Δελτίο της Ελληνικής Γεωλογικής Εταιρίας
Bulletin of the Geological Society of Greece

Τόμος XLVII, No3

Volume XLVII, No3

13° Διεθνές Συνέδριο της Ελληνικής Γεωλογικής Εταιρίας
Έρευνα και Εκμετάλλευση Ορυκτών Πόρων

13th International Congress of the Geological Society of Greece
September 5-8 2013, Chania, Crete, Greece

13th International Congress of the Geological Society of Greece
Exploration and Exploitation of Mineral Resources

Χανιά/Chania
2013

ΔΕΛΤΙΟ ΤΗΣ ΕΛΛΗΝΙΚΗΣ ΓΕΩΛΟΓΙΚΗΣ ΕΤΑΙΡΙΑΣ

Τόμος XLVII, No 3

BULLETIN OF THE GEOLOGICAL SOCIETY OF GREECE

Volume XLVII, No 3

13ο Διεθνές Συνέδριο της Ελληνικής Γεωλογικής Εταιρίας

Έρευνα και Εκμετάλλευση Ορυκτών Πόρων

13th International Congress of the Geological Society of Greece

Exploration and Exploitation of Mineral Resources

13th International Congress of the Geological Society of Greece
September 5-8 2013, Chania, Crete, Greece

ΕΠΙΜΕΛΕΙΑ ΕΚΔΟΣΗΣ

ΜΑΝΟΥΤΣΟΓΛΟΥ ΕΜΜΑΝΟΥΗΛ

ΠΥΛΙΩΤΗΣ ΙΩΑΝΝΗΣ

Πολυτεχνείο Κρήτης

EDITORS

MANOUTSOGLOU EMMANOUIL

PYLIOTIS IOANNIS

Technical University of Crete

Χανιά/Chania 2013

ΔΟΜΗ ΤΩΝ ΠΡΑΚΤΙΚΩΝ / SCHEME OF THE PROCEEDINGS

ΤΟΜΟΣ 1 / VOLUME 1

Opening Lectures/Εναρκτήριες Ομιλίες

Palaeontology, Stratigraphy and Sedimentology/Παλαιοντολογία, Στρωματογραφία και Ιζηματολογία

Geomorphology/Γεωμορφολογία

Petrology and Mineralogy/Πετρολογία και Ορυκτολογία

ΤΟΜΟΣ 2 / VOLUME 2

Tectonics and Geodynamics/Τεκτονική και Γεωδυναμική

Hydrology and Hydrogeology/Υδρολογία και Υδρογεωλογία

Geochemistry and Biogeochemistry/Γεωχημεία και Βιογεωχημεία

Environmental Geology/Περιβαλλοντική Γεωλογία

Geosciences in Education and Geosites/Γεωεπιστήμες στην Εκπαίδευση και Γεώτοποι

ΤΟΜΟΣ 3 / VOLUME 3

Geophysics and Seismology/Γεωφυσική και Σεισμολογία

Natural Hazards/Φυσικές Καταστροφές

Remote Sensing and GIS/Τηλεπισκόπηση και ΓΣΠ

Marine Geology/Θαλάσσια Γεωλογία

ΤΟΜΟΣ 4 / VOLUME 4

Ore Geology, Mining Technology and Economic Geology/Κοιτασματολογία, Μεταλλευτική Τεχνολογία και Οικονομική Γεωλογία

Engineering Geology and Geotechnical Engineering/Τεχνική Γεωλογία και Γεωτεχνική Μηχανική

Geothermics/Γεωθερμία

Exploration and Exploitation of Mineral Resources/Ερευνα και Εκμετάλλευση Ορυκτών Πόρων

Industrial Minerals and Rocks/Βιομηχανικά Ορυκτά και Πετρώματα

Energy Resources/Ενεργειακές Πρώτες Ύλες

ΠΕΡΙΕΧΟΜΕΝΑ/CONTENTS

ΤΟΜΟΣ 1 / VOLUME 1

Εναρκτήριες Ομιλίες
Opening Lectures

Παλαιοντολογία, Στρωματογραφία και Ιζηματολογία
Palaeontology, Stratigraphy and Sedimentology

Γεωμορφολογία

Geomorphology

Πετρολογία και Ορυκτολογία
Petrology and Mineralogy

ΤΟΜΟΣ 2 / VOLUME 2

Tectonics and Geodynamics/Τεκτονική και Γεωδυναμική

Hydrology and Hydrogeology/Υδρολογία και Υδρογεωλογία

Geochemistry and Biogeochemistry/Γεωχημεία και Βιογεωχημεία

Environmental Geology/Περιβαλλοντική Γεωλογία

Geosciences in Education and Geosites/Γεωεπιστήμες στην Εκπαίδευση και Γεώτοποι

Τεκτονική και Γεωδυναμική
Tectonics and Geodynamics

Υδρολογία και Υδρογεωλογία
Hydrology and Hydrogeology

Γεωχημεία και Βιογεωχημεία
Geochemistry and Biogeochemistry

Περιβαλλοντική Γεωλογία
Environmental Geology

Γεωεπιστήμες στην Εκπαίδευση και Γεώτοποι
Geosciences in Education and Geosites

ΤΟΜΟΣ 3 / VOLUME 3

Geophysics and Seismology/Γεωφυσική και Σεισμολογία

Natural Hazards/Φυσικές Καταστροφές

Remote Sensing and GIS/Τηλεπισκόπηση και ΓΣΠ

Marine Geology/Θαλάσσια Γεωλογία

Γεωφυσική και Σεισμολογία
Geophysics and Seismology

Φυσικές Καταστροφές
Natural Hazards

Τηλεπισκόπηση και ΓΣΠ
Remote Sensing and GIS

Θαλάσσια Γεωλογία
Marine Geology

ΤΟΜΟΣ 4 / VOLUME 4

Κοιτασματολογία, Μεταλλευτική Τεχνολογία και Οικονομική Γεωλογία
Ore Geology, Mining Technology and Economic Geology

Τεχνική Γεωλογία και Γεωτεχνική Μηχανική
Engineering Geology and Geotechnical Engineering

Γεωθερμία
Geothermics

Έρευνα και Εκμετάλλευση Ορυκτών Πόρων
Exploration and Exploitation of Mineral Resources

Βιομηχανικά Ορυκτά και Πετρώματα
Industrial Minerals and Rocks

Ενεργειακές Πρώτες Ύλες
Energy Resources

Δελτίο της Ελληνικής Γεωλογικής Εταιρίας, τομ. XLVII , 2013
Πρακτικά 13ου Διεθνούς Συνεδρίου, Χανιά, Σεπτ. 2013

Bulletin of the Geological Society of Greece, vol. XLVII 2013
Proceedings of the 13th International Congress, Chania, Sept. 2013

GEOELECTRIC PROSPECTING IN UNIVERSITY CAMPUS REGION FOR DETECTION OF POSSIBLE GEOLOGICAL DISCONTINUITIES, RIO, PATRA, GREECE

Angelis G.L.[1], Stephanopoulos P.[1], Papamarinopoulos St.P. [1]

[1] University of Patras, Department of Geology, Sector of Applied Geology & Geophysics, Laboratory of Geophysics 26 504 Campus, Rio Patras aggelisg@upatras.gr, stefanop@upatras.gr

Abstract

Geophysical prospecting is a non catastrophic technique, applicable on a wide range of problems, including archaeological, environmental and geological problems. At Campus University of Patras, a detailed geophysical investigation applied for detection of possible existing geological discontinuities, which produced serious problems at buildings and main roads of Campus. As main technique used the electric mapping and electric imaging. These were applied on already prepared geophysical grids by measuring parallel profiles along and perpendicular to the geomagnetic north. The two geophysical grids were separated 100 meters away each other. Firstly, an electric mapping procedure took place by using twin-probe array with four electrodes in distance between 0.5-3 meters. As result was the recording of soil resistance on horizontal layer with constant depth. By processing the data through Geosoft Oasis Montaj software, the distribution of this physical property was illustrated on color scale maps. Secondly, electric imaging technique applied with twenty-five equal space electrodes along straight lines, with one meter space by using the hybrid arrangement Wenner-Schlumberger (Stephanopoulos, 2002). As result was the recording of distribution of soil apparent resistivity on a vertical layer in eight separated depths. Resistivity calculated by processing imaging data through 2D mathematical algorithm based on least squares inversion (Res2Dinv). Further processing by Oasis Montaj, had as a result the production of horizontal slices (Stephanopoulos 2002) and 3D maps, where the resistivity distribution was illustrated on separated depths, in color and grey schedule format. The combined geophysical investigation with the contribution of the HVSR (Horizontal to Vertical Spectral Ratio) technique confirmed the existence of geological discontinuity.
Key words: *geoelectric imaging, geoelectric mapping, HVSR technique.*

Περίληψη

Η γεωφυσική διασκόπηση αποτελεί μια τεχνική διερεύνησης που χαρακτηρίζεται ως μη καταστροφική, με δυνατότητα εφαρμογής σε μεγάλη πλειονότητα προβλημάτων. Πραγματοποιήθηκε συνδυασμένη γεωφυσική έρευνα μέσω εφαρμογής ηλεκτρικής χαρτογράφησης, ηλεκτρικής τομογραφίας και καταγραφών εδαφικού θορύβου σε περιοχή της Πανεπιστημιούπολης. Σκοπός ήταν η λεπτομερής γεωφυσική διερεύνηση για τον εντοπισμό γεωλογικών ασυνεχειών στον ευρύτερο χώρο του Πανεπιστημίου. Οι προαναφερόμενες τεχνικές εφαρμόστηκαν στο πεδίο επί προκαθορισμένων γεωφυσικών δικτύων που απείχαν μεταξύ τους απόσταση 100 μ., με σάρωση επάλληλων διατομών παράλληλα και κάθετα στην διεύθυνση του γεωμαγνητικού βορρά. Ως πρώτη τεχνική

επιλέχτηκε η ηλεκτρική χαρτογράφηση με χρήση της δίδυμης διάταξης και άνοιγμα ηλεκτροδίων 0.5-3 μέτρων, που απέδωσε την κατανομή της ηλεκτρικής αντίστασης του εδάφους επί οριζόντιου επιπέδου σε γνωστό βάθος. Ως δεύτερη τεχνική εφαρμόστηκε η ηλεκτρική τομογραφία. Με χρήση 25 συνευθειακών ηλεκτροδίων σε απόσταση 1 μέτρου, μέσω της διάταξης Wenner-Schlumberger (Στεφανόπουλος 2002), επιτεύχθηκε η καταγραφή της κατανομής της φαινόμενης ειδικής αντίστασης επί κατακόρυφου επιπέδου σε 8 διαφορετικά βάθη. Μέσω του ειδικού λογισμικού Res2DINV, υπολογίστηκε η τιμή της ειδικής ηλεκτρικής αντίστασης, με δημιουργία μαθηματικού προτύπου δύο διαστάσεων βασιζόμενο στην επίλυση των ελάχιστων τετραγώνων. Με την βοήθεια του ειδικού λογισμικού Geosoft Oasis Montaj, πραγματοποιήθηκε η επεξεργασία των δεδομένων της ηλεκτρικής χαρτογράφησης και της ειδικής ηλεκτρικής αντίστασης. Ως αποτέλεσμα ήταν η παραγωγή έγχρωμων χαρτών όπου απεικόνιζαν την κατανομή της ηλεκτρικής αντίστασης, ενώ από την δεύτερη τεχνική παρήχθησαν οριζόντιες κατόψεις όπου απέδιδαν την ειδική αντίσταση σε ορισμένο βάθος καθώς και τρισδιάστατη απεικόνιση αυτής. Οι γεωφυσικές έρευνες με χρήση των καταγραφών εδαφικού θορύβου, χρησιμοποιήθηκαν επικουρικά για να ταυτοποιήσουν τα παραγόμενα αποτελέσματα των ηλεκτρικών μεθόδων γεωφυσικής διασκόπησης. Από την ερμηνεία των παραγόμενων έγχρωμων χαρτών έγινε σαφής ο εντοπισμός της υπάρχουσας γεωλογικής ασυνέχειας στην παραπάνω περιοχή και κατασκευάστηκε τρισδιάστατο μοντέλο απεικόνισης κατανομής της ειδικής ηλεκτρικής αντίστασης.
Λέξεις κλειδιά: *Ηλεκτρική χαρτογράφηση, ηλεκτρική τομογραφία,, εδαφικός θόρυβος.*

1. Introduction

Geophysical prospecting techniques were based on the study of physical fields (gravitational, magnetic, electrical, seismic, electromagnetic, acoustic). Such kind of Measurements are applicable on the surface of the earth, in the air and underground (wells and shafts). The recorded information can be used to determine the location of geological structures, ore bodies, and so forth and their fundamental characteristics (Papamarinopoulos et al., 2001). All geophysical techniques are based on the use of physicomathematical principles for the development of theory. Each of them focus on a target from a different perspective, emphasized on the differential measured quantity among potential target and the surrounding soil material. These techniques are characterized by non-destructive application, as a result, they can be applicable to areas with possible archaeological targets, aquifers and subsurface geotechnical problems (Stephanopoulos, 2002). This study deals with some of electrical prospecting techniques and the application of them for exploring possible geological discontinuities (Angelis, 2013). HVSR (Horizontal to Vertical Spectral Ratio) technique was used as an assistant method to determine the dynamic characteristics of geological formations (Lane et al., 2008). The contribution of HVSR was the identification of potential geologic discontinuities (faults) in the area of Patras University plus mapping of their characteristics. The survey was conducted to oriented geophysical grids for the application of electrical mapping and electrical imaging (Zorbas et al., 2012).

2. General Area Description

University of Patras is located between Rio and Patras town. Inside Campus there are main and assist roads and also the students union building. One of the main problem was the damaging in students union building, where a substitution episode took place. The building abandoned for a short period. Same circumstances found on the main road of Campus, where crack impacts were easily observed on surface main road, for a long distance. Laboratory of Geophysics decided to apply a detailed geophysical research for mapping the existing geological discontinuity. The investigated area was separated in two branches. One nearby the Administration Building of

Campus (Figure 2 left), second approximately 100 m away, in front the existing Campus Church (Figure 2 right). From previous geomorphology research in this area was known the existence of Rio – Patras Fault zone (Figure 1).

The Rion-Patras fault zone has a NE-SW general direction and extends along the rangefront that is found behind the large alluvial fans of the Rion-Patras coastal plain (Palyvos et al., 2007).

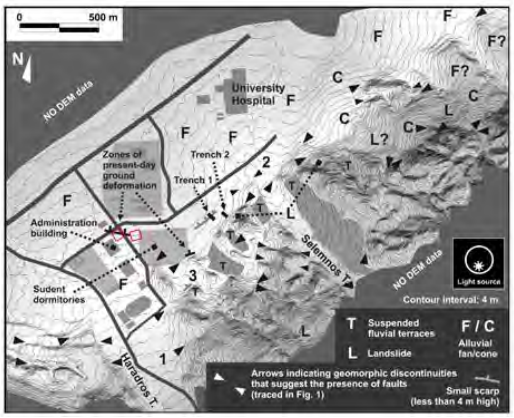

Figure 1 - Detailed morphology along part of the Rion-Patras fault zone at the longitude of the University of Patras Campus, larger geomorphic discontinuities indicative of faults are indicated by arrow heads (Palyvos┼ et al. 2007).

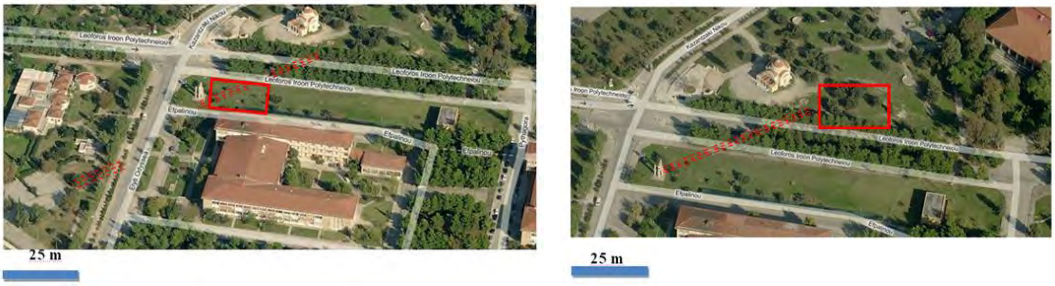

Figure 2 – Left: The boundary area of the Grass region (red square) located near Administrator building. Right: The boundary area of the Church region (red square) located between the Church and the student residence of Campus. Red lines represents the impact of geological discontinuity.

Figure 3 – Impact Crack on the main road of Campus.

3. Geology and Seismicity

The geology of wide area in University Campus, consisted by Quaternary deposits, Plio-pleistocene sedimentary rocks and unconsolidated soils. Inside are included, coastal sands, fluvial sands and gravels, Holocene deposits, weathering mantle of Plio-pleistocene sediments, as well as alluvial and diluvial deposits. In general, the total thickness of the Quaternary deposits exceeds 80 meters (Rozos et al., 2006).

The high seismicity of the area is closely related to the above mentioned fault tectonics and to existence of grabens with a recent geodynamic evolution. The dynamic loading on the various geological formations encountered in Patras area shallow and high magnitude earthquakes, apart from the direct results on the constructed environment, may also activate landslides, rockfalls, and liquefaction (Tselentis et al., 1994).

4. Methodology

Detailed geophysical prospecting applied on ground geophysical grids, located on two separated region, geoelectric mapping with twin-probe array through different electrode spacing, geoelectric imaging with twenty-five equal spaced electrodes through the hybrid Wenner-Schlumberger arrangement an as assistant HVSR technique. Processing of the measured data through specific software, had as result the creation of coloured maps where the distribution of measured physical property was illustrated.

5. Geophysical Field Prospecting

The geophysical procedure in the area of study, applied by three different techniques, geoelectric mapping, geoelectric imaging and HVSR technique.

Geoelectric mapping applied by using four electrodes with space 0.5-3 m distance through the twin-probe array arrangement. As a result was the recording of soil resistance on a constant depth equal to 3 times the electrode space. As main objective was the delimitation of region in high and low interest subareas, while other techniques focused on the scope of the survey, the mapping of geologic discontinuities. As main electrometer was chosen the Geoscan Rm4 and the Rateu system.

Beside the Administration building, was located the Grass area, where a geophysical grid with dimension 10 x 20 m researched. In the second area (Church area), researched a geophysical grid with dimension 15 x 15.

The measured physical property was given in colour schedule map format by processing the geoeletric mapping data through the Oasis Montaj software.

6. Geolectric Imaging

Geoelectric imaging recorded the distribution of resistivity on a vertical layer on eight different separated depths. On the ground surface, twenty-five equal spaced electrodes were located on a straight line, with constant space equal to 1 meter. As main electrometer was chosen the Campus geopulse signal which could produced external electric field in square pulse formation with intensity 0.5 to 100 mA. During the field procedure each measurement became by the combination of four electrode. Two external was used an current, while the two internal as potential. Between the two potential electrodes the apparent resistivity was measured by adopting the hybrid Wenner-Schlumberger arrangement (Stephanopoulos 2002). As result by this technique was the distribution of apparent resistivity on an inverse triangle, due to the geometric factor of the technique. On the maximum depth was located the corner of the triangle, while its base, near the ground surface. The central electrode was located on the middle distance of the profile (maximum depth), while the rest 24 electrodes were delimitation beside the central with equal space. By using

this tip, the discreet ability of the technique increased. The current intensity was in low level at shallow depths, while in deeper levels increased until 20 mA, while the number of cycles were extended from 2 to 3. The average of measurement was set equal to one and the field error had been set to 1%. In case of bad connections between electrode and surrounding soil, a little moisture of salty water was introduced in the base of electrodeby using a injection (Stephanopoulos 2002, 2009). By applying special software depth-slice (Stephanopoulos, 2002, 2009), horizontal slices were produced, while by further processing through Oasis Montaj software, the distribution of resistivity in horizontal plan view and in 3D format obtained.

In Grass area, which located beside the administration Campus building, 19 parallel profiles were researched, while in second area (Church area), 16 parallel profiles. In second area the geoelectric imaging technique applied along and perpendicular to geomagnetic north axis.

7. HVSR Technique

In 1989 Nakamura suggested estimating the amplification factor from the ratio of amplitude spectra of the horizontal to vertical components of ground acceleration recorded on the surface. The relation between this ratio and the frequency is called the HVSR curve and has a peak with in dominating frequencies of the recording. The peak amplitude is the amplification factor estimate, and its frequency is the principal frequency of surface layer. Furthermore, Nakamura ascertained that such a characteristic peak of the HVSR curve is strictly related to local geology, being independent of source parameters and signal frequency (Nakamura, 2000). He also indicated that the HVSR method would give the most accurate results when the spectral ratio were evaluated from the horizontal and vertical component of S wave (Nakamura et al., 2002).

8. Geophysical Inversion

Geophysical inversion was separated in two parts. Firstly was focused on processing the data from geoelectric mapping through the world standard software Oasis Montaj. As result was the creation of colour schedule maps where the distribution of soil resistance illustrated in Ohms. During the processing applied correction in case of base moving, while the data were extremely searched for instantly existing bad datum points.

Secondly the data from geoelctric imaging were processed by using three different software. During the measuring procedure in field, inside the data had been introduced the geometric factor of the applied electrode arrangement. The elimination of this was successful during the transformation of the data in format for Res2dinv software (Stephanopoulos, 2002). By using 2D special mathematical algorithm based on least square inversion, the calculation of resistivity in Ohms·m was real. The depth of first level was set equal to 0.5 times the electrode spacing, while the sequence deeper depths were increased by a value of 10%. The ratio of vertical to vertical filter was set equal to one and the damping factor was limited between 0.001 to 0.16, while the ability of recalculation was enabled. The radius search was set to be applied if the rms error was not decreased about 5%. Maximum number of iteration was chosen equal to 5 and the starting model was set to be scheduled by using the apparent resistivity values.

Horizontal slices from geoelectric imaging data, were produced by adopting special depth-slice software (Stefanopoulos, 2002), which had the ability to reformat the processed data in Oasis Montaj format. Horizontal slices illustrated the distribution of resistivity on constant depth, while there was the ability to be compared with results from geoelectrical mapping. Statistical analysis by using the mean value each profile, applied before the main process before 3D procedure. By adopting 3D subroutine of Oasis Montaj software, a 3D presence of resistivity values obtained.

9. Geophysical results

The result of geoelectric mapping in Grass area is illustrated in Figure 4.

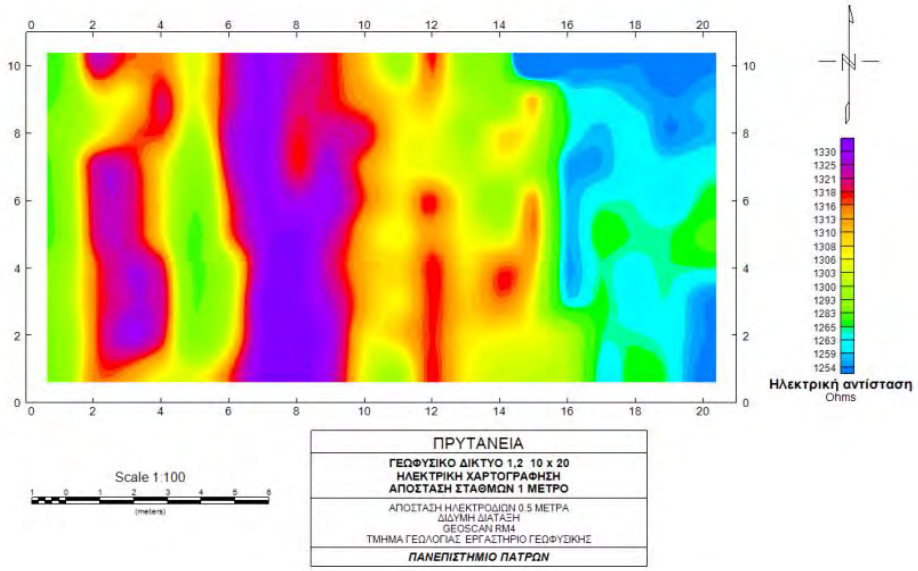

Figure 4 - Distribution of electrical resistance in Grass area by applying the Twin Probe Array (N-S).

At the west corner of the map in figure 4 there are high values of soil resistance, while in the opposite side these seemed to be decreased. The illustrated geophysical anomalies does not have any geometrical formation, while between 4 and 5 is obvious a discontinuity of geological material.

The application of geoelectric imaging illustrated in Figure 5.

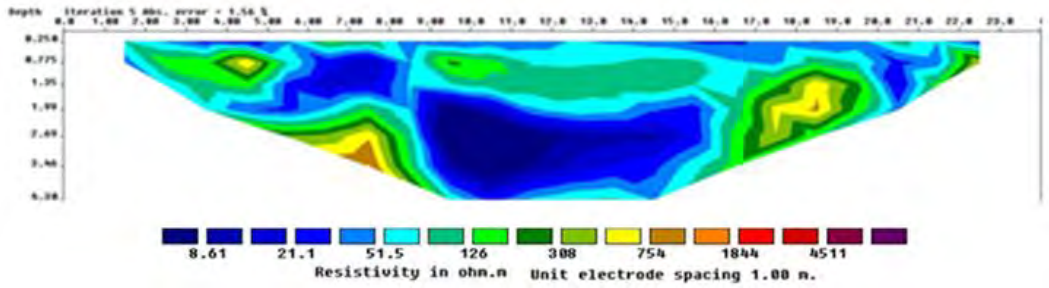

Figure 5 - Vertical electrical section of geoelectric imaging.

As it is obvious from Figure 5 the depth of investigation limits at 4.3 meters. In this section the resisitivity varies from 0.6 - 754 Ohms·m. Low values of that physical property seemed to be visible mostly on the center of the profile, while highest values are located peripheral of that. Between electrode 8 & 9, the transformation of the geological material is obvious by the discontinuity. By applying the depth-slice software, in collaboration with the Oasis Montaj software, the horizontal slices illustrated in Figure 6.

Figure 6 presents the distribution of resistivity in horizontal slice at approximately 1 meter depth. High resistivity values located almost on all over the illustrated map. In some cases these are given a geometric schedule, but not so clearly. On the East side of the map the geologic material have been shifted for a distance equal to 1 m at least, while the high resistivity values have been substituted by lower. In the centre of the map between 16 -18, there is a certificated separation of this geological material along the N-S axis.

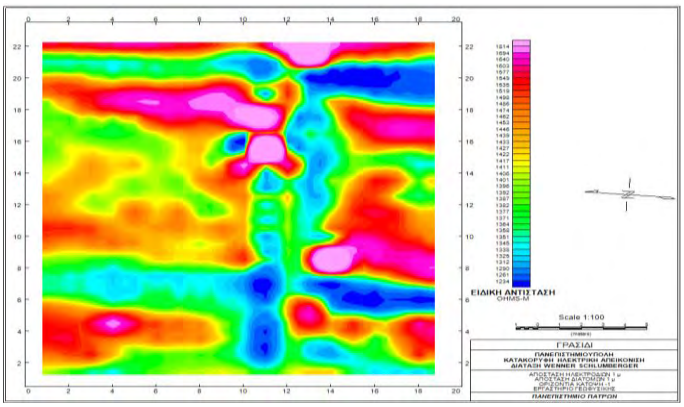

Figure 6 - Distribution of electrical resistance meter in 1 m depth on Grass area using the hybrid arrangement Wenner-Schlumberger with 1 m distance between electrodes (E-W).

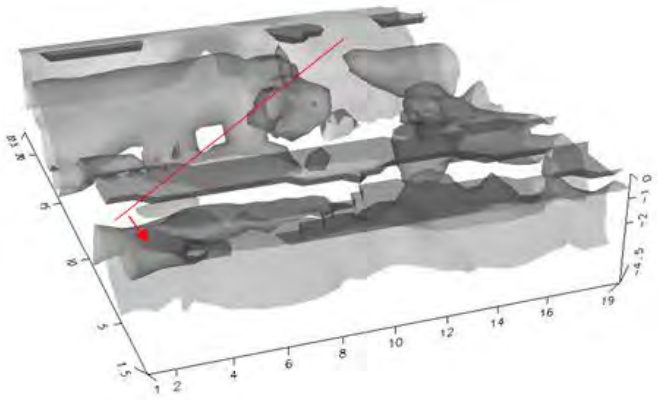

Figure 7 - 3D distribution of resistivity in 1480 Ohms·m in Grass area.

Figure 7 is given the 3D distribution of resistivity in Grass area. The red arrow means the existence of metallic pipes which are using for grass watering. The red line indicates the impact of the geological discontinuity in that area (Mourelatos et al., 2012).

In Figure 8 is given the result by using the geoelectric mapping in Church area. At the left, mapping has been applied parallel to geomagnetic axis, while at the right, perpendicular to that.

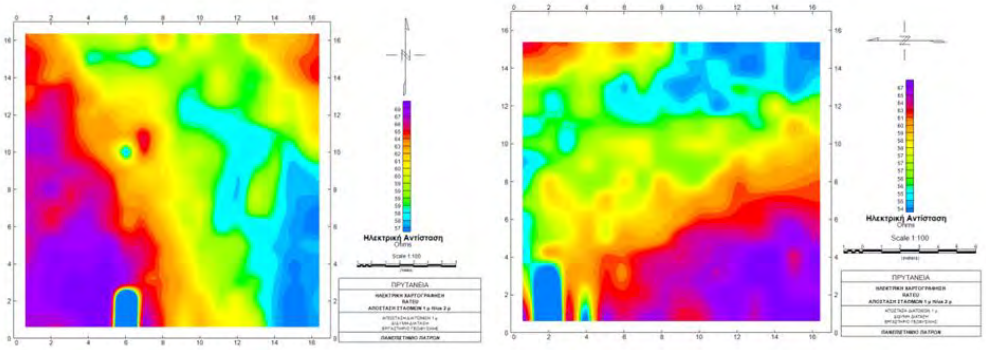

Figure 8 - Distribution of electrical resistance in Church area by applying the Twin Probe Array (N-S, E-W).

In this region the geoelectric mapping applied with electrodes at 2 m distance, through twin-probe array. Both of processing gave the same result. High values of soil resistance at the top and bottom of the map, with non well geometric formation. In the middle of each map, the high resistance values separated by the existence of lower level values, while the first formation is shifted at least 1 m away.

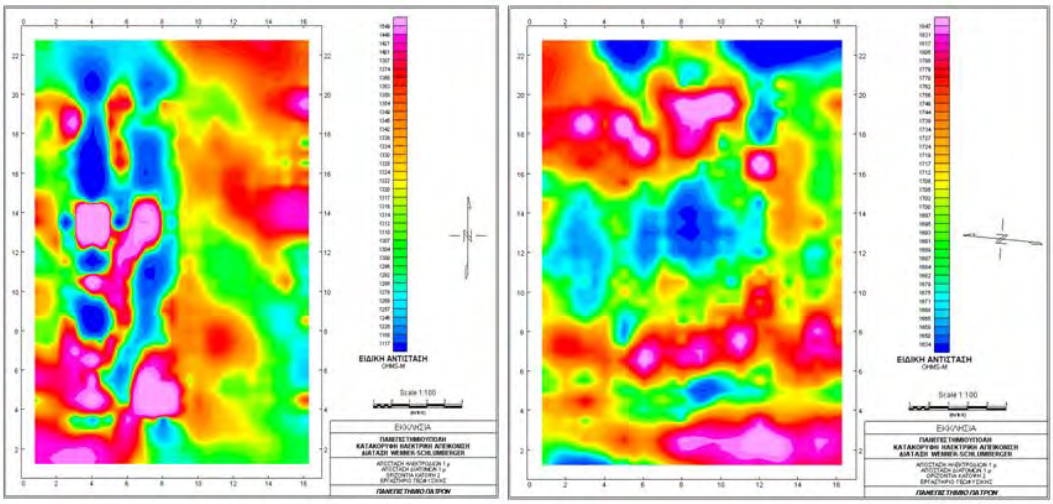

Figure 9 - Distribution of electrical resistance meter in 2 m depth on Church area using the hybrid arrangement Wenner-Schlumberger with 1 m distance between electrodes (N-S,E-W).

High values of resistivity occur almost all over in both maps, while non-well geometric formation appears. In some cases and especially in the centre and towards to the top of map a shift of geologic formations is obvious. From Figure 9 certificated that the continually of material are separated by existence of lower resistivity values.

By processing the above data set in 3D the result in Figure 10 produced, where the impact of possible geological discontinuity is emphasized by the red line (Mourelatos et al., 2012).

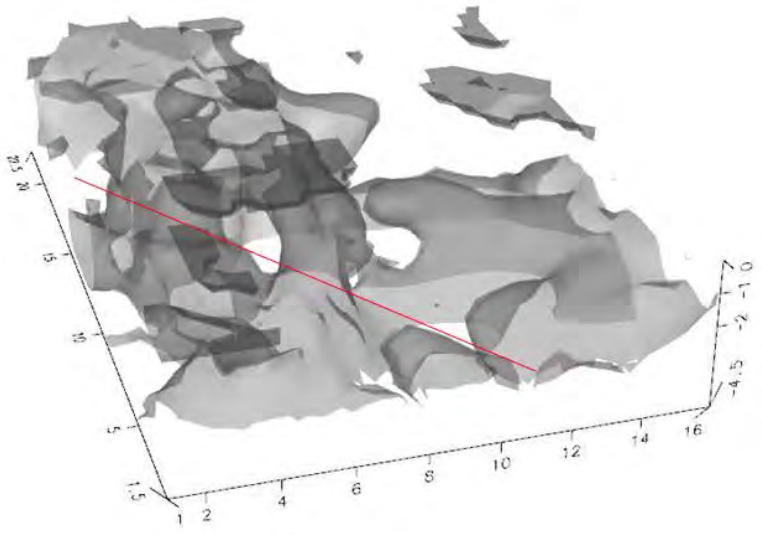

Figure 10 - 3D resistivity distribution in 1300 Ohms·m in Church area.

10. Conclusion

Detailed geophysical research in Campus of University of Patras, gave the chance for the well mapping of an existing impact of geological discontinuity. Geoelectric mapping with twin-probe array recorded the distribution of soil resistance and separated the researched region in subareas with low and high interest. Geoelectric imaging technique focused on high interest area location. By chosen the appropriate electrode space, in collaboration with suitable electrode arrangement, increased the resolution of that technique. Electric mapping gave well description of general geological statement, while imaging gave the expecting result where the existing fault was mapped. Further processing with 3D gave the chance to the observer to see details which were not seemed directly, while the underground pipe and geological discontinuity were well recorded. Also the existence of the above geological evidence was found by geomorphological prospecting which was applied by Palyvos┼ et. al. 2007. At this point the geomorphological research is certificated by geophysical investigation. The HVSR technique, found that the geological discontinuity is extended until 50 meters depth. That depth couldn't be reached by geoelectric imaging due to the existence of physical and artificial obstacles, limited the electrode spacing.

11. Acknowledgements

This work is a part of the Msc Thesis "Detailed Geophysical Prospecting for the investigation of possible geological discontinuities in University Campus area of Patras, Greece".

We are grateful to the Rector and the staff of the Technical Service of the University of Patras, for giving permission to investigate in the University Campus. We warmly thank Dr. P. Paraskevopoulos for valuable ideas and discussion in the field about HVSR technique, also we would like to thank Dr. K. Nikolakopoulos, Associate Professor in Department of Geology, University of Patras for his help in the construction of 3D mapping. We also thank undergraduate students for their help in the field (P. Zorbas, E. Metaksa, M.-E. Norda, Ch. Gakou, A. Oikonomou, K. Stratopoulos, D. Tsakiris, P. Chatzileontiadis, S. Mourelatos, L. Smailis) and Mrs E. Kouzeli, Msc student.

12. References

Angelis G.L. 2013. Detailed Geophysical Prospecting for the investigation of possible geological discontinuities in University Campus area of Patras, *Msc Thesis,* Greece.

Lane J.W.Jr., White E.A., Steele G.V. and Cannia J.C. 2008. Estimation of bedrock depth using the horizontal-to-vertical (H/V) ambient-noise seismic method, in Symposium on the Application of Geophysics to Engineering and Environmental Problems, April 6-10, 2008, Philadelphia, Pennsylvania, *Proceedings: Denver, Colorado, Environmental and Engineering Geophysical Society*, 13.

Mourelatos S. and Smailis L. 2012. Processing of Geoelectric imaging data through 3D algorithms for the detection of existing geological discontinuation in region of University Campus, *Bachelor Thesis*, Lab of Geophysics, Department of Geology, Sector of Applied Geology and Geophysics, University of Patras.

Nakamura Y. 2000. Clear identification of fundamental idea of Nakamura's method for dynamic characteristics estimation of subsurface using microtremor on the ground surface, *Proceedings of 12th World Conference on Earthquake Engineering,* New Zealand.

Nakamura Y., Sato T. and Nishinaga M. 2002. Local site effect of Kobe based on microtremor measurement.

Palyvos N., Pantosti D., Stamatopoulos L. and De Martini P.M. 2007. Geomorphological reconnaissance of the psathopyrgos and Rion-Patras fault zones (Achaia, NW Peloponnesus), *Bulletin of the Geological Society of Greece* vol. XXXX.

Papamarinopoulos St. and Stephanopoulos P. 2001. Laboratory notes for the course Introduction to Applied Geophysics, University of Patras, Greece.

Rozos D., Koukis G. and Sabatakakis N. 2006. Large-scale engineering geological map of the Patras city wider area, Greece, *IAEG paper number 241*.

Stephanopoulos P. 2002. The contribution of Geophysics with geoelectric imaging in solution of Archaeological and Environmental problems, *PhD Thesis,* University of Patras, Department of Geology, Sector of Applied Geology & Geophysics.

Stephanopoulos P. 2009. Geophysical hardware and software notes, Vol. I, II, University of Patras, Greece.

Tselentis G. Melis N. and Sokos E. 1994. The Patras (July 14, 1993; Ms=5.4) earthquake sequence, *Proc. Of the 7th Congress of the Geol. Society of Greece*.

Zorbas P., Metaxa Ev., Norda M., Economou A., Stratopoulos K., Tsakiris D. and Chatzileodiadis P. 2012. Detailed Geophysical Research in Region of University Campus for detection of existing geological discontinuation. *Bachelor Thesis,* Lab of Geophysics, Department of Geology, Sector of Applied Geology and Geophysics University of Patras.

Δελτίο της Ελληνικής Γεωλογικής Εταιρίας, τομ. XLVII , 2013
Πρακτικά 13ου Διεθνούς Συνεδρίου, Χανιά, Σεπτ. 2013

Bulletin of the Geological Society of Greece, vol. XLVII 2013
Proceedings of the 13th International Congress, Chania, Sept. 2013

GEOPHYSICAL INVESTIGATION AND ITS GEOLOGICAL INTERPRETATION IN THE FRAME OF AN INTERGRATED SURVEY PRIOR TO A DAM CONSTRUCTION IN PLATI RIVER VALLEY, RETHYMNO, GREECE

Apostolopoulos G.[1], Pavlaki C.[2], Perleros V.[3] and Amolochitis G.[4]

[1] *School of Mining and Metallurgical Engineering, Applied Geophysics Laboratory, National Technical University of Athens, 9 Iroon Polytechniou Str., 15780 Zografou, Greece, gapo@metal.ntua.gr*

[2] *Consultant for Geological Surveys, 56 Tzanakaki Str., 73134 Chania, Greece,catrpaul@otenet.gr*

[3] *Consultant for Geological Surveys, 56 Dionysou Str., 15234 Chalandri, Greece,perlerosv@gmail.com*

[4]*School of Mining and Metallurgical Engineering, Applied Geophysics Laboratory, National Technical University of Athens, 9 Iroon Polytechniou Str., 15780 Zografou, Greece, amoloh@metal.ntua.gr*

Abstract

A geophysical survey using electrical resistivity tomography (ERT) method(25 ERT profiles of 240m total length and 2 ERT profiles of 1000m total length) in the area of Plati River valley gave valuable information regarding the stratigraphy, related to loose sediments, various faces of flysch and limestone, the tectonic status and the detection of areas of thick and extensive sheared siltstone, that geoelectrically is similar to clay,material useful for the core of the future dam. Both branches of river and valley and in greater detail the area near the position of the dam have detected showing the underground in a 2D and 3D manner. The thickness of neogene and flysch exceeds 40m. Alternations of siltstones-sandstones are met in flysch and in places cohesive sandstones are also met without continuation in an extended area. The siltstonelayers due to their shear character present clayey characteristics in respect of their resistivities. In general zones of limestone uplift have not been detected, which may create problems of leakages apart of the dam area where lateral inhomogeneity between flysch and limestone has been detected (probable fault). The various limestone bodies met in flysch or neogene do not have continuation in depth and they are isolated.

Key words:*Resistivity, Tomography, Schlumberger Array, Pole-Dipole Array.*

Περίληψη

Γεωφυσική έρευνα χρησιμοποιώντας την μέθοδο της γεωηλεκτρικής τομογραφίας (25 τομές μήκους 240μ και 2 τομές μήκους 1000μ) στην περιοχή της κοιλάδας του Ποταμού Πλατύ στον Νομό Ρεθύμνου έδωσε χρήσιμη πληροφορία σχετικά με την στρωματογραφία (χαλαρά ιζήματα, φάσεις του φλύσχη, ασβεστόλιθος), την τεκτονική και τον εντοπισμό περιοχών μεγάλου πάχους και έκτασης διατμημένων ιλυολίθων που προσομοιάζουν γεωηλεκτρικά με στρώματα αργίλων και θα μπορούσαν να

χρησιμοποιηθούν για τις ανάγκες του πυρήνα του φράγματος. Οι δύο κλάδοι του ποταμού και της κοιλάδας και με μεγάλη ακρίβεια η περιοχή που σχεδιάζεται να κατασκευαστεί το φράγμα έχουν ερευνηθεί με το υπέδαφος να αποτυπώνεται στις δύο και τρεις διαστάσεις. Το πάχος των νεογενών και του φλύσχη ξεπερνά τα 40μ. Εναλλαγές ιλυολίθων ψαμμιτών συναντώνται στον φλύσχη και σε περιοχές υπάρχουν συνεκτικοί ψαμμίτες που δεν παρουσιάζουν συνέχεια στην ευρύτερη περιοχή.Τα ιλυολιθικά στρώματα λόγω διάτμησης παρουσιάζουν χαρακτηριστικά αργιλικών υλικών ως προς τις ειδικές αντιστάσεις.Δεν εντοπίστηκαν στις ζώνες των διασκοπήσεων αναθολώσεις του ανθρακικού υποβάθρου που θα μπορούσαν να δημιουργήσουν προβλήματα διαφυγών. Στην περιοχή του υπό μελέτη φράγματος εντοπίστηκε παράπλευρη ανομοιογένεια μεταξύ φλύσχη και ασβεστόλιθου (πιθανό ρήγμα).Οι διάσπαρτοι ασβεστολιθικοί όγκοι που συναντώνται εντός του φλύσχη και των νεογενών δεν παρουσιάζουν σε βάθος συνέχεια και είναι απομονωμένοι.
Λέξεις κλειδιά:*Γεωηλεκτρική Τομογραφία, Μέθοδος Ειδικής Αντίστασης, Διάταξη Schlumberger, Διάταξη Πόλου-Διπόλου.*

1. Introduction

The quality of an integrated geological-geotechnical survey is one of the critical aspects for the "health" and durability of big construction projects as they are the dam and artificial lake construction. A useful tool for the better understanding of the subsurface along with the necessary drillings is the appropriate geophysical investigation. Appropriate since the expected geological formations will judge which geophysical methods can distinguish interfaces, local features, possible tectonic structure. The use of geophysical investigation proved important prior or after dam construction in Greece,Louis et al. (1992), Apostolopoulos et al. (1999), Karastathis et al. (2002) or elsewhere Sjödahl et al. (2006), Hunterand Powers (2008).

Main objectives of a geophysical survey in these applications are the detection of the stratigraphy, the tectonic status and the detection of places for large amounts of fine grain clay material useful for the dam construction. The design of this geophysical survey is such to see these objectives a) with scattered profiles in the whole valley covered by water and nearby region in order to predict phenomena after water coverage and b) with dense coverage of profiles in the area of the dam to give information to construction issues and possible leakage phenomena.

Finally the design of the geophysical survey is the result of the collaboration between geologists and geophysicists who consider all aspects both the demands of the project and qualitative geophysical data. Some displacements occur during the field work due to local obstacles (fences, human activities, etc.)

2. Geology of the Area

The geological structure of the Platy River region bears characteristics of compressional tectonics with old over-thrusting structures related to plate convergence followed by extensional tectonics with the development of normal faults developed during the southern migration of the subduction zone.

The study area comprises of geological formations of the Pindos and Arvis geotectonic units that correspond to the upper tectonic nappes of Crete. These formations include (Figure 1):

- Flysch transition beds of siltstone, calcareous sandstone and clay and the upper Pindos Flysch. The upper Pindos Flysch predominates in the foundation zone and catchment basin of the Platis dam and is composed mainly of sandstone and siltstone intercalations and occasional clay and low grade metamorphic formations. In the dam zone, intense tectonic deformation has resulted in fractured sandstone formations and faulted siltstone formations.

- Transition beds composed of intercalations of thin-bedded limestone, sandstones, siltstones and chert.
- Local outcrops of thin-bedded platy Pindos limestone with chert intercalations that develop below the dam zone, and outcrops in the form of an exhumed overthrust ridge that dip at high angles to the North along a normal fault trace. The thin-bedded limestones also outcrop in the catchment basin along the Lygiotis stream gorge.
- Local outcrops of unstratified residual limestone, thrusted over the flysch in the form of minor tectonic nappes, boulders or relics that developed during the overthrust process. Due to the variable mechanical properties of limestone they were separated and thrusted independently over the flysch. Limestone boulders of various dimensions were recorded on the left buttress overlying the elluvial layer of flysch, scattered in various locations in the catchment basin and its limits. These outcrops were studied by geophysical exploration.
- Neogene and Quaternary sediments, comprising conglomerates, marls, sandstones, clays, silts and sands.

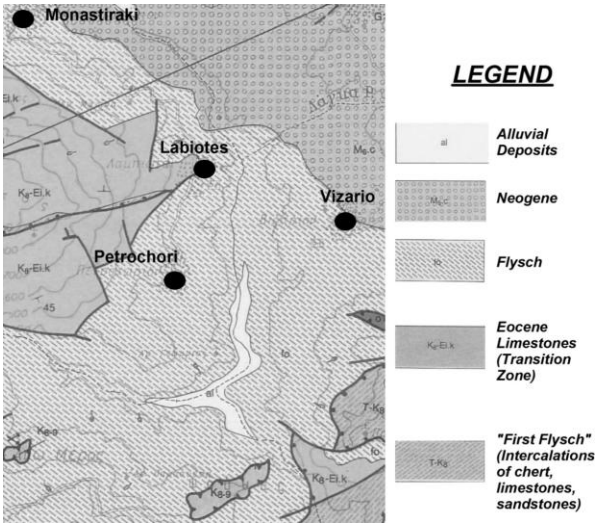

Figure 1 -Geological map of the survey area (part of IGME geol. map "Melambes", 1985).

3. Geophysical Survey

The best geophysical method in order to distinguish formations of different grain size in loose sediments, the various phases of flysch and interfaces with limestone is the resistivity method and in particular the Electrical Resistivity Tomography (ERT) technique to detect in great detail both stratigraphy and local features.

The geological formations of the area have different resistivities. Clay has 10-50Ohm.m (depending on the grain size, the moisture, the compaction), pebbles 200-500Ohm.m, flysch 80-170Ohm.m (depending on its phase), limestone 500-3000Ohm.m. In greater detail coloring and classification of various resistivities shown in resistivity sections is shown in Figure 2

Twenty-five (25) ERT profiles of 240m total length and 5m electrode spacing are scattered in the two branches of the valley and densely positioned in the area of the dam (labeled with R* in Figure 2). These profiles will give the stratigraphy and local features in great detail. Two (2) ERT profiles of 1000m total length and 50m electrode spacing are positioned along the big (N-S) branch of the valley to detect deeper geological formations (labeled R100* in Figure 2).Schlumbereger electrode configuration was selected since accuracy in stratigraphy is the main target of the survey. One (1) ERT profile (Figure 2, "RPD") at the position of the dam with 355m

total length and 5m electrode spacing used Pole-Dipoleelectrode configuration in order to detect both lateral and horizontal discontinuities in great detail.

Accurate positioning and leveling of the profiles and their electrodes was made with Differential LeicaGPS1200. Resistivity measurements were acquired with two instruments ABEM SAS1000 and IRIS SYSCAL-PRO-72.

Analysis of the results as shown with resistivity sections of some indicative profiles (Figures 3, 4) as we go from north and west to the position of the dam in the south is following.

ERT section "R-23" (Figure 3) shows a fine grain clayey-sandy material of very low resistivities on the top overlying clay material (dashed line shows their interface) while to the south-east there is a body of sandstone. These are characteristically Neogene formations.

ERT section "R-18" (Figure 3) shows on its northwest part a highly resistive surface layer of coarse material (pebbles) which overlays on clay with some coarse material (intermediate resistivities) and all of them on clay that extends in the whole section. ERT section "R-16", been on the opposite west side of the valley in respect of "R-18", south of Petrochori village, shows a surface layer of intermediate resistivities consisting clay and gravels that overlays on a layer of a fine grained clayey-sandy material and this one overlays to clay. In the north-west part of this last clayey layer there is a body of higher resistivities possibly sandstone.

In the left branch of the valley both sections "R-2" and "R-4" (Figure 3) show a surface layer of high resistivities with pebbles which overlays a layer of fine grain clay material (clayey phase of flysch, low resistivities) and that overlays a "sandstone phase of flysch" (intermediate resistivities) and in "R-4" been underneath of it as well.

In the area of the future dam construction both ERT sections "R-6" and "R-7" (Figure 4) show a surface layer of high resistivities with pebbles which overlays flysch. In the layer of flysch there is a medium of higher resistivities which can be cohesive sandstone and where there are intermediate resistivities a loose sandstone phase of flyschmay exist. The lower resistivities correspond to the clayey phase of flysch. The ERT section "RPD" (Figure 4) with the pole-dipole electrode configuration with greater depth detection and sensitive to lateral inhomegeneities, shows the highly resistive surface layer of pebbles followed deeper by low resistivity clay layer. Deeper there is the highly resistive limestone whose top is outlined by a small dashed line. At distance of -250m there is a deep lateral interface separating flysch and limestone probably showing a fault. Surface manifestations indicate that as well.

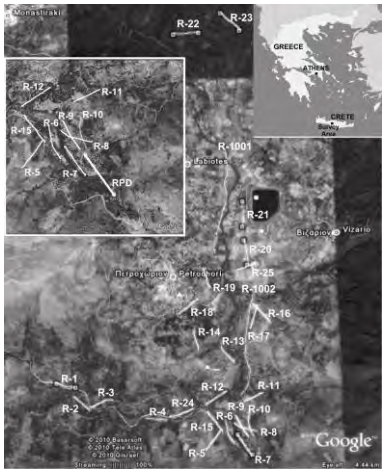

Figure 2 - ERT profiles on a Google map scattered in the two branches of Platis River valley near Petrochori village. In the small picture with greater detail more dense coverage of profiles in the area of future dam.

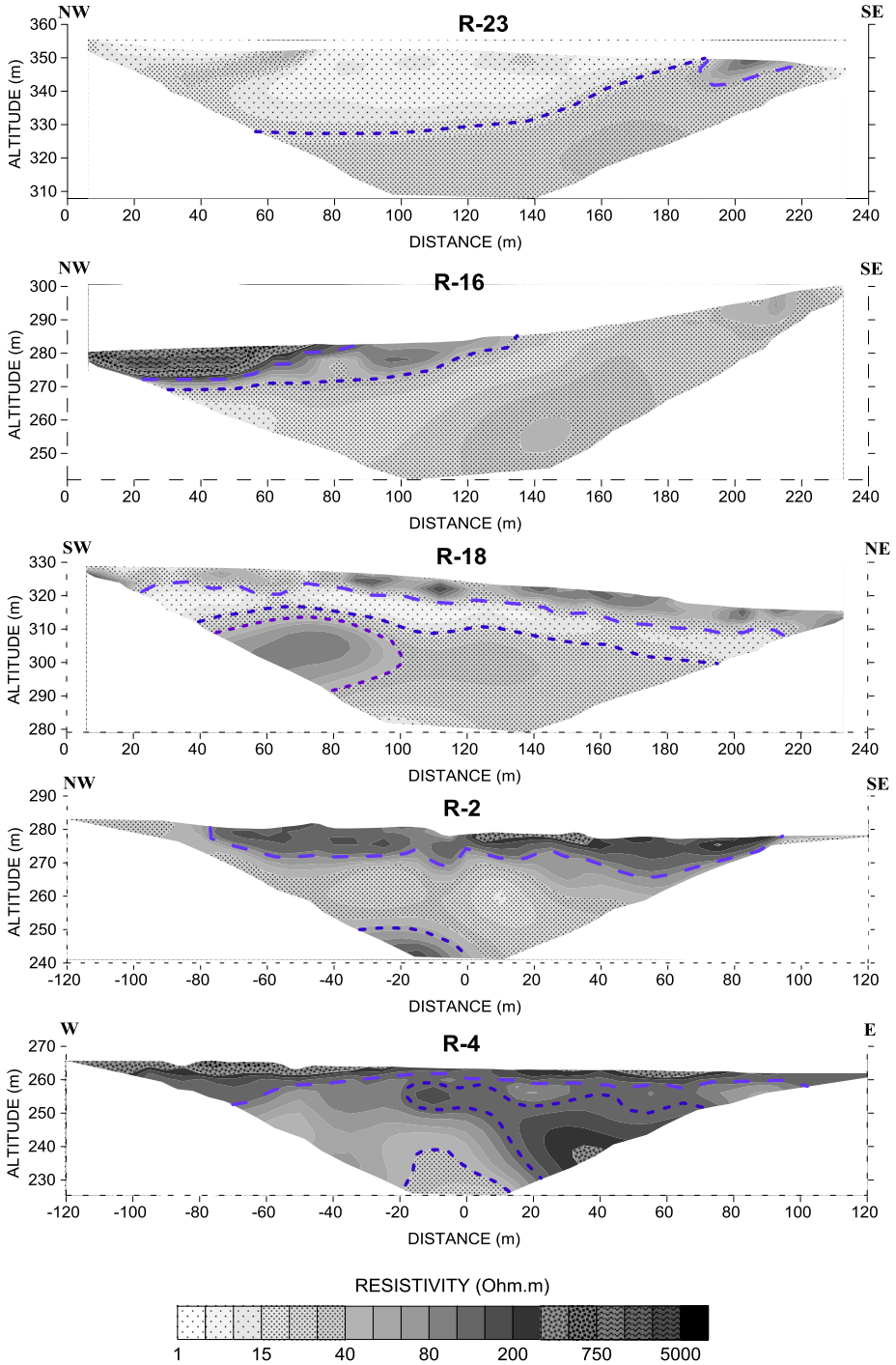

Figure 3 -ERT sections "R-23", "R-16", "R-18", "R-2" and "R-4". Resistivity distribution with depth is shown along with the main interfaces between main formations with dashed lines.

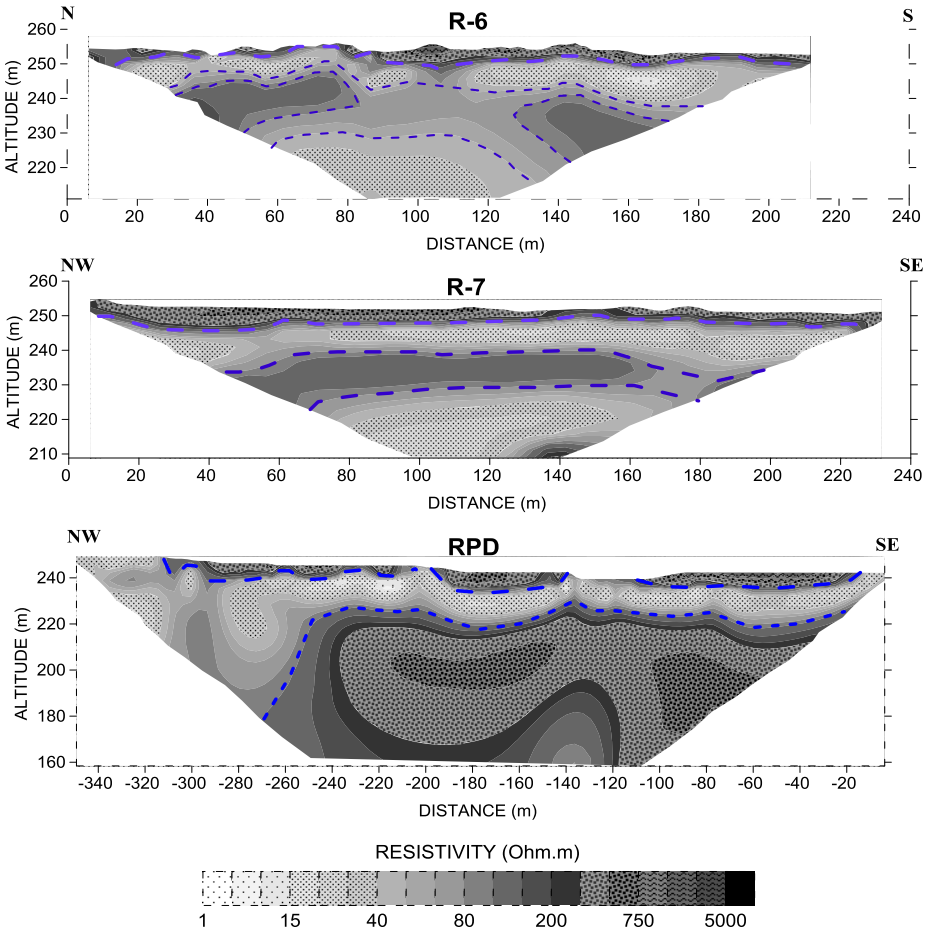

Figure 4 -ERT sections "R-6", "R-7" and "RPD". Resistivity distribution with depth is shown along with the main interfaces between main formations with dashed lines.

Long ERT sections of 800m length and greater depth of detection (80-100m), "R-1001" and "R-1002" (Figure 5) made to see the general stratigraphy along the north-south branch of the valley. These two ERT long sections show that from the north part of the survey area to the region where the two branches of the river meet together there is a surface layer of coarse material and deeper fine grain clayey materials exist. These clayey materials show different resistivities (the presence of sand increases the resistivity value) and the very low resistivities of the deep layer in section "R-1001" represent Neogene formations while in its southern part as well as in the whole section "R1002" the deeper low to intermediate resistivities represent flysch formations.

All resistivity sections southwards from R-20 and eastwards from R-4, can lead to the following results:

- From the north part of the survey to the area where the two branches of the river meet together there is a surface layer of coarse material and deeper fine grain clayey materials exist.
- In the area of left west branch of the river and in the area of the dam construction the surface layer of coarse material overlays flysch of various phases, high resistive corresponding to the cohesive sandstone, intermediately resistive to the loose sandstone phase and conductive to the clayey phase.

– At the dam construction site, where "RPD" ERT profile is, there is a lateral interface between flysch and limestone probably related to a fault.

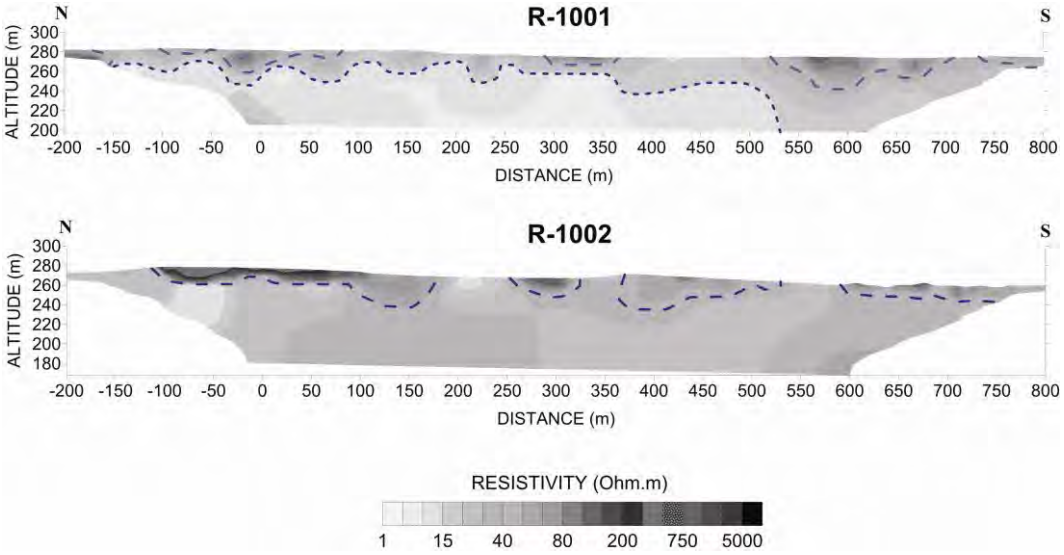

Figure 5 -Long ERT sections (800m length) with great depth of detection along the north-south branch of the valley. Resistivity distribution with depth is shown along with the main interfaces between main formations with dashed lines.

The previous observations can be seen in Figure 6 where horizontal distribution of resistivity is presented in various levels – altitudes. We see the low resistivities dominating the northern part (altitudes: 320m -290m) with fine grained clayey material, an accumulation of high resistivities at altitude 300m related to coarse material (gravels, river activity), the presence of flysch with higher resistivities in the south part at altitude 290m, the presence of cohesive sandstone phase at altitudes 280m -270m and deeper the clayey phase of flysch be dominant.

4. Conclusions

The objective of the geophysical survey was to detect the underground in the zone of the dam foundation and in the catchment area in respect of layer thickness of flysch and neogene and the probable uplift of the bedrock (limestone). It was also detected the continuation in depth of various limestone bodies which are in Flysch or above neogene.

The design and parameters of the geophysical survey by the application of electrical resistivity tomography have followed the demands of the project as well rules for their best quality.

The geophysical survey has shown that in the whole catchment area the thickness of neogene and flysch exceeds 40m. Alternations of siltstones-sandstones are met in flysch and in places cohesive sandstones are also met without continuation in an extended area. The mudstone layers due to their shear character present clayey characteristics in respect of their resistivities. In general zones of limestone uplift have not been detected, which may create problems of leakages apart of the dam area where lateral inhomogeneity between flysch and limestone has been detected (probable fault). The various limestone bodies met in flysch or neogene do not have continuation in depth and they are isolated.

Boreholes after the geophysical survey were positioned in the best manner to interpret in geological-geotechnical aspect the conclusions of the geophysical results.

The two subsequent borehole projects confirmed the geophysical results (Pavlaki and Perleros, 2012).

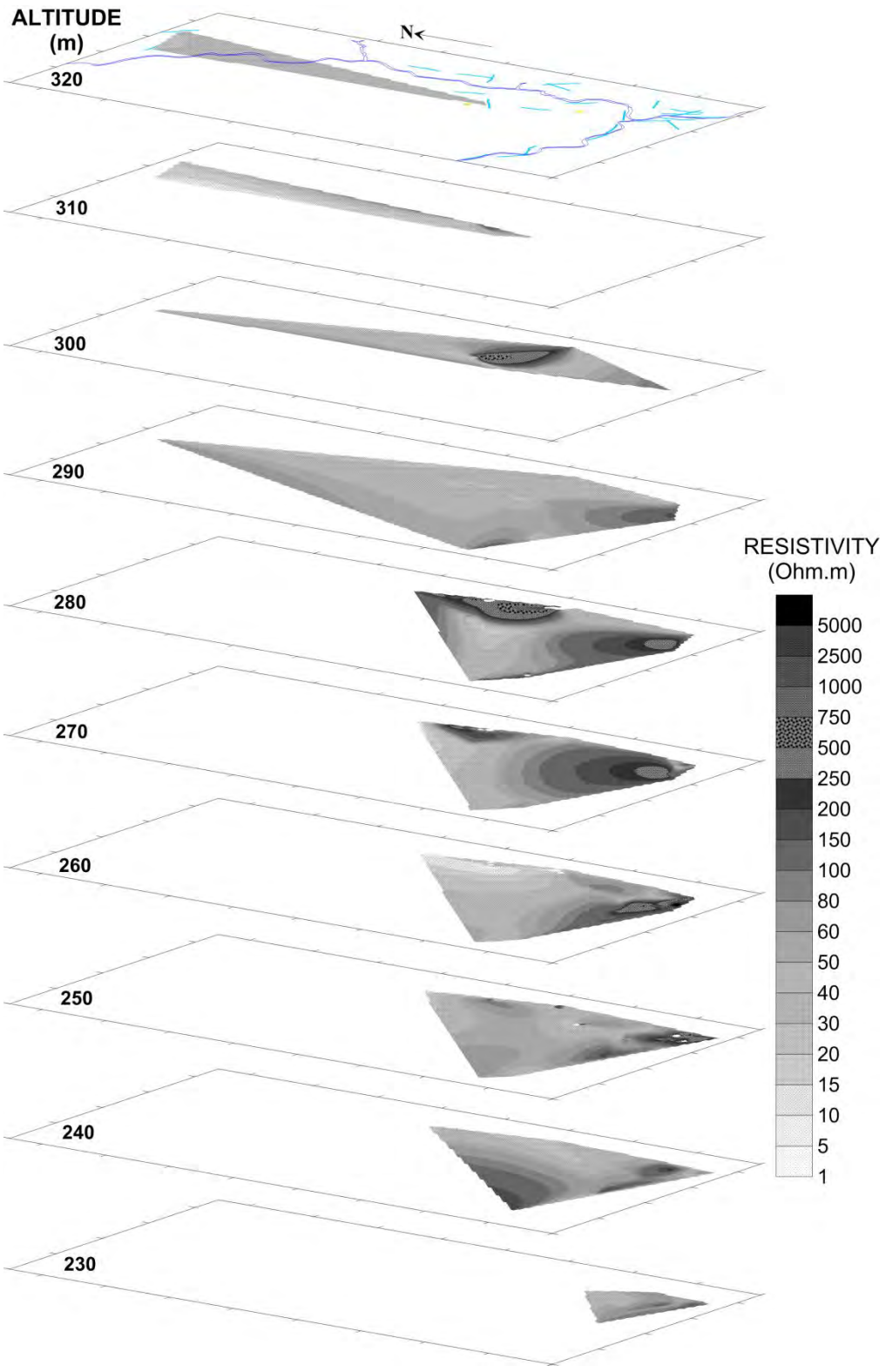

Figure 6 -Horizontal resistivity distribution in various altitudes in the survey area.

5. Acknowledgments

The authors wish to thank for their valuable help during the data acquisition as well as processing the mining engineers – geophysicists Dr. C. Orfanos, Dr. K.Leontarakis, C.Polychronopoulou (M.Sc.) and Dr. G.Fragogiannis.

6. References

Apostolopoulos G., Antoniades K. and Pavlopoulos K. 1999. The electrical resistivity method – a useful tool in evaluating geological and geotechnical conditions for construction and engineering projects, *Proceedings of 2nd Conference of the Balkan Geophysical Society (BGS)*, Istanbul, Turkey.

Hunter L. and Powers M. 2008. Geophysical Investigations of Earthen Dams. An Overview, *Symposium on the Application of Geophysics to Engineering and Environmental Problems,* 1083-1096.

Karastathis V.K., Karmis P.N., Drakatos G. and Stavrakakis G. 2002. Geophysical methods contributing to the testing of concrete dams. Application at the Marathon Dam, *Journal of Applied Geophysics* 50, 247– 260.

Louis J.J., Papadopoulos T., Pantzartzis P. and Apostolopoulos G. 1992. Geophysical engineering conditions at Ilarion damsite, *Annales Geologiques des Pays Helleniques* 35, 147-163.

Pavlaki C. and Perleros V. 2012. Reconnaissance and final geological study of the area zone of Platy dam. Preliminary and final study of Platy dam in Rethymno County and final study of water pipe to Messara.*HMRDF Report*.

Sjödahl P., Dahlin T. and Zhou B. 2006. 2.5D resistivity modeling of embankment dams to assessinfluence from geometry and material properties, *Geophysics*71, no. 3, G107–G114.

Δελτίο της Ελληνικής Γεωλογικής Εταιρίας, τομ. XLVII , 2013
Πρακτικά 13ου Διεθνούς Συνεδρίου, Χανιά, Σεπτ. 2013

Bulletin of the Geological Society of Greece, vol. XLVII 2013
Proceedings of the 13th International Congress, Chania, Sept. 2013

QUALITATIVE PRECURSORY PATTERN BEFORE SEVERAL STRONG EARTHQUAKES IN GREECE

Baskoutas I.[1] and Papadopoulos G.[2]

[1]*Institute of Geodynamics, National Observatory of Athens, Greece. Email: i.baskoo@noa.gr*

[2] *EPPO, Seismotect. Div., Xanthou32, 15451 Athen, Greeces.Email: gpapadopoulos@oasp.gr*

Abstract

The temporal variation of the seismicity, based on the analysis of three seismic parameters i.e., number of earthquakes, b-value and energy released, were investigated before several strong earthquakes occurrence in Greece the time period 2000-2008. The seismic parameters estimates were obtained by the means of new tool, suited to analyze earthquake catalogue, and visualize their spatio-temporal variation behaviour. The seismic data used were taken from the earthquake catalogue of the Geodynamic Institute of National Observatory of Athens, Greece. The obtained temporal variation series shows significant changes around their relative mean values, which specific phases can be related to the strong earthquakes preparation stages. This relation shows remarkable temporal regularity so that it can be establish considered as a precursor seismicity pattern. These results suggest that identification of this behaviour, by the continuous monitoring of the temporal variation of the seismic parameters, can contribute to the assessment of the current seismic hazard and to the impending strong earthquake parameters evaluation, in a given area.

Περίληψη

Μελετήθηκε η χρονική μεταβολή τριών σεισμικών παραμέτρων, δηλαδή, του αριθμού των σεισμών N, της παραμέτρου b-value και της εκλυόμενης σεισμικής ενέργειας, πριν από την εκδήλωση ισχυρών σεισμών στην Ελλάδα, για το χρονικό διάστημα 2000-2008. Η ανάλυση έγινε με τη χρήση δεδομένων του καταλόγου σεισμών του Γεωδυναμικού Ινστιτούτου του Εθνικού Αστεροσκοπείου Αθηνών. Συγκεκριμένες φάσεις της χρονικής διακύμανσης των σεισμικών παραμέτρων, γύρω από σχετικές μέσες τιμές τους, σε δεδομένο χρονικό διάστημα, μπορούν να συσχετιστούν με τις φάσεις προετοιμασίας και εκδήλωσης ενός ισχυρού σεισμού. Η επαναλαμβανόμενη κανονικότητα της αυτής της συσχέτισης μπορεί να θεωρηθεί ως ποιοτικό μοτίβο (pattern) πρόδρομης συμπεριφοράς. Η συνεχής παρακολούθηση της μεταβολής της σεισμικότητας και η αναγνώριση των φάσεων του παραπάνω μοτίβου, μπορεί να συμβάλει στην αξιολόγηση του σεισμικού κινδύνου και της πρόγνωσης μιας επικείμενης ισχυρής σεισμικής δραστηριότητας, σε μια δεδομένη περιοχή.

Keywords: *Seismic energy released, b-value, temporal variation of seismicity, precursory seismicity pattern.*

1. Introduction

Precursory seismicity changes have attracted the attention of researchers over the years and several types of patterns preceding large earthquakes have been proposed worldwide, including preseismic activation, quiescence, clustering, earthquake migration and combinations of these. In the overwhelming majority, the study of these precursory patterns were based mainly on the statistical analysis or the spatiotemporal characteristics of the seismicity (Habermann, 1981; Kanamori H., 1981; Caputo et. al., 1983; Papadimitriou and Papazachos 1985; Matthews and Reasenberg, 1988; Eneva and Hamburger, 1989; Shaw, et al., 1992; Romanowicz, 1993; Kossobokov and Carlson, 1995; Press and Allen, 1995; Shebalin et al., 2000; Di Giovambatista and Tyupkin, 2000; Keilis-Borok, et al., 2002; Papadopoulos et al., 2002; Tiampo et al.; 2002; Papadopoulos et al., 2003; Zavyalov, 2003; Papazachos et al., 2004; Baskoutas et al., 2004; Matsumura, 2006; Sobiesiak, et al., 2007; Papadimitriou P., 2008).

Seismic precursors may reflect changes in rock properties connected with the earthquake preparatory process, but the results obtained in the identification of these precursors may differ, in size and shape, depending on differences in experimental method or regional characteristics and can be interpreted in different ways. Alternatively, such precursors may result from systematic spatio-temporal seismicity fluctuations in areas of spatially varying rock properties. In this direction, Papadopoulos and Baskoutas (2003; 2009; 2011) have introduced the FastBEE algorithm for the seismic hazard assessment, base on the hypothesis that temporal changes of the seismicity reflects the influence of the physical process. The analysis tool, in this algorithm, was designed to obtain temporal variation profiles of some basic seismicity parameters, by the elaboration of common earthquake catalogue data. The retrospective application of this algorithm (Baskoutas et al., 2004; Baskoutas et al., 2011; Papadopoulos and Baskoutas, 2011) has shown that the obtained temporal variation profiles, over a long time interval, present a clear precursory regularity, which can be related to strong earthquake occurrence. This behaviour, introducing a new model regarding the intermediate term earthquake prediction, was interpreted (Papadopoulos and Baskoutas 2011) in term of the phases of the phenomelogical «Consolidation Model" of the earthquake preparation process, proposed by Dobrovolski (1991). Given that the geodynamic regime in the Hellenic arc and trench system controls the physical process of strong earthquakes occurrence, this paper describe the characteristic of the above mentioned precursory pattern, observed before all strong earthquakes, with magnitudes M>6.0 occurred in Greek territory in the time period 2000 to 2008.

2. Qualitative Temporal Variation Precursory Seismicity Pattern

In applying the FastBEE tool analysis, the temporal variation series of the seismic parameters estimates were obtained by a simple moving-window technique, with one-month step. In continuation the smoothed estimates were filtered, with the same width filter, in order to avoid side lobs effect. This procedure makes the temporal changes, with periods equal or greater of the half filter width, to pass undistorted. The final output includes the temporal variation of all three examined seismic parameters, which each one appears as a complex of two superposed curves, (figure 3). The first thin violet curve represents the smoothed time series and the second bolder red line the filtered one. The standard errors for the b-value and the confidence limit 1σ of the parameters logN and $\log E^{2/3}$, in the same graph can be seen as lines parallel to their mean values in the examined time period. The observed clear fluctuation of all parameters, over and above their relative mean values, forms consecutive relative minima and maxima. These changes, although their qualitative characters are believed to reflect the changes in stress in the broader area. The positive relation of the observed significant fluctuations with strong earthquakes occurrence were considered by Papadopoulos and Baskoutas (2009; 2011) as prognostic anomalies. The regularity of temporal prognostic anomalies appearance, over a long time variation profiles can be formulated, in the ambit of the FastBEE algorithm, as a qualitative precursor seismicity pattern.

The general trend of this pattern, in all three parameters, appears schematically in the figure 1 and its characteristics can be summarized as follow:

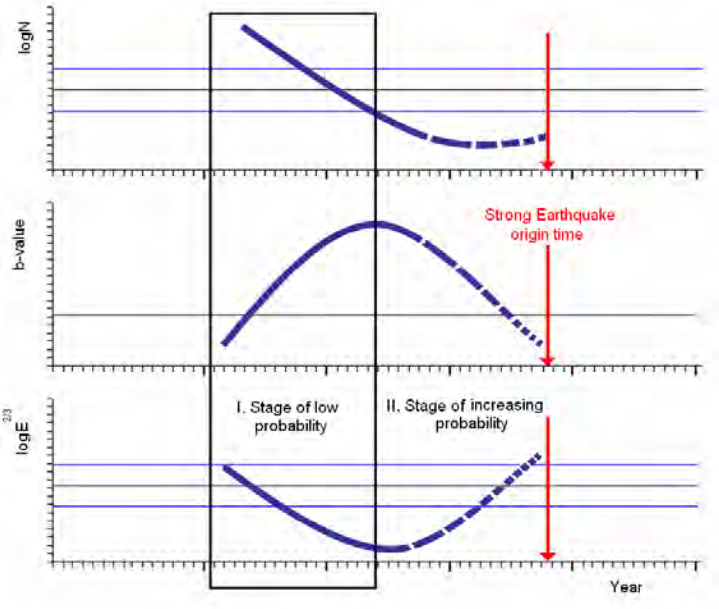

Figure 1 - Schematic representation of the temporal prognostic anomaly. Open rectangular parallelogram denotes the first, low probability stage, which is followed by an increasing probability stage. Vertical red arrow shows the earthquake origin time.

The temporal variation of the parameter logN, shows, in the majority of the cases a clear decreasing phase toward to the relative mean value, in the examined time interval and bellow to the confidence level of 70%, reaching to a relative minimum. Usually the relative mean values, especially when the examined time interval is long enough, some how represent the background ("normal') seismicity in a given region and the previously decreased stage denote kind of "quiescence" period. This parameter usually reflects the fluctuation of the number of earthquakes despite the present of a strong earthquake. In case of strong earthquake occurrence the influence of its aftershock activity can add information of the evaluation of the two other considered seismic parameters. Nevertheless it was found that the use of a declustered, for aftershocks, earthquake catalogue doesn't change the qualitative character of the observed precursory seismicity pattern.

Parameter b-value, in the same pattern, shows at the beginning an increasing trend until it reaches a relative maximum. After that this parameter starts to decreases constantly toward to the relative mean value and even lower. Usually the strong earthquake occurrence falls within this time interval. Finally the parameters $\log E^{2/3}$, contrary to the b-value, is characterized by a gradual decrease toward to the relative mean value and even lower to the confidence limit. The inversion of this trend to toward to the mean value, signalize the impending strong earthquake occurrence.

It was observed that the temporal evolution of the foresaid prognostic anomaly can be divided in two distinct probability stages. During the time evolution of the first period the probability for a strong earthquake occurrence is very low; contrary the second period the probability for a earthquake occurrence is high, which become higher, as the temporal anomaly is approaching to its end and no earthquake is yet occur (dashed line in figure 1).

Previous studies have shown that among all three examined seismic parameters, b-value and the seismic energy releases, in the form $\log E^{2/3}$, are more informative in respect to the parameter logN, although this last can add information when anomalous temporal variation appears in the

seismicity of the region. From the physical point of view, the quantity $logE^{2/3}$, is proportional to the rate of accumulation of the dynamic ruptures in the strong earthquakes preparation process area, (Keilis-Borok 1959; Sadowski & Pisarenko, 1983) reflecting the variations of the tectonic stress in the region of the observation. For this reason, parameter $logE^{2/3}$ seems to describe much better the observed temporal variation of the seismicity, due to the temporal changes of the stress field influence precursory seismicity pattern case studies before several strong earthquakes in Greece.

3. Precursory Seismicity Pattern Before Several Strong Earthquakes in Greece.

Earthquakes, with magnitude Ms≥6.0 in Greek territory, represents according to Papazachos and Papazachou (2003), the lower magnitude of a destructive earthquake with a return period of about one year. For this reason all events above this magnitude threshold, in the time period 2000-2008 were investigated in relation to the observed foresaid temporal variation anomaly. The seismic data used was taken from the Earthquake Catalogue of the Geodynamic Institute, of the National Observatory of Athens (NOA), Greece. Table 1 show the parameters of the examined strong earthquakes and figure 2 shows their epicentres, numbered according to the serial numbers of the Table 1.

The Skyros 2001, July 26, with Ms=5.8 earthquake, although smaller than the defined threshold (nevertheless reported by NEIC, as M=6.5), was included in this study, because it belongs to a remarkable strong earthquake activity of a cluster of eight (8) events, with magnitude Ms ≥ 5.5, which have been occurred within the short time interval of 14 hours (Table 2).

Table 1 - Earthquakes catalogue parameters with magnitude M_S≥6.0, in the time period 2000-2008.

s/s	Date	Orig Time	Lat	Lon	Depth	Magn GINOA	Magn NEIC
1	2001 JUL 26	00:21	39.06	24.24	10	5.8	6.5 MwGS
2	2003 AUG 14	05:14	38.79	20.56	12	6.4	6.3 MwHRV
3	2005 OCT 17	05:45	38.13	26.59	29	6.0	5.5 MwHRV
4	2005 OCT 18	15:25	37.58	20.86	22	6.1	5.7 MwHRV
5	2007 MAR 25	13 57	38.34	20.42	15	6.0	5.7 MwGS
6	2008 FEB 14	10 09	36.50	21.78	41	6.7	6.9 MwGCMT
7	2008 JUN 8	12 25	37.98	21.51	25	7.0	6.4 MwGCMT
8	2008 JUL 15	03 26	35.85	27.92	56	6.7	6.4 MwGCMT
9	2008 OCT 14	02 06	38.85	23.62	24	6.1	5.2 MwGCMT

The temporal variation of the seismicity, before each strong earthquake is based on the elaboration of a seismic data set for a period of ten years within a rectangular area around the earthquake epicenter and with size of 100x100Km. Figure 3 shows, as an example, the characteristic FastBEE output, with the seismic parameters temporal variation, for the Skyros 2001 earthquake. The inspection of this figure shows the characteristic temporal behaviour of the previously described "prognostic anomaly". The curve of the parameter logN starts to decrease continuously after the middle of the year 1998, when it crosses the relative mean value. This behaviour somehow depicts a "quiescence period". In the same time interval curves of the parameters b-value and $logE^{2/3}$, start to increase and decrease respectively, signalizing the first, low probability for an earthquake occurrence, stage (see also figure 1), and lasting till the middle of the year 1999, where both reach

their respective relative maximum and minimum. After this date starts the beginning of the second stage high probability stage, which becomes critical in the middle of 2000 and especially when the $logE^{2/3}$ parameter crosses the lower confidence limit (70%) line concluding with the strong earthquake occurrence one year later (July 26, 2001).

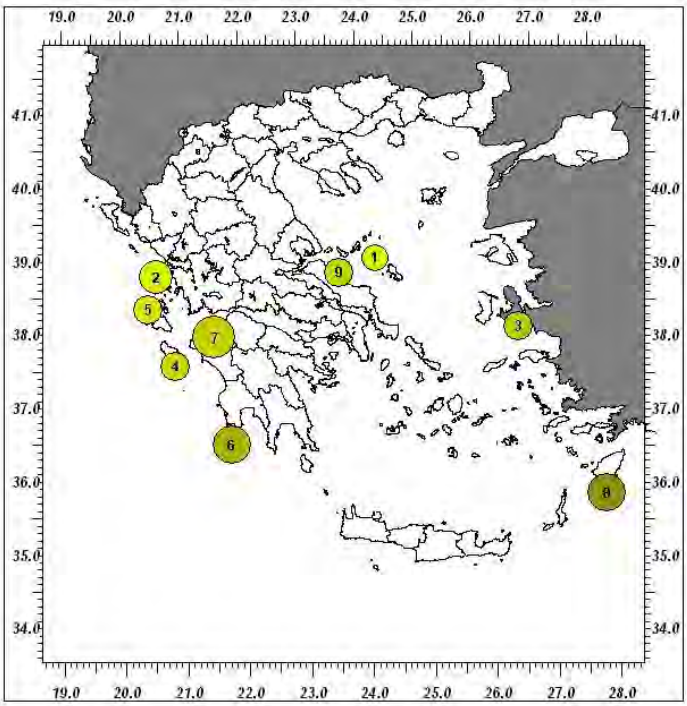

Figure 2 - Map of seismic epicenters of the shallow strong earthquakes with magnitude $M_S \geq 6.0$, in the time period 2000-2008.

Table 2 - List with the parameters of the Skyros, July 26, 2001 mainshock and the after-shocks with magnitude $M_S \geq 5.0$ (Catalogue of Geodynamic Institute of National Observatory of Athens).

	Date	hh:mm	Lat	Lon	Depth	Magn
1	2001 JUL 26	00:21	39.06	24.24	10	5.8
2	2001 JUL 26	00:34	39.04	24.35	18	5.3
3	2001 JUL 26	02:01	39.10	24.31	21	5.0
4	2001 JUL 26	02:06	38.96	24.45	23	5.2
5	2001 JUL 26	02:09	38.92	24.52	24	5.3
6	2001 JUL 26	02:40	38.97	24.57	5	5.1
7	2001 JUL 26	04:53	39.06	24.38	22	5.1
8	2001 JUL 26	14:24	39.11	24.27	5	5.1

Figure 4 shows the temporal course of the "prognostic anomaly", for the Skyros 2001 earthquake, as it regards the parameter $logE^{2/3}$ and its polynomial fitting line (red line). The regression equation and the respective R-squared value follow as:

$$\mathbf{y = 1^{-06}x^2 - 0{,}089x + 16 \text{ and } R^2 = 0{,}67}$$

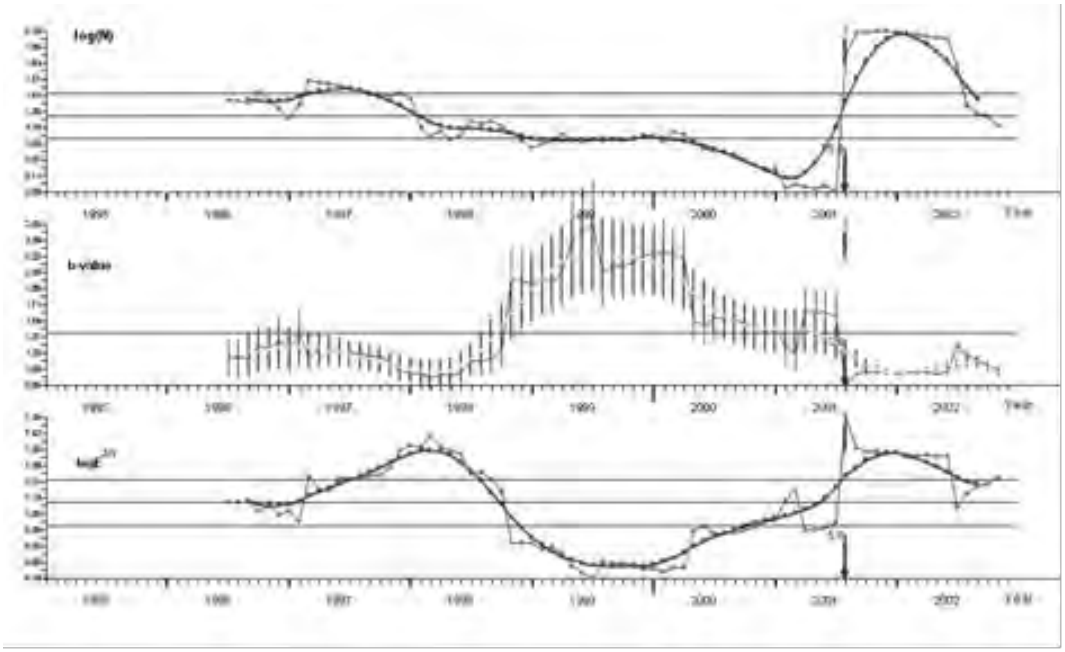

Figure 3 - Temporal variation of the seismic parameters logN(t), b-value and $logE^{2/3}$, with their respective standard errors, for the Skyros 2001 July 26, Ms=5.8 strong earthquake. The numbered arrow perpendicular to the time axis denotes the earthquake origin time.

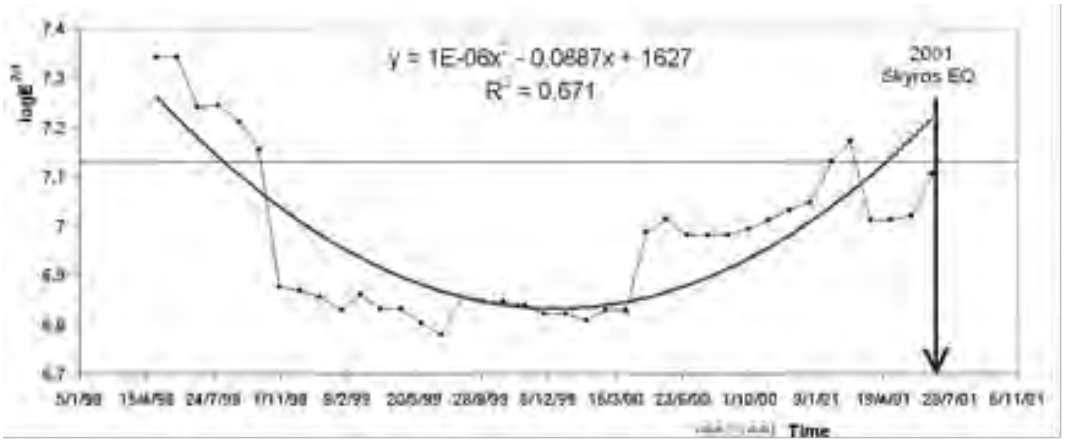

Figure 4. Prognostic anomaly for the Skyros 2001 July 26, Ms=5.8 earthquake and the respective polynomial fitting line (red line).

In the same way were obtained the prognostic anomalies, before all examined strong earthquakes, which shape, duration and their respective polynomial fitting line can be seen in the figure 5. The regression equations and their respective R-squared values for all cases are reported in table 3. The mean polynomial equation is:

$$logE=2{,}01^{-01}t^2-8{,}13^{-02}t$$

Table 3 shows also the "prognostic anomaly" duration in months and the respective magnitudes of the examined strong earthquakes. Its mean duration is equal as 45±28, ranging between a minimum of 17 and maximum of 73 months. Figure 6 shows the dependence of the "prognostic anomaly" total duration, measured form the parameter $logE^{2/3}$ and the magnitude. This relation

shows a slight proportionality, with significant, in some cases, deviation around the same order of magnitude and is expressed by the following linear regression equation:

$$T_{Dur} = 28,056Ms - 140,3$$

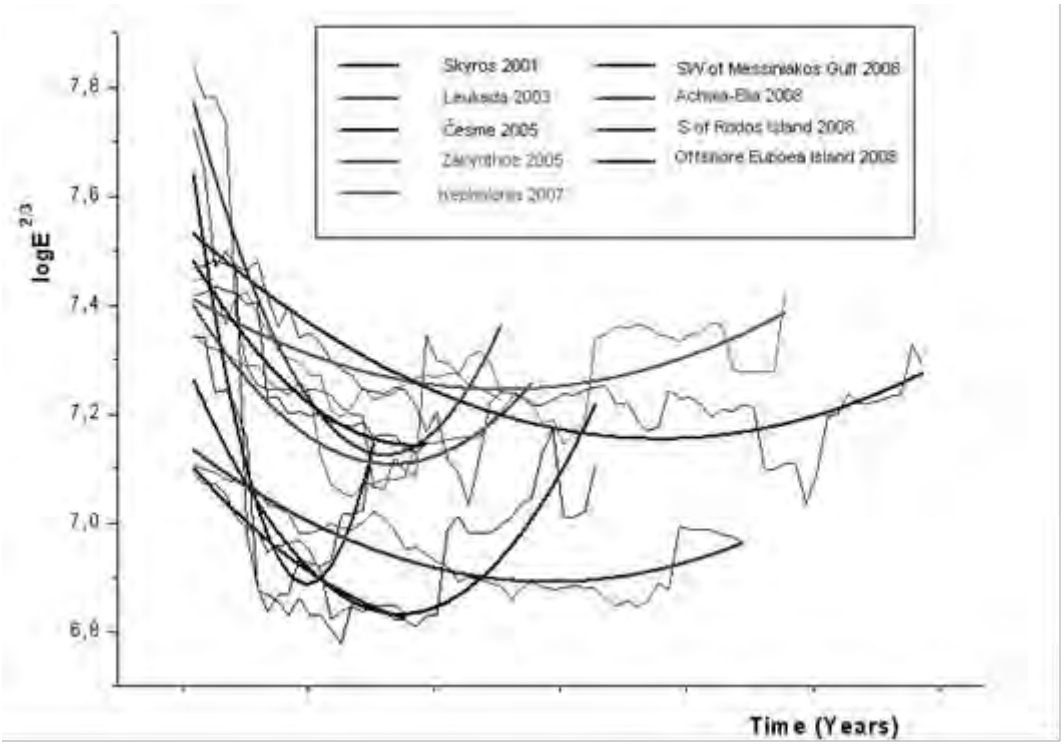

Figure 5 - The shapes and the durations of the seismic parameter $logE^{2/3}$ prognostic anomalies for each examined strong earthquake and their respective polynomial fitting.

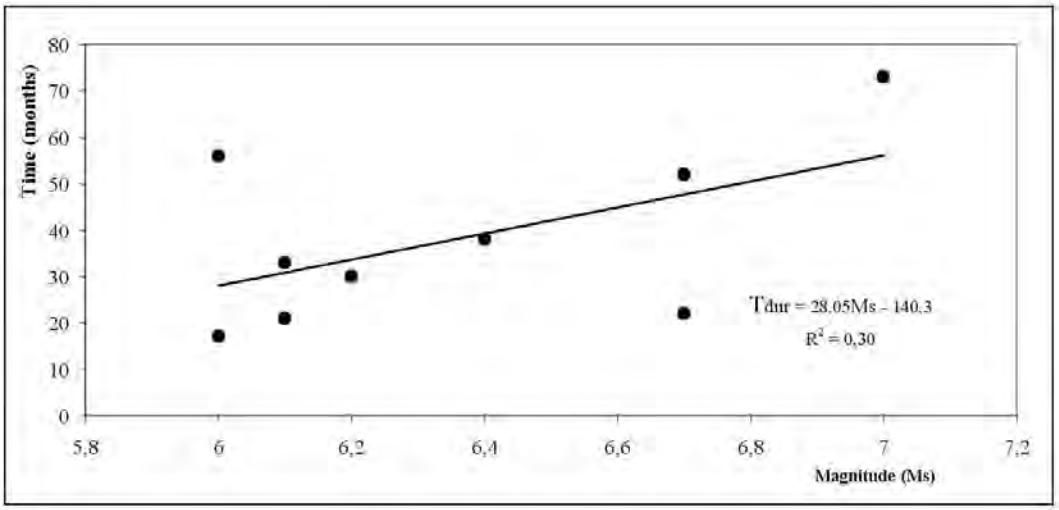

Figure 6 - The dependence between magnitude of the examined strong earthquakes and total duration of the prognostic anomaly measured in the parameter $logE^{2/3}$.

Table 3. The duration of the prognostic anomalies, in the parameter $logE^{2/3}$ temporal variation and the magnitudes of the examined cases. (Magnitudes were taken from the catalog of Geodynamic Institute of National Observatory of Athens)

	Case of earthquake	Prognostic anomaly duration (in months)	Regression Equation	R^2
1	Skyros 2001	38	$y = 1^{-06}x^2 - 0,09x + 16$	0,67
2	Leukada 2003	30	$y = 2^{-06}x^2 - 0,17x + 32$	0,78
3	Cesme 2005	17	$y = 9^{-07}x^2 - 0,069x + 13$	0,80
4	Zante 2005	33	$y = 2^{-07}x^2 - 0,016x + 32$	0.42
5	Kephalonia 2007	56	$y = 8^{-07}x^2 – 0,06x + 13$	0,89
6	S Messiniakos 2008	22	$y = 2^{-07}x^2 - 0,02x + 32$	0,70
7	Rodos 2008	73	$y = 2^{-07}x^2 - 0,02x + 32$	0,70
8	Achaia Elia 2008	52	$y = 2^{-06}x^2 - 0,16x + 31$	0,90
9	Evia 2008	21	$y = 4^{-07}x^2 - 0,03x + 68$	0,93

4. Discussion and Conclusions

The temporal variation analysis of a set of three seismicity parameters, with FastBEE algorithm, was performed in Greek territory in the time period 2000-2008. The prognostic anomaly observed before all examined strong earthquakes establish a precursory pattern, which characteristics, as it regards the parameters $logE^{2/3}$ were expressed in term of a polynomial fitting equation. The duration of such qualitative precursory anomalies shows a slight proportionality with the earthquake magnitude and varies, from case to case, between 17 and 73 months. The obtained theoretical polynomial prediction curves can be divided in two distinct and can be recognizable as low and high probability periods. In all examined cases, the earthquake occurrence falls within the second high probability period and especially in its later stage. It is obvious that this probability increases more and more, as this anomaly is reaching to its end and no earthquake has occurred yet Nonetheless, the earthquake occurrence can be observed in the earlier stage of this second high probability period or it can be delayed. This behaviour is an additional evidence of the influence of the geodynamic field regime acting in the wider area together with the geotectonic environment features. These factors can accelerate or delay the earthquake occurrence, although we don't know exactly how.

The result suggests that, by the constant monitoring the temporal variation of some basic seismicity parameters, in a given area and the identification of the seismic precursory pattern, can contribute to the assessment of the current seismic hazard. As a consequence the evaluation of the time evolution and the recognition of the periods of low and high probability stages can act as an alarm for an impending strong earthquake occurrence.

5. References

Baskoutas I., Papadopoulos G. and Panopoulou G. 2004. Long temporal variation of seismic parameters for seismic patterns identification in Greece, *Bull. Geol. Soc. Greece,* XXXVI/3, 1362-70. Available online at: http://geonet.geo.auth.gr/ege2004/articles/SE23_251.pdf

Baskoutas I., Papadopoulos G. and Chingtham Pr. 2011. Temporal variation of seismic parameters in the western part of the India-Eurasia Plate Collision Zone, *Research in Geophysics*, 1(1). doi:10.4081/rg.2011.e3

Dobrovol'skii I. P. 1991. *Theory of Preparation of a Tectonic Earthquake*, Moscow, Inst. of the P hys. of the Earth, RAS, Publications.

Jenkins G.M. 1970. Time Series Analysis: Forecasting and Control. Ed.Holden Day, San Francisco. Available online at: http://www.mendeley.com/research/time-series-analysis-forecasting-and-control-third-edition/

Caputo R., Console A., Gabrielov M., Keilis-Borok V.I. and Sidorenko T.V. 1983. Long-term premonitory seismicity patterns in Italy, *Geophys. J. R. Astron. Soc.*, 75, 71-75, doi: 10.1111/j.1365-246X.1983.tb01913.x

Eneva M. and Hamburge, M.W. 1989. Spatial temporal patterns of earthquake distribution in Soviet central Asia: application of pair analysis statistics, *BSSA*, 79(4), 1457-76.

Di Giovambattista R. and Tyupkin Yu.S. 2000. Spatial and temporal distribution of seismicity before the Umbria-Marche September 26, 1997 earthquakes, *Journal of Seismology*, 4(4):589-598.

Habermann R. E. 1981. Precursory seismicity patterns: Stalking the mature seismic gap. *In Earthquake Prediction*: *An International R*eview (eds) Simpson, D. W., and Richards, P. G., American Geophysical Union, Washington, D.C., 29-42.

Kanamori H. 1991.The nature of seismicity patterns before large earthquakes. In: *Earthquake Prediction: An International Review* (eds) Simpson, D. W., and Richards, P. G., American Geophysical Union, Washington, D.C., 1-19.

Keilis-Borok V.I. 1959. On Estimation of the Displacement in An Earthquake Source and of Source Dimensions, *Ann Geofis.*, 12, 205–214.

Keilis-Borok V., I., Shebalin P.N. and Zaliapin I.V. 2002. Premonitory patterns of seismicity months before a large earthquake: five case histories in Southern California, *Proc. Natl. Acad. Sci. USA*, 99(26), 16562–67.

Kossobokov V. G., Carlson J. M. 1995. Active zone size versus activity: A study of different seismicity patterns in the context of the prediction algorithm M8, *J. Geophys. Res.*, 100(B4), 6431-41.

Matsumura S. 2006. Preparatory process reflected in seismicity-pattern change preceding the M=7 earthquakes off Miyagi prefecture, Japan, *Earth Plan Space*, 58(12), 1581-86.

Matthews M. V. and Reasenberg P. A. 1988. Statistical methods for investigating quiescence and other temporal seismicity patterns, *PAGEOPH*, 126(2-4), 357-372.

Papadimitriou E. E. and Papazachos B. C. 1985. Evidence for precursory seismicity patterns in the Ionian islands (Greece), *Earth. Pred. Res*., 3, 95-103.

Papadimitriou P. 2008. Identification of seismic precursors before large earthquakes: Decelerating and accelerating seismic patterns, J Geophys. Res., 2008, 113/ B04306, 1-19.

Papadopoulos G., Ganas A. and Plessa A. 2002. The Skyros earthquake (Mw 6.5) of 26 July 2001 and precursory seismicity pattern in the north Aegean Sea, *BSSA*, 92(3),1141.

Papadopoulos G., Baskoutas I. and Stavrakakis G. 2003.Tools for the Fast Estimation of Expected Big Earthquake in predefined seismic prone areas, *1th International Workshop on Earthquake Prediction*, Athens, Greece.

Popandopoulos G. A. and Baskoutas I. 2011. Regularities in the Time Variations of the Seismic Parameters and Their Implications for Prediction of Strong Earthquakes in Greece, *Izv Akad Nauk. Fiz Zemli*, 11, 1-12.

Papadopoulos G. A. and Baskoutas I. 2009. New tool for the temporal variation analysis of seismic parameters, *Nat. Hazards Earth Syst. Sci.*, 9, 859-64.

Papazachos B.and Papazachou K. 2003. *Earthquakes of Greece*, Thessaloniki, Greece, Ziti Publications, 412 pp.

Press F. and Allen C. 1995. Pattern of seismic release in the Southern California region, *J. Geophy s. Res.*,100(B4), 6421–30.

Romanowicz B. 1993. Spatiotemporal patterns in the energy-release of great earthquakes, *Science*, 260, 1923–1926.

Shaw B. E., Carlson J. M. and Langer J. S., 1992. Patterns of seismic activity preceding large earthquakes*, J. Geophys. Res.*, 97, 479-89.

Shebalin P., Keilis-Borok V. I., Gabrielov A., Zaliapin I. and Turcotte D. 2006. Short-term earthquake prediction by reverse analysis of lithosphere dynamics, *Tectonophysics*, 413(1-2), 63-75.

Sadovski M. A. and Pisarenko V. F. 1983. On the Dependence of the Duration of Earthquake Preparation on its Energy, *Dokl. Akad. Nauk SSSR*, 272(2), 330–333.

Sobiesiak M. and Clark S. A. 2007. Levander A, Palma, M, Romero G. Seismicity pattern and first b-value mapping of the Caribbean - South American plate boundary in North-eastern Venezuela, *American Geophysical Union*. Available online at: http://adsabs.harvard.edu/abs/2007AGUSM.S33A..07S

Tiampo K. F., Rundle J. B., McGinnis S. A. and Klein W. 2002. Pattern Dynamics and Forecast Methods in Seismically Active Regions, *PAGEOPH*, 159(10), 2429-67.

Zavyalov A. D. 2003. Map of Expected Earthquakes in Greece for the 1996–2002 Period: Predicti on and Realization, *Izvestiya, Physics of the Solid Earth*, 39(1),1–6.

Δελτίο της Ελληνικής Γεωλογικής Εταιρίας, τομ. XLVII , 2013
Πρακτικά 13ου Διεθνούς Συνεδρίου, Χανιά, Σεπτ. 2013

Bulletin of the Geological Society of Greece, vol. XLVII 2013
Proceedings of the 13th International Congress, Chania, Sept. 2013

GROUND DEFORMATION MEASUREMENTS OVER LAKE TRICHONIS BASED ON SAR INTERFEROMETRY

Benekos G.[1], Parcharidis I .[1], Foumelis M .[2] and Ganas A [3].

[1] Harokopio University of Athens, Department of Geography, El. Venizelou 70 Kallithea, 17671 Athens, Greece, parchar@hua.gr, benekos@hua.gr

[2] European Space Agency (ESA-ESRIN), Via Galilieo Galilei, 00044 Frascati, Italy, michael.foumelis@esa.int

[3] National Observatory of Athens, Geodynamic Institute, 11810 Athens, Greece, aganas@noa.gr

Abstract

The aim of this study is to detect and measure ground deformation over the broader area of Lake Trichonis (Western Greece), focusing mainly on the April 2007 earthquake swarm which occurred at the vicinity of the Lake. The area, forming a pull-apart basin, presented historically an intense seismic activity along the two active normal faults at the northern and southern part of the Lake. The swarm initiated by small magnitude events on the 8th of April 2007 followed by the three strongest events of the entire sequence on the 10th of April 2007, with magnitudes ranging from 5.0 to 5.2 Mw. The seismic activity continued for longer with smaller seismic events. Based on seismological data this activity was attributed to two unmapped NW SE trending normal faults that bounds the SE bank of the Lake. Using a dataset of 28 ENVISAT ASAR scenes covering the period from February 2003 until February 2010 (~7 yr), different Interferometric Stacking techniques was applied in order to quantify the ground deformation induced by the earthquake swarm as well as its effect on the inter-seismic deformation pattern of the area. Our results indicate that co-seismic motion differs significantly from that observed during the pre- and post- swarm periods. The co-seismic pattern reveals subsidence at the northern and uplift at the southern lake sides, consistent with the structural model already proposed for the area. For the pre- and post-seismic periods both sides of the Lake show stability or low rates of subsidence with higher deformation velocity rates for the period after the seismic activity, possibly attributed to post-seismic relaxation. Our findings imply that inter-seismic ground deformation does not necessary follow the deformation pattern observed during seismic triggering, thus, long-term geodetic observations such as those provided by SAR interferometry are valuable in order to fully characterize the geodynamic behavior of an active region.

Key words: *SAR interferometry, ground deformation, earthquake swarm, Trichonis Lake, Greece*

Περίληψη

Ο σκοπός της παρούσας μελέτης είναι ο εντοπισμός της παραμόρφωση του εδάφους στην ευρύτερη περιοχή της Λίμνης Τριχωνίδας (Δυτική Ελλάδα), εστιάζοντας κυρίως

στο σεισμικό φαινόμενο του Απριλίου 2007 με την σμήνοσειρά σεισμών που σημειώθηκε στην περιοχή της λίμνης. Η περιοχή συνιστά μία pull-apart λεκάνη, η οποία παρουσιάζει γενικότερα μία έντονη σεισμική δραστηριότητα λόγο των δύο ενεργών ρηγμάτων κατά μήκος του βόρειου και νότιου περιθωρίου της. Η σμηνοσειρά ξεκίνησε με μικρού μεγέθους σεισμούς, στις 9 Απριλίου 2007 ενώ ακλούθησαν τρία ισχυρότερα σεισμικά γεγονότα στις 10 Απριλίου 2007, με μεγέθη που κυμαίνονται από 5,0 έως 5,2 Mw, τα οποία και αποτέλεσαν τα μεγαλύτερα ολόκληρης της ακολουθίας. Η σεισμική δραστηριότητα συνεχίστηκε για περισσότερο από ένα μήνα με μικρότερα σεισμικά γεγονότα. Βάσει των σεισμολογικών δεδομένων οριοθετήθηκαν δύο νέα κανονικά ρήγματα ΒΔ-ΝΑ διεύθυνσης κατά μήκος της νοτιοανατολικής όχθης της λίμνης. Χρησιμοποιώντας ένα σύνολο 28 εικόνων Ραντάρ, του δορυφόρου ENVISAT για την περίοδο από το Φεβρουάριο του 2003 μέχρι τον Φεβρουάριο του 2010 εφαρμόστηκε η τεχνική της διαφορικής συμβολομετρίας και πιο συγκεκριμένα διαφορετικές τεχνικές σώρευσης συμβολογραφημάτων με σκοπό την ανίχνευση και χαρτογράφηση των παραμορφώσεων του εδάφους που προκλήθηκε από την «σμηνοσειρά σεισμών». Σύμφωνα με τα αποτελέσματά των συγκεκριμένων τεχνικών αποδεικνύεται ότι η περιοχή παρουσιάζει εντελώς διαφορετικό καθεστώς εδαφικής παραμόρφωση κατά τη διάρκεια της προ-σεισμικής και μετα-σεισμικής περιόδου σε σχέση με την συν-σεισμική.
***Λέξεις κλειδιά:**, Συμβολομετρία Ραντάρ, εδαφική παραμόρφωση, σμηνοσειρά, Λίμνη Τριχωνίδα, Ελλάς*

1. Introduction

During the last two decades spaceborne Synthetic Aperture Radar (SAR) interferometry has become a useful geodetic tool for ground deformation detection and monitoring (Massonnet et al., 1993; Zebker et al., 1994; Galloway et al., 1998; Wright and Stow, 1999; Carnec and Fabriol, 1999; Strozzi et al., 2001; 2002; Foumelis et al., 2009).

The potentials of SAR interferometry has motivated many scientists to apply this technique for a wide range of applications related to seismo-tectonics. The utilization of an appropriate interferometric dataset allows measuring the various components of the seismic cycle, namely the pre-seismic, co-seismic, and post-seismic deformation (Massonnet et al., 1993; Peltzer et al., 1998; Peltzer and Crampé, 1999; Donnellan et al., 2002). Such analysis was performed in the present study to investigate the deformation caused by the April 2007 Trichonis's Lake Basin earthquake swarm as well as its effect on the inter-seismic pattern of the area.

The seismic sequence initiated by small events on the 8th of April 2007, while two days later, three of the strongest events in the whole sequence occurred (10th of April at 03:17, 07:15 and 10:41 GMT), with magnitudes ranging from 5.0 Mw to 5.2 Mw. The seismic activity continued for more than a month with smaller events (Sokos et al., 2010; Evangelidis et al., 2008; Kiratzi et al, 2008). The above studies provided insights on the activation of an unmapped NW–SE fault zone.

2. Geological Setting

Trichonis is the largest natural lake in Greece, covering an area of 97 km^2 and located in the western part of the country. On the northeastern side of the lake, there is the high slope of the Panaitoliko Mountain, whereas to the southwestern, the ridge of Arakintho Mountain (Figure 1). The broader Trichonis basin is a 30-km-long by 10-km-wide neo-tectonic graben (Doutsos et al., 1987). Its southern border is marked by a major WNW-ESE trending normal fault. The main geological formations belong to the External Hellenides, namely the Pindos and Gavrovo geotectonic units. The lake of Trichonis occupies the east edge of the fractured tectonic trough that retains a semi-circular shape. The formation of this trough is mainly due to the intense tectonism

of the area and partly to the falling down of limestone masses into the existing underground caverns, which form a quite extensive underground karstic network (Figure 2). The underground caverns of this network are being enlarged due to the erosive and solvent action of the water, resulting thus to the fall of the overlying layers and, finally, to the change of the morphology of the region (Evangelidis et al., 2008 and Kiratzi et al., 2008).

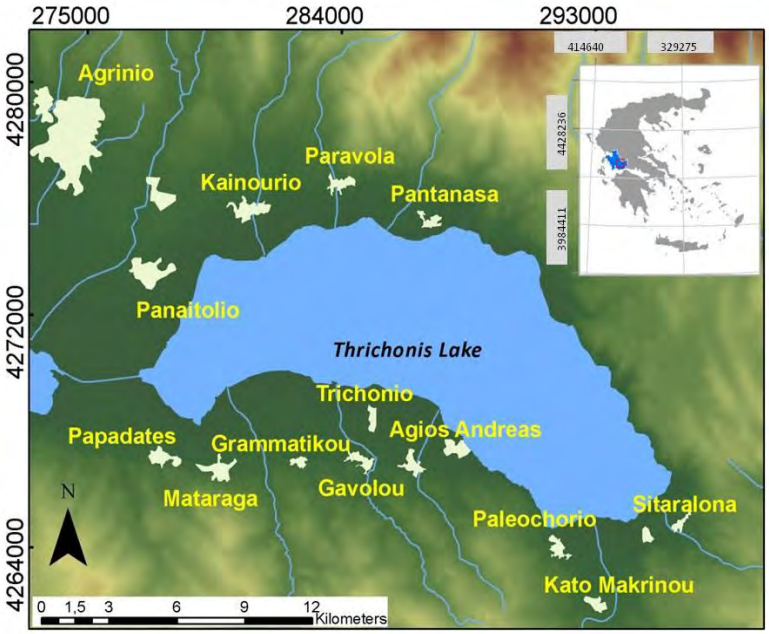

Figure 1 - Location map of the study area

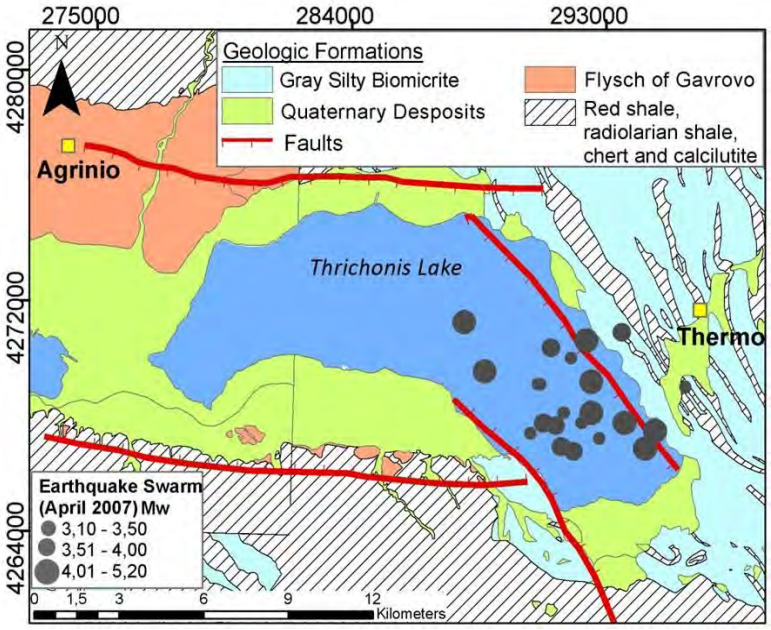

Figure 2 - Simplified geological map of the broader study area (IGME 1977). Epicenters of the earthquake swarm of April 2007 are also shown (Kiratzi et al., 2008).

3. Geodynamic Regime

3.1. Tectonic Settings

The Trichonis graben is a well-known Quaternary structure that strikes WNW–ESE for a distance of about 32 km and has a width of about 10 km. The graben cuts across the Pindos Mountains and strikes almost parallel to the Gulf of Patras graben about 30 km to the south. The Trichonis Fault zone is the major, topography controlling north-dipping normal fault, which bounds the south shore of the lake where it is locally buried under Pleistocene deposits and thick alluvial cones (Doutsos et al., 1987). The fault forms a distinct topographic escarpment with clear drainage incision in the footwall block.

3.2 Seismicity

The majority of the seismic events in the area are well-constrained along the southeastern side of the lake. Historical records exist since 1841 for that region, illustrating an average yearly earthquake magnitude of 5 in the Mercalli-Sieberg scale until 1959 (Delibasis and Carydis, 1977). It should be mentioned that in 1975 from June to December there was a sequence of earthquakes in the southern part of the lake. The first of the largest earthquakes took place on 30 June 1975 (M 5.4) whereas on 21 December 1975 an M 5.1 event was followed by another on 31 December 1975 with a magnitude of 5.1 (Papazachos et al., 1997; Evangelidis et al., 2008; Kiratzi et al., 2008). Specifically, in the southeastern part of the lake a strong seismic activity with a series of relative strong earthquakes started in April 2007 (Figure 2). The swarm began with small events, on April 9 and two days later occurred the three strongest events of the entire sequence (10 April at 3:17, 07:15 and 10:41 GMT), with sizes ranging from 5.2 to 5.0 Mw (Table 1). The seismic activity continued for a month with smaller magnitude events (Evangelidis et al., 2008; Kiratzi et al., 2008). It was shown that this seismic activity does not correlate with any of the two fault zones at the northern and southern edges of the lake, but with two unmapped NNE-SSW and NW-SE faults along its eastern shore (Sokos et al., 2010; Evangelidis et al., 2008; Kiratzi et al., 2008). Also the seismic activity of 1975 associated with these normal faulting along a NNW–ESE striking fault, combined with a left lateral component of the slip vector. This strike-slip is linked with the vertical rotation axis of the cortex and the left fracture associated with fault zones, Trichonis and the Corinthian Gulf (Kiratzi et al., 2008 and Sokos et al., 2010).

4. Data Used and Methodology

For the scope of the study, a total number of 28 ENVISAT ASAR scenes acquired along the ascending track 279 and covering the period between 2003 and 2010 (~7 yr) (Table 2), were processed using the GAMMA software. Initial estimations of the interferometric baselines were calculated from the Deflt precise orbit state vectors (Scharoo and Visser, 1998). The topographic phase was simulated based on SRTM V3 DEM of approximate spatial resolution of 90 m.

Stacking of differential interferograms aims to combine the information from several observations, in order to extract common information (Sandwell and Sichoix, 2000; Parcharidis et al., 2006; Raucoules et al., 2008). The most straightforward procedure is to compute linear combinations by averaging of interferograms. Interferometric Stacking (IS) is useful in overcoming drawbacks of conventional Differential SAR Interfeometry (DInSAR) such as the temporal decorrelation while minimizing error sources related to atmospheric phase screen.

The main process steps followed comprise the co-registration of single look complex images (SLCs), simulation of the topographic phase , generation of differential interferograms, filtering, phase unwrapping, baseline refinement, and geocoding from SAR to map geometry. All possible interferometric combinations with baselines less than 150 m were computed resulting in a total number of 68 interferograms. These interferograms were filtered using an adaptive filtering

Table 1 - Epicenters of the 2007 earthquake (the strongest events of the swarm are marked with red), modified by (Kiratzi et al., 2008).

No	Year	Month	Day	h:min:s	Lat °N	Lon °E	Depth	Mw
1	2007	4	9	23:27:15.71	38,539	21,626	15,66	4,40
2	2007	4	10	00:54:56.35	38,529	21,629	14,91	3,40
3	2007	4	10	03:17:56.09	38,551	21,626	14,29	5,00
4	2007	4	10	03:27:38.33	38,534	21,612	5,28	3,90
5	2007	4	10	03:32:34.20	38,524	21,619	14,15	3,70
6	2007	4	10	03:39:18.86	38,549	21,663	12,49	3,30
7	2007	4	10	04:16:15.65	38,550	21,605	2,95	3,10
8	2007	4	10	04:29:58.11	38,535	21,607	10,96	3,70
9	2007	4	10	04:47:17.99	38,535	21,622	12,94	3,30
10	2007	4	10	05:55:12.15	38,531	21,602	9,70	3,10
11	2007	4	10	06:03:39.12	38,570	21,638	8,54	3,70
12	2007	4	10	07:13:03.67	38,532	21,651	14,60	4,70
13	2007	4	10	07:14:12.39	38,567	21,624	12,42	4,40
14	2007	4	10	07:15:40.44	38,555	21,584	5,06	5,10
15	2007	4	10	08:13:45.40	38,526	21,614	14,59	3,80
16	2007	4	10	09:59:01.51	38,560	21,618	11,63	3,50
17	2007	4	10	10:34:47.97	38,550	21,606	13,62	3,30
18	2007	4	10	10:41:00.14	38,525	21,647	22,47	5,20
19	2007	4	10	12:55:17.70	38,539	21,615	12,91	3,30
20	2007	4	10	13:51:00.93	38,564	21,610	17,81	3,60
21	2007	4	13	12:58:14.45	38,526	21,616	9,38	3,10
22	2007	4	15	02:16:32.58	38,574	21,576	17,86	4,10
23	2007	6	5	11:50:20.46	38,535	21,639	16,57	4,80

algorithm proposed by (Goldstein and Werner, 1998) to reduce phase noise. The levels of coherence, independently of the acquisition time intervals, were high only over build environment that reflects the villages around the lake. The majority of the arable areas around the lake exhibit significantly low coherence due to that don't reflected constant over time the signal. Subsequently, we reconstructed the unwrapped phase from the obtained differential interferograms, based on the assumption of the structured "phase unwrapping" rule; that is the phase difference between two neighbor pixels does not exceed the half cycle (π), and using the minimum cost network algorithm (Constantini, 1998).

Following phase unwrapping a baseline refinement procedure was adopted in order to more precisely define acquisition geometry and hence the simulation of topographic component. Finally, the unwrapped interferograms of the highest quality in terms of coherence levels was stacked in order to estimate ground deformation rates. In this step the selection of the reference points is considered to be one of the critical parts of the processing since it affects significantly the final deformation estimates. Some selection criteria are quantitative, such as the high coherence of the point in terms of phase stability overtime. Others are qualitative and are related to the regional tectonic setting of the area and the related pattern of deformation which needs to be extracted. The local reference point selected for the processing is located close to Agrinio town at the north-east part of the study area.

Also, a specific stacking strategy be followed, in order to develop two different time period IS processings. The first involves the pre-seismic period with 17 interferograms from the total 27 before the seismic swarm. The second one involves the post-seismic period with 9 from the 11

total interferograms. The selection of pairs is according to the criteria of quality as the residual phase and the noise in the unwrapped interferograms.

For the co-seismic period, there are no suitable interferometric pairs to follow the aforementioned IS procedure. In the case of non instantaneous (for example linear) deformation, summing interferograms on equivalent periods (approximately same start and end dates) partly reduce the atmosphere to deformation ratio and the obtained pseudo-interferograms will have an increased accuracy respect to initial ones. The sum of pairs covering successive periods was also computed to provide long time span pseudo-interferograms that could not be reliably covered by a single interferogram due to geometric (baseline) and temporal (coherence) limitations (Parcharidis et al., 2006). The linear combination in this case a sum of four interferograms covering the periods (i) 2007-01-16/2008-04-15, (ii) 2008-04-15/2008-09-02, and (iii) 2008-11-11/2009-12-20 resulted in the formation of a pseudo-interferogram spanning the period 2007–2009, where the co-seismic deformation signature of the earthquake swarm was identified.

Table 2 - List of ENVISAT ASAR.SLC dataset used in the analysis. Reference image in bold, Bp: perpendicular baseline and dT: temporal separation between acquisitions.

No	Master (Date)	Slave (Date)	Bp (m)	dT (days)
1	20050531	20030211	787	-840
2	20050531	20030805	-227	-665
3	20050531	20031014	38	-595
4	20050531	20031223	-439	-525
5	20050531	20040406	-69	-420
6	20050531	20040511	18	-385
7	20050531	20040720	-343	-315
8	20050531	20040824	340	-280
9	20050531	20040928	-683	-245
10	20050531	20041102	-551	-210
11	20050531	20050111	-494	-140
12	20050531	20050426	1001	-35
13	**20050531**	**20050531**	**0**	**0**
14	20050531	20060620	-656	385
15	20050531	20060725	1107	420
16	20050531	20061003	-587	490
17	20050531	20070116	375	595
18	20050531	20070220	-326	630
19	20050531	20080311	35	1015
20	20050531	20080415	308	1050
21	20050531	20080729	-269	1155
22	20050531	20080902	411	1190
23	20050531	20081007	-331	1225
24	20050531	20081111	156	1260
25	20050531	20090120	120	1330
26	20050531	20090224	-299	1365
27	20050531	20090505	-463	1435
28	20050531	20100209	138	1715

5. Results

By transforming the interferometric results from range–Doppler coordinates into map geometry, the interferometric analysis results were imported in a GIS environment for further interpretation. The obtained deformation maps for the pre-, co- and post-seismic periods are shown in (Figure 3).

The pre-seismic displacement field (Oct. 2003–Oct. 2006) shows relative stability, while locally low subsidence rates are observed. In the northern part of the lake subsidence prevails with the highest rate of -7 mm/yr in Paravola village. Similar deformation patterns are observed on the south side of the lake (up to -8 mm/yr). In the southeastern part of the lake, which should be considered separately because of the presence of the two active NW–SE fault zones, subsidence rates varies between -1 and-5 mm/yr (Figure 4).

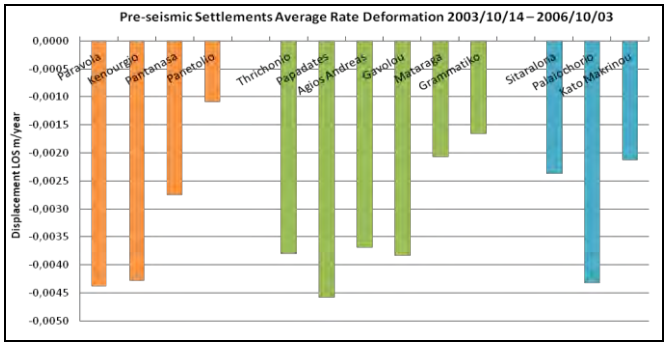

Figure 3 - Settlements' average deformation rates (along the Line-of-Sight - LOS) for the pre-seismic period, (Northern part – Orange columns, Southern part - Green columns, Southeast part - Blue columns).

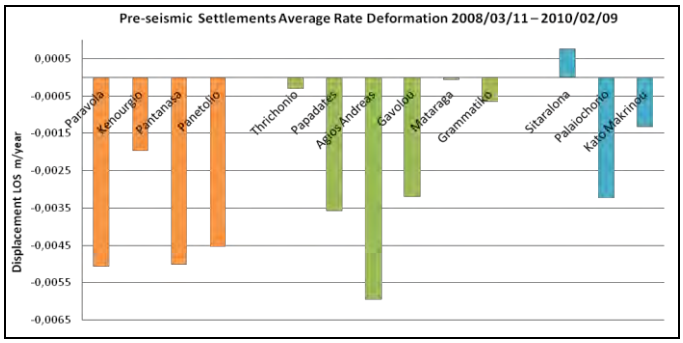

Figure 4 - Settlements' average deformation rates (in LOS) for the post-seismic period, (Northen part – Orange columns, Southern part - Green columns, Southeast part - Blue columns).

Moreover, the surface deformation is examined for the post-earthquake swarm period. Making a first reading in this post-seismic deformation map for the period Mar. 2008 – Febr. 2010, increased subsidence rates are observed compared to the pre-seismic results for the same areas. Specifically, the northern part of the Trichonis Lake subsides by up to -10.2 mm/yr. The southern part of the lake roughly follows the same pattern with rates up to 10 mm/yr. On the southeastern part of the lake, the Paleochori settlement subsides up to -1 mm/yr and Kato Makrinou shows subsidence until -8 mm/yr. But the Sitaralonona village shows mixed deformation patterns from 5 to -5 mm/yr (Figure 5).

The resulting pseudo-interferogramthat includes the effect of the earthquake swarm shows a different deformation pattern compared to the previously examined periods. The northern part of

the Trichonis' Lake shows subsidence patterns, on the contrary to the southern part where uplift is detected. This characteristic deformation pattern is also present on the southeastern part of the lake. This regions is examined separately because of two NW–SE faults resulting in uplifts at the western part while the eastern one shows significant subsidence rates (Figure 6).

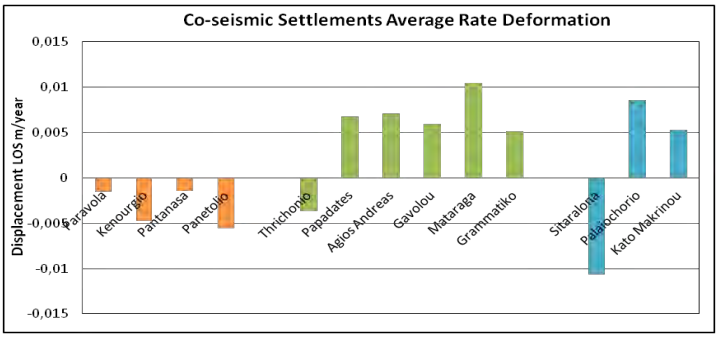

Figure 5 - Settlements' average deformation rates (in LOS) for the cot-seismic period, (Northen part – Orange columns, Southern part - Green columns, Southeast part - Blue columns)

6. Conclusion-Discussion

The IS technique was implemented to the Trichonis' lake area for the seismic event (earthquake swarm) on April 2007, showing the following results:

- The major subsidence rate in the post-seismic period compared to pre-seismic period. Probably the seismic event caused higher deformation velocities.
- This processing and the different deformation patterns in the displacement maps in the southeastern part of the lake verify the studies that promote the new tectonic settings that determined by the earthquake's swarm on April 2007 with two active faults in the southeastern part of the lake.
- Both the co- and inter-seismic displacement fields of the Trichonis Lake, the latter calculated for the periods before (2003-2006) and after (2007-2009) the swarm of earthquake in 2007, were investigated by means of SAR interferometric analysis.

  Regarding the co-seismic ground deformation, the adopted procedure to compensate for the lack of an appropriate single interferometric pair to cover the entire period of seismic activity, namely the linear combination of consecutive differential interferograms, led to the reduction of the error budget from possible atmospheric effects. Although this procedure provided acceptable results over build-up areas, the increase of the level of noise from individual pairs especially over agricultural and generally vegetated areas, which exhibit in turns high decorrelation, did not allowed deriving robust displacement observation.
- However, the relatively large number of villages in the region permitted the recognition of a characteristic co-seismic deformation pattern, with the entire northern part of the lake subsiding with an average rate of -5mm/yr, contrary to the southern part where uplift dominates by approximately 10mm/yr.
- Nonetheless, for an exact determination of the geometry of the activated fault zones as well as the amount of slip that took place, further modeling of the obtained InSAR results is necessary.
- As for the inter-seismic part, it was shown that the sign of motion is retained, though differences in the displacement rate do exist. Specifically, higher subsidence rates are

calculated for the post-seismic period, yet these differences lay within the uncertainty of the estimates and could be therefore neglected. It is worth to mention that no significant seismic activity was recorder during these periods.

- Finally, further analysis are required in order to identify and separate from the observed inter-seismic (pre- and post-) motion rates the effects of non-tectonic deformation-induced phenomena.

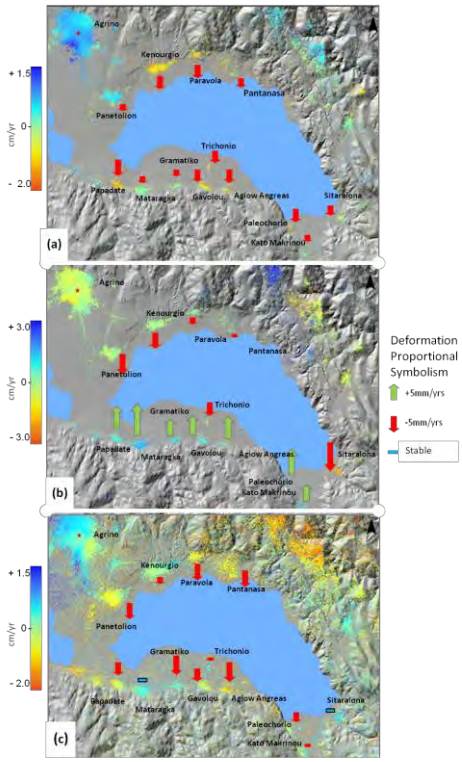

Figure 6 - Deformation rates maps of the broader area of Trichonis Lake by Interferometric Stacking for the (a) pre-seismic (2003-2006), (b) co-seismic (2007-2009) and (c) post-seismic (2008 -2009) periods. The red star represents the selected reference area.

7. Acknowledgments

ENVISAT ASAR scenes were provided by the European Space Agency (ESA) in the frame of TERRAFIRMA-X GMES project.

8. References

Carnec C. and Fabriol H. 1999. Monitoring and modeling land subsidence at the Cerro-Prieto geothermal field, Baja California, Mexico, using SAR interferometry, *Geophys. Res. Lett. 9*, 1211–1214.

Costantini M. 1998. A novel phase unwrapping method based on network programming, 1998, *IEEE Trans. GARS*, 36 (3), 813 – 821.

Delibasis N. and Carydis P. 1977. Recent earthquake activity in Trichonis region and its tectonic significance, *Ann. Geofis.* 30, 19–81

Donnellan A., Parker and Peltzer G., 2002. Combined GPS and InSAR models of postseismic deformation from the Northridge earthquake, *Pure and Applied Geophysics* 159, 2261–2270.

Doutsos T., Kontopoulos N. and Frydas D. 1987. Neotectonic evolution of northwestern-continental Greece, *Geol. Rundsch*. 76, 433–450.

Evangelidis C.P., Konstantinou K.I., Melis N.S., Charalambakis M. and Stavrakakis G.N. 2008. Waveform relocation and focal mechanism analysis of an earthquake swarm in Trichonis lake, western Greece, *Bull. Seism. Soc. Am.* 98(2), pp. 804-811.

Foumelis M., Parcharidis I., Lagios E. and Voulgaris N. 2009. Evolution of post-seismic ground deformation of the Athens 1999 earthquake observed by SAR interferometry, *J. Appl. Geophys.* 69 (1), 16–23.

Galloway D.L., Hudnut K.W., Ingebritsen S.E., Phillips S.P., Peltzer G., Rogez F. and Rosen P.A. 1998. Detection of aquifer system compaction and land subsidence using interferometric synthetic aperture radar, Antelope Valley, Mojave Desert, California, *Water Resources Research*, 34 (10), pp. 2573-2585.

Goldstein R. and Werner C. 1998. Radar interferogram filtering for geophysical applications, *Geophys. Res. Lett*. 25 (21), 4035–4038.

IMGE 1977. Geological Map of Greece, Scale 1:50.000, Thermon Sheet, D.L. Loftus, N. Philippakis and A. Mavridis, The Institute of Geological and Minning Researche,

Kiratzi A., Sokos E., Ganas A., Tselentis A., Benetatos C., Roumelioti Z., Serpetsidaki A., Andriopoulos G., Galanis O. and Petrou P. 2008. The April 2007 earthquake swarm near Lake Trichonis and implications for active tectonics in western Greece, *Tectonophysics* 452, 51- 65.

Massonnet D. and Adragna F. 1993. A full-scale validation of Radar Interferometry with ERS-1: the Landers earthquake, Earth Observation Quarterly, 41.

Massonnet D., Rossi M., Carmona C., Adragna F., Pelmtzer G., Feigl K. and Rabaute T. 1993. The displacement field of the Landers Earthquake mapped by radar interferometry, *Nature* 364, 138–142.

Scharoo R. and Visser P.N.A.M. 1998. Precise orbit determination and gravity field improvement for the ERS satellites, *Journal Geophysical Research*, vol. 103, 8113-8127.

Papazachos B. and Papazachou K. 1997. The Earthquakes of Greece, Ziti Editions, Thessaloniki, Greece.

Parcharidis Is., Lagios E., Sakkas V., Raucoules D., Feurer D., Le Mouelic S., King C., Carnec C., Novali F., Ferretti A., Capes R. and Cooksley G. 2006, Subsidence monitoring within the Athens Basin (Greece) using space radar interferometric techniques, *Earth Planets Space*, 58, 505–513, 2006.

Peltzer G. and Crampé F. 1999. Evidence of non-linear elasticity of the crust from the Mw7.6 Manyi (Tibet) earthquake surface displacement field, *Science* 286 (5438), 272–276.

Peltzer G., Rosen P. and Rogez F. 1998. Poro-elastic rebound along the Landers 1992 earthquake surface rupture, *Journal of Geophysical Research B: Solid Earth 103 (B12), 30131–30145.*

Raucoules D., Parcharidis I., Feurer D., Novalli F., Ferretti A., Carnec C., Lagios E., Sakkas V., Le Mouelic S., Cooksley G. and Hosford S. 2008. Ground deformation detection of the greater area of Thessaloniki (Northern Greece) using radar interferometry techniques, *Natural Hazards Earth Syst. Sci. J.* 8 (4), 779–788.

Sokos E., Pikoulis V.E, Psarakis E.Z. and Lois A. 2010. THE APRIL 2007 SWARM IN TRICHONIS LAKE USING DATA FROM A MICROSEISMIC NETWORK, Bulletin of the Geological Society of Greece 2010, *Proceedings of the 12th International Congress* Patras May, XLIII, No 4 – 2183.

Strozzi T., Wegmuller U., Tosi L., Bitelli G. and Spreckels V. 2001. Land subsidence monitoring with differential SAR interferometry, *Photogramm. Eng. Remote Sens.* 67, 1261–1270.

Wright P., Stow, R., 1999. Detecting mining subsidence from Space, *Int. J. Remote Sens.* 20 (6), 1183–1188.

Zebker H.A., Rosen P.A., Goldstein R.M., Gabriel A. and Werner C.L. 1994. On the derivation of coseismic displacement-fields using differential radar interferometry: the Landers earthquake, *J. Geophys. Res. Solid Earth* 99 (B10), 19617–19634

Δελτίο της Ελληνικής Γεωλογικής Εταιρίας, τομ. XLVII , 2013
Πρακτικά 13ου Διεθνούς Συνεδρίου, Χανιά, Σεπτ. 2013

Bulletin of the Geological Society of Greece, vol. XLVII 2013
Proceedings of the 13th International Congress, Chania, Sept. 2013

MICROTREMOR HVSR STUDY OF SITE EFFECTS IN THE URBAN AREA OF THE TOWN OF MYTILENE, LESVOS (GREECE) – PRELIMINARY RESULTS

Bouranta E.[1], Vallianatos F.[2], Hatzopoulos J.N.[1], Papadopoulos I.[2] and Gaganis P.[1]

[1] University of Aegean, Department of the Environment University Hill, Mytilene, Greece

[2] Laboratory of Geophysics & Seismology, Technological Educational Institute of Crete, Chania, Crete, Greece

Abstract

Mytilene is the capital of Lesvos, the eighth largest island in the Mediterranean Sea and the largest in the North Aegean. The region of North Aegean is a geotectonically complex area, because its geodynamic status is directly affected by the North Anatolian Fault Zone. In the present paper, microtremor data have been analyzed for the city of Mytilene using Nakamura technique of Horizontal to Vertical Spectral Ratio (HVSR) to ascertain the structure in terms of the predominant frequency. 100 microtremor measurements have been performed in the city of Mytilene. At each point of microtremor measurement, the natural frequency and amplification factor have been determined. The predominant frequency varies from 0.4 Hz to 6.6 Hz. The amplification factor in 0.4-8.07 range has been obtained from the HVSR analysis. The results are presented in terms of maps, including the spatial variability of the predominant frequency and developed GIS database. The results of this study make it clear that the characteristics of microtremors depend on the type of soil deposits.
Key words: *Nakamura method, amplification factor, natural frequency, GIS*

Περίληψη

Αντικείμενο της παρούσας ερευνητικής εργασίας είναι η εκτίμηση της επίδρασης των τοπικών εδαφικών συνθηκών στη σεισμική κίνηση, στο αστικό συγκρότημα της πόλης της Μυτιλήνης. Για το σκοπό αυτό, έχουν αναλυθεί δεδομένα μικροθορύβου για την πόλη της Μυτιλήνης, χρησιμοποιώντας τη Μέθοδο Φασματικού Λόγου Οριζόντιας προς Κατακορυφη Συνιστώσα. Πραγματοποιήθηκαν 100 μετρήσεις εδαφικού θορύβου στην πόλη της Μυτιλήνης. Για κάθε σημείο μέτρησης προσδιορίστηκε η θεμελιώδης συχνότητα των επιφανειακών στρωμάτων και το πλάτος ενίσχυσης της εδαφικής κίνησης. Η τιμή της θεμελιώδους συχνότητας κυμαίνεται από 0.4 Hz έως 6.6Hz, ενώ η τιμη του παράγοντα ενίσχυσης κυμαίνεται από 0.4 έως 8.07. Τα αποτελέσματα δίδονται υπό μορφή χαρτών και περιλαμβάνουν τη χωρική κατανομή της θεμελιώδους συχνότητας και του παράγοντα ενίσχυσης. Δημιουργήθηκε βάση δεδομένων GIS, η οποία λειτούργησε ως υπόβαθρο για την παρουσίαση των παραγόμενων χαρτών. Συμπερασματικά, οι τοπικές εδαφικές συνθήκες επηρεάζουν σημαντικά τις μετρήσεις εδαφικού θορύβου.
Λέξεις κλειδιά: *Μέθοδος Nakamura, παράγοντας ενίσχυσης, θεμελιώδης συχνότητα, Γ.Σ.Π.*

1. Introduction

The seismic action has considerably negative repercussions in the material and technical infrastructure and by extension in the social and economic life. In the economic cost that involves the alleviation of affected regions and the reset of damage should be added also the loss of markets (products and services) in a continuously more competitive economic environment at international level. This fact makes the need for mitigation of repercussions of seismic destructions imperative.

The distribution of earthquake damage is directly dependent on local site conditions. In the present paper we have attempted to study the site effects and the site ground response in the case of an earthquake in the urban area of Mytilene (Lesvos, Greece). This area is exposed to seismic hazard because is a very active area with high seismicity. The Nakamura technique has been adopted for the microtremor measurements analysis (HVSR) to determine the predominant frequency of the soil**s** in this area.

The Nakamura technique has gained much popularity over the past years because it is inexpensive method and can be applied to regions of low seismicity. Also, it requires only a single station. One drawback of the HVSR technique is the theory on which it is based. There is a disagreement among various researchers on the nature of the microtremor as there is no established theory concerning the kind of wave motions the microtremor survey provides (Bard, 1999).

Although the specific mechanism causing wave amplification can vary from site to site, several studies suggest that ambient noise, or weak motions, can be used to identify areas that might amplify earthquake ground motions in advance of earthquake occurrence (Nakamura 1989, 1997). In this paper, we investigate the use of microtremors, or ambient noise, using horizontal-to-vertical spectral ratios (HVSRs) to study potential site effects on seismic ground motions in the urban area of the town of Mytilene. We determine predominant frequencies and relative amplification derived from the microtremor measurements, and we interpret these results in the context of geotechnical studies and geological maps. The spatial locations of all measurements and their analysis are managed by a GIS data base which has been designed to accommodate this study.

2. Materials and Methods

2.1. Geological Characteristics and Seismicity of the Study Area

Lesvos is the eighth largest island in the Mediterranean Sea and the third largest island of the Greek Islands, with 1.632 square kilometres in extent. It is located in the northeastern Aegean Sea. The city of Mytilene is the capital of the island of Lesvos and of the Prefecture of Lesvos.

Several studies carried out by Hecht (1972, 1974a,b), Pe-Piper (1978), Katsikatsos et al. (1982, 1986), and Pe-Piper and Piper (1993) described the geology and provided the geological maps of Lesvos Island (Figure 1). The geology can be summarized as a basement composed of Alpidic and pre-Alpidic metamorphic rocks which were covered later by post-Alpine formations, mainly Miocene volcanic rocks and Neogene marine and lacustrine deposits. (Soulakellis et al., 2006).

The North Aegean region is a geotectonically complex area. Its geodynamic status is directly affected by the North Anatolian Fault Zone, is westward continuation in the Aegean Sea, known as the North Aegean Trough and the West Anatolia Graben System in Asia Minor with significant historical seismicity (Papazachos and Papazachou, 1997). The island belongs in the old volcanic arc that acted at the Middle Miocene 15-19 million years ago. This area is characterized by high seismicity hazard and it had been affected many times in the past by powerful devastating earthquakes.

Instrumental records and historic sources clearly indicate the high seismicity of Lesvos Island. Among the destructive earthquakes of the island, the most devastating was the 1867 event (estimated intensity IX to X in Mercalli scale).

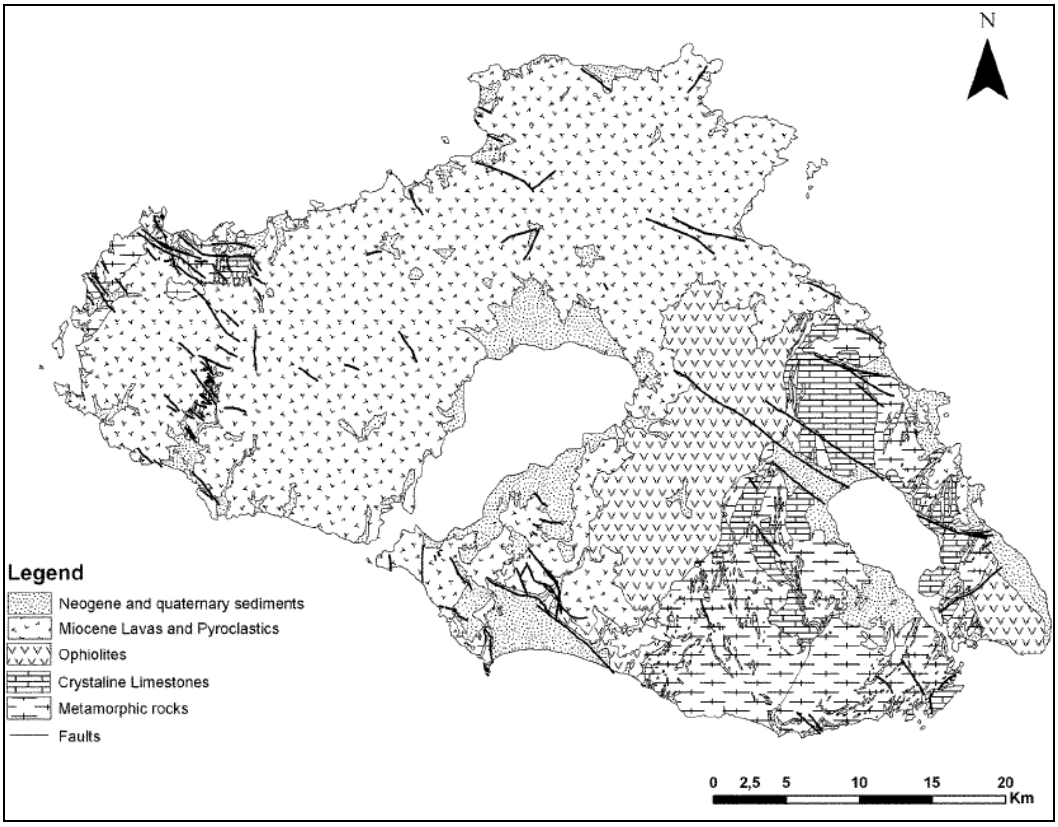

Figure 1- Simplified Geological Map of Lesvos Island (from Hecht, 1971-1974).

Mytilene is the capital of Lesvos and located at the eastern part of the island. The altitude fluctuates from 0 to 100 m and it has a smooth relief.

2.2. Methodology

In the present paper microtremor measurements have been conducted in order to study the site effects and the site ground response in case of an earthquake in the urban area of Mytilene. For this reason the Horizontal-to-Vertical Spectral Ratio (HVSR) technique has been applied on ambient noise measurements (Nakamura's technique). This method is particularly widespread the last years and several scientific studies that are referred to this have been published internationally. (Bonnefoy - Claudet et al. 2006a, 2006b; Field and Jacob, 1993; Gosar, 2007).

Although the microtremor method is well established, its ability to predict wave amplification and predominant frequency of strong motion has been debated. However, still a topic of debate, the use of microtremor is very attractive because it is fast and low-cost technique. Because of its sensitivity to spatial variations of near surface geology, the method is particularly attractive in urban areas.

This method utilizes the microtremor data from digital highly sensitive wideband seismographs with high dynamic range (24 bits). It aims to determine the fundamental frequency of local ground resonance and the empirical transfer function. Moreover, this method can be used as a powerful tool to estimate the thickness of soft-cover layers (Seht and Wohlenberg, 1999).

Microtremor measurements have been performed in the urban area of town of Mytilene. With the term "microtremors" we define Earth' s surface vibration caused by daily human activities such as machinery movement in factories, motor cars, people walking and natural phenomena (flow of

water in rivers, rain, wind, variation in atmospheric pressure and ocean waves). The microtremor record, as each seismic record, is a signal that gives information related to: a) seismic source mechanism, b) attenuation path and c) site conditions of the recording station.

Generally, microtremor data has been used to estimate fundamental frequency of a site in order to identify the site's response during an earthquake. This technique uses the spectral ratio between horizontal and vertical components (H/V ratio) of microtremors (Nogoshi and Igarashi, 1971; Nakamura, 1989). It is known as Nakamura's technique or HVSR method and has been applied in the present paper.

Afterwards, the microtremor records have been processed according to the steps proposed by Mucciarelli (1998) and Duval et al. (2004). In this way, the experimental Horizontal-to-Vertical Spectral Ratio and the fundamental frequency are calculated. Finally, a predominant frequency map is generated which reflects the fundamental characteristics of possible site effects. (Yamanaka et al., 1994; Duval et al., 1995; Field, 1996; Fäh et al., 1997; Ibs-von Seht and Wohlenberg, 1999; Jiménez et al., 2000; Delgado et al., 2000a; Delgado et al., 2000b; Alfaro et al., 2001; Navarro et al., 2001; Duval et al., 2001a,b; Woolery and Street, 2002; Hloupis et al., 2005; Vallianatos and Hloupis, 2008; Sarris et al., 2010; Moisidi et al., 2012; Moisidi et al., 2013).

2.3. Data Acquisition and Analysis

The acquisition of data has been performed using the CITYSHARK II recorder connected to the Lennartz Le3D/5s velocimeter. The CITYSHARK system was developed by the French Institute for Research and Development (IRD) and a local French company (LEAS) for specifically ambient vibration measurements (Chatelain et al., 2000).

Ambient noise measurements have been performed in the city of Mytilene from May 2012 to February 2013. 100 measurements of ambient noise have been conducted throughout the city. The measurements have been carried out from Monday to Friday at hours 23:00-02:30. A global Positioning System (GPS) module localizes the spatial position of each point of measurement (Hatzopoulos, 2008). The sampling rate was set to 200 Hz and the duration of recording 30 minutes. These data are acquired according to guidelines proposed by Duval et al., 2004. The sites of microtremor recordings were selected to cover all different geological formations of the area. Though the HVSR technique is independent of the sources, there are certain criteria that were taken into consideration. Sites very close to heavy traffics were avoided for nearby strong sources that can distort the recordings for the proper recording of ambient noise. Some of these measurements have been repeated to minimize artificial noises due to traffic human activities. Figure 2 shows the locations of measured points in the urban area of town of Mytilene.

The H/V ratios are calculated using the GEOPSY software (www.geopsy.org), for the frequency range 0.2 to 20 Hz, using 40s time windows and removing time windows contaminates by transients. The interpretation of the H/V curve has been carried out conformably to international consensus criteria (Duval et al., 2004). The Fourier amplitude spectra of each selected window are computed. The HVSR relation of Nakamura (1989) is applied for each individual window and the final predominant frequency is obtained.

3. Results and Discussion

Microtremor measurements have been performed in the urban area of the town of Mytilene for a preliminary evaluation of site response. The signals recorded have been analyzed for horizontal to the vertical (H/V) sprectral ratio. The scrutiny of H/V data set allows us to keep only reliable data for mapping resonance frequencies in the city of Mytilene.

The Figure 3 shows the results obtained through the analysis of microtremor. The dotted curves represent the upper and lower bound of 1 standard deviation around the mean spectral ratio,

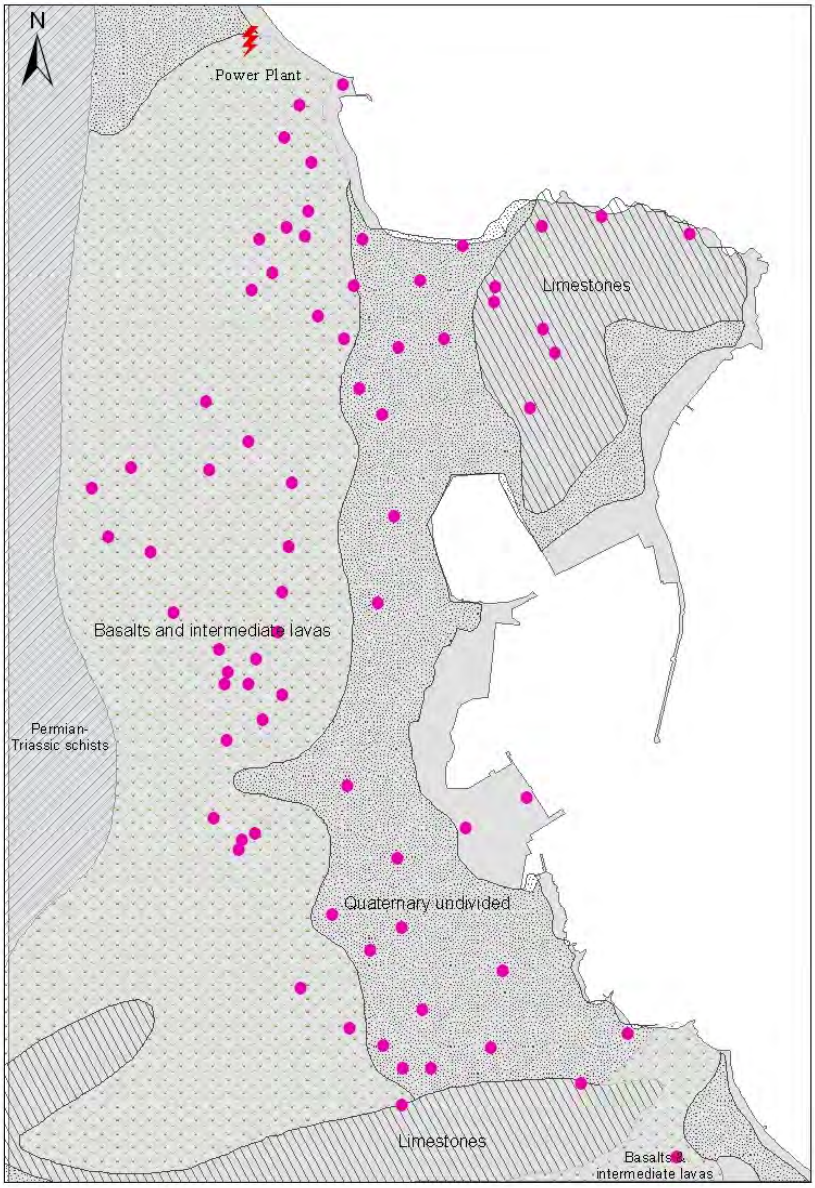

Figure 2 – Position map of microtremor measurements in the urban area of Mytilene.

respectively. Grey vertical bars show the selected H/V peak. The width of the vertical bars denotes the range of the peak frequency.

In order to represent the spatial distribution of the predominant frequency over the urban area of the town of Mytilene, interpolation between the microtremor positions has carried out using the geostatistical technique of nearest neighbour. Figure 4 shows the map of predominant frequency obtained from HVSR technique for the town of Mytilene. Moreover, using the same method of interpolation, the maximum amplification has been determined. Figure 5 represents the amplification factors of the predominant frequencies based on the H/V of the microtremors in investigation sites. The generated maps are managed through a properly developed GIS database (Hatzopoulos, 2008), and are elaborated in laboratory of Remote Sensing and GIS (Department of Environmental Studies, University of the Aegean).

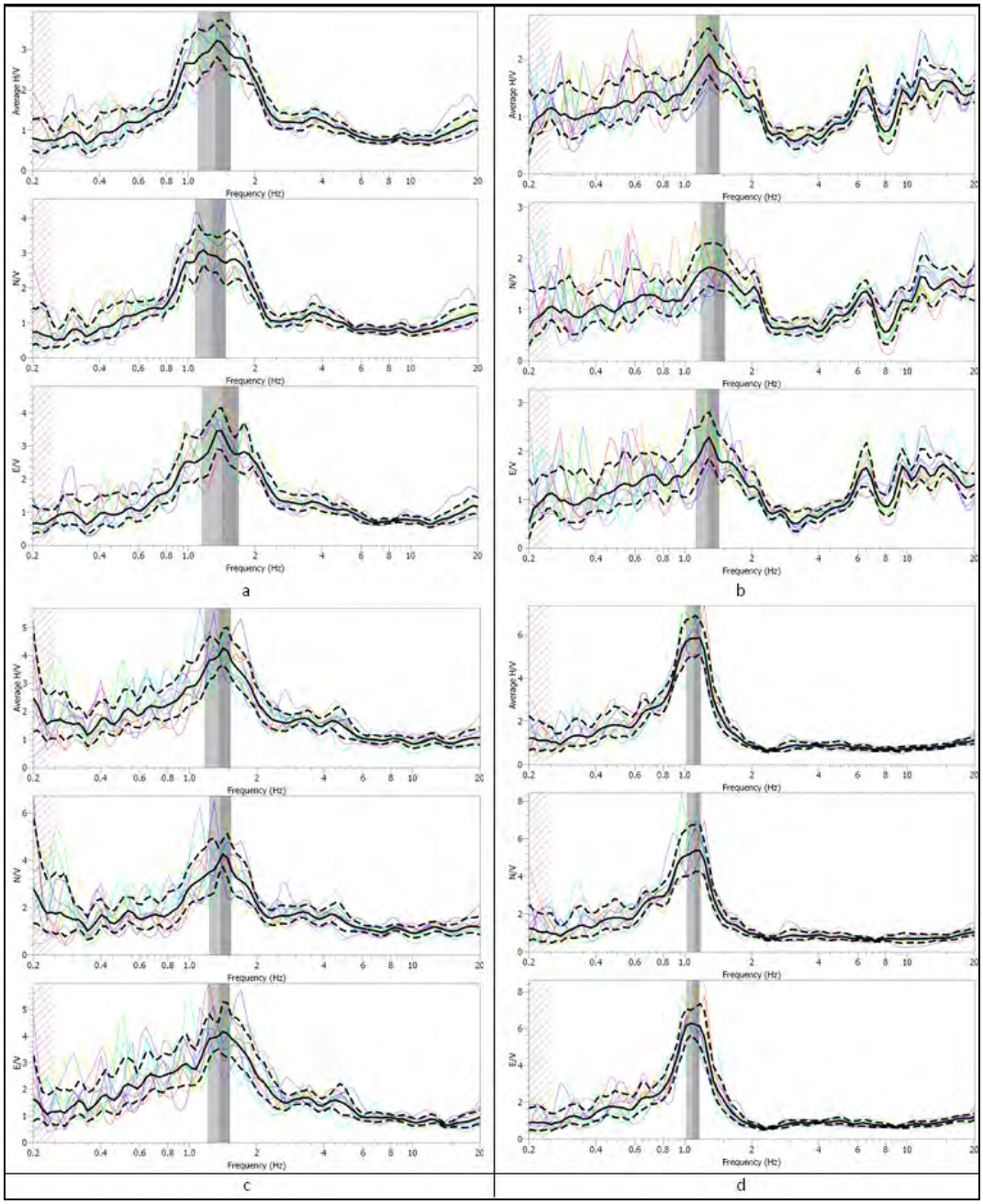

Figure 3 – Responses in sites 2, 11, 40, 89 as presented in Figure 4, 5.

The predominant frequencies ranged from 0.4 to 6.6 Hz. The main reason for such a wide range of results arises from the large differences in the near- surface geological conditions of the region. It is worth noting that there were some of sharp peaks due to an industrial origin (power plant). These peaks have been excluded from the results, and the second peak of natural origin has taken instead. The amplification factor in investigation sites ranges from 0.4 to 8.07.

Consequently, the frequency and amplification distribution maps reflect the geology of the region. The results obtained in the present study can be extended for the seismic hazard studies.

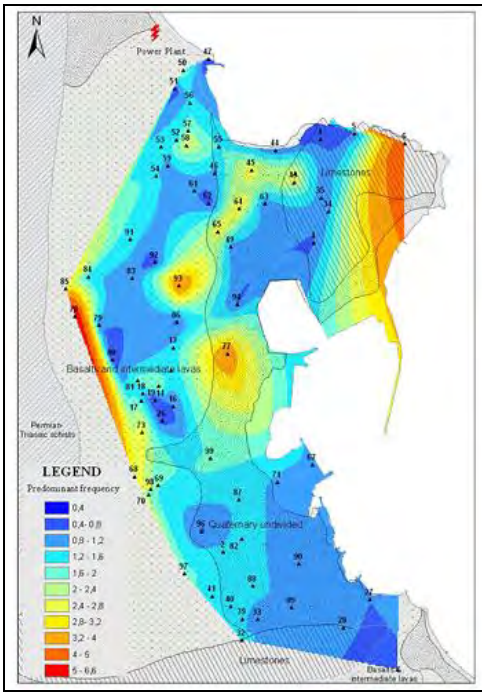

Figure 4 – Map of predominant frequency obtained from HVSR technique for the town of Mytilene.

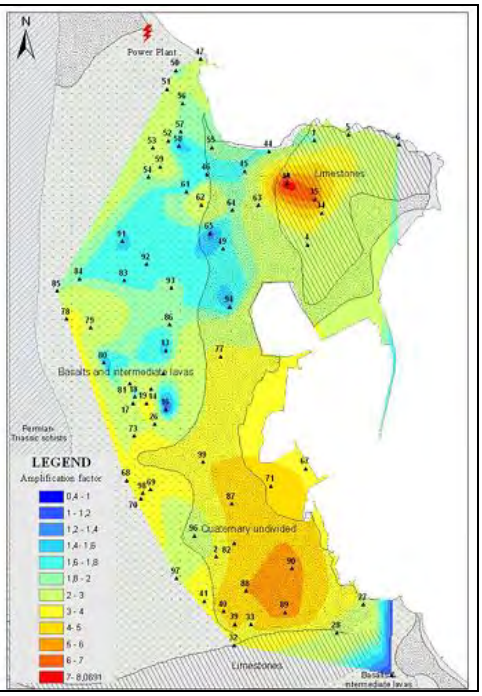

Figure 5 – Map of the H/V amplitude at fundamental frequencies for the town of Mytilene.

4. Conclusions

The microtremor records for the urban area of the town of Mytilene are analyzed for 100 positions. An attempt has been made to interpret variations of microtremor H/V spectral ratios in terms of the local site geology. The main conclusions can be summarized as follows:

The distribution of predominant frequency is relative uniform, ranging from 0.4 – 6.6 Hz, with the frequency value associated with the topographic pattern. Local high observed values are due to the ground surface geology. The amplification factor is ranging from 0.4 to 8.07. Amplification factor values lower than 1.2 are associated with areas where the bedrock appears at the ground surface. In these areas, ground shaking is not amplified. However, some high amplification factor values on NE part located on the limestone owing to possible anthropogenic noise and should be checked.

According to the observations and analysis presented earlier, the characteristics of microtremors are primarily dependent on the type of soils. As a further step, it would be recommendable to improve the spatial distribution of predominant frequency and amplification factor in Quaternary soils through a denser grid of microtremor measurements. Moreover, in the next stage of this research, a comparison of microtremors with the respective earthquake characteristics can be very beneficial and applicable in engineering.

The application of HVSR technique on microtremor measurements in the town of Mytilene showed encouraging results with regard to method potential and applicability. This method is proved very time and cost effective, and easy to implement.

The characteristics of microtremors are found to be mainly dependent on the type of soil deposits. Therefore, the H/V microtremor spectral ratios technique may also represent valuable tool for soil type evaluation in addition to providing a valuable input in urban seismic microzonation and in seismic hazard mitigation.

5. Acknowledgments

Bouranta Evangelia is supported by the Greek State Scholarships Foundation (IKY).

6. References

Alfaro A., Pujades L. G., Goula X., Susagna T., Navarro M., Sanchez J. and Canas A. 2001. Preliminary map of soil's predominant periods in Barcelona using Microtremors, *Pure Appl. Geophys., 158,*. 2499-2511.

Bard P. Y. 1999. Microtremor measurements: a tool for site effect estimation? *Proc. of 2nd International Symposium on the Effect of Surface Geology on Seismic Motion,* Yocohama, Japan, 1251-1279.

Bonnefoy-Claudet S., Cornou C., Bard P.-Y. Cotton F., Moczo P., Kristek J. and Fäh D. 2006a. H/V ratio: a tool for site effects evaluation. Results from 1-D noise simulations, *Geophys. J. Int*., 167, 827-837.

Bonnefoy-Claudet S., Cotton F. and Bard P.-Y. 2006b. The nature of noise wavefield and its applications for site effects studies, A literature review, *Earth.-Sci. Rev*., 79, 205-227.

Chatelain J. L., Guéguen P., Guillier B., Fréchet J., Bondoux F., Serrault J., Sulpice P. and Neuville J.M. 2000. CityShark: A user-friendly instrument dedicated to ambient noise (microtremor) recording for site and building response studies, *Seismological Research Letters*, Vol. 71(6), 698-703.

Delgado J., Lopez Casado C., Giner J., Estevez A., Cuenca A. And Molina S. 2000a. Microtremors as a Geophysical Exploration Tool: Application and Limitations, *Pure and Applied Geophysics*, 158, 2525-2541.

Delgado J., Lopez Casado C., Estevez A., Giner J., Cuenca A. and Molina S. 2000b. Mapping softsoils in the Segura river valley (SE Spain) a case study of microtremors as a e xploration tool, *J. Appl. Geophys., 42*, 19-32.

Duval A.-M., Bard P.-Y., LeBrun B., Lacave-Lacher C., Riepl J. and Hatzfeld D. 2001-b. H/V technique for site response analysis. Synthesis of data from various surveys. *Boull. Geof. Teor. Appl., 42*, 267-281.

Duval A.-M., Bard P.-Y., Meneroud J.-P., and Vidal S. 1995. Usefulness of microtremor measurements for site effects*, Proc. of 10th European Confer., Proc. of Earthquake Engineering,* Vienna, Austria, 521-528.

Duval A.-M., Vidal S., Meneroud J.-P., Singer A., DeSantis F., Ramos C., Romero G., Rodriguez R., Pernia A., Reyes N. and Griman C. 2001-a. Site effect determination with Microtremors, *Pure Appl. Geophys., 158,* Caracas, Venezuela, 2513-2523.

Duval A.-M., Chatelain J.-L., Guillier B. and the SESAME WP02 team. 2004. Influence of experimental conditions on H/V determination using ambient vibrations (noise), *13th World Conf. on Earthq. Engin.*, Paper No. 306.

Fäh D., Ruttener T., Noack T. and Kruspan P. 1997. Microzonation of the City of Basel, *Journal of Seismology 1*, 87-102.

Field E. 1996. Spectral amplification in a sediment-filled valley exhibiting clear basin-edge induced waves, *Bull. Seismol. Soc. Am., 86*, 991-1005.

Field E. and Jacob K. 1993. The theoretical response of sedimentary layers to ambient seismic noise, *Geophysical Research Letters, 20(24),* 2925-2928.

Gosar A. 2007. Microtremor HVSR study for assessing site effects in the Bovec basin (NW Slovenia) related to 1998 M_w56 and 2004 M_w52 earthquakes, *Engineering Geology*, 91, 178-193.

Hatzopoulos J. 2008. *Topographic Mapping*, Universal Publishers, pp. 208, 290.

Hecht J. 1972. Zur Geologie von Sudost Lesbos (Griechenland), *Z. Deutsch Geol.123*, 423-432.

Hecht J. 1974a. Geological map of Greece, 1;50000, *Mithimna sheet*, IGME.

Hecht J. 1974b. Geological map of Greece, 1:50000, *Polychnitos sheet*, IGME.

Hloupis G., Vallianatos F. and Stonham J. 2005. A wavelet representation of HVSR technique, *Bulletin of the Greek Geological Society, 36(3)*, 1269-1278.

Seht M. Ibs-von and Wohlenberg J. 1999. Ambient noise Measurements used to map thickness of soft sediments, *Bull. Seismol. Soc. Am., 89*, 250-259.

Jimenez M. J., Garcia-Fernandez M., Zonno G. and Cella F. 2000. Mapping Soil Effects in Barcelona, Spain, Through an Integrated GIS Environment, *Soil Dynamics and Earthquake Engineering, 19*, 289-301.

Katsikatsos G., Mataragas D., Migiros G. and Triantaphyllis E. 1982. Geological study of Lesvos Island*. IGME (interna report),* Athens.

Katsikatsos G. Migiros G., Triantaphyllis M. and Mettos A. 1986. Geological structure of internal Hellenides (E. Thessaly – SW. Macedonia, Euboea – Attica – Northern Cyclades islands and Lesvos, *IGME. Geol. & Geoph. Res. Special Issue*, 191-212.

Moisidi M., Vallianatos F., Soupios P. and Kershaw S. 2012. Spatial spectral variations of microtremors and electrical resistivity tomography surveys for fault determination in southwestern Crete, Greece, *J. Geophys. Eng. 9*, 261-270.

Moisidi M., Vallianatos F., Soupios P., Kershaw S., Rust D. and Piscitelli S. 2013. Modeling tectonic features of the Kissamos and Paleohora areas, Western Crete (Greece): combining geological and geophysical surveys, *J. Geophys. Eng., 10 025015* doi:10.1088/1742-2132/10/2/025015.

Mucciarelli M. 1998. Reliability and Applicability of Nakamura's technique using Microtremors: An experimental approach, *J. Earthq. Eng., 2*, 625-638.

Nakamura Y. 1989. A method for Dynamic Characteristics Estimation of Subsurface using Microtremor on the Ground Surface, *Quarterly Report of Railway Technical Research Institute (RTRI), vol. 30*, No. 1.

Nakamura Y. 1997. Seismic Vulnerability Indices For Ground and Structures Using Microtremor, *World Congress on Railway Research in Florence*, Italy, November 1997.

Navarro M., Enomoto T., Sanchez F. J., Matsuda I., Iwatate T., Posadas A. M., Luzon F. and Seo K. 2001. Surface soil effects study using short-period Microtremors observations in Almeria City, Southern Spain, *Pure Appl. Geophys., 158*, pp. 2481-2497.

Nogoshi M. and Igarashi T. 1971. On the Amplitude Characteristics of Microtremor (Part 2) (in Japanese with English abstract), *Jour. Seism. Soc. Japan, 24*, pp. 26-40.

Papazachos B. and Papazachou K. 1997. *Earthquakes of Greece*, Ziti editions (new edition*).* Thessaloniki, Greece.

Pe-Piper G. and Piper D.J.W. 1993. Revised stratigraphy of the Miocene volcanic rocks of Lesvos, Greece, *Neues Jahrbuch Geologie und Palaeontologie Munchen*, 2, 97-110.

Pe-Piper G. 1978. Cainozoic Volcanic Rocks of Lesvos Island, *Ph.D. Thesis,* University of Patras, 365p.

Sarris A., Loupasakis C., Soupios P., Trigkas V., Vallianatos F. 2010. Earthquake vulnerability and seismic risk assessment of urban areas in high seismic regions: application to Chania City, Crete Island, Greece, *Nat. Hazards, 54*, 395-412.

Soulakellis N., Novak I., Zouros N., Lowman P. and Yates J. 2006. Fusing Landsat-5/TM Imagery and Shaded Relief maps in Tectonic and Geomorphic Mapping: Lesvos Island, Greece, *Photogrammetric Engineering and Remote Sensing,*72(6), 693-700.

Woolery E. W. and Street R. 2002. 3D near-surface soil response from H/V ambient-noise ratios, *Soil Dyn. Earthq. Eng., 22,* 865-876.

Vallianatos F. and Hloupis G. 2008. HVSR Technique Improvement Using Redundant Wavelet Transform *in Increasing Seismic Safety by Combining Engineering Technologies and Seismological Data, NATO Science for Peace and Security Series C: Environmental Security ISSN1874-6519*, Spinger Netherlands.

Yamanaka H., Takemura M., Ishida H. and Niwa M. 1994. Characteristics of Long-Period microtremors and their applicability in exploration of deep sediments, *Bull. Seismol. Soc. Am., 84,* 1831-1841.

Δελτίο της Ελληνικής Γεωλογικής Εταιρίας, τομ. XLVII , 2013
Πρακτικά 13ου Διεθνούς Συνεδρίου, Χανιά, Σεπτ. 2013

Bulletin of the Geological Society of Greece, vol. XLVII 2013
Proceedings of the 13th International Congress, Chania, Sept. 2013

RESISTIVITY INVESTIGATION FOR WELL-SITE DEFINITION AROUND BARIKA VILLAGE, SOUTHEAST SULAIMANY CITY IRAQI KURDISTAN REGION

Ghaib F.A.[1], Abdulla H.[2] and Anwar H.[3]

[1]*Salahaddin University, College of Science, Department of Geology, Erbil-Iraq, f_ghaib@yahoo.com.*

[2]*Qandeel Swedish Organization, Erbil-Iraq*

[3]*Salahaddin University, College of Science, Department of Geology, Erbil-Iraq, f_ghaib@yahoo.com.*

Abstract

An electrical resistivity survey involving Vertical Electrical Soundings (VES) was carried out in the Barika collective village, southeast of Sulaimany City in the Iraqi Kurdistan Region, to study groundwater characteristics such as depth, thickness and aquifer boundaries. Vertical electrical soundings by Schlumberger array were conducted in this area. The resistivity Schlumberger soundings which have a maximum current electrode spacing (AB) of 800m were carried out at fourteen sites along lines in the NE-SW and NW-SE directions. Interpretation of these soundings showed the presence of three geo-electrical horizons. The upper one is representing the alluvial deposits with 3Ωm to 60Ωm range of resistivity values reflecting the heterogeneity of the slope deposits. The middle one is taken to be the unconfined jointed aquifer represented by the Tanjero Formation with a resistivity range of 10Ωm to 42Ωm and a thickness range of 24m to 106m. The third horizon is representing the lower part of the Tanjero Formation with a relatively high resistivity range of 51Ωm to 556Ωm. Based on these results and upon our recommendations, a successful water well was drilled yielding quite enough amount of fresh water.

Keywords: *Arbat, Iraq, resistivity, water.*

1. Introduction

The area of investigation is located about 20 km to the southeast of Sulaimany City at the cross of latitude 35°22'25"N longitude 45°36'25"E covering an area of about 19 km^2 (Figure 1). Barika village lacks sufficient surface and subsurface sources for water and devoid of springs and permanent streams. The villagers used to depend upon some shallow hand dug wells which may dry in summer during some years. Type of groundwater in the whole surrounding area is fresh. Among many wells drilled around the village during the last few years, one was yielding considerable amount of water. The present study aims to locate the best site/s to drill more wells in view of the population growth of the village. It aims to give the recommended depth and type of water.

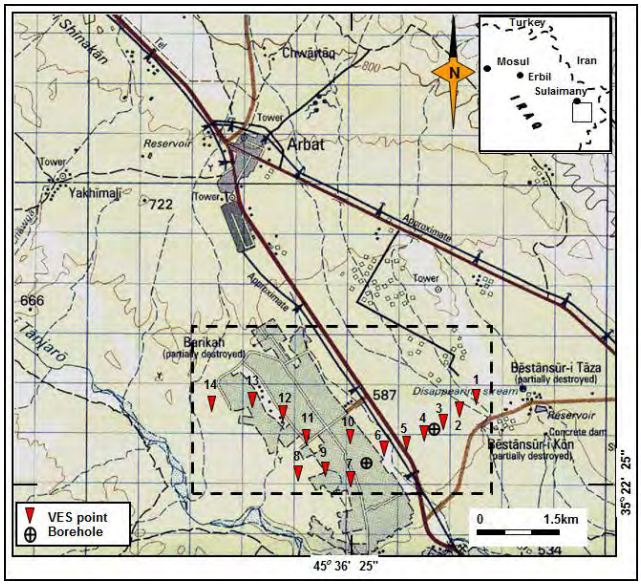

Figure 1 - Topographic map showing Barika collective village.

2. The Resistivity Method

The resistivity method involves measuring the electrical resistivity of earth materials, by introducing an electrical current into the ground and monitoring the potential field developed by the current. In most earth materials, electricity is conducted electrolytically by the interstitial fluid. The resistivity is controlled mostly by porosity, water content and water quality than by the resistivities of the matrix (Ayer, 1989). The main target is identification of the horizontal and vertical variations in lithology, which might lead to more structural information about the subsurface. The electrical resistivity is the resistance offered by the opposite faces of a unit cube of material to direct current. In geophysical literature the unit of resistivity is taken as the Ω.meter. The resistance (R) of the material having a resistivity (ρ) over a length (L) and surface area of current flow (A) is given by [$R = \rho (L/A)$]. This is governed by ohm's law. The inverse of resistance is called conductance. The resistivity of the geological formation is generally very high under dry conditions and decreases in clayey rock. The presence of water containing salt even in minor amounts makes them relatively conductive and as the moisture increases the resistivity falls considerably. As the salinity of water increases the resistivity of the rock formation decreases.

The vertical electrical sounding (VES) has been chosen for this study. The method has been proven to be an effective mean of solving groundwater problems (Mbonu *et. al.*, 1991, and Ghaib, F. 2009).

3. Geomorphology and Hydrology of the Study Area

The study area is located hydrologically within the Arbat sub-basin which is one of four sub-basins of the main Sharazor basin (Ali, 2008). The Barika village is located within a hilly terrain. All the surface runoff and the groundwater discharge of this sub-basin are drained exclusively to the Darbandikhan reservoir by the Tanjero stream some 10 kms to the south of Arbat town. Almost all the studied area consists of gently sloping plain which now makes up the main cultivation land in the sub-basin.

The basin boundary at the north, northeast, south and southwest are bounded by the summits of Goizha, Barda Kar, Baranan and Bakir Agha mountains (or anticline) respectively. Some hills are also present. They are formed due to the differential erosion of the surface rock types of sand and clay.

The climate of the studied area as is the case in the northern Iraq is characterized by clear seasonal differences, caused mainly by the change in the type of atmospheric circulation during the year, and by the intensity of the insulation It is generally classified as moist type, and from the metrological data, the area shows seasonal variation between cold, rainy, humid, low evaporation and low vapor pressure in winter months (January, February and March) and hot, low humidity, high vapor pressure and high evaporation rate in summer months (June, July and August), (Ali, Op. Cit.)

4. General Geology of the Area

The study area is covered by agricultural recent sediments with no signs about the underlying formations (Figure 2). However, a general reconnaissance revealed that the expected underlying rock unit is Tanjero Formation. This formation is composed of khaki to olive green sandstone, claystone, shale and occasionally conglomerate. These inter-bedded lithologies have no regular pattern in their distributions which makes direct interpretation of their subsurface positions unpredictable. In view of the general geology of the area, Tanjero Formation should be underlain by the Shiranish Formation which is composed of alternating marl and marly limestone. Shiranish Formation is expectedly underlain by the Komitan Formation which makes up the anticline situated to the northeast of Barika village area. Scattered exposures of compacted sandstone are present to the southwest of the village. They are believed to be remnants of the Tanjero Formation (Buday and Jassim, 1987).

5. Fieldwork

Vertical Electrical Sounding (VES) technique is the best resistivity way in investigations for water well sites. Here, a series of measurements of resistivity are made by increasing the electrode spacing in successive steps about a fixed point. This method of vertical exploration is known as the expanding electrode method, resistivity sounding or depth probing or vertical electrical sounding (VES). The apparent resistivity values obtained with increasing values of electrode separation are used to estimate the thickness and resistivities of the subsurface formations. VES is mainly employed in groundwater exploration to determine the disposition of the aquifers (Ahilan and Senthil Kumar, 2011)

Among many electrode spreading configurations, the Schlumberger method is more suitable. In this method the four electrodes are kept in a line with the outer electrode spacing kept large compared to inner electrode spacing usually by more than five times. For each measurement only the current electrodes are moved keeping the potential electrodes at the same locations. The potential electrodes are moved only when the signal become too weak to be measured.

This method was used in this study to collect the data in fourteen sites along lines in the NE-SW and NW-SE directions (Figure 1). The used maximum electrode spread in the NW-SE direction is 400 m on each side of the center-point. SAS300 Tetrameter present in Qandil Organization (Erbil) was used to collect the resistivity data which were of good quality while the coordinates of the investigation sites were measured by Global Positioning System (GPS-Garmen).

6. Sounding Curve and Interpretation

The basic interpretation of field curve for apparent resistivity is a correlation with a master curve and auxiliary curves, and through that the real resistivity and thickness of subsurface layers are calculated.

There are several methods for interpreting the field curve such as a complete curve matching and auxiliary point, in addition to some computer programs used for this purpose such as the commercial program IPI2WIN as shown in Figure (3). The VES curves were obtained by plotting the apparent resistivity against electrode spacing. The resistivity for each of the vertical electrical sounding was drawn on transparent double log graph paper.

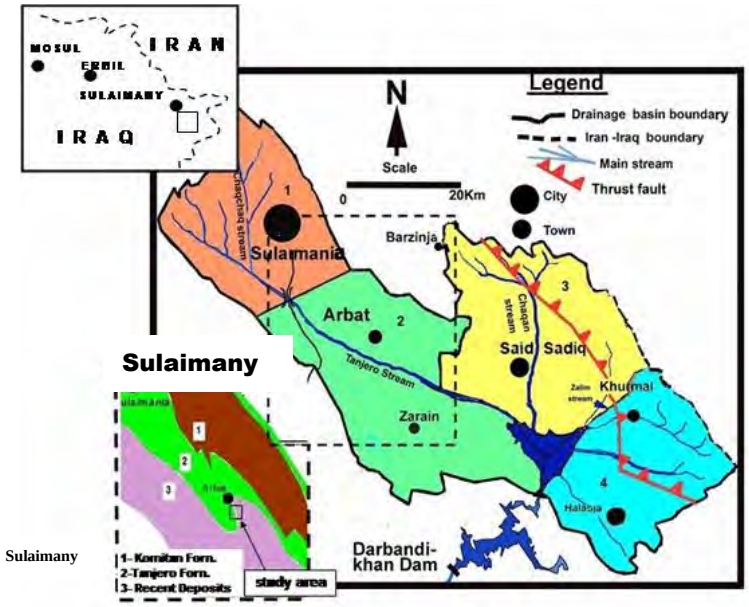

Figure 2 - A simplified geologic map of the study area relative to the hydrological basins.

7. Geo-electric Sections

The VES curves which are the plot of apparent resistivities collected in the field against AB/2 have been prepared by IPI2 Win software Program in order to estimate the true resistivities of different horizons and their thickness. Some examples are shown in Figure 3.

Geo-electrical sections show the vertical distribution of resistivities within a particular volume of the earth. The section consists of a sequence of uniform horizontal or slightly inclined layers (electrical horizons). The layers true resistivity is noted on each one for each VES sounding. After that several sections for VES points on a certain traverse can be linked together to show a cross sectional view of the traverse. Each layer (horizon) in a geo-electrical section may completely be characterized by its thickness and true resistivity. For the purpose of constructing geo-electrical sections, the VES points were grouped to three traverses (Figures 4, 5 and 6).

7.1. Traverse 1

This traverse extends in the NE-SW direction and involves six VES points (VES-1 to VES-6). All points are located on recent sediments (Fig. 4). The geo-electrical section shows three main horizons, they are:

(Z1) It is exhibited in all VES points along the traverse and is characterized by resistivity values ranging from 5.48 Ω.m at VES-5 and 52 Ω.m at VES-6. It has a maximum thickness of about 32 m below the VES-4, under which a relatively high resistivity lens is being revealed. The thickness is

decreasing to reach 4 m below the VES-3. Within this horizon, several horizontal and vertical lithological variations are present. This horizon is believed to consist of clayey soil having generally low resistivity values in some locations and a high resistivity values when gravel and sands are present such as under VES-6 and 3.

(Z2) It has a thickness of about 84.6 m underneath the VES-6, decreasing to about 37.6 m beneath the VES-1. The average thickness is about 63.93 m. Its resistivity varies from 16.5 Ω.m below VES-3 to 41.7 Ω.m below VES-1. This horizon is expected to be rich in gravel, sand and clay. It belongs to the upper part of Tanjero Formation.

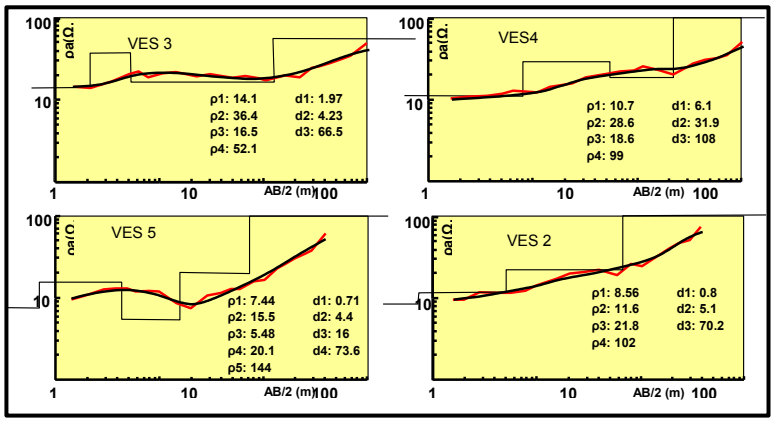

Figure 3 - Examples of Some Sounding Curves and interpretations.

(Z3) It most probably represents the Tanjero Formation which is expected to be composed of marl and marly limestone. The depth of this horizon is ranging from 57 m to 99 m below VES-1and 6, respectively. Resistivity has a minimum value of 52 Ω.m beneath VES-3 and a maximum value of 556 Ω.m beneath VES-1. In this horizon the ratio of the resistivity value has increased relatively to the second horizon. The lower boundary of this horizon is not defined in this survey.

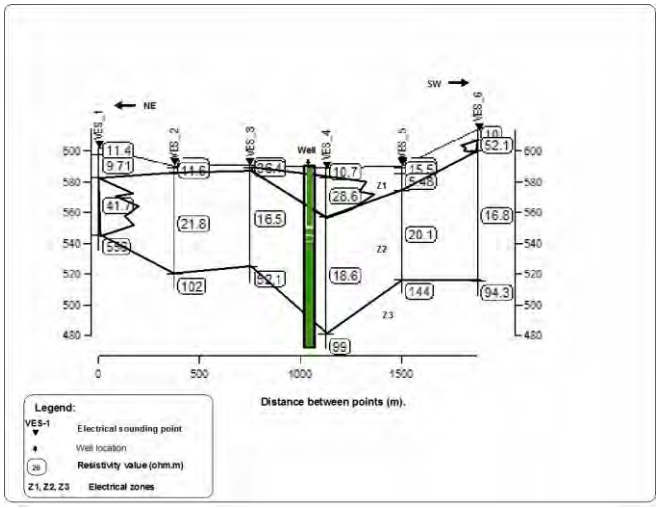

Figure 4 - Geo-electrical section along traverse 1.

7.2- Traverse 2

It involved six VES points (VES-7 through VES-14) which extends in the NW-SE bending to E-W along VES-13 and 14. The geo-electrical section shows three main horizons (Fig. 5), they are:

(Z1) It has a thickness of about 10.7 m that decreases to 0.75 m below VES-13 with an average thickness of 6.08 m. The resistivity values of this horizon range from 3.19 Ω.m to 46.9 Ω.m. Within this horizon, a vertical lithological variation is present beneath VES-11 which possibly represents the top soil, sand and gravel sediments that belong to Quaternary deposits.

Z2: It is characterized by resistivity values ranging from 13 Ω.m below VES-13 to 28 Ω.m below VES-7, averaging 22 Ω.m. The resistivity value is generally decreasing in the SE direction which is referred to the increase of sand, silt and clay materials. The maximum thickness of this horizon is about 106 m which is observed beneath VES-9, while the minimum thickness is about 24 m which is observed beneath VES-11. It is believed to represent the Tanjero Formation again.

Z3: The resistivity value of this horizon is ranging from 51 Ω.m below VES-14 to 114 Ω.m below VES-7, with an average value of 22 Ω.m.

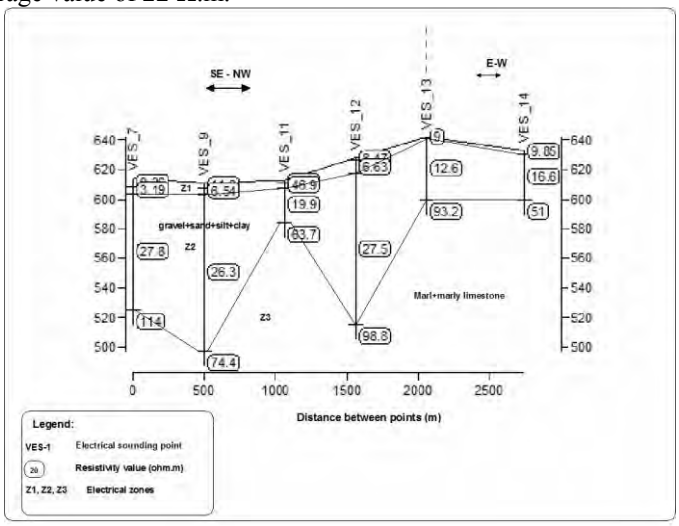

Figure 5 - Geo-electrical section along traverse 2.

7.3- Traverse 3

This section involves three points (VES-8, VES-9 and VES-10). The geo-electrical section shows three horizons:

(Z1) the resistivity values of this horizon vary from 6.5 Ω.m to 60 Ω.m, with an average of 20 Ω.m The average thickness is about 8 m; the maximum thickness is more than 9 m below VES-10, while the minimum thickness is more than 6 m below the VES-8. The horizon comprises alluvial deposits represented by clay, silt and gravel.

(Z2) It represents the upper part of the Tanjero Formation in the study area. It has a thickness of about 60 m below VES-8 increasing to 106 m below VES-9 with an average of about 83. The maximum resistivity values is 32 Ω.m. which is observed beneath VES-8 and a minimum resistivity values of 10 Ω.m. which is observed below VES-10, giving an average of about 24 Ω.m It is composed of gravel, sand, silt and clay materials.

(Z3) It mostly represents the marl and marly limestone of the the Tanjero Formation. The depth of this horizon is ranging from 67 m to 114 m and has a resistivity value of about 74 Ω.m beneath VES-9 increasing to 357 Ω.m below VES-10.

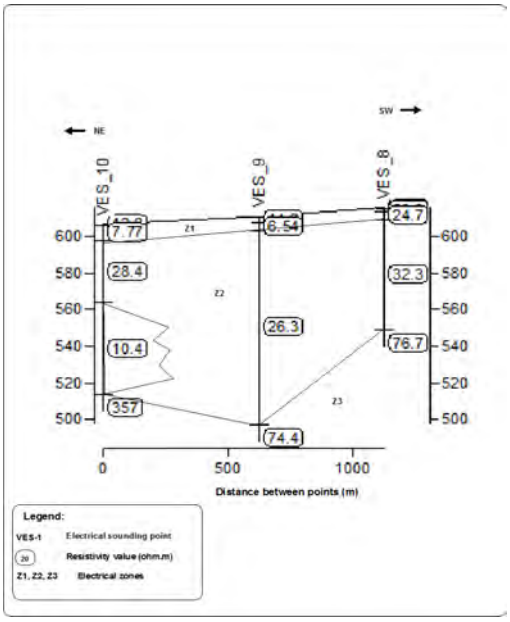

Figure 6 - Geo-electrical section along traverse 3.

8. Apparent Resistivity Maps

These maps are constructed by plotting the apparent resistivity value at each VES point for individually half distance current electrode (AB/2) and drawing the contour lines for similar values. Four apparent resistivity maps for (AB/2= 80m, 100m, 140m, 200m) were constructed (Figures 6 and 7).

These maps show the following:

1- Two prominent anomalies, one positive and the other negative that appear in all maps. The negative one appears at almost the same spacial location at maps AB/2 = 80 m and 100 m (Fig. 6), while is shifted towards southeast and east in the other two maps (i.e. AB/2 = 140 and 200m (Figure 7).

2- The negative anomaly on the other hand is shifted towards southeast in maps AB/2 = 100 m, 140 m and 200 m with respect to the map AB/2 = 80 m.

3- Both anomalies are shifted towards east and southeast.

4- The resistivity values generally increase with the increase in the value of AB/2.

5- The resistivity values are increased toward SE direction.

9. Results

The description of the present aquifer in the area comes only from the resistivity sounding interpretation results given in the form of geo-electrical sections (Figures 3, 4 and 5). All sections show the presence of three horizons. The upper one is representing the alluvial deposits with a broad

range of resistivity values reflecting the heterogeneity of the slope deposits. The middle one is taken to be the unconfined jointed aquifer. It is the Tanjero Formation which is composed of jointed sandstone, claystone, marl and some conglomerates. This was approved later on by the drilling of the recommended water well. The drilling site on the ground was recommended by the present authors after drawing the geo-electrical sections.
The potentiality of yielding water for a certain well depends upon the topography of the bedrock (i.e. underneath the aquifer) in addition to the lithological characteristics of the aquifer itself. In our case the lower boundary of the Tanjero Formation is taken as bedrock.

As a principle, depressions within the bedrock are the best sites for accumulating water hence are best sites for drilling. Davis and DeWieste (1976) stated such a situation (Fig. 8).

Few months after carrying out the fieldwork and submitting our recommendation, a water well sponsored by the same Swedish Organization was drilled. The recommended site was between the VES-3 and VES-4 (Fig. 4). It yielded more than 90 Gallon/minute when tested. This amount is quite enough for the present population of the village for domestic uses.

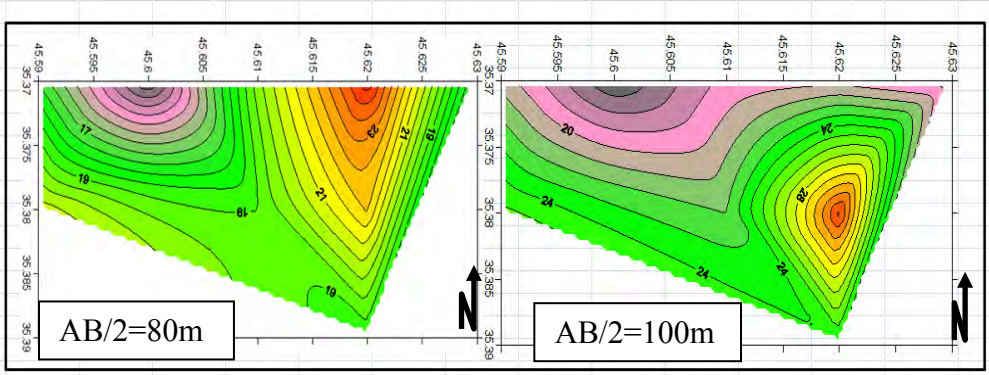

Figure 6 - Apparent resistivity map for AB/2 equal to 80 and 100m.

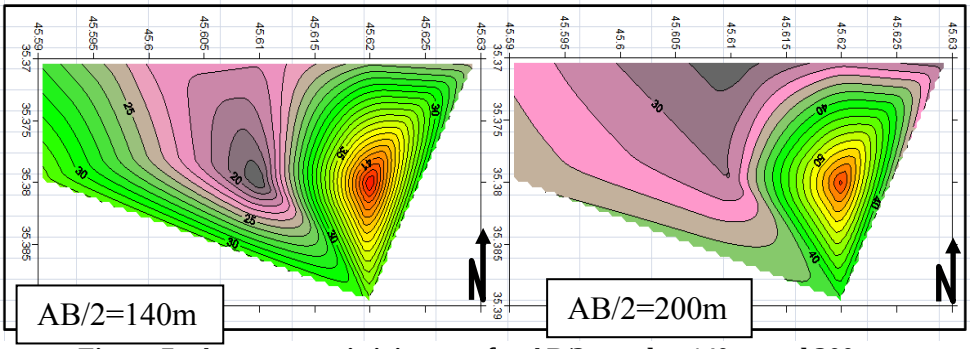

Figure 7 - Apparent resistivity map for AB/2 equal to 140 m and 200 m.

10. Conclusions

1- The subsurface is divided into three electrical horizons having different resistivity values and thicknesses.

2- The thickness of the uppermost recent deposit horizon that covers the Tanjero Formation was found to be between 0.75m and 32 m through the studied area. This horizon has resistivities ranging from 3 Ω.m to 60 Ω.m.

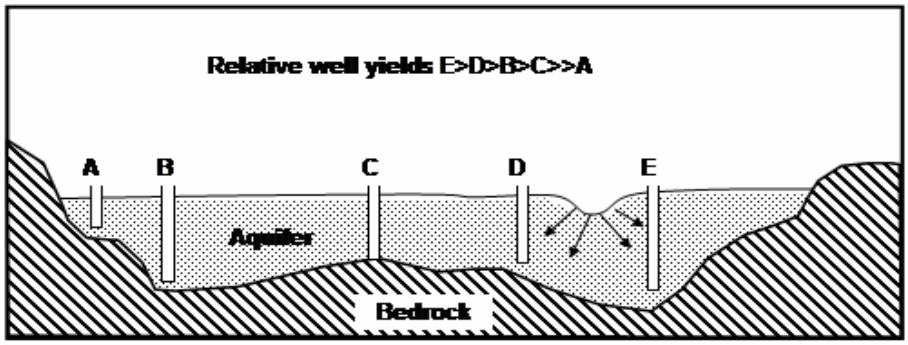

Figure 8 - Hypothetical cross section of a valley showing the effects of aquifer thickness and hydrogeologic boundaries on well yield (Davis and DeWiest, 1976).

3- The thickness of the second lower horizon ranges from 24 m to 106 m. with resistivity values ranging from 10 Ω.m to 42 Ω.m with an average value of 24 Ω.m which is a consistent value of holding water according to personal experience.

4- The third horizon is believed to represent the lower marly and marly limestone part of the Tanjero Formation with a relatively high value of resistivity ranging from 51 Ω.m to 55 6Ω.m with an average value of 201 Ω.m.

5- According to the authors recommendation a successful water well was drilled to yield quiet enough amount of water within the distance between the VES's 3 and 4.

11. Acknowledgements

The field data of this study was originally used for the assessment of the groundwater situation by the Swedish Qendeel NGO, Erbil. The present paper was prepared and published by their permission for which we are thankful.

12. References

Ali S.S. 2007. Geology and hydrogeology of Sharazoor-Piramagroon Basin in Sulaimai Area, Northeastern Iraq, *Unpublished Ph.D. Thesis*, University of Belgrade, Serbia.

Ayer J.F. 1989. Conjunctive use of geophysical and geological data in the study of an alluvial aquifer, *Groundwater*, 27 (5), 625-632.

Buday T. and Jassim S.Z. 1987. The regional geology of Iraq: Tectonism, Magmatism and Metamorphism, Vol.2, *D.G. of Geologic Survey and Mineral Investigation*, Baghdad, Iraq, 352 pp.

Davis S.N. and DeWiest R.J.M. 1976. *Hydrogeology*, John Wiley and Sons, U.S.A., 463 pp.

Ghaib F.A. 2009. The Assessment of Erbil Aquifer Using Geo-electrical Investigation (Iraqi Kurdistan Region), *Journal of Applied Sciences in Environmental Sanitation*, 4 (1), 43-54.

Jassim S.Z. and Goff J.C. 2006. Geology of Iraq, First Edition, Prague and Moravian, Zelnytrh 6, Brno, Czeck Republic, 245pp.

Mbonu P.D.C., Ebeniro J.O., Ofoegbu C.O. and Ekine A.S. 1991. Geoelectric sounding for determination of aquifer characteristics in parts of the Umuahia area of Nigeria, *Geophysics*, 56, 284-291.

Δελτίο της Ελληνικής Γεωλογικής Εταιρίας, τομ. XLVII , 2013
Πρακτικά 13ου Διεθνούς Συνεδρίου, Χανιά, Σεπτ. 2013

Bulletin of the Geological Society of Greece, vol. XLVII 2013
Proceedings of the 13th International Congress, Chania, Sept. 2013

STOCHASTIC ANALYSIS OF EARTHQUAKE ACTIVITY IN TWO SEISMOGENIC FAULT SYSTEMS IN GREECE

Gkarlaouni Ch.[1], Papadimitriou E.[1], Lasocki S.[2], Lizurek G.[2], Karakostas V.[1] and Kilias A.[3]

[1] *Geophysics Department, School of Geology, Faculty of Exact Sciences, Aristotle University of Thessaloniki, GR54124, Thessaloniki, Greece*

[2]*Institute of Geophysics, Polish Academy of Sciences, Księcia Janusza 64,*

01452, Warsaw, Poland

[3] *Geology Department, School of Geology, Faculty of Exact Sciences, Aristotle University of Thessaloniki, GR54124, Thessaloniki, Greece*

Abstract

Possible systematic variations in earthquake occurrence and fluctuations in seismicity behaviourof two seismically active regions in Greece which share common seismotectonic properties, is the aim of this study. Mygdonia graben in northern Greeceis characterized by arather moderate background seismicity, with small earthquakes between 2008-2012 whereas Corinth Gulf in southern Greece exhibits a constantly high seismicity rate with several seismic activations during the recent instrumental period or before. The statistical approach of seismicity was accomplished, regardingthe magnitude, the inter-event time and distance for recent seismicity as a tool to quantify complex earthquake occurrence ordense spatial and temporal clustering. For this reason, complete catalogues were compiled for the time period of the study. Probabilistic tests such as the smoothed bootstrap test for modality and bump–hunt were employed in order to unveil the complexity of the probability density function distribution of the above parameters. On the other hand spatial earthquake distribution wasalso investigated under the frameof their fractal properties since the fractal coefficientcan largely express the clustering degree of seismicity. The goal of this stochasticanalysisis the quantification of the differentiationin seismicity propertiesinthese two important seismogenic normal fault populations in the back arc Aegean area.
Keywords:*Seismicity, complexity, fault basins.*

Περίληψη

Οι πιθανές συστηματικές διαφοροποιήσεις στη γένεση σεισμών καιοι διακυμάνσεις στη σεισμική συμπεριφορά δύο ενεργών περιοχών της Ελλάδας, αποτελούν το σκοπό αυτής της εργασίας. Η λεκάνη της Μυγδονίας στη Β. Ελλάδα, χαρακτηρίζεται από σεισμική ηρεμία κατά το χρονικό διάστημα 2008-2012, ενώ η λεκάνη του Κορινθιακού κόλπου στη Ν. Ελλάδα παρουσιάζει σταθερά υψηλό ρυθμό σεισμικότητας με συχνές σεισμικές εξάρσεις κατά την ενόργανη σεισμολογική περίοδο, η οποία εξετάζεται στην παρούσα εργασία και πριν. Η στατιστική ανάλυση της

σεισμικότητας αφορά τη μελέτη τουμεγέθους, τουενδιάμεσου χρόνου και της απόστασης μεταξύ διαδοχικών σεισμών, χρησιμοποιώντας τα κατάλληλα εργαλεία προκειμένου να ποσοτικοποιηθείο βαθμός πολυπλοκότητας της σεισμικότητας καθώς και η ισχυρή ομαδοποίηση των σεισμών στο χώρο και στο χρόνο. Για τον λόγο αυτό, κατασκευάστηκαν πλήρεις κατάλογοι σεισμικότητας για τις δύο περιοχές και για τοχρονικό διάστημα 2000-2012. Χρησιμοποιήθηκαν στοχαστικέςδοκιμές όπως η δοκιμή της πολυτροπικότητας και η ομαλοποιημένη δοκιμήBootstrap, χρησιμοποιήθηκαν ώστε να αποκαλυφτεί η πολυπλοκότητα την οποία παρουσιάζει η κατανομή της συνάρτησης πυκνότητας των παραπάνω παραμέτρων. Μελετήθηκαν οι κλασματικές ιδιότητες της σεισμικότητας στο χώρο, δεδομένου ότι ο κλασματικός συντελεστής εκφράζει τον βαθμό αυξημένης συγκέντρωσης.Ο σκοπός αυτής τηςστοχαστικής ανάλυσηςαποτελεί η ανάδειξη και ποσοτικοποίηση τωνδιαφορετικώνιδιοτήτων σεισμικότητας των δύο σημαντικών πληθυσμών κανονικών ρηγμάτων στην οπισθότοξη περιοχή του Αιγαίου.
Λέξεις κλειδιά:*Σεισμικότητα, πολυπλοκότητα, ενεργές τεκτονικές λεκάνες.*

1. Introduction

Intensive researchwork has been conducted on the development of stochastic tools which among others investigatethesystematic properties of earthquake occurrence associated with the spatial, temporal and magnitude distribution of regional seismicity (e.g. Ogata, 1988; 1998; Console et al., 2006).Thisapproachis widely accepted and applied because of the urgent need to fully exploit all the available information and develop hypotheses on the systematics which govern seismicity processes at all scales, like clustering which is expressed as the dense occurrence of earthquakes and triggering between them.The stochastic approach of seismicity also reveals additional implications about the seismic behaviourof the causative fault systems which preferably prevail in each seismotectonic setting. The concern about seismicity systematics and their complicated behaviour stemmed from Omori law which expressed the time decay of aftershocks in time (Omori, 1894) and it was supplemented by the Gutenberg–Richter relation (Gutenberg and Richter, 1944) considering the frequency-magnitude distribution. Further modifications about G-R scaling law were proposed by Utsu(1999) whereasits temporal descriptionwasintroduced byBak et al.(2002). However, in each case, this analysis is susceptible to a variance of factors such as the seismotectonic framework of the study area,the seismologicalinstrumentation, the homogeneity and consistency of the seismic catalogue as well as the time period that the data refer to, and all of them enforce their impact on theresearch outcome.In our case, magnitude, time and space distribution, for two independent seismogenic zones located in the Greek mainland, Mygdonia basin (in Northern Greece) and Corinth Gulf (in Central Greece) bothsharing common seismotectonic properties and strong seismicity are investigated regardingtheir seismicity properties, such as the degree of clustering and complexity under the stochastic framework. In particular, the magnitude distribution of earthquakes as well as the lapse and the inter-event distance for consecutive pairs of earthquakes are investigated, taking into account the distribution of probability density function (PDF) of these parameters. The obtained results will provide a further insight into the seismicity behaviour in each case andwill be evaluated.

2. Seismotectonic Setting

The two study areas(Figure 1a), are located in the Greek mainland where strong extensional forces driven by the relative movement of microplates such asthe subduction and rolling-back of the eastern Meditterranean oceanic microplate along the South Hellenic Arc have given birth to the formation of numerous back – arc neotectonic basins, oriented perpendicular to the extensional stress axis. Geodetic and other measurements show that the deformation rate in the back-arc area,

varies in space, therefore northern regions where Mygdonia region belongs (Figure 1b) demonstrate a reduced rate of deformation with rates equal to 1mm/year (Kotzev et al., 2001) compared to the fast moving southern Aegean zone and the Corinth Gulf (Figure 1c) where extension dominates with rates equal to 1cm/y (Briole et al., 1993). However, important processes of fault nucleation and seismogenesis are taking place in both areas where North – South extension definesthe dominant pattern of active deformation.

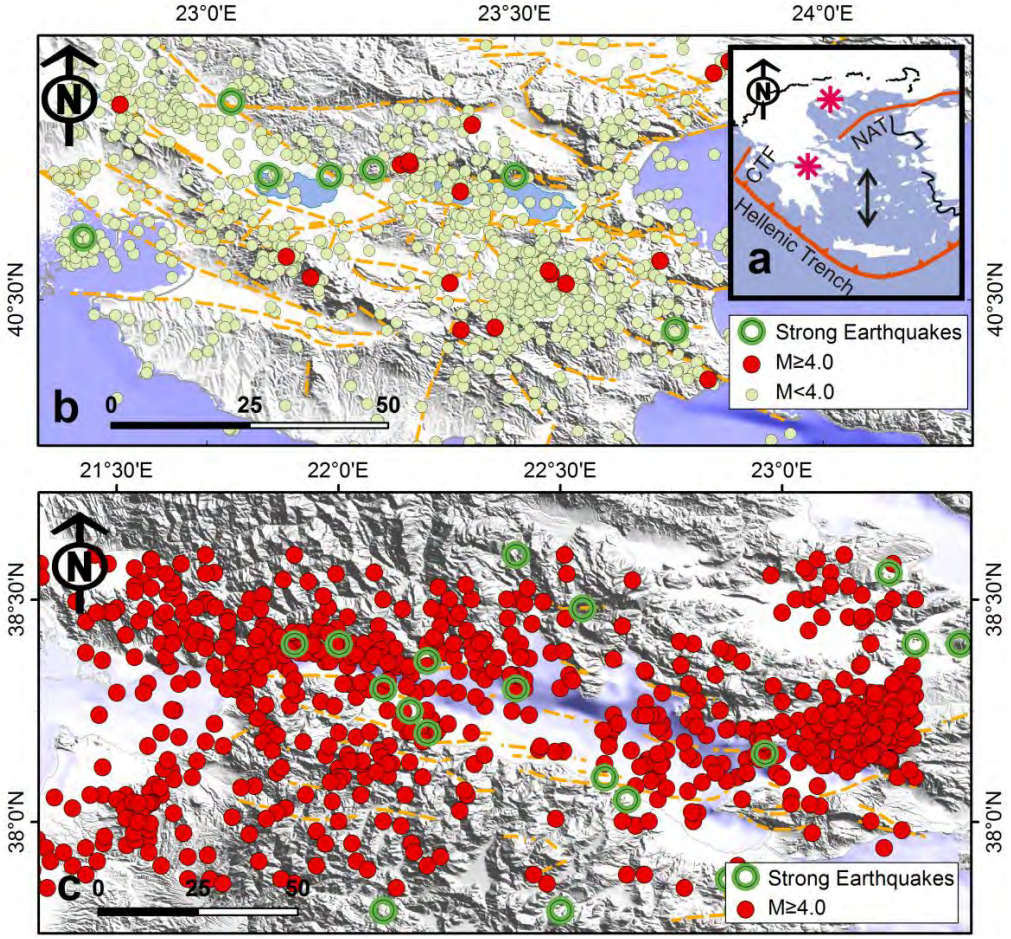

Figure 1 - a) Simplified seismotectonic map of the Aegean region (Hellenic Trench, NAF: North Aegean Trough, CTF: Cephalonia Transform Fault). The locations of the two study areasare highlighted with asterisksb) Mygdonia region in Northern Greece and c) Corinth gulf in Central Greece. Green circles correspond to strong historical earthquakessince 1700 (Papazachos and Papazachou, 2002). Earthquakes with strong magnitudesduring2000 - 2012are alsoillustrated.

Mygdonia basin and the surrounding mountainous volumes accomodate a dense normal faulting network mainly developed in an E–W direction especially in the central part of the basin (Tranos et al., 2003) and is recently characterized by earthquake quiescence sincerecent seismicity is deprived of strong earthquakes after the occurrence of 1978 (M6.5) strong seismic triplet and Arnea Earthquake in 1995(M_w5.8). However, according to the historical record the area was repeatedly struck by moderate and strong events in the past, and thus this information evidences the necessity of a thoughtful investigation of seismicity by all available means.

Our second study area, Corinth graben constitutes a half graben bounded by segmented normal faults in an E-W direction dipping both to the North and the Southwith the southern faults to be the most active ones (Armijo et al., 1996).Constantlyintense seismicity and several strong earthquakes accompanied by aftershock sequences occurred in the last years (Achaia, M_w =6.4, 2008; Efpalio,M_w=5.5, 2010; Xilokastro, M_w=5.0, 2012).

3. Data

Differentiations in seismological networks and magnitude estimation through time have an influence on the long-term distribution of magnitudes and finally contribute to the different completeness threshold. The compilation of precisely defined focal earthquake parameters along with complete and homogeneous data sets seem to be a primal and fundamental step before exploiting seismicity catalogues.The data used, include all the earthquakes that occurred during 2008–2012 in the study areas and were instrumentally recorded by the Unified National Seismological Network of Greece. Thisstudy period was selected because it coincides with the higheraccuracy and stability of the permanently operated seismological network. These improvements, undoubtedly lead to a significant lowering of the magnitude threshold for detecting earthquakes.The magnitude threshold was found equal toM_C=1.6 for Mygdonia region (Figure 2a) and equal toM_C=2.4 for Corinth Gulf(Figure 2b) by applying the algorithm ofLeptokaropoulos et al. (2012) for the best linear fit (method by Wiemer and Wyss, 2002).Magnitudes were acquired from the monthly bulletins of the Seismological Station (A.U.Th.) and they refer to M_L magnitude obtained by applying the methodology of Hutton and Boore (1987) on simulated Wood Anderson earthquake recordings.

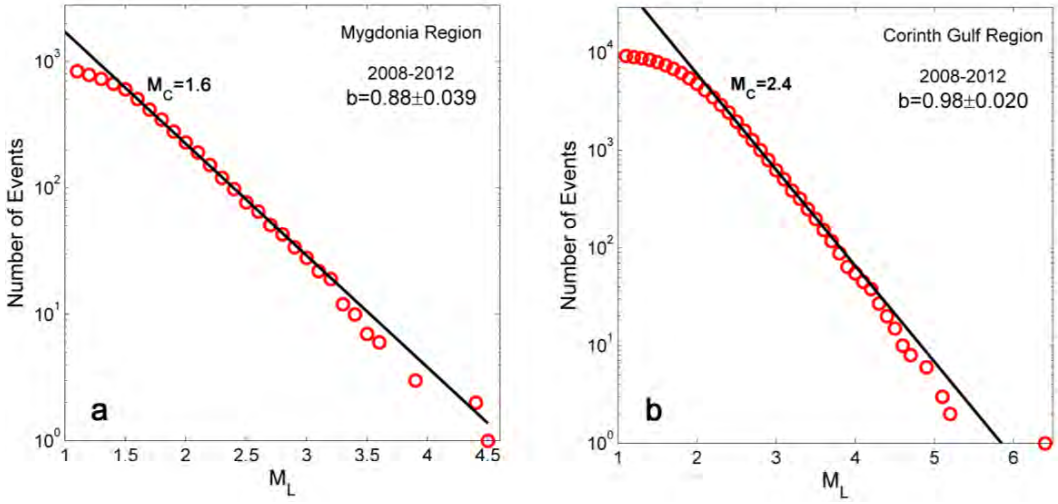

Figure 2 - Cumulative frequency–magnitude distribution (FMD) of earthquakes for the two study areas for the time period2008–2012The completeness threshold is determined by detecting the smaller residual for a maximum likelihood estimation fitting a) FMD for Mygdonia Region, where M_C=1.6 b) FMD for Corinth Gulf Region, where M_C=2.4.

There is strong evidence that in a case of seismic excitations there is always an increased probability for aftershock sequences to occur. This dense occurrence of earthquakes in time and space is often misleading when long term variations and clustering are being studied because the degree of clustering phenomenais amplified. For this reason in the case of Corinth Gulf, Reasenberg's declustering algorithm (Reasenberg, 1985) wasapplied for the compilation of a catalogue data set deprived as possible of aftershock sequences. However, as far as the magnitude distribution is concerned tests wereapplied to both data sets(the initial set and the declustered) in

order to investigate the properties of both catalogues and provide a comparison between them, if any.

4. Methodology used

4.1. Smoothed Bootstrap Test

The methodology adopted for the investigation of the PDF of the studied parameters,concerns the smoothed bootstrap test for multimodality and the bump hunt test, which isa non-parametrical procedure(fully described by Lasocki and Papadimitriou, 2006). The methodology (Silverman, 1986; Efron and Tibshirani 1994) has been applied in both fields of mining (Lasocki and Orlecka–Sikora, 2008) and natural seismicity (Lasocki and Papadimitriou, 2006). The method firstly investigates the distributionon the existence of modes or bumpsand secondly their number, since it is hypothetically stated that the distribution is not complex.Two hypotheses are assumed: H_1^0 presents the hypothesis that the probability density of magnitude distribution is unimodal, whereas H_2^0 refers to the assumption that the probability density of magnitude has one bump to the right from the mode.The distribution complexity, revealing multimodality, is accepted when the significance of either of these null hypotheses is low. Briefly, in a non–parametric approach the kernel estimator of probability density function $\hat{f}$ given byEquation 1where, M_i is the magnitude of n given data, h is a positive smoothing factor and $K(\bullet)$is a kernel function strongly dependable on h .

Equation 1 - The kernel estimator of probability density function, $\widehat{f}$

$$\hat{f}(M \mid \{M_i\}, h) = \frac{1}{nh}\sum_{i=1}^{n} K\left(\frac{M - M_i}{h}\right)$$

To determine the significance of the two hypothesesit is necessary to determine the critical smoothing factor, $h_{crit}(l), l = 1,2$ such that there is only one mode or bump, for every $h \geq h_{crit}(l)$for the two hypotheses, respectively.A number of smoothed bootstrap samplesderived from the original data sets, are compiled in order to approximate the significance of the two assumptions.

4.2. Fractal Dimension

The fractal dimension D_F expressesthe degree of object clustering and is widely used in seismicity in order to quantify possible dense occurrence of earthquakesin time or space (Kagan and Jackson, 1991). Fractal geometry was first introduced by Mandelbrot (1983) who attempted to characterize self-similar properties of scale independent sets of data. The fractal analysis in this study is performed with the use of the algorithm introduced by Grassberger and Procaccia (1983) according to which, a volume containing N objects, earthquakes in this case, which correspond to $\bar{x}$ variable, is covered by boxes exhibiting a specific length side. The correlation integral for this variable is given by the Equation 2, where $\|\bar{x}_i - \bar{x}_k\|$ is the measured distance between two earthquakes i and k in the $\vec{x}$ domain, r corresponds to a reference distance and $\Theta(\bullet)$refers to the known Heaviside function.The correlation integral, which behaves as a power to r is proportional to the fractal dimension and is defined from the linear part of $-\log r$ empirical relation. When the studied objects are scale invariant, the number $N(r)$, of boxes covering the objects scales with r is given by D_F , which corresponds to the fractal dimension.

Equation 2 - The Correlation integral which is proportional to the fractal dimension

$$C^{(2)}(r) = \frac{1}{N(N-1)} \sum_{i=1}^{N} \sum_{k \neq i} \Theta\left(r - \left\|\vec{x}_i - \vec{x}_k\right\|\right)$$

This parameter illustrates the degree of clustering of a set of objects and is used to express their similarities or heterogeneities. In our case, the parameter that is investigated in terms of fractal analysis using the methodology above, concerns the two dimensional spatial distance between consecutive events.

5. Test Results

5.1. General

The above described methodologies were employed in the current study because they provide a direct indication about the complexity of the parametersdistribution that are examined and can besuccessfully revealed under the frameof stochastic means. In this chapter, the outcome of this investigation in the two study regions is presented and the expectation of rejecting the initial hypotheses are analysed.Parameters like size, interevent time and interevent distance are examined with the use of smoothed bootstrap test for multimodality and bump hunt, whereas the spatial distribution of epicentres is investigated with the use of the fractal dimension in a two dimensional space.

5.2. Size Distribution

The smoothed bootstrap multimodality test was applied in three data sets,two of them corresponding to complete catalogues of the two study areas and the thirddeprived of aftershocks(Corinth Gulf). The same procedure was followed in all cases and thus 1000 bootstrap samples were compiled in order to estimate the significance of the null hypothesis. Rejecting the null hypothesis does not claim the existence of the alternative hypothesis, however, when the estimated probability is less than 0.15 the significance of this state depends on the value of H_1^0. In every casethat the size distribution is complex, revealing more than one bumpor mode, the location of the minimum and maximum points provide information onthe evolution of the seismicity processes and the prevalence of certain magnitudes. Two smoothing factors, $h_{crit}$and h_{critb} were calculated for both real and calibrated data and the resulting analysis for the three cases isprovided in Table 1 and Figure 3.

Table 1 -Results for the smoothed bootstrap test for multimodality and the bump hunt test, applied for magnitude PDF where M_C is the magnitude threshold, n is the number of the data in each sample and H_1^0,$H_2^0$is the significance of the tests. For the case of rejecting null hypothesis the location of modes or bumps according to the test are given.

Study Area	M_C	n	hcrit	H_1^0	$hcrit_b$	H_2^0	Location of Modes or Bumps				
							Modes			Bumps	
Mygdonia	1.6	505	0.246	0.19	0.363	0.06	-			2.1	4.2
Cor. Gulf	2.4	2446	0.443	0.12	0.505	0.08	2.7	6.2	6.3	3.1	6.2
Cor. Gulf (decl.)	2.2	2248	0.434	0.12	0.520	0.01	2.4	6.0	6.3	2.9	6.1

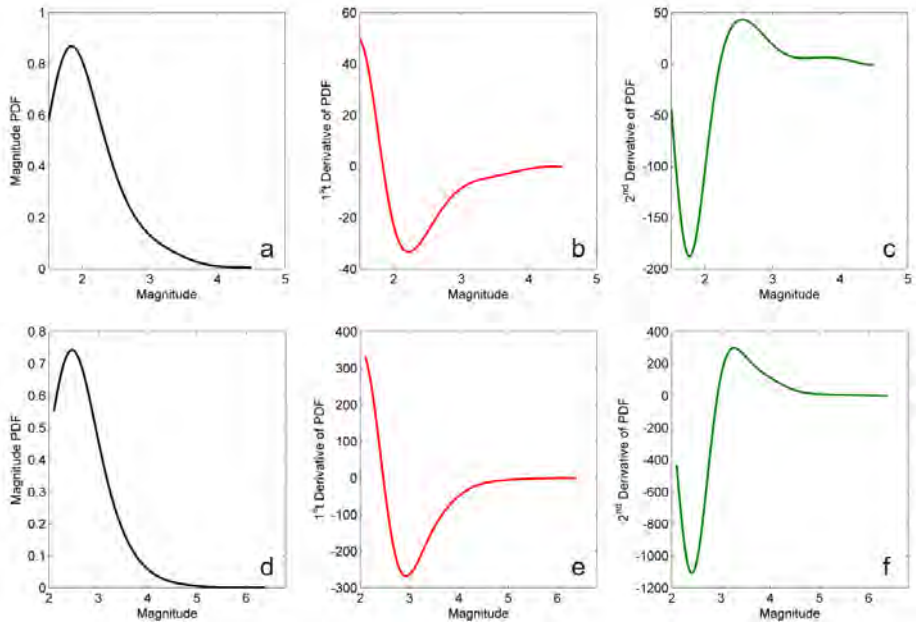

Figure 3–a) The magnitude PDF for Mygdonia region, b)The 1st derivative of PDF, c) the 2nd derivative of PDF, d) The magnitude PDF for Corinth region, e) The 1st derivative of PDF and f) the 2nd derivative of PDF estimated using the declustered catalogue.

ThePDF distribution shows that there is not an important indication for complexity and mode existence in the case of magnitudes in Mygdonia,however the significance of characteristic more than one bumpsappearance is important (H_2^0:0.06)and suggests that there is a 6% percentage of failing when the null hypothesis about uniformity is rejected. The bumps in the distribution correspond to lower real magnitudes than expected according to G-R law and are located at M=2.2 and M=4.2. On the other hand,in both data sets forCorinth Gulf it is observed that both null hypotheses for unimodality are rejected and multiple modes and bumps are present in both cases (since $H_1^0$and H_2^0<0.15). Characteristic clustering of magnitudes is observed at small magnitudes in both cases (2.7, 2.4) and at the highest magnitudeslocated in the tail of the PDF distribution. It is observed that in the case of the declustered data modes and bumps are met at lower magnitudes compared to the original set.

5.3. Interevent Distance Distribution

The interevent distance, Δs, ($\Delta s = r_{(i+1)} - r_i$), corresponds to the respective distance of one event from its preceding, within the Euclidian space. Investigation of the distribution of theinterevent distance PDF provides a measurement of quantification of earthquake clustering in space and a degree of relativity and interaction between epicentres close in space.Results of the tests are presented in Table 2. It can be deduced that there is an indication of modes and bumps in the spatial distribution because the probability that the null hypothesisto be real scenario is important in the case of Mygdonia, while in the case of Corinth gulf it remains doubtable.

5.4. Interevent Time Distribution

The distribution of the lapse time, dt, between a pair ofconsecutive events, that corresponds to the time that mediates the occurrence of two consecutive earthquakes, $\tau = t_{(i+1)} - t_i$, was also examined. In the last years, the analysis of waiting times between subsequent earthquakes was the subject of various works (Corral, 2006) supporting that the use of interevent time is beneficial since it is deprived of relative errors that origin time carries and may describecharacteristic attributes depending on the study area(Jonsdottir et al., 2006). The investigation of the multimodality test for

this temporal parameterreveals that the behaviour of seismicity in time is not occurring in a uniform way in the two cases as it can be observed at Table 3.In Mygdonia the possibility of mistake, when rejecting the unimodal distribution hypothesis is about 11% and in Corinth even smaller. Therefore, there is stronger evidence that interevent time distribution is complex in both cases.

Table 2 -Results for the smoothedbootstrap test for multimodality and bump hunt test, for interevent distance PDF between consecutive events, where M_C is the magnitude threshold, n is the numberof the data in each sample and H_1^0,$H_2^0$is the significance of the tests.

Study Area	M_C	n	hcrit	H_1^0	$hcrit_b$	H_2^0	Location of Modes or Bumps				
							Modes			Bumps	
Mygdonia	1.6	505	0.002	0.04	0.002	0.15	0.0012	0.037	0.051	0.09	0.011
Cor. Gulf (decl.)	2.2	2248	0.002	0.17	0.003	0.18	-			-	

Table 3 -Results for the smoothedbootstrap test for multimodality and bump hunt test, for interevent distance PDF between consecutive events, where M_C is the magnitude threshold, n is the number of the data in each sample and H^0_1,H^0_2 is the significance of the tests.

Study Area	M_C	n	hcrit	H_1^0	$hcrit_b$	H_2^0	Location of Modes or Bumps			
							Modes		Bumps	
Mygdonia	1.6	505	14.60	0.108	17.78	0	5.7	9.6	4.76	6.34
Cor. Gulf (decl.)	2.2	2248	1.00	0.24	1.46	0.011	-		2.12	10.38

5.5. Spatial Distribution

Long term spatial clustering was approached with the investigation of fractal properties for the two dimensional space of the seismogenic volume and the fractal dimension of the earthquake epicentral distribution for the complete earthquake catalogue. The calculation of the fractal dimension derives from the double logarithmic plot between the correlation dimension and the Euclidian distance located on a planar surface upon which the epicentres were projected. This approach is close to reality since the study area is not very extended and can be approximated with a planar surface. As mentioned before, the correlation integral corresponds to the best fittedleast–square regression line to the linear part of the slope of a log–log plot.Clustering is as stronger as smaller the value of the corresponding fractal dimension.Results are presented in Figure 4. The fractal dimension in two-dimensional space was found equal to 1.3 for both areas. In Figure 4 the linear part of the plots without the minimum and maximum cutoff of the logarithmic plot are presented.The fractal dimensions of three dimensional data including focal depths were excluded from the calculations, since it seems that focal depths are concentrated in a specific band of the crust, i.e. the seismogenic layer, and they do not provide any additional information.

6. Discussion

The stochastic approach of seismicity along with faulting identification studies both share the satisfying determination of a potential threat in a seismogenic region (Ouillon and Sornette, 2011).Therefore, the target of our study was the full exploitation of seismicity data for two seismo-

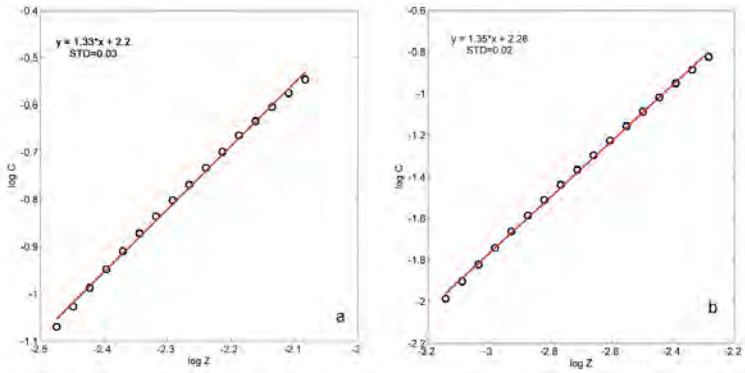

Figure 4 - Fractal Dimension of the two–dimensional spatial distribution where lgC and lgZ correspond to the logarithm of the distance reference and the distance for a) Mygdonia and b) Corinth Gulf region.

genic regions in Greece, one exhibiting a seismic quiescenceperiod with the maximum magnitude 4.8 and the other experiencing strong seismicity with maximum magnitude equal to 6.4. Accurate complete data for the study period where taken into consideration and the tools chosen for this purpose concern methodologies that were applied in regions with low magnitudes and localized earthquakes such as mines. Bootstrap techniques are the most suitable to be used because of the resampling process of the imported data, despite the small seismicity sample. The aim of this approach was the quantification of clustering effects of seismicity, in two cases, with or without main strong events. The smoothed bootstrap testfor the probability density function of magnitudes, interevent time and space shows a strong evidence for a multi–modes shape, leading to the conclusion that both regions behave in the same way without a uniform occurrence of small and stronger events. Maximum concentrations of magnitudes are met at lowest magnitudes (2.7, 2.4) of the distribution as well as in the tails. The probabilistic analysis for time and distance in general are not contradictory to the results obtained from the fractal analysis. Interevent time and interevent space depicts a multi mode shape with three distinct locations of modes, for all cases, however in Gorinth gulf there is not a characteristic interevent time distance between events. According to the fractal dimensions, their values do not exhibit significant variations in the two areas, or in the entire study area and clustering in the spatial distribution of epicentres in the entire study area is evident and strong enough. Even in the case of Mygdonia small earthquakes trigger the occurrence of each other along their neighbour faults. There was a complete use of all available data, and observations seem to be in a good agreement thus complexity was revealed in both study areasdespite the rate of seismicity, with different characteristic properties for each case.

7. Acknowledgments

This work was co–financed by the European Union (European Social Fund–ESF) and Greek national funds through the Operational Program "Education and Lifelong Learning" of the National Strategic Reference Framework (NSRF) – Research Funding Program: Heracleitus II Investing in knowledge society through the European Social Fund.Geophysics Department contribution 000.

8. References

Armijo R., Meyer B., King G.C.P. Rigo A. and Papanastassiou D. 1996. Quaternary evolution of the Corinth Rift and its implications for the Late Cenozoic evolution of the Aegean, *Geophys J. Int.*, 126, 11-53.

Bak P., Christensen K., Danon L. and Scanlon T. 2002. Unified scaling law for earthquakes, *Phys. Rev. Lett.,* 88, doi:10.1103/PhysRevLett.88.178501.

Briole P., Rigo A., Lyon-Caen H., Ruegg J.C., Papazissi K., Mitsakaki C., Balodimou A., Veis G., Hatzfeld D. and Deschamps A. 2000. Active deformation of the Corinth rift, Greece: results from repeated Global Positioning System surveys between 1990 and 1995, *J. Geophys. Res.*, 105, 25605–25625.

Console R., Murru M. and Catalli F. 2006. Physical and stochastic models of earthquake clustering, *Tectonophysics*, 417, 1–2, 141-153.

Coral A. 2006. Dependence of earthquake recurrence times and independence of magnitudes on seismicity history, *Tectonophysics* 424, 177–193.

Efron B. and Tibshirani R.J., 1993/1998. *An Introduction to the Bootstrap*, Chapman and Hall, London

Grassberger P. and Procaccia I. 1983. Characterization of strange attractors, *Phys. Rev. Lett.,* 50, 346–349.

Gutenberg B. and Richter C.F. 1944. Frequency of earthquakes in California, *Bull. Seismol. Soc. Am,*. 34 185–188.

Hutton L.K. and Boore D.M. 1987. The M scale in southern California, *Bull. Seismol. Soc. Am*., 77, 2074 – 2094.

Jonsdottir K., Lindman M., Roberts R., Lund B. and Bödvarsson R. 2006. Modelling fundamental waiting time distributions for earthquake sequences, *Tectonophysics*, 424, 195–208.

Kagan Y.Y. and Jackson D.D. 1991. Long-term earthquake clustering, *Geoph. J. Int.,* 104, 117–133.

Kotzev V., Nakov R., Georgiev Tz., Burchfiel B.C. and King R.W. 2001. Crustal motion and strain accumulation in western Bulgaria, *Tectonophysics,* 413, 189 – 200.

Lasocki S. and Orlecka–Sikora B. 2008. Seismic hazard assessment under complex source size distribution of mining–induced seismicity, *Tectonophysics*, 456, 28–37.

Lasocki S. and Papadimitriou E. 2006. Magnitude distribution complexity revealed in seismicity from Greece, *J. Geophys. Res*., 111,B11309, doi:10.1029/2005JB003794.

Leptokaropoulos K. Karakostas V. Papadimitriou E. Adamaki A. Tan O. and Inan S. 2012. A homogeneous earthquake catalogue compilation for western Turkey and magnitude completeness determination (submitted manuscript).

Mandelbrot B.B. 1983. The fractal geomtery of nature, *Freeman*, San Francisco, 468 pp.

Ogata Y. 1988. Statistical models for earthquake occurrence and residual analysis for point process, *J. Am. Stat. Assoc.* 83, 9–27.

Ogata Y. 1998. Space-time point-process models for earthquake occurrences, *Ann. Inst. Stat. Math.* 50, 379–402.

Omori F. 1894. On aftershocks of earthquakes, *J. College Sci. Imp. Univ*., Tokyo 7, 111–200.

Papazachos B.C. and Papazachou C. 2002. *The earthquakes of Greece, Ziti Publ.,* Thessaloniki, Greece, 317pp.

Ouillon G. and Sornette D. 2011.Segmentation of fault networks determined from spatial clustering of earthquakes, *J. Geophys. Res.,* 16, doi:10.1029/2010JB007752.

Reasenberg P. 1985. Second-order moment of central California seismicity, 1969–1982, *J. Geophys. Res.*, 90, 5479– 5495.

Silverman B.W. 1986. Density Estimation for Statistics and Data Analysis, *Monographs on Statistics and Applied Probability*, Chapman and Hall, London, 175 pp.

Tranos M., Papadimitriou E. and Kilias A. 2003. Thessaloniki-Gerakarou fault zone (TGFZ): the western extension of the 1978 Thessaloniki earthquake fault (northern Greece) and seismic hazard assessment, *J. Struct. Geol.,* 25, 2109-2123.

Utsu T. 1999. Representation and analysis of the earthquake size distribution: a historical review and some new approaches, *Pure Appl. Geophys*., 155, 509–535.

Wiemer S. and Wyss M. 2000. Minimum magnitude of completeness in earthquake catalogs: examples from Alaska, the Western United States, and Japan, *Bull. Seismol. Soc. Am*., 90, 859–869.

Δελτίο της Ελληνικής Γεωλογικής Εταιρίας, τομ. XLVII , 2013
Πρακτικά 13ου Διεθνούς Συνεδρίου, Χανιά, Σεπτ. 2013

Bulletin of the Geological Society of Greece, vol. XLVII 2013
Proceedings of the 13th International Congress, Chania, Sept. 2013

SPATIO-TEMPORAL EARTHQUAKE CLUSTERING IN THE WESTERN CORINTH GULF

Karagianni E.[1], Paradisopoulou P.[1] and Karakostas V.[1]

[1] Geophysics Department, School of Geology, Aristotle University of Thessaloniki, GR54124, Thessaloniki, Greece, elkarag@geo.auth.gr, ppara@geo.auth.gr, vkarak@geo.auth.gr

Abstract

Corinth Gulf has been studied, thoroughly using multidisciplinary approaches (geological, seismological, geodetic etc), which revealed its complicated tectonic behaviour. In the last five years or more, an intense continuous microseismic activity is observed in the westernmost part of the gulf covering the area from west of Aigio to the area west of Rio Antirrio strait, near the city of Patras. Aiming to study in detail the properties of this microseismic manifestation, the recordings of the Hellenic Unified Seismological Network (HUSN) are used to accurately determine the focal coordinates of earthquakes with magnitudes M=1.5 or more. Relocation was performed using the HYPOINVERSE program, for all available data for the period 2010-2011 when earthquakes up to magnitude M=5.5 occurred. The space time plot of the epicentres shows that seismicity is not random in the area but formed distinctive clusters, indicating an E-W striking seismic zone whose patches are successively activated for certain periods. The present work deals with the investigation of spatio-temporal evolution of seismicity with the intention to examine the migration of seismicity and multi-segment activation.

Key words: *Seismicity relocation, migration of seismic activity, focal mechanisms.*

Περίληψη

Η ευρύτερη περιοχή του Κορινθιακού κόλπου λόγω της πολύπλοκης και ενδιαφέρουσας σεισμοτεκτονικής συμπεριφοράς που παρουσιάζει έχει αποτελέσει το αντικείμενο έρευνας πολλών μελετών (γεωλογικών, σεισμολογικών, γαιωδαιτικών κ.λ.π.). Τα τελευταία πέντε τουλάχιστον χρόνια έχει παρατηρηθεί μία έντονη σεισμική δραστηριότητα η οποία καλύπτει την περιοχή δυτικά του Αιγίου, το στενό Ρίου-Αντιρρίου μέχρι την πόλη της Πάτρας. Τα δεδομένα της παρούσας εργασίας καλύπτουν τη χρονική περίοδο 2010-2011 κατά την οποία καταγράφηκε έντονη σεισμική δρστηριότητα με ισχυρούς σεισμούς (μέχρι M=5.5) και χωροχρονικές συγκεντρώσεις της σεισμικότητας. Οι καταγραφές των σεισμών από το Ενιαίο Ελληνικό Σεισμολογικό δίκτυο χρησιμοποιήθηκαν για τον ακριβή επαναπροσδιορισμό των εστιακών παραμέτρων των σεισμών με μέγεθος M≥1.5 χρησιμοποιώντας το πρόγραμμα HYPOINVERSE. Με βάση τα δεδομένα και τα αποτελέσματα από τον επαναπροσδιορισμό των εστιακών συντεταγμένων, η χωροχρονική κατανομή έδειξε ότι η σεισμικότητα συγκεντρώνεται σε κάποιες συστάδες σεισμών σε περιοχές που είναι πιθανό να συνδέονται και με ροή ρευστών λόγω της θέσης των σεισμών σε υποθαλάσσια περιοχή. Η παρούσα εργασία μελετά τη χωρική και χρονική κατανομή της σεισμικότητας στο δυτικό τμήμα του Κορινθιακού κόλπου με σκοπό να ελεγχθεί τυχόν "μετανάστευση" της σεισμικότητας και σύνδεσή της με τις σεισμοτεκτονικά καθορισμένες περιοχές.

Λέξεις κλειδιά: *Σεισμικότητα, μετανάστευση επικέντρων, μηχανισμοί γένεσης.*

1. Introduction

Earthquakes are usually observed in clusters both in time and space. A significant part of these clusters is caused by the aftershock sequences of major earthquakes. However, smaller earthquakes (M<5.0) also generate aftershocks and at least some of the space time clustering in short time and distances is probably caused by triggering among small earthquakes. The spatial distribution of microseismicity is very useful in deciphering complicating fault structures at depth.

The Gulf of Corinth is one of the most seismically active zones in Europe (e.g. Hatzfeld et al. 2000; Burton et al. 2004). It is the fastest continental rift in the world, with the geodetically measured extension varying from ~5mm/yr at the eastern part, to ~15mm/yr at the western part (Briole et al., 2000; Avallone et al., 2004). The rift initiated sometime in the late Pliocene and was superimposed on the NNW-SSE trending Hellenides orogenic belt of Oligocene age. The seismicity as shown in many works is very different in the western part of the rift with the occurrence of (frequent earthquake swarms with magnitudes smaller than 4.5. The focal mechanisms show a consistent pattern of E-W trending normal faulting, with a shallow plane dipping toward the north (Baker et al. 1997). This pattern is consistent with microseismic observations obtained by dense temporary networks (Hatzfeld et al. 1990, 2000; Rigo et al. 1996) as well as with high resolution seismic reflection and multibeam bathymetric data (McNeil et al. 2005; Bell et al. 2008).

In this work, we study the spatio-temporal evolution of seismicity in the western part of Corinth gulf, trying to examine the migration of seismicity and multi-segment activation, as this later has been mentioned in previous studies (e.g. Doutsos et al., 1992; Flotte et al., 2005; Tselentis et al., 2007).

2. Data and Location Procedure

2.1. Data Processing

The recordings of P- and S- seismic waves, from the (HUSN), were used to obtain the earthquake location for the year 2011. The network in the study area is quite dense and hence the focal coordinates could be defined with considerable accuracy even for weak seismic events (M≤2.0). In order to achieve a satisfactory hypocentral depth resolution special attention was paid to the manual S-picks and to the adequate azimuthally station coverage. Although some earthquakes of the dataset were recorded by many seismological stations, the recordings of the 27 stations in epicentral distances up to 140 km were used, with most of them located at distances less than 100 km (Figure 1). The recordings of 365 earthquakes were manually picked and merged with 724 earthquakes from Efpalio sequence (January 18, 2010–March 09, 2010) in order to capture the seismic activity evolution from 2010 (Karakostas et al., 2012). The final catalogue contains M_L magnitudes (obtained from the monthly bulletins of the Geophysics Department of the Aristotle University of Thessaloniki) estimated using the formula proposed by Hutton and Boore (1987), after appropriate filtering of the data to simulate Wood Anderson recordings.

2.2. Relocation of Events

Two moderate earthquakes (M5.5 and M5.4) occurred in January 2010 near the town of Efpalio in the western part of Corinth Gulf, and that was the beginning of smaller magnitudes swarms that spread from Aigio to the west up to Rio-Antirrio strait, near the city of Patras. It was interesting to study the dense microseismic activity that appeared in this area for the period 2010-2011 and hence the relocation of the data was necessary in order to describe sufficiently the space-time distribution of the events. Since the 2010 events were relocated in a previous work (Karakostas et al., 2012), only the 2011 events were relocated here, using the computer program HYPOINVERSE

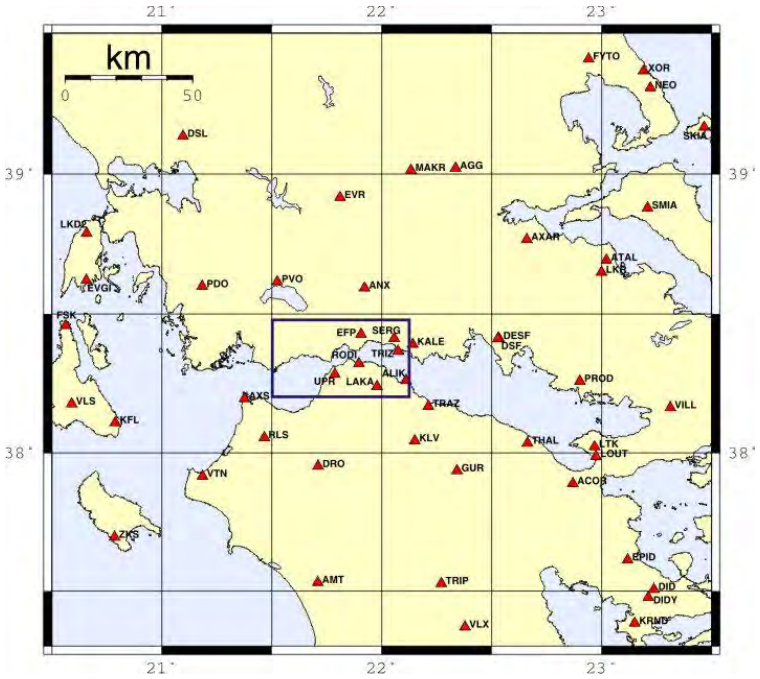

Figure 1 – Geographical distribution of the seismological stations of HUSN used in the present study. The study area is depicted by the rectangle.

(Klein, 2000) and, mainly, the one dimensional velocity model proposed for the area by Novotny et al. (2008). Because not only local seismological stations are used, one more layer added from the depth of 31 km with P_n-waves velocity equal to v_n=7.9km/s (Panagiotopoulos and Papazachos, 1985), in the final velocity model given in (Table 1).

Table 1 – Crustal model used in this study for the hypocenter determination (Novotny et al., 2008; Panagiotopoulos and Papazachos, 1985).

P-wave velocity (km/sec)	Thickness (km)
5.36	3.55
5.37	3.10
5.59	1.37
5.97	2.20
6.30	4.78
6.5	15.3
7.9	∞

The mean value of velocity ratios (v_p/v_s) was found equal to 1.81±0.06 using the Wadati method for 141 earthquakes with seven or more S-arrivals. Previous studies in the western part of the Corinth Gulf (Rigo et al. 1996; Novotny et al. 2008; Pacchiani and Lyon Caen 2010) have shown a noteworthy variation in the values of velocity ratios that probably could be attributed to the complicated geological conditions and rheological changes.

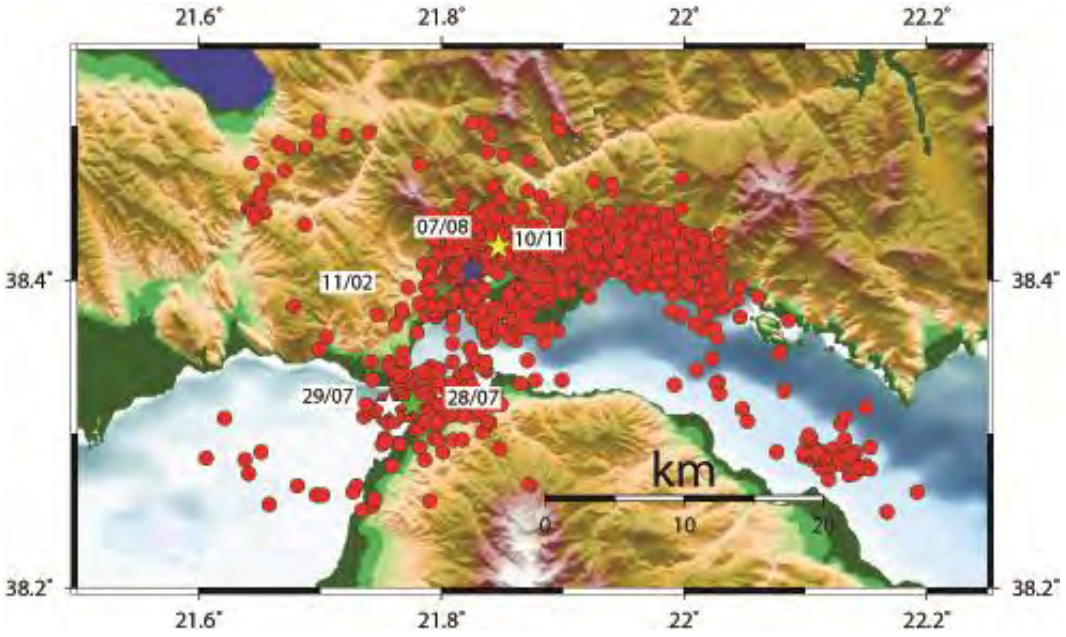

Figure 2 - Epicentral distribution of the relocated data set. The stars indicate the earthquakes with M≥4.0 occurred in 2011.

Time corrections relative to the crustal model were calculated considering as origin time of each earthquake the one estimated from Wadati method. An iterative procedure (Karakostas et al., 2012) applied until the time corrections for all the stations to obtain a stable value. In fact, the procedure was repeated until the differences between the observed and the theoretical travel times to be 0.1sec or less in all stations used. For the relocation of the 365 shocks (Figure 2) the calculated time delays were taken into account. The average values for the estimated errors in origin time, epicenters and focal depths are RMS=0.12 sec, ERH=0.42 km and ERZ=1.09 km, respectively.

3. Fault Plane Solutions

For the larger earthquakes of the data set of 365 events located in the study area we determined the fault plane solutions using the FPFIT Computer program (Reasenberg and Openheimer, 1985). The first step was to define manually the P-wave first onsets using only events with at least 10 impulse arrivals. For each fault plane solution, FPFIT calculates several uncertainty indices to characterize the quality of the final solution. The main indices are the misfit function F_j which indicates the fit of the solution and can potentially range from 0 (for a perfect fit) to 1(for a complete misfit), the station distribution ratio varying in the range 0 to 1.0, as well as the uncertainties in strike, dip and rake of the final solution which for a reliable solution should be smaller than 20^0. At this preliminary work we determined the focal mechanisms for 9 events for which we had adequate number (at least 10) of first onsets (Table 2, figure 3A) with mean misfit function F_j, equal to 0.19, mean STDR equal to 0.6 and errors in strike, dip and rake smaller than 15^0. Although there is a variety in the faulting type, where normal faulting coexist with thrust, the T axis (figure 3B) is found to be sub-horizontal and striking almost N-S to NNW-SSE in full agreement with the regional stress pattern. An adequate number of focal mechanisms provide the tool of revealing spatial variations of the stress field.

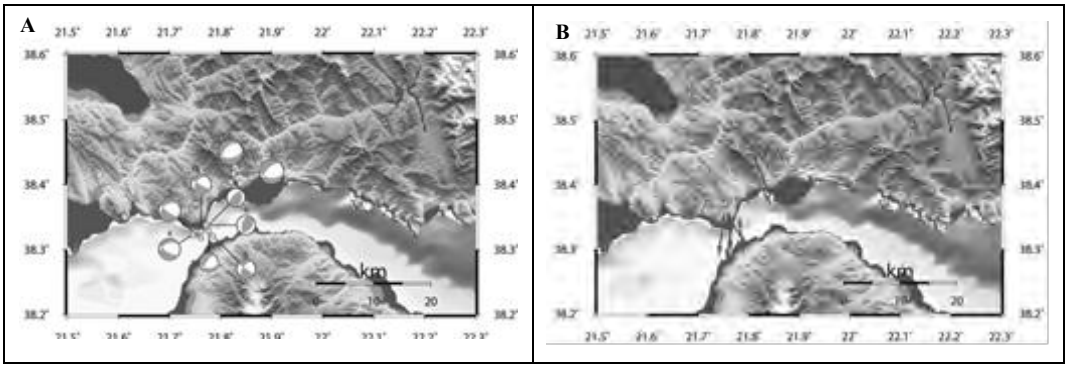

Figure 3 – A. Fault plane solution for selected earthquakes. The numbers correspond to the time order of earthquakes (Table 2) B. Horizontal projection of the T axis for the same data set of focal mechanisms. The orientation of the vectors is mainly NNW-SSE in agreement with the regional stress field.

Table 2 - Fault plane solutions for the 9 earthquakes used in the present work. The strike, dip and rake correspond to the one nodal plane of the focal mechanism. The dip and azimuth of the P- and T- axis for each earthquake are given in last four columns.

	Origin Time		Epicenter				Fault Plane Solution			P-axis		T-axis	
a/a	Date	Time	φ(°)	λ(°)	Depth (km)	M_w	Strike (°)	Dip (°)	Rake (°)	Azimuth	Dip	Azimuth	Dip
1	24-Jul-2011	07:00:59.1	38.328	21.762	8.53	3.9	210	85	-45	67	34	176	25
2	28-Jul-2011	09:18:09.98	38.317	21.762	10.05	4.3	215	75	-55	72	47	189	22
3	29-Jul-2011	00:26:53.83	38.329	21.777	9.5	3.7	185	40	-35	81	53	327	16
4	29-Jul-2011	19:52:26.28	38.323	21.746	8.43	4.2	210	62	-60	72	58	188	14
5	7-Aug-2011	14:35:34.24	38.404	21.820	9.713.7	4.7	170	50	-65	56	70	152	2
6	14-Sep-2011	19:20:21.4	38.321	21.785	8.11	3.7	35	90	30	75	19	173	21
7	10-Nov-2011	17:25:39.82	38.417	21.825	13.35	4.7	185	45	-50	80	62	337	6
8	26-Nov-2011	16:41:22.75	38.336	21.774	12.14	3.6	95	35	55	299	14	175	65
9	27-Nov-2011	15:09:13.36	38.338	21.771	12.42	3.7	135	40	115	297	7	51	72

4. Space-Time Clustering of Seismicity

4.1. Space-Time Analysis

To explore the evolution of seismic activity with time, a space-time plot in the NNE-SSW direction (38.5°N-22.5°E to 38.2°N-21.65°E) is obtained according to the prevalent direction of the spatial distribution of the microearthquake activity (figure 4). Seismicity is started (0 day on the time axis) with the Efpalio earthquake in the central part of Corinth Gulf where two major earthquakes occurred, M=5.5 and four days later M=5.4 (Karakostas et al., 2012). As time advances (~100 days) a migration of activity is observed in the western part of Corinth Gulf where a swarm of low magnitude earthquakes is appeared. The seismicity from this time forward until the end of 2010 is characterized from sparse microearthquakes without a specific bunch. Swarms are started to appear early in 2011 where an earthquake with magnitude M=4.2 occurred. After

five months two clusters are shown in almost the same period. The first cluster is located in the southern part of the study area occupying a region with a length of 5 km. Two moderate earthquakes (M=4.2 and M=4.3) occurred here on 28 and 29 of July. After one month the second cluster is observed in the northern part of the study area where an earthquake of M=4.7 occurred. The length of this northern cluster is about 5 km, almost equal to the previous one. The activity seems to continue in both the aforementioned clusters until the end of the year where an earthquake of M=4.7 occurred in the northern cluster.

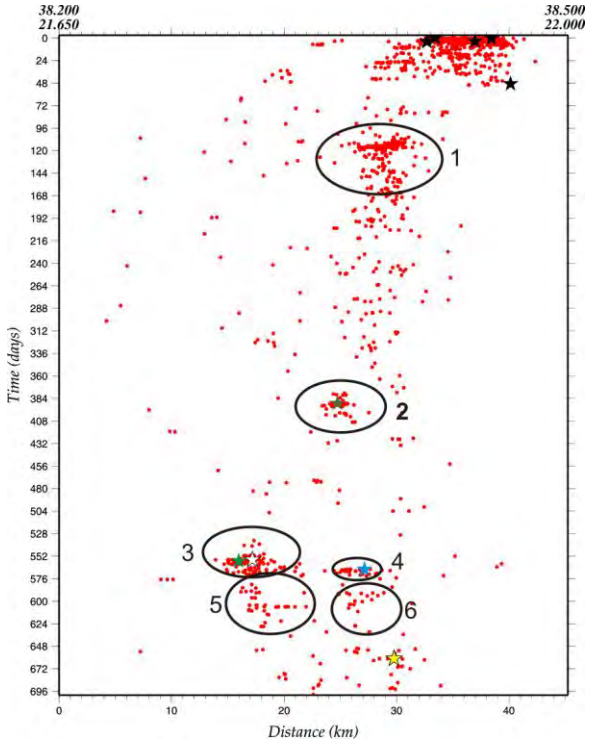

Figure 4 - Space time plot in the NNE-SSW direction of the seismicity distribution in the area under study. Coloured stars are same as in figure 2. Numbers indicate the time order of clusters.

4.2. Discussion

This paper deals with the characteristic seismicity that occurred in the western part of Corinth Gulf in 2011 after the 2010 seismic sequence of Efpalio. For this purpose 324 well-located events recorded by seismological stations in distances up to 140 km are used whereas these data enhanced using the 724 earthquakes from Efpalio seismic sequence. The distribution of relocated events (figure 2) indicates that the seismicity was spreading to the west forming two main clusters, in the northern part (as a continuation from the 2010 sequence) and in the southern part along the Rio-Antirrio strait. Generally the epicenters revealed an almost E-W striking seismic zone. The focal mechanisms (figure 3A, B) show that the orientation changes from ENE-WSW (northern cluster) to E-W (southern cluster).

Aiming to seek for more details in the evolution of the swarms, space-time plots in different periods was performed (figure 5). It is evidenced that the events are concentrated in clusters and can be correlated with the earthquakes with M≥4.0 that occurred in the study area in 2011. The increased seismicity along the Rio Antirrio strait is probably correlated to the fluids presence, as it is believed that fluids play an important role to the triggering of tectonic earthquakes (Nur and Booker 1972; Brodsky et al., 2000; Scholz, 2002; Prejean et al., 2004).

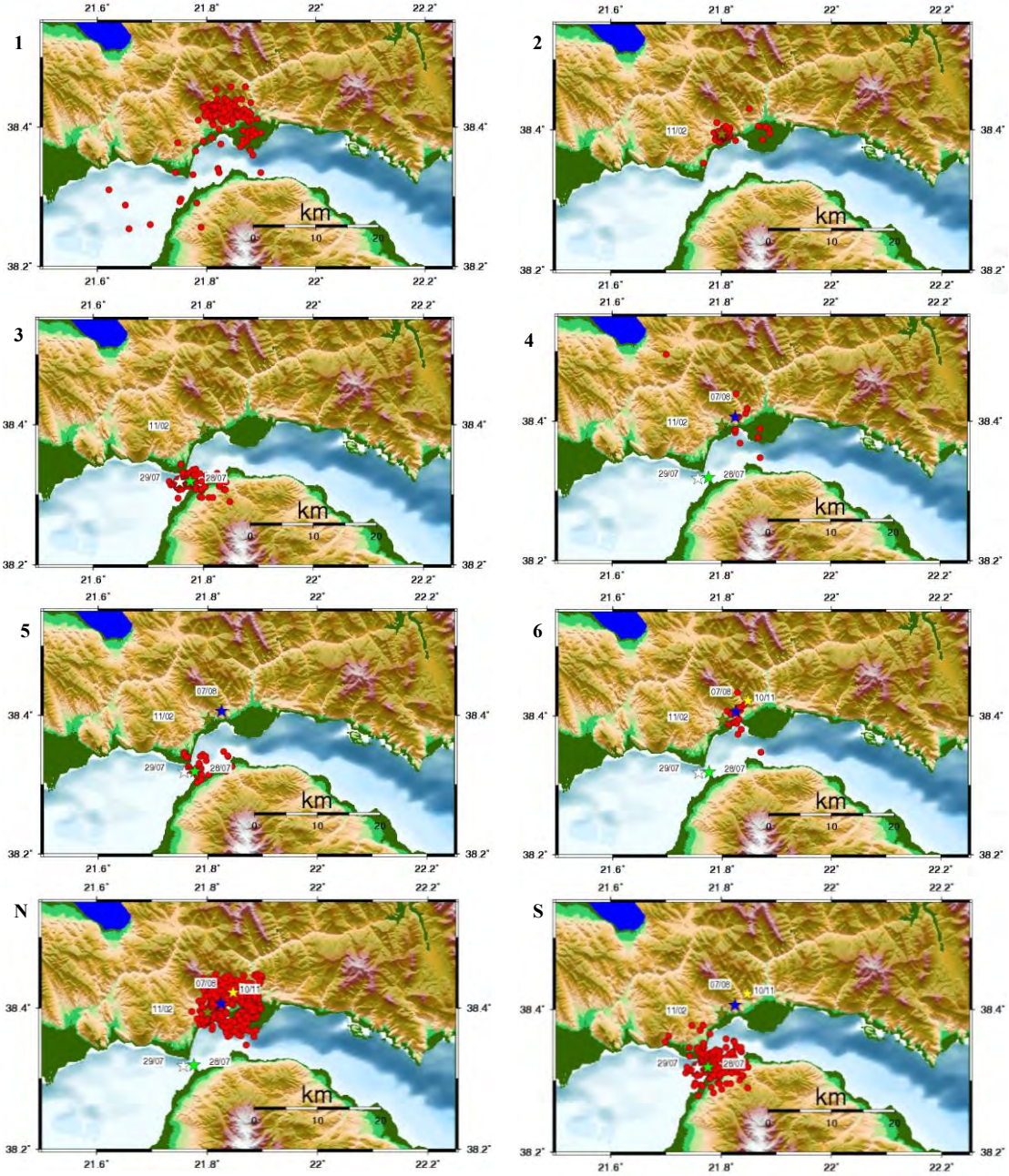

Figure 5 – Horizontal projection of seismic activity for the time period 2010-2011. Numbers (1 to 6) represent the seismic swarms that are referred in figure 4. The last two images (indicated as N and S) obtain the space distribution of north and south clusters respectively.

5. Acknowledgments

The GMT system (Wessel and Smith (1998) was used to plot the figures. We would like to thank the two anonymous reviewers for their comments and useful suggestions. Geophysics Department Contribution 809/2013.

6. References

Avallone A., Briole P., Agatza-Balodimou A.M., Billiris H., Charade O. and Veis G. 2004. Analysis of eleven years of deformation measured by GPS in the Corinth Rift Laboratory area, *C.R.Geoscience,* 336 (4-5):301-312.

Baker C., Hatzfeld D., Lyon–Caen H., Papadimitriou E. and Rigo A. 1997. Earthquake mechanisms of the Adriatic Sea and Western Greece: implications for the oceanic subduction–continental collision transition, *Geophys. J. Int.*, 131, 559–594.

Bell R.E., McNeill L.C., Bull J.M. and Hantstock T.J. 2008. Evolution of the western Gulf of Corinth, *Bull. Geol. Soc. Am.*, 120(1/2), 156-178, doi:10.1130/B26212.1.

Briole P., Rigo A. Lyon-Caen H., Ruegg J.C., Papazissi,K. Mitsakaki C., Balodimou A., Veis G., Hatzfeld D. and Deschamps A. 2000. Active deformation of the Corinth rift, Greece: Results from repeated Global Positioning System surveys between 1990 and 1995, *J. Geophys. Res.*, 105, 605–625.

Brodsky E.E., Karakostas V. and Kanamori H. 2000. A new observation of dynamically immerged regional seismicity: earthquakes in Greece following the August, 1999 Izmit, Turkey Earthquake, *Geophys. Res. Lett.,* 27, 2741-2744.

Burton P.W., Xu Y., Qin CH., Tselentis G., Sokos E. 2004. A catalogue of seismicity in Greece and the adjacent areas for the twentieth century, *Tectonophysics*, 390, 117-127.

Doutsos T. and Poulimenos G. 1992. Geometry and kinematics of active faults and their seismotectonic significance in the western Corinth-Patras rift (Greece), *Journal of Structural Geology*, 14 (6), 689-699.

Flotte N., Sorel D., Muller C. and Tensi J. 2005. Along strike changes in the structural evolution over a brittle detachment fault example of the Pleistocene Corinth-Patras Rift (Greece), *Tectonophysics*, 403, 77-94.

Hatzfeld D., Pedotti G., Hatzidimitriou P. and Makropoulos K. 1990. The strain pattern in the western Hellenic arc deduced from a microearthquake survey, *Geophys. J. Int.*, 101, 181–202.

Hatzfeld D., Karakostas V., Ziazia M., Kassaras I., Papadimitriou E., Makropoulos K., Voulgaris N. and Papaioanou C. 2000. Microseismicity and faulting geometry in the Gulf of Corinth (Greece), *Geophys. J. Int.*, 141, 438–456.

Hutton L.K. and Boore D.M. 1987. The M_L scale in southern California, *Bull. Seism. Soc. Am.*, 77, 2074-2094.

Karakostas V., Karagianni E. and Paradisopoulou P. 2012. Space-time Analysis, faulting and triggering of the 2010 earthquake doublet in western Corinth Gulf, *Natural Hazard*, doi:10.1007/s1 1069-012-0219-0.

Klein F.W. 2000. User's Guide to HYPOINVERSE–2000. A Fortran program to solve earthquake locations and magnitudes, *U. S. Geol. Surv. Open File Report,* 02–171 Version 1.0.

McNeil L.C., Cotterill C.J., Henstock T.J., Bull J.M., Stefanos A., Collier R.E.L., Papatheodorou G., Ferentinos G. and Hicks S.E. 2005. Active faulting within the offshore western Gulf of Corinth, Greece:Implication tops models of continental rift deformation, *Geology*, 33, 241-244.

Novotny O., Jansky J., Plicka V. and Lyon-Caen H. 2008. A layered model of the upper crust in the Aigio region of Greece, inferred from arrival times of the 2001 earthquake sequence, *Stud. Geophys. Geod.*, 52, 123–131.

Nur A. and Booker J.R. 1972. Aftershocks caused by pore fluid flow? *Science*, 275, 885-887.

Pacchiani F. and Lyon-Caen H. 2010. Geometry and spatio–temporal evolution of the 2001 Agios Ioanis earthquake swarm (Corinth Rift, Greece), *Geophys. J. Int.*, 180, 59–72.

Panagiotopoulos D.G. and Papazachos B.C. 1985. Travel times of Pn waves in the Aegean and surrounding area, *Geophys. J. R. astr. Soc.*, 80, 165–176.

Prejean S.G., Hill D.P., Brodsky E.E., Hough S.E., Johnston M.J.S., Malone S.D., Oppenheimer D.H., Pitt A.M. and Richards-Dinger K.B. 2004. Remotely triggered seismicity on the United States west coast following the M_w 7.9 Denali Fault earthquake, *Bull. Seism. Soc. Am*. 94(6B), S348-S359.

Reasenberg P. and Openheimer D. 1985. FPFIT, FPPLOT, and FPPAGE: FORTRAN computer programs for calculating and displaying earthquake fault-plane solutions, *U.S. Geological Survey Open–File Report,* 85-739.

Rigo A., Lyon-Caen H., Armijo R., Deschamps A., Hatzfeld D., Makropoulos K., Papadimitriou P. and Kassaras I. 1996. A micro-seismic study in the western part of the Gulf of Corinth (Greece): implications for large–scale normal faulting mechanisms, *Geophys. J. Int.*, 126, 663–688.

Scholz C.H., 2002. *The Mechanics of Earthquakes and Faulting*, 2nd Edn, Cambridge University Press, Cambridge.

Tselentis G-A. Serpetsidaki A. Martakis N. Sokos E. Paraskevopoulos P and Kapotas S. 2007. Local high resolution passive seismic tomography and Kohonen neural networks, application at the Rio-Antirrio Strait, Central Greece, Geophysics, Vol. 72, (4) 93-106.Wessel, P. and Smith, W. H. F., 1998. New, improved version of the Generic Mapping Tools Released, *EOS Trans. AGU,* 79, 579.

Δελτίο της Ελληνικής Γεωλογικής Εταιρίας, τόμ. XLVII, 2013
Πρακτικά 13ου Διεθνούς Συνεδρίου, Χανιά, Σεπτ. 2013

Bulletin of the Geological Society of Greece, vol. XLVII, 2013
Proceedings of the 13th International Congress, Chania, Sept. 2013

HYDROGEOPHYSICAL EXPLORATION FOR ESTIMATING GROUNDWATER RESERVOIRS AREAS IN SOUTHERN RHODES THROUGH ERT (ELECTRICAL RESISTIVITY TOMOGRAPHY) METHOD

Karmis P.[1], Giannoulopoulos P.[2], Sofos F.[1] and Lappas I.[2]

[1]National Centre of Sustainable Development – Institute of Geology and Mineral Exploration, Sector of Basic and Applied Geology, Department of Geophysics, 13677 Acharnai, Athens, Greece

[2]National Centre of Sustainable Development – Institute of Geology and Mineral Exploration, Sector of Water Resources and Environment, Department of Hydrogeology, 13677 Acharnai, Athens, Greece

Abstract

The present study deals with the groundwater investigation of hydrogeological conditions of Southern Rhodes, in the search for additional groundwater supplies to support the water needs of the area. An extensive Hydrogeological – Geophysical research was conducted, aimed to identify exploitable groundwater zones. This geophysical survey was carried out along alluvial basins, looking for more permeable geological formations within the sequence of the Neogene and Quarternary deposits. The use of a high resolution geophysical method (ERT) was selected for targeting the shallow geological structures and hydrostratigraphy. Thirteen ERT sections of total length of approximately 34000m were measured, laid out primarily at the south eastern part of the island. The geophysical survey revealed that alluvial sediments have an average thickness of about 30m while nearby the coastal zone increase locally up to 50m. The hydrostratigraphical structure is characterized by three distinct sections, the overlying alluvial deposits, the intermediate clay-marls and the underlying coarse formations. Moreover, almost all fault zones which are reflected in the surface geological map are revealed in greater depths. Result of vertical tectonic movements is the uplift of geological formations with increased resistivity. Finally, the target areas were selected based on hydrogeological criteria and specifically taking into account the increased possibility of groundwater reservoirs within the alluvial aquifer.

Key words: *Groundwater supplies, exploitable groundwater zones, high resolution geophysical method, hydrostratigraphy.*

Περίληψη

Η παρούσα μελέτη ασχολείται με την έρευνα των υπόγειων νερών και των υδρογεωλογικών συνθηκών της Νότιας Ρόδου, στην αναζήτηση υπόγειων υδατικών αποθεμάτων για την υποστήριξη των αναγκών της περιοχής σε νερό. Μια εκτεταμένη Υδρογεωλογική – Γεωφυσική έρευνα διεξήχθη, με στόχο τον εντοπισμό εκμεταλλεύσιμων ζωνών υπόγειων υδάτων. Η γεωφυσική έρευνα πραγματοποιήθηκε κατά μήκος αλλουβιακών λεκανών, αναζητώντας υδροπερατούς γεωλογικούς

σχηματισμούς εντός της ακολουθίας του Νεογενών και Τεταρτογενών αποθέσεων. Η χρήση της γεωφυσικής μεθόδου υψηλής ανάλυσης (ERT) επιλέχθηκε για τη στόχευση των ρηχών γεωλογικών δομών και της διερεύνησης της υδροστρωματογραφίας. Δεκατρείς ERT τομές συνολικού μήκους περίπου 34000m μετρήθηκαν στο νοτιοανατολικό τμήμα του νησιού. Η γεωφυσική έρευνα αποκάλυψε ότι οι προσχωματικές αποθέσεις έχουν μέσο πάχος περίπου 30m, ενώ κοντά στην παράκτια ζώνη παρατηρείται αύξηση έως και 50m. Η υδροστρωματογραφική δομή χαρακτηρίζεται από τρία διακριτά τμήματα, τις υπερκείμενες προσχώσεις, τις ενδιάμεσες πηλο-μαργαϊκές αποθέσεις και τους υποκείμενους αδρόκοκκους σχηματισμούς. Επιπλέον, σχεδόν όλες οι ρηξιγενείς ζώνες που αποτυπώνονται επιφανειακά, εκδηλώνονται και σε μεγαλύτερα βάθη. Αποτέλεσμα των κατακόρυφων τεκτονικών κινήσεων είναι η αναθόλωση των γεωλογικών σχηματισμών με αυξημένη ειδική αντίσταση. Τέλος, οι περιοχές ενδιαφέροντος επιλέχθηκαν, βάσει υδρογεωλογικών κριτηρίων και λαμβάνοντας ιδιαίτερα υπόψη την αυξημένη ύπαρξη υπόγειων θυλάκων νερού εντός του προσχωσιγενούς υδροφόρου ορίζοντα.
Λέξεις κλειδιά: *Υπόγεια υδατικά αποθέματα, εκμεταλλεύσιμες ζώνες υπόγειου νερού, γεωφυσική μέθοδος υψηλής ανάλυσης, υδροστρωματογραφία.*

1. Introduction

The present study investigates the hydrogeological conditions of Southern Rhodes with regards to the search for additional groundwater resources for supporting the water needs of the study area. Taking into account the acute water supply problem during the summer season, due to the population rise, the extended drought as well the quantitative and qualitative aquifers degradation because of the excessive pumping, the need for finding groundwater permeable areas becomes crucial. Given the available data from previous geological and hydrogeological studies taken place by the Institute of Geology and Mineral Exploration, an extensive Hydrogeological – Geophysical campaign was conducted, aimed to identify exploitable groundwater zones.

2. Methodology

The hydrogeophysical exploration aims to quantify the subsurface hydrogeological parameters based on experience in oil and mineral investigation. Yet in hydrogeological applications the contrast between the target's physical properties and environment's is small making the geophysical response obscure. For that reason, the use of high resolution geophysical methods is necessary in order to determine the nature and geometry of the shallow geological structures. The geophysical survey was conducted along the alluvial basins of Asklipio – Gennadi, Vati, Kolonitis and Lachania, exploring systematically the potential groundwater ability of the geological formations.

The choice of the most suitable geophysical method depends on the geological – hydrogeological settings, the penetration depth and the topographic relief. On sedimentary basins, the DC Vertical Electrical Sounding (VES) method (Koefoed, 1979) provides information of the geological stratigraphy and identifies the existence or not of the potential groundwater zones. In cases, however, of lateral geological variations and complex topographic relief, the above method has limited reliability and effectiveness, taking into consideration the need of large electrode arrays in the field (Rubin et al., 2005). The growth of geophysical data inversion techniques along with the development of hardware has resulted to the emerging of subsurface imaging methods, such as the Electrical Resistivity Tomography (ERT) as one of the most effective methods (Dahlin, 2001), combining advantages such as: a) imaging reliability of the actual distribution of the subsurface resistivity, b) high definition of the two-dimensional geoelectrical structure and c) topographic correction removing the effect of topographic relief (Kirsch, 2005, Rubin et al., 2005).

In case of Southern Rhodes the Syscal Pro (Iris) system (Kim, 2009) was used with a multiprobe array of 48 electrodes of 20m dipole length, with the penetration depth reaching 200m. This was considered satisfactory taking into account the seawater intrusion and the relatively mild topographic relief of the study area. With the constant movement of the array and a 50% overlap of the electrodes spread, long lines of length up to 4800m were covered. Thirteen (13) ERT sections with total length of 34000m were surveyed, focused on the Eastern part of the study area. The selection of target areas was based on hydrogeological criteria and taking into account the increased possibility of groundwater reservoirs within the alluvial aquifer.

3. Geological, Tectonics and Hydrogeological Settings

3.1. Geology

The Rhodes island's stratigraphy is characterized by the presence of Neogene sediments and the formations of the Ionian geotectonic zone (Figure 1). Specifically it consists of:

- Plio – Pleistocene deposits: consisted of talus and land deposits. They mostly appear at the Southern part of the island between the hilly area of Katavia and Prasonissi over Sgourou formations. The latter consists of porous limestones and greenish – grey marls with sand and gravels over Levantine deposits, which are consisted of fluvial conglomerates, sands and silty marls.
- Oligocene – Miocene deposits: comprised of Mesanagros sandstone, Agios Minas marls and Kortiatis conglomerates derived from ophiolites, limestones and radiolarites as well Thari formation consisting of ophiolithic, carbon and silicate conglomerates. This sedimentary sequence lies unconformably between the overlying Levantinian deposits and the underlying flysch of Ionian geotectonic zone.
- Ionian geotectonic zone: Katavia flysch, Hocene limestones, marly and silicate limestones (upper Jurassic – upper Cretaceous) are included.
- Pindos geotectonic zone: consisted of Malona limestones with silica and radiolarites, Elafokampos silicate, well-bedded dolomitic limestones, Kopria diavases – radiolarites and Ophiolites (Triassic – Jurassic).
- Parnassos geotectonic zone: Archipolis flysch (Paleocene – Hocene), Salakos limestones and Koumouli limestones (Triassic – Hocene) are included.
- Gavrovo – Tripolis geotectonic zone: consisted of thick-bedded, crystallic Lindos limestones (Cretaceous) of maximum thickness 450m.

3.2. Tectonics

The study area is characterized by the post alpine sediments monoclinic structure. Katavia flysch is the geological bedrock, overlaid by Kortiatis conglomerates, Mesanagros sandstones, Agios Minas marls, Levantinian sediments and gray – greenish Sgourou formations. Stratigraphic unconformities exist almost to all above formations' contacts. At the central and eastern part of the study area the formations have monoclinic structure with a Southeastern dip, while at the western part of Apolakia a West – Northwestern dip prevails. The folding tectonics is almost completely absent however the presence of faulty structure is significant with faults intersecting both alpine and post – alpine formations: the prevailing fault systems are of Southwest – Northeast and Northwest – Southeast direction, perpendicular to each other.

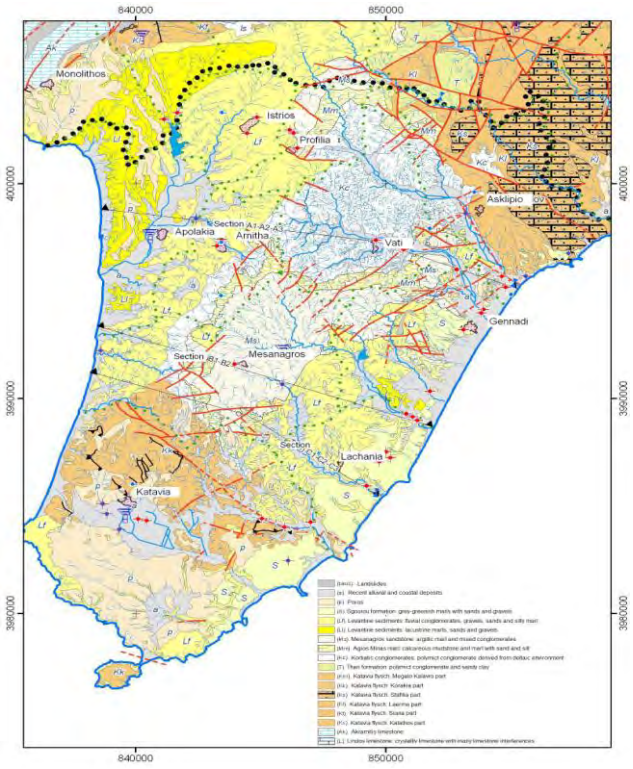

Figure 1 - Geological map of Southern Rhodes (Mutti et al., 1965 with modifications).

3.3. Hydrogeology

The aquifers directly depend on the hydrogeological behavior and the tectonics of geological formations, according to which they are divided into impermeable, semi-permeable and permeable ones (Giannoulopoulos and Lappas, 2008, 2010).

- Impermeable formations: Katavia flysch, clay phase of Levantinian sediments and Agios Minas marls are included.
- Semipermeable formations: Mesanagros sandstones, Levantinian sediments, Sgourou formation and Kortiatis conglomerates are included. Drilled boreholes to the above mentioned formations yield 5 – 15m^3/h.
- Permeable formations: Alluvial and fluvial deposits of the coastal zones and within the valleys which are included from Asklipio to Katavia. Drilled boreholes to these sediments yield over 60m^3/h. At Katavia alluvial aquifer boreholes yield between 10 – 20m^3/h.

The region's aquifers are the followings (Figure 2):

- Alluvial aquifer of Asklipio – Gennadi - Lachania: consisted of coarse sediments which are derived from the underlying Kortiatis conglomerates and Levantine sediments. Drilled boreholes to these sediments exceed yields locally over 60m^3/h.
- Alluvial aquifer of Apolakkia: developed in the western part and lithologically consists of erosion materials derived from Levantine sediments which are finer than those in the eastern part. That is the reason why boreholes yield less than those in the eastern zone and range from 10 to 20m^3/h.

- Alluvial aquifer of Katavia: developed in the southern part of the island, surrounded mostly by flysch and consisted of fine thin sediments, while the boreholes yields do not exceed $20m^3/h$.
- Aquifers of Levantine sediments: two separate aquifers are identified, the one of the eastern part and that of the western. In the eastern part, the aquifer is developed at the hilly region of Gennadi – Lachania, while at the western one the aquifer covers the hilly regions of Arnitha, Apolakia and Istrios. Boreholes yields range from 5 to over $30m^3/h$ and depend directly on sediments's lithological in-homogeneities.

Mesanagros sandstone has flyschoid texture and is not expected to host remarkable groundwater resources. A borehole drilled at depth greater than 150m is reported to yield only $10m^3/h$. Kortiatis conglomerates are coarse derived from gravels and sands with relatively limited clay phase participation. Vati's borehole yields almost $10m^3/h$, while it is estimated that the formation may yield significantly higher groundwater quantities taking into account its lithological texture.

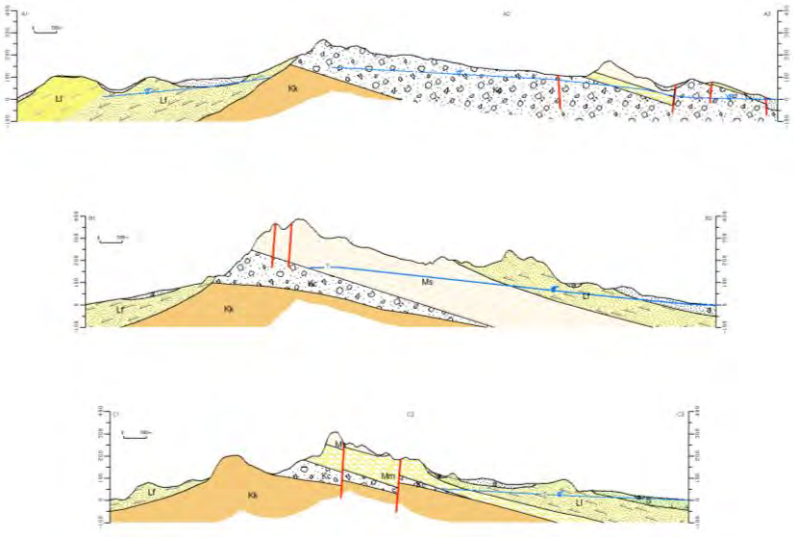

Figure 2 - Schematic hydrolithological sections (Giannoulopoulos and Lappas, 2008).

4. Geophysical Investigation, Processing and Interpretation

The data processing followed the steps: i) measuring the coordinates of the start and end of each line, the intermediate centers of the arrays, as well as the altitude of each electrode through a digital elevation model (DEM), ii) calculation of the Digital elevation model (DEM) of the island with a cell size of 20m which was utilized in assigning the actual coordinates of the electrodes, calculating the correct geometrical factors of the array and correcting the topographic relief and iii) inversion of data with an iterative smoothness constrain scheme (DC2Dpro, Kim, 2009). The location of ERT lines is shown in Figure 3.

4.1. Gennadi Area – Section 1

The results of the inversion – interpretation are shown in Figure 4. Numbers 1 to 9 correspond to successive spread centers along the line. All sections are plotted from West to East or NW to SE.

Gennadi 1-1: The largest part of the line (0 - 1500m) exhibits surface cover of coarse sediments with resistivity values in the range of 70 - 200Ω.μ, thickness of 40-50m, implying possible association with water reservoir. These sediments are consisted of fluvial conglomerates, gravels

and sands included in Levantine deposits. Stratigraphically under the conglomerates, conductive clay and marly sediments can be detected which are attributed to Levantine sediments and Agios Minas marls. Also, resistive anomalies possibly associated with conglomerates of Levantine sediments or more likely with the underlying Mesanagros sandstones can be recognized. The ERT image explains the satisfactory yield of G41 and G42 boreholes, which despite their shallow depth they exploit areas with increased thickness of the surface layer of permeable conglomerates.

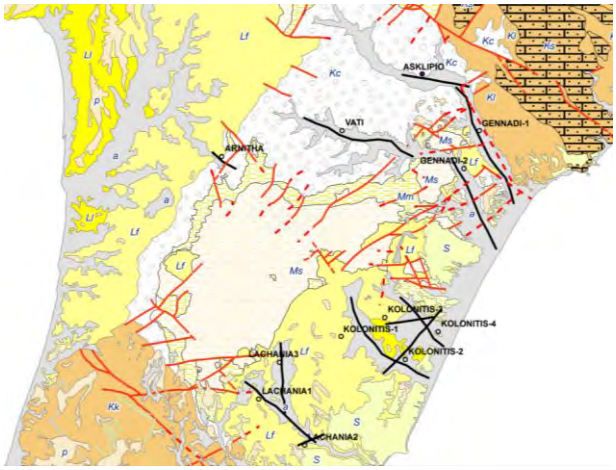

Figure 4 - Location map of ERT lines.

Gennadi 1-2: Tectonic discontinuities are identified mainly within the high resistivity conglomerates or sandstones. The surface layer of coarse sediments is detected in the second half of the line with relatively lower thickness and anomalies that may prove potential groundwater areas.

Gennadi 1-3: The surface layer of coarse sediments reaching 35m of thickness is occasionally detected. The conductive layer of clays and marls under the conglomerates is detected while antistatic anomalies are identified at depth, associated with the carbonate parts of Katavia flysch and determined by tectonic discontinuities. The shape of the anomaly and resistivity values of 100 – 150Ω.μ suggests a possible relationship with a paleovalley. The existence of tectonic discontinuity within the margins favors the potential permeable formation's supply.

4.2. Gennadi Area – Section 2

The top layer of fluvial conglomerates with thickness up to 30m is detected, underlain by a conductive layer of fine sediments associated to clays and marls. Resistive anomalies are located below, confined by tectonic discontinuities, possibly associated to permeable carbonate formations. To the South of the spread center 6 the boundaries of seawater intrusion are detected with characteristically very low resistivity values of 2Ω.μ. At the proximity of the limits of the seawater intrusion in the area, two active boreholes G43 and G106 exist, of very shallow depth (40m) exploiting the surface permeable layer of conglomerates. These boreholes will be most likely contaminated by seawater intrusion at deeper levels and their exploitation should be carefully monitored.

4.3. Asklipio Area

The top resistive layer of fluvial layer of conglomerates is clearly seen, with thickness of 30m, underlain by conductive clay – marly sediments with low resistivity values of 5Ω.μ. Resistive anomalies are recorded at deeper levels, possibly associated to probable permeable formations, bounded by tectonic discontinuities (Figure 5a).

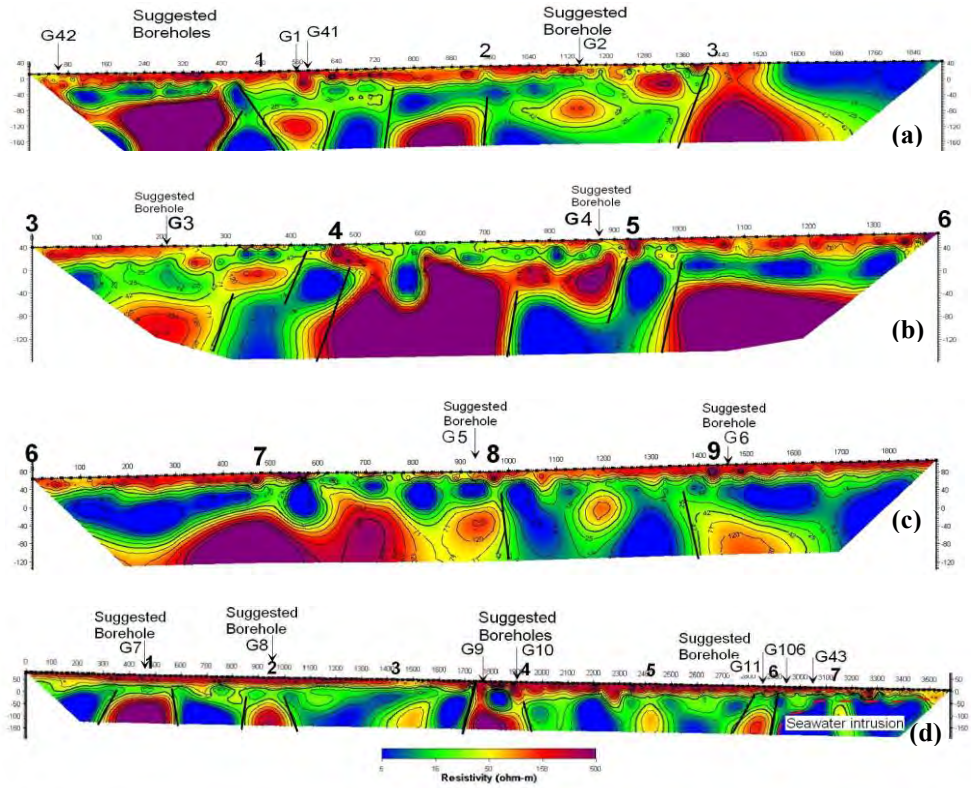

Figure 4 - ERT inversion results along Gennadi lines 1-1 (a), 1-2 (b), 1-3 (c) and line 2 (d).

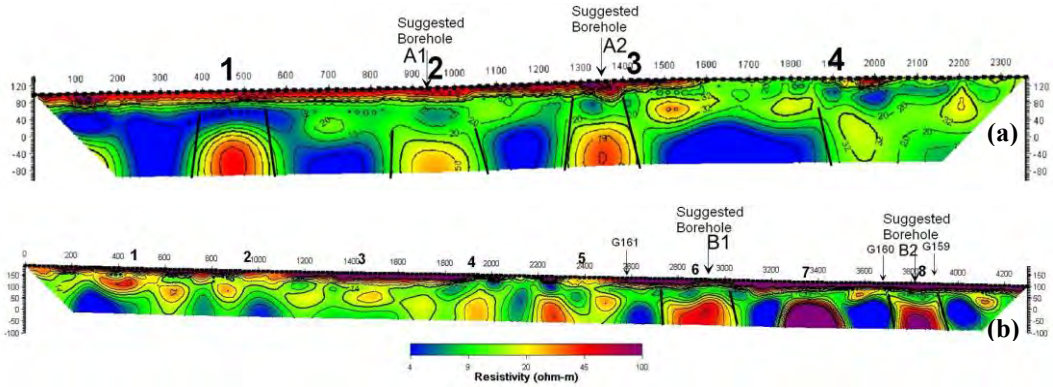

Figure 5 - ERT inversion results along Asklipio (a) and Vati (b) lines.

4.4. Vati Area

The surface layer of conglomerates is detected, along the entire length of the line, reaching a maximum thickness of 35m at the Eastern part of the section (Figure 5b). This is underlain by conductive clay materials, belonging to Agios Minas marls. The position of three existing boreholes G159, G160 and G161 is drawn on the ERT section and it can be clearly seen that the limited thickness of the conglomerates explains the fact that all three boreholes are dry or yield very small groundwater quantities.

4.5. Kolonitis Area

Line 1: The shallow layer of gravels and sands reaches the thickness of 20m (Figure 6a). To the Southeast and between the centers 6 and 8, the layer's thickness increases up to 50m approximately and the nearby boreholes (G45, G171 and G172) exploit this particular layer. Tectonic discontinuities are also identified which delineate the carbonate parts of Levantine sediments. The negative aspect in hydrogeological prospect is that these carbonate formations are surrounded by strongly conductive formation associated to impermeable silty marl, diminishing the groundwater potential of the area. An important point of interest is the extended seawater intrusion reaching up to 1700m from the coast so it is assumed there is a serious risk of boreholes contamination. From the above data it is concluded that no borehole drilling can be proposed in this area.

Line 2: In the first 600m along the line, the shallow layer of gravels reaching the maximum thickness of 38m is recognized (Figure 6b). The conductive layer of silty marl is detected below. Between the stations 700 and 1100 a conductive layer of very low resistivity (<2Ω.μ) is identified which is attributed to seawater intrusion. Tectonic discontinuities are also identified at stations 200, 400 and 700. The seawater intrusion as well as the general resistivity image of the line does not justify any borehole target proposal.

Line 3: It is concluded through ERT image that the geological structure is consisted of Levantine sediments with conglomerates, gravels, sands and marls (Figure 6c). At the center of the line a resistive anomaly is recorded with possible association to sandstone. At the Eastern part of the line a shallow layer of conglomerates with underlying marl is also identified.

Line 4: The shallow layer of conglomerates with an average thickness of 15m is recognized, underlain by Levantine fine sediments (Figure 6d). Moreover, tectonic discontinuities can be observed. At station 500 the shape of the resistivity image suggests a possible paleovalley bounded by tectonic discontinuities.

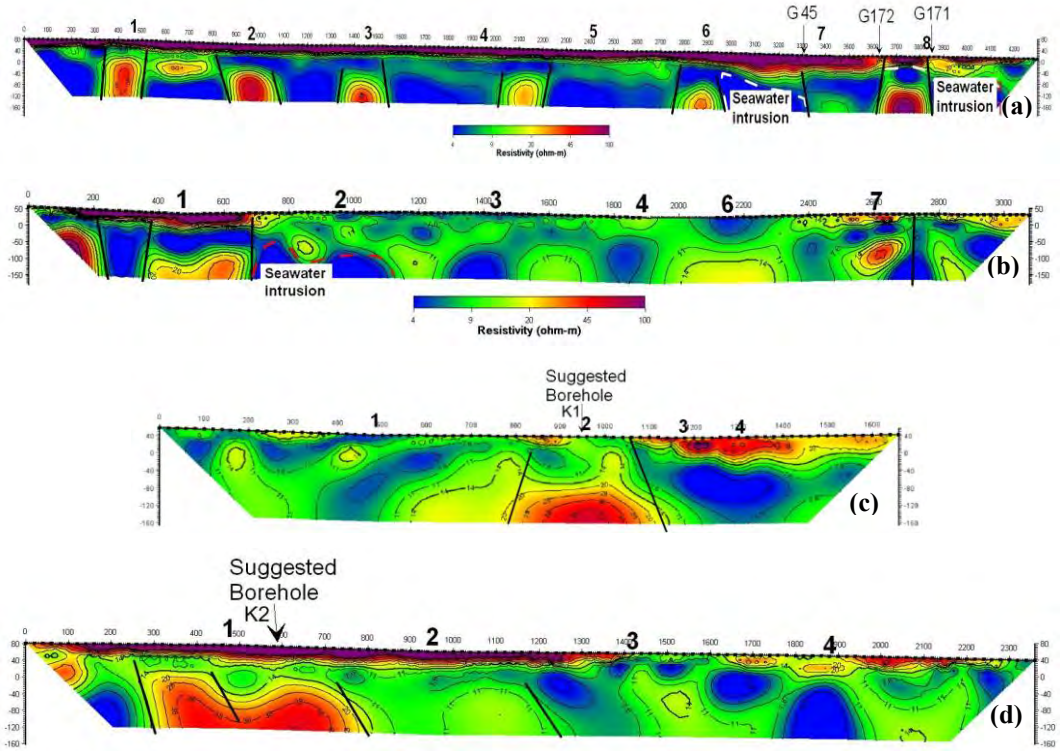

Figure 6 - ERT inversion results along Kolonitis lines 1(a), 2(b), 3(c) and 4 (d).

4.6. Lachania Area

Line 1: The line is entirely structured by fine thin sediments, alluvial deposits, sands and marls (Figure 7a).

Line 2: A surface thin layer of conglomerates at the center of the section with a maximum thickness of 20m is detected while the underlying one is attributed to marls (Figure 7b). Between the locations 560 and 700 a low resistivity value area is recognized indicating seawater intrusion. The seawater intrusion may be taking place in the first half of the ERT too where the resistivities are also very low.

Line 3: The hydrogeological interest of this line is focused on the first half and especially on the existence of successive tectonic discontinuities limiting the extent of resistive blocks uplifted within a regionally conductive environment of impermeable marls (Figure 7c). These are probably sandstone blocks belonging to Mesaoagros sandstones.

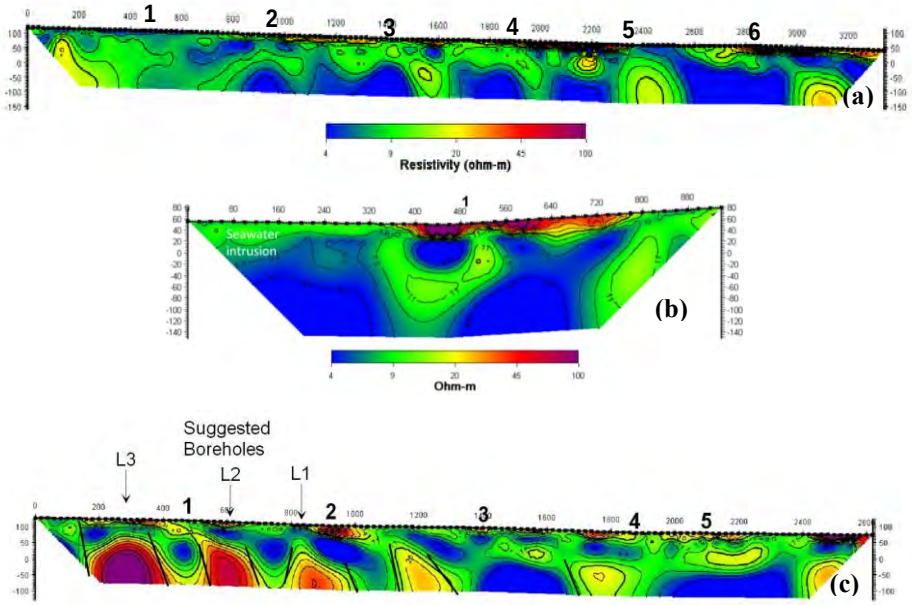

Figure 7 - ERT inversion results along Lachania lines 1(a), 2(b) and 3 (c).

4.7. Arnitha Area

The top layer of resistive conglomerates reaching a thickness of 30-35m covers the whole extent of the line. This is underlain by marly and clastic parts of Kortiatis conglomerates as well as the Levantine marls. The suggested borehole at station 100 is expected to drill increased thickness of surface conglomerates and a resistive block probably associated to the Kortiatis conglomerates.

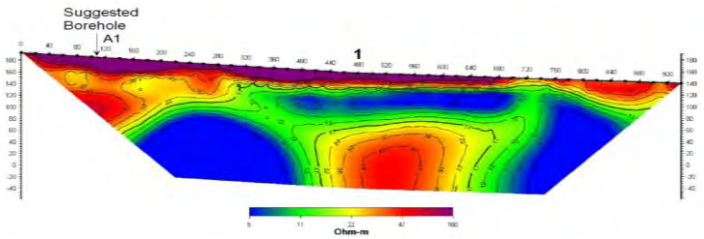

Figure 8 - ERT inversion results along Arnitha line.

5. Concluding Remarks

From the hydrogeophysical survey conducted on the Southern part of Rhodes island, the following conclusions can be drawn:

- The fluvial deposits between Asklipio and Lachania basins have an average thickness of 30m which in some places mostly nearby the coastal zone increase locally up to 50m forming favorable groundwater conditions.
- The hydrogeological – geophysical structure is characterized by three distinct sections: 1) the overlying alluvial – fluvial deposits, 2) the intermediate clay – marly formations (Agios Minas marls and the clay phase of Levantine sediments) and 3) the underlying coarse formations (Mesanagros sandstone and Kortiatis conglomerates). The groundwater potential of the shallow alluvial aquifer is mainly concentrated near the coastal zone. West from the coastal zone, groundwater is expected in areas with strong lithological inhomogeneities as well as in the vicinity of fracture zones.
- All fracture zones mapped in the area have been detected by the ERT survey along with additional structural discontinuities with no surface expression. From geophysical evidence it is suggested that these structural lines are related to the uplift of resistive geological formations, possibly attributed to Mesanagros sandstones or Kortiatis conglomerates.
- At the area of Gennadi the seawater intrusion has advanced at 800m from the coast line and it may affect the existing wells G43 and G106. This problem is more severe at the Kolonitis area, where the seawater intrusion has advanced at 1700m from the coastline probably affecting the wells G45, G171 and G172.
- A number of boreholes have been selected for drilling, as shown in Figures 4 to 9 and they are all expected to intersect coarse groundwater permeable formations.

6. Acknowledgements

The authors would like to thank the board of the municipality of Southern Rhodes for the hospitality and the unconditional help offered to all phases of the field work for the whole project's accomplishment.

7. References

Dahlin T. 2001. The development of DC resistivity imaging techniques, *Computers & Geoscience*, 27, (9), 1019-1029.

Giannoulopoulos P. and Lappas I. 2008. Hydrogeological Identification and Mapping of Water Supply Conditions in the Municipality of Southern Rhodes, Rhodes Island, Prefecture of Dodecanese, *I.G.M.E.,* Athens.

Giannoulopoulos P. and Lappas I. 2010. Hydrogeological Study of the Water District of Aegean Islands. Water Resources Assessment, Quality Control and Development Proposals. 3rd Community Support Framework, *I.G.M.E.,* Athens.

Kim Y.H. 2009. DC2Dpro – User's Manual, KIGAM, Daejon, Korea.

Kirsch R.2005. *Groundwater Geophysics*. Springer, 492 pp.

Koefoed O.1979. *Geosounding principles, 1, Resistivity Sounding Measurements*. Elsevier, Amsterdam.

Mutti E., Orombelli G. and Pozzi R. 1965. *Geological Map of Rhodes Island,* University of Milan Italy.

Rubin Y. and Hubbard S. 2005. *Hydrogeophysics,* Springer, 521 pp.

Δελτίο της Ελληνικής Γεωλογικής Εταιρίας, τομ. XLVII , 2013
Πρακτικά 13ου Διεθνούς Συνεδρίου, Χανιά, Σεπτ. 2013

Bulletin of the Geological Society of Greece, vol. XLVII 2013
Proceedings of the 13th International Congress, Chania, Sept. 2013

THE 1912 GANOS EARTHQUAKE: SOURCE CONSTRAINTS USING GROUND MOTION SIMULATIONS

Kiratzi A.

Department of Geophysics, Aristotle University of Thessaloniki, Greece (Kiratzi@geo.auth.gr)

Abstract

We study the source characteristics of the 9 August 1912, Mw 7.4, Mürefte (Ganos) earthquake that ruptured the Ganos Fault in the westernmost segment of the North Anatolian Fault. We apply the stochastic method for finite-faults in order to simulate strong ground motion acceleration using different fault geometries in terms of the rupture initiation and the length of the fault. A first-order approximation of the site effect variation is achieved following an empirical approach based on the topography gradient as a proxy for site-effect. The simulated ground motions, which are calculated at phantom stations, over a grid covering the area of study, satisfactorily produce the regions which were more severely shaken during the 1912 event. We simulate ground motions using a conservative fault length of 50 km (one land segment) which is able to explain the location of the surface ruptures but is not able to reproduce the surface extent of strong shaking. We then use a longer fault of approximately 120 km, extending to Saros Bay in the west and to Marmara Sea in the east. The synthetic peak ground acceleration values, indicate a segmented nature of the fault, have at least two patches of strong shaking and significantly predict the observed macroseismic intensities of the 1912 earthquake. Further constrain in our modelling is posed by surface ruptures, with small releasing and restraining structures and 1.5–5.5 m right-lateral offsets, that have been previously measured by others, at 45 sites of the on-land ~50-km-long fault section.
Key words: *Ganos fault; North Anatolian fault; Mürefte; deformation.*

Περίληψη

Ο σημαντικότερος σεισμός στο δυτικό άκρο του ρήγματος της Β. Ανατόλιας είναι αυτός της 9ης Αυγούστου 1912, Mw 7.4. Για τη μελέτη των χαρακτηριστικών της πηγής, και ειδικότερα του μήκους του ρήγματος που τον προκάλεσε καθώς και του σημείου έναρξης και διάδοσης της διάρρηξης, γίνεται στοχαστική προσομοίωση των εδαφικών κινήσεων. Στους κόμβους ενός πλέγματος που καλύπτει την ευρύτερη περιοχή υπολογίζεται η μέγιστη εδαφική επιτάχυνση από δυο σενάρια: κατά το πρώτο σενάριο το μήκος του ρήγματος είναι μόνο 50 km, όπως η επιφανειακή εμφάνιση στην ξηρά. Οι τιμές της επιτάχυνσης, διορθωμένες και για τις εδαφικές συνθήκες, αποτυπώνουν τις περιοχές στην ξηρά με τις μέγιστες μετρήσεις ολίσθησης, αλλά η συνολική επιφάνεια μέγιστης παραμόρφωσης είναι μικρότερη από την παρατηρηθείσα. Καλύτερη αποτύπωση γίνεται για ένα ρήγμα μήκους 1200 km, το οποίο πέρα από την ξηρά εκτείνεται τόσο στη θάλασσα του Μαρμαρά στα ανατολικά, όσο και στον Κόλπο του Σάρου στα δυτικά. Οι μέγιστες εδαφικές επιταχύνσεις αποτυπώνουν τουλάχιστον δυο περιοχές με ισχυρές εδαφικές κινήσεις, το οποίο μπορεί να εκληφθεί και ως

ένδειξη πολλαπλών πηγών κατά τη διάρρηξη. Για την αξιολόγηση των αποτελεσμάτων των στοχαστικών προσομοιώσεων συνεκτιμήθηκαν και οι μετρήσεις της επιφανειακής ολίσθησης κατά μήκος του ρήγματος
Λέξεις κλειδιά: *Μυριόφυτο, ρήγμα Ganos, παραμόρφωση, Ρήγμα Βόρειας Ανατόλιας.*

1. Introduction

The most significant earthquake at the western end of the North Anatolian Fault Zone (Figure 1), along the Ganos Fault Zone (GFZ) is the 9 August 1912 event (40.7°N, 27.2°E; UTC 01:29; Ms 7.0 to 7.6; Mw7.4) also known as Sarköy-Mürefte or Saros-Marmara earthquake (Ambraseys and Jackson, 1998, 2000; Janssen et al., 2009). The Ganos Fault Zone extends from the Tekirdag Basin in the east, up to the Island of Samothrace in the west, passing through the town of Gaziköy and the Saros Trough (Armijo et al., 1999; Seeber et al., 2004; Karabulut et al., 2006).

The earthquake caused the loss of 2,836 people, while more than 7,000 were injured. More than 300 villages suffered damage (Altinok et al., 2003; Papazachos and Papazachou, 2003), mainly to the north of Dardanelles. Liquefaction was observed to distances up to 180 km from the epicentre, indicating the level of strong ground motions. Long period ground motions were responsible for serious damage to public buildings as far as Edirne to the north and Istanbul to the east of the epicentre, The mainshock was followed by many aftershocks; the strongest was the one that occurred within hours after the mainshock (UTC 09:23; Ms 6.2). On 13 September 1912 (UTC 23:32) a second shock occurred of Ms 6.7 (Mw6.8), with an epicentre (40.1°N, 26.8°E) located at the westernmost edge of the August mainshock rupture, and was considered as a triggered event (Papadimitriou et al., 2001).

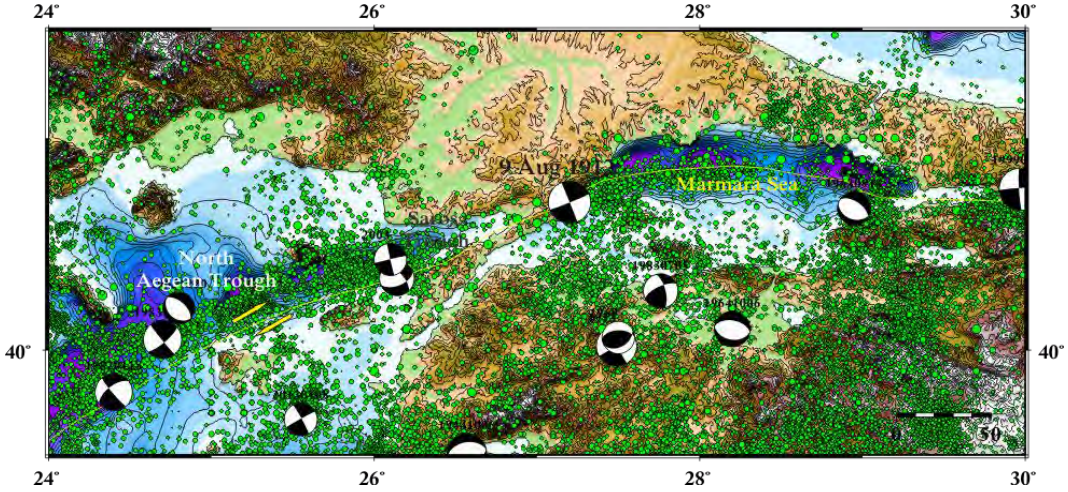

Figure 1 - The location of the 9 August 1912 earthquake along the Ganos Fault Zone. The beach- balls (from Kiratzi and Louvari, 2003; Kiratzi et al., 2007) denote the available focal mechanisms for previous events with Mw>6.0. The seismicity of the period 550BC- 2012 with M>5.0 is also plotted (green circles).

The 1912 earthquake has attracted the attention of many scientists mainly because it is connected with the inferred sub-marine fault system to the Marmara Sea, which poses a constant threat to the metropolitan city of Istanbul. Moreover, the connection of the Ganos Fault with other fault segments capable to produce strong earthquakes makes it even more significant.

The Ganos Fault Zone (GFZ) joins the northern strand of the North Anatolian Fault Zone (NAFZ) in the Marmara Sea and the North Aegean Sea. The western continuation of the NAFZ into the

North Aegean Trough is portioned and two main branches can be identified. The GFZ is clearly visible on satellite images. The northern part of the zone is bounded by the Ganos Mountains, which are considered to develop during the end of Miocene due to an episode of transpressional uplift, resulting from right lateral strike-slip motion, which in total is ~40 km.

The total rupture length of the 1912 earthquake is a matter of dispute. Most people agree that the length is well above the 50 km land segment, but what is the extent of the rupture into the Saros Trough and what is its extent into the western Marmara Sea is again controversial. For example, the rupture length is considered between 90 to 150 km (Aksoy et al., 2010 and references therein). The purpose of the present study is to examine a number of locations of the rupture initiation and two fault lengths in order to test their capability to reproduce the gross characteristics of the measured surface slip along-strike of the fault and to the distribution of damage (Figure 2) in the most affected region (Ambraseys and Finkel, 1987). To do so, stochastic ground simulations are performed using the method of Boore (1983) as used by Beresnev and Atkinson (1997, 1998).

2. Observations for Ground Motion Validation

The 9 August 1912 mainshock produced a surface expression of the fault with a distinct right lateral strike-slip motion (see Table 1 for parameters). The measured length on land was 45 - 50 km (Ambraseys and Finkel, 1987; Altunel et al., 2004). The long-period records from a small number of Wiechert seismographs were used to estimate the magnitude of this earthquake (Ambraseys and Jackson, 1998; Aksoy et al., 2010). The large magnitude ($M_w = 7.4$), declares that complimentary to the ~50 km land segment co-seismic faulting must have extended off-shore, towards the south-west into the Gulf of Saros, and towards the north-east into the Marmara Sea near Güzelkoy.

Table 1 – Information on the focal mechanism solutions reported for the 1912 shocks.

Date Y/MM/DD	Origin Time hh:mm	Lat	Long	Mw	NODAL PLANE 1 Strike° Dip° Rake°			NODAL PLANE 2 Strike° Dip° Rake°			Ref
19120809	01:29	40.7	27.2	7.3	41	60	-135	284	52	-39	1
#	#	40.7	27.2	7.4	68	88	180	158	89	2	2
19120809	09:23	40.8	27.5	6.2							1
19120913	23:32	40.7	27.0	6.8							1

References 1: Jackson and McKenzie 1988; 2: Aksoy et al., 2010

The distribution of the isoseismals for the 1912 mainshock clearly shows that in the mezoseismal region intensities were of the order of IX (Figure 2). The length of the major-axis of the contour of intensity IX is about 110 km. Complimentary to the distribution of observed intensities, there are data from the slip measured at 45 sites, along the land segment of the fault (Aksoy et al., 2010). These slip values range from 1.4 meters to 5.5 meters, with a median value of 4 m (Figure 3). The average slip is of the order of 2.5 m.

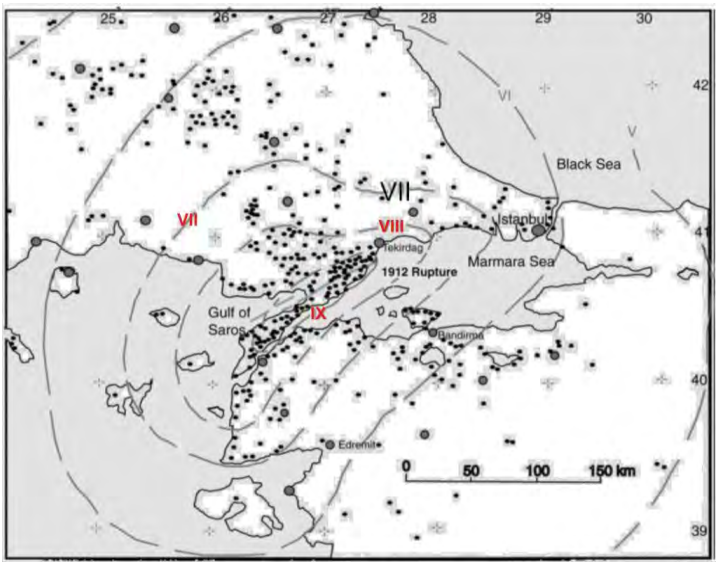

Figure 2 - Isoseismal map for the 1912 mainshock (from Ambraseys and Finkel, 1987). Note the distribution of intensity IX, which roughly has a length of ~110 km.

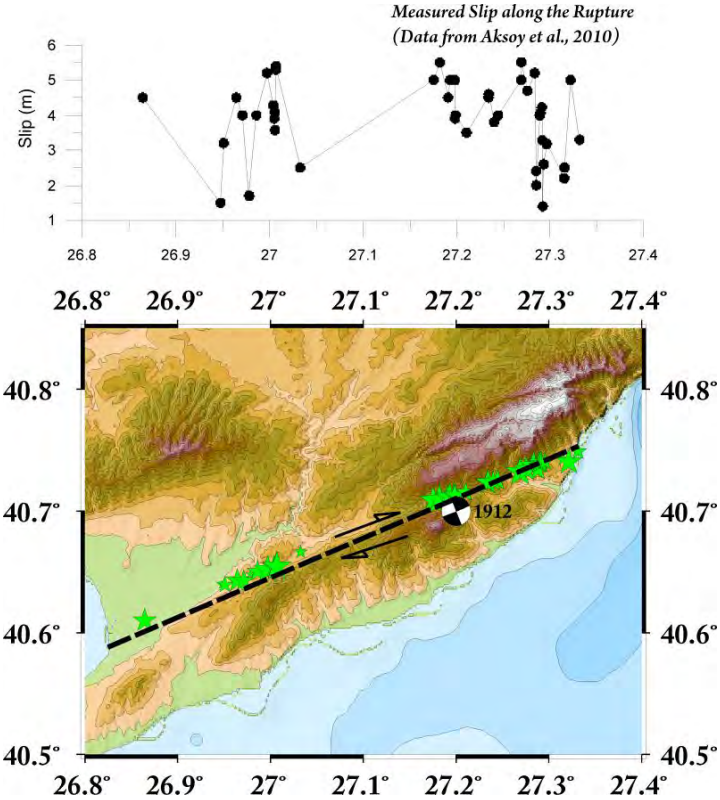

Figure 3 - Measured surface slip for the 1912 Ganos earthquake (top) as given by Aksoy et al., 2010, to compare with the assumed land fault segment and the assumed epicentre location, given by the beach-ball (bottom). Green asterisks denote the points where slip was measured.

3. Strong Ground Motion Modelling

3.1 Method

The core of the method used relies on the observation that a considerable portion of the strong ground motion, mainly related to the onset of S-waves, can be approximated as white noise. In parallel, the Fourier Amplitude Spectrum of a Brune omega-squared type source is stable and independent of frequency, for the frequencies between the corner frequency, fc and fmax. This led to the hypothesis that the strong ground motion, between the frequencies of fc and fmax, can be approximated by white noise.

The applied method requires a simple representation of all factors affecting strong ground motion. The source is approximated by a rectangular fault, and the propagation parameters (geometric spreading, inelastic attenuation, near-surface attenuation and site amplification) are described by empirical relations and factors. As mentioned, the method involves discretization of the fault plane into a number of sub-faults, each of which is assigned an ω^{-2} spectrum. Contributions from all sub-faults are empirically attenuated to the observation site using $Q(f) = 50f^{1.09}$ (Pulido et al., 2004) and appropriately summed to produce the synthetic accelerograms. Near-surface attenuation of the seismic waves was modelled using the kappa, κ, operator and diminishing the simulated spectra by $exp(-\pi\kappa f)$. Simulations at all sites of interest were performed assuming rock site conditions at the ground surface.

A first-order incorporation of the site effect in the computed ground motion parameters was based on the work of Wald and Allen (2007). They correlate the topography gradient of a region with VS_{30} (average shear-wave velocity at the top 30 meters of the soil column), which are often used as a proxy for soil characterization. Based on the VS_{30} value and the amplitude of the peak ground acceleration in the synthetic accelerograms at the specific grid point an appropriate empirical amplification factor for the PGA (Borcherdt, 1994) was selected.

3.2 Case 1: Conservative Fault Length

In this case the total along-strike length of the fault is taken equal to 50 km; the fault is placed on its surface expression on the land (Figure 3). The width of the fault is taken to be 17 km. The number of sub-faults along strike and along dip is 9 and 3, respectively. The purpose of the simulation is to see what the land segment of the rupture, can reproduce. The fault strike is taken as 68°, the dip is taken equal to 88° (Aksoy et al., 2010; see Table1).

The rupture starts from sub-fault [9, 3] that is at the easternmost and deepest location of the fault and propagates towards west. This rupture initiation point was chosen after a number of trial runs, and was found to reproduce better the observed surface deformation. The simulations were performed over a grid covering the broader region and spaced at 0.05°. At each grid point a simulated horizontal component of shear wave from the finite fault was computed.

Figure 4 summarizes the simulations results. To produce this figure the simulated accelerations at each grid point, were corrected first for the site – effect and then they were converted to intensities in order to compare the predicted values within the mezoseismal area with those reported by Ambraseys and Finkel (1987).

A conservative fault length that aligns along the observed surface expression of the rupture is capable to reproduce the level of damage at the mezoseismal region. For example the simulated intensities are of the order of 8.5 to 9, as in the observed intensities (Figure 2). The area covered though by isoseismal IX though, is considerably smaller compared to the regional extent of IX in the case of observed damage.

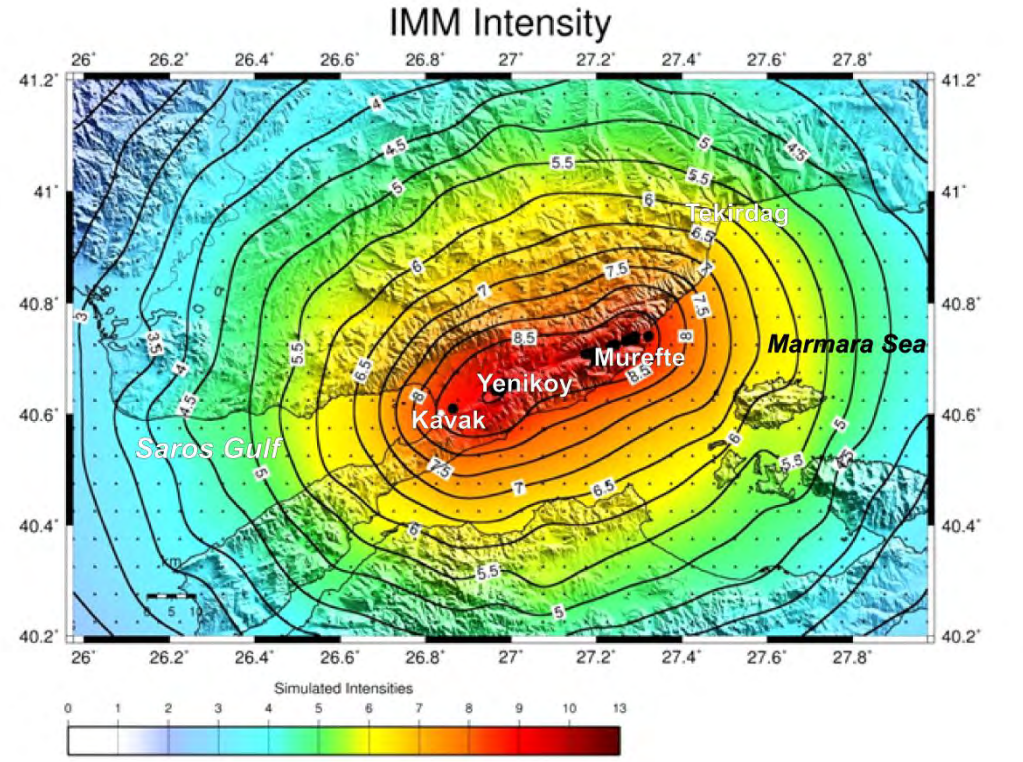

Figure 4 - Simulated distribution of intensities for the 1912 Ganos earthquake, using a finite fault with length equal to 50 km. The fault location is placed along the land expression of the rupture. The model predicts intensities 8 to 9 in the mezoseismal area, but of considerable smaller area, compared to the area observed (see Figure 2). The points where surface slip exceeded 4 m are marked as black dots. The white dot marks the western edge of the model finite-fault which extents 50 km to the east.

3.3 Case 2: Large Fault Length

The next step was to imply the largest length for the causative fault and to examine the percentage of the length extent in the west (e.g. Saros Gulf) as well as the length required at the eastern end, at the Marmara Sea. A number of fault lengths and end-member extents were tested and finally the value adopted was for a 120 km length fault of 18 km width along dip, in agreement with empirical scaling relations (Wells and Coppersmith, 1994). The same focal mechanism was used in this case, also. In this simulation the fault was discretized in 24×3 sub-faults, along strike and along dip, respectively. The rupture initiated at sub-fault (14, 3) using the local coordinates, which is at the deepest point of the fault and close to the epicentre.

More specifically for this fault length the length of the rupture into the Saros Bay was 40 km, 50 km on land and 30 km into the Marmara Sea. The simulated ground motions are presented in Figure 5. The map represents the distribution of simulated PGA's at the broader region, and it is observed that the simulations predict two patches of strong shaking: one extending east of the adopted hypocenter and into the Marmara Sea, with the strongest shaking observed ~25 km east of Tekirdag. The second patch of strong shaking is extending to the west of the hypocenter and its shape is two-lobe. One lobe is observed near Kavak while the other is further to the west, at the opening of the Saros Bay, north of Yeniköy.

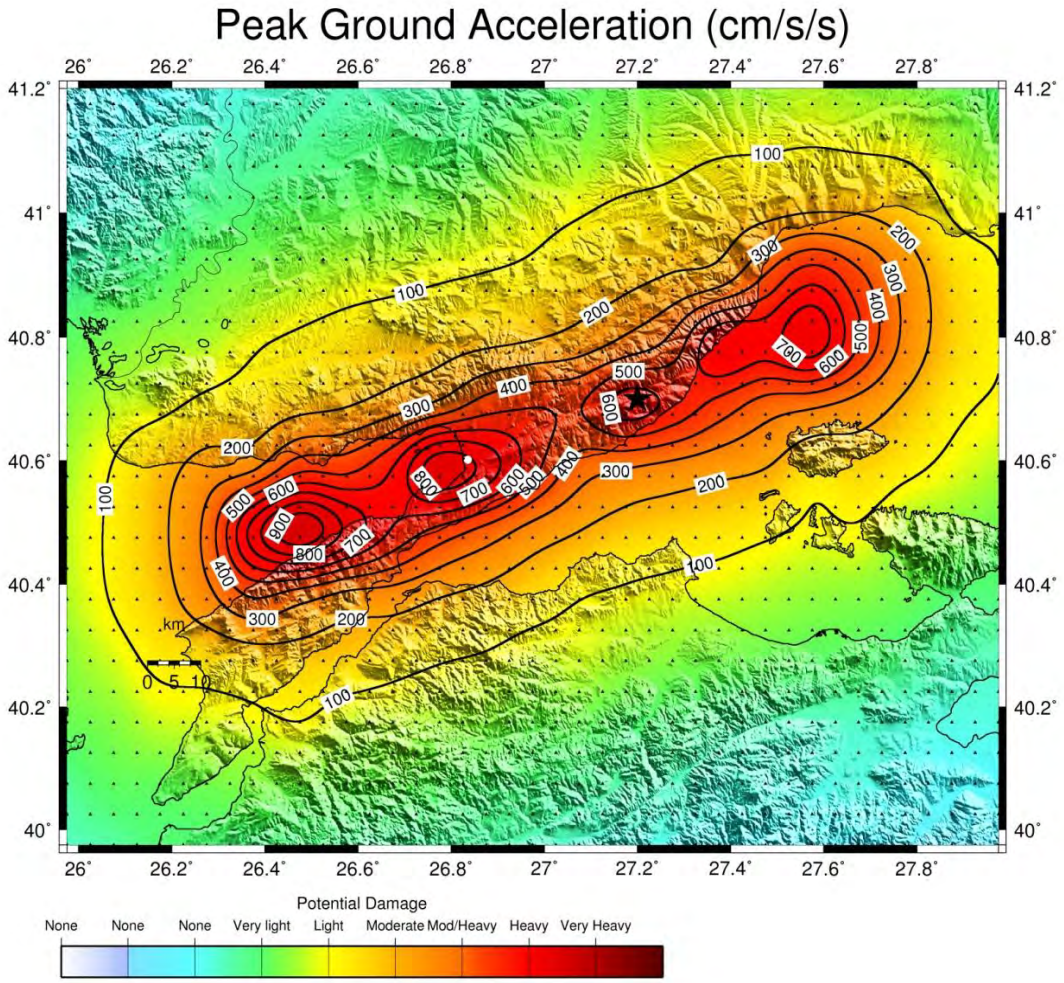

Figure 5 - Distribution of Peak Ground Acceleration at the broader region of the Ganos Fault, using stochastic simulations for a finite fault of length equal to 120 km and width of 18 km. The dots denote the grid nodes at which simulated acceleration time-histories were calculated, using the code of Beresnev and Atkinson (1998). The black star denotes the epicentre location.

Figure 6 provides the predicted level of intensities using the simulated accelerations at each node of the grid. It is observed that the mezoseismal region is well defined by the distribution of VIII to IX intensity level. For example the along major axis length of the area outlined by intensity 8 is approximately 120 km, as observed in the isoseismal maps of figure 2.

In conclusion, it is evident that to reproduce the gross characteristics of the distribution of damage of the 1912 Ganos earthquake a fault that extends both in Sea of Marmara as well as into the Saros Bay in the west, is required. In the simulations tested here, the results reproduce patches of strong shaking that are located at the ends of the fault, near Tekirdag in the east and north of Gelibolu in the west.

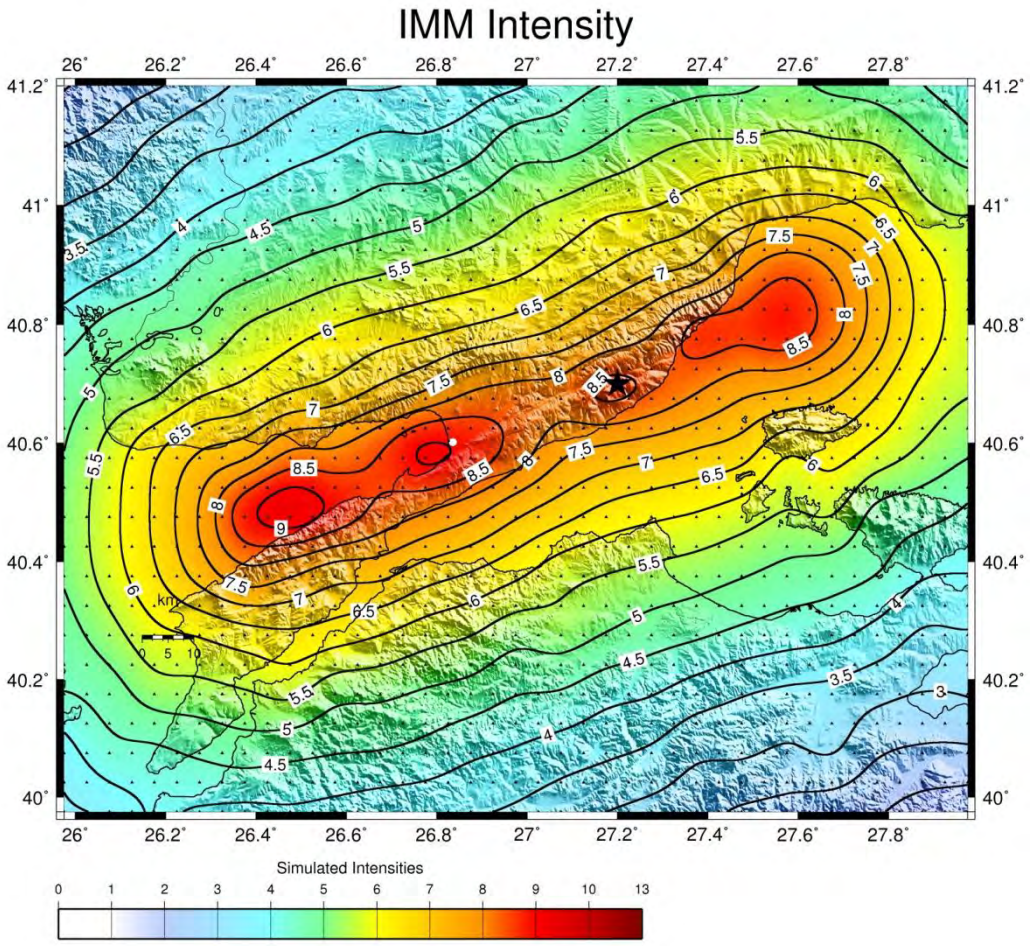

Figure 6 - ShakeMap for the 1912 Ganos mainshock, obtained from the simulated ground motions (PGA) at each node (dots) of the grid covering the broader region.

4. Conclusions

The 9 August 1912 Ganos fault earthquake (also known as Mürefte – Sarköy earthquake) together with the 1999 Izmit earthquake, are the two earthquakes which ruptured considerable part of the North Anatolian Fault, leaving its segments within the Marmara Sea un-ruptured. To this end, both events are significant mainly due to the imposed risk for the metropolitan city of Istanbul. The 9 August 1912 mainshock, Mw7.4, caused heavy damage, at the towns located along the Gaziköy – Saros segment of the North Anatolian Fault. It produced a well-mapped surface expression of the fault (Ambraseys and Finkel, 1987) along which slip measurements were performed (Altunel et al., 2004; Aksoy et al., 2010). The mainshock of August 9 was followed within hours by an Mw6.2 aftershock with an epicentre closer to the Marmara Sea. On 13 September 1912 another strong event occurred close to the Saros Bay, which is considered as a separate event rather as a late aftershock.

Even though most of the studies conclude that the focal mechanism of the 1912 earthquake is a N68°E dextral pure strike-slip fault (e.g. Aksoy et al., 2010), the length of the causative fault, is controversial. It is reported to be well above the 50km of the rupture mapped on land, and is considered to range between 90 and 150 km.

The purpose of this work was to test two end-members regarding the length of the causative fault. The method used was to stochastically simulate the level of strong ground motions, suing the approach of Beresnev and Atkisnson (1998) at a grid whose nodes cover the broader region. In one case the fault length is very conservative and is assumed to be only 50 km, and is placed on land exactly along the observed surface expression. In the other case, after many trials the fault length is chosen to be 120 km, which was found to better reproduce the observed pattern of damage. In both cases I examine the simulated PGA maps with respect to their ability to reproduce the gross characteristics of the observed surface faulting for the 1912 rupture.
In the first case, where a length of 50 km was used, that corresponds to the along –strike extent of the surface faulting the simulated ground motions can predict the areas of strong shaking but the area of strong shaking is considerably smaller than the one depicted within intensity VIII to IX in the observed isoseismal map. In the second case, where the fault length is taken 120 km, with 30 km extending in the Sea of Marmara, 50 km on land and 40 km in the Saros Bay, the simulated ground motion shaking better approximates the observed area of strong intensities as well as the regions where the measured slip exceeded 4 m (as reported in Aksoy et al., 2010). In both cases, the hypocenter was placed at the eastern end of the fault and the rupture initiation point was placed at the deeper part of the finite-fault. This means that the best results were obtained for unilateral rupture propagation from east towards west. As a result, the present study confirms the previous results for a fault length of approximately 120 km, as well as the fact that only a small segment within the western edge of the Sea of Marmara ruptured during the 1912 mainshock. The sea-bottom topography and the change of strike near Tekirdag, has affected the propagation of the rupture towards east.

5. Acknowledgments

This work was financed by **a)** the European Union (European Social Fund – ESF) and Greek national funds through the Operational Program "Education and Lifelong Learning" of the National Strategic Reference Framework (NSRF) - Research Funding Program: Thales “Investing in knowledge society through the European Social Fund and **b)** the General Secretariat for Research & Technology (GSRT) of Greece (Project Number: 10 TUR/1-3-52) in the framework of the Turkey-Greece bilateral project with title: “Turkey – Greece cross border seismicity: velocity models, moment tensors, slip models, shake maps based on knowledge- transfer and a joint database repository”. Figures were produced using the General Mapping Tools software (Wessel and Smith, 1998).

6. References

Aksoy E. M., Meghraoui M., Vallée M. and Cakir Z. 2009. Rupture Characteristics of the 1912 Mürefte (Ganos) Earthquake Segment of the North Anatolian Fault (Western Turkey), *Eos Trans. AGU 90(52)*, Fall Meet. Suppl., Abstract T13C-1884.

Altınok Y., Alpar B. and Yaltırak C. 2003. Şarköy- Mürefte 1912 earthquake’s tsunami, extension of the associated faulting in the Marmara Sea, Turkey, *Journal of Seismology*, 7, 329–346.

Altunel E., Meghraoui M., Akyuz S. and Dikbas A. 2004. Characteristics of the 1912 co-seismic rupture along the North Anatolian Fault Zone (Turkey): implications for the expected Marmara earthquake, *Terra Nova*, *16* (4), 198-204.

Ambraseys N.N. and Finkel C.F., 1987. The Saros-Marmara earthquake of 9 August 1912, *Earthquake Eng. and Struct. Dyn.,* 15, 189–211.

Ambraseys N.N. and Jackson J.A. 1998. Faulting associated with historical and recent earthquakes in the Eastern Mediterranean region, *Geophys. J. Int*., 133, 390–406.

Ambraseys N.N. and Jackson J.A. 2000. Seismicity of Sea of Marmara (Turkey) since 1500, *Geophys. J. Int*., 141, F1–F6.

Armijo R., Meyer B., Hubert A. and Barka A.A. 1999. Westward propagation of the North Anatolian fault into the northern Aegean: Timing and Kinematics, *Geology,* 27, 267–270.

Beresnev I. A. and Atkinson G. M. 1997. Modeling finite-fault radiation from the ωn spectrum, *Bull. Seism. Soc. Am.,* 87, 67 – 84.

Beresnev I. A. and Atkinson G. M. 1998. FINSIM – a FORTRAN program for simulating stochastic acceleration time histories from finite faults, *Seism. Res. Lett*., 69, 27 – 32.

Boore D. M. 1983. Stochastic simulation of high-frequency ground motions based on seismological models of the radiated spectra, *Bull. Seism. Soc. Am.,* 73, 1865 – 1894.

Borcherdt R. D. 1994. Estimates of site-dependent response spectra for design (methodology and justification), *Earthquake Spectra,* 10, 617- 653.

Shebalin N. and Karnik V. 1974. Catalogue of Earthquakes in the Balkan Region, UNESCO survey of seismicity of the Balkan Region, Part I, *Atlas of Isoseismal Maps*, Skopje, Yugoslavia.

Karabulut H., Roumelioti Z., Benetatos C., Ahu Komec M., Özalaybey S., Aktar M. and Kiratzi A. 2006. A source study of the 6 July 2003 (*M*w 5.7) earthquake sequence in the Gulf of Saros (northern Aegean Sea): Seismological evidence for the western continuation of the Ganos fault, *Tectonophysics*, 412, 195– 216.

Kiratzi A. and Louvari E. 2003. Focal mechanisms of shallow earthquakes in the Aegean Sea and the surrounding lands determined by waveform modelling: a new database, *Journal of Geodynamics,* 36 (1–2), 251–274.

Kiratzi A., Benetatos C. and Roumelioti Z. 2007. Distributed earthquake focal mechanisms in the Aegean Sea, *Bulletin of the Geological Society of Greece*, Vol. XXXX, 1125-1137.

Papadimitriou E.E., Karakostas V.G. and Papazachos, B.C. 2001. Rupture zones in the area of the 17.08.99 Izmit (NW Turkey) large earthquake (Mw 7.7) and stress changes caused by its generation, *J. Seismol.,* 5, 269–276.

Papazachos B. C. and Papazachou C. 2003. *The earthquakes of Greece*, Ziti Publ. Co., Thessaloniki, Greece, pp. 286 (in Greek).

Pulido N., Ojeda A., Atakan K. and Kubo T. 2004. Strong ground motion estimation in the Sea of Marmara region (Turkey) based on scenario earthquake, *Tectonophysics,* 39, 357-374.

Seeber L., Emre O., Cormier M.-H., Sorlien C. C., McHugh C. M. G., Polonia A., Ozer N. and Cağatay N. 2004. Uplift and subsidence from oblique slip: the Ganos–Marmara bend of the North Anatolian Transform, Western Turkey*, Tectonophysics,* 391, 239-258.

Wald D. J. and Allen T. I. 2007. Topographic slope as a proxy for seismic site conditions and amplification*, Bull. Seism. Soc. Am.,* 97(5), pp. 1379-1395.

Wells D. L. and Coppersmith K. J. 1994. New empirical relationships among magnitude, rupture length, rupture width, rupture area and surface displacement, *Bull. Seism. Soc. Am.,* 84, 974-1002.

Wessel P. and Smith W.H.F. 1998. New improved version of the Generic Mapping Tools released, *EOS Trans.* AGU, 79, 579.

Δελτίο της Ελληνικής Γεωλογικής Εταιρίας, τομ. XLVII , 2013 Πρακτικά 13ου Διεθνούς Συνεδρίου, Χανιά, Σεπτ. 2013	Bulletin of the Geological Society of Greece, vol. XLVII 2013 Proceedings of the 13th International Congress, Chania, Sept. 2013

THE 10 JUNE 2012 MW6.0 EARTHQUAKE SEQUENCE IN THE EASTERNMOST END OF THE HELLENIC ARC

Kiratzi A.[1], Aktar M.[2] and Svigkas N.[1]

[1] Department of Geophysics, Aristotle University of Thessaloniki, Greece

[2] Kandilli Observatory and Earthquake Research Institute, Bogaziçi University, Istanbul, Turkey

Abstract

The 10 June 2012 (UTC 12:44:17.3; lat. 36.441°N, long. 28.904°E, Mw6.0) earthquake sequence, 60 km to the west of Rodos Island, is studied, in an attempt to shed light to the obscure deformation pattern at the easternmost end of the Hellenic Arc. Moment tensor solutions for the mainshock and the strongest aftershocks revealed the operation of WNW-ESE dextral strike-slip faulting, with slip vector at ~N295°E, approximately orthogonal to the GPS velocity vectors. The strike of the activated structure generally aligns with bathymetric linear escarpments observed in the region, bordering the eastern section of the Rodos basin. The best constrained focal depths are in the range 10 to 25 km, with the mainshock at the depth of 24 km. The slip model for the mainshock, obtained through a finite-fault inversion scheme, showed that slip was mainly concentrated in a single patch, with the locus of peak slip (~125 cm) located ~ 4km to the NW of the hypocenter. The sequence which lies in the western continuation of the Fethiye – Burdur sinistral strike-slip zone into the Aegean Sea and Rodos basin, is not connected with activation of this zone. Its characteristics comply with the activation of a dextral strike-slip structure, oblique to this zone, which accommodates along – arc NE-SW extension.
Key words: *Rodos Basin; slip model; rupture; focal mechanism.*

Περίληψη

Μελετάται η σεισμική ακολουθία της 10ης Ιουνίου 2012 (UTC 12:44:17.3; 36.441°B; 28.904°E, Mw6.0), 60 χιλιόμετρα δυτικά της Ρόδου, στο ανατολικότερο άκρο του ελληνικού τόξου. Οι μηχανισμοί γένεσης του κύριου σεισμού και των ισχυρότερων μετασεισμών έδειξαν τη λειτουργία ενός ΔΒΔ-ΑΝΑ ρήγματος δεξιόστροφης οριζόντιας συνιστώσας, με διάνυσμα ολίσθησης ~Β295°Α. Η παράταξη της δομής που ενεργοποιήθηκε ακολουθεί την τοπογραφία του βυθού στην ευρύτερη περιοχή του ανατολικού τμήματος της λεκάνης της Ρόδου. Τα καλύτερα προσδιορισμένα εστιακά βάθη κυμαίνονται από 10 έως 25 χλμ, με την εστία του κύριου σεισμού στον κατώτερο φλοιό, σε βάθος 24 χιλιομέτρων. Το μοντέλο ολίσθησης για τον κύριο σεισμό, έδειξε ότι η ολίσθηση στην επιφάνεια του ρήγματος είναι συγκεντρωμένη σε ένα μεμονωμένο τμήμα. με το μέγιστο της τιμής της να είναι ~ 125 εκατοστά. Το μέγιστο δεν εμφανίζεται στο υπόκεντρο, αλλά ~4 χλμ στα βορειοδυτικά αυτού. Η σεισμική ακολουθία του Ιουνίου 2012 βρίσκεται στην δυτική συνέχεια της αριστερόστροφης ζώνης Fethiye – Burdur προς την πλευρά του Αιγαίου Πελάγους και της λεκάνης της Ρόδου. Εντούτοις, ο σεισμός του Ιουνίου 2012 δεν συνδέεται με την ενεργοποίηση αυτής της ζώνης, ούτε συνηγορεί για την προς δυσμάς συνέχειά της. Τα

χαρακτηριστικά της ακολουθίας δείχνουν την ενεργοποίηση ενός δεξιόστροφου ρήγματος οριζόντιας μετατόπισης, με πλάγια παράταξη ως προς τη ζώνη, που απορροφά εφελκυσμό παράλληλα προς το ελληνικό τόξο κατά διεύθυνση ΒΑ-ΝΔ.
Λέξεις κλειδιά: *Μοντέλο ολίσθησης, Λεκάνη Ρόδου, διάρρηξη, μηχανισμός γένεσης.*

1. Introduction

The Hellenic Subduction Zone has a significant role in the active tectonic pattern of Eastern Mediterranean Sea. It is formed from the subduction of Mesozoic African lithosphere beneath the overriding Aegean Sea material. Africa is moving north towards Eurasia at only 5 to 10 mm/year, whereas the Aegean is moving faster to the south-west with respect to Eurasia, resulting in about 35 mm/yr that have to be accommodated by deformation along the Hellenic Subduction zone. The eastern border of the Hellenic Trench, close to the coastal regions of western Anatolia, is poorly studied, mainly due to the insufficient number of strong events.

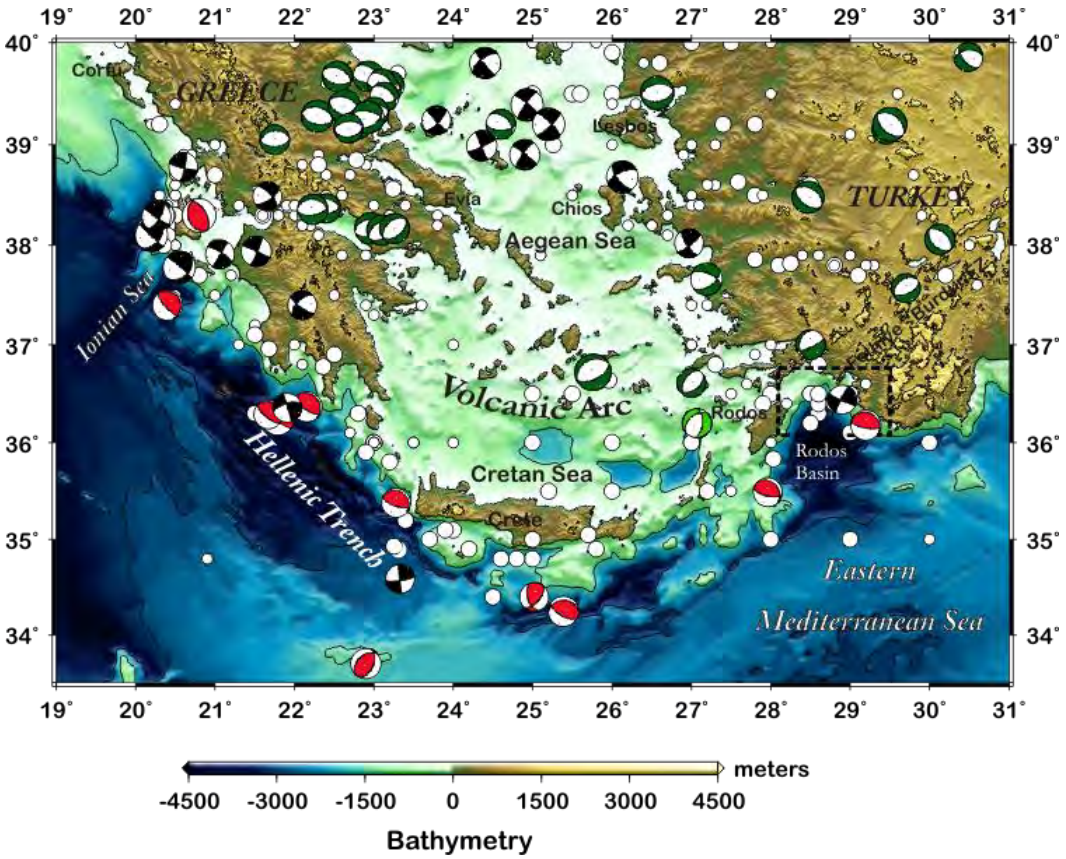

Figure 1 - The location of the 10 June 2012 sequence, marked with the dashed rectangle, at the easternmost section of the Hellenic Subduction Zone. The colour beach- balls (from Kiratzi and Louvari, 2003; Kiratzi et al., 2007) denote the available focal mechanisms for previous events with Mw>6.0. The seismicity of the period 550BC- 2012 with M>6.0 is also plotted (open circles).

The 10 June 2012 earthquake sequence occurred offshore and in the mid-distance between the Island of Rodos and the city of Fethiye in south-western Anatolia (Figure 1). From the Turkish side the broader region of occurrence is dominated by the presence of the transtensional left-lateral Fethiye - Burdur Fault Zone (FBFZ). It is a well known structure of pronounced NE-SW trending

faults and basins, which roughly align between the cities of Fethiye and Afyon (Taymaz and Price, 1992; Ocakoğlu, 2012). These faults are combined with N-S faults, to form an en-echelon basin configuration, which continues westward into the eastern Hellenic Arc. The sinistral strike-slip character of the FBFZ is mainly indicated by the analysis of structural data and of sediment deposits. More specifically, structural analyses on the Turkish coastal regions suggest that the Holocene – Recent deformation was taken up in a transtensional environment which required the progressive addition of a sinistral shear motion, to confront the NE propagating transcurrent motion of the Hellenic fore-arc (ten Veen, 2004).

To this end, the 10 June 2012 earthquake occurred in a region, of interaction between the western prolongations of the Fethiye – Burdur Fault Zone and the Hellenic Subduction. The sequence is studied here, in terms of the focal mechanisms, the time and space evolution and the slip model of the mainshock. The data for this study were derived from the broad band stations of the Greek and Turkish stations, thus providing a good coverage in most azimuths, except a gap in coverage in the southeast.

2. Moment Tensor (MT) Solutions and Relocation of Aftershocks

2.1 MT Inversions

Moment tensors of the mainshock and of the stronger events of the sequence were computed by the Time-Domain Moment Tensor inversion method (Dreger, 2003). The method is now routinely applied and for its applications in the Aegean Sea region the details are described in Roumelioti et al. (2010). We solved for the deviatoric seismic moment tensor only.

Table 1 – Information on the focal mechanism solutions of the strongest events of the June 2012 sequence (VR= Variance Reduction of the solution; Nst= number of stations used in the inversion).

Date Y/MM/DD	Origin Time hh:mm:ss.s	Lat	Long	Depth km	Mw	NODAL PLANE 1 Strike°	Dip°	Rake°	NODAL PLANE 2 Strike°	Dip°	Rake°	VR %	Nst
20120610	12:44:17.3	36.468	28.888	24	6.0	115	85	171	206	81	5	78	9
20120610	15:02:41.1	36.464	28.873	15	3.3	295	78	-173	204	83	-12	56	3
20120610	18:28:33.9	36.448	28.895	16	3.9	153	88	175	243	85	2	73	4
20120611	02:06:35.9	36.400	28.970	22	3.8	307	87	-172	217	82	-3	84	7
20120611	17:35:39.1	36.422	28.973	30	3.8	123	89	177	213	87	1	85	3
20120611	19:51:06.8	36.429	28.948	14	3.7	163	82	174	254	84	8	50	3
20120614	16:46:07.7	36.390	29.020	25.0	4.5	310	86	-177	220	87	-4	83	6
20120625	13:05:30.0	36.457	28.916	20.0	4.7	143	82	172	234	82	8	80	5

The inversion yields the M_{ij} which is decomposed into the scalar seismic moment, a double-couple (DC) moment tensor and a compensated linear vector dipole (CLVD) moment tensor. The decomposition is represented as percent DC and percent CLVD. Source depth is found iteratively by finding the solution that yields the largest variance reduction. It is assumed that the event location is well represented by the high frequency hypocentral location, and a low frequency centroid location is not determined. Moreover, the representation assumes that the source time

history is synchronous for all of the moment tensor elements and that it may be approximated by a delta function. Finally, it is assumed that the crustal model is sufficiently well known to explain low frequency wave propagation.

To apply the method, broad band waveforms were retrieved from the Hellenic Unified Seismic Network (HUSN) and the Turkish network operated by the Kandilli Observatory (KOERI). Prior to the inversion, full broadband waveforms of the three recorded components were band-pass filtered between 0.02–0.08 Hz or 0.05-0.10 Hz depending on the magnitude of the event and the signal-to-noise ratio of the waveforms. Theoretical Green's functions required to model the propagation of the seismic waves were constructed with the method and code described by Saikia (1994) using the velocity model of Novotný et al. (2001), which has proven to successfully describe low frequency wave propagation (e.g., Roumelioti et al.,2010; Kiratzi, 2010, 2011 and references therein). In Figure 2 we show the moment tensor solution and the waveform fit for the mainshock, while the parameters of the computed focal mechanisms of the aftershocks are listed in

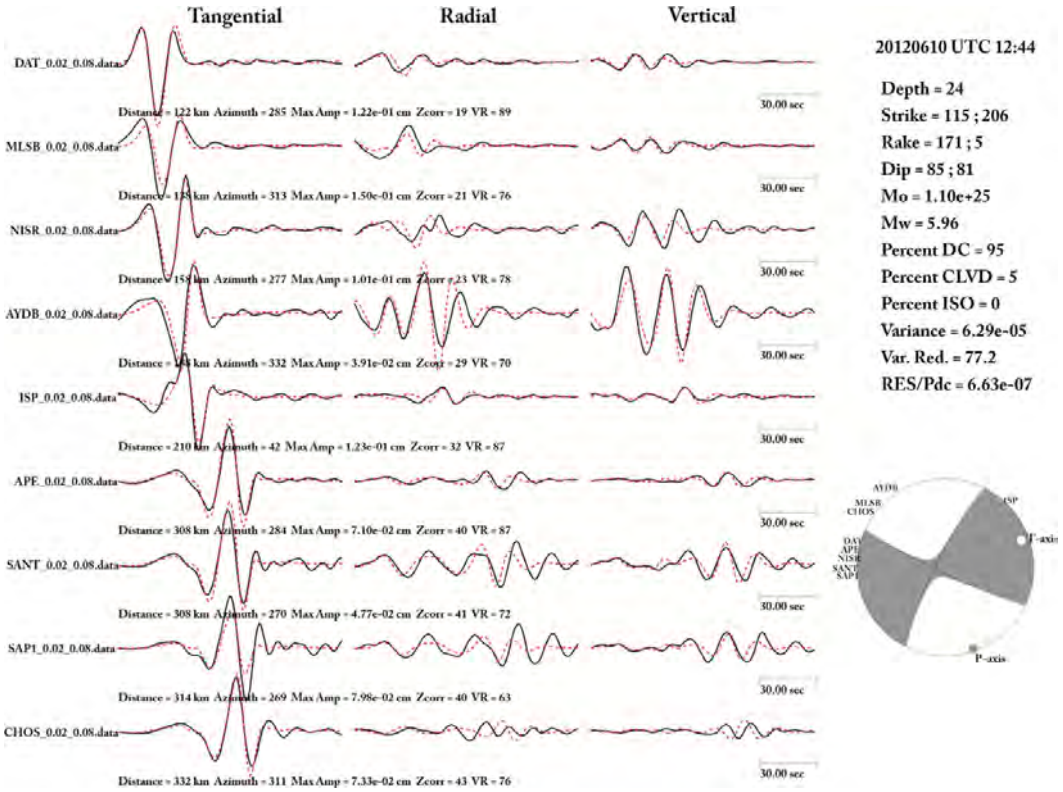

Figure 2 - Deviatoric moment tensor point-source inversion results for the 10 June 2012 mainshock using waveform data from the Greek and Turkish networks. For each station three component displacement seismograms (shown as solid lines) are compared to one-dimensional synthetic seismograms (dashed red lines), while the azimuth, the maximum three-component trace amplitude, cross-correlation samples (Zcorr) and Variance Reduction (VR) are also provided. The lower-hemisphere projection of the P-wave radiation pattern is shown at right, together with the azimuthal distribution of the stations included in the inversion. Solution information includes the strike, rake, and dip for the two possible double-couple planes, the scalar seismic moment, the moment magnitude, and percentage DC, CLVD. Fitting parameters as the variance, the variance reduction (Var. Red) and the variance modulated by the percent double-couple (RES/Pdc) are also given.

Table 1. Our solution is in very good agreement with those published by other agencies, as these can be retrieved from the site of the EMSC (http://www.emsc-csem.org).

2.2 Relocation Results

The strongest events of the sequence have already occurred by mid July 2012. More specifically the mainshock on 10 June 2012 (UTC 12:44:16.73) was followed within minutes by the strongest aftershock of Mw4.8 (UTC 12:49:36.97). Unfortunately, for this aftershock a moment tensor solution is not provided, because the waveforms were mixed with the coda of the mainshock.

In order to relocate the epicentres we joined phase data from the Greek and Turkish stations. We read ourselves P and S phases from the closest stations, particularly the S arrivals, in an attempt to increase the depth resolution. We used HypoDD (Waldhauser and Ellsworth, 2000) and LSQR for the relocation; from the initial set of 65 events, we were able to relocate a subset of 51 events with M>2.0, which passed the criteria. Our relocation was combined with waveform cross-correlation for the closest stations. Our relocated dataset is complete for M>2.6, e.g. including 42 events in total. Using the utilities of ZMAP we obtained a b –value equal to 0.61.

The distribution of the best located events, shown in Figure 3 and in cross-section in Figure 4, show a number of interesting features. From a close inspection of the aftershock cloud it is immediately noticed that the activated structure has a NW-SE trend, implying that from the two nodal planes of the focal mechanism, the NW-SE trending plane is the fault plane. The mainshock occurred at the northernmost cloud and within minutes the strongest aftershock occurred at the southern cloud, with most of the aftershocks located at that cloud. The length of the activated structure is about 9 Km, in accordance with the predictions of empirical scaling relations for an Mw6.0 earthquake. It is worth noting also (Figure 4) that the majority of the aftershock activity is concentrated at shallower depths (<15 km) compared to the mainshock and strongest aftershocks (>20 km), an observation previously made in the case of Adana 1998 sequence, located similarly next to an active subduction zone in Eastern Mediterranean Sea (Aktar et al., 2000).

3. Distribution of Slip onto the Fault Plane

3.1 Method

To obtain the slip distribution onto the ruptured fault plane for the 10 June 2012 mainshock the finite-fault inversion method of Kaverina et al. (2002), a nonnegative, least-squares scheme with simultaneous smoothing and damping was applied. The same code can be used to simulate ground motions from a slip model.

In brief, this method inverts for fault slip distributed over a grid of point sources that are triggered according to the passage of a circular rupture front. A Laplacian-smoothing operator, slip positivity, and a scalar moment minimization constraint is applied to stabilize the inversions. Green's functions based on the Novotný et al. (2001) velocity profile, shown to be effective in modelling regional wave propagation, were used to invert the seismic waveforms, and were calculated using the frequency–wavenumber integration method (Saikia, 1994) for 1-km intervals in distance and 1-km intervals in depth. The source model used is a single fault plane with constant rupture velocity and constant dislocation rise time.

3.2 Application Results

The seismic data consist of three component broad band displacement waveforms recorded at regional stations of the Greek and neighbouring networks. Both the data and the synthetic Green's functions were bandpass filtered between 0.02 to 0.08 Hz. From a standard grid search of the parameter space, the rupture velocity was found to be 2.9 km/s and the rise time 0.5 s.

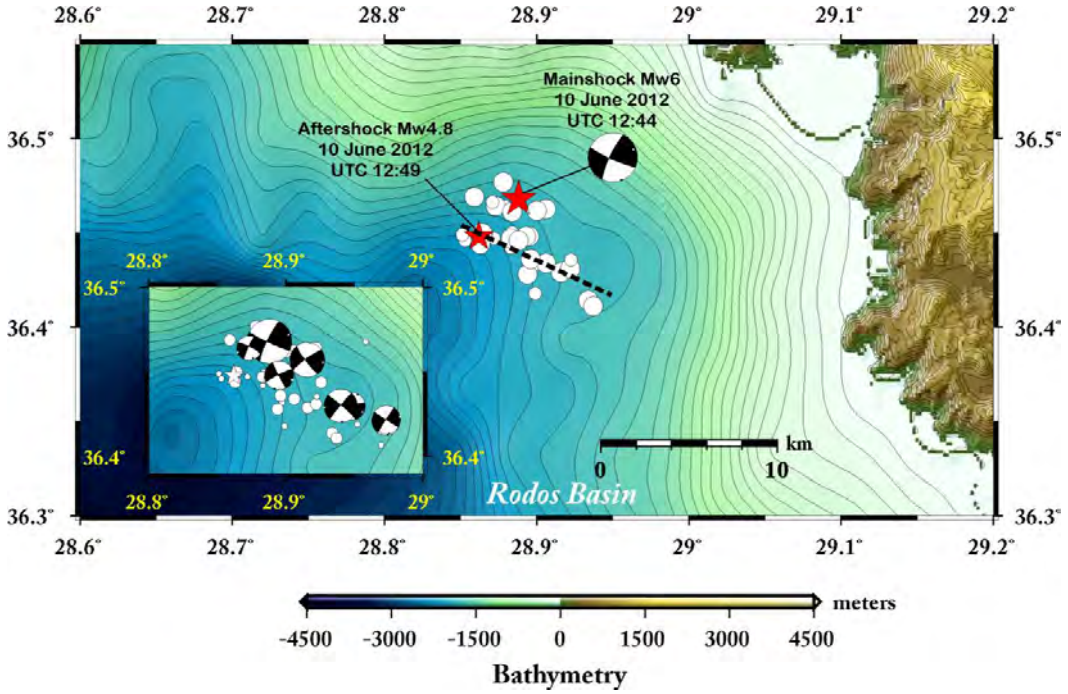

Figure 3 - HypoDD relocated epicentres of the June 2012 sequence, together with the focal mechanism of the mainshock for comparison. Note that the cloud of aftershocks clearly denotes the NW-SE nodal plane as the fault plane. The dashed line is parallel to the fault plane to visually show this. The inset to the left shows the focal mechanisms of the stronger aftershocks computed by moment tensor inversion (listed in Table 1).

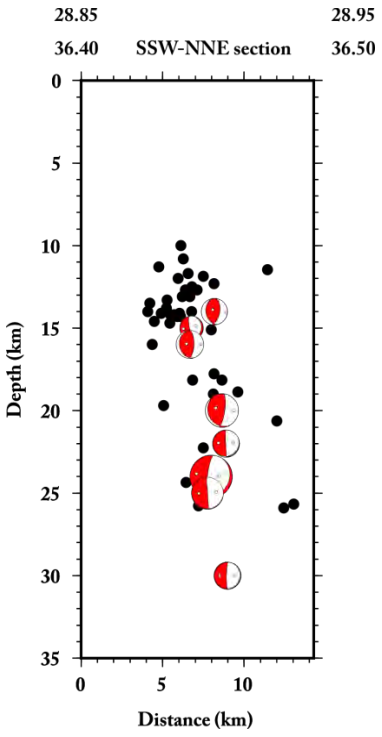

Figure 4 - Cross-section along a plane perpendicular to the fault plane (coordinates shown on top of the section), to show that the sequence operated in the depth range 10 to about 25 km, with the majority of the aftershocks in the range 10 to 15 km.

The results of the inversion show that slip is confined in a main patch, and the maximum slip is located ~4 km to the WNW of the hypocenter location (Figure 5), providing evidence for a mainly unilateral rupture to NW. A deeper patch of slip is also observed to the SE of the hypocenter, at a depth of ~32 Km that fits large lapse time signal in the data. This patch was a stable feature in all trial inversions, and is not very likely to be an artifact. Average slip in the ruptured area is ~19 cm and peak slip reaches 125 cm. The total scalar seismic moment for the slip model is M_o=1.80x10^{25} dyn-cm, resulting in moment magnitude Mw6.1, slightly larger than the Mw obtained in the moment tensor solution (Figure 2).

The total data variance reduction for the solution, calculated as a normalized squared misfit, is 85%, indicating a very satisfactory level of fit, between observed and slip-model produced synthetic waveforms, which are shown in Figure 6.

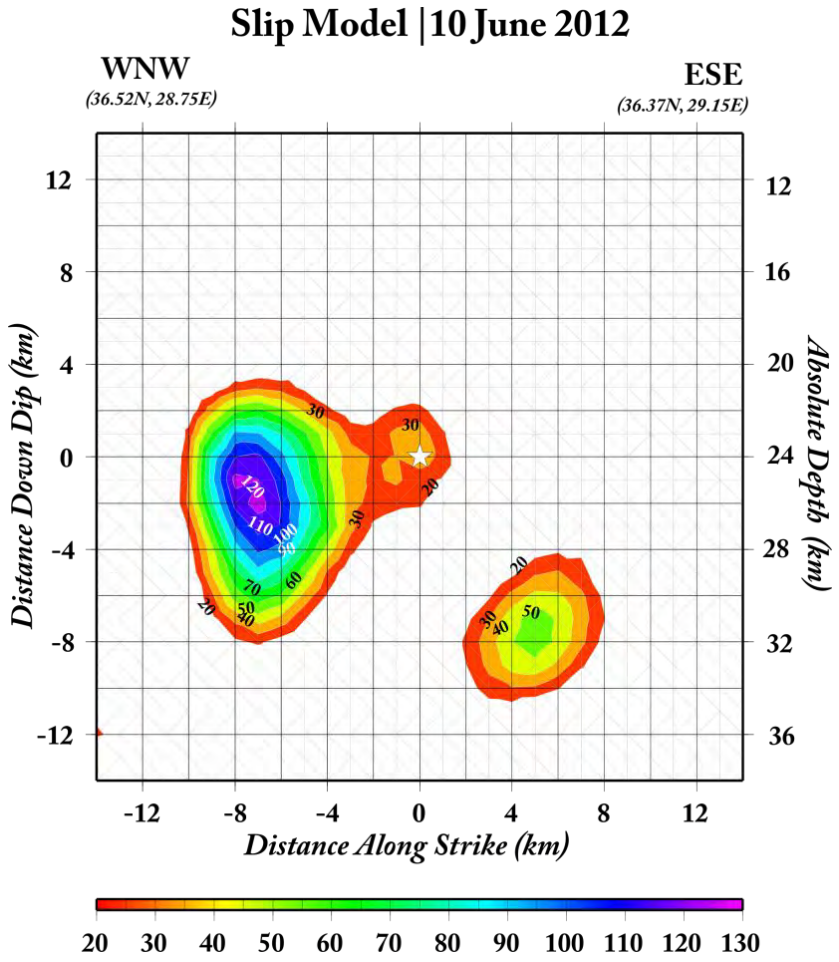

Figure 5. Slip model for the event of 10 June 2012 Mw6.0 event obtained from the inversion of broad band waveforms, for the N115°E trending fault plane, adopting a rupture velocity of 2.9 km/s, found from a standard grid search of the parameter space. One main slip patch is calculated where the peak slip value (~125 cm) was observed, with approximate dimensions 5x5 km². The asterisk denotes the hypocentre location, which lies at an absolute depth of 24 km. Note that the locus of slip is concentrated ~ 4 km to the NW of the hypocenter, and if directivity is present, it should be in that direction. A second slip patch is also observed, which is deeper than the previous and less pronounced, but which was a stable feature in all test inversions and fits the long lapse time in the data.

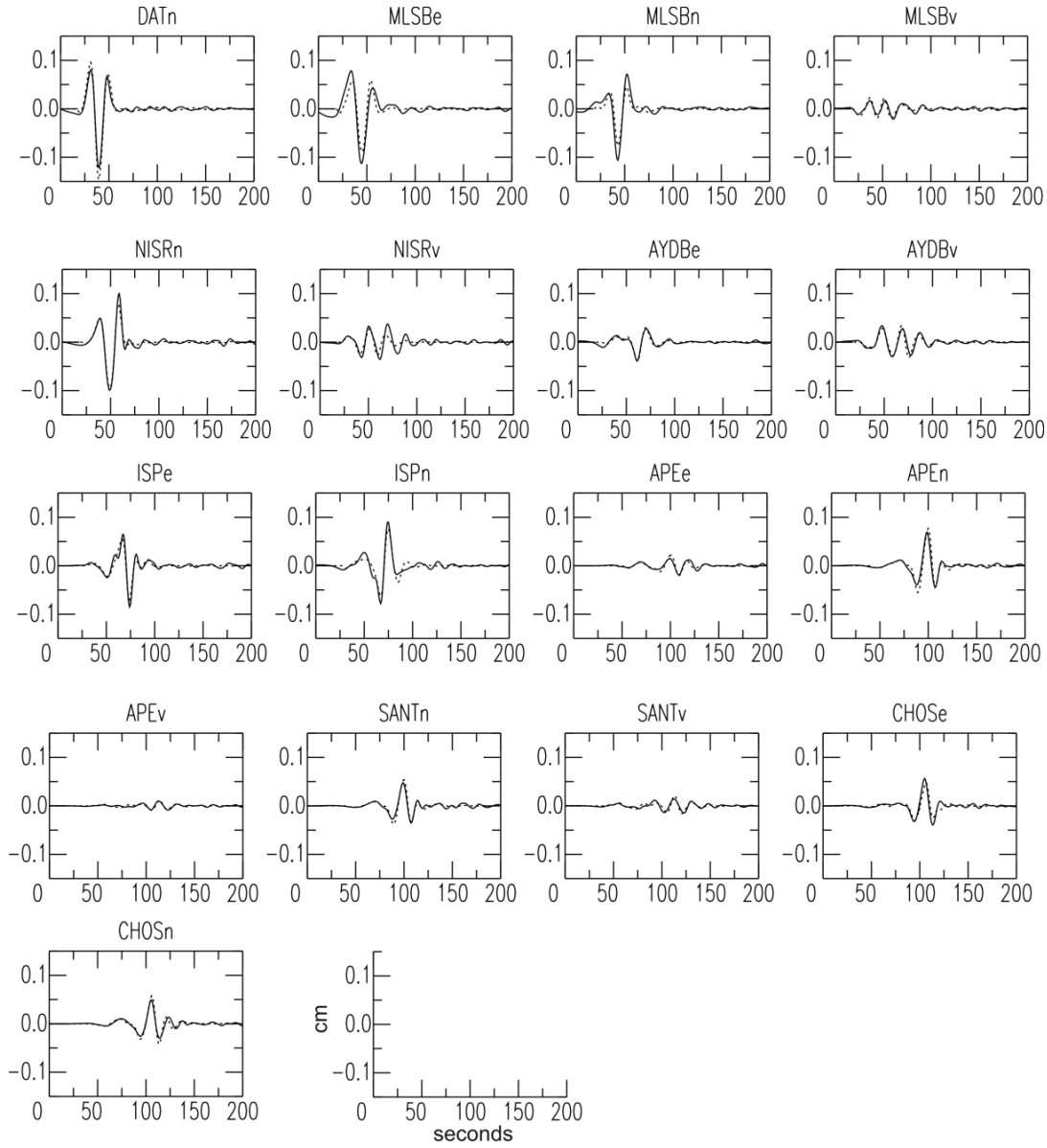

Figure 6. Comparison of observed (straight lines) and of synthetic (dashed lines) waveforms. Synthetics were calculated using the slip model for mainshock of 10 June 2012 Mw6.0 (Fig. 5). The fit in most of the stations is very good, resulting in a large Variance Reduction (85%) for the inversion.

4. Conclusions

The eastern termination of the Hellenic Subduction Zone is insufficiently studied compared to its western and central part, mainly due to the lack of strong earthquakes to be instrumentally recorded by the present seismological networks in Greece and Turkey (Shaw and Jackson, 2010; Shaw, 2012). The 10 June 2012 event Mw6.0 with an epicentre in the mid distance between Rodos Island and the city of Fethiye in coastal western Anatolia was studied in an attempt to shed light to

the seismotectonic features of the region. Moment tensor solutions of the mainshock and of the strongest aftershocks revealed the operation of strike-slip faulting in the region, in the depth range 10 to 25 km, while the strongest events nucleated at the lower crust. The HypoDD relocated epicentres of the sequence led to the identification of the fault plane, which strikes NNW-ESE (N115°E) indicating dextral strike-slip motion. The 2012 sequence is located in the western prolongation of the Fethiye – Burdur Fault Zone (FBFZ) towards the Aegean Sea and Rodos Basin. This zone is considered to be connected with sinistral strike-slip faulting. To this end, the sequence studied here is not connected with this zone, neither does it support its western extension, but on the contrary it involves rupture of a rather deep strike-slip fault that is oblique to the FBFZ (see Fig. 1), in a sense reflecting the interaction of Africa – Anatolia lithospheres at their easternmost sections.

Finite – fault inversion applied to broad band displacement waveforms of the Greek and Turkish networks, revealed that the slip onto the causative fault is concentrated at main patch of 5×5 Km². The locus of the peak slip which was calculated to be 125 cm is located 4 Km to the NNW of the hypocenter, providing evidence for rupture propagation mainly towards that direction. The average slip onto the fault plane is 19 cm and the resolved total seismic moment is 1.80×10^{25} dyn-cm. The obtained slip model provides very good fit to the observed waveforms.

The T-axes of the focal mechanisms of the 2012 sequence indicate extension approximately NE-SW in accordance with the regional stress field. This along-arc extensional field is characterising the entire region south of the Hellenic Volcanic Arc and is considered to be related to the outward growth of the Hellenic Arc in response to the westward Anatolia extrusion. In conclusion the 10 June 2012 Mw6.0 sequence is characterized by dextral strike-slip faulting associated with the activity of NW-SE trending faults that accommodate NE-SW extension, as observed in many regions south of the Hellenic Volcanic Arc (Benetatos et al., 2004; Kiratzi, 2012 and references therein).

5. Acknowledgments

This work was financed by TUBITAK of Turkey (Project Number: 109Y402) and the General Secretariat for Research & Technology (GSRT) of Greece (Project Number: 10 TUR/1-3-52) in the framework of the Turkey-Greece bilateral project with title: “Turkey – Greece cross border seismicity: velocity models, moment tensors, slip models, shake maps based on knowledge-transfer and a joint database repository”. AK also acknowledges co-finance by the European Union (European Social Fund – ESF) and Greek national funds through the Operational Program "Education and Lifelong Learning" of the National Strategic Reference Framework (NSRF) - Research Funding Program: Thales “Investing in knowledge society through the European Social Fund”. Broad band waveforms used in this study were retrieved from the Hellenic Unified Seismological Network of Greece, and the network operated by Kandilli Observatory in Turkey. Moment tensors were computed using the tdmt-invc_iso package developed by Douglas Dreger and Sean Ford of the Berkeley Seismological Laboratory, and Green’s functions were computed using the FKRPROG software developed by Chandan Saikia. Figures were produced using the General Mapping Tools software (Wessel and Smith, 1998). The SAC software (Goldstein and Snoke, 2005) was used to process the waveforms. Special thanks are extended to our colleagues Vasilis Karakostas, K. Leptokaropoulos and H. Garlaouni who provided many helpful scripts to manage the data.

6. References

Aktar M., Ergin M., Özalaybey S., Tapirdamaz C., Yörük A. and Biçmen F. 2000. A lower-crustal event in northeastern Mediterranean: the 1998 Adana earthquake (Mw=6.3) and its aftershocks, *Geophys. Res. Lett*., Vol. 27, N:16, 2361-2364.

Benetatos C., Kiratzi A., Papazachos C. and Karakaisis G. 2004. Focal mechanisms of shallow and intermediate depth earthquakes along the Hellenic Trench, *Journal of Geodynamics*, 37, 253-296.

Dreger D. S. 2003. TDMT_INV: Time Domain Seismic Moment Tensor INVersion, *International Handbook of Earthquake and Engineering Seismology*, Volume 81B, p 1627.

Goldstein P. and Snoke A. 2005. SAC Availability for the IRIS Community, Incorporated Institutions for Seismology Data Management Center Electronic Newsletter.

Kaverina A., Dreger D. And Price E. 2002. The Combined Inversion of Seismic and Geodetic Data for the Source Process of the 16 October 1999 Mw 7.1 Hector Mine, California, Earthquake, *Bulletin of the Seismological Society of America,* 92, 1266-1280.

Kiratzi A. 2010. The 24 May 2009 Mw5.2 earthquake sequence near Lake Doirani (FYROM - Greek borders): focal mechanisms and slip model using empirical Source Time Function's inversion, *Tectonophysics*, 490, 115-122.

Kiratzi A. 2011. The 6 September 2009 Mw5.4 earthquake in Eastern Albania – FYROM Border: focal mechanisms, slip model, ShakeMap, *Turkish Journal of Earth Sciences,* 20 (4), 475–488.

Kiratzi A. 2013. The January 2012 earthquake sequence in the Cretan Basin, south of the Hellenic Volcanic Arc: Focal mechanisms, rupture directivity and slip models, *Tectonophysics*, http://dx.doi.org/10.1016/j.tecto.2012.11.019

Kiratzi A. and Louvari E. 2003. Focal mechanisms of shallow earthquakes in the Aegean Sea and the surrounding lands determined by waveform modelling: a new database, *Journal of Geodynamics,* 36 (1–2), 251–274.

Kiratzi A., Benetatos C. and Roumelioti Z. 2007. Distributed earthquake focal mechanisms in the Aegean Sea, *Bulletin of the Geological Society of Greece*, Vol. XXXX, 1125-1137.

Novotný O., Zahradník J., and Tselentis G.A. 2001. North-Western Turkey earthquakes and the crustal structure inferred from surface waves observed in Western Greece, *Bulletin of the Seismological Society of America*, 91, 875-879.

Ocakoğlu N. 2012. Investigation of Fethiye-Marmaris Bay (SW Anatolia): seismic and morphologic evidences from the missing link between the Pliny Trench and the Fethiye-Burdur Fault Zone, *Geo-Marine Letters*, (2012) 32, 17–28.

Roumelioti Z., Kiratzi A. and Benetatos C. 2010. Time Domain Moment Tensors of Earthquakes in the broader Aegean Sea for the years 2006-2007: the database of the Aristotle University of Thessaloniki, *Journal of Geodynamics*, doi: 10.1016/j.jog.2010.01.011.

Saikia C. K. 1994. Modified frequency-wavenumber algorithm for regional seismograms using Filon's quadrature; modeling of Lg waves in eastern North America, *Geophysical Journal International*, 118, 142-158.

Shaw B. 2012. Active Tectonics of the Hellenic Subduction Zone, Springer Theses, 1, doi: 10.1007/978-3-642-20804-1_1, © *Springer-Verlag Berlin.*

Shaw B. and Jackson J. A. 2010. Earthquake mechanisms and active tectonics of the Hellenic subduction zone, *Geophysical Journal International*, 181 (2), 966-984.

Taymaz T. and Price S. 1992. The 1971 May 12 Burdur earthquake sequence, SW Turkey: a synthesis of seismological and geological observations, *Geophysical Journal International,* 108, 589-603.

Ten Veen J. 2004. Extension of Hellenic forearc shear zones in SW Turkey: the Priocene-Quaternary deformation of the Esen Cay Basin, *Journal of Geodynamics*, 37, 181-204.

Waldhauser F. and Ellsworth W. L. 2000. A double-difference earthquake location algorithm: Method and application to the northern Hayward fault, *Bull. Seismol. Soc. Am.,* 90, 1353–1368.

Wessel P. and Smith W.H.F. 1998. New improved version of the Generic Mapping Tools released, *EOS Transactions, AGU* 79, 579.

Δελτίο της Ελληνικής Γεωλογικής Εταιρίας, τομ. XLVII , 2013
Πρακτικά 13ου Διεθνούς Συνεδρίου, Χανιά, Σεπτ. 2013

Bulletin of the Geological Society of Greece, vol. XLVII 2013
Proceedings of the 13th International Congress, Chania, Sept. 2013

CHARACTERIZATION OF SITE CONDITIONS IN GREECE FOR REALISTIC SEISMIC GROUND MOTION SIMULATIONS: PILOT APPLICATION IN URBAN AREAS

Kiratzi A.[1], Klimis N.[2], Theodoulidis N.[3], Margaris V.[3], Makra K.[3], Christaras B.[1], Chatzipetros A.[1], Papathanassiou G.[1], Savvaidis A.[3], Pavlides Sp. [1], Roumelioti Z.[4], Sapountzi L.[1], Diamantis I.[2], Lazaridis Th.[2], Petala E.[2] and Mimidis K.[2]

[1] Aristotle University of Thessaloniki, School of Geology, kiratzi@geo.auth.gr, christar@geo.auth.gr, ac@geo.auth.gr , gpapatha@ auth.gr, stavsapountzi@yahoo.gr, pavlides@geo.auth.gr

[2] Democritus University of Thrace, Department of Civil Engineering, nklimis@civil.duth.gr, jdiam@civil.duth.gr, theo.laza@gmail.com, epetala@civil.duth.gr, komimidi@civil.duth.gr

[3] Institute of Engineering Seismology & Earthquake Engineering, Thessaloniki, ntheo@itsak.gr, margaris@itsak.gr, alexandros@itsak.gr, makra@itsak.gr

[4] Aristotle University of Thessaloniki, Department of Civil Engineering, zroum@auth.gr

Abstract

We present the structure and first results of the "Thales" project on site classification in Greece. The aim of the project is twofold: to develop and present a methodology for the characterization and classification of site conditions based on their geological, geomorphological and geophysical characteristics and to apply the proposed methodology to case studies in Greece, including the urban areas of Xanthi, Edessa and Grevena. In particular, the units described on a surficial geological map will be correlated to shear-wave velocity data, corresponding to the upper 30m (Vs30) of the soil column, aiming to produce first order maps to help practitioners and provide the tools to realistically predict ground motions triggered by an earthquake. The classification will be based on information provided by borehole logs, where velocity profiles were measured and will be validated using the three case studies. The outcome of the project will be usable by national agencies and decision makers for urban planning.
Key words: *site characterization, surface geology, earthquake, Vs_{30}.*

Περίληψη

Αντικείμενο της παρούσας εργασίας είναι η παρουσίαση των βασικών ερευνητικών στόχων και των πρώτων αποτελεσμάτων του προγράμματος «Θαλής» για την ταξινόμηση των εδαφικών συνθηκών στον ελλαδικό χώρο. Οι κύριες ερευνητικές κατευθύνσεις του προγράμματος είναι α) η ανάπτυξη μεθοδολογίας για τον χαρακτηρισμό και την ταξινόμηση των εδαφικών συνθηκών με βάση τα γεωλογικά, γεωμορφολογικά και γεωφυσικά χαρακτηριστικά τους και β) η πιλοτική εφαρμογή των αποτελεσμάτων για την ανάλυση και πρόβλεψη των σεισμικών κινήσεων σε αστικά κέντρα στην Ελλάδα

όπως α) στην πόλη της Έδεσσας, β) στην πόλη της Ξάνθης, και γ) στην πόλη των Γρεβενών. Η έρευνα βασίζεται στη συσχέτιση των διαφορετικών γεωλογικών σχηματισμών με την ταχύτητα των εγκαρσίων (διατμητικών) σεισμικών κυμάτων σε βάθη έως 30m, Vs_{30}, χρησιμοποιώντας ως ενδιάμεσο κρίκο γεωτεχνικές παραμέτρους. Η παραπάνω μεθοδολογία πρόκειται να χρησιμοποιηθεί για την καλύτερη χωρική αποτίμηση των σεισμικών εδαφικών κινήσεων από έναν πραγματικό σεισμό ή από ένα σενάριο σεισμού, συνυπολογίζοντας με τον τρόπο αυτόν και την επιρροή της τοπικής γεωλογίας στη διαμόρφωση της σεισμικής κίνησης. Δυο είναι οι βασικοί στόχοι του έργου: α) η ταξινόμηση των εδαφών και συσχέτισή τους με τις ταχύτητες των εγκαρσίων κυμάτων για την Ελλάδα έτσι ώστε να είναι ευχερέστερος ο χαρακτηρισμός των εδαφικών συνθηκών σε κάθε περιοχή και β) η καλύτερη χωρική αποτίμηση των σεισμικών εδαφικών κινήσεων από έναν πραγματικό σεισμό ή η πρόβλεψη αυτών από ένα σενάριο σεισμού, αφού ο παράγοντας της ενίσχυσης λόγω εδαφικών συνθηκών, θα έχει αξιόπιστα συνυπολογιστεί.
Λέξεις κλειδιά: *τεκμηρίωση εδαφικών συνθηκών, επιφανειακή γεωλογία, σεισμική εδαφική κίνηση, Vs_{30}.*

1. Introduction

Consideration of site conditions is a vital step in analyzing and predicting earthquake ground motion in order to estimate structural failure in urban areas endangered by large or even moderate magnitude earthquakes. It is well known from historical reports and post-earthquake reconnaissance field surveys that damage is usually greater at sites lying on soils than on rocks. Characteristic examples of site amplification is the 1985 Michoacán earthquake (Mexico) that induced severe structural damage to 10 and 20-stories buildings in Mexico City, at an epicentral distance of more than 400km and the 1989 Loma Prieta earthquake that caused serious damage to structures built on non-engineered fill materials at the marina district of San Francisco and at the city of Oakland where structures were built on alluvial deposits (Wills et al., 2000).

The outcome of numerous studies regarding the factors that play an important role to site amplification is that soils modify seismic waves in at least three ways: generating reflected, refracted and/or diffracted waves at velocity discontinuities (Olsen and Archuleta, 1996), scattering the incoming wave as it encounters inhomogeneity within the soil (Zeng, 1993) and increasing the amplitude of the incoming wave in soils that are less tightly packed (Joyner and Boore, 1988; Borcherdt, 1994).

A widely used method for assessing site amplification is based on the evaluation of shear-wave velocity in the shallow subsurface. In particular, Borcherdt et al. (1991) showed that the shear wave velocity averaged over the upper 30m (Vs_{30}) can be correlated to the amplification of ground motions. The evaluation of the Vs_{30} can be achieved using the equation:

Equation 1 – Formula for evaluating the Vs_{30}

$$V_{S30} = \frac{30}{\sum_i \frac{h_i}{V_i}}$$

where h_i is the thickness of the i_{th} layer in the upper 30m of the soil column and V_i the shear-wave velocity within it.

The importance of site amplification has been recognized and prompted strong efforts to map site conditions at regional scales (Holzer et al., 2005). Such maps are useful both for code applications and input to earthquake loss models.

Initially, Joyner et al. (1981) proposed that the velocity to a depth equal to one quarter wavelength of the period of interest could represent the site conditions. They used quaternary mapping units and assigned a mean shear-wave velocity to each geological unit within the studied area. A few years later, Borcherdt et al. (1991) proposed a map that grouped the geologic units in San Francisco into four shear-wave velocity classes. Similar methodology was used by Park and Elrick (1998) in order to classify the geological units in southern California. The outcome of their study is the grouping of geological units into eight units with similar Vs_{30} values.

At the same period, the classification suggested by National Earthquake Hazards Reduction Program was incorporated in the building code in the United States of America (Building Seismic Safety Council - BSSC, 1995; 2001). This classification grouped soil and rock units into five categories (Table 1) based on the Vs_{30} values of Dobry et al. (2000).

Table 1 - Classification of sites adopted by the Building Seismic Safety Council of U.S.A (BSSC, 2001).

Site class	Vs_{30} (m/sec)	Geotechnical description
A	>1500	Hard rock
B	$760 \leq VS_{30} \leq 1500$	rock
C	$360 \leq VS_{30} \leq 760$	Very dense soil and soft rock
D	$180 \leq VS_{30} \leq 360$	Stiff soil
E	<180	Soft soil

During the last decade, mapping of site conditions generally follows this model and the proposed classifications of geological units are based on the shear-wave velocity on the upper 30m. Wills et al. (2000) attempted to group geological formations according to Vs_{30} in seven classes. In particular, they grouped geological units of similar age and properties and then assigned them to shear wave velocities groups (Wills et al., 2000).

Wills and Clahan (2006) developed a map of geological units that can be distinguished by their shear-wave velocity. In order to develop this map, they used data regarding the age as well as the properties of the geological units and their depositional environment (Figure 1).

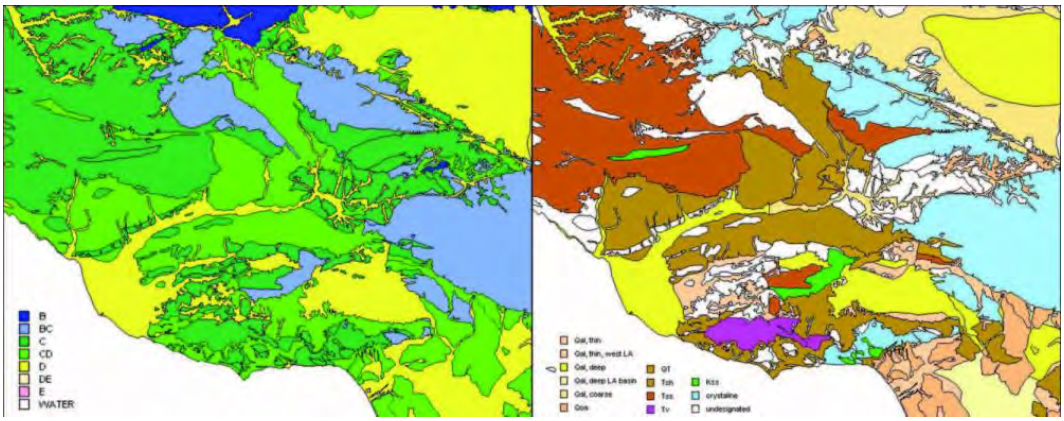

Figure 1 - Preliminary site-conditions map of California (Wills et al., 2000) and geological map based on shear-wave velocities categories on the right (Wills and Clahan, 2006).

Furthermore, Holzer et al. (2005) investigated the correlation of Vs_{30}-geology by taking into account the impact of the thickness of shallow geologic units and local measurements of Vs. They developed a map on 1:24.000 scale, based on in-situ S_{CPT} data.

Recently, both Eurocode8 (EC8, CEN 2004) in Europe and the International Building Code (ICC, 2012) in USA adopted the same basic principles and approaches regarding soil classification (Pitilakis et al., 2012). In particular, the Vs_{30} parameter is used in EC8 along with N_{SPT} blow count, plasticity index (PI) and un-drained shear strength, C_u to define five soil types (A–E), while two extra special ground types (S1 and S2) are also proposed for soils that special attention should be paid (liquefaction, etc).

The aim of this project is to develop a classification of surficial geological units based on their geophysical and geomorphological characteristics that could be used for the development of simplified maps to be used by practitioners and for the estimation of the ground motions triggered by an earthquake.

Table 2 - Soil classification based on EC 8 (CEN, 2004).

		Parameters		
Site class	**Description**	**Vs_{30} (m/s)**	**N_{SPT} (blows/30cm)**	**C_u (kPa)**
A	Rock or other rock-like geological formation, including at most 5 m of weaker material at the surface	>800		
B	Deposits of very dense sand, gravel, or very stiff clay, at least several tens of meters in thickness, characterized by a gradual increase of mechanical properties with depth	360–800	>50	>250
C	Deep deposits of dense or medium-dense sand, gravel or stiff clay with thickness from several tens to many hundreds of meters	180–360	15–50	70–250
D	Deposits of loose-to-medium cohesionless soil (with or without some soft cohesive layers), or of predominantly soft-to-firm cohesive soil	<180	<15	<70
E	A soil profile consisting of a surface alluvium layer with Vs values of type C or D and thickness varying between about 5 m and 20 m, underlain by stiffer material with Vs >800 m/s			
S1	Deposits consisting, or containing a layer at least 10 m thick, of soft clays/silts with a high plasticity index (PI>40) and high water content	<100		10-20
S2	Deposits of liquefiable soils, of sensitive clays, or any other soil profile not included in types A–E or S1			

2. Structure of the Project

Recently reported earthquake-induced failures in Italy and Greece confirmed that the scale of structural damage depends on site conditions. In particular, the 1986 Kalamata and 1999 Athens events, regarding Greek territory, showed that one of the basic parameters influencing the severity of structural failures is the spatial distribution of alluvial deposits.

Taking into account the fact that the spatial distribution of sediments and particularly the alluvial ones is a basic factor for the amplification of seismic ground motion, it can be assumed that it is crucial to map and classify the quaternary geological units. This classification can be achieved by correlating the value of the shear-wave velocity on the upper 30m (Vs_{30}) with the type of deposits.

Thus, this project aims to provide a useful tool for the evaluation of site effects by establishing a relationship and proposing a relevant classification between geological formation of the Greek area and Vs_{30}. This classification could be used by urban planners and decision makers for designing the extension of urban areas or in near real time seismological applications for seismic hazard and seismic impact assessment. In order to achieve this goal, the spatial distribution of quaternary deposits is going to be examined in conjunction with their physical and mechanical properties following widely-used methodologies for evaluating seismic ground motion. The main tasks of our project are outlined below:

- Initially, the geological units will be grouped using criteria related to the depositional process, material, age and physical properties.
- Afterwards, by taking into account published classifications and data provided by in-situ tests, shear-wave velocity values will be assigned to each group of geological units
- One of the most important tasks of the project is the geological field reconnaissance of suitable sites for field testing using SCPT seismic cone. These tests will be performed at sites specifically selected for their geological structure: formations would be homogenous or at least with clearly defined stratigraphy based on their granulometry (the classification will be the one proposed by the Unified Soil Classification System (USCS; http://www.astm.org/), (i.e. coarse grained or unconsolidated and fine grained or consolidated). The results of this task are expected to clarify the contacts between overlapping geological formations and define the proposed classification of the geological formations based on shear wave velocity. The methodology that will be followed is described in the following subtasks:

  -Literature review and data extraction concerning homogenous geological formations from published 1:50,000 I.G.M.E. geological maps, papers, technical reports, etc.

  -Fieldwork at selected sites for the reconnaissance of the geological structure and the characterization of the formations based on their sedimentation facies and age.
- An additional field task deals with surface geology and structure reconnaissance at sites where accelerographs have already been installed and ground motions records are available. In this way, the processes and the deposition environment of each formation will be clarified and they will be characterized and classified. The field work will consist of geological characterization of surface soil and rock formations based on the published 1:50,000 I.G.M.E. maps, papers, technical reports and field reconnaissance.
- A task will deal with the collection and evaluation of existing information regarding the extent of the geological formations at the selected sites, compilation of geological maps and geological profiles showing the structure, stratigraphic position and thickness of each formation. The methodology that will be followed for this objective consists of:
  - Literature review on the surface geology of the selected sites based on the published 1:50,000 I.G.M.E. maps, papers, technical reports etc.

Fieldwork at selected pilot sites in order to define the geological structure and, when possible, the basement outcrops.

- Characterization of the geological formations based on their depositional environment, age and, when possible, their granulometry, in order to comprehend the local geological conditions.

- Finally, having classified the geological units, a task will deal with the application of the proposed methodology to selected urban areas. In particular, the cities of Xanthi, Grevena and Edessa were selected as pilot areas due to their characteristic topography (Edessa) and/or their seismotectonics setting (Xanthi and Grevena). Single station ambient noise measurements as well as ambient noise array measurements are currently implemented within the aforementioned cities in order to determine selected soil dynamic properties of geologic surface layers. Finally, the new soil classification scheme will be validated/verified in simulations of recorded strong ground motion at specific points (i.e. those of permanently installed accelerographs) and if judged qualified, it will be incorporated in a methodology for the computation of shake maps from scenario earthquakes.

3. Accomplished Tasks

The initial task of this project was the collection of existing geological information and data provided in literature, maps and geotechnical boreholes concerning the urban areas of Edessa, Xanthi and Grevena.

The outcome of this research is a compilation of a database where data provided by more than 100 borings are employed (Figure 2). In particular, regarding the urban area of Xanthi, 60 geotechnical boreholes with NSPT measurements have been collected. The depth of the boreholes ranges from 1.9m to 30m, whereas 33% of them were drilled down to 10m. In the area of Grevena, the review of published reports and articles resulted to the compilation of a database with 31 geotechnical boreholes that were mainly drilled within the city. The depth of the boreholes varied between 2m and 20m, while the majority of the information (circa 68%) is provided by boreholes of depth from 10m to 15m. Finally, regarding the third pilot area (city of Edessa), data provided by 22 geotechnical boreholes in the city of Edessa were collected. Most of them were drilled before the 90's, during the construction of state buildings and their depth varies from 8 to 28m.

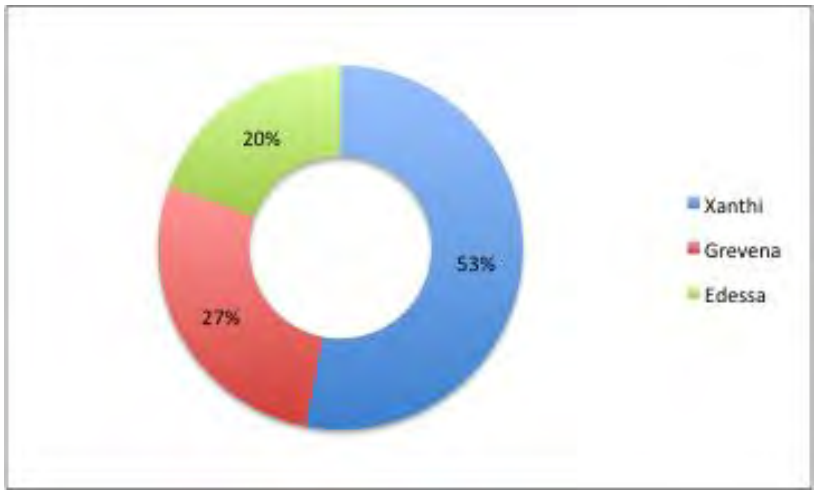

Figure 2 - Comparative presentation of the amount of borehole data collected for each of the three pilot areas (Xanthi, Grevena, and Edessa) as a percentage of the entire database that was created for the pilot studies.

The collected data are organised in an excel database, where all basic information is presented in 25 columns (Figure 3). In particular, borehole ID, its location (coordinates), depth and water table level are employed in the first 6 columns followed by information on the upper and lower level of the geological units (per layer) and a relevant brief geological-geotechnical description based on N_{SPT} values and Atterberg limits (Liquid limit and Plasticity index) of the soil units. In addition, data provided by laboratory tests (e.g. grain size analysis) are also employed and used for the classification of the geological units according to USCS. Finally, 6 fields are used to include information regarding the recorded shear wave velocity Vs per unit, the average value of Vs on the upper 30m and the relevant classification based on Eurocode 8.

J	K	L	M	N	O	P	Q	R
GRAIN SIZE ANALYSIS (%)			ATTERBERG LIMITS		U.S.C.S. CLASSIFICATION	SIMPLIFIED CLASSIFICATION	N_{30} (SPT)	Depth of SPT (m)
Gravels (>No4)	Sand	Fines (<No200)	W_L%	PI%				
3,5	88,5	8			SM-SW	S	11	2,00
2	80,5	17,5			SM	S	45	4,00
1	61	38			SC	S	19	6,50
15	63,5	21,5			SM	S	18	8,00
							21	10,00
							20	12,50
							20	14,50
							30	16,50
							42	18,50
							24	21,00
							>50/10cm	23,5

Figure 3 - Part of the excel database designed and created to include all information necessary to proceed to the soil classification in Greece.

The single station ambient noise measurements were given priority for the city of Xanthi where detailed geological/geotechnical information is available. As a passive geophysical method it requires a preliminary stage of carefully selected sites before a dense mesh of measurements is accomplished throughout the city. For this purpose, two measurements were performed at the accelerograph stations and six in selected sites based on available geological maps. Each measurement had duration of 30 minutes and sensor's coupling was ground. Following the SESAME guidelines instructions (SESAME Project, 2004) the H/V spectral ratio method was calculated in order to define fundamental frequency and its corresponding amplification due to surface geologic layers.

Results of the analysis are shown in Figure 4. It is observed that a systematic “bump” of the H/V curve is apparent for frequencies less than 1.5Hz. Almost all sites do not show a clear H/V fundamental peak but rather a broad one between 0.4Hz to 1.Hz. However, for the site 027 a clear fundamental frequency peak is apparent around 0.25Hz. Taking into account the preliminary results of the H/V spectral ratio together with all available geological and geotechnical information for the city of Xanthi, a dense mesh of ambient noise measurements is going to be implemented. Based on the H/V zonation of the city as well as on available geological information, ambient noise array for a few sites will be also performed in order to define V_{sz} shear wave velocity values as a function of depth z, at least for the upper 30 meters.

4. Results - Discussion

Although the "Thales" project is still in its beginning, we have managed to accomplish several important tasks i.e. the collection of geotechnical borehole data for the three pilot areas (Xanthi, Edessa and Grevena) and most importantly the design and implementation of a database that will host this data. This database is continuously growing with the addition of relevant geotechnical information from boreholes throughout the Greek mainland. Apart from the expected scientific results of the project, the database itself is a major deliverable to the scientific community.

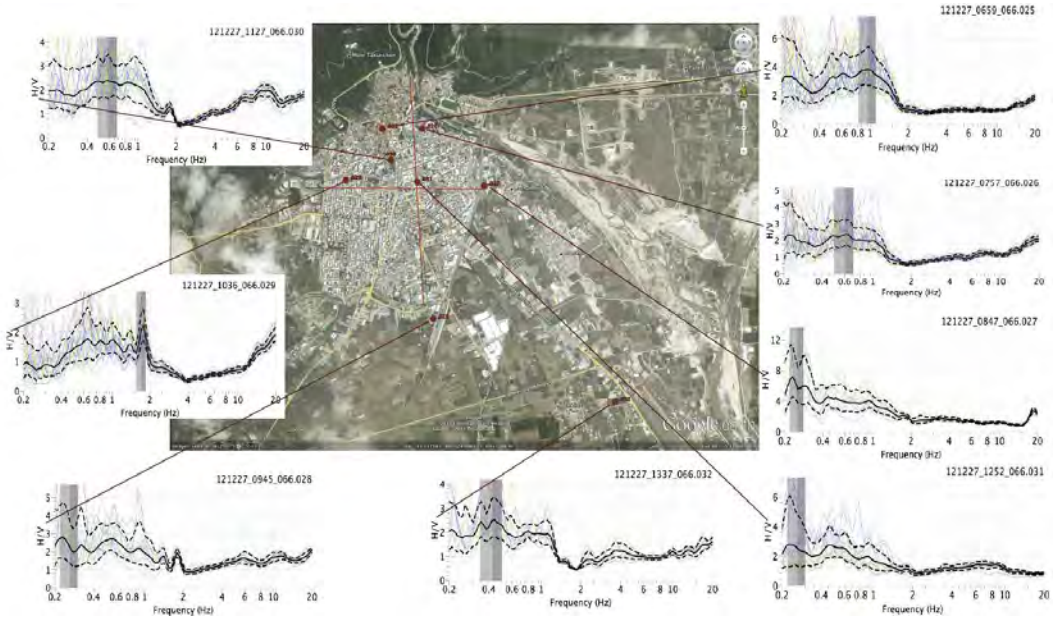

Figure 4 - H/V spectral ratio in selected sites of Xanthi, based on single station ambient noise measurements.

At present, the "Thales" project on site classification in Greece continues with the geological reconnaissance surveys at selected sites and field measurements to augment our geotechnical database and improve our knowledge on the relation between data at hand and surface geology.

5. Acknowledgments

This research has been co-financed by the European Union (European Social Fund – ESF) and Greek national funds through the Operational Program "Education and Lifelong Learning" of the National Strategic Reference Framework (NSRF) – Research Funding Program: "Thales". Investing in knowledge society through the European Social Fund.

6. References

Borcherdt R. D., Wentworth C. M., Janssen A., Fumal T. and Gibbs J. 1991. Methodology for predictive GIS mapping of special study zones for strong ground motion in the San Francisco Bay region, CA, *Proc. Fourth Int. Cont. on Seismic Zonation*, Earthquake Engineering Research Institute, Oakland, California, 545–552.

Borcherdt R. D. 1994. Estimates of site-dependent response spectra for design (methodology and justification), *Earthquake Spectra,* 10, 617–653.

Building Seismic Safety Council (BSSC) 1995. 1994 Edition, NEHRP Recommended Provisions for Seismic Regulations for New Buildings, FEMA 222A/223A, Vol. 1 (Provisions) and Vol. 2 (Commentary), developed for the Federal Emergency Management Agency, Washington, D.C.

Building Seismic Safety Council (BSSC) 2001. 2000 Edition, NEHRP Recommended Provisions for Seismic Regulations for New Buildings and Other Structures, FEMA-368,Part1 (Provisions): developed for the Federal Emergency Management Agency, Washington, D.C.

CEN (European Committee for Standardization) 2004. Eurocode 8: design of structures for earthquake resistance, part 1: general rules, seismic actions and rules for buildings. EN 1998-1:2004. Brussels, Belgium

Dobry R., Borcherdt R. D., Crouse C. B., Idriss I. M., Joyner W. B., Martin G. R., Power M. S., Rinne E. E. and Seed R. B. 2000. New site coefficients and site classification system used in recent building code provisions, *Earthquake Spectra,* 16 (1), 41–68

Holzer T. L., Padovani A. C., Bennett M. J., Noce T. E. and Tinsley J. C. III 2005. Mapping V_{s30} site classes, *Earthquake Spectra,* 21 (2), 353–370.

Joyner W.B., Warrick R.E. and Fumal T.B. 1981. The effect of Quaternary alluvium on strong ground motion in the Coyote Lake, California, earthquake of 1979, *Bull. Seism. Soc. Am*., 71, 1333-1350

Joyner W. B. and Boore,D. M. 1988. Measurement, characterization, and prediction of strong ground motion, *Proc. Earthquake Engineering, #38,* Soil Dynamics II GT Div/ASCE, Park City, Utah, June 27–30, 1988.

ICC (International Code Council) 2012 International Building Code. International Code Council, Inc. www.iccsafe.org/Pages/default.aspx

Olsen K. B. and Archuleta R. J. 1996. Three-dimensional simulation of earthquakes on the Los Angeles fault system, *Bull. Seism. Soc. Am*., 86, 575–596.

Park S. and Elrick S. 1998. Predictions of shear-wave velocities in southern California using surface geology, *Bull. Seism. Soc. Am*., 88, 677– 685.

Pitilakis K., Riga E. and Anastasiadis A. 2012. Design spectra and amplification factors for Eurocode 8*, Bulletin of Earthquake Engineering*, Vol 10(5), 1377-1400.

SESAME Project., 2004. Guidelines, Final Report, 2004; (http://sesame-fp5.obs.ujf-grenoble.fr/index.htm).

Wills C. J., Petersen M., Bryant W. A., Reichle M., Saucedo G. J., Tan S., Taylor G. and Treiman J. 2000. A Site-Conditions Map for California Based on Geology and Shear-Wave Velocity, *Bull. Seism. Soc. Am*., 90 (6B), S187–S208.

Wills C.J. and Clahan K.B. 2006. Developing a Map of Geologically Defined Site-Condition Categories for California, *Bull. Seism. Soc. Am*., 96(4A), 1483–1501.

Zeng Y. 1993. Theory of scattered P and S waves energy in a random isotropic scattering medium, *Bull. Seism. Soc. Am*., 83, 1264–1276.

Δελτίο της Ελληνικής Γεωλογικής Εταιρίας, τομ. XLVII , 2013
Πρακτικά 13ου Διεθνούς Συνεδρίου, Χανιά, Σεπτ. 2013

Bulletin of the Geological Society of Greece, vol. XLVII 2013
Proceedings of the 13th International Congress, Chania, Sept. 2013

MODELING SEISMICITY RATE CHANGES ALONG THE HELLENIC SUBDUCTION ZONE (GREECE)

Leptokaropoulos K. M.[1], Papadimitriou E. E.[1], Orlecka–Sikora B.[2] Karakostas V. G.[1] and Vallianatos F.[3]

[1]*Geophysics Department, School of Geology, Aristotle University of Thessaloniki, GR54124 Thessaloniki, kleptoka@geo.auth.gr, ritsa@geo.auth.gr, vkarak@geo.auth.gr*

[2]*Seismology and Physics of the Earth's Interior, Institute of Geophysics, Polish Academy of Sciences, Warsaw, Poland, orlecka@igf.edu.pl*

[3]*Laboratory of Geophysics and Seismology, Technological Educational Institute of Crete, fvallian@chania.teicrete.gr*

Abstract

The Dieterich (1994) Rate/State formulation was applied for the seismicity rate changes in the western part of the Hellenic arc to be investigated. The completeness magnitude of the shallow seismicity (h<60km) was firstly evaluated for different time windows. The spatio-temporal changes of these seismicity rates (reference rates) were studied then for the interevent periods between successive strong (M≥6.0) earthquakes. These changes were correlated with the Coulomb stress changes (ΔCFF) produced by the stronger events, through a Rate/State model which incorporates physical parameters associated with fault dynamics such as the tectonic stressing rate, fault constitutive parameters and frictional response of the rupture zones. The influence of the former parameters in the model performance was tested by evaluating the linear correlation coefficient between modeled and real earthquake production rates along with their confidence limits. Application of different parameter values was attempted for the sensitivity of the calculated seismicity rates and their fit to the real data to be tested. Given the geographical peculiarity of the Hellenic Subduction zone, that yields to high uncertainties in the earthquake focal parameter determination, the results demonstrate that the present formulation and the available data sets are sufficient enough to contribute to a robust seismic hazard assessment.

Key words: *Coulomb stress changes, Rate/state stress transfer, smoothed seismicity.*

Περίληψη

Οι μεταβολές των ρυθμών σεισμικότητας στο δυτικό τμήμα του Ελληνικού Τόξου μελετήθηκαν με βάση το μοντέλο Ρυθμού/Κατάστασης (Dieterich, 1994). Καθορίστηκε το μέγεθος πληρότητας του καταλόγου επιφανειακών σεισμών (h<60km) για διαφορετικά χρονικά διαστήματα και έγινε μελέτη των μεταβολών των ρυθμών σεισμικότητας αναφοράς στο χώρο και το χρόνο για τις περιόδους μεταξύ διαδοχικών ισχυρών (M≥6.0) σεισμών. Οι μεταβολές αυτές συσχετίσθηκαν με τις μεταβολές των στατικών τάσεων Coulomb (ΔCFF), που συνδέονται με τη γένεση των ισχυρών σεισμών, σε ένα μοντέλο που συνδυάζει φυσικές παραμέτρους των ρηγμάτων όπως οι ρυθμοί τεκτονικής φόρτισης, οι καταστατικές παράμετροι και η τριβή. Η επίδραση των

τιμών αυτών των παραμέτρων εκτιμήθηκε με τον υπολογισμό του συντελεστή γραμμικής συσχέτισης μεταξύ των πραγματικών και των υπολογισμένων με βάση το μοντέλο ρυθμών σεισμικότητας και του διαστήματος εμπιστοσύνης του. Εφαρμόστηκαν διαφορετικές τιμές των παραμέτρων που υπεισέρχονται στο μοντέλο για να ελεγχθεί η ευαισθησία υπολογισμού των εκτιμώμενων ρυθμών στη διακύμανση των τιμών αυτών. Με δεδομένη την γεωγραφική ιδιαιτερότητα της περιοχής μελέτης, εξαιτίας της οποίας προκύπτουν σημαντικές αβεβαιότητες στον προσδιορισμό των εστιακών παραμέτρων των σεισμών, τα αποτελέσματα της εργασίας δείχνουν ότι η συγκεκριμένη μεθοδολογία και τα διαθέσιμα δεδομένα μπορούν να προσφέρουν μια αξιόπιστη εκτίμηση σεισμικής επικινδυνότητας.
Λέξεις κλειδιά: Μεταβολές Τάσεων Coulomb, Μοντέλο Ρυθμού/Κατάστασης, Ομαλοποιημένη Σεισμικότητα.

1. Introduction

The Hellenic subduction zone (Figure 1) constitutes one of the most rapidly deforming parts of the Alpine-Himalayan mountain belt, exhibiting intense shallow and intermediate depth seismic activity and experiencing several devastating earthquakes known from both historical reports and instrumental recordings. The strongest earthquake that ever occurred in the broader Aegean region, was located at the southwestern part of the Hellenic Arc, near Crete Island (M8.3), in AD 365 (Papazachos & Papazachou, 2003; Papadimitriou & Karakostas, 2008; Shaw, 2012). The subduction thrust belt is the most prominent feature of the broader Aegean region between the slowly converging Eastern Meditteranean oceanic lithosphere and Aegean microplate with a well constrained, from GPS data and the geological history, rate of convergence of about 4cm/yr (Clarke et al., 1998; McClusky et al., 2000). This deformation rate is enough to induce a roll-back at the Hellenic Trench leading to significant extension of the overriding plate with the back-arc

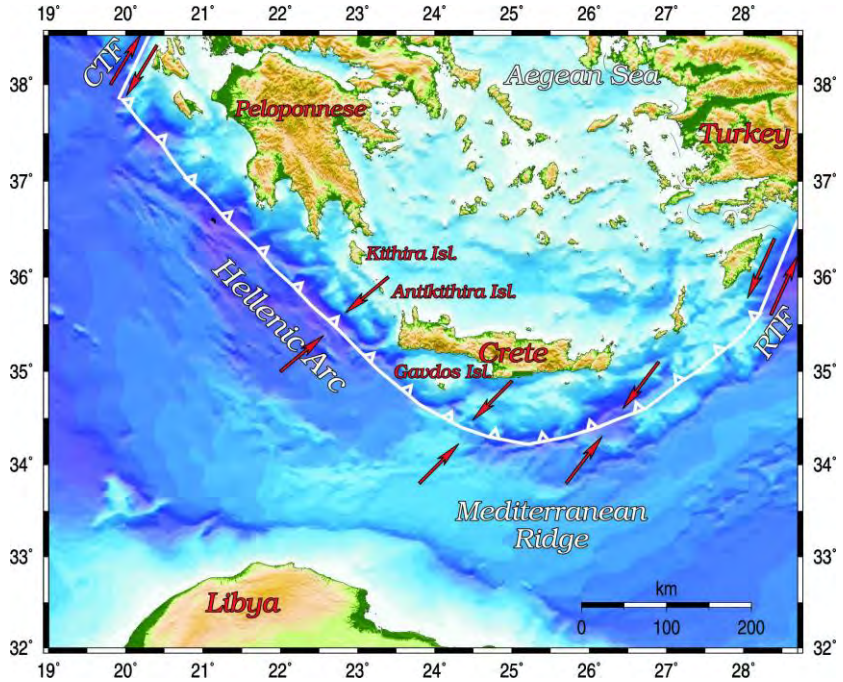

Figure 1 - Morphology and main seismotectonic properties of the study area (Papadimitriou & Karakostas, 2008).

stretching direction being oblique to the trench roll-back direction. This zone is extended between the two Subduction-Transform Edge Propagators (STEP) of the dextral Cephalonia Transform Fault in the west (Scordilis et al., 1985) and the sinistral Rhodos fault in the east (Papazachos and Papazachou, 2003) over a distance of approximately 1000km.

The existence of a Wadati-Benioff zone which is dipping about 30^o at its shallow segment until 100km depth and then descending with a steeper angle of 45^o was first recognized by Papazachos & Comninakis (1971) and it was then confirmed from seismic hypocenter studies (Hatzfeld and Martin, 1992; Papazachos et al., 2000). Seismic tomography revealed the deeper branches of subducted lithosphere at a depth of 600 km (Spakman et al. 1988, Papazachos and Nolet 1997).

Seismic deformation is not uniformly distributed throughout the region as the tectonic structures are related to complex tectonic evolution and deformation patterns. Both extensional and compressive regimes are evident in the region (Taymaz et al., 1990, 1991; Papazachos & Kiratzi, 1996; Benetatos et al., 2004; Yolsal-Çevikbilen & Taymaz, 2012) resulted to three major faulting types. The shallow earthquakes in the external part of the subduction system are associated with low angle, reverse faulting with the P-axis being almost perpendicular to the subduction front. This latter seismic activity is responsible for the most destructive earthquakes throughout the entire Arc. The second type involves crustal earthquakes in a backarc narrow extensional continental zone with the T-Axis orientated in an almost east-west direction and faults striking almost N-S running parallel to the arc (Papazachos et al., 1998; Benetatos et al., 2004). The intermediate depth events occur onto the descenting slab and are associated with strike slip faulting with a considerable thrust component, with maximum tension trending parallel to the dip of the Wadati–Benioff zone and maximum compression being almost horizontal and parallel to the arc direction (Kiratzi and Papazachos 1995, Papazachos 1996). Normal faulting with E-W orientated strike dominate the backarc region.

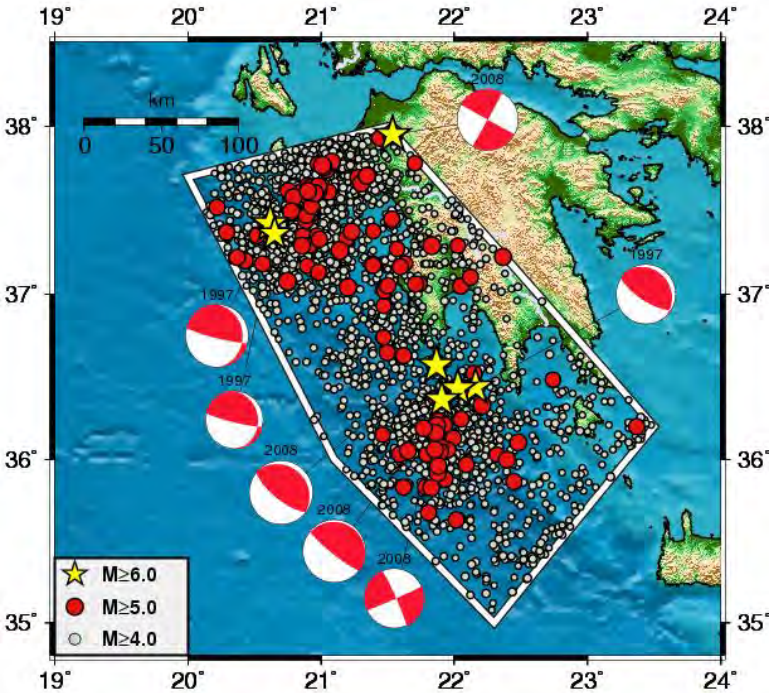

Figure 2 – Earthquake (M≥6.0) fault plane solutions that occurred in the study area since 1997, shown as lower hemisphere equal area projections. Epicenters of the earthquakes with M≥4.0 since 1971 are also depicted. Information about these strong events is also given in Table 1.

2. Method

The evaluation of seismicity rate changes in terms of Coulomb static stress changes is performed on the basis of a Rate/State model, proposed by Dieterich (1994). According to Rate/State stress transfer concept, a sudden positive stress step, results to an immediate increase of the seismicity rate, which is temporary and attenuates with time following the Omori's decay law. Similarly, a sudden stress drop brings on a seismicity rate decrease, which also tends to recover with time to the initial rate, due to the effect of the stressing rate (constant or variable). These rate changes can be observed either along the fault, which caused the main shock (along fault aftershocks), or in nearby faults (off-fault triggering) up to a distance proportional to the final slip distribution regardless the dynamics of the rupture (Gomberg et al., 2005). Applications of the model (e. g. Toda et al., 1998; Toda et al., 2005; Catalli et al., 2008) have shown that seismicity rate changes, **R**, strongly depend on clock–advanced failure, the fault stressing rate, $\dot{\tau}$, and the reference rates of earthquake production, **r**, expressed as:

$$R = \frac{r}{\gamma \cdot \dot{\tau}_r} \qquad (1)$$

Where **γ**, is the state variable for seismicity formulation that evolves with time and stressing history and alters its value because of the stress perturbations, causing seismicity rate changes. The seismicity rate equation, as a function of time, **t**, has the form (Dieterich & Kilgore, 1996):

$$R(t) = \frac{r}{\left[\exp\left(\frac{-\Delta CFF}{A\sigma}\right) - 1\right]\exp\left(\frac{-t}{t_a}\right) + 1} \qquad (2)$$

Here, $\mathbf{t_a}$, is the characteristic relaxation time for the perturbation of earthquake rate, **A** is a fault constitutive parameter, **σ** is the total normal stress and **ΔCFF** is the coseismic Coulomb stress changes, given by $\mathbf{\Delta CFF = \Delta\tau + \mu' \Delta\sigma_n}$, with **Δτ**, being shear stress change, $\mathbf{\Delta\sigma_n}$, stands for the normal stress change and **μ′**, the apparent coefficient of friction, including pore pressure effects (Simpson and Reasenberg, 1994). Product **Aσ**, describes the instantaneous response of friction to a step change in slip speed (Toda & Stein, 2003). Reference and observed seismicity rates for any inter-event time interval are computed by spatially smoothing the seismicity. For this purpose we use a probability density function (PDF) of epicenters distribution. This function determines the seismicity rates at the center of each cell of a normal grid superimposed on the study area and these values are considered constant in time as the same is considered for the secular tectonic stressing rate. The PDF is estimated by a bivariate kernel density estimator of the form (Silverman, 1986):

$$f(x,y) = \frac{1}{nh^2}\sum_{i=1}^{n} K\left(\frac{x - X_i}{h}, \frac{y - Y_i}{h}\right) \qquad (3)$$

Where K stands for the Gaussian Kernel of the form:

$$K(x,y) = \frac{1}{2\pi} e^{\frac{-(x^2+y^2)}{2}} \qquad (4)$$

Where $\mathbf{X_i}$, $\mathbf{Y_i}$, are the epicentral coordinates of earthquakes (longitude, **λ** and latitude, **φ**, respectively), **x**, **y**, are the coordinates of the centers of the bins, on which the PDF value is going to be estimated, **n**, is the number of the events and **h**, is the smoothing parameter (or window width), having the same units with $\mathbf{X_i}$, $\mathbf{Y_i}$, **x**, **y**. The kernel determines the regularity and the shape of the estimator, whereas the window width controls the degree of smoothing. From equations (3) and (4) the probability is derived:

$$P = \frac{1}{4n}\sum_{i=1}^{n}[erf(\frac{y_2 - Y_i}{h\sqrt{2}})\cdot(erf(\frac{-x_1 + X_i}{h\sqrt{2}}) - erf(\frac{-x_2 + X_i}{h\sqrt{2}})) + erf(\frac{y_1 - Y_i}{h\sqrt{2}})\cdot(erf(\frac{-x_2 + X_i}{h\sqrt{2}}) - erf(\frac{-x_1 + X_i}{h\sqrt{2}}))] \quad (5)$$

With $erf(x) = \frac{2}{\sqrt{\pi}}\int_0^x e^{-t^2} dt$ (6)

which is twice the integral of the Gaussian distribution with mean zero and variance of 1/2. Finally the seismicity rate is estimated for the given time period, **Δt** as, **R=n/Δt**. This corresponds to the real seismicity rate of the given time period and is compared with the value of expected seismicity rate for the respective period resulted from (2).

2.1 Data Selection

We selected the shallow seismicity (h<60km) data in the western part of the Hellenic arc between the Kephalonia transform fault and Crete Island, since 1970. Then the completeness magnitude, M_c, was evaluated for different time increments with the methodology of Leptokaropoulos et al. (2012) as shown in Table 1. In each case two different periods with different duration and M_c were considered to calculate the reference seismicity rates. These periods were selected for data sufficiency and longest possible duration to be achieved.

Table 1 – Magnitude of completeness as calculated for different periods

Period		Period	Mc	Period	Mc
1971-1980	4.0	1991-2000	3.6	2001-2007	3.6
1981-1990	3.7	2001-2012	3.6	2008-2012	3.5

2.2 ΔCFF Calculations

Coulomb stress changes were calculated from the coseismic displacements of the stronger (M≥6.0) events (Table 2) that occurred in the study areas since 1996. Fault lengths, L, were determined following the spatial distribution of the stronger, well located aftershocks. The respective widths were estimated from the dip angle of the fault and the distance measured down–dip from the surface to the upper and lower edges of the rectangular dislocation plane, respectively, as h/sin(dip), where H, is the width of the seismogenic layer (3 – 20km). For the low angle dipping faults the constraint L≥W was set. The mean coseismic slip, u, was calculated from the seismic moment, M_o, of an earthquake, as M_o=G·u·L·w, where, **G**, stands for the shear modulus and equals to $3.3\cdot10^5$ bars. All ΔCFF calculations were done at the depth of 8km, which represents approximately the nucleation depth. The calculation of the stress field changes was done according to the representative fault plane geometry and sense of slip as found for each one of the study sub-areas. The apparent coefficient of friction, **μ΄**, and the Poisson ration, **ν**, were considered equal to 0.4 and 0.25, respectively.

Table 2 – Source mechanisms of the events considered in this study.

Year	Date	Lat(oN)	Lon(oE)	h(km)	M	strike	dip	rake	Reference
1997	13OCT	36.440	22.160	13.0	6.3	123	72	84	Kiratzi & Louvari, 2003
1997	18NOV	37.420	20.619	10.0	6.6	354	20	159	
1997	18NOV	37.360	20.650	5.0	6.1	354	20	159	
2008	14FEB	36.570	21.868	20.0	6.7	312	18	93	GCMT
2008	14FEB	36.430	22.026	8.6	6.6	292	8	74	
2008	20FEB	36.360	21.907	9.4	6.3	336	85	178	
2008	8JUN	37.950	21.537	15.0	6.4	301	74	7	

2.3 Expected Seismicity Rates – Rate/State Parameters

The expected seismicity rates were therefore calculated in each cell from eq. 2, given the reference seismicity rate, **r**, the static Coulomb stress changes, **ΔCFF**, the characteristic relaxation time, $\mathbf{t_a}$, which was considered to range between 2.5yr-25yrs and the product **Aσ** (fault constitutive parameter, **A**, total normal stress, **σ**). This product is connected with the characteristic time and the long term tectonic loading, $\boldsymbol{\tau_r}$, as $\mathbf{A\sigma=\tau_r \cdot t_a}$. The tectonic loading was selected ranging from 0.005bar/yr to 0.06bar/yr. The aforementioned values of $\mathbf{t_a}$ and $\boldsymbol{\tau_r}$, lead to an **Aσ** ranging from 0.0125 – 1.5 bars.

3. Qualitative and Quantitative Analysis

Once the modeled seismicity rates are calculated, they are compared with the observed ones for the respective time windows. A qualitative fitting was accomplished by comparison of the patterns of observed and expected seismicity and the locations of the events that occurred during the respective periods and for specific parameter values (Figure 3). One more qualitative representation was done by mapping the ratio of expected/observed seismicity rates in the study areas (Figure 4). Thus, the declination of the modeled from the real values becomes more evident. Quantitative comparison was done by calculation of the Pearson's linear correlation coefficient (PCC) and its 95% confidence intervals (Figure 5). Significance testing for PCC was also performed by estimating the corresponding p-value that is the highest level of significance at which the null hypothesis stating that PCC=0 can still be rejected.

The infuence of 7 strong events (3 in 1997 and 4 in 2008) was taked into consideration to calculate ΔCFF and to model expected seismicity rates (Figure 3). The reference seismicity rate was calculated for 1971-1997 (M_c=4.0). The June 2008 event occurred outside the area borders but it was close enough to alter the regional stress field. In the first period (1997-2008) the correlation is much stronger, especially in the central and northern part of the area. The second period (2008-2012) is not long enough to contain sufficient data and therefore the correlation coefficient is relatively low (h=0.08^o, t_a=10yrs, τ_r=0.01 bar/yr). Similar results for the first period yielded when reference seismicity rates were calculated from 1981-1997 (M_c=3.7), although they were somewhat amplified in comparison with the previous approach, because in this period the dataset contains a larger number of events (smaller M_c). For the second period, more events are available, but the correlation does not show any improvement with a significant number of earthquakes taking place in stress shadows.

The ratio of expected/observed seismicity rate for the two study periods is shown in Figure 4 with calculations done considering reference seismicity rate evaluated for 1981-1997 (M_c=3.7). The ratio is close to 1 for the first period but it diverges to higher values for the second one, indicating that the modeled rates are higher than the expected ones (h=0.08^o, t_a=10yrs, τ_r=0.01 bar/yr). The patterns are similar if we consider reference seismicity rate calculated for 1971-1997, but here are more obvious in the second period (2008-2012) due to larger sample available.

The quantitative analysis shows that there is a relatively high correlation between observed and modelled seismicity rates for the first of the study periods. This correlation is even stronger in areas experiencing positive ΔCFF values and reaches over 70% in most of the cases. For the time interval from February to June 2008, there is no correlation at all (~0) because of the very small span of the time window resulted to shortage of data. Finally, for the period 2008-2012 a moderate correlation is evident which become higher for positive ΔCFF areas. This happens due to the fact that the catalog is dominated by along-fault aftershocks, that took place in the close vicinity of the faults segment connected with these main events. Therefore, it is very likely that the correlation will be improved as time passes and the aftershock sequence decay at the reference rate.

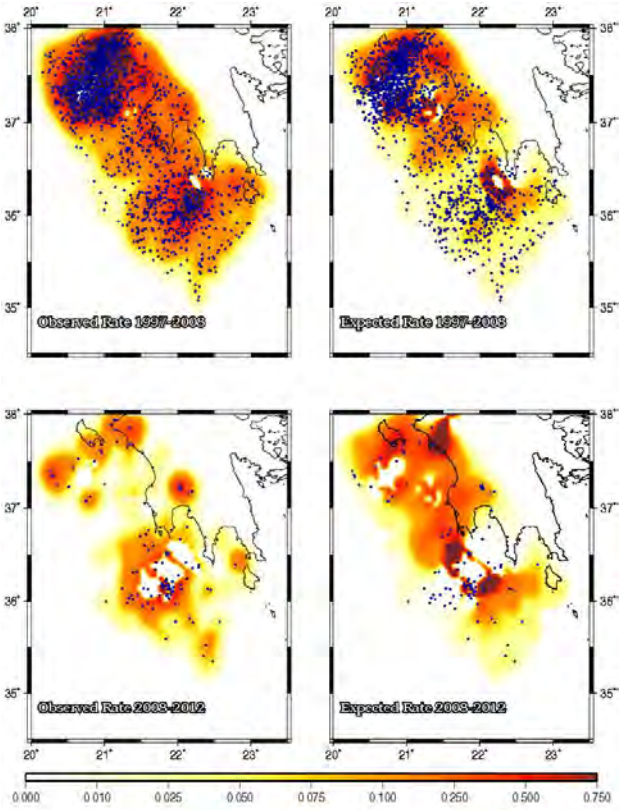

Figure 3 – Observed (left frames) and modelled (right frames) seismicity rates. Blue dots represent the epicentres of the earthquakes occurred during the respective periods. The reference seismicity rate was calculated during 1971-1997 (M≥4.0).

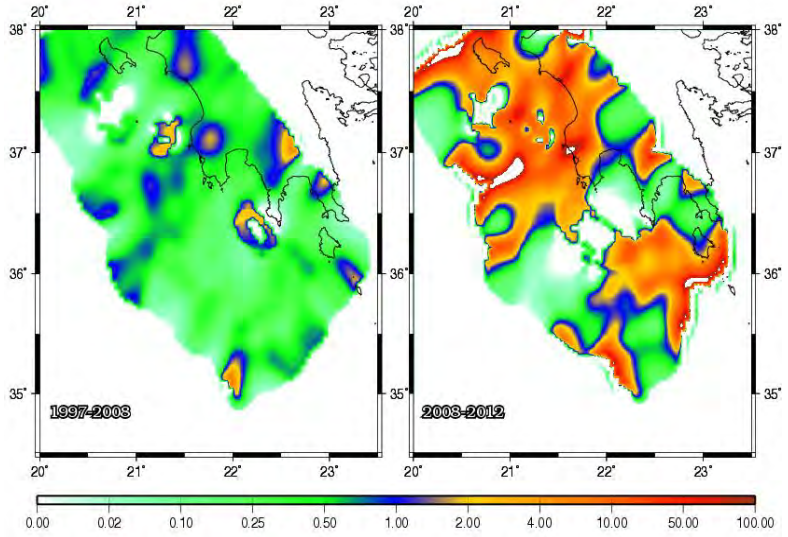

Figure 4 - Ratio of expected/observed seismicity rates for the inter event periods. Green colors indicate regions where expected seismicity rates are lower than the observed ones while warmer colors stand for regions with higher expected rates in comparison with the observed ones. Applied parameter values were: h=0.08^{o}, t_a=10yrs, τ_r=0.01 bar/yr, Aσ=0.1bar. Reference seismicity rate was considered from the period 1981-1997 (M≥3.7).

4. Discussion and Conclusion

In the application of the Dieterich (1994) rate/state model, we started with a "learning period" (either 1971-1997 or 1981-1997) and a reference seismicity rate was then evaluated. The static Coulomb stress changes (ΔCFF), caused by strong earthquakes' occurrence were calculated and their influence to the reference seismicity rates were estimated. The impact of the constant tectonic loading (stressing rate) during the inter-seismic periods (or 'testing periods') was embodied to the modeled seismic rates. Summarizing, the simulated earthquake occurrence rates were estimated as a result of the effect of the successive coseismic ΔCFF and the steady-rate tectonic loading on the reference rates evaluated from the learning period's seismicity. These calculations are performed just before and after a strong earthquake takes place, and therefore the real (observed) seismicity rates during the inter-event periods are also evaluated (following the same procedure as with the reference seismicity rates). The results are qualitatively and quantitatively compared with the modeled ones in order to seek for correlation between observed-expected seismic rates and improve the modeling by selection/combination of parameter values applied.

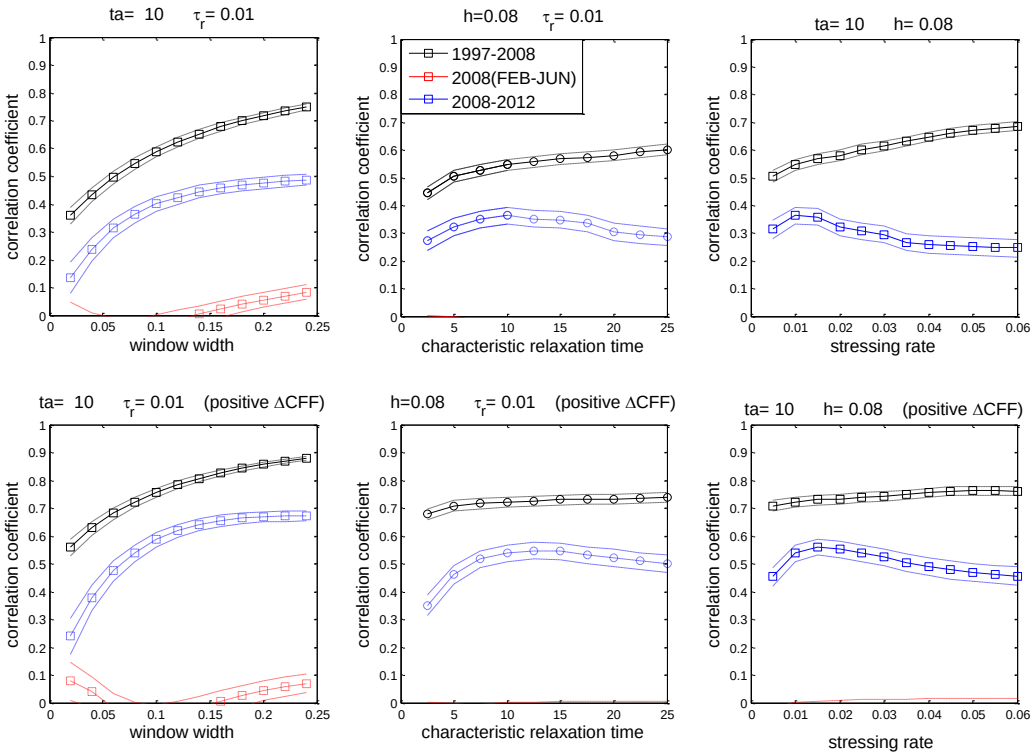

Figure 5 - Quantitative evaluation of the difference between observed-synthetic seismicity rates during the inter-event time periods (colored lines). Solid lines indicate the value of Pearson linear Correlation Coefficient (PCC) while dashed lines indicate its lower and upper bounds for a 95% confidence interval for each coefficient. The upper frame figure yielded from the whole data, while the figure below by taking into account only those cells which experience positive ΔCFF.

The results indicate that the correlation between observed and simulated seismicity rate values is quite high when the study periods last enough for the respective dataset exhibiting sufficient size and including adequate number of off-fault earthquakes. In some of the cases the expected rates are very close to the observed ones, whereas, in the remaining cases the model tends to overestimate the seismicity rates in comparison with the real ones, although the spatial distribution

of expected seismicity rates fits well to the observed one. When a different learning period was considered in order to obtain bigger sample, both qualitative and quantitative correlation was slightly improved. When cells experience positive ΔCFF are only considered in the calculations, stronger correlation is obtained. Even if several assumptions were taken into consideration (uniform stressing rate, ΔCFF calculation according to a specific type of faulting, influence of strong events before 1997 was not considered), the results show that successful modeling seismicity rate changes through this approach is feasible. Implication of the current analysis to earthquake probabilities is expected to significantly contribute to time dependent seismic hazard assessment. Given a magnitude frequency relation the rates of the strongest events occurrence can be easily transformed to probability of earthquake occurrence

5. Acknowledgments

This work was supported by the THALES Program of the Ministry of Education of Greece and the European Union in the framework of the project entitled "Integrated understanding of Seismicity, using innovative Methodologies of Fracture mechanics along with Earthquake and non extensive statistical physics – Application to the geodynamic system of the Hellenic Arc. SEISMO FEAR HELLARC". The GMT system (Wessel and Smith, 1998) was used to plot some of the figures. Geophysics Department, AUTH, contribution number 814.

6. References

Benetatos C., Kiratzi A., Papazachos C. and Karakaisis G. 2004. Focal mechanisms of shallow and intermediate depth earthquakes along the Hellenic Arc, *J. Geodyn.,* 37, 253-296.

Catalli F., Cocco,M., Console R. and Chiaraluce L. 2008. Modeling seismicity rate changes during the 1997 Umbria–Marche sequence (central Italy) through a rate-and-state dependent model, *J. Geophys. Res.,* 113, B11301, doi:10.1029/2007JB005356.

Clarke P.J., Davies R.R., England P.C, Parsons B., Billiris H., Paradissis D., Veis G., Cross P. A., Denys P.H., Ashkenazi V., Bingley R., Kahle H. G.,. Muller M.V. and Briole P. 1998. Crustal strain in central Greece from repeated GPS measurements in the interval 1989–1997, *Geophys. J. Int.,* 135, 195– 214.

Dieterich J.H. 1994. A constitutive law for rate of earthquake production and its application to earthquake clustering, *J. Geophys. Res.*, 99, 2601–2618.

Dieterich J.H. and Kilgore B. 1996. Implications of fault constitutive properties for earthquake prediction, *Proc. Natl. Acad. Sci.*, 93, 3787–3794.

Gomberg J., Bodin P. and Reasenberg P.A. 2003. Observing Earthquakes triggered in the near field be dynamic deformations, *Bull. Seimol. Soc. Am.,* 93, 118-138.

Hatzfeld D. and Martin C. 1992. Intermediate depth seismicity in the Aegean defined by teleseismic data, *Earth Planet. Sci. Lett*., 113, 267– 275.

Kiratzi A.A. and Papazachos C.B. 1995. Active seismic deformation in the southern Aegean Benioff zone, *J. Geodynamics,* 19, 65-78.

Leptokaropoulos K.M., Karakostas V.G., Papadimitriou E.E., Adamaki A.K., Tan O. and İnan S. 2013. A homogeneous earthquake catalogue compilation for western turkey and magnitude of completeness determination (*submitted manuscript*).

McClusky S., Balassanian S., Barka A., Demir C., Ergintav S., Georgiev I., Gurkan O., Hamburger M., Hurst K., Kahle H., Kastens K., Kekelidze G., King R., Kotzev V., Lenk O., Mahmoud S., Mishin A., Nadariya M., Ouzounis A., Paradissis D., Peter Y., Prilepin M., Reilinger R., Sanli I., Seeger H., Tealeb A., Toksöz M. N. and Veis G. 2000. Global Positioning System constraints on plate kinematics and dynamics in the eastern Mediterranean and Caucasus, *J. Geophys. Res.*, 105, 5695-5719.

Papadimitriou E.E. and Karakostas V.G. 2008. Rupture model of the great AD 365 Crete earthquake in the southwestern part of the Hellenic Arc, *Acta Geophys.,* 56, 293-312.
Papazachos B. C. and Comninakis P.E. 1971. Geophysical and tectonic features of the Aegean Arc, *J. Geophys. Res.,* 76, 8517-8533.
Papazachos B. C. 1996. Large seismic faults in the Hellenic Arc, *Annali Geof.,* 39, 891-903.
Papazachos B.C. and Kiratzi A. 1996. A detailed study of the active crustal deformation in the Aegean and surrounding area, *Tectonophysics*, 253, 129–153.
Papazachos B.C., Papadimitriou E.E., Kiratzi A.A., Papazachos C.B. and Louvari E.K. 1998. Fault plane solutions in the Aegean and the surrounding area and their tectonic implications, *Boll. Geof. Teor. Appl., 39*, 199–218.
Papazachos B.C., Karakostas B.G., Papazachos C.B. and Scordilis E.M. 2000. The geometry of the Benioff zone and lithospheric kinematics in the Hellenic Arc, *Tectonophysics,* 319, 275-300.
Papazachos B.C. and Papazachou C. 2003. *The Earthquakes of Greece*, Ziti Publ., Thessaloniki, 317 pp.
Papazachos C.B. and Nolet G. 1997. P and S deep velocity structure of the Hellenic Arc obtained by robust nonlinear inversion of travel times, *J. Geophys. Res*., 102, 8349-8367.
Scordilis E.M., Karakaisis G.F., Karakostas B.G., Panagiotopoulos D. G., Comninakis P.E., and Papazachos B.C. 1985. Evidence for transform faulting in the Ionian Sea: The Cephalonia Island earthquake sequence, *Pure Appl. Geophys.,* 123, 388-397.
Shaw, B., 2012. *Active tectonics of the Hellenic subduction zone*, Springer Theses, 169 pp.
Silverman B.W. 1986. *Density Estimation for Statistic and Data Analysis*, Chapman and Hall, London, pp 9, 21.
Simpson R.W. and Reasenberg P.A. 1994. Earthquake–induced static stress changes on central California faults, in the Loma Prieta, California earthquake of October 17, 1989 – *Tectonic processes, and models*, ed. Simpson R. W., *U. S. Geol. Surv. Prof. Pap.,* 1550–F, F55–F89.
Spakman W., Wortel M.J.R. and Vlaar N.S. 1988. The Hellenic subduction zone: a tomographic image and its geodynamic implications, *Geophys. Res. Lett.,* 15, 60-63.
Taymaz T., Jackson J. and Westaway R. 1990. Earthquake mechanisms in the Hellenic trench near Crete, *Geophys. J. Int.,* 102, 695-731.
Taymaz T., Jackson J. A. and McKenzie D. 1991. Active tectonics of the north and central Aegean Sea, *Geophys. J. Int,* 106, 433–490.
Toda S., Stein R. S., Reasenberg P. A. and Dieterich J. H. 1998. Stress transferred by the 1995 M_w = 6.9 Kobe, Japan, shock: Effect on aftershocks and future earthquake probabilities, *J. Geophys. Res.*, 103, 24, 543–24,565.
Toda S. and Stein R.S. 2003. Toggling of seismicity by the 1997 Kagoshima earthquake couplet: A demonstration of time-dependent stress transfer, *J. Geophys. Res.,* 108, 2567, doi:10.1029/2003JB002527.
Toda S., Stein R. S., Richards-Dinger K. and Bozkurt S. 2005. Forecasting the evolution of seismicity in southern California: Animations built on earthquake stress transfer, *J. Geophys. Res.,* 110, doi:10.1029/2004JB003415.
Yolsal-Çevikbilen S. and Taymaz T. 2012. Earthquake source parameters along the Hellenic subduction zone and numerical simulations of historical tsunamis in the Eastern Mediterranean, *Tectonophysics*, 536-537, 61-100.

Δελτίο της Ελληνικής Γεωλογικής Εταιρίας, τομ. XLVII , 2013
Πρακτικά 13ου Διεθνούς Συνεδρίου, Χανιά, Σεπτ. 2013

Bulletin of the Geological Society of Greece, vol. XLVII 2013
Proceedings of the 13th International Congress, Chania, Sept. 2013

EARTHQUAKE CLUSTERS IN NW PELOPONNESE

Mesimeri M.[1], Papadimitriou E.[1], Karakostas V.[1] and Tsaklidis G.[2]

[1] *Aristotle University of Thessaloniki, Geophysics Department, mmesimer@geo.auth.gr, ritsa@geo.auth.gr,vkarak@geo.auth.gr.*

[2] *AristotleUniveristy of Thessaloniki, Department of Statistics and Operational Research, tsaklidi@math.auth.gr*

Abstract

Clusters commonly occur as main shock – aftershock (MS-AS) sequences but also as earthquake swarms, which are empirically defined as an increase in seismicity rate above the background rate without a clear main shock. A delcustering algorithm is employed to identify clusters from a complete catalog of earthquakes that occurred in the area of NW Peloponnese (Greece) during 1980-2007. In order to distinguish these clusters we calculate the skewness and kurtosis of seismic moment release for each cluster, since swarm-like sequences generally have lower skew value of moment release history than MS-AS. The spatial distribution of b-value was calculated for the entire catalog as for the declustered one, in order to correlate them with seismicity behavior of the region. Finally, the pre-stress field of Achaia 2008 earthquake was calculated aiming to associate the stress accumulation with the occurrence of the identified clusters.

Key words: *earthquake swarms, static stress changes, statistical seismology*

Περίληψη

Οι σεισμικές συγκεντρώσεις εκδηλώνονται ως ακολουθίες του τύπου κύριος σεισμός – μετασεισμοί αλλά και ως σμηνοσειρές, οι οποίες ορίζονται ως απότομες μεταβολές της σεισμικότητας χωρίς να κυριαρχεί κάποιος σεισμός σε μέγεθος. Εφαρμόστηκε αλγόριθμος με σκοπό την αναγνώριση των σεισμικών συγκεντρώσεων από ένα πλήρη κατάλογο για την περιοχή της ΝΔ Πελοποννήσου κατά την περίοδο 1980-2007. Ένα χαρακτηριστικό των σμηνοσεισμών αποτελεί η χαμηλή τιμή της λοξότητας της σεισμικής ροπής ως προς το χρόνο. Με σκοπό την διάκριση των σεισμικών συγκεντρώσεων σε σμηνοσεισμούς και μετασεισμικές ακολουθίες υπολογίζονται οι τιμές της λοξότητας και της κύρτωσης της σεισμικής ροπής ως προς το χρόνο για κάθε σεισμική συγκέντρωση. Επιπλέον υπολογίστηκε η χωρική κατανομή της παραμέτρου b τόσο για τον πλήρη κατάλογο όσο και για τον κατάλογο που προσεγγίζει την κανονική σεισμικότητα της περιοχής. Τέλος, υπολογίστηκε η κατανομή των τάσεων πριν την γένεση του σεισμού της Αχαΐας του 2008 με σκοπό την συσχέτιση της φόρτισης της περιοχής με την εκδήλωση σεισμικών συγκεντρώσεων.

Λέξεις κλειδιά: *σμηνοσεισμοί, μεταβολές πεδίου τάσεων, στατιστική σεισμολογία*

1. Introduction

Clustering of earthquakes in space and time indicates that interaction between earthquakes is an important component of the seismic cycle. There are three different types of earthquake sequences: (i) a mainshock followed by a number of aftershocks of decreasing magnitude and frequency, (ii) a slow buildup of seismicity (foreshocks) leading to a type (i) sequence and (iii) a gradual increase and decay of seismicity in time without a distinct mainshock. Earthquake sequences (i) typically occur in homogeneous material with a uniform external stress. Sequences (ii) tend to occur in material that is heterogeneous to some degree, or a moderate fracture density, with a non-uniform external stress. Sequences (iii) or swarms, occur in material that is extremely heterogeneous, or have high fracture density, with very concentrated external stress (Mogi, 1963).

One case of earthquake clustering is the occurrence of 'earthquake swarms', which can be defined as an increase in seismicity rate that lacks a clear main shock (Mogi, 1963; Sykes, 1970; Hill, 1977). Seismic swarms occur in a variety of different environments and might have a diversity of origins. Several studies were conducted to identify earthquake clusters and their spatiotemporal properties (Vidale and Shearer, 2006; Farell et al., 2009; Roland and McGuire, 2009; Holtkamp et al., 2011, among others).

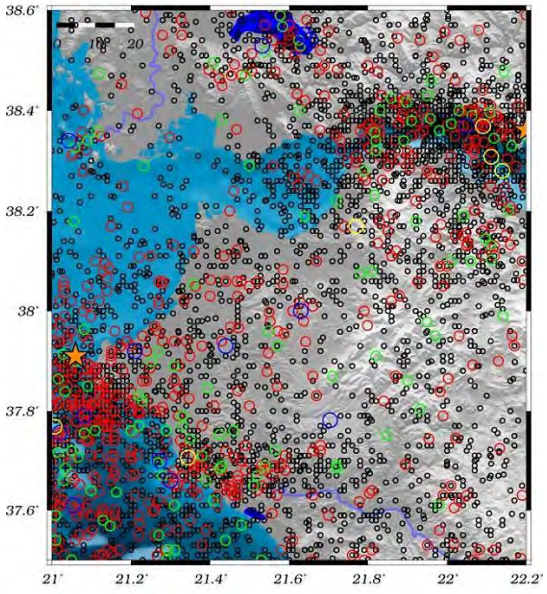

Figure 1 - Seismicity map of the complete catalogue (Mc ≥ 3.5) for the region of NW Peloponnese (1980-2007). Earthquakes with 3.5 ≤ M<6.0 are denoted by circles increasing in size according to the magnitude and M ≥ 6.0 are denoted by stars.

NW Peloponnese (Figure 1), which was selected as our target area, has experienced several moderate earthquakes in the last decades. In addition, several seismic sequences were recorded without a main shock with clearly discriminative magnitude. In the present work an effort is made for identifying earthquake clusters of both types that occurred in the region in the last decades and to investigate their spatio-temporal distribution, aiming to associate their occurrence with certain seismicity patterns.

2. Methods

In order to identify earthquake clusters from an earthquake catalogue and define their spatiotemporal properties, the following methods were applied.

2.1. Swarm Identification

Various algorithms are available to detect foreshock, mainshock and aftershock sequences (Reasenberg, 1985; Zhuang et al., 2002, among others). In this study, Reasenberg's (1985) algorithm was used to identify clusters from a complete catalogue. After the performance of declustering algorithm, we extract the catalogue that contains the clusters and we analyze them statistically (**see 2.3**) to distinguish swarm-like sequences from MS-AS. A swarm is defined if the following criteria proposed by Mogi (1963) are met: i) the maximum of the daily number of events in the sequence (N) is greater than twice the square root of the swarm duration in days (T): $N>2\sqrt{T}$ and ii) the total number of earthquakes in a sequence is at least 10 .

2.2. Calculating b-values

The b-value is a measure of the relative number of small to large earthquakes that occur in a given area and in a given time interval. In particular, the b-value is the slope of the frequency-magnitude distribution (Ishimoto and Iida, 1939; Gutenberg and Richter, 1944) for a given population of earthquakes. Studies have shown that the b-value changes with material heterogeneity (Mogi, 1962), thermal gradient (Warren and Latham, 1970), and applied stress (Scholz, 1968; Wyss, 1973; Urbancic et al., 1992; Schorlemmer et al., 2004; Schorlemmer and Wiemer, 2005; Schorlemmer et al., 2005).

The b-values determined in this study were calculated using the Zmap algorithm (Wiemer, 2001). Maximum-likelihood b-values were computed using equation 1 (Utsu, 1965; Aki, 1965; Bender, 1983):

Equation 1- b value calculation

$$b = \frac{1}{\bar{M} - M_{\min}} \log e$$

where $\bar{M}$ is the mean and M_{min} the minimum magnitude, respectively, of the given sample.

To examine how reliable our estimations are, a standard deviation δb of the b-value is estimated from the equation first derived by Aki (1965), or the improved formulation (eq. 2) by Shi and Bolt (1982):

Equation 2- error in b-value calculation

$$\delta b = 2.3 b^2 \sqrt{\frac{\sum_i (M_i - (M))^2}{n(n-1)}}$$

where n is the sample size.

2.3 Skewness and Kurtosis

Seismic swarms are distinguished from typical MS-AS by their unique seismicity patterns: the largest swarm events tend to occur later in the sequence, swarms contain several events as opposed to one clear mainshock, and swarm seismicity is more prolonged in time. One simple way to quantitatively identify earthquake clusters with swarm-like properties is through characterizing the timing of the largest event relative to the rest of the seismicity. To accomplish this, we calculate the skewness of moment release history and the kurtosis for each of the sequences that we analyze (Mesimeri, 2013). As described by Roland and McGuire (2009), a larger positive value of skewness is observed for pure aftershock sequences (approximately 30) while a lower or even negative value is observed for swarms (between -2 to 2). In addition, a large value of kurtosis is expected for MS-AS (kurtosis≥3) and a lower one for swarm-like sequences (kurtosis≤3) by the definition of kurtosis.

As proposed by Chen and Shearer (2011), for each swarm we normalize the time for each event since the beginning of the sequence by the mean time delay,

Equation 3- Mean time delay

$$t_i = \frac{(T_i - T_o)}{mean(T_i - T_o)} \quad i = 1, N$$

.

Next we consider the normalized timing of the largest event in the sequence t_{max}. Chen and Shearer (2011) classify clusters with $t_{max} \leq 0.4$ as early M_{max} (more similar to MS-AS) and clusters with $t_{max} \geq 0.4$ as late M_{max} (more swarm like) but in our study we consider $t_{max} \leq 0.3$ and $t_{max} \geq 0.3$ for MS-AS and swarm-like sequences, respectively. We use the skewness of moment release history

Equation 4-Skewness of moment release history

$$F(t) = \int_{t_0}^{t} M_o \, dt$$

to further quantify the difference between early M_{max} and late M_{max} clusters. For each event, the moment is estimated from the catalog magnitude (Hanks and Kanamori, 1979):

Equation 5

$$M_o(i) = 10^{1.5ML\,(i)+16.1},$$

where M_L is the local magnitude for each earthquake.

The centroid time of moment release is obtained from the weighted mean time (Jordan ,1991):

Equation 6- Centroid time

$$\bar{t} = \frac{\sum_1^N t_i \cdot M_o(i)}{\sum_1^N M_o(I)}$$

.

Individual moments (M_o) are normalized by

Equation 7

$$m_o(i) = \frac{M_o(i)}{\sum_1^N M_o(I)}$$

so that $F(t \rightarrow \infty) = 1$. The third ($\mu_3$) and the fourth ($\mu_4$) central moment of this sequence are

Equation 8-Third central moment

$$\mu_3 = \sum_1^N \left([\![ti - \bar{t}]\!] \right)^3 m_o(i) \,,$$

Equation 9 – Fourth central moment

$$\mu_4 = \sum_1^N \left([\![ti - \bar{t}]\!] \right)^4 m_o(i)$$

and the standard deviation:

Equation 10 –Standard deviation

$$\sigma = \sqrt{\sum_1^N \overline{ti - (t)}^2 \, m_o(i)}$$

.

The skewness and the kurtosis of moment release of each sequence are

Equation 11-Skewness

$$skewness = \mu_3/\sigma^3 \,,$$

Equation 12-Kurtosis

$$kurtosis = \mu_4/\sigma^4 \,.$$

2.4 Prestress Field Changes Calculations

In the pre-seismic stage, the main fault is locked and background seismicity is distributed in the surrounding area across small faults due to the raise of the stress level. King and Bowman (2003) have shown that a strong earthquake occurs when the distribution of the Coulomb stress around the fault has a certain pattern capable to trigger this rupture. This pattern depends on the geometry and kinematics of the ensuing rupture.

In the present study, Coulomb stress changes were calculated with the sense of slip opposite to the observed slip of the 2008 Achaia mainshock, according to the back-slip model suggested by Bowman and King (2001). This approach is based on the idea that before a strong earthquake the stress must accumulate not only on the fault itself, but also to a large region surrounding the fault prior to its failure. For the identification of this region, calculation of the stress field required for moving the causative fault with the orientation, displacement, and rake observed in the main shock is needed (Karakostas, 2009).

2.5 Data

The data used for the current study are taken from the monthly bulletins of the Geophysics Department of the Aristotle University of Thessaloniki (AUTH) and the Institute of Geodynamics of the National Observatory of Athens (NOA). The latitude and longitude appears with 3 digits in the AUTH dataset and with 2 digits in the NOA dataset. We did not proceed to any modifications since the error is larger than the accuracy of our data and the result is not affected. For the compilation of these bulletins, the recordings of the Hellenic Unified Seismographic Network (HUSN), maintained by the above Institutions as well as by Department of Geophysics of the University of Athens and the Laboratory of Seismology of the University of Patras were used. The catalogue that covers the time from 01/01/1980 to 31/12/2007, was checked for completeness and a threshold magnitude was identified.

3. Results

3.1 Clusters and their Statistical Properties

Wiemer and Wyss (2000) suggest that a careful estimate of the spatial and temporal homogeneity of the completeness magnitude (M_c) is required before deviations from a power law behavior for small magnitudes can be made. We employed the maximum curvature method and the M_c was found to be equal to M_c=3.5 for the entire period. We also calculate M_c for shorter time intervals (1980-1990, 1990-2007, 2000-2007) in which M_c remained unaltered.

The complete catalogue was declustered dividing the catalogue in 3 datasets, (i) the entire complete catalog, (ii) the one that contains only the clusters (1,383 events) and (iii) the declustered catalog (3262 events). The seismicity rate for the 3 datasets is shown in Figure 2 along with the events with magnitude M≥5.0, denoted by stars on the curve which contains the entire catalogue. From a visual inspection, we can recognize if the increase of the seismicity is due to a strong event or not.

The catalogue that contains the clustered events was thoroughly examined in order to more strictly define clusters and then distinguish MS-AS from earthquake swarms. From the initially 1,383 clustered events, 632 are kept that are distributed into 18 potential clusters. The spatial distribution of these clusters is shown in Figure 3, where the mean geographical coordinates of each cluster were plotted by stars. Additional information on the clusters properties such as starting time, duration and mean epicenter, is given in Table 1. For now on we will refer to each cluster by the code number given in Table 1.

In order to separate the swarm-like sequences from the MS-AS we calculate the skewness and the kurtosis of the seismic moment release for each event (Table 1). The t_{max} were also calculated for

this discrimination. If t_{max} is greater than 0.3 we have a swarm-like sequence and if t_{max} is lower than 0.3 is MS-AS or a swarm like sequence with an early main event, as mentioned above.

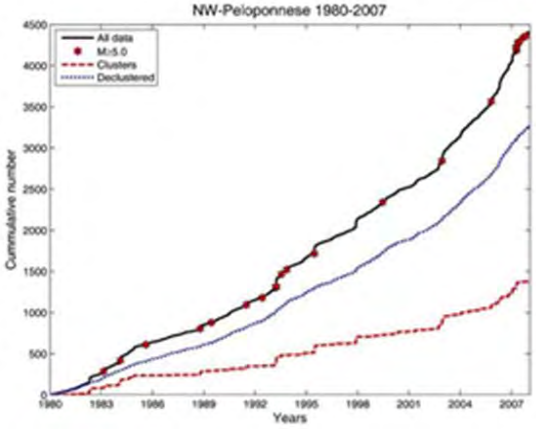

Figure 2 – Seismicity rates for the three data sets. Solid, dotted and dashed lines correspond to complete, declustered and clusters catalogues, respectively. Stars denote events with M≥5.0.

In Figure 4 the value of skewness of each cluster is plotted against to the value of kurtosis. For our data, it seems that clusters with skewness <2 and kurtosis<5 can be characterized as swarms, while clusters with skewness>2 and kurtosis>5 are MS-AS. Considering the value of t_{max} we conclude that clusters 03, 04, 07, 08, 10, 12, 18 are of MS-AS type, clusters 01, 02, 13-16 are swarms and clusters 05, 06, 09, 11, 17 are swarm like sequences with an early main event (t_{max} approximately zero).

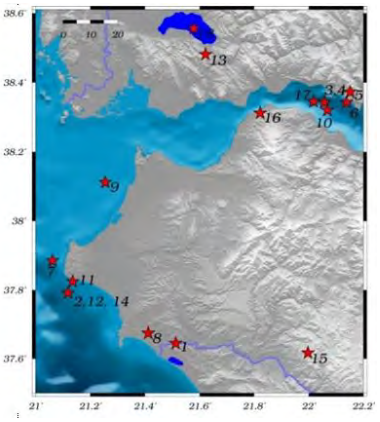

Figure 3 – Spatial distribution of earthquake clusters centres (denoted by star) for 1980-2007. The numbers are referring to Table 1

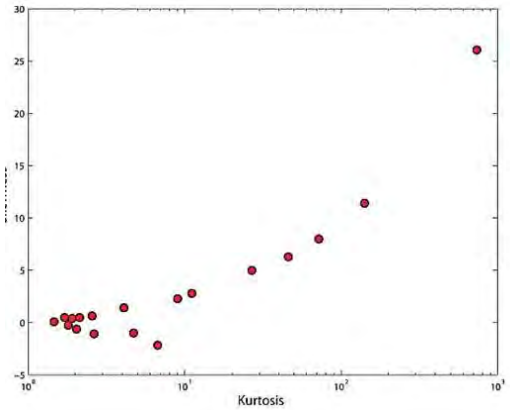

Figure 4 –Calculated skewness of seismic moment release plotted against the kurtosis of each cluster

3.2 b-value Distribution

In Figure 5 the b-value spatial distribution of the complete (Figure 5a) and the declustered (Figure 5b) catalogue is shown, as been calculated by Zmap, along with earthquakes epicentral distribution. Calculations were performed on the nodes of a normal grid superimposed on the study area. A constant 15km radius was chosen to calculate b-values, compromising maximum coverage and details in b-values spatial variation. The number of events with $M \geq M_c$ are set to 25 and the grid selection is 0.01^o x 0.01^o. In addition, two more limitations are applied to get reliable results. Firstly we consider only values estimated from datasets with magnitude range $\Delta M \geq 1.0$, where ΔM is the difference between M_{max} and M_c of each bin, and finally we choose b-values with $\delta b < 0.4$.

Table 1 - Basic properties of the clusters shown by asterisks in map of Figure 3. The two last columns correspond to the statistical parameters skewness and kurtosis, respectively

S/N	Starting Time	Days	M_{max}	# of events	Lon. (°E)	Lat. (°N)	T_{max}	Sw	K
1	1982/04/23,02:24	14.8	4.8	57	21.513	37.645	0.4	0.4	1.7
2	1983/03/13,13:48	4.2	4.3	13	21.119	37.792	1.1	-1.0	4.7
3	1984/01/02,07:07	5.3	4.5	14	22.023	38.346	0.0	2.27	9.01
4	1984/02/11.05:04	6.9	5.6	37	22.064	38.351	0.08	11.4	141
5	1984/11/09,09:51	0.7	3.9	10	22.151	38.373	0	0.3	1.9
6	1984/11/20,19:30	10.7	3.7	13	22.133	38.340	0	-0.6	2.0
7	1988/10/16,12:34	16.3	6	27	21.062	37.885	0	7.9	71.9
8	1993/03/26,11:45	8.4	5.4	86	21.413	37.675	0	2.7	11.1
9	1994/10/13,12:40	12.2	4	13	21.255	38.112	0.1	0.4	2.1
10	1995/06/15,00:15	24.8	6.5	82	22.068	38.320	0	26.0	735
11	2002/09/14,19:46	16.04	4.6	35	21.128	37.823	0	1.4	4.1
12	2002/12/02,04:58	23.03	5.4	47	21.115	37.795	0	6.28	46.0
13	2012/12/29,22:22	2.5	4.2	12	21.662	38.481	1.35	-1.0	2.6
14	2003/01/04,20:00	18.88	4.7	26	21.126	37.795	0.07	-0.2	1.8
15	2005/01/26,05:46	0.55	4.5	4	21.997	37.617	1.16	-2.1	6.73
16	2005/10/17,22:15	4.02	4.0	22	21.822	38.321	0.3	0.07	1.46
17	2007/01/07,14:47	13.94	4.3	60	22.018	38.341	0	0.63	2.55
18	2007/04/09,05:02	5.88	5.3	66	21.579	38.556	0.67	4.98	26.8

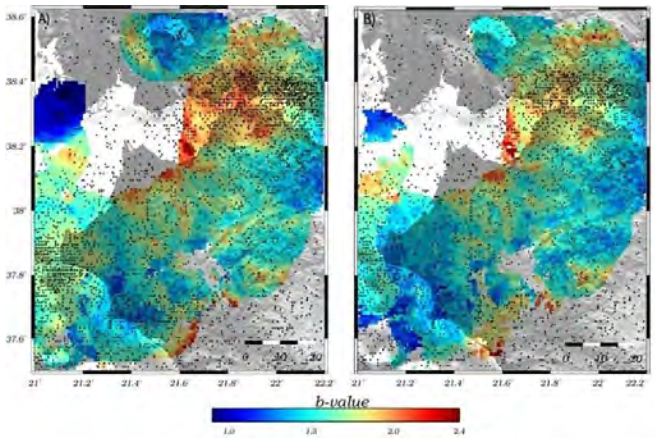

Figure 5 – b-value distribution a) for the complete catalogue and b) for the declustered catalogue (1980-2007). Bright and dark zones indicate high and low b-values, respectively.

In order to associate the b-value with the seismicity of the region we use both the entire catalogue and the declustered one. It is pictured (Figure 5) that regions with high seismicity, such as the western part of Corinth Rift, exhibit high b-values both in the declustered and the entire catalogue. For the regions that experience low seismicity, a b-value was not possible to be calculated.

3.3 Coulomb Stress Changes

In order to examine the relation between the spatial appearance of clusters and the pre-stress field of Achaia 2008 earthquake, we adopted the GCMT fault plane solutions for the strongest event in each cluster with a main event of M≥5.0 (Table 2).The pre-stress field was calculated inverting the sense of slip on the fault of 2008 earthquake according to the faulting type of the main event of each cluster (Figure 6). In these figures, dark regions denote negative changes in ΔCFF and inferred decrease likelihood of fault rupture. These regions are called stress shadows (Harris and Simpson 1993, 1996). Bright regions represent positive ΔCFF and increased likelihood of fault plane rupture. Most of the clusters were in the areas of high stress concentration (bright zones) with only the exception of cluster 8.

Table 2 – Information on the source parameters of M≥5.0 earthquakes that occurred in NW Peloponnese during 1980-2008 Fault plane solutions are taken from GCMT catalogue.

Origin Time	Epicenter		Mw	Mechanism			Depth	Event
	Lon.	Lat.		Strike	Dip	Rake		
1984/02/11,08:02	22.09	38.36	5.6	77	28	-121	15	4
1988/10/16,18:40	20.9	37.95	5.8	301	76	-3	29	7
1993/03/26,11:58	21.3	37.66	5.4	30	86	150	15	8
1995/06/15,00:15	22.2	38.36	6.5	265	43	-103	15	10
2002/12/02,04:59	21.08	37.79	5.6	36	56	-160	15	12
2007/04/10,03:17	21.63	38.55	5.0	320	41	-69	13.9	18
2008/06/08,12:25	21.53	37.95	6.5	208	88	178	24.7	Achaia

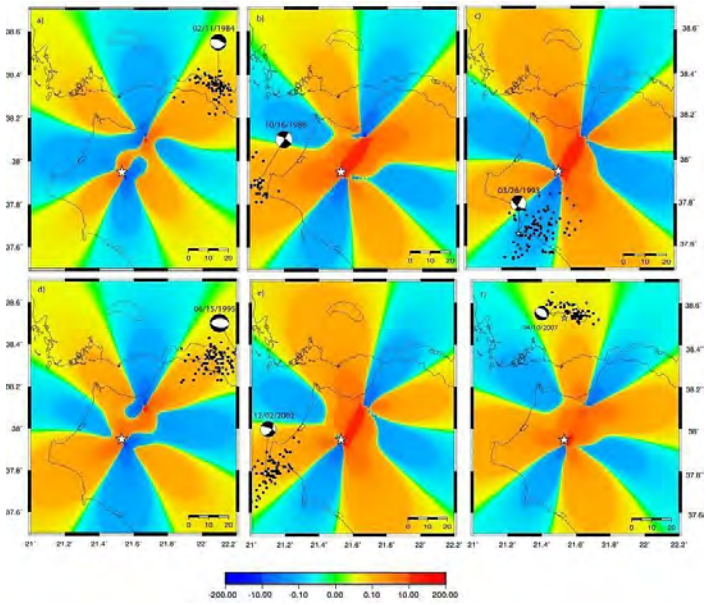

Figure 6 – Stress field modelled by reversing the sense of slip observed in Achaia 2008 earthquake (M=6.4) for the fault plane solution of events in Table 2. Dots represent the epicenters of each cluster, the big star depicts the epicentre of Achaia 2008 earthquake. In a) is cluster 4, b) cluster 7, c) cluster 8, d) cluster 10 (Aigio earthquake), e) cluster 12 and f) cluster 18.

4. Discussion – Conclusions

For the period 1980-2007 18 clusters were identified in the area of NW Peloponnese, with the employment of a declustering algorithm in a complete earthquake catalogue. Clusters were divided into three types (MS-AS, swarms and swarm-like sequences) according to their history of seismic moment release (skewness and kurtosis) and the occurrence time of the main event. Spatial distribution of calculated b-values on a normal grid superimposed on the study area reveals that high b-values are in areas that experience high seismicity. The stress associated with the preparation procedures of 2008 Achaia main shock (M=6.4) is in agreement with the 5 major clusters, as those are placed in the red lobes, indicating that the stress was accumulated in the region around the fault and swarm-like activity was encouraged.

5. Acknowledgments

The GMT system (Wessel and Smith, 1998) was used to plot the figures and the Zmap software (Wiemer, 2001) for the b-value calculations. The stress tensors were calculated using a program written by J. Deng (Deng and Sykes, 1997) who used the DIS3D code of S. Dunbar and Erikson (1986) and the expressions of G. Converse. The paper is benefitted by the thorough revision of Antonis Vafidis and an anonymous reviewer. This work was supported in part by the THALES Program of the Ministry of Education of Greece and the European Union in the framework of the project entitled "Integrated understanding of Seismicity, using innovative Methodologies of Fracture mechanics along with Earthquake and non extensive statistical physics – Application to the geodynamic system of the Hellenic Arc, SEISMO FEAR HELLARC". Geophysics Department Contibution 812.

6. References

Aki K. 1965. Maximum likelihood estimate of b in the formula log N=a−bM and its confidence limits, *Bull. Earthq. Res. Inst. Univ. Tokyo,* 43, 237–239.

Bender B. 1983. Maximum likelihood estimation of b values for magnitude grouped data, *Bull. Seismol. Soc. Am.*, 73, 831–851.

Bowman D. and King G. 2001. Accelerating seismicity and stress accumulation before large earthquakes, *Geophys. Res. Lett.,* 28, 21, 4039-4042,DOI: 10.1029/2001GL013022.

Chen X. and Shearer P. 2011. Comprehensive analysis of earthquake source spectra and swarms in the Salton Trough, California, *J. Geophys. Res.*, 116, B09309, doi:10.1029/2011JB008263.

Deng J. and Sykes L. 1997. Evolution of the stress field in southern California and triggering of moderate-size earthquakes: A 200-year perspective*, J. Geophys. Res.*, 102, B5, 9859-9886, DOI: 10.1029/96JB03897.

Erikson L. 1986. User's Manual for DIS3D: A Three-Dimensional Dislocation Program with Applications to Faulting in The Earth, *Master's Thesis*, Stanford University, Stanford, CA, 167 pp.

Farrell J., Husen S. And Smith R. 2009. Earthquake swarm and b-value characterization of the Yellowstone volcano-tectonic system, *J. Volcanol. Geotherm. Res.*, 188, 260–276.

Gutenberg B. and Richter C.F. 1944. Frequency of earthquakes in California, *Bull. Seismol. Soc. Am.* 34, 185–188.

Hanks T. C. and Kanamori H. 1979. A moment magnitude scale, *J. Geophys. Res.,* 84, 2348-2350.

Harris R. and Simpson R. 1993. In the shadow of 1857:An evaluation of the static stress changes generated by the M8 Ft. Tejon, California, earthquake, *EOS Trans. Am. Geophys. Un.,* 74, 427.

Harris R. and Simpson R. 1996. In the shadow of 1857: The effect of the great Ft. Tejon earthquake on subsequent earthquakes in southern California, *Geophys. Res. Lett.*, 23, 229–232.

Hill D. 1977. Model for earthquake swarms, *J. geophys. Res.*, 82, 1347–1352.

Holtkamp S., Pritchard M. and Lohman R. 2011. Earthquake swarms in South America, *Geophys. J. Int.*, 187, 128-146.

Jordan T. 1991. Far-field detection of slow precursors to fast seismic ruptures, *Geophys. Res. Lett.*,18, 2019-2022.
Ishimoto M. and Iida K. 1939. Observations of earthquakes registered with the microseismograph constructed recently, *Bull. Earthq. Res. Inst. Univ. Tokyo*, 17, 443–478.
Karakostas V. 2009. Seismicity patterns before strong earthquakes in Greece, *Acta Geophys.*, 57, 2, 367-386, DOI: 10.2478s11600-009-0004-y.
King G. and Bowman D. 2003. The evolution of regional seismicity between large earthquakes, *J. Geophys. Res.,* 108, B2, 2096, DOI: 10.1029/2001JB000783.
Mesimeri M. 2013. Spatio-temporal properties of earthquake swarms, *MSc thesis*, Aristotle University Thessaloniki, Thessaloniki, Greece, 84 pp (in Greek).
Mogi K. 1962. Magnitude–frequency relation for elastic shocks accompanying fractures of various materials and some related problems in earthquakes, *Bull. Earthq. Res. Inst. Univ. Tokyo,* 40, 831–853.
Mogi K. 1963. Some discussions on aftershocks, foreshocks and earthquake swarms—the fracture of a semi-infinite body caused by an inner stress origin and its relation to the earthquake phenomena, *Bull. Earthq. Res. Inst. Univ. Tokyo,* 41, 615–658.
Reasenberg P. 1985. Second-order moment of central California seismicity, 1969–1982, *J. Geophys. Res.*, 90, 5479–5495.
Roland E. and McGuire J. 2009. Earthquake swarms on transform faults, *Geophys. J. Int.*, 178, 1677–1690.
Scholz C. 1968. The frequency–magnitude relation of microfracturing in rock and its relation to earthquakes, *Bull. Seismol. Soc. Am.,* 58, 399–415.
Schorlemmer D., Weimer S. and Wyss M. 2004. Earthquake statistics at Parkfield: 1.Stationarity of b values, *J. Geophys. Res.,* 109, B12307. doi:10.1029/2004JB003234.
Schorlemmer D. and Wiemer S. 2005. Microseismicity data forecast rupture area, *Nature,* 434, 1086.
Schorlemmer D., Wiemer S. and Wyss M. 2005. Variations in earthquake-size distribution across different stress regimes, *Nature,* 437, 539–542.
Shi Y. and Bolt B. 1982. The standard error of the Magnitude-frequency b value, *Bull. Seism. Soc. Am.*, 72, 1677-1687.
Sykes L. 1970. Earthquake swarms and sea-floor spreading, *J. geophys.Res.,* 75, 6598–6611.
Utsu T. 1965. A method for determining the value of b in a formula log N=a−bM showing the magnitude frequency for earthquakes, *Geophys. Bull. Hokkaido Univ.*, 13, 99–103.
Urbancic T., Trifu C., Long J. and Toung R. 1992. Space–time correlations of b values with stress release, *Pure Appl. Geophys.,* 139, 449–462.
Vidale J. and Shearer P. 2006. A survey of 71 earthquake bursts across southern California: Exploring the role of pore fluid pressure fluctuations and aseismic slip as drivers, *J. Geophys. Res.*, 111, B05312, doi:10.1029/2005JB004034.
Warren N. and Latham G. 1970. An experimental study of thermally induced microfracturing and its relation to volcanic seismicity, *J. Geophys. Res.*, 75, 4455-4464.
Wessel P. and Smith W. 1998. New, improved version of the generic mapping tools released, *EOS Trans. AGU,* 79, 579.
Wiemer S. 2001. A software package to analyze seismicity: ZMAP, *Seism. Res. Lett.*, 72, 373-382.
Wiemer S. and Wyss M. 2000. Minimum magnitude of completeness in earthquake catalogs: examples from Alaska, the western United States, and Japan, *Bull. Seismol.Soc. Am.*, 90, 859–869.
Wyss M. 1973. Towards a physical understanding of the earthquake frequency distribution, *Geophys, J. R. Astron. Soc.*, 31, 341-359.
Zhuang J., Ogata Y. and Vere-Jones D. 2002. Stochastic Declustering of Space-Time earthquake Occurrences, *Journal of the American Statistical Association*, 97, 458, 369-380.

Δελτίο της Ελληνικής Γεωλογικής Εταιρίας, τομ. XLVII , 2013
Πρακτικά 13ου Διεθνούς Συνεδρίου, Χανιά, Σεπτ. 2013

Bulletin of the Geological Society of Greece, vol. XLVII 2013
Proceedings of the 13th International Congress, Chania, Sept. 2013

A NON-EXTENSIVE APPROACH IN INVESTIGATING GREEK SEISMICITY

Michas G.[1], PapadakisG.[1] and Vallianatos F.[1,2]

[1]*Institute for Risk and Disaster Reduction, University College London, Gower Street, London, WC1E 6BT, UK,georgios.michas.10@ucl.ac.uk*

[2] *Laboratory of Geophysics and Seismology, Technological Educational Institute of Crete, Chania, GR 73133, Crete, Greece*

Abstract

In this work the Greek seismicity is being investigated by means of Non-Extensive Statistical Physics [NESP]. NESP is a generalization of Boltzmann-Gibbs statistical physics and has been successfully used for the analysis of a variety of complex dynamic systems, where fractality and long- range interactions are important. We use a non-extensive model that is derived from the first principles to describe the frequency-magnitude distribution of the Greek seismicity for the period 1976-2009 by using a recent earthquake catalogue for the Hellenic region compiled by Makropoulos et al. (2012). The results indicate that the non-extensive model can describe quite well the observed magnitude distribution for the entire magnitude range. Furthermore, the q parameter of the non-extensive model, along with the b-value of the Gutenberg-Richter relation, are being estimated for different time windows along the time expansion of the catalogue and the variations of these values are being discussed.
Key words:*Frequency – magnitude distribution, non-extensive statistical physics, Gutenberg-Richter relation.*

Περίληψη

Στην παρούσα εργασία εξετάζεται η σεισμικότητα του ελληνικού χώρου χρησιμοποιώντας τη γενικευμένη θεωρία της μη-εκτατικής στατιστικής φυσικής. Η θεωρία αυτή αποτελεί γενίκευση της στατιστικής φυσικής των Boltzmann-Gibbs και έχει επιτυχώς χρησιμοποιηθεί στην ανάλυση πολύπλοκων συστημάτων που παρουσιάζουν κατανομές fractal και συσχέτιση μεταξύ των δεδομένων τους. Χρησιμοποιώντας ένα μοντέλο το οποίο προκύπτει από τις αρχές της θεωρίας αυτής, εξετάζουμε την κατανομή συχνότητας - μεγέθους της ελληνικής σεισμικότητας κατά την περίοδο 1976-2009, όπως αναφέρεται στον πρόσφατο κατάλογο των Makropoulosetal. (2012). Τα αποτελέσματα υποδεικνύουν ότι το μοντέλο αυτό περιγράφει πολύ καλά την κατανομή συχνότητας – μεγέθους για όλο το εύρος τιμών. Επιπλέον, η παράμετρος q του μοντέλου αυτού, καθώς και η παράμετρος b της σχέσης των Gutenberg-Richter, υπολογίζονται σε διαφορετικά χρονικά διαστήματα στη χρονική διάρκεια του καταλόγου και σχολιάζονται οι μεταβολές που εμφανίζουν στο χρόνο.
Λέξεις κλειδιά: *Κατανομή συχνότητας – μεγέθους, μη-εκτατική στατιστική φυσική, σχέση των Gutenberg-Richter.*

1. Introduction

Earthquakesaregenerallyoccurringduetothedeformationandsuddenruptureofpartsoftheearth'sbrittlec rust due to the relative motion of the tectonic plates releasing energy. The energy distribution of earthquakes has a fractal power-law distribution (Turcotte, 1997; Rundle et al., 2003) that in terms of the cumulative magnitude distribution can be expressed through the Gutenberg – Richter (G-R) relation (Gutenberg and Richter, 1944) as:

Equation 1 – Power-law form of the Gutenberg-Richter relation

$$N(>M) \propto 10^{-bM},$$

where $N(>M)$ is the number of earthquakes greater than a threshold magnitude M and b is the slope that describes the size distribution of the earthquake events. This relation is empirical and has not been associated with general physical principles, except a recent attempt (Varotsos et al., 2004), where the G-R relation and the stability of the b-value in the range $0.8 \leq b \leq 1.2$ (Rundle et al., 2003) is simply explained by the maximum entropy principle, if the analysis is performed in the natural time domain (Varotsos et al., 2001).

In 2004, Sotolongo-Costa and Posadas starting from first principles developed a general physical model for the earthquake generation mechanism that contains the G-R relation as a particular case. In this model, the local breakage and the displacement of the asperities and the fragments between the fault planes are the cause of the earthquake energy release. Then, the released energy can be considered proportional to the volume of the fragments and the energy distribution function can be obtained in terms of the fragment size distribution (Sotolongo-Costa and Posadas, 2004).Sotolongo-Costa and Posadas have considered that interactions between the fragments exist and derived the model in the frame of non-extensive statistical physics (NESP). NESP has been proposed by Tsallis (1988) as a possible generalization of Boltzmann-Gibbs (BG) statistical physics and provides a consistent theoretical framework for the analysis of complex dynamical systems that exhibit fractal structures and long-range correlations (Tsallis, 2009). The NESP concept has been successfully applied to various fields of geophysics (see Vallianatos and Telesca, 2012 and references therein) including earthquakes (e.g. Vallianatos et al., 2012; 2013; Vallianatos and Sammonds, 2013).

The non-extensive model for the earthquake energy distribution, as was later revised by Silva et al. (2006), has been successfully applied to regional seismicity (Silva et al., 2006; Telesca, 2010a; 2010b) covering diverse tectonic regions and volcano related seismicity (Vallianatos et al., 2013). The question of whether this model can also describe the earthquake activity at the Hellenic region is addressed in this work. We use this model, along with the G-R relation, to study the earthquake activity during the period of 1976-2009, as it is referred in the recent earthquake catalogue for the area of Greece by Makropoulos et al. (2012). We perform the analysis for the entire time period as well as in different time intervals, in order to recognize patterns that are related to the evolution of the earthquake activity and the results are being discussed.

2. Dataset

In this work we use a recent catalogue for the area of Greece, compiled by Makropoulos et al. (2012) that expands from 1901 to 2009. In our analysis we consider the moment magnitudes (M_w) of the shallow seismicity (depth $\leq$ 40 km) that occurred in the period 1976 – 2009, as for this period the catalogue can be considered complete for magnitudes (M_w) greater than 4.1 (Makropoulos et al., 2012). We decluster the catalogue in order to remove the aftershocks from the dataset and to perform the analysis directly to the main earthquake events. For this purpose, we use the window method by Gardner and Knopoff (1974), as it was later on modified by Uhrhammer (1986). After the declustering procedure, a dataset of 2153 earthquakes emerges that is used further on in the analysis.

3. Non-extensive Model for Earthquake Energies

The non-extensive model for the earthquake energies distribution is derived in the frame of NESP. This concept refers to the non-additive Tsallis entropy S_q(Tsallis, 1988) that incorporates the parameter q, which is a measure of the non-extensivity of the system. In the limit of $q \to 1$, S_q reduces to the ordinary BG entropy S_{BG}. The main difference among them is that S_{BG} is additive while S_q is non-additive. According to this property S_{BG} includes only short-range correlations, while S_q allows all length-scale correlations between the elements of the system (Tsallis, 2009). In terms of the probability $p(\sigma)$ of finding a fragment of surface σ, S_q is expressed as:

Equation 2 – Integral formulation of Tsallis entropy

$$S_q = k_B \frac{1 - \int p^q(\sigma) d\sigma}{q - 1},$$

where k_B is Boltzmann's constant and q is the non-extensive index. For the sake of simplicity we set k_B=1. To find the probability $p(\sigma)$ the maximum entropy principle is applied, under the constraint of the normalization of $p(\sigma)$:

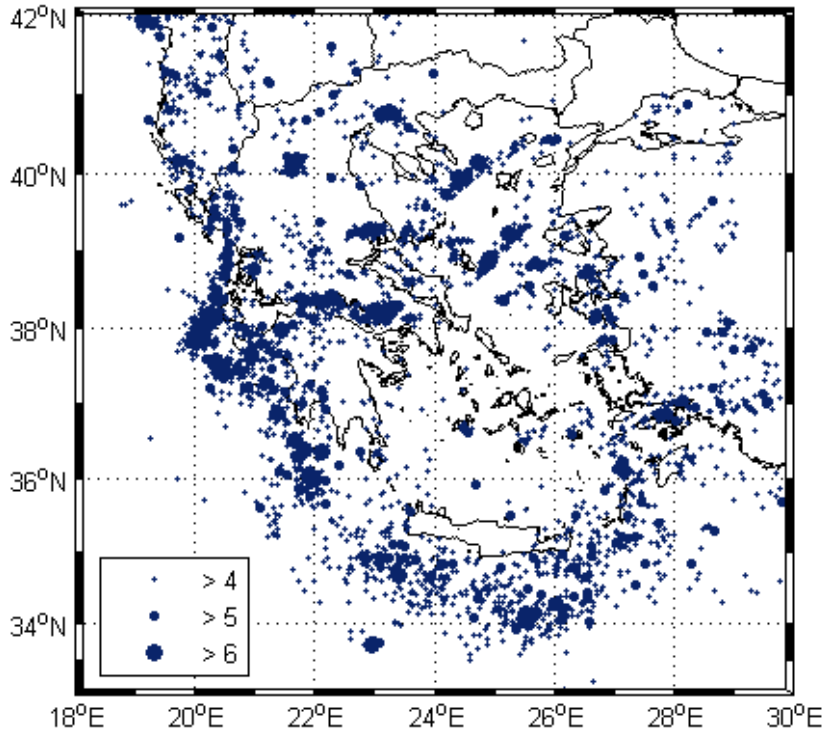

Figure 1 – Spatial distribution of the shallow earthquake activity (depth ≤ 40 km) in the area of Greece and the adjacent areas during 1976 – 2009.

Equation 3 – Normalization condition

$$\int_0^\infty p(\sigma) d\sigma = 1$$

and the condition about the q-expectation value (Tsallis, 2009):

Equation 4 – Definition of *q*-expectation value

$$\sigma_q = \langle \sigma \rangle_q = \frac{\int_0^\infty \sigma p^q(\sigma) d\sigma}{\int_0^\infty p^q(\sigma) d\sigma}.$$

After the maximization procedure, the following expression for the fragment size distribution function is derived (Silva et al., 2006):

Equation 5 – Probability distribution function for the size of the fragments

$$p(\sigma) = \left[1 - \frac{(1-q)}{(2-q)} (\sigma - \sigma_q) \right]^{1/(1-q)}.$$

Assuming that the energy release E is proportional to the volume of the fragments $E \sim r^3$ (Silva et al., 2006), in accordance to the standard definition of seismic moment scaling with rupture length (Lay and Wallace, 1995), this proportionality becomes:

Equation 6 – Relation between the size of the fragments and the earthquake energy

$$\sigma - \sigma_q = \left(\frac{E}{\alpha} \right)^{2/3}.$$

In the last equation, σ scales with r^2 and α is the proportionality constant between E and r^3. By using the latter deformation, the energy distribution function becomes:

Equation 7 – Probability distribution function for earthquake energies

$$p(E) = \frac{C_1 E^{-\frac{1}{3}}}{\left[1 + C_2 E^{\frac{2}{3}} \right]^{1/(q-1)}},$$

with $C_1 = \frac{2}{3\alpha^{\frac{2}{3}}}$ and $C_2 = -\frac{(1-q)}{(2-q)a^{\frac{2}{3}}}$.

In the last equation, the probability of the energy is $p(E)=n(E)/N$, where $n(E)$ is the number of earthquakes with energy E and N is the total number of earthquakes. The cumulative number of earthquakes with energy E can be now estimated by integrating Eq. (7):

Equation 8 –Integration of the probability density function

$$\frac{N(E > E_{th})}{N} = \int_{E_{th}}^\infty p(E) dE,$$

where $N(E>E_{th})$ is the number of earthquakes with energy E greater than the threshold energy E_{th} and N the total number of earthquakes. The cumulative distribution in terms of the earthquake

magnitude M can now be obtained, if we consider that the magnitude M is related to the energy E as $M = \frac{2}{3}\log(E)$ (Kanamori, 1978). Thus:

Equation 9 – Normalized cumulative distribution of earthquake magnitudes

$$\frac{N(>M)}{N} = \left[1 - \left(\frac{1-q}{2-q}\right)\left(\frac{10^{M}}{\alpha^{2/3}}\right)\right]^{\frac{2-q}{1-q}}.$$

The last expression describes from the first principles and in NESP formalism, the cumulative distribution of the number of earthquakes N greater than the threshold magnitude M in a seismic region, normalized by the total number of earthquakes. Above a certain threshold, the G-R relation can be deduced as a particular case with $b = (2-q)/(q-1)$ (Telesca, 2012). Taking in account the minimum magnitude M_0 of an earthquake catalogue, Eq. (9) should be slightly changed to (Telesca, 2012):

Equation 10 – Normalized cumulative distribution of earthquake magnitudes taking in account the minimum magnitude M_0

$$\frac{N(>M)}{N} = \left[\frac{1 - \left(\frac{1-q}{2-q}\right)\left(\frac{10^{M}}{\alpha^{2/3}}\right)}{1 - \left(\frac{1-q}{2-q}\right)\left(\frac{10^{M_0}}{\alpha^{2/3}}\right)}\right]^{\frac{2-q}{1-q}}.$$

4. Data analysis

The non-extensive model that has been described in the previous section is now applied to the normalized cumulative magnitude distribution for our dataset. We estimate the values of q and α by fitting the observed distribution to the non-extensive model of Eq.(10) by applying a non-linear least squares algorithm. The results of this analysis are presented in Figure 2. The non-extensive model describes quite well the data for the values of q=1.46 ±0.018 and α=3.25·10^5±1.7·10^5. For comparison, a power-law fit that corresponds to the G-R relation (Eq. (1)) is also plotted in Figure 2 for the value of b=1.076 ±0.027. The b-value is estimated according to the maximum likelihood technique (Aki, 1965), as was later revised by Utsu (1978).The mean square error estimation for the non-extensive model and the power-law fit indicates that the former describes better the observed magnitude distribution, as it has been also observed in previous studies (e.g. Vallianatos et al., 2013).

An interesting feature is whether the q and b parameters vary with time and how these variations are related to the evolution of the earthquake activity. This kind of analysis can provide useful insights into the physical mechanism of seismogenesis. We perform such an analysis by estimating q and b in different time intervals along the time spanning of the earthquake catalogue. We define these intervals by a sliding window, which is characterized by the length l and the sliding factor w. These factors should be defined in a way that optimal estimations, concerning the statistical significance of the results and the resolution, can be obtained. In our case we set l=200 and w=20, illustrating that the estimation of q and b is performed for time intervals that contain 200 events and slide every 20 events, resulting on 90% overlapping between the successive windows. Though the selection we made may produce large deviations, it is preferred here in order to gain better

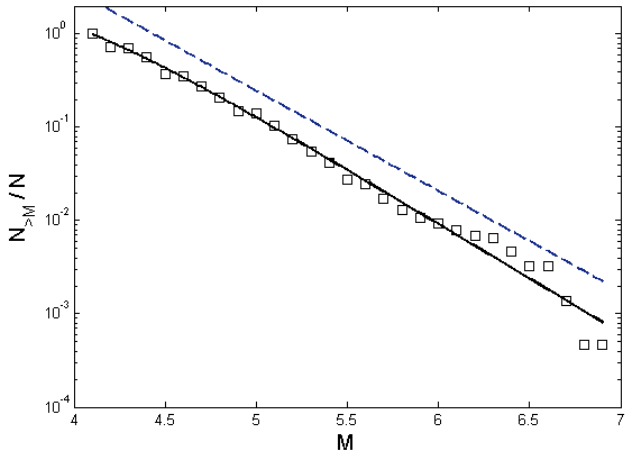

Figure 2 – Normalized cumulative magnitude distribution (squares) and the model of Eq. (10) (solid line) for the values of q=1.46 ±0.018 and α=3.25·10^5±1.7·10^5. The dashed line represents the G-R relation for b=1.076 ±0.027 (transposed vertically).

resolution in the variations with time. The estimated values are then associated to the time of the last event in each window.

The results of this analysis are presented in Figure 3a and Figure 3b for b and q respectively, along with their standard deviations. Both parameters exhibit variations during the different time periods. The b-value varies between 0.9 and 1.37, while q between 1.26 and 1.54. In Figure 3c the cumulative earthquake energy in each time interval, according to $E \sim 10^{1.5M}$ (Kanamori, 1978), is also presented. The time and the magnitude of the earthquakes with $M_w \geq 6$ are also presented in Figure 3c.The b-value seems to increase during more quiescent periods and reduce to a value close to 1 during periods where higher magnitude earthquakes occur, though this is not evident for the period 1982-1984 where b suddenly increases and the released earthquake energy obtains higher values as well. In the other hand, there is a clear correlation between the q-value variations and the cumulative energy in each time interval. Such a result can be interpreted in terms of the physical meaning of q that measures the degree of non-extensivity. For q approaching 1, equilibrium and the transition to Boltzmann-Gibbs statistical physics is obtained. In the other hand, as q increases, the system is getting away from equilibrium and larger earthquakes occur. Thus, q may be considered as a characteristic parameter for the seismic history of a particular area. A closer inspection of Figure 3b and Figure 3c also implies a periodicity in the q-values and the released earthquake energy during 1980 – 2009, where 5 – 7 years periods of increased activity and higher q s are followed by more quiescent periods that last 7 – 10 years.

5. Conclusions

In the present work, the earthquake activity at the Hellenic region during 1976 – 2009 is studied by means of non-extensive statistical physics. We use a physical model, derived in a NESP formalism, to investigate the frequency - magnitude distribution of the shallow earthquake activity that occurred during 1976 – 2009. In terms of this model, the cumulative magnitude distribution can be well reproduced for the values of q=1.46 ±0.018 and α=3.25·10^5±1.7·10^5. For the sameperiod, the b-value of the G-R relation is b=1.076 ±0.027. By performing the analysis in different time intervals along the evolution of the earthquake activity, variations in the values of b and q emerge that for the latter correlate well with the relative cumulative earthquake energy in each time interval. Thus, the non-extensive analysis and particularly the q-value can provide valuableinformation on the state of the seismogenic process in a particular area and should be considered in future seismological studies.

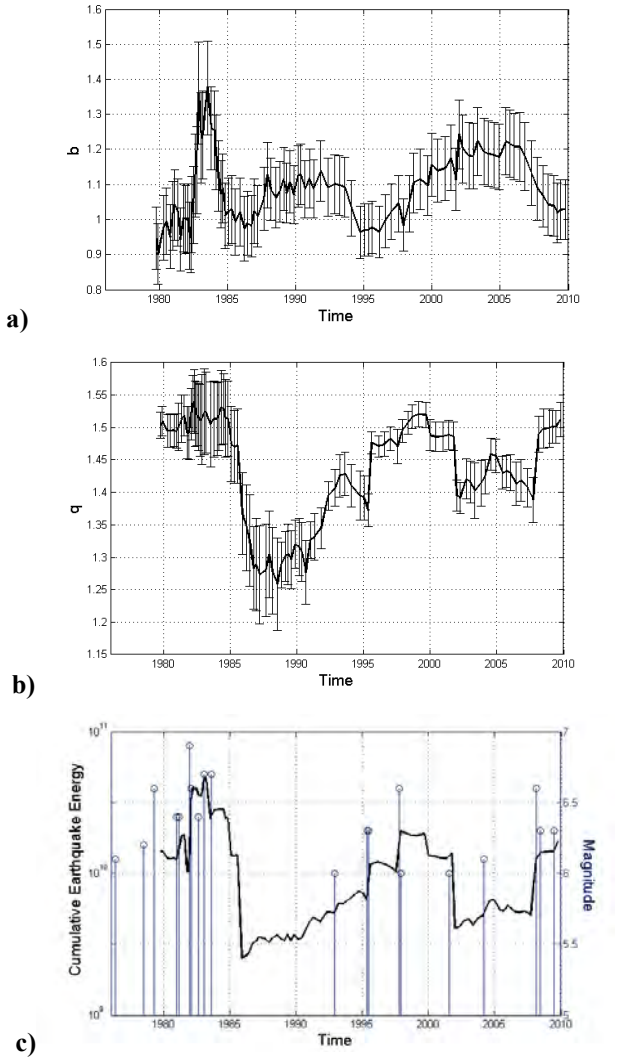

Figure 3 – a) Variations of the *b*-value with time, estimated in successive time intervals with 90% overlapping and the associated standard deviations, plotted as error bars, b)*q*-value variations with time, estimated as previously and theassociated standard deviations, plotted as error bars, c) cumulative earthquake energy in each time interval (solid line) and the magnitude of earthquakes with $M \geq 6$ with time.

6. Acknowledgements

G. Michasand G. Papadakis wish to acknowledge the financial support of the Greek State Scholarships Foundation (IKY). The completion of this work has been accomplished in the framework of the postgraduate program and co-funded through the action "Program for scholarships provision I.K.Y. through the procedure of personal evaluation for the 2011-2012 academic year" from resources of the educational program "Education and Life Learning" of the European Social Register and NSRF 2007-2013.

7. References

Aki K. 1965. Maximum likelihood estimate of b in the formula log N = a – bM and its confidence limits, *Bull. Earthq. Res. Inst. Tokyo Univ*., 43(2), 237-239.

Gardner J. K. and Knopoff L. 1974. Is the sequence of earthquakes in Southern California, with aftershocks removed, Poissonian?, *Bull. Seism. Soc. Am*., 64(5), 1363-1367.

Gutenberg B. and Richter C.F. 1944. Frequency of earthquakes in California, *Bull. Seism. Soc. Am*., 34(4), 185-188.

Kanamori H. 1978. Quantification of earthquakes,Nature, 271, 411-414, doi:10.1038/271411a0.

Lay T. and Wallace T.C. 1995.*Modern Global Seismology*, Academic Press, New York.

Makropoulos K., Kaviris G. and Kouskouna V. 2012. An updated and extended earthquake catalogue for Greece and adjacent areas since 1900, *Nat. Hazards Earth Syst. Sci*., 12, 1425-1430, doi:10.5194/nhess-12-1425-2012.

Silva R., Franca G.S., Vilar C.S. and Alcaniz J.S. 2006. Nonextensive models for earthquakes, *Phys. Rev. E*, 73, 026102, doi:10.1103/PhysRevE.73.026102.

Sotolongo-Costa O. and Posadas A. 2004. Fragment-asperity interaction model for earthquakes, *Phys. Rev. Letter*, 92, 048501, doi:10.1103/PhysRevLett.92.048501.

Telesca L. 2010a. Nonextensive analysis of seismic sequences, *Phys. A*, b389, 1911–1914.

Telesca L. 2010b. Analysis of Italian seismicity by using a nonextensive approach, *Tectonophysics*, 494, 155–162, doi:10.1016/j.tecto.2010.09.012.

Telesca L. 2012. Maximum likelihood estimation of the nonextensive parameters of the earthquake cumulative magnitude distribution, *Bull. Seismol. Soc. Am*., 102, 886-891, doi: 10.1785/0120110093.

Tsallis C. 1988. Possible generalization of Boltzmann–Gibbs statistics, *J. Stat. Phys*., 52, 479-487, doi:10.1007/BF01016429.

Tsallis C. 2009. Introduction to nonextensive statistical mechanics: *Approaching a complex world*, Springer, Berlin, 378 pp.

Turcotte D.L. 1997. *Fractals and Chaos in Geology and Geophysics*, Cambridge University Press, Cambridge, UK, 2nd ed., 398 pp.

Rundle J.B., Turcotte D.L., Shcherbakov R., Klein W. and Sammis C. 2003. Statistical physics approach to understanding the multiscale dynamics of earthquake fault systems, *Rev. Geophys*., 41, 4.

Uhrhammer R. 1986. Characteristics of Northern and Central California Seismicity, *Earthquake Notes*, 57(1), 21.

Utsu T. 1978. Estimation of parameter values in the formula for the magnitude-frequency relation of earthquake occurrence, *Zisin*, 31, 367–382.

Vallianatos F. and Sammonds P. 2013. Evidence of non-extensive statistical physics of the lithospheric instability approaching the 2004 Sumatran–Andaman and 2011 Honshu mega-earthquakes, *Tectonophysics*, 590, 52-58, doi: 10.1016/j.tecto.2013.01.009.

Vallianatos F. and Telesca L. 2012. Statistical mechanics in earth physics and natural hazards, *Acta Geophys.*, 60, 499-501.

Vallianatos F., Michas G., Papadakis G. and Sammonds P. 2012. A non-extensive statistical physics view to the spatiotemporal properties of the June 1995, Aigion earthquake (M6.2) aftershock sequence (West Corinth rift, Greece), *Acta Geophys*., 60(3), 758-768, doi:10.2478/s11600-012-0011-2.

Vallianatos F., Michas G., Papadakis G. and Tzanis A. 2013. Evidence of non-extensivity in the seismicity observed during the 2011-2012 unrest at the Santorini volcanic complex, Greece, *Nat. Hazards Earth Syst. Sci*., 13, 177–185, doi:10.5194/nhess-13-177-2013.

Varotsos P.A., Sarlis N.V. and Skordas E.S. 2001.Spatio-temporal complexity aspects on the interrelation between seismic electric signals and seismicity,*Practica Athens Acad*., 76, 294-321.

Varotsos P.A., Sarlis N. V., Skordas E.S. and Tanaka H. K., 2004.A plausible explanation of the b-value in the Gutenberg-Richter law from first principles, *Proc. Japan Acad*., 80, 429-434.

Δελτίο της Ελληνικής Γεωλογικής Εταιρίας, τομ. XLVII , 2013
Πρακτικά 13ου Διεθνούς Συνεδρίου, Χανιά, Σεπτ. 2013

Bulletin of the Geological Society of Greece, vol. XLVII 2013
Proceedings of the 13th International Congress, Chania, Sept. 2013

IMPROVED EARTHQUAKE LOCATION IN THE AREA OF NORTH EUBOEAN GULF AFTER THE IMPLEMENTATION OF A 3D NON-LINEAR LOCATION METHOD IN COMBINATION WITH A 3D VELOCITY MODEL

Mouzakiotis E.[1] and Karastathis V. K.[1]

[1] National Observatory of Athens, Institute of Geodynamics, aggelmo@geol.uoa.gr, Karastathis@noa.gr

Abstract

Considerably improved hypocentral locations of the 274 earthquakes, with magnitudes between 1.5 to 4.1 Ml recorded during the period from 2009 to 2010 by the Hellenic Unified Seismographic Network (HUSN), have been obtained for the area of North Euboean Gulf after the implementation of a 3D non-linear location algorithm and a previously calculated local 3D velocity model for both P and S wave phases. To assess the effectiveness of the 3D locations we compared the results with the solutions obtained with alternative 1D velocity models such as the minimum 1D model calculated with the VELEST algorithm and the 1D model used by the National Observatory of Athens (NOA) for daily earthquake analysis. We were further able to assess the location accuracy of each model by comparing the location results for a number of quarry blasts that occurred in the area in that period. The use of the local 3D velocity model provides considerably more accurate than the minimum 1D model which in turn provides more constrained locations from the 1D model of NOA. The epicentral locations calculated by each model are almost similar; however the depth distribution of the events varies, with depth differences of up to 12 km for some earthquakes. The results prove that accurate, local models are necessary in order to achieve more accurate locations for the events in a local area.
Key words: Re*location; Euboean Gulf Seismicity; Central Greece.*

Περίληψη

Σημαντικά βελτιωμένη ακρίβεια στον προσδιορισμό των εστιών των σεισμών που έγιναν στην περιοχή του Βόρειου Ευβοϊκού κόλπου και καταγράφηκαν από το σεισμολογικό δίκτυο του Εθνικόύ Αστεροσκοπείου Αθηνών, κατά την περίοδο 2009 με 2010 επιτεύχθη με τη χρήση τρισδιάστατου μη γραμμικού αλγόριθμου καθορισμού των εστιακών συντεταγμένων σε συνδυασμό με τοπικό τρισδιάστατο μοντέλο ταχυτήτων για τα P και για τα S κύματα. Για να εκτιμηθεί η ακρίβεια του μοντέλου έγινε σύγκριση των εστιακών συντεταγμένων που υπολογίστηκαν από αυτό, με αυτά που υπολογίστηκαν από το βέλτιστο μονοδιάστατο μοντέλο της περιοχής και από το μονοδιάστατο μοντέλο που χρησιμοποιείται από το Εθνικό Αστεροσκοπείο Αθηνών για την ανάλυση της σεισμικότητας. Επί πλέον εκτίμηση της ακρίβειας των μοντέλων έγινε συγκρίνοντας τα αποτελέσματα καθορισμού εστιακών συντεταγμένων ενός

αριθμού λατομικών εκρήξεων. Το τριδιάστατο μοντέλο παρουσίασε τα μικρότερα σφάλματα. Το βέλτιστο μονοδιάστατο μοντέλο (minimum 1D) παρουσίασε με τη σειρά του μικρότερα σφάλματα από το μοντέλο του Εθνικού Αστεροσκοπείου Αθηνών. Οι επικεντρικές συντεταγμένες είναι παρόμοιες για τα 3 μοντέλα, υπάρχει όμως διαφοροποίηση στην κατανομή των βαθών. Από τα αποτελέσματα αποδεικνύεται ότι ένα αξιόπιστο τοπικό μοντέλο ταχυτήτων είναι σημαντικό για τον ακριβή προσδιορισμό των εστιακών συντεταγμένων της σεισμικότητας μιας τοπικής περιοχής.
Λέξεις κλειδιά: *Επανακαθορισμός εστιακών συντεταγμένων; Σεισμικότητα Ευβοϊκού κόλπου; Κεντρική Ελλάδα.*

1. Introduction

Inadequate knowledge of the earth's velocity structure can lead to systematic errors in hypocentral location of the earthquakes (Douglas, 1967; Dewey, 1971, 1972; Engdahl and Lee, 1976; Jordan and Sverdrup, 1981; Pavlis and Hokanson, 1985; Pavlis, 1992) and it can subsequently lead to incorrect evaluation of earthquake spatial patterns. This problem is more severe in cases of small local earthquakes, since they are usually recorded only locally, where the velocity structure can be much different than the average velocity structure of the region covered by the seismographic network. The construction of three–dimensional models is required to correctly calculate the ray paths, however, is not always feasible, since their calculation requires dense and well distributed seismicity. Therefore in most cases for the regional seismicity monitoring the data are analyzed with the use of 1D velocity models, representing the average velocity structure of the earth's crust in a regional scale.

In this study we assess the performance of the 3D velocity model for the area of North Euboean Gulf, previously calculated by Karastathis *et al*. (2011), in locating earthquakes. This is accomplished by relocating the seismicity data of the Hellenic Unified Seismographic Network (HUSN) for this particular area and for a two years period between 2009 and 2010. The results were assessed by comparing the location results of quarry blasts and by examining the error ellipsoids and the event spatial distribution. It is important to note that the seismicity data used for the evaluation of the model are totally independent to the ones used for the calculation of the 3D model.

2. Tectonics

The area of the North Euboean Gulf (Figure 1) is located in central Greece, between two major structures: the North Aegean Trough and the Gulf of Corinth. The area itself contains a number of notable fault zones. The most important and well documented fault structure is the Atalanti fault zone (Poulimenos and Doutsos, 1996; Ganas 1998; Pantosti et al., 2001; Karastathis et al., 2007; Pavlidis et al., 2004) with a NW–SE strike. Two other notable fault zones are the Kamena Vourla fault zone and the Kallidromo fault zone, north of the Atalanti fault zone. Additionally, the Knimis fault zone (Jackson et al. 1982) and some additional smaller fault zones in Malesina peninsula with NE-SW direction (Palyvos, 2001) appear in the area.

3. Methodology and Data

Data from seven local stations belonging to the HUSN network, plus the additional station of CHLKS, installed for the seismic monitoring of Athens, were utilized in this study (Figure 1). These stations were the ones within the 3D velocity model area. Although we could not use the outer stations, the information loss was not significant since the most of the events were of low magnitude (< 3 Ml) and recorded only locally.

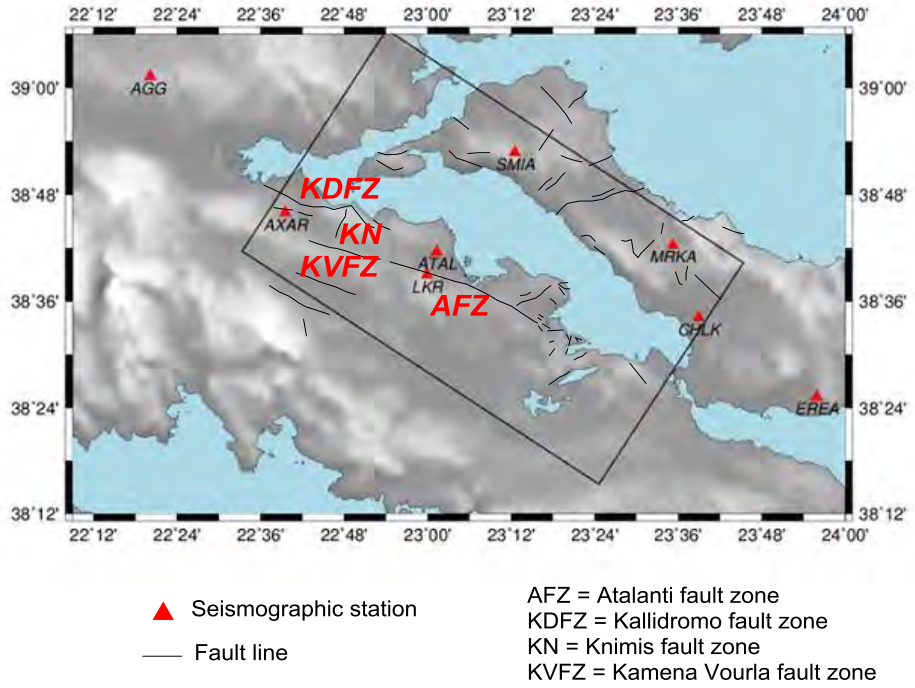

Figure 1 – The study area, the stations that were incorporated and the major fault zones (Institute of Geology and Mineral Exploration — IGME, 1993; Jackson et al., 1982; Palyvos, 2001; Tzanis et al., 2009).

In total 274 events were recorded with magnitudes larger than 1.5 Ml. The events recorded by five local stations at minimum. We selected the 217 most reliably located events, with azimuthal gap lower than 180^{o} and with at least 5 P and 3 S wave phases. Many of the phases used have been obtained by NOA's bulletins and then revised when necessary. The dataset was completed with other local phases not previously considered by NOA after manual picking.

The 1D velocity models utilized are: a) the 1D velocity model used for daily earthquake analysis by NOA, b) the minimum 1D velocity model calculated by VELEST algorithm (Kissling, 1995) by Karastathis *et al*. (2011) (Figure 2). The 3D velocity model (Figure 3) was suggested by Karastathis *et al.* (2011) using a dataset acquired by a local seismographic network including 24 land and 6 OBS stations. The creation of the model was based on a successive application of the 1D minimum velocity model algorithm (Kissling et al., 1994) and linearized 3D inversion (Thurber, 1989; Emberhard-Philips, 1990).

To accurately locate the earthquakes, the probabilistic non-linear location method provided by the NonLinLoc software package was implemented. The velocity model is imported as a cubic grid with a velocity value in each node. Travel-times between each node and each station are calculated using a 3D version (Le Maur, 1994; Le Maur et al., 1997) of the Eikonal finite difference scheme (Podvin and Lecomte, 1991).

The complete location probability density function (PDF) is accurately obtained by the Oct-Tree importance sampling algorithm, which is based on recursive subdivision and sampling of cells in 3D space. Location PDF is calculated using the Equal Differential Time function (Lomax, 2005), which is robust in the presence of outlier data:

$$pdf(x) \propto k\left[\sum_{obs_a obs_b} \frac{1}{\sqrt{\sigma_a^2 + \sigma_b^2}} \exp\left(-\frac{\{[Tobs_a(x) - Tobs_b(x)] - [TTcalc_a(x) - TTcalc_b(x)]\}^2}{\sigma_a^2 + \sigma_b^2}\right)\right]^N$$

This method is not depended on the origin time, thus reducing the initial 4D problem to a 3D search over latitude, longitude and depth.

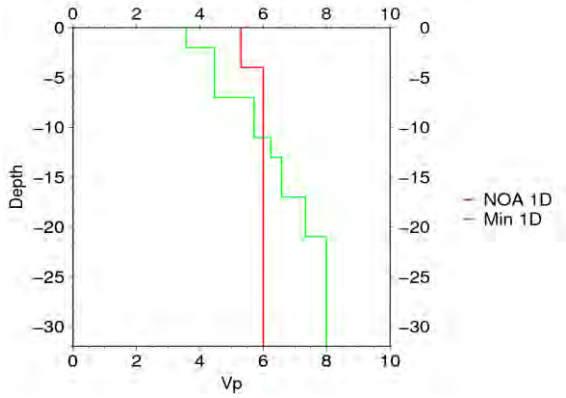

Figure 2 – NOA 1D (red line) and the minimum 1D (green line) models used in the study.

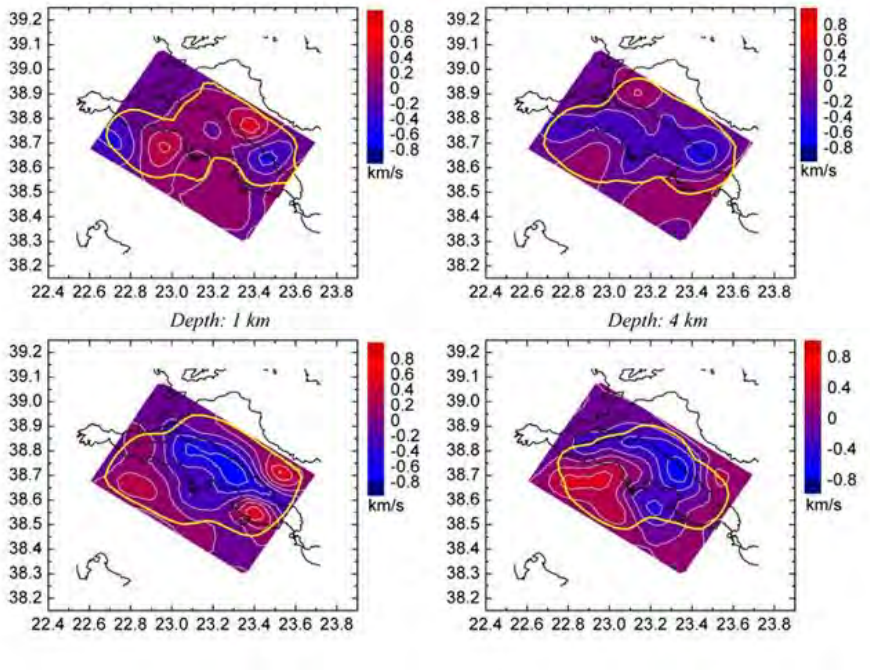

Figure 3 – Local normalized 3D velocity model (Karastathis et al., 2011).

4. Results

Each model's validity was initially assessed by locating three quarry blasts, shot in the Tragana area and recorded by the HUSN network. The locations of the blasts given in the NOA's catalog as it can be seen in Figure 4 are obviously far from the actual site of the quarry.

The 1D minimum model concentrated the blasts at the same position but epicenters are systematically mislocated to the south by approximately 7Km. This was expected due to the lack of seismographic stations south of the quarry. In spite of this limitation, however, the three blasts were accurately located within the quarry, when using the local 3D model. These results prove the validity of the model in a local scale.

The next step was to evaluate the model by a direct comparison of the location results of the seismicity with those obtained by the 1D models. The results proved that the 3D model achieved significantly better constrained event locations, compared to the other two models. In turn the minimum 1D model provided more constrained locations compared to the NOA 1D model. The average confidence ellipsoid volume was 55.4 Km^3 for the 3D model, 78.9 Km^3 for the minimum 1D model and 106 Km^3 for the NOA 1D model. The average major semi-axis lengths were 4.8 Km, 5.3 Km and 6.8 Km, respectively, for the 3 models (Figure 5).

It is worth to note that despite the small number of seismographic stations, we obtained highly constrained event locations for a large number of events, mainly in the central area, where the azimuthal coverage was optimal. Thus, the unrealistic results given by the usual RMS error minimizing procedure were considerably eliminated.

The results did not show any significant shift in the epicentral distribution for most of the events, between the 3 models (Figures 6, 7). The picture however is quite different for the distribution of

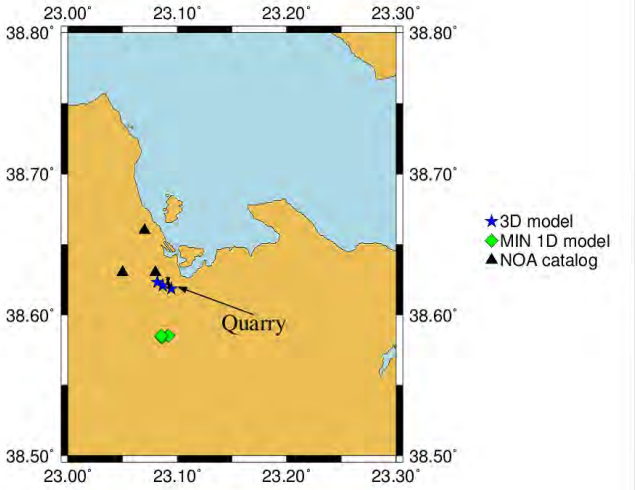

Figure 4 – Map showing the location of the quarry blasts as obtained by the NOA's catalogue (black), the minimum 1D model (green) and the 3D model (blue).

the hypocentral depths between the 3 models, as seen in Figure 8. For the NOA 1D model this distribution is quite unrealistic with a large number of events being located above the depth of 2 Km. The minimum 1D model showed an almost symmetrical distribution centered around the depths of 10-12 Km with the majority of the events being located between 6 to 14 km. For the local 3D model most events are located within 6 to 12 km. The number of events increases almost linearly from 2 to 12 km and then drops rapidly, which indicates that the brittle-ductile transition zone is at this depth. We can see from the results that the majority of the seismicity is located on the western coast of the island of Euboea (Figure 9). The rest of the events are concentrated at known fault areas. The two clusters in the NW part of the area are probably related to the Knimis and Kalidromo fault zones. An exception is the cluster located offshore, east of Malesina peninsula since the seismicity cannot be safely related to the Atalanti fault. The possibility that this cluster is

related to an active zone at the opposite coast cannot be dismissed. Finally no significant seismicity appears to be attributed to the major fault zone of Atalanti.

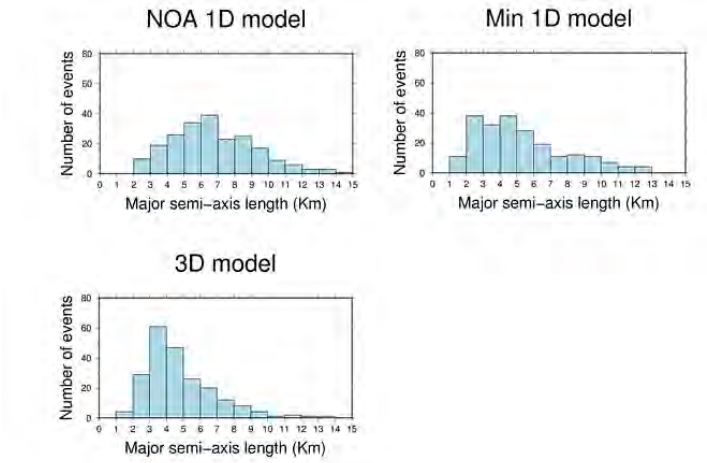

Figure 5 – Distribution of the major ellipsoid semi-axes for the NOA 1D model (top left), the minimum 1D model (top right) and the 3D model (bottom left).

The results proved clearly that the local 3D velocity model is valid for the area and could assist towards more accurate hypocentral locations. As it has already been mentioned, the velocity model has been calculated on the basis of a totally different dataset, with different stations, event locations and ray coverage. The successful location of the earthquakes is an indicator of the independency of the model from the initial dataset used for its calculation. However we are skeptical about the value of constructing such models for use in daily earthquake analysis. Indeed locating events with this method requires a dense and evenly distributed seismographic network within the area of the model, something not feasible due to the geomorphology limitations of Greece.

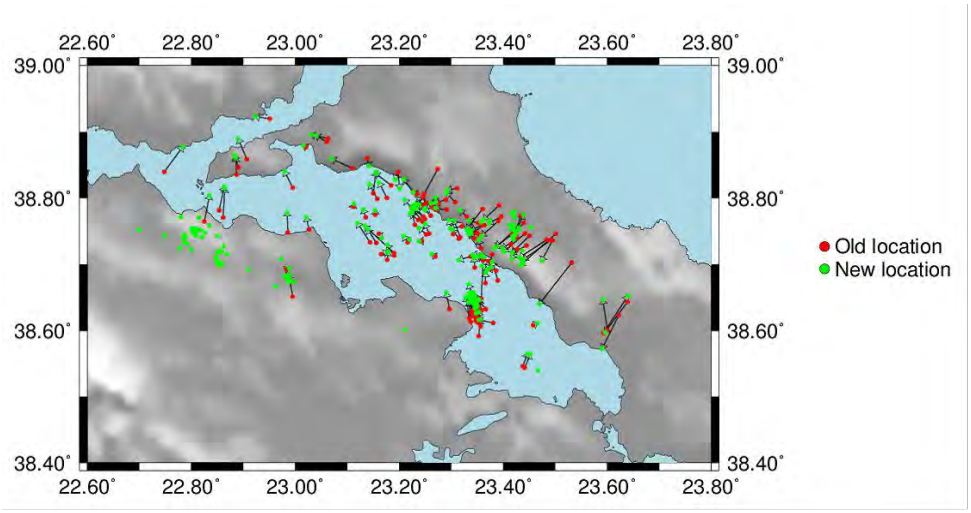

Figure 6 – Locations obtained by the NOA 1D model (red) and the 3D model (green). Only the events located with azimuthal gap lower than 180° are shown.

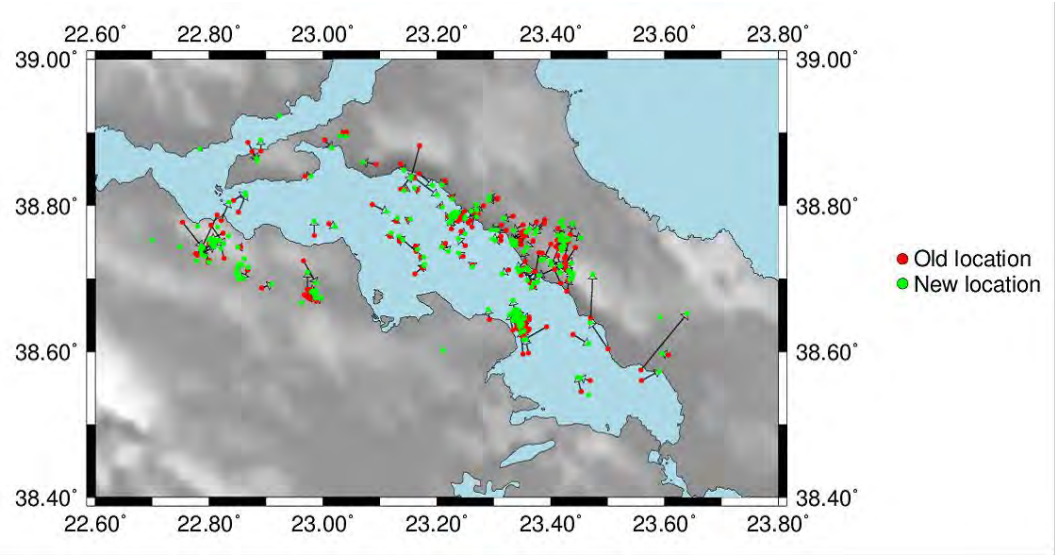

Figure 7 – Locations obtained by the minimum 1D model (red) and the 3D model (green). Only the events located with azimuthal gap lower than 180° are shown.

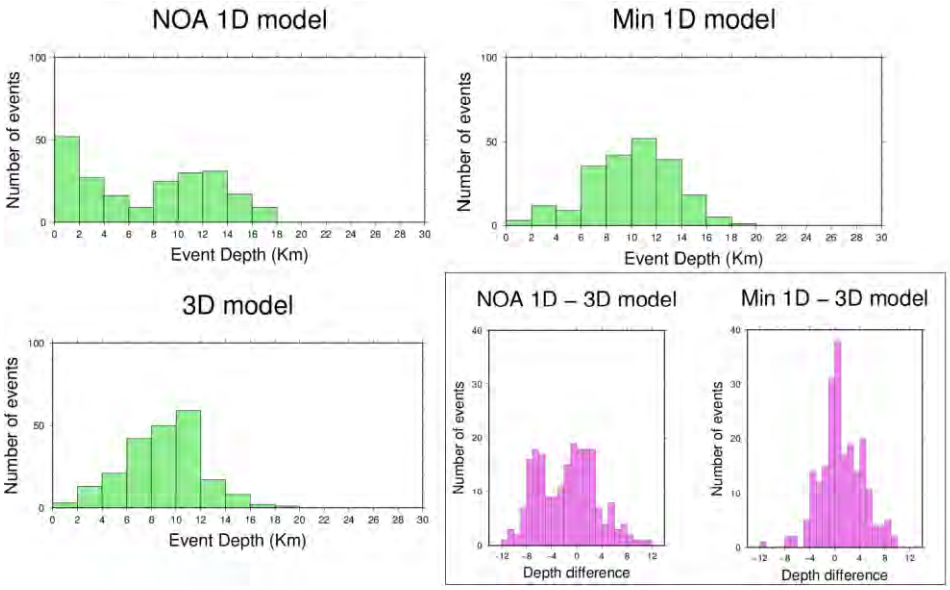

Figure 8 – Depth distribution of the events for the NOA 1D model (top left), the minimum 1D model (top right) and the 3D model (bottom left). Depth differences for the located earthquakes, between the 3D and the 1D models are also presented in this figure (bottom right.

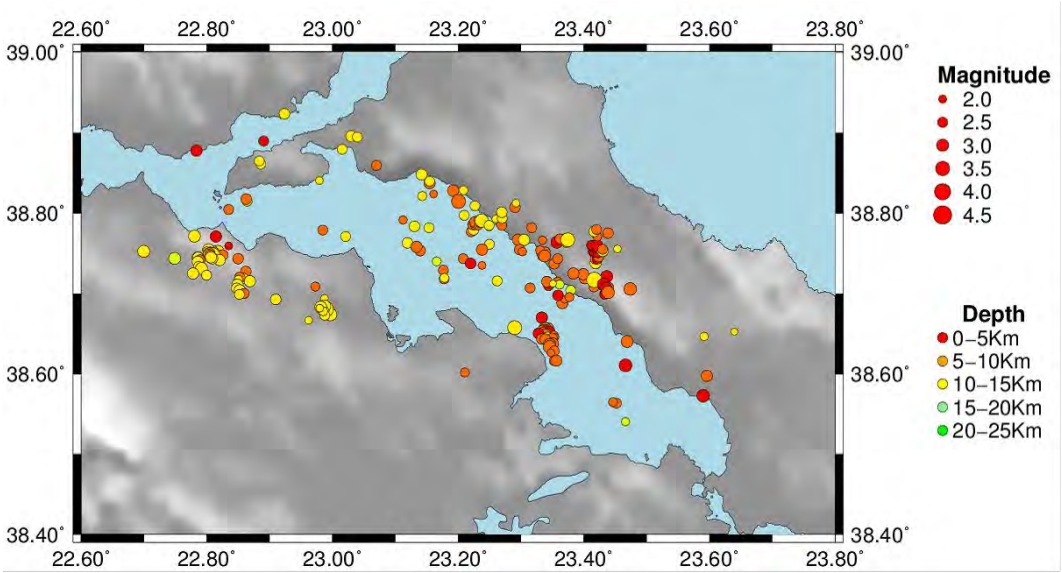

Figure 9 – Event locations map calculated with the use of the local 3D velocity model.

5. Acknowledgments

The seismicity data used were gathered by the Hellenic Unified Seismograph Network in the period of 2009-10. We would like to thank the scientific and technical personnel who worked for the creation of this dataset. Thanks are also due to Dr G. Papadopoulos who provided the waveform data of CHLK station for the entire study period. The CHLK station was part of the network established for the monitoring of the metropolitan area of Athens for the Olympic Games of 2004. We would also like to thank Lafarge Beton who provided us with information on the quarry blasts used in that period. The calculation of the 3D local velocity model of the North Euboean Gulf was based on the data funded by the General Secretariat for Research and Technology of Greece, through the research project "AMPHITRITE".
Thanks are due to professor Eleftheria Papadimitriou and professor Antonis Vafidis for their constructive comments which improved the initial version of the paper.

6. References

Dewey J.W. 1971. Seismicity studies with the method of joint hypocenter determination, *Ph.D. Thesis,* University of California, Berkeley, California.

Dewey J.W. 1972. Seismicity and tectonics of western Venezuela, *Bull. Seism. Soc. Am.* 62**,** 1711–1751.

Douglas A. 1967. Joint epicentre determination, *Nature* 215**,** 47–48.

Eberhart-Phillips D. 1990. Three-dimensional P and S velocity structure in the Coalinga Region, California, *Journal of Geophysical Research* 95, 15 343–15 363.

Engdahl E.R.and Lee W.H.K. 1976. Relocation of local earthquakes by seismic ray tracing, *J. Geophys. Res.* 81**,** 4400–4406.

Ganas A., Roberts G. and Memou P. 1998. Segment boundaries, the 1894 ruptures and strain patterns along the Atalanti Fault, central Greece, *Journal of Geodynamics* 26, 461–486.

Jordan T. H.and Sverdrup K. A. 1981. Teleseismic location techniques and their application to earthquake clusters in the south-central Pacific, *Bull. Seism. Soc. Am.* 71**,** 1105–1130.

Karastathis V.K.,Ganas A.,Makris J., Papoulia J.,Dafnis P., Gerolymatou E.and Drakatos G. 2007. The application of shallow seismic techniques in the study of active faults: the Atalanti normal fault, central Greece, *Journal of Applied Geophysics* 62, 215–233.

Karastathis V.K., Papoulia J., Di Fiore B., Makris J., Tsambas A., Stampolidis A. and Papadopoulos G.A. 2011. Deep structure investigations of the geothermal field of the North Euboean Gulf, Greece, using 3-D local earthquake tomography and Curie Point Depth analysis. J*ournal of Volcanology and Geothermal Research* 206, 106–120.

Kissling E., Ellsworth W.L., Eberhart-Phillips D.and Kradolfer U. 1994. Initial reference models in local earthquake tomography, *Journal of Geophysical Research* 99, 19635–19646.

Kissling E. 1995. Velest User's Guide, *Internal report, Institute of Geophysics,* ETH, Zurich.

Le Meur H. 1994. Tomographie tridimensionnelle a partir des temps des premieres arrivees des ondes P et S, application a la region de Patras (Grece), *These de Doctorat,* Paris VII, France.

Le Meur H., Virieux J.and Podvin P. 1997. Seismic Tomography of the gulf of Corinth: a comparison of methods, *Annali di Geofisica,* 40, 6, 1-24.

Lomax A. 2005. A reanalysis of the hypocentral location and related observations for the great 1906 California earthquake, *Bull. Seism. Soc. Am*., 9, 861 – 877.

Palyvos N. 2001. Geomorphological study of the broader area of Atalanti, Fthiotis. *Ph.D. Thesis.* University of Athens, Greece, (in Greek).

Pantosti D., De Martini P.M., Papanastassiou D., Palyvos N., Lemeille F. and Stavrakakis G. 2001. A reappraisal of the 1894 Atalanti earthquake surface ruptures, central Greece, *Bulletin of the Seismological Society of America 91,* 760–780.

Pavlides S.B., Valkaniotis S., Ganas A., Keramydas D. and Sboras S. 2004. The active fault of Atalanti — re-evaluation with new geological data. *Bulletin of the Geological Society of Greece* 36, 1560–1567 (in Greek).

Pavlis G.L. and Hokanson N. B. 1985. Separated earthquake location. *J. Geophys. Res.* 90**,** 12,777– 12,789.

Pavlis G.L. 1986. Appraising earthquake hypocenter location errors - a complete, practical approach for single-event locations, *Bull. Seism. Soc. Am.,* 76, 1699-1717.

Pavlis G. L. 1992. Appraising relative earthquake location errors, *Bull. Seism. Soc. Am.* 82**,** no. 2, 836–859.

Podvin P. and Lecomte I. 1991. Finite difference computation of traveltimes in very contrasted velocity models: a massively parallel approach and its associated tools, *Geophys. J. Int*., 105, 271-284.

Poulimenos G.and Doutsos T. 1996. Barriers on seismogenic faults in central Greece, *J. Geodyn.* 22 (1-2), 119 – 135.

Thurber C.H. 1983. Earthquake locations and three dimensional crustal velocity structure in the Coyote lake area, central California, *Journal of Geophysical Research* 88, 8226–8236.

Tzanis A., Kranis H.and Chailas S. 2009. An investigation of the active tectonics in central-eastern mainland Greece with imaging and decomposition of topographic and aeromagnetic data, *J. Geodyn.,* doi:10.1016/j.jog.2009.09.042.

Δελτίο της Ελληνικής Γεωλογικής Εταιρίας, τομ. XLVII , 2013
Πρακτικά 13ου Διεθνούς Συνεδρίου, Χανιά, Σεπτ. 2013

Bulletin of the Geological Society of Greece, vol. XLVII 2013
Proceedings of the 13th International Congress, Chania, Sept. 2013

THE EARTHQUAKE INTERVENT TIME DISTRIBUTION ALONG THE HELLENIC SUBDUCTION ZONE

Papadakis G.[1], Vallianatos F.[1,2] and Michas G.[1]

[1]*Institute for Risk and Disaster Reduction, University College London, Gower Street, London, WC1E 6BT, UK (georgios.papadakis.10@ucl.ac.uk)*

[2]*Laboratory of Geophysics and Seismology, Technological Educational Institute of Crete, Chania, GR 73133, Crete, Greece*

Abstract

The Hellenic Subduction Zone (HSZ) is the most seismically active region in Europe (Becker and Meier, 2010). The evolution of such an active region is characterized by complex phenomenology and is expressed through seismicity. Seismicity temporal patterns remain as one of the most important topics in earth sciences. The Weibull distribution has been used as a recurrence time model for large earthquakes (Rikitake, 1976; Rikitake, 1991). Moreover,Hasumi et al. (2009) used the Weibull-log Weibull distribution for the study of the interoccurrence times of earthquakes in Japan.The dataset formed in this study concerns the seismic belt of the HSZ during the period 1976-2009. We use the external seismic sources of shallow earthquakes in the Aegean and the surrounding area (Papaioannou and Papazachos, 2000) along with the updated and extended earthquake catalogue for Greece and adjacent areas (Makropoulos et al., 2012).The application of the Weibull distribution to the interevent times of the formed dataset is analyzed and discussed.
Key words: *HellenicSubduction Zone, Weibull distribution,seismicity*

Περίληψη

Η ελληνική ζώνη υποβύθισης είναι η πιο σεισμική περιοχή της Ευρώπης. Η κατανομή Weibullέχει χρησιμοποιηθεί σαν μοντέλο για την περιγραφή των χρονικών διαστημάτων μεταξύ διαδοχικών σεισμών σε συγκεκριμένες ρηξιγενείς ζώνες (Rikitake, 1976; Rikitake, 1991), καθώς και για την περιγραφή της σεισμικότητας μίας ευρύτερης περιοχής (Hasumietal., 2009). Ταδεδομένα που αναλύουμε σε αυτή την εργασία αφορούν την ελληνική ζώνη υποβύθισης και καλύπτουν την περίοδο 1976-2009. Χρησιμοποιούμε τις σεισμικές πηγές επιφανειακών σεισμών όπως αυτές ορίζονται από τους PapaioannouandPapazachos(2000), καθώς και τονκατάλογο σεισμών των Makropoulosetal. (2012) για την Ελλάδα και τις παρακείμενες περιοχές. Η εφαρμογή της κατανομής Weibullστα χρονικά διαστήματα μεταξύ διαδοχικών σεισμών αναλύεται και περιγράφεται σε αυτή την εργασία.
Λέξεις κλειδιά: *Ελληνική ζώνη υποβύθισης, κατανομή Weibull, σεισμικότητα*

1. Introduction

The eastern Mediterranean region presents a remarkable record of major earthquakes (Ambraseys and Jackson, 1998).The Hellenic Subduction Zone (HSZ) is an active seismic belt (Becker and Meier, 2010; Meier et al., 2004). Many destructive earthquakes have taken place along the HSZ (Papathanasiou et al., 2005; Papazachos and Papazachou, 2003). This high seismic activity is caused by the subduction of the Adriatic continental lithosphere in the north and the Ionian oceanic lithosphere in the south (Royden and Papanikolaou, 2011). The Kephalonia Transform Zone (KTZ) separates the northern part (N.HSZ) of the Hellenic subduction boundary from the southern one (Fig. 1).The evolution of such an active region is characterized by complex phenomenology and is expressed through seismicity.

Seismicity temporal patterns remain as one of the most important topics in earth sciences.Over the past years, much has been written about the distribution of interevent times, which are defined asthe time intervals between successive earthquakes. Various distributions have been used to fit earthquake interevent time statistics (Abaimov et al., 2008). Among them, one of the most recent is proposed by Vallianatoset al., (2012), where the spatiotemporal properties of the 1995 Aigion (Greece) earthquake aftershock sequence were investigated using the concept of Nonextensive Statistical Physics formalism (Tsallis, 1988; Tsallis, 2009). The aforementioned authors conclude that Tsallis entropic term describes very well the observed distributions and the spatiotemporal earthquake patterns. An alternative approach is based on theapplication of the Weibull distribution to the interevent times of an earthquake sequence asithas been performed by many authors (Hagiwara, 1974; Rikitake, 1976; Rikitake 1991).Hasumi et al. (2009) used the Weibull-log Weibull distribution for the study of the interoccurrence times of earthquakes in Japan.The latter distributions haverenewedtheir use in geosciences, since theycan be used in seismic hazard assessment (Votsi et al., 2011).It is the scope of the present work to use the Weibulldistribution for the analysis ofthe cumulative distributionof the interevent times along the seismic zones of the HSZ.

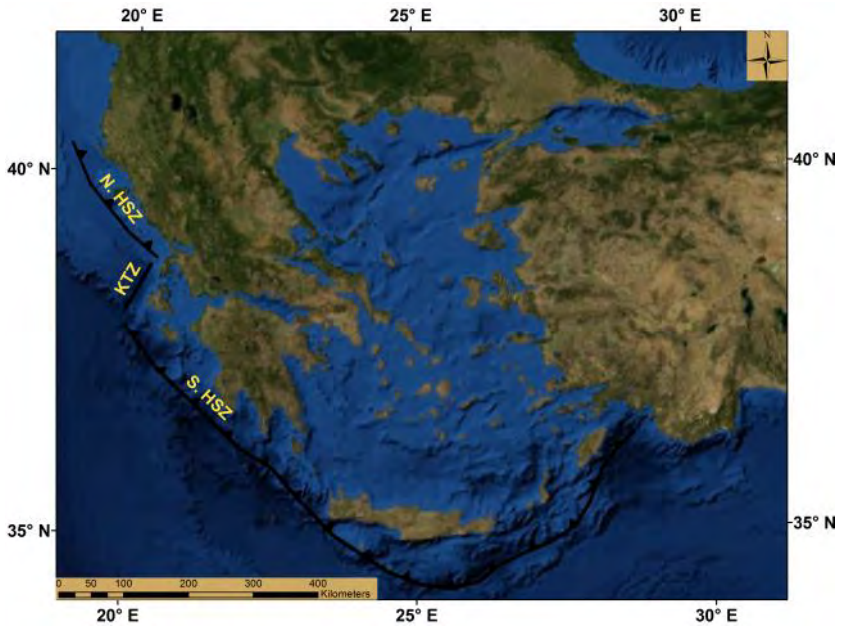

Figure 1 - The active trenches (thick dark lines with solid barbs) for the HSZ, as Royden and Papanikolaou (2011) indicate them. The Kephalonia Transform Zone (KTZ) separates the northern part (N. HSZ) of the Hellenic subduction boundary from the southern one (S. HSZ).

2. Seismic Zones and Earthquake Dataset

Papaioannou and Papazachos (2000) separated the region of the Aegean and the surrounding area in 67 seismogenic sources. This separation is based on previous work on seismic zonation, work on seismicity and active tectonics, as well as on geological and geomorphological information. In the present work, we use the external seismic sources, which are associated with the compressional stress field to define a dataset regarding the subduction zone. These sources have axes parallel to the external coast of the area, to the strikes of the seismic faults (thrust or strike- slip), and are associated with the lithospheric convergence (Papazachos, 1990).In order to create a dataset with a significant number of events that will lead us in a confidence result,we merge the external seismic sources to form larger areas of study called seismic zones, as it is proposed in Papadakis et al., (2013). It should be noticed that the latter process is in fully agreement with the zonation study originally proposed in Papaioannou and Papazachos (2000).Table 1 provides the composition of each seismic zone as regards the seismic sources forming them and the correspondent number of seismic events used in each of the zones.We note that the dataset used in this study is based on the updated and extended earthquake catalogue for Greece and the adjacent areas by Makropoulos et al. (2012). It concerns shallow earthquakes (focal depth ≤ 60km) and covers the period 1976-2009 (Figure 2).

Table 1 – The composition of the seismic zones used in this study and the correspondent number of seismic events.

Seismic Zones	Seismic Sources	Seismic Events
1	4,5	111
2	6,7,8,11	265
3	9,10,12,13	248
4	14,15,16,17	327
5	18,19,20	179

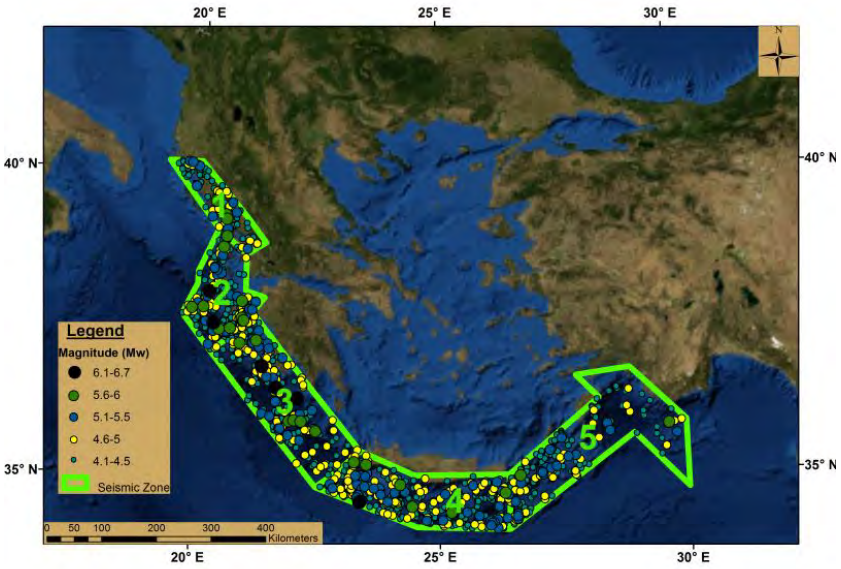

Figure 2 - The seismic zones (polygons 1-5) (Papaioannou and Papazachos, 2000) of the HSZ, and the seismic events (colored circles) (Makropoulos et al., 2012) of shallow earthquakes (focal depth ≤ 60km) covering the period 1976-2009.

Moreover, Makropoulos et al. (2012) have computed the magnitude of completeness (Mc) of their updated catalogue for the period 1976-2009 to be as Mc = 4.1.The final dataset used in this study, is extracted usingthe application of the window method, introduced by Gardner and Knopoff (1974) and modified by Uhrhammer (1986)for thedeclustering of the original earthquake catalogue.

3. The Weibull Distribution

The probability density function (pdf) for a Weibull distribution is given as:

Equation 1–The probability density function (pdf)

$$p(t) = \frac{\beta}{\tau}\left(\frac{t}{\tau}\right)^{\beta-1} exp\left[-\left(\frac{t}{\tau}\right)^{\beta}\right],$$

whereβ is the shape parameter or the Weibull modulus and τ is the scale parameter.

The cumulative distribution (cdf) of the Weibull distribution is given as:

Equation 2–The cumulative distribution function (cdf)

$$P(t) = 1 - exp\left[-\left(\frac{t}{\tau}\right)^{\beta}\right],$$

where P(t) is the fraction of the recurrence times that are shorter than t.

The survival function R(t) is given as:

Equation 3–The survival function

$$R(t) = 1 - P(t).$$

The hazard function h (t_0) is the pdfthat an event will occur at a time t_0 after the occurrence of the last event (Abaimov et al., 2008). The hazard function exhibits a power-law behavior and it is given as:

Equation 4–The hazard function

$$h(t_0) = \frac{pdf}{1 - cdf} = \frac{\beta}{\tau}\left(\frac{t_0}{\tau}\right)^{\beta-1}.$$

If β>1 the probability that an earthquake will occur increases as a power of the time t_0 since the last earthquake. For β=1 the Weibull distribution reduces to the exponential distribution. That means that earthquakes occur randomly.For β<1 the Weibull distribution is known as the stretched exponential distribution(Yakovlev et al., 2006).

4. Interevent Time Cumulative Distribution

The cumulative distribution of the interevent times for each seismic zone and for the HSZ as a unified system is given in Figure 3. The best fit of the Weibull distribution using the maximum likelihood estimation is also presented.

The calculated Weibull parameters are presented in Table 2. An inspection to the obtained values of the shape parameter β suggests its increase as we move from seismic zone 1 to seismic zone 5. The β value is equal to 0.92 for the HSZ as a unified system. It becomes equal to 0.77 in seismic zone 1. Moving southward it increases and becomes equal to 0.88 and 0.89 in seismic zones 2 and 3, respectively. This trend continues to appear along the northeast portion of the Hellenic arc

presenting values equal to 0.95 and 1.08 in seismic zones 4 and 5 respectively. On the other hand the scale parameter τ shows variations that do not follow the trend of the shape parameter and has a value equal to 9.15*105(sec) for the HSZ as a unified system.

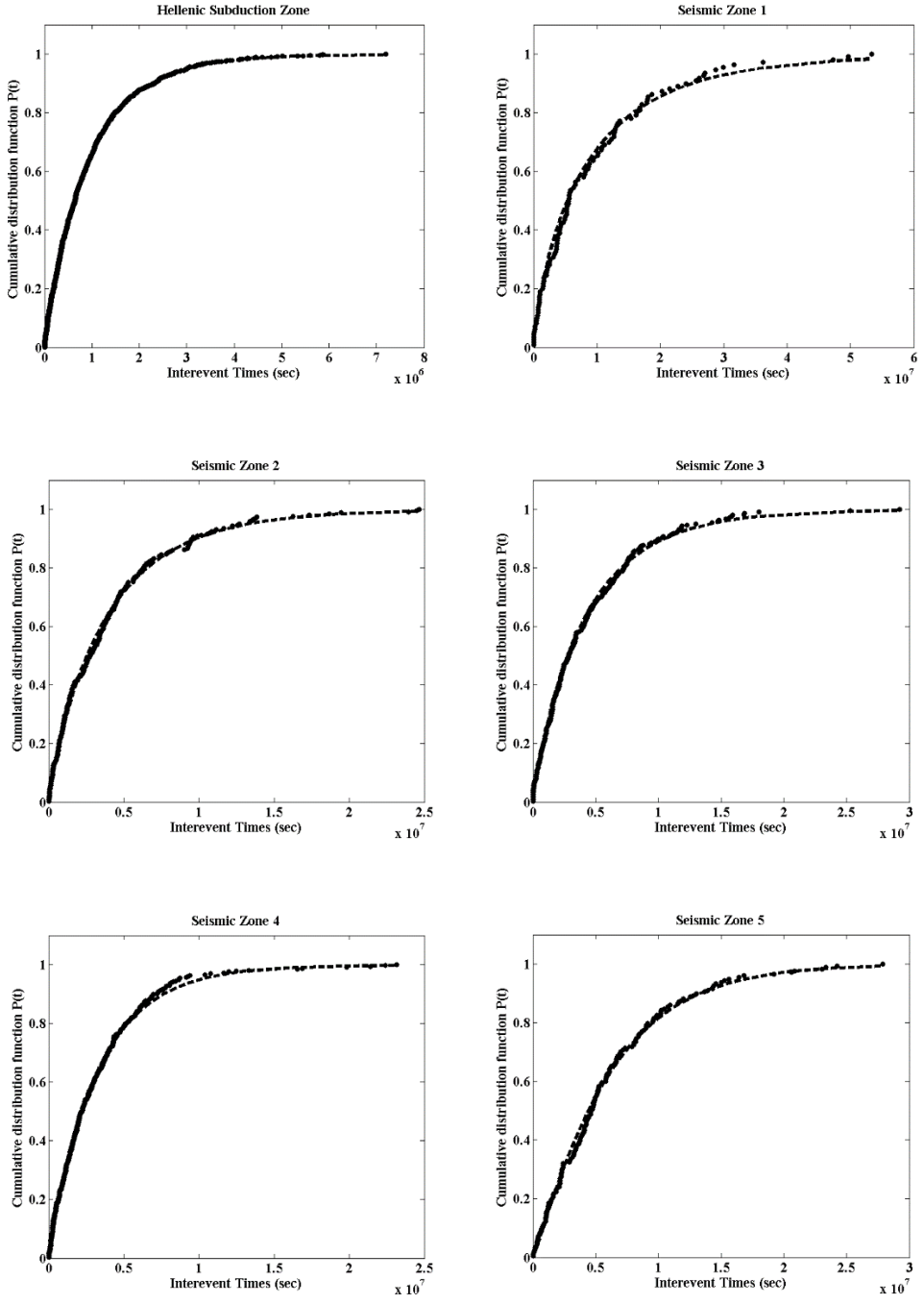

Figure 3 - The cumulative distribution ofinterevent times for each seismic zone and for the HSZ as a unified system. The black discontinuous line is the best-fit Weibull distribution. The estimation of the Weibull parameters has been performed using the maximum likelihood estimation.

Table 2 - The Weibull parameters β and τ and their 95% confidence intervals [β1, β2] and [τ1, τ2] for each seismic zone and for the HSZ as a unified system.

Seismic Zones	β	τ(sec)	[β1,β2]	[τ1, τ2]
HSZ	0.92	$9.15*10^5$	[0.88, 0.96]	[$8.56*10^5$, $9.77*10^5$]
1	0.77	$8.50*10^6$	[0.66, 0.90]	[$6.61*10^6$, $1.09*10^7$]
2	0.88	$3.81*10^6$	[0.80, 0.97]	[$3.30*10^6$, $4.40*10^6$]
3	0.89	$4.12*10^6$	[0.81, 0.99]	[$3.56*10^6$, $4.76*10^6$]
4	0.95	$3.17*10^6$	[0.87, 1.03]	[$2.81*10^6$, $3.57*10^6$]
5	1.08	$6.15*10^6$	[0.96, 1.22]	[$5.34*10^6$, $7.09*10^6$]

5. Conclusions

In the present work the analysis of the interevent timedistribution using the Weibull distribution is being investigated. The studied area is the Hellenic subduction belt divided in 5 seismic zones as it is recently used in Papadakis et al., (2013) and as it is originally proposed in Papaioannou and Papazachos (2000)for the separation of the Aegean and the surrounding area in 67 seismogenic sources. The declusteredearthquake dataset concerns earthquakes with Mc= 4.1 and covers the period 1976-2009.The Weibull distribution used in this study fits rather well to the observed distributionsimplying its usefulness in the investigation of the interevent time distribution along the HSZ.The shape parameter βpresents increasing values as we move from the northwestern (seismic zone 1) to the southeastern part (seismic zone 5) of the Hellenic subduction boundary. On the other hand the scale parameter τ presents variations that do not follow the trend of the shape parameter along the seismic zones of the HSZ.

6. Acknowledgments

This work was supported by theTHALES Program of the Ministry of Education of Greece and theEuropean Union in the framework of the project entitled “Integrated understanding of Seismicity, using innovative Methodologies of Fracture mechanics along with Earthquake and non-extensivestatistical physics – Application to the geodynamic system of theHellenic Arc. SEISMO FEAR HELLARC”.

7. References

Abaimov S.G., Turcotte D.L., Shcherbakov R., Rundle J.B., Yakovlev G., Goltz C. and Newman W.I. 2008. Earthquakes: Recurrence and Interoccurrence Times, *Pure Appl. Geophys.*, 165, 777-795.

Ambraseys N.N. and Jackson J.A. 1998. Faulting associated with historical and recent earthquakes in the eastern Mediterranean area, *Tectonophysics*, 60, 1-42.

Becker D. and Meier T. 2010. Seismic Slip Deficit in the Southwestern Forearc of the Hellenic Subduction Zone, *Bull. Seismol. Soc. Am.,* 100, 325-342.

Gardner J.K. and Knopoff L. 1974. Is the sequence of earthquakes in Southern California, with aftershocks removed, Poissonian?, *Bull. Seismol. Soc. Am.*, 64, 1363–1367.

Hagiwara Y. 1974. Probability of earthquake occurrence as obtained from a Weibull distribution

analysis of crustal strain, *Tectonophysics*, 23, 313-318.
Hasumi T., Akimoto T. and Aizawa Y. 2009. The Weibull-log Weibull distribution for interoccurrence times of earthquakes, *Phys. Stat. Mech. Appl.*,388, 491-498.
Makropoulos K., Kaviris G. and Kouskouna V. 2012. An updated and extended earthquake catalogue for Greece and adjacent areas since 1900, *Nat. Hazards Earth Syst. Sci.*, 12, 1425-1430.
Meier T., Rische M., Endrun B., Vafidis A. and Harjes H.P. 2004. Seismicity of the Hellenic subduction zone in the area of western and central Crete observed by temporary local seismic networks, *Tectonophysics*, 383, 149-169.
Papadakis G., Vallianatos F. and Sammonds P. 2013.Evidence of Non Extensive Statistical Physics behaviour of the Hellenic Subduction Zoneseismicity, *Tectonophysics*, DOI: 10.1016/j.tecto.2013.07.009.(In press)
Papathanassiou G., Pavlides S. and Ganas A. 2005. The 2003 Lefkada earthquake: Field observations and preliminary microzonation map based on liquefaction potential index for the town of Lefkada, *Eng. Geol.*, 82, 12-31.
Papaioannou C.A. and Papazachos B.C. 2000. Time-independent and time-dependent seismic hazard in Greece based on seismogenic sources, *Bull. Seismol. Soc. Am.*, 90, 22-33.
Papazachos B.C. 1990. Seismicity of the Aegean and surrounding area, *Tectonophysics*, 178, 287-308.
Papazachos B.C. and Papazachou C.B. 2003. *The earthquakes of Greece*, Thessaloniki, Ziti Publications.
Rikitake T. 1976. Recurrence of great earthquakes at subduction zones, *Tectonophysics*, 35, 335-362.
Rikitake T. 1991. Assessment of earthquake hazard in the Tokyo area, Japan, *Tectonophysics*, 199, 121-131.
Royden L.H. and Papanikolaou D.J. 2011. Slab segmentation and late Cenozoic disruption of the Hellenic arc, *Geochem. Geophys. Geosyst.*, 12, Q03010.
Tsallis C. 1988. Possible generalization of Boltzmann-Gibbs Statistics, *J. Stat. Phys.*, 52, 479-487.
Tsallis C. 2009. *Introduction to Nonextensive Statistical Mechanics: Approaching a Complex World*, New York, Springer.
Uhrhammer R. 1986. Characteristics of northern and central California seismicity, *Earthquake Notes*, 57, 21.
Vallianatos F., Michas G., Papadakis G. and Sammonds P. 2012. A non-extensive statistical physics view to the spatiotemporal properties of the June 1995, Aigion earthquake (M6.2) aftershock sequence (West Corinth rift, Greece), *ActaGeophys.*, 60, 758-768.
Votsi I., Tsaklidis G.M. and Papadimitriou E.E. 2011. Seismic hazard assessment in central Ionian Islands area (Greece) based on stress release models, *ActaGeophys.*, 59, 701-727.
Yakovlev G., Turcotte D.L., Rundle J.B. and Rundle P.B. 2006. Simulation-based distributions of earthquake recurrence times on the San Andreas Fault System, *Bull. Seismol. Soc. Am.*, 96, 1995-2007.

Δελτίο της Ελληνικής Γεωλογικής Εταιρίας, τομ. XLVII , 2013
Πρακτικά 13ου Διεθνούς Συνεδρίου, Χανιά, Σεπτ. 2013

Bulletin of the Geological Society of Greece, vol. XLVII 2013
Proceedings of the 13th International Congress, Chania, Sept. 2013

RESULTS FOR THE SHALLOW STRUCTURE OF THE BROADER REGION OF CHANIA BY HVSR MEASUREMENTS OF AMBIENT NOISE AND THEIR VALIDATION USING SIMULATION OF AMBIENT NOISE AND INDEPENDENT GEOLOGICAL INFORMATION

Papadopoulos I.[1], Papazachos C.[2], Savvaidis A.[3], Theodoulidis N.[3], Vallianatos F.[1] and Tsourlos P.[2]

[1] Technological Institute of Crete, Department of Natural Resources and Environment, ilias@chania.teicrete.gr, fvallian@chania.teicrete.gr

[2] Aristotle University of Thessaloniki, Department of Geology, kpapaza@geo.auh.gr, tsourlos@geo.auth.gr

[3] Institute of Engineering Seismology and Earthquake Engineering, alekos@itsak.gr, ntheo@itsak.gr

Abstract

The city of Chania is located at the Western-North part of the island of Crete. It is mostly built over Neogene sediments of unknown thickness. In the southern part of the city the Chania basin is developed, filled mainly by Quaternary deposits overlying the deep Neogene sediments. In this complex geological setting, we conducted over 200 single station measurements of ambient noise, aiming to estimate the predominant frequency of the subsurface formations. The obtained results for the HVSR data show a different behavior between sites located on Neogene and Quaternary deposits. In general, Neogene sediments show a single peak at low frequencies (below 1Hz, typically in the range 0.4-0.6Hz), indicating a very thick layer overlying the bedrock (Trypalion and Plattenkalk limestones). On the other hand, measurements at Quaternary deposits show two peaks, with the first one similar to the Neogene formations, while the second one is identified at higher frequencies, typically ~0.8-4.0 Hz. Simulation of ambient noise 1-D models show a good correlation between the experimental and theoretical HVSR curves, especially when the initial model consists of two layers (typically Neogene sediments overlying high-velocity bedrock formations) with a clear identification of the lower frequency HVSR peak, while for three layered models (typically Quaternary sediments and underlying softer Neogene and Neogene/bedrock high-velocity formations) results are more complicated, although both HVSR frequencies can be partly reconstructed.
Key words: *Microtremor, Resonance frequency, Site effects.*

Περίληψη

Η πόλη των Χανίων βρίσκεται στο Βορειοδυτικό τμήμα της Κρήτης, χτισμένη σε Νεογενή ιζήματα αγνώστου πάχους. Νότια της πόλης σχηματίζεται η λεκάνη των Χανίων, η οποία είναι πληρωμένη με Τεταρτογενείς αποθέσεις που επικάθονται των μεγάλου πάχους Νεογενών ιζημάτων. Σε αυτό το πολύπλοκο γεωλογικό περιβάλλον

πραγματοποιήθηκαν 200 μετρήσεις εδαφικού θορύβου με τη μέθοδο μονού σταθμού, με σκοπό τον προσδιορισμό της συχνότητας ενίσχυσης των επιφανειακών σχηματισμών. Τα αποτελέσματα του φασματικού λόγου της οριζόντιας προς την κατακόρυφη συνιστώσα (HVSR) δείχνουν διαφορετική συμπεριφορά των Νεογενών και Τεταρτογενών σχηματισμών. Γενικά, τα Νεογενή εμφανίζουν ενίσχυση σε μια χαμηλή συχνότητα (κάτω του 1 Hz, μεταξύ 0.4-0.6 Hz), υποδεικνύοντας την ύπαρξη μεγάλου πάχους ιζημάτων πάνω από το γεωλογικό/σεισμικό υπόβαθρο (ασβεστόλιθοι Τρυπαλίου και Plattenkalk). Οι μετρήσεις σε περιοχές που καλύπτονται επιφανειακά από Τεταρτογενείς σχηματισμούς εμφανίζουν διπλές κορυφές συχνότητας ενίσχυσης, μια παρόμοια με αυτή των περιοχών που καλύπτονται από Νεογενή ιζήματα και μια υψηλότερη, μεταξύ 0.8-4 Hz. Η προσομοίωση του εδαφικού θορύβου με μονοδιάστατα μοντέλα δείχνει καλή συνάφεια με τα πειραματικά αποτελέσματα, ειδικά όταν το αρχικό μοντέλο αποτελείται από ένα στρώμα πάνω από ημιχώρο, με καθαρή διάκριση της κορυφής ενίσχυσης. Στην περίπτωση δύο στρωμάτων επί ημιχώρου τα αποτελέσματα είναι πιο περίπλοκα, κατορθώνοντας όμως να κάνουν εφικτή την διάκριση μεταξύ των δύο κορυφών.
Λέξεις κλειδιά: *Εδαφικός θόρυβος, συχνότητα ενίσχυσης, προσομοίωση.*

1. Introduction

Amplification of earthquake ground motion due to the effect of local geological site conditions (e.g. thick sedimentary deposits) is an important factor when determining the seismic risk of areas not located on bedrock formations. Determining the ground response of different geological formations with traditional methods is not an easy task, especially in urban areas (e.g. due to anthropogenic factors) or when a large area needs to be covered in high density. During the past decades the usage of ambient noise recordings has been extensively employed as a tool to determine the eigenfrequency of sedimentary formations due to seismic excitation and possibly their lower level of expected amplification. The most common approach is the calculation of spectral ratio of horizontal to vertical component of ambient noise-HVSR (Nakamura, 1989), despite the lack of a rigorous theoretical basis (Bard, 1999). In the present study 200 measurements of ambient noise with a single recording station have been performed in the urban area of Chania and its southern basin in order to determine the eiganfrequency of excitation. Measurements are grouped based on the spatial similarity of the HVSR curve in order to define common properties of the geological formations. Using Hisada's method for the calculation of Green function (Hisada, 1994, 1995), five (5) groups of measurements have been simulated using a 1-D model. The simulation of ambient noise sources has been performed by the use of the RANSOURCE algorithm (Moczo and Kristek, 2002).

2. Geological Setting and Experiment Setup

2.1. Geological Setting

The broader study area consists, according to the available IGME geological map, of Tripalion and Plattenkalk limestones in the mountainous area south of the basin of Chania, Quaternary deposits filling the basin of Chania south of the main city complex and Neogene sediments filling the urban area at the North. Bastelli (2002) presented a more detailed description of the Neogene sediments covering the city of Chania. The largest part of the eastern and southern Chania city area is covered with alternations of white and grey marly limestones, marls and yellow marly limestones with thin layers of sandstone. The western section of the city region is covered with alluvial Quaternary deposits, while at the coast there are human deposits, medium thickness sand formations, as well as fluvial sediments. At the southwestern area we find compact marly limestone with colors rang-

ing from white to grey, within which bioclastic limestone lenses can be found, along with marly gravels (Figure 1).

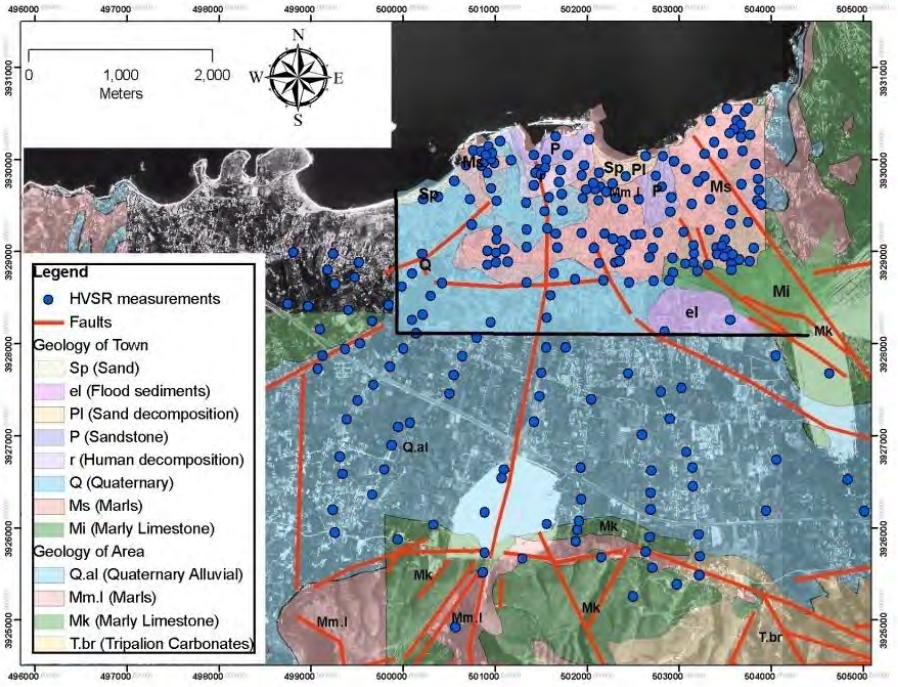

Figure 1 - Geological map of the broader Chania area (based on IGME map and Bastelli, 2002). The HVSR recording sites are also presented (blue dots).

2.2. Experiment Setup

The 200 measurements of ambient noise have been conducted in the broader area of interest, using a Lennarz 3D/5s sensor coupled with City Shark II digitizer. All measurements lasted 30 minutes and were obtained at night hours (typically 24:00-06:00) to minimize human and traffic noise influence. For all measurements a common processing approach was adopted, removing the mean value and filtering them with a bandpass Butterworth filter in the 0.2-20 Hz range, which corresponds to the main frequency window of interest. Measurements were split in smaller time-windows of 40 seconds length. The spectrum of each component's window was calculated using a Fast Fourier Transform (FFT) with tapering of 5% and smoothed using the Konno-Ohmachi approach, with a *b* constant of 40 (Konno and Ohmachi, 1998). The horizontal components were then geometrically averaged and divided with the vertical component to obtain the Horizontal to Vertical Spectral Ratio (HVSR) of each measurement. The lowest peak in frequency exceeding the amplitude value of 1.8-2.0 was chosen as the resonance frequency of sediments overlying the geological bedrock. If more than one peak was observed, we checked the spectrum of measurement to define whether its origin was human related, e.g. by observing spikes in the FFT spectrum at the same frequency. If the origin of peak was considered as of possible geological origin, then a second frequency was picked, following the same amplitude criteria as above.

Measurements were visually inspected in a GIS system and spatial distribution maps were created regarding the selected frequencies and amplitudes. Measurements were grouped based on the similarity of the corresponding HVSR curve in order to recognize patterns reflecting different geological formations. Using Hisada's method (Hisada, 1994, 1995) a calculation of the theoretical Green function was performed for 1-D geophysical models derived on the basis of independent geophysical (noise array) measurements (Papadopoulos, 2013). The usage of the RANSOURCE

algorithm (Moczo and Kristek, 2002) provided the ambient noise input signal calculated for an area much similar in size to the study area.

3. Theoretical Approach

3.1. Horizontal to Vertical Spectral Ratio

Nogoshi and Igarashi (1970) presented the first usage of the HVSR of ambient noise for site response estimation, showing the relationship between the HVSR curve and the ellipticity curve of the Rayleigh waves around the fundamental resonance frequency. Nakamura (1989) showed that it is possible to estimate the resonance frequency of sediments, proposing that the ambient noise consists of S-waves, and showing that a good approximation of the amplification can be achieved, making HVSR a useful tool to reveal some of the dynamic characteristics of local site effects. Until today, the applicability of HVSR technique has been the subject of numerous studies around the World (e.g. Field and Jacob, 1995; Horike et al., 2001), and in some extent some theoretical and numerical investigations have been published regarding the physics of the subject (e.g. Bonnefoy-Claudet et al., 2007). Most of the authors agree that the method is quite reliable in defining the resonance frequency of soft soil over bedrock using ambient noise (e.g. Bard et al., 1997), but should not be considered as safe for the estimatation of the amplification due to seismic excitation by using HVSR curves (Haghshenas et al., 2008). In most cases amplitude measured with ambient noise is considered a low boundary of the actual amplification given by other geophysical and geotechnical methods, like Standard Spectral Ratio (e.g. Maresca et al., 2003). Moreover, the geometry of the sedimentary formation e.g. basin shape, plays an important role to both frequency and amplitude measured with the HVSR technique. When lateral discontinuities are observed, especially at the edges of basin, HVSR peaks appear broader and lower as the slope of basement increases (Cornou et al., 2006)

3.2. Parametric Numerical Investigation

To create the source signal for ambient noise recorded in a receiver, we used the RANSOURCE algorithm (Moczo and Kristek, 2002). The algorithm creates random sources either on the surface or in small depth of a given volume. A large number of receivers can be set at the surface or at a depth anywhere in the simulation volume. The time function of the noise sources can be either delta type or pseudo-monochromatic of random length and eigenfrequency, randomly chosen by the algorithm, in an attempt to imitate as much as possible the most common noise sources (impact and pseudo-harmonic).

Hisada (1994, 1995) modified the generalized Transmitter/Receiver coefficient method (Luco and Apsel, 1983), solving the difficulty of calculating Green's function when sources and receivers are located in similar or the same depth. Soil column must be heterogeneous and viscoelastic, horizontally stratified above bedrock, with parameters varying only with depth (1D models). Green functions are calculated for every pair of source-receiver and the time series is the summation of every recording couple. In order for the Green function to be calculated, the 1D geophysical model needs to be provided, consisting of the velocity parameters of the layers for P- and S- waves, thickness and density of layers, and quality factors Qp and Qs.

The volume we chose for creating the noise signal is similar to the size of the Chania basin, namely 2500x2500x10 meters. Receiver is centred on the surface of the volume, with source positions randomly distributed at the surface or down to the depth of 10m, with an equal contribution (50%) of delta and pseudo-monochromatic sources. In total 549 sources are created, effecting for 50 seconds. Minimum and maximum simultaneous working sources are set to 1 and 25, respectively, the minimum distance between sources was 10 meters and the minimum and maximum distance between source and receiver was set to 50 and 2500 meters, respectively. Combining RANSOURCE with Hisada's method produced 50 seconds time series of ambient noise over 1-D model, which by convolution of the time series was increased to 250 seconds.

4. Results

4.1. HVSR Results

In Figure 1 the HVSR measurements covering most of the extent of the Chania basin are superimposed to the geological map of the study area. In Figure 2 the spatial map of the lower resonance frequency of the area, as defined by the HVSR data, is presented, overlying the geology. Within the area of the city of Chania this fundamental frequency exhibits a peak around 0.4-0.6 Hz which extends throughout almost to the whole basin. This peak is possibly associated with the impedance contrast between the total column of Quanternary-Neogene sediments and the underlying bedrock formations. At the South, where the mountainous area consisting mainly of marly limestones is located, the peak frequency rises to values ranging 10-18 Hz, corresponding most probably to the superficial cover of soil or weathered bedrock. At the western and southern region of the basin, the peak frequency is lower, ranging between 0.28-0.35 Hz. In Figure 3 the amplitude of the corresponding frequency peak is presented, showing a value between 2-2.5 for the largest part of the urban area, indicating a relatively low impedance between the bedrock and the overlying (mostly Neogene) sediments. In the central part of the basin the observed amplitudes rise to values above 3.7.

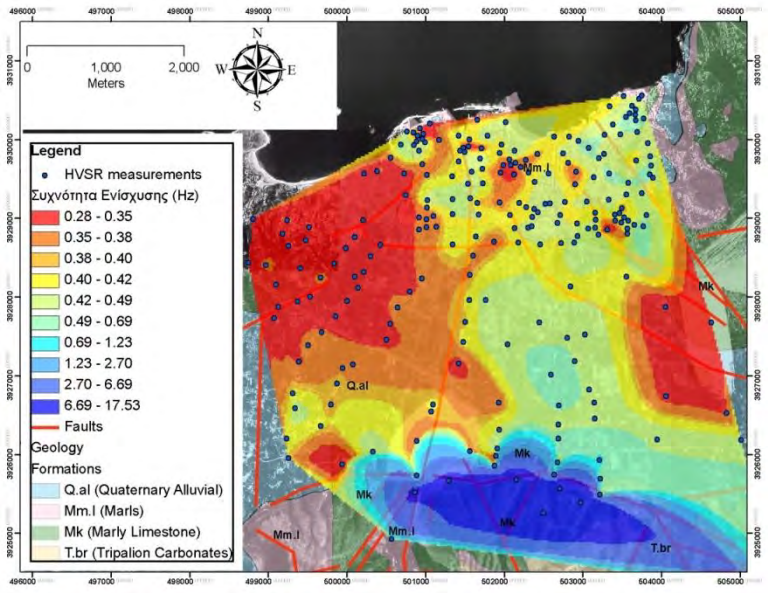

Figure 2 – Spatial distribution of the fundamental frequency defined from HVSR measurements within the broader Chania area.

For many recording sites, especially inside the Quaternary basin of Chania south of the main city complex, a second peak was observed in frequency range of 0.8-4 Hz. Although several research works consider higher frequency HVSR peaks as an indication of higher modes of Rayleigh waves in the ambient noise wavefield, an alternative approach is to consider them as a result of impedance contrast between sediments, corresponding to different layers inside the soft soil formations. In Figure 4 the measurements for which a second frequency peak appears in the HVSR curve are presented along with the spatial map of this higher frequency peak. In the urban area of Chania HVSR measurements appear to have a second peak mostly in the range 3-10 Hz, which can be interpreted as a result of the presence of small lenses of soft Quaternary or Neogene sediments locally placed above stiffer Neogene formations (e.g. stiffer marls).

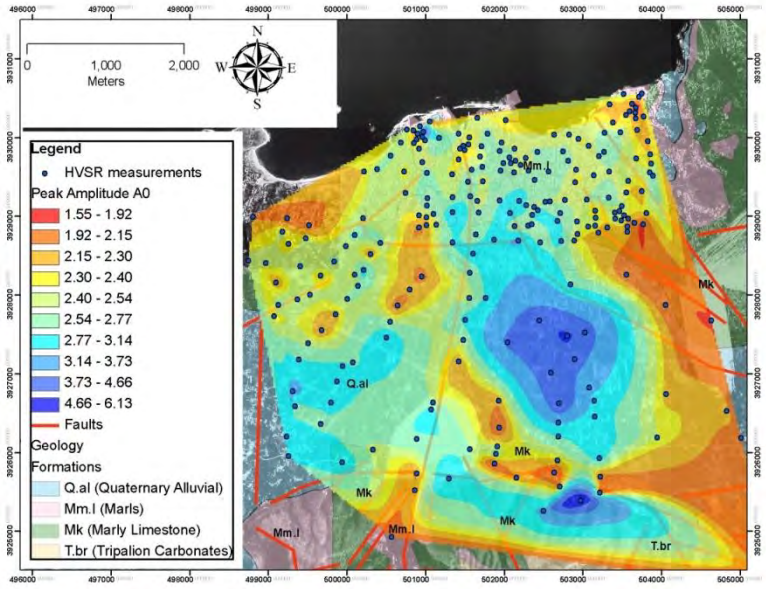

Figure 3 - Spatial distribution of the amplitude of the fundamental frequency peak defined from HVSR measurements within the broader Chania area.

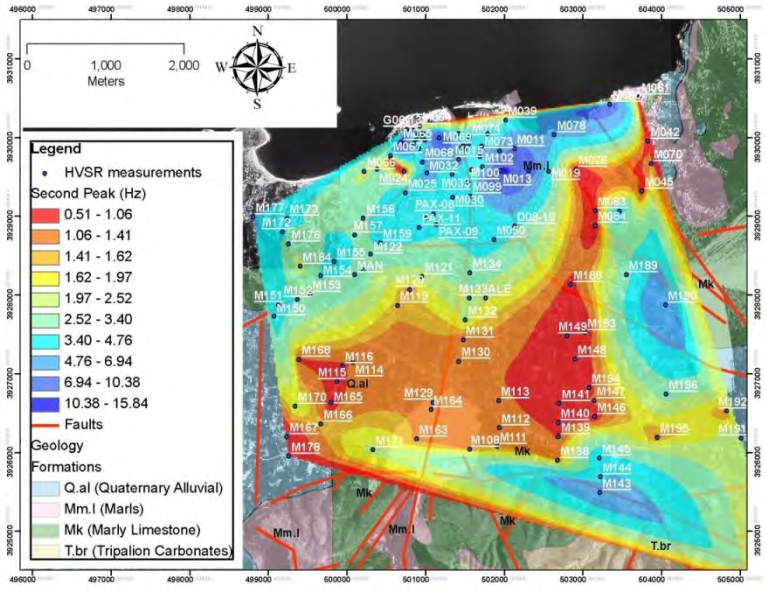

Figure 4 - Spatial distribution of the higher frequency defined from HVSR measurements within the broader Chania area.

Moving to the South, it is evident that the whole basin, which is covered with Quaternary deposits, has a second peak frequency around 1 Hz, which gradually lowers up to 0.5 Hz towards its centre. We interpret the existence of the second frequency in the basin as related with the impedance ratio between the low velocity Quaternary deposits and the higher velocity Neogene sediments. The difference in frequency between the central section and the basin edges depicts the corresponding difference in thickness of the Quaternary deposits. In Figure 5 the amplitude of the higher frequency peak is presented, showing a maximum again at the centre of the basin, with a value exceeding 3, while at the edges of the basin and in the urban area the value is between 1.8-2.5.

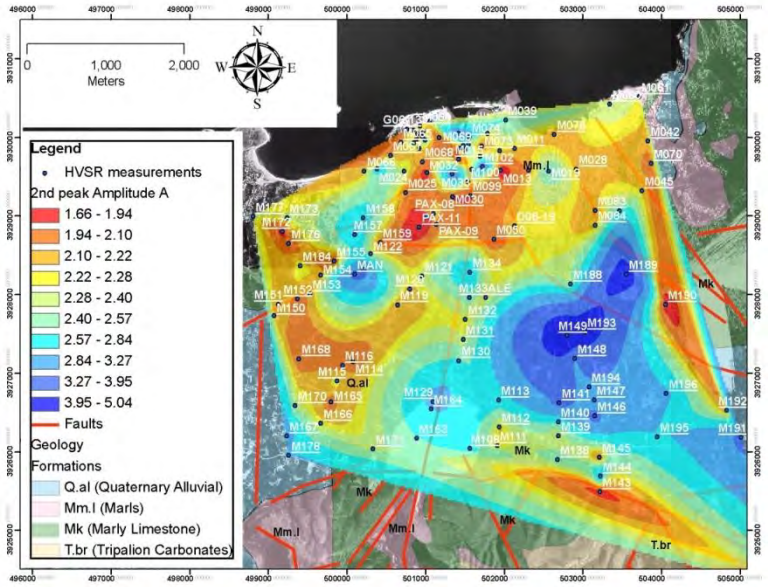

Figure 5 –Spatial distribution of the amplitude corresponding to the higher frequency defined from HVSR measurements within the broader Chania area.

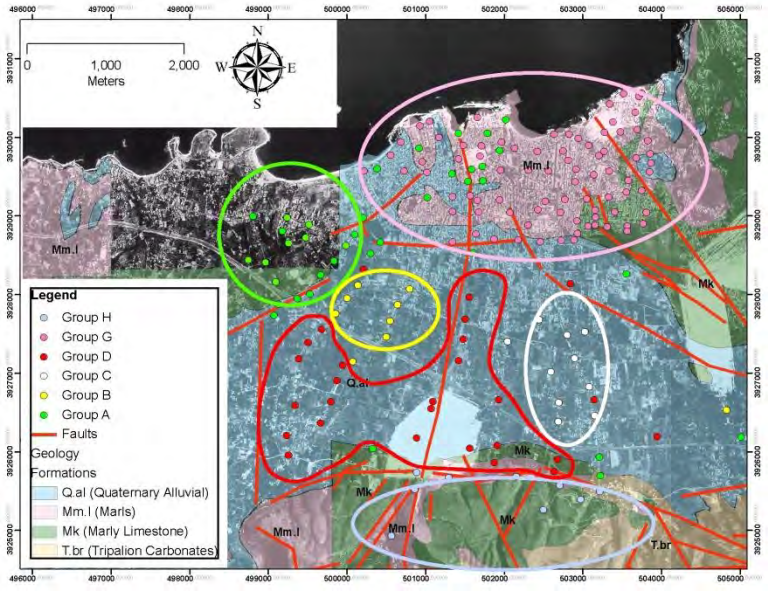

Figure 6 – Spatial grouping of HVSR measurements in the broader Chania area, performed on the basis of the HVSR curve similarity.

4.2. Parametric Investigation Results

HVSR curves were correlated on the basis of their similarity into groups, in order to define patterns possibly reflecting the local geological formations. Six (6) groups of HVSR curves have been identified and for each group a parametric investigation was performed using Hisada's method in an attempt to estimate the 1-D model of geological formations for each HVSR group. In Figure 6 the grouping of measurements is presented, showing each area in different colours. Group H represents all measurements with no significant amplification or amplification in frequencies

above 12 Hz, mainly identified in the mountainous area at the South, which can be considered as typical for a rock formation. For all other groups, we considered 1-D models for Hisada's calculation of theoretical transfer function. The S-wave velocities employed for these models were derived from independent results (Papadopoulos, 2013), using ambient noise array recordings, which show velocities of the order or 300m/s for Quaternary formations and between 700 (shallower) and 1700m/s (deeper) for Neogene formations (mainly marls), with an average velocity of ~1100m/s. Using these velocities as a base for all models, we allowed the Quaternary/Neogene and Neogene/bedrock interfaces to vary, in order to allow the synthetic HVSR curves to match the observed ones. A typical example is presented in Figure (7), where the fit of the synthetic HVSR against observed ones is presented for groups A and G. In general, the modelling allows the efficient simulation of the observed HVSR data, suggesting that their features, especially the higher HVSR frequencies can be efficiently explained by the determined 1-D of each sub-area.

The final modelling results are presented in Table 1, showing 2-layer formations in the area covered by the city of Chania (Neogene sediments-bedrock, groups G), and 3-layer geological formations in the basin or the hill area west of the city complex (Quaternary deposits-Neogene sediments-bedrock, groups A, B, C and D). The results show a single clear peak in frequency for Group H, covering the urban area, with a 1D model of Neogene sediments overlying the bedrock. The remaining four models describing the basin geology consist of two layers over bedrock, showing a second peak in frequency that varies, depending on the thickness of the upper layer of mainly Quaternary (locally softer Neogene) deposits. In general the amplitude of a two-peak HVSR curve is low, making the peak identification more difficult; however their presence is still evident, confirming the presence of a velocity contrast between the sedimentary formations (typically Quaternary/Vs~300m/s against stiffer Neogene/Vs~1100m/s layers).

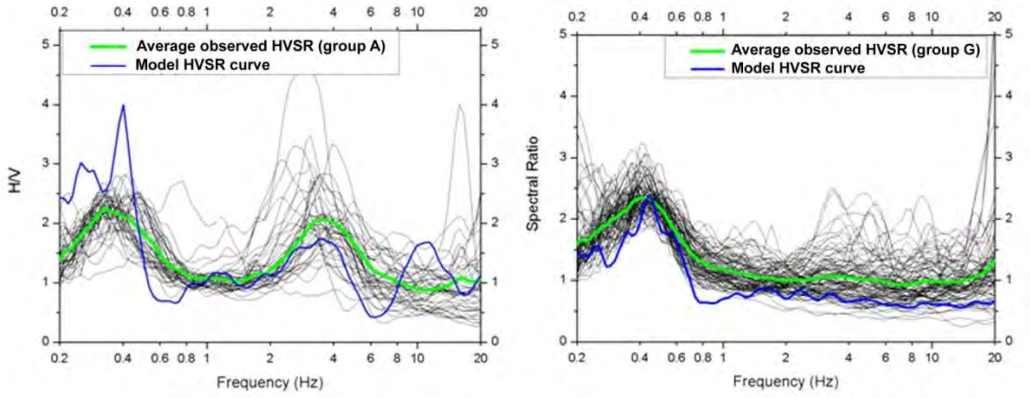

Figure 7 - Theoretical and observed HVSR curves for the spatial HVSR groups A and G, as these are presented in figure 6. Notice the fit of the higher frequency peak for group A, as a result of the presence of shallower low-velocity Quaternary/Neogene formations, and the fit of the fundamental frequency peak ~0.4-0.5 Hz for both groups (see also Table 1).

5. Conclusions

We have studied the complex geological environment of the broader area of the city of Chania, using HVSR measurements that were conducted in order to define the resonance frequency of sediments overlying the bedrock formations (typically Trypalion and Plattenkalk limestones) and estimate the general structure of the main geological formations (Quaternary and Neogene deposits) of the broader area. Results show that for the whole area a peak can be observed in the HVSR curves at a low frequency, around 0.4-0.6 Hz, associated with the velocity contrast between sediments of unknown thickness and the geological/seismic bedrock. A second peak in higher

frequency appears in the Chania basin, ranging between 0.8-4 Hz, which has been interpreted as the result of the impedance difference between the low velocity Quaternary deposits that cover the basin and the underlying Neogene sediments with higher velocity. Amplitude of the peak frequencies is in the vicinity of 1.5-3.5 for the lower frequency peak and 1.6-2.8 for the higher frequency peak, except for the centre of the basin, where it rises to values of 4-6 and 3-5, respectively.

Simulation of ambient noise confirmed in general the results by calculating the theoretical transfer function using Hisada's method, and providing an estimation of the thickness of the various formations. For all simulations Quaternary deposits have an average velocity of 300 m/sec, overlying Neogene sediments with velocity around 1100 m/sec and bedrock appears with velocity of 3500 m/sec, as controlled by independent noise array results. Simulation shows that when a two-layer over bedrock model is used, a second peak appears in the HVSR curve, as long as the impedance contrast between the sediments is high enough. At higher frequency (over 6 Hz) a third peak appears in the simulation that does not exist at the experimental HVSR curve, which is interpreted as a result of the multiple reflections of the surface waves that is not present in actual HVSR curves, due to model deviations from the 1D structure. The simulation results verify that the higher peak frequency decrease observed for the central part of the Quaternary Chania basin is due to an increase of the thickness of the Quaternary deposits, with group C depicting the higher Quaternary formation thickness of ~100m (see Table 1), while other models depict significantly lower estimates (e.g. 20m for group A). On the other hand, the Neogene thicknesses vary between 500 and 800m, verifying the dominant presence of Neogene formations (mainly marls and marly limestones) above bedrock, in excellent agreement with geological observations and models.

Table 1. Geological models used for the simulation of HVSR curves.

Group	Formation	Vp (m/sec)	Vs (m/sec)	H (m)	Qp	Qs	ρ (gr/cm^3)
A	Quaternary	460	300	20	30	15	1.9
	Neogene	2000	1100	800	90	30	2.0
	Bedrock	5400	3500	-	300	90	2.1
B	Quaternary	800	500	80	30	15	1.9
	Neogene	2500	1100	800	90	30	2.0
	Bedrock	5400	3500	-	300	90	2.1
C	Quaternary	460	300	100	30	15	1.9
	Neogene	2100	1100	500	90	30	2.0
	Bedrock	5400	3500	-	300	90	2.1
D	Quaternary	460	300	60	30	15	1.9
	Neogene	2000	1100	800	90	30	2.0
	Bedrock	5400	3500	-	300	90	2.1
G	Neogene	2300	1400	750	90	30	2.0
	Bedrock	5400	3500	-	300	90	2.1

6. Acknowledgments

This work has been partly financed by the PYTHAGORAS research project of the Hellenic Ministry of Education (Research Committee of Aristotle University Thessaloniki proj. #21945#).

7. References

Bastelli G. 2002. Microzonazione di Chania (Creta), *Tesi di laurea,* Universita degli Studi della Basilicata (in Italian)

Bard P-Y, Duval AM, Lebrun B, Lachet C, Riepl J and Hatzfeld D. 1997. Reliability of the H/V technique for site effect measurement: an experimental assessment, *17th International conference on soil dynamics and earthquake engineering, Istanbul,* 19–24 July 1997.

Bard P.-Y. 1999. Microtremor Measurements: A tool for site effect estimation*?, In The Effects of Surface Geology on Seismic Motion,* 1251-1279, ed. Irikura, Kudo, Okada and Sasatani, Balkema, Rotterdam.

Bonnefoy-Claudet S., Köhler A., Cornou C., Wathelet M. and Bard P.Y. 2008. Effects of Love waves on microtremor H/V ratio. *Bulletin of the Seismological Society of America*, 98(1), 288-300.

Cornou C, Guillier B, Kristek J, Bonnefoy-Claudet S, Bard P.Y, Faeh D. and Moczo P. 2006. Simulation of seismic ambient vibrations: does the H/V provide quantitative information in 2D–3D structure, *Proceedings of the third international symposium on the effects of surface geology, Grenoble (France),* August 30–September 1, 2006, paper # 153

Field E. and Jacob K. 1995. A comparison of Various Site-Response Estimation Techniques, Including three that are not Reference-Site Dependent, *Bull. Seismol. Soc. Am.,* 85, 1127–1143.

Haghshenas E., Bard P.Y. and Theodulidis N. 2008. Empirical evaluation of microtremor H/V spectral ratio, *Bulletin of Earthquake Engineering*, 6(1), 75-108.

Hisada Y. 1994. An efficient method for computing Green's functions for a layered halfspace with sources and receivers at close depths, *Bull. Seism. Soc. Am*., 84, 5, 1456-1472.

Hisada Y. 1995. An efficient method for computing Green's functions for a layered halfspace with sources and receivers at close depths (Part 2), *Bull. Seism. Soc. Am.,* 85, 4, 1080-1093.

Horike M., Zhao B. and Kawase H.2001. Comparison of site response characteristics inferred from microtremor and earthquake shear waves, *Bull. Seism. Soc. Am., 91, 1526–1536.*

Konno K., and Ohmachi T. 1998. Ground-motion characteristics estimated from spectral ratio between horizontal and vertical components of microtremor, *Bull. Seism. Soc. Am.,* 88, no. 1, 228–241.

Luco J.E. and Apsel R.J. 1983. On the Green's functions for a layered half-space, part 1, *Bull. Seism. Soc. Am* . 73, 909-929.

Maresca R., Castellano M., DeMatteis R., Saccorotti G. and Vaccariello P. 2003. Local Site Effects in the town of Benevento (Italy) from Noise Measurements, *Pure Appl. Geophys.,* 160, 1745–1764.

Moczo P. and Kristek J. 2002. FD code to generate noise synthetics, *SESAME EVG1-CT-2000-00026 project, Deliverable D02.09, 31 p,* http://SESAME-fp5.obs.ujf-grenoble.fr.

Nakamura Y. 1989. A method for dynamic characteristics estimation of subsurface using ambient noise on the ground surface*, QR Railway Tech. Res. Inst., 30, 25-33.*

Nogoshi M. and Igarashi T.1970. On the propagation characteristics of microtremors. *J. Seism. Soc. Japan*, 23, 264-280.

Papadopoulos H. 2013. Experimental and theoretical study of the local site-effect amplification using microtremor recordings and field geophysical measurements, *Ph.D. Thesis,* Geophysical Laboratory, Aristotle Univ. Thessaloniki, 411pp.

Δελτίο της Ελληνικής Γεωλογικής Εταιρίας, τομ. XLVII , 2013
Πρακτικά 13ου Διεθνούς Συνεδρίου, Χανιά, Σεπτ. 2013

Bulletin of the Geological Society of Greece, vol. XLVII 2013
Proceedings of the 13th International Congress, Chania, Sept. 2013

COSEISMIC STRESS DISTRIBUTION ALONG ACTIVE STRUCTURES AND THEIR INFLUENCE ON TIME-DEPENDENT PROBABILITY VALUES

Paradisopoulou P.[1], Papadimitriou E.[1], Mirek J.[2] and Karakostas V.[1]

[1] *Geophysics Department, School of Geology, Aristotle University of Thessaloniki, GR54124, Thessaloniki, Greece, ppara@geo.auth.gr, ritsa@geo.auth.gr, vkarak@geo.auth.gr*

[2] *Faculty of Geology, Geophysics and Environmental Protection, AGH University of Science and Technology, Krakow, Poland, jmirek@seismo.geol.agh.edu.pl*

Abstract

Based on the fact that stress changes caused by the coseismic slip of strong events can be incorporated into quantitative earthquake probability estimates, the goal of this study is to estimate the probability of the next strong earthquake (M≥6.5) on a known fault segment in a future time interval (30 years). The probability depends on the calculation of ΔCFF and the estimate of the occurrence rate of a characteristic earthquake, conditioned to the elapsed time since the previous event. The Coulomb stress changes caused by previous earthquakes are computed and their influence are considered by the introduction of a permanent shift on the time elapsed since the previous earthquake or by a modification of the expected mean recurrence time. The occurrence rate is calculated, taking into account both permanent and temporary perturbations. The estimated probability values correspond to the probabilities along each fault segment with discretization of 1km, illustrating the probability distribution across the specific fault. In order to check whether the estimated probability vary with depth, all the estimations were performed for each fault at depths of 8, 10, 12 and 15 km.

Key words: *Faults, strong earthquakes, renewal process, Greece.*

Περίληψη

Στόχος της παρούσας εργασίας είναι η εκτίμηση της πιθανότητας γένεσης ισχυρών σεισμών (M≥6.5) στα ενεργά ρήγματα της Ελλάδας και της ευρύτερης περιοχής της. Πιο συγκεκριμένα δίνεται η κατανομή της πιθανότητας κατά μήκος και ανά 1km σε κάθε ενεργό δομή που συνδέεται με κάποιο ισχυρό σεισμό (M≥6.5). Για να γίνει εκτίμηση της πιθανότητας λήφθηκε υπόψη η μεταβολή της τάσης που προκύπτει μετά από κάθε ισχυρό σεισμό και η οποία έχει ως αποτέλεσμα να επιταχύνει ή να επιβραδύνει τη γένεση ενός επόμενου σεισμού. Γίνεται δηλαδή ενσωμάτωση των μεταβολών των τάσεων στη χρονικά εξαρτώμενη πιθανότητα, με σκοπό να δειχθεί κατά πόσο μία μεταβολή στην τάση συμβάλλει στη διαδικασία του να γίνει ένας σεισμός σ' ένα ρήγμα. Το μοντέλο της δεσμευμένης πιθανότητας είναι αυτό που χρησιμοποιήθηκε για τους υπολογισμούς οι οποίοι γίνονται για τα επόμενα 30 χρόνια. Οι υπολογισμοί πραγματοποίηθκαν σε διάφορα βάθη (8, 10, 12 και 15km) για να ελεγχθεί κατά πόσο μεταβάλλονται οι τιμές των πιθανοτήτων, οι οποίες παρουσιάζονται σε χάρτες για την άμεση οπτική αντίληψη της χωρικής κατανομής τους.

Λέξεις κλειδιά: *Ενεργά ρήγματα, ισχυροί σεισμοί, περίοδος επανάληψης, Ελλάδα.*

1. Introduction

Studying the distribution of strong (M>6.5) historical and recent earthquakes it is found that they may occur on the same fault (after a time recurrence) or in adjacent faults activated by previous earthquakes. Fault interaction along with the time and space where an earthquake can occur led to the development of many methodologies, one of which being the incorporation of stress changes to the calculation of earthquake probabilities. The so-called Coulomb stress changes resulting from coseismic slip strongly affect the time and the location of subsequent events (mainshocks or aftershocks) making stress changes a useful tool for indentifying risk areas.

The field of time dependent models for earthquake probability estimations were introduced, based on various geologic and geophysical data such as fault slip rates, the interevent times of prior strong earthquakes (e.g., Working Group on California Earthquake Probabilities, 1990). Stress triggering and fault interaction are also starting to be incorporated into time-dependent earthquake probability estimates by Stein et al., 1997; Toda et al., 1998; Working Group on California Earthquake Probabilities, 1999; Parsons et al., 2000.

Following these methodologies Paradisopoulou et al. (2010a) used 67 strong earthquakes ($M \geq 6.5$) that occurred in Greece and its adjacent areas since the beginning of 20th century (instrumental era) and calculated the coseismic stress changes due to these earthquakes. Incorporating the effect of stress change into the time–depended probability estimates using an earthquake nucleation constitutive relation, which includes both permanent and transient effects of stress changes the probability during the next years, was calculated in each known fault of the study area. The present study is a step forward in the application of the same methodology. The goal here is to calculate probabilities along each fault of the study area with discretization of 1km, illustrating the probability distribution across the specific fault. In order to demonstrate whether the estimated probabilities vary with depth, all calculations were performed in each case at depths of 8, 10, 12 and 15 km. Probability calculations were carried out and given for the entire study area during the next 30 years.

2. Coseismic Stress Changes

Static stress change is a mechanism of earthquake triggering. “Triggering” has the meaning that one earthquake causes another earthquake which would not have otherwise occurred at that time. Rupture perturbs the state of stress on neighboring faults that in turn “encourages” or “suppresses” earthquakes on adjacent faults depending on the increase or decrease of stress. Our study uses the assumption that an earthquake can be modeled as a moving dislocation in an elastic half space (Okada, 1992) enabling estimation of stress transfer to other faults. Earthquakes occur when stress exceeds the strength of the fault. The closeness to the failure is quantified using the change in Coulomb failure function (ΔCFF). The Coulomb failure stress change is given by eq. 1:

Equation 1 - Coulomb failure stress change formulation

$$\Delta CFF = \Delta\tau + \mu(1 - B)\Delta\sigma$$

where $\Delta\tau$ is the change in shear stress on a fault, $\Delta\sigma$ is the change in normal stress, μ is the friction coefficient and B is the Skempton’s coefficient (in this study we assume μ =0.75 and B=0.5 as in Robinson and McGinty, 2000 among others). $\Delta\sigma$ and $\Delta\tau$ are calculated for a fault plane at the observing (field) point. For increasing shear stress in the direction of relative slip on the observing fault $\Delta\tau$ is positive. $\Delta\sigma$ is positive for tensional normal stress. The shear modulus and Poisson’s ratio are fixed at $3.3 \cdot 10^5$ bar and 0.25, respectively. Coulomb stress changes are calculated according to the geometry of the target fault, which is the fault of the anticipated strong earthquake, and at the appropriate depth. In our study area it is known that the majority of the foci of the

crustal earthquakes are located in the depth range of 3 to 15 km, which defines the brittle part of the crust. Considering all the above information the seismogenic layer in our calculations is taken to be in this range for all the strong events (M≥6.5) modeled.

3. Earthquake Probability Estimation

In this section we estimate the probabilities for the occurrence of future strong (M>6.5) events along the fault segments associated with events of M>6.5 that occurred either during the instrumental period or in the past centuries and for which information exists. The adequate proposed methodology followed is that by Stein et al. (1997), Toda et al. (1998) and Parsons (2000, 2004, 2005) who support an earthquake renewal process in which the probability of a future event grows as the time of previous event increases considering both permanent and transient effects of the stress changes on earthquake probabilities. To calculate such a renewal probability, ideally, one needs an earthquake catalog containing several strong events on each fault to deduce earthquake magnitudes, the mean interevent time of similar events, and the elapsed time since the last shock on each fault.

3.1. Probability Models

Two models for earthquake probabilities estimates are generally in use: the stationary Poisson model and the conditional probability model (Cornell et al., 1968; Hagiwara, 1974). Using both of the mentioned models we estimate the probability of an earthquake to occur in the next 30 years from 2012.

Poisson model: This model is one that treats earthquakes as occurring randomly in time (t) about a mean recurrence interval (T_r). The probability of at least one event in the time interval (t, t+Δt) is given by:

Equation 2 - Poisson probability model

$$P(t \le T \le t + \Delta t) = 1 - e^{-\Delta t / T_r}$$

Conditional Probability model: This model is time-dependent and includes knowledge of the time elapsed since the last event and may also include the effects of a given stress change. Following Working Group of California Earthquake Probabilities (1988) the probability that an earthquake will occur at time T in the interval (t, t+Δt) is:

Equation 3 - Conditional probability formulation

$$P(t \le T \le t + \Delta t) = \int_t^{t+\Delta t} f(t)dt$$

Where f(t) is the probability density function for the earthquake occurrence. We assume a lognormal probability distribution of recurrence time (e.g. Nishenko and Buland, 1987):

Equation 4 - Probability density function for lognormal distribution

$$f(t, \alpha, \beta) = \frac{1}{\beta t \sqrt{2\pi}} \exp\left[\frac{-(\ln \frac{t}{\alpha})^2}{2\beta^2} \right]$$

where $\beta^2 = \ln(\frac{s_t^2}{T_r^2} + 1), \alpha = \ln\left[T_r \exp(-0.5\beta^2)\right]$, T_r is the average interevent time, s_t: the standard deviation of interevent time. The probability conditioned on the fact that the earthquake has not occurred prior to t is:

Equation 5 - Conditional probability (an earthquake not occurring prior to t)

$$P(t \le T \le t + \Delta t \mid T > t) = \frac{P(t \le T \le t + \Delta t)}{P(T \ge t)}$$

3.2. Incorporating Stress Changes into Earthquake Probability Calculations

3.2.1. Permanent effect of stress change: To include the permanent effect of a stress change (ΔCFF), an assumption is made that a sudden stress increase (or decrease) linearly shortens (or lengthens) the time until the next earthquake. The advance or delay, termed a clock change (T′), can be calculated by dividing the stress change by the tectonic stressing rate ($\dot{\tau}$): T′=ΔCFF/ $\dot{\tau}$. Thus, an adjusted time by the clock change is taking into account and the conditional probability is now equal to:

Equation 6 - Static probability change formulation

$$P_c(t_1) = \frac{\int_{t_1}^{t_1+\Delta t} f_t(t + T')dt}{\int_{t_1}^{\infty} f_t(t + T')dt}$$

3.2.2. Transient probability change: The method is based on the model of Dieterich (1994), which incorporates changes in stress caused by a prior earthquake to changes in seismicity rate. The transient change in expected earthquake rate R(t) after a stress step can be related to the probability of an earthquake of a given size over the time interval Δt (30 years in this study) through a non stationary Poisson process as (Dieterich and Kilgore, 1996):

Equation 7 - Transient probability change formulation

$$P(t, \Delta t) = 1 - \exp\left[-\int_t^{t+\Delta t} R(t)dt\right] = 1 - \exp\left[-N(t)\right]$$

Integrated for N(t) yields:

Equation 8 - The expected number of earthquakes in the interval Δt

$$N(t) = r_p \left\{ \Delta t + t_\alpha \ln \left[\frac{1 + \left[\exp(-\frac{\Delta CFF}{A\sigma}) - 1 \right] \exp\left[\frac{-(\Delta t)}{t_\alpha} \right]}{\exp\left(\frac{-\Delta CFF}{A\sigma} \right)} \right] \right\}$$

Where t_α is the characteristic duration of the transient effect, σ, is the normal stress, A, is a fault constitutive constant and ΔCFF is the calculated Coulomb stress change. Note that the transient effect disappears if ΔCFF=0, that is $N=r_p \cdot \Delta t$. r_p is the expected rate of earthquakes associated with the permanent probability change (Toda et al., 1998). This rate can be determined again by applying a stationary Poisson probability expression as:

Equation 9 - Permanent background component of earthquake rate

$$r_p = -\frac{1}{\Delta t} \ln\left[1 - P_c\right]$$

where P_C is the conditional probability taken from eq. 6.

4. Input Parameter Calculations

Mean interevent time (T_r). For the calculation of time dependent probability of an earthquake of a given magnitude (in our case M≥6.5 under the renewal model), it is necessary to know or to estimate the mean interevent time and the time elapsed since the last earthquake of comparable size. These parameters are most commonly drawn from historic and paleoseismic record. Historical information is mainly taken from Papazachos and Papazachou (2003), Ambraseys and Jackson (2000) and Ambraseys (2002). For some faults information is taken from specific published works and used for assigning T_r onto them. Results on paleoseismic records on the North Anatolian Fault (NAF) are given by Rockwell et al. (2001), Klinger et al. (2003), Parsons, 2004, Palyvos et al. (2007), Pondard et al. (2007), Kurcer et al. (2008), Pantosti et al. (2008), which support Tr~207 - 275years. In the area of Corinth Gulf, for Eliki's (S43) and Xylokastro (S44) fault, mean interevent times of 242±60 and 119±20 years, respectively, was found (Briole et al., 2000; Koukouvelas et al. 2001). Collier et al. (1998) give a calculated mean interevent time equal to 330 years. Pavlides et al. (2004) suggest a mean interevent time of 1000 years on Atalanti's fault whereas Pantosti et al. (2004) estimated for the same fault 660-1200 years (faults S59-S61). In cases where only one or two events were reported for a particular fault segment, the interevent times are set equal to 500 years.

Rate and state parameters. Two parameters must be chosen for use of the rate- and state-dependent model of Dieterich (1994). The one is the tectonic stressing rate ($\dot{\tau}$) which is obtained directly from the chosen yearly slip rate for each fault segment. For parts of North Anatolian Fault, is found equal to 0.04-0.25bar/yr with a mean value 0.10 bar/yr. These values are in agreement with the ones from Stein et al. (1997), who estimated a value of 0.15bar/yr along most of the NAF system and from Parsons et al. (2000) and Parsons (2004) who proposed 0.1-0.064 bar/yr. For the remaining part of the study area the values of stressing rate are in the range of 0.003-0.25 bar/yr.

The second parameter is the duration of transient effect t_α. Following Dieterich (1994) we set t_α equal to 10% of the minimum mean interevent time. Thus, for the area of North Anatolian fault t_α=25 yr, considering a minimum return period of 250 years. For the same area a regional aftershock decay time for M>6.7 earthquakes was found to be ~35 years by Parsons et al. (2000). A value of t_α=50 yr was set for the rest part of our study area due to the longer observed interevent times (~ 500 years). For the southern part of Corinth Gulf the t_α was set equal to 30 years and for the Ionian Sea equal to 10 years due to the more frequent occurrence of such events in these areas.

5. Discussion and Conclusions

Until now the probability estimations were performed (Paradisopoulou et al., 2010a, b) for one value (minimum, maximum or average) of ΔCFF not allowing us to discriminate the exact location of this value on the fault (Figure 1). In this study, probabilities are calculated taken into account Coulomb stress changes along each fault at points with 1km spacing between them, and in four different depths onto the fault, thus giving us the advantage to observe the probability value and the stress influence at every fault patch.

5.1. Assumptions on Calculations

Some assumptions are made in this study and concern both stress calculation and probability estimation. At the outset, all stress calculations are performed in a homogeneous elastic half space and require a coefficient of friction (μ) and the Skempton's coefficient (B). An additional assumption of stress change calculation uncertainty is the dip and rake angles of the target fault which are known approximately, e.g. from surface projection, or they are defined from structural information or by moment tensors or focal mechanisms. In all cases there are uncertainties that lead to variation in stress change calculations. An effort was made in order to investigate to which extend the uncertainties, involved in the fault parameters, influence the calculated stress pattern by Paradisopoulou et al. (2010a). The correlation between calculated stress changes and different val-

ues of Skempton's coefficient (B), rake and dip angle of the fault are tested following the technique of Parsons (2005).

To pass from stress changes to probability estimations a second set of assumptions was done based on historical, paleoseismic data (needed for the calculation of T_r and elapsed time) and geodetic data (required for estimation of stressing rate, $\dot{\tau}$). These assumptions are necessary for the permanent probability change calculation due to advance or delay of time until the next earthquake. The conditional probability model using, in our case, the lognormal distribution, intrinsically involves uncertainties on the mean earthquake interevent time (T_r) and on the elapsed time.

For the dominant transient effect of the stress changes on earthquake probability, rate-state constitutive relations were applied, which require parameters such as t_α (aftershock duration) and Aσ (a state parameter). We assume, according to seismicity of each subarea of the study area and the mean recurrence time (Dieterich, 1994) that t_α is equal to 10% of T_r. With given values of the parameters t_α and $\dot{\tau}$, the Aσ was calculated using the equation: $A\sigma=t_\alpha \cdot \dot{\tau}$. The stressing rate $\dot{\tau}$ is related with the time, T΄, and therefore it could for example lead to smaller clock changes for a given stress change, and hence to smaller probability values. For this reason several values of $\dot{\tau}$ were used for each fault zone as already mentioned.

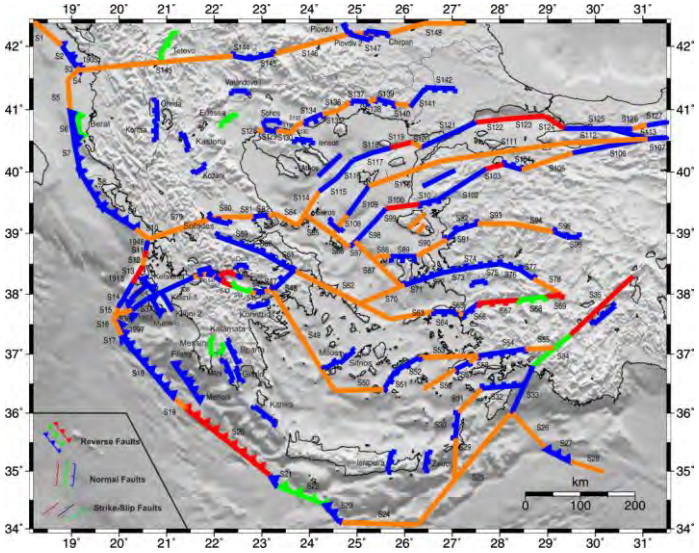

Figure 1 - Map of estimated time dependent probabilities for the occurrence of an earthquake with magnitude M≥6.5 for the next 30 years (after 2009), on each fault segment of the study area (modified from Paradisopoulou et al., 2010b). High probabilities are shown with red color, and lower values with green and blue colors. Orange color is corresponding to the faults for which no probability value is estimated.

5.2. Results

Detailed earthquake occurrence probabilities are provided by gridding the target fault areas and performing calculations on the nodes of the grid spacing 1km (Figures 2). In these figures, green colors denote faults where the probability values are low (P<0.09) due mostly to the effect of negative changes in Coulomb stress. Yellow to red colors represent higher probability values (0.09 ≤ P < 0.30 and P≥0.30, respectively) due mainly to positive ΔCFF values on these faults. The entirely green lines represent faults that have already failed whereas red lines correspond to faults that are candidate to host an incoming earthquake. Additionally to the effect of stress step (ΔCFF), rate and state parameters such as the duration of transient effect (t_α), the stressing rate ($\dot{\tau}$), mean interevent time (T_r) and elapsed time have influence to the results. Thus, for some faults illustrated

by yellow to red (or green) color, the probability changes are generally significant (or negligible) only for time intervals which are short (or long) compared to the repeat time of the fault. As far as the depth dependence concerns, there are no significant differences between the values corresponding to different chosen depths (e.g. ±0.03 for S122, ± 0 for S123, ± 0.016 for S124, ± 0 for 125, ± 0.0016 for Tetovo and ± 0.046 for SW Crete).

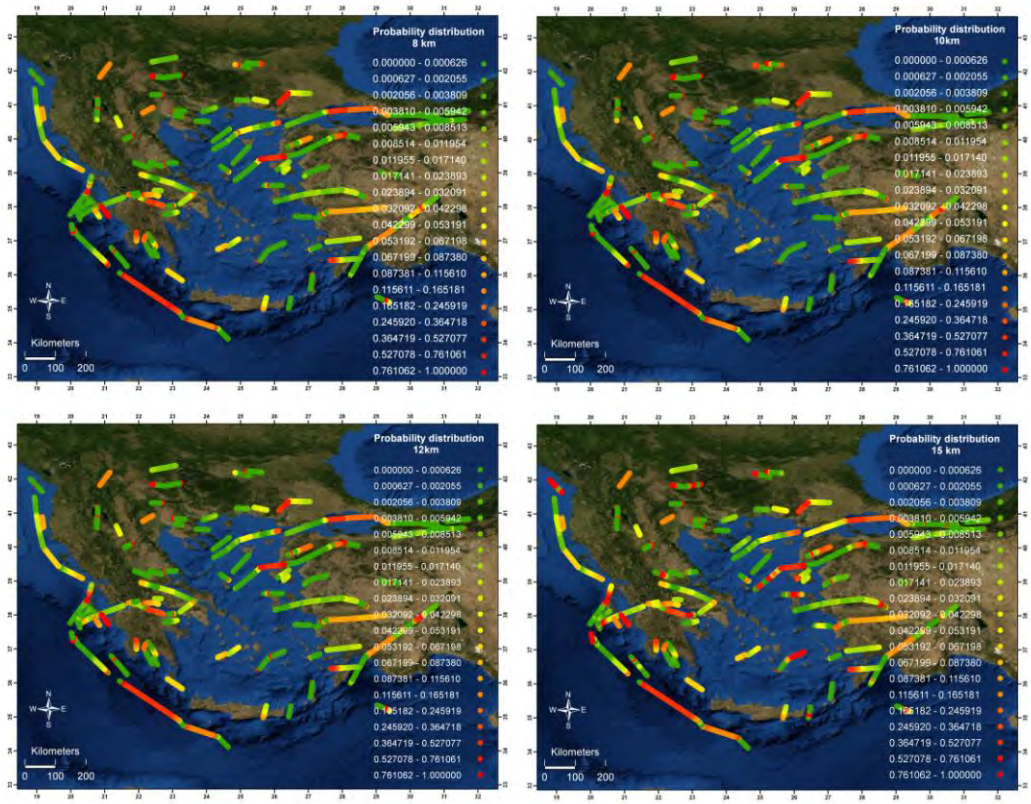

Figure 2 – Probability distribution along each fault of the study area. Calculations were performed at 8km, 10 km, 12km and 15km depth. Colors between green and yellow correspond to low probability values (P<0.09) and colors between yellow and red indicate higher probability values (0.09 ≤ P < 0.30 and P≥0.30).

Observing the probability values (Figure 2), unusually high ones (red color) were found at the edges of some faults. More precisely, neighbouring faults such as S95–S96, S122-S123-S124, S144 – S145, Plovdiv 2 – Chirpan, Sohos – S129 and individual faults such as Filiatra, Ohrida, S125, Valandovo, Kozani, S30, S35, S37, S77, S82, display low probability values while the faults boundaries exhibit one or more values that exceed the 80%. These values are uncertainties that introduced to the calculations due to the effect of stress changes. The method of calculating probabilities with the use of 1km grid onto the fault, enabling us to reduce any contingency to the estimated values. Figure 3 exemplifies the graphs of 30-years conditional probability along the fault, for six segments (S22 (south Crete), S122, S123, S124, S125 (Izmit) and S144 faults). The counting on x-axis starts from the left edge of each fault. All plots represent a further illustration (addition to Figure 2) of probability grid along the faults. Taking into account the above, the following results may be drawn:

a) There are some distinct values which can contaminate our results; therefore they can easily be removed for calculation improvement. Notice that these discrete values are observed at the fault boundaries (focus for example on S22 fault) and see in more detail

that the probabilities are under the influence of stress transfer between adjacent faults. S22 fault is located between two faults that have already ruptured and hence large values of ΔCFF and consequently higher probability values displayed at S22 edges.

b) Generally the probability results are more correctly and acceptable due to fact that there is a range of estimated probability values onto the fault instead of one value (minimum, maximum, average). On S122 fault for example (at 10 km depth) probability values ranging from 0.008 to 0.40 and 0.50 at the most part of the fault, while 0.38 was the estimated mean probability for the entire fault using the average value of ΔCFF on permanent and transient effect.

Consequently the methodology used could be useful for identifying those areas or cities with enhanced probability for large and damaging mainshocks. Additionally if the aforementioned assumptions will be reduced the estimation of the earthquake probabilities has profound implications for seismic hazard analysis.

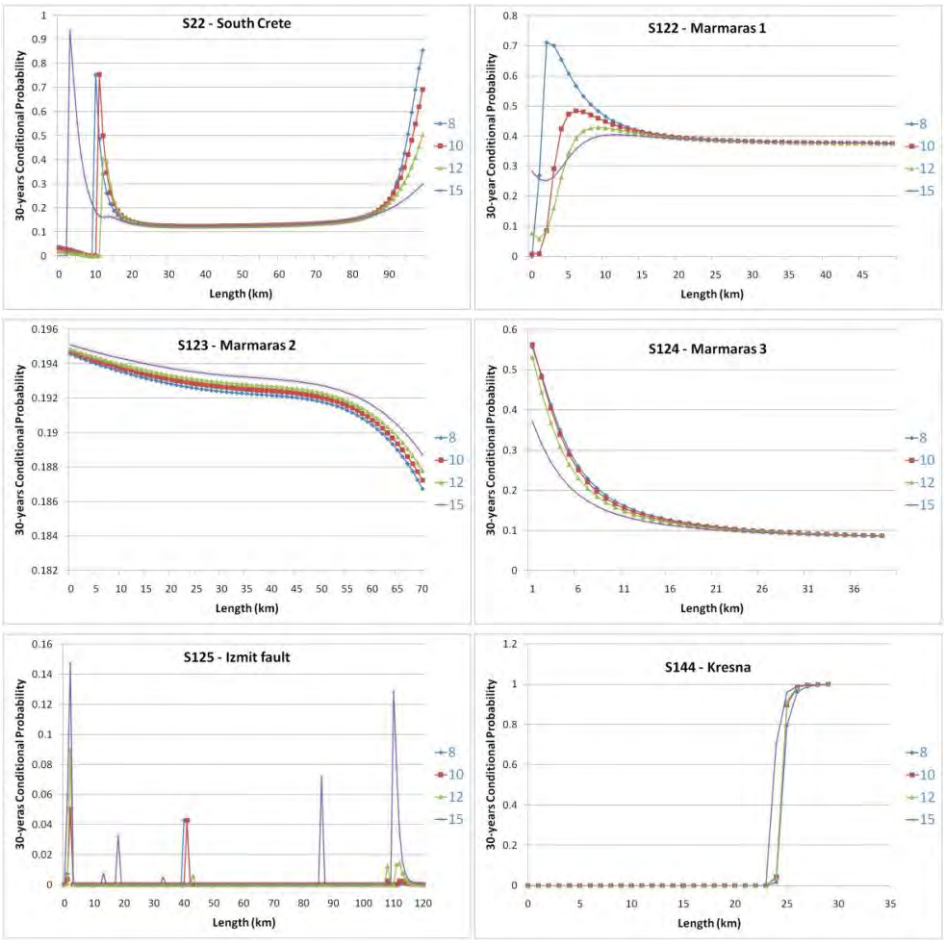

Figure 3 - Graph of 30 years estimated probability values along the strike of the fault for six faults of our data sample, indicating the uncertainties and singularities in probability distrib ution along the fault.

6. Acknowledgments

The stress tensors were calculated using a program written by J. Deng (Deng and Sykes, 1997) based on the DIS3D code of S. Dunbar, which later improved (Erikson, 1986) and the expressions of G. Converse. Maps are from ESRI. This work was partially supported by the research project 11.11.140.767 financed by the Polish State Committee for Scientific Research, AGH University of Science and Technology, Faculty of Geology, Geophysics and Environmental Protection. Geophysics Department contribution number 810.

7. References

Ambraseys N.N. 2002. The seismic activity of the Marmara Sea region over the last 2000 years, *Bulletin Seismological Society of America*, 92, 1-18.

Ambraseys N.N. and J. A. Jackson 2000. Seismicity of Marmara (Turkey) since 1500, *Geophysical Journal International,* 141, F1-F6.

Briole P., Rigo A. Lyon-Caen, H. Ruegg J.C., Papazissi K., Mitsakaki C., Balodimou A., Veis G., Hatzfeld D. and Deschamps A. 2000. Active deformation of the Corinth rift, Greece: Results from repeated Global Positioning System surveys between 1990 and 1995, *Journal of Geophysical Research 105, 605-625.*

Collier, R. E., Pantosti D., D'addezio G., De Martini P.M., Masana E. and Sakellariou D. 1998. Paleoseismicity of the 1981 Corinth earthquake fault: seismic contribution to extensional strain in central Greece and implications for seismic hazard, *Journal of Geophysical Research* 103, 30001-30019.

Cornell C.A., Wu S.C., Winterstein S.R., Dieterich J.H. and Simpson R.W. 1968. Seismic hazard induced by mechanically interactive fault segments, *Bulletin Seismological Society of America* 83, 436–449.

Dieterich J.H. 1994. A constitutive law for rate of earthquake production and its application to earthquake clustering, *Journal of Geophysical Research,* 99, 2601–2618.

Dieterich J. H. and Kilgore B. 1996. Implications of fault constitutive properties for earthquake prediction, *Proceedings of the National Academy of Sciences U.S.A,* 93, 3787–3794.

Hagiwara Y. 1974. Probability of earthquake occurrence as obtained from a Weibull distribution analysis of crustal strain, *Tectonophysics,* 23, 313-318.

Klinger Y., Sieh, K., Altunel, E., Akoglu, A., Barka A., Dawson T., Gonzalez T., Meltzner A. and Rockwell T. 2003. Paleoseismic Evidence of Characteristic Slip on the Western Segment of the North Anatolian Fault, Turkey, *Bulletin of Seismological Society of America,* 93, 2317–2332.

Koukouvelas I.K., Stamatopoulos L., Katsanopoulou D. and Pavlides S. 2001. A palaeoseismological and geoarchaeological investigation of the Eliki fault, Gulf of Corinth, Greece, *Journal of Structural Geology,* 23, 531-543.

Kurcer A., Chatzipetros A., Tutkun S. Z., Pavlides S., Ates O. and Valkaniotis S. 2008. The Yenic Gonen active fault (NW Turkey): Active tectonics and palaeoseismology, *Tectonophyics* 453, 263–275.

Nishenko S. P. and Buland R. 1987. A generic recurrence interval distribution for earthquake forecasting, *Bulletin Seismological Society of America*, 77, 1382–1399.

Okada Y. 1992. Internal deformation due to shear and tensile faults in a half space, *Bulletin of Seismological Society of America,* 82, 1018-1040.

Palyvos N., Pantosti D., Zabci C. and D' Addezio G. 2007. Paleoseismological evidence of recent earthquakes on the 1967 Mudurnu valley earthquake segment of the North Anatolian Fault zone, *Bulletin Seismological Society of America,* 97, 1646–1661.

Pantosti D., De Martini P.M., Papanastassiou D., Lemeille F., Palyvos N. and Stavrakakis G. 2004. Paleoseismological Trenching across the Atalanti Fault (Central Greece): Evidence for the Ancestors of the 1894. Earthquake during the Middle Age and Roman Times, *Bulletin Seismological Society of America,* 94, 2, 531-549.

Pantosti D., Pucci S., Palyvos N., De Martini P.M., D' Addezio G., Collins P.E.F. and Zabci C. 2008. Paleoearthquakes of the Düzce fault (North Anatolian Fault Zone): Insights for large surface faulting earthquake recurrence, *Journal of Geophysical Research* 113, doi: 10.1029/2006JB004679.

Papazachos B. C. and Papazachou C. 2003. *The earthquakes of Greece*, Ziti publications, Thessaloniki, 289 pp.

Paradisopoulou P.M., Papadimitriou E.E., Karakostas V.G., Taymaz T., Kilas A., and Yolsal S. 2010a. Seismic hazard evaluation in western Turkey as revealed by stress transfer and time-dependent probability calculations, *Pure and Applied Geophysics* doi: 10.1007/s00024-010-0085-1.

Paradisopoulou P.M., Papadimitriou E.E., Karakostas, V.G., Lasocki S., Mirek J. and Kilias A. 2010b. Influence of stress transfer in probability estimates of M≥6.5 earthquakes in Greece and surrounding areas 2010, *Bulletin of the Geological Society of Greece,* XLIII, 2114–2124.

Parsons T. 2004. Recalculated probability of M≥7 earthquakes beneath the Sea of Marmara, Turkey, *Journal of Geophysical Research,* 109, doi:10.1029/2003JB002667.

Parsons T. 2005. Significance of stress transfer in time–dependent earthquake probability calculations, *Journal of Geophysical Research,* 110, doi: 10.1029/2004JB003190.

Parsons T., Toda S., Stein R. S., Barka A. and Dieterich J.H. 2000. Heightened odds of large earthquakes near Istanbul: An interaction–based probability calculation, *Science,* 288, 661–665.

Pavlides S.B., Valkaniotis S., Ganas A., Keramydas D. and Sboras S. 2004. The Atalanti active fault: re-evaluation using new heological data, *Bulletin of the Geological Society of Greece* vol. XXXVI, *Proceedings of the 10th International Congress*, 1560-1567, Thessaloniki.

Pondard N., Armijo R., King, G. C. P., Meyer B. and Flerit F. 2007. Fault interactions in the Sea of Marmara pull–apart (North Anatolian Fault): earthquake clustering and propagating earthquake sequences, *Geophysical Journal International,* 171, 1185–1197.

Robinson R. and McGinty P.J. 2000. The enigma of the Arthur's Pass, New Zealand, earthquake. 2. The aftershock distribution and its relation to regional and induced stress fields, *Journal of Geophysical Research,* 105, 16139-16150.

Rockwell T., Barka A., Dawson T., Akyuz S. and Thorup K. 2001. Paleoseismology of the Gazikoy–Saros segment of the North Anatolia fault, northwestern Turkey: Comparison of the historical and paleoseismic records, implications of regional seismic hazard and models of earthquake recurrence, *Journal of Seismology,* 5, 433–448.

Stein R.S., Barka A.A. and Dieterich J.D. 1997. Progressive failure on the North Anatolian fault since 1939 by earthquake stress triggering, *Geophysical Journal International,* 128, 594-604.

Toda S., Stein R.S., Reasenberg P.A. and Yoshida A. 1998. Stress transferred by the 1995 Mw=6.9 Kobe, Japan shock: Effect on aftershocks and future earthquake probabilities, *Journal of Geophysical Research,* 124, 439-451.

Working Group on California Earthquake Probabilities (WGCEP), 1990. Probabilities of large earthquakes in the San Francisco Bay region, California, *U.S. Geol. Surv. Circ.* 1053, 51pp.

Working Group on California Earthquake Probabilities (WGCEP), 1999. Probabilities of large earthquakes in the San Francisco Bay region, California, *U.S. Geological Survey, Open File Report,* 99-517.

Δελτίο της Ελληνικής Γεωλογικής Εταιρίας, τομ. XLVII , 2013
Πρακτικά 13ου Διεθνούς Συνεδρίου, Χανιά, Σεπτ. 2013

Bulletin of the Geological Society of Greece, vol. XLVII 2013
Proceedings of the 13th International Congress, Chania, Sept. 2013

THE WEB PORTAL OF THE EUROSEISTEST STRONG GROUND MOTION DATABASE

Pitilakis K.[1], Roumelioti Z.[1], Manakou M.[1], Raptakis D.[1], Liakakis K.[2], Anastasiadis A.[1] and Pitilakis D.[1]

[1] Research Unit of Soil Dynamics and Geotechnical Earthquake Engineering, Department of Civil Engineering, Aristotle University of Thessaloniki, P.O. Box 424, 54124, Thessaloniki, Greece, kpitilak@civil.auth.gr, zroum@auth.gr, manakou@civil.auth.gr, raptakis@civil.auth.gr, anas@civil.auth.gr, dpitilak@civil.auth.gr

[2] Department of Physics, Aristotle University of Thessaloniki, 54124 Thessaloniki, Greece, kostas@physics.auth.gr

Abstract

Strong motion data that have been recorded during the 20-years of operation of the permanent network of EUROSEISTEST (Mygdonia basin, Northern Greece) have been homogenized and organized in an easily accessible, via the web, database. The EUROSEISTEST web portal and the application server running underneath are based solely on free and open source software (F/OSS; MySQL v5.5; RubyOnRails, SAC, Gnuplot and numerous GNU supporting utilities). Its interface allows the user to easily search strong motion data from approximately 200 events and 26 strong motion stations using event-related, record-related or station-related criteria. Further investigation of the data is possible in a graphical environment which includes plots of processed and unprocessed acceleration waveforms, velocity and displacement time histories, amplitude Fourier and response spectra and spectrograms. A great effort was directed toward the inclusion of accurate and most updated earthquake metadata, as well as a wealth of stations related information such as geotechnical and geophysical site characterization measurements, subsoil structure and site effects. Acceleration data can be easily downloaded in either SAC or ASCII format, while all stations metadata are also available to download.
Key words: *subsoil structure, site effects, Mygdonia.*

Περίληψη

Οι καταγραφές της εδαφικής επιτάχυνσης του πολυδύναμου πεδίου δοκιμών EUROSEISTEST (Μυγδονία λεκάνη, Βόρεια Ελλάδα), που έχουν συλλεχθεί κατά τη διάρκεια των 20 χρόνων λειτουργίας του, ομογενοποιήθηκαν και οργανώθηκαν σε μια εύκολα προσβάσιμη, μέσω του διαδικτύου, βάση δεδομένων. Η δικτυακή πύλη του EUROSEISTEST και όλες οι λειτουργίες του διακομιστή της έχουν σχεδιαστεί με αποκλειστική χρήση ανοιχτού λογισμικού (MySQL v5.5; RubyOnRails, SAC, Gnuplot, διάφορα άλλα GNU εργαλεία). Το γραφικό περιβάλλον της δικτυακής πύλης παρέχει τα κατάλληλα εργαλεία για την εύκολη αναζήτηση δεδομένων από τους 26 σταθμούς του μόνιμου δικτύου του EUROSEISTEST και τους 200 περίπου σεισμούς που έχουν καταγραφεί μέχρι σήμερα. Παρέχεται επίσης δυνατότητα επισκόπησης των δεδομένων μέσω εικόνων με χρονοϊστορίες της επιτάχυνσης, ταχύτητας και μετάθεσης, φάσματα

πλάτους Fourier, απόκρισης, καθώς και φασματογραφημμάτων. Ιδιαίτερη βαρύτητα έχει δοθεί στην υψηλή ποιότητα πληροφορίας των μετα-δεδομένων (σεισμών, σταθμών καταγραφής και εδαφικής δομής) που έχουν συμπεριληφθεί στη βάση. Όλα τα δεδομένα επιτάχυνσης του EUROSEISTEST και τα μετα-δεδομένα που αφορούν τον γεωτεχνικό-γεωφυσικό χαρακτηρισμό και την απόκριση του εδάφους στις θέσεις των σταθμών καταγραφής είναι διαθέσιμα μέσω της σχετικής δικτυακής πύλης.
Λέξεις κλειδιά: *δομή υπεδάφους, αποτέλεσμα εδαφικών συνθηκών, Μυγδονία.*

1. Introduction

EUROSEISTEST is a multidisciplinary European experimental site (e.g. Pitilakis et al., 2011) for integrated studies in earthquake engineering, engineering seismology, seismology, geotechnical engineering and soil dynamics. It is the longest running (for 20 years) basin-instrumentation project worldwide, and is located in the Mygdonia valley (epicentral area of the 1978, M6.4 earthquake), about 30km to the NE of the city of Thessaloniki in northern Greece (Figure 1). It consists of a 3D accelerograph array and an instrumented single-degree-of-freedom structure (EuroProteas), the latter to be used in studies of soil foundation – structure interaction studies.

Figure 1 – Location (triangle) of the EUROSEISTEST experimental site.

The initial development of EUROSEISTEST was mainly funded by the European Commission - Directorate General for Research and Development under the framework of consecutive EU research projects (EuroseisTest, 1993-1995; EuroseisMod, 1996-1999; Euroseisrisk, 2002-2005). In years after 2005, the maintenance and improvement of the array, as well as the construction of the EuroProteas structure, have been funded through resources of the Research Unit of Soil Dynamics and Geotechnical Earthquake Engineering (SDGEE, http://sdgee.civil.auth.gr) of the Aristotle University of Thessaloniki, as well as by several other European Union (e.g. SERIES, NERA) and international projects. The establishment and operation of the experimental site have been the responsibility of SDGEE with the contribution of the Institute of Engineering Seismology and Earthquake Engineering of the Earthquake Planning and Protection Organization of Greece (ITSAK-EPPO, http://www.itsak.gr), among other partners.

During its 20-years-long life, the permanent accelerograph network of EUROSEISTEST has recorded more than 190 events of local magnitude, M_L in the range 1.5-6.6 and at epicentral distances from 1 to 500 km. These events have provided circa 1000 three-component acceleration records, which along with stations and earthquakes metadata constitute a significant dataset, useful in different kinds of ground motion and site effects studies. These data and metadata were recently organized in a well-structured and easily extendable database, which is accessible through the internet at the web address http://euroseisdb.civil.auth.gr.

In this paper, we present an overview of the EUROSEISTEST database web portal aiming to describe its fundamental functions and thus further facilitate the dissemination of our data.

2. The Permanent Strong Motion Network of the EUROSEISTEST and its Database

The permanent strong motion network of EUROSEISTEST was initially designed as a linear array of instruments along the small axis (~north-south direction) of the Mygdonia graben, between the villages of Profitis and Stivos. In 2003, another branch was added, this time along the long axis of the graben, thus oriented ~east-west. Overall, 26 strong motion stations have operated in the area since the establishment of the network in 1993. Today, the permanent network includes 21 modern strong motion accelerographs, 15 of which are located at the ground surface and 6 in down-hole arrays at the centre and at the northern edge of the instrumented area (Figure 2).

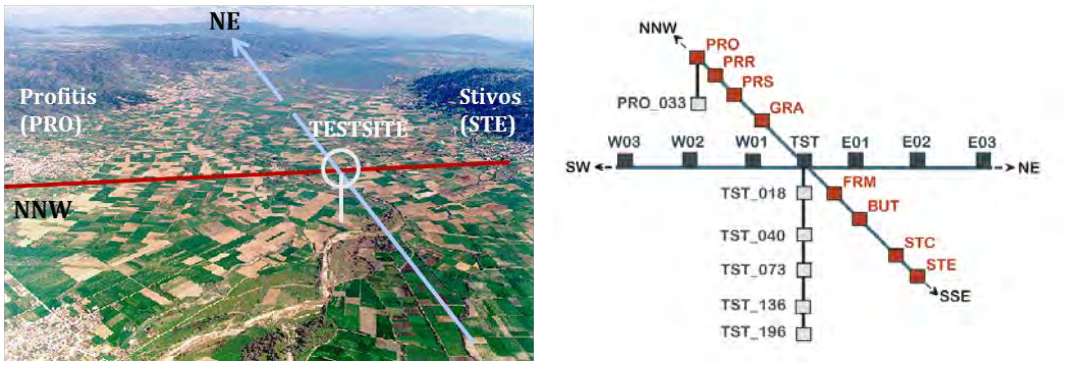

Figure 2 – The permanent accelerometric network of EUROSEISTEST. Left: Air photograph of the central part of the Mygdonia graben. The directions of the two branches of the surface array are noted as thick lines. The centre of the network (Test site) is the location of TST station and the deepest downhole array that reaches the underlying bedrock at circa 200m depth. Right: the current configuration of the EUROSEISTEST network with station codes.

Stations instrumentation has undergone many changes during the lifetime of the network. Initial installations included low resolution (12 and 16 bits) accelerographs without absolute timing (Global Positioning System, GPS). In 2003, when the east-west array was added, the entire network was upgraded with modern instruments of high resolution and GPS installed at all stations.

By the end of 2012, the network had recorded 190 events, which provided 997 three-component acceleration records. Most of the recorded events are from within and around the Mygdonia basin i.e. from epicentral distances, R, smaller than 50 km although the entire range of distances in the database is $1 \leq R \leq 500$ km. Magnitude distribution (local magnitude, M_L) of the events covers the range $1.5 \leq M_L \leq 6.6$.

3. The Web Portal

3.1. Technical Information

All components of the EUROSEISTEST web portal, including its database, have been built using solely Free/Open Source Software (F/OSS). The web server is using the NGINX platform, which combines high security standards with a friendly configuration scheme, increased functionality, robustness and smaller (compared to the more common Apache server) processing and memory requirements. Acceleration data and all accompanying stations and earthquakes metadata have

been stored in a MySQL v5.5 relational database through a content management system (CMS), which has been built especially for our application. The background programming language is Ruby, combined with the well supported and very extensible web application framework called Rails (the combination often referred to as RubyonRails).

Part of the data processing is performed offline, mostly using the Seismic Analysis Code (SAC, Goldstein et al., 2003; Goldstein and Snoke, 2005). After the data upload through a user-friendly web interface, a second part of processing including data integration to velocity and displacement time histories, Fourier spectra and spectrograms computation, and production of the corresponding graphical plots, is taking place automatically. Several other pieces of F/OSS are used in this phase, notably SAC, GNUPLOT and other GNU utilities.

3.2. Contents

The EUROSEISTEST database web portal is hosted at the address: http://euroseisdb.civil.auth.gr. Its home page (Figure 3) includes basic information on the contents of the portal and a list of most recent announcements related to EUROSEISTEST in general and new event uploads to the web database. It also provides links to the major sections of the web portal, which are "The EUROSEISTEST", the "Database Search" and "SFSI" (Soil Foundation – Structure Interaction). Each section is described in the following.

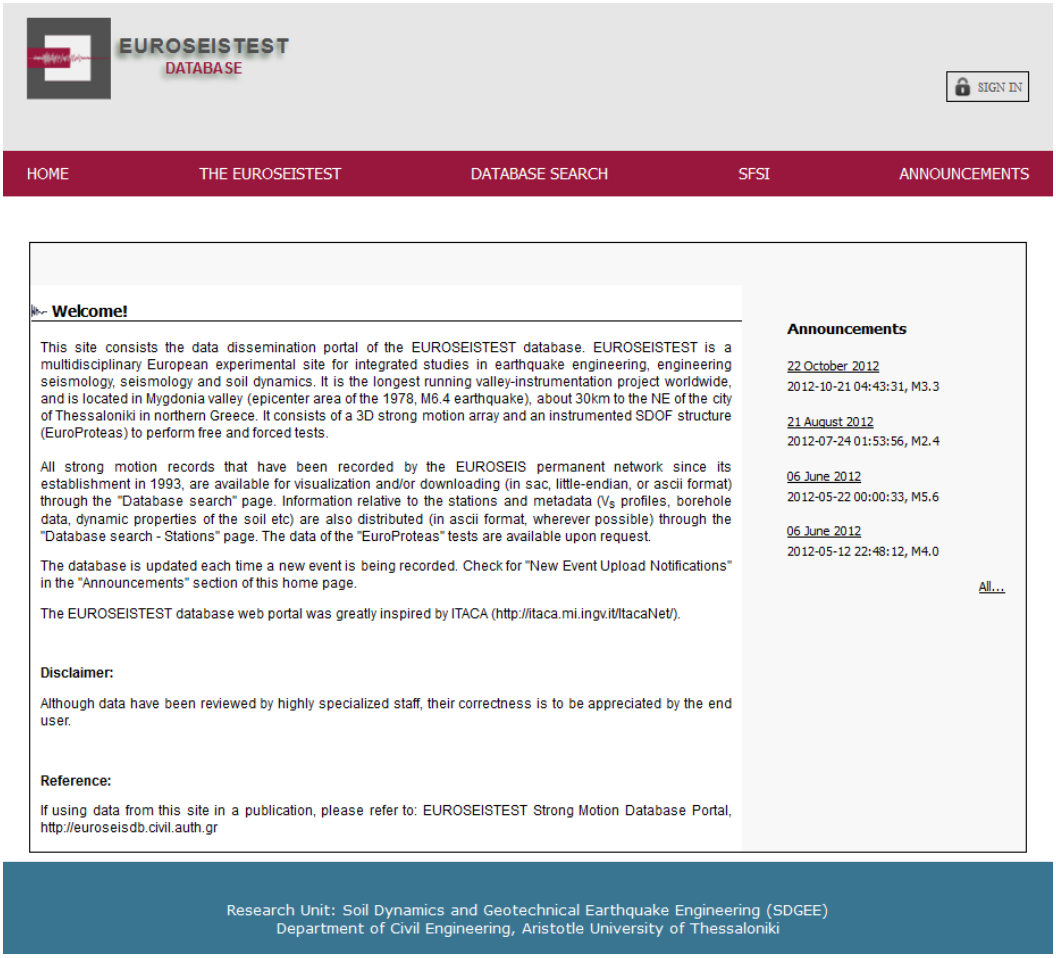

Figure 3 – The home page of the EUROSEISTEST web portal (http://euroseisdb.civil.auth.gr).

3.2.1. "The EUROSEISTEST" section

This part of the EUROSEISTEST web portal is dedicated to the history of the test site and so far scientific achievements (Figure 4). More specifically, under this menu one can find information on:

- The establishment and operation status of the test site
- Its facilities
- The regional geology and tectonics
- The geotechnical/geophysical experiments and results that have taken place in the broader area since the establishment of the permanent accelerograph network (in 1993)
- A brief overview of the current knowledge of the 2D and 3D subsoil structure of the Mygdonia basin
- A full list of EUROSEISTEST-related scientific publications, etc.

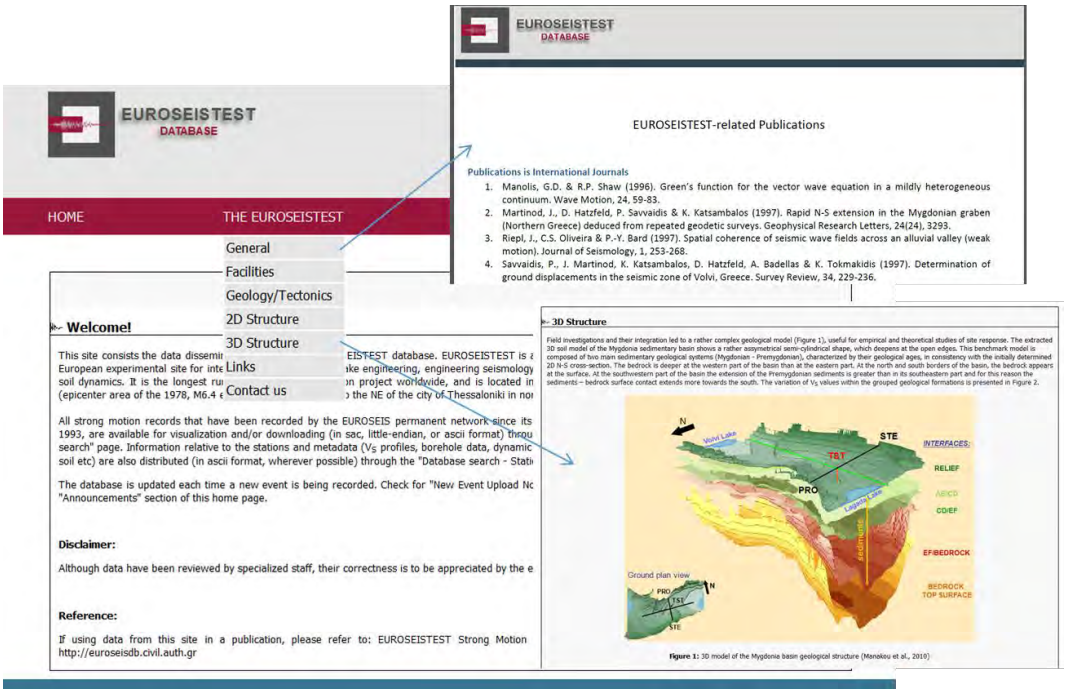

Figure 4 – Section of the web portal dedicated to the history of the test site and the so far scientific accomplishments.

3.2.2. Database search

The main section of the web portal is the one named "Database search". It constitutes an interface where the user can choose among several criteria to search the contents of the database (Figure 5). Following the common practice in other web-based acceleration databases (e.g. Pakor et al., 2011 and references therein), search criteria are grouped in record-related e.g. epicentral distance or peak ground acceleration, event-related e.g. the magnitude or the location of the earthquake and station-related e.g. soil category at the installation site. Query results are presented in the form of a table, on the same page, which provides links to several other sub-pages dedicated to either the requested station(s) or the requested event(s).

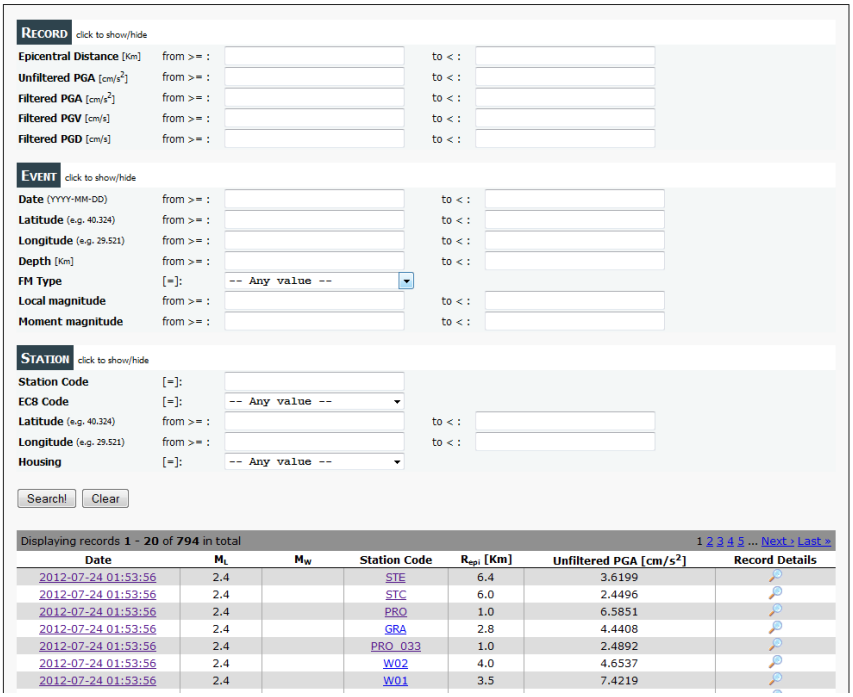

Figure 5 – Online form provided for searching the database contents. Three types of criteria related to the acceleration record, the earthquake event or the recording station can be used either individually or in combination. Query results are presented in the lower part of the web page in the form of a table.

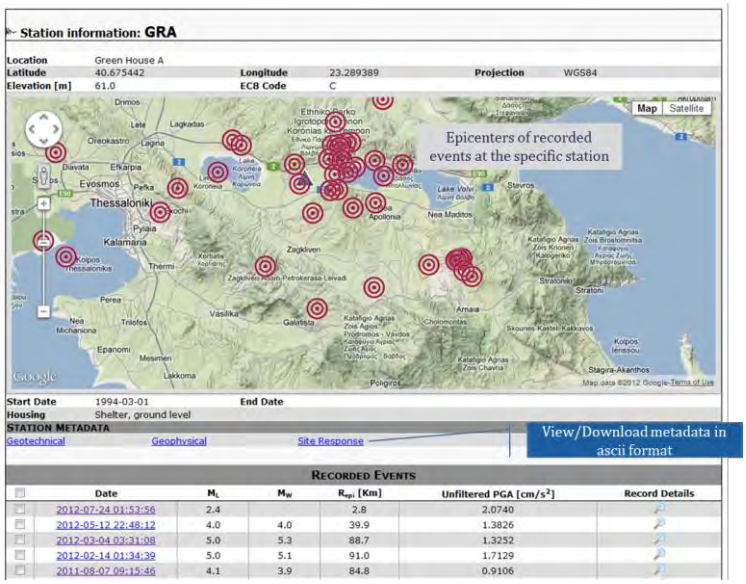

Figure 6 – Example of a station-dedicated web page. Includes all trivial information such as the location, housing, installation date etc., a Google map with the location of the station (triangle) and the epicentres of all events that have been recorded at the specific site, and links to different sets of station metadata.

Station-dedicated web pages (Figure 6) include all trivial information such as the exact location (geographical coordinates and altitude/depth) of the installation site, the housing and the soil category characterization. It also includes a Google map showing the location of the station, as well as epicentres of all events that have been recorded at the specific site. Most importantly, it provides links to station metadata for the geotechnical and geophysical site characterization, as well as results on the site response with relative references (e.g. Jongmans et al., 1998; Raptakis et al., 2000, 2005; Manakou et al., 2010). It must be noted that all this information is available in both graphical and numerical formats and can be easily downloaded.

Event-dedicated web pages (Figure 7) provide basic metadata such as the location and focal mechanism of the event with relative references, a Google map (dynamic) showing the epicentre and the locations of stations that have recorded the specific earthquake, and a table with links to the actual records. At the bottom of the page there is a form for data downloading, where the user can choose the available data set(s) and download format(s). At present we provide two data formats (ascii and SAC, little endian) and three sets of acceleration data: raw, basically processed (mean, linear trends removal and units converted from counts) without any filtering, and filtered. The relevant response spectra are also available for download.

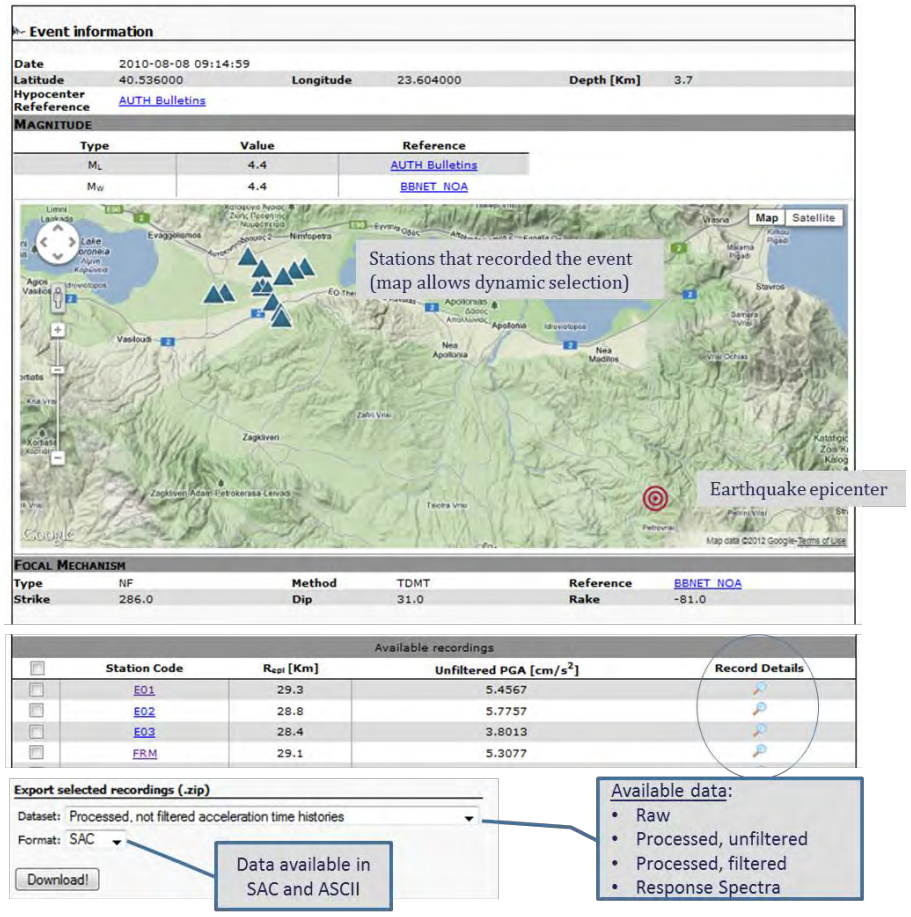

Figure 7 – Example of an event-dedicated web page. Apart from location and focal mechanism information, a map is provided with the locations of epicentre and recording stations. At the lower part of the web page a table summarizes parameters of the actual records and provides links (Record Details) to the corresponding waveforms. A form for facilitating data download is also included.

If the user decides to further investigate the “record details” (Figures 5, 6, 7), he will find a group of plots for each recorded component of ground motion. An example of such plots is presented in Figure 8. These static graphs serve as a first screening of the quality of the data and basic characteristics of the ground motion e.g. peak values, duration, frequency content etc.

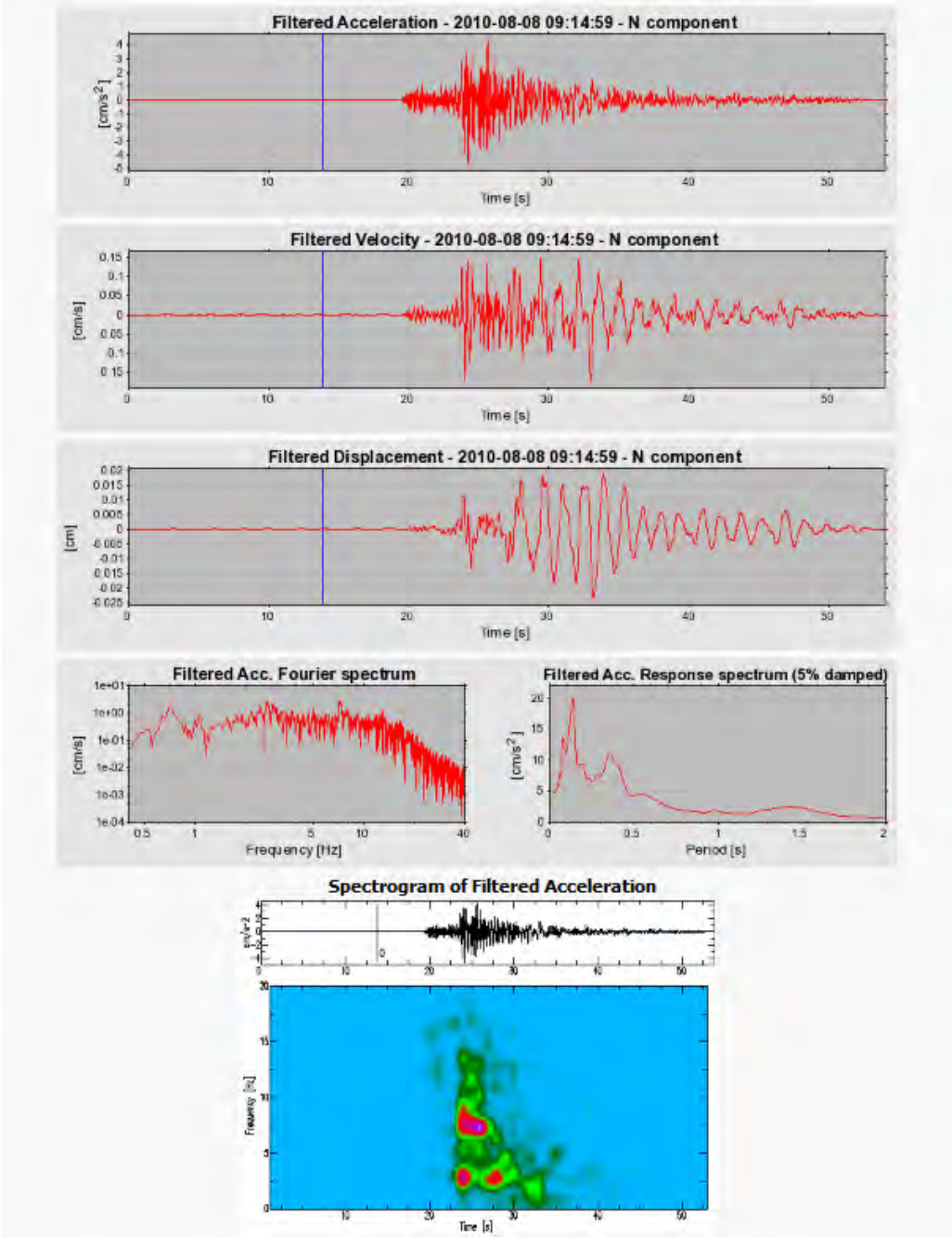

Figure 8 – Part of data plots available for a recorded component of acceleration. From top to bottom: acceleration, velocity and displacement time histories, Acceleration amplitude Fourier and response (5% damped) spectra and spectrogram of the acceleration time history.

3.2.3. Soil - Foundation - Structure Interaction (SFSI)

During the last few years, significant research effort in EUROSEISTEST is put on the topic of interaction between the soil, the foundation and the superstructure. Toward this research direction, EUROSEISTEST facilities were enriched with a large-scale prototype soil-foundation-structure system named "EuroProteas". EuroProteas conforms to the provisions of modern codes and regulations (e.g. Eurocode, EKOS2000, EAK2000) and has a simplified and reconfigurable structure in terms of mass and stiffness, designed to promote the effects of SFSI and wave propagation on the superstructure and in the soil.

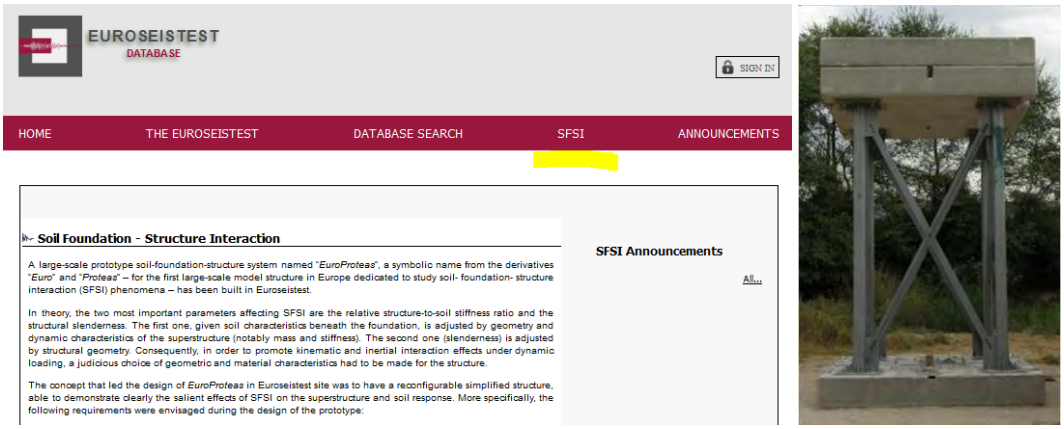

Figure 9 – Section of the web portal dedicated to the Soil Foundation – Structure Interaction (SFSI) research in EUROSEISTEST. Photo: EuroProteas, facility specially designed for SFSI studies.

The "SFSI" menu of the EUROSEISTEST web portal (Figure 9) has been designed to host information on EuroProteas and related experiments and scientific results. In the future, this section will be further extended to include a second database of data collected on EuroProteas during free-vibration, forced-vibration and ambient noise experiments accounting for soil-foundation-structure interaction.

4. Discussion

The EUROSEISTEST experimental site has served for many years, most than any other similar test site in the world, the scientific community by providing high quality data for strong ground motion and site effect studies. Its data has already been used in more than 200 scientific publications, while its facilities have been used in many European and other international projects. One of the most significant advantages of this test site is the well-known subsoil structure, which makes it an ideal place to test/validate/verify methods and software for ground motion and site effects studies.

Through the EUROSEISTEST web portal we aim to facilitate further use of our dataset by an even larger number of scientists from around the globe. Toward this direction, we put our effort in the proper maintenance of all the existing facilities of EUROSEISTEST, but also in the continuous upgrade of the test site as a whole. A recent major addition has been the EuroProteas structural model, already present in the web portal in a dedicated section to SFSI studies. Data collected from dynamic vibration experiments on EuroProteas are, at the moment, available upon request, although in the near future relative datasets will be available through the EUROSEISTEST web portal.

We intend to keep the EUROSEISTEST portal continuously updated by adding to its underlying database any newly recorded event. At present, such updates are performed within hours to few days after the earthquake occurrence. Scientists who are interested in being kept informed about EUROSEISTEST news and new event uploads can visit the "Announcements" section of the portal's home page or subscribe to the EUROSEISTEST mailing list in https://lists.auth.gr/sympa/info/euroseisdb.

5. Acknowledgments

Thanks are due to Stavrina Kykalou, graphic designer of the Research Committee of the Aristotle University of Thessaloniki, for kindly helping us to improve the web portal's graphical environment. The overall design concept of the EUROSEISTEST database portal was greatly inspired by ITACA (Working group ITACA, 2010; Luzi et al., 2008), the Italian Accelerometric database. Finally, we would like to express our gratitude to all free/open source software developers that provided us with the tools to perform this work.

6. References

EAK 2000. National Greek Earthquake Design Code, Athens, Publication of Earthquake Planning and Protection Organization of Greece.

EKOS 2000. National Greek Reinforced Concrete Design Code, Athens, Publication of the Earthquake Planning and Protection Organization of Greece.

Goldstein P., Dodge D., Firpo M. and Minner Lee 2003. SAC2000: Signal processing and analysis tools for seismologists and engineers, Invited contribution to "*The IASPEI International Handbook of Earthquake and Engineering Seismology*", Edited by WHK Lee, H. Kanamori, P.C. Jennings, and C. Kisslinger, Academic Press, London.

Goldstein P. and Snoke A. 2005. SAC Availability for the IRIS Community, *Incorporated Institutions for Seismology Data Management Center Electronic Newsletter*.

Jongmans D., Pitilakis K., Demanet D., Raptakis D., Riepl J., Horrent C., Tsokas G., Lontzetidis K. and Bard P.-Y. 1998. Euroseistest: Determination of the Geological Structure of the Volvi Graben and Validation of the Basin Response to one Earthquake and one Shot, *Bull. Seism. Soc. Am.,* 88(2), 473-487.

Luzi L., Hailemikael S., Bindi D., Pacor F., Mele F. and Sabetta F. 2008. ITACA (ITalian ACcelerometric Archive): A web portal for the dissemination of Italian strong-motion data, *Seism. Res. Lett.,* 79, 716-722.

Pakor F., Paolucci R., Luzi L., Sabetta F., Spinelli A., Gorini A., Nicoletti M., Marcucci S., Filippi L. and Dolce M. 2011. Overview of the Italian strong motion database ITACA 1.0, *Bull. Eq. Eng.,* 9, 1723–1739.

Pitilakis K., Raptakis D., Makra K., Manakou M. and Chávez-García F. J. 2011. Euroseistest 3D array for the study of complex site effects, in *Earthquake Data in Engineering Seismology*, Geotechnical, Geological, and Earthquake Engineering 14, S. Akkar et al. (eds), doi 10.1007/978-94-007-0152-6_11, Springer Science + Business Media B. V.

Raptakis D. G., Chavez-Garcia F., Makra, K. A. and Pitilakis K. D. 2000. Site Effects at Euroseistest-I. 2D Determination of the Valley Structure and Confrontation of the Observations with 1D Analysis, *Soil Dyn. and Eq. Eng.,* 19(1), 1-22.

Raptakis D., Manakou M., Chávez-García, F. J., Makra K., and Pitilakis K. 2005. 3D configuration of Mygdonian basin and preliminary estimate of its site response, *Soil Dyn. and Eq. Eng.,* 25, 871-887.

Manakou M. V., Raptakis D. G., Chávez-García F. J., Apostolidis P. I. and Pitilakis K. D. 2010. 3D soil structure of the Mygdonian basin for site response analysis, *Soil Dyn. and Eq. Eng.,* 30(11), 1198-1211.

Δελτίο της Ελληνικής Γεωλογικής Εταιρίας, τομ. XLVII , 2013
Πρακτικά 13ου Διεθνούς Συνεδρίου, Χανιά, Σεπτ. 2013

Bulletin of the Geological Society of Greece, vol. XLVII 2013
Proceedings of the 13th International Congress, Chania, Sept. 2013

CONSTRAINTS ON THE LOCATION OF THE 2008, M_W6.4 ACHAIA-ILIA EARTHQUAKE FAULT FROM STRONG MOTION DATA

Roumelioti Z.[1], Theodoulidis N.[2] and Bouchon M.[3]

[1] *Research Unit of Soil Dynamics and Geotechnical Earthquake Engineering, Department of Civil Engineering, P.O. Box 424, 54124 Thessaloniki, Greece, zroum@auth.gr*

[2] *Institute of Engineering Seismology and Earthquake Engineering (ITSAK-EPPO), P.O. Box 53, 55102 Thessaloniki, Greece, ntheo@itsak.gr*

[3] *Université Joseph Fourier, BP 53, 38041 Grenoble, France, bouchon@ujf-grenoble.fr*

Abstract

The June 2008, M_w6.4 Achaia-Ilia earthquake was the first recorded dextral strike-slip event of considerable magnitude in western Peloponnese, which, nevertheless, could not be related to any of the known/mapped structures at the ground surface. Published locations of the mainshock focus by various agencies/researchers differ by as much as 6 km and 16 km in the horizontal and vertical dimensions, respectively, making even more difficult the accurate siting of the seismogenic fault. However, the 2008 earthquake provided a valuable set of near-fault strong motion data, which could shed some light on the problem of accurately locating the earthquake source. To this end, we use the discrete wavenumber method to forward model the strong ground motion records at three stations, located close to the prolongation of the 2008 strike. We test different locations and lengths for the ruptured plane and compare synthetic polarities and amplitudes of the first strong S-wave pulse to actual data. We conclude that the line of maximum moment release (our fault models are vertical planes) during the 2008 earthquake is located to the east of the imaginary line connecting stations PAT2 and AMAA and to the west of station PYR1.
Key words: *Andravida, Western Greece, acceleration.*

Περίληψη

Στην παρούσα εργασία γίνεται χρήση των καταγραφών της επιτάχυνσης του σεισμού του 2008 (M_w6.4), που εκδηλώθηκε στη συνοριακή περιοχή των νομών Αχαΐας-Ηλείας, προκειμένου να προσδιοριστεί με μεγαλύτερη ακρίβεια η θέση του σεισμογόνου ρήγματος. Ο σεισμός αυτός είναι ο πρώτος με σημαντικό μέγεθος που παρείχε ενόργανες αποδείξεις για τη δράση μεγάλων δεξιόστροφων ρηγμάτων οριζόντιας μετατόπισης στη Δυτική Πελοπόννησο. Λόγω, όμως, της έλλειψης σαφούς επιφανειακής εκδήλωσης της ρηξιγενούς δομής, η θέση και οι διαστάσεις της έχουν προσδιοριστεί μόνο έμμεσα και κατά κύριο λόγο από τη χωρική κατανομή των επικέντρων της μετασεισμικής ακολουθίας. Ωστόσο, ο προδιορισμός των σεισμικών επικέντρων στη συγκεκριμένη περιοχή της ελληνικής επικράτειας εμπεριέχει σημαντικά σφάλματα, γεγονός που αποτυπώνεται στις διαφορές των δημοσιευμένων λύσεων για τον κύριο σεισμό της ακολουθίας που είναι της τάξης των 6 και 16 χλμ

στην οριζόντια και κατακόρυφη διεύθυνση, αντίστοιχα. Με τη μέθοδο των διακριτών κυματαρίθμων και την προσομοίωση των καταγραφών της επιτάχυνσης σε τρεις σταθμούς, κατά μήκος της παράταξης του ρήγματος αλλά σε αντίθετες κατευθύνσεις, εξετάζονται διαφορετικά σενάρια για τη θέση και το μήκος της ρηξιγενούς δομής. Από τη συγκριτική εξέταση των αποτελεσμάτων των σεναρίων και των πραγματικών καταγραφών προκύπτει ότι η γραμμή μέγιστης έκλυσης της σεισμικής ροπής (τα μοντέλα της πηγής είναι κατακόρυφα επίπεδα) κατά την εκδήλωση του σεισμού του 2008 βρίσκεται ανατολικά της νοητής γραμμής που συνδέει τους σταθμούς PAT2 και AMAA και στα δυτικά του σταθμού PYR1.
Λέξεις κλειδιά: *Ανδραβίδα, Δυτική Ελλάδα, επιτάχυνση.*

1. Introduction

On June 08, 2008 an M_w6.4 earthquake shook the Achaia-Ilia prefectures in NW Peloponnese (Greece). This event attracted the interest of many researchers not only because of its impact (two deaths, hundreds injured, small to significant damage to masonries and life-lines; e.g. Margaris et al., 2010) but also because it was the first recorded dextral strike-slip event of considerable magnitude in this part of Greece. Shortly after the earthquake, it was concluded that the rupture did not reach the surface and the seismogenic fault could not be related to any of the known, mapped structures (Koukouvelas et al., 2010).

The 2008 Achaia-Ilia earthquake has been the subject of numerous scientific studies (e.g. Ganas et al., 2009; Gallovic et al., 2009; Feng et al., 2010; Konstantinou et al., 2010, 2011; Margaris et al., 2010; Papadopoulos et al., 2010; Zahradnik et al., 2010). Most of the aforementioned studies tend to converge on the idea that a deep, newly formed right lateral strike-slip fault zone has started taking the deformation in NW Peloponnese in a way similar to the Cephalonia transform fault. A different opinion is given by Konstantinou et al. (2011), who found that the 2008 seismogenic fault was significantly different in orientation (by 68◦) with respect to the maximum principal stress axis in NW Peloponnese. This finding argues against the birth of a new fault and thus Konstantinou et al. (2011) relate the 2008 event to a pre-existing structure that was reactivated in an over-pressured lower crust. The most recent, pertinent to the 2008 earthquake, study, which performs a crustal anisotropy analysis (Giannopoulos et al. 2012) favors the latter opinion.

Scientific controversy is not restricted to the geological age of the ruptured fault; it also extends to routine earthquake locations. A characteristic example is the comparison of the absolute locations of the aftershock sequence of the 2008 earthquake in two independent studies i.e. Gallovic et al. (2009) and Konstantinou et al. (2010) (Figure 1). Although both research teams performed relocation techniques, the independently computed aftershock clusters appear clearly separated in space with a mean shift between clusters of the order of 2 km. Of course, such a difference lies within the expected uncertainties in earthquake locations, which are quite large in this part of Greece due both to the complicated earth structure and the lack of seismological stations to the W-NW (i.e. in the Ionian Sea). Differences in mainshock location solutions are not smaller. In fact, published locations differ by as much as 6 km in the horizontal direction and 16 km in the vertical.

Since the 2008 earthquake appears to significantly alter/complement the pre-existing scientific knowledge of the on-going seismotectonic processes in NW Peloponnese, its source characteristics are of great importance. In the present study we put additional constraints on the location of the 2008 seismogenic source and its dimensions by exploiting information carried in near-fault strong ground motion recordings. The discrete wavenumber method is used to simulate acceleration waveforms recorded in the vicinity of the 2008 earthquake. We test several models incorporating different locations and lengths of the seismogenic fault. The optimum location is the one that reproduces the recorded low-frequency signal polarities and amplitudes of strong ground motion.

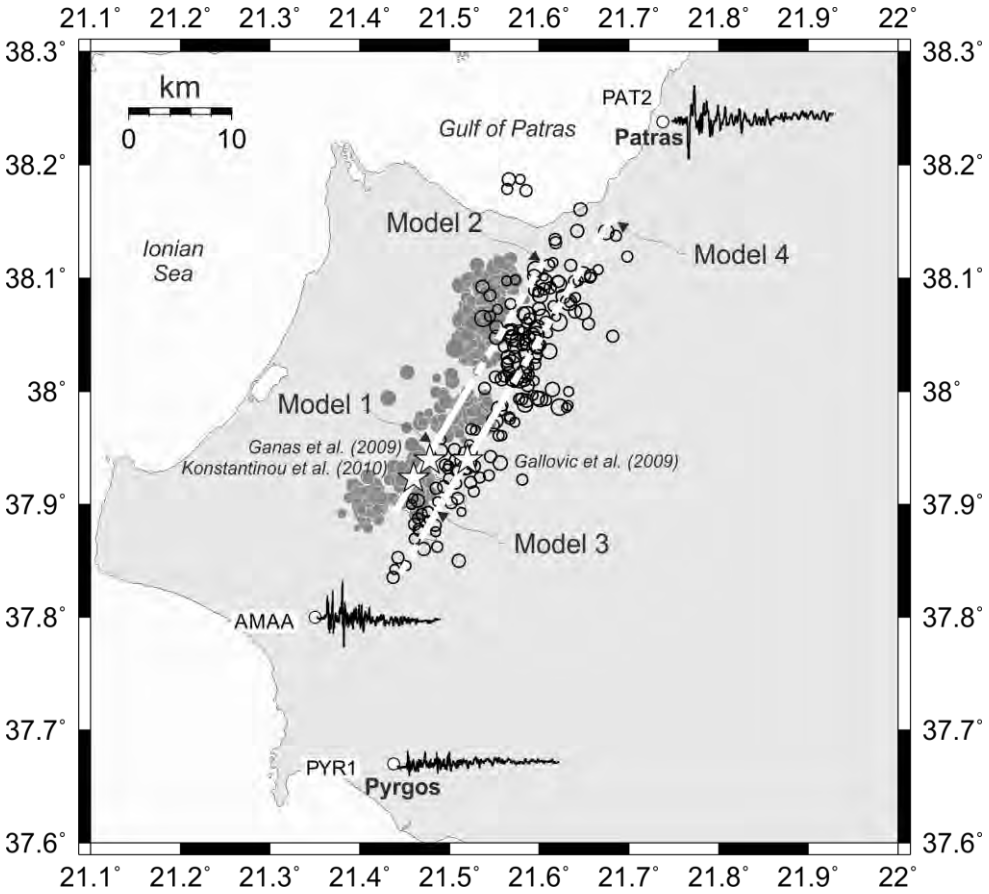

Figure 1 – Regional map showing relocated epicenters of the 2008 Achaia-Ilia earthquake (star symbols) suggested by different researchers and aftershock locations as computed by Konstantinou et al. (2010; dark grey solid circles) and Gallovic et al. (2009; open black circles). The locations and acceleration waveforms (one of the horizontal components) of stations PAT2, AMAA and PYR1 are also shown. Thick white lines, continuous and dashed, indicate the surface projections of the four tested source models.

2. Strong Ground Motion Data

The 2008 earthquake was recorded by 27 strong motion stations (Margaris et al., 2010), nine of which were located at relatively close distance (<50 km) from the seismic source. Among the latter, six stations are clustered in the city of Patras. In the present work, we selectively deal with the recordings at stations PAT2 (among the six stations installed in Patras), AMAA and PYR1, which are located along the line of the rupture, at opposite directions with respect to the 2008 epicenter (Figure 1). Information on the strong motion stations used herein is provided in Table 1.

Prior to any processing, data were carefully checked for polarity reversals. Original acceleration records were integrated to velocity without applying any filtering in order to preserve all information at low frequencies. The velocity waveforms at the three examined stations, PAT2, AMAA and PYR1, are plotted in Figure 2. Transverse component at station PAT2 appears quite simple with one dominant low-frequency pulse, while corresponding recordings at stations AMAA and PYR1 show larger complexity with at least three distinct pulses. At a first glance, one could conclude rupture directivity toward the north, where PAT2 station is located.

Table 1 - Information on the three accelerograph stations used in this study. Orientations (LVT, modified LVT as used in SMA-1) have been converted to XYZ for reasons of uniformity (positive polarity i.e. positive output for positive acceleration).

Station Code	Location	Lat° (N)	Lon° (E)	Az (X)	PHA (g)	Az (Y)	PHA (g)	Operator*
AMAA	Amaliada	37.795	21.350	280**	0.244	190**	0.241	NOA
PAT2	Patra – Agios Dimitrios	38.238	21.738	15	0.091	285	0.100	ITSAK
PYR1	Pyrgos	37.670	21.438	80	0.085	350	0.056	ITSAK

* NOA: National Observatory of Athens; ITSAK: Institute of Engineering Seismology and Earthquake Engineering.

** Revised orientation of AMAA instrument was provided by I. Kalogeras of NOA (personal communication).

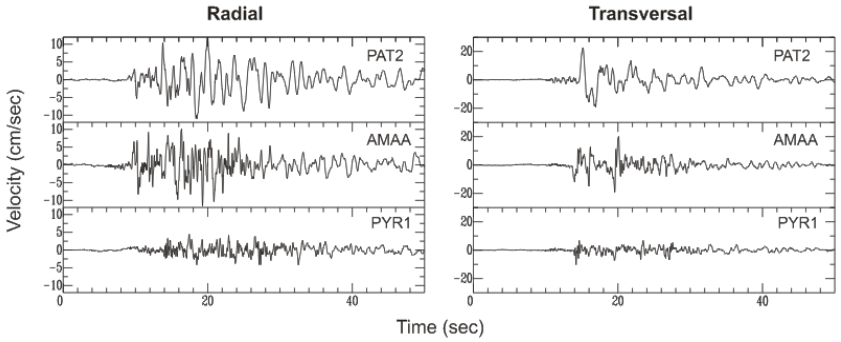

Figure 2 – Velocity records at the two horizontal components of stations PAT2, AMAA and PYR1. Originally recorded accelerograms have been integrated to velocities and rotated to obtain the fault-parallel (Radial; left) and fault-normal (Transversal; right) components of ground motion.

3. Investigating Different Source Scenarios

3.1. Method

The method used to simulate observed ground motion at stations PAT2, AMAA and PYR1 is the Discrete Wavenumber Number (DWN) originally introduced by Bouchon and Aki (1977) and extensively reviewed in Bouchon (2003). For reasons of space economy, we do not include a description of the DWN herein and, thus, the reader is referred to the aforementioned studies.

3.2. Application and Results

We tested four different fault models, which were defined based on the two different pictures of the relocated 2008 sequence, as suggested by Gallovic et al. (2009) and Konstantinou et al. (2010). The surface projections of the four fault models (all of them considered to be vertical and with a strike of 211°) are shown in Figure 1. Apart from different location, we also investigated different fault lengths, L, i.e. by including or not the northernmost cluster of afteshocks, which appears to deviate from the strike suggested by the moment tensor of the 2008 mainshock. Details on the geometry of the tested models are summarized in Table 2.

In all our applications rupture velocity, V_r, was considered equal to 3.0 km/sec, i.e. close to 80% of the S-wave velocity at the depth of the hypocentre and identical to the value used in Gallovic et al.

(2009). Dislocation rise time was taken to be equal to 10% of the total rupture duration (Heaton, 1990), T, where $T=L/V_r$. Average slip varied depending on the dimensions of each fault model, although in all cases total slip (mean slip × fault surface) was constant.

Table 2 - Parameters of the four fault models (Figure 1) tested in the present study.

	MODEL1	MODEL2	MODEL3	MODEL4
Location	37.89N – 21.44E 38.01N – 21.53E	37.89N – 21.44E 38.12N – 21.62E	37.87N -21.47E 37.99N – 21.56E	37.84N – 21.45E 38.16N – 21.70E
Length (km)	16	30	16	42
Depth of top of fault (km)	15	15	15	15
Depth of bottom of fault (km)	30	30	30	30
No of subfaults (strike×dip)	16×15	30×15	16×15	42×15
Focal Depth	24	24	24	24
Subfault of hypocentre along strike	11	25	9	29
Rupture Velocity (km/sec)	3.0	3.0	3.0	3.0
Rise time (sec)	0.5	1.0	0.5	1.4

In Figures 3, 4 and 5, we present the results from all four tested models and for the two horizontal components of ground velocity at stations PAT2, AMAA and PYR1, respectively. The main conclusions drawn from the comparative study of these Figures are the following:

- Model 1 is the only one among the four tested models that places stations PAT2 on the western, northward moving part of the fault. The result is that the synthetic S-wave pulse in the radial component (Figure 3b) is negative, i.e. of reversed polarity compared to observations. Thus, the true location of the seismogenic fault is to the east of model 1.
- Overall, amplitude and shape of the S-wave pulses at the three examined stations are better fitted with models 1 and 3. Models 2 and 4 include larger rise time (because of the proportionality of this quantity with the rupture length, which is quite larger in models 2 and 4) and result in longer period S-wave pulses.
- Duration of observed records seem to require rupture length greater than 16 km assumed in models 1 and 3. However, larger length should then be combined with values of rise time much smaller than those predicted by empirical equations (Heaton, 1990), i.e. the 2008 would be unusually fast. In fact, Feng et al. (2010) concluded that the studied event was unusually strong in terms of high-frequency energy.
- Although the transversal component is overall well fitted by models 1 and 3, the radial component shows poorer fit. Among the many factors that affect the amplitude of this component, is the distance of the station from the fault on the perpendicular to the strike direction. For example, the radial component of PYR1 (Figure 5b) in model 3 is over-predicted and this implies that the station should be closer to the true fault (closer to nodal) than it is in the specific model. The opposite is observed in Figure 3b, i.e. at the radial

component of PAT2. Assumed location of PAT2 relative to the fault of model 3 is obviously too small, resulting to very low amplitudes in the synthetic waveforms.

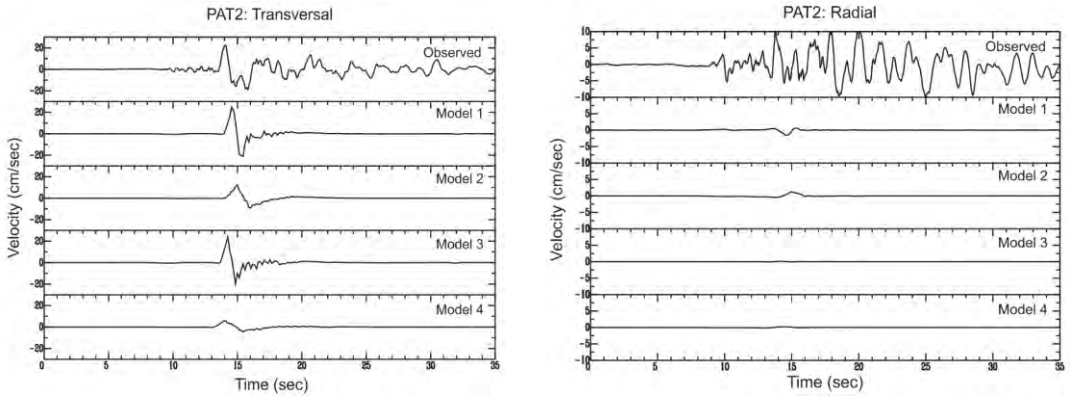

(a) **(b)**

Figure 3 – a) Comparison of observed velocity at the transversal component of station PAT2 with synthetic waveforms based on four different fault models (Figure1, Table 2). All waveforms are high-pass filtered at 0.08 Hz. b) Corresponding results for the radial component at station PAT2.

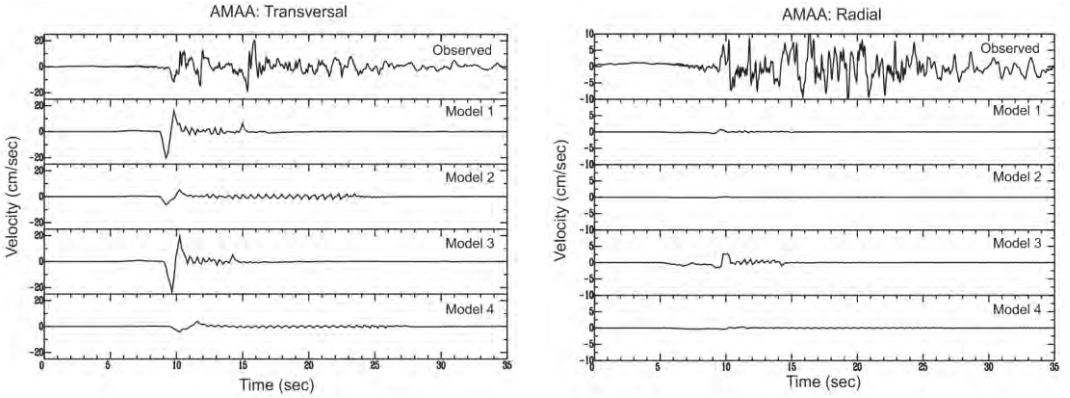

(a) **(b)**

Figure 4 – a) Comparison of observed velocity at the transversal component of station AMAA with synthetic waveforms based on four different fault models (Figure1, Table 2). All waveforms are high-pass filtered at 0.08 Hz. b) Corresponding results for the radial component at station AMAA.

Keeping in mind the aforementioned conclusions, we tested several other locations of the fault model and achieved, by trial and error, the best overall match between synthetic and observed amplitudes in all three components of ground motion. The most important constraint comes from the amplitude of the initial S-wave pulse in the radial components of the three examined stations. To optimally reproduce strong motion amplitudes at all three stations, a shift of our fault model further to the east is required i.e. further away from stations PAT2 and AMAA and closer to station PYR1. Our best synthetics are compared to observed acceleration time histories in Figure 6. We should once more note that we focus on reproducing the rough shape and amplitude of the initial S-wave pulse in each record. The location of the 2008 seismogenic fault, as constrained by the near-fault strong motion data, is shown in Figure 7.

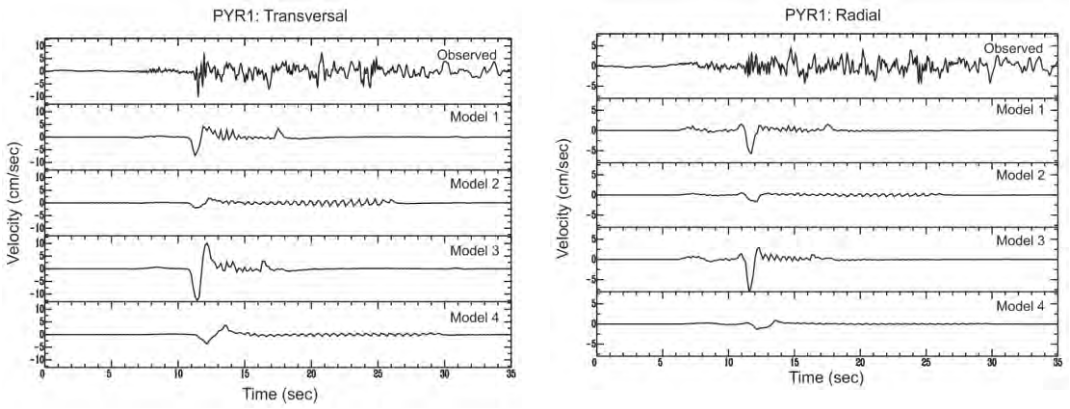

(a) **(b)**

Figure 5 – a) Comparison of observed velocity at the transversal component of station PYR1 with synthetic waveforms based on four different fault models (Figure1, Table 2). All waveforms are high-pass filtered at 0.08 Hz. b) Corresponding results for the radial component at station PYR1.

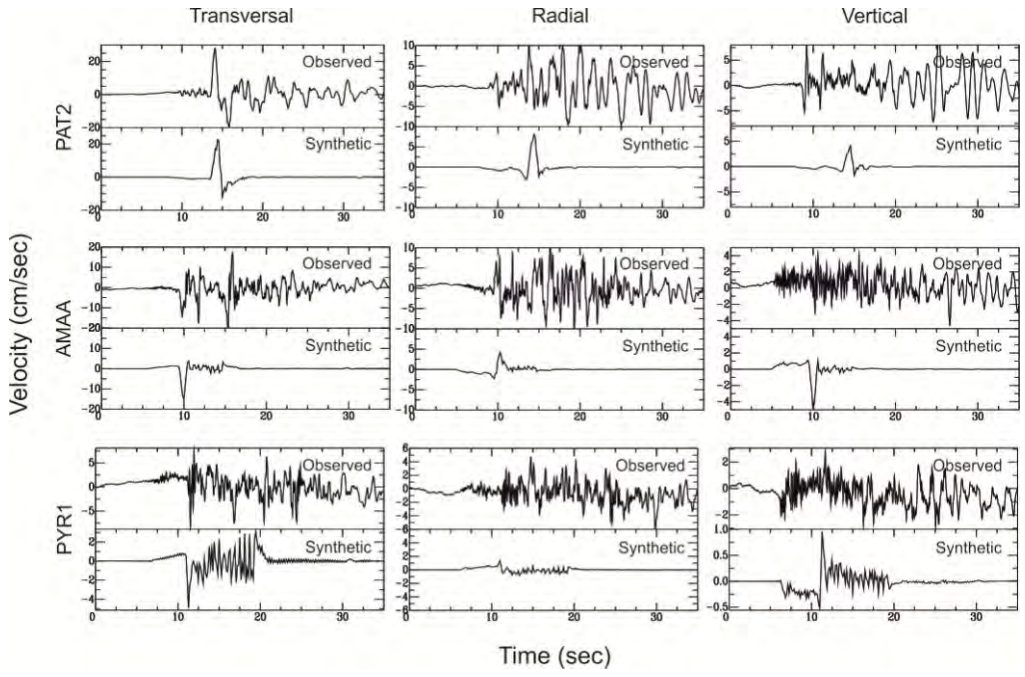

Figure 6 – Comparison of observed and synthetic velocity time histories from our preferred location of the 2008 seismogenic fault (Figure 7) at stations PAT2 (top), AMAA (center) and PYR1 (bottom).

4. Conclusions – Discussion

The 2008 Achaia-Ilia earthquake undoubtedly changed the so-far existing knowledge on the seismotectonic processes in the area of NW Peloponnese. It comprises the first dextral strike-slip earthquake of considerable magnitude that has been recorded from this part of Greece and provides further evidence for the possible existence of a second transform fault zone that accommodates the relative motion between Apulia and Aegean plates, similarly to the Cephalonia

transform fault zone to the west. However, the imprints of the 2008 earthquake on the ground surface were limited and its role on the general seismotectonic setting can be revealed only through detailed studies of its source rupture characteristics.

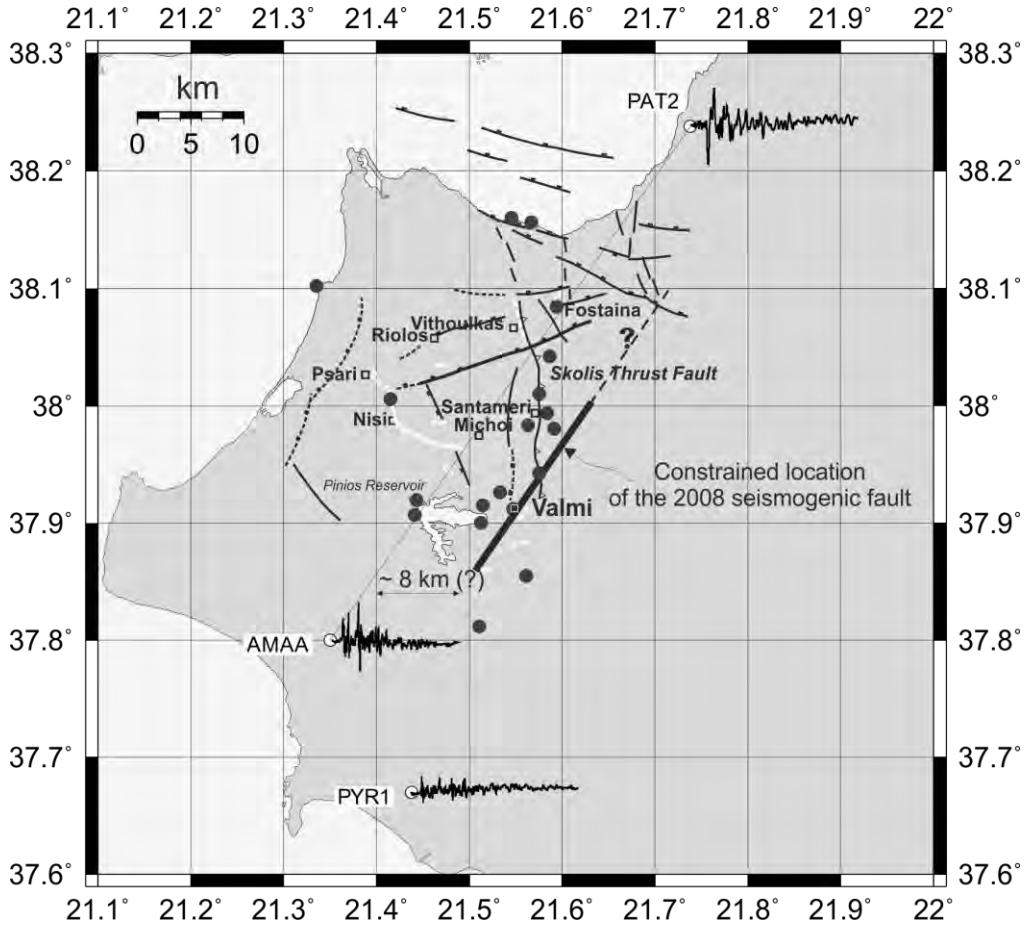

Figure 7 – Regional map showing the main tectonic structures of the 2008 epicentral area and 2008 surface ruptures (white lines) (reproduced from Figure 2 of Koukouvelas et al., 2010), and the herein constrained location (black thick line) of the 2008 seismogenic fault. Black dots denote areas of rock falls or liquefaction phenomena observed during the 2008 event (Margaris et al., 2010; Papadopoulos et al., 2010).

In this work we put additional constraints on the exact location of the 2008 seismogenic source through forward modeling near-fault strong motion data. We emphasized on correctly reproducing the theoretically expected sign and overall shape of long-period S-wave pulses. We conclude that the 2008 seismogenic fault (i.e, major moment release) is located to the east of stations AMAA and PAT2 and to the west of station PYR1. A preferred fault location is at approximately 8 km to the east of the imaginary line connecting stations AMAA and PAT2. This is very close to the limited surface ruptures mapped to the east of Pinios reservoir, close to the village of Valmi, by Koukouvelas et al. (2010), and, also close to the area where the majority of other ground failures i.e. rockfalls and liquefaction phenomena were observed. However, it must be clearly stated that in using the amplitude of the S-wave pulse to constrain the fault location, we assume the theoretically expected near-extinction of the radial displacement at near-nodal locations. However, this does not really occur in the real earth because crustal heterogeneities make the ray paths deviate from

straight lines and thus the ~8 km distance should be considered as an upper limit in our computations.

Although relative results are not presented herein, our analysis favors a fault that slipped at depths larger that 10-15 km. This last finding is in accordance with the lack of surface expression of the fault (Koukouvelas et al., 2010) and the absent or limited permanent ground deformation in the broader epicentral area (Feng et al., 2010; Papadopoulos et al., 2010). Regarding the length of the rupture, we found that models of 16 km length sufficiently reproduce the salient features of the recorded motions. However, the overall duration of observations is better matched when the assumed length exceeds 30 km. To better constrain the length of the ruptured area, more detailed modeling of the source, including inhomogeneous distribution of slip, is required.

5. Acknowledgments

This research was financially supported by EC-Project "International Transfer of Seismological Advanced Knowledge and Geophysical Research", a Transfer of Knowledge Marie-Curie action; MTKD-CT-2005-0296270. Z.R. acknowledges hosting in the facilities of ITSAK during the preparation of the present work. We thank Dr. Anna Serpetsidaki of the Seismological Laboratory of Patras University for providing raw data of locations used in Gallovic et al. (2009). Maps were produced using the GMT software (Wessel and Smith, 1998).

6. References

Bouchon M. 2003. A review of the discrete wavenumber method, *Pure and Ap. Geophys.,* 160, 445-465.

Bouchon M. and Aki K. 1977. Discrete wave number representation of seismic source wave fields, *Bull. Seism. Soc. Am.,* 67, 259-277.

Feng L., Newman A. V., Farmer G. T., Psimoulis P. and Stiros S.C. 2010. Energetic rupture, coseismic and post-seismic response of the 2008 Mw 6.4 Achaia-Elia earthquake in northwestern Peloponnese, Greece: an indicator of an immature transform fault zone, *Geophys. J. Int.,* 183, 103 – 110.

Gallovic F., Zahradnik J., Krizova D., Plicka V., Sokos E., Serpetsidaki A. and Tselentis G.A. 2009. From earthquake cetroid to spatial-temporal rupture evolution: Mw6.3 Movri mountain earthquake, June 8, 2008, Greece, *Geophys. Res. Lett.,* 36, L21310, doi: 10.1029/2009GL040283.

Ganas A., Serpelloni E., Drakatos G., Kolligri M., Adamis I., Tsimi Ch. and Batsi E. 2009. The M_w 6.4 SW-Achaia (Western Greece) earthquake of 8 June 2008: Seismological field, GPS observations, and stress modeling, *J. Eq. Eng.,* 13(8), 1101-1124.

Gianopoulos D., Sokos E., Konstantinou K. I., Lois A. and Tselentis G.A. (2012). Temporal variation of shear-wave splitting parameters before and after the 2008 Movri Mountain earthquake in northwest Peloponnese (Greece), *Annals of Geophys.,* 55(5), doi: 10.4401/ag-5586.

Heaton T. H. 1990. Evidence for and implications of self-healing pulses of slip in earthquake rupture, *Phys. of the Earth and Plan. Int.,* 64, 1-20.

Konstantinou K. I., Melis N. S., Lee S.-J., Evangelidis C. P. and Boukouras K. 2010. Rupture process and aftershocks relocation of the 8 June 2008 M_w 6.4 earthquake in Northwest Peloponnese, Western Greece, *Bull. Seism. Soc. Am.* 99(6), 3374 – 3389, doi: 10.1785/0120080301.

Konstantinou K. I., Evangelidis C. P. and N. S. Melis, 2011. The 8 June 2008 M_w 6.4 earthquake in northwest Peloponnese, western Greece: A case of fault reactivation in an overpressured lower crust?, *Bull. Seism. Soc. Am.* 101 (1), 438 – 445.

Koukouvelas I. K., Kokkalas S. and Xypolias P. 2010. Surface deformation during the Mw6.4 (8 June 2008) Movri Mountain earthquake in the Peloponnese, and its implications for the seismotectonics of western Greece, *Int. Geol. Rev.* 52, 249 – 268.

Margaris B., Athanasopoulos G., Mylonakis G., Papaioannou Ch., Klimis N., Theodulidis N., Savvaidis A., Efthymiadoy V. and Stewart J. P. 2010. The 8 June 2008 M_w 6.5 Achaia-Elia, Greece earthquake: Source characteristics, ground motionsandground failure, *Earthquake Spectra,* 26(2), 399- 424.

Papadopoulos G. A., Karastathis V., Kontoes Ch., Charalampakis M., Fokaefs A. and Papoutsis I. 2010. Crustal deformation associated with east Mediterranean strike-slip earthquakes: The 8 June 2008 Movri (NW Peloponnese), Greece, earthquake (Mw6.4), *Tectonophysics,* 492, 201 – 212.

Wessel P. and Smith W.H.F. 1998. New improved version of the Generic Mapping Tools released, *EOS Trans*. *AGU*, 79, 579.

Zahradnik J. and Gallovic F. 2010. Toward understanding slip-inversion uncertainty and artifacts, *J. Geophs. Res.,* 115, B09310, pp. 16, doi: 10.1029/ 2010JB007414.

Δελτίο της Ελληνικής Γεωλογικής Εταιρίας, τομ. XLVII , 2013
Πρακτικά 13ου Διεθνούς Συνεδρίου, Χανιά, Σεπτ. 2013

Bulletin of the Geological Society of Greece, vol. XLVII 2013
Proceedings of the 13th International Congress, Chania, Sept. 2013

LOCAL MAGNITUDE ESTIMATION IN GREECE, BASED ON RECORDINGS OF THE HELLENIC UNIFIED SEISMIC NETWORK (HUSN)

Scordilis E.[1], Kementzetzidou D.[1] and Papazachos B.[1]

[1] Aristotle University of Thessaloniki, Faculty of Geology, Department of Geophysics, manolis@geo.auth.gr, dkementz@auth.gr

Abstract

A new relation is proposed for calculation of local magnitudes in Greece. For this purpose, there were used synthetic Wood-Anderson (SWA) recordings of 98 digital broad-band stations operating between 2007 and 2011. These stations are installed at the sites of the seismological networks of: a) the National Observatory of Athens (HL), b) the Department of Geophysics of the Aristotle University of Thessaloniki (HT), c) the Seismological Laboratory of the University of Athens (HA) and d) the Seismological Laboratory of the University of Patras (HP). All these institutions constitute the recently (2004) established Hellenic Unified Seismic Network (HUSN). These recordings are used to calculate a refined geometrical spreading factor and an anelastic attenuation coefficient, representative for Greece and surrounding area, proper for estimating local magnitudes in this region. Individual station corrections are also calculated in order to further ameliorate magnitude estimation accuracy. Comparison of such calculated local magnitudes with corresponding original moment magnitudes revealed that these two scales are equivalent for a wide range of values ($2.9 \leq M_W \leq 6.4$).

Key words: *Synthetic Wood-Anderson records, geometrical spreading, anelastic attenuation.*

Περίληψη

Προτείνεται μια νέα σχέση για τον υπολογισμό τοπικών μεγεθών (M_L) στην Ελλάδα. Για το σκοπό αυτό χρησιμοποιούνται συνθετικές καταγραφές Wood-Anderson (SWA) που προέρχονται από 98 ψηφιακούς σεισμολογικούς σταθμούς ευρέος φάσματος και καλύπτουν το χρονικό διάστημα 2007-2011. Οι σεισμολογικοί αυτοί σταθμοί ανήκουν σε τέσσερα σεισμολογικά δίκτυα που ελέγχονται από: α) το Γεωδυναμικό Ινστιτούτο του Εθνικού Αστεροσκοπείου Αθηνών (HL), β) το Εργαστήριο Γεωφυσικής του Αριστοτέλειου Πανεπιστημίου Θεσσαλονίκης (HT), γ) το Εργαστήριο Σεισμολογίας του Εθνικού Καποδιστριακού Πανεπιστημίου Αθηνών (HA) και δ) το Εργαστήριο Σεισμολογίας του Πανεπιστημίου Πατρών (HP). Τα δίκτυα αυτά συνιστούν από το 2004 το Ενιαίο Εθνικό Δίκτυο Σεισμογράφων (Ε.Ε.Δ.Σ.). Οι καταγραφές των 98 αυτών σταθμών χρησιμοποιούνται για τον καθορισμό συντελεστών γεωμετρικής διασποράς και ανελαστικής απόσβεσης, αντιπροσωπευτικών για την Ελλάδα και τις γύρω περιοχές, κατάλληλων για τον υπολογισμό τοπικών μεγεθών στις περιοχές αυτές. Υπολογίζονται, επίσης, σταθερές διορθώσεις, που σχετίζονται με τις τοπικές συνθήκες της θέσης κάθε σταθμού, για την περαιτέρω βελτίωση της ακρίβειας στον καθορισμό

του μεγέθους. Τέλος επιχειρείται συσχέτιση του υπολογιζόμενου μεγέθους με αυθεντικά μεγέθη σεισμικής ροπής, η οποία αναδεικνύει ισοδυναμία των δύο αυτών κλιμάκων μεγεθών για ένα ευρύ φάσμα τιμών ($2.9 \leq M_W \leq 6.4$).
Λέξεις κλειδιά: *Συνθετικές καταγραφές Wood-Anderson, γεωμετρική διασπορά, ανελαστική απόσβεση.*

1. Introduction

This To measure the "size" of earthquakes, Richter (1935) introduced the *local magnitude scale*, M_L, using trace amplitudes of local earthquakes recorded on typical Wood Anderson seismographs with magnification 2,800; natural period 0.8sec; damping 0.8 (Anderson and Wood, 1924, 1925). Recent studies (Uhrhammer and Collins, 1990; Uhrhammer et al., 1996) have showed that the effective magnification of the typical WA seismograph is around 2,080, which means a systematic error in M_L estimations. Other magnitude scales (m_b, m_B, M_S, M_D) which were introduced soon after the definition of M_L did not overcome the limitations introduced by the instruments' response and the frequency content of the seismic waves. However, the important role of the local magnitude scale in earthquake hazard assessments has been emphasized for years by several workers (Kanamori and Jennings, 1978; Hutton and Boore, 1987; Boore, 1989).

The M_W scale (Kanamori, 1977; Hanks and Kanamori, 1979), solved the problem of confusing plurality and limited applicability of the existing magnitude scales. This scale is reasonably reliable since it is controlled by the fault size and dislocation. The robustness of the M_W estimation is due to the fact that seismic moment estimation is based on spectral amplitudes. On the other hand, M_W does not saturate, since it is directly proportional to the logarithm of seismic moment. As a result M_W exhibits a uniform behavior for all magnitude levels. For these reasons, this magnitude is considered as the most reliable earthquake magnitude, because it accurately describes the size of earthquakes and its relation with other magnitude scales has been also accurately defined (Heaton et al., 1986; Johnston, 1996; Shedlock, 1999; Papazachos et al., 2002, Scordilis, 2006).

The relation between M_L and M_W has been extensively studied by several authors and for different seismotectonic environments (Heaton et al., 1986; Kim et al., 1989; Uhrhammer et al., 1996; Papazachos et al., 1997, 2002; Utsu, 2002; Grünthal and Wahlström, 2003; Brazier et al., 2008). In most of the relative works it is shown that these two magnitude scales are equivalent for a wide range of magnitudes.

In 2002, a working group of IASPEI proposed relations for different scale magnitude estimations. That is, for M_L magnitude they adopted a poly-parametric estimation of distance correction by relations of the form of equation 1 where, A is the 0-peak (in mm) amplitude on a typical WA seismograph (recorded or synthesized), R is the hypocentral distance (in km), n is the geometrical spreading factor, K is the anelastic attenuation coefficient and c_i is a standard correction. This relation was initially proposed by Bakun and Joyner (1984). Especially, for regions with attenuation similar to this of southern California IASPEI proposed the above relation with n=1.11 and K=0.00189 estimated by Hutton and Boore (1987).

Equation 1 - Formula for for M_L magnitude estimation proposed by IASPEI working group.

$$M_L = \log A + n \cdot \log(R/100) + K(R-100) + c_i .$$

In Greece, a WA seismograph was installed at the seismological station of Athens in 1965. Its records were used for a long time period by HL for regular determinations of local magnitudes in Greece by adopting the calibration function, $-\log A_0 = f(R)$, of Richter (1935, 1958). Kiratzi and Papazachos (1984) used these WA records to define new relations for the estimation of local magnitudes, M_{LG}, in Greece and surrounding areas, valid for epicentral distances $100 < \Delta \leq 1000$km. They also noticed a possible inconsistency between M_{LG} and M_W. Kiratzi (1984) and Scordilis

(1985) calibrated the recordings of short period instruments of the HT network for defining relations to estimate magnitudes equivalent to M_{LG} for a wide range of epicentral distances. Papazachos et al. (1997) in searching the relations between M_W and other magnitude scales in Greece observed the same inconsistency between the M_{LG} and M_W. This inconsistency has been confirmed (and extensively discussed) by Margaris and Papazachos (1999) who used strong motion recordings of earthquakes in Greece to estimate typical M_L (M_{LSM}). Papazachos et al. (2002) compared the M_W of 329 earthquakes, which occurred in the broader area of Greece during the period 1959-2001, with magnitude scales that are used in Greece (i.e. M from Wiechert and Mainka, M_L, M_{LSM}) confirming the previous results on M_{LG}.

For the last 5 years, M_L in Greece is estimated by the recordings of the digital broadband stations of HUSN, using the relation proposed by Hutton and Boore (1987) after applying a proper level-correction. However, even though this relationship gives better results than in the past, some inconsistencies with *Mw* are still noticeable.

The purpose of this work is to estimate new attenuation parameters (and individual station corrections) better adapted to Greece and surrounding areas, which allow more accurate magnitude determination for the earthquakes of this area.

2. The Data

Digital recordings of 98 seismological stations (Figure 1) belonging to the HUSN and operated by its four participants (HL, HT, HP and HA), are used to carry out this study. These recordings correspond to shallow earthquakes (focal depths up to 40km) which occurred in the area bounded by the coordinates 33^0N-43^0N, 18^0E-30^0E for the time period October of 2007 - end of 2011.

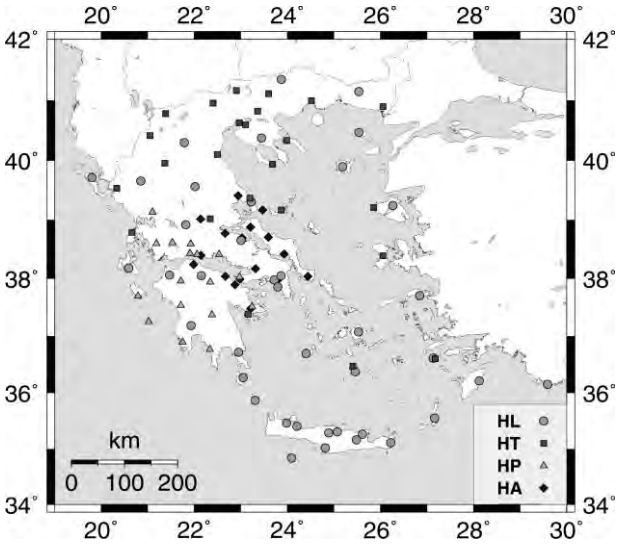

Figure 1 - The 98 stations of the HUSN of which the recordings are used in the present study.

After de-convolving the instrument response of each recording and re-convolving with the WA response, synthetic WA seismograms (SWA) were generated (Kanamori and Jennings, 1978; Bakun *et al.*, 1978; Uhrhammer and Collins, 1990), considering both the instrumentation characteristics of each employed station and the characteristics of the standard WA seismograph (*V=2080*, T_0*=0.8sec*, critical dumbing *0.8*).

For each station and for each earthquake, maximum trace amplitudes were measured on both N-S and E-W SWA components, where it was feasible. The mean amplitude was used to constitute a single measurement that corresponds to each station and each shock, since M_L was originally de-

fined as a function of the mean maximum trace amplitudes of NS and EW WA components. The finally produced data-base includes a total of 177,234 SWA picks corresponding to 23,354 earthquakes. The epicentral distances of the 98 stations that recorded these earthquakes reach up to 600 km and their magnitudes range from 2.9 to 6.4 (in the M_W scale)..

3. Method and Results

Starting with relation 1 and assuming that the frequency independent geometrical spreading factor, n, and the anelastic attenuation coefficient for the path (frequency dependent), K, should each have

Equation 2 – Calibration function used to fit the available data.

$$M_L - \log A = n \cdot \log(R/100) + K \cdot (R - 100) + c + d_i$$

the same value for the whole area under study, equation 2 was fitted to the data, where, A is the average 0-peak amplitude (in mm) of the two horizontal components of the SWA, R is the hypocentral distance (in km), c is a standard correction and d_i is an additional level correction due to the site conditions of each station, i. In order to define these parameters a reference magnitude was

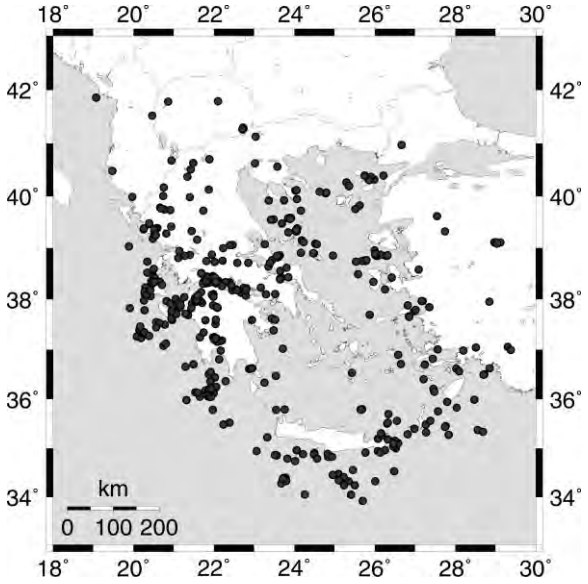

Figure 2 - Epicenters of 453 earthquakes with available M_W used in the present study.

necessary. Considering previous studies which confirmed the consistency (equivalence) between M_L and M_W (i.e. Heaton et al., 1986; Bollinger et al., 1993; Uhrhammer et al., 1996; Utsu, 2002; Brazier et al., 2008) the M_W is chosen as such reference magnitude. Several sources (GCMT, NEIC, EMSC, NOA, AUTH, UPSL, NKUA) provided M_w values for 453 earthquakes, satisfactorily covering the study area (Figure 2).

The data (moment magnitudes, SWA amplitudes and hypocentral distances) were elaborated with the code MINUIT ver94.1 (James, 1998) which is based on the simplex method of Nelder and Maed (1965) and the variable metric method of Fletcher (1970), in order to fit equation 2. The data sample consists of 5270 data points corresponding to mean SWA records of the 473 earthquakes with available M_W. The derived coefficient-values are $n=1.2614$, $K=0.0031$ and $c=0.9043$ (Figure 3).

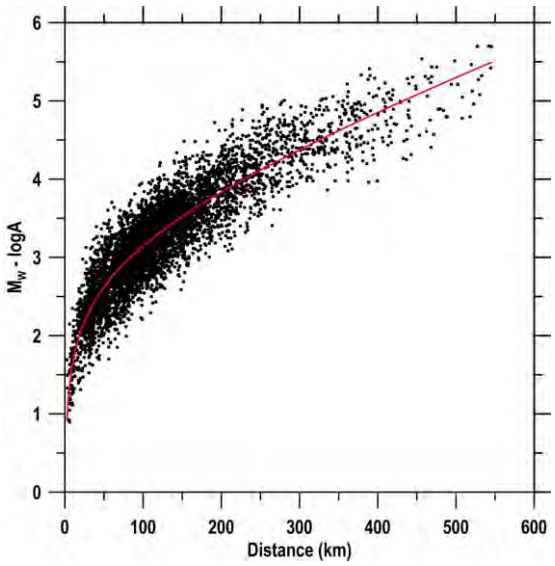

Figure 3 - Calibration function for shallow (h<40km) earthquakes. The line represents the best fitting the data curve.

Individual differentiations from M_W values have been calculated and used as level-corrections for each station in order to avoid biases related to possible inconsistencies in instruments responses. The procedure has been repeated for defining this way more representative n, K and c values. To further ameliorate the correlation of the estimated magnitude with M_W, individual correction, d_i, was estimated for each station, by keeping the n, K and c values and using each station's data separately. Such corrections are attributed to the local conditions of each station. The results for all 98 available stations are shown on Table 1.

Table 1. Station corrections attributed to local conditions.

Net	Station Code	d_i
HA	ACOR	-0.1791
HT	AGG	0.0488
HT	ALN	0.0910
HP	AMT	-0.2016
HL	ANKY	0.0740
HP	ANX	-0.1302
HT	AOS	0.0740
HL	APE	0.1551
HL	ARG	0.0038
HA	ATAL	0.2638
HL	ATH	-0.0863
HA	ATHU	0.4175
HA	AXAR	-0.3430
HT	CHOS	-0.0804
HT	CMBO	-0.3415

Net	Station Code	d_i
HP	DID	-0.0418
HA	DIDY	-0.0081
HP	DRO	-0.2160
HP	DSF	0.0874
HP	DSL	-0.0285
HP	DYR	0.1284
HP	EFP	-0.0753
HA	EREA	-0.0227
HL	EVR	0.0515
HT	FNA	-0.0859
HA	FYTO	0.2408
HT	GRG	-0.0206
HP	GUR	-0.2064
HL	GVD	-0.1377
HT	HORT	0.2369

Net	Station Code	d_i
HL	IACM	-0.4053
HL	IDI	0.2022
HT	IGT	0.1432
HL	IMMV	-0.1219
HL	ITM	0.0998
HL	JAN	-0.0397
HA	KALE	-0.0236
HL	KARP	-0.0557
HA	KARY	0.0722
HT	KAVA	0.0737
HL	KEK	0.0770
HL	KLV	0.2570
HT	KNT	0.1258
HT	KPRO	0.0368
HT	KRND	-0.0786

Net	Station Code	d_i
HL	KSL	0.1163
HL	KYTH	-0.0315
HL	KZN	0.0296
HA	LAKA	0.0622
HL	LAST	0.1948
HL	LIA	-0.0255
HT	LIT	0.0672
HT	LKD2	-0.0201
HL	LKR	0.0448
HA	LOUT	0.0922
HP	LTK	0.0299
HA	MAKR	-0.3116
HL	MHLO	-0.4520
HA	MRKA	-0.0310
HL	NEO	-0.1274

Net	Station Code	d_i
HT	NEST	0.0261
HT	NIS1	-0.1998
HL	NISR	-0.0927
HL	NPS	0.0451
HL	NVR	0.1136
HT	OUR	-0.0729
HT	PAIG	0.1837
HP	PDO	-0.3495
HL	PLG	0.2552
HL	PRK	-0.2960

Net	Station Code	d_i
HL	PTL	0.0252
HP	PVO	0.0360
HP	PYL	0.1229
HL	RDO	0.0863
HL	RLS	0.2043
HL	SANT	-0.0699
HP	SERG	0.0203
HP	SFD	-0.3116
HT	SIGR	-0.0494
HL	SIVA	-0.2834

Net	Station Code	d_i
HA	SKIA	-0.0694
HL	SMG	-0.1667
HA	SMIA	-0.4173
HL	SMTH	0.0625
HT	SOH	-0.0077
HT	SRS	0.2114
HA	THAL	-0.3020
HT	THE	0.4064
HL	THL	0.1755
HL	VAM	-0.0273

Net	Station Code	d_i
HA	VILL	-0.1367
HL	VLI	0.0213
HL	VLS	0.0842
HP	VLX	-0.1923
HL	VLY	-0.0486
HT	XOR	-0.0255
HL	ZKR	0.1078
HP	ZKS	-0.3141

The final graph representing the dependence of M_w–$logA_0$ upon the hypocentral distance, R, is given in Figure 4. The hypocentral distances are up to ~550km while the parameters best fitting the relation 2 are n=1.2328 (geometrical spreading), K=0.0031 (anelastic attenuation) and c=3.1465, with high correlation (R=0.9247). These values can be considered as representative for Greece and surrounding areas since they are based on data of earthquakes with epicenters satisfactorily covering this area. The respective values for the area of southern California (Hutton and Boore, 1987) are n=1.11 and K=0.00189. Figure 5 shows that the formed calibration function fits well the data of each one of the four contributing networks (HL, HT, HP and HA).

Comparison of these two curves shows (Figure 6) that while the attenuation in Greece is slightly weaker than that of southern California for hypocentral distances up to ~100km, it becomes clearly stronger for distances between 100 and 550km.

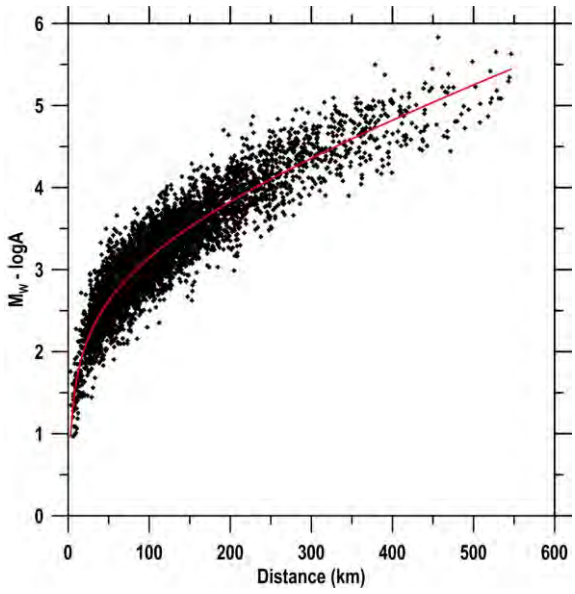

Figure 4- Calibration function for shallow (h<40km) earthquakes after applying the stations' corrections listed on table 1. The line represents the best fitting the data curve.

A data-set consisting of amplitude readings of recent earthquakes which occurred in the broader Aegean area within the year 2012 was used to check the consistency of M_W with the M_L estimated by the relation proposed in the present study. This data-set is completely independent since it didn't participate in geometrical spreading factor and anelastic attenuation parameter estimation and, therefore, it can be used to test new relation's reliability. Thus, using the values of parameters *n, K, c* and d_i in relation 2, the average magnitude for each of these events was re-calculated and its consistency with the respective moment magnitude (only earthquakes with at least two reported M_w values were used to strengthen test reliability) was checked (Figure 7a). Despite the small number of the available pairs (77) and the lack of enough M_WGCMT observations, the regression analysis showed clear linearity expressed by the relation $M_W=M_L+0.04$, with high correlation (R=0.94) and low standard deviation (σ=0.18). Clear equivalence of these two magnitude scales is also revealed by using 192 M_W/M_L pairs concerning earthquakes of the time period 2007-2011 ($M_W=M_L-0.003$, R=0.96, σ=0.17, Figure 7b). This objective test shows clear equivalency between the original M_W and the M_L derived from the relation proposed in the present study, for a wide range of values (~3.5-6.5). The high correlation can be attributed to the good quality of readings of digital recordings, to the stable behavior of the digital sensors and to the robustness of the geometrical spreading factor and anelastic attenuation coefficient, defined in the present study.

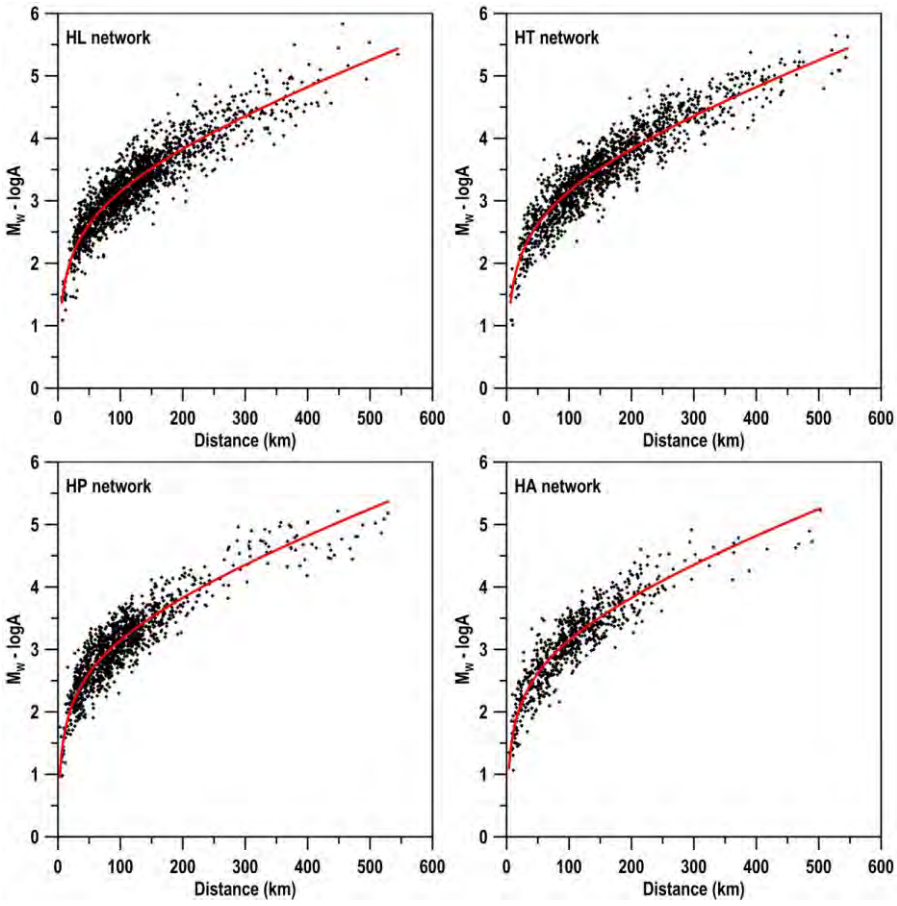

Figure 5 - Plot of *M-logA* versus hypocentral distance for the stations of each one of the four participating networks (the lines represent the final calibration function defined in the present work).

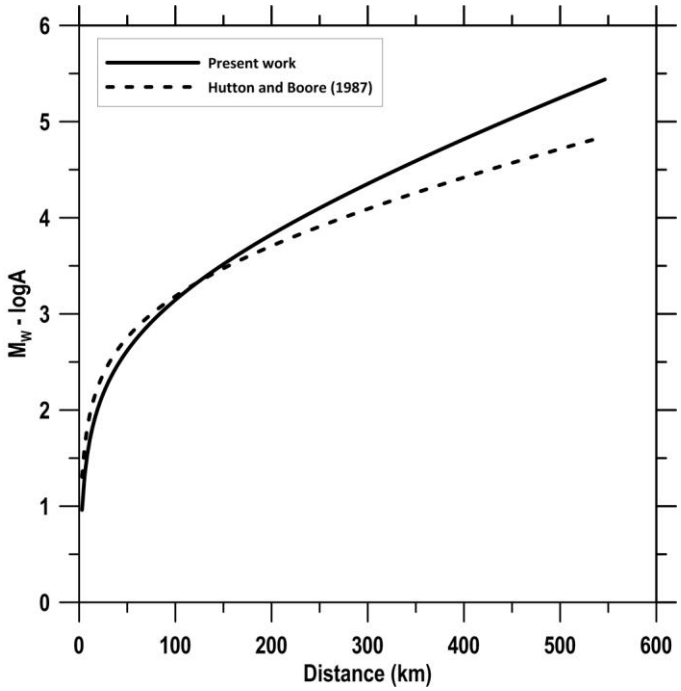

Figure 6 - Comparison of calibration functions for Greece (defined in the present work, solid line) with that (dashed) for southern California (Hutton and Boore, 1987).

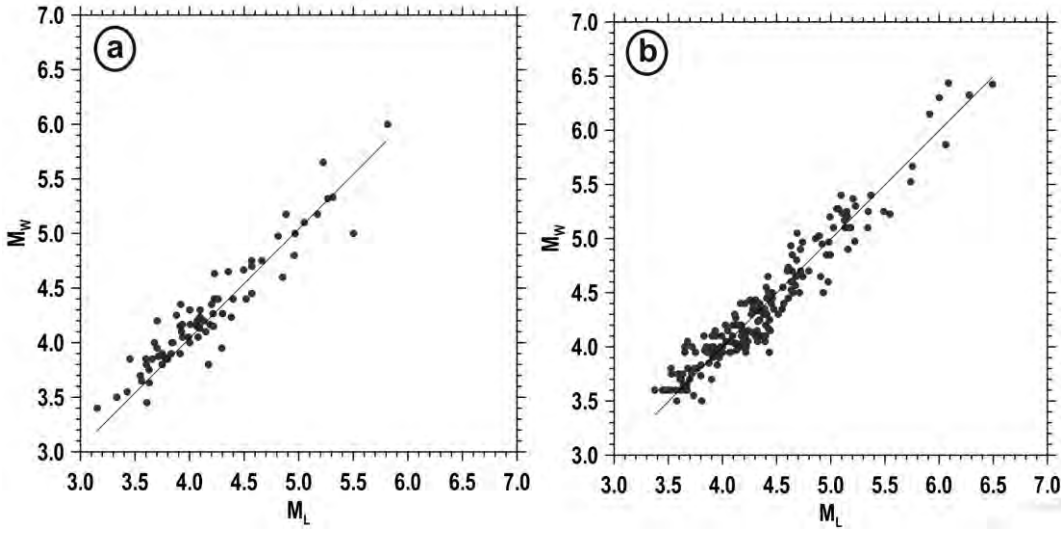

Figure 7 - Comparison between original M_W and M_L estimated by relation 2 of this work for two data-sets: a) independent data-set (2012) used to test new relation's reliability and b) main data-set (2007-2011) used for new geometrical spreading factor and anelastic attenuation parameter estimation. Straight lines represent the lines best fitting the data, in the least-squares' sense.

4. Conclusions

The goal of the present work is to define new reliable attenuation parameters and station-level corrections for local magnitude estimation in Greece based on reliable recordings of digital broad-band instruments of the HUSN. For this reason an adequate amount of high quality data has been used assuring the robustness of the result.

Amplitude readings measured on synthetic Wood-Anderson (SWA) recordings produced by digital broad-band instruments, form our data-tank. Only records that correspond to shallow earthquakes (focal depths up to 40 km) which occurred in Greece and surrounding areas during the time-period October 2007 – December 2011 are considered.

Both geometrical spreading and anelastic attenuation were examined. The finally estimated parameters, n=1.2328 for the geometrical spreading factor, K=0.0031 for the anelastic attenuation coefficient and $c=3.1465$ for the correction term, were used in order to define leveling correction corresponding to each station (tables 3 and 4). It is obvious that geometrical spreading plays the main role while anelastic attenuation is rather negligible. Comparison of the derived calibration function with that of southern California, defined by Hutton and Boore (1987), shows slightly weaker attenuation in Greece for hypocentral distances up to ~100km, but noticeably stronger for distances between 100 and 550km.

Comparison of the magnitudes, M_L, which are estimated by the relation proposed in this study, with original M_W (Figure 7) for two data-sets, one of recent earthquakes (not used to produce the relation) and a second one with earthquakes occurred during 2007-2011, shows that these two magnitude scales are equivalent with high correlation coefficients ($R=0.94$ and $R=0.96$, respectively), for a wide range of magnitudes.

The proposed relation can be used in the routine analyses for reliable estimation of earthquake magnitudes in Greece. It can be also used to create homogeneous earthquake catalogs with reliable magnitudes accurately estimated and expressed in a common and widely used scale such as the local magnitude scale.

5. Acknowledgments

The maps were produced with the GMT software (Wessel and Smith, 1995). This research has been co-financed by the European Union (European Social Fund – ESF) and Greek national funds through the Operational Program "Education and Lifelong Learning" of the National Strategic Reference Framework (NSRF) - Research Funding Program: THALES. Investing in knowledge society through the European Social Fund. Project SEISMO FEAR HELLARC. Geophysics Department Contribution Number 807/2013.

6. References

Anderson J.A. and Wood H.O. 1924. A torsion seismometer, *J. Opt. Soc. Am. Rev. Sci. Inst.,* 8, 817–822.

Anderson J.A. and Wood H.O. 1925, Description and theory of the torsion seismometer, *Bull. Seism. Soc. Am.,* 15, 1–72.

Bakun W.H. and Joyner W.B. 1984. The M_L scale in central California, *Bull. Seism. Soc. Am.,* 74, 1827-1843.

Bakun W.H., Houck S.T. and Lee W.H.K. 1978. A direct comparison of "synthetic" and actual Wood-Anderson seismograms, *Bull. Seism. Soc. Am.,* 68, 1199-1202.

Bollinger G.A., Chapman M.C. and Sibol M.S. 1993. A comparison of earthquake damage areas as a function of magnitude across the United States, *Bull. Seim. Soc. Am.,* 83, 1064-1080.

Boore D.M. 1989. The Richter scale: its development and use for determining earthquake source parameters, *Tectonophysics*, 166, 1-14.

Brazier R.A., Miao Q., Nyblade A.A., Ayele A. and Langston C.A. 2008. Local magnitude scale for the Ethiopian Plateau, *Bull. Seism. Soc. Am.*, 98, 5, 2341-2348.
Fletcher R. 1970. A new approach to variable metric algorithms, *Comput. J.*, 7, 308-313.
Grünthal G. and Wahlström R. 2003. An M_W based earthquake catalogue for central, northern and northwestern Europe using a hierarchy of magnitude conversions, *J. Seismol.,* 7(4),507-531.
Hanks T. and Kanamori H. 1979. A moment magnitude scale, *J. Geophys. Res.,* 84, 2348–2350.
Heaton T., Tajima F. and Mori A. 1986. Estimating ground motions using recorded accelerograms, *Surv. Geophys*. 8, 25–83.
Hutton L.K. and Boore D.M. 1987. The M_L scale in southern California, *Bull. Seism. Soc. Am.*, 77, 2074-2094.
James R. 1998. MINUIT: Function minimization and error analysis, *Reference Manual, Ver 94.1, CERN Geneva, Switzerland*, 54pp.
Johnston A.C. 1996. Seismic moment assessment of earthquakes in stable continental regions-I. Instrumental seismicity, *Geophys. J. Int.,* 124, 381–414.
Kanamori H. 1977. The energy release in great earthquakes, *J. Geophys. Res.,* 82, 2981–2987.
Kanamori H. and Jennings P.C. 1978. Determination of local magnitude, M_L, from strong motion accelerograms, *Bull. Seism. Soc. Am.*, 68, 471-485.
Kim W.Y., Wahlström R. and Uski M. 1989. Regional spectral scaling relations of source paramet ers for earthquakes in the Baltic Shield, *Tectonophysics,* 166, 151-161.
Kiratzi A.A. 1984. Magnitude scales for earthquakes in the broader Aegean area, *Ph.D. Thesis,* Aristotle University of Thessaloniki, 189 pp.
Kiratzi A.A. and Papazachos B.C. 1984. Magnitude scales for earthquakes in Greece, *Bull. Seism. Soc. Am.,* 74, 969–985.
Margaris B.N. and Papazachos C.B. 1999. Moment-magnitude relations based on strong-motion re cords in Greece, *Bull. Seism. Soc. Am.,* 89, 442–455.
Nelder J.A. and Mead R. 1965. A simplex method for function minimization, *Comput. J.*, 7, 308-3 13.
Papazachos B.C., Kiratzi A.A. and Karakostas B.G. 1997. Toward a homogeneous moment-magnitude determination for earthquakes in Greece and surrounding area, *Bull. Seism. Soc. Am.,* 87, 474–483.
Papazachos B.C., Karakostas V.G., Kiratzi A.A., Margaris B.N., Papazachos C.B. and Scordilis E. M. 2002. Uncertainties in the estimation of earthquake magnitudes in Greece, *J. Seismol.,* 6, 557–570.
Richter C. 1935. An instrumental earthquake magnitude scale, *Bull. Seism. Soc. Am.,* 25, 1–32.
Richter C.F. 1958. *Elementary Seismology*, W.H. Freeman, San Francisco, 578pp.
Scordilis E. 1985. A microseismicity study of the Serbomacedonian zone and the surrounding area , *Ph.D. Thesis,* University of Thessaloniki, 250 pp.
Scordilis E.M. 2006. Empirical global relations converting M_S and m_b to moment magnitudes, *J. Seismology,* 10, 225-236.
Shedlock K.M. 1999. Seismic hazard map of North and Central America and the Caribbean, *Ann. Geofis.,* 42, 977–997.
Uhrhammer R. and Collins E. 1990. Synthesis of Wood Anderson seismograms from broadband digital records, *Bull. Seism. Soc. Am.,* 80, 702–716.
Uhrhammer R.A., Loper S.J. and Romanowicz B. 1996. Determination of local magnitude using B DSN broadband records, *Bull. Seism. Soc. Am.,* 86, 1314–1330.
Utsu T. 2002. Relationships between magnitude scales, *International Handbook of Earthquake an d Engineering Seismology,* 81, 733–746.
Wahlström R. and Grünthal G. 2000. Probabilistic seismic hazard assessment (horizontal PGA) for Sweden, Finland and Denmark using different logic tree approaches, *Soil Dyn. Earthq. Eng.,* 20, 45–58.
Wessel P. and W. Smith 1995. New version of the Generic Mapping Tools, *EOS,* 76**,** 329.

Δελτίο της Ελληνικής Γεωλογικής Εταιρίας, τομ. XLVII , 2013
Πρακτικά 13ου Διεθνούς Συνεδρίου, Χανιά, Σεπτ. 2013

Bulletin of the Geological Society of Greece, vol. XLVII 2013
Proceedings of the 13th International Congress, Chania, Sept. 2013

SIMULATION OF ERT SURFACE-TO-TUNNEL MEASUREMENTS

Simyrdanis K.[1], Tsourlos P.[1], Soupios P.[2] and Tsokas G.[1]

[1] *Aristotle University of Thessaloniki, Faculty of Geology, Department of Geophysics, ksimirda@geo.auth.gr, tsourlos@geo.auth.gr, gtsokas@geo.auth.gr*

[2] *Technological Educational Institute of Crete, Department of Natural Resources and Environment, soupios@chania.teicrete.gr*

Abstract

The applicability of surface-to-tunnel electrical resistance tomography (ERT) measurements using a simulation tank for imaging subsurface targets is studied in this work. The tank was filled with water and inside of it was placed firmly a plastic construction where all targets were placed. Some of the targets that used were: a void plastic cylinder (resistive target) and metal plates (conductive target). Data were collected with a multichannel resistivity meter.

The initial scope for these tests was to verify the reliability of developed inversion software which was modified to cope with the specific measurements (surface-to-tunnel). Furthermore, during several experiments different electrode arrays (standard as well as new optimized) were validated. In our attempt to show the advantages of surface-to-tunnel measurements we analyzed the resolution for each configuration of traditional (surface) and surface-to-tunnel arrays. Studies also included testing the electrode displacement effect and also the effect of the tunnel size into the measurements.

Key words: *surface-to-tunnel, ERT, simulation-tank.*

Περίληψη

Στην παρούσα εργασία με τη χρήση μίας δεξαμενής προσομοίωσης πραγματικών συνθηκών πραγματοποιήθηκαν μία σειρά πειραμάτων ώστε να μελετηθεί η εφαρμογή της διάταξης επιφανειακών-τούνελ ηλεκτροδίων. Στη δεξαμενή τοποθετήθηκε ειδικά κατασκευασμένη διάταξη για την τέλεση των πειραμάτων. Χρησιμοποιήθηκαν μία σειρά από ετερογενείς στόχους (αντιστατικούς και αγώγιμους) και η δεξαμενή πληρώθηκε με ομογενές μέσο (νερό). Για τη λήψη των μετρήσεων χρησιμοποιήθηκε πολυκάναλο όργανο.

Ο αρχικός σκοπός των πειραμάτων ήταν να επιβεβαιωθεί η ορθότητα του κώδικα, ο οποίος προσμαρμόσθηκε ώστε να είναι εφικτές αυτού του είδους οι μετρήσεις. Επιπλέον εφαρμόσθηκαν καινούρια πρωτόκολλα, όπως επίσης και έγινε χρήση βέλτιστων μετρήσεων. Τέλος, μελετήθηκε η επίδραση των λανθασμένης θέσης των ηλεκτροδίων και η επίδραση του μεγέθους του τούνελ στα δεδομένα.

Λέξεις κλειδιά: *Τούνελ, δεξαμενή προσομοίωσης.*

1. Introduction

ERT measurements are routinely being used in order to map the subsurface. Initial limitations of surface electrode arrays regarding the resolution with depth were overcome by introducing electrodes in boreholes. Among existing electrode arrangements one special case is when electrodes are used in tunnels. Actually, installing electrodes in tunnels is an easy way to obtain information of increased sensitivity by taking advantage of the proximity of the tunnel to the prospected targets. Application of electrodes in tunnels has been proposed in geotechnical investigation (Danielsen et al., 2010), as well as in the case of in-tunnel mining prospection (van Schoor et al., 2010). The present study deals with the case of ERT measurements obtained in a combined mode using electrodes both on surface and in tunnel. Such an arrangement is expected to provide an increased imaging resolution for the area in-between the tunnel and surface and can be used for geological, geotechnical and mining applications. Only limited application of such a measuring mode has been reported in literature describing surface-to-tunnel application for very deep mining (Sasaki et al., 1993).

Although this arrangement shares many similarities with the cross-hole ERT mode the major difference has to do with the fact that measurements associated with surface electrodes exhibit different sensitivities compared to measurements involving tunnel electrodes. Further, the tunnel itself may be a source of significant noise for the measurements. Other issues that need to be investigated have to do with the sensitivity of the results in relation to the accuracy of the electrode positioning which may be problematic for the case of surface-to-tunnel measurements.

Simulation tank simulations are being used as a bridge between synthetic and real data. Simulation tank data verify computer simulations and at the same time provide more realistic measurements which reassemble more closely the actual field data. At the same time simulation tank data allow to use not only simple but also complicated models. Several such models were tested using different array protocols in order to evaluate the tunnel-to-surface measuring mode.

2. Methodology

2.1. Electrode Arrays - Protocols

An existing Matlab based 2.5D modelling /inversion algorithm (Karaoulis 2009; Tsourlos , 1995) has been modified in order to accommodate the tunnel-to-surface measuring mode. The scheme is being based on a finite element forward solver (Figure 1) while inversion is performed via an iterative smoothness constrained scheme. The forward solver, given the coordinates of the electrodes, generates an appropriate mesh so that the forward and inverse calculations can take place.

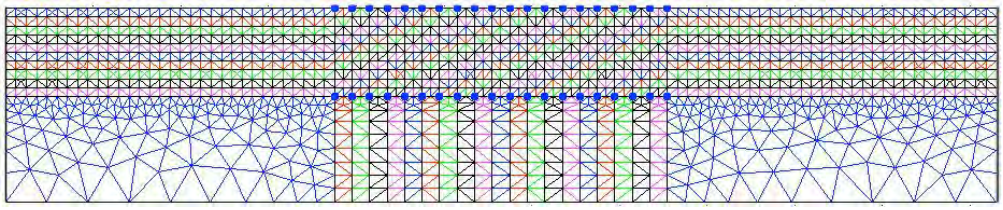

Figure 1 – Mesh (created by FEM) used using surface to tunnel measurements.

Tunnel-to-surface measuring mode can be applied in order to increase the investigation depth of the geoelectrical measurements when there is the possibility of installing electrodes within an existing tunnel (see Figure 2).

It is noted that for the tunnel-to-surface there are no standard array configuration that can be used. However due to the analogy with the cross-hole ERT arrangement arrays proposed and used in this mode can be transferred and used in the tunnel-to-surface case. The electrode arrays that have been

used are: bipole-bipole (bb), pole-dipole (pd) and pole-tripole (pt), where A, B are the current electrodes and M, N are the potential electrodes (Figure 3).

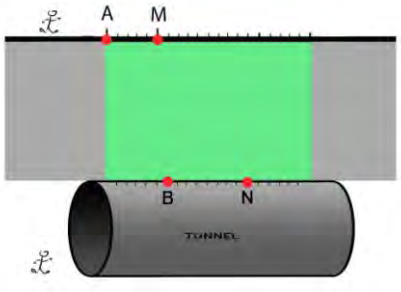

Figure 2 – Application of surface-to-tunnel arrays (A, B current electrodes, M, N potential electrodes).

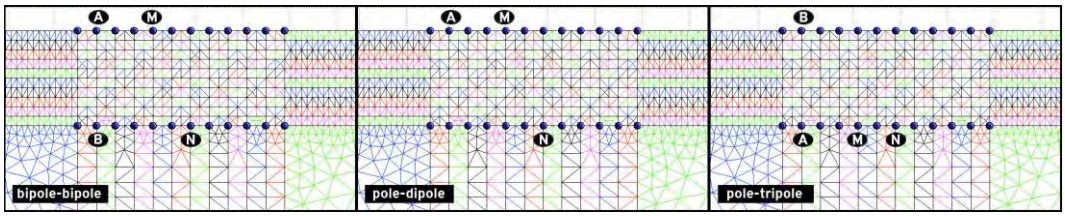

Figure 3 – Protocols that were used for this work: Bipole-bipole, Pole-dipole and Pole-Tripole.

3. Simulation Tank – Experiment Setup

The simulation tank experiments took place at the Laboratory of Geophysics & Seismology, Department of Natural Resources & Environment (Technological Educational Institute of Crete) (Figure 4). The simulation tank is made by Plexiglas and is placed within a metal framework to increase its stability. The capacity is $1m^3$ and can hold weight more than 10^3 liters of water. During the experiment the tank was filled with drinking and deionized water, so conductivity could be altered at will.

Figure 4 – Simulation tank used for the experiments in Laboratory of Geophysics & Seismology (Department of Natural Resources & Environment).

On top of the tank a special construction to simulate tunnel-to-surface measurements was placed. The construction consists of three parallel plastic pipes: green, blue and black (each has a different purpose) (Figure 5). The green pipe contains a series of electrodes that are situated on surface of water. Blue coloured part contains electrodes that will be induced inside medium and black pipe contains electrodes that simulate a "tunnel" condition since is fully sealed and air filled. The whole construction was built with plastic parts (for conductivity reasons) and additionally has the ability to adjust the distance between the series of "surface" and "tunnel" electrodes (form 5 to 25cm). The probe spacing between electrodes is fixed to 2 cm while 20 electrodes have been placed in each of the pipe. (60 electrodes total). The blue pipe has the extra ability to slightly shift its position horizontally so that the effect of electrode displacement can be studied. The black pipe has a diameter of 7 cm. The whole construction can be firmly placed on tank so that can be stable as experiment takes place.

Figure 5 – Construction used for the experiments. It consists of three parts (green, blue and black) which distance can be chosen by will. Whole construction is made by plastic parts for conductivity reasons.

The equipment that was used for obtaining the measurement is the single channel resistivity meter Syscal R1 Plus (Iris Instruments) (Figure 6, left) while a pocket conductivity meter was used to measure in situ the conductivity of the water that filled the tank (Figure 6, right).

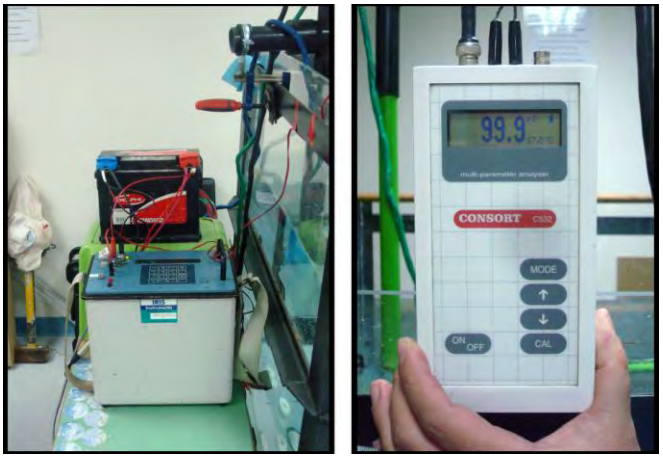

Figure 6 – (left) "Iris" instrument for acquiring electrical data, (right) "Consort" a conductivity meter for measuring medium inside tank.

Some typical targets that were used include: void plastic cylinder filled with air or polystyrene pieces (resistive objects) and metal plates (as conductive objects) (Figure 7). The distance between the surface and "tunnel" arrays that was tested was 10, 15 and 20 cm. The conductivity of drinking water was measured to 34 ohm and for deionized water to 100 ohm.

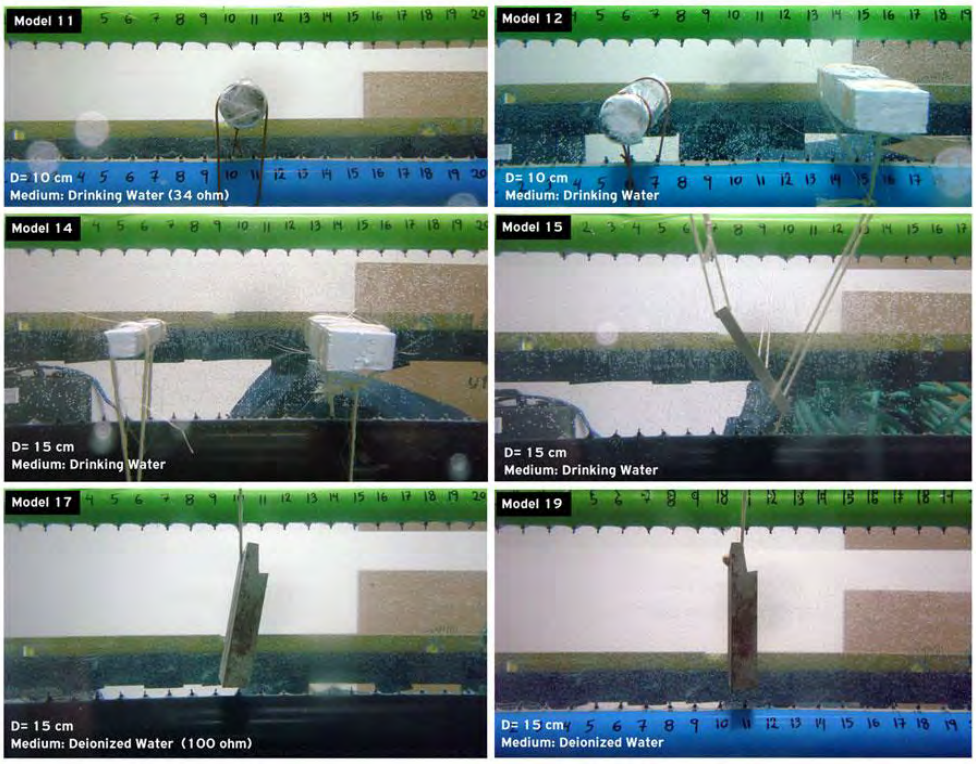

Figure 7 - Targets for detection embedded inside water (void cylinder, polystyrene, metal plates).

4. Results

4.1. Resolving ability of tunnel-to-surface measuring mode

Initial tests are related to establishing the increased resolving ability of surface-to-tunnel array over standard measuring modes (i.e. surface measurements). For the particular example the tank was filled with deionized water (100 ohm resistivity) and a metal plate (see Figure 8) was used as a target. Protocols tested involved bipole-bipole, pole-dipole and pole-tripole arrays.

For all cases individual surface and tunnel data sets were inverted and results are compared with the inversions of the surface-to-tunnel arrays. The results are presented in Figure 9 and it is clear that surface measurements sensitivity is limited only to the top part of the model: the metal target is identified only close to electrodes for all tested arrays. Same happens when electrodes inside earth since only the part of the target which is close to interior electrodes is reconstructed. On the other hand when surface-to-tunnel array is used resolution is increased and the modeling body is clearly depicted throughout its length suggesting that this type of measuring mode is optimum. Comparing the protocols it can be observed that pole-tripole describes better the limits of the target. Bipole-bipole depicts the conductive body is less accurate and pole-dipole is more accurate at bottom area.

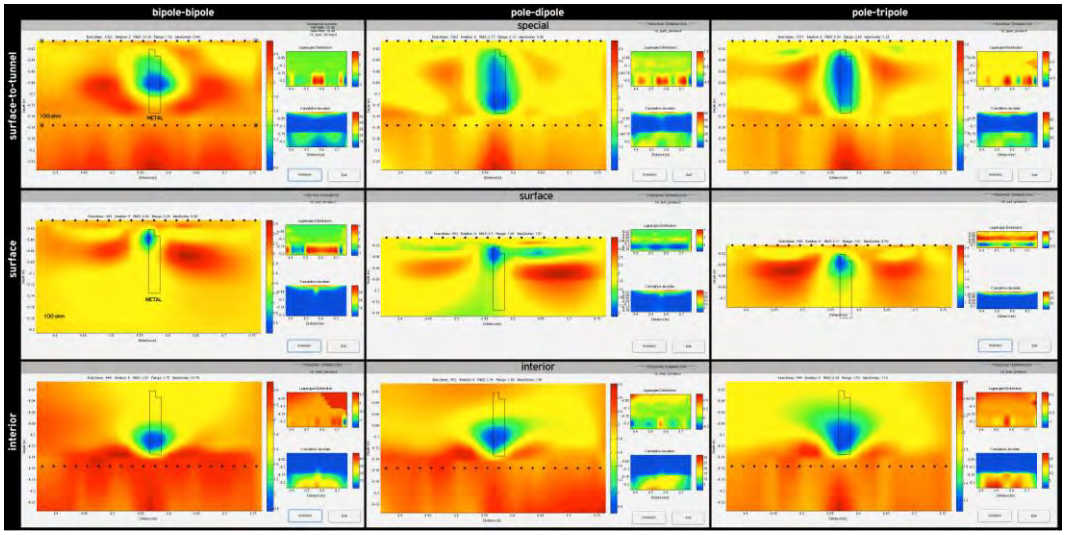

Figure 8 - Inversion results using conductive target inside water.

4.2. Comparing Array Protocols

Furthermore optimum measurements were created in order to reduce acquisition time and inversion procedure time. Starting from a complete large data set a limited initial set is generated using a criterion based on Jacobian matrix (Athanasiou et al., 2007). Subsequently, this initial set is enriched with additional optimum measurements which are selected on the basis of a resolution matrix analysis following the procedure proposed by Wilkinson et al (2006).

As it can be seen in Figure 10 inverted results of the optimized data sets for the model 12 (see Figure 8) produce at least equally good results and in many cases their inverted images are superior to the standard arrays' results. Bipole-Bipole optimum sets have resistivity values closer to the target resistivity than the standard data set. Pole-Dipole optimum protocols define better the target limits than the standard data set. Pole-Tripole optimum protocol has better results (taking into account % RMS error) than the standard set of measurements.

The obvious benefit of choosing optimum arrays instead of standard protocols is that they can produce these results by just using only a small portion of the complete set of measurements. In the presented model (Figure 10) and for all tested arrays all standard sets of measurements include more than 1900 measurements while all optimum sets involve less than 500 measurements. Apparently both measuring and inversion time is reduced in the case of optimum arrays.

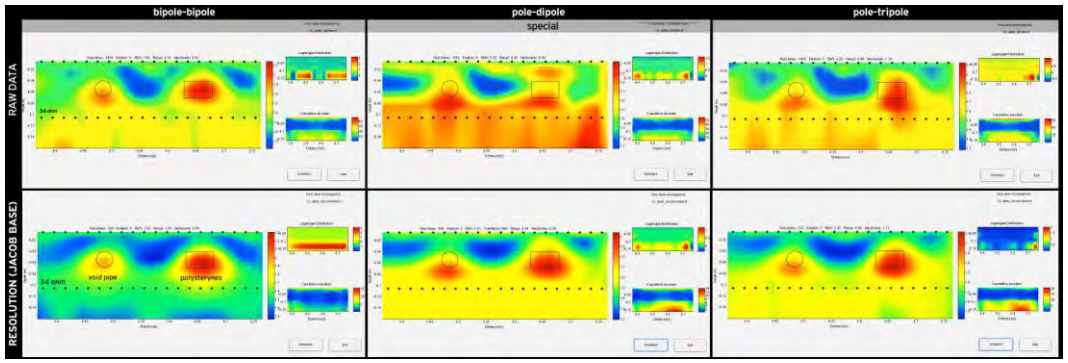

Figure 9 – Inversion results using optimum measurements: Jacobian matrix (second row), Resolution matrix (third row).

4.3. Tunnel Effect

A particular problem of the tunnel-to-surface measuring mode has to do with the effect that an air-filled tunnel has to our measurements and subsequent inversions. Several model and array configurations were tested to study this effect by using an air filled pipe (black pipe in Fig. 11) to simulate the effect of a tunnel to our measurements.

Figure 10, depicts the raw data inversions (top row) for several arrays when an air filled "tunnel" is considered. It is clear that the existence of the tunnel affects inversions severely generating major artifacts. Actually it can be easily seen that the amount of induced noise has to do with the size of the tunnel (tunnel diameter) in relation to the inter-electrode spacing. There are many possible procedures to alleviate this affect but the simplest (and crudest one) is to ignore measurements which have spacing comparable (i.e equal or smaller) to the diameter for the tunnel (figure 11, bottom row).

As it can be seen in Figure 11 for all protocols after applying this type of correction target appears more clearly this procedure may affect the resolving ability of the measuring mode near the tunnel area.

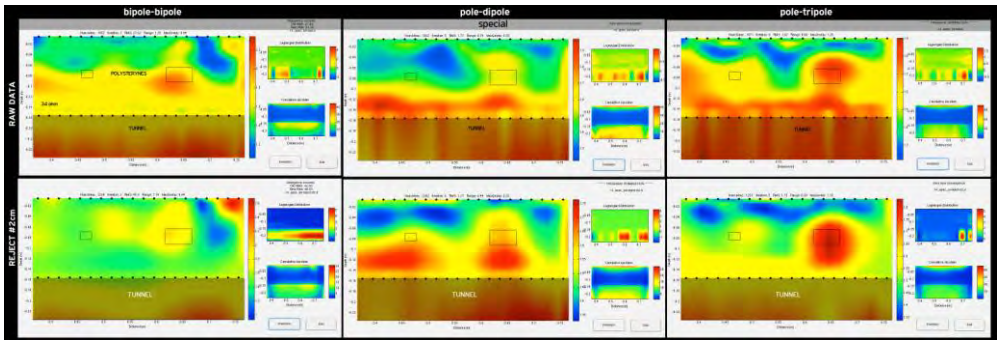

Figure 10 – Inversion results depicting target above a tunnel raw data (top row) and corrected data (bottom row).

4.4. Electrode Displacement

In real case situations many times electrode displacement can occur and this can lead to erroneous results. We used the simulating tank to test this effect using all different protocols (bb, pd, pt). The "tunnel" electrodes were slightly displaced (1 inter-electrode spacing step) and measurements were obtained for different modes. Data were then inverted as if top and "tunnel" electrodes were aligned.

The derived results suggest that protocols have varying sensitivity to this source of noise. Figure 11 shows the misfit that occurs when there is offset between the two arrays, using all protocols.

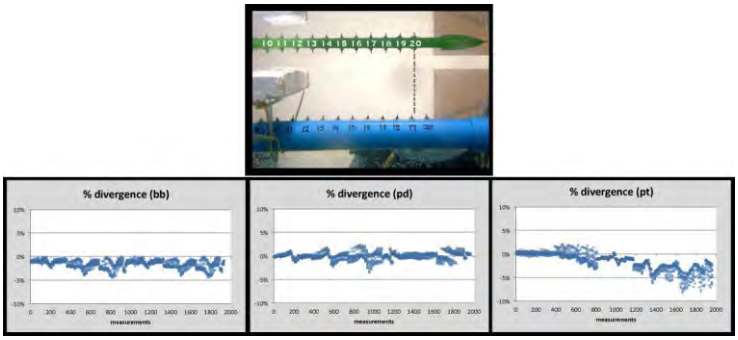

Figure 11 – Offset calculated with electrode displacement (top), % divergence occurred (bottom).

Results show that bb and pd are the two less sensitive protocols. In Figure 12 we can see inversion results for 0% and 100% offset for protocol bb and pt. The distortion of the target shows clearly how electrode displacement effects data in pt protocol.
All tests suggest that bb is the least sensitive protocol to the electrode displacement, which means the most appropriate to use, when the electrode position is not accurate.

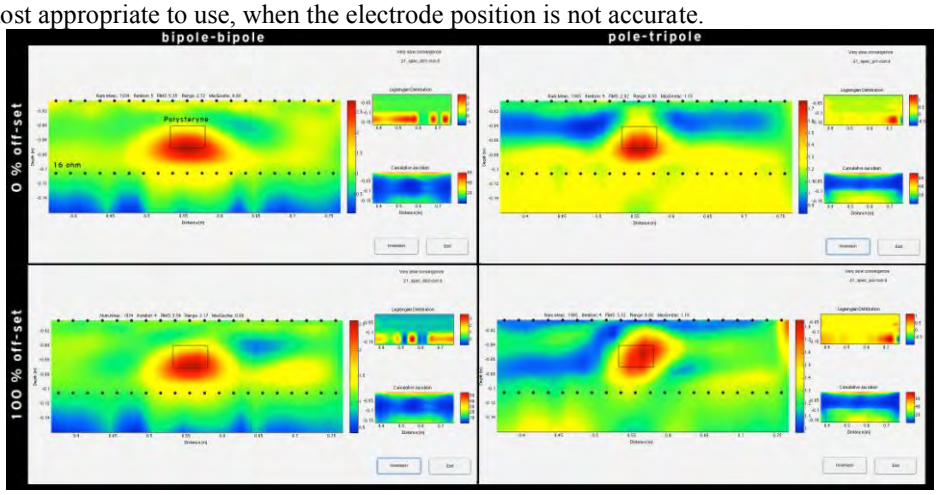

Figure 12 – Inversion results with 0% (top row) and 100% (bottom row) electrode displacement for protocol bb (left column) and pt (right column).

5. Conclusions

The simulation tank experiments proved a valuable tool that can act as a bridge between computer simulated data and reality since many scenarios can be studied in a fully controlled environment. Experiments have clearly demonstrated that the surface-to-tunnel array has increased resolution over the standard surface array therefore this type of measuring mode, when feasible, is preferable.

Optimum measurements were generated in order to reduce acquisition and inversion procedure time. Bipole-bipole optimum sets have resistivity values closer to the target resistivity than the standard data set. Pole-dipole optimum protocols define better the target limits than the standard data set and pole-tripole optimum protocol has better results than the standard set of measurements.

A particular problem of the tunnel-to-surface measuring mode has to do with the effect that an air-filled tunnel has to our measurements and subsequent inversions. It is shown that this effect can be very important and that it need to be taken in to account. There are many possible procedures to alleviate this affect and in this work we have chosen to ignore measurements which have spacing comparable (i.e. equal or smaller) to the diameter for the tunnel. Results suggest that inversion quality is significantly improved when this correction is applied.

Finally the electrode displacement effect was studied and results suggest that that bipole-bipole is the least sensitive protocol to this source of noise. Therefore it is suggested that this array is used when a limited positioning accuracy can be achieved.

6. Acknowledgements

This work is supported by the EU project: “Operational Program Educational and Lifelong Learning, investing in knowledge society, Ministry of Education, Lifelong Learning and Religious Affairs, NSFR, 2007-2013”

European Union
European Social Fund
OPERATIONAL PROGRAMME
EDUCATION AND LIFELONG LEARNING
investing in knowledge society
MINISTRY OF EDUCATION, LIFELONG LEARNING AND RELIGIOUS AFFAIRS
MANAGING AUTHORITY
NSRF 2007-2013
EUROPEAN SOCIAL FUND
Co- financed by Greece and the European Union

7. References

Athanasiou E., Tsourlos P. and Vargemezis G. 2007. Optimizing Electrical Resistivity Array Conf igurations for Hydrogeological Studies, in Coastal Aquifers: Challenges and Solutions, (eds Pulido Bosch, A. ,Lopez- Geta,J.A.& Ramos Gonzalez, G.). *Hidrogeologia y agues subter raneas*, Instituto Geologico y Minero de Espana, Madrid. n23, 243-252

Danielsen B.E. and Dahlin T. 2010. Numerical modeling of resolution and sensitivity of ERT in h orizontal boreholes, *Journal of Applied Geophysics* 70, p. 245–254

Sasaki Y. and Matsuo K. 1993. Surface-to-Tunnel Resistivity Tomography at the Kamaishi Mine, Batsuri- Tansa, vol. 46, 128–133.

Tsourlos P. 1995. Modelling, Interpretation and Inversion of Multielectrode Resistivity Survey Dat a, *Thesis.*

van Schoor M. and Binley A. 2010. In-mine (tunnel-to-tunnel) electrical resistance tomography in South African platinum mines, *Near Surface Geophysics*, 8, 563-574.

Paul B., Wilkinson P.I., Meldrum J.E., Chambers O.K. and Richard D.O. 2006. Improved strategies for the automatic selection of optimized sets of electrical resistivity tomography measu rement configurations, *Geophys. J. Int.,* 167, 1119-1126

Καραούλης Μ.. 2009. Ανάπτυξη Αλγορίθμων Αντιστροφής Διαχρονικών Γεωηλεκτρικών Δεδομένων, *Διδακτορική Διατριβή*.

Δελτίο της Ελληνικής Γεωλογικής Εταιρίας, τομ. XLVII , 2013
Πρακτικά 13ου Διεθνούς Συνεδρίου, Χανιά, Σεπτ. 2013

Bulletin of the Geological Society of Greece, vol. XLVII 2013
Proceedings of the 13th International Congress, Chania, Sept. 2013

RECONSTRUCTING CONCEALED CULTURAL REMAINS THROUGH INTEGRATED GEOPHYSICAL TOMOGRAPHIC METHODS

Soupios P.[1], Papadopoulos N.[2] and Sarris A.[2]

[1] Department of Natural Resources & Environment, Technological Educational Institute of Crete, Greece, email: soupios@chania.teicrete.gr

[2] Laboratory of Geophysical-Satellite Remote Sensing & Archaeo-environment, Institute for Mediterranean Studies - Foundation for Research & Technology, Hellas (IMS/FORTH), emails: nikos@ims.forth.gr, asaris@ret.forthnet.gr.

Abstract

The purpose of this work was to compare the mapping of shallow subsurface archaeological structures through Seismic Refraction Tomography (SRT), Electrical Resistivity Tomography (ERT) and Ground Penetrating Radar (GPR) methods. For achieving the goals of the project, a specific section of the archaeological site in Delphi has been surveyed through the employment of the above techniques. For the SRT survey, twenty four P-wave geophones were installed randomly in a 50 by 40 m area. Totally seventy three (73) shots were made by striking a metal plate with a sledgehammer to collect about 1752 travel-times. The pole-dipole array was employed to capture the ERT data along twenty densely spaced parallel profiles. The GPR data were collected along parallel sections with a resolution of 50 cm between the lines. The SRT and ERT field data were processed with modern tomographic inversion algorithms for the reconstruction of the 3-D velocity and resistivity models describing the buried archaeological remains and the subsurface matrix up to the depth of 5 meters below the ground surface. GPR signals were enhanced with specific filters signifying the shallow structures up to 2 meters below the ground surface. The integrated processing results indicate the existence of walls buried in a relatively uniform background soil. The outcome of this approach signifies that SRT, ERT and GPR methods can be used as a validation tool in any archaeological investigation by providing accurate tomographic subsurface models and contribute in cultural resources management.

Key words: *resistivity tomography, seismic refraction tomography, GPR, 3D, Delphi.*

Περίληψη

Σκοπός της εργασίας είναι να συγκρίνει τα αποτελέσματα της χαρτογράφησης θαμμένων αρχαιολογικών δομών από μία περιοχή στους Δελφούς με τις μεθόδους της ηλεκτρικής και σεισμικής τομογραφίας και τη μέθοδο του Γεωραντάρ. Για την συλλογή των περίπου 1752 χρόνων διαδρομής των επιμήκων κυμάτων, τοποθετήθηκαν 24 γεώφωνα σε μία περιοχή που κάλυπτε μία έκταση 50x40 μέτρα και πραγματοποιήθηκαν 73 κρούσεις μέ ένα σφυρί πάνω σε μεταλλική επιφάνεια. Τα δεδομένα της τρισδιάστατης ηλεκτρικής τομογραφίας συλλέχθηκαν κατά μήκος

πυκνών παράλληλων γραμμών με την διάταξη πόλου-διπόλου όπου η απόσταση μεταξύ των τομών ήταν 1 μέτρο. Η χωρική ανάλυση παράλληλων τομών για τα δεδομένα του γεωραντάρ ήταν 0,5 μέτρα. Τα γεωηλεκτρικά και σεισμικά δεδομένα επεξεργάστηκαν με αλγόριθμους τρισδιάστατης μη-γραμμικής αντιστροφής με σκοπό την ανακατασκευή τρισδιάστατων μοντέλων αντίστασης και ταχύτητας. Τα μοντέλα αυτά περιγράφουν την χωρική κατανομή των αρχαιολογικών λειψάνων μέσα στο υπέδαφος αλλά και τα επιφανειακά γεωλογικά στρώματα μέχρι το βάθος των 5 μέτρων από την επιφάνεια. Επιπλέον τα σήματα του γεωραντάρ ενισχύθηκαν με την εφαρμογή συγκεκριμένων φίλτρων με σκοπό την ενίσχυση της αρχαιολογικής πληροφορίας μέχρι το βάθος των δύο μέτρων από την επιφάνεια του εδάφους. Η συνδυαστική ερμηνεία των γεωφυσικών αποτελεσμάτων δείχνει την ύπαρξη αρχιτεκτονικών δομών μέσα σε ένα αργιλικό περιβάλλον. Τα αποτελέσματα δείχνουν γενικά τη σημασία των τομογραφικών γεωφυσικών μεθόδων προς την κατεύθυνση της πιο ολοκληρωμένης αποτύπωσης των φυσικών ιδιοτήτων του υπεδάφους στο πλαίσιο αρχαιολογικών προσεγγίσεων και της διατήρησης της πολιτισμικής κληρονομιάς .
Λέξεις κλειδιά: *Ηλεκτρική τομογραφία, σεισμική τομογραφία, γεωραντάρ, 3D, Δελφοί.*

1. Introduction

Delphi is both an archaeological site and a modern town in lower central Greece on the south-western side of Mount Parnassus. The site is well known for its Delphic oracle, the most important oracle in the classical Greek world, and a major site for the worship of the god Apollo. The Pythian Games were held every four years, starting in 776 BC. The first excavations in Delphi started in 1892 with the excavation to the sanctuary of Apollon to initiate in 1887. Excavations required the displacement of the old medieval village of Kastri, which was built on the top of the archaeological site, to the outer limits of the site, where now the modern town of Delphi is located. Below the soil depositions due to landslides, the sanctuary of Apollon, the Gymnasium, the Stadium, the settlement and its cemeteries started to be revealed.

In 2012, a three-year archaeological mission was initiated by the French School of Athens having three components (Luce 2012). Through the cleaning of the 19th century trenches, the topographic mapping of the surface monuments and the architectural relics, and the geophysical mapping of the area, the archaeological campaign aims to study the urban organization of the city and its development since the beginning of the occupation in the 16th century BC to its abandonment in the 7th century AD. The first phase of the geophysical investigations was completed within July 2012 focussing mainly at the north-west section of the archaeological site. In this particular area the archaeologists of the 19th century opened a series of about 30 roughly parallel exploratory trenches that brought to light a number of architectural remains. The goals of the geophysical campaign were to reveal the plan of structures between the trenches, with particular attention to those who are continuing from the open ones.

The steep slopes of the terrain of Delphi (~30-40%), the wooded areas, the fire-fighting hoses, the various metal fragments distributed randomly around the site and the deep old trenches made the geophysical prospection of Delphi a real challenge. In order to maximize the results of the geophysical prospection and test the quality of the signals collected, five methods were applied in the site: magnetic gradiometry, electrical resistivity tomography (ERT), multi-frequency controlled source electromagnetic (CSEM), ground penetrating radar (GPR) and seismic refraction tomography (SRT). The investigations were focused below the road that leads to the stadium and above the main road that leads to the sanctuary. The layout of the geophysical grids and the locations of the geophones or the resistivity tomography transects was carried out by a total station and a differential GPS survey (Figure 1).

This work will focus on the results of an integrated geophysical approach that was applied in a small section of the site. This 50 by 40 meters area is outlined with the black thick rectangle in Figure 1. The plateau and the road that exist close to the facilities of the performances of the theatre and the storage area of epigraphic stones found in the site were scanned through by seismic refraction and resistivity tomography methods in order to enhance the information context up to the depth of 5 meters below the ground surface. A complementary GPR survey was used to highlight the superficial structures up to 2 meters. These geophysical techniques were the only ones allowed in the area, as the rest of the methods could not have been employed due to the modern metallic structures that existed in the area. In the following paragraphs the field strategy, the processing steps and the results by the integrated interpretation are explained.

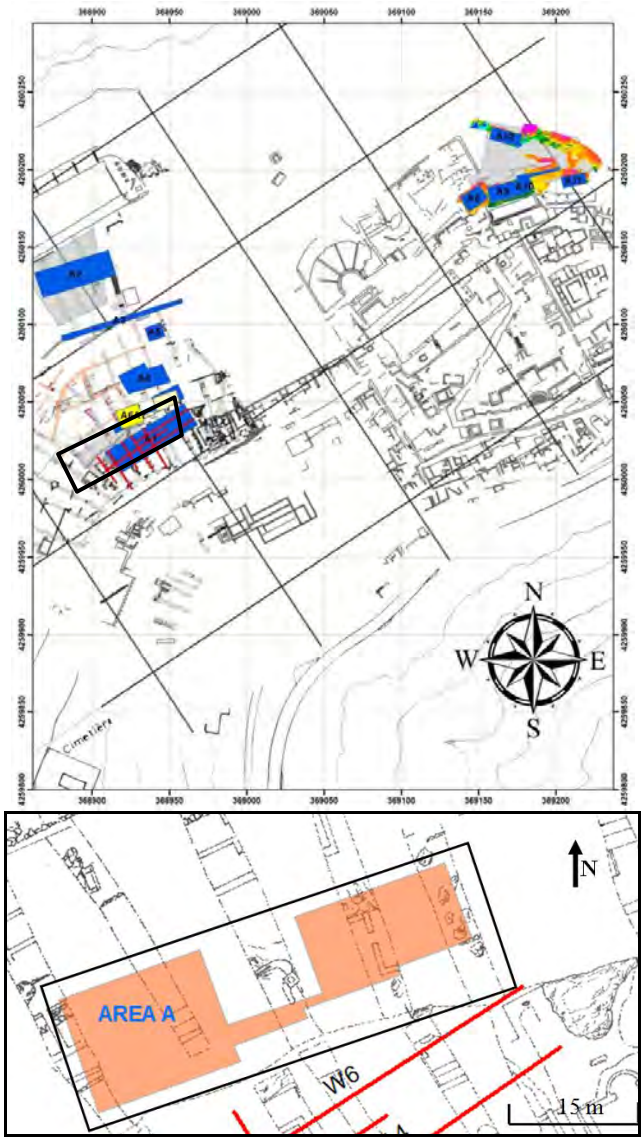

Figure 1 - Overlay of the geophysical grids and transects from the 2012 survey in the area of investigation as it is depicted by the topographic plan of Delphi. The blue areas were all scanned with the GPR. The red lines denote the individual 2-D ERT profiles. The thick rectangular depicts the section (Area A) where the experimental 3-D ERT, SRT and GPR techniques were employed.

2. Data Collection and Processing

2.1. Electrical Resistivity Tomography

The specific scheme of collecting measurements within a dense network of parallel 2-D ERT sections was followed (Papadopoulos et al., 2006) in order to survey an area of about 400 square meters, excluding the inaccessible parts due to modern constructions that prohibited the employment of electrodes in these cases. The basic inter-electrode interval along each profile and the inter-line spacing was one meter (a=1m). The lines had variable length due to obstacles that were scattered in the area. A protocol of a sequence of measurements employing the pole-dipole configuration was programmed into the Syscal Pro Switch resistivity instrument in order to capture the apparent resistivity data with maximum Nsep=10. Additional data with multiple "a" spacing (1a, 2a) were also collected to enhance the signal to noise ratio while trying to investigate at larger depths. Figure 2 (center) shows details of the instrumentation during the collection of the ERT data. The pre-processing stages of the ERT data include the geometry correction of the individual lines and the removal of erroneous extreme high or low apparent resistivity values through despiking filters.

After cleaning the data and bringing them to a suitable format an iterative inversion algorithm (Papadopoulos et al., 2011) was used to reconstruct a 3-D resistivity model of the site. The algorithm uses a 3-D Finite Element Method scheme to numerically solve the Poisson's equation and the adjoint equation technique to calculate the sensitivity matrix. The augmented system $\begin{bmatrix} \mathbf{J}_k \\ \sqrt{\lambda_k}\mathbf{C} \end{bmatrix} \cdot \mathbf{dx}_k = \begin{bmatrix} \mathbf{dy}_k \\ \mathbf{0} \end{bmatrix}$ is solved with an iterative solver (LSMR-Fong and Saunders 2011), where k is the iteration number, $\mathbf{J}_k$ is the Jacobian matrix estimate of the $\mathbf{x}_k$ resistivity distribution, $\mathbf{dx}_k$ is the resistivity correction vector, $\mathbf{dy}_k = \mathbf{y}\text{-}\mathbf{F}(\mathbf{x}_k)$, where $\mathbf{F}(\mathbf{x}_k)$ is the forward modelling operator and $\mathbf{y}$ is the measured data vector, λ_k the Lagrangian multiplier, and $\mathbf{C}$ is the 2nd order smoothness matrix operator. The vector $\mathbf{dx}_k$ is added to the previous vector $\mathbf{x}_k$ to obtain the updated resistivity parameters. The procedure is repeated until an acceptable misfit is reached between the measured and modelled data. The Lagrange multiplier is used to weight the model constraints against the data misfit and the strategy of decreasing λ beginning from a starting value (λ=1) down to a minimum value (λ=0.125) was adopted. Furthermore the choice of calculating only the significant part of the Jacobian matrix was enabled in order to reduce the overall 3-D processing time. The algorithm converged to a final resistivity model after 8 iterations with an RMS less than 10%, describing the subsurface resistivity up to the depth of 5 meters below the surface. Finally horizontal depth slices every 0.5 meter were extracted by the final 3-D inversion resistivity model. Specific sections of the slices were masked illustrate areas with no valid information due to the surface obstacles that prohibited the extension of the lines.

2.2. Seismic Refraction Tomography

The seismic refraction tomography survey covered the whole area of interest. Totally twenty four P-wave geophones were randomly installed on the ground following arbitrary directions in order to have a 3D coverage of the study area. The seismic energy was created by vertically striking a metal ground plate with a 7Kg sledgehammer (Figure 2-right). The shots in each location were repeated at least 4 times to ensure the good quality of signal by stacking the recorded waveforms. Totally 73 shots were used to collect about 1752 traveltimes (73 shots x 24 geophones = 1752 raypaths). Prior the application of seismic tomography, all the collected seismic data were processed using the PickWIN (ver. 3.2.0.1) module of SeisImager processing software in order to pick the first arrivals, the traveltimes and the source – receivers location.

The data were afterwards pre-processed providing information about a) source and receiver exact locations including topographic corrections, b) the experimental geometry and c) the traveltimes recorded per source-receiver pair. Non-commercial software (ATOM_3D, Koulakov 2009) was

used for the inversion and interpretation of the seismic refraction traveltime data. The program uses a ray tracing bending algorithm for solving the forward problem. The model parameterization can be applied by using nodes or cells, polygons or analytical laws. It is only necessary to define an initial velocity model of the study area. The raytracing starts from a straight line connecting source and receiver and iteratively (by using bending method) changes in order to finally achieve the minimum traveltime raypath. The calculated ray tends to travel through high velocity anomalies and avoids low velocity patterns. An iterative routine (LSQR- Paige and Saunders 1982) is used to solve the inverse seismic refraction problem. The amplitude and smoothness of the tomographic solution is controlled by applying regularization constraints. In order to reduce the effect of grid orientation, the inversion is applied in several differently oriented grids (i.e. 0°, 22°, 45° and 67°) and the results are stacked. The final velocity tomographic model was achieved after nine iterations and the final Root Mean Square (RMS) error was 1.03 ms. Finally horizontal velocity tomograms every 0.5 meter up to the depth of 5.5 meters were extracted by the 3-D velocity model.

2.3. Ground Penetration Radar

The GPR data were collected from an area of about 300 square meters with the Noggin Plus Smart Cart system using the 250 MHz antennas (Figure 2-left) partly overlapping the southern part of the investigated area. The effort of the GPR survey was to map the vertical subsurface stratigraphy through parallel profiles. The distance between the individual lines was 0.5 meter while the resolution along each transect was 0.05 meters. This particular field set up can increase the spatial resolution of the subsurface reflections that are related to archaeological structures. The GPR sections were corrected for the local coordinate system. Then the first peak was estimated in order to define the initial useful signal from each line based on the intensity percentage of the first reflected wave (5-30%). Specific filters (AGC, Dewow and DCshift) enhanced the reflected signal, while the rejection of the background noise and the data smoothing was accomplished by a trace-to-trace averaging filter. Finally, horizontal depth slices with thickness 0.2 meters were created by the original vertical sections assuming a velocity for the electromagnetic waves equal to 0.1m/nsec, reaching the maximum depth of 2 meters below the ground.

Figure 2 - Details of the geophysical methods with GPR (left), ERT (center) and SRT (right) that were applied in the area A of the site.

3. Integrated interpretation of geophysical results

The results of the geophysical mapping are presented through colour scale maps depicting the horizontal and vertical variation of the ground resistivity and velocity of seismic waves, as well as the intensity of the reflected electromagnetic waves. The diverse applied geophysical techniques contributed in extracting horizontal slices that describe the spatial variation of the different physical properties in multiple depths below the ground. Reddish colours in the maps indicate increase of the physical property (resistivity, velocity and reflection amplitude) that can be potentially attributed to the existence of buried archaeological structure. The integrated and efficient interpretation of the geophysical results was made possible with the rectification of all the

maps on a common coordinate system and the overlay of them on the topographic plan of the site through a Geographical Information System platform (Figures 3, 4, 5).

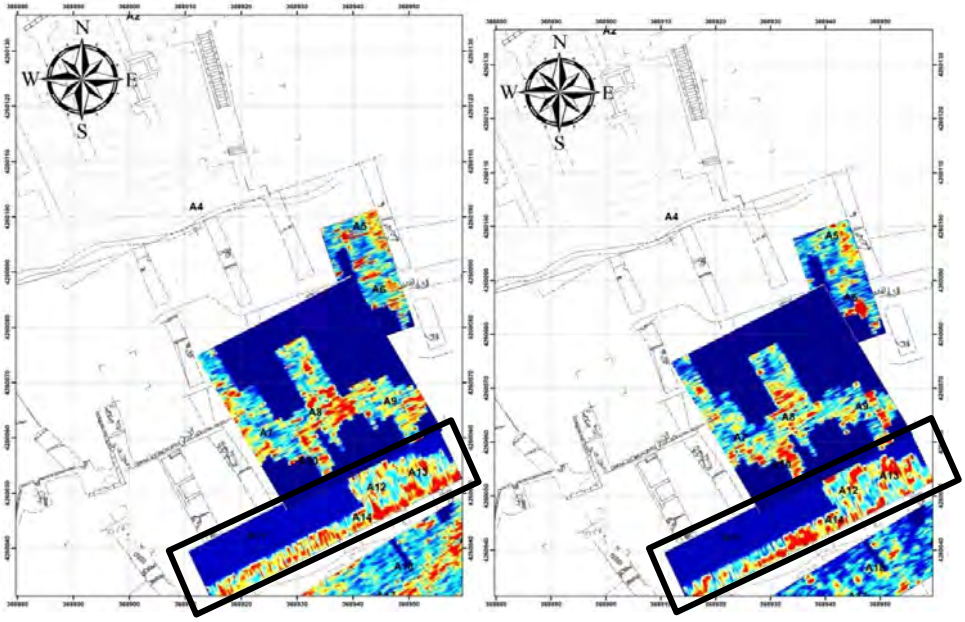

Figure 3 - GPR depth slices for depth less than 1 meter (left) and depth more than 1.5m (right). The section of the area A that was surveyed with the GPR is depicted within the black rectangular.

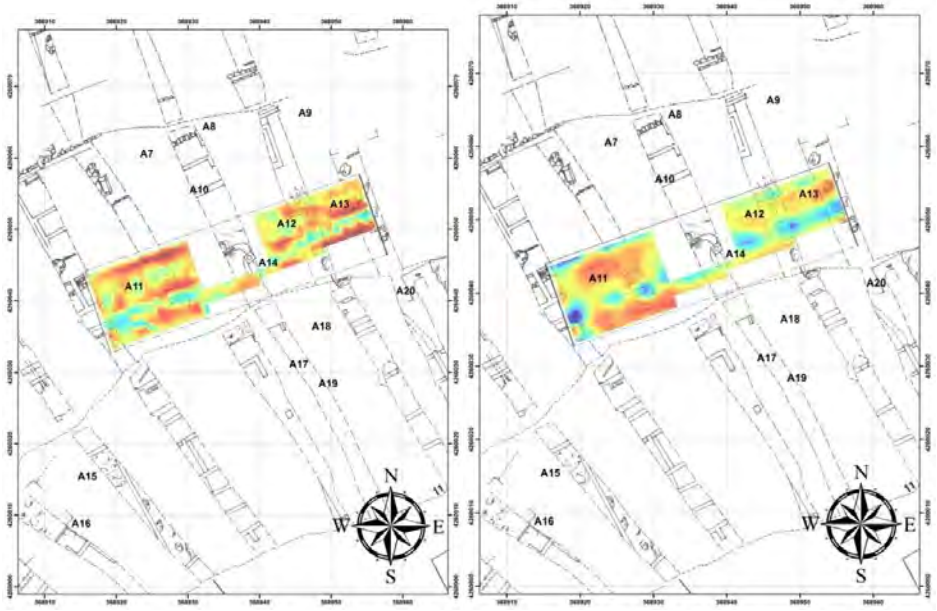

Figure 4 - ERT depth slices of the distribution of the soil resistivity of area A for depth 1 meter (left) and depth 2 meters (right).

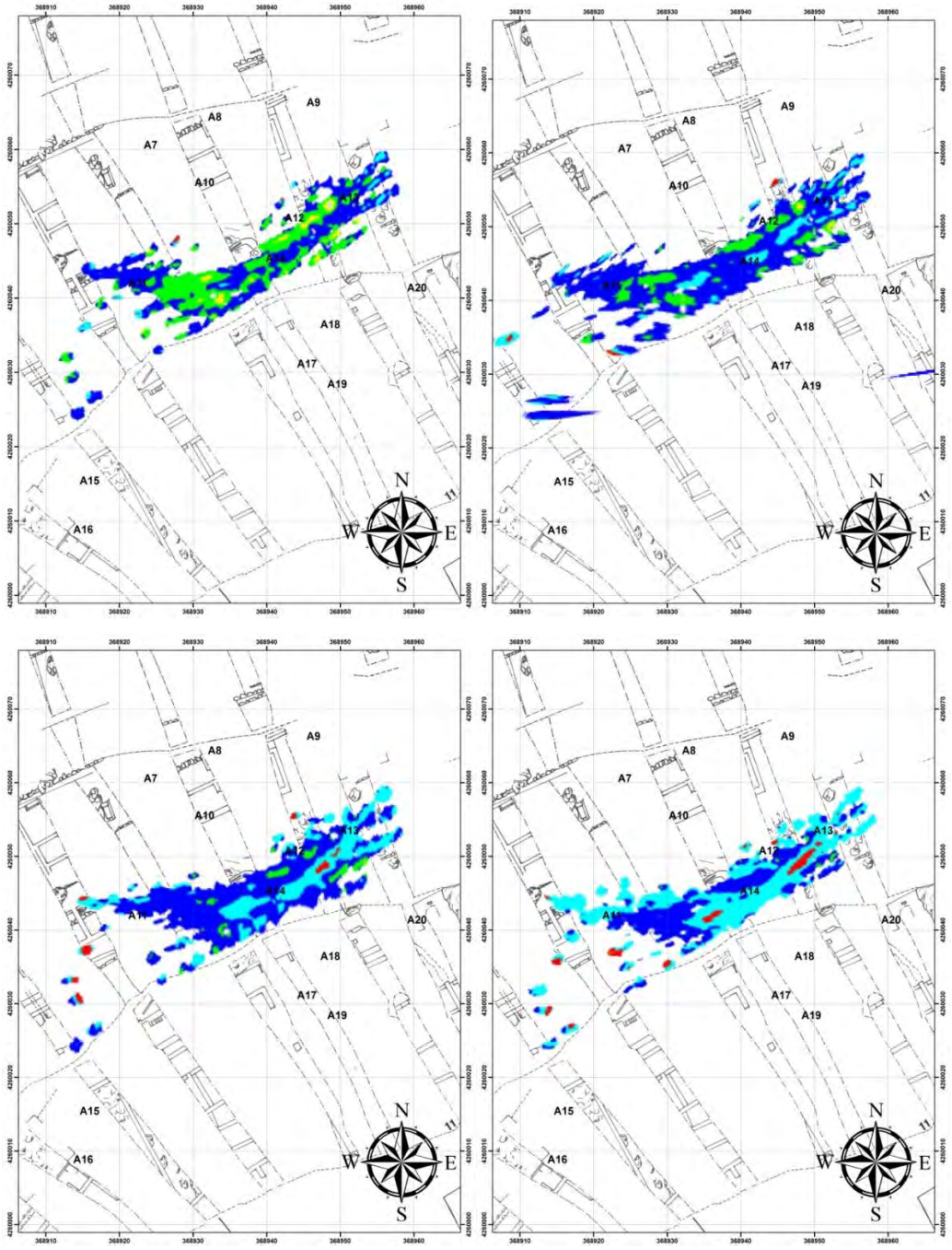

Figure 5 - Seismic depth slices for depth 1 meter (upper left), depth 2 meters (upper right), depth 3 meters (lower left) and depth 4 meters (lower right).

The results of all methods pinpointed to a number of anomalies. The ERT and GPR anomalies had the highest degree of correlation (Figures 3 and 4). The continuation of the wall structures to the east seems to be confirmed by the linear anomalies existing at A11. An elongated linear anomaly (A14) extending for more than 35 meters along the SW-NE direction seems to be consistently present in all datasets and may constitute another supporting wall (see also Figure 5). Towards the

NE of this anomaly, two clusters of features appear at the location of A12 and A13, even if they are not clearly described. The GPR measurements indicate also the existence of vertical sections extending from the supporting wall, probably belonging to other architectural structures. Figure 6 presents the integrated diagrammatic interpretation of the geophysical anomalies resulted by all methods and different depth slices.

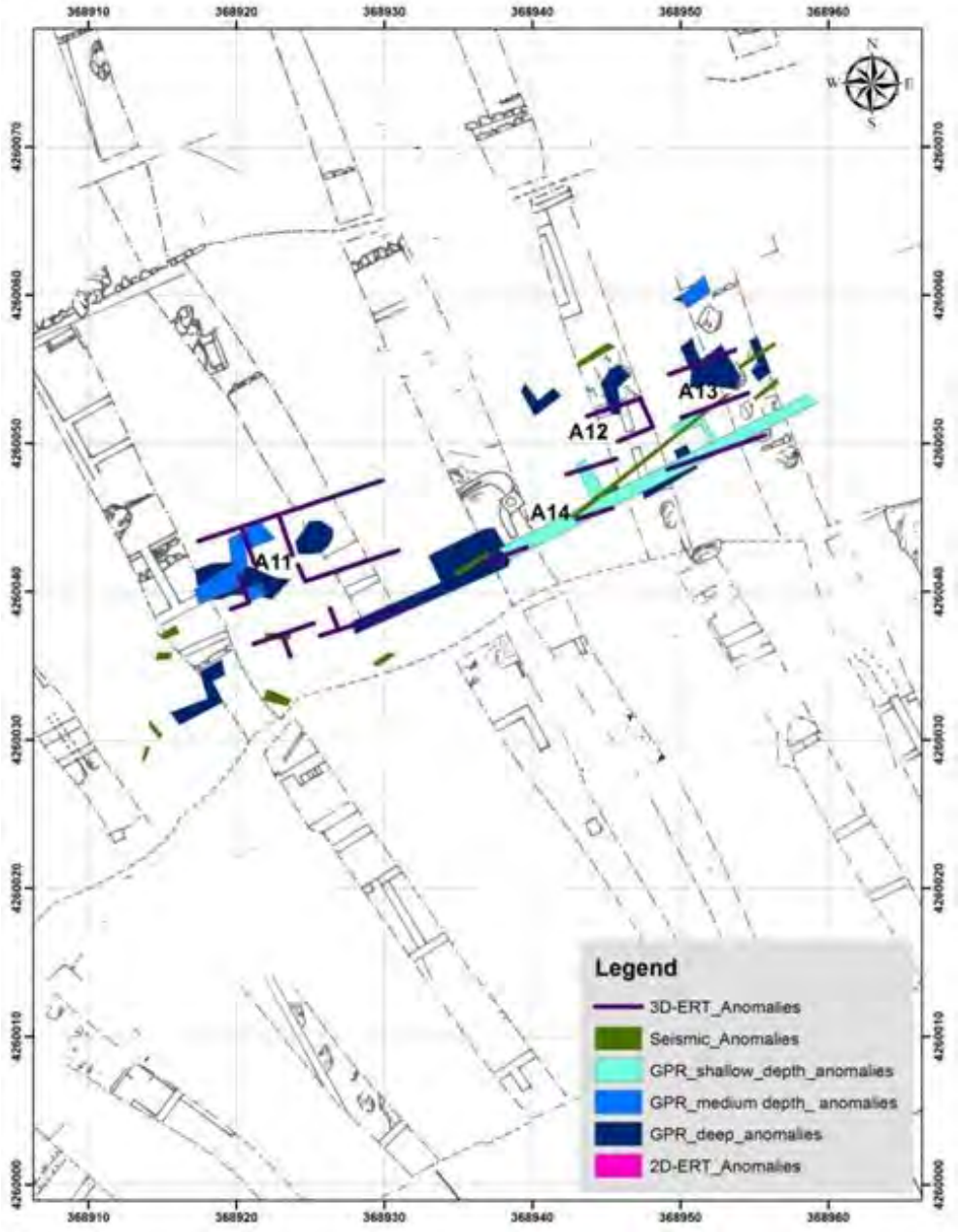

Figure 6 - integrated diagrammatic interpretation of the high resistivity, high velocity and high amplitude GPR reflection anomalies resulted by the interpretation of the ERT, SRT and GPR data that were collected in the area A of Delphi.

4. Conclusions

The interpretation of electrical resistivity and seismic refraction tomographic geophysical data through inversion methods face the possibility to get different tomographic results from the same data file by applying different regularization or inversion parameters. This is caused by the geophysical ambiguity or uncertainty of geophysical interpretation, but also from the fact that each method is based on the measurements of different physical properties of the soil. Since in general, a unique solution cannot be reconstructed from a data set, geophysical interpretation is concerned either to determine properties of the subsurface that all possible solutions share, or to introduce assumptions to restrict the number of admissible solutions. In this sense a manifold geophysical field strategy has to be pursued (Sarris 2012).

The application of different tomographic techniques in the archaeological site of Delphi signifies the importance of the manifold geophysical strategy in order to extract the maximum subsurface information in a more efficient way. Each one of the methods applied has been able to suggest specific targets in terms of the physical quantity measured and the properties of the subsurface. The employment of different methods for the scanning of the site was valuable, since they provided complementary information and thus helped the delineation of the most significant features that were suggested by the various approaches.

5. References

Fong D. C.-L. and Saunders M.A. 2011. LSMR: An iterative algorithm for sparse least-squares problems, *SIAM Journal of Scientific Computing*, 33, 2950-2971.

Koulakov I. 2009. LOTOS code for local earthquake tomographic inversion, Benchmarks for testing tomographic algorithms, *BSSA*, Vol. 99(1) 194-214 doi: 10.1785/0120080013.

Luce J-M. 2012. Exploration du secteur Nord-Ouest de Delphes. La mission du 9 au 30 juillet 2012, *unpublished report*.

Paige C C and Saunders M A.1982. LSQR: An algorithm for sparse linear equations and sparse least squares, *ACM trans. Math Soft*., 8, 43-71.

Papadopoulos N.G., Tsourlos P., Tsokas G.N. and Sarris A. 2006. 2D and 3D Resistivity Imaging in Archaeological Site Investigation, *Archaeological Prospection*, 13, 3, 163-181.

Papadopoulos N.G., Tsourlos P., Papazachos C., Tsokas G.N., Sarris A. and Kim J.H. 2009. An Algorithm for the Fast 3-D Resistivity Inversion of Surface Electrical Resistivity Data: Application on Imaging Buried Antiquities, *Geophysical Prospecting*, 59, 557-575.

Sarris A. 2012. *Multi+ or Manifold Geophysical Prospection? Computer applications and Quantitative methods in Archaeology*, University of Southampton, 26-30 March 2012.

Δελτίο της Ελληνικής Γεωλογικής Εταιρίας, τομ. XLVII , 2013
Πρακτικά 13ου Διεθνούς Συνεδρίου, Χανιά, Σεπτ. 2013

Bulletin of the Geological Society of Greece, vol. XLVII 2013
Proceedings of the 13th International Congress, Chania, Sept. 2013

EARTHQUAKE RELOCATION FOR NORTHWESTERN GREECE USING 3D CRUSTAL MODEL; METHOD COMPARISON AND SEISMOTECTONIC INTERPRETATION

Stavroulopoulou O.[1], Sokos E.[1], Martakis N.[2] and Tselentis G-A.[1]

[1] University of Patras, Faculty of Geology, Seismological Laboratory, ostavrol@upatras.gr, esokos@upatras.gr, tselenti@upatras.gr

[2] LandTech Enterprises, nmartakis@landtechsa.com

Abstract

A dense microseismic network was installed in Northwestern Greece for a period of eleven months. A total of 1368 events were recorded and located using a 1D model. These events were also used to derive a 3D velocity model for the area. This work presents results from further processing of the data using (a) simple location method of events in a 1D medium through Hypo71 standard procedure; (b) location via the probabilistic, non-linear earthquake location method in 3D medium; (c) relocation of the events using the Double - Difference method in 1D medium; and (d) the same relocation procedure invoking 3D medium. The application of different location methodologies results in slightly different locations, which are evaluated using as criterion the compactness of hypocenter distribution. The three point method was used in order to derive linear characteristics from the hypocenter distribution and the final results were compared against the focal mechanisms of the events as computed using the polarity method and the 3D velocity model. The combination of accurately computed hypocenters and focal mechanisms provides important information for the seismotectonics of Epirus.

Key words: *Epirus, Focal mechanisms, Non Linear Location, Three-point method.*

Περίληψη

Για χρονική περίοδο ένδεκα μηνών, εγκαταστάθηκε στην Ήπειρο ένα πυκνό μικροσεισμικό δίκτυο. Κατά το διάστημα αυτό καταγράφηκαν συνολικά 1368 σεισμοί, τα επίκεντρα των οποίων προσδιορίστηκαν με χρήση μονοδιάστατου μοντέλου ταχυτήτων. Οι σεισμοί αυτοί χρησιμοποιήθηκαν στη συνέχεια για τον υπολογισμό 3Δ μοντέλου ταχυτήτων. Η παρούσα εργασία παρουσιάζει τα αποτελέσματα της περεταίρω επεξεργασίας των δεδομένων αυτών με εφαρμογή (α) της απλής μεθόδου προσδιορισμού υποκέντρων Hypo71 με χρήση 1Δ μοντέλου ταχυτήτων, (β) της πιθανολογικής, μη γραμμικής μεθόδου προσδιορισμού υποκέντρων NonLinLoc με χρήση 3Δ μοντέλου ταχυτήτων, (γ) της μεθόδου Double-Difference με χρήση 1Δ μοντέλου ταχυτήτων, για τον επαναπροσδιορισμό των υποκέντρων των σεισμών τα επίκεντρα των οποίων αρχικά είχαν εντοπιστεί με τη μέθοδο Hypo71, και (δ) την εφαρμογή της ίδιας μεθόδου επαναπροσδιορισμού υποκέντρων με χρήση 3Δ μοντέλου ταχυτήτων. Η εφαρμογή των διαφορετικών μεθόδων οδήγησε σε ελαφρώς διαφορετικές κατανομές υποκέντρων, οι οποίες χρησιμοποιήθηκαν για

λεπτομερέστερη σκιαγράφηση των γραμμικών δομών της περιοχής, με χρήση της Μεθόδου των Τριών Σημείων. Οι δομές αυτές συγκρίθηκαν με τους μηχανισμούς γένεσης των σεισμών, οι οποίοι υπολογίστηκαν με τη μέθοδο πολικότητας και το 3Δ μοντέλο ταχυτήτων. Η υπολογισμένη με μεγάλη ακρίβεια θέση των υποκέντρων σε συνδυασμό με τους μηχανισμούς γένεσης παρείχαν σημαντικές πληροφορίες για το σεισμοτεκτονικό καθεστώς της Δυτικής Ελλάδας.
Λέξεις κλειδιά: *Ήπειρος, Μηχανισμοί γένεσης, Μη Γραμμικός Προσδιορισμός Επικέντρου, Μέθοδος Τριών Σημείων.*

1. Introduction

Seismic event location and relocation is a critical task in seismology and can be accomplished with various methodologies. This study uses high quality data to evaluate four methods on location/relocation. The methods are, (a) simple location method of events in a 1D medium through Hypo71 (Lee and Lahr, 1975), (Lee and Valdes, 1985), standard procedure, (b) location via the probabilistic, non-linear earthquake location method in 3D medium (Lomax et al., 2000), (c) relocation of the events whose epicenters were initially located with Hypo71 within the area defined by the microseismic network, using the Double - Difference method in 1D medium (Waldhauser and Ellsworth, 2000), (Waldhauser, 2001) and (d) the same relocation procedure invoking 3D medium. Data were recorded in the Epirus region, northwestern Greece, using a dense seismic network (Martakis, 2003). This unique dataset offers an opportunity to test the performance of location/relocation algorithms especially in the case of 3D velocity model use. As expected the different methodologies provide different results, and we estimate their performance based on the linear characteristics of the located/relocated seismicity. We present here results from location/relocation in 1D and 3D medium and discuss the results in relation to the region's seismotectonics.

Epirus lies between the Pindus Mountains and the Ionian Sea and has been the subject of several detailed geodynamic studies, as it is considered an area of particular interest in terms of its geodynamics. Geologically belongs to External Hellenides which are formed by three isopic zones (Brunn, 1956; Aubouin 1959; Bernoulli & Laubsher. 1972; Jacobshagen, 1986), namely the Pindos, Gavrovo and Ionian zone. Starting from the eastern end, the Pindos zone is thrusted on the Gavrovo zone and the latter on the Ionian zone (Avramidis et al., 2000).

Previous microearthquake studies in Epirus performed by Kiratzi et al., (1987), Waters, (1994) and Hatzfeld et al., (1995), propose an ENE-WSW shortening, which is in agreement with the continental convergence west of Corfu and a NNW extension, further east, close to the Pindos foothills. Geomorphological work performed by King et al., (1983) using boundary-element modelling, identified a substantial left lateral strike-slip component in addition to the compressional motion. Furthermore, geological and geomorphological research which was conducted by IGSR and IFP, (1966) and King et al., (1993) as well as crustal deformation studying of the Aegean area by Papazachos and Kiratzi, (1996), implied similar results.

From the geodynamical point of view, the study area is in a strategic position where the extensional Inner Aegean regime switches to the compressional outer Aegean. Studies of the focal mechanisms from earthquakes within the area, have shown that the tectonic regime of the area varies from thrust and strike slip to normal (Mercier et al., 1972; King et al., 1983; Doutsos et al., 1987; Underhill, 1989; Waters, 1994; Hatzfeld et al., 1995).

The E-W shortening generates thrust belts that trend N-NW (Taymaz et al., 1991) and are cut by almost perpendicular strike slip or normal faults. Hatzfeld et al., (1995), assert that the jump of active thrusting from the Pindos to the Ionian zone, which continues to present time, causes the compressional regime in Epirus.

Tselentis et al., (2006), based on the seismicity distribution and the stress-inversion results, concluded that the existence of evaporites have played an important role in the change of the stress regime, just at the internal Ionian thrust, which seems to be the boundary between the transtensional regime in the east to transpressional to the west.

In this article we extent the work of Tselentis et al., (2006), by applying four different location/relocation methodologies to high-quality seismological data for the area of Epirus. The application of different location methodologies results in slightly different locations. The compactness of hypocenter distribution computed from each method was used as the criterion to evaluate the location accuracy. Furthermore, it provides important information regarding the ability of the hypocenter distribution to delineate linear structures. Finally, we compare the obtained results with the known active structures within the study area.

2. Seismograph Network and Data

The data analyzed in this study were recorded during a 12-month period (August 1998 - June 1999) by a dense microseismic network of 44 portable seismographs which was installed in the study area by the Seismological Laboratory, University of Patras, Greece.

The network consisted of 44 three component seismic stations. Thirty eight stations were Earthdata PR2400-type 24bit seismographs and SIG SR2 short period type seismometers. They were installed in boreholes of 15m depth; the remaining 6 stations consisted of Teledyne PDAS100- type 16bit recorders and of 3 Teledyne S13 short period seismometers. The recording was continuous at 100 samples/sec. Recorded data were collected every 15 days and stored in 80 Gb hard discs. For time synchronization each station was equipped with a high-precision Magellan-type GPS, with measurement error of less than 20m. The location of the stations was based on the criteria indicated by Lee and Stewart, (1981). They determine the required minimum number of stations, the azimuthal gap and the relationship between the focal depth and the epicentral distance from the closest station.

Event selection and time correlation of the identified events was performed by custom-developed software, based on the STA/LTA (short-term average/long-term average) algorithm and a minimum number of 8 stations as a criterion. Data processing was performed using Sismwin software (Xanalatos and Tselentis, 1997).

During the aforementioned 12-month operation 1368 earthquakes were recorded, with duration magnitude ranging from 1.11 to 4.69 and focal depths ranging from a few hundred meters to 46km; the majority was in the 0-10km range.

3. Methodology

3.1. Location 1D (HYPO71)

The initial location of the 1368 events in 1D medium was performed using the standard location program HYPO71 (Lee and Lahr, 1975; Lee and Valdes, 1985). The velocity model adopted for this procedure was calculated by 1D tomographic inversion performed by Martakis, (2003) in the study area.

3.2. Location 3D (NLLoc)

To improve the initial location results, the NonLinLoc, probabilistic, non-linear earthquake location method in 3D medium (Lomax et al., 2000), was applied to the same seismological data. The velocity model which was used for this procedure was derived by 3D tomographic inversion performed by Martakis, (2003) in the study area. The earthquake location algorithm implemented in the program NLLoc follows the probabilistic formulation of inversion presented in Tarantola and Valette, (1982) and Tarantola, (1987), which produces comprehensive uncertainty and

resolution information represented by a probability density function (PDF) over the unknown hypocentral parameters. The errors in the observations (phase time picks) and in the forward problem (travel-time calculation) are assumed to be Gaussian. This assumption allows the direct, analytic calculation of a maximum likelihood origin time given the observed arrival times and the calculated travel times between the observing stations and a point in XYZ space. For accurate, efficient and complete mapping of earthquake location probability density functions (PDFs) in 3D space, the oct-tree importance sampling algorithm was chosen (Lomax and Curtis, 2001). This method is faster than grid-search (factor 1/100) and uses very few parameters (initial grid size, number of samples).

Figure 1shows the epicentre distribution and the cross-section across the study area of the located events with the NonLinLoc method in 3D medium. The hypocenter determination is similar to HYPO71, as expected since the events are well recorded, but the non linear location provides a better view of the location errors.

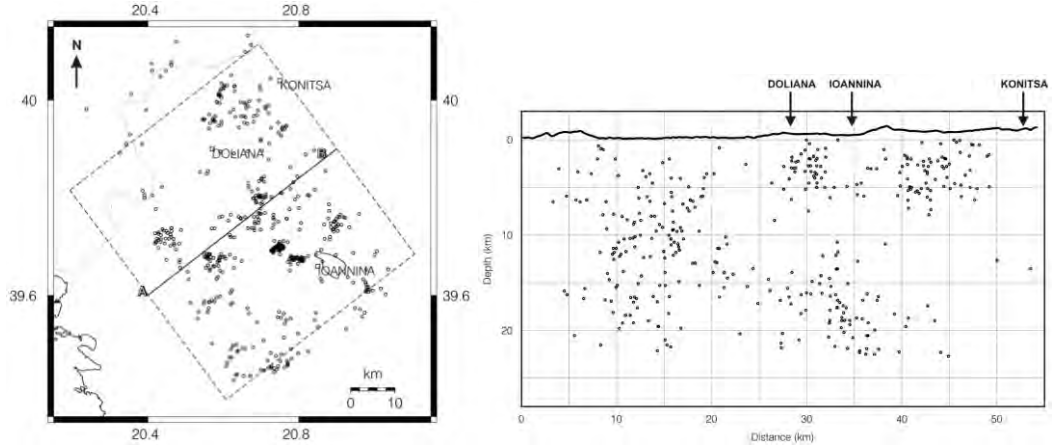

Figure 1 - The epicentre distribution (left) and the cross-section across the study area (right) of the located events with the NonLinLoc method in 3D medium.

3.3. Relocation 1D (HypoDD 1.0)

The events whose epicenters were initially located with HYPO71 standard procedure within the area defined by the microseismic network, were relocated using the Double - Difference method in 1D medium (Waldhauser and Ellsworth, 2000), as implemented in HypoDD 1.0 program (Waldhauser, 2001), to improve relative location accuracy by removing effects due to un-modelled velocity changes. The velocity model which was used for this procedure was the same that was used for the location in 1D medium. Using this method, residuals between observed and theoretical travel-time differences (or double-differences) were minimized for pairs of earthquakes at each station while linking together all observed event-station pairs. A least-squares solution is found by iteratively adjusting the vector difference between hypocentral pairs. For the relocation procedure all 452 events which had initially been located inside the microseismic network were selected. A total of 271 of them formed 10 clusters including more than 10 events each, with maximum hypocentral separation between the event-pairs, 2km. These were chosen to be further analysed below.

Figure 2 shows the epicentre distribution (left) and the cross-section across the study area (right) of the relocated events with the HypoDD method in 1D medium. As expected the hypocenter distribution is more compact, since events collapse to clusters and thus linear features were revealed.

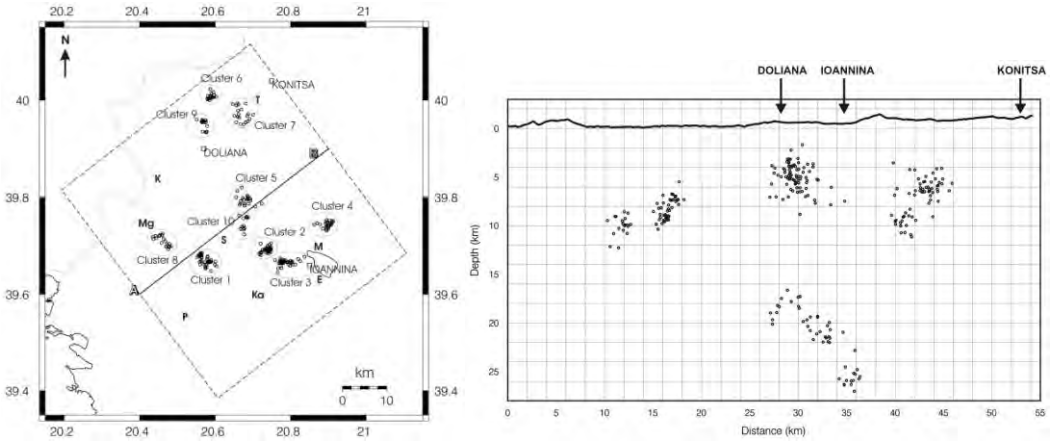

Figure 2 - The epicentre distribution (left) and the cross-section across the study area (right) of the relocated events with the HypoDD method in 1D medium. P, Paramythia; Mg, Mourgana mountain; K, Kourendon; S, Soulopoulo; Ka, Kassidiares; E, Evaporite outcrop; M, Mitsikeli mountain; T, Tymfi mountain.

3.4. Relocation 3D (HypoDD 2.1)

For further enhancement of the hypocentral parameters, the relocation procedure was further applied to the seismological data, invoking 3D medium using the Double - Difference method in 3D medium (Waldhauser and Ellsworth, 2000), as implemented in HypoDD 2.1 program (Waldhauser, 2001). The velocity model which was used for this procedure was the same that was used for the location in 3D medium, as described above. This is a recently proposed enhancement of HypoDD algorithm and the current application is one of the first worldwide, thus it serves as a benchmark of the algorithms performance. HypoDD relocation in 3D medium produces slightly different results if we compare with the relocation in 1D medium, this is probably due to method's independence of the crustal model or in the data quality.

4. Focal Mechanisms

The fault-plane solutions were determined using the FPFIT program (Reasenberg and Oppenheimer, 1985), a grid search routine that minimizes the misfit between nodal planes and observed first-motion data. For this procedure, the azimuth and the angle of incidence of the 271 events included into the 10 clusters computed by the HypoDD relocation method were used. The minimum number of P-wave first-arrival observations was 10. More than 90% of the solutions were unique. From the events with multiple solutions we selected those with the highest quality, as estimated from the uncertainty measurements determined by FPFIT. The nodal planes are well-constrained, with mean misfit function F_j, equal to 0.11, mean STDR equal to 0.6 and errors in strike, dip and rake (ΔSTR, ΔDIP, ΔRAK) smaller than 10^o. The focal mechanisms derived from this procedure, is in agreement with the previous observations within the area, as normal, reverse, srike-slip, and oblique surface structures were identified.

In the following paragraphs we discuss in detail the results obtained per cluster. We are mainly interested in the geometrical characteristics of the clusters and their connection with the focal mechanisms in order to derive results about the seismic sources involved. To define more clearly the geometry of the clusters, the Three-Point Method (Fehler et al., 1987) was applied to the relocated events. It consists in calculating, the poles of the planes that pass through each combination of three hypocenters and then, the pole density for the elements of equivalent area that form the lower hemisphere of a stereographic projection. If the pole density distribution has a clear maximum, it defines the geometry of the multiplet, that is, of its associated plane. Instead of calculating the plane's pole we calculate here the dip direction of the planes of each cluster and

check if it is in agreement with the observed directions indicated by the fault plane solutions as they were described above. (Figures 3, 4, 5)

Cluster 1 is located at the SE corner of the study area, close to Soulopoulo (Figure 2) and contains 54 relocated hypocenters with depth range of 5 to 12km. The focal mechanisms vary from strike slip and normal for most of the earthquakes, which changes to thrust along NW-SE direction for some earthquakes. This observation agrees with the previous studies in the area performed by IGSR and IFP, (1966); King et al., (1993); Hatzfeld et al., (1995) and Tselentis et al., (2006) who mapped normal and oblique-normal focal mechanisms which became pure strike-slip and even the reverse for some earthquakes. According to them, the variety of faulting type implies the existence of two groups of faults, a group of oblique to normal faults that trend N-NW-SE and a group of almost vertical reverse faults of N-S trend. The reverse fault could be the Kourenton fault (Figure 2), which has been described as backthrust by IGSR and IFP, (1966).

Figure 3 shows the epicentre distribution (left), the cross-section across the cluster area (middle) and the orientations of faults (dip-direction) on equal-area projection (right), of the relocated events. The WSW dip of the cluster can be clearly observed. This suggests that this cluster is connected to a back thrust fault, most probably the Kourenton fault.

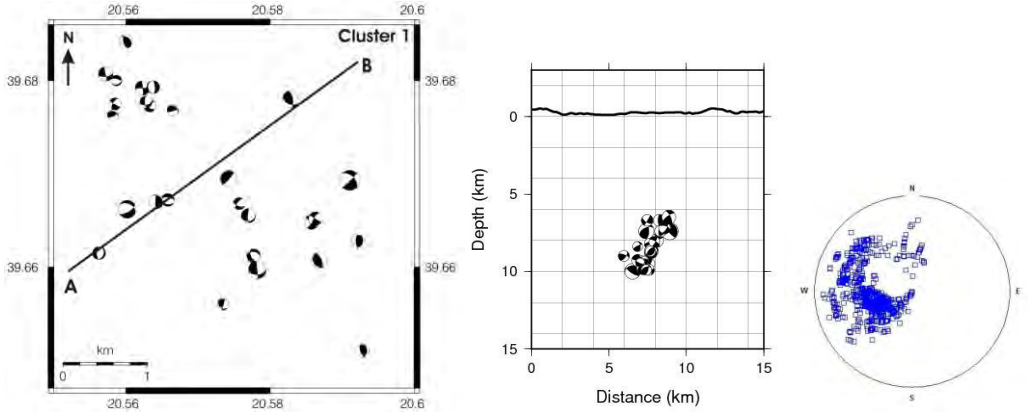

Figure 3 - The epicentre distribution (left), the cross-section across the cluster 1 area (middle) and the orientations of faults on equal-area projection (right), of the relocated events.

Cluster 2 and cluster 3 lie west of lake Pamvotis and contain 46 and 39 relocated hypocenters respectively. The majority of earthquakes occur at shallow depths up to 5km with just a few deeper events limited at 10km. This area between Mitsikeli (M) and Kourenton (K) thrust (Figure 2) was referred by King et al., (1993) as Ioannina basin. Tselentis et al., (2006), found normal focal mechanisms in this area and related them with a set of conjugate normal faults, structures that can develop on top of evaporite domes. Also, they attributed the absence of seismicity below the depth of 5km, to the existence of a large evaporite body close to the surface which extends to the north. This idea was corroborate by the presence of an evaporite outcrop (Figure 2) close to the two clusters and by additional information from geophysical and geological data (IGMR, 1967). The fault plane solutions derived here for these earthquakes show pure normal and strike-slip faults which are bounded at the north part of the area by a few reverse faults with E-W strike. The depth of the earthquakes increases to the NE direction for both clusters. These results are in good agreement with Tselentis et al., (2006) and support further the idea of normal faulting associated with an evaporite dome (Figure 2) very close to the Ioannina basin surface.

Cluster 4 extends east of the mountain Mitsikeli (Figure 2) and consists of 24 relocated events with depth range of 2 to 12km. A variety of focal mechanisms can be observed from strike slip and normal faulting for the shallower events, to thrust faulting for the deeper ones. More specifically,

strike slip structures are detected at the NE part of the cluster area, which are cut towards the NS direction by normal faults. These results agree with the fault plane solution proposed by Martakis, (2003) and with the extension referred by Papazachos and Kiratzi, (1996) for this area. At the SW part of the area the hypocenters become deeper and the focal mechanisms denote thrust.

Figure 4 shows the epicentre distribution (left), the cross-section across the cluster area (middle) and the orientations of faults (dip-direction) on equal-area projection (right), of the relocated events. High inclination of the faults towards a mean west direction can be observed.

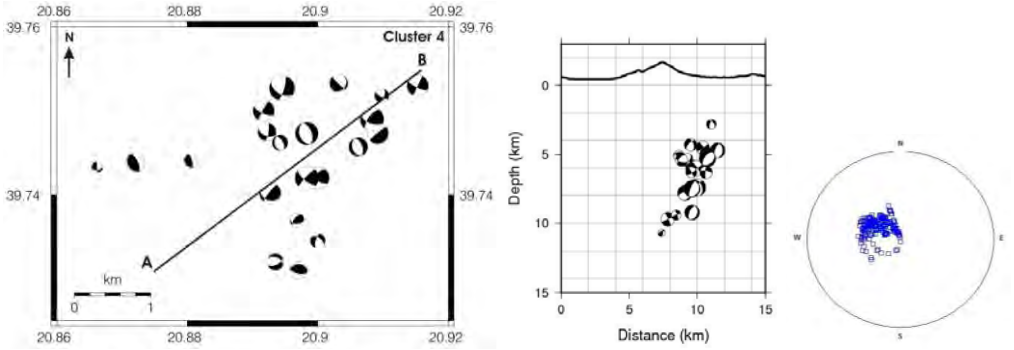

Figure 4 - The epicentre distribution (left) and the cross-section across the cluster 4 area (middle) and the orientations of faults on equal-area projection (right), of the relocated events.

In the centre of the study area, east of Soulopoulo (S) and the Kasidiares (K) thrust (Figure 2) two hypocenter clusters are located with focal depths significantly different from the average depth of the study area. These are cluster 5 which contains 21 events and its depths range from 18 to 24km and a smaller one, cluster 10 which contains 13 events and its depths range from 16 to 20km. Similar deepening of the hypocenters was observed by Hatzfeld et al., (1995) and Tselentis et al., (2006). The fault plane solutions observed for these two clusters show pure reverse faulting, with a few, scattered, oblique-normal focal mechanisms. Furthermore, in cluster 5 a deepening of the hypocenters towards the NE direction occurs. These events are connected with a deep thrust zone that dips to the east and this is probably the middle Ionian thrust or some other blind thrust.

Figure 5 shows the epicentre distribution (left), the cross-section across the cluster 5 area (middle) and the orientations of faults (dip-direction) on equal-area projection (right), of the relocated events. The dip direction of the faults towards the ENE direction can be observed.

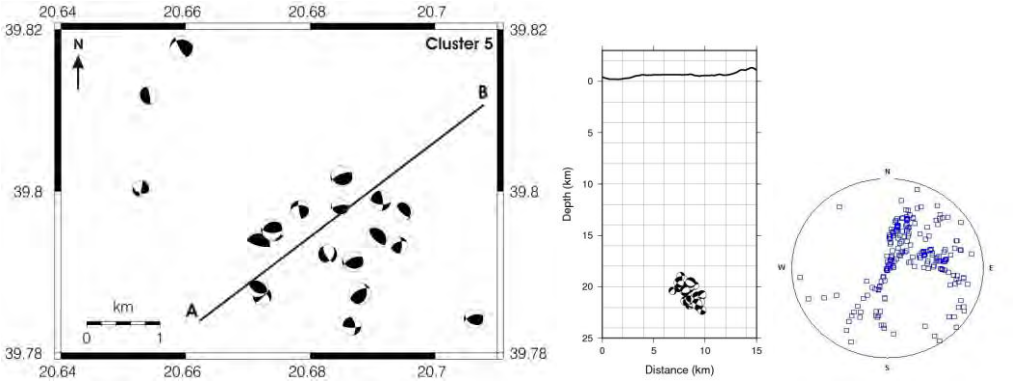

Figure 5 - The epicentre distribution (left) and the cross-section across the cluster 5 area (middle) and the orientations of faults on equal-area projection (right), of the relocated events.

Cluster 6 is the northeast group of 20 relocated events, close to the Greek-Albanian border. Even though hypocentral depths range from 4 to 12km, most of the relocated events are concentrated around 10km. Fault plane solutions are normal and oblique-normal, which is in agreement with IGSR and IFP, (1966) reference. This cluster is probably connected with a normal oblique fault, following the general NE-SW trending of the Konitsa normal fault system (Galanakis et al., 2007) (Figure 2).

Cluster 7 contains 20 shallow events located in the area of the mountain Timfi (Figure 2). Their depths range from 2 to 10km. Most of the fault plane solutions for these earthquakes are of normal and oblique normal type. These can be explained as a result of the extension which is taking place in this area (Papazachos and Kiratzi, 1996) and (Doutsos and Koukouvelas, 1998). Additional information comes from Tselentis et al., (2006) seismotectonic study in Epirus, who detected N-NE strike-slip focal mechanisms and sometimes clear N-S mechanisms.

Cluster 8 is located at the eastern part of the study area which is referred to as the Paramythia (P)-Mourgana (Mg) area (Figure 2), where the main observed structure is thrust with NW-SE epicentre distribution. This is probably connected with the middle Ionian thrust further west, described by IGSR and IFP, (1966). In the same direction there are also a few strike-slip and oblique-normal focal mechanisms. The fault plane solution variation agrees with observations in the same area by Tselentis et al., (2006). This cluster contains 19 relocated hypocenters with focal depths around 10km while a few scattered ones are located at depths of 6 to 14km

Cluster 9 is a small cluster of 15 events extended from 24 to 35km depth at the Doliana basin (King et al., 1993), (Figure 2). The fault plane solutions derived for these events show thrust and oblique thrust faulting with a mean strike at NW-SE direction. Hypocenter distribution suggests that cluster dips to the east. These structures could be connected with the middle Ionian thrust (IGSR and IFP, 1966) or another major thrust west of Doliana basin (e.g. the northern part of Kasidiares thrust) (Figure 2).

5. Results

In this paper we make use of a high quality seismic dataset in order to test a number of location/relocation methods and derive accurate location of seismicity in Epirus. In detail we investigate the effect of 3D crustal model in earthquake location/relocation using the most recently proposed methods in this area i.e. non-linear location in 3D medium (Lomax et al., 2000) and relocation in 3D medium (Waldhauser, 2001). Our results, based on a very good dataset, suggest that the hypocenters obtained by 3D non linear location are similar to 1D location methods.

Nevertheless, the associated location errors are defined in a transparent way in the non linear location method and this is a major advantage. Similarly the relocation by HypoDD in 3D medium didn't provide significantly better results in comparison to standard HypoDD in 1D medium. This was in some extend expected since the relocation methodology itself doesn't depend on crustal model accuracy. Since all the methods were tested in a high quality dataset we cannot rule out a bias by the data quality i.e. we don't suggest that similar results can be obtained using a lower quality dataset.

Results from the seismicity relocation procedure and focal mechanisms obtained using the relocated hypocenters and the first polarity method were used to derive results about the seismotectonic environment in Epirus. In general results are in agreement with Tselentis et al., (2006), although a more detailed image is provided here. The active structures in the study area agree with a thrust belt zone at the west, combined with an extensional regime at the eastern end. The presence of evaporite bodies is clearly defined from seismic data in good connection to geological findings.

6. Acknowledgments

All the figures were produced with the GMT software package (Wessel and Smith, 1991). The first author thanks Vasilis N. Nikolaidis and Paraskevas Paraskevopoulos for their assistance in software development and use.

7. References

Aubouin J. 1959. Contribution a l'etude geologique de la Greece, septentrionale, les confins de l'Epire et de la Thessalie, *Ann. Geol. Pays. Hellen* 10, 1–483.

Avramidis P., Zelilidis A. and Kontopoulos N. 2000. Thrust dissection control of deep-water clastic dispersal patterns in the Klematia - Paramythia foreland basin, western Greece, *Geol. Mag.* 137, no. 6, 667–685.

Bernoulli D. and Laubscher H. 1972. The palinspastic problem of the Hellenides, *Eel. geol. Helv.,* 65, 107-118.

Brunn J.H. 1956. Contribution a l'etude geologique du Pinde Septentrional et d'une partie de la Macedonie occidentale. *Annales Geologique des pays Helleniques*, Vol. VII.

Doutsos T. and Koukouvelas I. 1998. Fractal analysis of normal faults in northwestern Aegean area, *J. Geodyn*. 26, 197–216.

Doutsos T., Kontopoulos N. and Fridas D. 1987. Neotectonic evolution of northwestern continental Greece, *Basin Res*. 1, 177–190.

Fehler M., House L. and Kaieda H. 1987. Determining planes along which earthquakes occur: method and application to earthquakes accompanying hydraulic fracturing, *J. geophys. Res.*, 92(B9), 9407–9414.

Galanakis D., Paschos P., Rondoyanni T. and Georgiou C. 2007. Neotectonic Activity of Konitsa Area and the 1996 Earthquakes, *Hellenic Journal of Geosciences*, vol. 42, 57-64.

Hatzfeld D., Kassaras L., Panagiotopoulos D., Amorese D., Makropoulos K., Karakaisis G. and Coutand O. 1995. Microseismicity and strain pattern in northwestern Greece, *Tectonics* 14, 773–785.

Institute of Geology and Mineral Resources (IGMR), 1967. Geological map of Greece*, Ioannina and Klematia sheet (1:50,000),* Athens, Greece.

Institute for Geology Subsurface Research of Greece and Institute Francais de Petrole (IGSR and IFP), 1966. Etude geologique de l'Epire, Paris, *Technip*, 306 pp.

Jacobshagen V. 1986. *Geologie von Griechenland,* Beiträge Zur Regionalen Geologie der Erde, 19, Berlin.

King G., Tselentis A., Gomberg J., Molnar P., Roecker S., Sinvhal H., Soufleris C. and Stock J. 1983. Microearthquake seismicity and active tectonics of northwestern Greece, *Earth Planet Sc. Lett.* 66, 279–288.

King G., Sturdy D., and Whitney J. 1993. The landscape geometry and active tectonics of the northwest Greece, *Geol. Soc. Am. Bull*. 105, 137–161.

Kiratzi A., Papadimitriou E., and Papazachos B. C. 1987. A microearthquake survey in the Steno dam site in northwestern Greece, *Ann. Geophys*. 592, 161–166.

Lee W.H.K. and Lahr J.C. 1975. HYPO71 (Revised): A computer program for determining hypocenter, magnitude, and first motion pattern of local earthquakes, *U.S. Geol. Surv. Open-File Rept. OF* 85-749.

Lee W.H.K., and Stewart S. W. 1981. Principles and Applications of Microearthquake Networks, *Adv. Geophys*., Supplement No. 2, Academic Press, New York, 293 pp.

Lee W.H.K. and Valdes C. M. 1985. HYPO71PC A personal computer version of the HYPO71 earthquake location program, *U.S. Geol. Surv. Open-File Rept. OF* 85-749.

Lomax A., Virieux J., Volant P. and Berge C. 2000. Probabilistic earthquake location in 3D and layered models: Introduction of a Metropolis-Gibbs method and comparison with linear locations, In: *Advances in Seismic Event Location Thurber*, *C.H*., and N. Rabinowitz (eds.), Kluwer, Amsterdam, 101-134.

Lomax A. and Curtis A. 2001. Fast, probabilistic earthquake location in 3D models using oct-tree importance sampling, *European Geophysical Society*, March 2001, Nice.

Martakis N. 2003. *Passive seismic tomography survey in Epirus*, *Ph.D. thesis*, University of Patras - Faculty of Geology and Geophysics – Seismological Laboratory, p. 116-126, 145, 189 (In Greek).

Mercier J., Bousquet B., Delibasis N., Drakopoulos I., Keraurden B., Lemell F., and Sorel D. 1972. Deformations en compression dans le quartinaire des ravages Ioniens. Donnes neotectoniques et seismiques, *C. R. Acad. Sci.* Paris 275, 2307–2310.

Papazachos C. and Kiratzi A. 1996. A detailed study of the active crustal deformation in the Aegean and surrounding area, *Tectonophysics* 253, 129–153.

Reasenberg P. and Oppenheimer D. 1985. FPFIT, FPPLOT and FPPAGE: Fortran computer programs for calculating and displaying earthquake fault plane solutions, *U.S. Geol. Surv. Open-File Rept. OF* 95-515, 24 pp.

Tarantola A. 1987. Inverse problem theory: Methods for data fitting and model parameter estimation, *Elsevier*, Amsterdam, 613p.

Tarantola A. and Valette B. 1982. Inverse problems = quest for information, *J. Geophys*., 50, 159-170

Taymaz T., Jackson J. A., and McKenzie D. 1991. Active tectonics of the north and central Aegean Sea, *Geophys, J.* Int. 106, 433–490.

Tselentis G-A., Sokos E., Martakis N. and Serpetsidaki A. 2006. Seismicity and Seismotectonics in Epirus, Western Greece: Results from a Microearthquake Survey, *Bull. Seism. Soc. Am*., Vol. 96, No. 5, pp. 1706–1717.

Underhill J.R., 1989. Late Cenozoic deformation of the Hellenide foreland, western Greece, *Geol. Soc. Am. Bull*. 101, 613–634.

Waldhauser F. and Ellsworth W.L. 2000. A double-difference earthquake location algorithm: Method and application to the northern Hayward fault, *Bull. Seism. Soc. Am*., 90, 1353-1368.

Waldhauser F. 2001. HypoDD: A computer program to compute double-difference earthquake locations, *U.S. Geol. Surv. open-file report*, 01-113, Menlo Park, California.

Waters D. 1994. The tectonic evolution of Epirus, Northwest Greece*, Ph.D. thesis*, University of Cambridge, Cambridge, p. 248.

Wessel P. and Smith W. H. F. 1991. Free software helps map and display data, *EOS Trans. AGU* 72, 441, 445–446.

Xanalatos N. and Tselentis G-A. 1997. Seismwin, An Algorithm For Processing Seismological Waveforms. *Proc. Geol. Soc*., Athens, 22, 235-246.

Δελτίο της Ελληνικής Γεωλογικής Εταιρίας, τομ. XLVII , 2013
Πρακτικά 13ου Διεθνούς Συνεδρίου, Χανιά, Σεπτ. 2013

Bulletin of the Geological Society of Greece, vol. XLVII 2013
Proceedings of the 13th International Congress, Chania, Sept. 2013

DETAILED ARCHAEOMAGNETIC STUDY OF A CERAMIC WORKSHOP AT KATO ACHAIA: NEW DIRECTIONAL DATA AND ARCHAEOMAGNETIC DATING IN GREECE

Tema E.[1]

[1]*Dipartimento di Scienze della Terra, Università degli studi di Torino, via Valperga Caluso 35, 10123, Torino, Italy, evdokia.tema@unito.it*

Abstract

New archaeomagnetic results from two ancient kilns excavated at Kato Achaia, southern Greece, are presented. According to archaeological evidence, both kilns were part of a bigger ceramic workshop, probably used for the production of bricks or ceramics. Systematic archaeomagnetic sampling was carried out collecting 9 brick samples from the first kiln (KL3) and 12 brick samples from the second kiln (KL5). Magnetic mineralogy measurements have been carried out in order to determine the main magnetic carrier of the samples and to check their thermal stability. Standard thermal demagnetization procedures have been used to determine the archaeomagnetic direction registered by the bricks during their last firing. The direction of the Characteristic Remanent Magnetization (ChRM) has been obtained from principal component analysis and the kilns mean directions were calculated using Fisher statistics. The archaeomagnetic ages of both kilns were determined using the most recent developments in data elaboration and were calculated after comparison of the kilns declination and inclination with the reference curves produced by the SCHA.DIF.3K European regional geomagnetic field model. Dating results are in good agreement with archaeological evidence of the site and suggest that both kilns were in use during Hellenistic times.

Key words: *Archaeomagnetism, magnetic mineralogy, kilns, Kato Achaia, Greece.*

Περίληψη

Στην παρούσα εργασία παρουσιάζονται τα αποτελέσματα από την αρχαιομαγνητική μελέτη δυο αρχαίων κλιβάνων που ανακαλύφθηκαν στην Κάτω Αχαΐα. Σύμφωνα με τα ευρήματα της αρχαιολογικής ανασκαφής, οι δυο αυτοί κλίβανοι αποτελούσαν μέρος ενός μεγαλύτερου κεραμικού εργαστηρίου που λειτουργούσε στην περιοχή, πιθανότατα για την παραγωγή τούβλων ή κεραμικών. Συστηματική αρχαιομαγνητική δειγματοληψία πραγματοποιήθηκε σε συνεργασία με τους αρχαιολόγους και συνολικά λήφθηκαν 9 δείγματα από τον πρώτο κλίβανο (KL3) και 12 από τον δεύτερο (KL5). Συστηματικές μετρήσεις της μαγνητικής ορυκτολογίας των δειγμάτων πραγματοποιήθηκαν με σκοπό τον καθορισμό του βασικού φορέα της μαγνήτισης των δειγμάτων. Η διεύθυνση της Χαρακτηριστικής Παραμένουσας Μαγνήτισης καθορίστηκε κατόπιν ανάλυσης της κύριας συνιστώσας μαγνήτισης και οι μέσες τιμές διεύθυνσης για τους δυο κλιβάνους υπολογίστηκαν σύμφωνα με την στατιστική του Fisher. Η ηλικία των κλιβάνων υπολογίστηκε χρησιμοποιώντας τις πιο σύγχρονες εξελίξεις στην αρχαιομαγνητική έρευνα και κατόπιν σύγκρισης της διεύθυνσης των

κλιβάνων με τις καμπύλες αναφοράς, όπως αυτές υπολογίστηκαν από το SCHA.DIF.3K γεωμαγνητικό μοντέλο που περιγράφει την μεταβολή του μαγνητικού πεδίου στον Ευρωπαϊκό χώρο. Τα αποτελέσματα της αρχαιομαγνητικής χρονολόγησης συμφωνούν πολύ ικανοποιητικά με τις αρχαιολογικές ενδείξεις για την περίοδο χρήσης των κλιβάνων και υποδεικνύουν ότι οι κλίβανοι ήταν σε χρήση κατά την διάρκεια της ελληνιστικής περιόδου και εγκαταλείφτηκαν προς το τέλος αυτής.
Λέξεις κλειδιά: *Αρχαιομαγνητισμός, μαγνητική ορυκτολογία, κλίβανοι, Κάτω Αχαΐα, Ελλάδα.*

1. Introduction

During last decades, important progress in archaeomagnetic studies has been done and archaeomagnetism is now established as a useful tool in archaeological research. One of the most common applications of this method is the archaeomagnetic dating. This dating technique is based on the ability of several archaeological structures and artifacts (e.g., kilns, hearths, bricks, pottery) to acquire, under certain conditions, a thermal remanent magnetization (TRM) with direction parallel and magnitude proportional to the local field when heated at high temperatures and cooled in the presence of the Earth's magnetic field. The date of the TRM acquisition can thus be determined by comparing the geomagnetic field elements (Declination, D, Inclination, I and intensity, F) obtained from the remanent magnetization measured on the undisturbed archaeological artifacts with reference secular variation (SV) curves that report the chronological geomagnetic field variations within a certain region.

The accuracy of archaeomagnetic dating depends on several factors such as the suitability of the studied materials as recorders of the Earth's magnetic field, the experimental uncertainty, the rate of change of the geomagnetic field in the considered period and the availability of a detailed reference SV curve for the given territory. In Europe, well established directional SV curves have been recently published for several countries, e.g. France (Gallet et al. 2002), the United Kingdom (Zananiri et al., 2007), Iberian Peninsula (Gómez-Paccard et al., 2006), Italy (Tema et al., 2006), Germany (Schnepp & Lanos 2005), Hungary (Márton, 2010), Bulgaria (Kovacheva et al., 2009), Balkan Peninsula (Tema & Kondopoulou, 2011). In Greece, archaeomagnetic investigations started at the early 60's and since then various studies have been carried out (e.g. Liritzis & Thomas, 1980; Downey & Tarling, 1984; Papamarinopoulos, 1987; Kovacheva et al., 2000; Spatharas et al. 2000, 2011; De Marco et al., 2008a, 2008b; Spassov et al., 2010; Aidona & Kondopoulou, 2012; Fanjat et al., 2012; Tema et al., 2012; De Marco et al., 2013 and references there in). Recently, De Marco et al. (2013, *submitted*) compiled a database with all the available up to now directional results from Greece and proposed a reference secular variation curve for the last 4500 years.

Apart from the secular variation curves available for single countries, during the last years, great progress on geomagnetic field modeling at regional scale has also been done. Nowadays geomagnetic field models, able to represent the past geomagnetic field vector variation in Europe, are available. These models can provide reference curves for a precise location (Pavón-Carrasco et al., 2009, 2010) and be used for archaeomagnetic dating in Europe (Pavón-Carrasco et al., 2011). Regional models present the advantage to predict the geomagnetic field at the site of interest, avoiding this way any eventual relocation error. They can also provide well-constrained palaeosecular variation curves for regions and time periods that are poorly covered by archaeomagnetic data of local scale.

This paper presents the results of the archaeomagnetic investigation of two circular brick kilns excavated at Kato Achaia, southern Greece. The rock magnetic properties of the studied material have been investigated and the calculated mean archaeomagnetic direction for each kiln has been used for archaeomagnetic dating. The most probable dates of the last firing of the kilns have been

obtained using recent developments on data statistical treatment and archaeomagnetic dating (Pavón-Carrasco et al., 2011).

2. Archaeological Context and Archaeomagnetic Sampling

The studied kilns were excavated in an habitation area of Kato Achaia village (38.15^{o} N, 21.55^{o} E), Parodos Papaflessa street, during the works for the construction of a new building. Both of the sampled kilns, named KL3 and KL5, are circular (Figure 1) and were part of a bigger production workshop. At least three other kilns were found in the same excavation area and according to archaeological evidence they were used for the production of bricks or ceramics. Based on some ceramics found in the site, archaeologists suggest that both kilns were in use during Hellenistic times (Tsaknaki 2013, personal communication).

(a) (b)

Figure 1 - Photos of the studied kilns where the position of the collected samples is shown: a) kiln KL3 and b) kiln KL5.

Systematic archaeomagnetic sampling was carried out collecting 9 brick samples from the first kiln (KL3) and 12 brick samples from the second kiln (KL5). All samples were oriented *in situ* using a magnetic and a solar compass. Most of the bricks were positioned horizontally in the kilns' walls and the central pillar (Figure 1). From each independently oriented sample, one to three cylindrical specimens of standard dimensions (diameter = 25.4 mm, height = 22 mm) were drilled in the laboratory.

3. Magnetic Mineralogy

The magnetic properties of representative samples collected from both kilns have been investigated by isothermal remanent magnetization (IRM) acquisition curves and thermal demagnetization of three IRM components (Lowrie, 1990). All measurements have been performed at the ALP Palaeomagnetic laboratory (Peveragno, Italy). The IRM was given by applying stepwise magnetic fields, with an ASC pulse magnetizer, up to 1.2 T. The magnetic remanence was measured with a JR6 spinner magnetometer (AGICO). The IRM acquisition curves obtained for different specimens are quite similar for both kilns and show that more than 90% of saturation is reached at applied fields of 0.2-0.4 T while no fraction remains unsaturated after 1.2 T peak field (Figure 2 a and b), indicating the presence of a low coercivity mineral such as magnetite and/or Ti-magnetite.

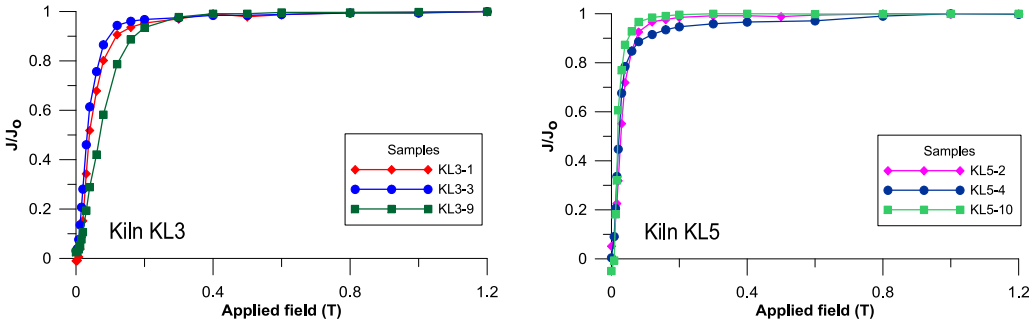

(a) (b)

Figure 2 - Representative IRM acquisition curves from selected samples from a) kiln KL3 and b) kiln KL5.

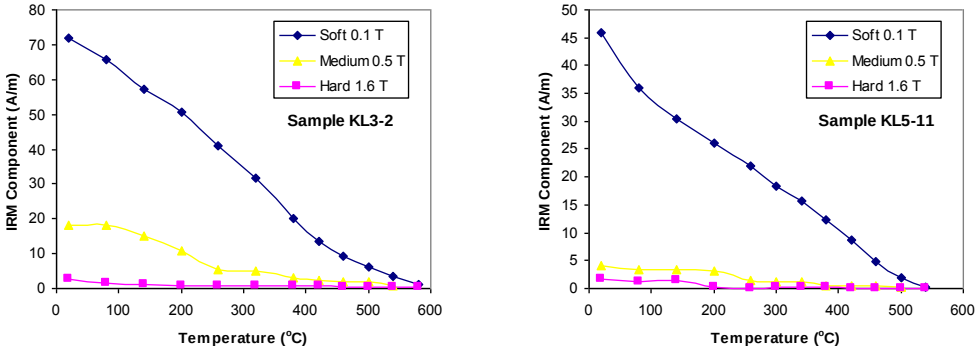

Figure 3 - Stepwise thermal demagnetization of three IRM components for a) sample KL3-2 (kiln KL3) and b) sample KL5-11 (kiln KL5).

Stepwise thermal demagnetization of the three IRM components (Lowrie, 1990) induced along the three sample axes, applying first the maximum field (1.6 T) along Z-axis, then the intermediate field (0.5 T) along the Y-axis and finally the minimum field (0.1 T) along the X-axis, shows thedominating role of the magnetically soft fraction (< 0.1 T) with unblocking temperatures ranging between 460 and 540 ^{o}C (Figure 3). These results point to magnetite or Ti-magnetite as the main magnetic carrier in the studied samples.

4. Archaeomagnetic Direction: Experiments and Results

The Natural Remanent Magnetization (NRM) of all specimens has been measured using a JR-6 spinner magnetometer. Subsequently, specimens have been stepwise thermally demagnetized up to 580 ^{o}C using a TSD-2 Schonstedt furnace. Demagnetization results (Figure 4) show that the magnetic remanence is very stable and it consists of one well defined Characteristic Remanent Magnetization (ChRM). In some samples (mainly from KL3 kiln) a secondary component is also visible but it is easily removed during thermal demagnetization.

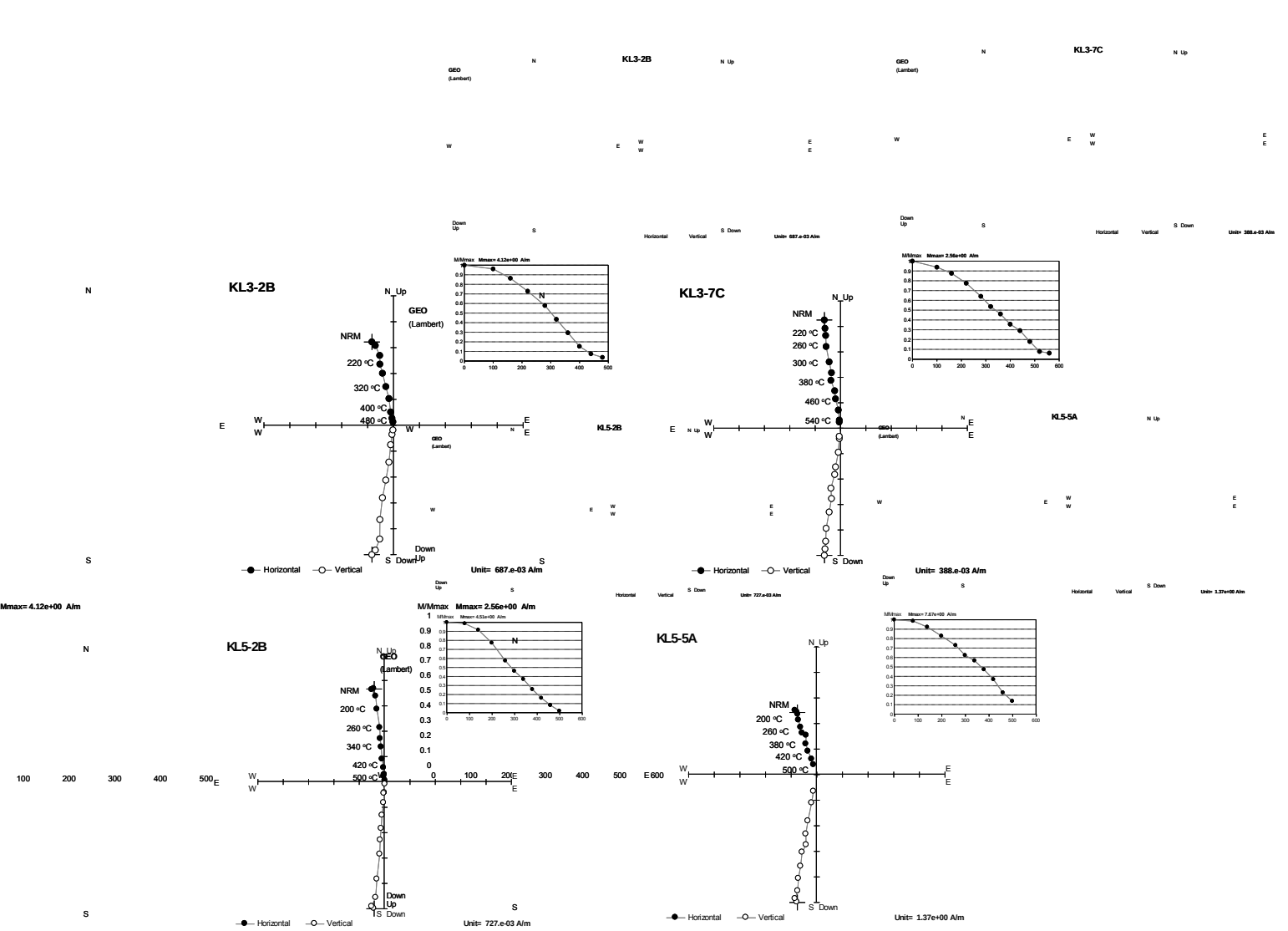

Figure 4 - Zijderveld diagrams and demagnetization curves from stepwise thermal demagnetization of representative samples from KL3 (upper part) and KL5 (lower part) kilns.

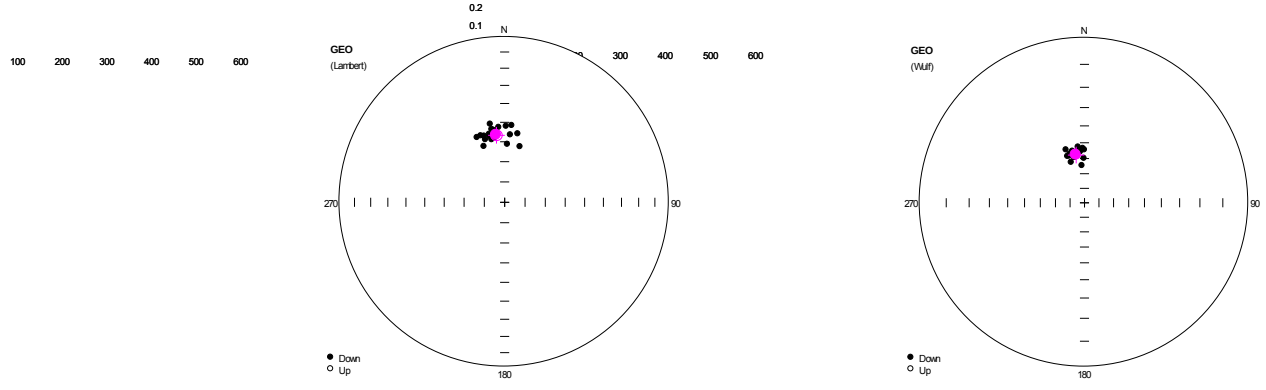

(a) (b)

Figure 5 - Equal area projection of the ChRM directions for kiln a) KL3 and b) KL5.

The direction of the ChRM for each specimen has been obtained from principal component analysis (Zijderveld, 1967; Kirschvink, 1980) using the Remasoft software (Chadima & Hrouda, 2006). All results at specimen level from kiln KL3 and KL5 are reported in Table 1 and Table 2 respectively, together with the mean direction for each kiln, calculated according to Fisher

statistics (Fisher, 1953). Equal-area projections of the ChRM directions (Figure 5) show a good concentration around the mean directions. The calculated mean direction for kiln KL3 is: D= 353.0°, I= 56.5°, k= 147, α_{95}= 2.7° and for kiln KL5 is: D= 350.1°, I= 57.3°, k= 246, α_{95}= 2.4°.

Table 1 - Archaeomagnetic directional results for kiln KL3.

Sample	Temperature range (°C)	D (°)	I (°)
KL3-1a	400-560	348.8	58.6
KL3-1b	400-560	350.2	56.5
KL3-1c	280-560	351.9	58.0
KL3-2a	220-480	1.6	52.3
KL3-2b	220-480	347.7	55.6
KL3-2c	220-480	343.7	55.9
KL3-3a	320-480	5.8	51.7
KL3-3b	160-520	337.2	55.3
KL3-4a	280-480	347.7	56.7
KL3-4b	280-520	351.7	54.0
KL3-6a	400-560	343.3	57.8
KL3-6b	220-560	340.6	55.2
KL3-7a	220-560	355.9	52.8
KL3-7b	160-520	350.4	53.4
KL3-7c	220-560	349.9	50.6
KL3-8a	100-520	340.0	60.8
KL3-8b	280-520	5.4	56.6
KL3-8c	280-520	11.4	55.5
KL3-9a	400-520	3.3	61.5
KL3-9c	220-520	16.1	61.6

Mean value:

N= 8	n= 20	D_m= 353.0°	I_m= 56.5°	k=147	α_{95}= 2.7°

Columns: Sample; Temperature interval used for the calculation of the direction of the ChRM at specimen level; Declination (°); Inclination (°); N= number of independently oriented samples; n= number of specimens; D_m= mean declination; I_m= mean inclination; k= precision parameter; α_{95}= 95% semi-angle of confidence.

Table 2 - Archaeomagnetic directional results for kiln KL5.

Sample	Temperature range (^{o}C)	D (^{o})	I (^{o})
KL5-1a	200-500	351.7	56.0
KL5-1b	200-500	343.8	56.2
KL5-2a	200-500	347.4	54.8
KL5-2b	140-500	354.0	52.8
KL5-3a	140-500	358.9	53.8
KL5-3b	140-500	0.5	54.7
KL5-4a	140-500	356.9	64.9
KL5-5a	140-500	342.3	61.5
KL5-5b	80-500	348.1	59.0
KL5-7b	200-500	341.1	52.9
KL5-8a	300-500	348.1	59.0
KL5-8b	200-500	356.1	56.0
KL5-10a	140-500	0.1	60.2
KL5-11a	140-500	342.6	57.3
KL5-11b	140-500	340.4	57.1

Mean value:

N= 9	n= 15	D_m= 350.1^o	I_m= 57.3^o	k=246	α_{95}= 2.4^o

Columns: (as in Table 1).

5. Archaeomagnetic Dating

The mean direction values obtained for each kiln have been separately used for the archaeomagnetic dating of the two structures after comparison with the reference secular variation curves calculated from the SCHA.DIF.3K model (Pavón-Carrasco et al., 2009). The SCHA.DIF.3K is a regional archaeomagnetic model that represents the geomagnetic field variations in Europe for the last 3000 years modeling together the three geomagnetic field elements. It is based on reference data coming from instrumental measurements for the last 400 years and on data from archaeological material for older times. For the 400 BC-500 AD period the directional curve obtained from the SCHA.DIF.3K model is statistically the same with the Greek SV curve calculated using the Bayesian statistics (De Marco et al., 2013, *submitted*). For this reason, both curves should give the same dating results. In this study, the SCHA.DIF.3K model reference curve was used because, in respect to the local SV curves, it presents the advantage that predicts the geomagnetic field at the site of interest, avoiding this way any eventual relocation error.
Archaeomagnetic dating of the KL3 and KL5 kilns has been carried out using the Matlab *archaeo_dating* tool (Pavón-Carrasco et al., 2011). Reference curves have been directly calculated at the geographic coordinates of Kato Achaia and have been used for the calculation of probability

density functions separately for declination and inclination. The final dating of the two kilns is obtained after the combination of the separate density functions (Figure 6).

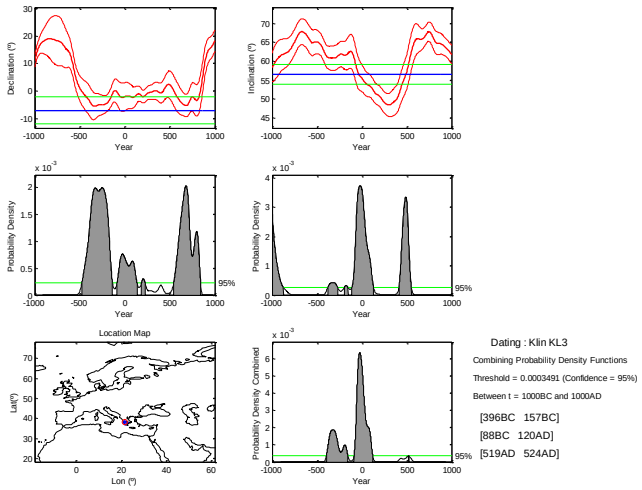

a)

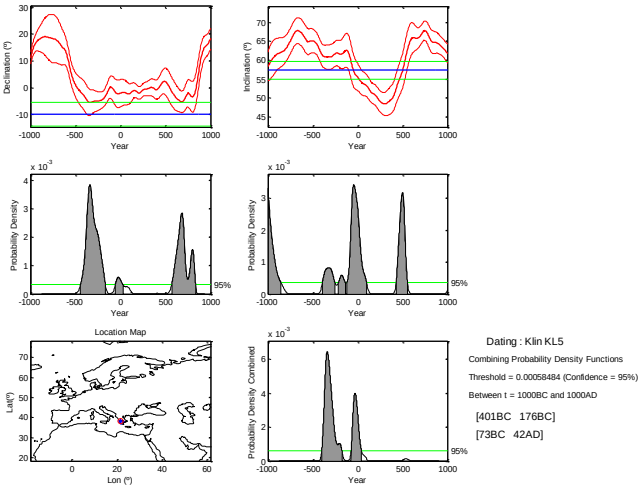

b)

Figure 6 - Archaeomagnetic dating results for a) KL3 and b) KL5 kilns. Dating intervals have been calculated at 95% of probability using the matlab *archaeo_dating* tool (Pavón-Carrasco et al., 2011).

Archaeomagnetic dating of KL3 and KL5 kilns calculated at 95% of probability shows several dating intervals in the 1000 BC-1000 AD period (Figure 6). However, taking into consideration the archaeological information available for the studied site, indicating that the kilns were in use during Hellenistic times, the older time intervals can be excluded. It is thus suggested that the last use of KL3 kiln took place around 88 BC to 120 AD while kiln KL5 was abandoned between 73 BC and 42 AD.

6. Conclusions

Archaeomagnetic investigation of two ancient kilns brought into light during a rescue excavation at Kato Achaia (Southern Greece), showed that the studied materials were heated at high temperatures and proved to be reliable recorders of the Earth's magnetic field at the time of their last firing. Thermal demagnetization procedures yielded well defined archaeodirection values for both kilns. The obtained results were compared with the reference curves produced by the SCHA.DIF.3K European regional geomagnetic field model and the archaeomagnetic dates of the kilns last use were calculated at 95% of probability. The obtained dating intervals are in very good agreement with the archaeological evidence, suggesting that both kilns were in use during Hellenistic times and were abandoned around 88 BC-120 AD for KL3 and 73 BC-42 AD for KL5 kiln. These results suggest that KL5 kiln could have been abandoned slightly before the KL3; nevertheless such short time differences should be cautiously interpreted because up to nowadays variations of the Earth's magnetic field in the past at time scales less than 100 years can not be reconstructed with such precision. Future investigation of the archaeointensity of the Earth's magnetic field registered by the kilns could further restrict the obtained dating intervals. These results show that precise archaeomagnetic dating in Greece is possible and can be used as a valuable dating tool in archaeological research.

7. Acknowledgments

The archaeologist Vaso Tsaknaki is warmly acknowledged for sampling permission, fruitful collaboration and important information provided for the studied archaeological site. Dr. Christina Rathosi is particularly thanked for sampling assistance. Dr. Ioannis Iliopoulos and an anonymous reviewer are acknowledged for their careful review of the paper.

8. References

Aidona E. and Kondopoulou D. 2012. First archaeomagnetic results and dating of Neolithic structures in northern Greece, *Stud. Geophys. Geod.,* 56, 827-844.

Chadima M. and Hrouda F. 2006. Remasoft 3.0 a user-friendly paleomagnetic data browser and analyser, *Travaux Géophysiques*, XXVII, 20-21.

De Marco E., Spatharas V., Gómez-Paccard M., Chauvin A. and Kondopoulou D. 2008a. New archaeointensity results from archaeological sites and variation of the geomagnetic field intensity for the last 7 millennia in Greece, *Phys. Chem. Earth*, 33, 578-595.

De Marco E., Spassov S., Kondopoulou D., Zananiri I. and Gerofoka E. 2008b. Archaeomagnetic study and dating of a Hellenistic site in Katerini (N. Greece), *Phys. Chem. Earth*, 33, 481-495.

De Marco E., Tema E., Lanos Ph. and Kondopoulou D. 2013. An updated catalogue of Greek archaeomagnetic data and a directional secular variation curve for the last 4500 *years, Stud. Geophys. Geod., (Submitted).*

Downey W.S. and Tarling D.H. 1984. Archaeomagnetic dating of Santorini volcanic eruptions and fired destruction levels of Late Minoan civilization, *Nature*, 309, 519-523.

Fanjat G., Aidona E., Kondopoulou D., Camps P., Rathossi C., Poidras T. 2012. Archaeointensities in Greece during the Neolithic period: New insights into material selection and secular variation curve, *Phys. Earth Planet. Int.*, 215, 29-42, doi:http://dx.doi.org/10.1016/j.pepi.2012.10.011.

Fisher R.A. 1953. Dispersion on a sphere, *Proceedings of Royal Society*, London, pp.295.

Gallet Y., Genevey A., Le Goff M., 2002. Three millennia of directional variation of the Earth's magnetic field in Western Europe as revealed by archaeological artefacts, *Phys. Earth Planet. Inter*., 131, 81-89.

Gómez-Paccard M., Lanos P., Chauvin A., McInstosh G., Osete M.L., Catanzariti G., Ruiz-Martınez V.C. and Núnez J.I. 2006. First archaeomagnetic secular variation curve for the

Iberian Peninsula: Comparison with other data from Western Europe and with global geomagnetic field models, *Geochem. Geophys. Geosyst.,* 7, Q12001, doi:10.1029 /2006GC001476.
Kirschvink J.L. 1980. The least-square line and plane and the analysis of palaeomagnetic data, *Geophys. J. Astron. Soc.,* 62, 699-718.
Kovacheva M., Spatharas V. and Liritzis I. 2000. New archaeointensity results from Greek materials, *Archaeometry*, 42 (2), 415-429.
Kovacheva M., Boyadziev Y., Kostadinova-Avramova M., Jordanova N. and Donadini F. 2009. Updated archaeomagnetic data set of the past 8 millennia from the Sofia laboratory, Bulgaria, *Geochem. Geophys. Geosyst.*, 10, Q05002, doi: 10.1029/2008GC002347.
Liritzis Y. and Thomas R.C. 1980. Palaeointensity and thermoluminescence measurements on Cretan Kilns from 1300 to 2000 BC, *Nature,* 283, 54-55.
Lowrie W. 1990. Identification of ferromagnetic minerals in a rock by coercivity and unblocking temperature properties, *Geophys. Res. Lett.*, 17, 159-162.
Márton P. 2010. Two thousand years of geomagnetic field direction over central Europe revealed by indirect measurements, *Geophys. J. Int.*, 181, 261-268.
Papamarinopoulos S.P. 1987. Geomagnetic intensity measurements from Byzantine vases in the period between 3000 and 1650 AD, *J. Geomagn. Geoelectr.,* 39, 261-270.
Pavón-Carrasco F.J., Osete M.L., Torta J.M. and Gaya-Piqué L.R. 2009. A regional archaeomagnetic model for Europe for the last 3000 years, SCHA.DIF.3K: applications to archaeomagnetic dating, *Geochem. Geophys. Geosyst.,* 10 (3), Q03013.
Pavón-Carrasco F. J., Osete M.L. and Torta J. 2010. Regional modeling of the geomagnetic field in Europe from 6000 BC to 1000 BC, *Geochem. Geophys. Geosyst*, 11, Q11008.
Pavón-Carrasco F.J., Rodriguez-Gonzalez J., Osete M.L. and Torta J. 2011. A Matlab tool for archaeomagnetic dating, *J. Archeol. Sci.*, 38 (2), 408-419.
Schnepp E. and Lanos Ph. 2005. Archaeomagnetic secular variation in Germany during the past 2500 years, *Geophys. J. Int.*, 163, 479-490.
Spassov S., Valet J.P., Kondopoulou D., Zananiri I., Casas L. and Le Goff M. 2010. Rock magnetic property and paleointensity determination on historical Santorini lava flows, *Geochem. Geophys. Geosyst., 11 (7),* Q07006.
Spatharas V., Kondopoulou D., Liritzis I. and Tsokas G. 2000. Archaeointensity results from two ceramic kilns from N. Greece, *J. Balkan Geophys. Soc.*, 4, 67-72.
Spatharas V., Kondopoulou D., Aidona E. and Efthimiadis K.G. 2011. New magnetic mineralogy and archaeointensity results from Greek kilns and baked clays, *Stud. Geophys. Geod.,* 55 (1), 131-157.
Tema E. and Kondopoulou D. 2011. Secular variation of the Earth's magnetic field in the Balkan region during the last eight millennia based on archaeomagnetic data, *Geophys. J. Int*., 186, 603-614, doi: 10.1111/j.1365-246X.2011.05088.x.
Tema E., Hedley I. and Lanos Ph. 2006. Archaeomagnetism in Italy: a compilation of data including new results and a preliminary Italian secular variation curve, *Geophys. J. Int.*, 167, 1160-1171. doi:10.1111/j.1365-246X.2006.03150.x
Tema E., Gómez-Paccard M., Kondopoulou D. and Ylenia A. 2012. Intensity of the Earth's magnetic field in Greece during the last five millennia: New data from Greek pottery, *Phys. Earth Planet. Int*., 202-203, 14-26, doi: 10.1016/j.pepi.2012.01.012.
Zananiri I., Batt C., Lanos Ph., Tarling D. and Linford P. 2007. Archaeomagnetic secular variation in the UK during the past 4000 years and its application to archaeomagnetic dating, *Phys. Earth Planet. Int.,* 160 (2), 97-107.
Zijderveld J. 1967. AC demagnetization of rocks: analysis of results, in: Collinson D., Creer K., Runcorn S. (Eds.), *Methods in Paleomagnetism*. Elsevier, New York, pp. 254-256.

Δελτίο της Ελληνικής Γεωλογικής Εταιρίας, τομ. XLVII , 2013
Πρακτικά 13ου Διεθνούς Συνεδρίου, Χανιά, Σεπτ. 2013

Bulletin of the Geological Society of Greece, vol. XLVII 2013
Proceedings of the 13th International Congress, Chania, Sept. 2013

LATE BRONZE AGE POTTERY AS INDICATOR OF THE DEPOSITION TEMPERATURES OF THE MINOAN PYROCLASTIC PRODUCTS, SANTORINI, GREECE

Tema E.[1], Pavlides S.[2] and Kondopoulou D.[3]

[1] *Dipartimento di Scienze della Terra, Università degli Studi di Torino, Italy, evdokia.tema@unito.it*

[2] *Department of Geology, Aristotle University of Thessaloniki, Greece*

[3] *Department of Geophysics, Aristotle University of Thessaloniki, Greece*

Abstract

The Minoan eruption of Santorini volcano (Greece) took place in the Late Bronze Age (17th century BC) and produced a great volume of volcanic products that covered the whole island and buried every human settlement under meters of pyroclastic deposits. In this study we used thermal analysis of the magnetic remanence carried by pottery fragments buried under the pyroclastic deposits in order to estimate the thermal effect of the Minoan volcanic products on the pre-eruption habitation level. A total of 70 samples, prepared from 45 independent pottery fragments, have been studied. Samples were collected from three different sites, situated at the southern part of the island. Stepwise thermal demagnetizations reveal that the pottery fragments generally carry a two-component remanent magnetization. Interpretation of the demagnetization results using the normalised intensity decay curves and the orthogonal projection diagrams indicates that most samples were re-heated at temperatures around 160-260 ^{o}C. The obtained results represent the equilibrium temperatures reached after the deposition of the pyroclastic fall and show that the pyroclastic fall deposits at distances around 6 to 9 km from the eruption vent were still hot enough to reheat the buried pottery at such temperatures.

Key words: *Palaeomagnetism, Pyroclastic deposits, Deposition temperature, Potery, Santorini.*

Περίληψη

Η Μινωική έκρηξη του ηφαιστείου της Σαντορίνης που έλαβε χώρα κατά την Ύστερη Εποχή του Χαλκού (17^{o} αιώνα π.Χ.) απέθεσε έναν τεράστιο όγκο ηφαιστειακών προϊόντων που κάλυψαν όλο το νησί και έθαψαν κάθε ανθρώπινο κτίσμα. Στην παρούσα μελέτη, παρουσιάζονται τα αποτελέσματα της θερμικής απομαγνήτισης κεραμικών θραυσμάτων που βρέθηκαν στην επαφή του προ-Μινωικού παλαιοεδάφους με τις πρώτες πυροκλαστικές αποθέσεις, με σκοπό την μελέτη της θερμικής επίδρασης των θερμών ηφαιστειακών υλικών στο παλαιοέδαφος όπου κατοικούσαν οι άνθρωποι πριν την έκρηξη. Συνολικά μελετήθηκαν 70 δείγματα που προέρχονται από 45 κεραμικά θραύσματα. Τα δείγματα συλλέχθηκαν από τρεις διαφορετικές τοποθεσίες στο νότιο μέρος του νησιού. Τα αποτελέσματα της σταδιακής θερμικής απομαγνήτισης των δειγμάτων δείχνουν ότι τα κεραμικά φέρουν δύο συνιστώσες μαγνήτισης που υποδεικνύουν ότι τα περισσότερα από αυτά αναθερμάνθηκαν σε θερμοκρασίες της

τάξεως 160-260 ^{o}C. Αυτές οι θερμοκρασίες αντιπροσωπεύουν τις θερμοκρασίες απόθεσης των πρώτων πυροκλαστικών προϊόντων που αποτέθηκαν πάνω στο Μινωικό έδαφος, μετά την αποκατάσταση της θερμικής ισορροπίας ανάμεσα στις θερμές αποθέσεις και το κρύο υπόβαθρο. Η μελέτη αυτή δείχνει ότι τα πρώτα πυροκλαστικά υλικά που αποτέθηκαν σε αποστάσεις 6 με 9 χιλιομέτρων από τον κρατήρα της Μινωικής έκρηξης, ήταν αρκετά ζεστά έτσι ώστε να προκαλέσουν αναθέρμανση των κεραμικών σε τέτοιες θερμοκρασίες.
Λέξεις κλειδιά: *Παλαιομαγνητισμός, Πυροκλαστικές αποθέσεις, Θερμοκρασία απόθεσης, Κεραμικά, Σαντορίνη.*

1. Introduction

Santorini has been, and still is, a unique natural laboratory where several disciplines found a prosperous ground for their development. A relatively less known one is the use of the magnetic properties of suitable materials (lithic clasts and/or archaeological artefacts) to estimate the deposition temperatures of the volcanic products produced by the various eruptions. This method has been already applied on lithic clasts from various series of the large explosive events which the island has experienced during the past 250000 years (McClelland & Druitt, 1989; Bardot & McClelland, 2000; Bardot, 2000). Several relevant studies have been also conducted in Italy, Mexico and Argentina (e.g. Cioni et al., 2004; Zanella et al., 2007; Sulpizio et al., 2008; Porreca et al., 2008; Di Vito et al., 2009; Lesti et al., 2011) and recently this technique was improved and extended involving also the study of human artefacts such as tiles and pottery.

The Minoan eruption (1613+/- 13 BC, Friedrich & Heinemeier, 2009) is the last large volcanic event which changed the morphology of the island to its actual aspect and is related to the destruction of the Cycladic culture and the Minoan civilization. Archaeological excavations, past and ongoing, put in light a rich evidence of human occupation which flourished during the Bronze age. The most prominent settlement, close to the modern village of Akrotiri, was totally buried by pumice and ash of the Minoan eruption which destroyed it, but at the same time also preserved it until its unearthing.

As a consequence of the island's "blanketing" by the Minoan eruption volcanic deposits, human artefacts among which pottery, were completely covered by the pyroclastic products and constitute today an additional source of information on the pyroclastic products deposition temperatures. It is well-known that baked clays contain various amounts of iron-oxides and can be magnetized during firing and subsequent cooling, under exactly the same physical principles which allow the magnetization of volcanics. Therefore, baked clays, abundant in archaeological sites, and in the present case lying under the Minoan eruptional products, can be used to reconstruct the deposition temperatures of the pyroclastic fall deposits within the sampling area.

In the present study we used carefully selected pottery fragments found on the surface of the pre-Minoan palaeosol and covered by the first eruption products. Standard palaeomagnetic techniques were used to estimate the prevailing temperatures reached after the deposition of the pyroclastic fall and the thermal equilibrium subsequently reached.

2. Materials and Methods

2.1. Palaeomagnetic Sampling

During two field campaigns carried out at 2011 and 2012, systematic sampling of ceramic fragments has been carried out at three locations: Megalochori Quarry (36^{o} 22' 00" N, 25^{o} 25' 12.0" E), Apothikes (Remezzo) (36^{o} 21' 36.6" N, 25^{o} 24' 14.7" E) and Vlichada (Bar Theros) (36^{o} 20' 42.9" N, 25^{o} 25' 30.0" E). Samples from Megalochori Quarry were first collected on May 2011 and the obtained results have been previously presented by Tema et al. (2013, *submitted*) while

samples from Apothikes and Vlichada were collected on August 2012 (Tema et al., 2013). All sampling sites are situated at the southern part of Santorini island (Figure 1), in distances that range from 6 to 9 km from the inferred vent of the Minoan eruption, probably located somewhere between the Nea Kameni Island and the present Fira town (Heiken & McCoy, 1984; McCoy, 2009). Identifying the sampling sites that could be appropriate for such study, was not an easy task: i) each studied site should offer a section of the Minoan eruption volcanic products. Moreover, the contact between the Minoan palaeosol and the first pyroclastic deposits should be clearly visible and approachable; ii) it should be an area occupied by human activity during the Minoan period in order to provide fragments from pottery and ceramic artefacts; iii) the collected ceramic fragments should be directly in contact and completely covered by the first pumice fall in order to be considered as reliable indicators of the re-heating temperature caused by the volcanic products. For this study, a total of 45 independent ceramic fragments have been collected; 22 from Megalochory Quarry, 16 from Apothikes and 7 from Vlichada (Bar Theros).

Figure 1 - Map of Santorini whith the location of the studied sites.

All collected ceramics were completely covered by the precursory volcanic activity ashes and/or incorporated at the first three centimetres of the pumice fall. They are small fragments with dimensions varying from 1-4 cm (Figure 2) and probably belonged to some vases or plates for domestic use spread on the palaeosol surface during the eruption. Due to the small size of the collected ceramics the preparation of standard cylindrical specimens (diameter 25.4 mm; height 22.5 mm) was not possible. To measure such small pieces, plastic boxes and white plasticine were used, following the procedures described by Cioni et al. (2004). In the case of samples larger than 2 cm, two specimens were prepared from individual fragments in order to improve the accuracy in the estimation of the deposition temperature interval (Zanella et al., 2008). Following this approach, from the 45 independent ceramic fragments, 70 specimens have been prepared and studied.

2.2. Contribution of Palaeomagnetic Methods to the Estimation of Deposition Temperatures

Palaeomagnetism has been widely applied in the last decades to tectonics, magnetostratigraphy, geomagnetic field modelling and to archaeology (archaeomagnetism). An additional and less known application consists to the estimation of pyroclastic deposits depositional temperature

Figure 2 - Photo of two ceramic fragments sampled at Vlichada.

through the determination of the partial thermal remanent magnetization (pTRM) of lithic clasts and/or ceramic fragments incorporated and/or covered by the volcanic deposits. This method has been thoroughly described by several authors (e.g. McClelland & Druitt, 1989; Zanella et al., 2007; Paterson et al. 2010) while others analysed potential factors affecting the reliability of the emplacement temperature estimates using palaeomagnetic methods (Bardot & McClelland, 2000; Porreca et al., 2008; Lesti et al., 2011).

The method is based on the following assumption: the lithic clasts found in the pyroclas-tic deposits and probably coming from cold lavas of previous eruptions contain magnetic minerals and carry a remanent magnetization acquired during their initial formation, oriented towards the Earth's magnetic field at the time of their cooling. These clasts are partially re-heated when incorporated in the hot mixture of ash and gases produced by a new volcanic eruption. A portion of their original magnetization is lost and they acquire a new partial thermoremanent magnetization, oriented along the Earth's magnetic field at the time of the emplacement. As a consequence, the natural remanent magnetization (NRM) of a lithic clast will consist of two TRM components of magnetization; an original, randomly oriented, high temperature component and a new, uniformly oriented, low temperature component.

Through an analogous procedure, ceramic fragments carry an initial magnetization acquired during heating at high temperatures and subsequent cooling at ambient temperature in a kiln during their production procedure. In the case of volcanic eruptions affecting inhabited areas, such ceramics are often found in contact with or incorporated into pyroclastic deposits that cover the human habitation surface (Di Vito et al., 2009). Since the volcanic products are usually hot when deposited over the ceramic fragments, then once the thermal equilibrium between the hot pyroclas-tics and the cold ceramics is reached , the ceramics will be partially demagnetized and will acquire a secondary, low temperature, magnetic component.

In order to obtain reliable equilibrium deposition temperatures, the secondary magnetization component should be of thermal origin (thermal remanent magnetization, TRM) and not be altered by the effects of chemical overprinting (chemical remanent magnetization, CRM) due to field or laboratory alteration (McClelland & Druitt, 1989). For this reason, several tests are performed in order to assess the thermal origin of the secondary component. A serious advantage in using pottery fragments instead of lithic clasts for the estimation of emplacement temperatures lies in their origin. In fact, pottery resists better to chemical alteration than lithic clasts often fractured and trapping water and gases.

3. Measurements and Results

A total of 70 specimens from the three studied sites have been submitted to stepwise thermal demagnetization at the ALP Palaeomagnetic Laboratory (Peveragno, Italy). Thermal

demagnetization was performed with a TSD-2 Schonstedt furnace and the magnetic remanence of the samples was measured with a JR6 (AGICO) spinner magnetometer. Thermal demagnetization was carried out in steps of 40 °C between a starting temperature of 60 °C and a maximum of ~620 °C. Whenever sister specimens from individual ceramic fragments were available, a second demagnetization was carried out using the same 40 °C steps but starting from 80 °C. The results were then interpreted using the principal component analysis available as part of the Remasoft software (Chadima & Hrouda, 2006).

3.1. Thermal Stability of the Samples

In order to estimate the thermal stability of the samples, after each heating/cooling circle, the bulk magnetic susceptibility at room temperature was measured for all samples with a KLY-3 (AGICO) Kappabridge at the ALP Palaeomagnetic laboratory. Almost all pottery samples show a very stable behaviour and only negligible magnetic susceptibility variations with increasing temperature are observed (Figure 3). These results are also confirmed by the continuous thermomagnetic curves obtained for representative samples from Megalochori Quarry (e.g. sample MGC2- Figure 4). The continuous heating and cooling curves measured at IPGP (Paris) with a CS3 Kappabridge, show very good reversibility and suggest that the ceramics are thermally stable and there is no evidence for important magnetic mineralogy transformations during heating.

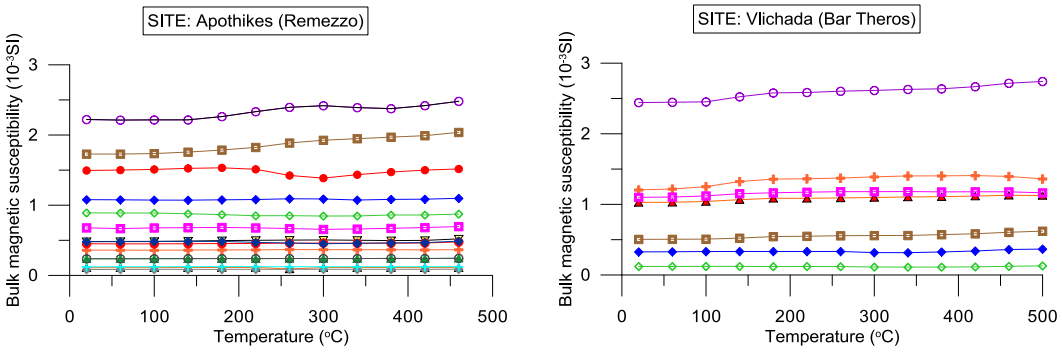

(a) (b)

Figure 3 - Variations of the bulk magnetic susceptibility at room temperature after each heating-cooling circle during stepwise thermal demagnetization for ceramics from a) Apothikes and b) Vlichada.

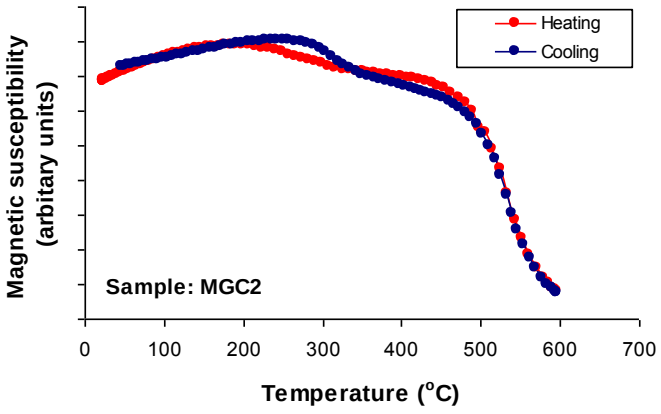

Figure 4 - Continuous variation of magnetic susceptibility with temperature (Sample MGC2, Megalochori Quarry).

3.2. Thermal Demagnetization Results

The thermal demagnetization results are interpreted using the normalised intensity decay curves and the orthogonal projection diagrams (Zijderveld, 1967). From the 70 demagnetized specimens, more than half of them (53 specimens) clearly show two components of magnetization: a high temperature component acquired during the initial heating of the ceramics (during their production involving heating in a kiln) and a low temperature component acquired during their partial re-heating caused by the overlapping hotter pyroclastic deposits. In most cases the two components are well defined and clearly distinguished from the Zijderveld diagrams, showing a sharp change in direction (Figure 5). In order to guarantee high quality of the obtained results, specimens

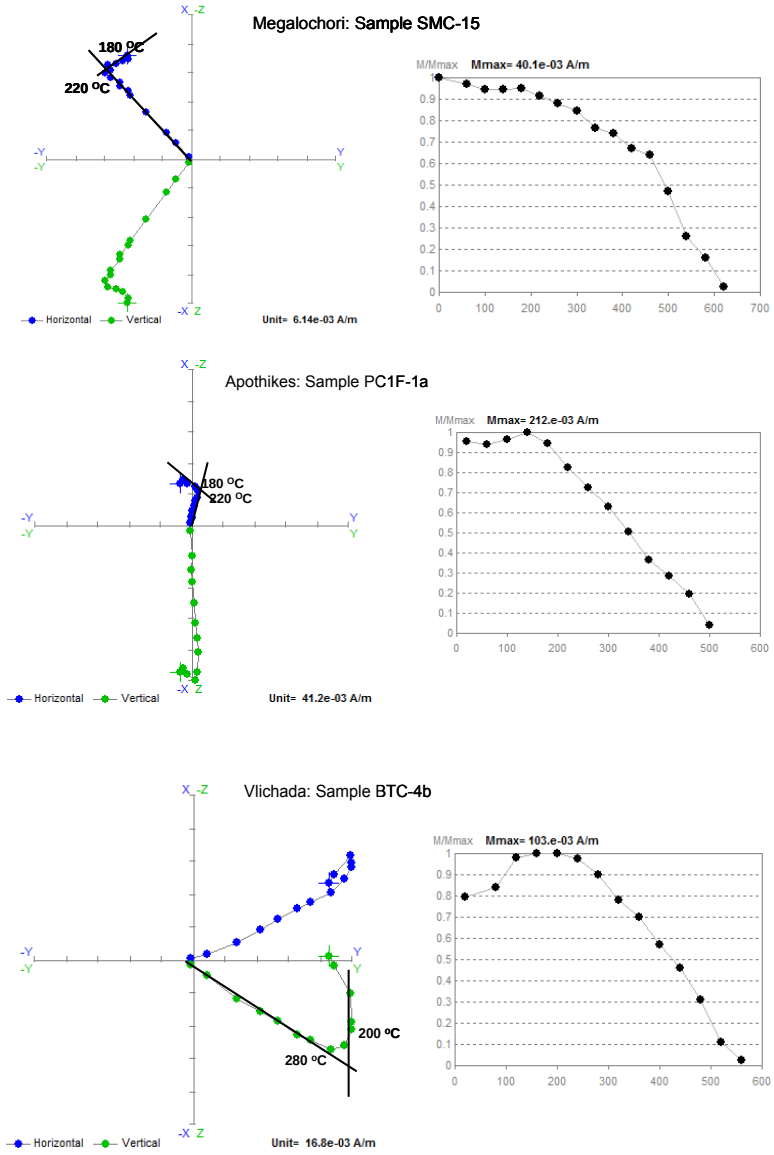

Figure 5 - Thermal demagnetization results illustrated as Zijderveld diagrams and NRM decay plots.

characterized by two magnetization components that however are not clearly separated, have been rejected. Few ceramic fragments show a three component magnetization; an initial characteristic magnetization component that is the one that passes through the origin of the axes in the Zijderveld diagrams and corresponds to the initial heating of the ceramics during their fabrication, a second high temperature component that indicates a partial re-heating at high temperatures around 420-460 ^{o}C, and a third low temperature component that indicates a final partial re-heating at lower temperatures around 180-220 ^{o}C. This intermediate temperature component, as already discussed by Tema et al. (2013, *submitted)* could be interpreted as a magnetization component acquired during the use of the ceramics that were often utilized to prepare and cook food and for this reason were in contact with fire or heated in domestic furnaces.

The ceramics re-heating temperatures have been estimated separately for each individual specimen from the intersection point of the low- and high- temperature magnetic component defined as the temperature interval between the highest temperature at which the low T_b component is present and the next temperature in the demagnetization sequence. Components with T_b< 130 ^{o}C have not been taken in consideration because they cannot be safely distinguished from a viscous magnetization overprint (Pullaiah et al., 1975; Bardot & McClelland, 2000). Estimated re-heating temperature intervals for each ceramic specimen based on the low-temperature magnetic component are illustrated in Figure 6 for each sampling site separately. The obtained results show that the estimated re-heating temperatures at specimen level vary from 120-240 ^{o}C at Megalochori, 120-300 ^{o}C at Apothikes and 140-280 ^{o}C at Vlichada. In all sites however, the maximum temperatures distribution is concentrated between 160 and 220 ^{o}C while 80% of the estimated temperatures from all sites are included in the 160-260 ^{o}C temperature range.

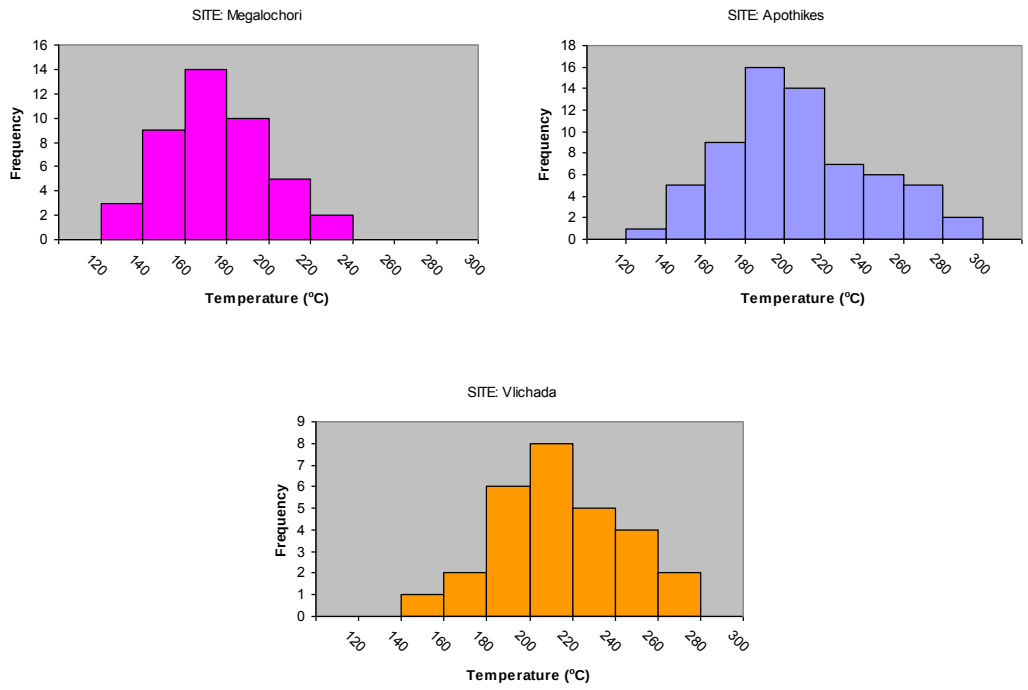

Figure 6 - Estimation of the re-heating temperatures of the studied ceramics from Megalochori, Apothikes and Vlichada sampling sites.

4. Conclusions

This study demostrates that pottery fragments can be successfully used as indicators of the deposition temperatures of the overlapping pyroclastic deposits. Samples collected from three sites situated at the southern part of Santorini island revealed two well defined magnetic components and showed that most of the studied samples have been re-heated at temperatures ranging from 160 to 260 ^{o}C. The obtained results are in good agreement with the Minoan plinial airfall emplacement temperatures estimated by McClelland et al. (1996). These authors studied lithic clasts collected from the Minoan Plinian tephra deposits at five sites and they found temperatures ranging from 130 to 250 ^{o}C at site level. However, no literature data for deposition temperatures of the Minoan deposits based on ceramic fragments are available, and the new results presented here are the only ones available up to now.

The estimated temperatures represent the equilibrium temperatures reached after the deposition of the first pyroclastic products and show that the pyroclastic fall deposits at a distances as far as 9 km from the eruption vent were still hot enough to reheat the buried ceramics at such temperatures. A continuation of this study involving the investigation of re-heating temperatures from sites located also at the Northern part of the island would be of particular interest in order to obtain a spatial distribution of the thermal effects of the Minoan volcanic products on the pre-Minoan habitation level.

5. Acknowledgments

Dr. Gerasimos Papadopoulos, Dr. Lefteris Zorzos, Mr. Elias Mastoras and the students A. Papadopoulos and G. Nikolaides are acknowledged for assistance during sampling. E. Tema acknowledges a post-doc fellowship from the Greek State Scholarship Foundation (IKY).

6. References

Bardot L. 2000. Emplacement temperature determinations of proximal pyroclastic deposits on Santorini, Greece, and their implications, *Bull. Volcanol*., 61, 450-467.

Bardot L. and McClelland E. 2000. The reliability of emplacement temperature Estimates using palaeomagnetic methods: A case study from Santorini, Greece, *Geophys. J. Int*. 143, 39-51.

Cioni R., Gurioli L., Lanza R. and Zanella E. 2004. Temperatures of A.D. 79 pyroclastic density currents deposits (Vesuvius, Italy), *J. Geophys. Res.,* 109, B02207, doi: 10.1029/ 2002JB002251.

Chadima M. and Hrouda F. 2006. Remasoft 3.0 a user-friendly paleomagnetic data browser and analyser, *Travaux Géophysiques*, XXVII, 20-21.

Di Vito M., Zanella E., Gurioli L., Lanza R., Sulpizio R., Bishop J., Tema E., Boenzi G. and Laforgia E. 2009. The Afragola settlement near Vesuvius, Italy: The destruction and abandonment of a Bronze Age village revealed by archaeology, volcanology and rock-magnetism, *Earth and Planetary Science Letters*, 277, 408-421.

Friedrich L.W. and Heinemeier J. 2009. The Minoan eruption of Santorini radiocarbon dated to 1613±13 BC: Geological and stratigraphic considerations, in: D. Warburton (Ed.), *Time's Up! Dating the Minoan Eruption of Santorini, Acts of the Minoan Eruption Chronology Workshop*. *Monographs of the Danish Institute at Athens*, Athens, vol. 10, 57-63.

Heiken G. and Mc Coy F. 1984. Caldera development during the Minoan eruption, Thera, Cyclades, Greece, *J. Geophys. Res.,* 89, B 10, 8441- 462.

Lesti C., Porreca M., Giordano G., Mattei M., Cas R.A.F., Wright H.M.N., Folkes C.B. and Viramonte J. 2011. High-temperature emplacement of the Cerro Galán and Toconquis Group ignimbrites (Puna plateau, NW Argentina) determined by TRM analyses, *Bull. Volcanol*., doi: 10.1007/s00445-011-0536-2.

McClelland E. and Druitt D.H. 1989. Palaeomagnetic estimates of emplacement temperatures of pyroclastic deposits on Santorini, Greece, *Bull. Volcanol*., 51, 16-27. doi:10.1007/ BF01086758.

McClelland E., Kondopoulou D., Westphal M. and Sophos Ph. 1996. Palaeomagnetic estimation of emplacement temperatures of plinian airfalls on Santorini, Greece. (Eds) Casale, R., Fytikas, M., Sigvaldasson, G., Vougioukalakis, G., The European laboratory volcanoes, *Proceedings of the 2nd workshop,* 2-4 May 1996, Santorini, Greece.

McCoy W. F.2009. The eruption within the debate about the date. In: D. A. Warburton (Ed.), Time's Up! Dating the Minoan Eruption of Santorini, Acts of the Minoan Eruption Chronology Workshop, *Monographs of the Danish Institute at Athens*, Athens, Vol. 10, 73-90.

Paterson G.A., Roberts A.P., Mac Niocaill C., Muxworthy A.R., Gurioli L., Viramonte J.G. and Navarro C. 2010. Paleomagnetic determination of emplacement temperatures of pyroclastic deposits: an underutilised tool, *Bull Volcanol.,* 72, 309-330, doi:10.1007/s00445-009-0324-4.

Porreca M., Mattei M., Mac Niocaill C., Giordano G., McClelland E. and Funiciello R. 2008. Paleomagnetic evidence for low-temperature emplacement of the phreatomagmatic Peperino Albano ignimbrite (Colli Albani volcano, Central Italy), *Bull. Volcanol*., 70, 877-893, doi:10.1007/s00445-007-0176-8.

Pullaiah G.E., Irving E., Buchan K.L. and Dunlop, D.J. 1975. Magnetization changes caused by burial and uplift, *Earth Planet. Sci. Lett*., 28, 133-143.

Sulpizio R., Zanella E. And Macías J.L. 2008. Deposition temperature of some PDC deposits from the 1982 eruption of El Chichón volcano (Chiapas, Mexico) inferred from rock magnetic data, *J. Volcanol. Geotherm. Res.*, 175, 494-500, doi:10.1016/j.jvolgeores.2008.02.024

Tema E., Kondopoulou D. and Pavlides S. 2013. How hot was the pyroclastic fall that covered the pre-Minoan palaeosol at Megalochory Quarry, Santorini (Greece)? Evidence from magnetic measurements*, Stud. Geophys. Geod., submitted.*

Tema E., Pavlides S. and Kondopoulou D. 2013. Investigating the deposition temperatures of the first pyroclastic products of the Minoan eruption (Santorini, Greece) through palaeomagnetic analysis on pottery, *EGU General Assembly, Vienna, Austria, 7-12 April 2013.*

Zanella E., Gurioli L., Pareschi M.T. and Lanza R. 2007. Influences of urban fabric on pyroclastic density currents at Pompeii (Italy): 2. Temperature of the deposits and hazard implications, *J. Geophys. Res.,* 112, B05214, doi: 10.1029/2006JB004775.

Zanella E., Gurioli L., Lanza R., Suplizio R. and Bontempi E.2008. Deposition temperature of the AD 472 Pollena pyroclastic density current deposits, Somma-Vesuvius, Italy, *Bull. Volcanol.*, doi: 10.1007/s00445-008-0199-9.

Zijderveld J.D.A. 1967. A.C. demagnetization of rocks: Analysis of results. In *Methods in Palaeomagnetism*, edited by Collinson, D.W., Creer K.M. and Runcorn S.K. Elsevier, Amsterdam.

Δελτίο της Ελληνικής Γεωλογικής Εταιρίας, τομ. XLVII , 2013
Πρακτικά 13ου Διεθνούς Συνεδρίου, Χανιά, Σεπτ. 2013

Bulletin of the Geological Society of Greece, vol. XLVII 2013
Proceedings of the 13th International Congress, Chania, Sept. 2013

NEAR-REAL-TIME EVALUATION OF THE EVOLUTION OF A SEISMIC EXCITATION: APPLICATION TO THE JANUARY 8, 2013 LEMNOS SEISMIC SEQUENCE

Teza E.[1], Scordilis E.M.[1], Papazachos C.B. [1] and Karakaisis G.F.[1]

[1] Department of Geophysics, Faculty of Geology, School of Science, Aristotle University, GR-54124 Thessaloniki, Greece., eteza@geo.auth.gr, manolis@geo.auth.gr, kpapaza@geo.auth.gr, karakais@geo.auth.gr.

Abstract

Monitoring the evolution of a seismic excitation in near-real-time sense is of high practical importance, as the quantitative results of this procedure may provide useful information to be used for the efficient planning of seismic protection measures. Furthermore, it may provide indications on the future evolution of this sequence, which is extremely important for both the public and authorities. A software package consisting of a number of sub-programs has been developed for this task. The main goal of this software is to obtain a semi-automatic evaluation of the possible evolution of a seismic excitation (sequence) already in progress. To achieve this target, successive determinations of basic parameters that characterize the sequence are performed and respective graphs are produced. In particular, the software automatically provides periodical snap-shots (within time periods defined by the user) describing how the shocks-members of the sequence are distributed in space, time, space-time and magnitude, allowing, this way, to detect possible variations in these parameters that could be connected to normal or non-normal evolution of the sequence. Application of this package has been performed during the recent seismic sequence which occurred SE of Lemnos island with a mainshock of M=5.9 (8/1/2013, 14:16 GMT). The snap-shots that described the evolution of the sequence and were produced by the application of the developed software package suggested a "normal" aftershock evolution during the first seven days of the main phase of this excitation.

Περίληψη

Η παρακολούθηση και εκτίμηση της εξέλιξης σεισμικών εξάρσεων σε σχεδόν πραγματικό χρόνο έχει μεγάλη πρακτική σημασία, καθώς μπορεί να παρέχει χρήσιμες πληροφορίες αξιοποιήσιμες για την αντισεισμική προστασία. Επί πλέον παρέχει ενδείξεις για την πιθανή εξέλιξη της διέγερσης κάτι εξαιρετικά σημαντικό τόσο για τους πολίτες όσο και για τις αρχές. Για την εξυπηρέτηση αυτού του σκοπού, υλοποιήθηκε ένα ημι-αυτοματοποιημένο λογισμικό το οποίο απαρτίζεται από ένα πλήθος επιμέρους υποπρογραμμάτων. Κύριος στόχος του λογισμικού αυτού είναι η σε σχεδόν πραγματικό χρόνο αυτοματοποιημένη παρακολούθηση μιας σεισμικής διέγερσης που είναι σε εξέλιξη. Έτσι, μέσω διαδοχικών υπολογισμών των παραμέτρων της διέγερσης και κατασκευής των αντίστοιχων διαγραμμάτων επιτυγχάνεται η εξαγωγή συμπερασμάτων σχετικά με την εξέλιξή της. Συγκεκριμένα, το λογισμικό

παράγει ανά τακτά χρονικά διαστήματα (οριζόμενα από το χρήστη) γραφήματα που περιγράφουν την κατά μέγεθος, χωρική, χρονική, και χωρο-χρονική κατανομή καθώς και τη μεταβολή του μέσου μεγέθους των σεισμών-μελών της διέγερσης, δίνοντας κατ' αυτόν τον τρόπο τη δυνατότητα διαμόρφωσης τεκμηριωμένης εκτίμησης σχετικά με την ομαλή ή μη εξέλιξη της διέγερσης. Εφαρμογή του λογισμικού επιχειρήθηκε κατά τη διάρκεια της σεισμικής ακολουθίας η οποία εκδηλώθηκε στις 8/1/2013 ΝΑ της Λήμνου με κύριο σεισμό μεγέθους M=5.9 (14:16 GMT). Τα διαδοχικά γραφήματα που προέκυψαν από την εφαρμογή του παραπάνω λογισμικού κατά τις πρώτες επτά μέρες, που αποτέλεσαν την κύρια φάση αυτής της διέγερσης, έδειξαν «ομαλή» εξέλιξη της διέγερσης με χαρακτηριστικά τυπικής μετασεισμικής ακολουθίας.

1. Introduction

Studies of seismic excitations can provide useful information of practical importance about their evolution. From this perspective, physical and statistical characteristics of their shocks-members such as their distribution in space, time and magnitude contribute to the understanding of the tectonic environment in which they occur and the stress distribution in the area.

Examination of spatial distribution of the earthquake hypocenters of a seismic sequence can provide useful information on both the length of the fault, and the rupture process on its surface. The first relatively accurate determination of epicenters of aftershocks, was performed by Nasu (1929) and concerned the aftershock sequence of the mainshock in Tango, Japan, on March 7, 1927 (M=7.3), focusing on the spatial and time distribution of the events. The study of the space-time distribution can provide indications on the way that the seismic fault ruptured, e.g. it can be assessed if the seismic activity is connected to a unilateral or a bilateral rupture. Such information could be used to "predict" the possible epicenter of a probable ensuing strong aftershock.

The time distribution of the aftershocks of a sequence, that is the rate of their occurrence, gives valuable information on how the sequence evolves with time. The first quantitative study of a seismic sequence was performed for the aftershocks of the mainshock of Nobi, Japan, (M=8.0, 28.10.1891). Omori (1894) observed that the number of these aftershocks decays with time according to the following formula:

Equation 1

$$n(t) = \frac{k}{t+c}$$

where t is the time from the main shock, $n(t)$ is the number of aftershocks per time unit and k and c are model parameters. Later studies on the Omori law (Mogi 1962, Ranalli 1969, Papazachos 1974, etc.) have showed that the number of aftershocks per unit-time roughly depends on the elapsed time from the mainshock according to the relation:

Equation 2

$$n = n_1 t^{-p} \Rightarrow \log n = a - p \log t$$

where n_1 is the aftershocks generation rate, n is the number of aftershocks occurred within time t from the mainshock and p is a parameter that depends on the physical characteristics of the focal area.

One of the most important relations in seismology is the one between the number and magnitude of the earthquakes that occur within a specific region during a certain time-period. This is the well-known Gutenberg and Richter (1944) relationship:

Equation 3

$$\log N_t = a_t - bM$$

where, N_t is the number of earthquakes with magnitude M or larger which occur in the region during a time period of t years, a_t, is the constant of this relationship for t years and b is a scaling coefficient. The latter is of great importance, since it is directly related to the stress-status of the excited area. It is known that small b-values are in general characteristic of fore-shock sequences while large b-values are connected to seismic swarms (e.g. Papazachos, 1974).

Another important feature that can be used to describe the excitation's identity is the mean magnitude of its member-shocks. This value should remain relatively constant in a normally evolving seismic sequence, whereas its increase may indicate upcoming strong aftershock (or a new main shock). The validation of the possible evolution of seismic excitations, in near real time sense, can provide useful information that can be used for the efficient organizing of seismic protection measures, since it is well-known that strong aftershocks may cause considerable damage.

In the present work, an effort was made to develop and apply a proper software, consisting of a number of sub-programs, in order to study the evolution of seismic sequences. The main goal of this software is to offer to the user the ability to automatically monitor the evolution of seismic excitation in a near real-time sense. This is achieved through successive calculations of parameters which reveal the excitations' identity with simultaneous production of relative graphs, plots and maps.

As a case-study we selected the strong earthquake of magnitude M=5.9 which occurred in the sea-area SE of Lemnos island on the 8th January 2013 (Figure 1) and its aftershock sequence.

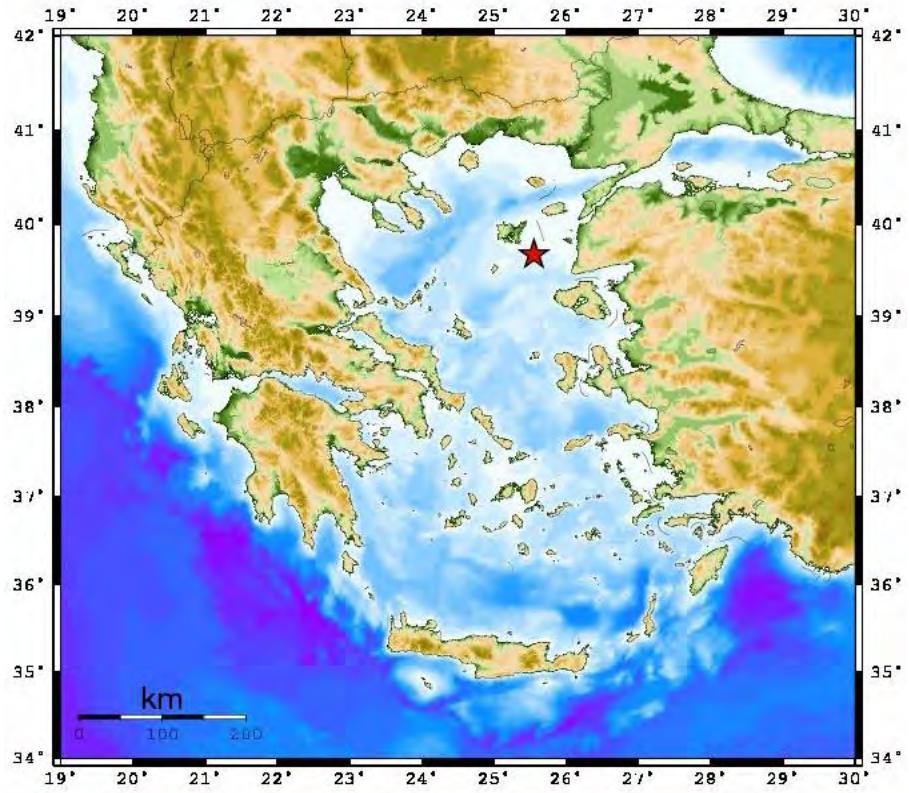

Figure 1- Epicentre map of the main shock of Lemnos 08/01/2013, 14:16 GMT, M=5.9.

2. Data

A prerequisite for the automated software which monitors the evolution of seismic sequences is an earthquake data-file (a catalogue of earthquakes). The main source for this database to be used in the analysis is the automatically recorded and analysed data through the freely distributed SeisComP software (http://geofon.gfz-potsdam.de/geofon/seiscomp, http://www.seiscomp3.org) that operates at the Seismological Station of the Geophysics Department of the Aristotle University of Thessaloniki (AUTH). This software detects and analyses earthquakes automatically, typically within less that 1 min after their occurrence, therefore, the database is updated in near-real-time sense. The quality of the focal parameters provided this way is sufficient for the purpose of monitoring a seismic excitation. However, it is well known that automatic locations are not as accurate as the manual ones. For that reason, a procedure was applied to import data of manually analysed earthquakes by replacing in the data-base the corresponding automatic locations. As sources of the manually analysed earthquakes we considered the preliminary bulletins (catalogues) of AUTH and of the Institute of Geodynamics of the National Observatory of Athens (NOA).

3. Software Configuration and Parameters' Determination

3.1. Software Configuration

The procedures executed by the software, after the necessary data file has been imported (namely the list of earthquakes that created), are outlined below:

- A theoretical circular region is defined, which is centred at the manually relocated epicentre of the main shock and has a radius proportional to its magnitude. The earthquakes enclosed within this circle are automatically selected, in order to create the catalogue of the seismic sequence.
- Based on the data that are recorded during the first 48 hours after the occurrence of the main shock, a completeness magnitude is estimated and a corresponding logN vs M plot-diagram is created.
- Based on the complete data of the first 48 hours, a mean magnitude, M_m, is estimated and simultaneously a corresponding plot of M_m vs time is generated.
- A mean strike azimuth is estimated based on the geographic distribution of the selected earthquakes (earthquakes contained in the region of interest, namely the seismogenic vol-ume).
- Based on this strike azimuth, along-strike and strike-normal cross-sections of the focal area are constructed.
- A space-time distribution graph of the aftershocks is also created.
- Based on the complete data of the first 48 hours, a graph of the time distribution of the earthquakes is automatically generated.

From the diagrams generated after the application of the integrated program, the user can obtain preliminary but reliable information on the evolution of the seismic excitation. In particular he may examine the geographical distribution of the earthquakes (spatial distribution), the potential rupture area as calculated from the data of the first 48 hours (longitudinal section and time-space distribution) and assess whether or not the evolution of the excitation over time evolves normally (time distribution and mean magnitude).

3.2. Parameters' Determination

After the application of this software, several quantitative parameters estimated are examined:

- The spatial distribution of the epicenters of the sequence roughly defines the seismogenic region. More specifically, the length of the fault, according to the magnitude of the mainshock, is estimated (Papazachos et al., 2004) (Equation 4) and then it is doubled in order to include all earthquakes that are considered as members of the sequence. This was because the automatically defined epicenters form a region almost double than the real one (Teza, 2011).

  Equation 4

  $$\log L = 0.51M - 1.85$$

- The magnitude distribution of earthquakes of the sequence demonstrates the completeness magnitude and the values of the parameters *a, b* of the G-R function. More specifically, the completeness magnitude is estimated based on the data of the first 48 hours in order to examine if this magnitude varies, through the evolution of the sequence, with time.
- The mean (average) magnitude distribution of the earthquakes of the sequence and its fluctuations are studied in order to identify possible changes over time. For this purpose, the data of the first 48 hours are used to determine the representative value of the mean magnitude and its standard deviation. Thereafter the magnitude of each new aftershock incorporated in the graph-plot in order to determine if that falls within the 68% confidence limits ($M_m \pm$ 1 standard deviation).
- The longitudinal section of the seismic region of the sequence provides a reliable estimation of the length of the seismic fault. In this way it can be checked whether the estimated fault length agrees with the one theoretically calculated by Equation 4. Moreover, the strike-normal cross-section provides information on the dipping direction of the fault.
- The time distribution of the earthquakes provides critical information on the normal (or not) evolution of the seismic sequence. In particular, through the use of Equation 2, both the coefficients of this relation and its 95% confidence limits (intervals) can be specified in order to delineate the deviations from this theoretical relation which can be considered as normal. These estimations are based on the complete data of the first 48 hours.
- The space-time distribution of earthquake epicenters of the sequence, in combination with the spatial distribution (seismicity map) can lead to valuable conclusions regarding the rupture propagation on the seismic fault, (e.g. unidirectional or bidirectional rupture, etc.).

4. Software Application and Results

An application of this software package, previously described, has been performed during the recent seismic sequence which occurred SE of Lemnos Island. The main shock occurred on 8 January 2013 14:16 GMT and its magnitude was M=5.9 (Figure 1).

The software was initially applied automatically, using as an input file a catalogue of earthquakes analysed by the software SeisComP. Due to shortage of data, a merged catalogue was eventually chosen to be used. This catalogue also incorporated manually elaborated data from AUTH and NOA. Therefore, the initial list of automatically analysed earthquake data was continuously supplemented with data derived by manual analysis. The software was activated periodically every 24 hours for a total duration of 9 days in order to obtain an objective view of the evolution of the sequence over time by checking for possible fluctuations of the values of the monitored parameters with the ones defined with the first 48 hours data. These repetitive daily applications allowed drawing conclusions in near real time sense about the evolution of the sequence.

In the present work, the values of the parameters as these were estimated 48 hours after the occurrence of the main earthquake (last event of the catalogue: 10/01/2013, 00:12:40 GMT) and for a period of 9 days after the occurrence of the main earthquake are presented (last event of the

catalogue: 17/01/2013, 23:11:14 GMT). In particular, the space distribution, the time distribution, the magnitude distribution, the variation of mean magnitude, the longitudinal and cross section of seismogenic region and the space-time distribution of the sequence were examined. The maps and the parameters which were defined by using the first 48 hours data were considered as representative of the sequence (Figure 2). Therefore, the completeness magnitude was automatically defined as M_C=2.2, while the mean magnitude for events above M_C was M_m=2.75 $\pm$ 0.44. The spatial distribution of the epicentres of the first 48 hours revealed a linear distribution of the aftershocks volume, trending in an azimuth of ~N68^{0}E. The longitudinal section suggested a fault length of ~15 km, which is in a very good agreement with the length derived from the spatial distribution of the epicenters (see the map of Figure 2). The cross-section of the earthquake foci shows an almost vertical fault. Both the azimuth and the dip of the fault plane are in good agreement with FPS published by GCMT, http://www.globalcmt.org, (azimuth 239^0, dip angle 80^0, slip 178^0). Finally, the space-time distribution of the aftershocks showed a clear unilateral rupture of the aftershocks, propagating in a NE direction. This evidence is also supported by the epicentral map, where the epicentre of the mainshock is located at the south westernmost edge of the seismogenic region.

The above procedure revealed the "identity" characteristics of the sequence, as they are quantitatively described by the employed parameters. Daily runs of the software allowed the frequent monitoring of the sequence's evolution, providing a clear picture of a normally evaluating aftershock activity. The values of the monitored parameters through this time-period (values in daily basis) are given in Table 1. Figure 3 gives a snap-shot of how the examined parameters varied up to the ninth day of the sequence. The final completeness magnitude was defined as M_C=2.0, while the mean magnitude of the aftershocks (following this completeness criteria) was M_m=2.6. The spatial distribution of the epicentres of the first 9 days clearly depicts the lineament of the aftershocks volume with an azimuth of ~N60^{0}E. The longitudinal section of the aftershocks foci (along this azimuth) continued to describe a fault length of ~15 km, while their strike-normal cross-section kept showing an almost vertical fault. The space-time distribution (and the epicentral map) of the aftershocks didn't change the picture obtained after the first 48 hours, showing unilateral rupture propagating in a NE direction (Figure 3).

5. Discussion

A software package to monitor seismic excitations in almost real-time sense was developed based on proposed definitions and semi-empirical formulations of certain aftershock sequence parameters, directly associated to the nature of the sequence. The software was tested on the recent sequence of the January 8th, 2013 earthquake, M=5.9, which occurred SE of the Lemnos island. The evolution of the sequence was daily monitored during the first nine days after its occurrence. Comparison of the graphs generated by this software 48 hours after the mainshock's occurrence with the respective graphs produced daily up to January 17th showed that the values of the monitored parameters of the sequence remained almost constant, without exhibiting significant variations. This observation was strong evidence that the sequence under study evolved normally during the monitored time period, confirming the characterization of the 5.9 magnitude earthquake as a mainshock.

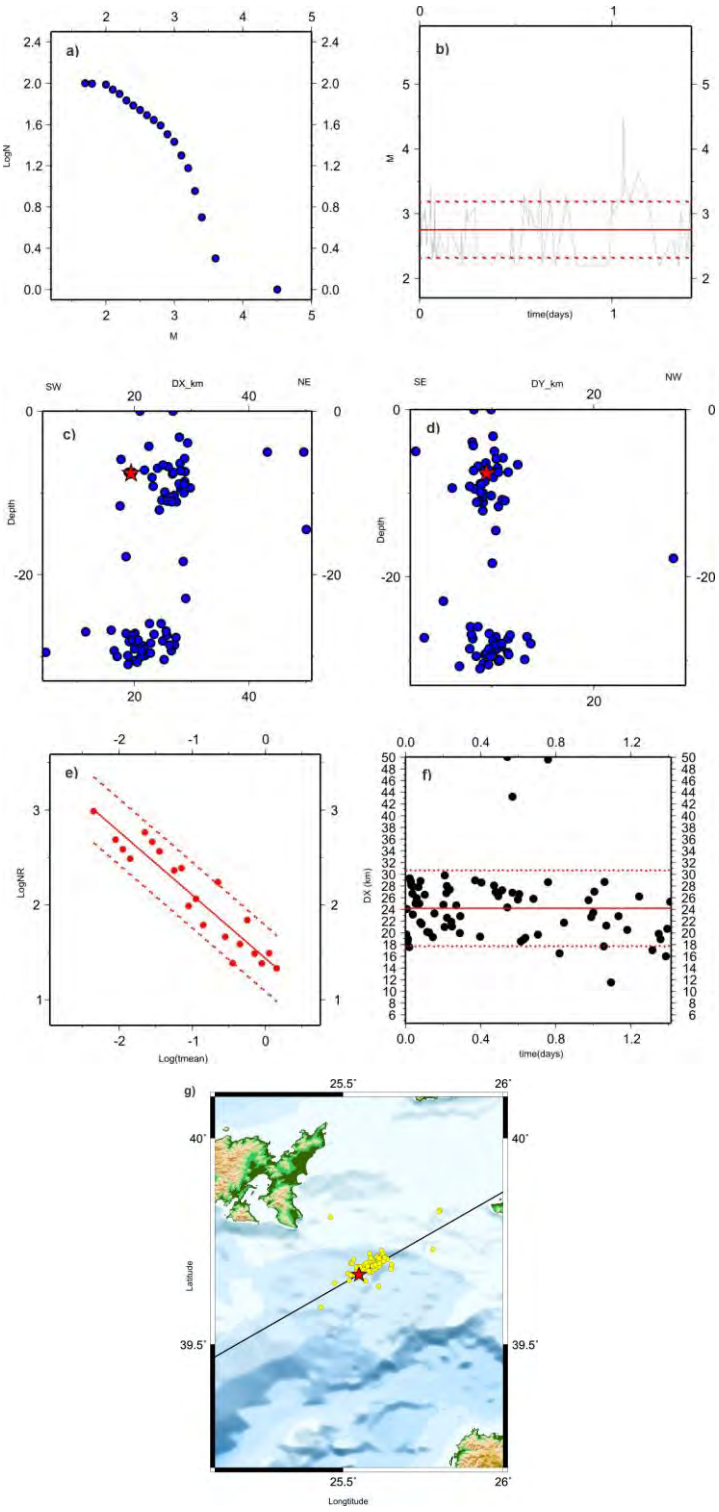

Figure 2 - Presentation of the software results, as estimated with the software application 48 hours after main shock: a) G-R distribution, b) mean magnitude, c) along-strike section, d) cross-strike section, e) time distribution, f) space-time distribution and g) seismicity map.

Table 1- Values of the parameters calculated by the software application. M_c is the magnitude of completeness, M_{mean} the mean magnitude, L the fault length.

Software Applications	Parameter	For the first 48hours	After 9days
G-R distribution	M_c	2.2	2.0
	b	0.94	0.88
	a	4.08	4.12
Magnitude distribution	M_{mean}	2.75	2.55
	SD	0.44	0.46
Seismicity map	Azimuth	$N60^0E$	$N68^0E$
Section along strike	*L* (km)	13	15
Time distribution	*b*	0.67	0.66
	a	1.44	1.56
Time distribution 95% 1st	*a*	1.79	1.99
Time distribution 95% 2nd	*a*	1.09	1.14
Space-time distribution	*Mean DX* (km)	24.18	21.95
	SD (km)	6.46	4.23

A general conclusion that can be drawn from the present study is that the evaluation of the possible evolution of a seismic excitation, already in progress, may be feasible. However, in order to achieve this target, certain requirements must be fulfilled. A self-evident prerequisite is that a reliable database is available, which can be continuously updated in near real-time sense. Automatic locations will be its basic data-source but it will be also enriched by manually analysed events in order to improve the accuracy of the estimated focal parameters. Following this requirement, the application of the presented software can provide useful information to be used for a reliable evaluation of the possible evolution of the monitored seismic excitation.

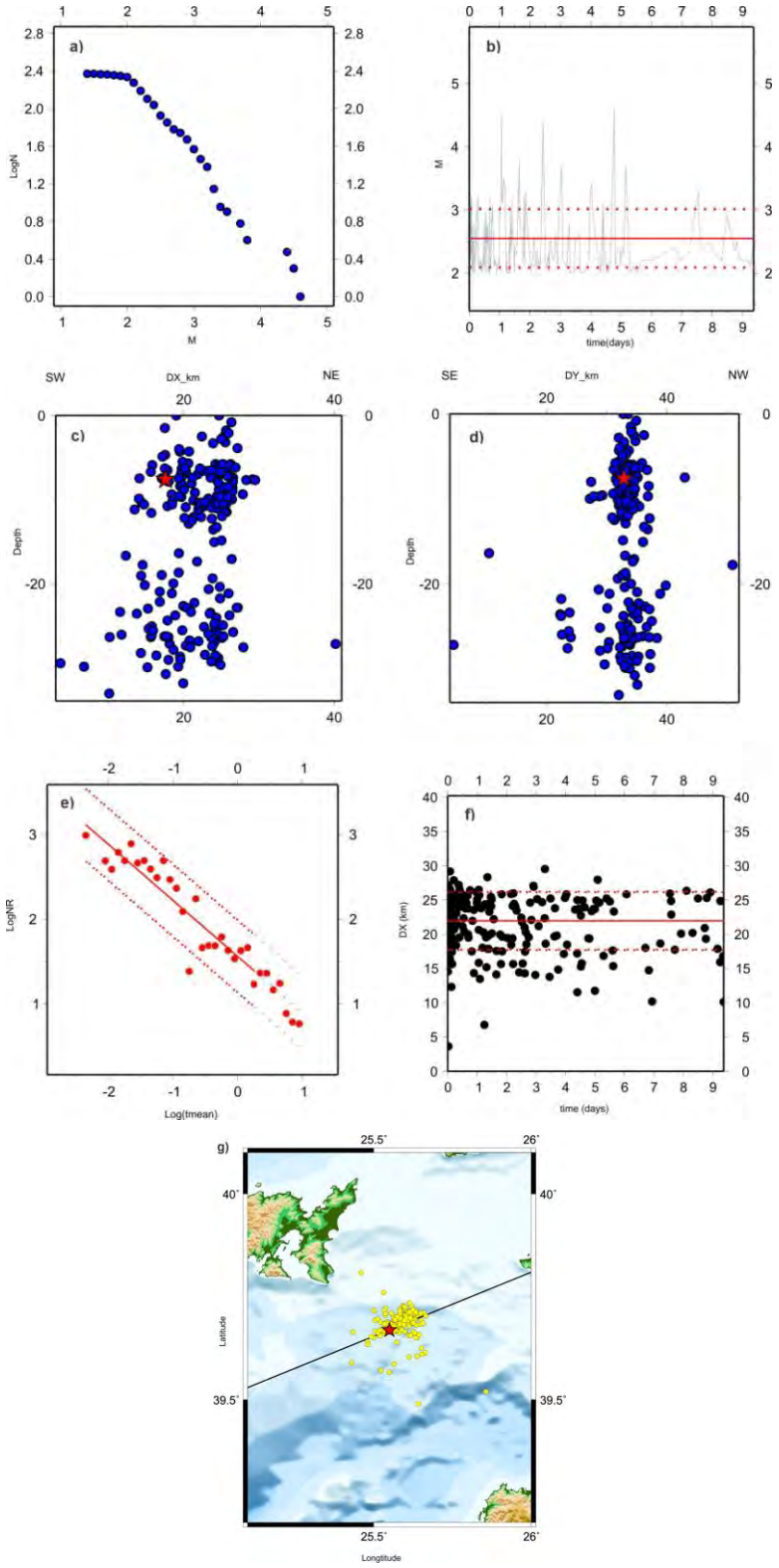

Figure 3 - Same as Figure 2 on the ninth day of the aftershock sequence.

6. Acknowledgments

The maps were produced with the GMT software (Wessel and Smith, 1995). This research has been co-financed by the European Union (European Social Fund – ESF) and Greek national funds through the Operational Program "Education and Lifelong Learning" of the National Strategic Reference Framework (NSRF) - Research Funding Program: THALES. Investing in knowledge society through the European Social Fund. Project SEISMO FEAR HELLARC. Geophysics Department Contribution 808/2013.

7. References

Gutenberg B. and Richter C.F. 1944. Frequency of earthquakes in California, *Bull. Seis. Soc. Am.*, 34, 185-188.

Mogi K. 1962. Study of elastic shocks caused by the fracture of heterogeneous materials and their relation to earthquake phenomena, *Bull. Earthq. Res. Inst., Univ. Tokyo*, 40, 125-73.

Nasu N. 1929. On the aftershocks of the Tango earthquake, *Bull. Earthq. Res. Inst.*, 6, 245-332.

Omori F. 1894. On aftershocks of earthquakes, *J. Coll. Sc. Imp. Univ. Tokyo*, 7, 111-200.

Papazachos B.C. 1974. On certain aftershock and foreshock parameters in the area of Greece, *Ann. Geofis.*, 27, 497-515.

Papazachos B.C., Scordilis E.M., Panagiotopoulos D.G., Papazachos C.B. and Karakaisis G.F. 2004. Global relations between seismic fault parameters and moment magnitude of earthquakes, *Bulletin of the Geological Society of Greece,* XXXVI, 3, 1482-1489.

Ranalli G. 1969. A statistical study of aftershock sequences, *Ann. Geophys.*, 22, 359-397.

Teza E. 2011. Automated procedure to monitor and evaluate the evolution of seismic excitations, *Msc. Thesis*, Aristotle University, Thessaloniki, 190pp.

Wessel P. and Smith W. 1995. “New version of the Generic Mapping Tools”, *EOS*, 76-329.

Δελτίο της Ελληνικής Γεωλογικής Εταιρίας, τομ. XLVII , 2013
Πρακτικά 13ου Διεθνούς Συνεδρίου, Χανιά, Σεπτ. 2013

Bulletin of the Geological Society of Greece, vol. XLVII 2013
Proceedings of the 13th International Congress, Chania, Sept. 2013

AUTOMATIC MOMENT TENSOR DETERMINATION FOR THE HELLENIC UNIFIED SEISMIC NETWORK

Triantafyllis N.[1], Sokos E.[2] and Ilias A.[1]

[1] *University of Patras, Department of Computer Engineering and Informatics, Rio 26504, Patras, Greece, triantafyl@ceid.upatras.gr, aristeid@ceid.upatras.gr*

[2] *University of Patras, Seismological Laboratory, Rio 26504, Patras, Greece, esokos@upatras.gr*

Abstract

Modern seismic networks with broadband sensors and real time digital telemetry made Moment Tensor (MT) determination a routine procedure. Automatic MT's are now provided by global networks and a few very dense regional networks, within minutes after a significant event. An automatic MT determination wasn't possible for the broader Hellenic area since seismic station density wasn't sufficient. The creation of the Hellenic Unified Seismic Network (HUSN) provided the opportunity to apply an automated MT procedure using the available broad band data from almost one hundred stations. Thus the ISOLA code was extended towards the automatic operation based on Linux OS shell scripts, stand alone Fortran codes and SAC2000. Software supports both manual and automatic mode; at the first case, the user manually runs the program with the desired input parameters while at the latter, the system monitors a mailbox or RSS feed and if it receives an appropriate notification triggers the MT inversion procedure based on certain conditions. As it is setup now it calculates automatically the moment tensor of earthquakes larger than 3.5Mw using data from HUSN. Application of an automated MT inversion procedure for HUSN will provide important real time information for studies like ground motion evaluation, tsunami warning etc.

Key words: *focal mechanism, inversion, ISOLA.*

Περίληψη

Τα σύγχρονα σεισμικά δίκτυα έχουν μετατρέψει τη διαδικασία αντιστροφής του τανυστή σεισμικής ροπής σε διαδικασία ρουτίνας. Οι αυτόματες λύσεις παρέχονται πλέον από παγκόσμια δίκτυα καθώς και από μερικά περιφερειακά δίκτυα, μέσα σε λίγα μόλις λεπτά από τη γένεση ενός σεισμού. Η αυτοματοποιημένη διαδικασία υπολογισμού του τανυστή σεισμικής ροπής δεν ήταν εφικτή για την Ελλάδα καθώς η πυκνότητα του δικτύου δεν ήταν επαρκής. Η δημιουργία όμως του Ενιαίου Εθνικού Δικτύου Σεισμογράφων (ΕΕΔΣ) με περίπου εκατό σεισμολογικούς σταθμούς εξασφάλισε αυτή τη δυνατότητα. Έτσι το λογισμικό ISOLA επεκτάθηκε ώστε να χρησιμοποιηθεί ως μια αυτοματοποιημένη διαδικασία η οποία βασίζεται σε εντολές κελύφους λειτουργικού συστήματος Linux, αυτόνομους κώδικες σε Fortran και το πρόγραμμα SAC2000. Το λογισμικό που δημιουργήθηκε υποστηρίζει αυτόματη λειτουργία αλλά και καθοδηγούμενη από το χρήστη. Στην πρώτη περίπτωση, το σύστημα παρακολουθεί ένα ηλεκτρονικό ταχυδρομείο ή ροές RSS και αν λάβει κατάλληλη ειδοποίηση ενεργοποιεί τη διαδικασία υπολογισμού του τανυστή σύμφωνα

με ορισμένες προϋποθέσεις. Στη δεύτερη περίπτωση ο χρήστης έχει τη δυνατότητα να εκκινήσει τη διαδικασία με τις κατάλληλες παραμέτρους. Μέχρι στιγμής το πρόγραμμα μπορεί να εκτελεί αυτόματα τις διαδικασίες υπολογισμού για σεισμούς μεγαλύτερους από 3.5Mw χρησιμοποιώντας τα δεδομένα από το ΕΕΔΣ. Μια εφαρμογή που υπολογίζει αυτόματα τον Τανυστή ροπής για το ΕΕΔΣ θα εξασφαλίσει πληροφορίες σε πραγματικό χρόνο σχετικά με θέματα όπως εκτίμηση της εδαφικής κίνησης, προειδοποίηση για τσουνάμι κτλ..
Λέξεις κλειδιά: *μηχανισμός γένεσης, αντιστροφή, ISOLA.*

1. Introduction

Automatic Moment Tensors (AMT) are provided by global networks and a few very dense regional networks. Global CMT (http://www.globalcmt.org) (Ekström et al., 2012) already supports a global AMT procedure for strong earthquakes for a few decades. Automatic solutions for global networks are as well provided by GFZ German Research Centre for Geosciences (http://edoc.gfz-pstsdam.de/gfz) (Saul et al., 2011). Berkeley Seismological Laboratory of University of California (http://seismo.berkeley.edu/), since 1993 developed a software (Dreger, 2002) that calculates AMT for regional networks and earthquakes larger than 3.5Mw. It has also been used at the Japan National Research Institute for Earth Science and Disaster Prevention (http://www.bosai.go.jp/e) and by independent researchers along USA, Europe and Asia. This distribution with different variations has been used by the Mediterranean Network (MedNet) of Italy (http://mednet.rm.ingv.it). Services that have performed respective efforts are the Swiss Seismological Service (SED) (http://www.seismo.ethz.ch) and the Earthquake and Volcano Information Center of Japan (http://wwweic.eri.u-tokyo.ac.jp/index-e.html); the last one applies a different approach. The creation of the Hellenic Unified Seismic Network (HUSN) provided the opportunity to apply an automated MT procedure using the available broad band data from almost one hundred stations. Thus the ISOLA code (Sokos and Zahradník, 2008) was extended towards automatic operation.

2. Method Description

2.1. ISOLA Moment Tensor Algorithm

The ISOLA moment tensor retrieval algorithm is based on the point source iterative deconvolution method; similar to (Kikuchi and Kanamori, 1991) multiple point source method for teleseismic events. In ISOLA the full wavefield is considered, and Green's functions are calculated by the discrete wavenumber method (Bouchon, 1981) and (Coutant, 1989) for local or regional distances. Moment tensor of subevents is found by least-square minimization of misfit between observed and synthetic waveforms, while position and time of subevents is optimized through grid search. The computational options include inversion to retrieve the full moment tensor (MT), the deviatoric MT, and pure double-couple MT. Finite-extent source inversions may also be performed in the case of a large event. The code has been extensively used at the University of Patras, Seismological Laboratory (UPSL), Greece, (http://seismo.geology.upatras.gr/), to routinely compute moment tensors for Mw > 3.5 events in western Greece, and, since 2012, at the National Observatory of Athens (http://www.noa.gr/). Besides that ISOLA has been used in various research studies worldwide e.g. (Sokos et al., 2012), (Gallovič et al., 2009), (Benetatos et al., 2012), (Fojtíková et al., 2010), (Reinoso, 2011), (Choi et al., 2010) and (Tan, 2012). Although ISOLA code is complemented by a Graphical User Interface (GUI) that simplifies its use during manual analysis of a seismic event, an automatic version of the code could be important for many applications e.g. rapid moment tensor estimation for shakemap generation or tsunami warning.

2.2. Algorithm Implementation for Automatic Use

The main phases of the automatic MT inversion procedure can be described as follows:

1. trigger the AMT inversion procedure

2. select stations based on the earthquake's location
3. retrieve data from selected stations
4. correct retrieved data for instrument effect and align them in time
5. compute green's functions
6. compute inversion
7. plot/distribute results

Figure 1 shows the flowchart diagram of automatic MT inversion process.

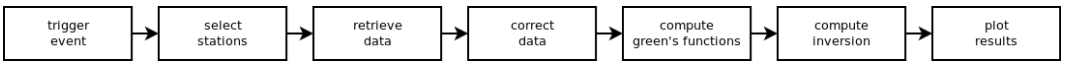

Figure 1 - Diagram of algorithm's procedure.

To implement these main phases of the automatic MT inversion algorithm we use the Bash scripting language of Linux OS. Bash is a high-level programming language and thus makes the process of developing/maintaining the code much simpler. During software development a Bash module was created for each main phase (Figure 1) and finally all modules were connected with each other. Besides Bash we use a few other programs also; like the GMT suite (Wessel and Smith, 1998) for distance determination between stations and epicentre, Nmxptool (http://mednet.rm.ingv.it/nmxptool.php) for data retrieval, Sac2000 (Goldstein et al., 2003) for data correction etc, all codes are open source. In the following paragraphs we describe in detail the main phases of the automatic MT inversion procedure.

2.3. Detailed Description of Main Stages

2.3.1. Trigger the Moment Tensor Procedure

There are two options to trigger the AMT inversion procedure, when the code is in automatic mode. Either through email, i.e. the program is monitoring an email account for incoming messages (in IMS 1.0 format, http://www.isc.ac.uk/standards/isf/download/ims1_0.pdf) or through RSS feeds. Once a valid trigger is declared i.e. the events parameters fulfil some criteria e.g. the automatic magnitude is larger than 3.5 and the epicentre is located within some geographical limits, the inversion procedure is triggered.

2.3.2. Select Stations Based on the Earthquake's Location

Just after a trigger is declared, station selection starts. It is based on a list of station coordinates and on event's automatic location. Based on these the program selects those stations that are within a predefined epicentral distance from the earthquake. An additional constrain is the total number of selected stations, which cannot exceed a predefined limit. Such a constrain is important e.g. in places where the station density is high a large number of data could be selected that could delay the inversion procedure significantly and in the same time provide redundant information only. Thus a fixed number of twenty stations was selected as a maximum; the program selects stations based on epicentral distance then sorts them according to this distance and selects the first twenty. It is also possible a station to be flagged by the user as not suitable for inversion, then the selection procedure will ignore it.

2.3.3. Retrieve Data from Selected Stations

The next step is to retrieve data for the selected stations. There are two possibilities up to now, a) to retrieve data from a NAQS server and b) to retrieve data from a Seedlink/SeisComP server (http://www.seiscomp3.org/). The Nmxptool is used for retrieving data from a NAQS server and the arclink_fetch client from the Seedlink/SeisComP server. Data are converted in SAC format (Goldstein et al., 2003) and stations whose data contain gaps or have less than three components are removed from the subsequent analysis. A test on the minimum number of available data is also

done here and if the available stations aren't enough the procedure stops, the minimum number of stations was set at four.

2.3.4. Correct Retrieved Data

After the data retrieval the program corrects them in four steps. During the first step the instrumental effect is removed, then data are aligned according to origin time, cut according to a predefined duration and finally resampled. All corrections are done using SAC2000 macros.

2.3.5. Compute Green's Functions

In parallel with the data correction, the Green's function computation starts. The code computes using a 1D crustal model (only one crustal model is currently possible) and the centroid trial position-station geometry the corresponding green's functions. These are later convolved with a delta time function and six elementary focal mechanisms in order to form elementary seismograms that will be used in the inversion (Sokos and Zahradnik, 2008). The centroid horizontal position is kept fixed at the epicentre location, provided by the automatic solution, but its depth is varied. In detail, starting from the automatic depth estimation, twenty trial sources are defined above it and twenty bellow it, the depth grid step is fixed at 2km. In order to reduce time the elementary seismogram calculation per trial centroid position is done in parallel.

2.3.6. Compute Inversion

As soon as corrected data and elementary seismograms are available the inversion procedure starts. Although the code offers various options for source inversion e.g. full moment tensor, deviatoric etc; the deviatoric type is predefined since it is adequate for most cases. The inversion frequency band is also kept fixed at 0.04 to 0.09Hz, since this is suitable for moment tensor inversion in local and regional distances (Roumelioti et al., 2011). Finally the centroid time is grid searched three seconds before and three seconds after the origin time. This step is important since it can capture small errors associated with event location, crustal model etc (Sokos and Zahradnik, 2008).

2.3.7. Plot/distribute Results

Finally, when the inversion procedure ends, the program a) produces text files suitable for email distribution, containing the results from the inversion and a graphic representation of the focal mechanism and b) updates a web page with the relevant information (http://seismo.geology.upatras.gr/amt). In the same web page the results of this paper are given in a graphical and numerical form.

3. Automatic and Manual Procedure Comparison

The automatic algorithm was tested using data from HUSN (Hellenic Unified Seismic Network). A total of fifty events triggered the system during six months of operation and we present here a statistical evaluation of the results. Comparison of the automatic solution validity is done against the manual MT solutions provided by GI-NOA (http://www.gein.noa.gr/el/). We make use of the so-called Kagan angle (Kagan, 1991) to calculate the difference between automatic and manual solution. This angle expresses the minimum rotation between two double couple focal mechanisms and is used here as a measure of the automatic solution quality. According to (Kagan, 1991) minimum angle is 0^o (same mechanism) and the maximum value is 120^o suggesting maximum divergence between two focal mechanisms. An acceptable agreement is represented by angles of the order of some tens of degrees, while a strong variance is given by angles larger than 50°-60° (Vannucci et al., 2004).

In Figure 2 we present the geographical distribution of the automatically analysed earthquakes and the corresponding Kagan angles, plotted as vertical bars. The Kagan angles vary between 2^o and 107^o with an average value of 37^o. In general the error's average value is acceptable, but extreme Kagan values exist and it is important for the automatic procedure evaluation to understand what is

causing them. These higher values are mainly connected with the edges of the seismic network (South Crete, Eastern Aegean etc). One of the problems here, is the large error in the automatic epicentre solution (due to network geometry) that causes subsequent problems in moment tensor inversion since the trial horizontal source position for the inversion is the automatic epicentre. For example, the two events south of Crete had differences between the automatic and manual epicentre location of the order of 30km.

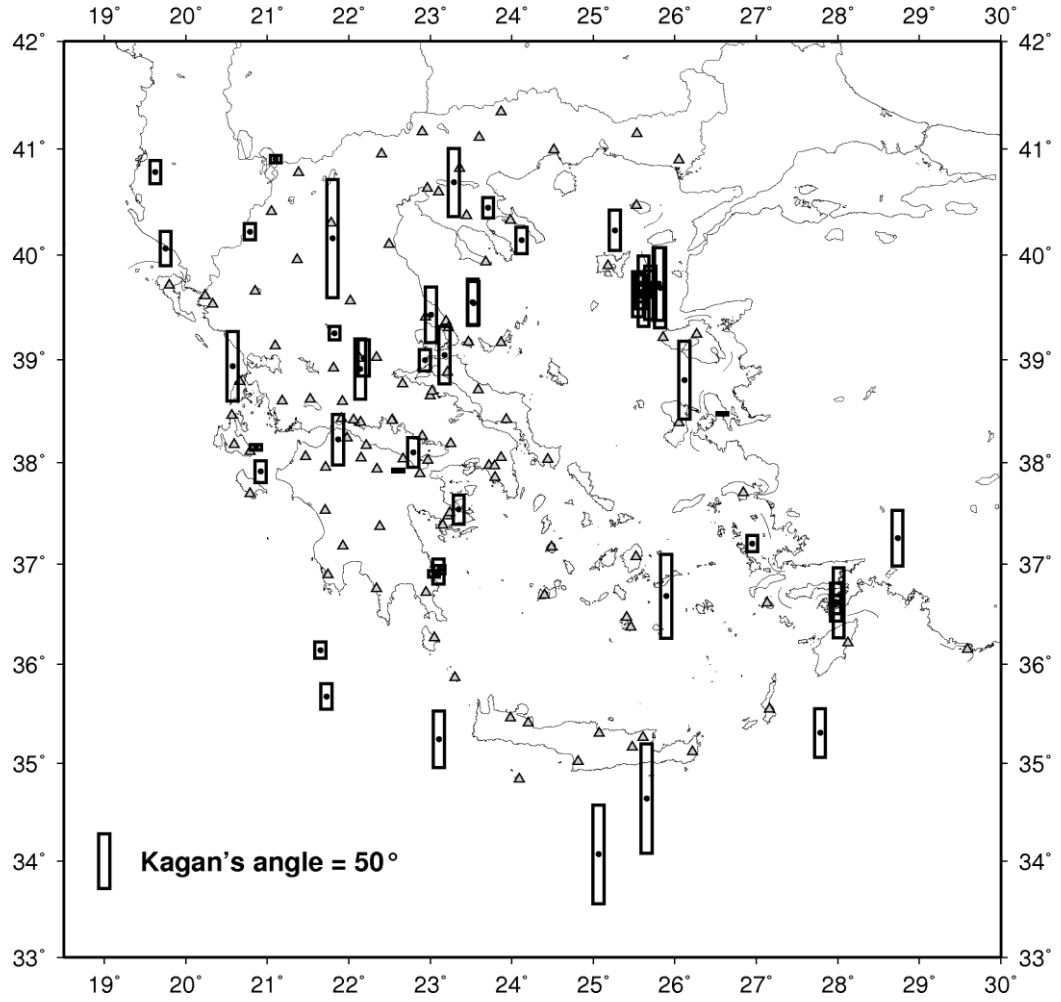

Figure 2 – Spatial distribution of Kagan's angle shown as bars at the epicentral locations of the analyzed events. Triangles are seismic stations of HUSN.

Nevertheless, large Kagan angles exist even in cases when the automatic-manual location difference is small. These problems are connected with either the use of different set of seismic data or the use of different crustal models. So far a single crustal model is used in the automatic procedure, the one proposed by (Novotny et al., 2001) using data from Central Greece. While the manual moment tensor solutions are based on region specific crustal models (Evangelidis C. pers.comm.); this could explain large Kagan angles in a few cases. Furthermore the manual solutions incorporate NOA's accelographic network data (http://www.gein.noa.gr/en/networks/accelerographic-network) also, which were not available in the automatic moment tensor inversion procedure. This is an additional explanation for large Kagan angles between manual and automatic solution. Finally another cause of error in the

automatic solution is the presence of disturbances in the data; such errors are hard to recognize in an automatic procedure and could affect the inversion (Zahradník and Plešinger, 2005).

Besides the focal mechanism, moment tensor inversion procedure provides another two parameters that are of significant importance during the first minutes after an event i.e. the moment magnitude and the centroid depth. In Figure 3a we present the comparison between the manual and the automatically retrieved moment magnitude, while in Figure 3b the corresponding centroid depth difference distribution is given. As regards the moment magnitude the automatic and manually derived results are almost identical having an average difference of 0.1 units. This result suggests that the moment magnitude is not so sensitive to the problems we described in previous paragraphs thus it can be regarded as a stable inversion feature. The automatically centroid depth is also similar to the manually derived one although a few extremes exist.

The above results suggest that the automatic moment inversion contributes to the recognition of the size and depth of the seismic source with adequate accuracy a few minutes after an event. This means that it is a valuable tool for estimating ground motions or tsunami hazard.

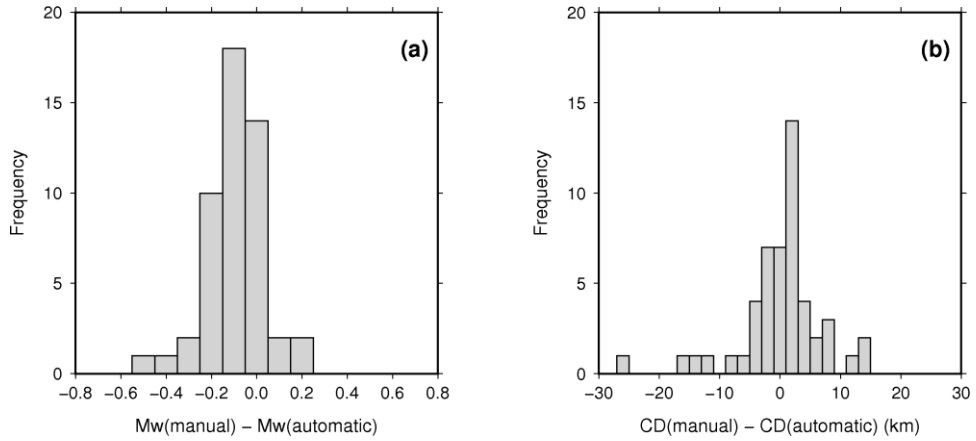

Figure 3 - a) Histogram of Mw difference between manual and automatic solution b) Histogram of centroid depth (CD) difference between manual and automatic solution.

4. Discussion

In this paper we present the first attempt to establish an automatic moment tensor retrieval procedure in Greece. We are using the waveform data from the Hellenic Unified Seismic Network, a modern digital seismic network of sufficient station density for advanced seismological applications. The ISOLA code, proposed by Sokos and Zahradnik, 2008 was modified in order to implement it in an automatic procedure. Comparison of fifty automatically retrieved moment tensor solutions with the manual ones produced by GI-NOA, revealed the ability of the procedure to accurately retrieve moment tensor under some conditions. Automatic moment magnitude calculation proved to be more robust and this is especially important in cases like shakemap generation or tsunami warning.

Moreover the comparison revealed drawbacks and possible extensions that would increase the reliability of automatic solutions. Based on these outcomes and to gained experience from automatic application of the method we have concluded to few improvements, described in the following paragraph.

As mentioned before a single crustal model is currently used in the automatic procedure. Thus a next step to improve our software is to implement multiple crustal models which will be selected depending on the geographic position of the seismic event. Another improvement that can be applied is to choose for the inversion, lower or higher frequency band values according to the

studied event's magnitude. In several cases seismic data depict various problems e.g. data transmission problems, noise, disturbances (Zahradník and Plešinger, 2005) etc. Thus it is clear that advanced signal processing methods to be applied to seismic waveforms is the key to improve the automatic procedure. These should detect erroneous waveforms and either remove from the procedure or even correct them. Another important point to enhance in the performance of the software is the station selection which should include an estimate of the azimuthal station distribution.

Although the automatic procedure as it is now can process an event within a few minutes (5-10) depending on stations used, computer power etc, it is clear that this has to be improved. This can be accomplished by e.g. pre-calculated green's functions or conversion of serial code to parallel since modern computers are based on parallel processors. This would allow the use of many trial sources and the search of the centroid could be done for a 3D grid surrounding the automatic hypocenter.

5. Acknowledgments

All the figures were produced with the GMT software package (Wessel and Smith, 1998). Waveform data from the Hellenic Unified Seismic Network are gratefully acknowledged.

6. References

Benetatos C., Málek J. and Verga F. 2012. Moment tensor inversion for two micro-earthquakes occurred inside the Háje gas storage facilities, Czech Republic, *J. Seism.,* in press, doi: DOI 10.1007/s10950-012-9337-0.

Bouchon M. 1981. A simple method to calculate Green's functions for elastic layered media, *Bul. Seism. Soc. Am.,* 71, 959-971.

Choi, H. and Noh M. 2010. Source parameters of the May 2, 2009 Andong earthquake in South Korea, *Geosci. J.*, 14, 269-276, doi: 10.1007/s12303-010-0025-1.

Coutant O. 1989. Program of numerical simulation AXITRA, Tech. rep., LGIT, Grenoble, France (in French).

Dreger D. S. 2002. Time-Domain Moment Tensor INVerse Code (TDMT_INVC), The Berkeley Seismological Laboratory (BSL), *Report*, (8511).

Fojtíková L., Vavryčuk V., Cipciar A. and Madarás J. 2010. Focal mechanisms of micro-earthquakes in the Dobrá Voda seismoactive area in the Malé Karpaty Mts, (Little Carpathians), Slovakia, *Tectonophysics,* 492, 213–229.

Ekström G., Nettles M. and Dziewoński A.M. 2012. The global CMT project 2004–2010: Centroid-moment tensors for 13,017 earthquakes, *Phys. Earth planet. Inter.*, Volumes 200–201, June 2012, Pages 1-9, ISSN 0031-9201, 10.1016/j.pepi.2012.04.002. Available online at: http://www.sciencedirect.com/science/article/pii/S0031920112000696

Gallovič F., Zahradník J., Křížová D., Plicka V., Sokos E., Serpetsidaki A. and Tselentis G.-A. 2009. From earthquake centroid to spatial-temporal rupture evolution: Mw 6.3 Movri Mountain earthquake, June 8, 2008, Greece, *Geophys. Res. Lett.,* 36, L21310.

Goldstein P., Dodge D., Firpo M. and Minner L. 2003. "SAC2000: Signal processing and analysis tools for seismologists and engineers", Invited contribution to "*The IASPEI International Handbook of Earthquake and Engineering Seismology*", Edited by WHK Lee, H. Kanamori, P.C. Jennings, and C. Kisslinger, Academic Press, London.

Kagan Y.Y. 1991. 3-D rotation of double-couple earthquake sources, *Geophys. J. Int.* 106, 709–716, doi: 10.1111/j.1365-246X.1991.tb06343.x.

Kikuchi M. and Kanamori H. 1991. Inversion of complex body waves—III., *Bul. Seism. Soc. Am.,* 81, 2335–2350.

Novotný O., Zahradník J. and Tselentis G.-A. 2001. Northwestern Turkey earthquakes and the crustal structure inferred from surface waves observed in western Greece, *Bul. Seism. Soc. Am.*, 91(4), 875-879.

Reinoso P.S. 2011. The upper crustal microseismicity image from the North Chilean subduction zone: implications for tectonics and fluid migration, *PhD Thesis*, Free University Berlin, Germany.

Roumelioti Z., Kiratzi A. and Benetatos C. 2011. Time-Domain Moment Tensors for shallow ($h \leq$ 40 km) earthquakes in the broader Aegean Sea for the years 2006 and 2007: The database of the Aristotle University of Thessaloniki, *J. Geodyn*, 51(2), 179-189.

Saul J., Becker, J. and Hanka W. 2011. Global moment tensor computation at GFZ Potsdam, *AGU 2011 Fall Meeting,* (San Francisco 2011).

Sokos E. N. and Zahradník J. 2008. ISOLA a Fortran code and a Matlab GUI to perform multiple-point source inversion of seismic data, *Comp. Geosc.*, 34, 967-977.

Sokos E. N., Zahradník J., Kiratzi A., Janský J., Gallovič F., Novotný O., Kostelecký J., Serpetsidaki A. and Tselentis G.-A. 2012. The January 2010 Efpalio earthquake sequence in the western Corinth Gulf (Greece), *Tectonophysics*, 530-531, 299-309.

Tan O. 2013. The dense micro-earthquake activity at the boundary between the Anatolian and South Aegean microplates, *J. Geodyn.*, 65, 199-217, doi:10.1016/j.jog.2012.05.005.

Vannucci G., Pondrelli S., Argnani A., Morelli A., Gasperini P. and Boschi E. 2004. *An atlas of Mediterranean seismicity*, Editrice Compositori.

Wessel P. and Smith W.H.F. 1998. New, improved version of generic mapping tools released, *Eos Trans, AGU,* 79, 579.

Zahradník J. and Plešinger A. 2005. Long-period pulses in broadband records of near earthquakes, *Bul. Seism. Soc. Am.*, Vol. 95, No. 5, 1928-1939.

Δελτίο της Ελληνικής Γεωλογικής Εταιρίας, τομ. XLVII , 2013
Πρακτικά 13ου Διεθνούς Συνεδρίου, Χανιά, Σεπτ. 2013

Bulletin of the Geological Society of Greece, vol. XLVII 2013
Proceedings of the 13th International Congress, Chania, Sept. 2013

GLOBALLY VALID RELATIONS CONVERTING MAGNITUDES OF INTERMEDIATE AND DEEP-FOCUS EARTHQUAKES TO M_W

Tsampas A.D.[1], Scordilis E.M.[1], Papazachos C.B.[1] and Karakaisis G.F.[1]

[1] Aristotle University of Thessaloniki, Faculty of Geology, Department of Geophysics, atsampas@geo.auth.gr, manolis@geo.auth.gr, kpapaza@geo.auth.gr, karakais@geo.auth.gr

Abstract

An essential step in the compilation of homogeneous and complete earthquake catalogs is the thorough investigation of potentially robust relations between different magnitude scales. The vast majority of already published relations usually concerns shallow-focus earthquake data with depths up to 60-70 km.

In the present study, several magnitude scales reported by 66 world-wide data providers in conjunction with published catalogs are examined within the depth range of 61-700 km, by applying least-squares regression analysis. Among other widely used scales, as body wave (m_b, m_B) and surface wave (M_s) magnitudes cited by International Centers (i.e. ISC, NEIC and IDC), the behavior of relevant magnitude scales determined by MOS (Moscow, Russia), BJI (Beijing, China), DJA (Djakarta, Indonesia) and the Japanese magnitude calculated by JMA, is also examined. By this way, robust calibrating relationships of 12 magnitude scales to the moment magnitudes provided by GCMT, NEIC and JMA are defined.

From the obtained results important observations on the behavior of certain magnitude scales were made. Thus, a remarkable variation of m_b scale cited by IDC could be noted for intermediate and deep focus events. Furthermore, a comparison with the M_w of NIED revealed an apparent lower "saturation" level around 5.0 below which the moment magnitude values published by GCMT and NEIC, are systematically overestimated.

Key words: *Homogeneous intermediate and deep-focus earthquake catalog, moment magnitude, converting relations.*

Περίληψη

Μία βασική διεργασία κατά τη σύνταξη ομογενών και πλήρων καταλόγων σεισμικότητας είναι η διεξοδική διερεύνηση των δυνητικά εύρωστων σχέσεων που συνδέουν μεταξύ τους κλίμακες διαφορετικών μεγεθών. Η συντριπτική πλειονότητα των ήδη δημοσιευμένων σχέσεων αφορά ως επί το πλείστον δεδομένα επιφανειακών σεισμών με εστιακά βάθη μέχρι και τα 60-70 χιλιόμετρα.

Στην παρούσα εργασία, διαφορετικές κλίμακες μεγέθους προερχόμενες από 66 κέντρα σε παγκόσμια κλίμακα, σε συνδυασμό με ήδη δημοσιευμένους καταλόγους, εξετάζονται για σεισμούς με εστιακά βάθη 61-700 χιλιομέτρων. Εφαρμόζοντας ανάλυση ελαχίστων τετραγώνων προέκυψαν 12 νέες αξιόπιστες σχέσεις βαθμονόμησης που συνδέουν τις αντίστοιχες κλίμακες μεγεθών με το μέγεθος σεισμικής ροπής. Μεταξύ άλλων

ελέγχθηκαν οι κλίμακες χωρικού (m_b) και επιφανειακού μεγέθους (M_s) που ανακοινώνονται από Διεθνή (ISC, NEIC και IDC) και εθνικά κέντρα (MOS από Μόσχα, BJI από Πεκίνο, DJA από Τζακάρτα) καθώς και το μέγεθος που υπολογίζεται από το JMA (Ιαπωνία).
Από τα παραπάνω αποτελέσματα προκύπτουν σημαντικές παρατηρήσεις σχετικά με την συμπεριφορά ορισμένων από τις κλίμακες μεγέθους. Αξιοσημείωτη είναι η διαφοροποίηση που παρατηρείται ως προς τους ενδιαμέσου και τους μεγάλου βάθους σεισμούς για το χωρικό μέγεθος m_b του IDC. Επιπλέον, η σύγκριση του μεγέθους σεισμικής ροπής του NIED με τα αντίστοιχα μεγέθη από GCMT και NEIC αναδεικνύει ένα εμφανώς κατώτερο επίπεδο "κορεσμού" προσδιοριζόμενο περίπου στη τιμή 5.0.
Λέξεις κλειδιά: *Ομογενής κατάλογος ενδιαμέσου-μεγάλου βάθους σεισμών, μέγεθος σεισμικής ροπής, σχέσεις μετατροπής.*

1. Introduction

Since Wadati presented his first results on the existence of a deep earthquake zone underneath Honshu (Wadati, 1928, 1929), research on intermediate-depth and deep-focus earthquakes has indicated the distinct nature of this particular type of seismic activity. It has been shown that intermediate-depth and deep-focus earthquakes can be clearly differentiated from the shallow ones since they occur only in certain geographical areas and follow different time and magnitude distributions (Dziewonski and Gilbert, 1974, Abe and Kanamori, 1979, Astiz et. al., 1988, Giardini, 1988, Okal and Kirby, 1995).

The size of earthquakes with focal depth h≥60 km remains a controversial issue since it is expressed in various magnitude scales. As it is known, body-wave magnitude is the conventional parameter for the quantification of the intermediate-depth and deep earthquakes. Recent relevant observations indicate a notable divergence in body wave magnitude (m_b) estimations that were based on standard methodologies applied for shallow events of the same size. Abe and Kanamori (1979) used the broad-band body-wave magnitude (with average period of the body-waves between 4 and 15 sec) to quantify a number of deep-focus earthquakes that occurred during 1904-1974. Seismic moment of earthquakes, however, is the most appropriate parameter that represents their physical size.

In the present work, following similar studies of global shallow seismicity (Utsu, 2002, Scordilis, 2006), an attempt is made to define reliable converting relations which will be used for creating a homogeneous, in respect to magnitude, global catalog. Such catalog of intermediate-depth and deep-focus earthquakes could then be used for seismicity and seismic hazard studies.

2. Data Compilation

As basic data source in our study we used the on-line bulletins of ISC and NEIC to create an initial global catalog with earthquakes of focal depths, h≥60 km since 1964. Earthquake parameters of events reported since 1964 were extracted and adopted as first-priority solutions in terms of origin-time, epicenter coordinates and focal depths, constituting the main body of our data set. To augment the data, additional information on intermediate-depth and deep-focus earthquakes has been extracted from GCMT and JMA. After discarding erroneous entries (doublets or false events), additional magnitude information originated from reliable published earthquake catalogs (Rothe, 1969; Bath and Duda, 1979; Abe, 1981; Karnik, 1996; Engdahl & Villaseñor, 2002) was also integrated in our dataset, thus enriching the earthquake catalog.

Moreover, reliable moment magnitude information published by GCMT, NEIC, JMA and the above mentioned earthquake catalogs, was adopted as well. Starting from 1962, according to first intermediate-deep entries mentioned by GCMT catalog, the extracted moment magnitudes were

classified by merging equivalent moment scales into three discrete categories (Table1). The M_wH group includes moment magnitude information originated from: a) Global Centroid Moment Tensor (GCMT) catalog based on long period waveforms, b) the solutions given by the source parameter catalog (SOPAR) of NEIC, c) moment magnitude referred by Engdahl and Villaseñor's (2002) centennial catalog (CEC). Components of the second moment magnitude category, M_wN, are: a) the NEIC moment magnitude, b) the so-called Preliminary Determinations of Epicenters (PDE) solutions provided by the source parameter catalog (SOPAR) of NEIC, c) the M_wGS of USGS referred in Engdahl and Villaseñor (2002). The third group includes only moment magnitudes calculated by the National Research Institute for Earth Science and Disaster Prevention (M_wNIED) of Japan, as cited in ISC on-line bulletins.

Table 1 - Classification of moment magnitude data published in global earthquake catalogs.

Moment Magnitude Group	Moment Magnitude Source	Time Period Coverage	Magnitude Range	Maximum Depth (km)
M_wH	GCMT	1962-2010	4.6 – 8.2	693
	SOPAR			
	CEC			
M_wN	NEIC	1980-2010	4.1 – 8.2	692
	PDE			
	GS			
M_wNIED	NIED	1997-2009	3.2 – 7.5	576

Corresponding M_wNIED moment magnitude values reach down to 3.2-3.3. On the other hand, M_wH and M_wN magnitudes exhibit their known global minima around 4.6 and 4.1 respectively. These variations in moment magnitude minima are due to different methodologies applied and the variety of the seismic waveforms' frequency content utilized through seismic moment measurements.

Thus, CMT methodology (Dziewonski et al., 1981) relies on long period seismic waves (T>45s) while moment tensors calculated by the USGS research group are based on body waveform analysis (T>15s) (Sipkin, 1982). On the other hand NIED's moment tensor inversion method (Fukuyama et al., 1999) is based on corrected ground displacements, filtered and resampled every 1Hz (Kubo et. al., 2002), by using waveforms of maximum three broadband stations (FREESIA seismic network).

Direct comparison between moment magnitudes of M_wH-M_wN subsets for earthquakes of $h \geq 60$km revealed their equivalence, confirming previous observations based on global shallow data (Scordilis, 2006). M_wNIED is also considered to be identical to M_wH and M_wN, respectively, for a wide range of magnitudes, even though some discrepancies may be noticed; as shown in Figure 1 the M_wH (open circles) and M_wN (light gray circles) exhibit lower saturation level around magnitude 5.0 as resulting from 289 and 101 values' pairs with M_wNIED, respectively.

Focusing on M_wH data and by fitting a 4^{th} degree polynomial equation (solid line), the saturation trend seems to insist, whereas moving upwards to this level, linear fitting across the bisector (dashed line) indicates equivalence of the examined subsets. This is also consistent with the systematic change in tendency that has been observed for moment values around at $2x10^{17}$ Nm (Kubo et. al., 2002), attributed to different methodologies implemented by NIED and GCMT for seismic moment estimation.

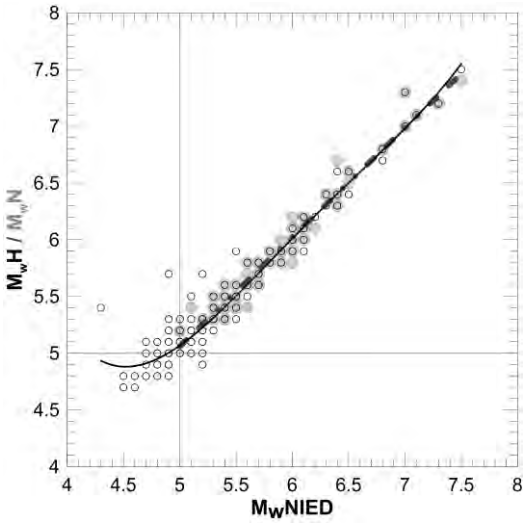

Figure 1 - Comparison between three distinguished categories of M_w, used in the present study. Dashed and solid lines represent linear and 4th degree polynomial fitting, respectively.

It should be also noted that the significantly low minima of M_wNIED's and the apparent lack of respective observations for M_wNIED-M_wN is due to facts such as:

- NIED's moment tensor determination is supported by the national dense coverage of Japan's broadband seismic network FNET, and
- Relevant high value of minimum M_w value according to the seismic moment calculations made by GCMT and NEIC research teams. Thus, only a small number of common events with relatively low moment magnitude data derived from both NIED and NEIC-USGS databases is available and consistently moment magnitude comparison is possible only for intermediate magnitude events (M_w>5.0) located in the broader East Asia region.

Therefore, in order to obtain calibration relations of various scales with M_w for a wide range of magnitude values, all the available moment magnitudes of NIED were adopted while only M_w of moderate and strong events reported by GCMT and NEIC were included.

To achieve higher accuracy in focal depth estimation for intermediate and deep-focus earthquakes, valuable information is offered by reflected on Earth's surface pP waves, recorded on distant long period seismograms and published in ISC bulletins. This approach can be applied for Δt in arrival times of pP and P ray-paths, since they are strongly depended on focal depths. Once reliable P and pP observations are available, accurate focal depths are obtained by using appropriate (pP-P) travel time curves or tables. This information was embedded in the catalog replacing focal depth values proposed by other sources.

3. Magnitude Conversion Relations

Following recent published results (Utsu, 2002, Scordilis, 2006) based on shallow global datasets, body wave (m_b) magnitudes, reported by ISC and NEIC, proved as well to be equivalent regarding intermediate-deep seismicity, composing a unified scale named m_bIN. Likewise, surface wave (M_s) magnitudes originated from above centers, both determined by applying the Prague formula (Vanek et. al., 1962), also turned to be equivalent in this study forming unified scale, M_sIN.

It is of interest to note that although M_s is not suitable for earthquakes of focal depths greater than ~50 km a considerable number of M_s concerning deeper earthquakes is reported by sources used in the present study, and implied in a number of seismicity studies (Ambraseys & Free, 1997, Gardini et. al., 1997 and others).

Body wave magnitude (m_B), estimated from long period records (Gutenberg, 1945c) is a scale of particular importance as concerning intermediate-deep seismicity (Frohlich, 2006), also utilized during this work.

3.1. Body Wave Magnitude Scale (m_b/m_B)

Body wave magnitude scales, m_b and m_B, derived from short and long period recordings respectively, comprise the vast majority of magnitudes participating in our dataset and they were calibrated against M_w. This wide use of m_b, is due to its nature since this particular scale suits to the determination of deep events' magnitude (Frohlich, 2006), as well as to the easy determination procedures.

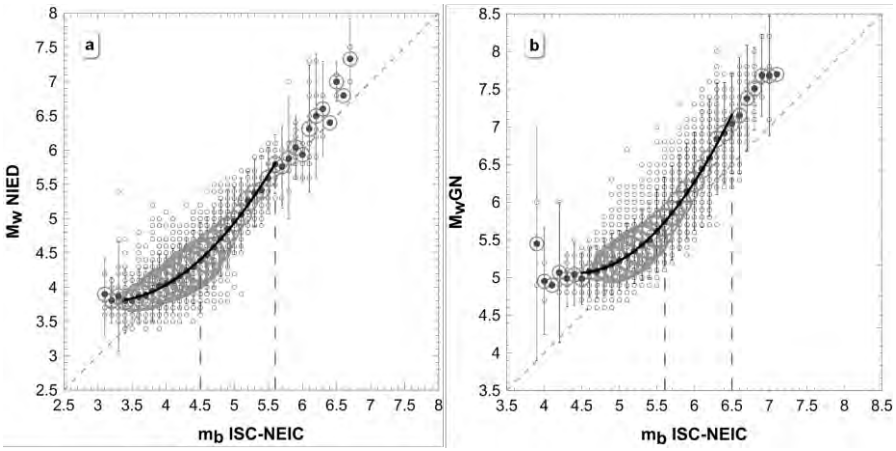

Figure 2 - Initial correlation plots between: a) M_wNIED and m_bIN (left), and b) M_wGN and m_bIN, (right) by applying 2nd degree polynomial fit (bisector is plotted as dashed line). Vertical dashed lines delimit the almost linear part of the fit. Solid circles represent the mean M_w NIED and M_wGN values corresponding to each m_bIN value while error-bars are for ±2 SD. Bubbles' size is related to the number of points used.

Direct comparison of m_bIN with M_wNIED (Figure 2a) and moment magnitudes from GCMT and NEIC (M_wGN) (Figure 2b), showed that a saturation-like behavior of M_w is revealed for m_bIN<5.6 summarizing both cases. Therefore, in order to have a reliable and representative set of data only ~6400 pairs of m_bIN and M_wGN values with M_wGN≥5.6 were integrated along with all the available pairs ~5150, of m_bIN and M_wNIED, despite their magnitude range.

The respective graph given in Figure 3, exhibits a clear linear relation between moment magnitude and m_bIN described in Table 1. This relation, produced by applying standard linear regression (SR), showed slight difference compared to corresponding general orthogonal regression (GOR) equation (proposed by Fuller, 1987 and Castellaro et. al., 2006). It holds for 4.5≤m_bIN≤7.0, in agreement with Sipkin (2003), where saturation at lower m_bIN values (around 5.5) is attributed to the non-completeness of GCMT data. From the above it is obvious that for intermediate and deep-focus earthquakes the m_b scale behaves completely different than for shallow ones (Kuge, 1992, Slipkin, 2003), not showing saturation for large (M>6.0) events.

Subsequently, by applying this type of composite regression analysis, body wave magnitudes from other sources as MOS, BJI, IDC and DJA are calibrated (Figure 4). A case of special interest, since noticeable variation in the defined equations for intermediate and deep-focus earthquakes has been observed, is m_bIDC. Linear regression fit for intermediate-depth events of IDC (60km≤h≤300km) was based on considerable more data, compared to that of deep seismicity (h>300km), resulting in more robust converting relation. Nevertheless, goodness of fit for m_bIDC calibration of deep-focus events is acceptable for lower-upper cutoffs of 4.2 and 7.0, respectively.

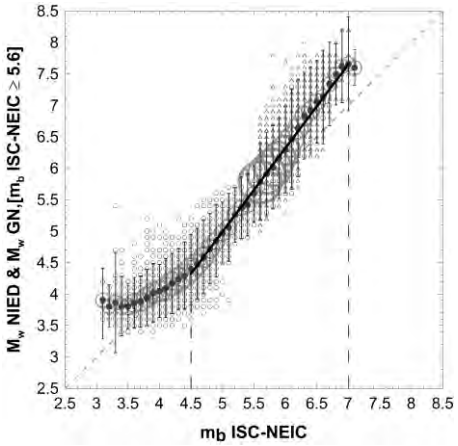

Figure 3 - Composite plot of M_WNIED-M_WGN against m_bIN by applying linear regression (SR). Open circles and triangles correspond to M_WNIED/m_bIN and M_WGN/m_bIN pairs, respe ctively. Solid circles represent the mean M_WNIED and M_WGN values corresponding to each m_bIN value while error-bars are for ±2 SD. Bubbles' size is related to the number of points u sed. The same symbols hold for Figures 4, 5 and 6.

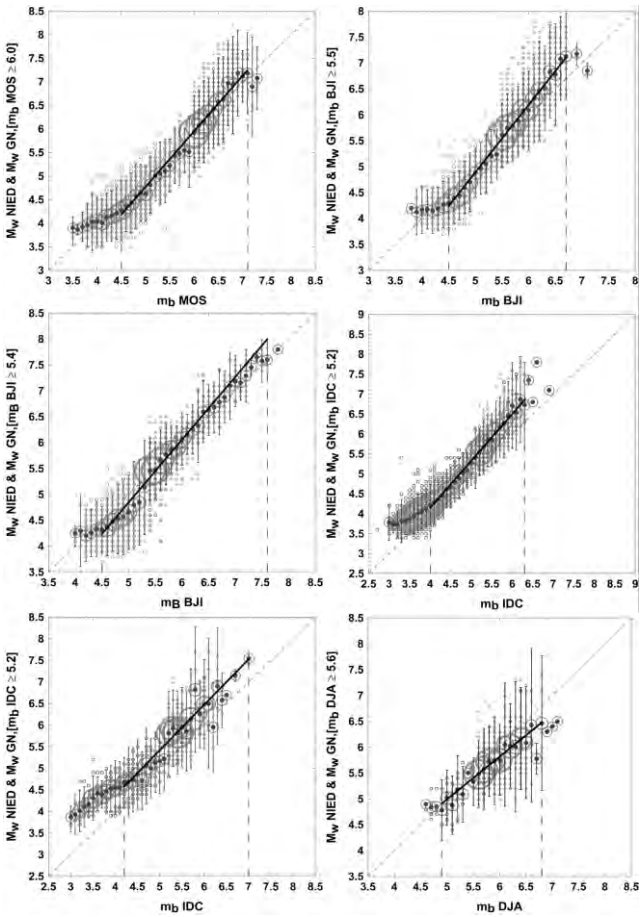

Figure 4 - From left to right, up to down raw: Composite plot of M_WNIED-M_WGN against m_bMOS, m_bBJI, m_BBJI, m_bIDC (h≤300km), m_bIDC (h>300km) and m_bDJA by applying standard linear regression (SR). The symbols are as in figure 3.

3.2. Calibration of Surface Wave Magnitude (M_s)

By comparing surface wave magnitudes M_s reported from ISC/NEIC with moment magnitudes, a robust linear correlation with significant low standard errors for the upper part of the composite regression is obtained (Figure 5). Therefore, as the 1150 events participated in M_sIN's regression analysis belong to depth range of 40-100 km, adjusted linear equation takes effect strictly for intermediate-depth earthquakes.

Besides, a few more M_s scales of great importance exhibiting linear behavior along with M_w were also calibrated (Figure 5). Regression analysis of M_sIDC and M_sBJI shows relative results to ISC/NEIC data and in the second case least squares' fit extends up to a value of 7.2 demonstrating also similarities to the respective M_sIN equation. By analyzing less, but sufficiently enough, data (~730 events), the M_sMOS vs M_W regression yields a linear equation for an impressively wide range of 4.2 to 7.9. In that case and in order to achieve lower fit error we preferred to utilize single intermediate depth information, by excluding deep-focus events reported by M_sMOS (h≥300km).

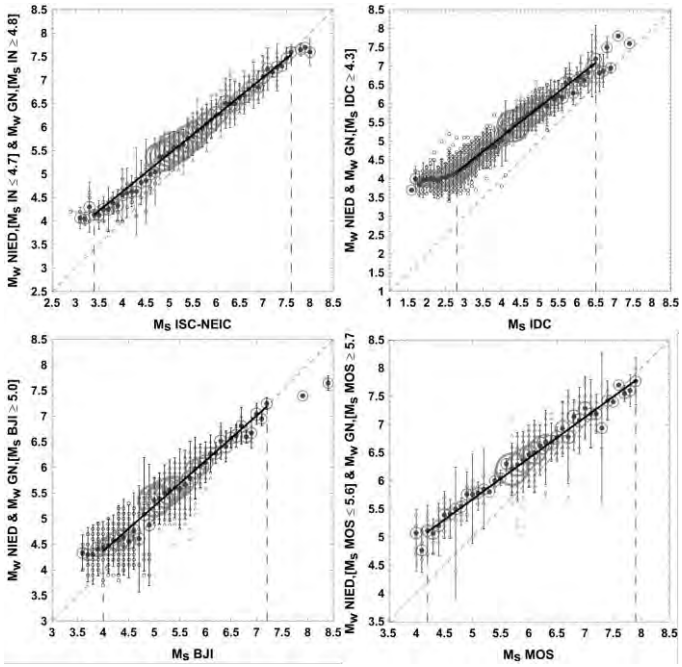

Figure 5 – From left to right, up to down raw: Composite plot of M_wNIED-M_wGN against M_sIN, M_sIDC, M_sBJI and M_sMOS (h≤300km) by applying standard linear regression (SR). The symbols are as in figure 3.

3.3. Calibration of Japan Meteorological Agency Magnitude Scale (M_{JMA})

Least squares correlation of moment magnitude with M_{JMA}, in the framework of a unified regression analysis, is depicted in Figure 6. As M_{JMA} is a local magnitude calculated for the broader region of Japan, its comparison with M_w exhibits a very tight linear adjustment for the lower part of the fit. A relative small number of events (~300) with M_{JMA}≥6.1 and reported M_wGN values give the option of extending the linear fit up to 7.6.

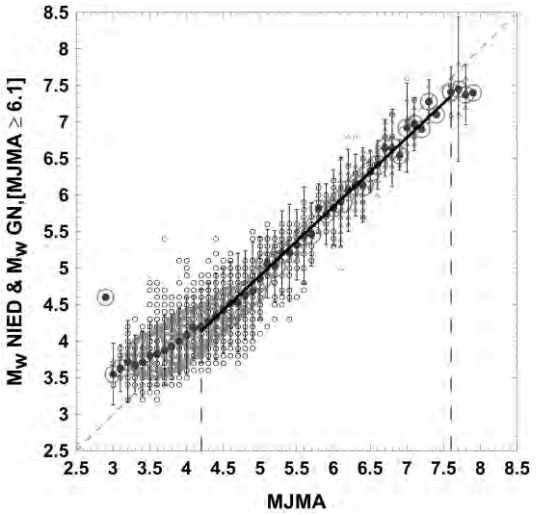

Figure 6 - Composite plot of M_wNIED-M_wGN against M_{JMA} by applying linear regression. The symbols are as in figure 3.

Table 2 - Linear regression coefficients derived after correlating M_w with 11 available magnitude scales for intermediate and deep-focus earthquakes globally

	Calibrated Magnitude Scales	b	a	σ	R^2	n	M_{min}	M_{max}
Body Wave Magntude	m_bIN	1.331	-1.669	0.33	0.82	8216	4.5	7.0
	m_bMOS	1.178	-1.110	0.38	0.83	3039	4.5	7.1
	m_bBJI	1.303	-1.625	0.33	0.83	3520	4.5	6.7
	m_BBJI	1.213	-1.224	0.31	0.84	3078	4.5	7.6
	m_bIDC h ≤ 300 km	1.177	-0.557	0.32	0.85	1749	4.0	6.3
	m_bIDC h > 300 km	1.052	0.158	0.49	0.61	430	4.2	7.0
	m_bDJA	0.826	0.865	0.42	0.37	556	4.9	6.8
Surface Wave Magnitude	M_sIN	0.810	1.384	0.20	0.89	1150	3.4	7.6
	M_sIDC	0.786	1.977	0.26	0.86	1810	2.8	6.5
	M_sBJI	0.881	0.844	0.30	0.80	1206	4.0	7.2
	M_sMOS	0.728	2.030	0.27	0.75	731	4.2	7.9
Other	M_{JMA}	0.945	0.170	0.28	0.89	1635	4.2	7.6

Additionally, two more observations concerning regression analysis of M_{JMA} could be done:

- homogeneity of error distribution between lower and upper section of the fit, with estimated errors remaining almost stable for both parts, and
- particularly high M_{JMA} value (6.1) around which integration of M_wNIED and M_wGN values is obtained.

4. Conclusions

The purpose of the present work was to define reliable empirical relations converting magnitudes expressed in several magnitude scales into moment magnitudes, valid for intermediate and deep-focus earthquakes globally. Such twelve new converting relations were derived for m_b, m_B and M_s magnitudes reported by ISC, NEIC, MOS, BJI, IDC, DJA, MOS and JMA (Table 2). A remarkable observation is that m_b scale doesn't appear to saturate for large magnitudes, an effect that is clearly observed for shallow earthquakes' body wave magnitudes around 6.2. The linear relation defined between m_b and M_w seems to extend up to the value of 7.0. The lack of such a saturation is also indicated by the distinct examination of m_b determined for intermediate and deep-focus earthquakes separately, confirming the fact in both of these cases.

Even though M_s is not recommended for intermediate and deep-focus earthquakes, surface wave magnitudes are reported for non-shallow earthquakes by international institutes. Correlation of M_s, reported by several centers, with M_w showed clear and robust linear dependence of these scales for a wide range of magnitude values. Strong linear connection was also revealed after comparing M_{JMA} with M_w.

A remarkable observation made in this study is the different behavior of M_w reported by GCMT and/or NEIC (M_wGN) and the M_w of NIED. Thus, the M_wGN for values bellow ~5.0 seems to be independent of the real magnitude while similar behavior is also observed for M_wNIED but for smaller magnitude values.

The relations proposed in the present study can be used to produce homogeneous, in respect to magnitude, earthquake catalogs of intermediate and deep-focus earthquakes globally.

5. Acknowledgments

This research has been co-financed by the European Union (European Social Fund – ESF) and Greek national funds through the Operational Program "Education and Lifelong Learning" of the National Strategic Reference Framework (NSRF) - Research Funding Program: THALES. Investing in knowledge society through the European Social Fund. Project SEISMO FEAR HELLARC. Geophysics Department Contribution Number 806/2013.

6. References

Abe K. 1981. Magnitudes of large shallow earthquakes from 1904 to 1980, *Phys. Earth Planet. Int*. 27, 72–92.

Abe K. and Kanamori H. 1979. Temporal variation of the activity of intermediate and deep focus earthquakes, *Journal of Geophysical Research*, 84, 87, 3589-3595.

Ambraseys N. and Free M. 1997. Surface-wave magnitude calculation for European region earthquakes., *Journ. Earthq. Eng.*, 1, 1, 1-22.

Astiz L., Lay T. and Kanamori H. 1988. Large intermediate-depth earthquakes and the subduction process, *Phys. Earth Planet. Int.*, 53, 80-166.

Bath M. and Duda S. J. 1979. Some aspects of global seismicity: Report No. 1-79, Seismological Institute, Uppsala, Sweden, 1- 41.

Castellaro S., Mulargia F. and Kagan. Y. Y. 2006. Regression problems for magnitudes, *Geophys. J. Int.,* 165, 913–930.

Dziewonski A. M. and Gilbert F. 1974. Temporal variation of the seismic moment tensor and the evidence of precursive compression for two deep earthquakes, *Nature,* 247, 185-188.

Dziewonski A. M., Chou T. A. and Woodhouse J. H. 1981. Determination of earthquake source parameters from waveform data for studies of global and regional seismicity, *J. Geophys. Res.,* 86(2), 825–852.

Engdahl E.R. and Villaseñor A. 2002. Global Seismicity: 1900-1999, In W.H.K. Lee, H. Kanamori, P.C. Jennings and C. Kisslinger (editors), *International Handbook of Earthquake and Engineering Seismology*, Part A, Chapter 41, Academic Press, 665-690.

Frohlich C. 2006. *Deep Earthquakes*, Cambridge University Press, Cambridge, England.

Fukuyama E., Ishida M., Horiuchi S., Inoue H., Hori S., Sekiguchi S., Kawai H. and Murakami H. 1999. NIED seismic moment tensor catalogue January – December, 1998. *TechnicalNote Natl. Res. Inst. Earth Sci. Disaster Prev*., 193, 1 - 35.

Fuller W. A. 1987. *Measurement Error Models*, Wiley, New York.

GCMT 2012. Global Centroid Moment Tensor (GCMT) project at Lamont-Doherty Earth Observatory (LDEO) of Columbia University, http://www.globalcmt.org/CMTsearch.html.

Giardini D. 1988. Frequency distribution and quantification of deep earthquakes, *J. Geophys. Res.* 93, 2095- 2105.

Gardini D., Donato M. di. and Boschi E. 1997. Calibration of magnitude scales for earthquakes of the Mediterranean, *Journal of Seismology,* 1, 161–180.

Gutenberg B. 1945. Magnitude determination for deep-focus earthquakes, *Bull. Seism. Soc. Am.* 35, 117-130.

International Seismological Centre (ISC) 2012. *On-line Bulletin*, http://www.isc.ac.uk, Internatl. Seis. Cent., Thatcham, United Kingdom, http://www.isc.ac.uk/iscbulletin/search/bulletin.

Karnik V. 1996. Seismicity of Europe and the Mediterranean, In: Klima, K. (ed.), *Academy of Sciences of the Czech Republic*, Geophysical Institute, 28 pp. plus earthquake catalogue.

Kubo A., Fukuyama E., Kawai H. and Nonomura K. 2002. NIED seismic moment tensor catalogue for regional earthquake around Japan: Quality test and application, *Tectonophys*., 356, 23-48 pp.

Kuge K. 1992. Systematic difference in the ISC body-wave magnitude - seismic moment relationship between intermediate and deep earthquakes, *Bull. Seismo. Soc. Amer*., 82, 819-835.

National Earthquake Information Center, (NEIC) 2011. *Earthquake Hazards Program*, URL: http://neic.usgs.gov/neis/epic/index.html.

Okal E.A. and Kirby S.H. 1995. Frequency-moment distribution of deep earthquakes; implications for the seismogenic zone at the bottom of slabs, *Phys. Earth Planet. Interiors,* 92, 169- 187.

Scordilis E.M. 2006. Empirical global relations converting Ms and mb to moment magnitude, *Journal of Seismology*, 10, 225-236.

Sipkin S.A. 1982. Estimation of earthquake source parameters by the inversion of waveform data: synthetic seismograms, *Physics of the Earth and Planetary interiors,* v. 30, no. 2-3, 242-259.

Sipkin S.A. 2003. A correction to body-wave magnitude mb based on moment magnitude Mw, *Seis. Res. Lett*., 74, 739-742.

SOPAR 2012. Source Parameter Search (SOPAR) - Moment Tensor and Broadband Source Parameter Search, USGS-NEIC, http://earthquake.usgs.gov/earthquakes/eqarchives/sopar.

Utsu T. 2002. Relationships between magnitude scales, *International Handbook of Earthquake and Engineering Seismology*, 81, 733–746.

Wadati K. 1928. Shallow and Deep Earthquakes, *Geophysical Magazine*, 1, 162-202.

Wadati K. 1929. Shallow and Deep Earthquakes, *Geophysical Magazine*, 2, 1- 36.

Δελτίο της Ελληνικής Γεωλογικής Εταιρίας, τομ. XLVII , 2013
Πρακτικά 13ου Διεθνούς Συνεδρίου, Χανιά, Σεπτ. 2013

Bulletin of the Geological Society of Greece, vol. XLVII 2013
Proceedings of the 13th International Congress, Chania, Sept. 2013

MULTIDIMENSIONAL EARTHQUAKE FREQUENCY DISTRIBUTIONS CONSISTENT WITH NON-EXTENSIVE STATISTICAL PHYSICS: THE INTERDEPENDENCE OF MAGNITUDE, INTEREVENT TIME AND INTEREVENT DISTANCE IN NORTH CALIFORNIA

Tzanis A.[1], Vallianatos F.[2] and Efstathiou A.[1]

[1] *National and Kapodistrian University of Athens, Faculty of Geology and Geoenvironment, Department of Geophysics and Geothermy, atzanis@geol.uoa.gr, aefstathiou@geol.uoa.gr*

[2] *Laboratory of Geophysics and Seismology, Technological Educational Institute of Crete, Chania, GR 73133, Crete, Greece, fvallian@chania.teicrete.gr*

Abstract

It is now accepted that the active tectonic grain comprises a self-organized complex system, therefore its expression (seismicity) should be manifested in the temporal and spatial statistics of energy release rates, and exhibit memory due to long-range interactions in a fractal-like space-time. Such attributes can be properly understood in terms of Non-Extensive Statistical Physics. In addition to energy release rates expressed by the magnitude M, measures of the temporal and spatial interactions are the time (Δt) and hypocentral distance (Δd) between consecutive events. Recent work indicated that if the distributions of M, Δt and Δd are independent so that the joint probability p(M, Δt, Δd) factorizes as p(M) p(Δt) p(Δd), earthquake frequency is related to M, Δt and Δd by well defined power-laws consistent with NESP. The present work applies these concepts to investigate the self-organization and temporal/spatial dynamics of North Californian seismicity. The results indicate that the statistical behaviour of seismicity in this area is consistent with NESP predictions and has attributes of universality, as its holds for a very broad range of spatial, temporal and magnitude scales. They also indicate that the expression of the regional active tectonic grain comprises a mixture of processes significantly dependent on Δd, which include near (<100km) and far (>400km) field interactions.

Key words: *Tsallis entropy*, *complexity*, *non-extensivity, statistical seismology.*

Περίληψη

Είναι πλέον δεκτό ότι ο ενεργός τεκτονικός ιστός αποτελεί αυτό-οργανωμένο πολύπλοκο σύστημα, οπότε και η έκφραση του (σεισμικότητα) θα πρέπει να εκδηλώνεται στην στατιστική της χωρικής και χρονικής εξάρτησης των ρυθμών έκλυσης ενέργειας και να εμφανίζει μνήμη λόγω αλληλεπιδράσεων μακράς εμβέλειας σε ένα μορφοκλασματικό χωροχρόνο. Τα χαρακτηριστικά αυτά μπορούν να κατανοηθούν στο πλαίσιο της Μη-Εκτατικής Στατιστικής Φυσικής. Εκτός από την έκλυση ενέργειας που εκφράζεται μέσω του μεγέθους M, μέτρο των χρονικών και χωρικών αλληλεπιδράσεων είναι ο χρόνος (Δt) και η υποκεντρική απόσταση (Δd) μεταξύ διαδοχικών σεισμών. Πρόσφατη έρευνα έδειξε ότι εάν οι κατανομές των M, Δt και Δd είναι ανεξάρτητες ώστε η κοινή πιθανότητα p(M, Δt, Δd) να παραγοντοποιείται

κατά το σχήμα p(M) p(Δt) p(Δd), η συχνότητα των σεισμών σχετίζεται με τα M, Δt και Δd μέσω καλώς προσδιορισμένων νόμων δύναμης συμβατών με την ΜΕΣΦ. Η παρούσα εφαρμόζει αυτές τις έννοιες στη διερεύνηση της αυτό-οργάνωσης και χρονικής/χωρικής δυναμικής της σεισμικότητας στην Βόρειο Καλιφόρνια (ΗΠΑ). Τα αποτελέσματα δείχνουν ότι η στατιστική συμπεριφορά της σεισμικότητας σ' αυτή την περιοχή είναι συμβατή με τις προβλέψεις της ΜΕΣΦ και εμφανίζει γενικότητα, καθώς ισχύει για σημαντικό εύρος μεγεθών και χρονικών/χωρικών κλιμάκων. Δείχνουν επίσης ότι η συνολική έκφραση του περιφερειακού τεκτονικού ιστού συγκροτείται από μείξη διεργασιών με σημαντική εξάρτηση από το Δd, οι οποίες περιλαμβάνουν αλληλεπιδράσεις εγγύς (<100km) και μακράν (>400km) πεδίου.
Λέξεις κλειδιά: *Εντροπία Τσάλλη, πολυπλοκότητα, στατιστική σεισμολογία.*

1. Introduction

The long term evaluation of earthquake hazard in terms of the regional statistical properties of earthquake occurrence and recurrence is usually based on the celebrated frequency – magnitude (F-M) distribution of Gutenberg and Richter (1944). This states that the frequency of earthquake occurrence is related to earthquake magnitude via a simple relationship of the form $\log N = a - bM$, where N is the number of earthquakes in a specified time interval. Barring the complications arising from studies of the F-M distribution on the global scale, the standard assumption about seismogenesis on regional and local scales was that it basically comprises a random (hence memoryless) extensive process and that individual events are uncorrelated, at least at the higher magnitude range. The Gutenberg – Richter F-M distribution was understood in this context and the standard tools currently used for earthquake hazard analysis are all based on this premise. Thus, it was generally accepted that seismicity (seismogenesis) obeys Boltzmann-Gibbs dynamics, although an apparent contradiction in that viewpoint is that the F-M distribution implies scale-free grading of frequency and magnitude, which cannot be derived from the Boltzmann-Gibbs formalism.

The concepts of fractal geometry, self-organized criticality and complexity introduced in the 1980's and 1990's have gradually shifted the paradigm. It is now accepted that the active tectonic grain comprises a complex dynamic system, the general understanding being that it is critical (e.g. Bak and Tang, 1989; Sornette and Sornette, 1989; many others since). A sizeable minority point of view proposes alternative complexity mechanisms, as for instance is the Epidemic-Type Aftershoc k Sequences model (e.g. Ogata, 1988), the Coherent Noise Model (Celikoglu et al, 2010), the Fertility Heterogeneity model (Saichev and Sornette, 2012), etc. At any rate, dynamic complex systems evolving in a fractal-like space-time are characterized by long-range interactions and long-term memory. This, in turn, implies that the statistics of earthquake occurrence, at least on a regional scale, should be manifested in certain traits of the F-M distribution and of all analogous frequency distributions pertaining to its temporal and spatial dependence. Specifically, one should expect power laws resulting from the tails generated by the long-term memory of the system.

The presently accepted interpretation of the Gutenberg – Richter F-M distribution is that it expresses the scale-free statistics of a fractal active tectonic grain; with relationships between the constant b and the fractal dimension of the tectonic grain having been derived in various ways. However, the F-M distribution is *static* and says nothing about the temporal and spatial dynamics of the seismogenetic system. A measure of the temporal dynamics is the time lapsed between consecutive events above a magnitude threshold over a given area: this parameter is variably referred to as *interevent time*, *waiting time, calm time* etc. Understanding the statistics of the earthquake frequency – interevent time (F-T) distribution is obviously key to understanding the seismogenetic system and has been studied by several researchers. The empirical F-T distributions generally exhibit power-law behaviour and long tails and have been investigated with standard statistical models with tails, reducible to power laws in some way or another (e.g. gamma distribution, Weibull distribution etc.). Several investigators have applied the gamma distribution and have suggested

universality analogous to the Gutenberg – Richter law (e.g. Corral, 2004), to which other investigators object on the premise of model-based studies, suggesting that the interevent times are mixed distributions of correlated aftershock and uncorrelated background processes (e.g. Touati et al, 2009). At any rate, these studies have generally been empirical or model-based; in the latter case, the underlying background process has always been conjectured to obey extensive thermodynamics (i.e. to be random). A measure of the spatial dependence is the *hypocentral* distance between consecutive events above a magnitude threshold over a given area (*interevent distance*). With less than a handful of direct (e.g. Abe and Suzuki, 2003) or indirect treatises, (e.g. Baiesi and Paczucki, 2004; Marsan and Legliné, 2008), the properties and statistics of earthquake frequency – interevent distance (F-D) distribution is practically terra incognita.

The most recent development in the statistical description of earthquake occurrence is the introduction of the concept of *non-extensivity*. A simple argument for this point of view is that if the frequency distributions of the relevant parameters exhibit the traits expected of non-extensive systems (power laws), then it is very likely that the system generating these distributions is universally non-extensive and not a mixture of extensive, or extensive *and* non-extensive processes, as the contesting view proposes. The Non-Extensive Statistical Physics (NESP) approach has attracted growing attention during the past few years (e.g. Vallianatos and Telesca, 2012) with several researchers studying the properties of the F-M and F-T distributions. However, if the seismogenetic process is indeed complex and long-range/long-memory, then the size, time and spatial statistics of earthquakes should be not be unrelated! Insofar as earthquakes occur by the triggering of successor events within the temporal and spatial interaction radius of predecessor events, (which depends on their size), or by long-range effects in the correlated space of the seismogenetic system, the frequency of earthquakes should be related to the magnitude, the interevent time and the interevent distance by multidimensional extensions of the one-dimensional power-laws predicted by the complexity model describing the system, in this case the NESP formalism.

The present paper marks the beginning of a systematic attempt to verify the conjecture and assist in validating/refuting the NESP approach to seismicity by studying the local and regional characteristics of different seismogenetic areas of the world, starting with Northern California (United States). The presentation will focus on the analysis of bivariate F-M-T distributions, while using the interevent distances as spatial constraints or spatial filters for studying the spatial dependence of the energy and time dynamics of North Californian seismicity. It shall be demonstrated that the frequency of earthquake occurrence at Northern California is multiply related to the magnitude, the interevent time by means of well defined multi-dimensional power-laws consistent with NESP and has attributes of universality, as its holds for a very broad range of spatial, temporal and magnitude scales. It shall also be demonstrated that the expression of the regional active tectonic grain (seismicity) is produced by an unexpectedly complex system comprising a mixture of processes that depend significantly on the distance between earthquakes.

2. Non-Extensive Statistical Physics

2.1. Tsalis Entropy and Probability Distribution

The context of *Non-Extensive Statistical Physics* (NESP), originally introduced by Tsallis (1988, 2009), has recently been suggested to comprise an appropriate tools for the analysis of complex dynamic systems with scale invariance, long-range interactions, long-range memory and systems that evolve in a fractal-like space-time (e.g. Gell-Mann and Tsallis, 2004).

Let X be a seismicity parameter (e.g. energy, interevent time etc.) and $p(X)dX$ the probability of finding its value in $[X, X+dX]$, such that $\int_W p(X)dX = 1$, where W is the support of X and expresses the total number of microscopic configurations of the system. Non-equilibrium states in systems with complex behaviour can be described by the Tsallis (1988) entropic functional:

$$S_q = k\frac{1}{q-1}\left[1-\int_W p^q(X)dX\right], \quad (1)$$

where k is the Boltzmann constant and q the *entropic index*. The latter is a measure of the *non-exte nsivity* of the system and for the particular case q = 1 Eq. 1 reduces to the Boltzmann–Gibbs entrop y $S_{BG} = -k\int_W p(X)\ln(p(X))dX$.

The Tsallis entropy shares properties with the Boltzmann-Gibbs entropy, including concavity and fulfilment of the H-theorem. However, it is *pseudo-additive* in the sense that it is not proportional to the number of the elements of the system as is S_{BG}. Thus, for a composite of two statistically independent systems, A and B, $S_q(A, B) = S_q(A) + S_q(B) + (1-q)\, S_q(A)\, S_q(B)$, leading to *super-additivity* for q<1, *additivity* for q=1, i.e. Gibbs-Boltzmann statistics, and *sub-additivity* for q>1.

Maximization of the Tsallis entropy yields the *q-exponential distribution*

$$p(X) = \frac{1}{Z_q}\exp_q\left[-\frac{\lambda}{I_q}\left(X-\langle X\rangle_q\right)\right], \quad (2)$$

where $\langle X\rangle_q = \int_W Xp_q(X)dX$ is the *q-expectation* value of X, λ is an appropriate Lagrange multiplier, $Z_q = \int_W dX \exp_q\left[-\lambda\cdot I_q^{-1}\cdot\left(X-\langle X\rangle_q\right)\right]$ is a generalized canonical partitioning function, and $I_q = \int_W dX[p(X)]^q$. In Eq. 2, the function $\exp_q(.)$ represents the *q-exponential* function

$$\exp_q(X) = \begin{cases}\left(1+(1-q)X\right)^{\frac{1}{1-q}} & 1+(1-q)X > 0\\ 0 & 1+(1-q)X \le 0\end{cases}, \quad (3)$$

and comprises a generalization of the exponential function: for q=1, $\exp_1(X) = e^X$. As evident from Eq. 2 and Eq. 3, the probability $p(X)$ is a power-law with a long tail if q>1, corresponding to *sub-additivity*, an exponential distribution if q=1, corresponding to *additivity*, and a *cut-off* if 0< q< 1, corresponding to *super-additivity*; the cut-off appears at $X_c = X_0(1-q)^{-1}$, with $X_0 = (1-q)\cdot\langle X_q\rangle + \lambda/I_q$.

If the *empirical* distribution of X (i.e. the *escort probability*) is $P_q(X)$, then the *cumulative* probability function (CDF) derived from the above analysis is:

$$P(>X) = \int_X^\infty dX\ P_q(X)\,.$$

In the case of q > 1 and $X \in [0, \infty)$, the CDF becomes:

$$P(>X) = \int_X^\infty dX\ P_q(X)\ldots\Rightarrow\ldots P(>X) = \exp_q\left(-\frac{X}{X_0}\right) = \left[1-(1-q)\left(\frac{X}{X_0}\right)\right]^{\frac{1}{1-q}}. \quad (4)$$

which is a *q-exponential distribution*. When q > 1 the CDF exhibits a long tail, which becomes longer with increasing q; the system experiences long-range correlations and has long-term memory. When q = 1, the q-exponential distribution reduces to the common exponential distribution: the system is a random process (uncorrelated and memory-less). When q < 1, the distribution exhibits a cut-off, i.e. P(>X) = 0 whenever the argument becomes negative and is characterized by a bounded correlation radius.

2.2. NESP Distribution Law for Earthquake Magnitude and Interevent Time

The frequency-magnitude distribution has been approximated with a number of NSEP-compatible models (Sotolongo-Costa and Posadas, 2004; Silva et al., 2006; Telesca 2011, 2012 etc.). These all consider the interaction of two rough fault walls (asperities) and the fragments filling space between them, which is supposed to modulate earthquake triggering (the fragment-asperity model). However, they differ in their assumption of how the total energy stored in the asperities and frag-

ments scales with their linear characteristic dimension. Herein, we propose that the assumption made by Telesca (2011, 2012), that the energy scales with the area of the fragments and asperities ($E \propto r^2$) so that $M = \frac{2}{3}\log(E)$, is representative of the seismogenetic process. Accordingly, we adopt his model, in which the cumulative frequency-magnitude distribution reads:

$$P(>M) = \log\left(\frac{N(>M)}{N_{M=0}}\right) = \left(\frac{2-q_M}{1-q_M}\right)\log\left(1-\left[\frac{1-q_M}{2-q_M}\right]\left[\frac{10^M}{\alpha^{2/3}}\right]\right) \quad (5)$$

This relationship describes from first principles and in NESP formalism, the cumulative distribution of the number of earthquakes N with magnitude greater than a threshold M in a seismic region, normalized by the total number of earthquakes. The constant α expresses the proportionality between the released energy E and the fragment size r and q_M is the entropic index.

The CDF expressed by Eq. 4 is the only NESP formulation proposed for the one-dimensional distributions F-T (Abe and Suzki, 2005) and F-D (Abe and Suzuki, 2003). The empirical application of NESP to interevent times has been taken up by a handful of authors. Abe and Suzuki (2005) investigated the temporal properties of the seismicity in California and Japan; Carbone et al (2005) investigated the Italian seismicity; more recently, Vallianatos et al. (2012) investigated the spatio-temporal properties of the 1996 Aigion (Greece) aftershock sequence, Vallianatos et al. (2013) the temporal behaviour of the 2011-2012 seismicity crisis in the Santorini volcanic complex (Greece) and Vallianatos and Sammonds (2013) the behaviour of global seismicity prior to the 2004 Sumatran and 2011 Honsu mega-earthquakes. In these studies, the F-T distribution $P(>T)$ were all nicely fitted with a one-dimensional q-exponential distribution of the form (4).

2.3. NESP Formulation of Joint Distribution Laws

We assume that the magnitude M, interevent time Δt distributions are due to independent processes in the sense that the joint probability $P(M \cup \Delta t)$ factorizes into the probabilities of M and Δt, i.e. $P(M \cup \Delta t) = P(M)\,P(\Delta t)$. Then, on removing the normalization, the joint probability above a magnitude threshold can be expressed by

$$\log N = \log(N_{M=0}) + \left(\frac{2-q_M}{1-q_M}\right)\cdot\log\left(1-\frac{1-q_M}{2-q_M}\cdot\frac{10^M}{\alpha^{2/3}}\right) + \frac{1}{1-q_t}\log\left[1-(1-q_t)\left(\frac{\Delta t}{\Delta t_0}\right)\right], \quad (6)$$

where q_M, q_t are the entropic indices for the magnitude and interevent times respectively and Δt_0, is the *q-relaxation time*, analogous to the relaxation (characteristic) time often encountered in the analysis of physical systems. Eq. 6 comprises a generalized (bivariate) Gutenberg – Richter law and is the general model to be implemented in the ensuing analysis.

3. Data Analysis

3.1. The North California Earthquake Catalogue

The earthquake data utilized in this study was extracted from the regional earthquake catalogue compiled by the USGS/Northern California Seismic Network and available through the Northern California Earthquake Data Centre (NCEDC @ http://www.ncedc.org); it comprises 13165 events recorded within the area 35ºN/ 42ºN and 234ºE/ 242EºE during 1967-2012.

Most earthquakes are reported in the local (M_L) and moment (M_w) magnitude scales, while there is a considerable number of events reported in the duration (M_d) and amplitude (M_x) scales. The latter have been exhaustively calibrated against the M_L magnitude scale: Eaton (1992) has shown that they are *within* 5% of the M_L scale for magnitudes in the range 0.5 to 5.5 and that they are virtually independent of the distance from the epicentre to at least 800 km. Thus, M_d and M_x are practically equivalent to M_L. For the purpose of the present analysis the M_w magnitudes were also converted to M_L using the empirical formula of Urhammer et al (1996): $M_w = M_L \cdot (0.997 \pm 0.020) - (0.050 \pm$

0.131). Thus, the entire catalogue has been reduced to a proxy-M_L scale. The NCEDC catalogue is practically homogeneous by construction and complete for $M_L \geq 3$, as demonstrated in Figure 1c.

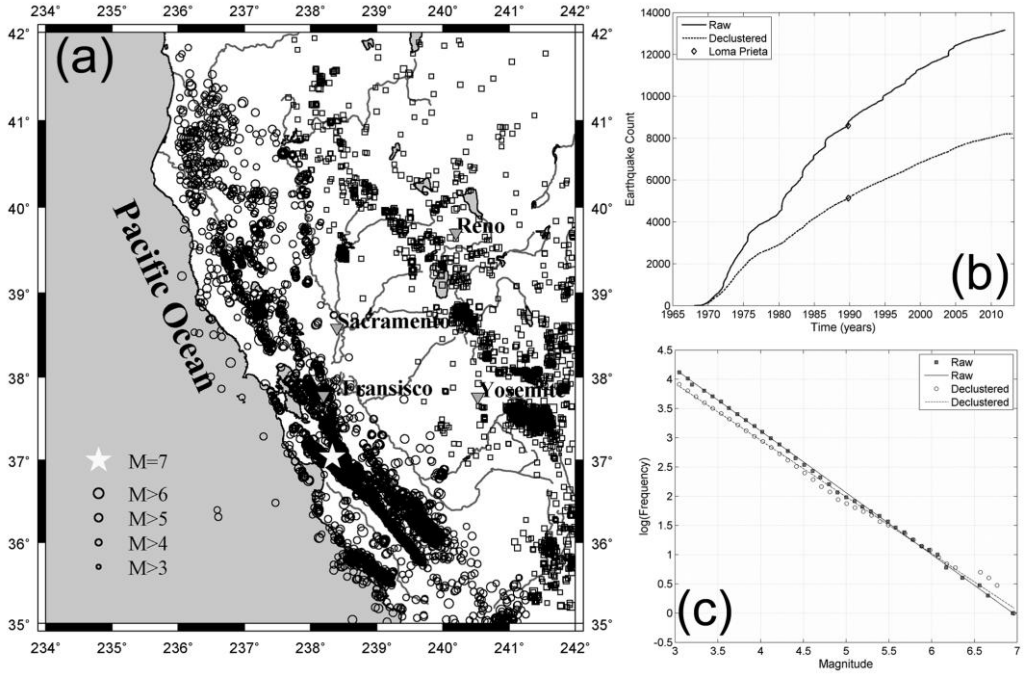

Figure 1 - The NCEDC catalogue, 1968–2012: (a) Epicentral distribution of the raw catalogue. (b) Cumulative earthquake counts of the raw and declustered catalogues. (c) The cumulative F-M distributions of the raw and declustered catalogues.

As stated in the introduction, there is an ongoing debate about the nature of interevent time frequency distributions with respect to whether they are characteristic and universal, or simply mixtures of correlated aftershock and uncorrelated background processes. This does not yet include the NESP formulation, but it is relevant nevertheless. In order to address this problem and compare the application of the NESP formalism to "mixed" and "background" processes, we have compiled a *de-clustered* version of the NCEDC catalogue using the approach of Reasenberg (1985). The declustered catalogue consists of 8210 events and its associated cumulative earthquake count is smooth and free of the time-local rate changes (jerks) evident in the corresponding curve of the raw catalogue due to aftershocks (Figure 1b); Consequently, it comprises mainly "background" earthquake activity; it is also homogeneous by construction and complete for $M_L \geq 3$ (Figure 1c).

3.2. Empirical Cumulative Frequency Distributions and Probabilities.

The joint F-M-T distribution is relatively easy to construct. A cut-off magnitude M_c is set and a bivariate frequency table (histogram) representing the incremental distribution is first compiled; the cumulative frequency distribution is then obtained from the incremental distribution by backward bivariate summation. A typical example is shown in Figures 2a and 2b, of the empirical F-M-T distribution compiled from the *raw* NCEDC catalogue for $M_c \geq 3.4$. It is apparent that it is a well defined and structured surface, with its end-member at [$M \geq M_c$, Δt=0] comprising the one-dimensional Gutenberg – Richter law. The opposite end member located at [M_c=0, Δt] comprises the one-dimensional F-T distribution. Both end-members of the distribution exhibit definite attributes of power-law dependence. In the above example, the cumulative frequency (earthquake count) can be written thus: $N(\{M \geq M_c, \Delta t : M \geq M_c\})$. Then, the empirical probability $P(>\{M \geq M_c,$

$\Delta t : M \geq M_c\}$) is simply $\dfrac{N(>\{M \geq M_c, \Delta t : M \geq M_c\})}{N(M_c, 0)}$, and $N(M_c, 0) = \|N\|_\infty$.

3.3. Modelling Procedure

The empirical F-M-T distributions of the form shown in Figure 2b, were approximated with the model of Eq. 6 using non-linear least-squares solver. Because the parameters of Eq. 6 are subject to positivity constraints and/or are bounded (e.g. the entropic indices), a solver implementing the trust-region reflective algorithm (e.g. Moré and Sorensen, 1983; Steihaug, 1983) was chosen, together with *Least Absolute Residual minimization* so as to down-weight possible outliers. A typical example is shown in Figure 2c and 2d. The quality of the approximation is exceptional, with the correlation coefficient (R^2) being as high as 0.99. The evaluation of the result is summarized in Figure 2d and is based on the analysis of the statistical distribution of the residuals. Thus, the observed cumulative probability of the sorted residuals is numerically approximated with a normal location-scale distribution (dashed line) and a Student-t location-scale distribution (solid line). Evidently, the residuals are not normally distributed and exhibit tails that are better approximated with the t-location-scale distribution. However, only 25 residuals deviate from the normal distribution, out of 173, or 14.45%; these represent outliers that have been effectively suppressed, since the solution is determined by the remaining 85.5% of the observations. It can also be seen that only 8 residuals are greater than |0.5|, or 3.16 earthquakes; these are, more or less scattered at the tails of the observed F-M-T distribution. Such statistics amply explain the quality of the solution and because they are typical, they strongly indicate that the NESP model represented by Eq. 6 is a "natural" description of earthquake (thermo)dynamics.

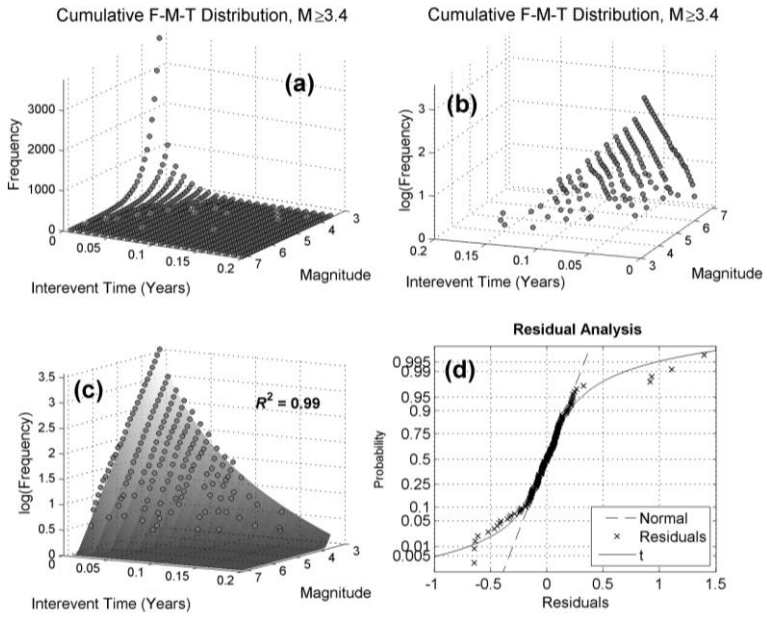

Figure 2 - (a) is the F-M-T distribution for the raw NCEDC catalogue and a cut-off magnitude of $M_c \geq 3.4$; (b) the same F-M-T but in logarithmic F-scale; (c) is as per (b) but with the predicted (fitted) distribution based on Eq. 6; (d) is a probability analysis of the residuals.

4. Results

As mentioned previously, the complexity and self-organization considered to characterize the seismogenetic system are associated with long-range interactions and long-term memory; these

properties are collectively referred to as "*correlation*". The NESP theory proposes that the entropic indices are a measure of such correlation: values approaching unity indicate low correlation (near randomness) and vice versa.

As a first step in investigating such correlations we apply the analysis described in Section 3.3, to F-M-T distributions compiled from the raw and declustered NCEDC catalogues for different cut-off magnitudes. The results are presented in Figure 3. Excellent approximations were generally obtained, the least-squares goodness of fit (R^2) being *invariably* higher than 0.93. In consequence, and for the sake of experimental vigour, this presentation will only discuss results obtained from empirical F-M-T distributions constructed with *more* than 300 earthquakes and associated with a goodness of fit *better* than 0.97.

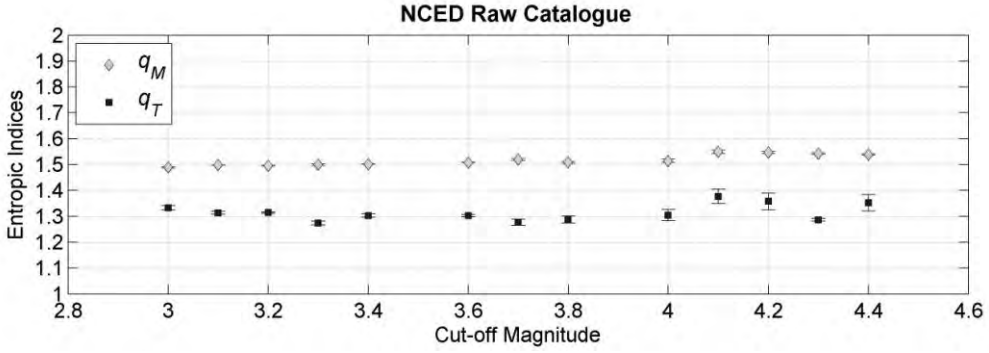

Figure 3 – The dependence of entropic indices estimated from the raw NCEDC catalogue on cut-off magnitudes. In all cases, error bars correspond to 95% confidence intervals

The raw NCEDC catalogue yields very stable q_M for all cut-off magnitudes, which varies from 1.49 at M_c=3.0 to 1.53 at M_c=4.4. It has been shown (e.g. Telesca, 2012) that Eq. 5 reduces to the conventional Gutenberg – Richter law and yields a proxy-*b* value expressed in terms of the entropic index: $b_q = (2\text{-}q_M)/(q_M\text{-}1)$. Application of this formula leads to proxy-*b* value estimates that vary linearly from ≈1 at M_c=3.0 to 0.88 at M_c=4.4 and can be verified to be consistent with corresponding determinations of *b*-values based on conventional methods. The entropic index q_M, like the *b*-value, represents the scaling of the size distribution of earthquakes and clearly indicates a correlated, scale-free process. Moreover, its small but persistent shift at the larger cutoff magnitudes indicates a corresponding increase in the size distribution of seismicity as a function of magnitude, albeit still correlated and scale-free. The temporal entropic index q_T exhibits small variation with magnitude: it indicates low to moderate correlation for $M_c \leq 3.8$, where $q_T \approx 1.3$, rising towards 1.4 thereafter (moderate correlation).

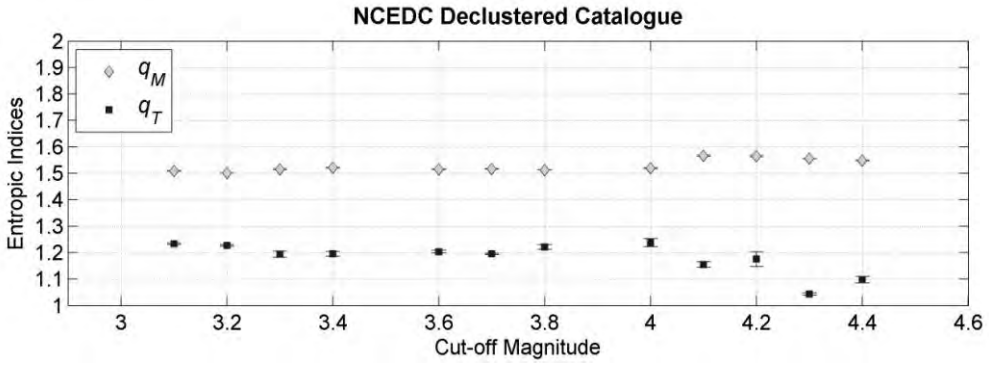

Figure 4 – As per Figure 3 for the *declustered* NCEDC catalogue.

The analysis of the declustered NCEDC catalogue is shown in Figure 4. q_M varies quasi-linearly from 1.5 at M_c=3 to and 1.53 at M_c=4.4 and is consistent with the corresponding index derived from the raw catalogue. This yields proxy-*b* values also quasi-linearly changing from 1 at M_c=3 to 0.88 at M_c=4.4, and is generally consistent with conventional determinations of *b*. Here as well, the small bt persistent shift of q_M at the larger cut-off magnitudes indicates a corresponding change in the size distribution of *background* earthquakes almost identical to that of the mixed background – aftershock process. The temporal entropic index q_T, however, behaves almost exactly opposite to its raw-catalogue counterpart: it is approximately equal to 1.2 for M_c=≤4 (low correlation) and gradually drops to 1.1 at M_c=4.4, which indicates very weak correlation or, equivalently, a practically random temporal sequence of earthquake occurrence, at least for cut-off magnitudes of the order of 4.2 – 4.3.

The comparison of the results from the raw and declustered catalogues shows that the size distribution of background earthquake processes on one hand, and mixed background – aftershock processes on the other, are compatibly correlated in a way consistent with the phenomenology expected from the SOC theory (e.g. Bak et al., 2002). Conversely, the temporal sequence of background earthquakes appears to be weakly correlated or random at worst, while the temporal sequence of the mixed process appears to be moderately correlated. At first sight, this would appear to be consistent with the model-based studies of Touati et al (2009). It is worth noting, however, that the moderate – good temporal correlation of the mixed process persists at $M_c \geq 4$ Although these results cannot be light-heartedly extrapolated to larger magnitude scales, the observation may suggest that at intermediate magnitude scales, aftershocks and background events are entangled and interact, thus producing SOC phenomenology in the temporal expression of regional seismicity. According to this view, aftershocks may be an integral part of the regional seismicity process and not just localized peculiarities (also see Marsan and Lengliné, 2008).

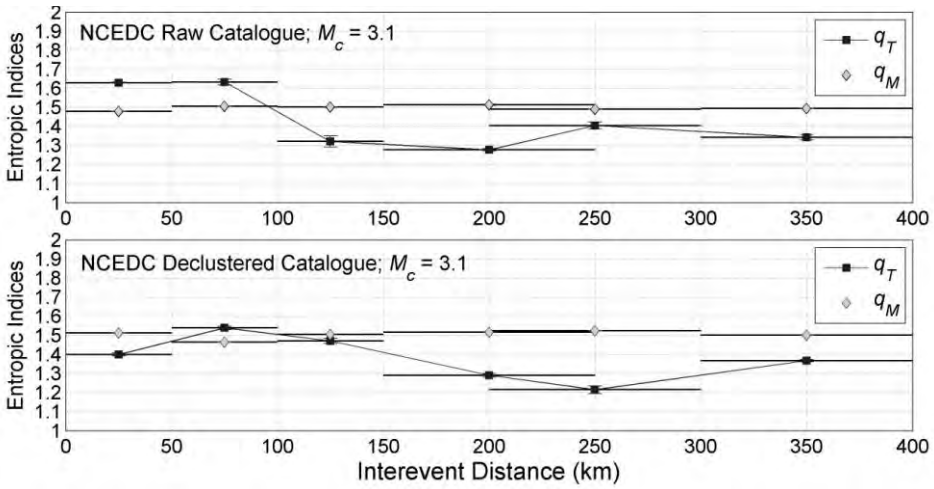

Figure 5 – The dependence of the entropic indices on interevent distance, for data subsets grouped according to interevent distance. (a) Analysis of the raw catalogue. (b) Analysis of the declustered catalogue.. The extent of *Δd* bins is indicated by horizontal line segments. Errors are 95% conf. intervals.

Next, we study the effect of spatial separation (interevent distance) on earthquake size distribution and temporal expression. The modelling procedure was applied to data subsets grouped according to the interevent distance between consecutive events, following the rule $C \supset \{C_D : M > M_c \wedge \Delta d_L \leq \Delta d \leq \Delta d_U\}$ where C is the catalogue, C_D is the subset catalogue, Δd is the interevent distance and Δd_L, Δd_U are the upper and lower group limits. The resulting variation of the entropic indices with respect to distance group is shown in Figure 5 for both the raw (top panel) and declustered (bottom

panel) catalogues. The breadth of the interevent distance bins is indicated by the horizontal line segments across the index symbols. The results have been derived for M_c=3.1.

The analysis of the raw NCEDC catalogue (Figure 5a) shows that q_M is consistently determined as a function of interevent distance. It can be seen to vary between 1.46 and 1.52 with the corresponding proxy *b*-values varying between 1.17 and 0.92. The temporal entropic index q_T exhibits significant variation with increasing interevent distance group. It begins by showing a very highly correlated process ($q_T \approx 1.6$ at Δd=0-100km), which is evidently due to the overwhelming effect of the tightly spaced and highly correlated aftershock sequences. At longer interevent distances q_T drops to 1.3 – 1.4 (moderate-good correlation). The high correlation at the short(er) interevent distances due to the tightly spaced aftershock sequences should have been expected, but the interesting observation here is that the time dependence of earthquake occurrence in the mixed background-and-aftershock process is correlated over long distances, implying the existence of long range interactions in the mixed process.

The analysis of the declustered NCEDC catalogue is shown in Figure 5b. The magnitude entropic index q_M behaves in a manner similar to its raw counterpart. It can be seen to vary between 1.48 and 1.52, with the corresponding proxy *b*-values varying between 1.08 and 0.92. The temporal entropic index q_T begins with a correlated process (q_T = 1.41 – 1.52 at Δd < 150km), which is attributed to near field interaction between nearby earthquake pairs and at longer interevent distances drops to 1.2 – 1.37 (low – moderate correlation).

5. Discussion and Conclusions

The present work marks the beginning of a systematic attempt to test this proposition: Insofar as earthquakes occur as manifestations of a complex non-extensive seismogenetic system, their frequency of occurrence should be related to the magnitude, the interevent time and the interevent distance by multidimensional power-laws consistent with the formalism of Non-Extensive Statistical Physics (NESP). The problem is addressed by constructing multivariate empirical earthquake frequency distributions with respect to the parameters quoted above, rigorously approximating them with theoretical models based on the NESP formalism and evaluating the results relative to the established ken on earthquake statistics. The case study reported herein is focusing on aspects of North Californian (USA) seismicity.

The results indicate that NESP is an excellent descriptor of the statistical physics of earthquakes. Provided that the multivariate empirical frequency distributions are based on a sufficient number of observations – a few hundred is an empirical lower limit – the results are stable and consistent with the established ken, irrespective of the magnitude and spatio-temporal range of the earthquake catalogue, or operations pertaining to re-sampling, bootstrapping or re-arrangement of the catalogue. In this sense the NESP formalism appears to apply to Northern Californian earthquake statistics and with time and due testing, may prove to comprise a universal descriptor of seismicity.

With respect to Northern Californian seismicity, the analysis of the size (energy) distribution of earthquakes yielded results consistent with a correlated sub-extensive system; the results are also compatible with observations based on conventional measures of scaling and self-organization, with particular reference to the *b*-value. There is also evidence for variation in the size distribution: the scaling of earthquake sizes appears to decrease for cut-off magnitudes larger than four, albeit by a very small factor. At this point, however, it cannot be positively determined whether this is a natural phenomenon, peculiarity of the catalogue, or a statistical/modelling artefact; the existing evidence is limited and does not warrant additional discussion and inference.

The analysis of interevent times, i.e. the time dependence of earthquake occurrence, has determined the existence of sub-extensivity and near-field interaction (correlation) in the complete record of North Californian seismicity (the raw catalogue comprising of mixed background

earthquake activity and aftershock processes), as well as in the background process alone (declustered catalogue). The former is attributed to the joint effect of near-field interaction between neighbouring earthquakes or seismic areas *and* interaction within the tightly spaced and correlated aftershock sequences. The latter is attributed to near-field interaction only. Good far-field correlation (between distant earthquake pairs) was detected only in the mixed process; which also yields evidence of the correlation strengthening for cut-off magnitudes larger than four. The background process appears to be moderately – weakly correlated at the far field. Properly random temporal processes ($q_T \approx 1$) have *not* been detected.

A general syllogism affordable by the above observations is that aftershock sequences may be an integral part of the seismogenetic process, as they appear to partake in long-range interaction. A formal explanation of such an effect is pending, but may nevertheless involve delayed remote triggering of seismic activity by (transient or static) stress transfer from the main shocks and large aftershocks and/or cascading effects already discussed by Marsan and Lengliné (2008). In this view, the effect weakens when aftershocks are removed because aftershocks are the link between the main shocks and their remote offshoot.

As a general conclusion, it may be stated that the expression of seismicity at Northern California is generally consistent with non-extensive (sub-extensive) thermodynamics. The NESP formalism, although far from having settled the questions and debates on the statistical physics of earthquakes, appears, nevertheless, to be an effective and insightful tool in the investigation of seismicity and its associated complexity.

6. Acknowledgments

This work was supported by the THALES Program of the Ministry of Education of Greece and the European Union in the framework of the project "Integrated understanding of Seismicity, using innovative methodologies of Fracture Mechanics along with Earthquake and Non-Extensive Statistical Physics – Application to the geodynamic system of the Hellenic Arc - SEISMO FEAR HELLARC".

7. References

Abe S. and N. Suzuki 2005. Scale-free statistics of time interval between successive earthquakes, *Physica A,* 350, 588-596.

Abe S., Suzuki N. 2003. Law for the distance between successive earthquakes. *J. Geophys. Res*., 108 (B2), 2113.

Baiesi M. and Paczucki M. 2004. Scale-free networks of earthquakes and aftershocks, *Phys. Rev. E*, 69, 066106; doi: 10.1103/PhysRevE.69.066106.

Bak P. and C. Tang 1989. Earthquakes as a self-organized critical phenomenon. *J. Geophys. Res.*, 94, 15635-15637.

Bak P., Christensen K., Danon L. and T. Scanlon 2002. Unified Scaling Law for Earthquakes. *Phys. Rev. Lett.*, 88, 178501.

Carbone V., Sorriso-Valvo L., Harabaglia P., Guerra I., 2005. Unified scaling law for waiting times between seismic events, *Europhys. Lett.*, 71 (6), p. 1036 (2005) doi: 10.1209/epl/i2005-10185-0

Celikoglu A., Tirnakli U., and Duarte Queir´os S., 2010: Analysis of return distributions in the coherent noise model, *Phys. Rev. E*, 82, 021124, doi:10.1103/PhysRevE.82.021124.

Corral A. 2004. Long-Term Clustering, Scaling, and Universality in the Temporal Occurrence of Earthquakes, *Phys. Rev. Lett.*, 92 (10), 108501; DOI: 10.1103/PhysRevLett.92.108501

Eaton J.P. 1992. Determination of amplitude and duration magnitudes and site residuals from short-period seismographs in Northern California. *Bull. Seism. Soc. Am*., 82 (2), 533-579.

Gell-Mann M. and Tsallis C. (eds.), 2004. Nonextensive Entropy – Interdisciplinary Applications. Oxford University Press, New York.

Gutenberg B. and Richter C.F. 1944. Frequency of earthquakes in California, *Bull. Seismol. Soc. Am.*, 34-4, 185-188.

Marsan D. and Lengliné O. 2008. Extending earthquakes's reach through cascading, *Science,* 319, 1076; doi: 10.1126/science.1148783

Moré J.J. and Sorensen D.C. 1983. Computing a Trust Region Step, *SIAM Journal on Scientific and Statistical Computing*, 3, 553–572.

Ogata, Y. 1988. Statistical models for earthquake occurrences and residual analysis for point processes, *J. Am. Statist. Assoc.,* 83, 9–27.

Reasenberg P. 1985. Second-order moment of central California seismicity, 1969-82, *J. Geophys. Res.*, 90, 5479

Saichev A. and Sornette D. 2012. Fertility Heterogeneity as a Mechanism for Power Law Distributions of Recurrence Times. arXiv:1211.6062, available online at http://arxiv.org/abs/1211.6062v1 (last access 31 January 2013).

Silva R., Franca G.S., Vilar C.S., Alcaniz J.,S., 2006. Nonextensive models for earthquakes. *Physical Review E*, 73, 026102. doi:10.1103/PhysRevE.73.026102.

Sornette A. and Sornette D. 1989. Self-organized criticality and earthquakes, *Europhys. Lett*., 9, 197-202.

Sotolongo-Costa O. and Posadas A. 2004. Tsalli's entropy: A non-extensive frequency-magnitude distribution of earthquakes, *Phys. Rev. Letters*, 92 (4), 048501; doi:10.1103/PhysRevLett.92.048501.

Steihaug T. 1983. The Conjugate Gradient Method and Trust Regions in Large Scale Optimization, *SIAM Journal on Numerical Analysis*, 20, 626–637.

Telesca L. 2011. Tsallis-based nonextensive analysis of the Southern California seismicity. *Entropy*, 13, 1267-1280.

Telesca L. 2012. Maximum Likelihood Estimation of the Nonextensive Parameters of the Earthquake Cumulative Magnitude Distribution, *Bull. Seismol. Soc. Am.*, 102, 886-891.

Touati S., Naylor M. and Main I.G., 2009. Origin and Nonuniversality of the Earthquake Interevent Time Distribution. *Phys. Rev. Letters,* 102, 168501; doi: 10.1103/PhysRevLett.102.168501

Tsallis C. 1988. Possible generalization of Boltzmann-Gibbs statistics. *Journal of Statistical Physics*, 52: 479–487. doi:10.1007/BF01016429.

Tsallis C. 2009. Introduction to Nonextensive Statistical Mechanics: Approaching a Complex World. *Springer Verlag*, Berlin, 378pp.

Uhrhammer B. R. A., Loper S. J., and Romanowicz B., 1996. Determination of local magnitude using BDSN Broadband Records, *Bull. Seism. Soc. Am.*, 86 (5), 1314-1330.

Vallianatos F. and Sammonds P. 2013. Evidence of non-extensive statistical physics of the lithospheric instability approaching the 2004 Sumatran-Andaman and 2011 Honshu mega-earthquakes, *Tectonophysics* (2013), doi: 10.1016/j.tecto.2013.01.009.

Vallianatos F., Michas G., Papadakis G. and Tzanis A., 2013. Evidence of non-extensivity in the seismicity observed during the 2011–2012 unrest at the Santorini volcanic complex, Greece, *Nat. Hazards Earth Syst. Sci.*, 13, 177–185; doi:10.5194/nhess-13-177-2013.

Vallianatos F., Michas G., Papadakis G., Sammonds P., 2012. A non-extensive statistical physics view to the spatiotemporal properties of the June 1995, Aigion earthquake (M6.2) aftershock sequence (West Corinth rift, Greece). *Acta Geophysica*, 60, 3, 758-768.

Vallianatos F. and Telesca L. (Eds.), 2012.. Statistical Mechanics in Earth Physics and Natural Hazards, *Acta Geophysica*, 60, 499–501.

Δελτίο της Ελληνικής Γεωλογικής Εταιρίας, τομ. XLVII , 2013
Πρακτικά 13ου Διεθνούς Συνεδρίου, Χανιά, Σεπτ. 2013

Bulletin of the Geological Society of Greece, vol. XLVII 2013
Proceedings of the 13th International Congress, Chania, Sept. 2013

THE CLEARWATER PROJECT: PRELIMINARY RESULTS FROM THE GEOPHYSICAL SURVEY IN TYMPAKI, CRETE, GREECE

Vafidis A.[1], Andronikidis N.[1], Hamdan H.[2], Kritikakis G.[1], Economou N.[1], Panagopoulos G.[1], Soupios P.[3], Steiakakis E.[1] and Manoutsoglou E.[1]

[1] Technical University of Crete, Department of Mineral Resources Engineering, vafidis@mred.tuc.gr

[2] A.C.E.S. Riyadh, Abn Rashiq Street, Building No. 6, Riyadh, Saudi Arabia,

[3] Technological Educational Institute of Crete - Branch of Chania, Department of Natural Resources & Environment

Abstract

One of the most important environmental problems in coastal areas is the salinization of ground water. The groundwater contamination due to seawater intrusion is usually caused by a violation of a delicate hydrogeological balance that exists between freshwater and seawater in coastal aquifers. The development of a methodology for the prediction of the systematic sea water intrusion can contribute to the planning of effective prevention measures in the coastal areas. The geophysical techniques offer a suitable non-invasive method for determining the geometric characteristics of an aquifer and monitoring the saline water intrusion. Among all geophysical techniques, the most successful methods, concerning the detection of salinization in the coastal areas, are the electric resistivity and electromagnetic methods. Seismic methods can also help in providing further geological information for the stratigraphy. In this work, we present the preliminary results from the geoelectrical survey conducted in Tympaki basin (Herakleio, Greece) within the framework of the project "geophysiCaL basEd hydrogeologicAl modeling to pRevent pollution from sea WATER intrusion at coastal areas".

Key words: *Seawater intrusion, electrical tomography, Tympaki, CLEARWATER.*

Περίληψη

Ένα από τα σημαντικότερα περιβαλλοντικά προβλήματα, που εντοπίζονται στις παράκτιες περιοχές, είναι η υφαλμύρινση. Η διείσδυση του θαλασσινού νερού οφείλεται στην ανατροπή του ευαίσθητου ισοζυγίου μεταξύ του γλυκού και θαλασσινού νερού. Η ανάπτυξη μιας ολοκληρωμένης μεθοδολογίας με στόχο τον εντοπισμό επέκτασης του μετώπου υφαλμύρωσης στους παράκτιους υδροφορείς, αποτελεί ένα χρήσιμο εργαλείο για τον αποτελεσματικό σχεδιασμό μέτρων αποτροπής της υφαλμύρινσης.. Οι γεωφυσικές τεχνικές αποτελούνμια κατάλληλη, μη καταστρεπτική μέθοδο, για τον προσδιορισμό των γεωμετρικών χαρακτηριστικών του υδροφορέαυ και την παρακολούθηση της διείσδυσης του θαλασσινού νερού. Η μέθοδος της ειδικής ηλεκτρικής αντίστασης και η ηλεκτρομαγνητική μέθοδος είναι οι πιο επιτυχείς γεωφυσικές μέθοδοι, στην παρακολούθηση επέκτασης του μετώπου

υφάλμυρου/γλυκού νερού, ενώ οι σεισμικές μέθοδοι συμπληρώνουν την πληροφορία που αφορά την στρωματογραφία. Στην παρούσα εργασία, παρουσιάζονται τα προκαταρκτικά αποτελέσματα της γεωηλεκτρικής γεωφυσικής διασκόπησης που πραγματοποιήθηκε στο Τυμπάκι Ηρακλείου, στα πλαίσια του ερευνητικού έργου «geophysiCaL basEd hydrogeologicAl modeling to pRevent pollution from sea WATER intrusion at coastal areas».
Λέξεις κλειδιά: *Υφαλμύρινση, ηλεκτρική τομογραφία, Τυμπάκι, CLEARWATER.*

1. The CLEARWATER Project

Coastal areas are densely populated, since they provide the best conditions for both economical development and quality of life. On the other hand, these regions suffer more than other areas from scarcity of fresh groundwater due to seawater intrusion into coastal aquifers. In most cases, the balance between freshwater/seawater is disturbed by groundwater over pumping and other human activities that lower groundwater level and ultimately cause seawater intrusion into the coastal area.

The consequences of this phenomenon can be catastrophic for the coastal aquifers, especially in the areas where the climate is arid or semi-arid, the groundwater is inadequate and the rainfall is the main source of freshwater. In such cases, the problem of sea water intrusion is irreversible and the effective prediction tools are of vital importance for preventing salinization.

The project "CLEARWATER" (geophysiCaL basEd hydrogeologicAl modeling to pRevent pollution from sea WATER intrusion at coastal areas) aims to develop an integrated approach for prediction the saltwater intrusion in coastal area that enhances the planning effective prevention measures in coastal areas. This methodology is based on modelling, monitoring and management of the groundwater. The key idea is the use of combinedgeophysical methods in order to monitor the evolution of the salinity boundaries, while the innovation of this project is the development of a comprehensive geophysical data processing tool which will guide the modelling and management process providing additional hydrogeological parameters.

The geophysical methods provide continuous subsurface structural information with low costs. Among all geophysical techniques, the most successful methods, concerning the detection of seawater intrusion, are the electrical and electromagnetic methods due to their sensitivity to the presence of the chlorine ion. Seismic methods can also help in providing information to locate fracture zones.

The geophysical methods have been widely used for assessing intrusion of seawater into coastal aquifers. Specifically, the electrical resistivity (Imhof et al., 2001; Kuras et al., 2005; Nguyen et al., 2009; Hamdan and Vafidis, 2009) and electromagnetic methods (Danielsen et al., 2003; Kafri and Goldman, 2005; Nielsen et al., 2007) have been proven to be powerful tools for the detection of the salt water presence in the aquifer. On the other hand, seismic methods are also widely used for depth imaging of complex structures (Haeni, 1986; Jarvis and Knight, 2002; Balia et al., 2003). The conventional way of combining the information provided by these methods is by means of joint interpretation of their processed data. This requires an experienced interpreter and often it's difficult to find a geological model which satisfies all available geophysical data.

Recently, different techniques have been developed to accommodate the interpretation process. Most of these techniques are based on the joint inversion of the different data sets, in order to achieve a unified geological model which will satisfy all the available geophysical data. The joint inversion techniques reduce the uncertainty arising from the non-uniqueness of the individual inversion (Zhang and Morgan, 1997; Gallardo and Meju, 2003; Candansayar and Tezkan, 2008). However, the efficiency of these techniques is still examined, especially in regions of complex geology. The CLEARWATER project focuses on the development of electric, electromagnetic and seismic joint inversion schemes, targeting to be applied at selected coastal areas for the detection of sea water intrusion.

More specifically, in the project CLEARWATER, two study areas were selected, namely Tympaki, Crete, Greece and Bafra Plain, Samsun, Turkey, using the following criteria: (a) The site must face sea water intrusion problems at early stages. (b) It must have agricultural, tourist or any other economical and social activity. (c) It must be located in the Black Sea region or in other region facing similar sea water intrusion problems. (d) It is necessary to have access to geological – hydrogeological data and boreholes.

A total of 8 sites were proposed from the partners. The evaluation system developed for the needs of the site selection is based on 15 factors extracted from the above criteria. Each factor is given a grade on a scale to 5, where the highest grade (5) denotes the most propitious condition for the application of the developed methodology, while zero value denotes that the site is inappropriate. In this work, we present the preliminary results from the geoelectrical survey conducted in Tympaki area in Crete.

2. Geological and Hydrogeological Setting of Tympaki Area, Crete, Greece

Tympaki area is located in the south central part of of Crete (Fig. 1). Tympaki is part of the Messara geological basin and was selected as test site for the application of the methodologies which will be developed by the project CLEARWATER. Farming, mainly greenhouses, citrus and olive groves comprise the main human activities in Tympaki resulting to widely developed irrigation systems. More than 7,800 hectares are cultivated, 4,000 of which are irrigated. Irrigation is performed exclusively by groundwater extraction, amounting to 7,000,000 m^3 per year.

In Crete, a large number of faults indicate an intense tectonic activity in the region. The tectonic setting affected the integrity and continuity of the lithostratigraphic units and the faults bring in contact different lithostatigraphic units with different hydrogeological characteristics.

Neogene deposits in Messara basin have undergone multidirectional extensional tectonic events with intervals of small, in duration and intensity degree of compression. Tympaki sub-basin is separated from the rest Messara basin by Festos horst. It is filled with Neogene deposits, which are regarded as aquitard and it separates hydrogeologically the Tybaki basin from the eastern part of Messara basin. There is only an approximately 2km - wide passage through the horst, on which Geropotamos river flows towards the west.

Tympaki sedimentary basin was formed and evolved during Miocene. Pleistocene and Holocene deposits dominate in the study area. The Neogene formation crops out mainly to the north of the study area and underlies the Pleistocene deposits.

The Pre-Neogene formation crops out mainly to the north of the study area. The geological contact of the Neogene with the Pre-Neogene formations (mainly represented by limestones) is tectonic in the form of a fault with major direction W-SW to E-NE.

All deposits show heterogeneous sequences of conglomerates, cobbles, sands, marls and clays with rapid lateral and vertical lithological changes, making the correlation of layers a difficult task.

Generally, the marly Neogene deposits act practically as impermeable layers, while the coarser and uncemented quaternary deposits are the permeable units. The upper Pleistocene and recent deposits have an average thickness of 120m in the south part of the basin and 90m in the north while the thickness of Pleistocene deposits is more than 200 m.

The availiable geological and hydrogeological studies (show that three hydrogeological units exist in the area: a) the Upper Pliocene to Quaternary formation aquifer, b) the Middle Miocene to Upper Pliocene formation aquitard and c) the Mesozoic aquifuge formations. The continuity of those formations is interrupted by several faults resulting in a block-faulting structure.

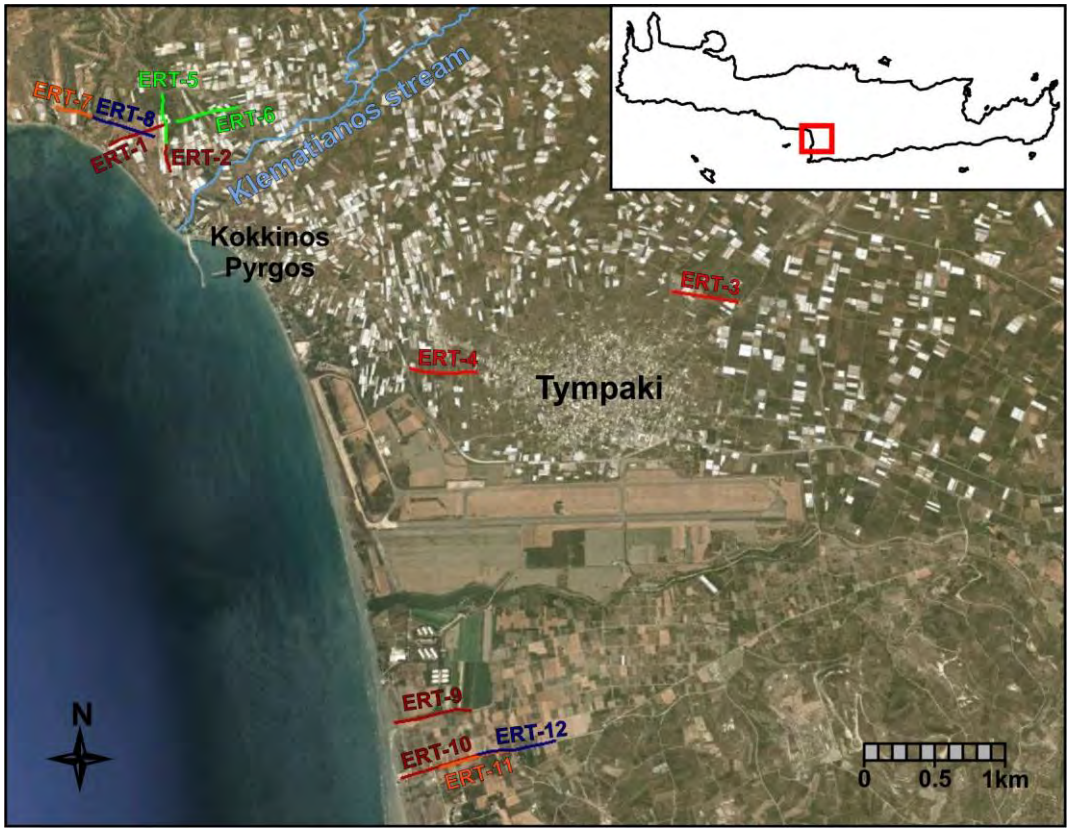

Figure 1 – The area under investigation and the surveyed lines (Google earth™).

The analysis and evaluation of the pumping test data (FAO, 1972), indicate that the average transmissivity (T) of the Neogene and Quaternary deposits reaches 1.7×10^{-1} m^2/sec corresponding to permeability (k) 1.8×10^{-3} m/sec (based on the apparent thickness of the formations/ drilling depth). Moreover, the storage coefficient (S) was estimated at 7.5×10^{-4}, while the specific yield (Sy) was calculated equal to 0.145. However, the above mentioned values are not considered representative for the geological formations of the aquifer. Specifically, the values of T and k are very high compared to values referred in literature (k should vary from 10^{-4} to 10^{-6} m/sec), while the large difference between S and Sy suggests confined aquifer, that is not the case.

These discrepancies in the results of the pumping tests with the expected values from the hydrogeological parameters, are mainly due to the following reasons:

- The wells are not perforated over the full thickness of the aquifer; therefore significant errors arise from the usage of the conventional methods (Dupuit, Jacob, Recovery method).
- The aquifer (Neogene and Quaternary deposits) is heterogeneous (with alternating coarse and fine materials); therefore the permeability varies with depth.
- The well screens extend for all the thickness of each permeable formation (aquifer).
- Aquifuge layers (clay, marl) which overlay water bearing formations (where the screens are extended), create local pressure conditions.

According to a review of the pumping test programme (Paritsis, 2005), transmissivity values in the alluvium exceed 1×10^{-1} m^2/sec. Storage coefficient values are on average around 10% and in coarser grained layers probably reach 15% or more. Transmissivities for the Lower Pleistocene range from 5×10^{-3} to 4×10^{-2} m^2/sec, and the average value being around 1×10^{-2} m^2/sec. Storage

coefficients are estimated to be around 6%. Well yields in the alluvium can exceed 300 m^3/h with a drawdown of a few meters and specific capacities of 100 m^3/h / m drawdown. The pumping levels range between 3 and 7 m above the sea level.

Well yields, ca 200 m^3/h, have been attained also in the Pleistocene, although the specific capacities are remarkably lower (about 15 to 40 m^3/h / m drawdown). Pumping levels range between 20 and 40 m below the sea level.

At the central part of the plain, between Tymbaki and the Klematianos stream (Fig. 1), well yields 100 m^3/h with specific capacities of 20 to 40 m^3/h/m drawdown are observed.

3. Preliminary Results of the Geophysical Survey

Geophysical data have been collected using electrical/electromagnetic geophysical methods in order to map the saline water intrusion. Twelve (12) electrical tomography lines of total 5913 m length were surveyed, using the Wenner-Schlumberger array. 55 electrodes were used in spacings 8.5, 9 and 10 m, resulting to line length ranged from 459 m to 540 m. Sting R1/Swift AGI system collected apparent resistivity data at 21 depth levels per line. The apparent resistivities were subsequently inverted using RES2DINV^{TM} software. The maximum depth of investigation was 100 m. Figure 1 shows the surveyed lines. Based on the preliminary evaluation of the geophysical data and the existing geological and borehole data, we observe that the electrical resistivity ranges from 5 Ohm.m (fine materials of the Pleistocene to recent deposits) to more than 120 Ohm.m (coarse materials). Saline water saturated zones of the Pleistocene and alluvium aquifers exhibit very low electrical resistivity values. Typical geophysical sections show that the Pleistocene deposits at the central part of the plain between Tympaki and Klematianos stream and at depths less than 100 m don't encounter saline intrusion. In particular, the geoelectrical section of ERT-12 (Fig. 2) indicates a low resistivity clay layer whose thickness is around 30 m on top of a higher resistivity zone, attributed to coarser material. According to the geoelectrical section ERT-4 (Fig. 3), the Pleistocene formations are highly heterogeneous. The lower resistivity zone at depths greater than 80 m in ERT-3 (Fig. 4) is attributed to Neogene formations according to a nearby borehole. Figures 5 and 6 present geoelectrical sections from the NE part of Tympaki sub-basin, where groundwater contamination due to sea water intrusion has been observed. More specifically, geoelectrical section ERT-2 indicates that seawater intrusion (very low resistivity) zone is present at depth greater than 30 m. Similar images are given by the electromagnetic method TEM which scanned the Tympaki sub-basin.

4. Conclusions

The preliminary investigation at Tympaki sub-basin, where Neogene deposits unconformably lie over the pre-Neogene basement and Pleistocene to recent deposits lie over the Neogene formation, indicate that the aquifers in these formations are heterogeneous with alternations of coarse and fine materials and exhibit seawater intrusion at depths less than 100 m at NW Tympaki.

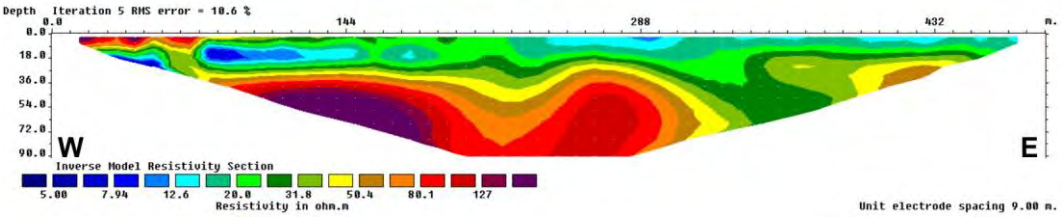

Figure 2 – Geoelectrical section of ERT-12.

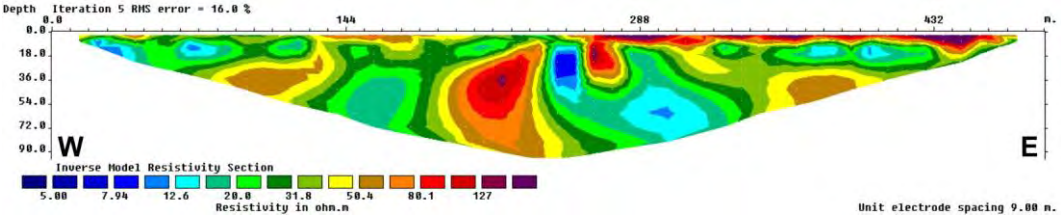

Figure 3 – Geoelectrical section of ERT-4.

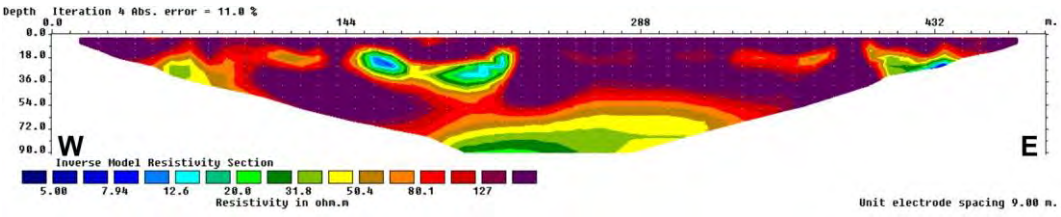

Figure 4 – Geoelectrical section of ERT-3.

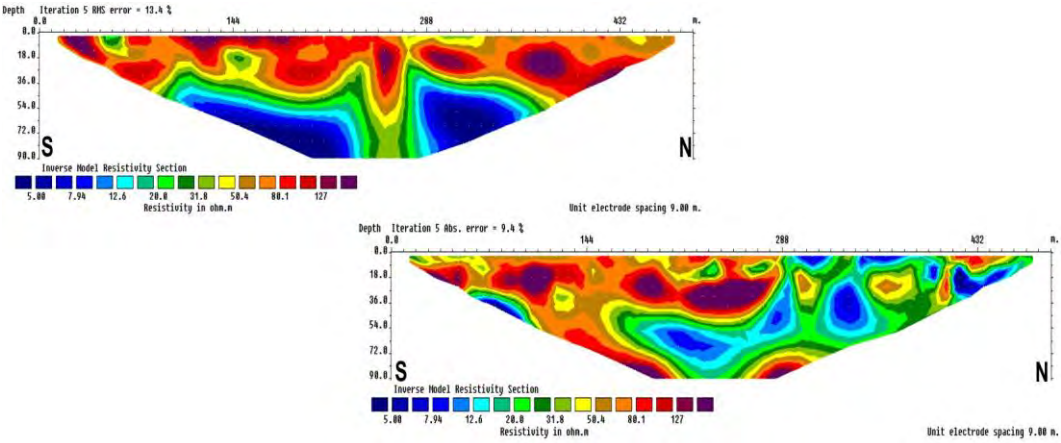

Figure 5 – Geoelectrical sections of ERT-2 (up) and ERT-5 (down). They are 46% overlapped.

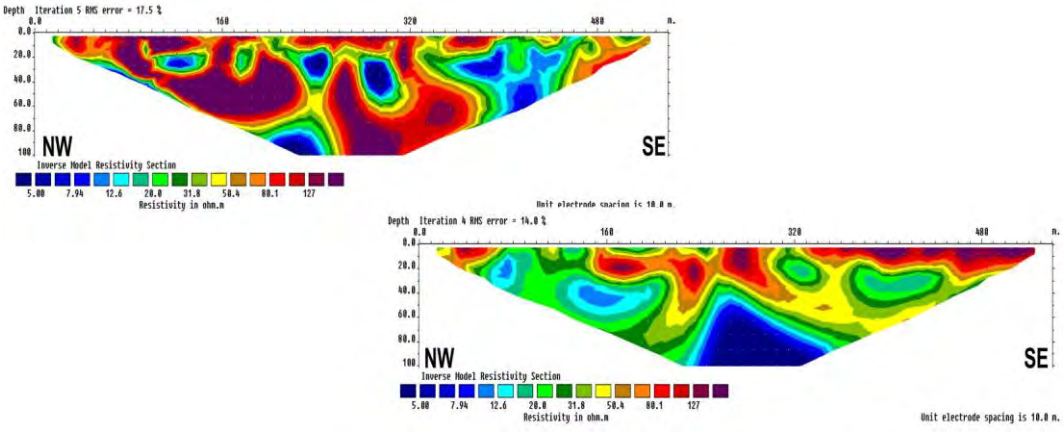

Figure 6 – Geoelectrical sections of ERT-7 (up) and ERT-8 (down). They are 40% overlapped.

5. Acknowledgments

This research has been financed by Greek national funds through the Operational Program "Education and Lifelong Learning" of the National Strategic Reference Framework (NSRF) - Research Funding Program: BS-ERA.NET. Networking on Science and Technology in the Black Sea Region.

6. References

Balia R., Gavaudo E., Ardau F. and Ghiglieri G. 2003. Geophysical approach to the environmental study of a coastal plain, *Geophysics*, Vol. 68, No. 5, 1446-1459.

Candansayar M.E. and Tezkan B. (2008). Two-dimensional joint inversion of radiomagnetotelluric and direct current resistivity data, *Geophysical Prospecting,* 56, 737-749.

Danielsen J.E., Auken E., Jorgensen F., Sondergaard V.H., Sorensen K. L. 2003. The application of the transient electromagnetic method in hydrogeophysical surveys, *Journal of Applied Geophysics*, 53, 181-198.

FAO, 1972. *Study of the water resources and their exploitation for irrigation in eastern Crete – Greece*. *Drillings and pumping tests in Messara AGL:SF/GRE 17/31 tech rep.26*, UNDP, Iraklio.

Gallardo L.A. and Meju M.A. 2003. Characterization of heterogeneous near-surface materials by joint 2D inversion of DC resistivity and seismic data, *Geophys. Res. Lett.*, 30(13), 1658.

Haeni F.P. 1986. Application of seismic refraction methods in groundwater modeling studies in New England, *Geophysics*, Volume 51, No. 2, 236-249.

Hamdan H., Vafidis A. 2009. Inversion techniques to improve the resistivity images over karstic structures, *Proceedings of the 15th European Meeting of Environmental and Engineering Geophysics*, 3–5 September 2009 Dublin, Ireland.

Imhof A. L., Guell A.E., Villagra S.M. 2001. Resistivity sounding method applied to saline horizons' determination in Colonia Loveras-San Juan Province-Argentina, *Brazilian Journal of Geophysics*, Vol.19 (3).

Jarvis K. D. and Knight R. J. 2002. Aquifer heterogeneity from SH-wave seismic impedance inversion, *Geophysics*, Vol. 67, No. 5, 1548-1557.

Kafri U. and Goldman M. (2005). The use of the time domain electromagnetic method to delineate saline groundwater in granular and carbonate aquifers and to evaluate their porosity, *Journal of Applied Geophysics*, 57, 167-178.

Kuras O., Meldrum P.I., Oglivey R.D., Gisbert J., Joretto S., and Sanchez Martos F. 2005. Imaging sea water intrusion in coastal aquifers with electrical resistivity tomography: initial results from the lower Andarax delta, SE Spain, *Proceedings, 11th Annual MeetingEAGE-Near-Surface Geophysics Conference*, Palermo, Sicily, Italy.

Nielsen L., Jorgensen N, O., and Gelting P. 2007. Mapping of the freshwater lens in a coastal aquifer on the Keta Barrier (Ghana) by transient electromagnetic soundings, *Journal of Applied Geophysivs*, Vol. 62, 1-15.

Nguyen F., Kemna A., Antonsson P., Engesgaard P., Kuras O., Ogilvy R., Meldrum Gisbert J., Jorreto S., Pulido-Bosh A. 2009. Characterization of sea water intrusion using 2D electrical imaging, *Near Surface Geophysics*, Special issue on Hydrogeophyics – Methods and Processes, Vol. 7, No.5-6, 377-390.

Paritsis S.N. 2005. Simulation of seawater intrusion into the Tymbaki aquifer, South Central Crete, Greece. *Report within MEDIS*, Study implemented on behalf of the Department of Management of Water Resources of the Region of Crete. Heraklion, Crete, Greece.

Zhang J. and Morgan F.D. 1997. Joint seismic and electrical tomography, *Ann. Symp. Environ. Geophys. Soc. (SAGEEP)*, Exp. Abst., 391- 395.

Δελτίο της Ελληνικής Γεωλογικής Εταιρίας, τομ. XLVII , 2013
Πρακτικά 13ου Διεθνούς Συνεδρίου, Χανιά, Σεπτ. 2013

Bulletin of the Geological Society of Greece, vol. XLVII 2013
Proceedings of the 13th International Congress, Chania, Sept. 2013

ROCK CHARACTERIZATION FOR THE FOUNDATION OF TWO WATER RESERVOIRS USING GEOPHYSICAL AND BOREHOLE DATA

Vafidis A.[1], Andronikidis N.[1], Hamdan H.[2], Kritikakis G.[1], Economou N.[1], Panagopoulos G.[1], Zanettidis S.[1], Merziotis D.[3], Pateras S.[3], Nikoforakis E.[4] and Blais J.P.[4]

[1] Technical University of Crete, Department of Mineral Resources Engineering, Applied Geophysics Lab., Polytechnioupolis, Chania 731 00, Greece, vafidis@mred.tuc.gr
[2] A.C.E.S. Riyadh, Abn Rashiq Str., Building No. 6, Riyadh, Saudi Arabia

[3] "ISTRIA" General Consulting Ltd, 5 Hatziyianni Mexi Str., Athens 115 28, Greece
[4] YDROAIOLIKI AIGAIOY, 15 Kastorias Str., Heraklion, Crete, Greece

Abstract

In this work, we present the results of a geophysical survey at Malia, Crete, Greece. This survey combines VES, electrical tomography and seismic refraction at two sites where equal number of water reservoirs is planned to be constructed for the needs of a hybrid power station using wind-hydro pumping renewable energy. The geophysical sections are interpreted using geological and borehole data. This survey determines the thickness of the overburden, defines the quality of the carbonate bedrock, detects faults and weathered zones in carbonates. One major very low resistivity anomaly was detected at the northern investigated area, which corresponds to completely fractured or weathered limestone, while a 25m deep fracture zone, was detected at the southern investigated area.
Key words: *Electrical tomography, seismic refraction, carbonates, fractured or weathered zones.*

Περίληψη

Σε αυτή την εργασία, παρουσιάζονται τα αποτελέσματα γεωφυσικής διασκόπησης στα Μάλια Κρήτης στην Ελλάδα. Η έρευνα αυτή συνδυάζει τις μεθόδους της ηλεκτρικής βυθοσκόπησης, της ηλεκτρικής τομογραφίας και της σεισμικής διάθλασης σε δύο περιοχές όπου πρόκειται να κατασκευαστούν ισάριθμες λιμνοδεξαμενές για τις ανάγκες ενός υβριδικού σταθμού ηλεκτρικής ενέργειας που θα χρησιμοποιεί αιολική ενέργεια. Η ερμηνεία των γεωφυσικών τομών πραγματοποιείται με τη χρήση γεωλογικών πληροφοριών και δεδομένων από γεωτρήσεις. Ο στόχος της έρευνας είναι ο προσδιορισμός του πάχους των υπερκειμένων σχηματισμών, η εκτίμηση της ποιότητας του ανθρακικού υποβάθρου, καθώς και ο εντοπισμός ρηγμάτων και μεγάλων ζωνών διάβρωσης ή σπηλαίων. Στην βορειότερη περιοχή, εντοπίστηκε κύρια ζώνη χαμηλών ειδικών ηλεκτρικών αντιστάσεων η οποία αποδίδεται στην παρουσία πλήρως διερρηγμένου ή αποσαθρωμένου ασβεστόλιθου, ενώ στην νοτιότερη περιοχή εντοπίστηκε ζώνη κατακερματισμένου ασβεστόλιθου έως τα 25 μέτρα βάθος.
Λέξεις κλειδιά: *Ηλεκτρική τομογραφία, σεισμική διάθλαση, ανθρακικοί σχηματισμοί, ρηγματογόνες ή αποσαθρωμένες ζώνες.*

1. Introduction

The investigated area, located southeast of Malia, Crete, Greece (Figure 1) consists of two sites, where equal number of water reservoirs is planned to be constructed for the needs of a hybrid power station using wind-hydro energy. Both Site M and Site K are located southeast of Malia. The mean elevation of Site M and K is approximately +270 m and +900 m, respectively.

Site M mostly consists of cretaceous carbonates belonging to the Tripoli's zone, covered by thin argillaceous sediments, while Site K consists of upper Triassic carbonates of the Tripoli's zone.

The seismic survey employed the method of seismic tomography. From the first arrivals of direct and head waves we obtained P-wave velocity sections. Twenty (20) seismic lines (11 at the site M and 9 at the site K), with total length of 2925 m, were surveyed. The length of the seismic lines was 55 m, 115 m or 230 m while the geophone interval, 5 m and 10 m distance. Explosives (80g-130g dynamite), seisgun and sledgehammer were used for seismic excitation. Five (5) to seven (7) shot positions per seismic line were utilized. The maximum depth of investigation was, in some cases, more than 25 m.

Seventeen (17) electrical tomography lines (10 at the site M and 7 at the site K) of total 3840 m length were surveyed, using both the dipole-dipole and Wenner-Schlumberger arrays (Hamdan and Vafidis, 2009, Zhou et al, 1999, 2008). The line length ranged from 80 m to 320 m, and the electrode spacing from 2 m to 8 m. Sting R1/Swift AGI system collected apparent resistivity data at 21 depth levels per line. The apparent resistivities were subsequently inverted using RES2DINV^{TM} software. The maximum depth of investigation was 50 m. Figures 1 and 2 illustrate the topographic maps of the investigated sites showing the surveyed lines. Additionally to the initial plan, eight (8) Vertical Electrical Soundings (VES) (5 at the site M and 3 at the site K) were also conducted (not shown on topographic maps) at selected locations. Based on the preliminary evaluation of geophysical data, 16 boreholes were proposed at selected locations of total length of 552 m. The subsequent drilling project, conducted by ISTRIA General Consulting Ltd, consisted of 13 boreholes with total length of 457.6 m. These boreholes were used for the calibration and interpretation of geophysical data (Figure 3).

2. Borehole Data

Borehole data were superimposed on the geoelectrical and seismic sections. Then, the borehole samples were classified according to a) the daily report and the detailed description of borehole logs, b) the electrical resistivity and c) seismic velocity values.

2.1. Rock Classes of Site M

The investigated subsurface of site M was classified to the following six rock classes:

- Completely Fractured and/or Weathered limestone (CFW) was found to correspond to electrical resistivity values 100-600 Ohm.m, seismic velocity less than 2800 m/s and RQD (Rock Quality Designation) values 0-25 at borehole MCD-1 from 8.8 to 34.1 m depth. Voids were also drilled at that range of depth. The same rock class (CFW) is also present in borehole MCD-2 from 12.1 to 17.0 m and from 20.4 to 25 m depth, where again the resistivity (line ML7) and the seismic velocity are relatively low (100-600 Ohm.m and < 2800 m/s, respectively), while the RQD values are less than 25.
- Completely Fractured and/or Weathered limestone to Fractured limestone filled With soil (CFW-FW) is a rock class between CFW and FW (Fractured limestone filled with soil) classes. It is characterized by resistivity values ranging from 450 to 1100 Ohm.m, seismic velocity < 2800 m/s and RQD values 15-35.

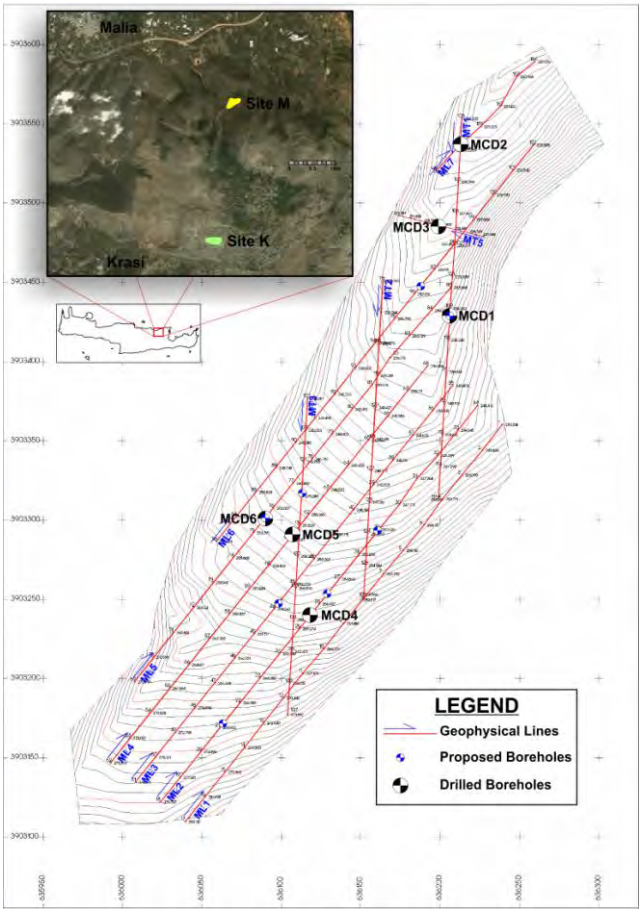

Figure 1 – The area under investigation and topographic map for site M. The surveyed lines and drilled boreholes are shown in red lines and B&W circles respectively. Blue-white circles indicate the positions of the initially proposed boreholes.

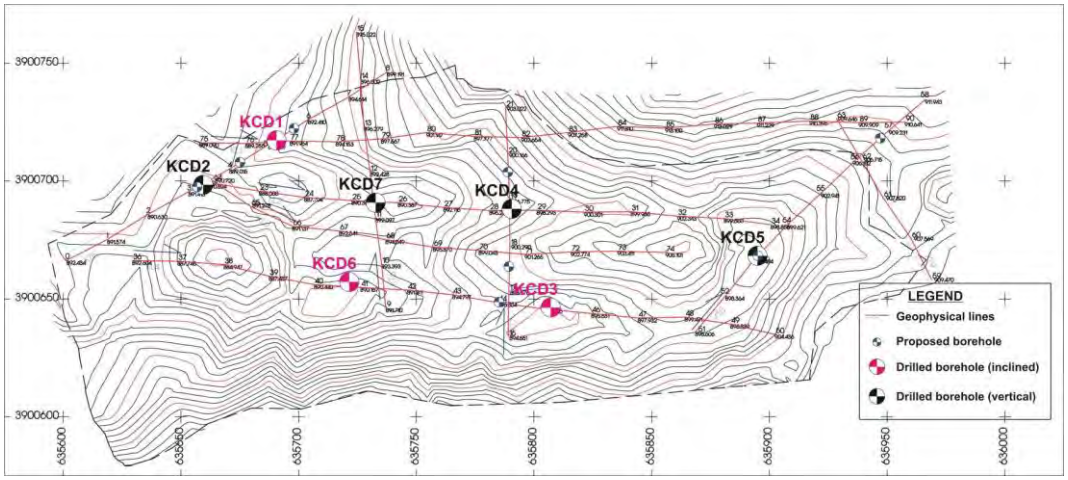

Figure 2 – Topographic map for site K. The surveyed lines are shown in red lines. Drilled boreholes are shown in B&W (vertical) and R&W (inclined) circles. Blue-white circles indicate the positions of the initially proposed boreholes.

- Fractured limestone filled With soil (FW) is present in borehole MCD-5 at depths 1.3 – 6.2 m, 8.1 – 10.1 m, 15.5 – 23.1 m and 25.2 – 30.3 m, where the resistivity values range from 800 to 2000 Ohm.m and the seismic velocity is (in general) less than 2800 m/s. RQD values range from 25 to 50.
- Fractured limestone filled With soil to Fractured limestone (FW-F) and Fractured to Healthy limestone (F-H) are two other rock classes They are characterized by medium (1500 – 3650 Ohm.m) to high (2700-6700 Ohm.m) resistivity values, while the RQD value ranges from 40 to 60 and from 50 to 75, respectively. These rock classes are present in boreholes MCD-4 and MDC-1 at depths 24.5 – 35.5 m and 4.0 – 8.8 m, respectively, and are in good agreement with the ERT sections (i.e. MT1).
- Healthy limestone is characterized by very high (>6700 Ohm.m) resistivity values, while the corresponding RQD value is greater than 75. This rock class has limited presence in boreholes. However, it was found in boreholes MCD-1 (3.0 – 4.0 m) and MCD-6 (7.4 – 11.9 m) which is in good agreement with the ERT sections (i.e. MT1).

2.2. Rock classes of site K

The investigated subsurface of site K was classified to the following four rock classes:

- Fractured - karstified limestones filled with soil, with the indication FW exhibit electrical resistivity values from 1700 to 2500 Ohm.m, seismic velocity from 1700 to 2200 m/s and RQD values 30-40 at borehole KCD-5 from 6.9 to 12.7 m depth. This formation exhibits electrical resistivity values around 800 Ohm.m, similar seismic velocity and RQD values around 50 at the same borehole from 12.7 to 14.8 m depth. At depth from 27 to 30 m the same formation exhibits 2300 m/s seismic velocity and RQD value 50. The formation FW present at borehole KCD-4 (depth from 2.5 to 4.5 m) exhibits seismic velocity below 1400 m/s and RQD 23. At borehole KCD-1 (depth from 38 to 44 m) the FW formation exhibits electrical resistivity values from 800 to 900 Ohm.m, seismic velocity less than 2000 m/s and RQD values from 27 to 51. At small depths (2-8 m, borehole KCD-6) FW exhibits electrical resistivity values less than 800 Ohm.m, seismic velocity less than 200 m/s and RQD values 20-57. Thus, the formation FW is characterized by electrical resistivity values ranging from 400 to 2500 Ohm.m at the geoelectrical sections, seismic velocity from 1800 to 2700 m/s at the seismic sections and RQD values from 23 to 60.
- Fractured - karstified limestones (F) exhibit electrical resistivity values of around 4500 Ohm.m and RQD from 46 to 49 at the borehole KCD-3 from depth of 22.3 m up to 30 m. The seismic velocity of this formation is less than 1800 m/s and RQD values range from 27 to 50 at boreholes KCD-7 and KCD-4.. At borehole KCD-1 this formation exhibited seismic velocity less than 2000 m/s and RQD values from 27-60. Thus, the formation F is characterized by electrical resistivity values around 4500 Ohm.m, seismic velocity less than 2000 m/s and RQD values from 23 to 50.
- Fractured-karstified limestones with voids (F&V) exhibits electrical resistivity values around 4500 Ohm.m, seismic velocity less than 2000 m/s and RQD values from 30 to 50 at borehole KCD2 (depths 17.4 m – 22.4 m). At borehole KCD-6 the same formation showed values lower than 2000 Ohm.m for electrical resistivity, seismic velocity lower than 2500 m/s and RQD values 34-54 at depths 8-16 m. The resistivity of the slightly weathered - fractured limestones (H) is higher than 8200 Ohm.m. The seismic velocity of this formation is higher than 2500 m/s and RQD values range from 63 to 99 at borehole KCD-5 (depths from 14.8 to 27 m). At borehole KCD-2 the seismic velocity of the same formation is around 1400 m/s and the RQD values range from 87 to 99. At the same borehole (depth more than 22.4 m) the seismic velocity exceeds 2500 m/s and RQD values, 90. Their

seismic velocity was more than 3200 m/s at borehole KCD-3 (depth 0-2.5 m and 31.9-40 m), while the corresponding RQD values ranges from 66 to 99 at both cases.

Table 1 - Rock classes at sites M and K

Site	Rock Class	Symbol	Resistivity (Ohm.m)	Velocity (m/s)	RQD
M	Completely Fractured and/or Weathered limestone	CFW	100-600	<2800	0-25
	Completely Fractured and/or Weathered limestone to Fractured limestone filled With soil	CFW-FW	450-1100	<2800	15-35
	Fractured limestone filled With soil	FW	800-2000	<2800	25-50
	Fractured limestone filled With soil to Fractured limestone	FW-F	1500-3650	-	40-60
	Fractured to Healthy limestone	F-H	2700-6700	-	50-75
	Healthy limestone	H	>6700	-	>75
K	Fractured and/or karstified limestone filled with soil	FW	400-2500	1800-2700	23-60
	Fractured and/or karstified limestone	F	4500	<2000	23-60
	Fractured and/or karstified limestone with voids	F & V	4500	2000	30-60
	Healthy or slightly fractured / karstified limestone	H	>8200	>2000	66-99

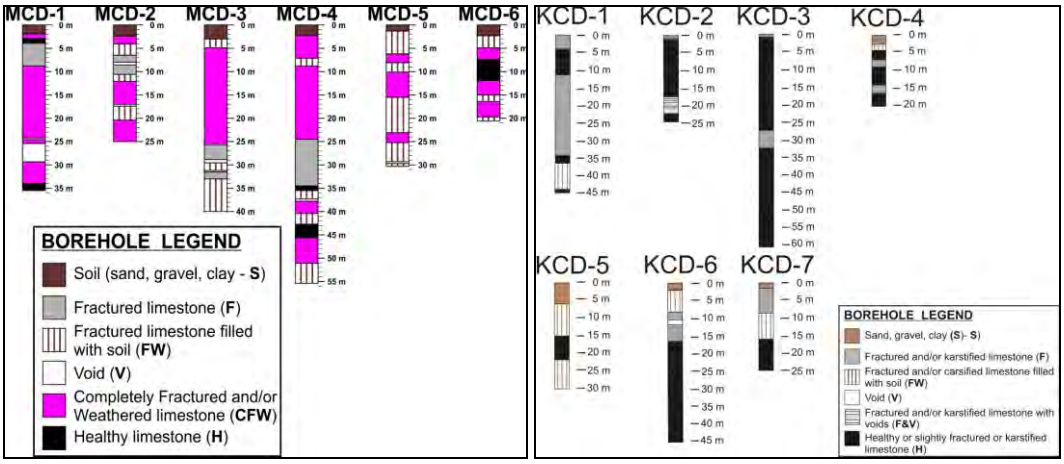

Figure 3 – Borehole logs for site M (left) and site K (right).

- Healthy limestones (H) at borehole KCD-1 (depth 4.5-12 m) exhibit electrical resistivity values more than 8200 Ohm.m and RQD values from 77 to 96, while at borehole KCD-6

(depth greater than 16 m) they exhibit resistivity values from 4000 to 8200 Ohm.m, seismic velocity more than 2600 m/s and RQD from 67 to 98. Thus, formation H is characterized by electrical resistivity values more than 8200 Ohm.m, seismic velocity more than 2500 m/s and RQD values from 66 to 99.

Table 1 and Figure 3 summarize the properties of rock classes drilled at site M and site K.

3. Selected Geophysical Sections

Taking into consideration all borehole and geological data from the Site M and K, we interpreted the geophysical sections. In this part the most representative sections, such as ML-7 and MT-1 from M site and KT-5 and KT-8 are presented.

3.1. Site M

A low resistivity zone (ρ< 600 Ohm.m) is present in the geoelectrical section ML-7 (Figure 4) from the beginning to the 70th m of the ERT line and exhibits seismic velocities less than 2800 m/s. This zone corresponds mainly to CFW class, reaches (according to seismic section) to the depth of 40 m and it is partially interrupted by a shallow high resistivity body (ρ> 3000 Ohm.m). One possible fault (ML7-F1) is indicated at the position where lateral transition from low to high resistivity and seismic velocity values are observed.

Apart from the southern part, the geoelectrical section MT-1 exhibits lower resistivity values (ρ< 600 Ohm.m) almost from the surface, while the seismic velocity is less than 2300 m/s (Figure 5). This zone, corresponds mainly to CFW class, reaches to the depth of 40 m and is partially interrupted by shallow medium to high resistivity (1100 - 3000 Ohm.m) bodies. A possible fault (MT1-F1) is present at the south part of the section.

A major low resistivity anomaly (100-1100 Ohm.m) (rock classes CFW and CFW-FW) is present and extends almost to the northern part of the surveyed area (Figure 6).

3.2. Site K

In the geoelectrical section KT-5 (Figure 7), several very high resistivity anomalies (ρ> 8200 Ohm.m) indicate slightly weathered and/or micro-karstified limestone (H), exhibiting RQD values more than 60. The seismic velocity gradually increases with depth. A lower velocity zone at the middle of the study line coincides with the lower resistivity anomaly from the 70^{th} to the 90^{th} m at the geoelectrical section. RQD values are less than 60 at this highly fractured zone (F) due to the presence of two faults F1 and F2. Lower resistivities in this zone at depths greater than 20 m are in accordance with the borehole which exhibits fracture limestone filled with soil (FW). The formations become highly karstified to the SW at depths greater than 5-10 m (F, FW and V), while the healthy limestone (H) outcrops to the NE.

In the geoelectrical section of KT-8 (Figure 8), a lower resistivity anomaly (ρ< 700 Ohm.m, from the 20th m to 50th m) at depth less than 15 m is attributed to formation S+FW, according to the borehole KCD-5. Seismic velocity is less than 2000 m/s, while RQD values are less than 60. After the 50th m of the ERT line a fractured zone related to faults F2 and F3, extends to 10 m depth. Micro-karstified slightly weathered limestone (H) underlies this zone with increasing RQD values (higher then 80). The same formation (H) outcrops to the NE. Still, moderately fractured limestones are visible in the borehole at depths greater than 22 m.

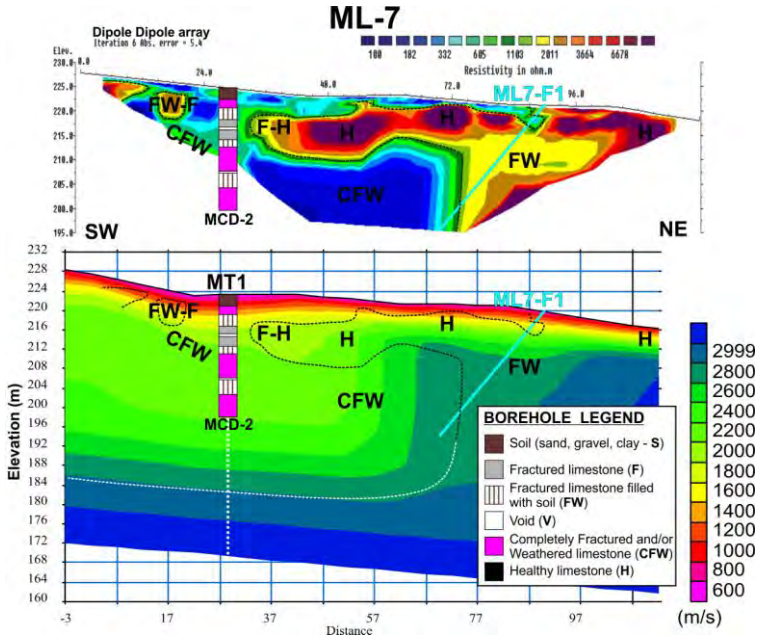

Figure 4 – Interpreted geoelectrical and seismic velocity sections for line MT1. The white dotted lines denote the location of the intersection with lines ML5, ML4, ML3 and ML2. Cyan line indicates possible fault. MCD-1, (projection of) MCD-2 and MCD-3 borehole logs and two VES profiles are also superimposed. Dashed lines separate the classes CFW and CFW-FW from the other classes.

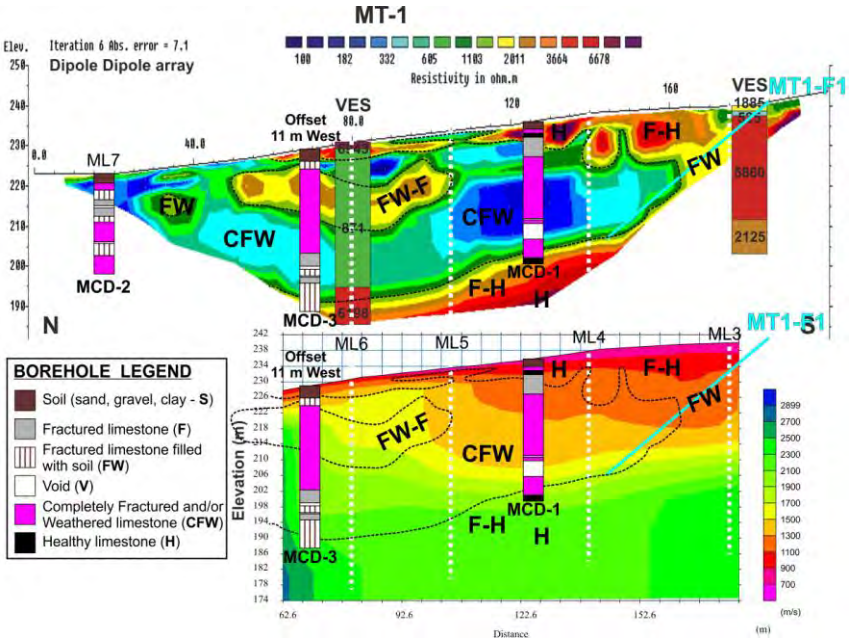

Figure 5 – Interpreted geoelectrical and seismic velocity sections for line MT1. The white dotted lines denote the location of the intersection with lines ML5, ML4, ML3 and ML2. Cyan line indicates possible fault. MCD-1, (projection of) MCD-2 and MCD-3 borehole logs and two VES profiles are also superimposed. Dashed lines separate the classes CFW and CFW-FW from the other classes.

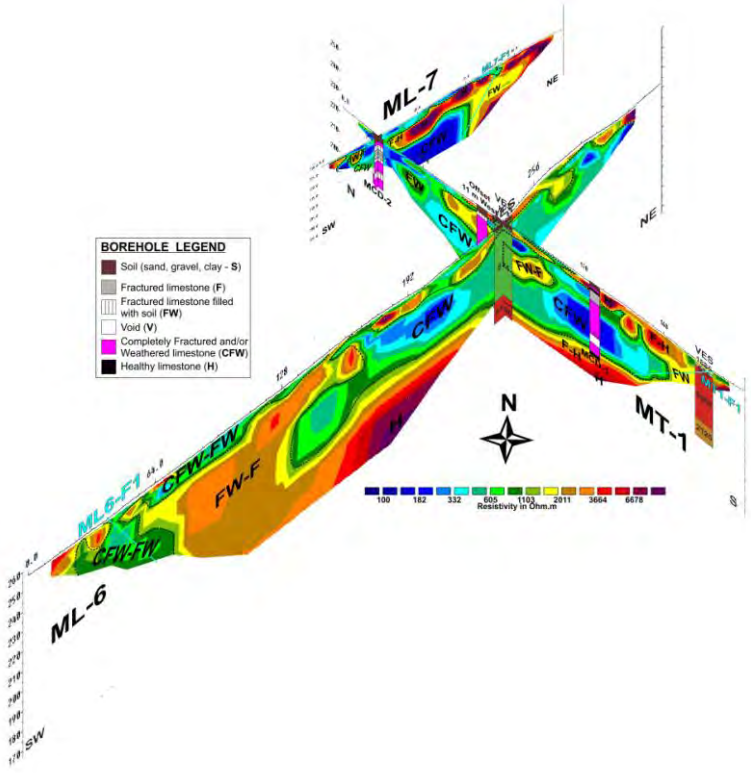

Figure 6 – 3D perspective view of the cross-section between geoelectrical sections of lines ML-6, MT-1 and ML-7. Dashed lines separate the classes CFW and CFW-FW from the other classes.

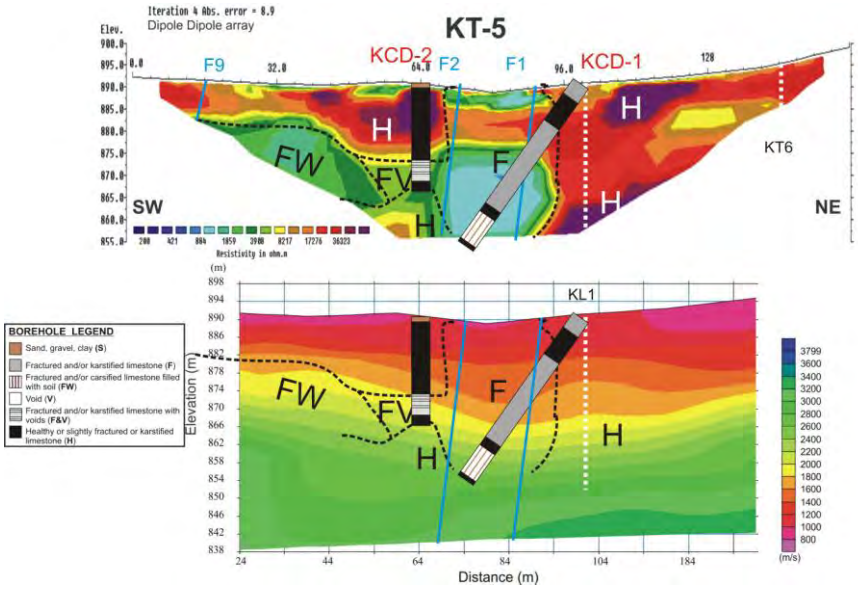

Figure 7 – Interpreted geoelectrical and seismic velocity sections for line KT-5. The white dotted lines denote the location of the intersection with lines KL-1 and MT6. KCD-1 (inclined) and KCD-2 borehole logs are also superimposed.

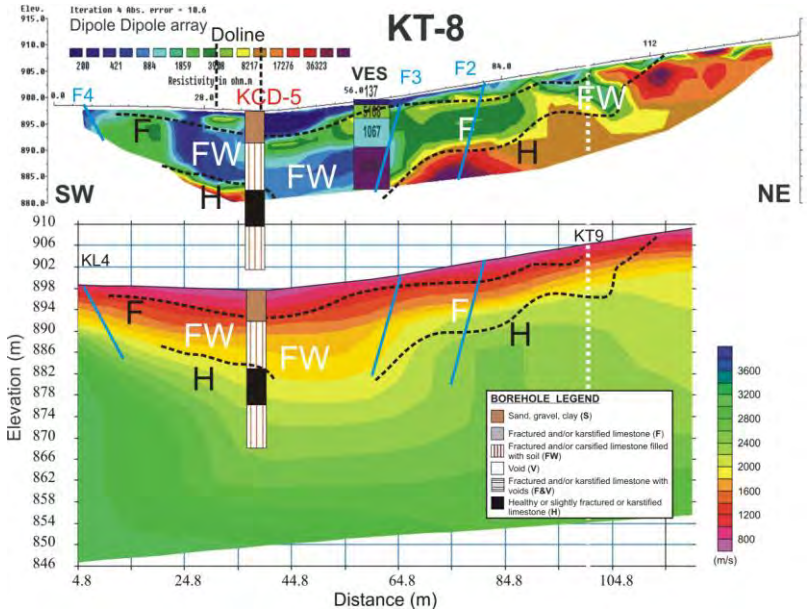

Figure 8 – Interpreted geoelectrical and seismic velocity sections for line KT-8. The white dotted lines denote the location of the intersection with lines KL-4 and KT-9. KCD-5 borehole log and VES are also superimposed.

4. Conclusion

At site M, a very low resistivity anomaly is present at the northern part of the surveyed area. This anomaly is attributed to Completely Fractured - Weathered (rock class CFW) limestone. At site K, based on the pseudo-3D image (Figure 9), the most fractured parts are at the south-east, west, north-west of the reservoir.

5. References

Hamdan H. and Vafidis A. 2009. Inversion techniques to improve the resistivity images over karstic structures, *Proceedings of the 15th European Meeting of Environmental and Engineering Geophysics*, 3–5 September 2009 Dublin, Ireland.

Zhou W.F., Beck B.F. and Stephenson B.J. 1999. Defining the bedrock/ overburden boundary in covered karst terranes using dipole–dipole electrical resistivity tomography. in: Powers MH, Ibrahim AB, Cramer L (eds) *Proc Symp Application of Geophysics to Engineering and Environmental Problems,* Oakland, California, 14–18 March 1999. Environmental and Engineering Geophysical Society, Colorado, pp 331–339.

Zhou W., Beck B. and Adams A. 2008. Effective electrode array in mapping karst hazards in electrical resistivity tomography, *Environmental Geology*, 42: 922-928.

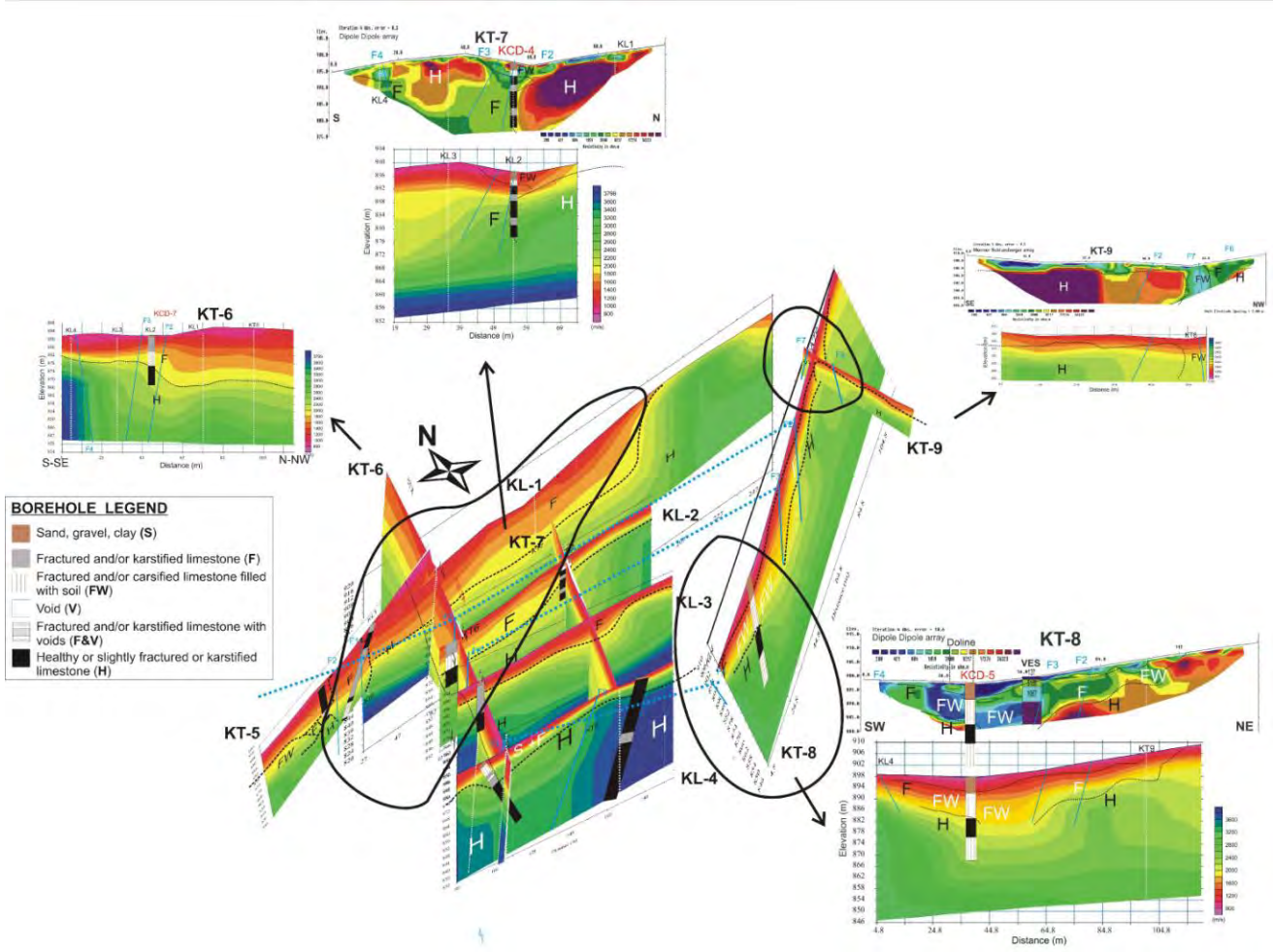

Figure 9 – 3D perspective view of interpreted seismic velocity sections for lines KL1, KL2, KL3, KL4, KT5, KT6, KT7, KT8 and KT9. Thick black lines indicate the most fractured zones.

Δελτίο της Ελληνικής Γεωλογικής Εταιρίας, τομ. XLVII , 2013
Πρακτικά 13ου Διεθνούς Συνεδρίου, Χανιά, Σεπτ. 2013

Bulletin of the Geological Society of Greece, vol. XLVII 2013
Proceedings of the 13th International Congress, Chania, Sept. 2013

GROUND PENETRATING RADAR AND ELECTRICAL RESISTIVITY TOMOGRAPHY FOR LOCATING BURIED BUILDING FOUNDATIONS: A CASE STUDY IN THE CITY CENTRE OF THESSALONIKI, GREECE

Vargemezis G.[1], Diamanti N.[1], Fikos I.[1], Stampolidis A.[1], Makedon Th.[2] and Chatzigogos N.[2]

[1] Aristotle University of Thessaloniki, School of Geology, Department of Geophysics, GR-54124, PO Box 352-1, Thessaloniki, Greece, ndiamant@geo.auth.gr, varge@geo.auth.gr, ifikos@geo.auth.gr, astamp@geo.auth.gr

[2] Aristotle University of Thessaloniki, School of Geology, Department of Geology, GR-54124, Thessaloniki, Greece, thomas@geo.auth.gr; chatzi12@gmail.com

Abstract

Ground penetrating radar (GPR) and electrical resistivity tomography (ERT) surveys have been carried out in the city centre of Thessaloniki (N. Greece), for investigating possible locations of buried building foundations. Geophysical survey has been chosen as a non-destructive investigation method since the area is currently used as a car parking and it is covered by asphalt. The geoelectrical sections derived from ERT data in combination with the GPR profiles provided a broad view of the subsurface. Regarding ERT, high resistivity values can be related to buried building remains, while lower resistivity values are more related to the surrounding geological materials. GPR surveying can also indicate man-made structures buried in the ground. Even though the two geophysical methods are affected in different ways by the subsurface conditions, the processed underground images from both techniques revealed great similarity. High resistivity anomalies and distinct GPR signals were observed in certain locations of the area under investigation, which are attributed to buried building foundations as well as the geological structure of the area.

Key words: *Archaeological prospection, geophysical survey, non-destructive testing, GPR, ERT.*

Περίληψη

Πραγματοποιήθηκε γεωφυσική διασκόπηση με τις μεθόδους του Ραντάρ Υπεδάφους και της Γεωηλεκτρικής Τομογραφίας, στο κέντρο της πόλης της Θεσσαλονίκης (Β. Ελλάδα) για τον εντοπισμό πιθανών οικοδομικών λειψάνων. Οι γεωφυσικές μέθοδοι είναι μη-καταστροφικές και χρησιμοποιήθηκαν σε αυτή την έρευνα μιας και η συγκεκριμένη έκταση λειτουργεί ως πάρκινγκ και είναι καλυμμένη με άσφαλτο. Οι γεωηλεκτρικές τομές σε συνδυασμό με τις οδεύσεις του ραντάρ μας έδωσαν λεπτομερείς εικόνες του υπεδάφους. Οι μεγάλες τιμές στις γεωηλεκτρικές τομογραφίες σχετίζονται με θεμέλια κτιρίων ενώ οι χαμηλές τιμές αποδίδονται στις γεωλογικές αποθέσεις της περιοχής. Επιπλέον, οι μετρήσεις του ραντάρ αποκαλύπτουν τις θαμμένες ανθρωπογενείς δομές. Παρά το γεγονός ότι οι δύο μέθοδοι χαρτογραφούν

διαφορετικές φυσικές ιδιότητες του υπεδάφους, εντούτοις αποκαλύπτουν παρόμοιες δομές. Τελικά, οι γεωηλεκτρικές ανωμαλίες και οι ξεκάθαρες ανακλάσεις στις μετρήσεις ραντάρ παρατηρούνται σε συγκεκριμένες θέσεις της περιοχής που ερευνήθηκε και αποδίδονται σε θαμμένα θεμέλια κτιριακών εγκαταστάσεων αλλά και υφιστάμενες γεωλογικές δομές.
Λέξεις κλειδιά: *Αρχαιολογική έρευνα, γεωφυσική διασκόπηση, μη-καταστροφικές μέθοδοι, ραντάρ υπεδάφους, γεωηλεκτρική τομογραφία.*

1. Introduction

It is well documented during the last decades that geophysical prospecting is increasingly used for detecting and mapping buried archaeological remains and standing monuments. Further, the combination of geophysical methods offers high resolution, detecting features in the order of a few tens of centimetres depth and/or thickness to several metres. Resistivity methods, and more specifically electrical resistivity tomography (ERT), (Tsokas et al., 1994; Diamanti et al., 2005, Papadopoulos et al., 2007, Tsokas et al., 2008a, Tsourlos and Tsokas, 2011) and ground penetrating radar (GPR) (Savvaidis et al., 1999; Leucci, 2002; Piro et al., 2003; Linford, 2004; Tsokas et al., 2007) are two of the most popular methods for doing so.

In this study we present the geophysical survey which was carried out at the parking area situated at the junction of Tsimiski St. and Ethnikis Aminis St., in the city centre of Thessaloniki (N. Greece). This survey was conducted in the framework for the construction of a new, underground parking area below the current one. There are records regarding modern building foundations in the area. The aim of the presented geophysical survey was (a) to study the subsurface geological structures at the location of the parking area and (b) to detect and possibly map buried antiquities under the ground surface. The case presented here comprises an example of a combined geophysical survey for investigating the area of interest. The geophysical methods employed were: ERT and GPR.

2. Geophysical Methods

2.1. Electrical Resistivity Tomography (ERT)

Resistivity techniques are established and widely used to solve a variety of geotechnical, geological and environmental subsurface detection problems. The goal of resistivity methods is to measure the potential differences on the ground surface due to the current flow within the ground. This measured potential drop reflects the difficulty with which the electrical current flows within the subsurface and hence, it gives an indication of the earth's electrical resistivity. Knowledge of the subsurface material resistivity is used for distinguishing existing underground features, such as layering, voids, man-made structures etc.

ERT can be considered as the development of the standard geoelectrical method. The advent of fully automated measuring instruments with electrode multiplexing ability in combination with the development of advanced interpretation algorithms, allows the collection of a large amount of data and the production of electrical resistivity images of the subsurface. The rapid advanced in computer technology during the last decades, allowed the development of automated algorithms, known as inversion algorithms, which are able to create precise images of subsurface resistivity distribution (Tripp et al., 1984; Li and Oldenburgh, 1992; Tsourlos, 1995).

ERT has proved to be a successful method in providing fast and reliable shallow subsurface geoelectrical property images under various field conditions, even in complex geological environments. ERT has been extensively employed in various cases such as in archaeological, geological and hydrogeological studies (Tsourlos et al., 2003; Tsokas et al., 2008b; Vargemezis et al., 2007, Ogilvy et al., 2009; Vargemezis et al., 2009).

2.2. Ground Penetrating Radar (GPR)

GPR is the general term applied to techniques which employ radio waves, typically in the 1 to 1000 MHz frequency range, to map structures and features buried in the ground (or in man-made structures). A GPR unit sends out radio waves that partially reflect back when they meet objects

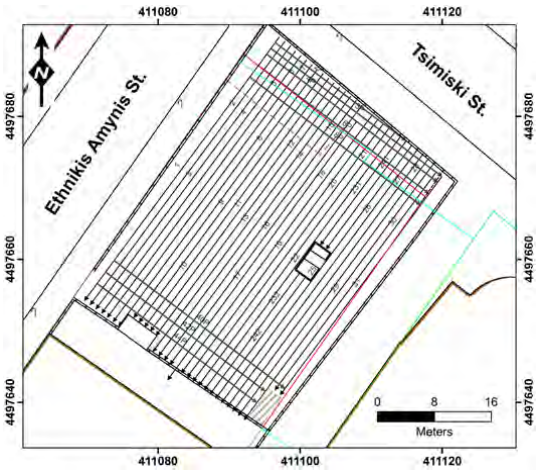

Figure 1 – (a) Plan view of the studied area (arbitrary coordinate system–coordinates in meters). Solid black lines denote the location & arrows the direction of ERT sections.

(b) Subdivisions of Thessaloniki's urban fill (implemented classification scheme proposed by Chatzigogos *et al.*, 2006). *Class A*: Historical fill, *Class B*: Modern fill (1st coastal expansion), *Class C*: Modern fill (2nd coastal expansion).

electrically different than their surroundings, and partially propagate in deeper layers. By recording the time interval between the instant at which the pulse is emitted by the transmitter and is recorded by the receiver, and by knowing its propagation velocity in the subsurface, it is possible to map underground reflectors.

GPR data is typically displayed in a cross-sectional format. We can also create three-dimensional (3D) views of data and also two-dimensional (2D) depth slices using appropriate software. These subsurface slices show how GPR signals vary over a grid area at a certain depth and they are very useful for data interpretation because they can reveal patterns that were not easily recognized while analyzing the cross-sections.

Today GPR is being used in many different areas including locating buried utilities, mine site evaluation, road / bridge / tunnel inspection, forensic investigations, archaeological digs, searching for buried landmines and unexploded ordinances, measuring snow, ice thickness, quality for ski slope management and avalanche prediction (Davis and Annan, 1989; Colla et al., 1997; Guy et al., 2000; Spikes et al., 2004; Diamanti et al., 2008; Solla et al., 2010; Diamanti and Redman, 2012).

3. Geophysical Survey

The geophysical prospecting using ERT and GPR was carried out simultaneously for both methods. One of our goals was to obtain indirect information regarding the near surface and deeper geometry and lithology of the subsurface at the area under study. The site is located just outside the SE part of the ancient city walls. According to geological information, the anticipated stratigraphy comprises of a superficial urban-historical fill of 2-4m thickness, overlying a 4-6m thick soil formation consisting of coastal river deposits (mostly sandy clays to clayey sands with calcareous bodies and rubble). The characteristic red-clay formation of Thessaloniki is expected to

be found 5-7m deep (Anastasiadis et al., 2001). In addition, the site is located very close to the natural coastline of the city, as illustrated in Figure 1b (Chatzigogos et al., 2006). This geophysical survey was part of a more extensive campaign of geological / geotechnical investigations at the area of interest.

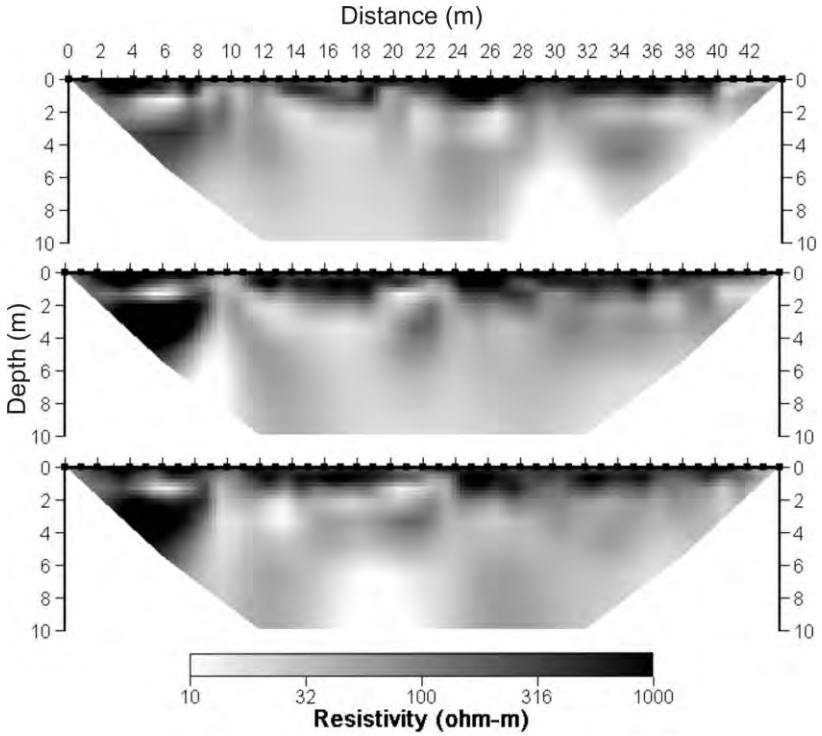

Figure 2 – Examples of the inverted ERT sections 1 to 3 (top to bottom). Depth (left vertical axis) and distance (horizontal axis) are in metres.

3.1. ERT: Data Acquisition, Processing and Results

The surface geological formations at the area of interest allowed for an effective ERT survey since the subsurface resistivity is expected to be small compared to the resistivity of the buried building foundations and antiquities.

We decided on the acquisition parameters of all geoelectrical tomographies so as to achieve ~10 meters depth of investigation. For the measurements we used the Iris Syscal-Pro resistivity meter. It has to be noted that a very important factor for the good quality of ERT measurements is the contact resistance between electrodes inserted into the ground and soil material. This quantity needs to be small so as electrical currents are easier injected into the subsurface. In our case, the ground is covered with asphalt which is a material completely unsuitable for current propagation. In order to restore direct coupling between the electrodes and the subsoil, we decided to drill the asphalt at the locations where the electrodes would be mounted to the ground.

Given the three-dimensional nature of the problem studied, we decided to acquire dense survey lines, to allow full 3D processing of the data (Papadopoulos et al., 2006). We measured a dense grid of parallel – and a few perpendicular – 2D ERT lines. We collected thirty-one linear ERTs in one direction (Figure 1a – NE–SW lines) and eight tomographies perpendicular to the first ones (Figure 1a – lines located almost parallel to Tsimiski St.), all being 1 m away from the other. We chose the dipole-dipole array to perform the survey as it has a good signal to noise ratio, provides the highest resolution and is most sensitive to vertical resistivity boundaries (Griffiths and Barker, 1993). The maximum potential to current electrode separation was n=8 (i.e., eight times the length

of the potential measuring dipole). The inter-electrode spacing was set to a=1.0 m for all ERT sections. In this way, we achieved a maximum penetration depth without sacrificing the resolution.

All measured ERT sections were inverted using DC2dPro (Kim, 2009), while a 3D resistivity model was constructed with DC3dPro (Yi et al., 2001). ERT data were collected on a grid and

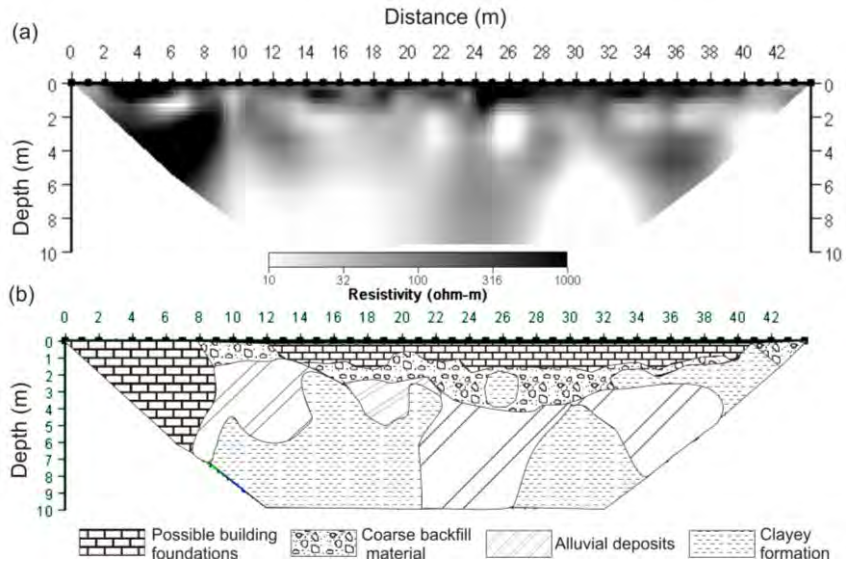

Figure 3 – (a) An inverted ERT section and (b) its possible interpretation.

therefore, apart from the traditional 2D inversion, it was possible to perform 3D processing and presentation of results, which is closer to reality. The 2D and 3D inversion schemes perform an iterative optimization based on a finite element forward modelling scheme. All inversions produced a low misfit error between the real and the predicted data (3%).

Figure 2 presents the inverted results of three indicative geoelectrical sections (the first three lines of Figure 1a, from NE towards SW). All ERT data are presented in either linear or logarithmic grey or rainbow scale. The x-axis of the ERT section is the horizontal distance along the survey line, while the y-axis is the depth, both in metres. All the inverted results of the 2D datasets obtained, depict a similar, characteristic variation in the subsurface resistivity. There seem to be horizontal layering consisting of areas of high resistivity, which is expected at the locations of building foundations. These areas differ significantly from the underlying clay layer. The corresponding layer for the backfill material has strong resistivity variations due to its heterogeneity.

An example of the inversion results with its interpretation is shown in Figure 3. As stated, the building ruins seem to cause a distinctive geoelectrical anomaly which is much different than the one caused by the surrounding formations. The thickness of the layer consisting of backfill / building foundation materials varies and its resistivity ranges from ~100 to ~1000 Ohm-m, since it consists of various materials (e.g., aggregates, cement blocks etc.). In most cases, the building foundations are located at a depth up to ~5 metres. Below this depth, there is a geological formation with resistivity ranging from ~10 Ohm-m – which corresponds to clay materials – to ~80 – 100 Ohm-m – which are values mainly matching materials such as sand, gravel, boulders and in general alluvial deposits (coarser materials).

As discussed previously, resistivity variation is in reality fully 3D. So, in the studied area, we collected parallel 2D ERT lines which were processed with a fully 3D approach, i.e. they were inverted altogether with the DC3dPro inversion software (Yi et al., 2001). The processing scheme

is based on a 3D finite element forward modelling solver. Note that this approach is much more time-consuming compared to the 2D one and can be applied only in areas where several parallel ERT lines (i.e., > 4) are collected. Although the data acquisition is a set of 2D measuring sections, it has been shown that in this case fully 3D imaging is possible when inversion is performed by fully 3D algorithms (Papadopoulos et al., 2006; 2007). Also, the data have to be collected along dense parallel traverses, which ideally should be spaced at intervals equal to the spacing of the electrodes along the traverse. Both these constraints are fulfilled in our case.

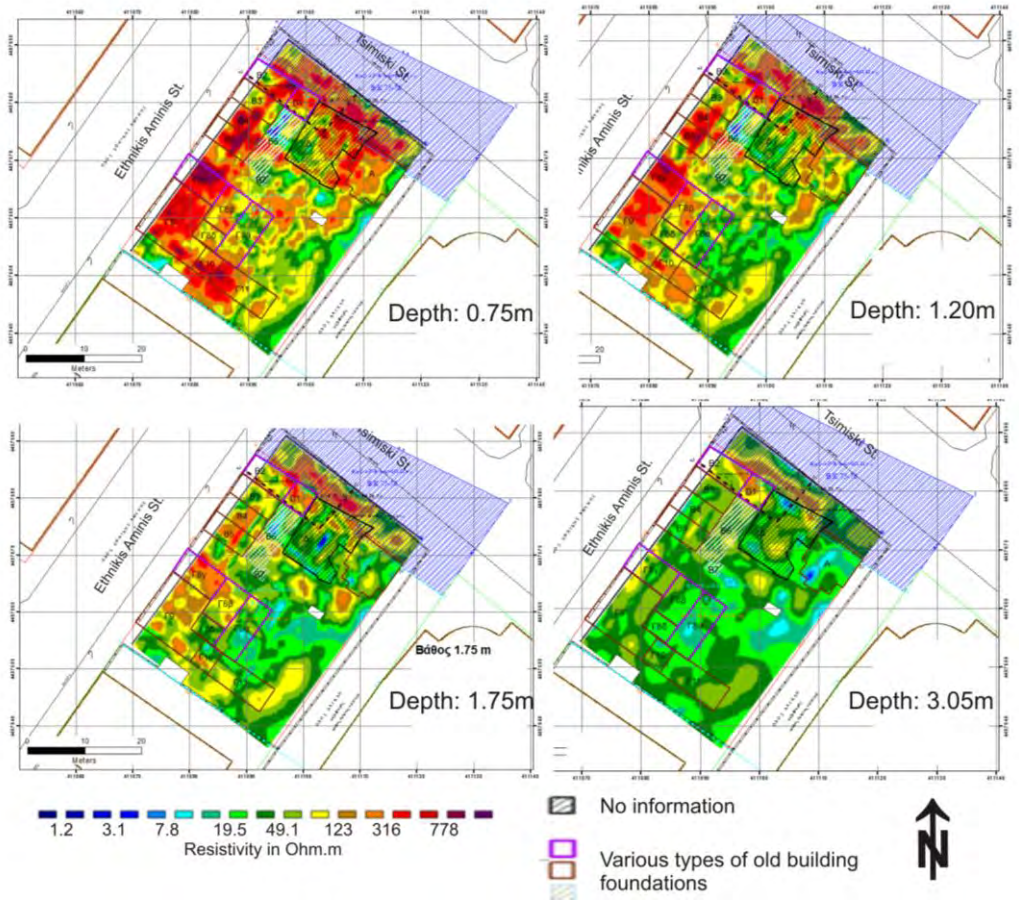

Figure 4 –Depth slices derived from the full 3*D* inversion of the set of ERT sections.

In Figure 4, two-dimensional depth-slices derived from the full three-dimensional inversion of the set of tomographies are presented. The highly resistive outline of the building foundations is clearly distinguished from the less resistive geological materials. The building remains are mainly located up to a depth of 2.5 metres, with the exception of the northern part (parallel to Tsimiski St.) where they extend up to 4.5 metres but with significantly lower values of resistivity. In Figure 5, the three-dimensional resistivity volume for the high and low resistivity values is presented: the high resistivity 3D image delineates realistically the building remains in contrast to the low resistivity image, which corresponds to the surrounding geological formations.

3.2. GPR: Data Acquisition, Processing and Results

We employed GPR to obtain higher resolution images of the subsurface than the ones we got using the ERT technology. We collected fifty-eight GPR profiles on the same locations and acquisition direction as the ERT sections (the sections with direction from NE to SW only–Figure 1a) and also

between them. So, each GPR profile was 0.5 m apart from the other. We used a cart-based 500 MHz GPR system produced by Mala. The trace sampling interval was 0.05 m. We present our GPR data in the standard cross-sectional format. Position is plotted on the horizontal axis, and depth and time on the vertical axes. To convert the time axis into depth, we assumed a constant signal velocity which. This velocity was set equal to 0.11 m/ns and it was determined by using a GPR velocity analysis software by Sensors & Software Inc. Moreover, we present our data as plan view maps (i.e., time/depth slices) which is one of the most widely used way of GPR data presentation, especially in archaeological prospection (Goodman et al., 1995).

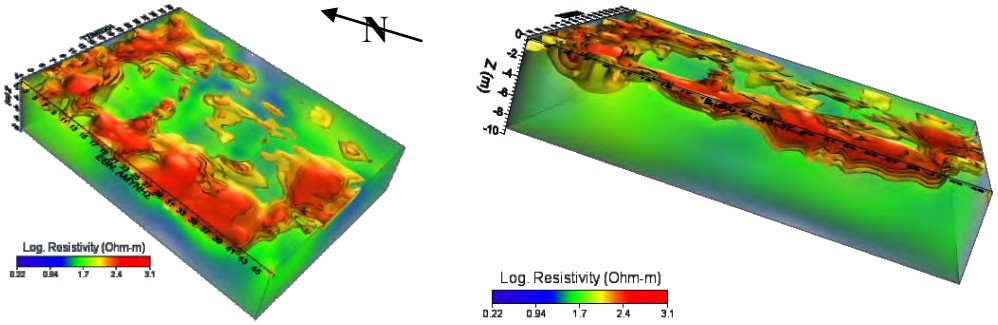

Figure 5 –Three-dimensional geoelectrical views of the subsurface. The bold red colours represent old building foundations under the studied area at various depths.

All GPR profiles were processed using Sensors & Software Inc. software, while the depth slices were produced using the software GPR-SLICE. We applied the same processing to all GPR sections and we purposely used a uniform signal velocity for comparisons between them. We applied a standard dewow filter to remove very low frequency components from the field data. Since GPR signals are very rapidly attenuated as they propagate into the ground, we applied a time dependent gain function to the data to compensate for this decrease in GPR signals from greater depths. We have applied a spherical exponential compensation (SEC) gain to enhance features in the data. We have also applied temporal filtering to the data to remove unwanted frequencies from our signals and to improve data quality and assist interpretation. It should be noted that all indications of targets presented in GPR data are true anomalies even though they may not be the desired targets. Similarly to all geophysical methods, GPR is incapable of giving a false positive reading, which is where experience in reading the records can help the investigator.

Figure 6 presents three cross-sections acquired from NE to SW at various locations of the survey area. Looking at the GPR profiles, it seems that we can obtain a reliable subsurface image up to a depth of ~2.0–2.5 metres. In all fifty-eight profiles collected in this area, we observe various reflections that could be possibly caused by old buildings foundations. Even though each GPR profile can be quite informative, one of the most useful presentations of GPR data sets collected along closely spaced parallel profiles is to display data in horizontal maps. These maps allow easy visualization of the location, depth, size and shape of GPR anomalies into the ground. Figure 7 presents selected depth slices developed from all GPR profiles. These slices are placed on a topographic map indicating locations of old buildings, information which was retrieved from historic records. The plan view maps show several features (orange/red colour) which are believed to be collapsed buildings/foundations.

3.3. Combined ERT and GPR

Even though ERT and GPR are two geophysical methods that are affected in different ways by the subsurface conditions, the processed underground images from both techniques revealed great similarity. An example is shown in Figure 8, which presents an ERT section and a GPR profile that were both acquired along the same line. Both interpreted ERT and GPR reveal similar lateral characterization (Figure 8 – white dashed line) of the near surface features. Moreover, there is a

good agreement on the interpreted thickness / depth of the underlying building foundations between the two methods.

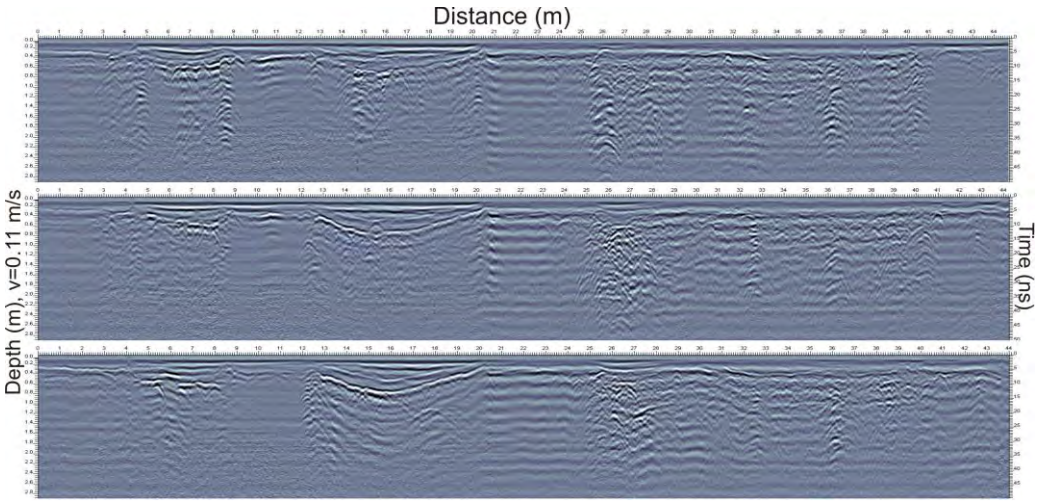

Figure 6 – GPR cross-sections acquired from NE to SW at various locations of the area.

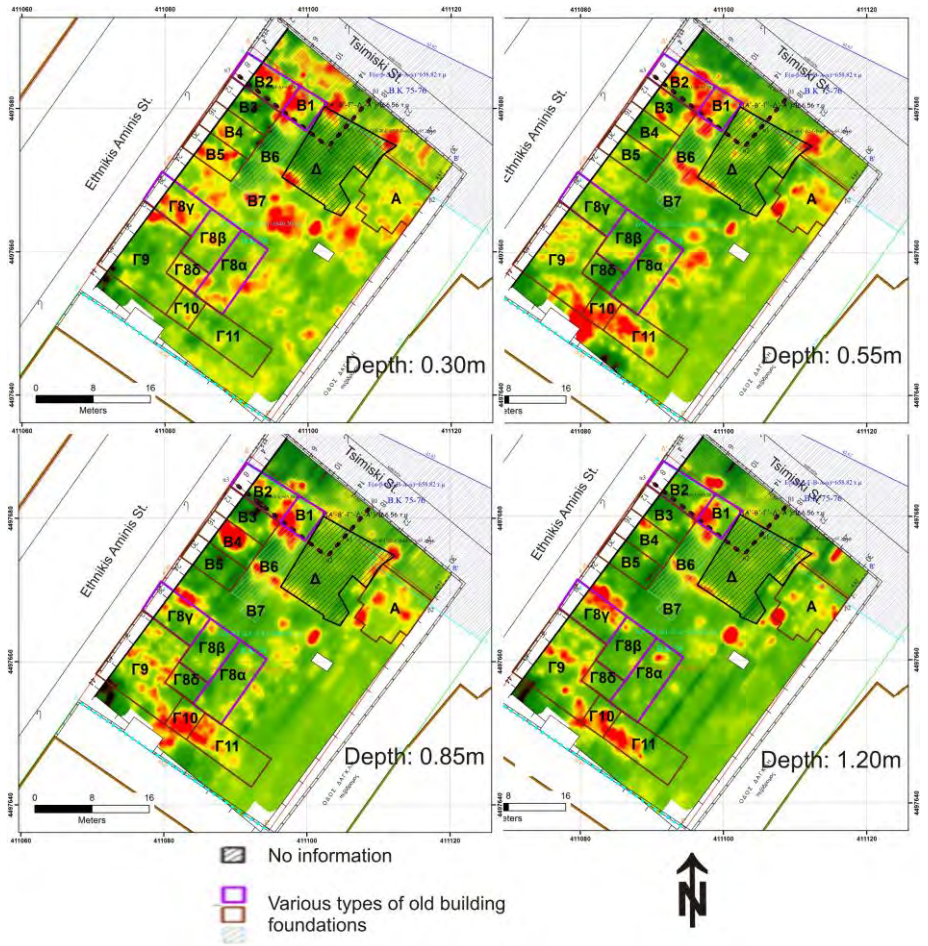

Figure 7 –GPR depth slices. Locations of old buildings are annotated on the map.

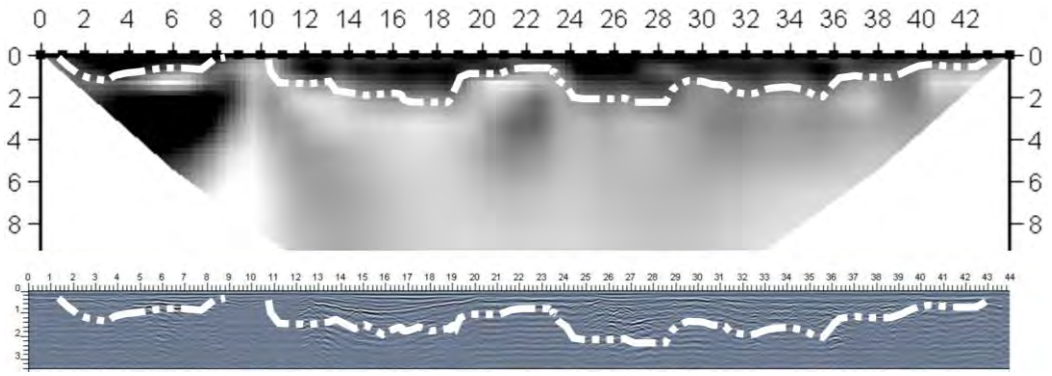

Figure 8 – An ERT section and a GPR profile acquired along the same line. The white dashed line indicates the area of similarity between the two sections.

It has to be noted that in many cases there are a few discrepancies between the depth positions of features deduced from GPR and ERT. This is due to the velocity variation of radar waves in the subsurface. GPR velocity is an average and does not remain constant while GPR waves travel in various soil conditions in the subsurface. For GPR profiles, to convert time-axis into depth-axis, we assume a constant GPR velocity and therefore, the actual depth of subsurface features is possible to slightly change from the one appearing on the vertical axis of GPR profiles and on depth slices. Though, the lateral positions of underground targets can be mapped in great detail using GPR.

Comparing both the cross-sections and depth slices of the two methods, it is obvious that ERT provides subsurface information for a greater depth than GPR, and maps quite satisfactorily the deeper subsurface geology. GPR, however, provides a more detailed image of the studied area. Both GPR profiles and depth slices image the near surface features with great resolution and detail regarding their lateral and vertical position.

4. Summary and Conclusions

A geophysical survey was performed in the city centre of Thessaloniki, Greece. This survey was part of a more extensive campaign of geophysical / geotechnical investigations which were carried out in the framework of the construction of new, underground parking area below the current one. We used both the ERT technique and the GPR method.

Both ERT and GPR were able to map and indicate locations of old building foundations, mainly buried near the surface. Depth slices seem to be very helpful in revealing subsurface patterns that cannot be easily seen while looking at the cross-sections of both methods. ERT cross- sections and depth slices provide a geoelectrical image of the subsurface for a greater depth than GPR. Apart from the anthropogenic structures, the ERT method also provides deeper geological subsurface information. On the other hand, GPR maps effectively features located in a smaller depth. Radar imaging provides great resolution in both lateral and vertical location of underground targets.

Based on the geological setting and the results of the geophysical investigation, the site seems to be located adjacent to a former stream-river bed running along Ethnikis Aminis St., very close to its coastal outflow. The geological model of the current survey also indicates stream cuts inside the red-clay formation (low resistivity areas) which may be branches of the outflow or estuary of the well-known Evangelistria stream. The interpretation and correlation of the geophysical results to the geological setting of the area, explains adequately the lack of archaeological ruins or findings in the specific area (despite the fact that such remains were found during the excavation of the neighbouring *YMCA* square to the east of the investigated site). This can be attributed to the

presence of an ancient stream-river bed with significant flow, bordering the ancient city walls, adjacent to the investigated site which possibly prohibited ancient urban constructions.

Our results show that combined ERT and GPR investigations are useful for providing an informative geophysical image of the subsurface. ERT imaging documents geoelectrical heterogeneities and GPR signatures depend on the dielectric/electromagnetic properties of subsurface materials. In some cases, there are a few discrepancies between the depth position of features obtained from GPR data and ERT interpretations. This depth variability is possibly caused by the radar wave velocity variation in the subsurface. Nevertheless, the combined use of ERT and GPR in conjunction with any other possible information (e.g., historic records) strengthens the geophysical/geological interpretations by reducing the ambiguous results. This effectively improves the accuracy of the lateral and vertical information about the investigated terrains.

5. References

Anastasiadis A., Raptakis D. and Pitilakis K. 2001. Thessaloniki's Detailed Micro zoning: Subsurface Structure as Basis for Site Response Analysis, *Pure and Applied Geophysics*, 158, 2597–2633.

Chatzigogos N., Makedon T., Tsotsos S. and Christaras B. 2006. Implementation of a ground investigation strategy on urban fills, *Proc. of the 10th IAEG Congress*, Nottingham, U.K., 6-10 September.

Colla C., Dast P.C., McCann D. and Forde M.C. 1997. Sonic, electromagnetic and impulse radar investigation of stone masonry bridges, *NDT&E International*, 30(4), 249–54.

Davis J.L. and Annan A.P. 1989. Ground-penetrating radar for high-resolution mapping of soil and rock stratigraphy, *Geophysical Prospecting*, 37, 531–551.

Diamanti N.G., Tsokas G.N., Tsourlos P.I., and Vafidis A. 2005. Integrated interpretation of geophysical data in the archaeological site of Europos (Northern Greece), *Archaeological Prospection*, 12, 79–91.

Diamanti N., Giannopoulos A. and Forde M.C. 2008. Numerical modelling and experimental verification of GPR to investigate ring separation in brick masonry arch bridges, *NDT&E International*, 41(5), 354-363

Diamanti N. and Redman J.D. 2012. Field observations and numerical models of GPR response from vertical pavement cracks, *Journal of Applied Geophysics*, 81, 106–116.

Goodman D., Nishimura Y. and Rogers J.D. 1995. GPR Time Slices in Archaeological Prospection. *Archaeological Prospection*, 2, 85–89.

Griffiths D.H. and Barker R.D. 1993. Two-dimensional resistivity imaging and modelling in areas of complex geology, *Journal of Applied Geophysics*, 29, 211–226.

Guy E., Daniels J., Holt J., Radzevicius S. and Vendl M.2000. Electromagnetic induction and GPR measurements for creosote contaminant investigation, *Journal of environmental and Engineering Geophysics,* 5, 11–19.

Kim J.H. 2000. DC2DPro-2D interpretation system of DC resistivity tomography, *User's Manual and Theory KIGAM,* S. Korea.

Leucci G. 2002. Ground penetrating radar survey to map the location of buried structures under two churches, *Archaeological Prospection*, 9, 217–228.

Li Y. and Oldenburg D.W. 1992. Inversion of DC resistivity data using an approximate inverse mapping, *Geophysical Journal International*, 116, 527–537.

Linford N. 2004. From hypocauset to hyperbola: Ground penetrating radar surveys over mainly Roman remains in the U.K., *Archaeological Prospection*, 11, 237–246.

Ogilvy R.D., Meldrum P.I., Kuras O., Wilkinson P.B., Chambers J.E., Sen M., Pulido-Bosch A., Gisbert J., Jorreto S., Frances I., and Tsourlos P. 2009. Automated monitoring of coastal aquifers with electrical resistivity tomography, *Near Surface Geophysics*, 7, 367-375.

Papadopoulos N.G., Tsourlos P.I., Tsokas G.N. and Sarris A. 2006. Two-dimensional and three-dimensional resistivity imaging in archaeological site investigation, *Archaeological Prospection* 13(3), 163–181.

Papadopoulos N.G., Tsourlos P., Tsokas G.N.and Sarris A. 2007. Efficient ERT measuring and inversion strategies for 3D imaging of buried antiquities, *Near Surface Geophysics*, 5, 349–361.

Piro S., Goodman D. and Nishimura Y. 2003. The study and characterization of Emperor Traiano's Villa (Altopiani di Arcinazzo, Roma) using high-resolution integrated geophysical surveys, *Archaeological Prospection*, 10, 1–25.

Savvaidis A., Tsokas G.N., Liritzis Y. and Apostolou M. 1999. The location and mapping of ancient ruins on the castle of Lefkas (Greece) by resistivity and GPR methods, *Archaeological Prospection*, 6, 63–73.

Solla M., Lorenzo H., Novo A. and Rial, F.I. 2010. Ground-penetrating radar assessment of the medieval arch bridge of San Antón, Galicia, Spain, *Archaeological Prospection*, 17, 223–232.

Spikes V.B., Hamilton G.S., Arcone S.A., Kaspari S. and Mayewski, P.A. 2004. Variability in accumulation rates from GPR profiling on the West Antarctic plateau, *Annals of Glaciology*, 39, 238–244.

Tripp A., Hohmann G. and Swift C. 1984. Two-dimensional resistivity inversion, *Geophysics*, 49, 1708–1717.

Tsokas G.N., Giannopoulos A., Tsourlos P., Vargemezis G., Tealby J.M., Sarris A., Papazachos C.B. and Savopoulou, T. 1994. A large scale geophysical survey in the archaeological site of Europos (N. Greece), *Journal of Applied Geophysics*, 32, 85–98.

Tsokas G.N., Stampolidis A., Mertzanidis I., Tsourlos P.I., Hamza R., Chrisafis C., Ambonis D. and Tavlakis I. 2007. Geophysical exploration in the church of Protaton in Karyes of Mount Athos (Holy Mountain) in Northern Greece, *Archaeological Prospection*, 14, 75–86.

Tsokas G.N., Tsourlos P.I. and Papadopoulos N. 2008a. Electrical resistivity tomography: a flexible technique in solving problems of archaeological research. In Seeing the Unseen, Campana, S. and Piro, S. (eds), *Geophysics and Landscape Archaeology*, ISBN 978-00415-44721-8, 83–104.

Tsokas G.N., Tsourlos P.I., Vargemezis G. and Novack M. 2008b. Non-destructive electrical resistivity tomography for indoor investigation: the case of Kapnikarea Church in Athens, *Archaeological Prospection*, 15, 47-61.

Tsourlos P.I.1995. Modeling, interpretation and inversion of multielectrode resistivity survey data, *Ph.D. Thesis*, Department of Electronics, University of York.

Tsourlos P., Ogilvy R., Meldrum P., and Williams G. 2003. Time-lapse monitoring in single boreholes using electrical resistivity tomography, *Journal of Environmental and Engineering Geophysics*, 8, 1-14.

Tsourlos P. and Tsokas G.N. 2011. Non-destructive electrical resistivity tomography survey at the South walls of the Acropolis of Athens, *Archaeological Prospection*, 18, 173–186.

Vargemezis G., Tsourlos P. and Stamoulis K. 2007. Application of Geophysical Methods to the study of the Mechanism of Springs, *Bull. Geol. Soc. Greece*, XXXVII, 605–615.

Vargemezis V., Zouros N., Tsourlos P.I. and Fikos I. 2009. High-resolution magnetic gradient and electrical resistivity tomography survey at the Plaka Petrified Forest Park in Lesvos Island, Greece, *Near Surface Geophysics*, 7, 207-215.

Yi M.J., Kim J.H., Song Y., Cho S.L., Chung S.H. and Suh J.H. 2001. Three-Dimensional Imaging of Subsurface Structures using Resistivity Data, *Geophysical Prospecting*, 49, 483-497.

Δελτίο της Ελληνικής Γεωλογικής Εταιρίας, τομ. XLVII , 2013
Πρακτικά 13ου Διεθνούς Συνεδρίου, Χανιά, Σεπτ. 2013

Bulletin of the Geological Society of Greece, vol. XLVII 2013
Proceedings of the 13th International Congress, Chania, Sept. 2013

OBTAINING INFORMATION ON THE Q-STRUCTURE OF THE SOUTHERN AEGEAN SUBDUCTION AREA BY SPECTRAL SLOPES FROM TEMPORARY AND PERMANENT NETWORKS

Ventouzi Ch.[1], Papazachos C.[1], Papaioannou Ch.[2], Hatzidimitriou P[1]. and the EGELADOS working group

[1] *Aristotle University of Thessaloniki, Faculty of Science, Department of Geology, Geophysical Laboratory, xrusven@geo.auth.gr, kpapaza@geo.auth.gr, chdimitr@geo.auth.gr*

[2] *Institute of Engineering Seismology & Earthquake Engineering, Thessaloniki, chpapai@itsak.gr*

Abstract

Anelastic attenuation studies have been considered one of the main controlling factors affecting seismic wave propagation, providing important information on the earth's structure. In order to investigate the attenuation structure of the southern Aegean subduction area, we employed ~400 intermediate depth earthquakes recorded by temporary and permanent networks. Using the recorded waveforms we have calculated a frequency-independent path attenuation operator t for both P and S waves. Initially an automated method was employed, where t* was automatically calculated by the slope of the acceleration spectrum produced above the corner frequency, f_c. Computations were performed in the 0.2-25Hz frequency band, using only spectra with a signal to noise ratio greater than 3, and above the noise level for at least the range 1-4Hz (for S and P waves, respectively). In the second approach, the selection of the segment of the spectrum was carried out manually for optimum fitting. No considerable linear trend revealing dependence of t* with distance could be observed on the original data, whereas strong clustering for different focal depth ranges was observed. The spatial variation of the obtained t* values shows that, in general, along-arc stations present low values of t*, while back-arc stations show much larger values. The observed t* difference becomes more pronounced as the depth of the earthquakes increases, suggesting a significant localized effect of the high-attenuation (low-Q) mantle wedge, in agreement with independent observations.*

Key words: *Anelastic attenuation, Quality factor, EGELADOS experiment.*

Περίληψη

Η μελέτη της ανελαστικής απόσβεσης η οποία θεωρείται ένας από τους σημαντικότερους παράγοντες στη διάδοση των σεισμικών κυμάτων, παρέχει πολύτιμες πληροφορίες για τη δομή της Γης. Για τη μελέτη της δομής απόσβεσης στη ζώνη κατάδυσης του Νοτίου Αιγαίου χρησιμοποιήθηκαν δεδομένα από περίπου 400 σεισμούς ενδιαμέσου βάθους που καταγράφηκαν από τοπικά και μόνιμα δίκτυα. Υπολογίστηκε ο χρόνος απόσβεσης t τόσο για τα επιμήκη (P) όσο και για τα εγκάρσια (S) κύματα ανεξάρτητα της συχνότητας. Αρχικά εφαρμόστηκε μια προσέγγιση όπου ο χρόνος απόσβεσης υπολογίστηκε αυτόματα από την κλίση του φάσματος επιτάχυνσης*

πάνω από τη γωνιακή συχνότητα, f_c. Οι υπολογισμοί πραγματοποιήθηκαν στο εύρος συχνοτήτων 0.2-25Hz, χρησιμοποιώντας μόνο τα φάσματα με λόγο σήματος προς θόρυβο μεγαλύτερο από 3, και τα οποία βρισκόταν πάνω από το επίπεδο θορύβου για 1-4Hz (για τα S και για τα P κύματα, αντίστοιχα). Στη δεύτερη προσέγγιση η επιλογή του τμήματος του φάσματος έγινε χειροκίνητα. Δημιουργήθηκαν διαγράμματα χρόνου απόσβεσης με την απόσταση αλλά δεν παρατηρήθηκε σημαντική εξάρτηση μεταξύ τους, ενώ αντίθετα υπήρξε σημαντική ομαδοποίηση ανάλογα με το εστιακό βάθος των σεισμών. Η χωρική μεταβολή των τιμών του t έδειξε ότι οι σταθμοί κατά μήκος του τόξου παρουσιάζουν χαμηλές τιμές του t* ενώ οι σταθμοί στο πίσω μέρος του τόξου εμφανίζουν σαφώς μεγαλύτερες τιμές. Η παρατηρούμενη αυτή διαφορά γίνεται εντονότερη καθώς το βάθος των σεισμών αυξάνει, ενδεικτικό της τοπικής επίδρασης της υψηλής απόσβεσης (χαμηλό Q) της σφήνας του μανδύα πάνω από την καταδυόμενη λιθόσφαιρα, σε συμφωνία με ανεξάρτητες παρατηρήσεις.*
Λέξεις κλειδιά: *Ανελαστική απόσβεση, Παράγοντας ποιότητας, πείραμα ΕΓΚΕΛΑΔΟΣ.*

1. Introduction

The under study area of the Southern Aegean is located where the eastern Mediterranean lithosphere subducts under the Aegean and the Aegean micropale overrides the Eastern Mediterranean along an active plate boundary forming the Hellenic Arc (Papazachos and Delibasis, 1969; Papazachos and Comninakis, 1971; McKenzie, 1972). Intermediate depth earthquakes occur at depths ranging between 60 to 180km (Papazachos et al., 2000) along a well-defined Wadati-Benioff Zone (Figure 1). Several studies on active tectonics of the area have been already done using seismological and geodetic data (Papazachos and Comninakis, 1971; Oral et al., 1995; Reilinger et al., 1997; Papazachos et al, 1999; McClusky et al., 2000) revealing that the subduction of the African plate beneath Crete which occurs at a rate of 35mm/yr, exceeds the convergence between Africa and Eurasia (5-10mm/yr), due to the fact that Southern Aegean moves more rapidly to the SW direction.

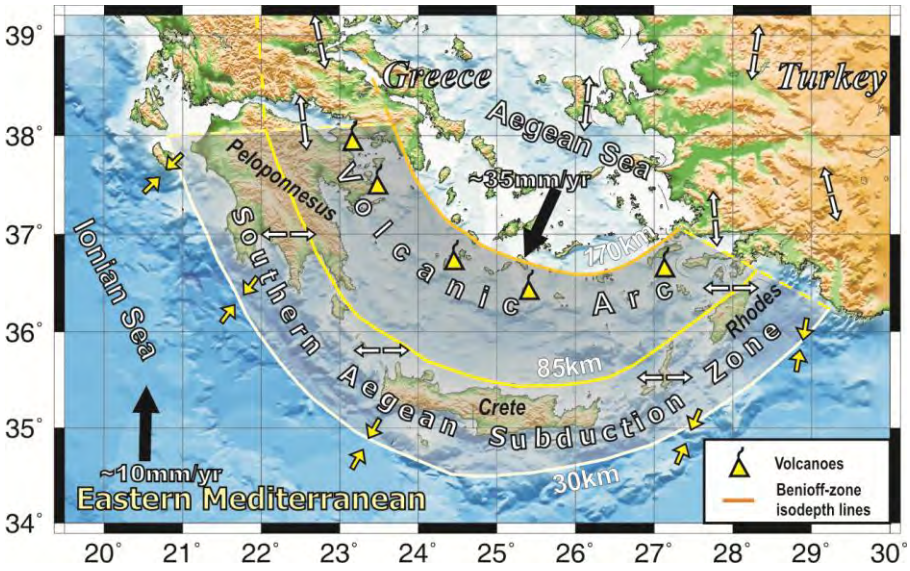

Figure 1 – Geotectonic setting of the broader Southern Aegean subduction area. Isodepths of the Benioff-zone, as well as the volcanic arc are shown. Single solid and double open vectors depict the plate motions and local stress field in the area, respectively (modified from Papazachos et al. 1998, Karagianni et al., 2005).

Anelastic attenuation studies are an important tool in complicated tectonic environments such as subduction zones, as they provide valuable information on subduction dynamics including slab dehydration and melt transport (Schurr et al., 2003; Pozgay et al., 2009), on the earth's interior including mantle wedge temperature (Stachnik et al., 2004; Pozgay et al., 2009) and the degree of partial melting. Seismic wave propagation is mainly controlled by attenuation which plays a significant role in strong ground motion predictions. It is therefore of high importance to understand the attenuation structure in the Hellenic subduction system. In the present study high-quality seismic data of intermediate-depth events from the large-scale local network of EGELADOS project are used in order to investigate the anelastic attenuation (Q) structure of the southern Aegean subduction system.

2. Data Used

The EGELADOS seismic monitoring project was a large-scale temporary amphibian broadband seismological network, consisted of 65 land stations and 24 ocean-bottom (OBS) recorders installed in the southern Aegean area. It operated from October 2005 until April 2007 by a large working group including the Aristotle University of Thessaloniki, the National Observatory of Athens, Technical University of Chania, Istanbul Technical University, University of Hamburg and GeoForschungszentrum Potsdam. Data from another local network were also taken into account for the research of the attenuation structure. CYCNET (Bohnhoff et al., 2004) was a digital broad-band/short period 22-station temporary seismic network installed in the central Hellenic Arc, in the Cyclades island group, which was in operation from September 2002 until September 2005. Finally recordings from the permanent networks of National Observatory of Athens and GEOFON were also included. The station distribution of all the above mentioned networks is shown in Figure 2. Red squares represent stations from EGELEDOS network; blue triangles show broadband stations from CYCNET network while inverted blue triangles display short-period sensors. Stations from the permanent seismological networks (NOA and GEOFON) appear with yellow stars and purple diamonds respectively. Finally the Ocean Bottom (OBS) instruments are denoted with green circles.

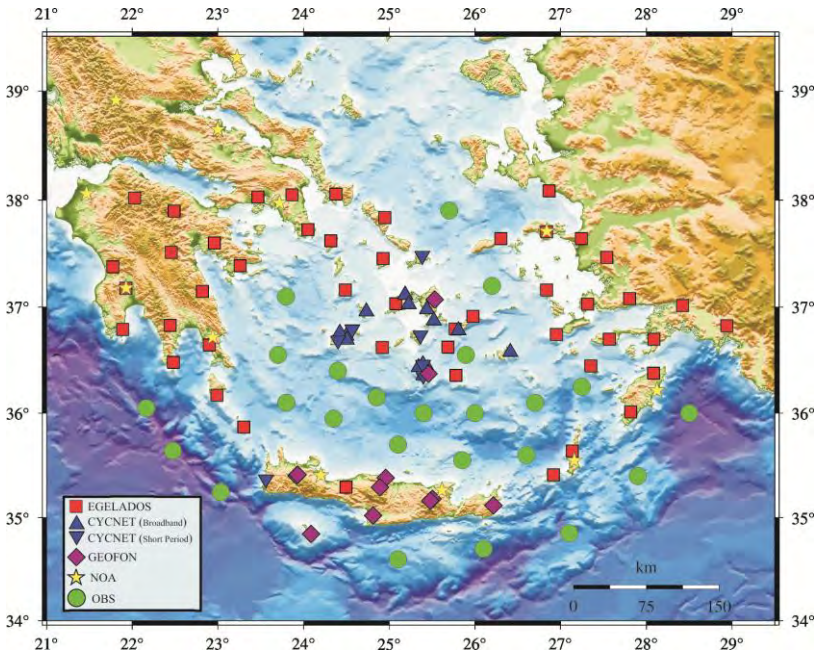

Figure 2 – Station distribution of all networks (temporary and permanent) used in the present study.

Data from these two experiments, together with the recordings of the permanent networks provided a large data set of high quality for studying the attenuation structure of the Hellenic Subduction Zone. About 400 intermediate-depth local events recorded by the on-land stations were finally adopted for the present study from the whole data set from both temporary and permanent networks. The epicentral, as well as the depth distribution, of the earthquakes studied is displayed in Figure 3.

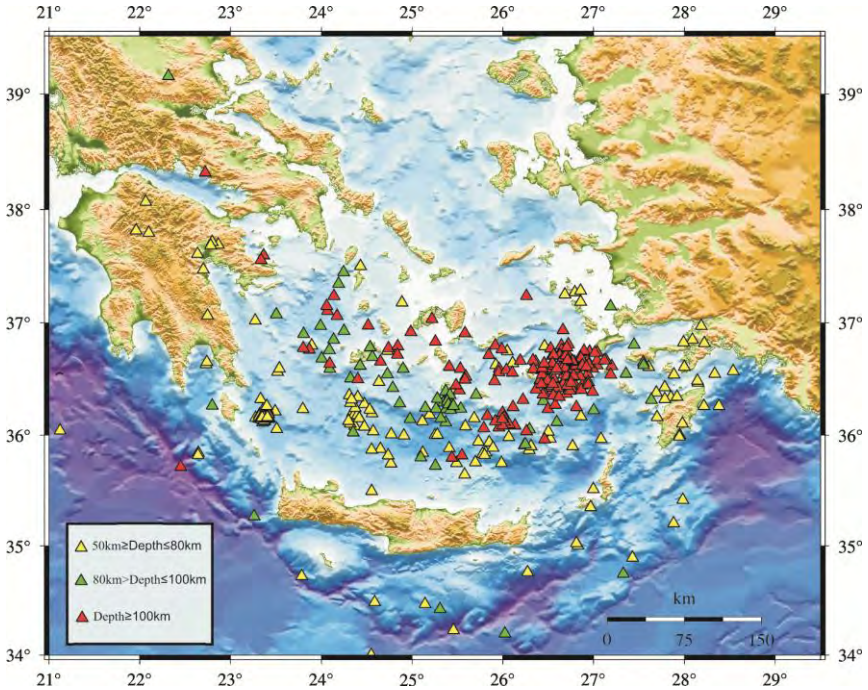

Figure 3 – Epicentral and depth distribution of all intermediate depth earthquakes employed for the Southern Aegean attenuation structure.

3. Estimating Attenuation Operator

Inelastic attenuation, i.e. the deviation of the behaviour of the Earth from a perfect elastic body, provides interesting information about the Earth's structure and in conjunction with geometrical spreading is a key factor in seismic wave propagation. Intrinsic attenuation is commonly described by the quality factor (Q-factor) which is the loss of elastic energy of a seismic wave while it propagates through an inelastic medium and can be defined as:

Equation 1 – Quality factor

$$(1)\quad Q = -\frac{2\pi E}{\Delta E}$$

where E is the energy of the seismic wave and ΔE is the amount of energy lost over a period or a wavelength. Due to this energy loss the amplitudes of seismic waves are reduced while they travel through Earth proportional to the quality factor. Therefore, the amplitude A of a wave at a distance r is given by Equation 2.

Equation 2 – Amplitude of a seismic wave at a distance r

$$(2)\quad A = \frac{A_0}{r}\exp\left(-\frac{\pi f}{QV}r\right)$$

In order to determine the quality factor we need to calculate the whole path attenuation operator t* for propagating seismic waves from the source to the recording station, which is given by (Equation 3).

Equation 3 – Whole path attenuation operator

(3) $t^* = \int_{path} \frac{dr}{QV}$ (Kanamori, 1967)

The whole path attenuation operator t* can be estimated from the slope of the amplitude spectrum above corner frequency f_c, by applying Fourier transformation (Cormier, 1982) according to (Equation 4).

Equation 4 – Fourier transformation spectrum

(4) $A(r,f) = A_0 \exp(-\pi f t^*)$ where

$A_0 = (2\pi f)^2 S(f)\, G(r,f)$

In equation (4) $G(r,f)$ is the geometrical spreading factor and $S(f)$ is the displacement source spectrum which assuming a Brune type source (Brune, 1970), is proportional to the corner frequency f_c. If we consider that the quality factor Q remains constant throughout the whole raypath, then equation 3 becomes:

Equation 5 – Whole path attenuation operator

(5) $t^* = \frac{t}{Q}$

Replacing the above relation in equation 4 we get (equation 6):

Equation 6 – Spectral slope estimation

(6) $ln[A(f)] = lnA_0 - \pi f t/Q$

which is a linear equation with slope $\pi t/Q$. By finding the slope of this linear equation we can practically compute the mean quality factor, Q, along the raypath since the $(2\pi f)^2 S(f)$ factor remains constant at frequencies above the f_c in acceleration spectrum and the geometrical spreading factor, $G(r,f)$, is considered to be depended only by distance.

In order to determine attenuation operator we need to know the arrival times of P and S waves respectively. Unfortunately, this information was not available for all recordings. For this reason we generated estimated arrival times as a function of epicentral distance, for different groups of focal depths, calculated from data provided by the CYCNET experiment. Figure 4 demonstrates the estimated arrival times as a function of epicentral distance for different groups of focal depth, and for both P and S waves.

Initially all available arrival times (original and estimated) were imported in the velocity waveforms for all three components and then differentiated to yield to the corresponding acceleration waveforms. We then obtained the amplitude spectra of 5% tapered P and S acceleration waveforms by applying the fast Fourier transform. The amplitude spectra were calculated for a 5sec time window after the P and S arrival times. Noise spectrum was also calculated 5sec before P and 5 sec before S arrival in order to estimate the signal-to-noise ratio and apply a quality control procedure. In order to obtain precise estimates of t*, we applied certain selection criteria. Therefore, we considered waveforms only if the amplitude of the acceleration spectrum was at least 3 times larger than the spectrum of the background noise for both P and S waves. In addition, only data with a frequency bandwidth greater than 4Hz for P waves and greater than 1Hz for S waves were processed. The lower limit of the frequency band that was considered for all calculations was 0.2Hz and the corresponding upper limit was set to 25Hz to reduce the effect of high-frequency noise.

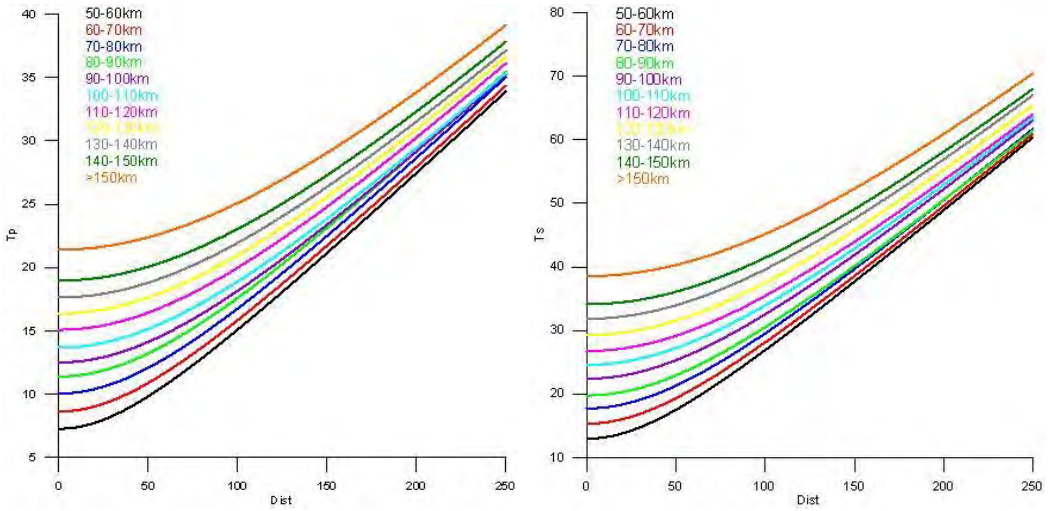

Figure 4 – Estimated arrival times of P (left) and S (right) waves in relation to epicentral distance for different focal depths.

To determine t^*, we have adopted two independent approaches. Initially an automated method was used, where t^* was automatically calculated by the slope of the acceleration spectrum produced above the corner frequency, f_c. In the second approach, the selection of the segment of the spectrum for the t^* estimation was carried out manually, by interactively picking each spectral

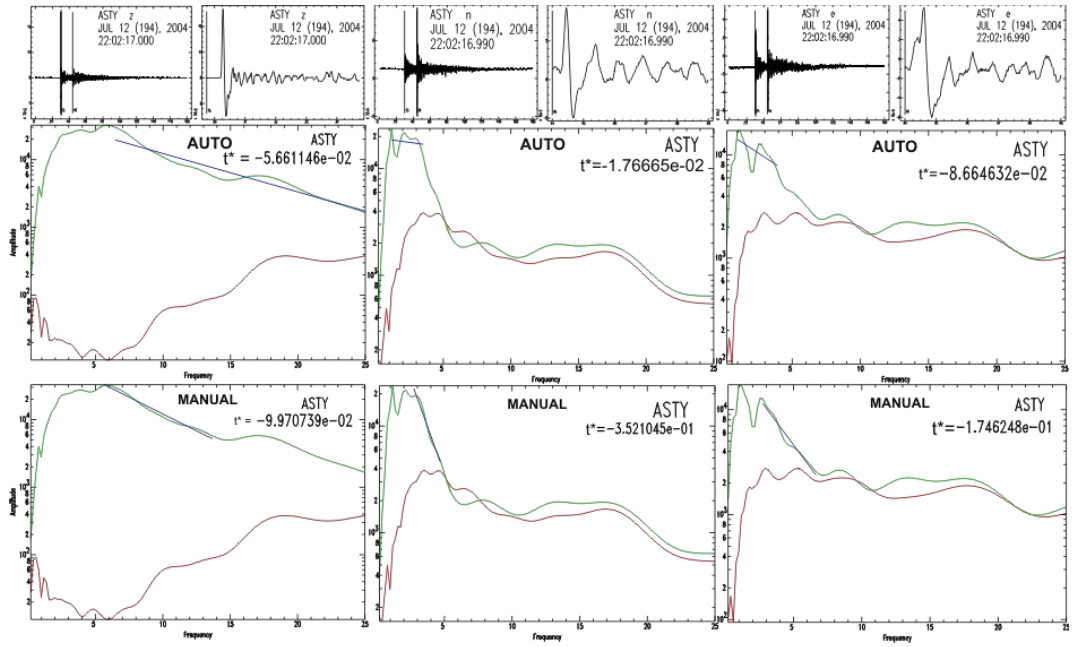

Figure 5 – Example of P and S velocity waveforms from one intermediate depth earthquake recorded by three-component station ASTY (CYC-NET network) as well as the best-fit linear slopes calculated both manually and automatic. The top frame shows the velocity waveform and the 5sec signal starting from the origin time. The middle frame shows the observed noise spectrum (red), the observed signal spectrum (green) and the best fitting line (blue) using the automatic approach, while bottom frame using the manual one. The calculated t* values are also listed.

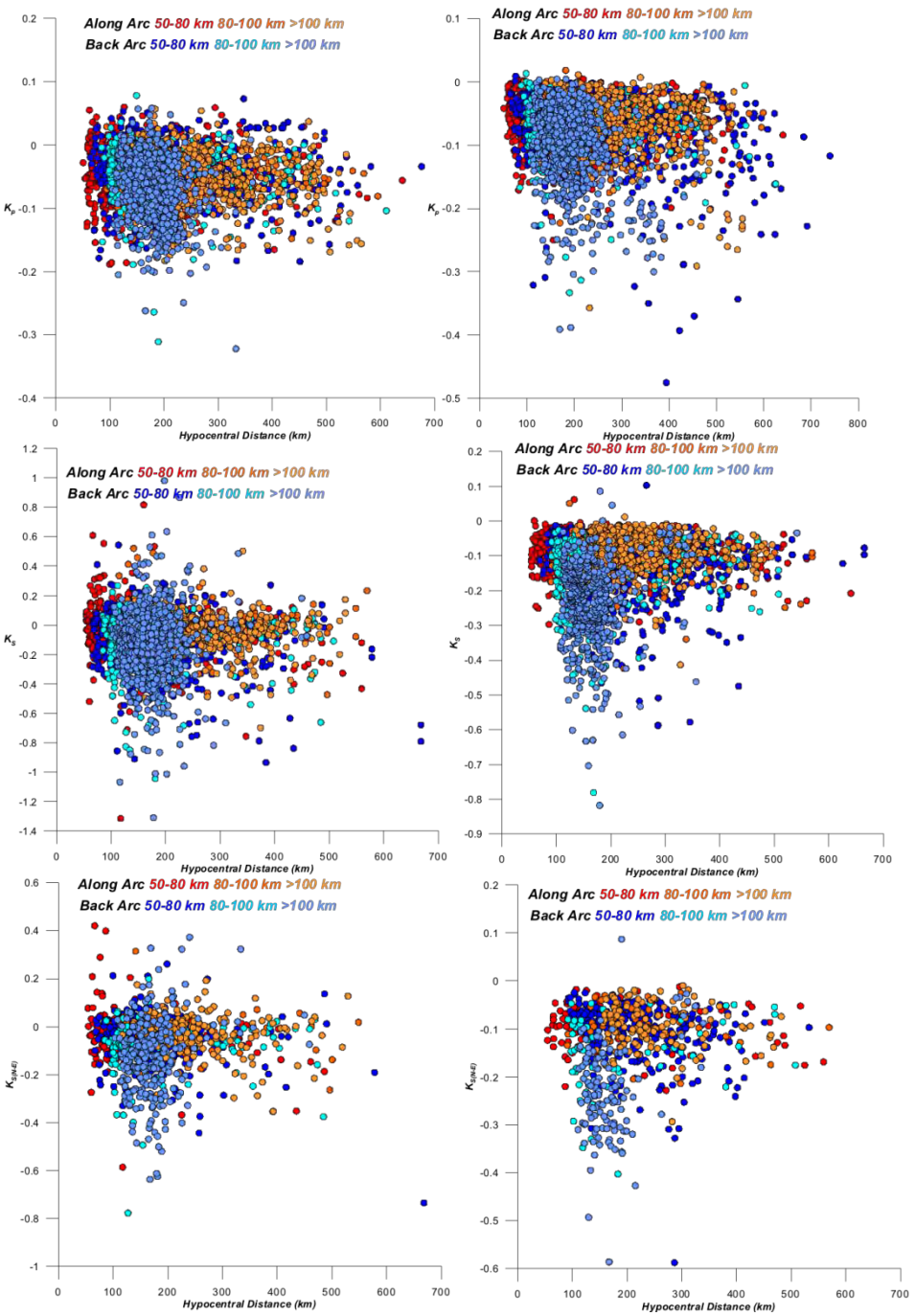

Figure 6 – Plots of t* versus hypocentral distance for P and S waves for all stations and for all intermediate depth events recorded and calculated with both approaches. On the left, the results from the automated method are presented, while on the right the results from the manual approach are shown. Top frame shows slope fits from P-waves, middle frame from S waves and bottom frame average S-wave slopes from both horizontal coordinates, when both where available. Back-arc stations have larger slope values revealing high attenuation in the area, similarly to deeper events (h>100km), which show the most pronounced attenuation effects.

frequency band over which to calculate *t**, ensuring at the same time that the frequencies are within the limits previously defined, and that the signal-to-noise ratio was above the desired level for optimum fitting. An example of velocity waveforms from one station with Z, N-S and E-W components with the appropriate fitting to the acceleration spectra produced, using both methods, is shown in Figure 5.

In order to examine the variation of t* with distance, plots of the estimated t* versus the hypocentral distance constructed using all the available data for both P and S waves. Moreover, following Skarlatoudis et al. (2013), data were sorted into three different depth categories (50≤depth≤80km, 80≤depth≤100km and depth≥100km respectively), and the recording stations were separated in along-arc and back-arc, according to their location. Figure 6 presents the observed t* as a function of hypocentral distance for both P and S waves, as well as for the average calculated from both horizontal components using both the automatic and manual approaches.

The results of Figure (6) show that no considerable linear trend revealing dependence of t* with distance could be observed on the original data, clearly a result of the significant spatial and depth variations of the anelastic attenuation structure. In order to further examine this issue, we studied the spatial variation of t* values. In general, along-arc stations present low values of t*, while back-arc stations show much larger values. The observed t* difference becomes more pronounced as the depth of the earthquakes increases revealing that attenuation is stronger for deeper events.
For a more detailed view of the spatial variations of the whole path attenuation operator we performed an approximate interpolation of t*, mapping each path value in the middle of the ray path. Interpolation was carried out for all stations for P, S and "mean S" waves using all the available t* values calculated with both approaches, for the same depth classification mentioned above. Examples of the results of this initial approximate interpolation for S waves are shown in plots in Figure 7.
The spatial variation of t*, as presented in Figure 7, display some interesting features. For hypocentral depths 50≤depth≤80km low values of t*, appear to be sparsely observed mainly in the back-arc area, while large values are found throughout the for-arc area. As hypocentral depths increase (80≤depth≤100km), low values of the whole path attenuation operator expand on a larger area in the back-arc/volcanic arc region. Finally, at depths larger than 100km, very low values of t* are clearly seen throughout the whole volcanic arc and back-arc area, defining a much larger area with higher attenuation.

4. Conclusions

High-quality data from two temporary networks were used in order to gain insight into the attenuation properties in the broader S. Aegean area. The whole path attenuation t* operator and the quality factor were determined by fitting seismic acceleration spectra adopting two independent approaches. Lateral variations of t* do not show any significant dependence of t* with distance. To examine possible spatial variations we examined t* in terms of focal depth and spatial variability. The results image a high attenuation area in the volcanic and back-arc region in accordance with P and S tomographic results (Papazachos et al., 1995, Papazachos and Nolet, 1997) which clearly outlines the spatial expanse of the low-velocity (high-attenuation) area beneath the Aegean volcanic arc. Attenuation is stronger for deeper events revealing that the source of the attenuation is the low-velocity mantle wedge above the subducting slab of the Mediterranean lithosphere, in accordance with earlier suggestions (Skarlatoudis et al., 2013). Further processing of the available data by inverting the observed t* values and constructing 1D and 3D tomographic models will reveal additional details on the attenuation structure of the whole S. Aegean area.

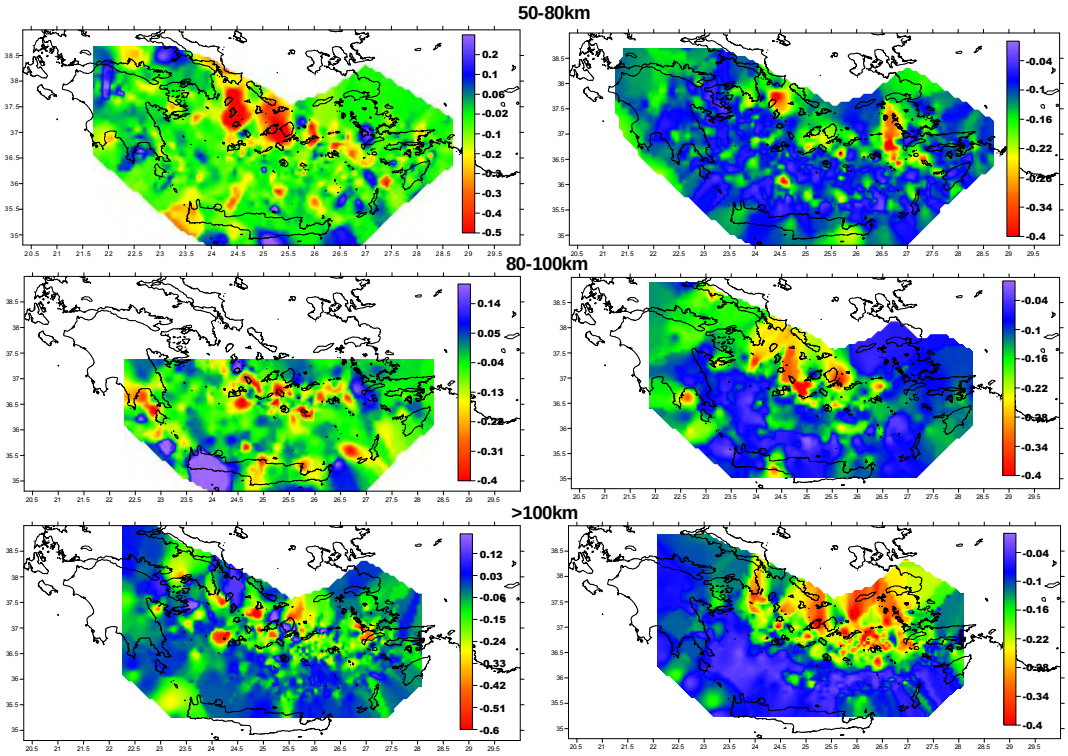

Figure 7 – Spatial variation of the t* for different focal depth ranges (50-80km, 80-100km, >100km) for the southern Aegean subduction area. Red regions show areas with low t* values (higher attenuation), while green and blue regions areas with larger values. On the left column the corresponding spatial distribution with the use of the automatic method is presented, while on the right with the use of the manual one.

5. Acknowledgments

The GMT system (Wessel and Smith, 1998) was used to plot some figures. This work has been partly supported by the 3D-SEGMENTS project of the ARISTEIA-I call funded by EC European Social Fund and the Greek Secretariat of Research and Technology.

6. References

Bohnhoff M., Riche M., Meier T., Endrun B., Harjes H.P. and Stavrakakis G. 2004. A temporary seismic network of the Cyclades (Aegean Sea, Greece), *Seismological Research Letters,* 75/3, 352-357

Brune J.N. 1970. New Tectonic stress and the spectra of seismic shear waves from earthquakes, *J. Geophys. Res.,* 75(26), 4997-5009.

Cormier V. F. 1982. The effect of attenuation on seismic body waves, *Bull. Seism. Soc. Am.* 72, . 169-200.

Kanamori H. 1967a. Attenuation of P-waves in the upper and lower mantle [with Japanese abs.]: *Tokyo Univ. Earthquake Res. Inst. Bull.,* v. 45, 299-312.

McClusky S., Balasdsanian A., Barka C., Demir I,. Georgiev M., Hamburger K., Hurst K., Kastens G., Kekelidze R.K.V., Kotzev O., Lenk S., Mahmoud A., Mishin M., Nadariya A., Ouzounis D., Paradissis Y., Peter M., Prilepin R., Reilinger I., Sanli H., Seeger A., Tealeb M.N., Toksoz and Veis G. 2000. Global positioning system constraints on crustal move-

ments and deformations in the eastern Mediterranean and Caucasus, *Journal of Geophysical Research,* 105, 5695–5719.

McKenzie D.P. 1972. Active tectonics of the Mediterranean region, *Geophysical. J. R. astr. Soc.,* 30*,* 109-185.

Oral M.B., Reilinger R.E., Toksoz M.N., King R.W., Barka A.A., Kiniki J. and Lenk D. 1995. Global Positioning System offers evidence of plate motions in eastern Mediterranean, *EOS,* 76, 9-11.

Papazachos B. C. and Delibasis N. D. 1969. Tectonic stress field and seismic faulting in the area of Greece, *Tectonophysics* 7, 231-255.

Papazachos B. C. and Comninakis P. E. 1971. Geophysical and tectonic features of the Aegean arc, *Journal of Geophysical Research* 76, 8517-8533.

Papazachos C.B., Hatzidimitriou P.M., Panagiotopoulosn D., and Tsokas G.N. 1995. Tomography of the crust and upper mantle in SE Europe, *J. Geophys. Res.*, 12, 405-12, 422.

Papazachos C.B., and Nolet G. 1997. P and S deep velocity structure of the Hellenic area obtained by robust non-linear inversion of travel times, *J. Geophys. Res.,* 102, 8349-8367.

Papazachos B.C., Papaioannou C.A., Papazachos C.B. and Savvaidis A.S., 1999. Rupture zones in the Aegean region, *Tectonophysics,* 106, 71-85.

Papazachos B.C., Karakostas B.G., Papazachos C.B. and Scordilis E.M. 2000. The geometry of the Wadati – Benioff zone and lithospheric kinematics in the Hellenic arc, *Tectonophysics,* 319, 275-300.

Pozgay S.H.*,* Wiens D.A.*,* Conder J.A.*,* Shiobara H. and Sugioka H. 2009. Seismic attenuation tomography of the Mariana subduction system: Implications for thermal structure, volatile distribution, and slow spreading dynamics*, Geochem. Geophys. Geosyst.*, 10, Q04X05.

Reilinger R.E., McClusky S.C., Oral M.B., King R.W., Toksoz M.N., Barka A.A., Kinik I., Lenk O. and Sanli. I. 1997. Global positioning system measurements of present crustal movements in the Arabia-Africa-Eurasia plate collision zone, *J. Geophys. Res. 102*, 9983-9999.

Schurr B., Asch G., Rietbrock A., Trumbull R., Haberland C. 2003. Complex patterns of fluid and melt transport in the Central Andean subduction zone revealed by attenuation tomography, *Earth Planet Sci Lett* 215(1–2), 105–119.

Skarlatoudis A.A., Papazachos C.B., Margaris B.N., Ventouzi Ch., Kalogeras I. and the EGELADOS group, 2013. Ground motion prediction equations of intermediate-depth earthquakes in the Hellenic arc, southern Aegean subduction area, *Bull. Seism. Soc. Am., in press.*

Stachnik J., Abers G. and Christensen D. 2004. Seismic attenuation and mantle wedge temperatures in the Alaska subduction zone, *Journal of Geophysical Research* 109(B10): doi: 10.1029/2004JB003018. issn: 0148-0227.

Δελτίο της Ελληνικής Γεωλογικής Εταιρίας, τομ. XLVII , 2013
Πρακτικά 13ου Διεθνούς Συνεδρίου, Χανιά, Σεπτ. 2013

Bulletin of the Geological Society of Greece, vol. XLVII 2013
Proceedings of the 13th International Congress, Chania, Sept. 2013

A MARKOV MODEL FOR SEISMIC HAZARD ANALYSIS ALONG THE HELLENIC SUBDUCTION ZONE (GREECE)

Votsi I.[1,2], Tsaklidis G.[2], Limnios N.[1], Papadimitriou E.[3] and Vallianatos F.[4]

[1] *Université de Technologie de Compiègne, Laboratoire de Mathématiques Appliquées de Compiègne, irene.votsi@utc.fr, nikolaos.limnios@utc.fr*

[2] *Aristotle University of Thessaloniki, Department of Mathematics, tsaklidi@math.auth.gr*

[3] *Aristotle University of Thessaloniki, Geophysics Department, ritsa@geo.auth.gr*

[4] *Technological Educational Institute of Crete, Laboratory of Geophysics and Seismology, fvallian@chania.teicrete.gr*

Abstract

A homogeneous finite–state discrete–time Markov model is applied for the earthquake occurrence in the Hellenic Subduction Zone (Greece), a region accommodating high seismic activity, being a key structure from a seismotectonic point of view. An attempt is made to provide a stochastic representation of the earthquake process and to assess the seismic hazard through the application of the Markov model. The model is applied on a complete data sample comprising strong ($M \geq 5.5$) earthquakes that occurred in the study area since 1911 up to present. The continuous magnitude scale is divided into appropriate intervals to specify discrete states of the model. As the stochastic behavior of the model is governed by its transition probability matrix, we firstly estimate its well–known maximum likelihood estimator. The estimation of the transition probability matrix leads to the estimation of important indicators of the Markov chain, including hitting times and failure rate functions. The mean number of steps for the first occurrence of an anticipated earthquake (belonging to the class with the stronger events, which we are more interested in) is estimated along with its variance. In a next step, we calculate the confidence interval of the aforementioned estimators.

Key words: *transition probabilities, earthquake occurrence probabilities, confidence intervals.*

Περίληψη

Εφαρμόζεται ένα ομογενές Μαρκοβιανό μοντέλο διακριτού χρόνου και χώρου καταστάσεων για τη γένεση σεισμών στο Ελληνικό Τόξο, περιοχή υψηλής σεισμικής δραστηριότητας και ιδιαίτερης σημασίας από σεισμοτεκτονική άποψη. Το μοντέλο παρέχει μια στοχαστική αναπαράσταση της γένεσης των σεισμών συμβάλλοντας στην εκτίμηση της σεισμικής επικυνδυνότητας για την περιοχή μελέτης. Τα δεδομένα που χρησιμοποιούνται λήφθηκαν από τον κατάλογο του Τομέα Γεωφυσικής του Αριστοτελείου Πανεπιστημίου Θεσσαλονίκης, ο οποίος θεωρείται ομογενής και πλήρης για σεισμούς με $M \geq 5.5$ από το 1911. Ο συνεχής χώρος καταστάσεων χωρίζεται σε κλάσεις μεγεθών καθορίζοντας με αυτό τον τρόπο τον χώρο καταστάσεων του μοντέλου. Η στοχαστική συμπεριφορά του μοντέλου καθορίζεται

από τον πίνακα πιθανοτήτων μετάβασής του, του οποίου υπολογίζεται αρχικά ο εκτιμητής μέγιστης πιθανοφάνειας. Στη συνέχεια εκτιμώνται σημαντικά χαρακτηριστικά της Μαρκοβιανής αλυσίδας, παρέχοντας προγνωστικά αποτελέσματα σχετικά με την πιθανότητα γένεσης ενός επερχόμενου ισχυρού σεισμού. Οι υπολογισμοί περιλαμβάνουν την εκτίμηση της μέσης τιμής, της διασποράς και του 95% διαστήματος εμπιστοσύνης του πλήθους των βημάτων που απαιτούνται ώστε η Μαρκοβιανή αλυσίδα να μεταβεί για πρώτη φορά σε μια ορισμένη κατάσταση (που σχετίζεται με τη γένεση ενός επερχόμενου ισχυρού σεισμού).
Λέξεις κλειδιά: *πιθανότητες μετάβασης, πιθανότητες γένεσης σεισμών, διαστήματα εμπιστοσύνης.*

1. Introduction

Until now deterministic approaches are not able to describe the earthquake dynamics appropriately. One reason for this is the limited access to important state variables of the underlying processes (e.g., stresses and material properties). Comparing the deterministic approach with the probabilistic one, we should note that the latter is the one most in favor today, relying on stochastic models to compute occurrence probabilities of strong earthquakes. Stochastic earthquake occurrence models are divided to memoryless and with-memory ones, where memory refers to time, size or location of preceding events. Usual probabilistic seismic hazard assessment is based on the assumption that the earthquake process is memoryless. This assumption is made by considering that the times of events above some threshold magnitude consist a realization of a time-homogeneous Poisson process. The Poisson model provides earthquake occurrence probabilities in a given period independently of the elapsed time since the previous one. The hazard rate describing the instantaneous earthquake occurrence rate at any time is constant confirming the stationary nature of the Poisson assumption. This is not in accordance with elastic rebound principles (Reid, 1910) and characteristic earthquake theory, which imply that if the accumulated strain of a fault section is released in an earthquake, then the initial value of the hazard should be zero and started to increase up to the next event.

Markov models were engaged for seismic hazard assessment since 1980. They are stochastic models with memory, where memory refers to the magnitude of the preceding event (one-step memory case). This type of memory can be incorporated into the definition of their state space via earthquake magnitudes. According to previous studies, it is observed that whereas the Poisson model may be applied to regions characterized by moderate frequent earthquakes, Markov models describe the sequences of events more adequately at regions with strong infrequent events (Anagnos and Kiremidjian, 1988 and the references therein), a very important implication for continental regions where there is shortage of multiple recurrent events into the same fault segment. The latter authors reviewed the basic assumptions of the various models, summarized their stochastic representations and discussed the parameters necessary for applications. Tsapanos and Papadopoulou (1999) applied a discrete-time Markov model for earthquake occurrences, in one of the most seismically active regions of the world, the area of Alaska and Aleutian Islands. The states of the model were defined on the basis of seismic zones (Papadimitriou, 1994). The frequency of visits and the transition probabilities in each one of the defined states were calculated for different magnitude thresholds. In a next step, the model was considered to visit an ‘‘active’’ or an ‘‘inactive’’ state. For each seismic zone, the transition probabilities between the active and inactive states were calculated along with the mean duration of an active period.

Here we focus on the application of a discrete-time Markov model, which assumes that the state duration is geometrically distributed depending on the current state of the Markov chain. Important indicators of the model are estimated, aiming to provide earthquake forecasting results. The transition probabilities of the chain are estimated along with its relevant measures, resulting to the calculation of earthquake occurrence probabilities. The Hellenic Arc is selected for this investigation because it exhibits high seismic activity, and therefore hazard assessment in this area

is of paramount importance. An adequate number of strong ($M \geq 6.4$) earthquakes, along with an adequate number of moderate ($M \geq 5.5$) events is available since 1911 (Figure 1). It is the first time that stochastic models are applied in the study area, and in particular the Markov model.

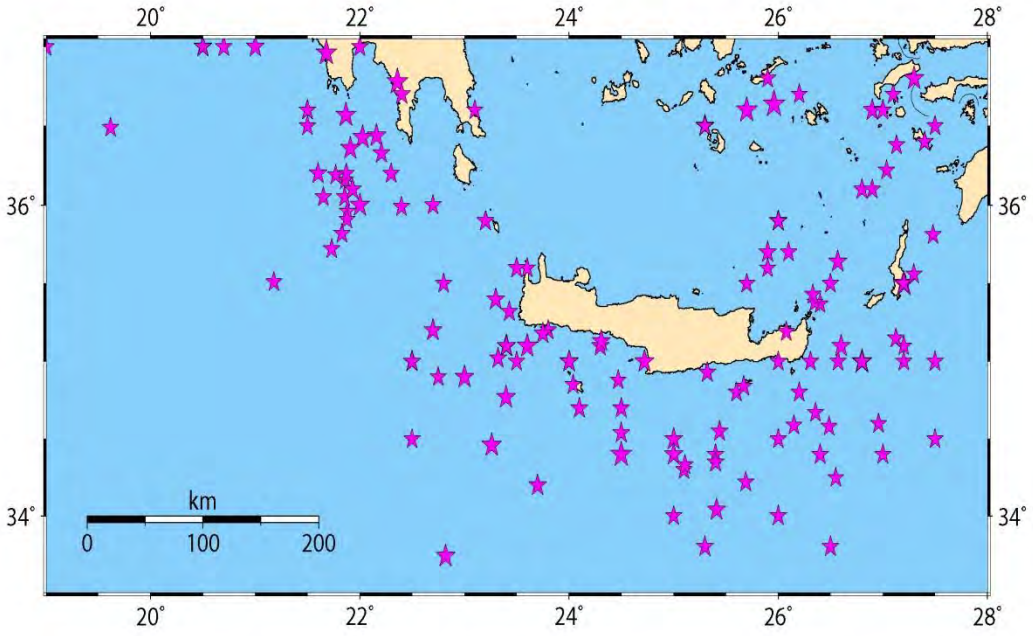

Figure 1 – Epicentral distribution of the earthquakes with $M \geq 5.5$ that occurred in the study area during 1911 -2012.

2. Seismotectonic Setting

Eastern Mediterranean active tectonics is dominated by slow convergence of Africa and Europe of about 1 cm/yr (Argus *et al*., 1989) that started about 83 Ma ago (Olivet *et al*., 1982) and lateral westward escapement of Anatolian microplate (McKenzie, 1978). In the eastern Mediterranean, the southern Aegean constitutes an area of intense seismic activity and in particular along the Hellenic Arc (Figure 2), which has been recognized as a subduction zone with a 30º–45º-dipping Wadati–Benioff seismic plane (Papazachos and Comninakis, 1971). The evolution of the orogen – back–arc basin system of the Hellenic–Aegean system is qualitatively explained by slab detachment at crust–lithosphere levels, and specifically lateral migration of the tear in the slab along the strike of the subduction zone. This provides a feasible mechanism for slab roll–back and arc migration, for orogenic collapse (and concurrent creation of large sedimentary depo–centers), and for changing chemical signatures of arc volcanism due to replacement of magma source regions by asthenospheric material (Wortel and Spakman, 1992).

Extension behind the subduction system began in the Middle to Late Miocene (10 – 13 Ma) (LePichon and Angelier, 1979; Jackson, 1994) or possibly as recently as 6 Ma (McKenzie, 1978). Extension of up to 100 per cent is thought to have affected the Aegean region in a north–south direction (McKenzie, 1978), with the greatest extensional strains located in the southern Aegean, north of Crete (Angelier *et al*., 1982; Jackson, 1994). Between the Hellenic trench and Africa, most of the region is comprised by the Mediterranean Ridge (MR), which terminates near the Calabrian arc in the west and south of Anatolia in the east. The Hellenic arc is laterally bounded by Subduction–Transform Edge Propagators (STEP), kinks in the plate boundary that are ongoing tearing of oceanic lithosphere near the horizontal terminations of subduction trenches (Govers and Wortel, 2005), the dextral Cephalonia Transform Fault in the west (Scordilis *et al*., 1985) and the

sinistral Rhodos fault in the east (Papazachos and Papazachou, 2003). Its western part is rectilinear and exactly perpendicular to the direction of underthrusting of the sea floor accommodating the largest known earthquake ($M = 8.3$) that has occurred in the Mediterranean region (Papazachos and Papazachou, 2003; Papadimitriou and Karakostas, 2008), while the eastern one is more complex and approximately parallel to it (Figure 2). The stresses related to subduction maintain the rectilinear boundary along the western convergent zone, while this containment does not exist on the eastern, mostly transform boundary (LePichon and Angelier, 1979).

Figure 2 – Morphology and main seismotectonic properties of the study area.

3. The Model

A Markov chain describes a stochastic process where transitions between states are governed by probability distributions. More formally, a Markov chain is a sequence of random variables $\boldsymbol{J} := (J_n)_{n \in N}$, where if the value $J_n = i$ is known, then the future evolution of the chain depends only on the last visited state i and it is stochastically independent of the visited states $J_{n-1}, \ldots, J_0$ ("Markov property"). We denote by E the state space of the Markov chain, which is considered to be a finite one. The initial probability distribution of the chain is denoted by $\boldsymbol{a} := (a(i); i \in E)$ (row vector), where $a(i) := P(J_0 = i)$, whereas its transition probability matrix is denoted by $\boldsymbol{P} := (p(i,j); i,j \in E)$, where $p(i,j) := P(J_{n+1} = j | J_n = i)$, for all $n \in N$. The transition probabilities are assumed to be independent of n, that is the chain is time-homogeneous.

For fixed time M, we define by

Equation 1 - Formula for the First Counting Process

$N_{\mathrm{M}}(i,j) \coloneqq \sum_{n=1}^{\mathrm{M}} 1_{\{J_{n-1}=i, J_n=j\}}$,

the number of transitions from state i to state j up to time M, whereas the number of visits to state i up to time M is defined by:

Equation 2 - Formula for the Second Counting Process

$N_{\mathrm{M}}(i) \coloneqq \sum_{n=1}^{\mathrm{M}} 1_{\{J_n=i\}}$.

The maximum likelihood function at time M is expressed in terms of the transition probabilities as follows:

Equation 3 - Formula for the Likelihood Function

$$L_{\mathrm{M}}(\boldsymbol{P}) = a(J_0)p(J_0,J_1)\cdots p(J_{\mathrm{M}-1},J_{\mathrm{M}}) = a(J_0)\prod_{(i,j)\in E^2}(p(i,j))^{N_{\mathrm{M}}(i,j)}.$$

By maximizing the corresponding log-likelihood function, we obtain the maximum likelihood estimator (MLE) of the transition probability $p(i,j)$ written as follows (see, e.g., Billingsley, 1961):

Equation 4 - Formula for the MLEs of the Transition Probabilities

$\hat{p}_{\mathrm{M}}(i,j) = \frac{N_{\mathrm{M}}(i,j)}{N_{\mathrm{M}}(i)}$,

for all $i,j \in E$.

4. Results

Concerning states classification, according to previous studies, the states of the Markov chain can be considered to be either the magnitudes or energy release levels of earthquakes. In our study the continuous magnitude scale is divided into appropriate intervals to specify discrete states visited by the Markov chain. In particular, we use three states corresponding to data magnitude intervals: *State* 1: [5.5, 5.6], *State* 2: [5.7, 6.0], *State* 3: [6.1, 7.5].

In the sequel, the discrete-time Markov model is applied to the above mentioned earthquake catalogue and the number of observed transitions in the dataset from each state i to each state j $(i,j \in E)$ are presented as elements of the following matrix:

$$Trans=\begin{pmatrix} 38 & 23 & 12 \\ 19 & 12 & 11 \\ 16 & 6 & 7 \end{pmatrix}.$$

Considering the earthquake sequence as a trajectory of the Markov chain in $[0,\mathrm{M}] \subset N$ we estimate the transition probability matrix $\hat{P}_{\mathrm{M}} = \left(\hat{p}_{\mathrm{M}}(i,j)\right)$ (Table 1), which governs the stochastic behavior of the Markov chain. The elements of the transition probability matrix describe the probabilities of the occurrence of an earthquake with a certain magnitude state, given that an earthquake with a certain magnitude state occurred. We go one step further and calculate the 95% confidence intervals of the transition probabilities resulting from the parametric bootstrap method. More specifically, the bootstrap confidence intervals are computed by means of the percentile method (Efron and Tibshirani, 1993) and they allow us to estimate the range of the values under consideration. The lower confidence bound (L.C.B.) is the $b \cdot a/2$-th order value of the transition probability, the upper confidence bound (U.C.B.) is the $b \cdot (1-a)/2$-th order value, where b denotes the number of bootstrap samples and $a/2$, $(1-a)/2$, stand for the percentiles of the

estimated quantity. New data sets (1000 in size) with each one containing 145 data points (the same size as the original dataset) are generated by using the MLEs of the transition probabilities. Then the model is applied to each dataset resulting in an empirical distribution around the MLEs of the transition probabilities and leading to the calculation of their 95% confidence intervals (Table 1).

Table 1 - Bootstrap percentile confidence intervals at 95% level of confidence for the transition probabilities of the Markov model.

	$\hat{p}_{\mathrm{M}}(1,1)$	$\hat{p}_{\mathrm{M}}(1,2)$	$\hat{p}_{\mathrm{M}}(1,3)$	$\hat{p}_{\mathrm{M}}(2,1)$	$\hat{p}_{\mathrm{M}}(2,2)$	$\hat{p}_{\mathrm{M}}(2,3)$	$\hat{p}_{\mathrm{M}}(3,1)$	$\hat{p}_{\mathrm{M}}(3,2)$	$\hat{p}_{\mathrm{M}}(3,3)$
MLE	0.5205	0.3151	0.1644	0.4524	0.2857	0.2619	0.5517	0.2069	0.2414
L.C.B.	0.3881	0.2169	0.0870	0.3111	0.1351	0.1400	0.3846	0.0741	0.0769
U.C.B.	0.6267	0.4286	0.2540	0.6000	0.4107	0.4054	0.7308	03600	0.3846

In what follows earthquake occurrence probabilities are calculated following Sadek and Limnios (2002). Let us denote by $1_{s,r} = (1, \dots, 1, 0, \dots, 0)^T$ the $s-$dimensional column vector whose r first elements are equal to 1 and the others are equal to 0. We further denote $1_r = 1_{r,r}$. At a next step we calculate the probability of the occurrence of an earthquake with $M \in [5.5, 6.0]$ at time $n \in N$, independently of the fact that an earthquake has occurred or not in $[0, n)$, which is defined as

Equation 5 - Formula for the Probability

$$A(n) = P(J_n \in \{1,2\}) = aP^n 1_{s,r} \ , n \in N,$$

with corresponding maximum likelihood estimator:

Equation 6 - Formula for the MLE of the Probability

$$\hat{A}_{\mathrm{M}}(n) = \hat{a}\hat{P}_{\mathrm{M}}^n 1_{s,r},$$

where $\hat{P}_{\mathrm{M}}^n = (\hat{P}_{\mathrm{M}})^n$, $n \in N$, and $1_{s,r} = 1_{3,2}$. Figure 3 represents the quantity under study along with its 95% confidence interval. This figure leads us to the conclusion that the occurrence probability of an earthquake with $M \in [5.5, 6.0]$ takes the constant value 0.792 after four steps ($n = 4$), given that the previous occurrences are not taken into account. The same conclusion is reached concerning its 95% confidence interval.

We further denote by P_{11} the restriction of the transition probability matrix to the set of states $\{1,2\}$ and by $\hat{P}_{\mathrm{M}11}$ its MLE. The probability of the occurrence of an earthquake with $M \in [5.5, 6.0]$ at time n and that up to time n there was no earthquake occurrence with $M \leq 6.0$, is given by

Equation 7 - Formula for the Probability

$$R(n) = P(J_u \in \{1,2\}, \forall u \in [0, n]) = a_1 P_{11}^n 1_r \ , n \in N,$$

with corresponding maximum likelihood estimator:

Equation 8 - Formula for the MLE of the Probability

$$\hat{R}_{\mathrm{M}}(n) = \hat{a}_1 \hat{P}_{\mathrm{M}11}^n 1_r.$$

Figure 4 represents the MLE of $R(n)$, along with its 95% confidence interval. In this figure we can see that as time elapses, the target-probability decreases. This result was expected in the sense that as time increases the occurrence probability of a stronger event ($M > 6.0$) increases, decreasing by this way the values of $\hat{R}_{\mathrm{M}}(n)$. After a certain number of steps, $\hat{R}_{\mathrm{M}}(n)$ and its confidence interval tend to zero. In other words, after a certain number of steps, the occurrence probability of an earthquake with $M > 6.0$ and its confidence interval tend to one. Let us now define as hitting time the occurrence time of an earthquake with $M \geq 6.1$ ("failure") denoted by T. The conditional

probability of the occurrence of an earthquake with $M \geq 6.1$ at time n, given that only earthquakes with $M \in [5.5,6.0]$ occurred up to time $n-1$, is given by

Equation 9 - Formula for the Conditional Probability

$$\lambda(n) = P(T = n | T \geq n) = \begin{cases} 1 - \dfrac{R(n)}{R(n-1)}, & R(n-1) \neq 0, \\ 0, & otherwise, \end{cases}$$

for every $n \in N^*$.

The maximum likelihood estimator for the target probability (known as BMP-failure rate), for every $n \in N^*$, is given by

Equation 10 - Formula for the MLE of the Conditional Probability

$$\hat{\lambda}_{\mathrm{M}}(n) = \begin{cases} 1 - \dfrac{\hat{R}_{\mathrm{M}}(n)}{\hat{R}_{\mathrm{M}}(n-1)}, & \hat{R}_{\mathrm{M}}(n-1) \neq 0, \\ 0, & otherwise. \end{cases}$$

and $\hat{\lambda}_{\mathrm{M}}(0) = 1 - \hat{R}_{\mathrm{M}}(0)$. Figure 5 depicts the MLE and the 95% confidence interval of the quantity under study. These results are significant in the sense that they take into account the history of earthquake occurrences up to time n in order to provide occurrence probabilities of strong events for time n. In particular, the probability of the occurrence of an earthquake with $M > 6.0$ at time n, given that only earthquakes with $M \in [5.5,6.0]$ occurred up to time $n-1$, takes the constant value 0.202 after the fourth step.

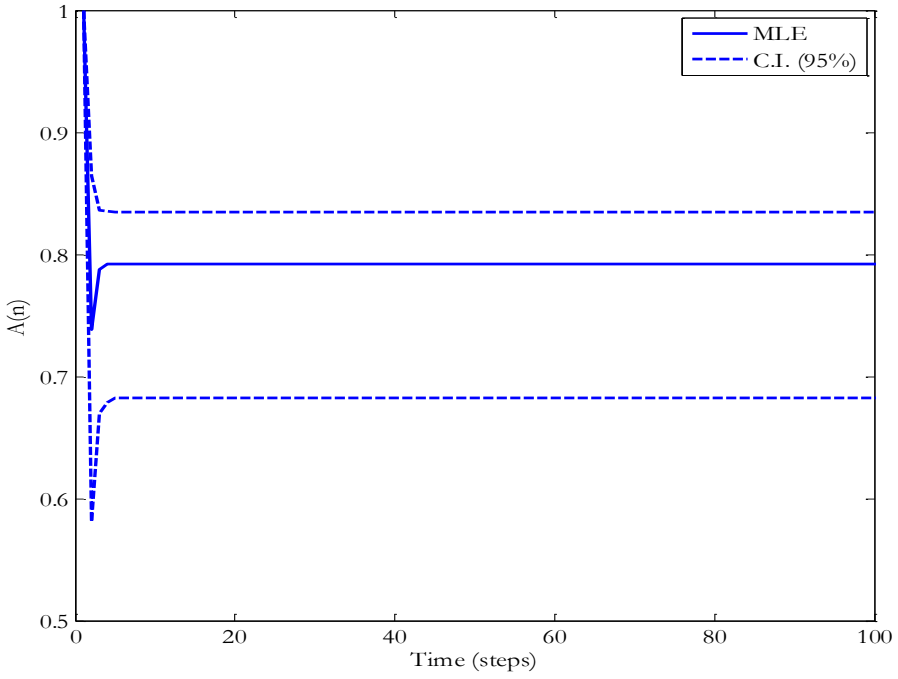

Figure 3 – Maximum likelihood estimator and 95% confidence interval for $A(n)$.

Remark. At this point we should note that although we work at the discrete-time case, we joined the values continuously, in order to observe their evolution in time more clearly.

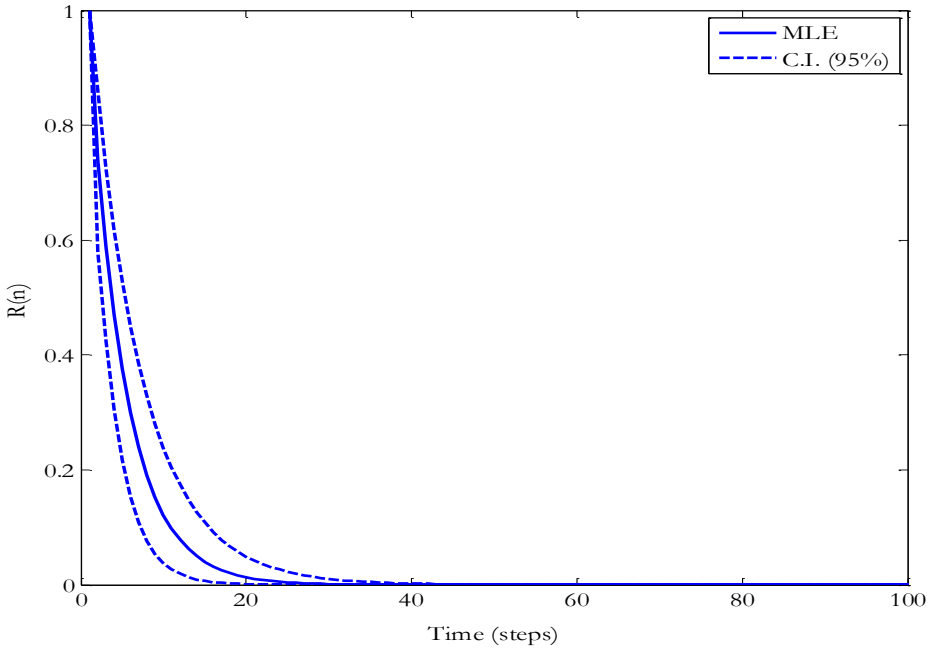

Figure 4 – Maximum likelihood estimator and 95% confidence interval for $R(n)$.

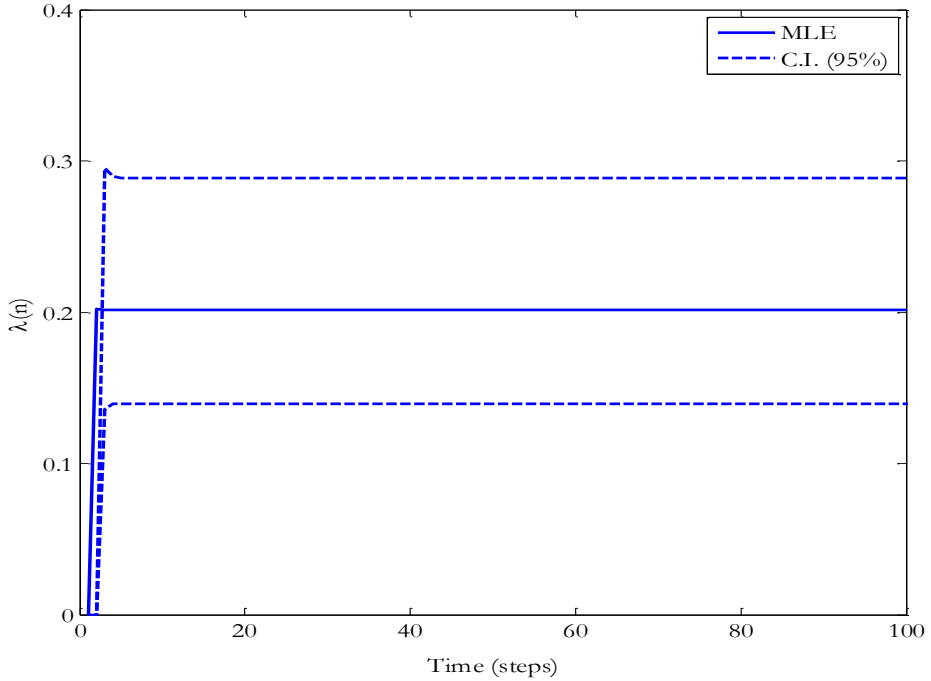

Figure 5 – Maximum likelihood estimator and 95% confidence interval for $\lambda(n)$.

Let us consider a partition $\boldsymbol{U}, \boldsymbol{D}$ of the state space $\boldsymbol{E}$, i.e., $\boldsymbol{E} = \boldsymbol{U} \cup \boldsymbol{D}$, with $\boldsymbol{U} \cap \boldsymbol{D}$=∅, $\boldsymbol{U} \neq \emptyset$ and $\boldsymbol{D} \neq \emptyset$. The random variable $\boldsymbol{T_{i'}}$ representing the number of steps for visiting for the first time a state $\boldsymbol{i'} \in \boldsymbol{D}$ is defined by $\boldsymbol{T_{i'}} := \boldsymbol{inf}\{\boldsymbol{n} \in \boldsymbol{N}: \boldsymbol{J_n} = \boldsymbol{i'}\}$. The mean number of steps for visiting for the first time the state $\boldsymbol{i'} \in \boldsymbol{D}$ starting from a state belonging to $\boldsymbol{U}$ is given by the formula (Kemeny and Snell, 1976) $\boldsymbol{E}[\boldsymbol{T_{i'}}] = \boldsymbol{a_1}(\boldsymbol{I} - \boldsymbol{P_{11}})^{-1}\boldsymbol{1_r}$. Index 1 means restriction of the transition probability matrix on $\boldsymbol{U}$, i.e., $\boldsymbol{P_{11}}$ means restriction of the matrix $\boldsymbol{P}$ on $\boldsymbol{U} \times \boldsymbol{U}$, $\boldsymbol{a_1}$ denotes the restriction of the raw vector $\boldsymbol{a}$ in $\boldsymbol{U}$, $\boldsymbol{r}$ is the number of states in $\boldsymbol{U}$ and $\boldsymbol{1_r}$ stands for the column vector of $\boldsymbol{r}$ ones. Let us now consider that set $\boldsymbol{U}$ contains all the states of $\boldsymbol{E}$ apart from the state $\boldsymbol{i'}$, which corresponds to the occurrence of an earthquake with $\boldsymbol{M} \geq \boldsymbol{6.1}$, i.e., the occurrence of an earthquake that belongs in the third magnitude state. The maximum likelihood estimator of the target number is given by the formula

Equation 11 - Formula for the MLE of the Mean Number of Steps

$$\widehat{E[T_{i'\mathrm{M}}]} = \hat{a}_1\left(I - \hat{P}^n_{\mathrm{M}11}\right)^{-1}\mathbf{1}_r.$$

Given that the current state of the Markov chain is $\boldsymbol{J_0} = \boldsymbol{2}$, the mean number of steps for the first occurrence of an anticipated earthquake with $\boldsymbol{M} \geq \boldsymbol{6.1}$ is 4.661. In other words, given that the last earthquake that occurred was of magnitude $\boldsymbol{M} \in [\boldsymbol{5.7}, \boldsymbol{6.0}]$, the first occurrence of an earthquake with $\boldsymbol{M} \geq \boldsymbol{6.1}$ is expected in an average number of 4.661 steps. The corresponding 95% bootstrap confidence interval turns out to be (3.270, 6.993).

5. Conclusions

The objective of this study is to describe a Markov model for characterizing the occurrence of strong ($M \geq 5.5$) earthquakes along the Hellenic Arc, which is consistent with the general physical process contributing to their occurrence. Contrary to the previous studies, where Markov models were applied as earthquake occurrence models, here we go one step further and estimate earthquake occurrence probabilities along with their 95% confidence intervals. The model provides important measures of the Markov chain leading to probabilistic seismic hazard results. It could serve as a basis for comparison with other stochastic models such as renewal ones as well as with more complicated models such as semi-Markov models. More accurate forecasting results could be feasible by the inclusion of the temporal and the spatial components to the model. Examples of extension are based on the assumption that the Markov chain is non-homogeneous or is a higher-order Markov chain, allowing second- or higher-order Markov dependence. The current research could be enriched by the calculation of other measures derived from the transition probability matrix (e.g., moments of the number of steps for the first earthquake occurrence of a certain magnitude state) to provide additional results. Alternative methods could be applied for the calculation of the confidence intervals for the quantities under study, and the derived results could be compared with the initial ones.

6. Acknowledgements

This work was supported by the THALES Program of the Ministry of Education of Greece and European Union in the framework of the project entitled “Integrated understanding of Seismicity, using innovative Methodologies of Fracture mechanics along with Earthquake and non extensive statistical physics - Application to the geodynamic system of the Hellenic Arc. SEISMO FEAR HELLARC”. Geophysics Department, AUTH, contribution number 815.

7. References

Anagnos T. and Kiremidjan A.S. 1988. A review of earthquake occurrence models for seismic hazard analysis, *Probabilist. Eng. Mech*., 3(1), 3-11.

Angelier J., Lyberis N., LePichon X. and Hucho X. 1982. The tectonic development of the Hellenic arc and the Sea of Crete: A synthesis, *Tectonophysics,* 86, 159-196.

Argus D.F., Gordon R.G., DeMets C. and Stein S. 1989. Closure of the Africa–Eurasia–North America plate motion circuit and tectonics of the Gloria fault, *J. Geophys. Res.,* 94, 5585-5602.

Billingsley P. 1961. Statistical Inference for Markov Processes. The University of Chicago, Chicago Press.

Barlow R.E., Marshall A.W. and Proschan F., 1963. Properties of Probability Distributions with Monotone Hazard Rate, *Ann. Math. Stat.*, 34, 375-389.

Barlow R.E., and Proschan F. 1975. Statistical Theory of Reliability and Life Testing, Probability Models, Holt, Rinehart and Winston, USA.

Roy D. and Gupta R.P. 1992. Classification of Discrete Lives, *Microelectron. Reliab.,* 32, 1459-1473.

Bracquemond C. 2001. Modélisation Stochastique du Vieillissement en Temps Discret, *Thesis*, Laboratoire de Modélisation et Calcul, Grenoble.

Bracquemond C., Gaudoin O. and Xie M. 2001. Towards a New Definition of Failure Rate for Discrete Distributions, *10th International Symposium on Applied Stochastic Models and Data Analysis*, 1, 266-270.

Efron B. and Tibshirani R.J. 1993. An introduction to the bootstrap. New York: Chapman and Hall.

Jackson J. 1994. Active tectonics of the Aegean region, *Annu. Rev. Earth Planet. Sci.,* 22, 239-271.

Govers R., and Wortel M.J.R. 2005. Lithosphere tearing at STEP faults: Response to edges of subduction zones, *Earth Planet. Sci. Lett.,* 236, 505-523.

Kemeny J.G. and Snell J.L. 1976. Finite Markov chains, *Springer-Verlag*, NY.

LePichon,X. and Angelier J. 1979. The Hellenic arc and trench system: A key to the neotectonic evolution of the eastern Mediterranean area, *Tectonophysics,* 60, 1-42.

McKenzie D. 1978. Active tectonics of the Alpine–Himalayan belt: The Aegean Sea and surrounding regions, *Geophys. J. Roy. Astron. Soc.,* 55, 217-254.

Olivet J.L., Bonnin J., Beuzart P. and Auzende J.M. 1982. Cinématique des plaques et paléo géographie: une revue, *Bull. Soc. Géol. France,* 24, 875-892.

Papadimitriou E.E. 1994. Long-term earthquakes prediction in the north Pacific seismic zone based on the time and magnitude predictable model, *Natural Hazards*, *9*, 303–321.

Papadimitriou E.E. and Karakostas V.G. 2008. Rupture model of the great AD 365 Crete earthquake in the southwestern part of the Hellenic Arc, *Acta Geophysica*, 56 (2), 293-312.

Papazachos B.C. and Comninakis P.E. 1971. Geophysical and tectonic features of the Aegean Arc, *J. Geophys. Res.* 76, 8517-8533.

Papazachos B.C. and Papazachou C. 2003. *The Earthquakes of Greece*, Ziti Publ., Thessaloniki, 317 pp.

Reid H.F. 1910. The mechanism of the earthquake, in: The California earthquake of April 18, 1906, *report of the state earthquake Investigation Commission*, Washington, D.C., Carnegie Institution, *2*, 1–92.

Sadek A. and Limnios N. 2002. Asymptotic properties for maximum likelihood estimators for reliability and failure rates of Markov chains, *Commun. Stat. A.-Theor.*, 31 (10), 1837-1861.

Scordilis E.M., Karakaisis G.F., Karakostas, B.G., Panagiotopoulos D.G., Comninakis P.E. and Papazachos B.C. 1985. Evidence for transform faulting in the Ionian Sea: The Cephalonia Island earthquake sequence, *Pure Appl. Geophys.,* 123, 388-397.

Tsapanos T.M. and Papadopoulou A. 1999. A discrete Markov model for earthquake occurren-ces in Southern Alaska and Aleutian Islands, *J. Balkan Geophys. Soc.*, 2 (3), 75–83.

Wortel M.J.R. and Spakman W. 1992. Structure and dynamics of subducted lithosphere in the Mediterranean region, *Proc. Kon. Ned. Acad. Sci.,* 95, 325-347.

Δελτίο της Ελληνικής Γεωλογικής Εταιρίας, τομ. XLVII , 2013
Πρακτικά 13ου Διεθνούς Συνεδρίου, Χανιά, Σεπτ. 2013

Bulletin of the Geological Society of Greece, vol. XLVII 2013
Proceedings of the 13th International Congress, Chania, Sept. 2013

FLOOD RECONSTRUCTION USING BOTANICAL EVIDENCE IN RAPENTOSA CATCHMENT, IN MARATHON, GREECE

Diakakis M.[1]

[1] *National and Kapodistrian University of Athens, Faculty of Geology and Geoenvironment, 15784, Zografou, Athens, Greece, Email: diakakism@geol.uoa.gr*

Abstract

Botanical evidence has been used in the past for flash flood analysis, especially when instrumental data were scarce. This work focuses on the use of such evidence as a tool to study flash flood phenomena in Rapentosa torrent, in Marathon, Greece. To this aim, impact scars induced during past flood events on trees along the torrent, were considered water stage indicators and were used to determine discharge magnitude of these flow episodes. Samples extracted from the scarred specimens with the aid of an increment borer, were used to date these impacts wounds. 1-D hydraulic modeling was used to provide a reconstruction of the highest-discharge event, while results were cross-examined with historical damages to verify the outcome of the analysis. Analysis showed a total of 22 impact wounds along the torrent indicating discharge values between 17.1 m^3/s and 84.9 m^3/s during past flow episodes. Three flash flood events were identified in 1996, 1998 and 2001. Hydraulic modeling of the 2001 event, which presented the highest flow values, illustrated its extent and water depth across the floodplain, presenting good correlation with the available documentary evidence.

Key words: *Dendrochronology, Dendromorphology, Flood hazard, Marathonas, Flood reconstruction.*

Περίληψη

Η δενδρομορφολογία έχει αποτελέσει στο παρελθόν σημαντικό εργαλείο στην ανάλυση πλημμυρών, ειδικότερα στις περιοχές όπου τα ενόργανα υδρολογικά δεδομένα είναι ελλειπή. Η παρούσα μελέτη εστιάζει στην ανάλυση πληγών πρόσκρουσης στη βλάστηση, οι οποίες δημιουργήθηκαν κατά τη διάρκεια πλημμυρικών επεισοδίων, στο ρέμα της Ραπεντώσας, στην περιοχή του Μαραθώνα. Για το σκοπό αυτό, εξετάσθηκαν οι συνθήκες ροής και οι διαστάσεις τις κοίτης στις υπό μελέτη θέσεις, και υπολογίσθηκε η απορροή. Παράλληλα, λήφθηκαν πυρήνες με τη χρήση ειδικού οργάνου με σκοπό την χρονολόγηση των πληγών αυτών. Ακολούθως, χρησιμοποιήθηκε η τεχνική της υδραυλικής προσομοίωσης με σκοπό την αναπαράσταση της πλημμύρας με τη μεγαλύτερη απορροή. Από την ανάλυση προέκυψαν απορροές μεταξύ 17.1 m^3/s και 84.9 m^3/s κατά τη διάρκεια τουλάχιστον τριών πλημμυρικών γεγονότων το 1996, το 1998 και το 2001. Από την μοντελοποίηση του συμβάντος του 2001, το οποίο παρουσίασε τις υψηλότερες τιμές απορροής, υπολογίσθηκε η έκταση και το βάθος της πλημμύρας.

Λέξεις κλειδιά: *Δενδροχρονολογία, Δενδρομορφολογία, Πλημμυρικός κίνδυνος, Μαραθώνας.*

1. Introduction

The analysis of botanical evidence is an established scientific tool in natural hazards research (Butler et al., 1987, Stoffel and Bollschweiler, 2008, Stoffel et al., 2010) used to study a range of geological and hydrometeorological phenomena, such as debris flows (Hupp, 1984), wildfires (McBride, 1983, Grissino-Mayer, 2010), earthquakes (Bekker, 2010), landslides (Hupp, 1983, Stoffel and Perret, 2006) and floods (Gottesfeld, 1996, Zielonka et al., 2008, George, 2010). In the field of flood risk analysis, especially in the case of ungauged catchments, dendromorphology has been proved a useful and increasingly reliable approach (Stoffel and Bollschweiler, 2008, Ruiz-Villanueva et al., 2010). One of the first descriptions of the impact of flooding on vegetation comes from Sigafoos (1964). Since then, several works have studied various disturbances of vegetation as source of information on past hydrologic episodes (Loomans, 1993, Ruiz-Villanueva et al., 2010). Scars caused on the stem of trees growing in channel banks, most likely formed by impact with woody debris and stones transported during intense flow episodes (Gottesfeld, 1996), have been used to identify floods, to examine raised water levels (Zielonka et al., 2008, George, 2010) and to date these events by tree-ring analysis (Ruiz-Villanueva et al., 2010).

Based on this principle several authors have exploited botanical evidence to estimate discharge in a single event or a series of floods (Jarrett, 1990, Gottesfeld, 1996, George, 2010), to reconstruct physical characteristics of flow (Loomans 1993, Tardif and Bergeron, 1997), to enrich flooding history and instrumental records (Yanoksy and Jarrett, 2002, Bollschweiler et al. 2011), to identify extreme floods (George and Nielsen, 2000), to estimate flood frequency (Hupp 1984) and to understand geomorphic processes of a river and their evolution (Baker 1994, Bollschweiler et al. 2011). Dendrochronology and dendromorphology have been used in conjunction with other hydrologic and hydraulic techniques to reconstruct and visualize characteristics of past flow episodes (Ballesteros et al. 2010).

Given the fact that flash flood analysis in ephemeral streams, in Greece, poses a significant challenge due to lack of instrumental data, this work analyses vegetation evidence along Rapenotsa catchment, in an effort to examine the applicability of the approach and improve our understanding on flood processes in the area, in terms of flood discharge and flood extent.

2. Study Area

The work carried out in this paper was conducted in Rapentosa catchment, in Attica, Greece, approximately 25 km northeast of the city of Athens (Figure 1). Rapentosa is an ephemeral mountain torrent with a basin area of 37.5 sq. km. draining the north slopes of Penteli Mt. At the last part of its course the torrent crosses Marathon plain, a fairly flat area dominated by agricultural land and the small settlements of Vranas and Tymvos. Directly upstream from the plain, which consists of Holocene alluvial deposits, the torrent passes through Mesozoic bedrock (mainly marble) forming a steep and narrow gorge.

The plain has been subject to flash flood phenomena several times in the past, claiming at least one life in 1980 (Diakakis 2010). According to historical evidence analyzed by Diakakis (2010) at least 13 distinct flash flooding events can be identified in 1805, 1959, 1980, 1987, 1988, 1996, 1998, 1999, 2001, 2003 and two in 2005. Examination of local wildfire history showed that three major forest fires have occurred in the area in 1995, 1998 and 2009 (Xanthopoulos 2002, Amiridis et al. 2012), leading, according to reports, to debris-laden river flows and increased amounts of sediments and vegetation fragments deposited across the plain and in the sea (Diakakis 2010).

This study was conducted in the 2730 m long section of the stream flowing through the gorge where dense coniferous vegetation is developed along the narrow riverbed and the banks of the torrent (Figure 1c).

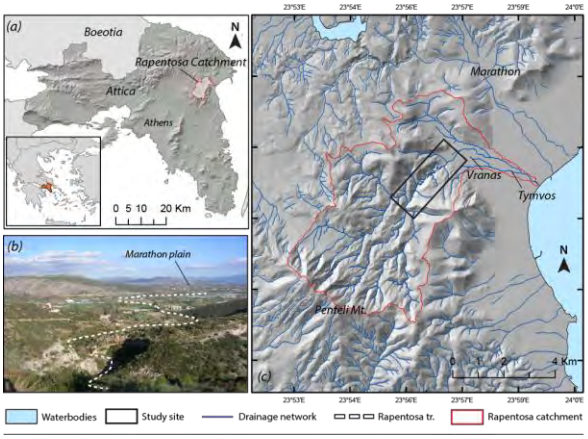

Figure 1 - (a) Location of the study area, (b) view of Rapentosa torrent flowing into Marathon plain (towards Northeast) and (c) overview of the Rapentosa drainage network and the study site.

3. Materials and Methods

The work carried out in this study can be divided into five main parts, namely: (i) field identification and mapping of flood-induced scars, (ii) recording of flow conditions and channel dimension at these locations, (iii) discharge calculations, (iv) core sampling and dating of scars and (v) 1-D modeling of highest calculated flood discharge.

3.1. Field Survey

The study started with field survey of the channel and its banks aimed to identify and map flood-induced external disturbances on vegetation. Tree trunks growing on the banks along the stream were carefully inspected for the presence of scars and other stem injuries. The survey confirmed 22 different cases of abrasion injuries (scars) on tree trunks of the conifer species *Pinus Halepensis* (Figure 2), created by either vegetation debris or stones transported violently during flood episodes. The scars were thoroughly inspected, photographed, measured and mapped with the aid of GPS equipment (Figure 3).

3.2. Recording Flow Conditions and Measuring Channel Dimensions

Flow conditions at the location of each injury were documented in order to calculate the channel's roughness coefficient for each spot according to the Aldridge and Garrett (1973) methodology. The cross sectional area was inspected, photographed and compared to the Aldridge and Garrett (1973) and Arcement and Schneider (1984) standards regarding six different variables affecting flow roughness, that is: (i) the channel's degree of irregularity, (ii) the variations in channel cross section, (iii) the channel's obstructions to flow, (iv) the amount of vegetation and (v) the degree of meandering.

Roughness coefficient (n) was then calculated according to the Cowan's (1956) equation:

Equation 1 – Cowan's (1956) equation for calculation of roughness coefficient.

$$n = \left(n_b + n_1 + n_2 + n_3 + n_4\right) \cdot m \,.$$

where n_b is a base value of n for a straight, uniform, smooth channel in natural materials, n_1 is a correction factor connected with the degree of the channel's irregularity, n_2 is a variable connected with the variations in the channel's cross section, n_3 is a factor connected with the effect of

obstructions to flow, n_4 is a factor connected with the amount of vegetation and m is a factor connected with the degree of meandering.

To calculate discharge of flow episodes detailed measurements of the channel cross sectional area and the wetted perimeter were carried out with the aid of laser rangefinders with an accuracy of 1.5mm. Two sets of measurements were carried out with the rangefinders and a third with typical measuring tape to assure accuracy. Following this step, simple geometry calculations were carried out to determine the two variables of the channel dimensions.

Figure 2 - Typical stem injuries (scars) along Rapentosa torrent banks.

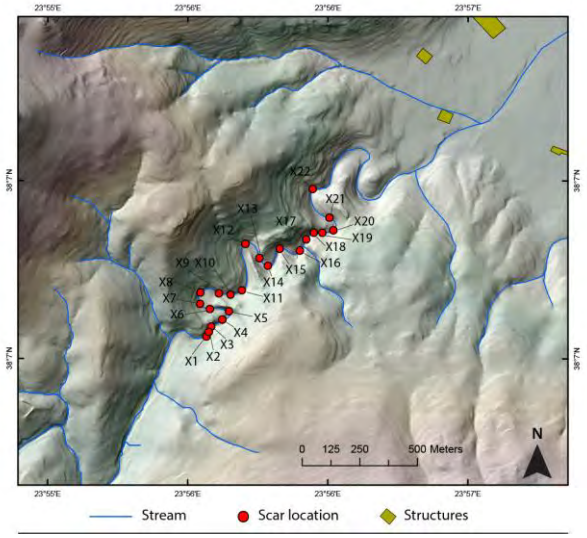

Figure 3 - Locations of abrasion scars identified in the study area.

3.3. Discharge Calculations

Given that injuries induced during flood episodes are considered water stage indicators, one can reconstruct discharge of a flow episode, using the Gauckler-Manning formula (Manning 1891):

Equation 2 – Gauckler-Manning formula

$$Q = \frac{1}{n} \cdot A \cdot R^{2/3} \cdot S^{1/2}$$

where Q is the flow discharge in m^3/s, n is the roughness coefficient, A is the cross sectional area in m^2, R is the hydraulic radius in m, S is the hydraulic slope. The hydraulic radius derives from the ratio of the cross sectional area (A) in m^2, to the wetter perimeter of the channel (P) in m.

3.4. Injury Dating

In order to determine the date of the injury, samples were extracted using a Haglof type increment borer of 16". Each tree specimen was sampled twice according to Barrett and Arno (1988) face-boring procedures for single scarred trees (Figure 4). After collection, cores were dried and sanded (surfaced) for ring analysis. Analysis was carried out using a 40x microscope and succeeded to determine the age of injury in 9 out of 22 samples.

3.5. Hydraulic Modelling

Hydraulic modeling was carried out to determine the extent of inundation and flow depth of the maximum discharge episode determined in prior steps of the methodology. To this aim, HEC-RAS model (HEC 2002) was used to simulate river flow downstream of the study site. Geometry of the channel and the floodplain was based on 1:5000 scale maps with 1m contours and accurate measurements of the channel dimensions in 30-meter intervals with the technique described in 3.2. The whole model was built and run in a GIS interface.

3.6. Uncertainties

One source of uncertainty is connected with the fact that the state of vegetation affecting flow conditions at the time of each flood could not be accurately known. For this reason today's flow conditions were used in discharge calculations. With regard to the channel dimensions it is consider safe to assume that channel measurements are the same because its bedrock nature wouldn't allow significant changes in a few years time. In addition, several of tree specimens were partly destroyed by a wildfire in August 2009 and therefore dating of some of the injuries as mentioned in 3.4 was impossible.

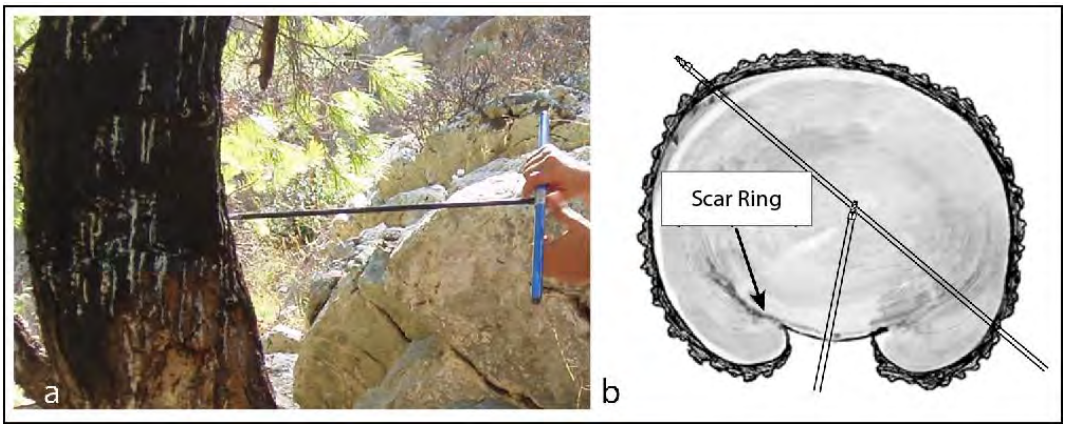

Figure 4 - Extracting samples using an increment borer (a), by a specific sampling approach illustrated on a schematic cross section of a tree trunk (b).

4. Results and Discussion

Discharge values indicated by each flood scar were calculated with the use of Gauckler-Manning formula between 17.1 m^3/s, and 84.9 m^3/s (Table 1).

Table 1 – Calculation of discharge (Q) for each impact location based on Manning formula and according to the channel parameters.

Location Name	A (m^2)	P (m)	S (m/m)	n	Q (m^3/s)
X1	11.1	15	0.04	0.128	14.3
X2	Speciment destroyed completely during the course of research, due to a wildfire				
X3	25.3	17	0.0349	0.143	42.9
X4	Speciment destroyed completely during the course of research, due to a wildfire				
X5	21.9	14.7	0.0305	0.119	41.9
X6	28.6	23.1	0.03143	0.079	74.2
X7	25.7	22.9	0.0325	0.064	78.1
X8	25.1	19.5	0.0325	0.093	57.5
X9	19.1	20.2	0.0278	0.09	34.1
X10	Speciment destroyed completely during the course of research, due to a wildfire				
X11	24.3	18	0.0186	0.081	50.1
X12	14.4	14.1	0.0186	0.0736	26.9
X13	26.3	15.4	0.044	0.113	69.5
X14	23.3	20.1	0.0494	0.071	80.4
X15	19.8	23	0.032	0.059	54.3
X16	20.4	20	0.0571	0.058	84.9
X17	20.8	23.5	0.0303	0.097	34.6
X18	20.6	15.7	0.0303	0.129	33.4
X19	15.7	13	0.0303	0.181	17.1
X20	29	19.9	0.036	0.13	54.5
X21	20.4	18.9	0.0421	0.144	30.5
X22	20.5	14.6	0.0415	0.083	63.2

Tree-ring analysis lead to the determination of impact year, in 9 out of 22 samples identifying three distinct flow episodes in 1996, 1998 and 2001 (Figure 5).

Analysis showed that the 2001 event presented the highest calculated flow value (84.9 m^3/s) (Table 2), indicating for the first time in this ungauged catchment the magnitude of flood episodes locally. Based on this value and with the aid of hydraulic modeling the study was able to determine the extent of flooding across the Marathon plain, delineating in this way the active part of the floodplain and determining the human infrastructure that is developed in this flood-susceptible area (Figure 6). In addition, the simulation calculated and visualized the depth of floodwaters for the 2001 scenario. This information can be valuable to estimate damage cost of future flooding in the area. Both flood extent and depth data improve our knowledge on the local flooding problem and can be used to define a long term strategy for flood risk mitigation planning, by illustrating its priorities, by identifying the flood-susceptible areas and by quantifying the impact of flooding. For verification purposes simulation results were compared with 2001 flood damages showing good correlation.

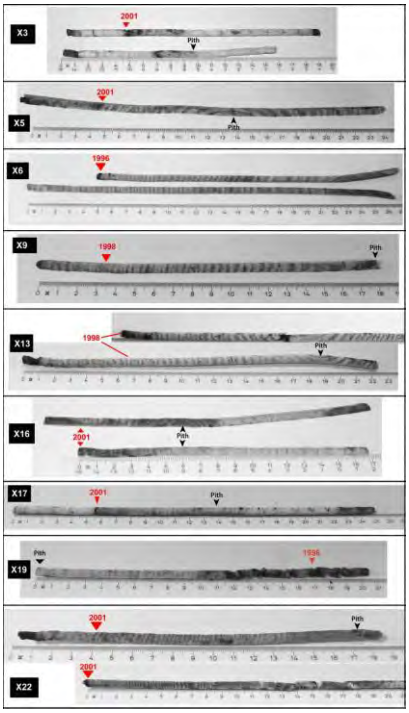

Figure 5 – Core samples extracted from scarred specimens in which determination of impact date was plausible. Impact year is appearing in red indicator, whereas scar codename appear in black rectangular in the left side of the image.

Table 2 – Date and discharge values indicated by 9 out of 22 impact scars.

Impact location	Year of impact	Discharge values (m^3/s)
X6, X19	1996	17.1-74.2
X9, X13	1998	34.1-69.5
X3, X5, X16, X17, X22	2001	34.6-84.9

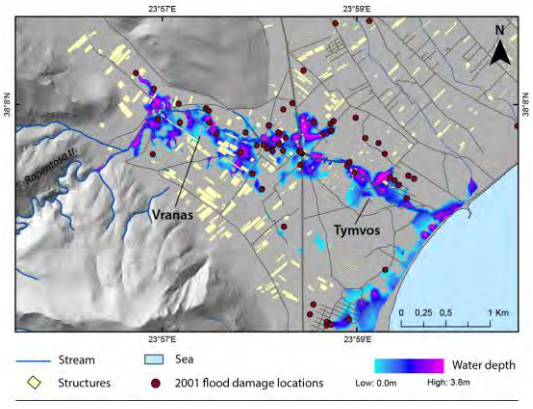

Figure 6 – Hydraulic simulation of 2001 flood discharge across Marathon floodplain showing water extent and depth, and the 2001 flood damage locations.

5. Conclusions

This work examines a series of flood impact scars along the ungauged torrent of Rapentosa, near Marathon in Greece. Based on hydraulic conditions and channel dimensions, this study manages to calculate discharge values reaching up to 84.9 m^3/s and identifies through tree-ring analysis at least three distinct flood events in 1996, 1998 and 2001. With the aid of hydraulic modelling, flood extent and water depth of the 2001 event are simulated and compared with historical flood damages, showing good correlation, verifying in this way the results of the analysis. The technique was proved to be a useful tool for determination of discharge values in ungauged catchments, delineation of the active floodplain and the physical characteristics of floodwaters as a basis for flood risk studies.

6. Acknowledgments

This work is dedicated with gratitude to the late Associate Professor of the National and Kapodistrian University of Athens, Ioannis Fountoulis, who always supported the author as an academic and as a friend. The author would like also to express his gratitude to Dr. Gavriil Xanthopoulos for offering his help and advice on the tree boring procedures and for lending equipment without which this research would not be completed. The author would also like to thank the friends and colleagues S. Mallis, P. Vamvakas, N. Papafakli, G. Glynos and K. Lazoglou for helping during fieldwork.

7. References

Acrement G.J. and Schneider V.R. 1984. Guide for selecting Manning's Roughness Coefficients for Natural Channels and Flood Plains, *United States Geological Survey Water-supply Paper 2339,* 67pp.

Aldridge B.N. and Garrett J.M. 1973. Roughness coefficients for stream channels in Arizona: *U.S. Geological Survey Open-File Report*, 87 pp.

Amiridisa V. Zerefosb C., Kazadzisd S., Gerasopoulos E., Eleftheratos K., Vrekoussis M., Stohl A., Mamouri R.E., Kokkalis P., Papayannis A., Eleftheriadis K., Diapouli E., Keramitsoglou I., Kontoes C., Kotroni V., Lagouvardos K., Marinou E., Giannakaki E., Kostopoulou E., Giannakopoulos C., Richter A., Burrows J.P. and Mihalopoulos N. 2012. Impact of the 2009 Attica wild fires on the air quality in urban Athens, *Atmospheric Environment*, 46, 536-544.

Baker V.R. 1994. Geomorphological understanding of floods, *Geomorphology*, 10, 139-156.

Ballesteros J.A., Eguibar M., Bodoque J.M., Diez-Herrero A., Stoffel M. and Gutierez-Perez I. 2010. Estimating flash flood discharge in an ungauged mountain catchment with 2D hydraulic models and dendrogeomorphic palaeostage indicators, *Hydrological Processes*, 25, 6, 970-979.

Barrett S.W. and Arno S.F. 1988. Increment-borer methods for determining fire history in coniferous forests, *United States Department of Agriculture. General Technical Report INT-244*. 20pp.

Bekker M.F. Tree rings and earthquakes, in: Stoffel M., Bollschweiller M., Butler D. R., Luckman, B. H. (eds), *Tree rings and natural hazards. A state-of-the-art*. 3-23, New York, Springer, 505pp.

Bollschweiller M., Stoffel M. and Schlappy R. 2011. Debris-flood reconstruction in a pre-alpine catchment in Switzerland based on tree-ring records of coniferous and broadleaved trees, *Geografiska Annaler: Series A*, *Physical Geography*, 93, 1, 1-15.

Butler D.R., Malanson G.P. and Oelfke J.G. 1987. Tree-Ring analysis and natural hazard chronologies: minimum sample sizes and index values, *The Professional Geographer*, 39, 1, 41-47.

Cowan W.L. 1956. Estimating hydraulic roughness coefficients, *Agricultural Engineering*, 37, 7, 473-475.

Diakakis M. 2010. Flood history analysis and its contribution to flood hazard assessment: the case of Marathonas, Greece, *Bull. Geol. Soc. Greece,* 43, 1323–1334.
George S.St. 2010. Dendrohydrology and Extreme Floods Along the Red River, Canada, in: Stoffel M., Bollschweiller M., Butler D.R. and Luckman B.H. (eds), *Tree rings and natural hazards. A state-of-the-art,* 3-23, New York, Springer, 505pp.
George S.St. and Nielsen E. 2000. Signatures of high-magnitude 19th-century floods in Quercus macrocarpa tree rings along the Red River, Manitorba, Canada, *Geology*, 28, 10, 899-902.
Gottesfeld A.S. 1996. British Columbia flood scars: maximum flood-stage indicators, *Geomorphology*, 14, 319-325.
Grissino-Mayer H.D. 2010. Wildfire Hazard and the Role of Tree-Ring Research, in: Stoffel, M., Bollschweiller, M., Butler, D. R., Luckman, B. H. (eds), *Tree rings and natural hazards. A state-of-the-art*. 3-23, New York, Springer, 505pp.
HEC 2002. HEC-RAS River analysis system. Hydraulic Reference Manual Version 3.1. Hydrologic Engineering Center, US Army Corps of Engineers.
Hupp C.R. 1983. Geo-botanical evidence of late Quaternary mass wasting in block field areas of Virginia, *Earth Surface Processes and Landforms*, 8, 439-450.
Hupp C.R. 1984. Dendrogeomorphic evidence of debris flow frequency and magnitude at Mount Shasta, California, *Environ. Geol. Water Sci.*, 6, 2, 121-128.
Jarrett R.D. 1990. Paleohydrology used to define the spatial occurrence of floods, *Geomorphology*, 3, 81-95.
Loomans S.A. 1993. Flood reconstruction in Southern Illinois using tree rings, *MSc Thesis,* University of Illinois at Urbana-Champaign. 87pp.
Manning R. 1891. On the flow of water in open channels and pipes, *Inst. Civ. Eng. Ireland Trans*. 20, 161–207.
McBride J.R. 1983. Analysis of the tree rings and fire scars to establish fire history, *Tree-ring Bull.*, 43, 51-67.
Ruiz-Villanueva V., Diez-Herrero A., Stoffel M., Bollschweiller M. and Ballesteros J.A. 2010. Dendrogeomorphic analysis of flash floods in a small ungauged mountain catchment (Central Spain), *Geomorphology*, 118, 383-392.
Sigafoos R.S. 1964. Botanical evidence of floods and flood-plain deposition, *United States Geological Survey Professional Paper*, 485-A, 35 pp.
Stoffel M. and Bollschweiller M. 2008. Tree-ring analysis in natural hazards research-an overview, *Nat. Hazards Earth Syst. Sci*., 8, 187-202.
Stoffel M., Bollschweiller M. Butler D.R. and Luckman B.H. 2010. Tree rings and natural hazards: An introduction, in: Stoffel, M., Bollschweiller, M., Butler, D. R., Luckman, B. H. (eds), *Tree rings and natural hazards. A state-of-the-art*. 3-23, New York, Springer, 505pp.
Stoffel M. and Perret S. 2006. Reconstructing past rockfall activity with tree rings: some methodological considerations, *Dendrochronologia*, 24, 1-15.
Tardif J. and Bergeron Y. 1997. Ice flood history reconstructed with tree-rings from the southern boreal forest limit, western Quebec, *Holocene,* 7, 291–300.
Xanthopoulos G. 2002. The forest fires of 1995 and 1998 on Penteli Mountain, *Proceedings of the International Workshop on "Improving Dispatching for Forest Fire Control".* December 6-8, 2001. Chania, Crete, Greece. G. Xanthopoulos, (ed) pp. 85-94, Mediterranean Agronomic Institute of Chania, Chania, Crete, Greece. 162 p.
Yanosky T.M. and Jarrett R.D. 2002 Dendrochronologic evidence for the frequency and magnitude of paleofloods, *Water Science and Application*, 5, 77-89.
Zielonka T., Holeksa J. and Ciapala S. 2008. A reconstruction of flood events using scarred trees in the Tatra Mountains, Poland, *Dendrochronologia,* 26, 173-183.

Δελτίο της Ελληνικής Γεωλογικής Εταιρίας, τομ. XLVII , 2013
Πρακτικά 13ου Διεθνούς Συνεδρίου, Χανιά, Σεπτ. 2013

Bulletin of the Geological Society of Greece, vol. XLVII 2013
Proceedings of the 13th International Congress, Chania, Sept. 2013

CHANGES IN FLOOD MORTALITY DURING THE LAST 50 YEARS IN GREECE

Diakakis M.[1] and Deligiannakis G.[2]

[1] *National and Kapodistrian University of Athens, Faculty of Geology and Geoenvironment, 15784, Zografou, Athens, Greece, Email: diakakism@geol.uoa.gr*

[2] *Department of Earth and Atmospheric Sciences Mineralogy - Geology Laboratory 75 Iera Odos Str., GR 11855, Athens, Greece*

Abstract

This work focuses on the changes that occur in the circumstances under which flood fatalities occur in Greece. To this aim, this paper develops and studies a database of 189 flood-related deaths, between 1960 and 2010, consisting of variables describing the conditions during the time of each incident. Changes in the number and the spatial distribution of fatalities, together with changes in the conditions, the surrounding environment and the demographics of the victims are investigated. Results showed that males, youngsters and elderly people presented an overrepresentation among the decedents, although individuals between 20 and 65 showed a significant increase among the victims, especially during the last decades of the study period. Fatal flood events were found to be approximately equally divided between urban and rural environments. However, fatal incidents appear to gradually migrate from urban centers to rural environments. Vehicle-related fatalities showed a gradual increase, whereas pedestrian victims and indoors incidents show an opposite trend. Fatalities per flood event presented a significant decline, although in absolute numbers, flood deaths did not show a respectively important decreasing trend. Among different causes of death drowning was found to be the most common throughout the study period.

Key words: *Flood deaths, Flood fatalities, Spatial Analysis, Flood Hazard.*

Περίληψη

Η παρούσα μελέτη εξετάζει την θνησιμότητα που συνδέεται με πλημμυρικά φαινόμενα στον Ελληνικό χώρο. Στο πλαίσιο αυτό αναπτύσσεται μια βάση δεδομένων 189 θανάτων, της περιόδου 1960-2010, με λεπτομερή στοιχεία για κάθε θανατηφόρο συμβάν. Με βάση το συστηματικό αυτό αρχείο εξετάζονται οι μεταβολές στον αριθμό, τη χωρική κατανομή, τις συνθήκες κάθε περιστατικού και τα δημογραφικά στοιχεία των θυμάτων. Από τα αποτελέσματα προκύπτει η υπερεκπροσώπηση των ανδρών, των νέων και των ηλικιωμένων ατόμων μεταξύ των θυμάτων, μολονότι τα άτομα μεταξύ 20 και 65 ετών καταγράφουν σημαντική αύξηση. Παρότι οι θάνατοι παρουσιάζονται μοιρασμένα σε αστικά και μη αστικά περιβάλλοντα, τα τελευταία χρόνια η πλειοψηφία των θανάτων καταγράφεται εκτός αστικού χώρου. Από την ανάλυση προκύπτει επίσης ότι οι θάνατοι που σχετίζονται με τη χρήση οχημάτων παρουσιάζουν αυξητική τάση αντίθετα με τους θανάτους πεζών και τους θανάτους εντός οικημάτων. Τα πολύνεκρα πλημμυρικά συμβάντα παρουσιάζουν σταδιακά εξαφανίζονται, μολονότι ο αριθμός των νε-

κρών δεν παρουσιάζει σημαντική μείωση. Τέλος, προκύπτει ότι μεταξύ των διαφόρων αιτιών θανάτου ο πνιγμός παρουσιάζει τα μεγαλύτερα ποσοστά.
Λέξεις κλειδιά: *Πλημμύρες, Θάνατοι, Χωρική ανάλυση, Πλημμυρικός κίνδυνος.*

1. Introduction

Flooding is one of the most catastrophic types of natural hazards in southern Europe (Guzzetti and Tonelli, 2004, Llasat et al., 2010,) inducing extensive damages and a large number of fatalities every year (Kunkel et al., 1999, Barrero, 2009).

Several studies focus on mortality associated with flooding (Alderman et al., 2012) by examining the factors that affect the vulnerability of individuals (French et al., 1983, Coates, 1999, Rappaport, 2000, Jonkman and Kelman, 2005, Ashley and Ashley, 2008, Bern et al., 1993, Staes et al., 1994). The victims' age is considered one of these factors, as it is suggested that very young and elderly individuals are more vulnerable due to lack physical strength and their inability to flee (Chowdburry 1993, Ashley and Ashley 2008). Regarding the victims' gender several studies show that males are more vulnerable (Coates 1999; French et al. 1983, Rappaport, 2000, Ashley and Ashley 2008) due to their involvement in riskier activities during a disaster and their propensity towards risk taking. However, this distribution is not always verified (Pradhan et al., 2007, Yeo and Blong, 2010, Alderman et al., 2012).

The literature examines also the activity of the victims at the time of the incident (French et al., 1983, Staes et al., 1994, Rappaport, 2000) as a factor affecting vulnerability. It is suggested that the majority of fatal incidents are vehicle-related (French et al., 1983, Staes et al., 1994, Rappaport, 2000, Yale et al., 2003, Drobot et al., 2007, Ruin et al., 2007, Ashley and Ashley, 2008), whereas other activities such as walking, being in a building, attempting a rescue or doing sports, are appearing usually in smaller percentages (Jonkman and Kelman, 2005).

Drowning presents the highest percentages amongst different causes of death, although a number of fatalities is related also to physical traumas, electrocution and heart attacks (Chowdhury et al., 1993, Jonkman and Kelman, 2005). Other vulnerability factors suggested, concern previous flood experiences (Grothman and Greusswig, 2006), time of the day, flood type (Coates, 1999, Jonkman, 2005) and issuance of flood warnings (French et al., 1993, Staes et al., 1994).

Greece is no exception to this flood-rich regime, as the literature shows an abundance of flood phenomena during the last decades (Mimikou and Koutsoyiannis, 1995, Stathis, 2004, Diakakis, 2010, Koutroulis et al., 2010, Diakakis et al., 2011). Nikolaidou and Hatzichristou (1995) developed a catalogue of flood events between 1887 and 1994 identifying 29 catastrophic fatal floods inducing at least 179 fatalities. Diakakis et al. (2011b) studied the flooding history of western Athens recording 76 fatalities in 4 flood incidents and 10 more non-fatal events in this part of the city. Lately, Diakakis et al. (2012) developed a database of 545 flood events, causing a total of 586 fatalities across the country.

Although previous works indicate changes in flooding phenomena in the country (Stathis, 2004, Diakakis et al., 2011a, Diakakis et al., 2012), there is limited information on human vulnerability to floods and how it has changed over the last decades, as social and technological conditions gradually altered (i.e. increase of urban population, improvement of buildings, increase of vehicle use etc.).

Given the limited research carried out in this scientific field and the significance of flood disasters in the recent decades (Lekkas et al., 1997, Koutsoyiannis and Baloutsos, 2000, Diakakis et al., 2011b), this work examines an inventory of flood-related deaths, between 1960 and 2010, in an effort to improve our understanding on flood vulnerability and the circumstances under which these fatalities occur. To this aim, the paper analyzes their spatial distribution, the demographic characteristics of the victims, the incident details and their change over the course of this period.

2. Data and Methods

2.1. Data

Primary information on flood events and associated fatalities was based on the database developed by Diakakis et al. (2012). According to this inventory, 189 fatalities were induced by 57 fatal flood events between 1960 and 2010. This catalogue contained data on location, number of fatalities, and date of the floods and was used as the basic record upon which additional information, concerning the circumstances of flood deaths, was aggregated.

Detailed scientific reports (Mimikou and Koutsoyiannis 1995, Mimikou et al., 2002, Skilodimou et al., 2003, Evelpidou et al., 2009, Diakakis et al., 2011) and press articles based on police reports, stored in 13 national newspaper databases such as the Digital Newspaper Collection (2010) of the Greek National Library and the Greek National Newspapers Archive (2010) of the Library of the Hellenic Parliament, were used to obtain details on the victims and the specifics of each incident.

2.2. Methodology

Details on the demographics of the victims, their activity at the time and their cause of death were collected. Based on this information, a systematic database was developed. Each entry of this database, corresponding to one fatality, consisted of several variables that offered detailed and objective description of the incident. All deaths included in this database were immediately and directly attributable to a flood event. Long-term health effects and casualties caused by flood disasters that are documented in certain studies (Alderman et al., 2012), were not examined in this work due to lack of data. Each fatality was given one classification in each of the following variables:

1. Name of the victim (for reference purposes)

2. Exact location

3. Date

4. Activity of the victim at the time of the incident

5. Age and gender of the victim

6. Cause of death

7. Type of surrounding environment (urban or rural)

To examine the spatial distribution of fatalities and possible changes in it during the study period (1960-2010), their locations were plotted on the country's map in a GIS environment.

Regarding the activity of the victims, possible classifications included walking, using a vehicle, being in a building, camping, evacuating an open or a confined space and attempting a rescue. Regarding the cause of death, possible classifications included drowning, heart attack (caused during the flood and attributed directly to the events), physical trauma (included individuals that died as a result of being hit by debris, the collapse of a building, physical injuries suffered during the flood or as their vehicle crashed influenced by floodwaters) and electrocution (caused by contact with floodwaters). The temporal evolution of fatalities was analyzed on decadal basis by comparing the total number of deaths and the number of deaths per event. With respect to the distinction between rural and urban areas, it is important to note that the classification "urban" was used only in the case that the surrounding environment of the exact location of the incident was built and consisting of human infrastructure.

Formation of the database allowed the development of a systematic record of data based on evidence fragmented in several reports, provided standardization of information and allowed easy cross reference, comparison and quantitative analysis. After the development of the database, simple mathematical operations were used to quantify the results and examine possible changes.

2.3. Data Treatment and Uncertainties

One source of uncertainty was associated with the non-scientific nature of part of the data. Although press databases have been used before as data sources in the study of natural hazards (Llasat et al., 2009), to deal with the possibility of subjectivity, the variables selected to describe fatalities were specifically chosen in a way that they would not be subject to the reporter's opinion. In addition, to assure an accurate determination of the locations of fatalities, spatial data were cross-checked in two independent sources. In addition, it should be noted that due to unavailability of data regarding the demographics of the country throughout the study period, comparison of the victims' age and gender details with these of the general population, was carried out using the 2001 census (ELSTAT 2001), and should be therefore considered with caution.

3. Results and Discussion

During the 50 years of the study period, a total of 189 fatalities were examined. Fatal events were found to occur all over the country, mainly in coastal, low-lying areas (Figure 1). The capital, Athens, showed an increased clustering of deaths, a fact attributed to multiple-fatality events that occurred in the area between 1960 and 1980 (Mimikou and Koutsoyiannis, 1995). Examination of the evolution of their spatial distribution showed changes between the first and the second half of the study period (Figure 1). In particular, the first half of the study period (1960-1985) presents an increased clustering of fatalities near Athens, whereas during the second half fatality locations show a higher dispersion across the country, with the majority of them occurring outside urban centers.

Examination of the surrounding environment showed that 47.1% of the incidents occurred in urban setting, whereas 46.03% occurred in rural areas. In 6.88% of cases this detail was not reported. However, examination of the same variable, in decadal basis, showed that rural incidents present a gradual increasing trend, counter to the urban ones which present a decline (Figure 2). This trend is attributed to the gradual disappearance of flood events with very high fatality figures in urban environments probably due to the improvement of buildings. For instance, during 1961 and the 1977 events (Mimikou and Koutsoyiannis, 1995) in the city of Athens, several victims died due to building collapses.

With regard to the activity of the victims, using a vehicle was identified as the most common activity, followed by individuals that passed away inside buildings, walking, camping and doing sports, attempting a rescue and evacuating a location (Table 1). In 52 cases, the activity was not reported. Regarding the cause of death, analysis showed that drowning presented the highest percentage, followed by physical trauma, heart attack and electrocution (Table 1). In 23.2% of the cases this detail was not reported.

Examination of the temporal evolution of decedents' activities showed a gradual increase in vehicle-related fatalities and a significant decrease in victims that died as pedestrians or indoors. Attempting a rescue presented a slight increase, whereas evacuating, camping and doing sports showed extended fluctuations but inconclusive trends (Figure 3).

Changes in flood victims' activity are attributed to the increase in use of motor vehicles in Greece. The clear decline of indoor incidents supports also the assumption of improvement in the structural endurance of buildings. The higher percentage of vehicle-related incidents shows accordance with other studies (French et al., 1983 Staes et al., 1994, Rappaport, 2000) and it is ascribed by the literature to the tendency of vehicle occupants to underestimate the risk of entering into a flooded area with a vehicle (Yale et al., 2003, Drobot et al., 2007).

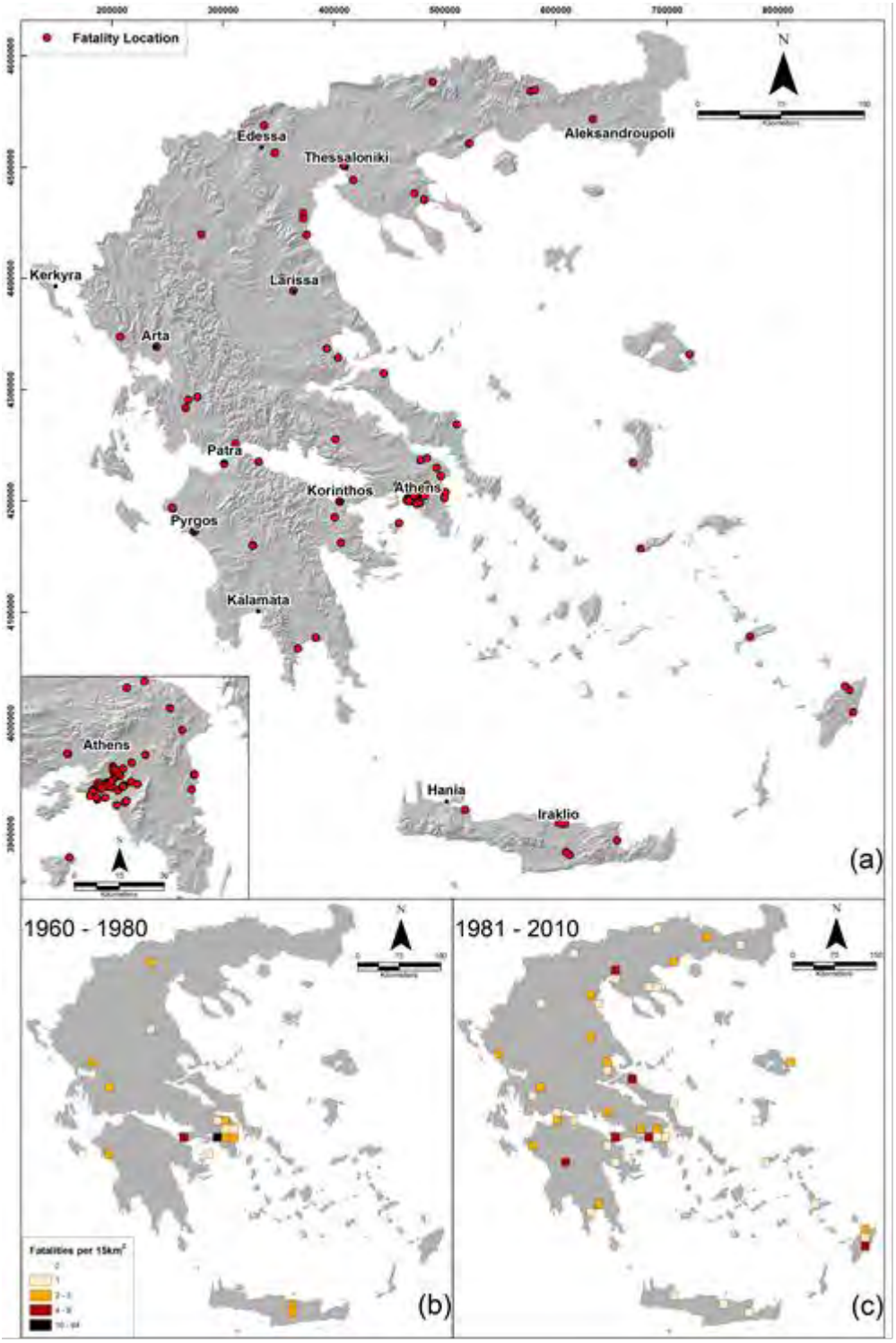

Figure 1 - (a) Spatial distribution of flood fatalities in Greece, between 1960 and 2010 and the changing spatial distribution of them in the two halves of the study period (b, c) expressed as the number of deaths in 15km X 15km grids.

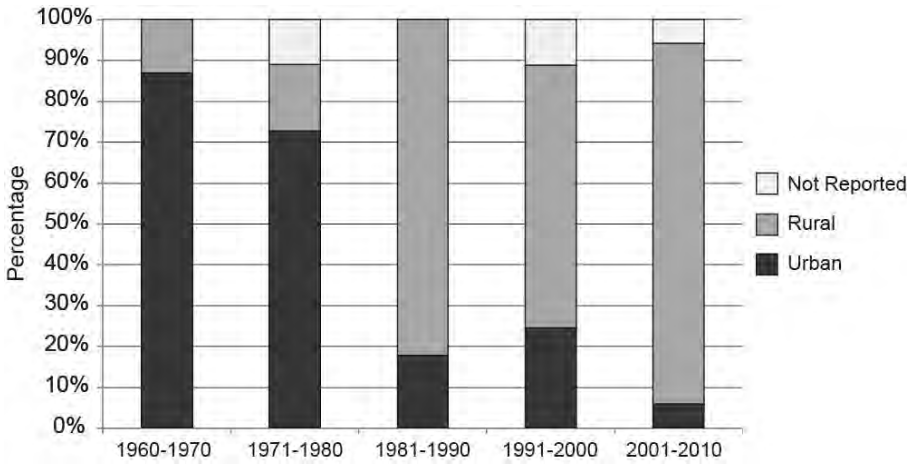

Figure 2 - Distribution of incidents with respect to their surrounding environment, showing a significant increase of rural events and a respective negative trend of urban ones.

Table 1 - Distribution of flood victims in Greece (1960-2010) with respect to their activity and their cause of death.

Activity	No. of cases	%	Cause of death	No. of cases	%
Using a vehicle	57	30.2	Drowning	119	63.0
Being in a building	28	14.8	Physical Trauma	19	10.1
Walking	24	12.7	Heart Attack	4	2.1
Camping	8	4.2	Electrocution	3	1.6
Doing sports	8	4.2	Not Reported	44	23.2
Attempting a rescue	7	3.7			
Evacuating a location	5	2.7			
Not Reported	52	27.5			
Total	189	100	Total	189	100

Examination of the evolution of causes of death showed that only negligible changes occurred during the study period.

Regarding the temporal evolution of deaths, significant fluctuations were identified in their numbers, presenting no clear trend during the study period. However, the number of fatalities per event showed a clear decreasing trend (Figure 4), showing too the gradual disappearance of multi-fatality events.

With respect to the victim demographics, it was found that the majority of the victims were males (58.74%), whereas females recorded a much smaller percentage (33.86%). In 7.4% of the cases this detail was not reported. This result is well-matched with the findings of the literature in other areas (Coates, 1999, Rappaport, 2000, Jonkman and Kelman, 2005, Ashley and Ashley, 2008) and is attributed to the increased propensity for risk taking, on behalf of males. No significant changes were identified regarding the victims' gender distribution throughout the study period, with the

exception of the first decade of the study period, which recorded 17 female fatalities, against 16 male ones. In all other decades males showed an overrepresentation amongst the decedents.

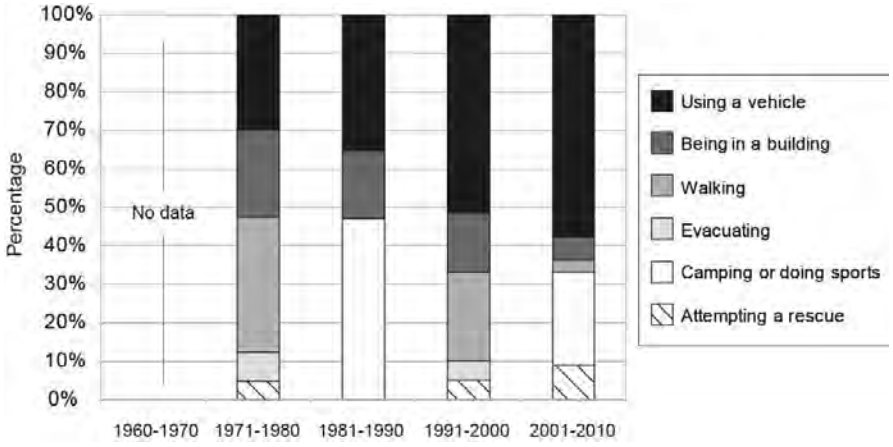

Figure 3 - Evolution of the distribution of decedents according to their activity at the time of the incident in 10-year segments.

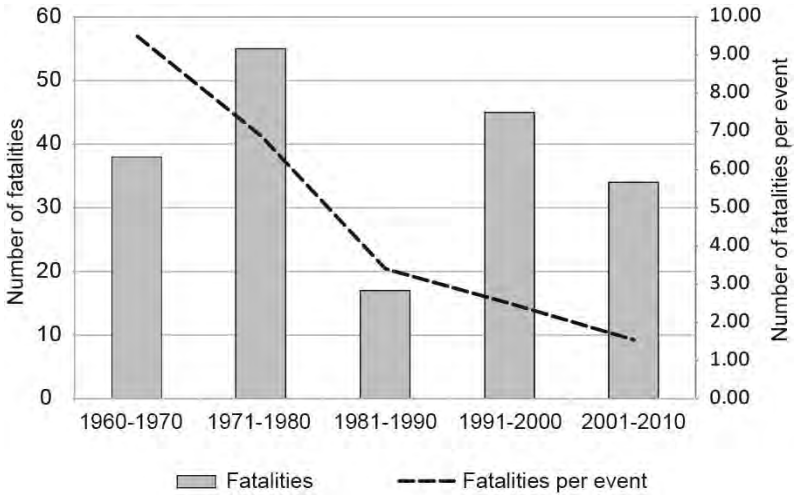

Figure 4 - Temporal evolution of flood-related deaths and deaths per flood event through the study period, in 10-year segments.

As far as the age of the victims is concerned, analysis showed an overrepresentation of youngsters (<15 years old) and elderly people (>75 years old) (Figure 5). This distribution is well-matched with the literature findings, which ascribes it to their physical inability to flee. Victims aged between 15 and 34 showed underrepresentation attributed probably to their increased physical agility. Individuals aged between 35 and 54 years old show are slightly overrepresented. In 25 cases (13.2% of total) the age was not reported.

Examination of the temporal evolution of the victims' age distribution showed that youngsters (<15 years old) and elders (>75 years old) presented a decline in percentage in the recent years. In fact, individuals between 20 and 64 years old showed a gradual increase among the decedents. This group recorded a 46.8% among the victims in the first ten years of the study period (1960-1970), a figure which increased to 82.4% in the last decade (2001-2010) (Figure 6). On the contrary, individuals younger than 20 years old presented a gradual decrease from 37.5% (in 1960-1970) to 5.88% (in 2001-2010). Victims over 65 years old increased until 2000, and then presented

a negative trend. This increase of victims between 20 and 64 is probably connected with the use of vehicle-related deaths, as individuals under 18 and over 65 are not entitled to a driving license in the country. However, the cause cannot be determined with confidence with the available data.

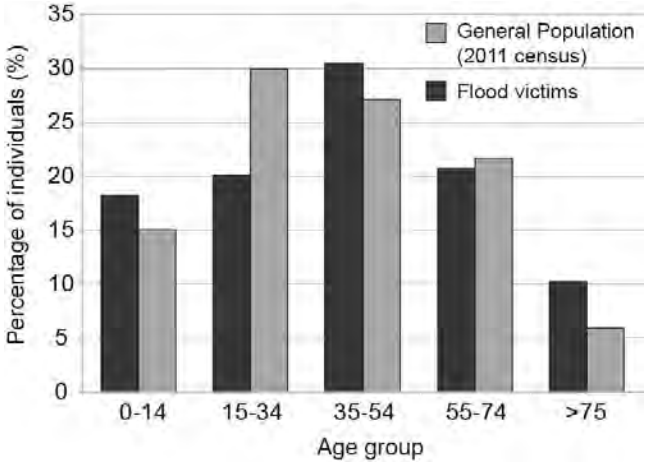

Figure 5 - Distribution of flood victims' age in comparison with the age of the general population of the country according to the 2001 census (ELSTAT 2001).

In general, this analysis shows that the development of a detailed record allows the systematic study of flood mortality and its changes and can be used as a useful tool to improve our knowledge on vulnerability of individuals to flooding. In this case, the analysis shows that the characteristics of flood mortality change in Greece, from urban high-fatality events, to low-fatality, vehicle-related incidents in rural areas.

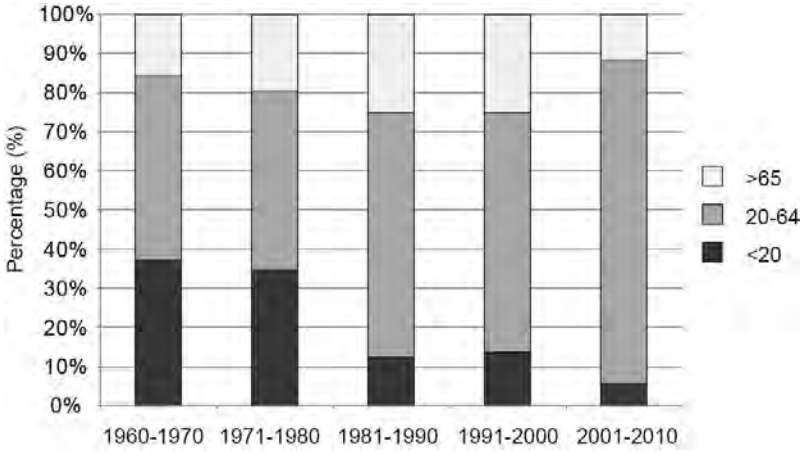

Figure 6 - Changes in distribution of flood victims' age in five segments of the time period. Individuals under 20 years old present a gradual decrease among the victims, whereas decedents between 20 and 64 years old show a continuing increase.

4. Conclusions

This study examines flood-related fatalities in Greece, between 1960 and 2010, and the changes that occurred in certain factors that affect flood mortality and the vulnerability of individuals to flooding. According to the findings, males, youngsters and elderly show overrepresentation among the victims, although individuals between 20 and 65 present a gradual increase during the last years of the study period.

Fatal flood events are approximately equally divided between urban and rural settings. However, fatal incidents appear to gradually migrate from urban centers to rural environments. In addition, vehicle-related incidents present also a gradual increase, whereas pedestrian and indoor incidents are declining. High-mortality flood events are decreasing, although fatality numbers do not show a clear tendency. Drowning presents the highest percentage throughout the study period among different causes of death.

5. References

Alderman K., Turner L. R. and Tong S. 2012. Floods and human health: A systematic review, *Environment International* 47:37–47.

Ashley S.T. and Ashley W.S. 2008. Flood Fatalities in the United States, *J. Appl. Meteor. Climatol*., 47, 805–818.

Barrero J.I. 2009. Normalised flood losses in Europe: 1970-2006, *Nat. Hazards Earth Syst. Sci*. 9, 97-104.

Bern C., Sniezek J., Mathbor G.M., Siddiqi M.S., Ronsmans C., Chowdhury A.M., Choudhury A.E., Islam K., Bennish M., Noji E. and Glass R. I. 1993 Risk factors for mortality in the Bangladesh cyclone of 1991, *Bull World Health Organ*. 71, 1, 73-78.

Chowdhury A.R. Mushtaque A.U., Bhuyia A.Y. and Choudhury R.S. 1993. The Bangladesh Cyclone of 1991: Why So Many People Died. *Disasters*. 17, 4, 291–304.

Coates L. 1999. Flood fatalities in Australia, 1788-1996, *Australian Geographer*, 30, 3, 391-408.

Diakakis M. 2010. Flood history analysis and its contribution to flood hazard assessment. The case of Marathonas in Greece. *Bulletin of the Geological Society of Greece* 43(3):1323-1334.

Diakakis M., Deligianakis G. and Mavroulis S. 2011a. Flooding in Peloponnese, Greece: a contribution to flood hazard assessment, in: Lambrakis, N., Stournaras, G., Katsanou, K. (Eds*) Advances in the Research of Aquatic Environment* vol.1:199-206, Springer.

Diakakis M., Foumelis M., Gouliotis L. and Lekkas E. 2011b. Preliminary flood hazard and risk assessment in Western Athens metropolitan area, in: Lambrakis N, Stournaras G, Katsanou K (Eds) *Advances in the Research of Aquatic Environment*, vol.1:147-154, Springer.

Diakakis M., Mavroulis S. and Deligiannakis G. 2012. Floods in Greece, a statistical and spatial approach, *Nat. Hazards*, 62 (2), 485-500.

Digital Newspapers Collection 2010. E-efimeris: digital newspapers collection of the Greek national library. Available online at: http://www.nlg.gr/digitalnewspapers/ns/main.html.

Drobot S.D., Benight C. and Gruntfest E. C. 2007. Risk factors for driving into flooded roads, *Env. Hazards*, 7, 227-234.

ELSTAT 2001. De facto population by sex and age groups. Greece Total, Geographic areas (NUTS I), regions (NUTS II), departments, municipalities/communities and municipal/Communal departments. Population census 18th March 2001. *Hellenic Statistical Authority ELSTAT.*

French J., Ing R., Von Allmen S. and Wood R. 1983. Mortality from flash floods: a review of Nati onal Weather Service reports, 1969-81, *Public Health Reports* 98 (6), 584-588.

Greek National Newspapers Archive, 2010. National Newspapers Microfilm Database of the Library of the Hellenic Parliament, *Hellenic Parliament, Greece.*

Grothmann T. and Reusswig F. 2006. People at risk of flooding: Why some residents take precautionary action while others do not, *Nat. Hazards*, 38, 101-120.

Guzzetti F. and Tonelli G. 2004. Information system on hydrological and geomorphological catastrophes in Italy (SICI): a tool for managing landslide and flood hazards, *Nat Hazards Earth Syst. Sci.* 4, 213–232.

Jonkman S.N. 2005. Global perspectives on loss of human life caused by floods, *Nat. Hazards*, 34, 151-175.

Jonkman S.N. and Kelman I. 2005. An analysis of the causes and circumstances of flood disaster deaths, *Disasters,* 29 (1), 75-97.

Koutroulis G., Tsanis I.K. and Daliakopoulos I.N. 2010. Seasonality of floods and their hydrometeorologic characteristics in the island of Crete. *J. Hydrol*. 394, 90-100.

Koutsoyiannis D. and Baloutsos G. 2000. Analysis of a long record of annual maximum rainfall in Athens, Greece, and design rainfall inferences, *Nat. Hazards* 29, 29-48.

Kunkel K.E., Pielke Jr.R.A. and Changnon S.A. 1999. Temporal fluctuations in weather and climate extremes that cause economic and human health impacts: a review, *Bull. Amer. Meteor. Soc.* 80, 1077-1098.

Lekkas E., Lozios S., Skourtsos E. and Kranis H. 1997. Floods, geodynamic environment and human intervention. The case of Corinth (Greece), *Risk Analysis, Eds. C.A.Brebbia, J.L.Rubio, J.L.Uso, Wit Press, Computational Mechanics Publications*, vol.2, p. 135-144.

Llasat M.C., Llasat-Botija M. and Lopez L. 2009. A press database on natural risks and its application in the study of floods in Northeastern Spain, *Nat. Hazards Earth Syst. Sci.* 9, 2049–2061.

Llasat M.C., Llasat-Botija M., Prat M.A., Porcu F., Price C., Mugnai A., Lagouvardos K., Kotroni V., Katsanos D., Michaelides S., Yair Y., Savvidou K. and Nicolaides K. 2010b. High-impact floods and flash floods in Mediterranean countries: the FLASH preliminary database, *Adv. Geosci*. 23, 47–55.

Mimikou M. and Koutsoyiannis D. 1995. Extreme floods in Greece: The case of 1994. *US – Italy Research Workshop on the Hydrometeorology, Impacts and Management of Extreme Floods*. Perugia, Italy, 13-17 November 1995.

Mimikou M., Baltas E. and Varanou E. 2002. A study of extreme storm events in the Greater Athens area, Greece, IAHS-AISH Publication, No 271, The Extremes of the Extremes; Extraordinary Floods, 161-166.

Nikolaidou M. and Hatzichristoun E. 1995. Registering and assessment of devastating floods in Greece and Cyprus, *Diploma thesis*, Department of Water Resources, Hydraulic and Maritime Engineering – National Technical University of Athens, Athens.

Pradhan E.K., West K.P.Jr., Katz J., LeClerq S.C., Khatry S.K. and Shrestha S.R. 2007. Risk of flood-related mortality in Nepal, *Disasters*, 1, 57-70.

Rappaport E.N. 2000. Loss of life in the United States associated with recent Atlantic tropical cyclones, *Bull. Amer. Meteor. Soc*., 81, 2065–2073.

Ruin I., Gaillard J.C. and Lutoff C. 2007. How to get there? Assessing motorists' flash flood risk perception on daily itineraries, *Environmental Hazards*, 7, 235-244.

Staes C., Orengo J.C., Malilay J., Rullan J. and Noji E. 1994. Deaths Due to Flash Floods in Puerto Rico, January 1992, Implications for Prevention. *International Journal of Epidemiology*. 23 (5) 968–975.

Stathis D. 2004. Extreme rainfall events and flood genesis in Greece. *Proceedings of the 7th Panhellenic Geografical Conference of the Hellenic Geographical Society (7PGC/HGS),* Mytilene, Greece, 1–8, 2004.

Yale J.D., Cole T.B., Garrison H.G., Runyan C.W. and RiadRuback J.K. 2003. Motor Vehicle-Related Drowning Deaths Associated with Inland Flooding After Hurricane Floyd: A Field Investigation, *Traffic Injury Prevention*. 4 (4), 279-284.

Yeo S.W. and Blong R.J. 2010. Fiji's worst natural disaster the 1931 hurricane and flood, *Disasters*, 34 (3), 657-683.

Δελτίο της Ελληνικής Γεωλογικής Εταιρίας, τομ. XLVII , 2013
Πρακτικά 13ου Διεθνούς Συνεδρίου, Χανιά, Σεπτ. 2013

Bulletin of the Geological Society of Greece, vol. XLVII 2013
Proceedings of the 13th International Congress, Chania, Sept. 2013

FLOOD FATALITIES IN ATHENS, GREECE: 1880-2010

Diakakis M.[1], Katsetsiadou K.[1], Pallikarakis A.[2]

[1] National and Kapodistrian University of Athens, Faculty of Geology and Geoenvironment, 15784, Zografou, Athens, Greece, Email: diakakism@geol.uoa.gr

[2] Department of Earth and Atmospheric Sciences Mineralogy – Geology Laboratory, 75 Iera Odos Str., GR 11855, Athens, Greece

Abstract

Flood-related deaths in urban environments constitute a major issue in flood risk management especially during the last decades, as global urban population grows larger. This work focuses on the analysis of flood-related fatalities in Athens metropolitan area, in Greece between 1880 and 2010. To this aim, a database is compiled, recording spatial and temporal distribution of fatal flood incidents, along with demographic information on the victims. GIS is used to map and spatially analyze the incidents in question and to examine possible migration trends. Results showed a total of 182 fatalities across Athens basin, presenting a decreasing trend, even though flood event numbers are rising. Males, youngsters and elderly people showed an overrepresentation amongst the victims in comparison with the country's general population. Fatal incidents presented a higher spatial density in the central and southwestern parts of the city indicating a higher persistence of flood phenomena in these areas. A gradual migration of fatality locations, from the central parts of the city, towards the outer suburbs during the study period was identified following the city's spatial expansion.
Key words: *Flood deaths, Flood mortality, Hazard, Spatial analysis, Flood migration.*

Περίληψη

Η επίπτωση των αστικών πλημμυρών σε ανθρώπινες ζωές είναι ένα από τα σημαντικότερα ζητήματα στην αντιμετώπιση του πλημμυρικού κινδύνου. Η παρούσα μελέτη εστιάζει στην ανάλυση των θανάτων από πλημμύρες στην περιοχή του Λεκανοπεδίου Αθηνών μεταξύ 1880 και 2010. Για το σκοπό αυτό, αναπτύσσεται μια βάση δεδομένων, σε περιβάλλον GIS, με αναλυτικά στοιχεία για τη χωρική και χρονική τοποθέτηση των συγκεκριμένων συμβάντων και δημογραφικές πληροφορίες για τα θύματα. Τα αποτελέσματα της ανάλυσης δείχνουν μια σταδιακή μείωση των θυμάτων, μολονότι τα πλημμυρικά φαινόμενα γίνονται ολοένα και πιο συχνά. Παράλληλα, προκύπτει υπερεκπροσώπηση των ανδρών, των νέων και των ηλικιωμένων ατόμων ανάμεσα στα θύματα. Η μεγαλύτερη συγκέντρωση θανάτων εμφανίζεται στα κεντρικά και δυτικά τμήματα του λεκανοπεδίου, ενώ παρατηρείται σταδιακή μετατόπιση των θέσεων θανατηφόρων συμβάντων από τα κεντρικά προς τα περιφερειακά τμήματα της πόλης, γεγονός που σχετίζεται με την παράλληλη επέκταση του αστικού ιστού και των ανθρώπινων δραστηριοτήτων στις περιοχές αυτές κατά την περίοδο μελέτης.
Λέξεις κλειδιά: *Θάνατοι, Πλημμύρες, Αθήνα, Επικινδυνότητα, Χωρική ανάλυση.*

1. Introduction

Floods are often cited as one of the most destructive and most lethal natural hazards, recording extensive economic (Barrero 2007; Barrero 2009) and life losses (Kundzewicz and Kundzewicz 2005; Jonkman 2005) worldwide. In Europe, increased population density and enhanced socioeconomic activities lead occasionally to the expansion of urban population into areas of elevated flood hazard. The region shows an abundance of flood phenomena (Llasat et al. 2010b) clustering in several occasions in urban areas (Barrera et al. 2006; Llasat et al. 2010a). Athens metropolitan area, in Greece, is no exception to this regime. The city has experienced too, several catastrophic events during the last century inducing a significant number of damages and fatalities (Nikolaidou and Hatzichristou 1995; Diakakis et al. 2012).

Athens, which is the largest urban area in Greece, is situated in the region of Attica, and is built in a morphologic basin that occupies an area of approximately 534 km^2 between Penteli, Parnitha, Ymitos and Aigaleo mountains and Saronikos Gulf in the south (Figure 1). During the last century, it has been a rapidly evolving urban centre, both in terms of population and spatial extension, leading to a gradual urbanization of a significant part of the basin (Evelpidou et al. 2009; Skilodimou et al. 2003; Papazoi et al. 2010; Baltas and Mimikou 2002). Nowadays, approximately 68% of the basin is occupied by urban expanses that are host to about 4 million people (ELSTAT 2001). The basin, in terms of morphology, is shaped primarily by Kifissos and Ilissos river networks. The area is mostly dry (Mimikou et al. 2002) with a mean annual rainfall of approximately 390mm (Koutsoyiannis and Baloutsos 2000) and a poorly developed river network dominated by streams, with small amounts of water for most of the year. The increased density of population, has led to the development of human activities and infrastructure in the vicinity of these ephemeral watercourses, in many cases in areas of elevated flood hazard, not suitable for building.

Due to the lack of instrumental data on river discharges, a large portion of information on local flooding history was until recently recorded in an anecdotal form (Diakakis 2010, Diakakis et al. 2011). Evidence of past flood events presented an increased level of fragmentation, which hampered the evaluation of the flooding problem as a whole. However, recent scientific work illustrated the severity of the problem by recording certain catastrophic events. Mimikou et al. (2002) and Evelpidou et al. (2009) stress the significance of high-intensity storm in flash flood triggering in the area. Mimikou et al. (2002), Baltas and Mimikou (2002), Alexoudi-Livaditi et al. (2007) and Papazoi et al. (2010) suggest that anthropogenic factors play a crucial role in flood generation in the area and that the rapid development of the city took place without implementing an appropriate plan of drainage works that would help the river network accommodate flood flows. In fact, several parts of the drainage network were shrunk or converted into streets and critical river cross sections were diminished (Baltas and Mimikou 2002). Skilodimou et al. (2003) study a flood in November 1993 in the south suburbs of the city and suggest too, that urbanization of the area is one of the most important factors in flood generation. Mazi and Koussis (2006) analyse the flood of July 2002 in the lower part of Kifissos River and conclude that human intervention to hydrologic processes was very critical in flood genesis.

Although several authors analyze flood hazard in Athens (Lekkas et al. 1997; Parharidis et al. 2000; Diakakis et al. 2011; Kandilioti and Makropoulos 2012), there is limited research regarding flood-related fatalities in the area. Nikolaidou and Hatzichristou (1995) developed a catalogue of flood events in Athens area between 1887 and 1994 identifying 29 fatal flood events that induced several fatalities across Athens basin. This catalogue was later adopted by Mimikou and Koutsoyiannis (1995) and Baltas and Mimikou (2002). Diakakis et al. (2011) studied the flooding history of western Athens recording 76 fatalities in 4 flood incidents and 10 more non-fatal events in this part of the city. Despite the existence of catalogues enlisting associated deaths, there are no works studying all the recorded fatalities in terms of their spatial distribution and the circumstances under which they occurred.

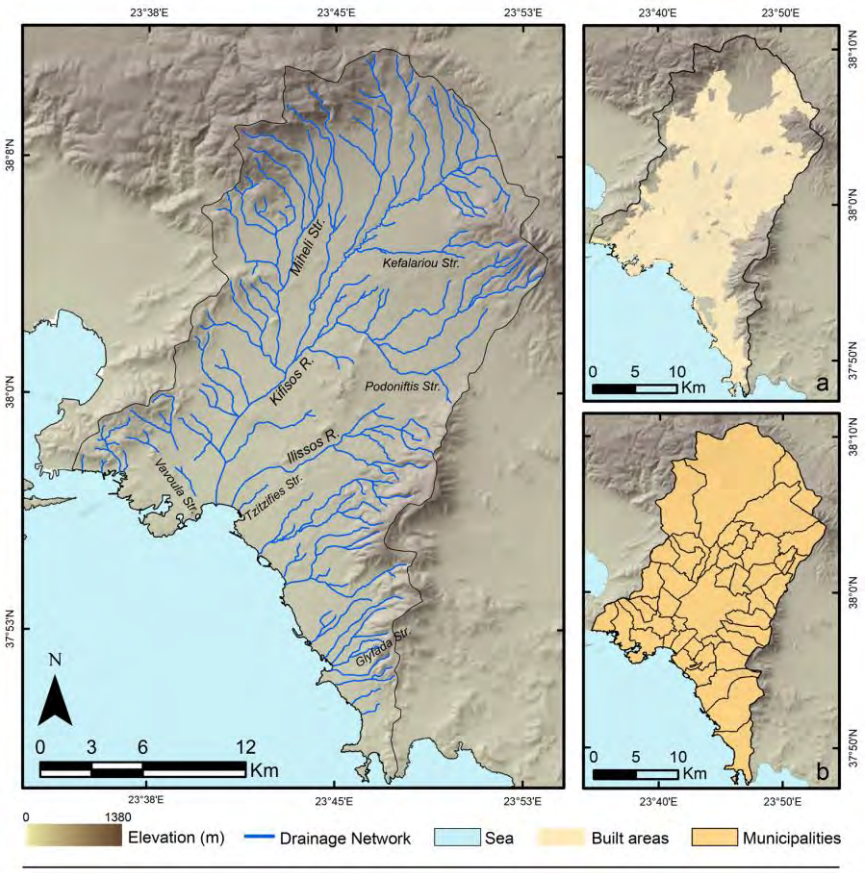

Figure 1 - Map of Athens basin showing the river network, the built areas (a) and the municipality administrative limits.

In this field, the literature discusses a number of different short and long-term consequences of floods to human health (Alderman et al. 2012). Several studies in different parts of the world analyse mortality attributed to flood disasters, focusing on the factors that affect vulnerability of individuals (Jonkman and Kelman 2005). Such factors include the victims' age (Coates 1999; Ashley and Ashley 2008; FitzGerald et al. 2010), their gender (Coates 1999; French et al. 1983, Rappaport 2000; Jonkman and Kelman 2005), their activity at the time of the flood (Staes et al. 1994; Rappaport 2000; Ashley and Ashley 2008) and several other parameters (Jonkman and Kelman 2005).

2. Materials and Methods

2.1. Data

Primary data on flood events were based on the flood database developed by Diakakis et al. (2012) for the Greek territory and for the period between 1880 and 2010. This catalogue contained data on the date and the number of fatalities that occurred during each flood along with a vague determination of their location. This inventory was used as the basic record upon which additional information was aggregated. Detailed scientific reports (Nikolaidou and Hatzichristou 1995; Mimikou and Koutsoyiannis 1995; Mimikou et al. 2002; Baltas and Mimikou 2002; Skilodimou et al. 2003; Evelpidou et al. 2009; Diakakis et al. 2011) and press articles were used to identify the exact location of each fatality and the age and gender of each victim. In total, 135 press reports were ana-

lysed, published in several issues of 13 national newspapers recovered from the Digital Newspaper Collection (2010) of the Greek National Library and the Greek National Newspapers Archive (2010) of the Library of the Hellenic Parliament.

2.2. Submission Steps

A systematic database was developed to link primary information deriving from the Flood Database of Diakakis et al. (2012) with information on location and demographic details of each victim. Each entry of the database, corresponding to one fatality, consisted of several variables that provided detailed information on each incident, recovered from the sources described above. An identical database was developed in a GIS environment, with the aid of which location of each fatality was plotted on the map. Following this step, an 800m X 800m grid was developed across the study area. Based on this grid, the number of fatalities in each cell was calculated, as a mean to illustrate the spatial distribution of fatalities across the study area and identify the locations with the higher concentration. The number of fatalities in the different administrative divisions (municipalities) of Athens Metropolitan area was calculated too. Calculation in both cases was carried out with the aid of ArcMap software (ESRI 2011).

Afterwards, the study period was divided in 13 decadal segments in order to examine the temporal evolution of fatalities. In addition, fatality locations were investigated in terms of changes in their spatial distribution in different parts of the study period. Finally, demographic details of the victims were analyzed and compared to the demographic distribution of the country's general population using simple mathematical operations.

2.3. Data Treatment and Uncertainties

In general, location information presented an overall good quality in all selected sources, mainly due to the stationarity of most city features, road network and landmarks during the study period. Regarding their spatial accuracy, it should be noted that in general the nature of data, allowed identification of location (through exact address or identified landmark) with a margin of error not more than 20m. However, one source of uncertainty was associated with the non-scientific nature of part of the data. Although press databases have been used before as data sources in the study of natural hazards (Llasat et al. 2009), to deal with the possibility of subjectivity, the variables selected to describe fatalities were specifically chosen in a way that they would not be subject to the reporter's opinion. In addition, to assure an accurate determination of the locations of fatalities, spatial data were cross-checked in two independent sources. With regard to the completeness of the catalogue, it should be noted that the record is considered complete given the continuous presence of human population in the area and the examination of multiple sources.

Finally, it should be noted that due to unavailability of data regarding the demographics of the country throughout the study period, comparison of the victims' age and gender details with these of the general population, was carried out using the 2001 census (ELSTAT 2001), and should be therefore considered with caution.

3. Results and Discussion

3.1. Inventory of Flood Events and Associated Fatalities

Analysis showed that Athens metropolitan area has suffered 52 major flooding events, 19 of which induced 182 fatalities between 1880 and 2010 (Table 1). The most lethal event occurred in 1896, inducing 62 deaths, followed by the November 1977 event (36 fatalities) and the November 1961 event (33 deaths). Sixteen other flood incidents were identified inducing 1 to 13 fatalities Thirty-three other flood events have taken place in the study area in 1886, 1901, 1906, 1928, 1930, 1934, 1936, 1939, 1949, 1950, 1952, 1955, 1965, 1972, 1978, 1980, 1981, 1986, 1987, 1988, 1993, 1997, 1998, 2002, 2004 and 2005 inducing no fatalities.

Regarding the activity of the victims at the time of each incident, for the 112 instances where this detail was known, it was found that outdoor activities (such as walking, evacuating and driving) accounted for 35.7% (40 cases). Amongst these, 18 cases, all of which occurred after 1960, were vehicle-related. In the rest 72 cases (50 before 1960 and 22 after this year) the victims passed away indoors.

Table 1 - Catalogue of fatal flood events in Athens between 1880 and 2010, their locations across the study area and the number of fatalities that they induced.

Date	Locations in summary	Deaths	Date	Locations in summary	Deaths
05-11-1896	City centre	1	14-10-1955	Tzitzifies, Chalandri	2
14-11-1896	Piraeus, Moschato	62	06-11-1961	Peristeri, Ilion	33
05-11-1899	Piraeus, City centre	7	02-11-1977	Ilion, Peristeri	36
23-11-1925	Nea Ionia, Fahlero	13	10-12-1977	Chalandri, Nea Ionia	3
22-02-1930	City centre	1	30-5-1979	Argiroupoli, Glyfada	1
27-10-1930	City centre, Fahlero	2	15-1-1991	Ilioupoli, Alimos	1
02-12-1933	City centre, Fahlero	2	31-1-1994	A. Liosia, Acharnes	2
22-11-1934	Nea Ionia, Fahlero	7	21-10-1994	Nea Ionia, Glyfada	5
05-11-1936	Kallithea, Moschato	2	08-7-2002	Moschato	1
30-09-1951	Petroupoli, Nikaia	1			

3.2. Temporal Evolution

Although significant variations were observed, results showed that fatalities present an overall decreasing trend during the study period. In the last 30 years only 9 deaths were identified (significantly less than the previous period), even though flood events are recording a noteworthy increase in the same time segment. Given the fact that the majority of deaths occurred indoors, and that the indoor deaths are showing a decline after 1960, the overall reduction of fatalities is attributed partly to the gradual improvement of buildings in terms of structural endurance. The decline may be connected also with improved education and awareness of the general public regarding natural disaster hazards.

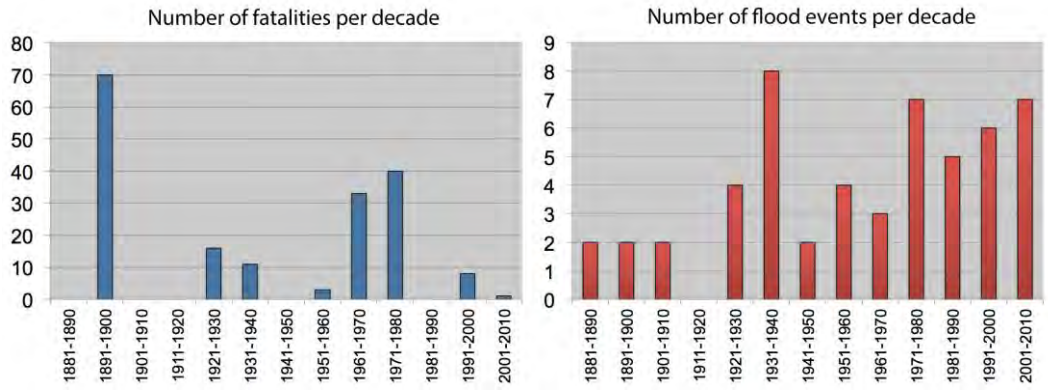

Figure 2 - Number of fatalities per decade showing a slight decreasing trend (left), despite the noteworthy increase of flood events in the same period (right).

3.3. Seasonal Distribution

Regarding their seasonal distribution, it was shown that autumn presents the vast majority of fatalities (94%) followed by winter (4.9%), summer (0.5%) and spring (0.5%). November was found to be the month presenting most deaths, as all three most-lethal floods occurred during this period. Although these results are not in disagreement with previous works findings (Diakakis et al. 2012), it appears that flood-related fatalities present stronger seasonality than flood events, which show a smaller autumn percentage. This fact is attributed probably to a difference in intensity of flooding between the seasons. However, a future revision of this distribution with a greater sample would improve the reliability of this analysis.

3.4. Demographic Analysis

Regarding the age of the victims, analysis shows an overrepresentation of youngsters (younger than 15 years old) and elderly people (older than 75 years old) in comparison with the general population (Figure 3). This result is in accordance with the conclusions of Chowdhurry et al. (1993), Rappaport (2000), Pradhan et al. (2007) and Ashley and Ashley (2008) who suggest that there is an increased vulnerability amongst the young and the elders, attributed to their physical inability to flee and occasionally to the propensity for risk-taking amongst the youngsters (Coates 1999; Ashley and Ashley 2008; FitzGerald et al. 2010). In 22.4% of the cases the age of the victims was not reported.

Regarding the gender of the victims, it was found that the majority of victims were males (51.1% of cases) whereas females showed an underrepresentation (40.7%) in accordance with the literature findings (French et al., 1983, Coates 1999). In 8.2% of cases the gender of the victim was not reported.

3.5. Spatial Analysis

Projection of fatality locations on the map of the study area shows a clustering of deaths in the central and western parts of the city near Piraeus and along the course of Kifissos River (Figure 4). Northern, eastern and southern suburbs present a very limited amount of casualties. This fact is attributed partly to the shorter history of these parts of the city and partly to the reduced density of buildings and urban fabric and the higher percentage of open spaces, leaving more space for drainage in these suburbs.

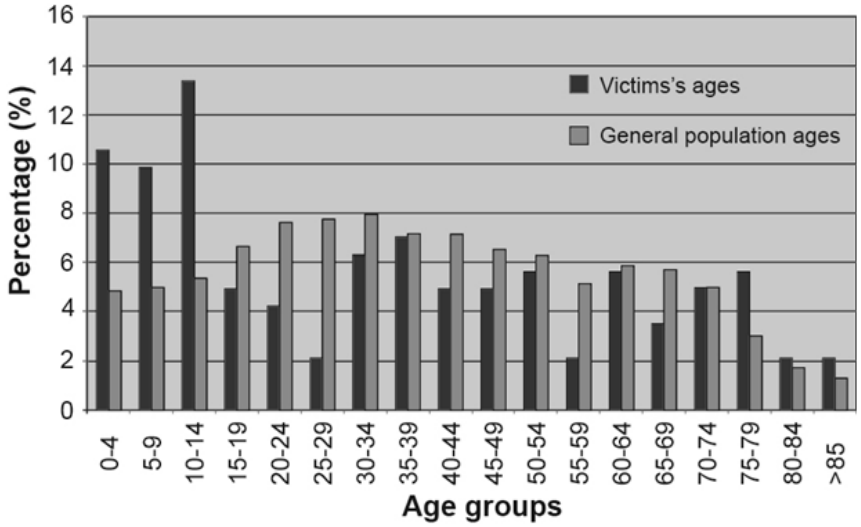

Figure 3 – Age distribution of flood fatalities (1880-2010) in comparison with the country's population in 2001 (ELSTAT 2001).

However, projection of incident locations in specific periods shows that, their distribution changes over time, presenting a gradually increasing dispersion (Figure 5). Comparison with the city's development shows that fatalities migrate towards the newly developed areas. In certain time segments when the city's development or population presents significant shifts or changes, fatality locations follow the same spatial pattern. In particular, between 1880 and 1920 when the city is very limited in space, fatality locations present a significant clustering. After 1920, when the city experiences a sudden population increase, fatalities too show a higher dispersion following the city's spatial expansion. In addition, flood deaths show a significant shift and an increased clustering in the western suburbs between 1945 and 1980, when this part of the city experienced a development boost. Finally, after 1980 when the city is developed across the whole basin, fatalities although much fewer seem to disperse across the whole area.

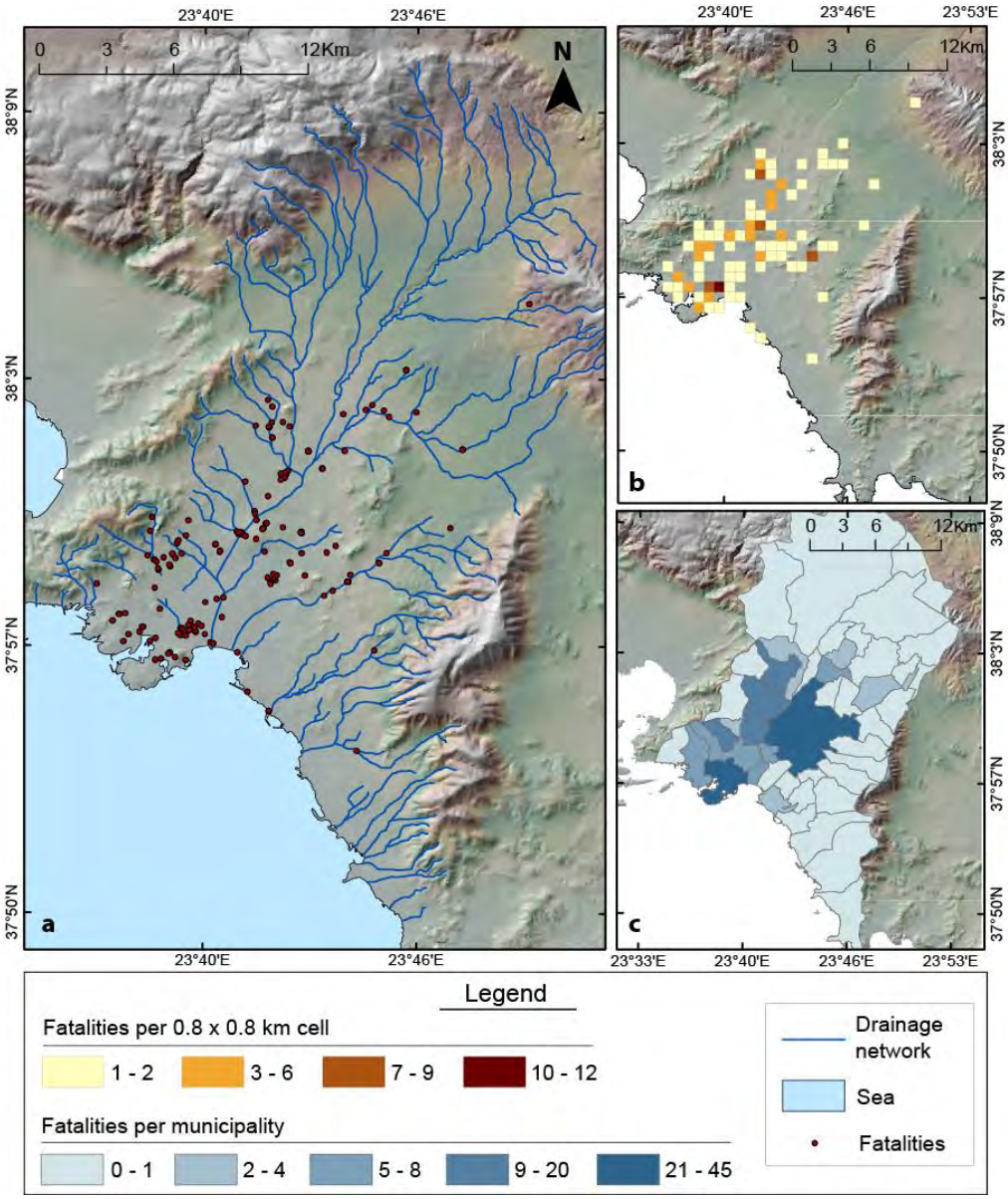

Figure 4 – (a) Locations of flood fatalities across Athens basin between 1880-2010, (b) number of fatalities on a 0.8 Km X 0.8 Km grid and (c) the number of fatalities per municipality.

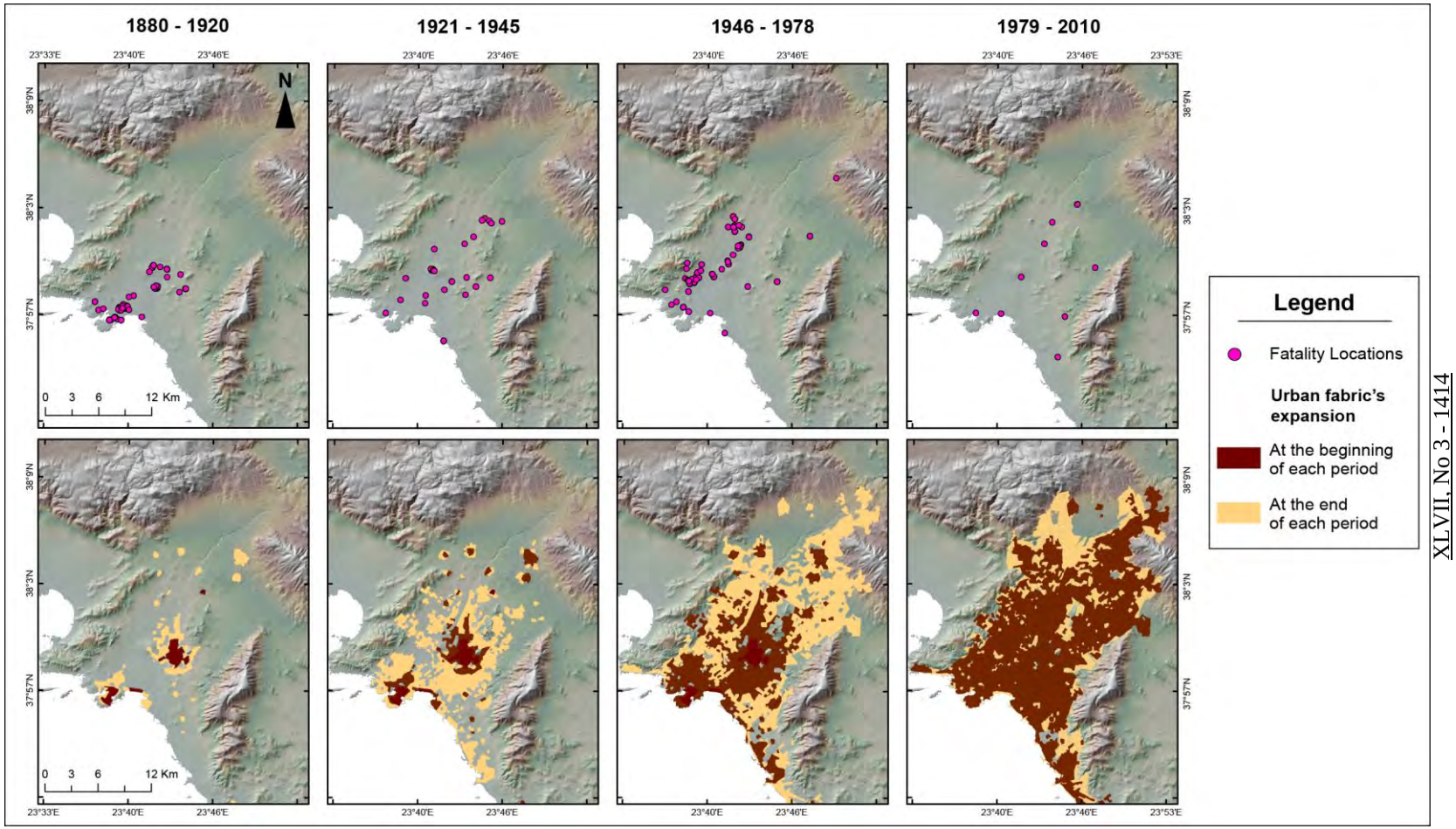

Figure 5 - Gradual migration of flood fatalities in 4 periods associated with the expansion of the city (EKKE 2000, Leontidou 2001, Avdelidi 2010) during the same time segments.

4. Conclusions

The study develops and analyzes a database of flood-related fatalities in Athens, Greece, between 1880 and 2010, identifying a total of 182 fatalities associated with flooding in the area. The record proves to be a useful tool for studying vulnerability of individuals and can be used as the basis for future research in flood risk mitigation. Flood mortality in the study area was found to present strong seasonality and a declining trend, more obvious during the last 30 years, even though flood events in the area are becoming gradually more frequent. Males, youngsters and elderly people show an overrepresentation amongst the victims. Spatial distribution of fatalities shows an increased clustering of deaths in the central and western parts of the metropolitan area, although their locations present a gradual migration, following the city's newly developed expansions throughout the study period.

5. References

Ashley S.T. and Ashley W.S. 2008. Flood Fatalities in the United States, *J. Appl. Meteor. Climatol*, 47, 805–818.

Avdelidi K. 2010. Spatial Evolution of 4 Major Greek Cities, *National Centre For Social Research*.

Barrera A., Llasat M.C. and Barriendos M. 2006. Estimation of extreme flash flood evolution in Barcelona County from 1351 to 2005*, Nat. Hazards Earth Syst. Sci.,* 6, 505–518.

Barrero J.I. 2007. Major flood disasters in Europe: 1950-2005, *Nat Hazards*, 42, 125-148.

Barrero J.I. 2009. Normalised flood losses in Europe: 1970-2006, *Nat. Hazards Earth Syst. Sci*., 9, 97-104.

Coates L. 1999. Flood fatalities in Australia, 1788-1996, *Australian Geographer*, 30, 3, 391-408

Diakakis M. 2010. Flood history and its contribution to flood hazard assessment. The case of Marathonas, Greece, *Bull. Geol. Soc. of Greece*, 43(3):1323-1334.

Diakakis M., Foumelis M., Gouliotis G. and Lekkas E. 2011. Preliminary flood hazard and risk assessment in Western Athens metropolitan area, in Lambrakis N., Stournaras G., Katsanou K. (eds.) *Advances in the Research of Aquatic Environmen*, 1, 147–154, Springer.

Diakakis M., Mavroulis S.and Deligiannakis G. 2012. Floods in Greece, a statistical and spatial approach, *Nat Hazards*, **62** (2), 485-500.

Digital Newspapers Collection 2010. E-efimeris: Digital Newspapers Collection, *Greek national Library.*

EKKE 2000. Social and Economic ATLAS of Greece, Athens: *National Centre For Social Research.*

ELSTAT, 2001. De facto population by sex and age groups. Greece Total, Geographic areas (NUTS I), regions (NUTS II), departments, municipalities/communities and municipal/Communal departments. Population census 18th March 2001, *Hellenic Statistical Authority ELSTAT.*

Evelpidou N., Mamassis N., Vassilopoulos A., Markopoulos C. and Koutsoyiannis D. 2009. Flooding in Athens: The Kephisos River flood event of 21-22/10/1994, *International Conference on Urban Flood Management*, Paris, UNESCO, 2009.

FitzGerald G., Du W., Jamal A., Clark M. and Hou X. 2010. Flood fatalities in contemporary Australia (1997-2008), *Emergency Medicine Australasia, 22,* 180-186.

French J., Ing R., Von Allmen S. and Wood R. 1983. Mortality from flash floods: a review of National Weather Service reports, 1969-81, *Public Health Reports 98*, 6, 584-588.

Guzzetti F. and Tonelli G. 2004. Information system on hydrological and geomorphological catastrophes in Italy (SICI): a tool for managing landslide and flood hazards, *Nat. Hazards Earth Syst. Sci,* 4, 213–232.

Greek National Newspapers Archive, 2010. National Newspapers Microfilm Database of the Library of the Hellenic Parliament, Hellenic Parliament, Greece.

Hollis G.E. 1975. The effect of urbanization on floods of different recurrence interval, *Water Resources Research* VOL. 11, NO. 3, P. 431.

Jonkman S.N. 2005. Global perspectives on loss of human life caused by floods, *Nat. Hazards*, 34, 151-175.

Jonkman S.N., Kelman I. 2005. An analysis of the causes and circumstances of flood disaster deaths, *Disasters*, 29, 1, 75-97.

Koutsoyiannis D. and Baloutsos G. 2000. Analysis of a long record of annual maximum rainfall in Athens, Greece, and design rainfall inferences, *Nat. Hazards*, 22 (1), 29-48.

Kundzewicz Z.W. and Kundzewicz W.J. 2005. Mortality in flood disasters, in: Kirch W., Menne B. and Bertollini R. (ed.) *Extreme Weather Events and Public Health Responses*, Springer Verlag, 197-206.

Leontidou L. 2001. Cities of Silence: Labor Colonization of Athens and Piraeus, 1909-1940, Athens, *Cultural Technological Foundation ETBA* (In Greek).

Llasat M.C., Llasat-Botija M., Rodriguez A. and Lindbergh S. 2010a. Flash floods in Catalonia: a recurrent situation, *Adv. Geosci*, 26, 105-111.

Llasat M.C., Llasat-Botija M., Prat M.A., Porcu F., Price C., Mugnai A., Lagouvardos K., Kotroni V., Katsanos D., Michaelides S., Yair Y., Savvidou K. and Nicolaides K. 2010b. High-impact floods and flash floods in Mediterranean countries: the FLASH preliminary database, *Adv. Geosci*, 23, 47–55.

Mimikou M. and Koutsoyiannis D. 1995. Extreme floods in Greece: The case of 1994, *US – Italy Research Workshop on the Hydrometeorology, Impacts and Management of Extreme Floods*, Perugia, Italy, 13-17 November, 1995.

Mimikou M., Baltas E. and Varanou E. 2002. A study of extreme storm events in the Greater Athens area, Greece, *The Extremes of the Extremes, Extraordinary Floods*, *IAHS-AISH Publication, No 271* pp. 161-166.

Nikolaidou M. and Hatzichristou E. 1995. Registering and assessment of devastating floods in Greece and Cyprus, Diploma thesis, Department of Water Resources, Hydraulic and Maritime Engineering – National Technical University of Athens, Athens.

Nipurama N. and Simonovic S.P. 2007. Increase of flood risk due to urbanization: a Canadian example, *Nat Hazards*, 40: 25-41.

Parcharidis I., Lekkas E. and Vassilakis Emm. 2000. SIR-C/X Space Shuttle Images Contribution in Assessment of Flood Risk: The Case of Athens Basin, IEEE IGARSS, 1, 328-330.

Rappaport E.N. 2000. Loss of life in the United States associated with recent Atlantic tropical cyclones, *Bull. Amer. Meteor. Soc*, 81, 2065–2073.

Skilodimou H., Livaditis G., Bathrellos G. and Verikiou-Papaspiridakou E. 2003. Investigating the Flooding Events of the Urban Regions of Glyfada and Voula, Attica, Greece: A Contribution to Urban Geomorphology, *Geografiska Annaler 85*, 2, 197–204.

Δελτίο της Ελληνικής Γεωλογικής Εταιρίας, τομ. XLVII , 2013
Πρακτικά 13ου Διεθνούς Συνεδρίου, Χανιά, Σεπτ. 2013

Bulletin of the Geological Society of Greece, vol. XLVII 2013
Proceedings of the 13th International Congress, Chania, Sept. 2013

SEISMIC HAZARD ASSESSMENT IN THE NORTHERN AEGEAN SEA (GREECE) THROUGH DISCRETE SEMI-MARKOV MODELING

Pertsinidou C.E.[1], Tsaklidis G.[1] and Papadimitriou E.[2]

[1] Aristotle University of Thessaloniki, Department of Mathematics, p.eli.christina@gmail.com, tsaklidi@math.auth.gr

[2] Aristotle University of Thessaloniki, Department of Geophysics, ritsa@geo.auth.gr

Abstract

Semi-Markov chains are used for studying the evolution of seismicity in the Northern Aegean Sea (Greece). Their main difference from the Markov chains is that they allow the sojourn times (i.e. the time between successive earthquakes), to follow any arbitrary distribution. It is assumed that the time series of earthquakes that occurred in Northern Aegean Sea form a discrete semi-Markov chain. The probability law of the sojourn times, is considered to be the geometric distribution or the discrete Weibull distribution. Firstly, the data are classified into two categories that is, state 1: Magnitude 6.5-7 and state 2 Magnitude>7, and secondly into three categories, that is state 1: Magnitude 6.5-6.7, state 2: Magnitude 6.8-7.1 and state 3: Magnitude 7.2-7.4. This methodology is followed in order to obtain more accurate results and find out whether there exists an impact of the different classification on the results. The parameters of the probability laws of the sojourn times are estimated and the semi-Markov kernels are evaluated for all the above cases. The semi-Markov kernels are compared and the conclusions are drawn relatively to future seismic hazard in the area under study.

Key words: *semi-Markov chains, Markov chains, transition probability matrix, sojourn time distribution function*

Περίληψη

Οι ημι-Μαρκοβιανές αλυσίδες χρησιμοποιούνται για τη μελέτη της σεισμικότητας στο Βόρειο Αιγαίο. Η βασική τους διαφορά από τις Μαρκοβιανές αλυσίδες είναι ότι επιτρέπουν μια οποιαδήποτε αυθαίρετη κατανομή για τους χρόνους παραμονής (χρόνοι μεταξύ διαδοχικών σεισμών). Υποθέτουμε ότι η χρονοσειρά των σεισμών που έχουν γίνει στο Βόρειο Αιγαίο αποτελεί μια διακριτή ημι-Μαρκοβιανή αλυσίδα. Θεωρείται ότι οι χρόνοι παραμονής ακολουθούν γεωμετρικές ή διακριτές κατανομές Weibull. Πρώτα ταξινομήθηκαν τα δεδομένα σε δυο κατηγορίες, όπου κατάσταση 1: Μέγεθος 6.5-7 και κατάσταση 2 Μέγεθος>7, και στη συνέχεια σε τρεις κατηγορίες, όπου κατάσταση 1: Μέγεθος 6.5-6.7, κατάσταση 2 : Μέγεθος 6.8-7.1 και κατάσταση 3 : Μέγεθος 7.2-7.4. Εκτιμήθηκαν οι παράμετροι των συναρτήσεων πιθανότητας των χρόνων παραμονής και υπολογίστηκαν οι πίνακες πυρήνες της ημι-Μαρκοβιανής αλυσίδας για όλες τις παραπάνω περιπτώσεις. Έγινε σύγκριση των πινάκων πυρήνων και προέκυψαν συμπεράσματα για τη μελλοντική σεισμική επικινδυνότητα στην υπό μελέτη περιοχή.

Λέξεις κλειδιά: *ημι-Μαρκοβιανές αλυσίδες, Μαρκοβιανές αλυσίδες, πίνακας πιθανοτήτων μετάβασης, συνάρτηση πιθανότητας χρόνων παραμονής*

1. Introduction

Stochastic models are widely used to obtain results concerning the seismic hazard assessment. In Patw-ardhan et al. (1980) a semi-Markov model is developed to estimate the likelihoods of occurrences of great earthquakes (M≥7.8). Fujinawa (1991) studied the earthquake occurrence via a Markov chain and data from China, whereas Al-Hajjar and Blanpain (1997) used a semi-Markov model in a swarm sequence and obtained the optimal value for the total duration of the sequence. Altinok and Kolcak (1999) estimated the earthquake occurrence probabilities by a semi-Markov model and studied the inte-rval transition probabilities. Nava et al. (2005) evaluated the seismic hazard of the Japan area via a Ma-rkov chain and Sadeghian (2010) applied a semi-Markov model to forecast the triad dimensions of ear- thquakes. Votsi et al. (2010a, b, 2012a, b) applied hidden Markov and hidden semi-Markov modeling for the description of seismicity patterns.

In this paper a discrete semi-Markov model is proposed for the area under study, which is the Northern Aegean Sea (Greece). This model can be successfully applied in Seismology, considering the earthqua-kes as discrete events of the chain. It allows the interevent times (sojourn times) between two earthqua-kes, to follow any arbitrary distribution, which makes the semi-Markov chains a generalization of Mar-kov chains (Kemeny and Snell, 1976). Using this model, important quantities can be estimated, such as the mean value of the first hitting times (the mean time that an earthquake of state j will occur for the first time given that the previous earthquake was of state i, (Howard, 2007).

The data are obtained by a complete, homogeneous and accurate catalogue from the Geophysics Depar-tment of the Aristotle University of Thessaloniki and cover the period 1845-2008.

In this paper the quantity that is studied, is the discrete semi-Markov kernel, which gives the probabili- ty that an earthquake of state j will occur after k time units, given that the previous earthquake was of state i. It is assumed that the probability law of the sojourn times is either the geometric or the discrete Weibull distribution and the results are compared.

2. Semi-Markov Kernel for the two Dimensional State Space

The state space is firstly assumed to be two dimensional by classifying the data into two categories, ac-cording to the range of magnitudes (smaller and larger earthquakes). The sojourn times are supposed to follow geometric or discrete Weibull distributions, in order to examine the differences of the probabili- ties related to the aforementioned distributions.

2.1 Geometric Sojourn Times

In this section, it is assumed that the sojourn time distribution law is the geometric which is a common distribution law and it can be well adapted in the area under study (Pertsinidou, 2012). The probability mass function of the geometric distribution is the following:

Definition 1-Geometric distribution

$$P(X = k) = (1-p)^{k-1}p, \quad k = 1,2,\dots$$

In the sequel we give some definitions concerning the semi-Markov chains which are necessary for what follows (Barbu and Limnios, 2008).

Let E={1,…,s} be a finite state space, whose evolution in time is governed by a stochastic process $Z = (Z_k)_{k\in N}$. Let us also denote by $S = (S_n)_{n\in N}$ the successive time points when state changes in $(Z_n)_{n\in N}$ occur and by $J = (J_n)_{n\in N}$ the chain which records the visited states at these time points. Let $X = (X_n)_{n\in N}$ be the successive sojourn times in the visited states. Thus, $X_n = S_n - S_{n-1}$, $n \in N^*$, and, by convention, we set X_0=S_0=0. If $P(J_{n+1} = j, S_{n+1} - S_n = k \,|\, J_0,\dots,J_n;S_0,\dots,S_n) = P(J_{n+1} = j, S_{n+1} - S_n = k \,|\, J_n)$, then $Z = (Z_n)_{n\in N}$ is called a semi-Markov chain and the couple (J_n, S_n) is call- ed a Markov renewal chain. The

visited-state chain $(J_n)_{n\in N}$ is called the embedded Markov chain. We denote by p_{ij} the transition probabilities, that is:

Definition 2 – Transition probabilities

$p_{ij} = P(J_{n+1} = j|J_n = i), i,j \in E, n \in N.$

The matrix $P = (p_{ij})$ is called the transition probability matrix. The distribution function of the sojourn times is defined as follows:

Definition 3 – Sojourn time distribution function

$f_{ij}(k) = P(X_{n+1} = k|J_n = i, J_{n+1} = j).$

The semi-Markov kernel probabilities that we study throughout this paper are defined as follows:

Definition 4 – Discrete-time semi-Markov kernel probabilities $q_{ij}(k)$

$q_{ij}(k) := P(J_{n+1} = j, X_{n+1} = k|J_n = i) = p_{ij}\, f_{ij}(k).$

Then the semi-Markov kernel is the matrix $Q(k) = (q_{ij}(k))$ and constitutes the essential quantity which defines a semi-Markov chain.

The data concerning earthquakes that occurred in Northern Aegean Sea from 1845-2008 are classified, according to their magnitude, into two categories which are state 1: Magnitude 6.5–7 and state 2: Magnitude>7. In order to study the semi-Markov kernel probabilities, we need first to estimate the transition probabilities. The estimators of the transition probabilities are (Barbu and Limnios, 2008):

Definition 5 – Estimators of the transition probabilities

$\hat{p}_{ij}(M) = N_{ij}(M)/N_i(M)$, if $N_i(M) \neq 0$,

where $N_i(M)$ is the number of transitions of the embedded Markov chain to state *i*, until time *M*, and $N_{ij}(M)$, is the number of transitions of the embedded Markov chain from state *i* to state *j*, until time M. If $N_i(M) = 0$ we set $\hat{p}_{ij}(M) = 0$ for all M and if $N_{ij}(M) = 0$ we set $\hat{f}_{ij}(M) = 0$ for all *M*. The time unit is considered to be the year and the transition matrix for our data is found to be

$P = \begin{pmatrix} 0.71 & 0.29 \\ 0.8421 & 0.1579 \end{pmatrix}$.

If we assume that the sojourn times follow geometric distributions, the maximum likelihood estimators of these geometric distributions are found to be (Pertsinidou, 2012):

$f_{11}(n) = \frac{39}{109}\left(\frac{70}{109}\right)^{n-1}$, $f_{12}(n) = \frac{2}{3}\left(\frac{1}{3}\right)^{n-1}$, $f_{21}(n) = \frac{8}{17}\left(\frac{9}{17}\right)^{n-1}$, $f_{22}(n) = \frac{3}{4}\left(\frac{1}{4}\right)^{n-1}$.

Then the kernel of the semi-Markov chain becomes

$Q(n) = \begin{pmatrix} 27.69 * 70^{-1+n} * 109^{-n} & 0.58 * 3^{-n} \\ 6.74 * 9^{-1+n} * 17^{-n} & 0.47 * 4^{-n} \end{pmatrix}$, n=1,2,3,…

The corresponding graphs, in which the decay of the kernel probabilities as time passes can be observed, are the following:

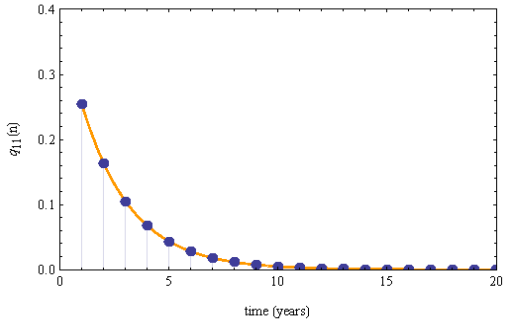

Figure 1 - Kernel probabilities $q_{11}(n)$, of the geometric distribution.

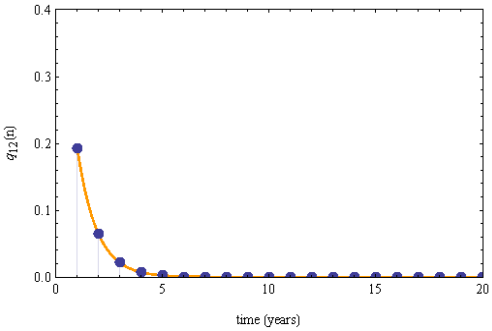

Figure 2 - Kernel probabilities $q_{12}(n)$ of the geometric distribution.

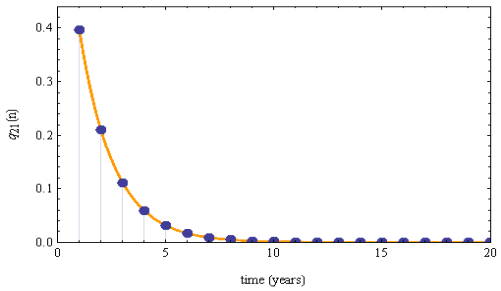

Figure 3 - Kernel probabilities $q_{21}(n)$, of the geometric distribution.

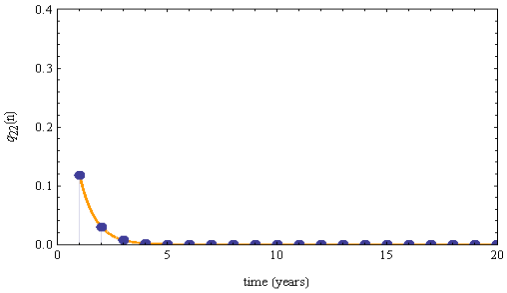

Figure 4 - Kernel probabilities $q_{22}(n)$, of the geometric distribution .

It is evident from Figure 1, that there is a higher probability for an earthquake of state 1 to be followed by an earthquake of state 1 during the next year (0.254). There is also a still high probability that such an earthquake will occur after two or three years, while these probabilities decay quickly from three years on. In Figure 2, given that the previous earthquake was of state 1, there is a high probability that the next earthquake of state 2 will occur in the next year. The probabilities $q_{12}(n)$ decay very quickly and, as we can also observe by the values given in Table 1 below, they become nearly 0 for n>5. Figure 3 shows that if the previous earthquake was of state 2, then it is very probable that the next earthquake of state 1 will occur in the next four years and for n>4 the probabilities become considerably smaller. Figure 4 shows that if the previous earthquake was of state 2 then there is a small probability that the next earthquake will also be of state 2, but if so, this is to be expected in the next four years. For n>4 the probabilities become zero. The aforementioned probabilities are given analytically below (for n∈[1,20]).

Thus, the probability that an earthquake of state 1, will be followed within three years by an earthquake of state 1, is high and from the third year on the probabilities decay quickly. If the next earthquake is of state 2, given that the last earthquake was of state 1, then this is expected to occur in the first five years. An earthquake of state 2, is more probable to be followed by an earthquake of state 1 in the next three years. Finally, if we assume that the an earthquake of state 2, will be followed by an earthquake of state 2, then this is more likely to happen within the next two years. As already mentioned, the probabilities $q_{12}(n)$ and $q_{22}(n)$ decay very quickly, which means that visiting state 2 (M>7) is less probable as the sojourn time increases.

2.2 Discrete Weibull Distributions for the Sojourn Times

It is now assumed that the transition probability matrix is the same as previously, but the sojourn time distribution function is the discrete Weibull of equation 2 that follows. This distribution allows the sojourn times to obtain greater values than the geometric, thus the time between two

Table 1 - Semi-Markov kernel probabilities of the geometric distribution (two dimensional case).

n	$q_{11}(n)$	$q_{12}(n)$	$q_{21}(n)$	$q_{22}(n)$
1	0.254	0.193	0.396	0.118
2	0.163	0.064	0.209	0.029
3	0.104	0.021	0.111	0.007
4	0.067	0.007	0.059	0.002
5	0.043	0.002	0.031	0.000
6	0.027	0.000	0.016	…
7	0.018	…	0.009	
8	0.011		0.005	
9	0.007		0.002	
10	0.005		0.001	
11	0.003		0.000	
12	0.002		…	
13	0.001			
14	0.000			
…	…	…	…	…
20	0.000	0.000	0.000	0.000

successive earthquakes can now be greater. In the sequel the probability mass function of the discrete Weibull distribution is cited, where x stands for the sojourn time and q and b are positive parameters.

Equation 2 – Discrete Weibull

$f(n)= q^{(n-1)^b} - q^{n^b}$, n=1,2,…. , 0<q<1 and b>0.

The parameters of the discrete Weibull distribution can not be estimated via the maximum likelihood method. There exists an empirical estimation effort (Kulasekera, 1994) which can not be used in our dataset, because of the small sample size of the sojourn times. Therefore, the parameters are estimated numerically and the distribution functions derived are (Pertsinidou, 2012):

$f_{11}(n) = 0.59^{(n-1)^{0.76}} - 0.59^{n^{0.76}}$, $f_{12}(n) = 0.53^{(n-1)^{0.94}} - 0.53^{n^{0.94}}$

$f_{21}(n) = 0.37^{(n-1)^{0.56}} - 0.37^{n^{0.56}}$, $f_{22}(n) = 0.4^{(n-1)^{0.62}} - 0.4^{n^{0.62}}$

Then the kernel matrix turns out to be

$$Q(n)= \begin{pmatrix} 0.71 * (0.6^{(-1+n)^{0.87}} - 0.6^{n^{0.87}}) & 0.29 * (0.25^{(-1+n)^{0.58}} - 0.25^{n^{0.58}}) \\ 0.8421 * (0.5^{(-1+n)^{0.89}} - 0.5^{n^{0.89}}) & 0.1579 * (0.34^{(-1+n)^{1.4}} - 0.34^{n^{1.4}}) \end{pmatrix}$$

The corresponding graphs of the discrete semi-Markov kernel functions are:

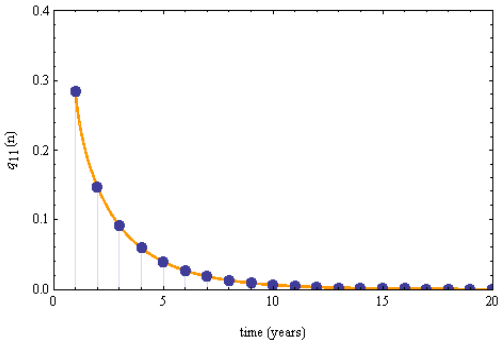

Figure 5 - Kernel probabilities $q_{11}(n)$, of the discrete Weibull distribution.

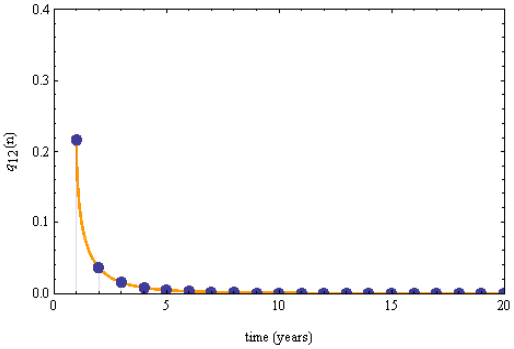

Figure 6 - Kernel probabilities $q_{12}(n)$, of the discrete Weibull.

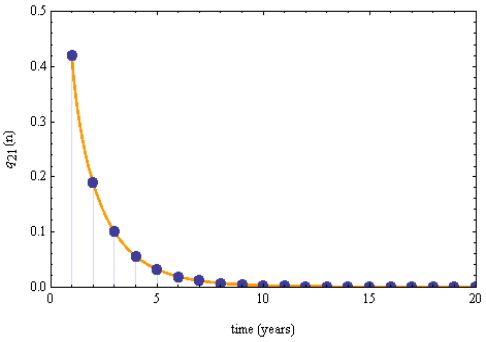

Figure 7 - Kernel probabilities $q_{21}(n)$, of the discrete Weibull distribution.

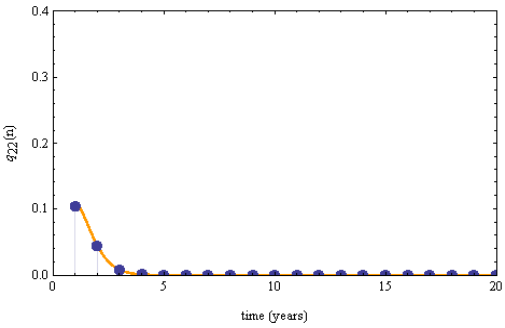

Figure 8 - Kernel probabilities $q_{22}(n)$, of the discrete Weibull distribution.

Comparing the above figures and also the values of the semi-Markov kernel probabilities given below, with the corresponding figures and values of the geometric distribution presented in the previous section, it can be seen that the results are similar, though we would expect the discrete Weibull kernel probabilities to decay much slower, than they do. This reinforces the previous conclusions concerning the expected seismicity. The values are given analytically (for comparison reasons) in the following Table 2.

3. Semi-Markov Kernel for the three Dimensional Transition Matrix

It is useful to classify the data into more than two categories, in order to observe if there are any differ- rences in the results. Now the data will be classified into three categories (we notice that more than three categories would lead to estimation problems due to the already small size of the dataset.) It is again firstly assumed that the times between two successive earthquakes follow the geometric distribu- tion and secondly the discrete Weibull distribution.

3.1 Geometric Sojourn Times

The data, concerning earthquakes that occurred in Northern Aegean Sea, are now classified into three categories, i.e. state 1: 6.5-6.7, state 2 : Magnitude 6.8-7.1, state 3 : Magnitude 7.2-7.4. The number $N_i(M)$ of visits in each state i and the transitions $N_{ij}(M)$ from state i to state j, until time *M* are found to be

Table 2 -. Semi-Markov kernel probabilities of the discrete Weibull distribution (two dimensional case)

n	$q_{11}(n)$	$q_{12}(n)$	$q_{21}(n)$	$q_{22}(n)$
1	0.284	0.217	0.421	0.104
2	0.147	0.035	0.188	0.045
3	0.091	0.015	0.099	0.008
4	0.059	0.008	0.055	0.000
5	0.039	0.005	0.032	…
6	0.027	0.003	0.018	
7	0.018	0.002	0.011	
8	0.019	0.001	0.006	
9	0.009	0.000	0.004	
10	0.006	…	0.002	
11	0.004		0.001	
12	0.003		0.000	
13	0.002		…	
14	0.001			
15	0.001			
16	0.000			
…	…	…	…	…
20	0.000	0.000	0.000	0.000

$N_1(M)$=29, $N_2(M)$=33, $N_3(M)$=12, $N_{11}(M)$=11, $N_{12}(M)$=14, $N_{13}(M)$=5, $N_{21}(M)$=15, $N_{22}(M)$=12, $N_{23}(M)$=5, $N_{31}(M)$=3, $N_{32}(M)$=7, $N_{33}(M)$=2.

The transition matrix is

$$P=\begin{pmatrix} 0.37 & 0.48 & 0.15 \\ 0.45 & 0.36 & 0.19 \\ 0.25 & 0.58 & 0.17 \end{pmatrix}.$$

Using the maximum likelihood function (Pertsinidou, 2012) we obtain the sojourn time distributions:

$f_{11}(n)=\frac{11}{25}\left(\frac{14}{25}\right)^{n-1}$, $f_{12}(n)=\frac{2}{5}\left(\frac{3}{5}\right)^{n-1}$, $f_{13}(n)=\frac{5}{7}\left(\frac{2}{7}\right)^{n-1}$

$f_{21}(n)=\frac{5}{12}\left(\frac{7}{12}\right)^{n-1}$, $f_{22}(n)=\frac{1}{2}\left(\frac{1}{2}\right)^{n-1}$, $f_{23}(n)=\frac{5}{7}\left(\frac{2}{7}\right)^{n-1}$

$f_{31}(n)=\frac{3}{13}\left(\frac{10}{13}\right)^{n-1}$, $f_{32}(n)=\frac{1}{2}\left(\frac{1}{2}\right)^{n-1}$, $f_{33}(1)=1$, and $f_{33}(n)=0$ for $n>1$.

The transitions from state 3 to state 3 found in the data are only two, which explains the fact that $f_{33}(1)=1$, and $f_{33}(n)=0$ for $n>1$.

The kernel matrix is

$$Q(n)=\begin{pmatrix} 4.07*14^{-1+n}*25^{-n} & 0.96*3^{-1+n}*5^{-n} & 0.75*2^{-1+n}*7^{-n} \\ 2.25*7^{-1+n}*12^{-n} & 0.36*2^{-n} & 0.95*2^{-1+n}*7^{-n} \\ 0.75*10^{-1+n}*13^{-n} & 0.58*2^{-n} & 0 \end{pmatrix}, n = 1,2,3,\ldots$$

The only difference is that the probabilities now decay faster, compared with the two dimensional case, in most of the cases. We cite as an example only the first graph.

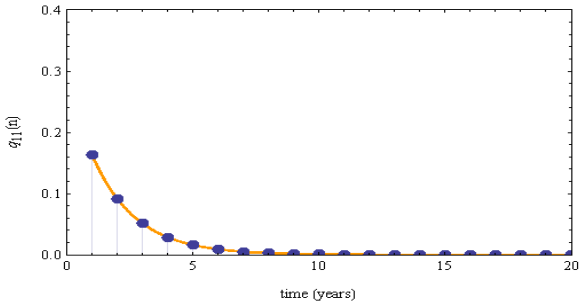

Figure 9 - Kernel probabilities $q_{11}(n)$, of the geometric distribution.

The kernel probabilities are the following (n∈[1,20]):

Table 3 - Semi-Markov kernel probabilities of the geometric distribution (three dimensional case).

n	$q_{11}(n)$	$q_{12}(n)$	$q_{13}(n)$	$q_{21}(n)$	$q_{22}(n)$	$q_{23}(n)$	$q_{31}(n)$	$q_{32}(n)$
1	0.163	0.192	0.107	0.187	0.18	0.138	0.057	0.29
2	0.091	0.115	0.031	0.109	0.09	0.039	0.044	0.145
3	0.051	0.069	0.009	0.064	0.045	0.011	0.034	0.073
4	0.028	0.041	0.002	0.037	0.022	0.003	0.026	0.036
5	0.016	0.025	0.000	0.022	0.011	0.000	0.02	0.018
6	0.009	0.015	…	0.013	0.005	…	0.015	0.009
7	0.005	0.009		0.007	0.003		0.012	0.005
8	0.003	0.005		0.004	0.001		0.009	0.002
9	0.002	0.003		0.002	0.000		0.007	0.001
10	0.000	0.002		0.001	…		0.005	0.000
11	…	0.001		0.000			0.004	…
12		0.000					0.003	
13							0.002	
14							0.002	
15							0.001	
…	…	…	…	…	…	…	0.001	…
20	0.000	0.000	0.000	0.000	0.000	0.000	0.000	0.000

We recall that $q_{33}(1) = p_{33}$ and $q_{33}(n)$=0 for n>1. We remind that in the two dimensional case it was $q_{11}(1)$=0.254. The corresponding probabilities appear to be smaller due to the different classification. We now expect fewer events of state 1, (6.5-6.7) given that the previous state was 1, which is reasonable since the class is smaller. From the values of Table 3, we realize that if the previous earthquake was of state 1, and the next one of state 2, then this is more probable to occur in the next 5 years. From the fifth year on, the probabilities decay and they become nearly zero for n>11 years. Furthermore, it is more likely for an earthquake of state 3 to be followed by an earthquake of state 1 in the next year and the probability that this transition will occur for n>4 years is almost zero. However, if the previous earthquake was of state 1, it is difficult to determine which one earthquake of the three classes is more likely to happen in the following year, because the related probabilities are found to be very close. We can also realize that if the last earthquake was of state 2, an earthquake of state 1 is more likely to happen after one or two years. For n>2 the probabilities are smaller and for n>10 they tend to zero. Also, given that the last earthquake was of state 2, an earthquake of state 2 is more likely to occur in the next five years, and for n>8 these probabilities become almost zero. If the previous earthquake was of state 2 and we assume that next one will be of state 3, then this is more likely to happen after one year, and the probability decays very quickly since for n>4 it is almost zero. Finally, comparing the values of $q_{31}(n)$ with $q_{32}(n)$ we find out that if the previous earthquake was of state 3, then an earthquake of state 2 is more likely to happen than an earthquake of state 1, in the next four years.

3.2 Discrete Weibull Distributions for the Sojourn Times

It is now assumed that the transition matrix is three dimensional, as estimated in the previous section, while the sojourn times follow discrete Weibull distributions. The parameters are estimated numerical- ly (Pertsinidou, 2012):

$f_{11}(n)= 0.54^{(n-1)^{0.98}} - 0.54^{n^{0.98}}$, $f_{12}(n)= 0.51^{(n-1)^{0.52}} - 0.51^{n^{0.52}}$

$f_{13}(n)= 0.4^{(n-1)^{1.4}} - 0.4^{n^{1.4}}$, $f_{21}(n)= 0.47^{(n-1)^{0.79}} - 0.47^{n^{0.79}}$

$f_{22}(n)= 0.51^{(n-1)^{0.83}} - 0.51^{n^{0.83}}$, $f_{23}(n)= 0.2^{(n-1)^{0.3}} - 0.2^{n^{0.3}}$

$f_{31}(n)= 0.89^{(n-1)^{1.4}} - 0.89^{n^{1.4}}$, $f_{32}(n)= 0.52^{(n-1)^{1.4}} - 0.52^{n^{1.4}}$

Then the kernel functions are found to be:

$q_{11}(n)= 0.37 * (0.54^{(-1+n)^{0.98}} - 0.54^{n^{0.98}})$, $q_{12}(n)= 0.48 * (0.51^{(-1+n)^{0.52}} - 0.51^{n^{0.52}})$

$q_{13}(n)= 0.15 * (0.4^{(-1+n)^{1.4}} - 0.4^{n^{1.4}})$, $q_{21}(n)= 0.45 * (0.47^{(-1+n)^{0.79}} - 0.47^{n^{0.79}})$

$q_{22}(n)= 0.36 * (0.51^{(-1+n)^{0.83}} - 0.51^{n^{0.83}})$, $q_{23}(n)= 0.19 * (0.2^{(-1+n)^{0.3}} - 0.2^{n^{0.3}})$

$q_{31}(n)= 0.25 * (0.89^{(-1+n)^{1.4}} - 0.89^{n^{1.4}})$, $q_{32}(n)= 0.58 * (0.52^{(-1+n)^{1.4}} - 0.52^{n^{1.4}})$

$q_{33}(n)=0$

We will cite, indicatively, only the graph of $q_{31}(n)$ which seems to differ from the others, which decay in a similar way to the already presented graphs in page 5.

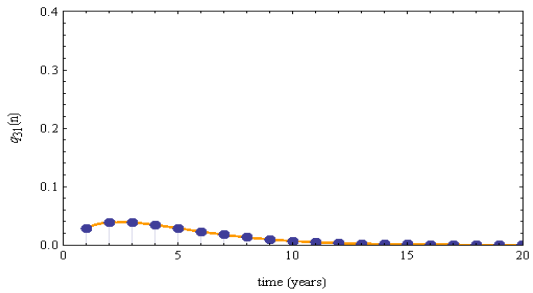

Figure 10 - Kernel probabilities $q_{31}(n)$, of the discrete Weibull distribution.

From the above graph we observe that the probabilities exhibit an increase for n=2,3. The values are shown in the following table.

Table 4 - Semi-Markov kernel probabilities of the discrete Weibull distribution (three dimensional case).

n	$q_{11}(n)$	$q_{12}(n)$	$q_{13}(n)$	$q_{21}(n)$	$q_{22}(n)$	$q_{23}(n)$	$q_{31}(n)$	$q_{32}(n)$
1	0.170	0.235	0.09	0.238	0.176	0.152	0.027	0.278
2	0.090	0.062	0.047	0.089	0.075	0.011	0.039	0.198
3	0.049	0.037	0.011	0.047	0.041	0.005	0.038	0.075
4	0.027	0.025	0.002	0.027	0.024	0.003	0.028	0.021
5	0.015	0.018	0.000	0.016	0.015	0.002	0.023	0.005
6	0.008	0.014	…	0.010	0.009	0.002	0.017	0.000
7	0.005	0.011		0.006	0.006	0.001	0.009	…
8	0.003	0.009		0.004	0.004	0.001	0.006	
9	0.001	0.008		0.003	0.007	0.000	0.005	
10	0.000	0.006		0.002	0.002	…	0.003	
11	…	0.005		0.001	0.001		0.002	
12		0.005		0.000	0.000		0.001	
13		0.004		…	…		0.000	
14		0.004					…	
15		0.003						
16		0.003						
17		0.002						
18		0.001						
19	…	0.001	…	…	…	…	…	…
20	0.000	0.000	0.000	0.000	0.000	0.000	0.000	0.000

From the above table we realize, that it is more probable for an earthquake of state 1, to be followed by an earthquake of state 2 or of state 1, and less probable of state 3, if the earthquake occurs during the next year. The probability of having a transition from state 2 to state 1 is more probable to happen after one year. The same holds for the probabilities $q_{22}(n)$ and $q_{23}(n)$. Also,

given the fact that an earthquake was of state 3, the probability that the next will be of state 1 is more likely to happen between 2-4 years, as we mentioned before in the graph of $q_{31}(n)$. Finally if an earthquake of state 3, will be followed by an earthquake of state 2, we expect this to happen in the next five years, since for n>5 $q_{32}(n) \approx 0$.

4. Conclusions

The use of semi-Markov chains is a useful tool that provides the probabilities that the chain will visit a state after a certain time given the previous state. In our case this means, that knowing the previous ear-thquake we can evaluate the probability that the next earthquake will occur after n time units and will be of state j. Classifying the states to earthquake clusters, allows us to obtain results concerning the sei-smic hazard. The discrete semi-Markov kernel, is studied in the Northern Aegean Sea. The kernel pro- babilities derived under the assumption that the sojourn times follow geometric or discrete Weibull di- stributions, in the two dimensional case, are very similar in most of the cases. Concerning the three di-mensional case we observe a mixed behavior for small number of steps, but as time increases the geo-metric probabilities decay faster than the discrete Weibull probabilities. A remarkable observation is that the $q_{31}(n)$ probabilities of the discrete Weibull distribution, are higher for n=2,3,4. This means that the occurrence of an earthquake of state 1, given that the previous earthquake was of state 3, is more li-kely to happen for n=2,3,4. We notice here that the mean hitting times of the various states for the mo-dels we studied in the present paper are also of main interest concerning seismic hazard assessment and have already being studied in Pertsinidou and Tsaklidis (2012).

5. Acknowledgments

This work was supported by the THALES Program of the Ministry of Education of Greece and the European Union in the framework of the project entitled "Integrated understanding of Seismicity, using innovative Methodologies of Fracture mechanics along with Earthquake and non-extensive statistical physics – Application to the geodynamic system of the Hellenic Arc. SEISMO FEAR HELLARC". Geophysics Department, AUTH, contribution number 813.

6. References

Al-Hajjar J. and Blanpain O. 1997. Semi-Markovian approach for modeling seismic aftershocks, *Engineering structures* 19, 969-976.

Altinok Y. and Kolcak D. 1999. An application of the semi-Markov model for earthquake occur-rences in North Anatolia, Turkey, *Journal of the Balkan Geophysical Society* 2, 90-99.

Barbu V.S. and Limnios N. 2008. Semi-Markov Chains and Hidden Semi-Markov Models toward Applications, New York, Springer, 7-26.

Fujinawa Y. 1991. A method for estimating earthquake occurrence probability using first- and multi-ple-order Markov chain models, *Natural Hazards* 4, 7-22 , Netherlands, Kluwer Academic Publishers.

Howard R.A. 2007. Dynamic probabilistic systems, Volume II: Semi-Markov and decision processes, Dover Publications, 642-644.

Kemeny J. and Snell L. 1976. Finite Markov Chains, Springer-Verlang, 24-38.

Kulasekera K.B. 1994. Approximate MLE's of the parameters of a discrete Weibull distribution with type I cencored data, *Microelectronics Reliability* 34, 1185-1188.

Nava F.A., Herrera C., Frez J. and Glowacka E. 2005. Seismic hazard evaluation using Markov chains: Application to the Japan area, *Pure and Applied Geophysics* 162, 1347-1366.

Patwardhan A.S., Kulkarni R.B. and Tocher D. 1980. A semi-Markov model for characterizing re-currence of great earthquakes, *Bulletin of the Seismological Society of America* 70, 323-347.

Pertsinidou C.E. 2012. Parametric estimation of the seismic hazard of the Aegean and the surrounding areas via the semi-Markov chains, *Master Thesis*, Aristotle University of Thessaloniki.

Pertsinidou C.E. and Tsaklidis G. 2012. Semi-Markov chains with sojourn times that follow the geometric or the discrete Weibull distributions, Application in the study of the seismic hazard of Greece, *25th Conference of the Greek Statistical Institute*, Volos, Greece.

Sadeghian R. 2010. The effects of zoning methods on forecasting of the next earthquake occurrences, according to semi-Markov models, *Annals of Geophysics* 53, 5-6.

Votsi I. 2013. Seismic Hazard Assessment through Hidden Markov and Semi-Markov Modeling and Statistical Estimation, *Thesis*, Aristotle University of Thessaloniki and Université de Technologie de Compiègne, 22-93.

Votsi I., Limnios N., Tsaklidis G. and Papadimitriou E. 2010a. Semi-Markov models for seismic hazard assessment in certain areas of Greece, *12th International Congress of the Geological Society of Greece*, Patra, Greece.

Votsi I., Limnios N., Tsaklidis G. and Papadimitriou E. 2010b. Nonparametric estimation of earthquake occurrence rate on northern Aegean sea, *28th European meeting of statisticians,* Piraeus, Greece.

Votsi I., Limnios N., Tsaklidis G. and Papadimitriou E. 2012a. Estimation of the Expected Number of Earthquake Occurrences Based on Semi-Markov Models, Methodology and *Computing in Applied Probability* 14, 685-703.

Votsi I., Limnios N. and Tsaklidis G. 2012b. Nonparametric estimation of the rate of occurrence of failures for semi-Markov chains, Bordeau Conference.

Δελτίο της Ελληνικής Γεωλογικής Εταιρίας, τομ. XLVII , 2013
Πρακτικά 13ου Διεθνούς Συνεδρίου, Χανιά, Σεπτ. 2013

Bulletin of the Geological Society of Greece, vol. XLVII 2013
Proceedings of the 13th International Congress, Chania, Sept. 2013

ROCKFALL HAZARD IN GREECE

Saroglou H[1].

[1] National Technical University of Athens, School of Civil Engineering, Department of Geotechnics, saroglou@central.ntua.gr

Abstract

The geological structure of Greece (frequent occurrence of rock formations, existence of faults and fracturing of rocks), the steep topography and mountainous terrain as well as its high seismicity, creates a significant rockfall hazard. During the last decades, rockfalls in Greece are becoming a frequent phenomenon due to the increase of intense rainfall events but also due to the extension of human activities in mountainous areas.

The paper presents rockfall hazard in Greece trough an inventory of rockfalls and investigates the correlation of specific factors, namely: a) triggering mechanism (rainfall, seismicity), b) slope angle, c) lithology, d) fault presence, e) block size on the probability of occurrence of these, based on a statistical approach. The time and space frequency of the events is also investigated. Finally, the impact of the events on human and infrastructures (transportation infrastructure, inhabited areas, archaeological sites) is discussed.

Key words: *Earthquake, slope, rainfall, risk, impact.*

Περίληψη

Η γεωλογική δομή της Ελλάδας (συχνή εμφάνιση βραχωδών σχηματισμών, παρουσία ρηγμάτων και κερματισμός των πετρωμάτων) σε συνδυασμό με το απότομο και ορεινό ανάγλυφο καθώς και την υψηλή σεισμικότητα, συμβάλλουν στην υψηλή διακινδύνευση έναντι καταπτώσεων βράχων. Τις τελευταίες δεκαετίες, οι καταπτώσεις βράχων είναι συχνό φαινόμενο στον Ελλαδικό χώρο εξαιτίας της αύξησης των ακραίων βροχοπτώσεων καθώς και τις επέκτασης της ανθρώπινης δραστηριότητας.

Το άρθρο παρουσιάζει την διακινδύνευση έναντι καταπτώσεων στην Ελλάδα με τη χρήση μιας βάσης δεδομένων και προσδιορίζει τη σχέση συγκεκριμένων παραμέτρων, όπως: α) μηχανισμός γένεσης (βροχόπτωση, σεισμός), β) κλίση πλαγιάς, γ) λιθολογία, δ) παρουσία ρήγματος, ε) μέγεθος πίπτωντων τεμαχών με την πιθανότητα εκδήλωσης αυτών με χρήση στατιστικής προσέγγισης. Διερευνάται επίσης η χρονική και χωρική συχνότητα και τέλος η επίπτωση των καταπτώσεων στις ανθρώπινες δραστηριότητες (δρόμους, κατοικημένες περιοχές, αρχαιολογικοί χώροι).

Λέξεις κλειδιά: *Καταπτώσεις βράχων, σεισμικότητα, διακινδύνευση, βροχοπτώσεις.*

1. Introduction

Rockfalls occur when a mass of rock is detached from bedrock and moves downward. They pose significant hazard on human activities and infrastructure. The assessment of rockfall risks along roads and on other human activities is of great importance. Rockfall intensity increases during

periods of low temperature and high rainfall. Geological assessment can lead to accurate prediction of the outbreak of such events, explain its mechanism of occurrence and assist in the effective design of protection measures. Koukis et. al. (1997) note that slope movements, which occur in the form of rockfalls have a relatively high frequency in Greece. The geological structure of Greece (frequent occurrence of rock formations, existence of faults and fracturing of rocks), the steep topography and mountainous terrain as well as its high seismicity, creates a significant rockfall hazard. The rockfall hazard poses a high to very high risk to transportation infrastructure (Highways and railways), domestic areas, archaeological and national heritage sites (ancient monuments, castles, etc.).

During the period 2000-2010, an increase in the number of rockfalls was noticed in Greece, due to intense rainfall events and earthquakes. A significant number of sites, prone to rockfalls, are known along the transportation infrastructure of Greece, near inhabited areas and archaelogical sites. Rockfall protection measures have been applied in relatively few places along highways and other sites in Greece.

The major rockfall at Tempi valley in 2009, led to a loss of human life death and the closure of a section of the Athens-Thessaloniki national road for several months. Other rockfall events, which have also led to human life loss, are those in Kakia Scala (2010), Santorini (2011) and Kefalari, Argos (2012).

2. Rockfall Inventory

2.1. Recorded Data

The case studies that were recorded are those, which have occurred as distinct rockfall episodes in natural slopes mainly and have impacted human activities, such as roads, inhabited areas and archaeological sites. Rockfalls, which occur from the road cut slopes along highways in the national road network, were not recorded in the present study. These are very often and especially encountered in Pindos mountain range but also in other mountainous areas. Some rockfalls on highways are

The following data were recorded for each rockfall episode: a) Location, b) Coordinates, Altitude, c) Type of site (roadway, inhabited area, archaeological site), d) Date (s) of rockfall events, d) Triggering mechanism (rainfall, earthquake, other), e) Fault scarp presence, f) Geological formation, g) Rock mass type, degree of fracturing, h) Slope height, i) Slope angle, j) Block size of fallen blocks, k) Impact type, l) Presence of vegetation (forest etc.), m) Energy level, n) Reference.

The recorded rockfalls are fifty-six events for the period between 1935 and 2013. The locations of these are presented in Figure 1. Additionally, the most important parameters of these events are given in Table 1.

It is evident that the frequency of rockfalls has increased significantly in the period between 2000 and 2010. This can be attributed to the increase of intense rainfall periods but also to the extension of human activities (infrastructure, increase of population etc.). In a number of sites, more than one event has occurred and thus it is possible to predict the return period of the phenomenon.

Koukis & Ziourkas (1991) and Koukis et. al. (2005) presented a landside frequency zone map for Greece. The relative frequency of rockfalls in these maps was 11 %. The maximum frequency of landslides in those maps, expressed in cases per surface area, is along the Pindos geotectonic zone,. Based on the present study, this maximum does not also depict the maximum frequency of rockfalls as it mainly reflects the large number of slope instabilities occurring in the flysch formation in the form of soil type or composite failures (rotational, translational etc.).

Rockfalls in Greece are more frequent in mountainous areas at slopes with angles greater than 50 degrees, as it can be seen by the concentration of events in Pindos Mt., Tempi valley and

Parnassos Mt., shown in Figure 1. Rockfalls also occur in low to medium altitude areas but with steep slope morphology, usually related to fault scarps, as it the case in Kakia Scala, Klokova, Monemvasia and elsewhere.

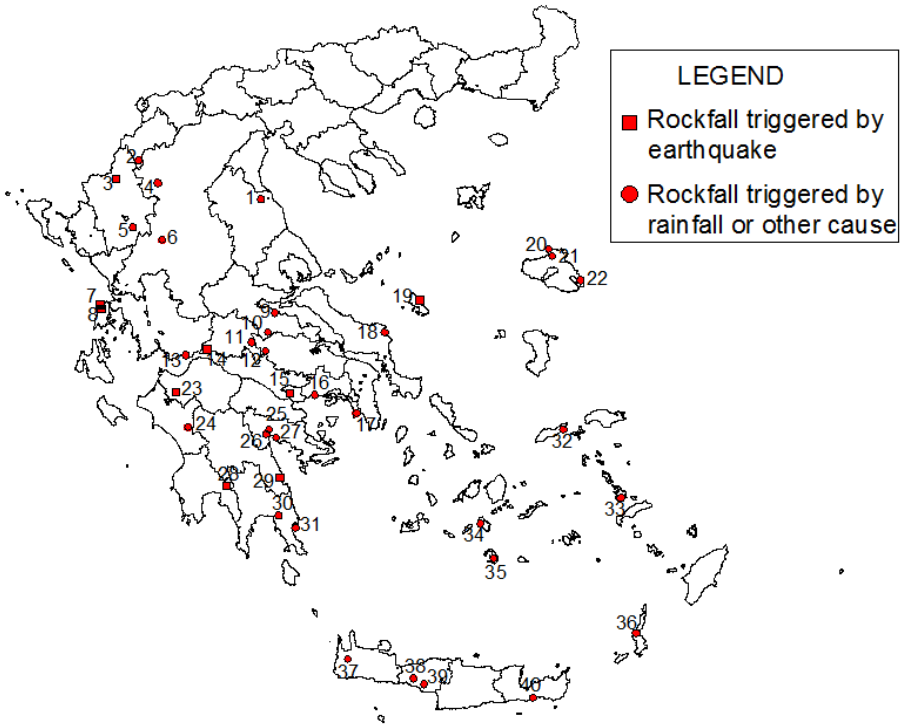

Figure 1 - Location of recorded rockfalls.

2.2. Time – space Frequency of Rockfalls

Based on the recorded data it was possible to define the frequency of rockfalls during the studied period. The frequency of rockfalls is shown in Figure 2.

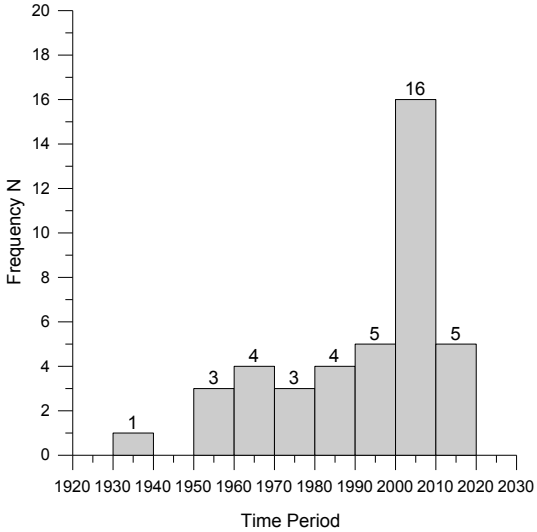

Figure 2 - Frequency of rockfalls in the period between 1930 – 2013.

Table 1 – Main data of recorded rockfalls in Greece.

Id	Location	Type	Date	Trigger	Rock type	Fault scarp	Block (m^3)	Impact	Ref.
1	Tembi Valley	R	17/12/2009 2004,1977[1]	ND	M		0.5 – 5, 50[2]	HLL, RC	R1, R2
2	Eptachori, Kastoria	D	1935, 51, 68, 70,87, 93, 94	R	M	Y	336[3]	DH	R3, R4
3	Konitsa,Ioaninna	D/A	8/1998	E	LA		2	DH	R5
4	Orliagas, Ziakas	D/R		ND	L	Y	1	ND	R6
5	Pramanta -Ioannina	R	9/3/2004	ND	L	Y	< 1	DR	
6	Nea Pefki, Trikala	R	20/10/2010	R	S		< 1	DR	
7	Drimonas,Lefkada	D/R	14/8/2003	E (6.4)	L	Y	< 1	DR	R7
8	Lefkada,Ag.Nikitas	D/R	14/8/2003	E (6.4)	L	Y	13.7	PDR	
9	Kamena Vourla	D	27/8/2012	ND	L		1	DH	
10	Tithorea, Parnassos	D	19/12/2010 1999, 1957	ND	L		10	DH	R8
11	Delfi ancient site	A	2003, 09[1]	R	L		8	V	R9, R10
12	Vageni Distomo	D/R		ND	C	Y	40	PDR	R11
13	Klokova Mt.	R	16/11/2012	ND	L		1-2	DR	
14	Itea, Monastiraki	R	18/1/2010	E (5.1)	L	Y	<1	DR	
15	Geraneia Mt.		24/2/1981	E (6.3)	L	Y			R12
16	Kakia Scala	R	20/11/2000	R	L	Y	0.5	HLL	
17	Vouliagmeni,Attica	D	1/1982	ND	L	Y	1-2		R13
18	Oksilithos, Paralia-Platana	R	13/8/2008	ND	MS		1.5	HI	R14
19	Skyros Island	A	26/7/2001	E (5.8)	L	Y	1-2	DC	R15
20	Mythimna, Lesvos	A	2001	R	A		0.3	ND	R16
21	Stypsi, Lesvos	D	1963, 1977	R	A		0.5-3.0	DH	R17,R18, R19
22	Taxiarches, Lesvos	D	1963, 3/11/ 09	ND	M	Y	1	DH	R20
23	Santomeri, Achaia	D	8/6/2008	E (6.5)	L	Y	4	DH	R21
24	Anc. Olympia	R	22/1/2013	R	L		0.5	DR	
25	Argos Castle	A	1987	ND	L			D	R22
26	Kefalari, Argos	D	20/4/2012	ND	L	Y	0.1	HLL	R23
27	Acronafplia	A	1/2010	ND	L		0.5	V	R24
28	Ladas, Eleochori, Poliani, Kalamata	D	13/9/1986	E (6.2)	L		<1	PDH	R25
29	Leonidio, Tiros	R	6/1/2008	E	L	Y	<1	RC	
30	Molaoi, Lakonia	D	2/2003	R	CA		1-2	PDH	R26
31	Monemvasia	A	2003, 2010[1]	R	L	Y	2	DH, V	R27

Id	Location	Type	Date	Trigger	Rock type	Fault scarp	Block (m^3)	Impact	Ref.
32	Therma Ikaria	D	10/1978	ND	M	Y	1	PDH	R28
33	Kalymnos	D	12/2002	R	L		4	PDH	R29
34	Chora, Ios	D	-	ND	S		1	PDH	R30
35	Santorini	D	2011	R	P		0.5	HLL	
36	Carpathos,Akropoli	D	-	ND	L			-	R32
37	Topolia, Chania	R	23/2/2012	R	L	Y	0.5	FB	
38	Kourtaliotis gorge	R	4/3/2012	R	L	Y	1	DR	
39	Heraklion (Pitsidia,Akoumia)	D	14/5/1959	E (6.3)	L	Y	<1	DH	R12
40	Ag. Fotia, Crete	R	-	ND	S		<1	DR	

[1] More rockfall events exist, which are not presented here, [2] A record of fallen blocks is given in Gazetas et. al. (2010), [3]the largest rock block, 15 smaller rocks have fallen in this site, Type: R=Roadway, D=Domestic, A: Archeological, Trigger: R=rainfall, E=Earthquake, ND=Not defined, Rock type: L= limestone, M=marble, CA= Calcitic agglomerate, LA=Limestone agglomerate, C= conglomerates, S=sandstone, M=marls, MS= marls/ sandstones, SG=Schist/gneiss, A= Andesite, P= Pyroclastics, Fault Scarp: Y=yes, Impact: HLL= Human loss, HI=Human injury, V=Potential impact on visitors, damage to archaeological site, DH=Damage to houses, PDH=Potential house damage, RC=Roadway closure, DR=Damage on roadway, PDR=Potential roadway damage, FB=fall on moving bus, DC=Damage on cars, ND= No damage. R1=IGME (1979), R2 Gazetas et. al. (2010), R3=IGME (1989), R4= Emmanouloudis & Filippidis (2000), R5= IGME (1998), R6= Papathanassiou et. al. (2010), R7= Vogiatzis et. al. (2004), R8= Papathanasiou et al. (2011), R9=Christaras & Vouvalidis (2010), R10=Marinos & Rondoyianni (2005), R11=IGME (2003), R12= Papazachos &Papazachou 1997, R13=IGME (1982), R14=Velissariou (2008), R15=Marinos & Tsiambaos (2002), R16=Marinos et. al. (2001), R17=Pangaea (1995), R18=IGME (2002), R19=Saroglou (2012), R20=Tsiambaos (2010), R21=Lainas et.al. (2010), R22=Sofianos et. al. (1988), R23=Kampouroglou & Chatzitheodorou (2012), R24=Konstantopoulou et. al. (2011), R25=Mariolakos et. al., (1987), R26= IGME (2003), R27=Saroglou et. al. (2012), R28= IGME (1979), R29= IGME (2003), R30=IGME (2002), R31=Antoniou, Lekkas (2010), R32=IGME (2003).

2.3. Triggering Mechanisms

The main triggering mechanism of rockfalls in Greece is rainfall. 13 rockfall events where triggered by rainfalls (frequency equal to 33%) and 1 event by a snowfall. A rise in rockfalls has occurred during the last years (2010 - 2013) due to heavy rainfall in limited time period usually during winter. Eighty six (86) instability phenomena were reported in 2010, from which 5% were rockfalls (Nikolaou et. al., 2011). The triggering factor of 95 % of those was intense rainfalls during February and November-December period. Additionally, the most affected area was Epirus Prefecture. Krautblatter & Moser (2009) proposed a model coupling rockfall and rainfall intensity.

The second most important triggering mechanism is seismic loading during earthquakes since 10 events by seismic loading (frequency equal to 25%). The rockfalls triggered by historical earthquakes in Greece, which are reported in literature (by Pavlides & Caputo, 2004, Ambraseys & Jackson, 1990), are summarized in Table 2. Recent earthquakes which have triggered large rockfall events are those in Skyros (2001), Lefkada (2003), Achaia (2008) and older events those during Alkyonides (1981) and Kalamata (1986) earthquakes. During Kalamata earthquake rockfalls occurred in the villages of Poliani, Eleochori and along the road linking Kalamata with Sparti (Papazachos & Papazachou, 1997). The rockfalls occurred along reactivated fault scarps (Mariolakos et. al., 1987). In some events the triggering mechanism was not defined.

Table 2 –Rockfalls during historical earthquakes.

Date	Location of Earthquake	Magnitude	Rockfall locations	Reference
550 BC	Sparta (Pelo-ponnese)	Mi7.0	Rock falls from Tay-getus Mt	Guidoboni 1989
469–464 BC	Sparta (Pelo-ponnese)	M>7.0	fault traces (?), rock falls	Guidoboni 1989, Armijo et. al. 1991
1893 February 9	Samothrace	M= 6.5	Ground cracks and rock falls	Papazachos &Papazachou 1997
Earthquakes of 1870	(Arachova-Delphi)	Ms=5.3 - 6.7	Rock falls	‘’
1402	Achaia Diakofto	M=7	Rockfalls Xylokastro, Diakofto, Evrostini	‘’
1633	Zakynthos	M=6.9	Rockfalls	Barbiani 1864, Chiotis 1887
1636	Cephallonia	M=7.1	Livatho, Argostoli, Liksouri	Papazachos &Papazachou 1997
1694	Athens	M=6.4	Ag. Dionysios rockfall	
1928	Corinth	M=6.3	Geraneia Mt. rockfalls	
1959 May 14	Heraklion	M=6.3	Rockfalls Pitsidia, Akoumia, Kamilari	
1783, 1825, 1885, 1914, 1915, 1948	Lefkada	M=5.7 - 6.7	Rockfalls	Papathanasiou

2.4. Impact of Rockfalls

Based on the analysis of the data, the main impact of rockfalls is damage and temporary closure of roadways (frequency equal to 32%) and secondly damage to houses (frequency equal to 20%). The percentage of potential damage to roadways and houses is 5% and 13% respectively. Additionally, the percentage of loss of human life is 11%, which is considered exceptionally high. Furthermore, the frequency of potential impact on visitors and damage to archaeological sites is equal to 11%.

According to Nikolaou et. al. (2011), from the 86 instability phenomena (5% rockfalls), which were reported in 2010, 34% of the cases impacted the roadway network and 66% inhabited areas.

The most known and studied events, which have occurred along highways and other roads, are that of Tempi (shown in Figure 3a), Kakia Skala and Klokova area. Significant rockfall events impacting roads have taken place in Ag. Nikitas in Lefkada island (Figure 3b), in Oksilithos (Velissariou, 2008), along roads in Kourtaliotis gorge, in Topolia and Ag. Fotia in Crete island.

Recent events that affected inhabited areas are those in Eptachori in 1994, in Skyros in 2001 (Marinos & Tsiambaos), Santomeri in 2008 (Lainas et al., 2010) and Tithorea in 2010 (Papathanasiou et. al., 2011), which is presented in Figure 3c. Sites of high risk in inhabited areas need to be identified in order to minimize rockfall risk.

Additionally, there are a large number of rockfall incidents, which have occurred in archaeological and national heritage sites. These pose a significant danger to tourists and visitors as well as they affect the integrity of the monuments itself. Well known example is that of Delfi site (Marinos & Rondoyanni, 2005), where part of the archeological site was closed in 2009. Other studied sites are Mythimna castle (Marinos et. al., 2002), Monemvasia castle (Saroglou et. al., 2012), as presented in Figure 3d and others.

Figure 3 - Impact of rockfall a) on highway in Tempi valley b) on roadway during Lefkada earthquake (photo from Geobrugg), c) Tithorea village, d) Monemvasia archaeological site.

3. DETERMINANT FACTORS

3.1. Slope Angle

Generally, Rockfalls occur at slopes with an inclination greater than 45 degrees. In the studied areas the slope angle ranged between 45 and 90 degrees with a mean value of 70 degrees.

3.2. Lithology – Degree of Fracturing

The most frequent geological formation encountered in the study areas, is limestone (with a frequency equal to 64%). The percentage of occurrence of the rocks forming the studied slopes is presented in Figure 4a. Generally, limestones are found broken to heavily broken, especially when in the vicinity of faults, resulting in blocky rock masses. Rockfalls are favoured in blocky or very blocky rock masses, since medium to large rock blocks are formed by intersecting discontinuities and can be relatively easily detached by the action of water or seismic loading.

In a large number of sites, scree is present at the foot of the slopes. The presence of a scree slope below the rock cliff suggests slope ravelling activity. According to Sartori et al. (2003), this activity can be linked to the progressive failure of the rock cliff, but can also be a precursory event of larger rockfalls. Dorren & Seijmonsbergen (2003) assigned rockfall susceptibility categories to

geological formations according to their nature and ability to produce rocks blocks. They considered limestone to have high susceptibility, while schists, slates, marls and sandstones low to medium. The block size of the fallen blocks ranges between 0.5 m^3 and 50 m^3 with an exception of Eptachori rockslide. The blocks size is less than 1m^3 in 22 sites and between 1 and 5 m^3 in 8 sites, as presented in Figure 4b.

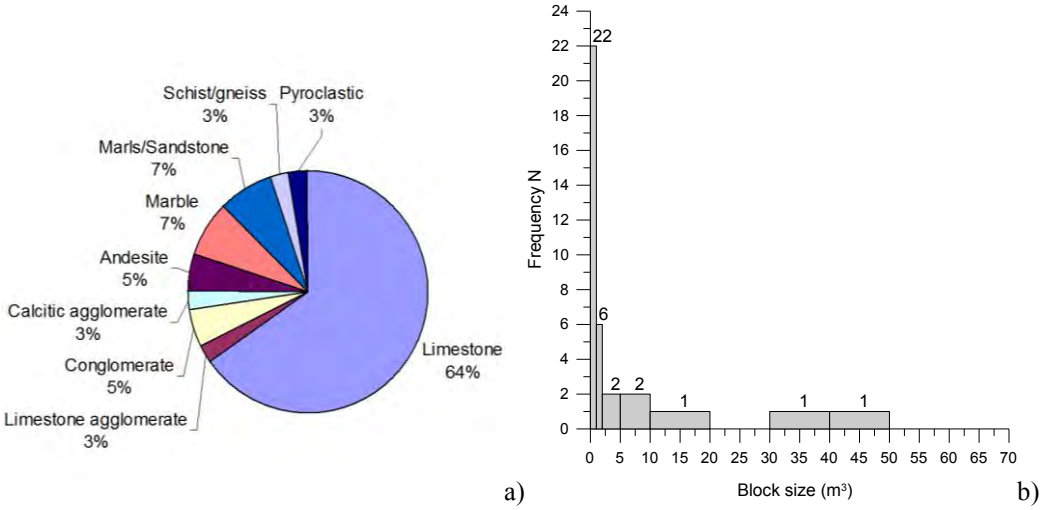

Figure 4 - a) Lithology in areas of rockfall events, b) Frequency of block size of fallen rocks.

3.3. Presence of Faults

Gallousi & Koukouvelas (2007) have correlated the triggering of the Marathias rockslide in Corinth Gulf with the seismicity of the area. The slide is formed along a fault scarp. In the study areas, twenty (20) slopes are related to the presence of faults and this contributes to the higher rockfall activity.

4. Conclusions

In the present paper a review of the rockfall activity in Greece was done for the period between 1930 until the present. A rockfall inventory was created, accounting for all the parameters determining the rockfall events. Based on the analysis of the data, it was shown that the number of rockfalls has increased substantially in the recent years. It is also concluded that the main triggering mechanism is rainfall, while a significant number of cases is related to earthquakes. Emphasis was given to the presence of faults and it was shown that almost half of the slopes were formed or relate to faults. In the study areas, limestone formations predominate, while the rock masses are blocky to very blocky resulting in block size range of the fallen block between 0.5 and 5 m^2 in the majority of the cases. Finally, the impact is severe in most cases having resulted in human life loss in four cases and usually in damages to roads and secondarily to houses, as well as potential risk to archaeological sites (visitors and structures).

5. References

Ambraseys N.N. and Jackson J.A. 1990. Seismicity and associated strain of central Greece between 1890 and 1988, *Geophys*. J. Int. 101, 663-708.

Antoniou A.A. and Lekkas E. 2010. Rockfall susceptibility map for Athinios port, Santorini island, Greece, *Geomorphology*, 118, 152-166

Armijo R., Lyon-Caen H. and Papanastassiou D. 1991. A possible normal-fault rupture for the 464 BC Sparta earthquake, *Nature*, 351, 137–139.

Asteriou P., Saroglou H. and Tsiambaos G. 2012. Geotechnical and kinematic parameters affecting the coefficients of restitution for rock fall analysis, *Int. Journal of Rock Mechanics and Mining Sciences*, Vol. 54, 103-113, ISSN 1365-1609, 10.1016/j.ijrmms.2012.05.029.

Christaras B., Filippides A., Vogiatzis D., Kantiranis N., Moraiti E., Dimitriou A. and Papathanassiou G. 2004. Rock falls and protective measures of the down slope area. The case of Drimon village, in Lefkas island, during the earthquake of 14/8/03 (Ms=6.4), 32 *IGC*, Florence.

Christaras B. and Vouvalidis K. 2010. Rockfalls in the archaeological site of Delphi, Greece, *Proc. of IAEG 2010 International Congress*, Auckland.

Dorren L. and Seijmonsbergen A. 2003. Comparison of three GIS-based models for predicting rockfall runout zones at a regional scale, *Geomorphology*, vol. 56, (1-2), 49-64.

Emmanouloudis D. and Filippidis E., 2000. A G.I.S. technique for volume calculation of Eptahori rockfalls, Macedonia, Greece, in Tsihrintzis et. al. (eds), *Proc. of Int. Conf.: Protection and Restoration of the Environment V*, Vol. I, pp. 429-435.

Gallousi C. and Koukouvelas I. 2007. Quantifying geomorphic evolution of earthquake-triggered landslides and their relation to active normal faults. An example from the Gulf of Corinth, Greece, *Tectonophysics,* 440, 85–104.

Gazetas G., Kavounidis S., Rozos D. and Tsiambaos G. 2010. Corollary Expert Committee for failures in Tempi, Technical Chamber of Greece (*in greek).*

Guidoboni, E. (Ed.) 1989. I terremoti prima del Mille in Italia enell'area mediterranea, *Instituto Nazionale di Geofisica* (ING), Bologna, 765 pp.

Andronopoulos B. and Koukis G. 1979. Geological – geotechnical study of slope stability along the national highway in Tempi area, *Unpublished report*, I.G.M.E, Athens.

Rozos D. 1979. Geotechnical investigation for slope stability of rockmass in Therma, Ag. Kirikos, Ikaria island, *Unpublished report*, I.G.M.E, Athens.

Chatzinakos I. 1989. Geotechnical investigation of the slope stability of Eptachori, Kastoria, *Unpublished report*, I.G.M.E, Athens.

Mpellas M. 1998. Geotechnical study for mitigation of detached blocks on slope of Konitsa Municipality, Ioannina, *Unpublished report*, I.G.M.E, Athens.

Andronopoulos V. 1982. Preliminary study of geotechnical conditions of the slopes in Vouliagmeni lake, *Unpublished report*, I.G.M.E, Athens.

Antonopoulos M. 2003. Engineering geological study report for instability phenomena in Akropoli area, Municipality of Carpathos, *Unpublished report*, I.G.M.E, Athens.

Rozos D. and Nikolaou N. 2002. Engineering geological investigation of rockfalls in Ios island, Cyclades, *Unpublished report*, I.G.M.E, Athens.

Pogiatzi E. and Konstantopoulou G. 2003. Engineering geological investigation of rock slopes in Molai, Lakonia, *Unpublished report*, I.G.M.E, Athens.

Nikolaou N. 2003. Engineering geological investigation of rockfalls in Vageni, Distomo, Voiotia, *Unpublished report*, I.G.M.E, Athens.

Apostolidis E. and Aleyras N. 2003. Engineering geological investigation of rockfalls in Kalymnos, island, *Unpublished report*, I.G.M.E, Athens.

Apostolidis E. 2002. Engineering Geological investigation of the instability phenomena in Stypsi, Petra prefecture, Lesvos Island,. *Unpublished report*, 37 pp., I.G.M.E, Athens.

Kampouroglou E. and Chatzitheodorou Th. 2012. Report on the geological, engineering geological conditions of cave and rock slope in Kefalari, Argos, Ministry of Culture (unpublished).

Konstantopoulou G., Spanou N. and Kontogianni V. 2011. Rockfall Susceptibility - Hazard and risk assessment of Akronafplia historical site, Nafplio, Greece, *The 2nd World Landslide Forum Abstracts*, WLF2 - 2011– 0300.

Koukis G. and Ziourkas C. 1991. Slope instability phenomena in Greece: A statistical analysis. *Bull. Int. Assoc. Eng. Geology*, vol. 43, 47-60.

Koukis G, Tsiambaos G and Sabatakakis N .1997. Landslide movements in Greece: engineering geological characteristics and environmental consequences, in: *Proceedings of International Symposium of Eng. Geol. and the Envar, IAEG, Balkema*, Rotterdam, pp 789–792

Koukis G., Sabatakakis N., Nikolaou N. and Loupasakis C. 2005. Landslide hazard zonation in Greece, in: Sassa K, Fukuoka H, Wang F, Wang G (eds) *Proc. 1st General Assembly and The 4th Session of Board of Representatives of the Int. Consortium on Landslides*, pp. 291–296.

Lainas S., Koulouris S., Vagenas S., Depountis N. ,Sabatakakis N. and Koukis G. 2010. Earthquake-induced rockfalls in Santomeri Village, Western Greece, *Proc. of the 12th International Congress,* Patras.

Marinos P., Kavvadas M., Tsiambaos G. and Saroglou H. 2002. Rock slope stabilization in Mythimna castle, Lesvos island, Greece*, 1st European conference on landslides*, Balkema, Rybar Stemberk & Wagner (eds), Prague, 635-639.

Marinos P, Tsiambaos G. 2002. Earthquake triggering rock falls affecting historic monuments and a traditional settlement in Skyros Island, Greece, *Proc. of the Int. Symposium: Landslide risk mitigation and protection of cultural and natural heritage*, Kyoto, Japan, pp. 343-346.

Marinos P., Kavvadas M., Tsiambaos G. and Saroglou H. 2002. Rock slope stabilization in Mythimna castle, Lesvos island, Greece, *1st European Conference on landslides*, Balkema publ, ed: Rybar Stemberk & Wagner, Prague, pp. 635-639.

Marinos P. and Rondoyanni Th. 2005. The archaeological site of Delphi, Greece: a site vulnerable to earthquakes, rockfalls and landslides, *Proc. of the 1st General Assembly of the international consortium on Landslides*: Landslides- Risk analysis and sustainable disaster management (2001), Ed. K. Sassa et al., Springer, Kyoto, ch. 31, pp. 241-249.

Mariolakos et. al. 1987. Presentation in Geological Society of Greece workshop.

Nikolaou N., Pogiatzi E. and Spanos N. 2011. *Report on landslides in Greece on 2010*, I.G.M.E. p.8.

Pangaea Consulting Engineers, 1994. Study for the protection of Stypsi village from rockfalls.

Papathanassiou G., Valkaniotis S. and Chatzipetros A. 2010. Rockfall susceptibility zoning and evaluation of rockfall hazard at the foothill of Orliagas Mountain, Greece, in: Christofides et al. (eds), *Proc.of the XIX Congress of them Carpathian-Balkan Geological Association, Special Pub*., vol. 99, 165-171.

Papathanasiou G., Marinos V., Vogiatzis D. and Valkaniotis S. 2011. A rock fall analysis study in Parnassos area, Central Greece*, Proc. 2nd World Landslide Forum*, Rome.

Papazachos B.C. and Papazachou C. 1997. *The Earthquakes of Greece*, Editions ZITI, Thessaloniki, 304 pp.

Pavlides S. and Caputo. 2004. Tectonophysics Magnitude versus fault's surface parameters: quantitative relationships from the Aegean Region, *Tectonophysics*, 380, 3-4, 159-188.

Saroglou H., Marinos V., Marinos P. and Tsiambaos G. 2012. Rockfall hazard and risk assessment: an example from the high promontory at the historical site of Monemvasia, Greece, *Nat. Hazards and Earth System Science*, Volume 12, Issue 6, 1823-1836.

Saroglou H. 2012. Engineering geological behaviour of volcanic formations. References to instability phenomena and town planning in Lesvos Island, Greece, *Bulletin of the Geological Society of Greece*, vol. XXXXVI, 90-104

Sartori M., Baillifard F., Jaboyedoff M. and Rouiller J.-D. 2003. Kinematics of the 1991 Randa rockslides (Valais, Switzerland), *Natural Hazards and Earth System Sciences*, 3.

Sofianos A., Constantinidis C., Christodou-lias J. and Anagnostopoulos A. 1988. Rockfall analysis at the ancient region of Argos, in Engineering Geology of Ancient Works, Monuments and Historical Sites", Marinos and Koukis (eds.), pp. 213-216, Bal-kema.

Tsiambaos G. 2010. Report for rockfall protection in Taxiarches village, Lesvos (unpublished)

Velissariou 2008. Geological report in the rockfall event in Oksilithos, Kymi (unpublished)

Vogiatzis D., Dimitriou A., Papathanasiou G., Christaras B., Kantiranis N., Filippidis A. and Moraiti E. 2004. Rockfalls during the earthquake of 14/8/03 and probable solutions at the upper level of Drimonas village slope, Municipality of Sfakioton, Leukada Island, *Bulletin of the Geological Society of Greece*, vol. XXXVI, 1735-1742.

Δελτίο της Ελληνικής Γεωλογικής Εταιρίας, τομ. XLVII , 2013
Πρακτικά 13ου Διεθνούς Συνεδρίου, Χανιά, Σεπτ. 2013

Bulletin of the Geological Society of Greece, vol. XLVII 2013
Proceedings of the 13th International Congress, Chania, Sept. 2013

"GEO-CHARACTERIZATION" OF SELECTED AREAS IN CRETE, GREECE, TOWARDS REALISTIC ASSESSMENT OF SEISMIC DESIGN ACTIONS

Vafidis A.[1], Steiakakis M.[1], Agioutantis Z.[1], Andronikidis N.[1], Kritikakis G.[1], Economou N.[1], Pandi K.[1], Spanoudakis N.[1], Savvaidis A.[2], Margaris B.[2], Theodoulidis N.[2], Lekidis V.[2], Karakostas Ch.[2], Mangriotis M.-D.[2], Kalogeras I.[3], Koutrakis S.[3], Rozos D.[4], Loupasakis C.[4], Rondoyanni Th.[4], Tsangaratos P.[4], Dikmen U.[5], Papadopoulos N.[6], Sarris A.[6], Soupios P.[7], Kokkinou E.[7], Papadopoulos I.[7], Kouli M.[7] and Vallianatos F.[7]

[1] Technical University of Crete, Department of Mineral Resources Engineering, vafidis@mred.tuc.gr*
[2] Institute of Engineering Seismology and Earthquake Engineering (EPPO), Thessaloniki, Greece
[3] Geodynamic Institute, National Observatory of Athens, Greece
[4] Laboratory of Engineering Geology and Hydrogeology, Department of Geological Sciences, School of Mining and Metallurgical Engineering, National Technical University of Athens, Greece
[5]Department of Geophysics, Ankara University, Turkey
[6]Laboratory of Geophysical-Remote Sensing & Archaeoenvironment, Institute for Mediterranean Studies, Foundation for Research & Technology Hellas, Greece
[7]Laboratory of Geophysics and Seismology, Department of Natural Resources and Environment, Technological Educational Institute of Crete, Chania, Grete, Greece

Abstract

The geo-characterization of site conditions is crucial for the estimation of regional elastic spectra. The work to be done in the framework of the "GEO-CHARACTERIZATION" THALIS-project, will combine geotechnical and geophysical methods and evaluate them to estimate critical geotechnical parameters. Although geotechnical tests in lab may provide more accurate estimates of geotechnical parameters, they require costly and time consuming drilling procedures. On the other hand geophysical methods are useful in providing estimates in situ of subsurface physical properties, which are not directly related to geotechnical parameters. Within "GEO-CHARACTERIZATION" THALIS-project a pilot survey for geotechnical characterization at selected sites of Hellenic Accelerometric Network in Crete will be conducted by employing geotechnical, geological and geophysical techniques. Subsequently, by correlating "geo-data" collected within this project, relations of certain mechanical parameters obtained in laboratory or/and in situ with geophysical parameters for typical geologic formations and soils will be established. The "GEO-CHARACTERIZATION" project, will focus on the influence of dynamic loads on geotechnical phenomena related to the static stress field variation, the estimation of site effects due to seismic motion and the proposal of regional elastic spectra for seismic provisions as well as their comparison with the corresponding elastic design spectra of Eurocode 8 (EC8).
Key words: *Natural Hazards, Earthquake Risk, Eurocode 8, Regional Elastic Spectra, Crete.*

Περίληψη

Η ποσοτική εκτίμηση των χαρακτηριστικών παραμέτρων της ισχυρής εδαφικής κίνησης στους επιφανειακούς γεωλογικούς σχηματισμούς έχει ιδιαίτερη σημασία στην τεχνική σεισμολογία και την εδαφομηχανική. Στο έργο "GEO-CHARACTERIZATION" ΘΑΛΗΣ, μελετώνται οι γεωτεχνικές και γεωφυσικές τεχνικές ως μέθοδοι διερεύνησης των γεωτεχνικών παραμέτρων του υπεδάφους. Ενώ οι γεωτεχνικές δοκιμές παρέχουν με ακρίβεια τις γεωτεχνικές παραμέτρους, η κατασκευή των γεωτρήσεων και η εκτίμηση των γεωτεχνικών παραμέτρων, είναι ιδιαίτερα δαπανηρή, ασαφής και χρονοβόρα διαδικασία. Οι γεωφυσικές μέθοδοι είναι αποτελεσματικές στη διερεύνηση του υπεδάφους, αλλά τα αποτελέσματά τους δεν μπορούν άμεσα να μεταφραστούν σε μεταβολή των γεωτεχνικών παραμέτρων. Με σκοπό τη πληρέστερη μελέτη του υπεδάφους, σε σταθμούς επιταχυνσιογράφων του Ε.Δ.Ε. (Εθνικού Δικτύου Επιταχυνσιογράφων), θα εκτελεστούν συμπληρωματικές γεωτεχνικές και τεχνικογεωλογικές εργασίες ενώ ταυτόχρονα θα εκτελεστούν γεωφυσικές διασκοπήσεις. Το σύνολο των δεδομένων θα επιτρέψει τη συσχέτιση των φυσικομηχανικών παραμέτρων (από εργαστηριακές/επιτόπου δοκιμές) με τις γεωφυσικές παραμέτρους. Επιπλέον, τα δεδομένα αυτά θα επιτρέψουν τη διερεύνηση γεωτεχνικών προβλημάτων καθώς και την απόκριση των σχηματισμών που δομούν την περιοχή σε ενδεχόμενη δυναμική – σεισμική φόρτιση, ενώ θα προταθούν και τοπικά κανονικοποιημένα ελαστικά φασμάτα σχεδιασμού τα οποία θα συγκριθούν με τα αντίστοιχα φάσματα του Ευρωκόδικα 8 (EC8).

Λέξεις κλειδιά: *Φυσικές Καταστροφές, Σεισμικός Κίνδυνος, Ευροκώδικας 8, Τοπικά Ελαστικά Φάσματα Σχεδιασμού, Κρήτη.*

1. Introduction

The estimation of the strong motion parameters for the shallow geological formations is essential for engineering seismology and soil mechanics. There is a plethora of studies which verify the correlation between site conditions and earthquake damages (Borcherdt, 1970; Bouckovalas et al, 1996; Atakan et al., 1997; Raptakis et al., 2005; Marka et al., 2005; Improta et al., 2005; Tyagunov et al., 2006; Lombardo et al., 2006; Rayhani et al., 2008; Razaei et al., 2009).

Wills et al. (2000) utilized the weighted velocity $V_{S,30}$ for the soil formations classification in California (USA), based on the U.B.C., while Kanli et al. (2006) classified soil formations based on the EC8 at Dinar, SW of Turkey. Carvalho et al. (2009) applied the seismic refraction method for both the characterization of soil formations (based on EC8) and the estimation of the Poisson ratio in the framework of a micro-zonation study at Western Portugal. Theodulidis et al. (2006) used stochastic methods for the calculation of synthetic accelerometer records for the 1978 Thessaloniki seismic event, based on geotechnical, geophysical and geological data.

Grasso and Maugeri (2009) performed seismic risk analysis in Catagnia (Italy) using seismicity (Barbano and Rigano, 2001), geological and geophysical studies (Cavallaro et al., 2006, Trovato et al., 2003, Beranzoli and Favali, 2005) as well as soil behavior studies of seismic loads (Grasso et al., 2005). Anagnostopoulos et al. (2008) created a GIS platform for the estimation of possible damages in Chania, Crete-Greece. This study involved spectral analysis of surface waves for the characterization of the site effects.

Pitilakis et al. (1992) utilized geophysical and lab measurements (e.g. triaxial compression tests on typical soil samples), in order to determine the Young's modulus. Raptakis et al. (1995) correlated the velocity V_S with in situ geotechnical parameters (SPR) for representative soils in Greece. Cicinioglou et al. (2007) used empirical relations for the seismic risk analysis in Instanbul, taking into consideration both the strong ground motion of shallow formations and the degradation (i.e. liquefaction) of formations subjected to seismic loads. In order to achieve this they calculated the Liquefaction Potential Index (LPI) (Iwasaki et al., 1978). For the estimation of the bearing capacity they utilized assumptions proposed by Richards et al. (1993). Inci (2002) studied the

influence of argillaceous soils water saturation on the maximum shear modulus (G_{max}) and Poisson ratio (ν). They utilized ultrasonics and compared their results with the empirical relations derived by Hardin and Black (1968).

Turesson (2007) compared the shear modulus derived by geophysical measurements (the seismic refraction method and the multi-channel surface wave analysis (MASW) method) with the corresponding modulus calculated by the empirical relation which was proposed by Hardin and Black (1968) and was modified by Higuchi et al. (1981). A lot of effort has been put also for the correlation of the seismic parameters of rocks with their mechanical behavior (Sjörgen et al., 1979, McCann et al., 1990, Isik et al., 2008). El-Naqa (1996) estimated the indices RMR, Q και RQD, from velocity of P and S waves, using empirical relations (Sjörgen et al., 1979). Finally, Tezcan et al. (2006) correlated P and S waves velocity with the specific weight and the bearing capacity of the subsurface.

The ***"GEO-CHARACTERIZATION" THALIS-project*** focuses on: a) the influence of dynamic loads on geotechnical phenomena related to the static stress field variation, b) the estimation of the site effects due to seismic motion and c) the proposal of regional elastic spectra for seismic provisions as well as their comparison with the corresponding Greek Seismic Code (GSC2000) and Eurocode 8 (EC8) elastic design spectra.

The specific study employs survey technologies based on geophysical and geotechnical methods as well as intensity and spectral characteristics of seismic motion. This study aims at the improvement of construction safety by determining representative earthquake spectral characteristics in Crete. More specifically, updating the elastic design spectra of the existing GSC2000 and Eurocode EC8, should lead to increased seismic safety through efficient and representative construction planning actions in southern Aegean area.

2. Methodology

The ***"GEO-CHARACTERIZATION" THALIS-project*** involves the following investigations in Crete:

- Selection of stations from the Hellenic Accelerometric Network (HAN) in Crete.
- Complementary geotechnical and engineering geology field work and lab tests.
- Geophysical survey.
- Correlation of physico-mechanical parameters with geophysical parameters.
- Regional elastic spectra for seismic provisions.

2.1. Complementary Geotechnical Engineering Geology Field Work and Lab Tests

This field work involves new geotechnical investigation and borehole drilling at the selected strong motion sites of HAN including engineering geological mapping and neotectonic study of the wider area, in situ tests (SPT, downhole etc) within the boreholes as well as high quality sampling at selected horizons not only from boreholes, but also from open pits and slopes. This field work complements existing geotechnical and engineering geological data in the literature and other available resources such as geotechnical companies and administrative authorities. Thus, the outcome of this investigation is detailed geological-geotechnical mapping of the area around selected HAN sites in Crete including tectonic and neotectonic data.

Laboratory tests on representative soil samples involve grain size analysis, Attenberg limits determination, moisture content, density, porosity, permeability tests, CUPP-triaxial compression tests. On the rock samples, lab tests provide estimates of moisture content, density and porosity, Young's (elastic) modulus (E) and Poisson ratio (ν), (axial compression and ultrasonics tests). All

the above mentioned tests follow the Technical Specifications E105-86 and ASTM. The mechanical parameters estimated by the lab tests will be subsequently correlated with the physical parameters deduced from the geophysical survey.

2.2. Geophysical Survey

After the geological/engineering investigation, a geophysical survey will be carried out. The geophysical survey consists of survey design, data acquisition and processing as well as combined interpretation for the geotechnical characterization of the soil formations. Survey design involves the selection of the proper geophysical techniques for imaging the subsurface and tests for the optimum survey parameters estimation. S-wave techniques using one (VSP) or more boreholes (cross-hole tomography) provide the most reliable V_S estimates, but their cost is high. The geo-characterization using borehole samples and geophysical measurements in boreholes, is extended using surface geophysical methods, such as seismic refraction and multichannel analysis of surface waves including microtremor spectral analysis of surface waves. The seismic methods will provide: (a) Detailed two-dimensional velocity (P and S) models, (b) Attenuation models (Q factor), (c) Mechanical characteristics of the bedrock.

Electrical methods are non-destructive high resolution methods, which are widely used in complex problems of geotechnical engineering. The development of modern multi-channel geophysical instruments for the automated and rapid acquisition permits a realistic subsurface imaging. All the above, make electrical methods and especially electrical tomography the most emerging methods in geotechnical geophysics. The application of electrical/electromagnetic methods including Vertical electrical sounding – (VES) and Transient electromagnetics (TEM) will provide: (a) Detailed two-dimensional electrical resistivity model, (b) Morphological characteristics of the bedrock, (c) Images of the fractured and water saturated zones.

2.3. Correlation of Physico-mechanical Properties with Geophysical Parameters

Although geophysical methods image the subsurface very effectively, most of the estimated physical parameters (such as electrical resistivity) cannot be explicitly related to geotechnical parameters because of the lack of relevant theoretical equations. Cross plots appropriate for certain lithologies are employed for the geotechnical characterization of the subsurface.

Existing empirical relations concerning soil formations will be initially, tested and modified for the soils under investigation. These empirical equations relate seismic velocity (V_P and V_S) and/or electrical resistivity with geotechnical parameters such as mechanical properties, porosity, moisture content, sand and clay percentage. Empirical equations for specific lithotypes are useful for the low cost and safe geo-characterization which employs high quality geophysical images as well as borehole and lab data. The ***"GEO-CHARACTERIZATION" THALIS-project*** will establish equations correlating mechanical and geophysical parameters deduced from geotechnical and geophysical investigations. Following the crossplots development and the assessment of the corresponding empirical equations, these equations will be employed for the geotechnical interpretation of geophysical sections.

Classification methods are an emerging technology concerning interpretation of seismic and electrical data. Still, the ads and pros of each classification method are not clearly specified. In general, one can employ automated or user defined classification methods. Automated classification methods are data dependent, while the latter classification methods require additional information (e.g. borehole data). Each geophysical method produces values (velocity, electrical resistivity etc) of soil properties, which define a multi dimensional vector. Every vector can be imaged on a scatter plot. Proximity of points on such a scatter plot corresponds to similar characteristics. Classification techniques control the organization of points in a multi dimensional scatter plot, searching for populations of points with similar measurements combination. These techniques differ from each other in the way they organize each population.

In this project algorithms of K-means and neural networks (SOM-Self Organizing Maps) will classify geophysical and geotechnical data. The above mentioned methods of classification will be assessed, regarding their use for the geotechnical interpretation of geophysical sections.

2.4. Regional Elastic Spectra

Site effects may drastically increase seismic hazard level and their assessment becomes a major concern in seismic risk mitigation. The most reliable methods for site effect estimation follow either an experimental or a theoretical approach: (i) The former approach, compares the spectral contents of the earthquake recordings obtained at the site of interest with a corresponding obtained at a nearby rock station called as reference site and (ii) The latter approach provides ground motion prediction based on a geophysical model of the site.

The European and American seismic codes regulation (EC8 and National Earthquake Hazards Reduction Program - NEHRP) employs a simple site classification based on time-averaged velocity of the first 30 m, $V_{S,30}$. The simplicity of this site classification and the relatively low cost of the background site survey made the $V_{S,30}$-based approach very popular, in particular because there is no alternative method which combines cost, simplicity, and physical relevance to the underlying phenomena. For seismic action estimation according to EC8 one has to characterize site conditions and suitably estimate soil amplification and corresponding peak ground motion for the site. Seismic provisions usually offer average design values covering nationwide needs. Variation in seismotectonic environment may significantly affect spectral content of ground motion resulting in turn to elastic design spectra that differ from corresponding seismic provisions' values. Thus, it becomes mandatory to investigate and test seismic code design spectral values over regions exhibiting a specific seismotectonic environment by employing either actual regional seismic recordings or/and new results from improved geophysical/geotechnical approaches for site characterization.

The ***"GEO-CHARACTERIZATION" THALIS-project*** will conduct a theoretical and experimental evaluation of the site effects in order to categorize selected HAN stations on Crete according to Eurocode 8. More specifically, using recorded ground motion data from intermediate depth events in Crete and surrounding area, the corresponding elastic response spectrum will be calculated for selected sites. These values are compared with those defined for the corresponding EC8 design spectrum for the seismic zone comprising the island of Crete.

The final outcome of this work is the proposal of regional normalized elastic spectra for seismic design of structures and urban development planning. By comparing them with Eurocode provisions we will pinpoint differences that could be taken into account for improving seismic design actions in southern Aegean area.

This project involves the creation of a database containing geophysical and geotechnical data as well as seismic event records from HAN sites. Intermediate depth seismic events will be highlighted due to their relation with the African plate and extended damages on Crete. If there is a lack of relevant seismic events, a simulation for similar seismotectonic environments will be implemented utilizing seismotectonic models of the south Aegean arc. Finally, this database will include additional information (pictures, construction sections, seismic vulnerability reports) of the buildings hosting the accelerometers of HAN.

3. Expected Results

The specific study will provide: (a) survey technologies based on geophysical and geotechnical methods, (b) new or upgraded equations relating physico-mechanical properties and the parameters estimated by geophysical investigation, (c) assessment of neural networks in the classification of geophysical and geotechnical parameters, d) theoretical and experimental estimation of the site effects at HAN sites on Crete, (e) database, (f) normalized elastic spectra for construction planning and comparison with the GSC2000 and EC8 and (g) webpage.

Summarizing, end-users may obtain data and technology for rapid and cost-effective high-resolution non-invasive evaluation of seismic risk.

Main target groups are public administration, the construction companies at national level and all construction engineers in Crete. Their benefits are in:

- Construction planning with improved seismic safety and
- soil characterization with reduced cost, as there is also a reduction of the number of boreholes needed

The ***"GEO-CHARACTERIZATION" THALIS-project*** leads to the establishment of a multi-disciplinary research group, whose main interest is the geo-characterization of selected sites on Crete using integrated geophysical and geotechnical methods. Similar studies, for the derivation of normalized elastic spectra are necessary at other earthquake prone regions in Greece. The members of this research group plan to continue their collaboration on the specific topic by carrying out such studies.

The effective dissemination of results will be achieved through the following levels:

- Presentations at conferences: The project includes a commitment to disseminate via presentations at conferences by academic partners.
- Scientific publications: The university participants are free to publish their results in open literature.
- Education: scientific knowledge will be disseminated within the involved Universities through research, education and training.
- Website: A website will be created, which will include the new technology created, application examples of the proposed methodology and restricted access of the end-users to the database of the project.
- Technological: Improvement of the services that the university and research institute laboratories can offer to the public administration and to private organizations operating in the construction and services sectors. The latter organizations can efficiently use the results in new constructions and re-evaluation of seismic safety of existing structures.
- Administration: dissemination at national and regional level of knowledge on safe and effective methods for assessment of seismic risk. This might have an important impact on new local and national regulations for seismic safety and urban land management.

4. Acknowledgements

This research has been financed by Greek national funds through the Operational Program "Education and Lifelong Learning" of the National Strategic Reference Framework (NSRF) - Research Funding Program: THALES. Investing in knowledge society through the European Social Fund.

5. References

Anagnostopoulos S., Providakis C., Salvaneschi P., Athanasopoulos G. and Bonacina G. 2008. SEISMOCARE: An efficient GIS tool for scenario-type investigations of seismic risk of existing cities, *Soil Dynamics and Earthquake Engineering*, Vol. 28, p. 73 – 84.

Atakan K., Brandsdottir B., Halldorsson P. and Fridleifsson G.O. 1997. Site response as a function of near-surface geology in the South Iceland seismic zone, *Natural Hazards*, Vol. 15 (2–3), 139 – 164.

Barbano M.S. and Rigano R. 2001. Earthquake sources and seismic hazard in south-eastern Sicily, *Annali di Geofisica*, Vol. 44 (4), 723 - 738.

Beranzoli L. and Favali P. 2005. SN-1—the first Italian seafloor observatory for seismic monitoring, in: Maugeri, M., (editor). Seismic prevention of damage: a case study in a Mediterranean city, Southampton, *WIT Press*, 367 – 376.

Borcherdt R D. 1970. Effects of local geology on ground motion near San Francisco Bay, *Bulletin of Seismological Society of America*, Vol. 60, 29 – 61.

Bouckovalas G., Anagnostopoulos A., Kapenis A. and Karantoni T. 1996. Analysis of soil effects and distribution of damage from the Pyrgos 1993 (Greece) earthquake, *Geotech. Geolog. Eng.* (Historical Archive), Vol. 14 (2), 111 – 128.

Carvalho J., Torres L., Castro R., Dias R. and Mendes-Victor L. 2009. Seismic velocities and geotechnical data applied to the soil microzoning of western Algarve, Portugal, *Journal of Applied Geophysics*, Vol. 68, 249 – 258.

Cavallaro A., Grasso S. and Maugeri M. 2006. Clay soil characterization by the new seismic dilatometer marchetti test (SDMT), *Proceedings of the second international conference on the flat dilatometer,* Washington; April 2 – 5, 2006.

Cinicioglu S.F., Bozbey I., Oztoprak S. and Kelesoglu M.K. 2007. An integrated earthquake damage assessment methodology and its application for two districts in Istanbul, Turkey, *Engineering Geology*, Vol. 94, 145 – 165.

El-Naqa A. 1996. Assessment of geomechanical characterization of a rock mass seismic geophysical technique, *Geotechnical and Geological Engineering*, Vol. 14, 291 – 305.

Grasso S., Laurenzano G., Maugeri M. and Priolo E. 2005. Seismic response in Catania by different methodologies, in: Maugeri, M., (editor). Seismic prevention of damage: a case study in a Mediterranean city. Southampton: WIT Press, 63 – 79.

Grasso S. and Maugeri M. 2009. The seismic microzonation of the city of Catania (Italy) for the maximum expected scenario earthquake of January 11, 1693, *Soil Dynamics and Earthquake Engineering*, Vol. 29, 953 – 962.

Hardin B.O. and Black W.L. 1968. Vibration modulus of normally consolidated clay, *Journal of the Soil Mechanic and Foundations Division*, ASCE, Vol. 94, 353 – 368.

Higuchi Y., Umehara Y. and Ohneda H. 1981. Evaluation of dynamic properties of the sand deposits under deep sea bed*, Proceedings of the 36th Annual Convention of the Japanese Society of Civil Engineering*, Vol. 3, 50 – 51.

Improta L., Di Giulio G., and Rovelli A. 2005. Variations of local seismic response in Benevento (Southern Italy) using earthquakes and ambient noise recordings, *Seismology*, Vol. 9 (2), 191 – 210.

Inci G. 2002. Small-strain elastic response of compacted clayey soils during drying – an empirical approach, Proceedings of SAGEEP, pp. 15.

Isik S. N., Doyuran V. and Ulusay R. 2008. Assessment of deformation modulus of weak rock masses from pressuremeter tests and seismic surveys, *Bull. Eng. Geol. Environ.*, Vol. 67, 293 – 304.

Iwasaki T., Tatsuoka F. and Takagi Y. 1978. Shear Moduli of Sands Under Cyclic Torsional Shear Loading. *Soils and Foundations*, Japanese Society of Soil Mechanics and Foundation Engineering, Vol. 18, (1), 39 – 56.

Kanli A.I., Tildy P., Pronay Z., Pinar A. and Hermann L. 2006. $Vs_{,30}$ mapping and soil classification for seismic site effect evaluation in Dinar region, SW Turkey, *Geophysical Journal International*, Vol. 165, 223 – 235.

Lombardo G., Langer H., Gresta S., Rigano R., Monaco C. and Deguidi G. 2006. On the importance of geolithological features for the estimate of the site response: the case of Catania Metropolitan area (Italy), *Natural Hazards*, Vol. 38, 339 – 354

Marka K., Chavez-Garcia F.J., Raptakis D.G. and Pitilakis K.D. 2005. Parametric analysis of the seismic response of a 2D sedimentary valley: implications for code implementations of complex site effects, *Soil Dyn. Earthqu. Eng.*, Vol. 25 (4), 303 – 315.

McCann D.M. Culshaw M.G. and Northmore K. 1990. Rock mass assessments from seismic measurements, in Field Testing in Engineering Geology, Bell, F.G., Culshaw, M.G., Cripps, J.C. and Coeffy, J.R. (eds), Engineering Special Publication No. 6, Geological Society, London, 257 - 266.

Pitilakis D.K., Anastassiadis A. and Raptakis D. 1992. Field and laboratory determination of dynamic properties of natural soil deposits, Earthquake Engineering, Tenth World Conference, Balkema, Rotterdam, 1275 - 1280.

Raptakis G.D., Manakou V.M., Chavez-Garcia J.F., Makra A.K. and Pitilakis D.K. 2005. 3D configuration of Mygdonian basin and preliminary estimate of site response, *Soil Dyn. Earthqu. Eng.*, Vol. 25, 871 – 887.

Raptakis G.D., Anastassiadis J.A., Pitilakis D.K. and Lontzetidis S.K. 1995. Shear wave velocities and damping of Greek natural soils, *10th European Conference on Earthquake Engineering, Balkema*, Rotterdam, 477 - 1280.

Rayhani M.H.T., El Naggar M.H. and Tabatabi S.H. 2008. Nonlinear analysis of local site effects on seismic ground response in the Bam earthquake, *Geotech. Geolog. Eng.*, Vol. 21 (1), 91 – 100.

Rezaei K., Guest B., Friedrich A., Fayazi F., Nakhaei M., Aghda F. and Beitollahi A. 2009. Soil and sediment quality and composition as factors in the distribution of damage at the December 26, 2003, Bam area earthquake in SE Iran (Ms=6.6), *Journal of Soils Sediments*, Vol. 9, 23 – 32.

Richards R., Elms D.G., Budhu M. 1993. Seismic bearing capacity and settlements of foundations, *Journal of Geotechnical Engineering*, Vol. 119 (4), 662 – 674.

Sjörgen B., Ofsthus A., and Sandberg J. 1979. Seismic classification of rock mass quality, *Geophysical Prospecting*, Vol. 27, 409 – 442.

Tezcan S.S., Keceli A. and Ozdemir Z., 2006. Allowable bearing capacity of shallow foundations based on shear wave velocity, *Geotechnical and Geological Engineering*, Vol. 24 03 – 218.

Theodulidis N., Roumelioti Z., Panou A., Savaidis A., Kiratzi A., Grigoriadis V., Dimitriu P. and Chatzigogos Th. 2006. Retrospective Prediction of Macroseismic Intensities Using Strong Ground Motion Simulation: The Case of the 1978 Thessaloniki (Greece) Earthquake (M6.5), *Bulletin of Earthquake Engineering*, Vol. 4, 101 – 130.

Trovato C., Vinciguerra S. and Imme G., 2003, Laboratory measurements of seismic velocities on rocks from Etna region (Italy), *European Geophysical Society*, Nice 2003, Vol. 1, 78 – 80.

Turesson A. 2007. A comparison of methods for the analysis of compressional, shear and surface wave seismic data and determination of the shear modulus, *Journal of Applied Geophysics*, Vol. 61, 83 – 91.

Tyagunov S., Hollnack D. and Wenzel F. 2006. Engineering–seismological analysis of site effects in the area of Cologne, *Natural Hazards*, Vol. 38, 199 – 214.

Wills J.C., Petersen M., Bryant W.A., Reichle M., Saucedo G.J., Tan S., Taylor G. and Treiman J. 2000. A Site Condition Map for California Based on Geology and Shear Wave Velocity, *Bull. Seism. Soc. Am.*, Vol. 90 (6B), 187 – 208.

Δελτίο της Ελληνικής Γεωλογικής Εταιρίας, τομ. XLVII , 2013
Πρακτικά 13ου Διεθνούς Συνεδρίου, Χανιά, Σεπτ. 2013

Bulletin of the Geological Society of Greece, vol. XLVII 2013
Proceedings of the 13th International Congress, Chania, Sept. 2013

NATURAL AND HUMAN HAZARD ASSESSMENT OF THE ARCHAEOLOGICAL SITES OF PAPHOS AREA (CYPRUS) WITH THE USE OF REMOTE SENSING AND GIS

Alexakis D. D.[1], Agapiou A.[2], Themistocleous K.[1], Lysandrou V.[2], Sarris A.[3] and Hadjimitsis D.G.[1]

[1] Department of Civil Engineering and Geomatics, Remote Sensing and Geo-environment Lab, School of Engineering and Technology, Cyprus University of Technology,2-8 Saripolou Str., Lemesos, Cyprus

dimitrios.alexakis@cut.ac.cy, athos.agapiou@cut.ac.cy, kt33@cytanet.com.cy, d.hadjimitsis@cut.ac.cy

[2] Museum of Kykkos, Cyprus, vaslysandrou@yahoo.it

[3]Institute for Mediterranean Studies, Foundation for Research and Technology - Hellas (FORTH) asaris@ret.forthnet.gr

Abstract

The study focuses on the creation of an innovative methodology for the development of a risk assessment model for the archaeological sites of western Cyprus (Paphos district). On site observation is the most common way for monitoring cultural heritage sites and monuments in Cyprus. However, this procedure which includes data collection, periodical observations, and multivariate risk assessment analysis, is practically difficult to be accomplished with the traditional practices and methods since it is time consuming and cost insufficient. Thus, the use of modern technologies such as Remote Sensing and GIS is anticipated to provide a tool of directives for the protection and preservation of cultural heritage sites from anthropogenic and environmental threats. These technologies provide to scientists integrated monitoring capabilities and have the unique advantage to store and manipulate a large amount of spatial and attribute data simultaneously. This study aims to integrate both satellite remote sensing techniques and GIS in a multidisciplinary approach, for monitoring natural and anthropogenic hazards with the use of archived and up-to-dated multi-temporal remotely sensed images in the study area, namely in areas nearby cultural heritage sites and monuments in Paphos area (Cyprus).According to the results, extensive construction and building development has taken placein the broader area. It was also proved that vast number of sites is established on areas prone to erosion and landslide phenomena

Key words: *Erosion, Landslides, Cultural Heritage, Urban Sprawl.*

Περίληψη

Η συγκεκριμένη εργασία εστιάζει στη χρήση σύγχρονων τεχνολογιών όπως είναι η Δορυφορική Τηλεπισκόπηση και τα Γεωγραφικά Συστήματα Πληροφοριών για τη δημιουργία ενός ολοκληρωμένου συστήματος εκτίμησης επικινδυνότητας αρχαιολογικών θέσεων και κατάλοιπων στη Κύπρο και συγκεκριμένα στην επαρχία

Πάφου. Τέτοιου είδους αναλύσεις οι οποίες περιλαμβάνουν συλλογή δεδομένων, συνεχείς παρατηρήσεις και πολυπαραμετρικές αναλύσεις εκτίμησης κινδύνου είναι δύσκολο να πραγματοποιηθούν με τις παραδοσιακές τεχνικές και μεθόδους, οι οποίες κοστίζουν και είναι χρονοβόρες. Οι σύγχρονες τεχνολογίες δίνουν τη δυνατότητα στους επιστήμονες για την συνολική επόπτευση της περιοχής μελέτης καθώς επίσης και το μοναδικό πλεονέκτημα της ταυτόχρονης αποθήκευσης κα διαχείρισης μεγάλου όγκου χωρικών και περιγραφικών δεδομένων που σχετίζονται με την διαχείριση και προστασία της πολιτιστικής κληρονομιάς. Αυτό το στόχο εξυπηρετεί και η συγκεκριμένη μελέτη που φιλοδοξεί να αναδείξει τις δυνατότητες που προσφέρει η χρήση δεδομένων δορυφορικής Τηλεπισκόπησης και ΓΣΠ για την προστασία της πολιτιστικής κληρονομιάς της ευρύτερης περιοχής της επαρχίας Πάφου στη Κύπρο από ανθρωπογενείς και φυσικούς κινδύνους.
Λέξεις κλειδιά: *Διάβρωση, Κατολισθήσεις, Πολιτιστική κληρονομιά, Άναρχη δόμηση.*

1. Introduction

Nowadays it has become obvious that in situ conservation of the archaeological heritage is endangered by different environmental and human factors such as landfills, erosion and urban sprawl (Carlon *et al*, 2002). Environmental, climatic changes and forces of nature, coupled with the anthropogenic interventions, increase the decay of archaeological remains. Both, the severe damages that most of these sites have suffered in the past and the accelerating pace of urban expansion within the last few decades, have made the protection of cultural heritage sites an essential task. Satellite remote sensing and Geographical Information Systems (GIS) can be employed to combine several different environmental and anthropogenic factors in order to proceed to the construction of a risk assessment model that could hierarchically classify an area of interest to different risk zones (Sarris, 2002; Alexakis *et al.,* 2012; Agapiou *et al.,* 2012; Themistocleous *et al.,* 2012; Hadjimitsis *et al.,* 2012). The use of GIS provides an effective methodology for an integrated analysis based on spatial information and the intrinsic and external parameters of a future instability (Canuti *et al,* 2000).

2. Study Area and Data

2.1. Study Area

The Paphos district is located in the SW part of Cyprus (Figure 1a). Several important monuments such as the *Nea Paphos* and the *Tombs of the Kings* archaeological sites, listed by UNESCO as World Heritage Monuments, are found in the broader area (Figure 2a). Paphos District was selected as the study area, since it combines both World Heritage Monuments, but in the same time one can find isolated monuments in the most in-accessible sites. Moreover monuments and sites in Paphos can be found both in urban and rural areas, near and far from the coastlines, in forest, or in industrial zones etc (Figure 1b). The urban sprawl pheromenon and the erosion hazard vulnerability were studied for all Paphos district. Concerning landslides hazard, the study area is located in the eastern part of Paphos district in the broader area of *Statos* and *Ayios Photios* villages, an area of 1393 km^2 in extent, historically vulnerable to such kind of phenomena (Figure 5a).

2.2. Data

For the study the following data were used and incorporated to GIS environment:

- 4 multispectral Landsat 5 TM, Landsat 7 ETM+ and Quickbird images. Specifically:
    1. 1990-08-04 / Landsat 5- TM

2. 2000-09-24 / Landsat 7 – ETM+

3. 2010-08-27 / Landsat 5 –TM

4. A panshαpened Quickbird image (0.6 m resolution – VIS, NIR part of spectrum) of 2010.

● A Digital Elevation Model (DEM) of 25m pixel size was used to generate geomorphologic parameters (slope, aspect and drainage network).

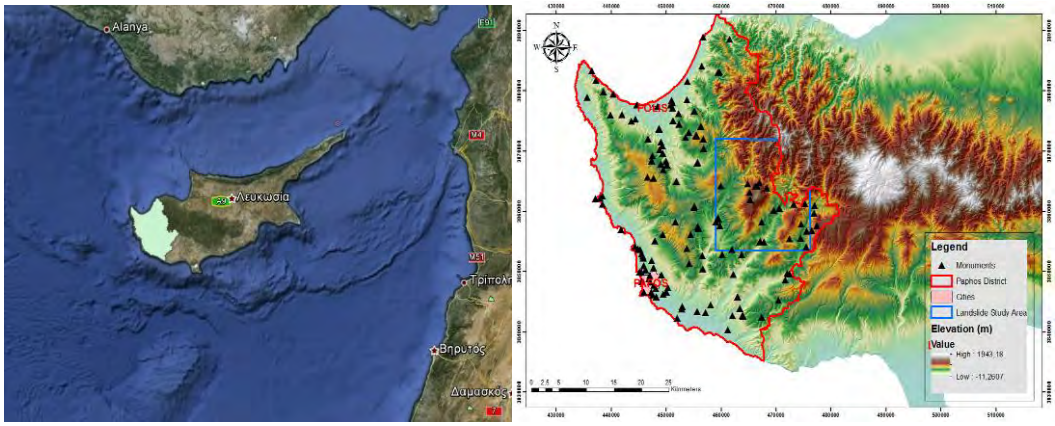

Figure 1 - Island of Cyprus (a). Study area (b).

3. Methodology

In order to map all known sites and monuments of Paphos District the necessary raw data from the Department of Antiquities of Cyprus were used. The authors explored the database of the «Cyprus Archaeological Digitization Programme», while at the same time all known sites were mapped using a customized GIS geodatabase. In total more than 170 monuments and sites exist in Paphos District (Figure 2b).

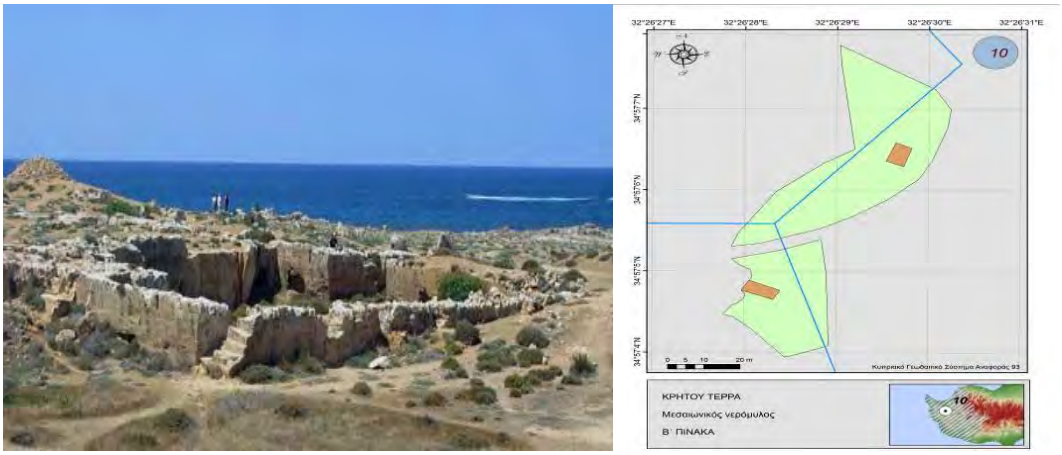

Figure 2 – *Nea Paphos* archaeological site (a). Digitization of cadastral maps in GIS environment (b).

After the construction of the archaeological database the research team proceeded to the natural and human risk assessment of Paphos archaeological sites in a threefold way: a) Evaluation of urban sprawl phenomenon and its impact to the archaeological sites, b) Estimation of erosion

hazard potential in the whole Paphos district c) Landslide hazard assessment in the eastern part of Paphos district.

For the urban sprawl phenomenon, besides the SVM classification algorithm, the Stohastic Markov Chain model was also applied in order to predict urban expansion tendency for 2020. The Markov chain equation was constructed using the land cover distributions at the beginning (Mt) and at the end (Mt+1) of a discrete time period as well as a transition matrix (MLc) representing the land cover changes that occurred during that period. The transition probability matrix records the probability that each land cover category will change to every other category. The extracted land use map of 2020 was added to the landslide hazard model of 2020. In addition AHP (Analytical Hierarchical Process) was applied to develop the landslide model. The AHP is a flexible way o f analyzing complicated and multi criteria problems. According to the specific methodology the final weight of significance for each factor can be defined using the eigen-vectors of a square reciprocal matrix of pairwise comparisons between the different factors.

Concerning satellite images preprocessing steps, geometric corrections were carried out using standard techniques with several ground control points (GCP's) and a second order polynomial fit. Following, atmospheric corrections were applied to satellite images. As it is shown by several studies (Hadjimitsis *et al.,* 2004) darkest pixel (DP) atmospheric correction methodology can be easily applied either by using dark targets located in the image or by conducting in situ spectroradiometric measurements.

4. Urban Sprawl Phenomenon

Initially several classification algorithms were applied to multitemporal Landsat TM images. Maximum likelihood, ISODATA, Nearest neighbour, SAM as well as SVM algorithms were implemented with the SVM algorithm to be proved to be the more accurate (Kappa coefficient accuracy ranges from 88-95%). As Heumann (2011) argues, SVM can be used for remote sensing applications, for classification of either multispectral or hyperspectral data, in which spectral separability is less than perfect. The basic difference of SVM comparedto other classifiers, is the fact that SVM aims to identify the boundary between classes in n-dimensional spectral-space rather that assigning points to a class based on mean values.

For that purpose classification analysis was applied to the images of 1984, 2000 and 2010. The Landsat dataset was classified into four main land cover types (built up areas; water bodies; vegetation and land) for all the three images. The classification results were examined in order to evaluate the urban expansion in the vicinity of the cultural heritage sites of Paphos (Figure 3a). A buffer zone of 500m around each monument was isolated and the percentage of each main land use class was calculated. The results indicated that the urban land cover in the vicinity of cultural heritage sites is increased during the period 1984 -2010. Specifically, urban expansion has been increased by 350% during the last 35 years. For the period 1984 until 2010, the new built up areas were found mainly in previous land classified areas (70%) while other built up areas have replaced vegetation land cover (15%). These land use change corresponds to approximately 51 km^2 and 9 km^2 for land and vegetation coverage respectively.

As it was proved a dramatic expansion was made especially during the last 10 years (2000-2010) in this region. Based on the results of SVM classification algorithm for 2000 and 2010 and with the use of Markov chain mode, an attempt was also made for the prediction of urban areas 2020. As it was proved (Figure 3b), the urban sprawl phenomenon will continue to expand and therefore the Paphos District archaeological sites and monuments will continue to suffer from the urban pressure.

4.1. RUSLE Methodology

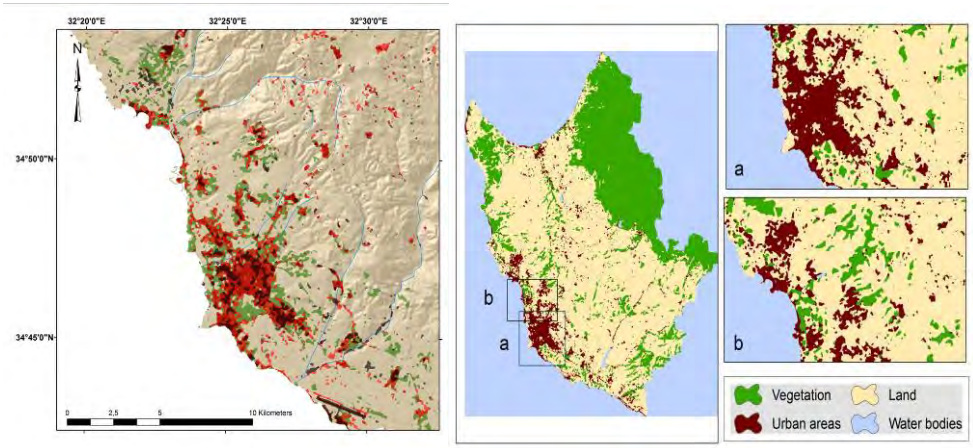

Figure 3 - Urban expansion of the Paphos city from 1984 to 2010. Black colour indicate urban areas back in 1984; orange colour the urban areas of 1990; red colour the urban areas of 2000 and green colour the urban areas of 2010 (a). Built up areas in red as calculated from the Markov model for 2020 (b).

Equation 1 –RUSLE equation

$$A = R * K * L * S * P$$

where A is the soil loss in t ha^{-1} year^{-1} ; K is the soil erodibility factor (t ha h ha^{-1}MJ^{-1} mm^{-1}), R is the rainfall – runoff erosivity factor in MJ mm ha^{-1} h^{-1} year^{-1} ; S is the slope steepness factor; P is the conservation practices factor r; L is the slope length factor and C is the cover and management factor.

4.1.1. Rainfall (R) Factor

The rainfall R factor is a measure of the erosive force of a specific rainfall**.** The Modified Fournier Index (MFI) is well correlated with the rainfall erosivity. The specific index is considered as an eff ective estimator of R factor because it takes into account the rainfall seasonal distribution. For the calculation of the R factor with the use of the Modified Fournier Index (MFI), two different approa ches were used (Equation 2).

Equation 2 – R factor

$$R_1 = 0.6120 * MFI^{1.56}$$

$$R_2 = 0.264 * MFI^{1.50}$$

The MFI was applied to take into account the monthly rainfall distribution during each year for a period of 20 years.

Equation 3 – R factor Regression Analysis

$$\text{MFI} = \sum_{J=1}^{N} \frac{Faj}{N} = \frac{1}{N} \sum_{j=1}^{N} \sum_{i=1}^{12} \frac{pij^2}{pj}$$

Where, p_{ij} is the rainfall depth in month / (mm) of the year j and P is the total rainfall for the same year. Then, the R factor was estimated for both equations (Equation 2) and its mean value was

finally calculated. After the calculation of the *R* factor for the area's rain-gauge stations, a continue surface was produced using the point data of the stations and the Kriging interpolation method in GIS (Figure 4a).

4.1.2. Soil Erodibility Factor (K)

The soil erodibility factor (*K*) refers to the average long-term soil and soil profile response to the erosive power associated with rainfall and runoff.

It is also considered to represent the rate of soil loss per unit of rainfall erosion index for a specific soil. A digital soil map of the study area was used and the main soil formations were categorized to 5 different major classes: coarse sandy loam, sandy loam and silty clay. According to Karydas et al., (2009) and Prasannakumar et al., (2011), the estimated *K* values of the textural groups vary from 0.15 t ha h ha^{-1} MJ^{-1} mm^{-1} for sandy loam - loam, 0.15 t ha h ha^{-1} MJ^{-1} mm^{-1} for clay loam-loam, 0.07 t ha h ha^{-1} MJ^{-1} mm^{-1} for coarse sandy loam, 0.13 t ha h ha^{-1} MJ^{-1} mm^{-1} for sandy loam and 0.26 t ha h ha^{-1} MJ^{-1} mm^{-1} for silty clay (Figure 4b).

4.1.3. Topographic Factor (LS)

The topographic factor is related to the slope steepness factor (*S*) and slope length factor (*L*) and is considered to be a crucial factor for the quantification of erosion due to surface run – off. The com bined *LS* factor was calculated by means of ArcGIS spatial analyst and Hydrotools extension librar y. In this study the equation 4 was adopted..

Equation 4 – LS factor

$$LS = \left(\frac{[FlowAccumulation * Cellsize]}{22.13} \right)^{0.4} * \left(\frac{\sin slope}{0.0896} \right)^{1.3}$$

4.1.4. Practice Factor (P)

Practice factor (*P*) is defined as the ratio of soil loss after a specific support practice to the corresponding soil loss after up and down cultivation. In order to delineate areas with terracing practices the Quickbird satellite images were used and the delineation was accomplished in GIS environment with extensive monitoring of the study area. Areas with no support practice were assigned with a *P* factor equal to 1. On the other hand the terrace areas which are considered to be less prone to erosion were assigned a 0.55 value according to expert's opinion (Figure 4c).

4.1.5. Cover Management Factor (C)

C factor represents the effect of soil-disturbing activities, plants, crop sequence and productivity le vel, soil cover and subsurface bio-mass on soil erosion.
The NDVI extracted from the study area (applied to Landsat 7 ETM+ image) has values that rang e from -0.65 to 0.99. The NDVI is used along with the equation 5 in order to calculate the *C* factor values of the study area in GIS environment.

Equation 5 – P factor

$$C = \exp[-a \frac{NDVI}{(b - NDVI)}]$$

where a and b are unitless parameters that determine the shape of the curve relating to NDVI and *C* factor. According to the final results the *C* factor values range from 0,67 to 1.26.

4.2. RUSLE Model Results

After the development of all the digital layers in GIS environment, with the use of equation 1 and through the use of Boolean algebra the final erosion hazard map was developed (Figure 4d). In the final RUSLE grid file due to the speckle phenomenon a 3x3 majority filter was applied to reduce the influence of the phenomenon. According to the final results the vast majority of sites are established on areas with recorded soil loss greater than the mean value soil loss of the whole district in tones/hectare * year.

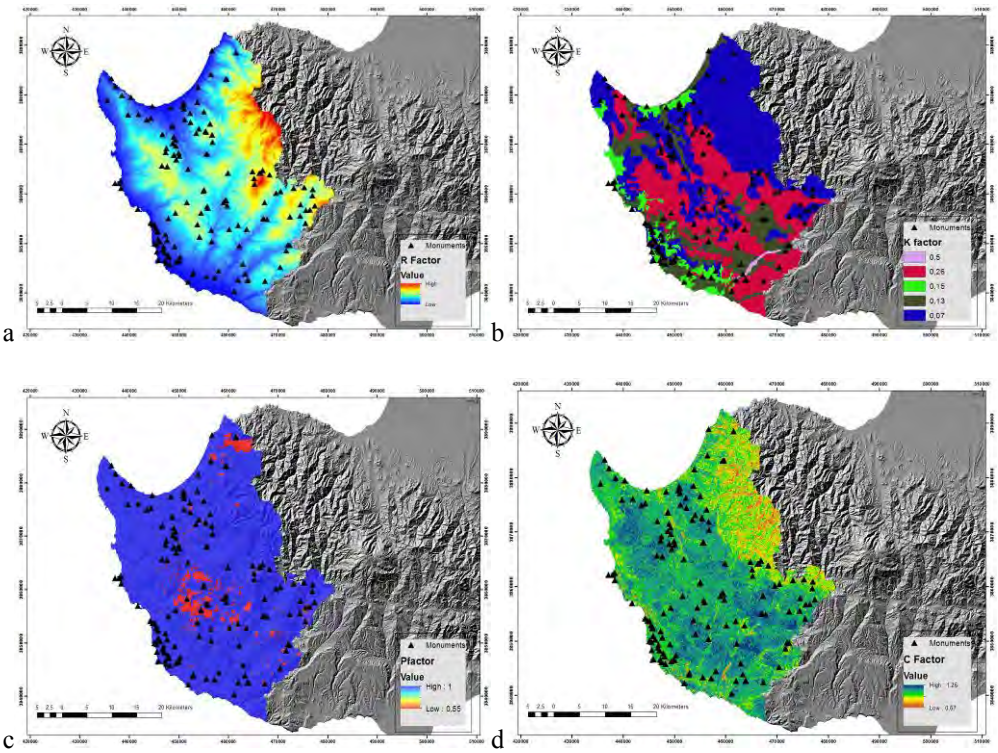

Figure 4 - *P* factor (a). *K* factor (b). *R* factor (c). RUSLE model of the study area (d).

5. Landslides Hazard Assessment

Landslide occurrence depends on complex interactions among a large number of partially interrelated factors. Information from remotely sensed data is digitally processed and combined with other ancillary environmental information incorporated in a GIS. In total 9 factors were considered in calculating landslide probability: Distance from drainage network, distance from faults, slope, aspects, relief, lithology, precipitation and land use regime. These parameters were extracted either from the area's DEM (relief, aspect, slope), from image's classification (land use), from digitization of geological and topographic maps (lithology, faults, road network) or from provided from Cyprus Meteorological Service annual precipitation data and application of Kriging interpolation method. All the final 9 digital layers were implemented in GIS environment and reclassified with certain rates, according to experts' opinion, for their contribution to possible landslide phenomena (Figure 5 b; c). In a next phase, AHP model was applied in order to compare the different parameters, their relative importance in estimating landslide risk and assign a final weight factor.

5.1. Implementation of AHP Methodology

According to AHP methodology, pairwise comparison of the contribution of each factor was acco mplished. Specifically, answers of several experts were collected on the reciprocal matrix, and the appropriate eigenvector solution method was then employed to calculate the factor weightings. Spe cifically a certain grade is assigned to all the different pairs from 1/9 when the factor is "not import ant at all" to 9 when the factor is "extremely important" (Table 1).

Table 1 - Implementation of AHP method.

Factors	F1	F2	F3	F4	F5	F6	F7	F8	F9	Total Sum	Normalized Weights
Lithology (F1)	1	5	5	3	9	7	5	9	3	47	0.245
Land Use (F2)	1/5	1	3	1/3	7	3	3	5	1/3	22.86	0.119
Distance from Streams (F3)	1/5	1/3	1	1/5	5	3	3	5	1/3	18.06	0.094
Slope (F4)	1/3	3	5	1	7	7	5	7	3	38.33	0.20
Aspect (F5)	1/9	1/7	1/5	1/7	1	1/3	1/5	3	1/7	5.12	0.026
Precipitation (F6)	1/7	1/3	1/3	1/7	3	1	1/3	3	1/7	8.41	0.043
Distance from road network (F7)	1/5	1/3	1/3	1/5	5	3	1	5	1/5	15.26	0.079
Relative Relief (F8)	1/9	1/5	1/5	1/7	1/3	1/3	1/5	1	1/7	2.65	0.013

After the calculation of the normalised weights, the consistency of the responses must be checked by calculating the Consistency Ratio. For that reason the Consistency index (CI) was calculated ac cording to equation 6:

Equation 6 – Consistency index

$$CI = \frac{\lambda \max - n}{n-1} = \frac{9.656-9}{9-1} = 0.082$$

Where λmax is the largest eigenvector and n is the number of criteria used in the study. The λmax value was calculated with the use of Matlab software.The final consistency ratio (CR) was estimat ed through the equation 7:

Equation 7 – Consistency ratio

$$CR = \frac{CI}{RI} = \frac{0.12}{1.45} = 0.082$$

where *RI* = Random Consistency Index. For the case of 9 different factors is equal to *1,45*. Accordi ng to Saaty (1980) if that ratio exceeds 0.1 the set of judgments may be too inconsistent to be reli- able. The Landslide Susceptibility Map with the corresponding weights of significance was calcu- lated according to equation 8:

Equation 8 – Landslide susceptibility map equation

$$\textit{Landslide Susceptibility Map} = F_1 * 0.245 + F_2 * 0.119 + F_3 * 0.094 + F_4 * 0.20 + F_5 * 0.026 + F_6 * 0.043 + F_7 * 0.079 + F_8 * 0.013 + F_9 * 0.176$$

Following, the initial hazard map was then transformed to Landslide Hazard Zonation Map (LHZM) (Figure 5d). Thus, the digital GIS layer was reclassified in GIS environment according to

Natural Breaks method to five major classes: Very High Hazard, High Hazard, Moderate Hazard, Low Hazard and Extremely Low Hazard. Over the final LHZM the digital road network was superimposed. Searching the results in GIS environment it was indicated that the vast majority of sites are established on areas of either High Hazard or Very High Hazard highlighting the vulnerability of sites in this specific natural threat.

Finally, the land use map of 2020 was incorporated in the final AHP model, which was implemented once again for 2020 period this time. The final results highlight a slight tendency for minimizing the landslide vulnerability of the study area.

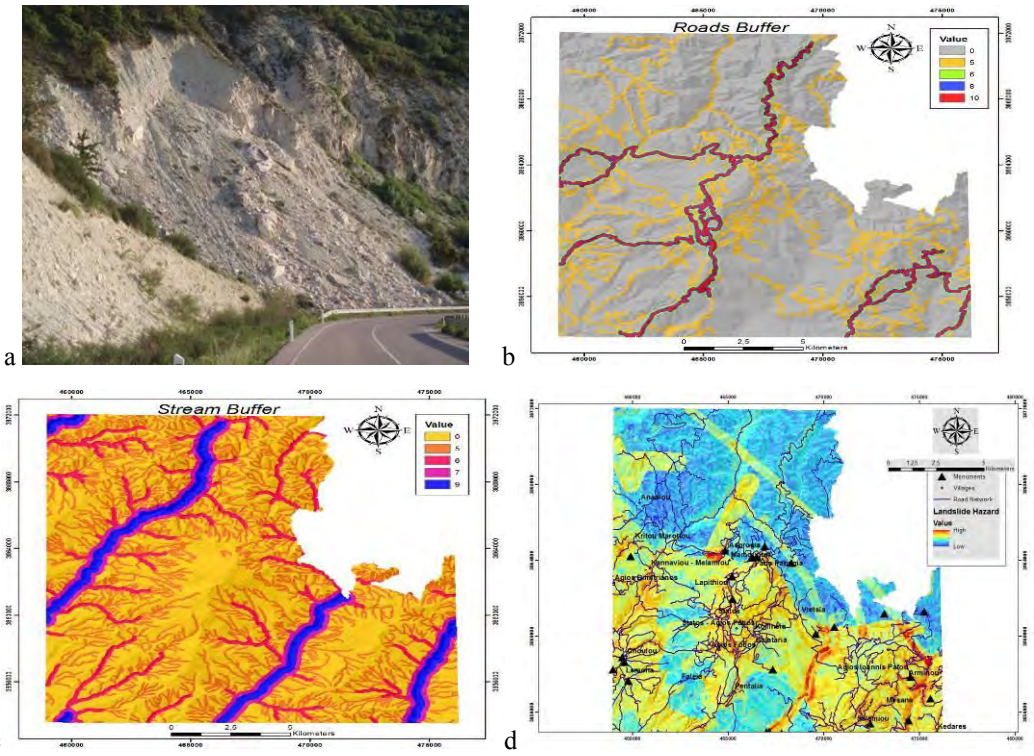

Figure 5 - Rock slide in chalk across a roadcut (a). Road buffer (b). Stream buffer (c). Landslide hazard assessment map (d).

6. Results

The environmental and human factors can contribute with equal or different participation to the damage of precious archaeological monuments and cultural reserves. The beneficial integrated use of satellite remote sensing with GIS has been demonstrated in this study for exploring the natural and anthropogenic hazard risk of the most significant cultural heritage sites in Paphos district in Cyprus.

As it was found, during the last years the phenomenon of urban sprawl has been recorded in the broader area of Paphos. Extensive construction and building development has taken place, and several areas of archaeological interest suffer from extensive urban pressure and the phenomenon is expected to intensify the next years. It was also proved vast number of sites is established on areas prone to erosion and landslide phenomena.This specific study revealed the different kind of natural and anthropogenic hazards that threatens the preservation of valuable CH sites. Additionally, this study provides the authorities with the essential knowledge that can help them to specify the actions they need to take for the protection of national heritage from natural

phenomena and anthropogenic impacts. The research team will continue the relevant study by supplementing the model with more potential hazards and proceeding to a final integrated model of overall hazard of Paphos archaeological sites.

7. Acknowledgments

The results reported here are based on findings of the Cyprus Research Promotion Foundation project "ΑΕΙΦΟΡΙΑ/ΚΟΙΑΦ/0311(BIE)/06". The project is funded by the Republic of Cyprus and the European Regional Development Funds. Thanks are also given to the Remote Sensing and Geo-Environment Laboratory of the Department of Civil Engineering & Geomatics at the Cyprus University of Technology for its continuous support (http://www.cut.ac.cy). The authors would like to thank the Director of the Department of Antiquities Dr. Maria Hadjicosti for her permission to access the data of the Department.

8. References

Agapiou A., Hadjimitsis D.G., Alexakis D.D. and Papadavid G. 2012. Examining the phenological cycle of barley (hordeum vulgare) using satellite and in situ spectroradiometer measurements for the detection of buried archaeological remains, *GIScience and Remote Sensing,* 49(6), 854-872.

Alexakis D., Agapiou A., Hadjimitsis D. and Sarris A. 2012. Chapter: Remote sensing applications in archaeology, *Remote Sensing/Book 2 (ISBN 979-953-307-231-8),* Book edited by: Boris Escalante.

Canuti P., Casagli N., Catani F. and Fanti R. 2000. Hydrogeological hazard and risk in archaeological sites: some case studies in Italy, *Journal of Cultural Heritage*, 1, 117 – 125.

Carlon C., Marcomini A., Fozzati L., Scanferla1 P., Bertazzon S., Bassa1 S., Zanovello F., Stefano F., Chiarlo R. and Penzo F. 2002. ArcheoRisk: a Decision Support System on the Environmental Risk for Archeological Sites in the Venice Lagoon, *Proceedings of the 1st Biennial Meeting of the iEMSs,* Lugano, Switzerland.

Hadjimitsis D.G., Clayton C.R.I. and Hope V.S. 2004. An assessment of the effectiveness of atmospheric correction algorithms through the remote sensing of some reservoirs, *Int. J. Remote Sens,* 25, 3651-3674.

Hadjimitsis D.G., Agapiou A., Alexakis D. and Sarris A. 2013. Exploring natural and anthropogenic risk for cultural heritage in Cyprus using remote sensing and GIS, *International Journal of Digital Earth,* 6(2*)*, 115-142.

Heumann B.W., 2011. An Object-Based Classification of Mangroves Using a Hybrid Decision Tree—Support Vector Machine Approach, *Remote Sensing,* 3, 2440-2460.

Karydas C., Sekuloska T. and Silleos, G. 2009. Quantification and site-specification of the support practice factor when mapping soil erosion risk associated with olive plantations in the Mediterranean island of Crete, *Environ Monit Assess.,* 149, 19–28, DOI 10.1007/s10661-008-0179-8.

Prasannakumar V., Vijith H. and Geetha N. 2011. Estimation of soil erosion risk within a small mountainous sub-watershed in Kerala, India, using Revised Universal Soil Loss Equation (RUSLE) and geo-information technology, *Geoscience Frontiers*, doi:10.1016/j.gsf.2011.11.003.

Saaty T. L. 1980. *The Analytic Hierarchy Process*, McGraw Hill International.

Sarris A., Topouzi S., Chatziiordanou E., Liu J. and Xu L. 2002. Space technologies in archaeological research & CRM of semi-arid & desertification affected regions. Examples from China & Greece, *European Space Agency, (Special Publication) ESA SP,* (515), 185-188.

Themistocleous K., Nisantzi A., Agapiou A., Alexakis D. Hadjimitsis D., Lysandrou V., Perdikou S., Retalis A. and Chrysoulakis N. 2012. Long term monitoring of air pollution on monuments and cultural heritage sites in Cyprus using satellite remote sensing, *International Journal of heritage in the digital Era,* 1(1)*,* 145-167.

Δελτίο της Ελληνικής Γεωλογικής Εταιρίας, τομ. XLVII , 2013
Πρακτικά 13ου Διεθνούς Συνεδρίου, Χανιά, Σεπτ. 2013

Bulletin of the Geological Society of Greece, vol. XLVII 2013
Proceedings of the 13th International Congress, Chania, Sept. 2013

SPATIAL AND TEMPORAL DISTRIBUTION OF RAINFALL AND TEMPERATURE IN MACEDONIA, GREECE, OVER A THIRTY YEAR PERIOD, USING GIS

Grimpylakos G.[1], Karacostas T. S.[2] and Albanakis K.[1]

[1] Aristotle University of Thessaloniki, Faculty of Geology, Department of Physical and Environmental Geography, grimpyl@geo.auth.gr, albanaki@geo.auth.gr

[2] Aristotle University of Thessaloniki, Faculty of Geology, Department of Meteorology and Climatology, karac@geo.auth.gr

Abstract

Due to increased demand and use of water resources, the European Union has established the (WFD) Water Framework Directive 2000/60 for Community action in the field of water policy. In order to achieve better water protection and management, Member States must identify and analyse European waters, on the basis of individual river basin and district.

Precipitation and air temperature are directly related and at the same way interacted to the hydrological cycle and therefore with water resources. The objective on this study is to present the spatial and temporal distribution of precipitation and air temperature in Macedonia, by using GIS software (ArcMap 9.3).

The data used were retrieved from 82 different meteorological stations, which belong to the Ministry of Rural Development and Food, and correspond to the thirty year period (1974-2004); all stations provided continuous daily data of precipitation while 43 of them provided also daily data of temperature. The annual temperature range and the annual total precipitation amount were calculated, at each individual station, for the thirty years of the examined period. By using GIS software and triangular interpolation scheme, the thematic maps of Macedonia for the aforementioned parameters and thermal continentality K were created. Furthermore, possible mean annual evapotranspiration for each meteorological station was estimated by Turc, Coutagne and Thornthwaite algorithms.

Key words: *Interpolation, Annual temperature range, Thermal continentality, Evapotranspiration, Water Framework Directive.*

Περίληψη

Η αυξημένη ζήτηση και χρήση των υδάτινων πόρων οδήγησε την Ευρωπαϊκή Ένωση στην καθιέρωση της Ευρωπαϊκής κοινοτικής Οδηγίας Πλαίσιο 2000/60 ΕΚ για τα ύδατα, η οποία έχει στόχο την καλύτερη πολιτική διαχείριση των υδάτων από τα κράτη μέλη. Προκειμένου να επιτευχθεί καλύτερη προστασία αλλά και διαχειρισή των υδάτινων πόρων, τα κράτη μέλη πρέπει να εντοπίσουνε και να αναλύσουνε τα ευρωπαϊκά ύδατα σε επίπεδο λεκάνης απορροής.

Ο υετός και η θερμοκρασία του αέρα συνδέονται άμεσα και αλληλεπιδρούν με τον υδρολογικό κύκλο και με τους υδάτινους πόρους. Ο στόχος αυτής της μελέτης είναι να

παρουσιάσει την χωρική και χρονική κατανομή του υετού και της θερμοκρασίας του αέρα στη Μακεδονία, με τη χρήση λογισμικού Γ.Σ.Π. (ArcMap 9,3).
Τα δεδομένα που χρησιμοποιούνται είναι οι ημερήσιες, μηνιαίες και ετήσιες τιμές των παραπάνω παραμέτρων, οι οποίες ανακτήθηκαν από 82 διαφορετικούς μετεωρολογικούς σταθμούς που ανήκουν στο Υπουργείο Αγροτικής Ανάπτυξης και Τροφίμων, και αντιστοιχούν στο χρονικό διάστημα τριάντα χρόνων (1974-2004). Συγκεκριμένα 82 σταθμοί παρείχαν συνεχή δεδομένα ημερήσιου υετού ενώ 43 από τους σταθμούς παρείχαν συνεχή δεδομένα της ημερήσιας θερμοκρασίας του αέρα. Το Ετήσιο Θερμοκρασιακό Εύρος, η θερμική Ηπειρωτικότητα, η μέση ετήσια θερμοκρασία και το μέσο ετήσιο ύψος υετού υπολογίστηκαν, σε κάθε σταθμό, για τα τριάντα χρόνια της εξεταζόμενης περιόδου. Χρησιμοποιήθηκε το λογισμικό GIS (ArcMap 9.3) για την εφαρμογή μεθόδων χωρικής παρεμβολής, προκειμένου να προσδιοριστούν οι τιμές των παραπάνω παραμέτρων στη Μακεδονία. Ακολούθησε έλεγχος αξιοπιστίας των μεθόδων και η πιο αξιόπιστη μεθοδος χρησιμοποιήθηκε για την δημιουργία χαρτών με τις προαναφερόμενες παραμέτρους. Έπειτα έγινε υπολογισμός της εξατμισοδιαπνοής για όλους τους μετεωρολογικούς σταθμούς με τρεις μεθόδους Thornthwaite, Turc και Coutange.
Λέξεις κλειδιά: *Ετήσιο θερμοκρασιακό εύρος, Βαθμός θερμικής ηπειρωτικότητας, Εξατμισοδιαπνοή, Κοινοτική Οδηγία 2000/60.*

1. Introduction

Precipitation, air temperature and evapotranspiration are directly related and interacted with the water cycle. This article is part of a research, which examines the spatial and temporal distribution of the aforementioned climatic parameters in Macedonia Greece, in order to decide if these parameters should be used as one of the alternative factors of System B for Greece's river typology according to the (WFD) Water Framework Directive 2000/60 for Community action in the field of water policy. According to the WFD, Member States are obliged to classify all surface waters by one of the two typology systems, A or B. System A has fixed types with specific categorisation. System B can include alternative factors alongside with the obligatory factors of System A, but leaves to the analyst's discretion the categorisation of these factors as long as the new typology achieves at least the same level of categorisation as System A. (Kanli, 2009).

2. Parameters, Data and Method

2.1. Climatic Parameters

2.1.1. Annual Temperature Range

The annual course of temperature depends on the deviation of sun (position of sun according to earth in general), place's latitude and the respective path of solar radiation. At North hemisphere, higher temperature is observed during July or August while minimum during January or February (Zampakas, 1981). Mean annual Temperature at each station, derives by calculating the mean monthly temperature for a 30-year period and abstracting from the maximum monthly temperature the minimum monthly temperature as shown at table 2. Annual temperature range can be used to categorise the climate type in 4 different types (Supan, 1880): i) $A \leq 15^{o}C$ Equator climate type, ii) $15^{o}C < A \leq 20^{o}C$ Transitional maritime climate type and iii) $20^{o}C < A \leq 40^{o}C$ Continental climate type, iv) $40^{o}C < A$ Extreme continental climate type.

2.1.2. Parameter K of Thermal Continentality

The index of thermal continentality, parameter K, which is most often used in Europe was proposed by Gorczynski in 1918, (Mikolaskova, 2009).

Equation 1 – Gorczynski for Thermal Continentality

$K = 1,7(A - 12\sin\theta)/\sin\theta$ or $K = 1,7A/\sin\theta - 20.4$

Parameter K is the index of continentality expressed as a percent, A is annual range of temperature in °C and θ is latitude in degrees (WGS84). Expression $A=12\sin\theta$ corresponds well to observations above sea (Gorczynski, 1922), constant 1.7 is calculated from the assumption that Verchojansk, in eastern Siberia, is representative of 100% continentality. K value range is 0-100, where 0 is observed at sea locations, where climate is no longer influenced by continental surface and 100 at purely continental areas, where there is no influence from maritime air masses. This parameter is not applicable at low latitudes (Conrad and Pollak, 1950) but it is applicable in Greece. Gorczynski suggests three degrees of continentality according to parameter K value: i) $0\% \leq K \leq 33\%$ Transitional maritime climate type, ii) $33\% < K \leq 66\%$ Continental climate type and iii) $66\% < K \leq 100\%$ Extreme continental climate type.

2.1.3. Evapotranspiration

Although several variations of the definition exist, potential evapotranspiration (PET) can be generally defined as the amount of water that could evaporate and transpire from a vegetated landscape without restrictions other than the atmospheric demand (Thornthwaite, 1948; Penman, 1948; Jensen et al., 1990). Evapotranspiration (ET) is the sum of evaporation and plant transpiration from the Earth's land surface to atmosphere. To estimate ET, three methods were used in this study: Turc, Coutagne and Thornthwaite. These methods need the mean monthly and annual precipitation and the mean monthly and annual temperature.

- Turc algorithm, equation 2, for estimating ET, uses P mean annual precipitation in mm and T which is the mean annual temperature in °C.

Equation 2 – Turc algorithm for Evapotranspiration

$E= P/\sqrt{(0,9+P^2/L^2)}$, with $L=300+25T+0,05T^3$

- Coutagne algorithm, equation 3, for estimating ET is applicable when the condition $1/8\lambda \leq P \leq 1/\lambda$ is valid, P is the mean annual precipitation in meters and T is mean annual temperature in °C.

Equation 3 – Coutagne algorithm for Evapotranspiration

$E= P-\lambda P^2$, with $\lambda=1/(0,8+0,14T)$

- Thornthwaite algorithm requires latitude, daylight coefficient, soil moisture, mean monthly precipitation in mm and mean monthly temperature in °C (Palmer & Havens, 1958; Pereira & Camargo, 1989; Kerkikdes et.al., 1996; Mardikis et al., 2005; Dalezios & Bartzokas, 2009).

Equation 4 – Thornthwaite algorithm for Evapotranspiration

$PET_i(L)=K*PET_i(0)$, $PET_i(0)=1,6*(10T_i/J)^c$, $J=\Sigma_{i=1}^{12}(I_i)$ and $I_i=(T_i/5)^{1,514}$

T_i=mean i monthly temperature and $C=0,000000675*J^3 - 0,0000771*J^2 + 0,01792*J +0,49239$

$PET_i(0)$ = Potential Evapotranspiration at 0 latitude. Constant K differs according to latitude. For our case study at all meteorological stations the same constant K values were used and these are shown at table 1.

Table 1 – Constant K values in Thornthwaite Method.

Month	Jan	Feb	Mar	Apr	May	June	July	Aug	Sep	Oct	Nov	Dec
K	0,83	0,83	1,3	1,11	1,25	1,26	1,27	1,19	1,04	0,96	0,82	0,8

Average monthly precipitation is estimated by averaging the overall precipitation for each month for 1974-2004. Mean annual precipitation is very reliable measured at points where meteorological stations are situated and was estimated by summing the average monthly precipitation for the same period. Average monthly temperature is estimated by averaging the average temperature for each month during the period of 1974-2004. Mean annual temperature was estimated by averaging the monthly average temperature for the aforementioned period.

2.2. Studying Area and Data

Macedonia is a district of North Greece as shown at figure 1. Studying area is a polygon that includes all the watersheds of Macedonia's torrents and rivers, resulting in a polygon the boundaries of which differ from the boundaries of Macedonia's political district. The boundaries were determined BY THE Ministry of Rural Development and Food in collaboration with the Institute of Geology and Mineral Exploration and always according to the WFD guidelines for water bodies. Studying area is 36290 km^2, has a perimeter of 2163 km and includes 77 different torrents in which main rivers are divided according to WFD and the watersheds are of 3-4775 km^2.

Ministry of Rural Development and Food provided data from 82 meteorological stations, which correspond to different time periods during an eighty year period (1930-2010) and include daily, monthly and annual measurements of precipitation, while 43 of them included also daily monthly and annual measurements of temperature. In order to study the climatic parameters for a given area, a 30-year period with good spatial and temporal distribution is needed. For our studying area, after sorting the data from all 82 meteorological stations the best period corresponded to 1974-2004, as all data were daily and continuous for this period.

Table 2 – Annual Temperature Range A at each station with the minimum and maximum mean T for period 1974-2004.

Station	County	A	Minimum T	Maximum T
Ano kalliniki	Florina	21,3	2,0 Jan	23,3 July
Limnochori	Florina	19,9	2,6 Jan	22,5 July
Amuntaio	Florina	20,0	3,0 Jan	23,0 July
Tropaiouxos	Florina	20,6	1,0 Jan	21,6 july
Monospita	Imathia	20,6	4,2 Jan	24,8 July
Rodochori	Imathia	19,9	3,7 Jan	23,6 July
Exaplatanos	Pella	20,0	4,5 Jan	24,5 July
Vrontous	Pieria	19,7	5,5 Jan	24,5 July
Moschopotamos	Pieria	19,5	4,9 Jan	24,3 July
Saint Paraskevi	Grevena	19,8	3,0 Jan	22,7 July
Alatopetra	Grevena	19,2	2,2 Feb	21,5 July
Krua Vrusi	Pella	20,5	4,0 Jan	24,5 July
Plana	Chalkidiki	19,1	5,3 Jan	24,5 Aug
Ano Theodoraki	Kilkis	19,2	4,0 Jan	23,2 July
Metaxochori	Kilkis	19,4	3,4 Jan	22,8 July
Melanthio	Kilkis	19,4	3,4 Jan	22,8 July
Nea Chalkidona	Thes\niki	20,5	4,7 jan	25,2 July
Chalastra	Thes\niki	20,2	4,7 jan	24,9 July
Drama	Drama	21,0	4,1 Jan	25,1 July
Kato Nevrokopi	Drama	20,8	0,2 jan	21 July
Kalampaki	Drama	20,5	4,2 Jan	24,7 July
Argyroupoli	Drama	21,6	3,7 Jan	24,3 Aug
Leukogia	Drama	21,7	0,6 Jan	22,1 July
Prinos Thasou	Kavala	20,0	4,9 Jan	24,9 July

Data from 43 meteorological stations, of the studying area, were available to be used in order to calculate the mean monthly and annual temperature, the annual temperature range A and the parameter K of thermal continentality. The data were of different periods during 1950-2010 and of different time continuity, 12-65 years. Period 1974-2004 was chosen to be used because most stations had data for this period. After sorting the data from the meteorological stations, 32 of them had data during the aforementioned period but only 24 had continuously data for the whole period of 30 years; therefore these stations were used (Table 2).

For the mean annual precipitation analysis, over the 82 meteorological stations only 64 had continuous data for the period 1974-2004 (Table 3) and included the 24 stations that were used to calculate the annual temperature range A. As there was a big diversity in the spatial distribution of the 24 and 64 meteorological stations, it was decided that two thematic maps should be constructed, with the spatial and temporal distribution of the precipitation through Macedonia. Afterwards, these thematic maps were checked for similarities and differences (Figure 6 and 7).

Table 3 –Mean Precipitation at each station for period 1974-2004 and the geographical position in EGSA 87 (meters).

Station	County	P(mm)	Altitude	Longitude	Latitude
Ano kalliniki	Florina	521,1	634,6	284948,045	4526799,972
Limnochori	Florina	541,3	598,9	294062,520	4500615,249
Amuntaio	Florina	438,1	579,0	304125,020	4507749,929
Polypotamos	Florina	619,0	1000,0	276016,096	4510396,803
Skopos	Florina	435,7	775,0	300399,873	4526365,940
Tropaiouxos	Florina	622,7	695,0	283109,746	4512037,983
Veui	Florina	535,1	734,7	297286,337	4515340,333
Aalexandria	Imathia	690,2	750,0	367360,434	4498948,430
Monospita	Imathia	596,9	47,0	346179,189	4497504,857
Koumaria	Imathia	1020,6	700,0	344499,751	4484582,860
Rodochori	Imathia	801,2	545,0	332288,798	4507060,477
Ergochori	Imathia	643,2	107,0	347437,793	4490075,164
Trilofos	Imathia	697,2	151,5	344653,693	4491983,540
Exaplatanos	Pella	635,6	133,0	342816,284	4538298,946
Notia	Pella	446,2	590,0	348692,164	4551133,402
Theodoraki	Pella	876,7	424,0	348348,671	4534480,631
Promachonas	Pella	890,2	250,0	329206,902	4433086,364
Skydra	Pella	550,7	46,0	343710,041	4514215,579
Ktima Kastorias	Kastoria	596,0	690,0	268286,411	4488408,209
Vrontous	Pieria	850,2	180,0	352321,397	4451109,708
Kolindros	Pieria	664,2	300,0	372715,011	4482198,998
Lofos	Pieria	821,8	250,0	362285,404	4452772,325
Mosxopotamos	Pieria	775,1	516,0	356858,373	4465828,328
Trilofos	Pieria	695,9	318,0	369664,889	4469296,912
Deskati	Grevena	668,0	850,0	311867,150	4422388,357
Saint Paraskevi	Grevena	727,1	615,0	281013,000	4439877,045
Alatopetra	Grevena	857,0	1250,0	262479,391	4438582,591
Anabruta	Grevena	920,2	860,0	282381,140	4437985,969
Kariotissa	Pella	533,1	9,0	356483,832	4514111,447
Krua Vrusi	Pella	524,2	8,0	356302,515	4504740,156
Trikala	Imathia	572,1	7,0	363097,862	4497174,779
Megali Panagia	Chalkidiki	679,8	440,0	471584,641	4477471,821
Plana	Chalkidiki	550,8	11,5	471556,731	4470071,868

Ormulia	Chalkidiki	472,8	40,0	461606,877	4460865,882
Rizes	Chalkidiki	742,0	350,0	451902,804	4483187,002
Ano Theodoraki	Kilkis	495,2	480,0	415959,912	4557455,098
Metaxoxori	Kilkis	565,1	63,0	411631,530	4546402,983
Melanthio	Kilkis	618,8	490,0	419912,640	4535205,366
Nea Chalkidona	Thessaloniki	508,6	29,5	381632,419	4509811,675
Chalastra	Thessaloniki	443,1	4,0	393266,166	4535543,332
Kalamoto	Thessaloniki	787,0	220,0	446284,268	4488778,629
Mavrouda	Thessaloniki	687,0	360,0	453583,750	4516454,322
Diavata	Thessaloniki	461,3	14,0	402694,802	4505804,818
Vraxia	Thessaloniki	415,6	2,0	384332,087	4502366,704
Drama	Drama	645,5	101,0	511038,602	4555131,545
Kato Nevrokopi	Drama	725,7	580,0	488696,344	4577334,585
Nikiforos	Drama	642,1	236,0	525017,441	4557016,570
Livadero	Drama	877,5	650,0	517855,148	4625457,932
Mikropoli	Drama	934,4	360,0	484478,409	4560689,863
Kalampaki	Drama	645,2	67,3	515257,514	4544037,941
Argyroupoli	Drama	746,5	74,0	502648,896	4551423,084
Leukogia	Drama	856,5	621,4	490098,077	4582883,456
Exochi	Drama	715,0	620,0	484529,212	4584743,409
Katafygio	Drama	745,1	761,0	473359,448	4577374,373
Ochyro	Drama	1127,5	543,0	487292,487	4571786,029
Iraklia	Serres	515,9	35,0	439744,333	4559070,950
Provatas	Serres	467,5	18,0	449439,899	4546045,337
Lower Kamila	Serres	554,4	10,0	456419,478	4542300,120
Worksite Serres	Serres	523,1	56,0	460652,182	4547827,040
Eleftheroupoli	Kavala	719,7	80,0	520902,445	4529250,503
Gialochoria	Kavala	485,6	7,0	498443,104	4508869,290
Prinos Thasou	Kavala	716,7	684,0	548325,837	4510168,565
Chrysoupoli	Kavala	569,8	18,0	558736,979	4536856,957
Moustheni	Kavala	701,0	151,0	509333,916	4522296,22

The data for calculating the potential evapotranspiration at each station derived from daily data of 24 stations at 1974-2004 period that were used for the estimation of annual temperature range, thermal continentality K and mean annual precipitation. These stations and data were chosen because Turc, Coutagne and Thornthwaite methods needed the mean monthly and annual temperature and precipitation in order to calculate PET. The high resolution Digital elevation model (DEM) with 28.3x28.3 cell size was used, which was constructed from the Advanced Spaceborne Thermal Emission and Reflection Radiometer (ASTER) of NASA Terra satellite.

2.3. Method

2.3.1. Spatial Interpolation

A very basic problem in spatial analysis is interpolating a spatially continuous variable from point samples. Spatial interpolation techniques predict values for cells in raster from a limited number of sample point data. According to first law of Geography, "Everything is related to everything else, but near things are more related than distant things" (Tobler, 1970). Unknown values are predicted with a mathematical formula that uses the values measured at nearby points. There are many different spatial interpolation techniques. Some of the most commonly used interpolation methods to model spatially distribution from point data are the following three: Inverse Distance Weighting

(IDW), spline and ordinary kriging. Overall, anomalies of local scale can be adjusted without affecting the values derived from interpolation at other points on the surface (Burrough and McDonnell, 1998).

2.3.2. Inverse Distance Weighted IDW

Inverse distance weighted (IDW) is a method of interpolation that estimates cell values by averaging the values of nearby measured data points. The main logic rule behind this technique is that the cell values next to each other are most likely to have same values, so the value of the predicted cell is more influenced by the value of cells closer than those that are further away. This technique weights the points closer to the prediction location greater than those farther away, hence the name inverse distance weighted (Watson and Philip, 1985). However the main problem with this technique is that it assumes that maximum and minimum values are measured at the sampled points and all other unsampled points have values between those values.

2.3.3. Spline Interpolation

Spline is an interpolation method in which cell values are estimated using a mathematical function that minimizes overall surface curvature, resulting in a smooth surface that passes exactly through the input points. It is a deterministic, locally stochastic interpolation technique, which represents two-dimensional curves on three-dimensional surfaces (Eckstein, 1989; Hutchinson and Gessler, 1994).

2.3.4. Kriging

The aforementioned methods are known as deterministic interpolation methods because they are directly based on the surrounding measured values and use specified mathematical formulas that determine the smoothness of the resulting surface. On the other hand, kriging uses statistical models that include autocorrelation among measured points, in order to predict the values at unknown points. The most commonly applied form uses “semivariogram” among pairs of sampled points. Kriging interpolation method was developed by Matheron in 1970.

2.3.5. Validation

All data were divided in 2 groups. The first group was named “training” and content 90% of sample points while the second group was named “test” and content 10% of the sample points. Training group’s measurements were used for predicting the values of the examined variable at whole Macedonia by using the aforementioned interpolation methods. Test’s group was used to validate the results of each method.

3. Results

3.1. Annual Temperature Range

In order to predict the Annual Temperature Range at Macedonia district, 24 sample points were used and divided in two subsets; the test group had 3 sample points which were randomly chosen from the 24 with only rule to be positioned within the rest and not at the edges of the study area, while the rest 21 sample points were the training group. Each interpolation method was applied at the training group and the predictions were validated using the test group (Table 4).

Table 4 – Estimated values of Annual Temperature Range by each method.

Meteorological Stations	Measured Values	Predicted Values			
		IDW	Krigging	Spline	Polynomial
Limnochori	19,9	20,19	20,11	19,9	20,31
Exaplatanos	20	20,23	20,33	20,56	20,34
Monospita	20,6	20,35	20,08	20,06	20,22
Root Mean Square Error		0,091	0,133	0,159	0,134

The validation showed that the best method was Inverse Distance Weighting. Furthermore, a raster file with cell value of 750m was created, by using IDW method and data from all 24 meteorological stations. Two thematic maps were constructed, the first visualised the spatial distribution of annual temperature range A at Macedonia (Figure 1) and the second one (Figure 2) showing the categorization of Macedonia in two climatic types, according to A values (Supan 1880). Finally possible correlation between A and elevation was checked and R^2=0,034 meaning not significant correlation.

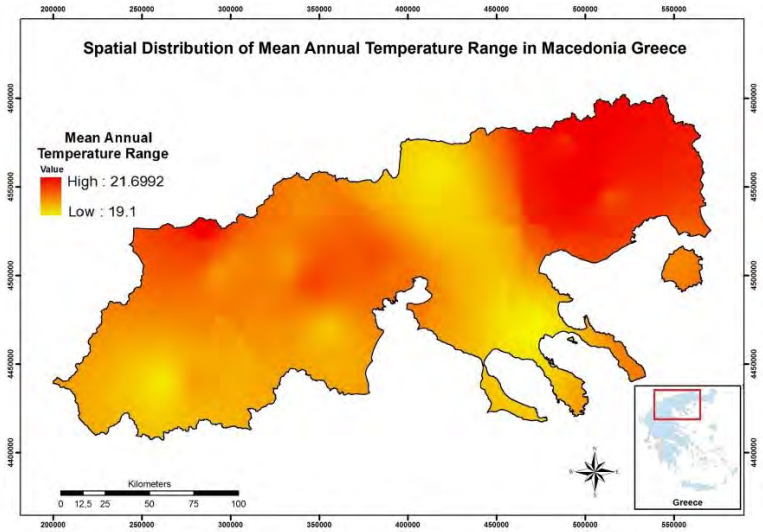

Figure 1 - Stretched map showing the gradual spatial distribution of A at Macedonia.

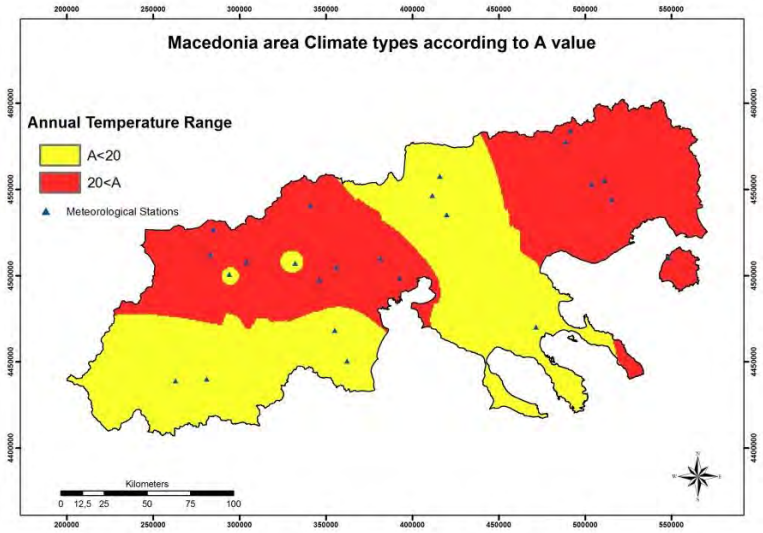

Figure 2 - Macedonia area climate types according to A value (Supan 1880).

3.2. Thermal Continentality K

Thermal continentality was constructed by applying the K algorithm at Raster calculator of ArcMap 9.3. In order to do this, two raster files of cell size 750 meters were used: one file with the annual temperature range value (the raster file thaw was previously constructed with IDW) and a second one with the latitude values per cell in WGS84. The results of the K were visualised with a

stretched thematic map, where K values ranged 29,18 - 35,42. Macedonia was divided in two different climate types according to the categorization of Gorczynski (Figure 3). Finally possible correlation between K and elevation was checked and R^2=0,025 meaning not significant correlation.

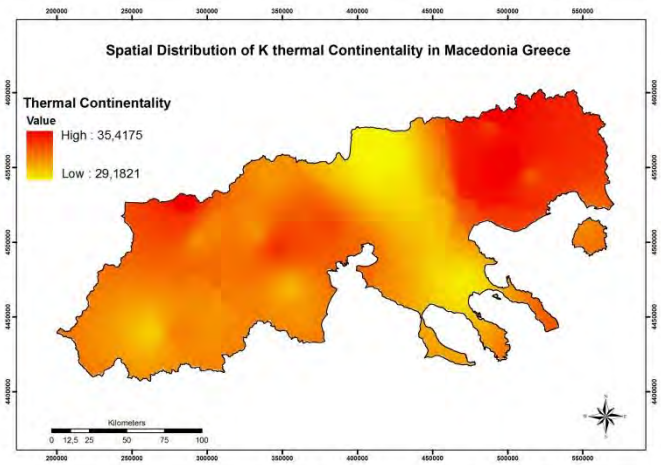

Figure 3 - Stretched map showing the gradual spatial distribution of K at Macedonia.

Mean annual temperature was estimated for each of the 24 meteorological stations that had continuous data for 1974-2004. Firstly, the mean monthly temperature for each meteorological station was calculated and then, the mean of these values gave the mean annual temperature. There is significant correlation between Mean annual Temperature and elevation where R^2 = 0,7234 as shown at Figure 4 and the corresponding equation 4 shows that the temperature declines as the elevation rises.

Equation 5 – Grimpylakos algorithm for Temperature at Macedonia

T = - 0,0038 * E + 14,904 (T is mean annual temperature and E is elevation).

The R square value (R^2), means that the mean annual temperature is 72,34% explained by elevation. Finally the equation was applied at raster calculator of ArcMap in order to estimate the temperature at the meteorological stations with no Temperature data.

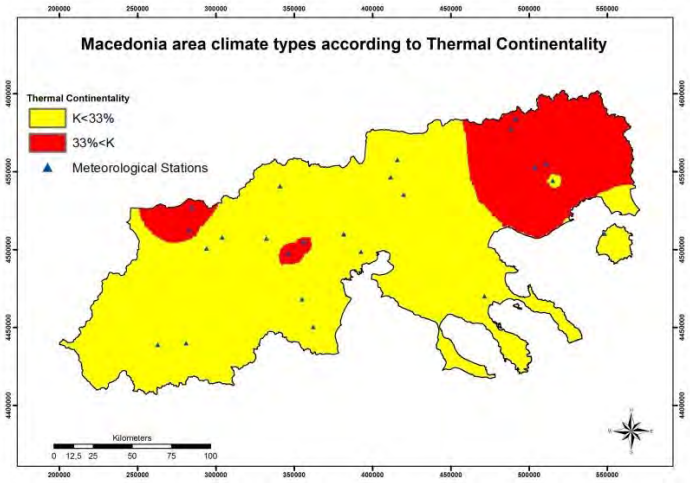

Figure 4 - Macedonia area climate types according to Thermal Continentality value.

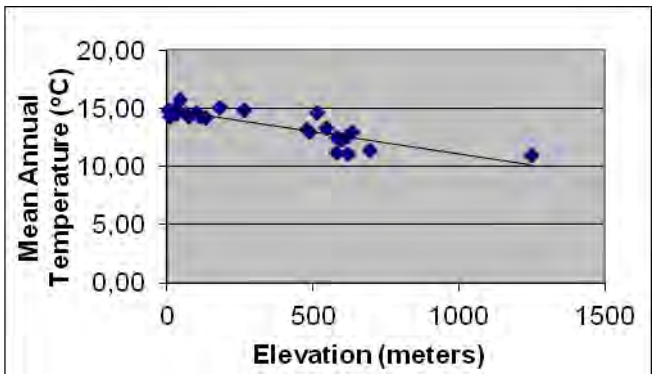

Figure 5 – Correlation of mean annual temperature with elevation.

3.3. Mean Annual Precipitation

Mean monthly precipitation was estimated for each month at all 24 and 64 meteorological stations and their total for mean annual precipitation was calculated. Two thematic maps were created showing the mean annual precipitation in Macedonia by using the interpolation method of Inverse distance weighted. The spatial distribution of the mean annual precipitation that derived from the data of 64 meteorological during 1974-2004 is projected at figure 6. The spatial distribution of the mean annual precipitation that derived from the data of 24 meteorological during 1974-2004 is projected at figure 7.The correlation between elevation and precipitation was checked with SPSS programme (Table 5). The highest possible correlation was not significant R^2<0,21 and so the mean annual precipitation for each cell of Macedonia could not be estimated and the corresponding thematic map using an equation between the elevation and the mean annual precipitation was not projected as it would have been inaccurate.

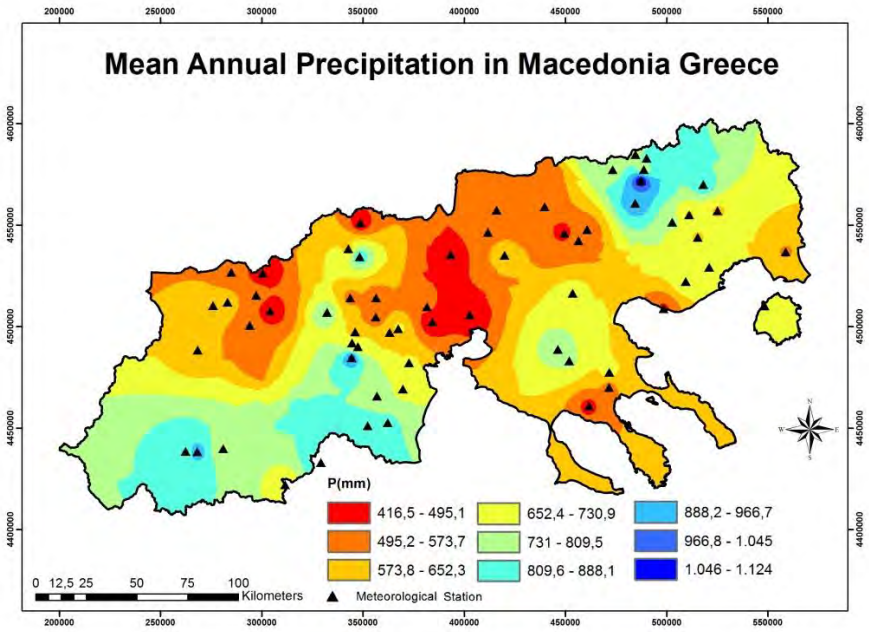

Figure 6 – Spatial distribution of mean annual precipitation at Macedonia Greece derived from 64 meteorological stations during period 1974-2004.

Table 5 – Correlation of Variables with Elevation.

Elevation	Examined Variable						
	T (°C)	P(mm)	K	A	Thornthwaite	Turc	Coutagne
Pearson	-0,851	0,306	-0,157	-0,184	0,156	-0,072	0,108
R-square	0,723	0,094	0,025	0,034	0,024	0,005	0,012

The thematic map that derived from the 24 stations missed mean annual precipitation values between 416,5 – 438,3 and 856,9 – 1124 as these data did not exist at the 24 stations. The data distribution of the 24 stations at West, central and South Macedonia is very sparse resulting in much less zones of precipitation. The map of 64 stations has good spatial distribution and is more accurate and should be used for analysis purposes.

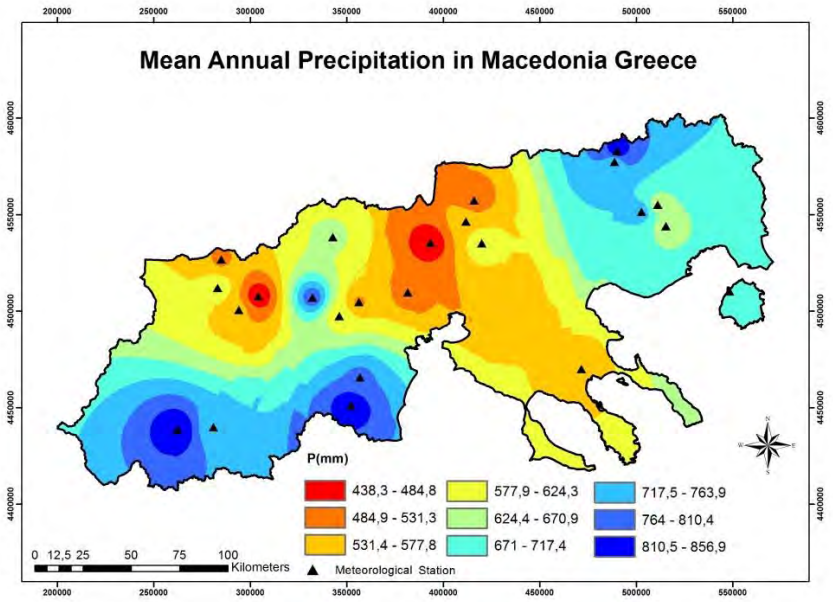

Figure 7 – Spatial distribution of mean annual precipitation at Macedonia Greece derived from 24 meteorological stations during period 1974-2004.

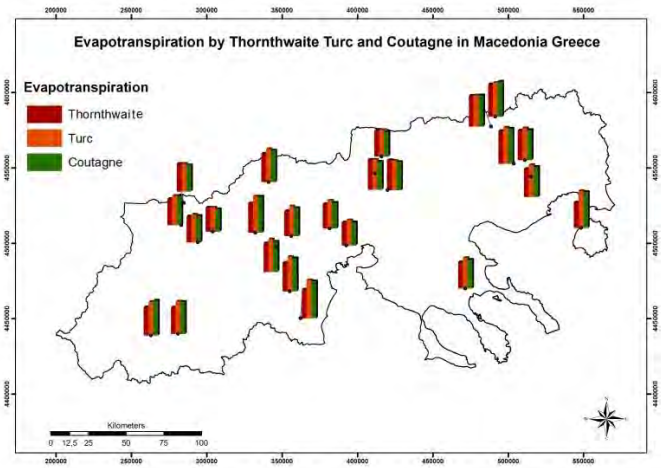

Figure 8 – Evapotranspiration in Macedonia Greece.

3.4. Evapotranspiration

Evapotranspiration was calculated with all three methods for each of the 24 stations (Figure 6). Evapotranspiration by Turc method is higher than Thornthwaite method at all stations and in 21 of 24 stations it is higher than Coutagne method, while Coutagne is higher than Thornthwaite method at 19 of 24 stations. On the other hand, Turc method is the most easily applied method of all, as Coutagne method is not always applicable and Thornthwaite's method uses parameters that differ according to elevation and the spatial distribution of each examined place, which makes it very difficult to apply this method at all stations. No significant correlation between elevation and evapotranspiration (Table 5). Finally Thornthwaite method is underestimating the evapotranspiration in comparison with the other two methods.

4. Discussion

There were small differences between predicted and measured values among the four interpolation methods that were tested for predicting A, annual temperature range, as noted also by Sailesh et al., 2012; in our case, IDW was the most accurate one as shown at table 4 as it has the smallest residuals. The spatial distribution of temperature data in central and Northwest Macedonia is very good. The estimation of annual temperature range A and thermal continentality K north of 4450000 meters and west of 525000 meters (GCS GGRS 1987) was accurate. On the other hand, the estimation of the variables, South and East of the aforementioned coordinates, needs to be crosschecked with meteorological data of nearby areas as data's spatial distribution at these areas is weak. Annual temperature range value is increasing as the distance from sea is increasing and while moving to the North (Nastos et al., 1995) as shown at figure 1a; classification by Supan (1880) divided Macedonia in two zones (figure 1b). Thermal continentality classification by Gorczynski (1922) divided Macedonia in two similar zones to A of Supan (1880) (Figure 4). From the combination of the results of A and K spatial distribution a final map was constructed and Macedonia was divided into the following three zones (Figure 7):

- $0\% \leq K \leq 33\%$ and $15^{o}C < A \leq 20^{o}C$ Transitional Maritime climate type
- $0\% \leq K \leq 33\%$ and $20^{o}C < A \leq 40^{o}C$ Transitional Continental climate type
- $15^{o}C < A \leq 20^{o}C$ and $33\% < K \leq 66\%$ Transitional Continental climate type
- $33\% < K \leq 66\%$ and $20^{o}C < A \leq 40^{o}C$ Continental climate type.

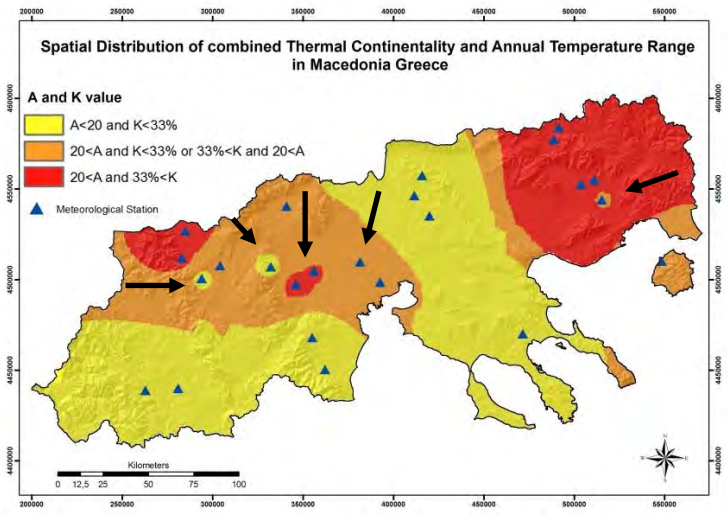

Figure 9 – Macedonia is divided in three climate types according to the author.

During the interpretation of the results as shown at figure 9, five anomalies can be observed at the map; at the two red arrows that show three stations with high A and K values, because the IDW method was not able to connect those two areas as it should have done, meaning this red small circles are not anomalies but a red zone situated Northwest of Katerini – Thessaloniki. The two yellow anomalies have A=19,9<20 classification by Supan (1880), while the orange has K=32,95% < 33%, classification by Gorczynski (1922); both cases can be included in the surrounding zone. The red arrows anomaly can be avoided with supervised classification. The elevation distribution of the meteorological stations was not adequate to check the possible correlation between Precipitation and Elevation at Macedonia and to create an equation. A map showing the spatial distribution of Evapotranspiration could not be created, as Precipitation values were necessary, that could not be precisely estimated. Mean annual precipitation, evapotranspiration and total runoff at each meteorological station were estimated and projected (Figure 10) alongside with the anaglyph. Total runoff is very strong correlated with high elevation and low temperature. Total runoff is higher at Southwest part of Macedonia west of Pindos mountain chain. The strong correlation with elevation is explained by the fact that at high elevation precipitation is higher while mean monthly and annual temperature is lower. This correlation is a proof that elevation distribution of each torrent watershed should be included in the classification of rivers typology; however in the elevation classification the relationship with the total runoff should be taken in consideration.

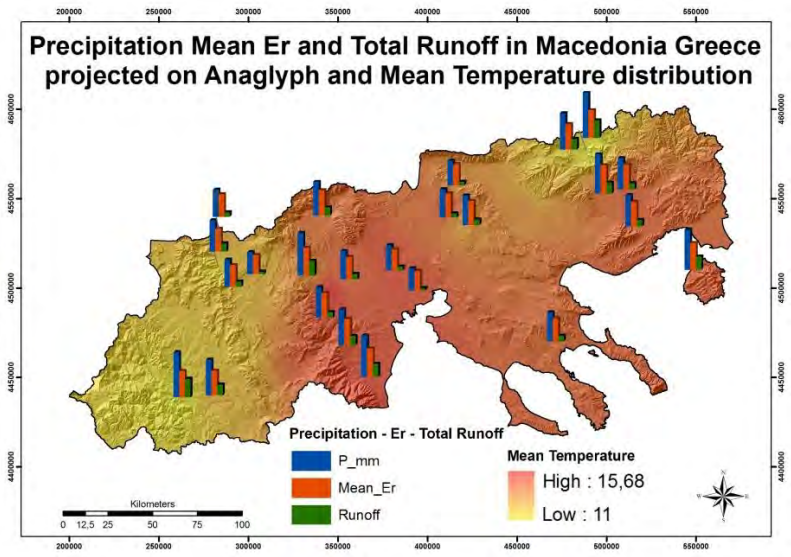

Figure 10 – Distribution of Precipitation Evapotranspiration and runoff in Macedonia Greece. On the background mean T and anaglyph is projected.

5. Acknowledgments

To Papadakou Stavroula, Drosos Efthumios, Pilalitos Konstantinos, Tsarmpos Vasileios and Leoutsarakos Nickolaos of Department of Geology and Hydrology of Ministry of Rural Development and Food, for providing the meteorological data for Macedonia. Grimpylakou Lina, for software advice in GIS-ArcMap. Tamtelen Anastasia, for data interpretation.

6. References

Apostolaki E.K. 2009. Typology and river type specific reference conditions at the basin of tauropo lake, Interdepartmental Postgraduate Program "Ecological Water Quality and Management at a River Basin level", *Master Thesis,* A.U.TH.

Burrough P.A and McDonnell R.A. 1998. *Principles of geographical information systems*, Oxford University Press, New York.
Conrad V., Pollak L.W. 1950. *Methods in climatology,* 2nd edition, Harvard University Press, Cambridge, Massachusetts.
Dalezios N.R. and Bartzokas A. 2009. Daily precipitation variability in semiarid agricultural regions in Macedonia, Greece, *Hydrological Siences Journal,* 569-585.
Eckstein B.A. 1989. Evaluation of spline and weighted average interpolation algorithms, *Comput Geosci,* 15, 79–94.
Gorczynski L. 1918. On a method of calculating the degree of continentality depending on the temperature, *Comptes Rendus, Societé des Sciences et des Lettres de Varsovie*, fasc. 4, 11, 500.
Gorczynski L. 1922. The calculation of the degree of continentality, *Monthly Weather Review*, Vol. 50, 370.
Hutchinson M.F. and Gessler P.E. 1994. Splines-more than just a smooth interpolator, *Geoderma,* Vol. 62, 45–67.
Jensen M.E., Burman R.D. and Allen R.G. 1990. Evapotranspiration and irrigation water requirements, *ASCE Manuals and Reports on Engineering practice*, New York, No. 70, 332.
Kanli L. 2009. Comparison of river typology systems in Greece, Interdepartmental Postgraduate Program "Ecological Water Quality and Management at a River Basin level, *Master Thesis,* A.U.TH.
Kerkidis P., Michalopoulou H., Papaioannou G. and Pollatou R. 1996. Water balance estimates over Greece, *Agricultural Water Management,* 32, 85-104.
Mardikis M.G., Kalivas D.P. and Kollias V.J. 2005. Comparison of Interpolation Methods for the Prediction of Reference Ecapotranspiration – An Application in Greece, *Water Resources Management,* 19, 251-278.
Matheron G. 1970. The theory of regionalized variables and its applications, *École Nationale Supérieure des Mine*, Les Cahiers du Centre de Morphologie Mathématique de Fontainebleau, Paris, Vol. 5, 212.
Mikolaskova K. 2009. A Regression Evaluation of Thermal Continentality, *Geografie*, *Proceedings of Czech Geographical Society*, Vol. 4, p. 114.
Nastos P, Evelpidou N. and Vasilopoulos A. 1999. Spatial distribution of Annual Temperature range at Greece using GIS, *1st Conference on Geographic Information Systems,* Greek Society of Geographic Information Systems.
Palmer W.C. and Havens A.V. 1958. A graphical technique for determining evapotranspiration by the Thornthwaite method, *U.S. Weather Bureau.*
Pereira A.R. and Camargo A.P. 1989. An analysis of the criticism of Thornthwaite's equation for estimating potential evapotranspiration, *Agricultural & Forest Meteorology,* 46, 149-157.
Penman H.C. 1948. Natural evapotranspiration from open water, bare soil and grass, *Proc. R. Soc. Lond.*, Vol A193, 120-145.
Sailesh S., Dilip K. P., Debasish L. and Babita P. 2012. Interpolation of climate variables and temperature modeling, *Theoritical Applied Climatology*, 107, 35–45.
Supan A. 1880. The distribution of the year union Warm variation on the earth's surface, Z. For knowledge, *Geographie, Vol.* 1.
Thornthwaite C.W. 1948. An approach towards a rational classification of climate, *Geographical Review*, 38, 55.
Tobler W. 1970. A computer movie simulating urban growth in the Detroit region, *Economic Geography*, 46(2), 234-240.
Watson D.F. and Philip G.M. 1985. A refinement of inverse distance weighted interpolation, *Geo-Processing,* 2, 315–327.
WFD 2007. Intercalibration technical report. Mediterranean GIG – Rivers Benthic Invertebrates.
Zampakas I. 1981. *General Climatology*, 176-177.

Δελτίο της Ελληνικής Γεωλογικής Εταιρίας, τομ. XLVII , 2013
Πρακτικά 13ου Διεθνούς Συνεδρίου, Χανιά, Σεπτ. 2013

Bulletin of the Geological Society of Greece, vol. XLVII 2013
Proceedings of the 13th International Congress, Chania, Sept. 2013

LANDSLIDE INVENTORY USING GISMA TECHNIQUES

Kordouli M.[1], Kavoura Kat.[1], Nikolakopoulos K.[1] and Sabatakakis N.[1]

[1] University of Patras, Department of Geology, Laboratory of Engineering Geology, kordouli@upatras.gr, kavoura@upatras.gr, knikolakop@upatras.gr,sabatak@upatras.gr

Abstract

The use of GIS for various types of data is considered to be of high importance, mainly because it is bringing together information from multiple sources. In addition, the new Internet technologies and applications of global world maps, like Google Maps, give the opportunity to build systems that the geographical information can be recorded and administrated by many users from anywhere. This kind of GIS systems is suitable for Business Administration, or Science, or Government Organizations, which need GIS systems with multiple users from many places and multiple kind of information. This system is defined as GISMA (Geographic Information System Multi Administration). In GISMA many users may input the data and use the information from different distance. Each user has specific permissions of use of data as the administrator sets.

In this work, the basic principles and rules of a building GISMA system are evaluated and an application is presented based on data and GIS techniques for the slope instability studies. Data obtained from historical landslide occurrences were verified with new locations obtained from high resolution orthophotos and Google Earth application. Landslide areas were mapped using Arc Map and finally the Landslide Inventory for the Achaia's Prefecture was created.

Keywords: *GIS, GISMA, WEBGISv.*

Περίληψη

Τα GIS συστήματα είναι πλέον ευρέως διαδεδομένα για την καταχώρηση και χρήση δημογραφικών, τεχνικογεωλογικών, τουριστικών κ.α. στοιχείων. Η τεχνολογία Google Maps και άλλων παρόμοιων παγκόσμιων χαρτών στο διαδίκτυο επέκτεινε την χρήση αυτών και σε άλλες εφαρμογές όπως η χρήση για εύκολη πρόσβαση σε πληροφορίες κάθε τόπου. Η χρήση όμως των GIS μπορεί να επεκταθεί και σε συστήματα διοίκησης και επιστημονικών εφαρμογών με πολλαπλούς χρήστες και πολλαπλές πληροφορίες. Τα συστήματα αυτά ορίζονται από την παρούσα εργασία σαν Γεωγραφικά Συστήματα Πληροφοριών Πολλαπλής Διαχείρισης (GISMA - GIS Multi Administration) τα οποία μπορούν να εφαρμοστούν σε επιχειρήσεις, επιστημονικές ανάγκες, κρατικούς οργανισμούς κ.α. Στην εργασία αυτή εισάγουμε την έννοια των GISMA και ορίζουμε τις βασικές αρχές που πρέπει να πληρούν. Επίσης παρουσιάζεται μια εφαρμογή GISMA, ενός συστήματος καταγραφής κατολισθήσεων για την περιοχή του Νομού Αχαΐας. Το σύστημα μετά από τις ανάλογες δοκιμές παρουσιάζει ικανοποιητική συμπεριφορά.

Λέξεις κλειδιά: *LANDSLIDES, LANDSLIDE INVENTORY, GIS, GISMA, WEBGIS.*

1. Introduction

Geographic information system (GIS) (Clarke, 1986) is a system designed to capture, store, manipulate, analyze, manage, and present all types of geographical data. The acronym GIS is sometimes used for geographical information science or geospatial information studies to refer to the academic discipline or career of working with geographic information systems. In the simplest terms, GIS is the merging of cartography, statistical analysis, and database technology.

A GIS can be thought of as a system—it digitally creates and "manipulates" spatial areas that may be jurisdictional, purpose, or application-oriented. Generally, a GIS is custom-designed for an organization. Hence, a GIS developed for an application, jurisdiction, enterprise, or purpose may not be necessarily interoperable or compatible with a GIS that has been developed for some other application, jurisdiction, enterprise, or purpose. What goes beyond a GIS is a spatial data infrastructure, a concept that has no such restrictive boundaries.

The aim of GISMA (Geographic Information System Multi Administration) is to manage geographical information from multiple sources. In GISMA, the data input, controlled and updated by different users. Users can be located either in the same or in different areas.

In GISMA the users have specific permissions of use of data as the administrator sets. So, the users can input information, take statistical or other results, update data e.t.c., according to their permissions defined by the system administrator.

The GISMA systems can be applied to administrative services, scientific applications, general applications of information where the information is managed directly correlated with topological data (coordinates in space) while simultaneously managing the volume of information and knowledge of these have multiple supply points.

The aim of this work is to give through an application of GISMA system a well documented landslide inventory of the studied area including the mapping of past and recent slope movements, together with the identification and mapping of the predisposing factors of slope instability. The data of the system include (a) past landslide occurrences and existing information on mass movements (historical catalogue) based on historical archives (review of scientific studies, technical reports, geological map descriptions, file reports, university theses, newspaper clippings etc) and (b) recent landslide occurrences based on a systematic interpretation of satellite images and aerial photographs.

2. Landslide Inventory Form

The primary requirement in predicting future landslides is a well documented landslide inventory of the studied area including the mapping of past and recent slope movements, together with the identification and mapping of the predisposing factors of slope instability. This constitutes the basic concept of landslide susceptibility which includes the spatial distribution of factors related to the instability processes in order to estimate zones of landslide – prone areas without any temporal implication (Radbruch, 1970) (Dobrovolny, 1971) (Fernandez et al., 2003) (Ayalew et al, 2004) (Chau. and Chan, 2005) (Chacón et al., 2006).

In this work a Landslide Inventory Form was used for data codification mainly based on landslide report (WP/WLI, 1990), summary (WP/WLI, 1991) and glossary (WP/WLI, 1993.) including the former suggestions regarding landslide causes (WP/WLI, 1994) and rate of movements (WP/WLI, 1995).

It also noted that Landslide inventory derived from historic archives is usually unrepresentative as regards its spatial distribution. This is because the landslide data recorded and obtained by the Authorities (Public Organizations) constitute only cases that have affected residential areas and road network causing financial damages with serious socio – economic consequences. Landslides

that occurred in uninhabited areas without causing damages, usually no recorded. In order to include all that occurrences, a systematic interpretation of satellite images and aerial photographs is needed. That means an inventory form suitably designed to include the obtained remote sensing information.

The inventory form shown in Fig. 1 was appropriately designed (Sabatakakis et al 2013) to include all the required information obtained from the above mentioned different data sources.

<table>
<tr><td colspan="6">Landslide Inventory Form</td><td colspan="2">Inventory Number: 214</td></tr>
<tr><td rowspan="2">Landslide location (Region, Municipality, city – village, area)</td><td colspan="5" rowspan="2">Western Greece, Achaia, Patras, Platani village</td><td colspan="2">Coordinates</td></tr>
<tr><td>lat (°)</td><td>long(°)</td></tr>
<tr><td>Land – use:</td><td colspan="3">Agriculture</td><td colspan="2">Crown elevation (m):</td><td>38°17′42″N</td><td>21°49′45″E</td></tr>
<tr><td>Date of landslide:</td><td colspan="3">22 February 1999</td><td colspan="2">Date of observation:</td><td colspan="2">23 February 1999</td></tr>
<tr><td colspan="3">Ground slope before landslide (degrees):</td><td>30°</td><td colspan="2">Slope orientation:</td><td colspan="2">N30E</td></tr>
<tr><td rowspan="2">Dimensions of landslide:</td><td>length (m):</td><td>300</td><td>width(m):</td><td>190</td><td>depth(m):</td><td>5 – 10</td></tr>
<tr><td>crown length(m):</td><td>120</td><td>volume(m^3):</td><td>210×10^3</td><td>area (m^2):</td><td>28×10^3</td></tr>
<tr><td>Rate of movement:</td><td colspan="3">10 m/day</td><td colspan="2">Orientation of movement:</td><td colspan="2">N50W</td></tr>
<tr><td>Landslide type:</td><td colspan="7">Composite (translational – rotational)</td></tr>
<tr><td>Geology (lithology – structure – weathering)</td><td colspan="4">Plio-Pleistocene stiff clayey marls (CL) and clayey sands (SC). Weathered zone mixed with recent materials.</td><td>mantle thickness (m):</td><td>3 – 5</td></tr>
<tr><td rowspan="2">Landslide causes:</td><td>Triggering</td><td colspan="6">intense and prolonged rainfall</td></tr>
<tr><td>Preparatory</td><td colspan="6">ground conditions, human causes (excavations, loading)</td></tr>
<tr><td>Impacts to:</td><td colspan="7">Residential (one two-story house destroyed), road (failures in cutting slopes 130 m long and in an embankment 90 m long)</td></tr>
<tr><td colspan="2">Landslide reported by (organization):</td><td colspan="6">Region of Western Greece</td></tr>
</table>

Figure 1 - Landslide inventory form completed with a recorded occurrence (Sabatakakis et al., 2013).

In this work, the form of the GISMA shown in Fig. 2, designed as the inventory form was introduced in a recent paper (Sabatakakis et al., 2013).

3. GISMA system

3.1. General Requirements and Principles

It is obvious that in GISMA there are two requirements:

1. The primary knowledge is in different places - users.
2. Data may be administered from various locations

The previous two requirements lead us to the following necessities:

1. Access to the GISMA application from different access points

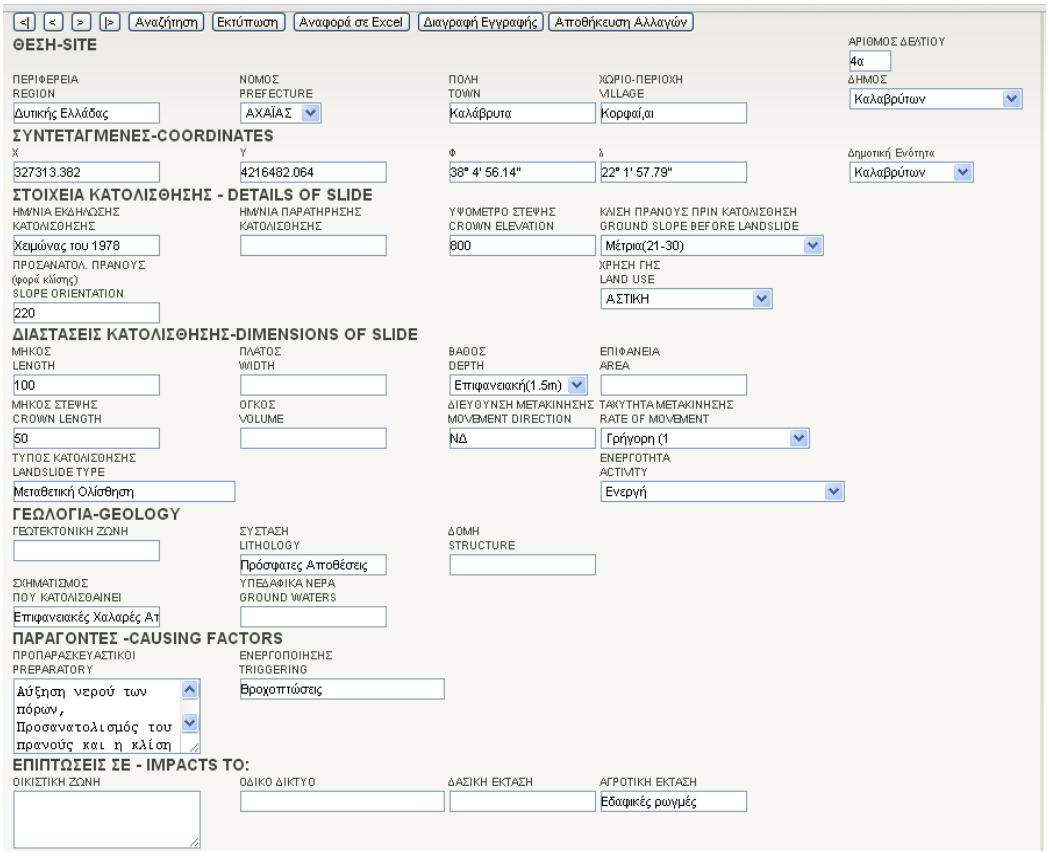

Figure 2 - Landslide inventory form in GISMA completed with a recorded occurrence.

2. Access and management of the application by different authorized users
3. Distinction between primary users in recording and updating information and administration-management users
4. Control whether the information is valid
5. Ability to collect information and process it according to the requirements of the central administration bodies.
6. The systems must be compatible to possible changes in system requirements

The above necessities give the following principles:

(a) Principle of Multiple Access (b) Principle of identity of the information (c) Principle of Role Graduation (d) Principle of Remote-Controlled Access (e) Principle of valid Information (f) Principle of Security (g) Principle of Adaptability/Compatibility

3.2. Implementation

The used technologies are PHP-MySQL (Kerner, 2008) and Google Maps API (Finley, 2011). PHP is an open source server-side scripting language designed for Web development to produce dynamic Web pages. It is one of the first developed server-side scripting languages to be embedded into an HTML source document rather than calling an external file to process data. The code is interpreted by a Web server with a PHP processor module which generates the resulting Web page. It has also evolved to include a command-line interface capability and can be used in standalone graphical applications. PHP can be deployed on most Web servers and also as a

standalone shell on almost every operating system and platform, free of charge. PHP was originally created by Rasmus Lerdorf in 1995 (Kemer, 2008). The main implementation of PHP is now produced by The PHP Group and serves as the formal reference to the PHP language. PHP is free software released under the PHP License, which is incompatible with the GNU General Public License (GPL) due to restrictions on the usage of the term PHP.

MySQL is the world's most used open source relational database management system (RDBMS) as of 2008 that runs as a server providing multi-user access to a number of databases. MySQL is a popular choice of database for use in web applications, and is a central component of the widely used LAMP open source web application software stack (and other 'AMP' stacks). LAMP is an acronym for “Linux, Apache, MySQL, Perl/PHP/Python.”

The following screenshots (Figure 3, Figure 4 and Figure 5) constitute the web page.

This GISMA system was installed in a Web Server with 1TB storage space and a bandwidth 50MBps.

Our GISMA system follows the basic principles of GISMA as described previously.

The system testing with the follow amount of users

24 Ordinary users

10 Registrars

5 Information managers

1 Guarantor

1 System Administrator

The volume of information that was applied was 120 MB.

The behavior of the system was quite satisfactory (maximum time of access record was 2sec).

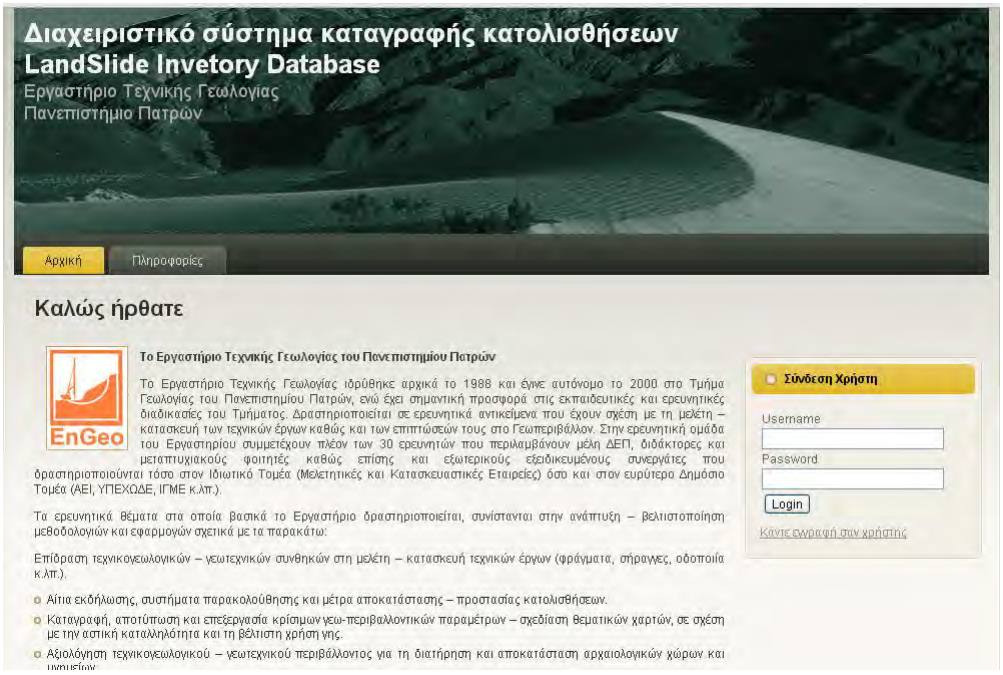

Figure 3 - The users give their username and passwords in order to have access in the system.

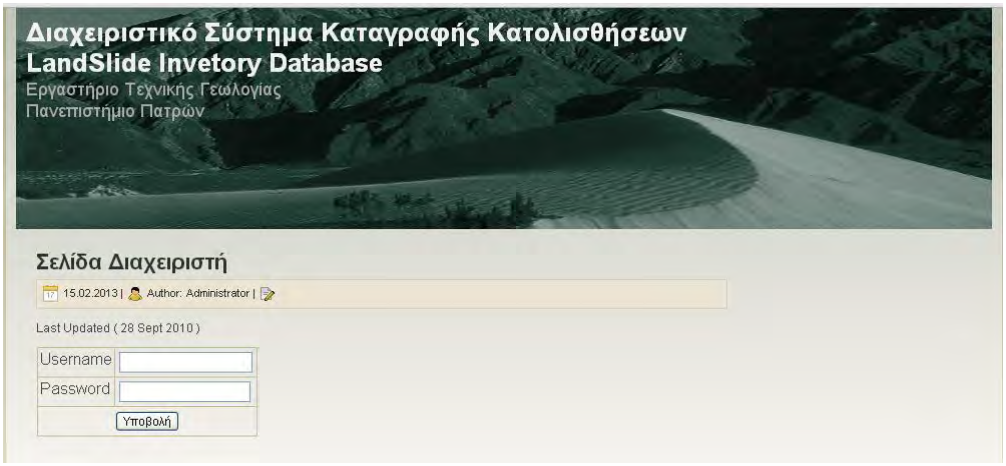

Figure 4 - The administrators give their username and password in order to have access in the system.

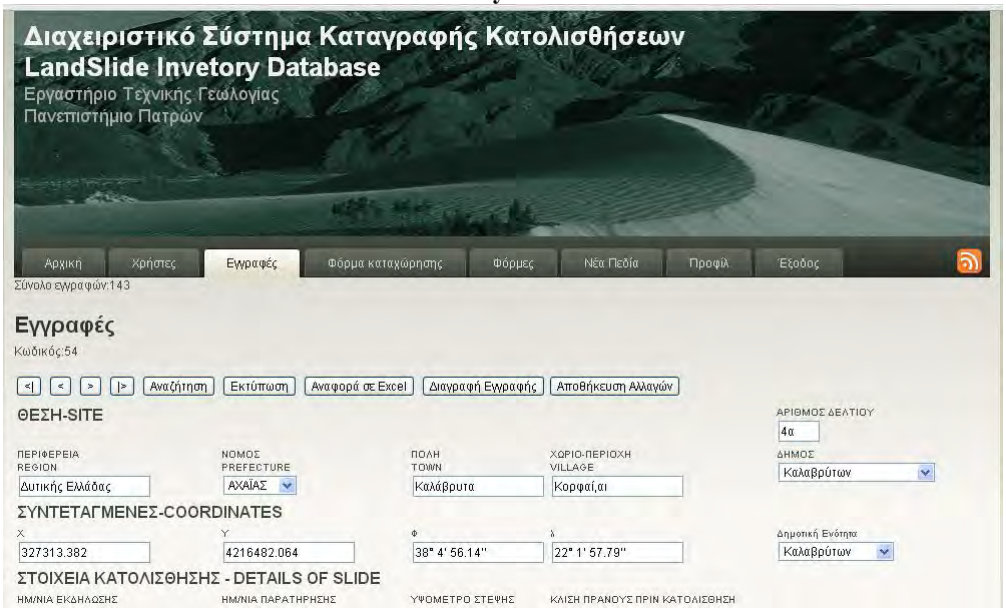

Figure 5 - A data page that the users or administrators can input or update data, take statistical results, take reports about the system.

4. Conclusion

Landslide occurrences are generally governed by numerous spatial predisposing factors that can be, for the purpose of susceptibility assessment, recorded and storage using a regional inventory. A reliable and accurate susceptibility assessment strongly depends on the proper identification and selection of these factors, while the inclusion or omission of some may change significantly the capability of that assessment.

A landslide inventory is usually derived from historical archives, meaning that is unrepresentative of the real spatial distribution, but also from systematic interpretation of satellite images and aerial photographs. The proposed inventory form in this work can be attempted through both sources of existing information on mass movements including historical and remote sensing data.

The created GISMA system already include over than 200 landslide cases occurred in Achaia Prefecture which have been selected as "pilot study". The system was properly designed to record and manage information from multiple users such as undergraduate, postgraduate students and other researchers of Patras University It also constitutes the basic tool for inventory-based, probabilistic approaches for landslide susceptibility zonation mapping.

5. References

Ayalew L. Yamagishi H. and Ugawa N. 2004. Landslide susceptibility mapping using GIS-based weighted linear combination, the case in Tsugawa area of Agano river, Niigata Prefecture, Japan, *Landslides,* 1,73–81, doi:10.1007/s10346-003-0006-9.

Chau K. and Chan J. 2005. Regional bias of landslide data in generating susceptibility maps using logistic regression: case of Hong Kong Island, *Landslides,* 2, 280-290, doi:10.1007/s10346-005-0024-x .

Chacón J., Irigaray C., Fernández T. and El Hamdouni. R. 2006. Engineering geology maps: landslides and geographical information systems, *Bull Eng Geol Environ,* 65, 341–411, doi:10.1007/s10064-006-0064-z.

Clarke C. 1986. Advances in geographic information systems, computers, environment and urban systems*, Computers, Environment and Urban Systems,* 10, 175–184.

Dobrovolny E. 1971. Landslide susceptibility in and near Anchorage as interpreted from topographic and geologic maps, in: *The great Alaska earthquake of 1964* - Geology volume, Publication 1603, U.S. Geological Survey Open-File Report 86-329, National Academy of Sciences, USA, 735–745.

Foresman T. 1997. *The History of GIS (Geographic Information Systems): Perspectives from the Pioneers,* (Prentice Hall Series in Geographic Information Science), Prentice Hall PTR, 1st edition November 10, 1997, 416 pp.

Kerner M. 2008. "PHP 4 is Dead-Long Live PHP 5". InternetNews, Retrieved 20 March 2013. Available online at: http://www.internetnews.com/dev-news/article.php/3725291

Fernández T, Irigaray C., El Hamdouni R. and Chacón J. 2003. Methodology for landslide susceptibility mapping by means of a GIS: application to the Contraviesa Area (Granada, Spain), *Nat Hazards*, 30(3), 297–308, doi:10.1023/B:NHAZ.0000007092.51910.3f .

Finley K. 2011. "7 Cloud-Based Database Services". ReadWriteWeb. Retrieved 20 March 2013. Available online at: http://readwrite.com/2011/01/12/7-cloud-based-database-service

Sabatakakis N., Koukis G., Vassiliades E. and Lainas S. 2013. Landslide susceptibility zonation in Greece, *Natural Hazards,* 65(1), 523 – 543, doi: 10.1007/s11069-012-0381-4.

WP/WLI. 1990. A suggested method for reporting a landslide. International Geotechnical Societies' UNESCO Working Party on World Landslide Inventory (Chairman D Cruden), *Bull Eng Geol Env,* 41(1), 5–12, doi:10.1007/BF02590201.

WP/WLI. 1991. A suggested method for a landslide summary, International Geotechnical Societies' UNESCO Working Party on World Landslide Inventory (Chairman D Cruden)*, Bull Eng Geol Env,* 43, 101–110, doi:10.1007/BF02590177.

WP/WLI. 1993. Multilingual landslide glossary. *International Geotechnical Societies' UNESCO Working Party on World Landslide Inventory* (Chairman D Cruden), BiTech, Richmond, p p 59.

WP/WLI. 1994. A suggested method for reporting landslide causes, International Geotechnical Societies' UNESCO Working Party for World Landslide Inventory (Chairman ME Popescu), *Bull Eng Geol Env,* 50(1),71–74, doi:10.1007/BF02594958.

WP/WLI. 1995. A suggested method for describing the rate of movement of a landslide. International Geotechnical Societies' UNESCO Working Party for World Landslide Inventory (Chairman ME Popescu)*, Bull Eng Geol Env,* 52(1), 75–78 doi:10.1007/BF02602683.

Δελτίο της Ελληνικής Γεωλογικής Εταιρίας, τομ. XLVII , 2013
Πρακτικά 13ου Διεθνούς Συνεδρίου, Χανιά, Σεπτ. 2013

Bulletin of the Geological Society of Greece, vol. XLVII 2013
Proceedings of the 13th International Congress, Chania, Sept. 2013

AN APPLICATION OF GIS ANALYSIS ON STRUCTURAL DATA FROM METAMORPHIC ROCKS IN SANTORINI ISLAND

Marsellos A.E.[1,2], Foster D.A.[2], Min K.[2], Kidd W.S.F.[3], Garver J.[4] and Kyriakopoulos K.[5]

[1] Dept. of Environment and Technology, University of Brighton, BN2 4GJ, U.K.

[2] Dept. of Geological Sciences, University of Florida, Gainesville, Florida 32611, U.S.A.

[3] Dept. of Earth & Atmos. Sciences, State University of New York, U.S.A.

[4] Dept. of Geology, Union College, Schenectady, NY 12308, New York, U.S.A

[5] Dept. of Geology & Geoenvironment, National & Kapodistrian University of Athens, Panepistimioupolis, GREECE 15784, E.U.

Abstract

The Santorini volcanic island is located in the northern Cretan Sea and is part of the recent subduction-related volcanic arc. The opening of Cretan Sea is the result of extension associated with a series of ductile and brittle detachment faults developed since the Middle Miocene. A detachment between two exhumed metamorphic units is exposed at Athinios, on Santorini Island. Two exhumed metamorphic units are identified that show evidence of similar brittle deformation, but distinctive ductile and ductile-brittle structures. Different thermal histories indicate that a Miocene metamorphic unit is juxtaposed structurally below an Eocene metamorphic unit. In this paper, a prediction map of structural observations in Athinios is generated with statistical and GIS software, and shows a spatial distribution consistent with the exposure of two metamorphic units. K-Mean Cluster analysis using SPSS software on lineation azimuths of the metamorphic rock units shows two populations with center values of 347.2^o ± 0.73^o degrees (NNW to N) and 003.4^o ± 0.83^o degrees (N to NNE). NNW-lineation (arc-parallel extension) population belongs to the lower Miocene metamorphic unit and the NNE-lineation represents the Eocene metamorphic unit that was affected by arc-normal extension. A geostatistical map of ordinary Kriging type displays the possible exposed tectonic contacts. This methodology provides a structural prediction map that after field verification facilitates efficient structural and thermochronological sampling.

Key words: *Geostatistical map, arc-parallel extension, brittle deformation.*

Περίληψη

Η ηφαιστειακή νήσος Σαντορίνη βρίσκεται στη βόρεια Κρητική θάλασσα και αποτελεί τμήμα του σύγχρονου ηφαιστειακού τόξου του Αιγαίου. Το άνοιγμα της Κρητικής θάλασσας είναι το αποτέλεσμα μίας σειράς πλαστικών και θραυστικών ρηγμάτων αποκόλλησης που διαμορφώθηκαν από το Μέσο Μειόκαινο. Ένα ρήγμα αποκόλλησης μεταξύ δύο μεταμορφωμένων ενοτήτων εντοπίζεται στην περιοχή Αθηνιό, της νήσου Σαντορίνη. Στις ενότητες των μεταμορφωμένων πετρωμάτων προσδιορίστικαν κοινά

χαρακτηριστικά δομών θραυστικής παραμόρφωσης αλλά διαφορετικά χαρακτηριστικά πλαστικής και πλαστικής-θραυστικής παραμόρφωσης δομές. Διαφορετικές θερμικές ιστορίες μεταξύ των δύο μεταμορφικών ενοτήτων αναδεικνύουν την Μειοκαινική μεταμορφωμένη ενότητα να βρίσκεται τεκτονικά κάτω από την Ηωκαινική μεταμορφωμένη ενότητα. Στην εργασία αυτή, δημιουργήθηκε ένας χάρτης πρόβλεψης της εμφάνισης τεκτονικών χαρακτηριστικών στην περιοχή Αθηνιός δημιουργήθηκε με στατιστικό και γεωγραφικό σύστημα πληροφοριών (G.I.S.) υπολογιστικό πρόγραμμα, όπου παρουσιάζεται μία χωρική κατανομή συναφή με την εμφάνιση των δύο μεταμορφωμένων ενοτήτων. K-Mean ανάλυση συστάδων χρησιμοποιώντας SPSS υπολογιστικό πρόγραμμα δείχνει μία χωρική κατανομή συναφή με την εμφάνιση των δύο μεταμορφωμένων ενοτήτων. Η K-mean ανάλυση συστάδων χρησιμοποιώντας SPSS υπολογιστικό πρόγραμμα σε αζιμούθια γραμμώσεων των μεταμορφωμένων ενοτήτων και δείχνει δύο πληθυσμούς με αντίστοιχες ιδιοτιμές $347.2^o \pm 0.73^o$ μοίρες (ΒΒΔ προς Β) και $004^o \pm 0.83^o$ μοίρες (Β προς ΒΒΑ). Ο πληθυσμός των ΒΒΔ-γράμμωσης (παράλληλη γράμμωση στο τόξο) ανήκει στην κατώτερη Μειοκαινική μεταμορφωμένη ενότητα και ο πληθυσμός της ΒΒΑ-γράμμωσης αντιπροσωπεύει την Ηωκαινική μεταμορφωμένη ενότητα που έχει επηρεαστεί από την κάθετη γράμμωση στο ηφαιστειακό τόξο. Ο γεωστατιστικός χάρτης τύπου ordinary Kriging δείχνει πιθανές εμφανίσεις των τεκτονικών επαφών των δύο ενοτήτων. Η μεθοδολογία αυτή μας παρέχει τη δυνατότητα δημιουργίας χάρτη πρόβλεψης εμφάνισης δομών που διευκολύνει την εργασία υπαίθρου για τεκτονικές και δομικές αναλύσεις καθώς και για πιο αποτελεσματική δειγματοληψία θερμοχρονολόγησης.
Λέξεις κλειδιά: *Γεωστατιστικός χάρτης, παράλληλος εφελκισμός τόξου, θραυστική παραμόρφωση.*

1. Introduction

Applied geographical information system (GIS) using structural data integrated with GPS data has become a routine in the field with the use of new and inexpensive technology for digital data collection. The Android platform and the iPhone and iPad have fundamentally changed mobile computing and suggest a new paradigm that will change the nature of field computing and data acquisition. There have been many discussions over the rapid evolution of digital mapping equipment and applications (e.g. Whitmeyer et al., 2010; Pavlis et al., 2012; Doublier & Hartley, 2012). This raises the need of hands-on geological and geostatistical exercises for students to increase proficiency using modern techonology for efficient high-resolution field data collection. Tablets or cell phones using integrated GPS, gyroscope, and digital compass sensors operating on numerous operational systems have allowed easier field mapping and abundant high-resolution structural data collection (McCaffrey, et al., 2005).

Statistical approach to structural field data applying normal distribution or/and cluster analysis has the potential to provide meaningful classification of metamorphic rocks. Geostatistical methods may reveal distinct structural fabrics thereby defining separate and unique metamorphic units and aid in interpreting tectonic contact. Metamorphic rocks of similar metamorphic conditions but slightly different stretching lineations may require geo- or/and thermo-chronology to provide adequate distinction of those rocks. An efficient method is to integrate all the field data into a GIS and to yield prediction maps to reveal possible tectonic contacts of more than one metamorphic units and suitable sampling locations for structural and thermochronological studies. We present in this paper a GIS technique that can be applied at the field. This methodology has been applied on structural data from metamorphic rocks that exhibit very similar lineations such as the metamorphic rocks of Santorini, and a GIS map has revealed possible locations of tectonic contact that brings two different metamorphic rock units exposed in Santorini.

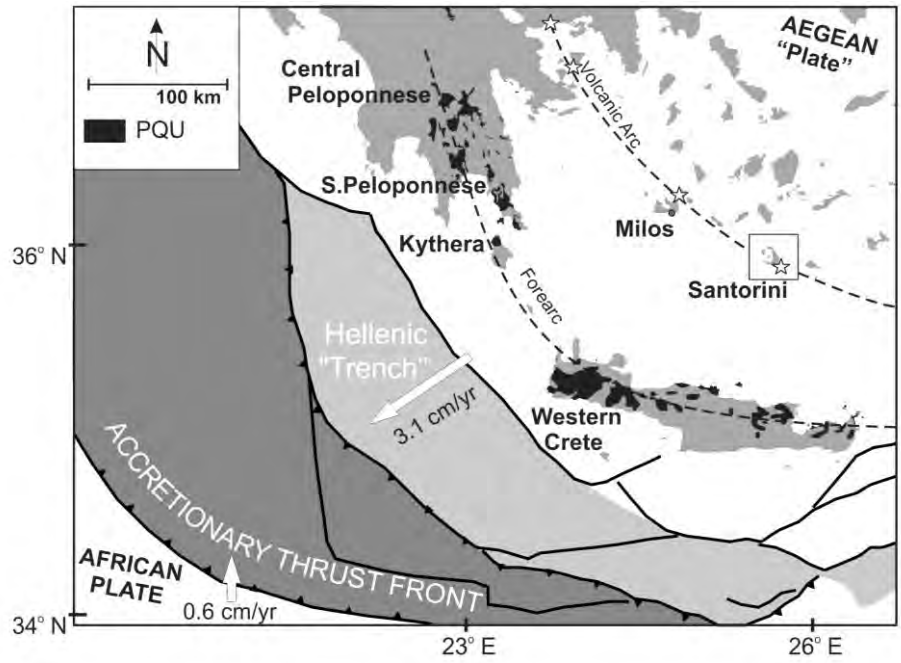

Figure 1 - Tectonic setting of the Hellenic volcanic and forearc which are the result of the interaction between the northward African subducting plate and the overriding Aegean micro-plate. Present GPS Eurasia-Africa relative velocity and average western Hellenic Arc-Africa relative velocity (derived from the average of five stations in western-central Crete, Kythera, and south Peloponnese) after McClusky et al., (2000).

The importance of those rocks is that they show two different post-metamorphic cooling ages and associated exhumation paths in Eocene and Miocene times, respectively (Marsellos et al., 2012). Other Aegean detachment faults such as the Potamos detachment fault in Kythera (Marsellos & Kidd, 2008) or the southeastern Peloponnese detachment (Marsellos et al., 2010) exhibit metamorphic rocks of similar age, but very different structural-oriented data such as lineations of perpendicular relationship. Very distinctive lineations of approximately 90^{o} degrees azimuth variation allow easier study of their distribution. On the contrary, lineation population data that comprise one normal distribution such as the Santorini metamorphic rocks may require an advanced statistical approach such as cluster analysis.

The Athinios site was selected because metamorphic rocks are exposed along an appropriate vertical profile allowing detailed analysis of fabric orientations in the exposed Santorini metamorphic rocks. In Athinios port, metamorphic rocks are exposed along an approximately 280 m vertical profile and a 3,200 m horizontal section along the road to the port from the mainland.

2. Tectonic Setting and Geology of Santorini

One of the most prominent tectonic features of the South Aegean is the Hellenic Arc, which consists of the forearc (Peloponnese, Kythera, Crete, Karpathos and Rhodes) and an inner volcanic arc (Attiki, Methana, Milos, Santorini, Nisiros, Kos). Both arcs are related to subduction of the African plate beneath the European plate and exhumation of high-pressure and low-temperature rocks, during multiple events and via multiple detachment faults (e.g. Fassoulas et al., 1994; Thomson et al., 1998; Lister et al., 2001, Brix et al., 2002, Jolivet et al., 2003, Brun & Faccena, 2008; Marsellos et al., 2010).

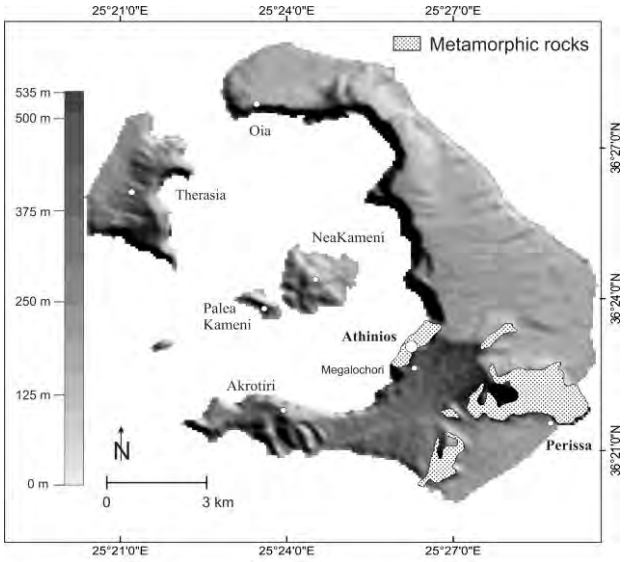

Figure 2 - A hillshade map of Santorini volcanic island. Dot-shaded areas show the exposure of the metamorphic rocks.

The Aegean Sea is an excellent example of episodic extension and exposes a wide range of regional detachment faults (e.g. Fassoulas et al., 1994; Thomson et al., 1999; Brix et al., 2002; Jolivet et al., 2003; Marsellos & Kidd, 2008; Ring et al., 2010; Skourtsos & Lekkas, 2010) and localized multi-detachments with more than one extension direction as observed in Kythera and Peloponnese (Marsellos et al., 2010). Correlation between structural data and thermochronological data has been shown to be useful in deconstructing multi-extensional complex tectono-low-thermal histories of HP-rocks associated with arc-normal or/and arc-parallel extensional detachments

Santorini is located at the center of the Recent South Aegean volcanic arc (Figure 1) where a series of active faults accommodate active extension and granitoid intrusion. The metamorphic basement of Santorini consists principally of schists, metapelites, metasandstones and quartzites, metaconglomerates, marbles and metavolcanics (Tataris, A, 1964; Skarpelis & Liati, 1987;1990). Santorini is dominated mainly by a NNW-SSE extensional stress regime (Mountrakis et al., 1996; Kilias et al., 1996). In Santorini Island, metamorphic rocks occur locally in the southeastern part (Perissa), in the caldera walls (Athinios), and in the outer rim of the island (Figure 2). These rocks have been affected by HP/LT (blueschist facies) metamorphism, and also, they have been intruded by an I-type granite of Late Miocene age (~ 9.5 Ma; Skarpelis et al., 1992) which is located at the southernmost part of the Miocene Cycladic granitoid province. Contact metamorphism has been also studied showing skarns and associated ore minerals (Skarpelis and Liati, 1987). Carbonate rocks occur above the metamorphic basement as recrystallized Triassic limestones (Papastamatiou, 1956; Blake et al., 1981). Carbonate and metamorphic rocks are overlain by numerous Pliocene to recent pyroclastics and lavas series. Santorini started to erupt since 200 ka (Druitt and Francaviglia, 1992), with caldera formation at~ 3.6 Ka during the Minoan eruption (Druitt et al., 1999), and recent activity including the latest eruption being in the 1950's.

3. Methods

3.1. Geographical Information System (GIS) Structural Maps

To explore the spatial distribution of the structural data of the metamorphic rocks in Athinios, we use GIS software (ArcGIS 10, ESRI). Structural data such as stretching lineation azimuth (n=131) were collected from the metamorphic rocks along a 3,200 m section from the road of the port of

Athinios towards Megalochori village (Figure 2, 3). Lineation data were used to develop a contour map using the ordinary krigering geostatistical procedure. A trend analysis was used to examine global trends and directional influences (anisotropy). Due to the topography of this study area data collection shows a persistent slope direction that occurs. This nonrandom component of the surface has been evaluated (Figure 5) and eliminated using a second-order polynomial function assigned by the program. The normality of the data has been verified with a quantile-quantile (QQ) plot (Figure 4). A semivariogram/covariance cloud allowed us to examine the spatial autocorrelation between the measured sample points. A surface map of stretching lineation azimuth data has been produced and shown in Figure 6. This map shows an interesting spatial distribution of two distinctive lineated rocks. Further sampling and dating of those has verified the existence of two metamorphic units (Marsellos et al., 2012).

Figure 3 - A Google Earth image (GeoEye scene of 29/07/2010 drapped over a digital elevation model) from the port Athinios in Santorini where a continuous outcrop of approximately 3,200 meters (dashed white line) of exposed metamorphic rocks has been studied.

3.2. Cluster Analysis

To statistically verify the existence of the two geological units in the examined location, we apply the statistical method of k-means cluster analysis in the azimuth lineation data. The k-means cluster analysis is a method of cluster analysis that aims to partition the observations (n=131 observations) into k clusters in which each observation belongs to the cluster with the nearest mean (Aldenderfer & Blashfield, 1984; Everitt, 1993). k-means cluster analysis showing two clusters of two different tectono-metamorphic rocks has validated at least two major sampling locations for thermochronological analysis. Those samples, later on, have indicated an Eocene and a Miocene metamorphic unit (Marsellos et al., 2012). Figure 7 and Table 1 shows the azimuth lineation data clusters after the application of the cluster analysis.

Cluster analysis was then implemented in a statistical software package (SPSS). Azimuth lineation data were normalized to avoid artifact clusters in which degree unit yields such as clusters nearby high values or very low values around North direction (000-030^o vs. 330^o-360^o). Two clusters were revealed and plotted on a stereonet with equal angle projection (Figure 7). The range of the lineation values for each population (cluster) has verified the GIS prediction map and shows the possible exposure of the two metamorphic rock units and their associated tectonic contact. This map (Figure 6) utilizes the azimuth of the lineation data to investigate the spatial distribution of those two clusters and determine possible locations of the tectonic contact that brings the Eocene metamorphic unit against the Miocene metamorphic unit.

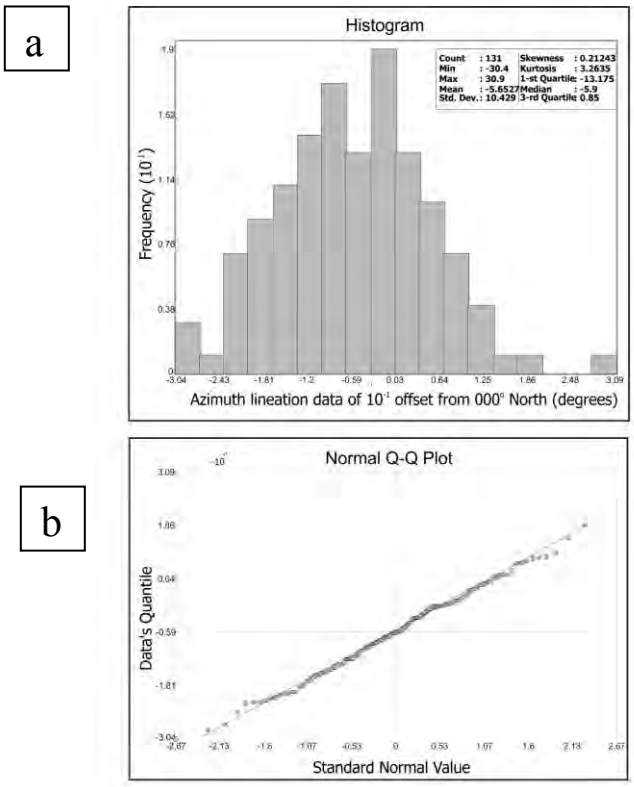

Figure 4 - (a) A histogram that shows the azimuth lineation data from the metamorphic rocks of Santorini. They follow a normal distribution. (b) A Quantile-Quantile (QQ) plot has verified the normality of the data.

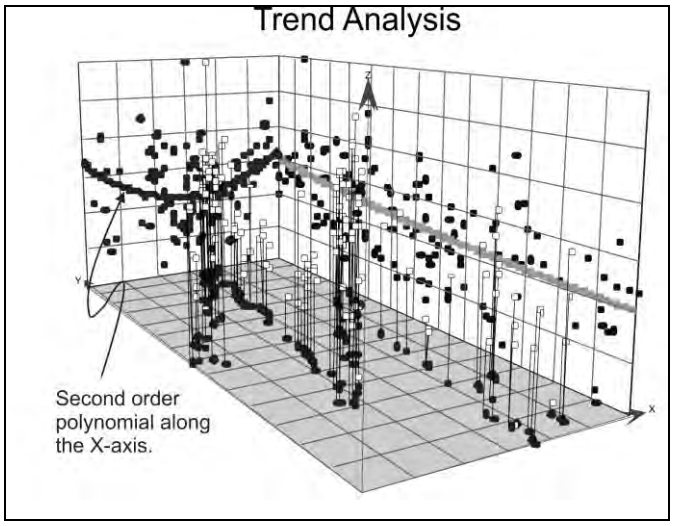

Figure 5 - Trend analysis of the azimuth lineation data along the 3.200 meters outcrop of metamorphic rocks in Athinios. X-axis projected points show the non-random surface component (black points; westward aspect of the slope), while the Y-axis projected points show no significant trend pattern.

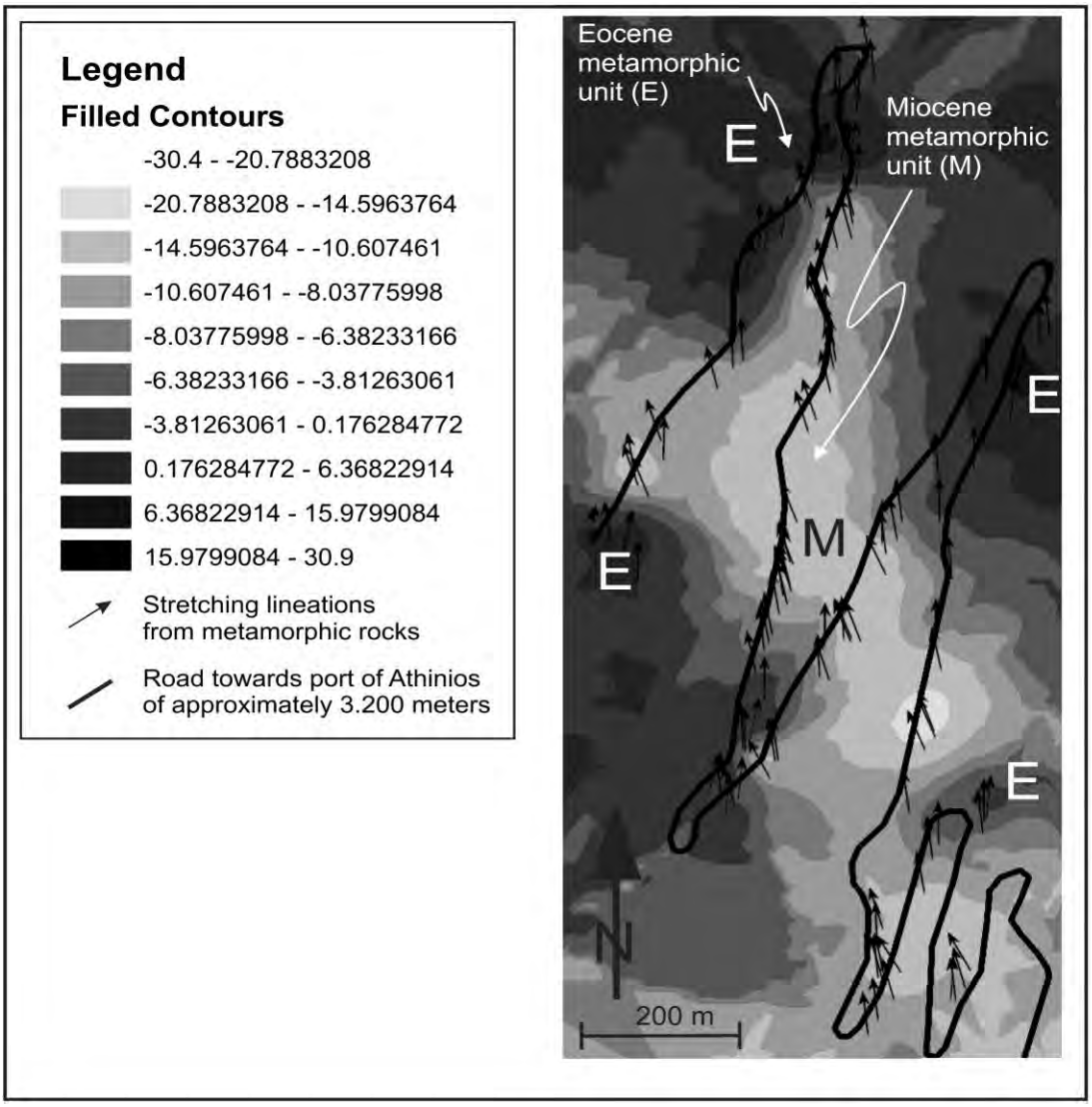

Figure 6 - Prediction map of the azimuth lineation data at the Athinios slope area where the Eocene metamorphic unit (E) rocks are in tectonic contact against the beneath Miocene metamorphic unit (M) of Santorini are exposed along the 3.200 meters outcrop of metamorphic rocks in Athinios. Considering zero as a North reference, data range from -30.4^{o} degrees (that is 329.6) to 30.9^{o} (030.9).

Table 1 - Cluster analysis of azimuth lineation data from the metamorphic rocks of Athinios, Santorini.

Rock Unit	N	Range	Minimum	Maximum	Mean	Std. Error	Std. Deviation
LMU	56	33.60	27.70	61.30	34.37	0.83	6.19
UMU	75	26.70	.00	26.70	17.57	0.73	6.34

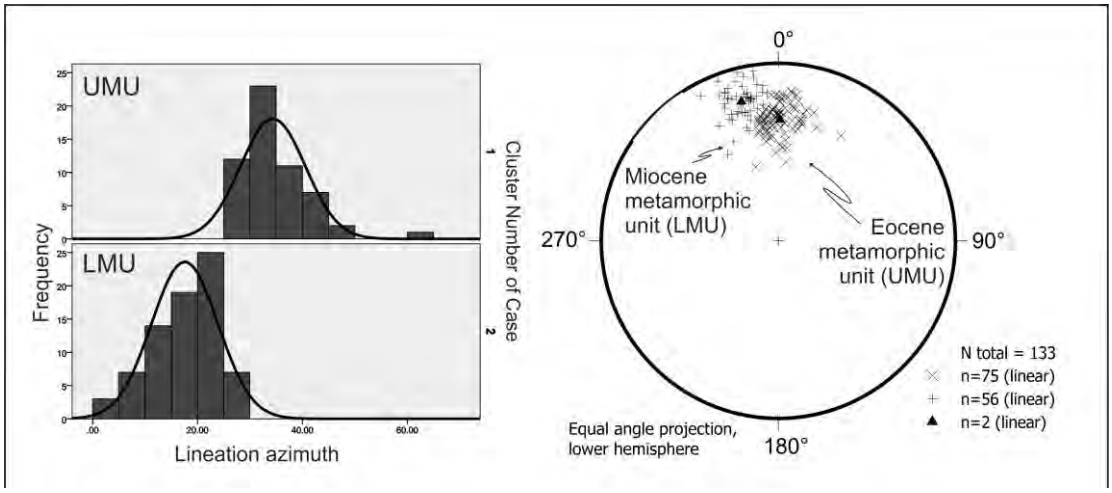

Figure 7 - Two populations of azimuth lineation data derived by cluster analysis from the upper metamorphic unit (UMU) rocks and lower metamorphic unit (LMU) rocks of Athinios, Santorini. Stereonet showing the two clusters projected on an equal angle projection, lower hemisphere.

4. Results and interpretation

4.1. Structural Data Interpolation Map Using GIS

Lineation directions (n=131) range from 329.6 ^{o} to 030.9 ^{o} degrees. Considering zero as a North reference, data range from -30.4^{o} (that is 329.6) to 30.9^{o} (030.9) (Figure 6). This is a range of approximately 60^{o} degrees, compared to some 90 ^{o} degrees of variation shown in the Kythera lineation data (Marsellos & Kidd, 2008; Marsellos et al., 2010). A lineation histogram (Figure 4) of the Santorini-Athinios azimuth data shows that they follow a normal distribution with a mean value at 354.3^{o} ± 0.9^{o}.

Cluster analysis in this normal distribution has shown two subsequent populations. The first ranges from 329.6 ^{o} to 356.3 ^{o} with a mean value at 347.2^{o} ± 0.73^{o} and a standard deviation of 6.2^{o}, and the second ranges from 357.3 ^{o} to 030.9^{o} with a mean value at 003.4^{o} ± 0.83^{o} and standard deviation of 6.3^{o}. Data were plotted in a stereonet and the two clusters may imply (Figure 7) that there are two metamorphic units with similar approximately N-S direction stretching lineations in contact with each other at the sudden changes of azimuth lineation directions.

All the tectonic contacts between the upper metamorphic cooling unit (Eocene) against the lower metamorphic cooling unit (Miocene) were almost impossible to locate in the field. Construction of a prediction map showing the lineation azimuth distribution of the metamorphic rocks, and the spatial distribution of the two clusters, has facilitated mapping and constraining locations of tectonic contacts. A classification map derived after assigning the two populations of lineation data to the known cooling ages of the Eocene and Miocene metamorphic rock units reveals the possible spatial distribution of those two units (Figure 6).

The results of the predicted locations of contacts were then verified in the field, which facilitated the entire mapping process and further sampling. It allowed us to locate major outcrops that show the occurrences of those two metamorphic units that exhibit two different clusters of stretching lineation populations, and may imply different extensional contexts.

The first population of lineation data shows a range from NNE- to N-trending (Figure 7), while the second population ranges from NNW- to N-trending lineation. Clustering of those lineations from the two metamorphic rocks may imply two different extensional contexts. The Hellenic arc ex-

tends along a NW-SE direction from Peloponnese through Kythera and western Crete, and it turns E-W in central and eastern Crete. It is reasonable to assume, therefore, that the NNE-trending lineation cluster of the Eocene metamorphic rocks was caused by Eocene arc-normal extension. Whereas, the arc-parallel extension previously documented from Miocene Kythera metamorphic extensional structures is likely equivalent to the NNW-trending lineation cluster from the Miocene Santorini metamorphic rocks. The Santorini Miocene extensional structures that show almost arc-parallel extension suggesting that arc-expansion enhanced by intensive arc-parallel extension has took place adjacent to the forearc and toward inner zones such as at the recent volcanic arc and nearby the backarc, as well as the forearc itself.

5. Conclusion

A geostatistical map of ordinary Kriging type displays the detailed distribution of two lineation populations corresponding to two distinctive metamorphic units. This methodology allows a quick mapping procedure for revealing tectonic contacts or locations for structural and/or thermochronological sampling, such as the Santorini metamorphic rocks, which show different cooling age and similar stretching lineations.

6. References

Aldenderfer M.S. and Blashfield R.K. 1984. *Cluster analysis*, Published in Beverly Hills, Sage Publications.

Blake M.C. Jr Bonneau M., Geyssant J., Kienast J.R., Lepvrier G., Maluski H. and Papanikolaou D. 1981. A geologic reconnaissance of the cycladic blueschist belt, Greece, *Geological Society of America*, 92, 247-254.

Brix M.R., Stockhert B., Seidel E., Theye T. Thomson N. and Kuster M. 2002. Thermobarometric data from a fossil zircon partial annealing zone in high pressure-low temperature rocks of eastern and central Crete, Crete, *Tectonophysics,* 349, 309-326.

Brun J.P. and Faccenna C. 2008. Exhumation of high-pressure rocks driven by slab rollback, *Earth and Planetary Science Letters*, 272, 1-7.

Doublier M.P. and Hartley G. 2012. Digital technologies and regional field mapping: an overview, *Structural Geology and Resources*, 70-74.

Druitt T.H. and Francaviglia V. 1992. Caldera formation on Santorini and the physiography of the islands in the late Bronze Age, *Bull. Volcanol.,* 54, 484-493.

Druitt T.H., Edwards L., Mellors R.M., Pyle D.M., Sparks R.S.J., Lanphere M., Davies M. and Barriero B. 1999. The Santorini Volcano, *Geological Society Special Memoir*, vol. 19, Geological Society Pub House, London, 165 pp.

Everitt B.S. 1993. *Cluster analysis*, 3rd ed., Published in London, E. Arnold, New York, Halsted Press.

Fassoulas C., Kilias A. and Mountrakis D. 1994. Post-nappe stacking extension and exhumation of the HP/LT rocks in the island of Crete, Greece, *Tectonics,* 13, 127–138.

Jolivet L., Faccenna C., Goffé B., Burov E. and Agard P. 2003. Subduction tectonics andexhumation of high-pressure metamorphic rocks in the Mediterranean orogens, *Am. J. Sci.,* 303, 353–409.

Kilias A., Mountrakis D., Tranos M. and Pavlides S. The prevolcanic metamorphic rocks of Santorini island: Structural evolution and kinematics during the Tertiary (South Aegean, Greece) - *EVOP, 2nd Workshop on European Laboratory Volcanoes*, In: Casale R., Fytikas M. et al., 23-36., 1996.

Lister G.S., Forster M.A., and Rawling T.J. 2001. Episodicity during orogenesis, *Geological Society, London*, Special Publications, 184, 89-113,

Marsellos A.E. and Kidd W.S.F. 2008. Extension and Exhumation of the Hellenic Forearc Ridge in Kythera, *J.Geology*, vol. 116, 640-651.

Marsellos A.E., Kidd W.S.F. and Garver J.I. 2010. Extension and exhumation of the HP/LT rocks in the Hellenic forearc ridge, *American Journal of Science*, vol. 310, 1-36.

Marsellos A.E., Foster D. A., Min K. , Kamenov G. D., Kidd W.S.F., Garver J. and Kyriakopoulos K. 2012. A structural and thermochronological study of Santorini detachment in Santorini Island, Aegean Sea, *American Geophysical Union*, December 2012, San Francisco, Abstr. Program. T43E-2722.

McCafrey K.J.W., Jones R.R., Holdsworth R.E., Wilson R.W., Clegg P., Imber, J., Holliman N. and Trinks I. 2005. Unlocking the spatial dimension: digital technologies and future of geoscience fieldwork, *J. of Geol. Soc. of London*, v. 162, 1-12.

McClusky S., Balassanian S., Barka A., Demir C., Ergintav S., Georgiev I., Gurkan O., Hamburger M., Hurst K., Kahle H., Kastens K., Kekelidze G., King R., Kotzev V., Lenk O., Mahmoud S., Mishin A., Nadariya M., Ouzounis A., Paradissis D., Peter Y., Prilepin M., Reilinger R., Sanli I., Seeger H., Tealeb A., Toksoz M.N. and Veis. G. 2000. Global Positioning System constraints on plate kinematics and dynamics in the eastern Mediterranean and Caucasus, *Journal of Geophysical Research*, Vol. 105, No. B3, 5695-5719.

Mountrakis D., Pavlides S., Chatzipetros A., Meletlidis M., Tranos G., Vougoukalakis G. and Kilias A. Active deformation of Santorini, *EVOP, 2nd Workshop on European Laboratory Volcanoes,* In: Casale R., Fytikas M. et al., 13-22., 1996.

Papastamatiou L. 1956. Sur l'ege des calcaires cristallins de l' ile de Thera (Santorin), *Bull. Geol. Soc. Greece*, 3, 1, 104-113.

Pavlis T., Hurdado J.M., Langford R.P. and Serpa L.F. 2012. Field geology in the 21st century: not what you learned in school, *Structural Geology and Resources,* 141-143.

Ring U., Glodny J., Will T. and Thomson S. 2010. The Hellenic Subduction System: High-Pressure metamorphism, exhumation, normal faulting, and large-scale extension. Reviews in advance, *Annu. Rev. Earth Planet. Sci.*, 38, 45-76.

Skarpelis N. and Liati A. 1987. Granite intrusion, skarn formation and mineralization in the metamorphic basement of Thera, Cyclades, Greece, *5th Meeting European Geological Societies*, Dubrovnik, Abstr., p. 81.

Skarpelis N. and Liati A. 1990. The prevolcanic basement of Thera at Athinios: Metamorphism, Plutonism and Mineralization, *Proc. of the Third International Congress "Thera and the Aegean World III"*, Hardy D.A. ed., The Thera Foundation, London, 2, 172- 182.

Skarpelis N., Kyriakopoulos K. and Villa I. 1992. Occurrence and $^{40}Ar/^{39}Ar$ dating of a granite in Thera (Santorini, Greece), *Geologische Rundschau 1992*, Volume 81, Issue 3, 729-735.

Skourtsos E. and Lekkas S. 2010. Extensional tectonics in Mt Parnon (Peloponnesus, Greece), *Int. J. Earth Sci. (Geol. Rundsch.)*, Volume 100, Issue 7, 1551-1567.

Tataris A. 1964. The Eocene in the semi-metamorphosed basement of Thera island, *Bull. Geol. Soc. Greece*, 6, 232- 238 (in Greek with English summary).

Thomson S.N., Stockhert B. and Brix M.R. 1998. Thermochronology of the high-pressure metamorphic rocks of Crete, Greece: implications for the speed of tectonic processes, *Geology,* 26, Vol. 259-262.

Thomson S.N., Stockhert B. and Brix M.R. 1999. Miocene high-pressure metamorphic rocks of Crete: rapid exhumation by buoyant escape, In Ring, U., Brandon, M., Lister, G.S., Willet, S. (editors), Exhumation Processes: Normal Faulting, Ductile Flow and Erosion. *Journal of Geological Society of London*, Special Publication, Vol. 154, 87-107.

Whitmeyer S.J., Nicoletti J. and De Paor D.G. 2010. The digital revolution in geologic mapping, *GSA Today*, 4-10.

Δελτίο της Ελληνικής Γεωλογικής Εταιρίας, τομ. XLVII , 2013
Πρακτικά 13ου Διεθνούς Συνεδρίου, Χανιά, Σεπτ. 2013

Bulletin of the Geological Society of Greece, vol. XLVII 2013
Proceedings of the 13th International Congress, Chania, Sept. 2013

LANDSLIDE DETECTION USING ALOS OPTICAL AND RADAR DATA. A CASE STUDY FROM THE ILIA PERFECTURE

Nikolakopoulos G. K.[1], Choussiafis Ch.[2] and Karathanassi V.[2]

[1] University of Patras, Department of Geology, Sector of Applied Geology and Geophysics, knikolakop@upatras.gr,

[2] National Technical University of Athens, School of Rural and Surveying Engineering, christos_hous@hotmail.com, karathan@survey.ntua.gr,

Abstract

In this study the usefulness of the ALOS optical and radar data for landslide monitoring is examined. ALOS contains three sensors, commonly referred to as the "three eyes" of ALOS. These sensors are: the Panchromatic Remote-Sensing Instrument for Stereo Mapping (PRISM), the Advanced Visible and Near Infrared Radiometer type 2 (AVNIR-2), and the Phased Array type L-band Synthetic Aperture Radar (PALSAR). The area of study is located in a small village named Sykies near to the city of Andritsena in Western Peloponnese. The area suffered during the last years from enormous fires. As a result many landslides have been recorded. One of the latest Landslides has been recorded on January 2009 as a consequence of heavy rains. That landslide was mapped in situ using differential GPS. The possibility of detecting and mapping the specific landslide using ALOS data is examined in this study and the results are presented. Thirty ALOS radar images within a period of three years, two ALOS Prism data sets and two ALOS AVNIR collected over the same area within a year were used.

Key words: *Interferometry, photogrammetry, landslide.*

Περίληψη

Στην εργασία αυτή παρουσιάζεται η χρήση οπτικών δεδομένων καθώς και ραντάρ δεδομένων από το δορυφόρο ALOS για τον εντοπισμό μίας κατολίσθησης. Ο δορυφόρος ALOS διαθέτει τρεις δέκτες. Έναν παγχρωματικό δέκτη (PRISM) που λαμβάνει στερεοεικόνες, ένα πολυφασματικό δέκτη (AVNIR-2) και ένα δέκτη ραντάρ (PALSAR). Η περιοχή μελέτης εντοπίζεται στη Δυτική Πελοπόννησο στην περιοχή της Ανδρίτσαινας και συγκεκριμένα στο χωριό Συκιές. Η περιοχή υπέστη σημαντικές καταστροφές από τις πυρκαγιές του 2007. Σαν αποτέλεσμα πολλές κατολισθήσεις καταγράφησαν τα επόμενα χρόνια. Η συγκεκριμένη κατολίσθηση σημειώθηκε τον Ιανουάριο του 2009 συνεπεία πολύ έντονων βροχοπτώσεων και χαρτογραφήθηκε στο πεδίο με χρήση DGPS. Η δυνατότητα εντοπισμού της κατολίσθησης από τα δορυφορικά δεδομένα ALOS εξετάζεται στην παρούσα εργασία και παρουσιάζονται τα αποτελέσματα. Γίνεται χρήση τεχνικών συμβολομετρίας για την επεξεργασία τριάντα εικόνων ραντάρ καθώς και χρήση φωτογραμμετρικών τεχνικών για την επεξεργασία των στερεοσκοπικών οπτικών δεδομένων.

Λέξεις κλειδιά: *Συμβολομετρία, φωτογραμμετρία, κατολίσθηση.*

1. Introduction

The term landslide includes a wide range of ground movement types, such as slides, falls, flows etc. mainly based on gravity with the aid of many conditioning and triggering factors. Especially in the last two decades, there is an increasing international interest on the landslide susceptibility, hazard or risk assessments.

Rockslide activity endangers surface and subsurface infrastructure, and is able to trigger other hazards, by, for instance, damming a river and causing a flood hazard. Digital image analysis techniques for mapping landslides and monitoring related elevation changes from repeated DEMs are comparably often applied (Mantovani et al, 1996; Mass et al., 1997; Weber and Herrmann, 2000; Chandler, 2001; Nikolakopoulos et al., 2005). Some other studies focused mainly on the use of remote sensing data on horizontal displacement measurements (Powers et al., 1996; Baum et al., 1998; Kaab, 2000).

In this paper a combined use of Remote Sensing, GIS and GPS data for landslide mapping is presented. The possibility of detecting and mapping the specific landslide using ALOS PALSAR radar data and interferometric techniques, ALOS PRISM stereo data and photogrammetric techniques and ALOS VNIR data is examined and the results are presented. Thirty ALOS radar images within a period of three years, two ALOS Prism data sets and two ALOS AVNIR collected over the same area within a year were used. The orthorectified ALOS optical data, the DSM produced by the stereo images, and the GPS measurements were implemented in ARCGIS in order to make the necessary measurements and create the final maps.

2. Study Area

The area of study is located in a small village named Sykies near to the city of Andritsena in Western Peloponnese. The area is characterized by large seismicity and the Landslides phenomena are very often. The area is covered by geological formations of the Pindos zone. The base of the Pindos zone is a clastic formation overlaid by resistant limestones of Upper Triassic to Liasian age. Alternations of radiolarites (Dogerian-Malmian age), consisting of mudstones and ribbon-bedded cherts and Lower Cretaceous limestones are next in the sequence (Jacobshagen et al., 1978). An Upper Cretaceous clastic formation (known in the literature as 1st flysch), including mudstones, cherts, terrigenous turbidites and pelagic limestones, with layers of chert is next in the sequence (Piper and Pe-Piper, 1980). The Eocene flysch rocks complete the sequence (Papanikolaou, 1986).

The area also suffered during the last years from enormous fires. As a result many landslides have been recorded. One of the latest Landslides has been recorded on January 2009 as a consequence of heavy rains.

3. Landslide Mapping

A few days after the landslide took place, in situ mapping was done using a Mobile Mapper GPS receiver with an external antenna and EGNOS correction (Figure 1).

The produced map of the landslide is presented in Figure 2. The Landslide has affected a small road in the village and a garden. The head of the landslide is just in front of two olive trees (Figures 3 and 4) about two meters from the house basement. The head of the landslide is about 27 meters long. At the south edge of the landslide a small river is present. The head and the foot of the landslide are mapped with the GPS (Figure 1). In Figure 2 the black dashed line represents the head of the landslide while the red one represents the foot of the landslide. The road network is presented with black color line. A part of the road has collapsed (Figure 4).

Figure 1 - The in situ mapping of the landslide using a Mobile Mapper GPS receiver with an external antenna.

4. ALOS Radar Data Processing

4.1. Method Description

Standard two pass Differential SAR Interferometry (DInSAR) was performed to detect the general ground deformation on the study area and specifically to identify and get information on the activity of the known landslide on Sykies. According to this technique the topographic phase contribution is removed from an interferogram in which interferometric phase surface displacement is recorded (Massonet et al., 1993). According to a general model, interferometric phase can be written as:

$$\varphi = \varphi_{flat} + \varphi_{topo} + \varphi_{defo} + \varphi_{atm} + \varphi_{noise} \quad (1)$$

where φ is the interferometric phase obtained from two SAR acquisitions, φ_{flat} is the flat earth phase, φ_{topo} is the topographic phase, φ_{defo} is the deformation phase, φ_{atm} is the atmospheric delay phase and φ_{noise} is the noise. In order to detect the ground deformation by unwrapping the phase φ, it is necessary to eliminate all the components of equation (1) apart from φ_{defo} component. The flat earth component can be removed by using the orbit information correction, as well as an external DEM to generate the topographic phase which is then subtracted from the interferogram (Zhou et al., 2005; Yu and Ge, 2010). The topographic phase cancellation performed by the generation and subtraction of the so-called synthetic or simulated interferogram. Within this study, the used external DEM which used for the elimination of φ_{flat} and φ_{topo} components, was a DEM provided by KTIMATOLOGIO S.A.. This DEM has a 5m pixel size, and its average accuracy was estimated to be 4.08m according to GCPs evaluation for confidence level 95%. The specific DEM is the most accurate official DSM covering the Greek territory. As far as the atmospheric component concerns, it mainly depends on the water vapor content of the atmosphere and is considered as an error in non atmospheric applications. Finally, the noise component refers to thermal noise and the contribution of changes of individual scatterers. The noise component is removed by applying filtering techniques (adaptive filters e.g. Goldstein) on the interferogram and/or SAR images. So, by removing or ignoring the components that do not contribute to height information, (1) can be written as following:

$$\varphi \cong \varphi_{defo} \quad (2)$$

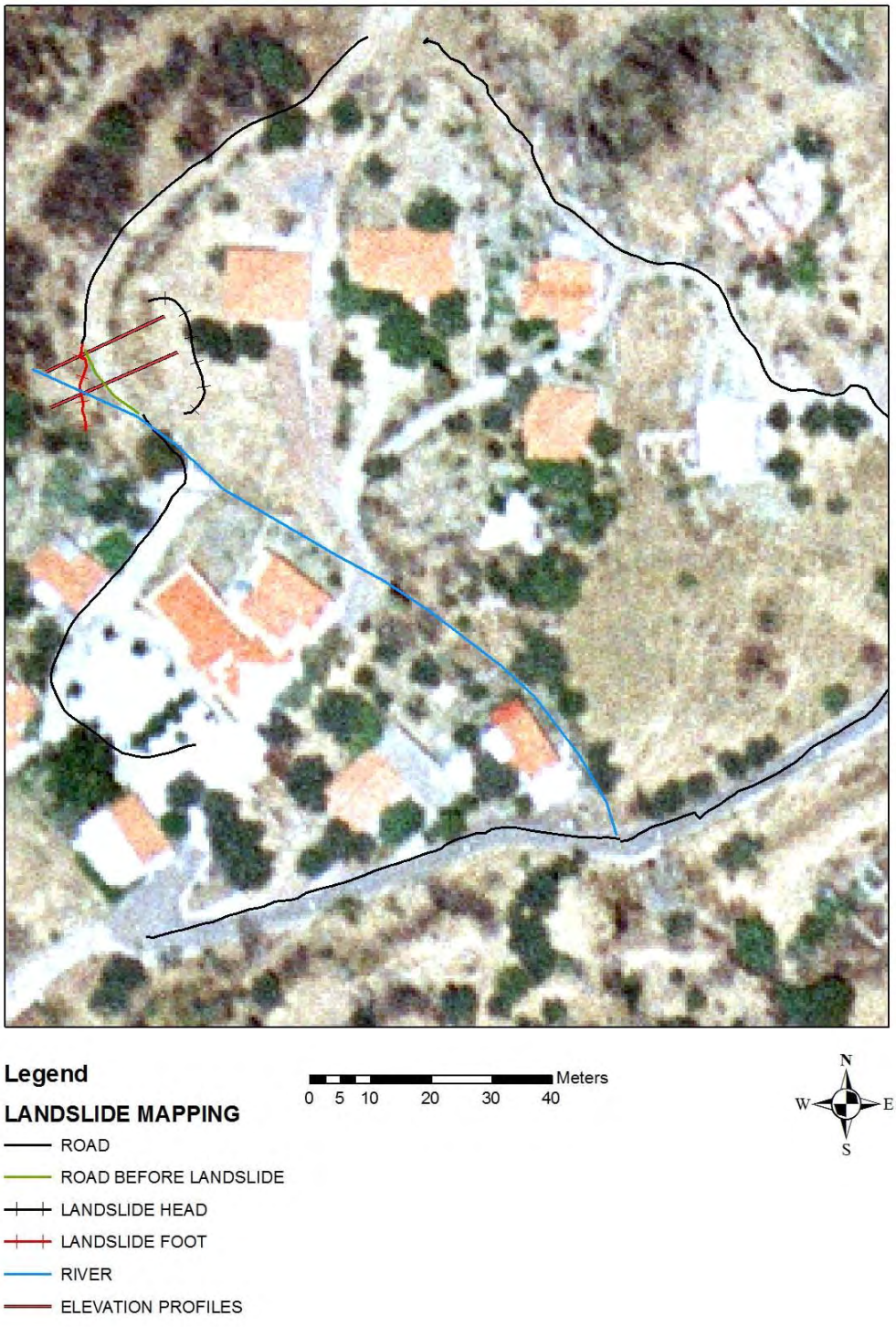

Figure 2 - The map of the landslide. The head of the landslide is in front of two olive trees. The black dashed line represents the head of the landslide while the red one represents the foot of the landslide. The road network is presented with black color line. A part of the road has collapsed.

Figure 3. Photo of the landslide taken from the southeast. The head of the landslide is in front of two olive trees about two meters from the house basement.

Figure 4 - Photo of the landslide taken from the northwest. Part of the small village road is collapsed.

Thirty ALOS PALSAR acquisitions within a period of three years were collected over the study area. As the landslide has been recorded on January 2009, the master and slave images of each interferometric pair had to be acquired before and after this date, respectively. Also, the interferometric pairs selected to have normal baseline component less than 1Km and time interval between 46 and 92 days (Ng et al., 2008; Blanco et al., 2008). These restrictions were set on to avoid geometric and temporal decorrelation phenomena. So, two interferometric pairs were formed according to the selected criteria. The interferometric methodology was applied on each pair using the SARscape software.

4.2. Results

In Figures 5 and 6, are presented the geocoded differential interferograms and the magnifications of the area around the landslide, respectively for each interferometric pair. With a red circle is

demonstrating the approximately site of the known landslide which has been measured by differential GPS.

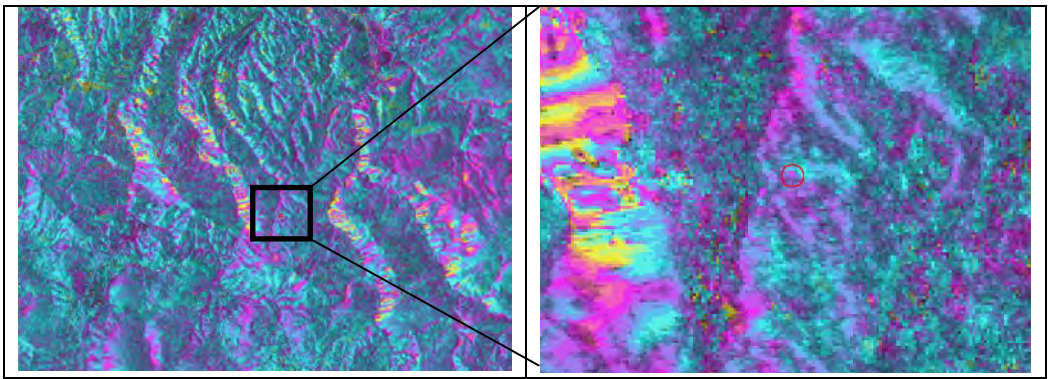

Figure 5 - (a) Geocoded Differential Interferogram from interferometric pair 20081110_20090210/ Bn=824m/ Δt=92 Days, (b) magnification of the area around the landslide.

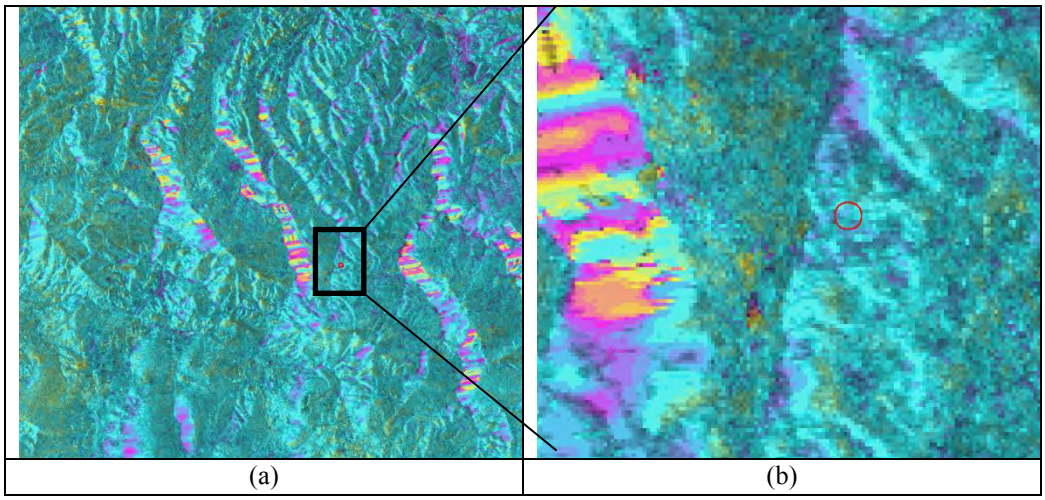

Figure 6 - (a) Geocoded Differential Interferogram from interferometric pair 20081226_20090210/ Bn=671m/ Δt=46 Days, (b) magnification of the area around the landslide.

There are many studies where the conventional DInSAR had been used successfully to detect and map landslide by exploiting SAR acquisitions in L-Band (Kimura and Yamaguchi, 2000; Strozzi et al., 2003; Wegmüller, et al., 2008). However, in this study the identification of the known landslide in Sykies was not achieved. There are error sources which had been reported in the international literature and are the main limitations of conventional DInSAR in landslide monitoring applications (Colesanti and Wasowski, 2006; Cascini et al., 2009). The atmospheric phase delay variation, the geometric and temporal decorrelation, the external reference DEM, the aspect and inclination of slope are few reasons which affect the result of the conventional two pass DInSAR.

The atmospheric phase delay has considered as an error since the detection of a landslide is a non atmospheric application. The geometric and temporal decorrelation phenomena have been limited by the adoption of specific criteria on interferometric pair selection. The inaccuracies of the external DEM involved in the cancellation of the topography component from the signal interferences are limited since the used external DEM has high precision and accuracy. Finally, the used SAR

images acquired over ascending orbits (line of sight pointing towards east) and the aspect of the study area is west/west-north. According to (Colesanti and Wasowski, 2006), the study area is affected by significant geometric distortions and especially by the distortion of foreshortening since the inclination of slope is about 22^o which is smaller than the off-nadir angle of ALOS sensor ($34,3^o$). Nevertheless, in this study the main limitation on landslide identification is the very small area of the deformation. Specifically, the cell size of the geocoded interferograms had been selected to be 10m (according to the best spatial resolution of ALOS Palsar data), so the area of the landslide mapped to three pixels approximately. The small area is linked directly to the spatial smoothing effect induced by interferogram filtering.

5. ALOS Optical Data Processing

Two ALOS Prism data sets with a spatial resolution of 2,5 meters and two ALOS AVNIR-2 sets with a spatial resolution of ten metes were used in this study. The first Prism and the first AVNIR-2 images were acquired on 2008 before the landslide while the other data sets were acquired on 2009 after the catastrophic event. ALOS data was provided by the European Space Agency.

The 2008 Prism data set contains three scenes collected from the three radiometers. The 2009 Prism data set contains only the nadir and forward images. Thus four different stereo-pairs were used for the creation of four ALOS DSMs over the same area. Twenty-five ground control points and more than one hundred tie points were used. For all the stereo-pairs the same gcp's were used. Four DSMs with a pixel size of 7,5m were created. No further processing (editing) was done to the four DSMs. The DSM difference and elevation profiles were used for the landslide detection.

The two AVNIR-2 data sets were orthorectified using the DSM created from the ALOS Prism data and the same ground control points. Band 3 and band 4 were used for the calculation of the NDVI indices before and after the landslide. Because most of the landslides are usually bare of vegetation cover they present high reflectance. As a result big landslides can be detected from satellite data. As the vegetation cover usually changes due to the landslide there should be a quite big difference to the NDVI indices before and after the event.

The accuracy of DSMs created from ALOS stereopair was discussed in a previous paper (Nikolakopoulos et al., 2010). According to that study the accuracy of ALOS DSM is similar to the accuracy of the DSM of the Ministry of Agriculture (created from airphotos). In this study different elevation profiles were used in order to detect the landslide. The landslide head was used as one of the elevation profiles before and after the landslide. As we can observe in Figure 7 there is a difference to the elevation profile before and after the event. The landslide head line was between 496 and 494 meters before the landslide (figure 7 top) and its elevation decreased to 492 after the landslide (figure 7 bottom).

Two other elevation profiles along the landslide were created (Figure 2 brown color lines). As it can be observed in Figure 8 (top) the elevation before the landslide ranged between 495 and 498 meters. Along the same profile (Figure 8 bottom) the elevation decreased after the landslide and ranged between 492 and 496 meters.

The study of the NDVI images presented in Figure 9 has confirmed the existence of the landslide. The two images present quite big differences in the tonality. As the landslide has destroyed the vegetation cover the NDVI image of 2009 (Figure 9 right part) present higher values than the NDVI image of 2008 (Figure 9 left part).

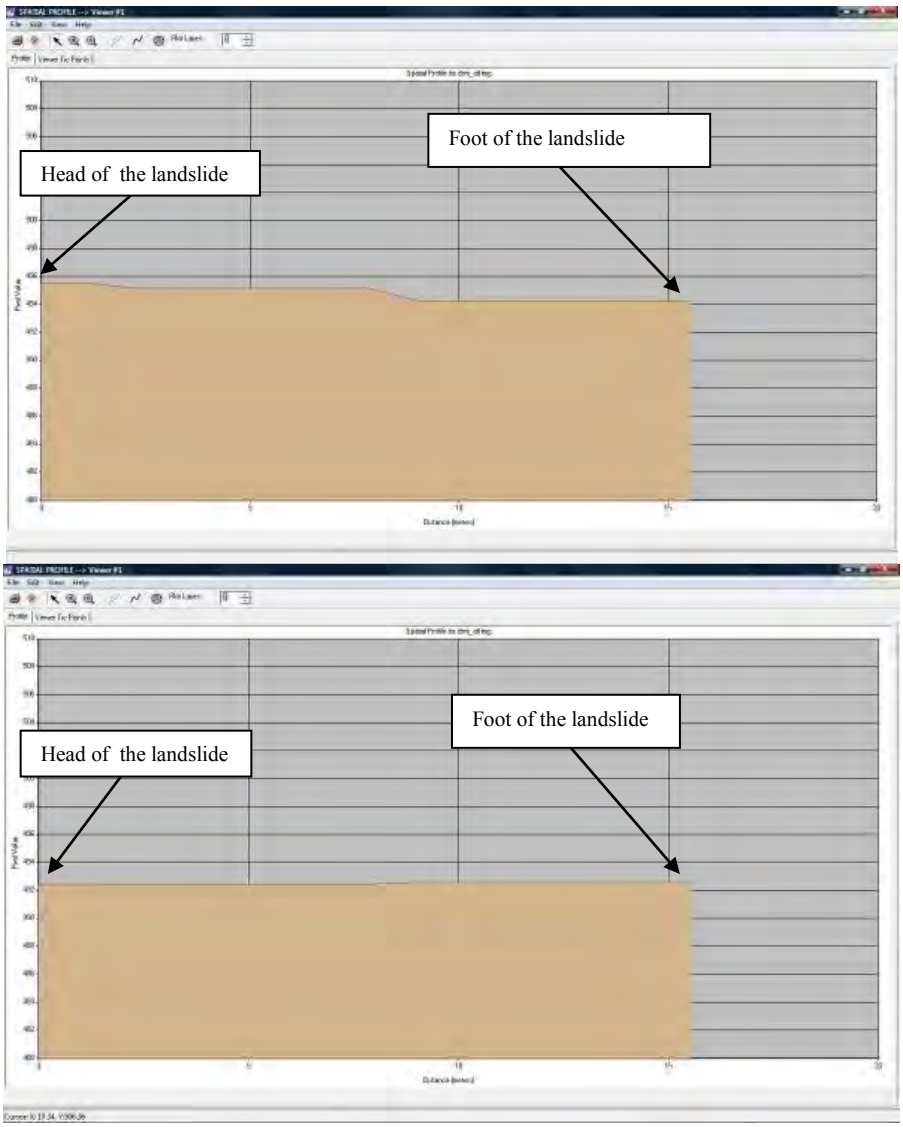

Figure 7. Elevation profiles along the landslide head. At the top the elevation profile from the 2008 stereopair. At the bottom the elevation profile of the 2009 stereopair.

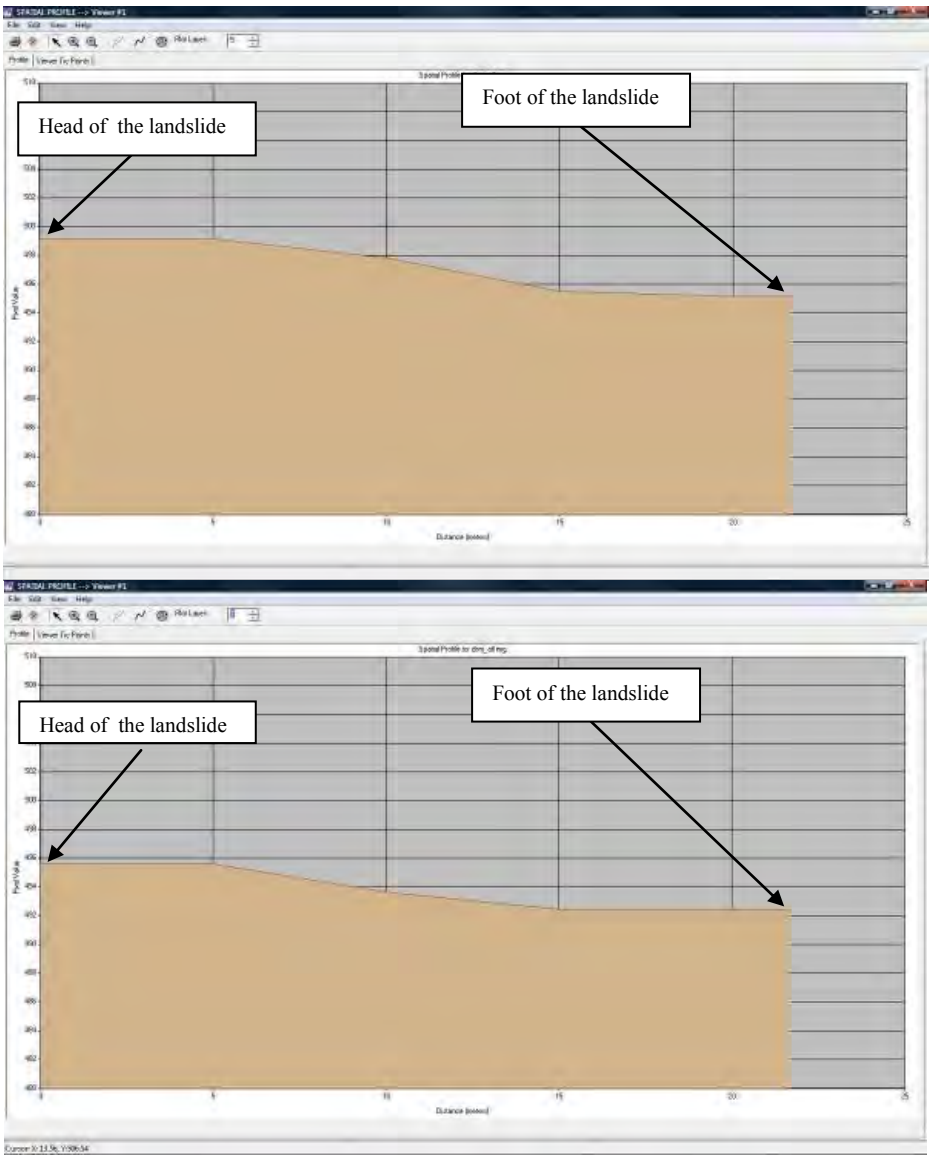

Figure 8. Elevation values along the profile no1. At the top the elevation profile from the 2008 stereopair. At the bottom the elevation profile of the 2009 stereopair.

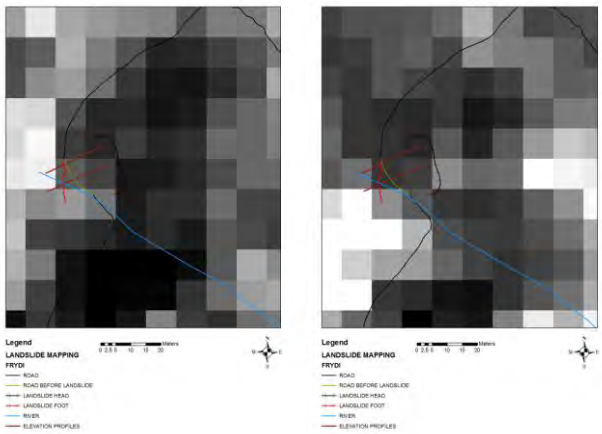

Figure 9. NDVI images produced from the ALOS VNIR-2 data before and after the landslide. At the left part the NDVI image of 2008 and at the right the respective image of 2009. The black dashed line represents the head of the landslide while the red one represents the foot of the landslide. The road network is presented with black color line.

6. Conclusions

In this paper the suitability of ALOS radar and optical data for landslide detection is discussed. A small landslide with a head of 27 meters length already mapped in situ with GPS was used for the testing. Thirty ALOS PALSAR acquisitions within a period of three years (before and after the event) were collected for the study area. Two ALOS Prism data sets with a spatial resolution of 2,5 meters and two ALOS AVNIR-2 sets with a spatial resolution of ten metes were used in this study. The first Prism and the first AVNIR-2 images were acquired on 2008 before the landslide while the other data sets were acquired on 2009 after the catastrophic event.

Standard two pass Differential SAR Interferometry was performed to detect the general ground deformation on the study area and specifically to identify and get information on the activity of the known landslide on Sykies. The detection of the landslide was not possible due to very small area of deformation. Specifically, the cell size of the geocoded interferograms had been selected to be 10m, so the area of the landslide mapped to three pixels approximately. The small area is linked directly to the spatial smoothing effect induced by interferogram filtering.

The DSM created from the ALOS PRISM data were proved suitable for the landslide detection. Different elevation profiles were examined and a decrease to the elevation values due the landslide has been marked.

7. Acknowledgements

The authors would like to acknowledge KTIMATOLOGIO S.A. for kindly providing the reference DEM for the study area. ALOS radar and optical data was provided by the European Space Agency under the PI project 6554.

8. References

Baum R.L., Messerich J. and Fleming R.W. 1998. Surface deformation as a guide to kinematics and three-dimensional shape of slow-moving, clay-rich landslides, Honolulu, Hawaii, *Environmental and Engineering Geoscience,* 4 (3), 283– 306.

Blanco P., Arbiol R. and Palà V. 2008. ALOS-PALSAR performances on a multiple sensor DInSAR scenario for deformation monitoring, *Proceedings of the ALOS PI 2008 Symposium organized by ESA*, Rhodes Island.

Cascini L., Peduto D., Fornaro G., Lanari R., Zeni G. and Guzzetti F. 2009. Spaceborne Radar Interferometry for Landslide Monitoring, *Proceedings of the 1st Italian Workshop on Landslides*, (1), 138-144.

Chandler J.H. 2001. Terrain measurement using automated digital photogrammetry in*:* Griffiths, J.S. (Ed.)*, Land Surface Evaluation for Engineering Practice*, *Geological Society of London*, vol. 18, 13– 18.

Colesanti C. and Wasowski J. 2006. Investigating landslides with space-borne Synthetic Aperture Radar (SAR) interferometry, *Engineering Geology,* 88, 173–199.

Jacobshagen V., Durr S., Kockel F., Kopp K.O. and Kowallczyck G. 1978. Structure and geodynamic evolution of the Aegean region, in*: Alps, Appenines, Hellenides,* H. Closs, D. Roeder & K. Schmidt (Eds.), 537–564.

Kääb A. 2000. Photogrammetry for early recognition of high mountain hazards: new techniques and applications, *Physics and Chemistry of the Earth*, Part B 25 (9), 765– 770.

Kimura H. and Yamaguchi Y. 2000. Detection of Landslide Areas Using Satellite Radar Interferometry, *Photogrammetric Engineering & Remote Sensing,* 66(3), 337-344.

Maas H.G. and Kersten T. 1997. Aerotriangulation and DEM/orthophoto generation from high-resolution still-video imagery—on the potential of digital cameras onboard an aircraft, *Photogrammetric Engineering and Remote Sensing,* 63 (9), 1079– 1084.

Mantovani F., Soeters R. and Van Westen C.J. 1996. Remote sensing techniques for landslide studies and hazard zonation in Europe, *Geomorphology,* 15 (3– 4), 213–225.

Massonet D., M. Rossi, C. Carmona, F. Adragna, G. Peltzer, K. Feigl and Rabaute T., 1993. The displacement field of the Landers earthquake mapped by radar interferometry, *Nature*, 364, 138-142.

Ng AH, Chang H., Ge L., Rizos C. and Omura M. 2008. Radar interferometry for ground subsidence monitoring using ALOS PALSAR data, in: *Proceedings of the XXI congress, The International Society for Photogrammetry and Remote Sensing*, Beijing.

Nikolakopoulos K.G., Vaiopoulos D.A., Skianis G., Sarantinos p. and Tsitsikas A, 2005. Combined use of Remote Sensing, GIS and GPS data for landslide mapping, *IEEE IGARSS* 7, 5196- 5199.

Nikolakopoulos K.G., Vaiopoulos A.D., and Tsombos P. 2010. DSM from ALOS data: the case of Andritsena, Greece, *Proc. of SPIE,* 7831, 78310K1-10.

Papanikolaou D. 1986. *Geology of Greece*, Eptalofos, Athens, 1-240.

Piper D.W.J. and Pe-Piper G. 1980. Was there an western (external) source of terrigenous sediment for the Pindos zone of the Peloponnese Greece? *Neues Jahrbuch Geologie und Paleontologie,* Monatsheft, 197–215.

Powers P.S., Chiarle M. and Savage W.Z. 1996. A digital photogrammetric method for measuring horizontal surficial movements on the Slumgullion earthflow, Hinsdale county Colorado, *Computers and Geosciences,* 22 (6), 651–663.

Strozzi T., Wegmüller U., Werner C., Wiesmann A. and Spreckels V., 2003. JERS SAR Interferometry for Land Subsidence Monitoring. *IEEE Transactions on Geoscience and Remote Sensing*, 41(7), 1702-1707.

Weber D. and Herrmann A. 2000. Contribution of digital photogrammetry in spatio-temporal knowledge of unstable slopes: the example of the Super-Saute landslide (Alpes-de-Haute-Provence, France), *Bulletin de la Societe Geologique de France,* 171 (6), 637– 648.

Wegmüller U., Werner C., Strozzi T., Wiesmann A. and Raetzo H. 2008. Slope stability monitoring using space-borne repeat-pass SAR interferometry, *Proc. of 13th FIG Symposium on Deformation Measurement and Analysis.*

Yu G.H. and Ge L. 2010. Digital Elevation Model generation using ascending and descending multi-baseline ALOS/PALSAR radar images, *In: FIG Congress 2010*.

Zhou C., Ge L., Dongchen E. and Chang H. 2005. A case study of using external DEM in InSAR DEM generation, *GeoSpatial Information Science*, 8(1): 14-18.

Δελτίο της Ελληνικής Γεωλογικής Εταιρίας, τομ. XLVII , 2013
Πρακτικά 13ου Διεθνούς Συνεδρίου, Χανιά, Σεπτ. 2013

Bulletin of the Geological Society of Greece, vol. XLVII 2013
Proceedings of the 13th International Congress, Chania, Sept. 2013

USING REMOTE SENSING MULTISPECTRAL DATA AND GIS TECHNIQUES FOR THE GEOLOGICAL MAPPING OF HALKI ISLAND

Nikolakopoulos G. K.[1], Tsombos I. P.[2], Photiades A.[2], Psonis K.[2] and Zervakou A.[2]

[1] University of Patras, Department of Geology, Sector of Applied Geology and Geophysics, knikolakop@upatras.gr,

[2] I.G.M.E.M, Olympic Village Entrance C, 13677 Acharnae, ptsombos@igme.gr, fotiades@igme.gr, zervakou@igme.gr

Abstract

In this paper we present the combined use of remote sensing and GIS techniques for the geological mapping of Halki Island at 1/50.000 scale. The geological formations, geotectonic units and tectonic structures were recognized in situ and mapped. Interpretation of multispectral satellite images (Landsat TM & ETM and Terra ASTER) has been carried out in order to detect the linear or not structures of the study area. Different band ratio was also used in order to distinguish and map the limits of the different geotectonic units. The in situ mapping was enhanced with data derived from the digital processing of the satellite data. All the analogical and digital data were imported in a geodatabase specially designed for geological data. After the necessary topological control and corrections, the data were unified and processed in order to create the final map layout at 1/50.000 scale.
Key words: *Halki, 1/50.000, geological map.*

Περίληψη

Στην εργασία αυτή παρουσιάζεται ο Γεωλογικός Χάρτης κλίμακας 1/50.000 Φύλλο "Νήσος Χάλκη" που εκδόθηκε από το ΙΓΜΕ. Για τη δημιουργία του χάρτη έγινε συνδυαστική χρήση δορυφορικών πολυφασματικών δεδομένων (Landsat TM & ETM and Terra ASTER), και χαρτογράφησης στο πεδίο με χρήση DGPS. Όλα τα δεδομένα εισήχθησαν στην ειδικά σχεδιασμένη γεωβάση του ΙΓΜΕ. Μετά τους απαραίτητους τοπολογικούς ελέγχους και τις αναγκαίες διορθώσεις τα δεδομένα ενοποιήθηκαν και έγινε η επεξεργασία τους με σκοπό τη δημιουργία του τελικού χάρτη.
Λέξεις κλειδιά: *Χάλκη, Γεωλογικός Χάρτης, 1/50.000.*

1. Introduction

The Institute of Geology and Mineral Exploration of Greece is the state's advisor on geoscientific issues. One of its main activities, which established the role of IGME in the field of the systematic research, study and mapping of the geological environment, at national and international level, is the geological mapping of Greece at various scales. The basic geological cartographic scale of

IGME is the 1:50.000. The whole country is covered by 326 map sheets, most of them accomplished during the last six decades by Greek and foreign geologists.

In many regions of Greece there is no continuity between adjacent geological maps (e.x. heterogeneity - discontinuity of geological features such as formations, tectonic lines, geological units). Furthermore a very few map sheets have not been published.

In order to heal these heterogeneities IGME has integrated a project involving the updating or publishing of fifty geological map sheets using GIS and Remote Sensing techniques, one of which was the geological map sheet of Halki. The project was founded in the framework of CSF 2000 – 2006 (Community Support Framework 2000-2006, Operational Program Competitiveness, Priority axis 7: Energy and Sustainable Development, Measure 7.3: Exploitation of natural recourses and support in meeting environmental commitments, Action 7.3.1) under the auspice of a project titled "Collection, Codification and documentation of geothematic information for urban and suburban areas in Greece - pilot applications".

In this paper we present the combined use of remote sensing and GIS techniques for the geological mapping of Halki Island at 1/50.000 scale. The geological formations, geotectonic units and tectonic structures were recognized in situ and mapped. Interpretation of multispectral satellite images (Landsat 7 ETM and Terra ASTER) has been carried out in order to detect the linear or not structures of the study area. Different band ratio was also used in order to distinguish and map the limits of the different geotectonic units. The in situ mapping was enhanced with data derived from the digital processing of the satellite data. All the analogical and digital data were imported in a geodatabase specially designed for geological data. After the necessary topological control and corrections, the data were unified and processed in order to create the final map layout at 1/50.000 scale.

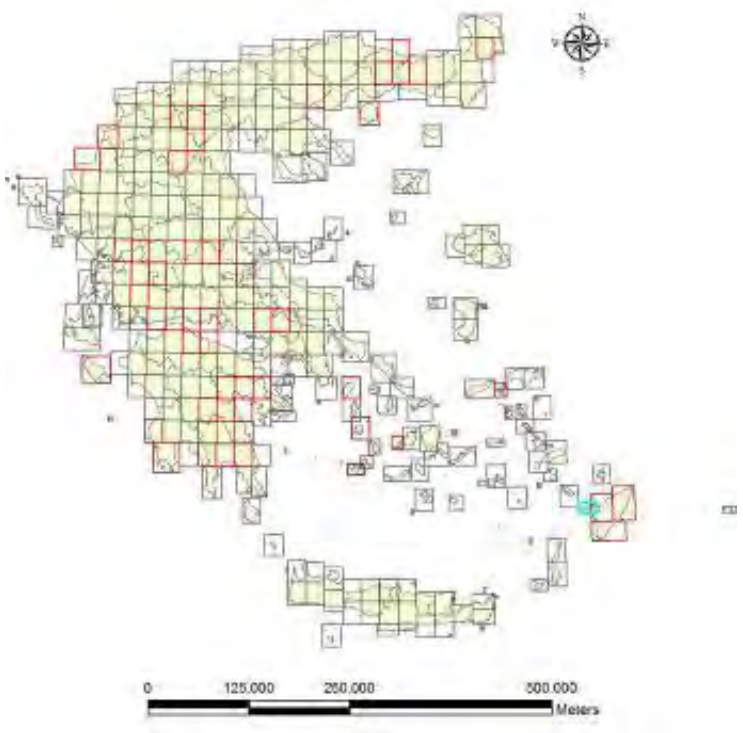

Figure 1 - The Greek territory is covered by 325 geological maps at 1/50.000 scale. With red color some of the geological maps that have been updated. With blue color the new Xalki Island map sheet.

2. Remote Sensing Data and Processing

2.1. Remote Sensing Data

Landsat imagery was successfully used throughout the years for geological structure recognition due to its synoptic view over large areas, enabling the detection of regional geological features. In particular, lineament analysis of remotely sensed data, either by visual or automatic interpretation, is a valuable source of information for studying the structural setting. Although, Landsat satellite TM data has proved useful for regional geological studies (Abrams et al., 1988), its coarse spectral resolution provoked difficulties to a detailed mapping of geological composition. This obstacle was overpassed with the launch of Landsat 7 and Terra satellites. Both ASTER instrument and ETM with a spatial resolution (for the Vnir and panchromatic band respectively) gave a new impulse to the use of satellite data for geological mapping .

Different algorithm has been applied in geological research, especially to detect geological lineaments such as fault, joints, dykes, and shear zones (Cross and Wadge, 1988). Other researchers (Wang and Howarth, 1990) used Hough transform for automated lineament analysis using parts of Landsat TM images. The synergistic use of optical and radar data for the detection of active faults was proposed (Parcharidis et al., 2001). Digital Elevation Models were also used for the detection of linear features and the extraction of the topographic structure (Jenson and Domingue, 1988).

Different RGB combinations and band ratios of ASTER data were used for geological mapping in different geological environments (Kavak, 2005; Nair and Mathew, 2012; Deller 2006; Nikolakopoulos et al., 2009; Oikonomidis et al., 2009). Visible, near-infrared and short wave infrared reflectance data (9 ASTER bands) have been processed and interpreted in framework of a mapping project concerning the western margin of the Kalahari desert (Gomez et al., 2005.). The same authors have also used Principal Component Analysis as a preliminary processing step before the classification of the ASTER data. In another study Gad Kusky, 2007) used different ASTER band ratios for lithological mapping in Egypt. Different combinations of ASTER band ratios were also used for lithological mapping in California (Rowan and Mars 2002). Principal Component Analysis method was applied in ASTER data in combination of NDVI and different False Colour Composite images for lineaments mapping in Crete (Papadaki et al., 2011).

In this study two ASTER, a Landsat TM and a Landsat ETM images were processed in order to detect different geological formations. In order to extract the maximum spectral info of each band the Principal Component Analysis, the Independent Component Analysis, the Tasseled cap and different combinations of band ratios were used. The results are presented in the next paragraphs.

2.2. Principal Component Analysis

Principal Components Analysis (PCA) was originally used as a method of data compression. It allows redundant data to be compacted into fewer bands--that is, the dimensionality of the data is reduced. The bands of PCA data are non correlated and independent, and are often more interpretable than the source data.

PCA was applied in ASTER SWIR data (Figure 2) and also in Landsat TM (Figure 3) and ETM (Figure 4) data. The upper formation with purple colour in Figure 2 and cyan to purple colour in Figure 3 corresponds to the limestone-dolomitic limestone of the Gavrovo Tripolis geotectonic zone. The lower formation presented with red colour in Figure 2 or with yellow colour in Figure 3 corresponds to the Lower Jurassic-Lower Cretaceous Limestones of the Gavrovo Tripolis geotectonic zone. Two small appearances of alluvial deposits (blue color in Figure 3 or purple colour in Figure 4) are easily detected inside the limestone formation in the east part of Halki Island while a more extensive appearance of alluvial is presented in the south part of the Island. Next to the alluvial deposits the Flysch of the Ionian zone can be distinguish with purple colour in Figure 3 or cyan to green colour in Figure 4.

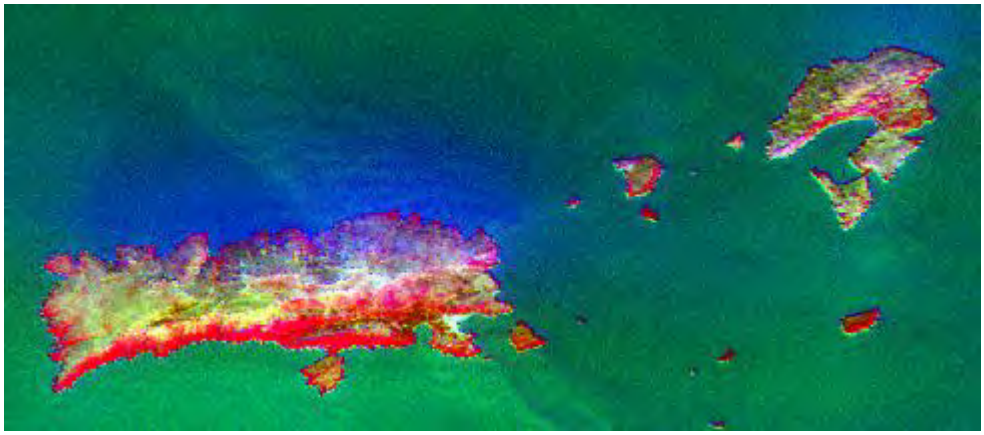

Figure 2 - RGB combination of the ASTER SWIR principal components 142. Four different geological formations can be recognized.

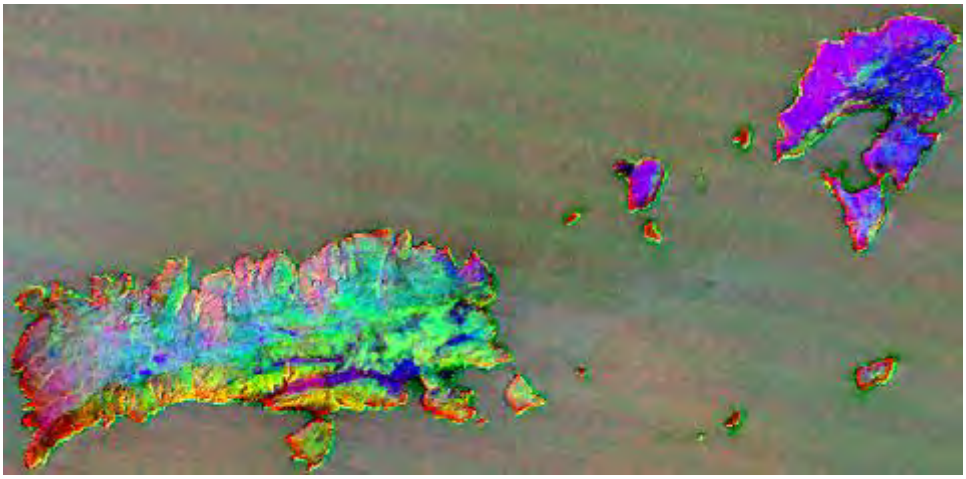

Figure 3 - RGB combination of the Landsat TM principal components 432. Four different geological formations can be recognized.

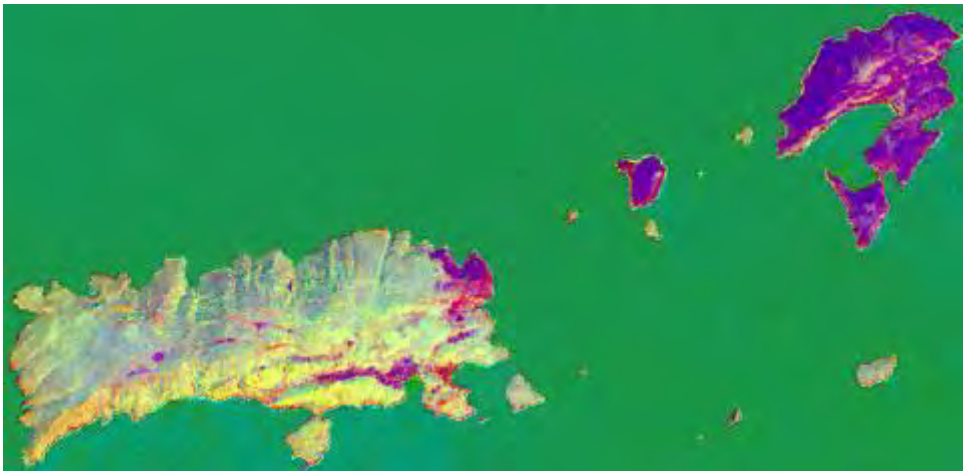

Figure 4 - RGB combination of the Landsat ETM principal components 142. Four different geological formations can be recognized.

2.3. Independent Component Analysis

Independent Components Analysis is a feature extraction technique which aims to decorrelate the spectral bands in order to recover the original features in the image. It performs a linear transformation of the spectral bands such that the resulting components are decorrelated. Each component will contain information corresponding to a specific feature in the original image.

Independent Components Analysis was applied in ASTER data (Figure 5) and also in Landsat TM and ETM data (Figure 6). The upper formation with green colour in Figure 5 and brown colour in Figure 6 corresponds to the limestone-dolomitic limestone of the Gavrovo Tripolis geotectonic zone. Two small appearances of alluvial deposits (pink colour) are easily detected inside the limestone formation in the east part of Halki Island while a more extensive appearance of alluvial is presented in the south part of the Island.

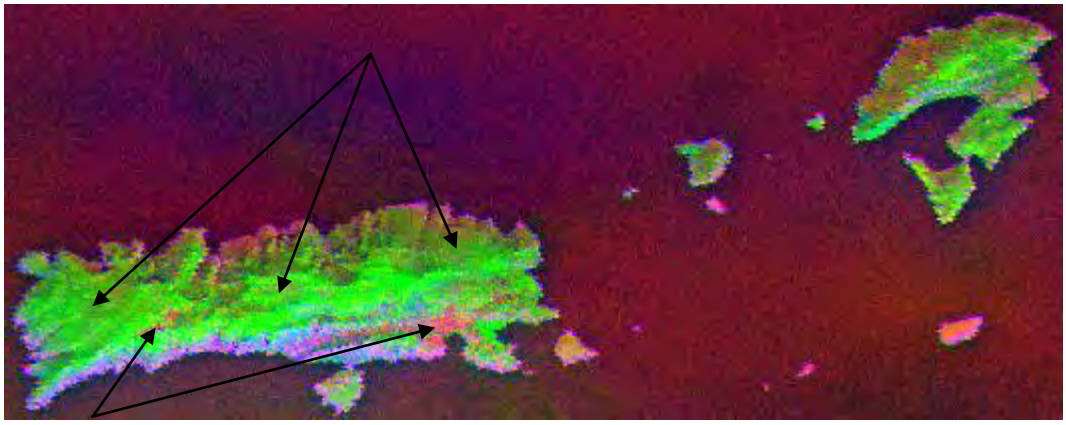

Figure 5 - RGB combination of the ASTER SWIR independent components 621. Four different geological formations can be recognized.

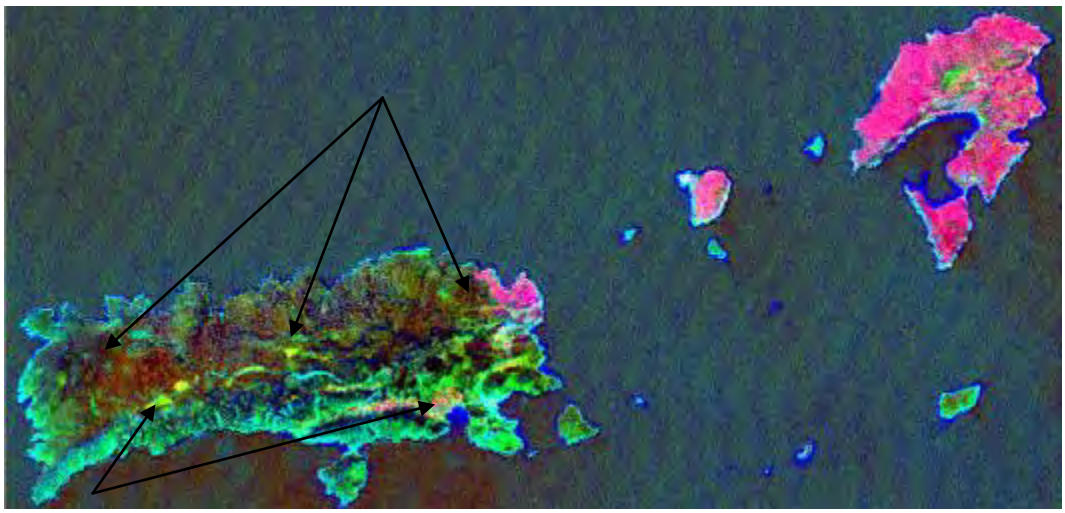

Figure 6 - RGB combination of the Landsat ETM independent components 431. Four different geological formations can be recognized.

2.4. Band Ratios

Band ratio images designed to display the spectral contrast of specific absorption features have been used extensively in geologic remote sensing (Rowan, 2003). Relative absorption depth

(RBD) images are an especially useful three-point ratio formulation for displaying Al-O-H, Mg-O-H and CaCO3 absorption intensities prior to conducting more detailed, time-consuming spectral analysis (Crowley et al., 1989). For each absorption feature, the numerator is the sum of the bands representing the shoulders (bands 1 and 2), and the denominator is the band located nearest the absorption feature minimum (band 3); removal of continuum increases the intensity of the absorption feature: RBD = (band 1 + band 2) / band 3 (according to Crowley et al., 1989)

Several different band ratio images have been created. The [(band 7 + band 9)/band 8] image which highlights the CaCO3 and Mg-O-H absorption feature at 2237.5 nm is presented in Figure 7. The specific band ratio image corresponds well with the limestone dolomite-limestone distribution in the north part of Halki Island. Another absorption RBD image [(band 6 + band 8)/band 7,)] exhibits correspondence with the dolomite distribution in the north part of Halki Island (Figure 8).

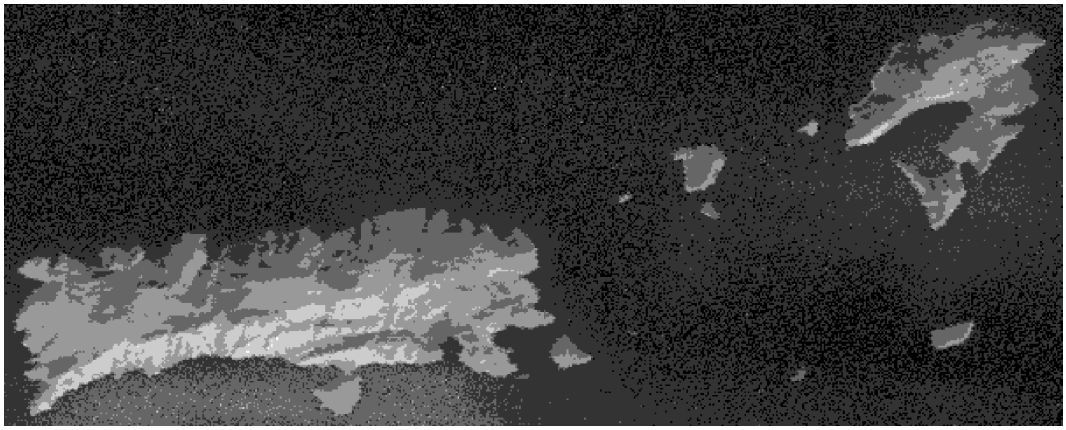

Figure 7 - Band ratio of the ASTER SWIR image. The formula was (band7+band9)/band8. The specific band ratio image corresponds well with the limestone dolomite-limestone distribution in the north part of Halki Island.

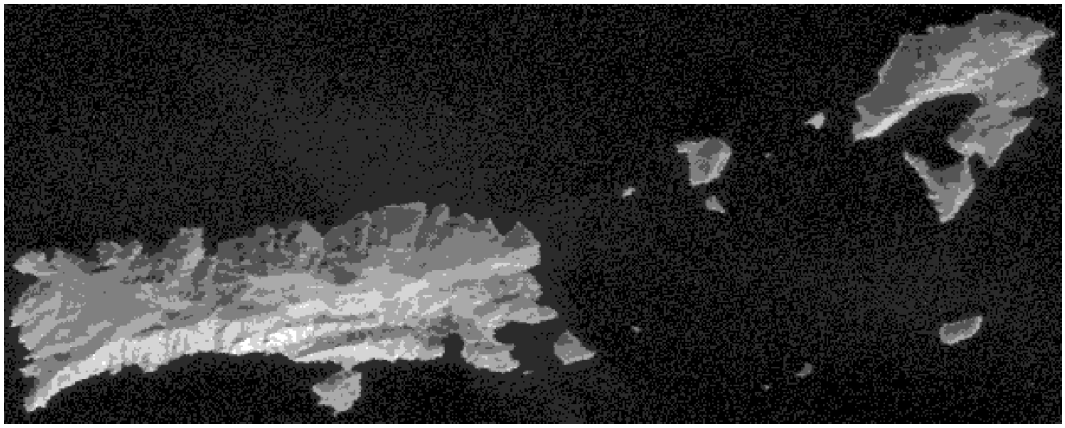

Figure 8 - Band ratio of the ASTER SWIR image. The formula was (band6+band8)/band7. The specific band ratio image corresponds well with the limestone dolomite-limestone distribution in the north part of Halki Island.

2.5. Tasseled Cap

Tasseled Cap transformation offers a way to optimize data viewing for vegetation studies. For example, a geologist and a botanist are interested in different absorption features. They would want to view different data structures and therefore, different data structure axes. Both would

benefit from viewing the data in a way that would maximize visibility of the data structure of interest. The tasseled cap image og the ETM data is presented in Figure 8. The difference in colour between the dolomitic-limestone and the limestone with silex is obvious.

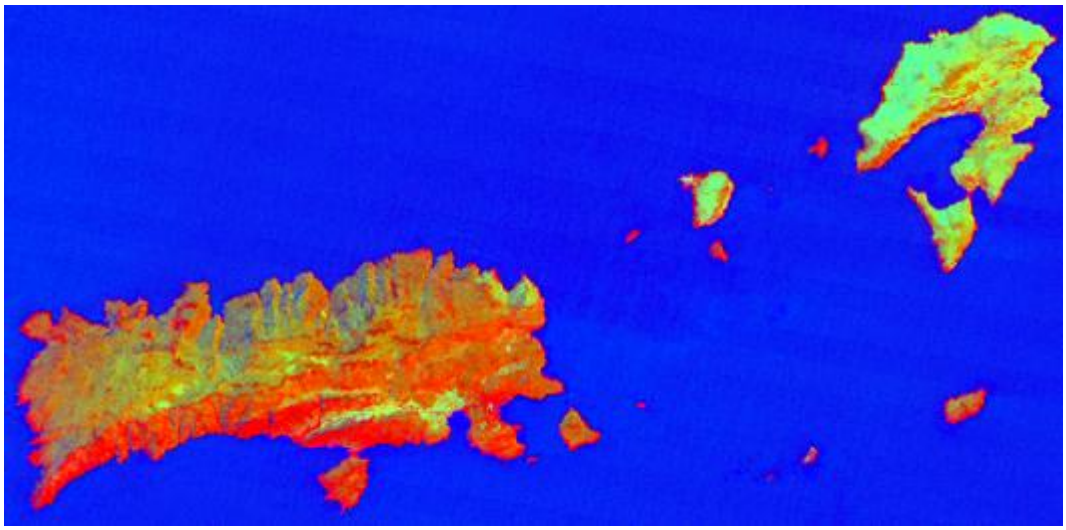

Figure 9 - The tasseled cap image of the ETM data. RGB combination of the bands 123.

3. In Situ Mapping.

Extended field work, including new geological mapping, GPS measurements and field data collection was undertaken in 2007 and 2008. All the small Islands around Halki were visited by a small boat (Figure 10) and mapped. Every tectonic line was checked and verified in the field. Every formation and all the geological boundaries were checked during the geological mapping and the boundaries were recorded digitally using the Arcpad GIS. The accuracy of the GPS measuremenwere ts was better than 3m (DGPS mode using EGNOS).

Formations of three geotectonic zones were recognized during the in Situ mapping. The bigger part of Halki Island is covered by limestone-dolomitic limestone of the Gavrovo Tripolis zone. At the south east coasts of the Island there are smaller appearances of limestone with silex and Flysch that belongs to the Ionian zone.

On Alimia Island the same formations with the exception of the Flysch of the Ionian zone were recognized. In addition an appearance of platy limestone with silex belonging to Pindos zone was mapped at the east part of the Alimia Island.

4. GIS

IGME has being implementing the project titled “Data digitizing for the Information System of IGME”.

The project comprises the following basic objectives:

- Digitizing – vectorization of data derived from 265 analogical and 60 digital geological map sheets of scale 1:50.000.
- Data import into an integrated standardized geographic database in the Hellenic Geodetic Reference System (EGSA87) called “Hellas GDB50K” (Geological Database 50 K) covering the whole country.
- Database updating and service.

The geographic database is built in GIS Environment with the use of ArcGIS 9x software (ArcInfo version, ESRI). The used format for editing and data management is ArcGIS Geodatabase, a native data structure for ArcGIS software. It is a collection of geographic datasets of various types held in a common file system folder, a Microsoft Access database, or a multi-user relational database (such as Oracle, Microsoft SQL Server, or IBM DB2).

All geoinformation is compiled in feature classes and grouped in thematically organized feature datasets:

- Feature Dataset "formations": It contains feature classes (point, linear, polygon geometry or annotation) concerning the geological linear objects and formations of the geological map.
- Feature Dataset "cross_section: It contains feature classes (point, linear, polygon geometry or annotation) concerning the crosses sections of the geological map.
- Feature Dataset "lithcolumn": It contains feature classes (point, linear, polygon geometry or annotation) concerning the lithological column of the geological map.
- Feature Dataset "legendboxes": It contains feature classes (point, linear, polygon geometry or annotation) concerning the legend boxes of the geological map.
- Feature Dataset "legend": It contains feature classes (point, linear, polygon geometry or annotation) concerning the legend of the geological map.

Through the integration of the specific geological database additional processes will be carried out

- Integrate legends (general and detailed) and codification for the entire geographic database.
- Local adjustments of point, linear, polygon features in the overlapping area of adjacent map sheets
- Domains and subtypes creation, common for the entire geodatabase.
- Metadata creation for the geographic database based on ISO standards.

5. Conclusions

In the frame of a more general project, concerning the updating and homogenizing in a common geodata base the 1/50.000 geological maps of Greece, we published the geological map sheet of Halki Island.

The geoligcal formations of Halki Island and the small islands around it have been recognized and corresponded to respective zones of the External Hellenides.

Remote sensing data, GPS and GIS techniques were extensively used in order to facilitate and make more accurate the geological mapping. All the data are implemented in the IGME integrated geographic database.

6. Acknowledgments

This study was implemented in the frame of the project "COLLECTION AND DOCUMENTATION of GEOTHEMATIC INFORMATION'S FOR URBAN AND SUBURBAN AREAS IN GREECE – PILOT APPLICATIONS". The program is funded from the Operational Program "Competitiveness" Priority Axis 7: Energy and Sustainable Development, Measure 7.3: Exploitation of natural resources and support in meeting environmental commitments. The Operational Program "Competitiveness" is co-funded by the European Regional Development Fund (ERDF).

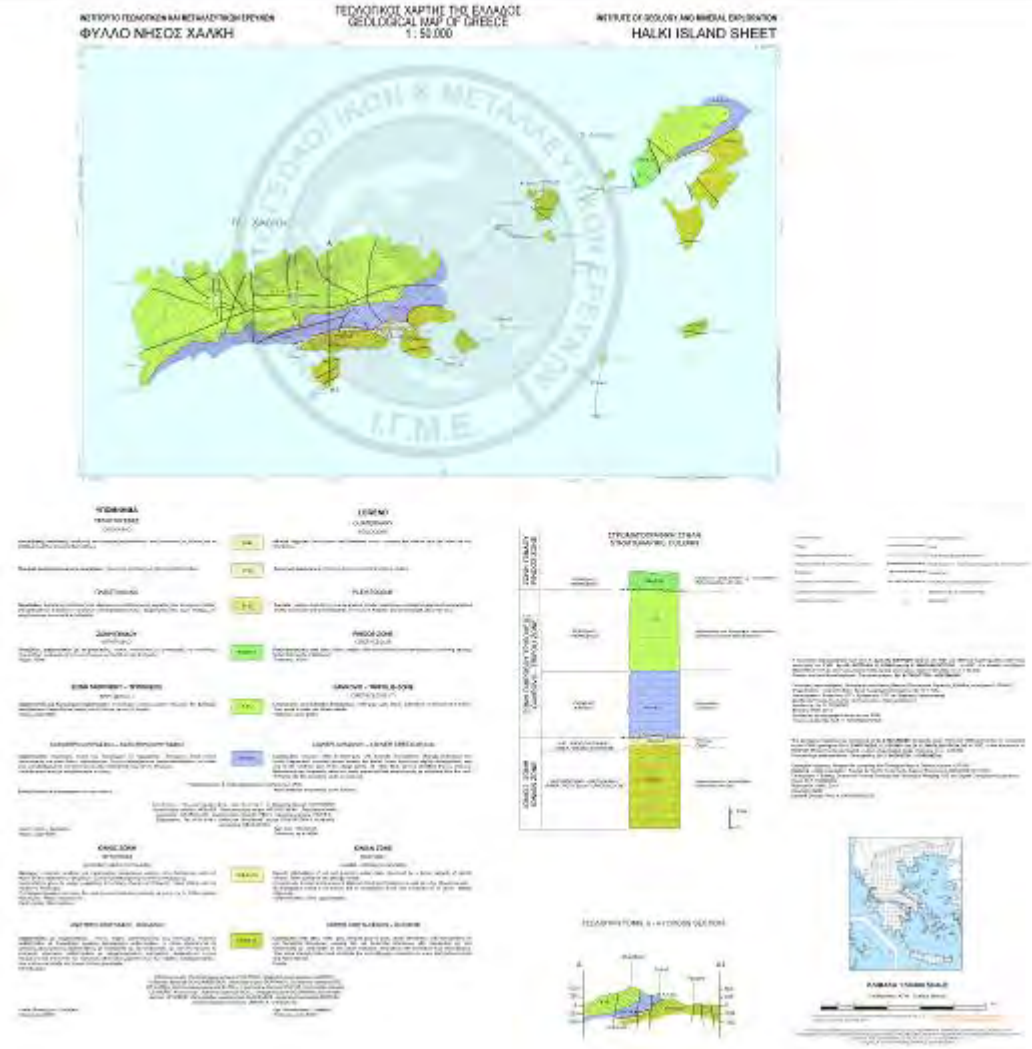

Figure 11 - The Geological map sheet Halki Island.

7. References

Abrams M.J., Rothery D.A. and Pontual A. 1988. Mapping in the Oman using enhanced Landsat Thematic Mapper images, *Tectonophysics*, (151), 387-401.

Cecile G., Delacourt C., Allemand P., Ledru P. and Wackerle R. 2005. Using ASTER remote sensing data set for geological mapping, in Namibia, *Physics and Chemistry of the Earth* (30), 97–108.

Cross A. and Wadge G. 1988. Geological lineaments detection using the Hough transform, *IGARSS'88 Proceedings*, 1779-1782.

Crowley J. K., Brickey D.W. and Rowan L.C. 1989. Airborne imaging spectrometer data of the Ruby Mountains, Montana: mineral discrimination using relative absorption band-depth images, *Remote Sensing of Environment*, 29, 121– 134.

Deller M.E.A. 2006. Facies discrimination in laterites using Landsat Thematic Mapper, ASTER and ALI data—examples from Eritrea and Arabia, *International Journal of Remote Sensing,* 27(12), 2389-2409.

Gad S. and Kusky T. 2007. ASTER spectral ratioing for lithological mapping in the Arabian–Nubian shield, the Neoproterozoic Wadi Kid area, Sinai, Egypt, *Gondwana Research,* (11) 326–335.

Jenson S.K and Domingue J.O. 1988. Extracting topographic structure from digital elevation data for geographic information system analysis, *Photogrammetric Engineering and Remote Sensing*, 54(11), 1593-1600.

Kavak K.S. 2005. Recognition of gypsum geohorizons in the Sivas Basin (Turkey) using ASTER and Landsat ETM+ images, *International Journal of Remote Sensing,* 26(20), 4583-4596.

Naira A. and Mathew G. 2012. Lithological discrimination of the Phenaimata felsic–mafic complex, Gujarat, India, using the Advanced Spaceborne Thermal Emission and Reflection Radiometer (ASTER), *International Journal of Remote Sensing,* 33(1), 198-219.

Nikolakopoulos K., Tsombos P., Mitropoulos D., Zervakou A., Grasemann B., Iglseder C., Petrakakis K., Müller M., Rice A.H., Voit K., Zámolyi A. and Draganits E. 2009. Updating the 1/50.000 geological maps of IGME with remote sensing data, GPS measurements and GIS techniques: the case of KEA Island, *Proc. of SPIE*, Vol. 7478, 74780O1-11.

Oikonomidis D., Mouratidis A., Astaras T. and Niarhos M. 2009. Geological Mapping by the Use of Multispectral and Multitemporal Satellite Images, Compared with GIS Geological Data. Case Studies from Macedonia Area, Northern Greece, *Imagin[e,g] Europe,* I. Manakos and C. Kalaitzidis (Eds)., IOS Press 2010, 311-319, doi: 10.3233/978-1-60750-494-8-311.

Papadaki E.S., Mertikas S.P. and Sarris A. 2011. Identification of lineaments with possible structural origin using ASTER images and DEM derived products in Western Crete, Greece, *EARSeL eProceedings* (10), 9-26.

Parcharidis I., Nikolakopoulos K., Serelis K. and Baskoutas I. 2001. Synergistic use of Optical and Radar data for active faults and corresponding displaced landforms detection in Kozani Basin (Greece), *Geocarto International, a multi-disciplinary journal of Remote Sensing and GIS*, Vol 16 No 3, 17-23.

Rowan Lawrence C. and John C.M. 2003. Lithologic mapping in the Mountain Pass, California area using Advanced Spaceborne Thermal Emission and Reflection Radiometer (ASTER) data, *Remote Sensing of Environment,* (84), 350–366.

Wang J. and Howarth P.J. 1990. Use of the Hough transform in automated lineament detection, *IEEE Transaction on Geoscience and Remote Sensing*, Vol. 28, No. 4, 561-566.

Zhang X. and Micha P. 2007. Comparison of Lithologic Mapping with ASTER, Hyperion, and ETM Data in the Southeastern Chocolate Mountains, USA, *Photogrammetric Engineering & Remote Sensing,* 73(5), 555–561.

Δελτίο της Ελληνικής Γεωλογικής Εταιρίας, τομ. XLVII , 2013
Πρακτικά 13ου Διεθνούς Συνεδρίου, Χανιά, Σεπτ. 2013

Bulletin of the Geological Society of Greece, vol. XLVII 2013
Proceedings of the 13th International Congress, Chania, Sept. 2013

BASIN AND LOCAL SCALE DETECTION OF GROUND SUBSIDENCE THROUGH PERSISTENT SCATTERER INTERFEROMETRY: THE ANTHEMOUNTAS BASIN (NORTHERN GREECE) CASE STUDY

Raspini F.[1], Loupasakis C.[2], Rozos D.[2] and Moretti S.[1]

[1] Department of Earth Sciences, University of Firenze, Via La Pira, 4 – 50121, Firenze, Italy, federico.raspini@unifi.it, sandro.moretti@unifi.it

[2] Laboratory of Engineering Geology and Hydrogeology, School of Mining and Metallurgical Engineering, National Technical University of Athens, 9 Iroon Polytechneiou, Athens, Greece, cloupasakis@metal.ntua.gr, rozos@metal.ntua.gr

Abstract

In the framework of the Terrafirma Extension project, a study has been established for ground motion detection and mapping in the Anthemountas basin (Central Macedonia). Terrafirma promotes the exploitation of Persistent Scatterer Interferometry (PSI) techniques, a remote sensing technology based on multi-temporal satellite Synthetic Aperture Radar (SAR) imagery. The potential of SAR interferometry has been exploited through the innovative Wide Area Mapping approach, recently implemented by the German Space Agency (DLR) and aimed at measuring land deformation over large areas.

Interferometric results from 1995-2001 by ERS1/2 satellites has been analyzed at a basin scale to investigate spatial patterns of land motion in the wider Anthemountas plain, where subsidence phenomena related to intense groundwater extraction is clearly manifested.

The WAP results turned out to be a valuable tool for the characterization at local scale of the land subsidence in the runaways area of the Macedonia airport and in the village of Perea, affected in 2005-2006 by a series of tensile ground ruptures due to excessive groundwater withdrawal.

Besides the study of the phenomenon, this work confirmed the suitability of PSI techniques to detect and measure surface displacements with millimetre accuracy and also to reconstruct the deformations history of the investigated areas through displacement time series analysis.

Key words: *multi-temporal satellite Synthetic Aperture Radar (SAR) imagery, intense groundwater extraction, Perea village, Macedonia airport.*

Περίληψη

Στο πλαίσιο του ευρωπαϊκού προγράμματος Terrafirma Extension πραγματοποιήθηκε έρευνα των εδαφικών υποχωρήσεων στην λεκάνη του Ανθεμούντα (Κεντρική Μακεδονία). Το Terrafirma προάγει τη χρήση των τεχνικών συμβολομετρίας σταθερών σκεδαστών (Persistent Scatterer Interferometry, PSI), μια τεχνική τηλεπισκόπησης που αξιοποιεί επαναλαμβανόμενες διαστημικές λήψεις από radar συνθετικού διαφράγματος (multi-temporal space-borne Synthetic Aperture Radar,

SAR). Οι εφαρμογές των τεχνικών συμβολομετρίας SAR διερευνήθηκαν πραγματοποιώντας επεξεργασία ευρείας έκτασης (Wide Area Processing, WAP), η οποία υλοποιήθηκε από την Γερμανική επιτροπή διαστήματος (DLR).
Για την έρευνα των εδαφικών υποχωρήσεων λόγω της υπεράντλησης των υδροφόρων στην λεκάνη του Ανθεμούντα αναλύθηκαν δεδομένα συμβολομετρίας, της περιόδου 1995 – 2001, από λήψεις των δορυφόρων ERS1/2.
Τα δεδομένα της επεξεργασία ευρείας έκτασης αποδέχτηκαν χρήσιμο εργαλείο για την μελέτη των εδαφικών υποχωρήσεων στο αεροδρόμιο Μακεδονία αλλά και στο οικισμό της Περαίας. Μάλιστα στον οικισμό της Περαίας τα φαινόμενα αυτά την περίοδο 2005 – 2006 προκάλεσαν μία σειρά εδαφικών διαρρήξεων εξ αιτίας του έντονου υποβιβασμού της στάθμης των υδροφόρων.
Εκτός από την μελέτη του φαινομένου η έρευνα ανέδειξε την καταλληλότητα των τεχνικών PSI στον εντοπισμό και την μέτρηση εδαφικών μετακινήσεων. Επίσης έδωσε την δυνατότητα παρατήρησης της διαχρονικής εξέλιξης του φαινομένου με την ανάλυση των χρονοσειρών των μετακινήσεων.
Λέξεις κλειδιά: Εδαφικές υποχωρήσεις, υπεράντληση υδροφόρων, αεροδρόμιο Μακεδονία, Περαία.

1. Introduction

At both regional and local scale studies satellite SAR (Synthetic Aperture Radar) interferometry has demonstrated its suitability to measure the spatial extent and magnitude of surface deformation associated with aquifer-system compaction (Galloway & Burbey, 2011). Furthermore, its complementarity with in situ measurements and geotechnical modelling provides substantial benefits.

The exploitation of Persistent Scatterer (PS) techniques has been recently promoted by several European initiatives, such as the Terrafirma project, a pan-European ground motion hazard information service supported by the ESA's (European Space Agency) GMES (Global Monitoring for Environment and Security) programme. Since the first two-year Stage 1 (which started in 2003), the project is based upon advanced interferometry products.

Launched in December 2009, Terrafirma Extension focuses on several thematic lines for terrain motion analysis: Tectonics, Flooding, Hydrogeology (ground water, landslides and inactive mines) and the innovative Wide Area service, aimed at measuring land deformation over very large areas. Terrafirma Stage 3 consortium is led by Altamira Information, with the Dutch Geological Survey leading the Flood Theme, the Italian National Institute of Geophysics and Volcanology leading the Tectonics Theme, the University of Firenze leading the Hydrogeology Theme, and the German Space Agency leading the Wide Area Mapping task.

Within the Terrafirma project collaboration between the Earth Science Department of the University of Firenze and the Laboratory of Engineering Geology and Hydrogeology of the School of Mining and Metallurgical Engineering of the National Technical University of Athens has been established. One of the main purposes of this study is to investigate ground motions in the Anthemountas basin, a region with a relatively short history of ground subsidence. This area draw the attention of the geo-scientists in 2005 when a series of fractures, causing damages to both buildings and roads, occurred at the Perea village, on the southern section of the basin`s coastal zone. These fractures were attributed to the overexploitation of the aquifers (koumantakis et al, 2008), although they manifested along the active Anthemountas Fault. The application of satellite SAR interferometry (InSAR) for the detection of land motion phenomena reviled that beside the Perea village big parts of the coastal zone subside. The main objectives of the current work are to identify the main causes of the observed ground deformations, to study their mechanisms and to validate the contribution of the remote sensing data on the study of the phenomena.

2. The Study Area

Anthemountas basin is located on the eastern side of Thessaloniki, named after the homonymous river. It extends with a NW-SE orientation from the Thermaikos gulf to the centre of the Chalkidiki peninsula (Figure 1).

The geological formations constituting the Anthemountas basin can be distinguished on the Mesozoic bedrock formations, occupying the bordering mountains, the Neogene deposits outcropping at the hilly areas and the foot of the mountains and the Quaternary deposits occupying the plain area (IGME, 1966; 1978a; b; c; Rozos et al, 1998; Anastasiadis et al., 2001). The Mesozoic formations consist of metamorphic (phyllite and gneiss with marble intercalations) and igneous (granite, gabbro and peridotite) rocks. The Neogene deposits consist of two sequences, the upper sand and gravel sequence and the lower sandy marls - red clays sequence, outcropping successively along the borders of the basin. The quaternary formations occupy the central part of the plain, with an increasing thickness towards the coastal area (Figure 1).

Considering the aquifers three systems can be distinguished in the abovementioned formations (Nagoulis & Loupasakis, 2001): a) the shallow phreatic aquifers system occupying the upper coarse-grained Quaternary deposits extending to a maximum depth of 30m, b) the semi-confined alternating aquifers, extending down to depths from 50 to more than 200m, occupying the lower Quaternary and the Neogene deposits as well as the fractured Mesozoic formations and c) Two deep confined (artesian) aquifers, the one gushing out at the Souroti spring (sub-acidic sparkling mineral water rich in calcium and magnesium) and the other at the thermal springs of Thermi. These systems do not seem to be affected by the ground water level variations of the two shallower aquifer systems.

The Anthemountas River basin has experienced both an increasing urbanization trend and significant population growth in the last few decades. Between 1991 and 2001 the municipality of Thermaikos, Vasilika and Anthemountas experienced an increase of population of about 108.3%, 34% and 3.44%, respectively (WATERinCORE, 2011). In the last decades, several industries, economic activities and infrastructures have developed around the Thessaloniki International Airport, one of the most important infrastructures of Northern Greece.

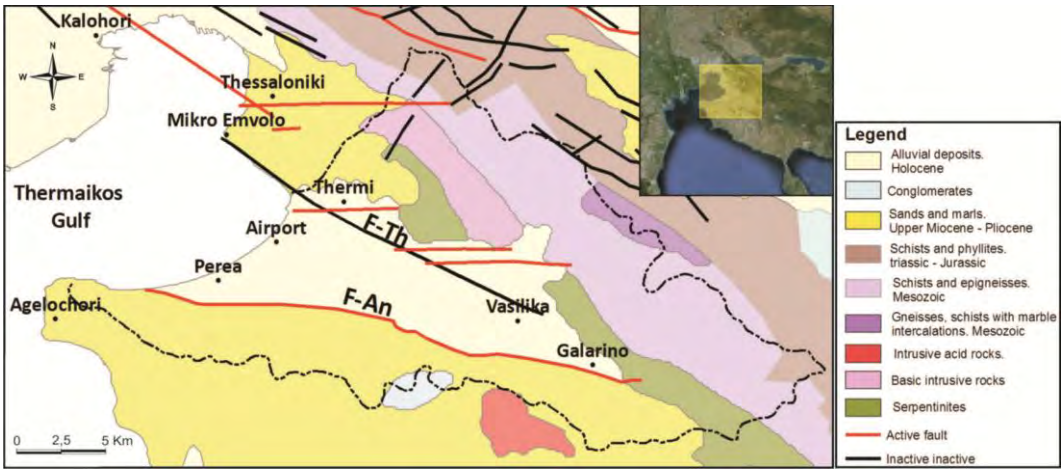

Figure 1 - Geological map of the wider study area (IGME, 1978). The abbreviations F-Th and F-An indicate the Thermi and the Anthemounta faults, respectively. The dotted line indicates the watershed line of the Anthemounta basin.

The continuously increasing demands on water are exclusively covered by the ground water exploitation. Despite the public network for water supply and distribution, several independent and usually uncontrolled water wells have been drilled, whose water abstraction is neither controlled nor systematically metered. Groundwater resources have been considered as renewable and unlimited and no attention was paid on their management. This resulted in the over-exploitation of the phreatic and the semi-confined aquifers, the decline of water levels with a mean annual rate of 1,5 - 2m and, finally, in the the loss of aquifers storage capacity.

3. Land Subsidence Evolution

3.1. Field Observations

The land subsidence phenomena draw the attention of the geo-scientists in 2005 when a series of fractures damaged at the upper Perea village. The fractures caused damages to both buildings and roads extending at a length of about one kilometre (Figure 2). The fractures occurred along the active Anthemounta fault confusing the scientific community. Finally, the phenomenon was attributed to the local overexploitation of the aquifers as in short distance, only a few tens of meters away, three public wells and an unknown number of private wells were operating (Koumantakis et al., 2008). So, the operating wells with a 2,2m mean annual drawdown rate generated an extra drawdown and inside the limits of the intersecting depression cones of the wells the raptures occur.

Apart from the tensile ruptures other visible traces of subsidence, like well-casing protrusion (Figure 3), has been reported northern to surface ruptures, at the same time period. Note that, no other effects related to the groundwater withdrawal can be clearly detected since 2005, not only at the narrow Perea village region but also at the entire basin.

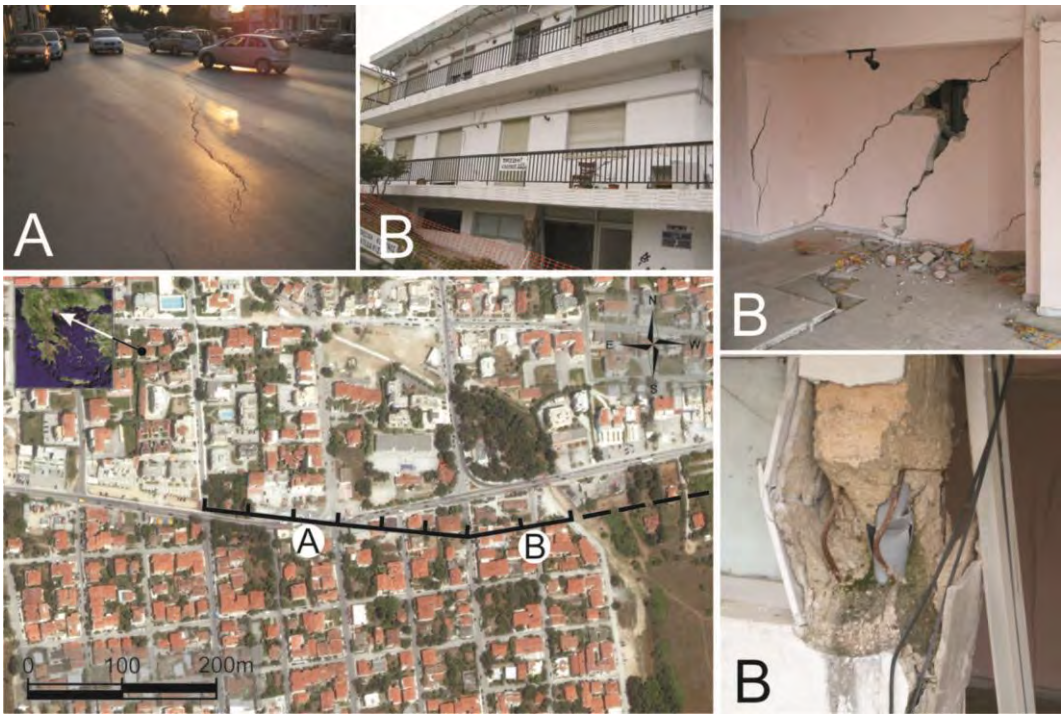

Figure 2 - Satellite picture indicating the 2005 ground rupture in upper Perea. The attached pictures present the damages witnessed at the road paving (A) and at the buildings (B).

Figure 3 - Well-casing protrusion, of about 20cm. The current well is located next to the G2 main well (Figure 6).

3.2. The PSI Interferometric Technique

The land subsidence phenomenon in the wider Anthemountas Plain was studied by exploiting the PSI technique, a remote sensing technology based on multi-temporal satellite SAR (Synthetic Aperture Radar) imagery. The PSI (Persistent Scatterer Interferometry) techniques are based on the processing of several multi-temporal satellite SAR imagery (at least 15-20, or more) of the same target area. The current technique uses long stacks of radar dataset and analyzes the signals backscattered from the observed scene aiming to estimate and remove atmospheric artifacts (Adam et al., 2011). The electromagnetic returns of electromagnetically stable, highly reflective point-wise targets (the so-called Permanent Scatterers, (PS) is statistically processed and analyzed to retrieve estimates of the displacements occurred between different acquisitions (Ferretti et al., 2000; 2011). PSs usually correspond to manmade structures (i.e. buildings, roads, bridge, monuments, pylons), as well as natural reflectors, such as outcropping rocks. Thanks to this multi-interferometric approach the LOS velocity can be estimated, at each Permanent Scatterer, with unprecedented accuracy, sometimes even better than 0.1 mm/year. Displacement time series can be retrieved, acquisition by acquisition, with accuracy on single measurements usually ranging from 1 to 3mm (Colesanti et al., 2003). Each measurement is temporally and spatially referred to a unique reference image and to a stable reference point, respectively.

3.3. SAR Data Used

In the framework of the ESA GMES Terrafirma project, a Wide Area Product (WAP) mapping, based on PSI, was demonstrated by the German Space Agency (DLR). Specifically, 9 satellite image frames were processed using a special semi-automated processor to produce a PSI ground motion map covering a 65,000 km^2 wide area of Greece. This WAP (Wide Area Product) mapping

over Greece is based on stripmap ERS1/2 images, obtained from the European Space Agency (ESA). Among these 9 satellite image frames, track 7_3 was employed for the reconstruction of the history and spatial patterns of land subsidence in the wider Anthemountas area. Track 7_3 consists of a dataset of 42 SAR imagery in C band (5.6cm wavelength), acquired along descending orbits from April 1995 to January 2001.

The reference points of the stack – to which the displacement estimates are referred – was selected in the southernmost part of Thessaloniki's urban fabric, in a sector unaffected by ground motions. The master image for Track 7_3 dataset has been chosen on December 31st, 1996.

3.4. Evaluation of the PSI Data

The analysis of the mean annual displacement velocities, retrieved by PSI processing, provides essential information. An overview of the WAP results for wider Anthemounta basin is presented in Figure 4, as measured by the SAR sensor along the satellite's line of sight and expressed in mm/y. The green dots refer to stable areas. The red dots represent increasing deformation rates, moving away from the sensor (subsidence). As expected, the density of measurement points is higher for the urban areas (maximum density up to about 300 PS/km^2), but lower for agricultural and vegetated terrains (few point/km^2).

The PSI results reveal that the city of Thessaloniki shows very low LOS deformation rates, ranging between -1.5 and 1.5 mm/yr (close to the PSI technique detection sensitivity), indicating stable ground conditions. Considering that a large part of the urban fabric is built over Neogene formations the above observation is reasonable. On the contrary the coastal area of the Anthemountas basin presents significant deformations (Figure 4).

Land subsidence can be clearly identified in the wide Anthemountas basin area with a mean deformation rate of 10mm/yr (Figure 4). In the airport area, observed LOS subsidence rates are 5–15mm/yr, with several points exceeding 20 mm/yr along the NNW-SSE oriented runaway area (Figure 5). PSI results reveal that the coastal area of the Perea village shows very low LOS deformation rates, ranging between -1.5 and 1.5 mm/yr, indicating relatively stable ground conditions since 1995. Nevertheless, in the southern part of the urban area subsidence can be observed, with maximum LOS deformation rates up to 10–15 mm/yr (Figure 6). The fact that the deformations have not affected the lower Perea as well supports the theory claiming that they were caused by the local overexploitation of the aquifers inside the intersecting depression cones of the active wells.

It is worth to notice that detected subsiding areas in the wider Anthemountas basin are distributed as either circular or as elongate patterns. The main "classical" subsidence bowl, corresponding to intense groundwater extraction, affects mostly the central part of the basin: here the measured subsidence rates seem to increase towards the coastline, where the thickest sequences of compressible Quaternary layers crop out.

Furthermore, a NW-SE oriented pattern, elongated parallel to the major normal Thermi fault (F-Th in Figure 1) bordering the NE part of the basin can be observed. This fault marks the geological boundary between the Quaternary alluvial sediments on the hanging wall and the Neogene over consolidated formations. According to the PSI data along the fault line a mean deformation of 5-7 mm/yr, with peak values up to 10mm/yr, is observed. These activity indications are of great interest as up to now this fault is referred to as inactive (Pavlides & Kilias, 1987; Tranos et. al., 1999, 2003; Zervopoulou, 2010). The lack of data across the fault prevent the calculation of the actual differential displacement across the fault, so the absolute deformation values deriving from the analysis (5-7mm/yr) seems to be excessive and they cannot be taken under consideration. In that case the PSI date can be considered only as activity indications.

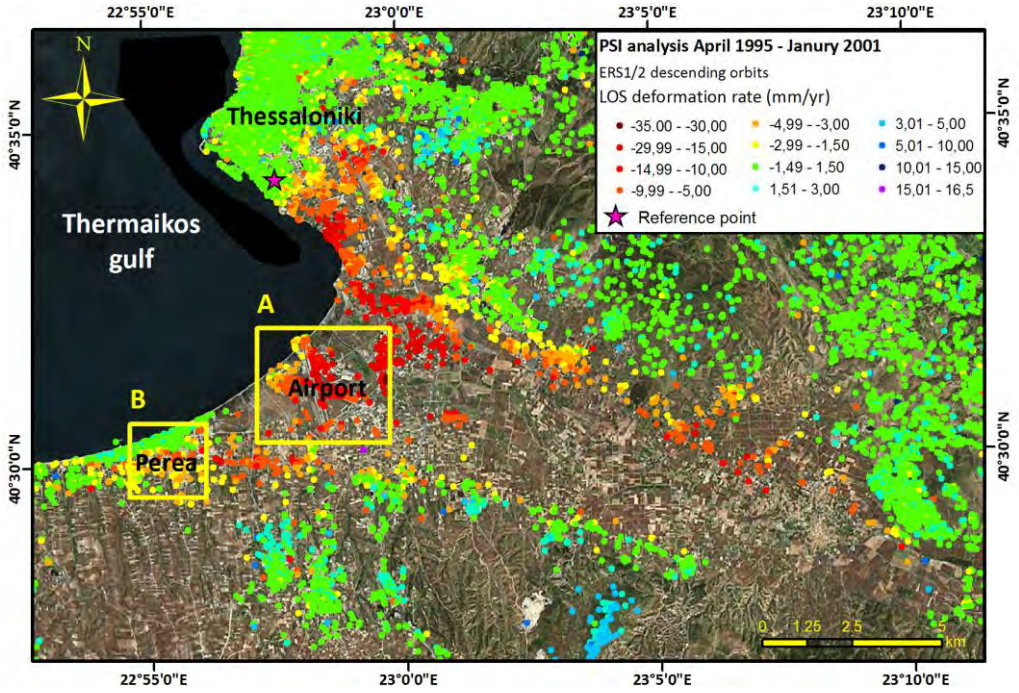

Figure 4 - Basin scale detection of ground subsidence through PSI. The Line of Sight - LOS deformation rates in the Anthemountas basin are presented. PSI map is overlaid on Visual Earth imagery. The polygons A and B indicate the areas subjected to local scale detection of ground subsidence.

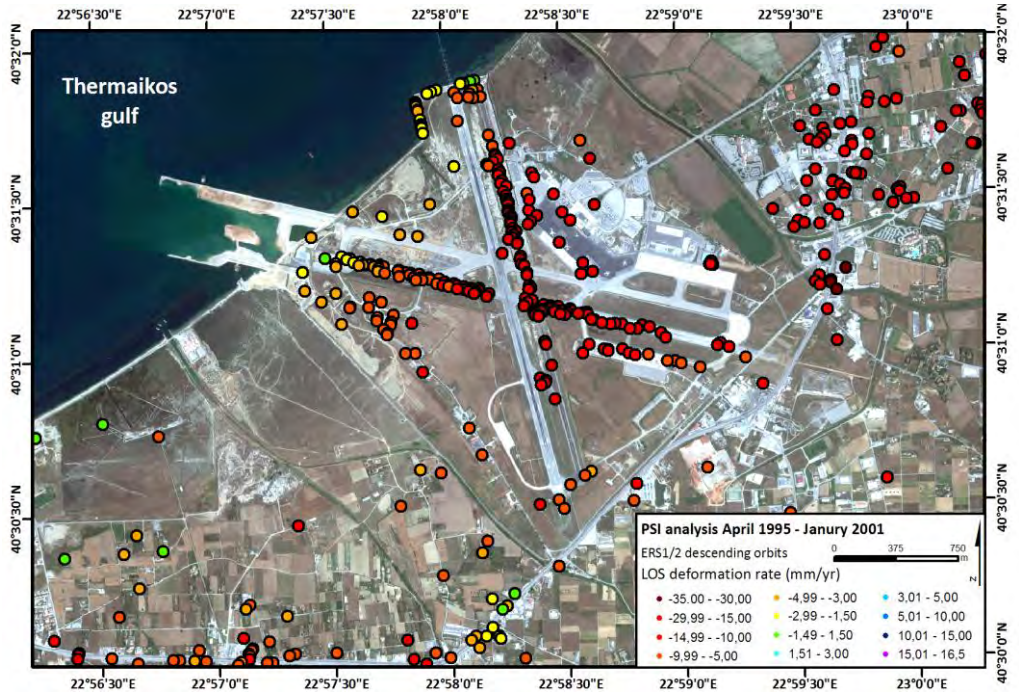

Figure 5 - Local scale detection of ground subsidence through PSI at the Macedonia International Airport. The location of the airport is clearly indicated in Figure 4.

Figure 6 - Local scale detection of ground subsidence through PSI at the Perea Village. The location of the village is clearly indicated in Figure 4.

4. Conclusions

The PSI results provided substantial information about the actual extent of the land subsidence phenomenon as, up to now, the only indications of this phenomenon were identified at the village of Perea. As already mentioned the Perea village was affected in 2005-2006 by a series of ground ruptures triggered by the excessive groundwater withdrawal, since then no further indications about the evolution of the phenomenon were recorded. The PSI data revealed that not only Perea but also the entire lower part of the Anthemountas plain area is affected by land subsidence phenomena. The most affected area includes a big part of the Thermi industrial zone as well as the Macedonia international airport.

The detection of the phenomena at an initial stage is extremely important, as further extension of the affected area and damages on settlements and infrastructure can be prevented. The information provided by this study can give rise to focused geotechnical and hydrogeological studies aiming to stop the phenomenon before it becomes an actual problem for the area.

This study proved that the repeat-pass satellite SAR interferometry can be exploited not only to map the extension of affected areas at a regional (basin) level but at a local level also, as it was proved valuable for the study of the phenomenon at the narrow airport or upper Perea region. Furthermore it should be noticed that this technique can also be exploited for the evaluation of the deformation history. The displacement time series, available for each PS in the area of interest, are ideal suited for large-scale, spatially continuous monitoring of geohazard-related ground motion.

5. Acknowledgments

The Terrafirma Extension project has funded the SAR imagery processing as well as the geological interpretation presented in this paper. The project is one of the many services being supported by the Global Monitoring for Environment and Security (GMES) Service Element

Programme, promoted and financed by the European Space Agency (ESA). The authors gratefully acknowledge the German Aerospace Centre (DLR) for having processed the SAR data.

6. References

Adam N., Rodriguez Gonzalez F., Parizzi A. and Liebhart W. 2011. Wide area persistent scatterer Interferometry*, Proceedings of IGARSS,* Vancouver, Canada.

Anastasiadis A., Raptakis D. and Pitilakis K. (2001). Thessaloniki's Detailed Microzoning: Subsurface Structure as Basis for Site Response Analysis, *Pure and Applied Geophysics,* 158, 2597-2633.

Colesanti C., Ferretti A., Prati C. and Rocca F. 2003. Monitoring landslides and tectonic motion with the Permanent Scatterers technique, *Engineering Geology,* 68(1–2), 3–14.

Ferretti A., Fumagalli A., Novali F., Prati C., Rocca F. and Rucci A. 2011. A new algorithm for processing interferometric data-stacks: SqueeSAR™, *IEEE Transactions on Geoscience and Remote Sensing*, (99), 1-11.

Ferretti A., Prati C. and Rocca F. 2000. Nonlinear subsidence rate estimation using Permanent Scatterers in differential SAR interferometry, *IEEE Transactions on Geoscience and Remote Sensing*, 38 (5), 2202– 2212.

Galloway D.L. and Burbey T.J. 2011. Review: regional land subsidence accompanying groundwater extraction, *Hydrogeology Journal* (19), 1459–1486.

I.G.M.E 1966. Geological Map of Greece, Scale 1:50.000, *Epanomi Sheet*, IGME, Athens.

I.G.M.E 1978a. Geological Map of Greece, Scale 1:50.000, *Thessaloniki Sheet*, IGME, Athens.

I.G.M.E 1978b. Geological Map of Greece, Scale 1:50.000, *Thermi Sheet*, IGME, Athens.

I.G.M.E 1978c. Geological Map of Greece, Scale 1:50.000, *Vasilika Sheet*, IGME, Athens.

I.G.M.E 1978d. *Geological Map of Greece*, Scale 1:500.000, IGME, Athens.

Koumantakis I., Rozos D. and Markantonis K. 2008. Ground subsidence in Thermaikos municipality of Thessaloniki County, Greece. *International Conference Gro-Pro – Ground water protection – Plans and Implementation in a North European Perspective*, (1), 177-184 Korsør Denmark.

Nagoulis A. and Loupasakis C. 2001. Hydrogeological conditions of the plain area of the Anthemounta basin (Macedonia, Greece), *Bulletin of the Geological Society of Greece*, (34), 1859 – 1868.

Pavlides S.B. and Kilias A.A. 1987. Neotectonic and active faults along the Serbomacedonian zone (Chalkidiki, N. Greece), *Annales Tectonicae,* (1), 97–104.

Rozos D., Hatzinakos I. and Apostolidis E. 1998. Engineering Geological Map of Thessaloniki wider area, Scale 1:25.000. *I.G.M.E.*, Athens.

Tranos M.D., Kilias A.A. and Mountrakis D.M. 1999. Geometry and kinematics of the Tertiary post-metamorphic Circum Rhodope Belt Thrust System (CRBTS), Northern Greece, *Bulletin of Geological Society of Greece*, (33), 5–16.

Tranos M.D., Papadimitriou E.E. and Kilias A.A. 2003. Thessaloniki–Gerakarou Fault Zone (TGFZ): the western extension of the 1978 Thessaloniki earthquake fault (Northern Greece) and seismic hazard assessment, *Journal of Structural Geology,* (25), 2109–2123.

WATERinCORE 2011. Sustainable Water Management through Common Responsibility enhancement in Mediterranean River Basins - Strategic Water Management Plan for Anthemountas River Basin.

Zervopoulou A. 2010. Neotectonic Faults of the Wide Area of Thessaloniki in association with foundation Soils, *Ph.D. Thesis*, University of Thessaloniki (in Greek).

Δελτίο της Ελληνικής Γεωλογικής Εταιρίας, τομ. XLVII , 2013
Πρακτικά 13ου Διεθνούς Συνεδρίου, Χανιά, Σεπτ. 2013

Bulletin of the Geological Society of Greece, vol. XLVII 2013
Proceedings of the 13th International Congress, Chania, Sept. 2013

REMOTE SENSING TECHNIQUES AS A TOOL FOR DETECTING WATER OUTFLOWS. THE CASE STUDY OF CEPHALONIA ISLAND

Stefouli M.[1], Vasileiou E.[2], Charou E.[3], Stathopoulos N.[2], Perrakis A.[3] and Giampouras P.[3]

[1] National Center of Sustainable Development, Unit of Environmental Policies, 241 Kifisias Avenue Vila Kazouli, 14561, Greece. stefouli@igme.gr

[2] National Technical University of Athens, School of Mining & Metallurgical Engineering, Laboratory of Engineering Geology & Hydrogeology, Heroon Polytechniou 9, 15780, Athens, Greece., elvas@metal.ntua.gr, nstath@metal.ntua.gr

[3] National Center for Scientific Research – Demokritos, Institute of Informatics and Telecommunications, Computational Intelligence Laboratory, 153 10, Agia Paraskevi, Athens Greece. exarou@iit.demokritos.gr, perrakisandreas3@gmail.com parisg@iit.demokritos.gr

Abstract

The amount of water flowing into the seas and oceans has slowly but steadily increased in recent years, signifying a possible speeding up of the water cycle due to climate change. The detection of the water outflows and the exploitation of them are very important to the rational water management. Remote sensing techniques has been proven a valuable tool for the detection and identification of submarine groundwater discharge-SGD (Submarine Groundwater Discharge). In this study the island of Cephalonia in Ionian sea, Greece is considered as a case study. A 6 Km sea buffer zone around the island is studied using Landsat images. Submarine groundwater discharge has been detected through remote sensing methods and the results have been combined with the tectonism and hydrogeological conditions of the island. A quantitative analysis of temperature in the buffer zone was carried out. The sea thermal anomalies in the same zone were also investigated.
Key words: *submarine springs, Ioanian sea, karstic system,GIS, Landsat, Thermal Infrared .*

Περίληψη

Η ποσότητα του νερού, που εκφορτίζεται στη θάλασσα και τους ωκεανούς, παρουσιάζει μια αργή αλλά σταθερή αύξηση τα τελευταία χρόνια, που σηματοδοτεί μια πιθανή επιτάχυνση του κύκλου του νερού λόγω των κλιματικών αλλαγών. Ο εντοπισμός των εκροών του υπόγειου νερού και η εκμετάλλευσή τους είναι πολύ σημαντική για την ορθολογική διαχείριση των υδάτων μια περιοχής. Οι τεχνικές τηλεπισκόπησης έχουν αποδειχθεί ένα πολύτιμο εργαλείο για τον εντοπισμό και την ταυτοποίηση των υποθαλάσσιων εκφορτίσεων μέσω των πηγών SGD. Στην παρούσα εργασία γίνεται εφαρμογή των μεθόδων αυτών στο νησί της Κεφαλονιάς στο Ιόνιο. Μια ζώνη επίδρασης 6 χιλιομέτρων γύρω από το νησί μελετήθηκε χρησιμοποιώντας εικόνες Landsat. Υποθαλάσσιες εκφορτίσεις εντοπίστηκαν με μεθόδους

τηλεπισκόπησης και τα αποτελέσματα αξιολογήθηκαν σε συνδυασμό με την τεκτονική και τις υδρογεωλογικές συνθήκες του νησιού. Μια ποσοτική ανάλυση της θερμοκρασία στα όρια επίδρασης των 6 km πραγματοποιήθηκε. Οι θερμικές ανωμαλίες που εμφανίζονται στη ζώνη αυτή διερευνήθηκαν.
Λέξεις κλειδιά: *υποθαλάσσιες πηγές, Ιόνιο πέλαγος, καρστικό σύστημα,GIS,Landsat, Θερμικό Υπέρυθρο.*

1. Introduction

GIS and Remote Sensing are powerful tools which provide solutions for water resources problems; such as assessing water quality, determining water availability, managing flood problems, understanding the natural environment, and managing water resources on local and regional levels.

Coastal aquifers have the tendency to discharge their subsurface flow into the sea either through seepage or submarine springs where fractures prevail. Karstic aquifers may have hydraulic links with the sea resulting in dominant flow of submarine springs. These springs were known to exist since the time of the Phoenicians (1000 years ago) where they used submarine springs. Recently submarine springs were discovered by divers and described by scientists in many countries such as Greece, France, Libya, Italy, Spain and South America and some other areas in the world. Although these springs are well documented no attempts were made to survey these areas in order to locate these springs (Al Bassam, 2005).

A basic driver of freshwater SGD is the amount of rainfall received by the drainage basin, coupled with evapo-transpiration rates and the surface geology (particularly the surface infiltration capacity) but flow through coastal marine sediments can occur for a variety of reasons. Flow may be induced by the terrestrial hydraulic gradient as well as by marine processes such as wave set-up, tidally driven oscillations, density-driven convection, and thermal convection(Al Bassam, 2005).

The mix will be different in different regions. It will depend, for example, on the hydraulic conductivity, hydraulic head, groundwater catchment area, recharge rates and many other factors. Density-coupled modelling of the saltwater interface indicates that seawater recirculation rates of 60% and more can occur due to dispersion and mixing within the aquifer even when wave and tidal effects are ignored. Since wave-induced and tidal effects are rarely completely absent, a great deal of seawater recirculation must occur on a global scale, while the local effects of freshwater SGD can be dominant in near shore environments (Al Bassam, 2005).

Coastal aquifers have the tendency to discharge their subsurface flow into the sea either through seepage or submarine springs where fractures prevail. Karstic aquifers may have hydraulic links with the sea resulting in dominant flow of submarine springs.

The contribution of the remotely sensed data to the geologic / geomorphologic mapping and identification of changes of fresh water outflow through time is indicated with the processed satellite imagery for the pilot project area. .

This paper is organized into the following 4 sections. Section 2, presents the Geology-Hydrogeology of the study –pilot area, the Cephalonia island, Greece. Section 3 describes the data set and the methodology used, the main pre-processing techniques adopted and Section 3 describes and discusses the experimental results obtained. Finally, Section 4 draws the conclusion of this paper.

2. Study-Pilot Area, Cephalonia Island

Cephalonia Island is used as pilot project area of study. The island is located in western Greece, in the Ionian sea. It covers a land of 781 km^2 and it has about 35.000 habitants and important touristic development (IGME, 2010). The hydrogeological conditions of the area are very complex. The

island could be characterized as mountainous in the major part of the land. Different karstic systems create a very interesting hydrodynamic regime, with high capacity aquifers, spring discharges and water outflows in the sea around it. Submarine springs have been detected through remote sensing methods. The detection of the water outflows and the exploitation of them are very important to the rational water management of the island.

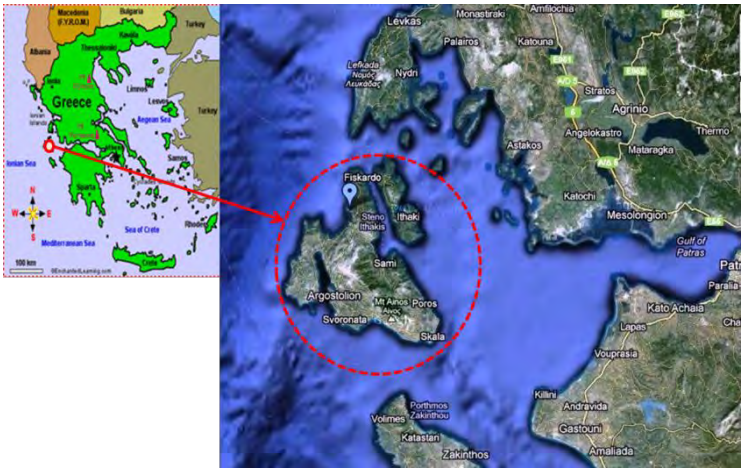

Figure 1 - The study area (www.googlemap.gr).

2.1. Geology-Hydrogeology of Cephalonia

Cephalonia Island belongs to Paxos and Ionios geotectonic zones. Paxos zone covers the widest part of the island. The main formations of the zone are the limestones of the Upper Cretaceous and smaller lanes of Paleocene and Eocene limestones. The Lower Cretaceous appears in small extent, with dolomitic limestones and dolomites in the area of Asos. Above the more recent limestones of this carbonic series, there are Oligocene and Miocene formations consisting of marbles, clays, or alternations of them with sandstones, conglomerates and limestones. In the eastern part of the island (Sami – Skala) the formations of the Ionian zone are overthrusted to Miocene deposits of Paxos zone (IGME, 2010).

The island's developing formations, from the more recent to the older ones, are the following:

- Alluvium and scree of the Oligocene
- Sandstones and conglomerates of the Pleistocene
- Conglomerates, sandstones and limestones of the Pliocene

Formations of Paxos Zone

- Conglomerate and lacustrine limestone of the Upper Oligocene – Upper Miocene
- Limestones Eocene – Oligocene
- Limestones Paleocene
- Limestones of the Upper Cretaceous
- Dolomites and limestones of the Upper Cretaceous

Formations of Ionian Zone

- Limestones of the Eocene
- Limestones of the Paleocene
- Lacustrines and limestones of the Upper Cretaceous
- Viglae limestones of the Upper Jurassic – Lower Cretaceous
- Schist and limestones of the Middle and Upper Dogger
- Pantocrator limestones of the Upper Trias – Middle Lias

As it is shown in geological map (Figure 2), there are many faults in total extent of Island. The main directions of the faults are NNW-SSE, N-S, NE-SW and E-W. Because of the actions of these faults, there is the tectonic sink of Argostoli bay and the lagoon of Koutavos.
The Island is mainly covered by carbonate formations, which are permeable. Because of the extended development of permeable formations, there is not significant surface run off, the total volume of rainfall infiltrates and recharges the karstic aquifers. The karstic systems of the Island are very complex because of the intense tectonism.

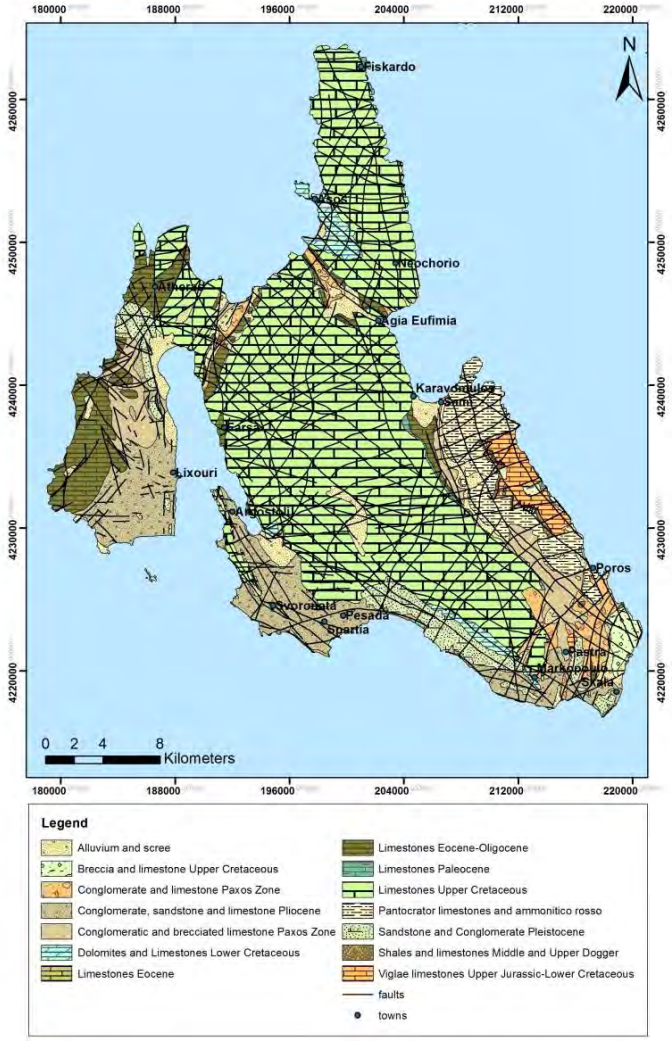

Figure 2 - Geological map of Cephalonia Island.

Six different karstic systems are developed in the Island. The karstic system of mountain Ainos (Ionian zone) is discharged by three coastal springs. These karstic systems have significant outflows to the sea, which are very difficult to quantify them. According to Koumantakis (1989), the most significant springs in the Island are : a) Springs of Agios Ioannis (200m^3/h) b) Papadatos springs (300 m^3/h) in Koutavos, c)Springs of Avuthos (100m^3/h), d) In the Sami moorage, the saline springs of Karavomilos and Agia Eufimia. All these springs are the surface discharge points from the respectively karstic systems, but there are also many submarine springs with significant outflows to the sea. The karstic system of mountain Atros is discharged surficial by Avuthos springs. The karstic system of Kalo Oros, at the north part of Cephalonia is exploited by drills and

it is in hydraulic connection by the sea. Outflows come also from the karstic sytem of Paliki, at the area of Aitheras. In Lixouri it is developed a semi-aquifer system in the alluvial deposits. In Argostoli there is a granular water system, confined and unconfined aquifers are developed.

The average annual precipitation in Cephalonia Island was estimated at about 890 mm for the period 1955-2008 in meteorological station of Argostoli. The evapotranspiration was estimated at 48% (427 mm) of the total precipitation. The surface flow and infiltration is about 52% of the rainfall, groundwater drainage is about the 43% of this amount (IGME, 2010). The rainfall was decreased during these 55 years. The recharge of the aquifers is characterized satisfactory and capacity of them remains high.

The water quality varies; the phenomenon of sea intrusion takes place in the coastal areas, because the most of the karstic systems are open to the sea, or due to overexploitation of the aquifers. High salinity has measured in many sampling. The geochemical ``pollution`` is also presented in many cases, because limestones are soluble, so the chemical reaction of ion exchange is performed.

The island has a significant touristic development; because of this the water needs are increased specially in summer time. The exploitation of the water resources are done by drillings wells and the springs. According to IGME (2010) 97 drills, 30 wells and 18 springs were recorded, but the real number of the subtraction works are definitely bigger than these (figure 3).

All these specific hydrological and hydrogeological conditions create the complex groundwater system interacting with the sea in Cephalonia Island. The need of investigating the submarine discharges is increased during the time, it is more imperative in nowadays, because of the climate changes. The exploitation of these outflows to the sea is demanded, as the water deposits are decreased, but the water demands are increased

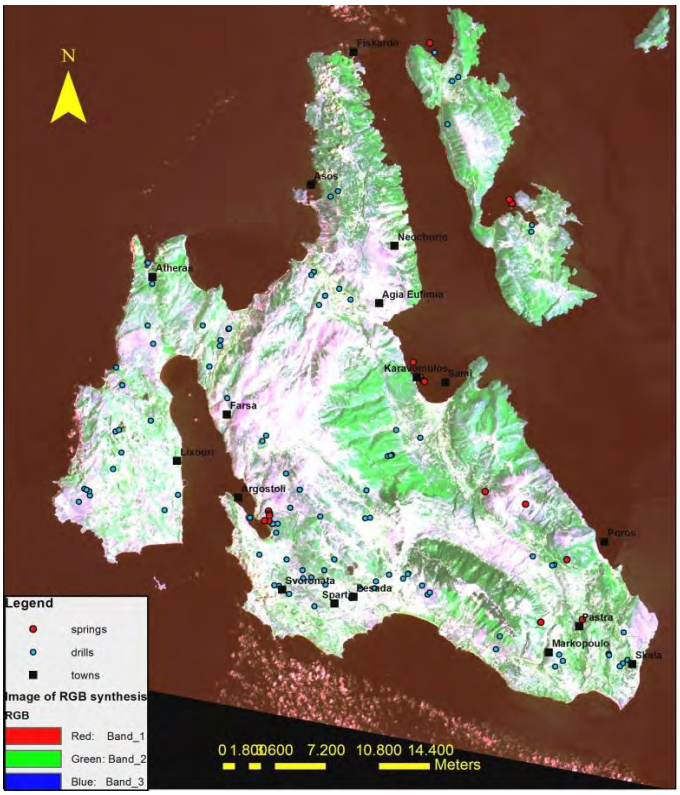

Figure 3 - Satellite image of Cephalonia with the water point subtractions.

3. Thermal Infrared Remote Sensing Data Analysis

Thermal Infrared radiation is emitted from warm objects such as the Earth's surface. Space borne remote sensing of this radiation is carried in certain parts (3μm-4μm and 10.5μm-12.5μm) of the thermal infrared region, of the EM Spectrum Thermal Infrared Images are used to quickly assess large areas and acquire useful information and measurements of the earth's land and sea surface temperatures, forest fires etc. Among various satellite derived thermal infrared Images that are currently available, the freely available Landsat TM/ETM are very popular.

Landsat thermal imagery have been used in monitoring evapotranspiration and managing water re sources (Anderson et all 2012) , land surface temperature,(Karnielli et al.2001, Jimenez-Munoz et al., 2003), lake surface temperature distributions (Charou et al., 2010). Since the 1970s, both satellite and airborne TIR have been used to detect groundwater discharge, either warmer or cooler than the surrounding surface water, by successfully detecting the contrast in water temperature from different sources. In coastal sea surface temperature variability Landsat Thermal Imagery have been used in synergy with AVHRR data (Thomas, 2003).

In this study Landsat TM/ETM Thermal Infrared images were used to identify surface temperature and specific locations of thermal anomalies. Thermal infrared only measures surface temperatures so its application is limited to the surface seawater. The groundwater temperature is relatively stable and it is as an average temperature of the area, while the temperatures of the surface water are changeable with the changing of the seasons

3.1 Thermal Variations Detection and Interpretation

A set of six Landsat 7 Enhanced Thematic Mapper Plus (ETM+) scenes for the years 1984, 1986, 1990, 2000, 2001 and 2005 and one Landsat5 image for the year 2011 was acquired over the Ionian islands have been downloaded from the USGS website (http://glovis.usgs.gov) and used forthe analysis. The Landsat 7 ETM+ of 2005, as all Landsat 7 images collected after May 31, 2003, when the Scan Line Corrector (SLC) failed has data gaps. However the image is still useful for thepart of the image that is to the west of the Cephalonia Island which is not corrupted.

Various image processing and GIS techniques have been used for the analysis of the satellite imagery using the TNTmips software package (www.microimages.com). Pre-processing and image enhancement for the identification of Areas of Interest AOI concerning sea water outflows have been applied. A 6 Km buffer zone around the Cephalonia island was drawn on the Landsat Thermal bands A land mask was created and extracted from all images in order to isolate/separate the sea zone. Variations of intensity in thermal bands were identified. A red color palette was applied to thermal bands for a better visualization (Figure 4). Dark red tones correspond to cold waters while light red to warmer waters.

3.2 Quantitative Assessment of Thermal Anomalies

In order to quantitatively assess the thermal anomalies the digital numbers of the original bands were converted to temperature (Celsius) using the relevant standard procedures for Landsat 5 and Landsat 7, available and well used in bibliography (Skianis, 2012) The temperature Map derived from the June, 6 of 2001 Landsat ETM Thermal Band 62 is shown in Figure 6. The sea surface temperatures were estimated for all images and the observed temperatures range from 19.5 ^{o} C to 23.5 ^{o} C.

Identified thermal anomalies in Cefalonia's coastal zone, were studied for their possible association with fresh water outflow by consulting topographic and geologic maps. A preliminary analysis reveals, that hydraulic gradients on land result in ground water seepage near shore. Artesian aquifers can extend from shore. In some cases, these deeper aquifers may have fractures in the overlying confining layers allowing fluid exchange between the ground water and the sea. This seems to be the case in Argostoli bay (Figure 5-b), where thermal anomalies have been identified in the Landsat thermal bands.

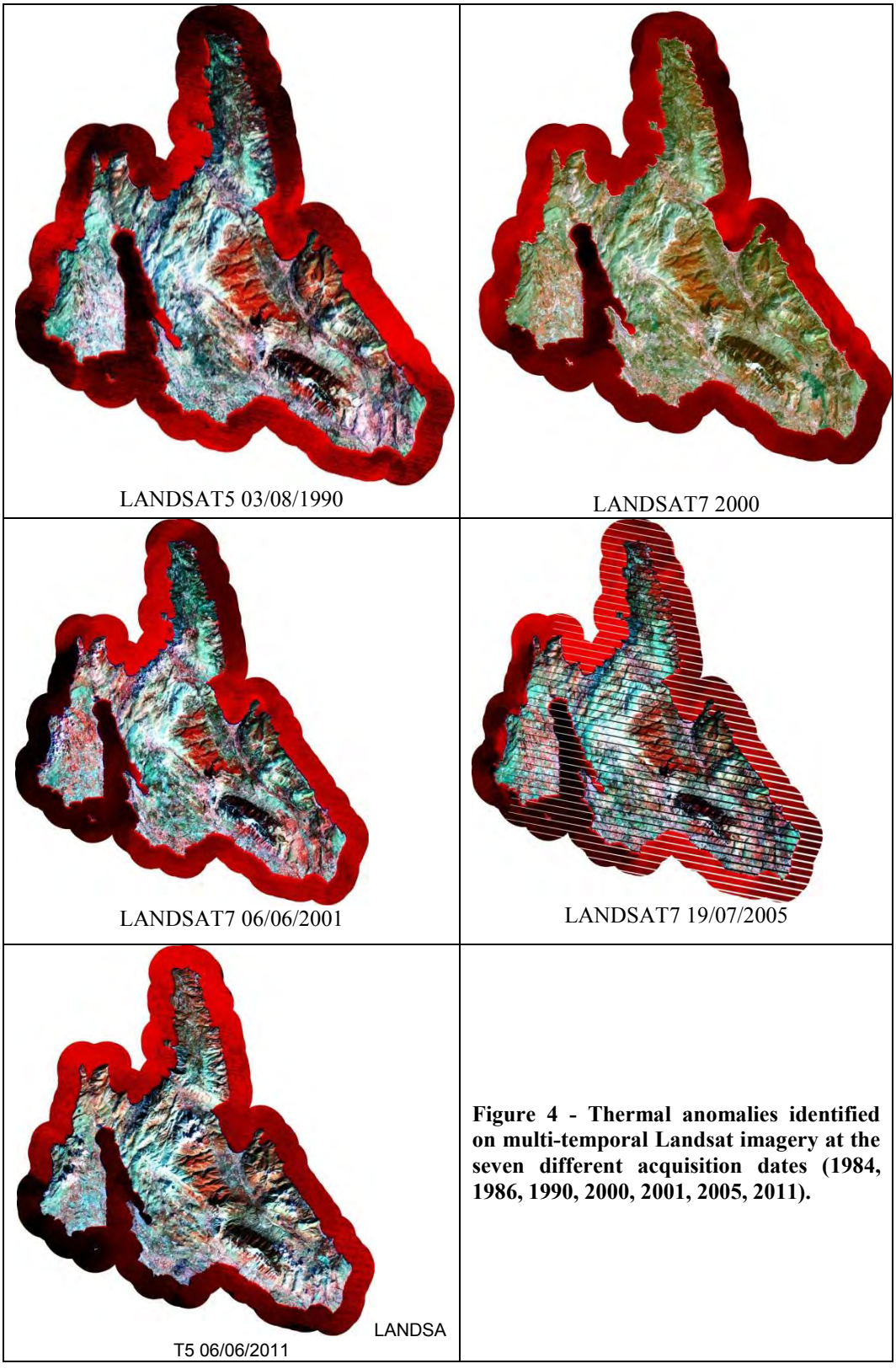

Figure 4 - Thermal anomalies identified on multi-temporal Landsat imagery at the seven different acquisition dates (1984, 1986, 1990, 2000, 2001, 2005, 2011).

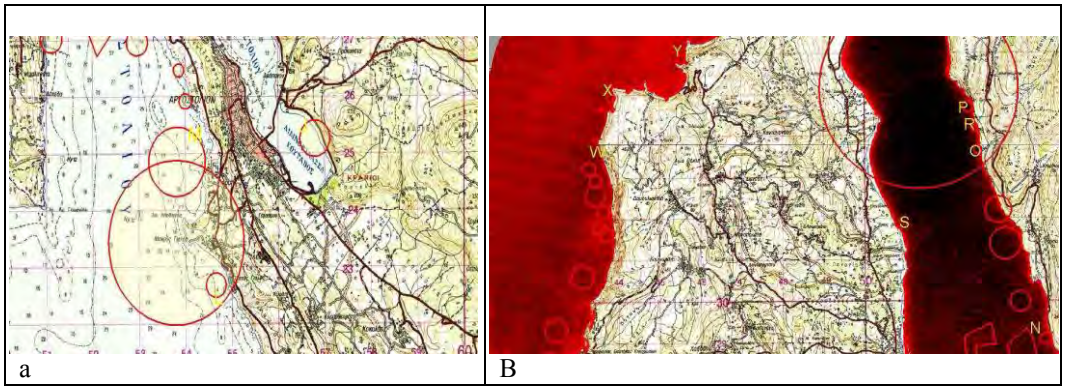

Figure 5 - Topographic Map superimposed in Thermal band with identifiable thermal anomalies.

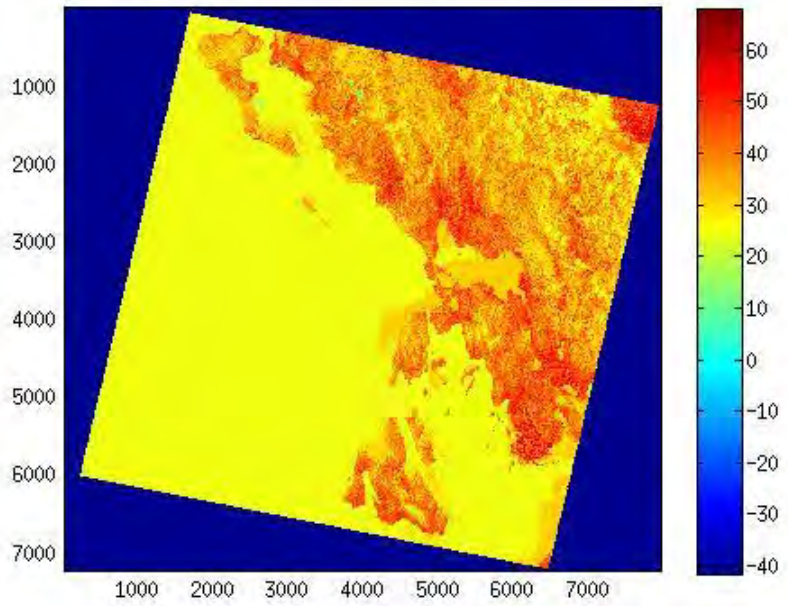

Figure 6 - Temperature Map derived from Thermal band 62 of Landsat 7 (06/06/2001).

In Figure 7, areas with water temperature lower than the surrounding sea water (deep blue colour) are identified. A subset of the imagery of 2001 image was extracted and for this subset the total area of low sea surface temperature was calculated. This is estimated to 1.4 Km^2.

4. Results and discussion

An approach of complementary techniques is applied to localise coastal ground water discharge in the widespread carbonate coastal aquifer of Cephalonia Island. Large coastal discharges have been observed using remote sensing techniques and this provides important information concerning different parameters of interest to a hydrological project. The locations of water outflows seem to be associated with tectonic discontinuities which can be mapped in detail on the satellite images. These discontinuities are used as conduits for the subsurface water flow. The geological

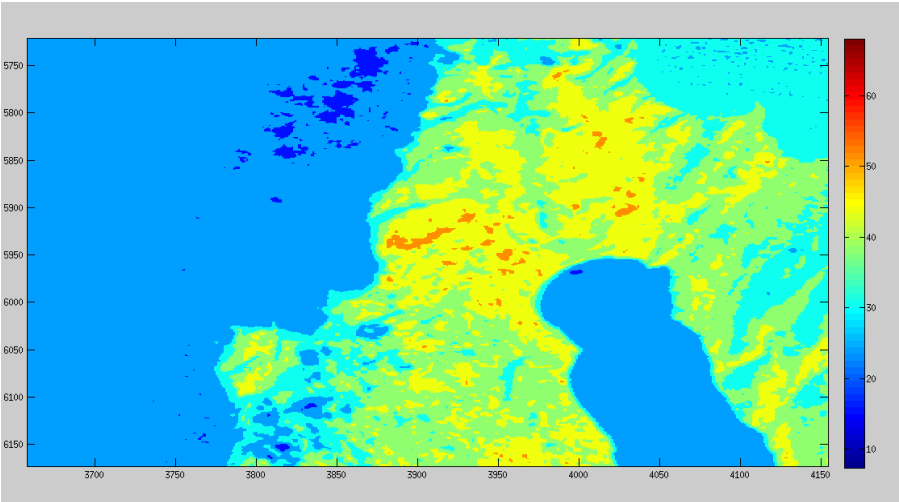

Figure 7 - Areas of low temperature sea water (dark blue).

formations of Cefalonia, which is covered by limestones, create favourable conditions for the occurrence of submarine discharges. Differences in the number and intensity of the identified water outflows between the various satellite image data are attributed to annual / seasonal differences of the hydrologic cycle inland and the ground water system in the coastal aquifers. Differences that are observed between the outflows, that have been recorded in the field and those interpreted on the satellite images, are due to the image resolution of the thermal bands and the prevailing hydrological conditions during the previous year, than the one when the field campaign has been carried out.

Monitoring is supported due to the multi-temporal character of the data. Additionally, satellite data can be analyzed to generate GIS database information required for hydrological studies. Generated database can be used to assess changes that are taking place for the fresh water outflows in coastal areas while tectonic features can be mapped effectively. The added advantage of the proposed approach, is that it makes available to end-users a variety of the data and that it helps in efficient analysis and prediction.

Although Landsat instruments are optimized for terrestrial targets they could be used for the study of possible water outflows into the sea. It is possible to identify thermal anomalies in sea surface and estimate the temperature as well as the area extent of these anomalies. The problem of using Landsat for such study is the large resolution of their images. However the processing of these images along with good knowledge of the geology, topography and hydrology may reveal a good possibility of detecting freshwater out flows. This must be coupled with field investigation and air borne TIR survey. Remote sensing technology has great potential for ground water monitoring and management by providing data to supplement the conventional field data. Considerable basic research and developments are indispensable in the future for enhanced and wide-scale applications of these two highly promising and economically viable techniques in groundwater hydrology.

5. References

Al Bassam Abdul Aziz, 2005. Using Remote Sensing and GIS for Submarine freshwater Springs exploration as a Plausible water source in Saudi Arabia" Faculty of Science/King Saud University Eng. Hiba Mohammed Tiro, GIS Department Manager / Engineering Department / Saudi Oger LTD.

Anderson M.C., Allen R., Morse A. and Kustas W. 2012. Use of Landsat thermal imagery in monitoring evapotranspiration and managing water resources, *Remote Sensing of Environment*, doi: 10.1016/j.rse.2011.08.025.

Ahlgren S. and Holmlund J. 2002. Outcrop Scans Give New View. American Association of Petrolum Geologists Explorer, July 2002. Available online at: http://www.aapg.org/explorer/geophysical_corner/2002/07gpc.cfm

Charou E, Stefouli M., Katsimbra E. and Chioni A. 2010. Monitoring lake hydraulics using remote sensing techniques in West Macedonia, *6th International Symposium on Environmental Hydraulics,* Athens, Greece, 887-892.

IGME 2010. Recording and evaluating of groundwater's hydrogeological characteristics and the aquifer system of Greece, 3rd Community Support Framework, Athens.

Jimenez-Munoz J.C. and Sobrino J.A. 2003. A generalized single-channel method for retrieving land surface temperature from remote sensing data, *Journal of Geophysical Research*, 108, doi: 10.1029/2003JD003480.

Karnieli Q. and Berliner P. 2001. A mono-window algorithm for retrieving land surface temperature from Landsat TM data and its application to the Israel-Egypt border region, *International Journal of Remote Sensing*, 22, 3719-3746.

Koumantakis I.E. 1989. Research of the aquifer system of Kefalonia Island: The regulation of the lake-spring of Megali Avuthos. Proposals for the exploitation of south-east Cephalonia Island. School of Mining and Metallurgy Engineering, Section of Geological Sciences, NTUA.

Skianis G., Nikolakopoulos K. and Vaiopoulos D. 2012. *Remote sensing*, IWN Editions.

Stefouli M., Tsompos P., 2004. Identification and monitoring of fresh water outflows in coastal areas:pilot study on Psahna area/Evia island Greece, *Bulletin of the Geological Society of Greece,* vol. XXXVI, Thessaloniki.

Thomas A., Byrne D. and Weatherbe R. 2002. Coastal sea surface temperature variability from Landsat infrared data, *Remote Sensing of Environment*, 81, 262–272.

http://landsathandbook.gsfc.nasa.gov/data_prod/

Δελτίο της Ελληνικής Γεωλογικής Εταιρίας, τομ. XLVII , 2013
Πρακτικά 13ου Διεθνούς Συνεδρίου, Χανιά, Σεπτ. 2013

Bulletin of the Geological Society of Greece, vol. XLVII 2013
Proceedings of the 13th International Congress, Chania, Sept. 2013

THE VALUE OF GEOLOGICAL DATA, INFORMATION AND KNOWLEDGE IN PRODUCING LANDSLIDE SUSCEPTIBILITY MAPS

Tsangaratos P.[1] and Koumantakis I.[1]

[1]National Technical University of Athens, School of Mining and Metallurgical Engineering, Department of Geological Studies, ptsag@metal.ntua.gr, koumantakisioannis@gmail.com

Abstract

The paper attempts to illustrate the value of Geological data, information and knowledge in studies that investigate landslide phenomena and how this is reflected in the production of landslide susceptibility maps. In particular, the concepts of data, information, knowledge and wisdom are defined and also the process of converting data into information and information into knowledge. The presented study continuous with a summary that introduces landslide phenomena and the available techniques and methods for identifying and classifying these natural phenomena. It describes the significance of landslide analysis and how this process is essential in order to orient intelligence decisions regarding strategies for regional and urban development. The susceptibility maps that are considered as the outcomes of the over mentioned process, reflects the Geological Knowledge that has been produced by involving expert knowledge and processing data.
Key words: *Landslide assessments, data processing, expert knowledge.*

Περίληψη

Στο άρθρο αυτό επιχειρείται να δοθεί μια συνοπτική παρουσίαση της αξίας που έχει η διαχείριση της γεωλογικής πληροφορίας σε μελέτες διερεύνησης κατολισθητικών φαινομένων και του τρόπου με τον οποίο αυτή αποτυπώνεται σε χάρτες κατολισθητικής επιδεκτικότητας. Συγκεκριμένα, ορίζονται οι έννοιες, δεδομένα, πληροφορία, γνώση, και παρουσιάζεται η διαδικασία μετατροπής των δεδομένων σε πληροφορία και της πληροφορίας σε γνώση, ενώ επιχειρείται και μια συνοπτική περιγραφή των κατολισθητικών φαινομένων και των τεχνικών που διαχειρίζονται τα δεδομένα και τις προκύπτουσες πληροφορίες.
Λέξεις κλειδιά: *Κατολισθητικά φαινόμενα, διαχείριση δεδομένων, γνώση ειδικών.*

1. The Concept of Data, Information, Knowledge and Wisdom

The concepts of data, information, knowledge and wisdom, which can be found in the process of Knowledge Discovery, are concepts mentioned in the research field of Information Science. Many definitions have been presented for these four concepts. The existence of different definitions is due to the different background of the researcher and their specific objectives that they analyze (Zins, 2007). One of the first reports on the hierarchical structure that these concepts follow and the potential link between them was made by Zeleny (1987) and Ackoff (1989) (Figure 1). According to Zeleny (1987) and Ackoff (1989), the data are non - organized or not - processed

events, associated with objects identified in the real world. They are considered as measurable values of variables and parameters that describe objects or events, characterized as "static" since, after being recorded, they do not change. To convert Data into Information requires a frame of reference and a conceptual model that allows their interpretation. Information is a set of Data that has undergone some form of processing and formatting. Unlike "static" data, information has meaning, purpose and relevance. Data are converted into Information mainly by following five (5) basic procedures (Davenport & Prusak, 1998):

- By placing them within a conceptual frame of reference, determined by the reason and the purpose for which the collection of data is done.
- By managing data in a more compact format, eliminating thus unnecessary details.
- By analyzing data, probabilistic or statistical data analysis.
- By categorizing or classifying data in specific classes or categories.
- By processing data.

Knowledge is referred as the Information that has undergone specific validation process. Knowledge is actually based on Information that has been organized, synthesized or summarized in order to increase understanding and awareness. Knowledge highlights the importance of Information and links Information with actionable conclusions (Benet & Benet, 2004). The usual questions about Data and Information are related to *who*, *what*, *where* and *when*, while questions referring to Knowledge are related mainly to the *how* and *why*.

Figure 1 - Hierarchical structure of data, information, knowledge and wisdom.

To reach the required wisdom reasoning is needed. Reasoning is the process by which we use existing knowledge in order to make inferences an integral component of the process that we call intelligence. It is the attempt to identify the consistency between two or more judgments, which are appreciated as the logical continuation of these judgments. It is the ability to recognize the truth and make sound judgments based on prior knowledge, experience and insight (Leibowitz, 2003). In particular, Knowledge is in a sense the familiarity which one acquires from an object or a phenomenon, the theoretical and practical understanding.

2. The Concept of Geological Data, Information and Knowledge

In complete correspondence with the foregoing, the Geological Information is the result of processing the primary geomorphological and geotechnical data. Raw data, non - organized associated with the geological environment, geological phenomena, geological and physical processes. Specifically, they could express values of measurable physical and mechanical parameters corresponding to certain geological formations. The collection of primary raw geological data and geological information is undertaken through:

- Reviewing the literature, studying geological maps, reports and geotechnical studies, environmental studies, examination of aerial photographs and satellite images, etc.
- Mapping of geological structures, lithological formations, tectonic features and areas of risk.
- Explore through sampling techniques, and performing appropriate field and laboratory tests (to assess the physical and mechanical properties of rocks and soils).
- Geophysical exploration through which one can achieve rapid preliminary identification of subsurface conditions.

The Geological Information is reflected primarily on maps, analogue or digital, adopting characteristics and technical symbols in diagrams and tables. Geological and Geotechnical particular maps are the main means of communication and flow of geological information between different disciplines (van Westen, 2004). The use of Geological Information can solve practical and theoretical issues in geosciences. Issues related to slope stability studies, forecasting geological hazards (Rosenbaum & Culshaw, 2003, Koumantakis et al., 2005), estimation of hydrocarbon reserves or aquifers (Mukerj et al., 2001, Schon, 2004), assessment of the geotechnical behavior the rock mass and soil formations (Tzamos & Sofianos, 2006, 2007, Ilia et al. 2009), assessment of suitability for the construction of underground space for various uses (Benardos & Kaliampakos, 2006, Koumantakis et al., 2007), decision making related to the design of underground infrastructure (Panou & Sofianos, 2002a, 2002b) etc. According to Wood & Curtis (2004), in most cases, the Geological Information is provided as an advance element, a priori component, a key component of the "function" that solves any geo-environmental problems. The use of reliable Geological Information is the key to successful implementation of the solution that is proposed for a given problem. As the authors note, where Geological Information is detailed and accurate, then and only then you can provide rational decisions with respect to critical environmental issues. The importance of the Geological Information and Knowledge in the methods and practice of Engineering Geology can be summarized into three (3) "equations" that are considered the central point of the philosophy of Engineering Geology, as currently configured towards safety and economics in any geotechnical project (Rozos, 1989, Rozos & Tsiambaos, 1991):

- Geological and geotechnical properties of the geological materials + 'mass characteristics' = geotechnical properties of geological 'mass'.
- Geotechnical properties of geological 'mass' + Environmental (climate, etc.) conditions = determining the precise location of the structure.
- Determine the exact location of construction + induced changes in the geological environment of the construction work = final mechanical response.

2.1. Transforming Geological Data into Geological Information and Knowledge

According to Wood & Curtis (2004), the transition from Geological Data to Geological Information requires three (3) basic elements:

- Input data managed by experts and specialists.
- The incorporation of uncertainty in the generated Geological Information.
- The Geological Information to be expressed in quantitative terms, whereas when plotted in a qualitative manner it must be fully defined so that the associated uncertainty has been assessed in the final output.

When these three (3) elements are present the quality of information generated increases and the configured information becomes more relevant and meaningful. For the transition of Geological Information in Geological Knowledge it is required to manage the Geological Information within a specific theoretical and mathematical background, whose most important result is the correlation

of information to actionable conclusions. The quality of knowledge generated reflects the understanding of the mechanism that drives the behavior of the environment. Increased quality implies more confident estimation of the response of the environment. The predictive modelling and simulation is designed to capture the knowledge of quantitative and qualitative characteristics, the application of which involves the necessary special checks for verification and certification of Information. Such transformation is shown in figure 2, where the 14 lithological units identified in the field surveys have been classified into 5 geotechnical units with the help of expert knowledge and analysis of laboratory and field tests. This process provides valuable knowledge.

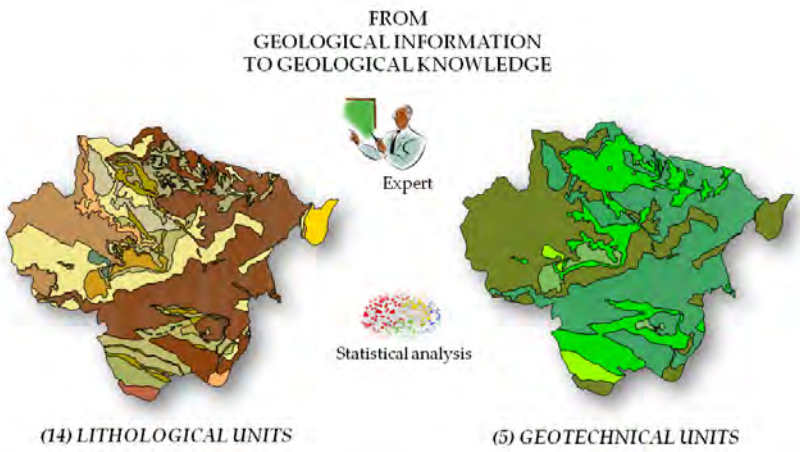

Figure 2 – Converting Geological Information to Geological Knowledge.

3. Managing Landslide Related Data

3.1. Landslide Phenomena

Landslides are one of the most complex and chaotic natural phenomena. Landslides are considered as unexpected and in most cases unpredictable movement that usually occur on unstable surface layers, making them one of the most frequent natural hazards with significant consequences to human life and incalculable social - economic consequences. According to Hutchinson (1995), landslides are the result of evolution or progressive extreme events that occur on the surface of the earth and due to the action of geological, geomorphological, climatic processes and also the negative impact of human activities.

3.2. Data Related to Landslide Phenomena

The process of identifying the causative factors and the related data is the basis of many methods of instability assessment. As for the nature of the data that one must investigate, they can be distinguished as dynamic (e.g. pore - water pressure), or passive (e.g. rock structure) and may also be considered in terms of the roles they perform in destabilising a slope (Crozier, 1986). In this sense, the factors from which data and information are collected could be recognised as pre-conditioning factors (e.g. slope steepness), preparatory factors (e.g. deforestation) and triggering factors (e.g. seismic shaking). The selection of the appropriate factors depends on the objective of the study and the complexity of the research area, the type of mass movement and the availability of existing data. It also depends by the analysis and method contacted. Morphological factors such as geometry (steepness, height, length, form, angle, and aspect) and basin / sub basin characteristics (order, magnitude, channel gradient) reflect the past and present geomorphlogical evolution of an area and provide fundamental data and information on landslide process. The acquisition of geological factors, such as rock composition, texture, structure, degree of weathering, fracture density / foliation attitude and stratigraphic settings is still not facilitated by the application of the GIS technologies but relay mainly on the traditional procedure of field

surveys and aerial photo – interpretation. These kinds of data are essential in any instability assessment. Table 1 gives a schematic overview of the main data layers that are required for a landslide susceptibility, hazard and risk assessment and also provides information about the importance of the data set for heuristic models, statistical models, physically-based models and probabilistic models (van Westen et al., 2008).

Table 1 – Data layers related to landslide phenomena (van Westen et al., 2008).

Data		Models			
Main type	**Data layer**	**Heuristic**	**Statistical**	**Physical based**	**Probabilistic**
Landslide inventory	Landslide inventory	Critical	High important	High important	High important
	Landslide activity	High important	Critical	Critical	Critical
	Landslide monitoring	Not relevant	Not relevant	High important	High important
Environmental factors	DEM	High important	Critical	Critical	Critical
	Slope geometry	High important	High important	High important	High important
	Slope hydrology	Not relevant	Not relevant	Critical	High important
	Lithology	High important	High important	High important	High important
	Geological structure	High important	High important	High important	High important
	Faults	High important	High important	Not relevant	Not relevant
	Soil type	Not relevant	Not relevant	Critical	High important
	Soil depth	Not relevant	Not relevant	Critical	High important
	Land use	High important	High important	High important	High important
Triggering factors	Rainfall	High important	High important	Critical	Critical
	Temparature/ evatranspiration	Not relevant	Not relevant	High important	Less important
	Earthquake data	-	-	-	Critical
	Ground acceleration	High important	High important	High important	Less important

3.3. Transforming Data Related to Landslide Phenomena into Information

The theoretical framework, through which one attempts to analyze the phenomenon of landslides, is formed by adopting some assumptions and specifications that summarize the knowledge of experts (Radbruch-Hall and Varnes, 1976, Varnes et al., 1984, Carrara et al., 1999, Hutchinson and Chandler, 1991, Hutchinson, 1995, Dikau et al., 1996, Turner and Schuster, 1996, Cruden and Varnes , 1996, Aleotti and Chowdhury, 1999, Guzzetti et al., 1999, Guzzetti et al., 2005):

- Landslide leave distinct mark on the surface of the earth, most of which can be identified, classified and mapped by field work or the analysis of stereoscopic aerial photographs.

- The morphological profile of a slope failure depends on the type and the rate of movement. In general, similar types of geological failures produce similar morphological profiles. By the presence of a geological failure, an expert can extract qualitative and quantitative information on the degree of activity, age and extent of geological failure.
- Slope failure does not occur randomly. It is the result of the interaction of natural processes that is a subject to mechanical and physical laws that can be determined empirically or statistically. The knowledge generated during the examination of the slope failures can be generalized.
- Slope failures of the past and present are evidence to predict future failures.

Therefore, the theoretical background and the mathematical model which are involved in the interpretation of the phenomenon of landslides are based on the following three (3) critical assumptions (Varnes et al., 1984, Hutchinson, 1995, Guzzetti et al., 1999, Chanon et a . 2006):

- Areas that in the past have a history on instability problems show great potential to failure.
- These areas, share common geotechnical characteristics.
- Similar conditions produce similar patterns of failures.

Within this conceptual frame of reference, data related to landslide phenomena could be analyzed, categorized or classified and transformed into valuable Information.

3.4. Transforming Information to Knowledge by Applying Methods of Analysis

Knowledge related to landslide phenomena is based on Information that has been organized, synthesized or summarized by applying specific methods of analyzes. These methods produce outputs of certain format that increase our understanding and awareness regarding with landslide phenomena. A variety of methods, qualitative or quantitative, direct or indirect are implement in order to rank slope – instability factors and assign different susceptibility and hazard levels to a region that is going to be analyzed (Carrara, 1989, van Westen et al., 2006). These methods embody expert-based analyses or complex mathematical-based systems. Particular, geomorphologic analyses and direct field mapping methods are considered qualitative methods since they don't provide numeric output with reference to landslide assessment. On the other hand, quantitative methods such as deterministic analyses, probabilistic approaches, statistical methods and data mining techniques, rely on mathematical models and produce numeric outputs that contain high value information (Glade et al., 2005, Tsangaratos et al., 2011).

Determining the spatial and temporal extent of landslide hazard requires to identifying areas which are, or could be, affected by a landslide and to assess the probability of such landslide occurrence within a specified period of time. To specify a precise time frame for the future occurrence of a landslide can be difficult. As a result, landslide hazard has often been represented by landslide susceptibility, where only the predisposing and preparatory landslide causes are described. Susceptibility zoning could be thought as a process that provides the spatial distribution and rating of the terrain units according to their propensity to produce landslides. It refers to the process that provides highly valued Knowledge that depends on the topography, geology, geotechnical properties, climate, vegetation and anthropogenic factors (Fell et al., 2008). The value of a landslide susceptibility map refers to its information and data content. The content of information depends mainly on the type of data shown, their quality and the extent to which the information is new and essential. According to Guzzetti et al. (2000), a landslide susceptibility map is valuable when the information and data shown are useful to the user and also when the map is both relevant and fully understood by the user. In more detail, reliable susceptibility maps could provide an explanation for the observed landslide spatial distribution pattern; provide in other words Knowledge of the instability state of the surroundings. In addition, by incorporating information on the instability factors that are known or supposed to control landslide spatial occurrence and

their underlying relationship, susceptibility maps are capable of predicting the location of landslides even in the areas where landslides were not recognized or mapped providing in a sense *Wisdom*.

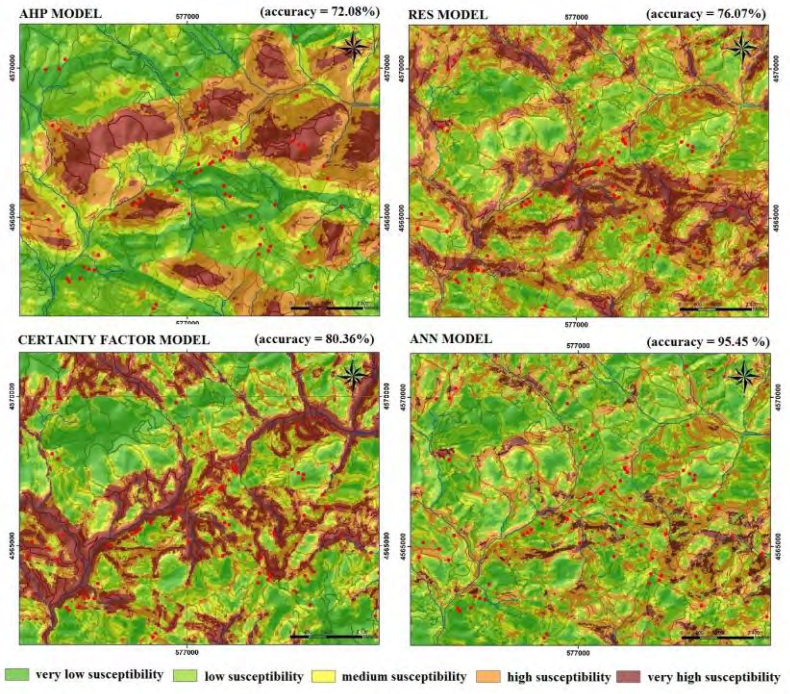

Figure 3 – Four different methods of analyzing landslide phenomena and producing highly valued Knowledge.

The four models that are shown in Figure 3 produce different landslide susceptibility maps and provide different level of Knowledge. The examples refer to an area that exhibits instability problems located in the prefecture of Xanthi, Greece (Tsangaratos, 2012). The level of Knowledge is clearly associated with the performance, indicated by the accuracy index. The first two models, Analytic Hierarchy Process (AHP) and Rock Engineering System (RES) are methods that embody expert-based analyses. They perform well concerning the predictive accuracy and the associated level of Knowledge they provide is of medium to high level. The level of *Knowledge* is determined by the fact that there is often an overestimation of the influence that certain factors have on the landslide susceptibility index and also by the fact that the mechanism of landsliding may not be fully understood. The Certainty Factor (CF) model performs better and provides additional information and knowledge about the underlying relationship that the landslide related factors have. The Artificial Neural Network model (ANN mode) has a higher performance and although it does not provide any additional information about how or why this happens it provides valuable Knowledge of where it will happen.

Table 2 shows the calculated weight of coefficient of the factors used in the four models for the same research area. The weights represent the significance each factor has during the estimation of landslide susceptibility. It is obvious that all models identify the lithological feature as the most significant despite the different approach they require during the estimation of the susceptibility.

The expert-based method, AHP seems to overestimate the influence of the lithological factor. However, the RES method gives a lower value to the lithological factor and may be closer expressing the actual significance. If one evaluates the influence of the geological boundaries the overall influence of the geological features reaches the same level of significance (0.2932) as

estimated by the AHP method. The nature of the other two models allows a more objective way to estimate the weight coefficients and the estimated level of significance may be more accurate.

Table 2 – Weight coefficient indicating the significance of each factor.

Factors	AHP model	RES model	CF model	ANN model
Lithological units	0.3422	0.1466	0.3142	0.2876
Elevation	0.0585	0.0681	0.0865	0.0975
Slope inclination	0.1181	0.1361	0.0899	0.1124
Slope orientation	0.0252	0.1047	0.0978	0.1021
Fault characteristics	0.1700	0.1257	0.0760	0.0490
Hydrological characteris-tics	0.0921	0.1361	0.0888	0.1011
Geological Boundaries	0.0921	0.1466	0.0990	0.0980
Infrastructure network	0.1038	0.1361	0.1478	0.1523

4. Discussion and Conclusion

To spatially identify landslide phenomena the process involves analyzes of a large set of interrelated data layers, often ill - known, unknown or in most cases unmappable. Landslide susceptibility is a function of the degree of the inherent stability of the slope as can be indicated by the factor-of-safety along with the presence of causative factors capable of reducing the excess strength and ultimately triggering movement. As illustrated in the present study, it is essential to produce landslide susceptibility maps, since they provide an explanation for the observed landslide spatial distribution pattern and the interrelationship between the factors that control instability. To extract Knowledge from any landslide susceptibility, hazard or risk assessment, it is necessary to develop a conceptual frame of reference that will enable the transformation of data, related to landslide phenomena, into information. A conceptual frame that is based on the belief that past and present provides evidence for the future, that failures do not occur randomly, that failures share common geotechnical characteristics and that similar conditions produce similar patterns of failures. The level of Knowledge that susceptibility maps provide is analogous to their usefulness and relevance and how well the explanation that they provide concerning the mechanism of instability is understood by the user. Each factor contributes to the overall susceptibility by a different level of significance, expressed with a weighted coefficient that is estimated through specific procedures according to different models. The provided Knowledge should be also accompanied by information of when a landslide will occur, and how large or destructive the mass movement is expected to be. This information is transformed from data that concern triggering factors and when analyzed produce landslide hazard and risk maps that provide a higher level of Knowledge. When landslide susceptibility maps predict successfully the location of landslides in areas where landslides were not yet recognized or mapped they provide in a sense Wisdom. In conclusion the landslide susceptibility maps provide to engineering geology experts a cost and time effective mean for tracing the most critical slope site with inherent instability potential. They may also serve as a valuable tool in decision-making, regarding the land use and development planning processes in landslide susceptibility areas.

5. References

Ackoff R. 1989. From Data to Wisdom, *Journal of Applied Systems Analysis*, vol.16, 3–9.

Aleotti P. and Chowdhury R. 1999. Landslide hazard assessment: Summary review and new perspectives, *Bulletin of Engineering Geology and the Environment*, 58(1), 21-44.

Benardos A.G. and Kaliampakos D.C. 2006. Design of an Underground Hazardous waste repository in Greece, *Tunneling and Underground Space Technology*, vol.21, 185-196.

Benet A. and Benet D. 2004. *Organizational survival in the new world*, Butterworth-Heinemann, US, 391 pp..

Carrara A. 1989. Landslide hazard mapping by statistical methods: a "black-box" model approach, *Proceedings International Workshop on Natural Disasters in European-Mediterranian Countries*, Perugia, June 27-July 1, 1988, CNR-ESNSF, pp. 205–224.

Carrara A., Guzzetti F., Cardinali M. and Reichenbach P. 1999. Use of GIS Technology in the Prediction and Monitoring of Landslide Hazard, *Natural Hazards*, vol. 20 (2-3), 117-135.

Chacon J., Irigaray C., Fernadez T. and El Hamdouni R. 2006. Engineering geology maps: Landslides and geographical information systems, *Bulletin of Engineering Geology and the Environment*, 65(4), 341-411.

Crozier M.J. 1986. *Landslides - Causes, Consequences and Environment*, Croom Helm, London, pp. 252.

Cruden D.M. and Varnes D. J. 1996. Landslide types and processes, In: Turner A.K.; Shuster R.L. (eds*) Landslides: Investigation and Mitigation*, Transp Res Board, Spec Rep 247, 36–75.

Davenport T.H. and Prusack L. 1998. Working Knowledge: How Organizations Manage What They Know. Boston: Harvard Business School Press, pp. 5.

Dikau R., Brunsden D., Sshrott L. and Ibsen M. 1996. *Landslide Recognition. Identification, Movement and Causes*, Wiley & Sons, Chichester, pp. 274.

Fell R., Corominas J., Bonnard C., Cascini L., Leroi E. and Savage W.Z. 2008. Guidelines for landslide susceptibility, hazard and risk zoning for land use planning, *Engineering Geology*, 102 (3‐4), pp. 85‐98.

Glade T., Anderson M. and Crozier M.J. 2005. *Landslide Hazard and Risk*, John Wiley & Sons, Ltd., Chichester, England, pp.802.

Guzzetti F., Carrarra A., Cardinali M. and Reichenbach P. 1999. Landslide hazard evaluation: a review of current techniques and their application in a multiscale study, Central Italy. *Geomorphology*, 31, pp. 181–216.

Guzzetti F., Cardinali M., Reichenbach P. and Carrara A. 2000. Comparing landslide maps: A case study in the upper Tiber River Basin, central Italy, *Environmental Management*, 25/3, 247-363.

Guzzetti F., Reichenbach P., Cardinali M., Galli, M. and Ardizzone F. 2005. Probabilistic landslide hazard assessment at the basin scale, *Geomorphology*, 72 (1‐4), 272‐299.

Hutchinson J.N. and Chandler M. P. 1991. A preliminary landslide hazard zonation of the undercliff of the Isle of Wight, in Slope stability engineering, development and applications. *Proc. Int. Conf. On Slope stability*, Isle of Wight, 15-18 April (Ed. R. J. Chandler), Thomas Telford, 197-206.

Hutchinson J.N. 1995. Keynote paper: Landslide hazard assessment, *Proceedings 6th International Symposium on Landslides*, Christchurch. Balkema, Rotterdam, 1805-1841.

Ilia I., Rozos D., Perraki Th. and Tsangaratos P. 2009. Geotechnical and mineralogical properties of weak rocks from central Greece, *Cent. Eur. J. Geosci*., 1(4), 431-442, DOI: 10.2478/v10085-009-0029-0.

Koumantakis I., Rozos D., Markantonis K. and Tsagaratos P. 2005. Engineering geological conditions, related ground failures and proposed measures, along the part of Peloponnesian railway line, Greece, *Proceedings of Intern. Symposium Geoline 2005*, BRGM (Abstracts in Proc., papers in CD-ROM), Lyon France 2005.

Koumantakis I., Rozos D. and Tsagaratos P. 2007. Underground space development in Attica County in relation with its geological structure, *11th ACUUS International Conference ''Underground space: Expanding the Frontiers''*. V1, 221-229, Athens, Greece.

Leibowitz J. 2003. *The Knowledge Management Handbook*, CRC Press LLC, pp. 328.

Mukerj T., Jorstad A., Avseth P., Mavco G. and Granli J. R. 2001. Mapping lithofacies and pore-fluid probabilities in a North Sea reservoir: seismic inversions and statistical rock physics, *Geophysics*, vol. 66, 988-999.

Panou K. and Sofianos A.I. 2002(a). A fuzzy multicriteria evaluation system for the assessment of tunnels vis a vis surface roads: theoretical aspects - Part I, *Tunnelling and Underground Space Technology*, 17, 195-207.

Panou K. and Sofianos A.I. 2002(b). A fuzzy multicriteria evaluation system for the assessment of tunnels vis a vis surface roads: the WPMA case - part II, *Tunnelling and Underground Space Technology*, 17, 209-219.

Radbruch-Hall D.H, Varnes D.J. and Savge W.Z. 1976. Gravitational speeding of steep-sided ridges ("sacking") in Western United States, *Bull. Int. Assoc. Eng. Geol.*, 14 (1976), 23–35.

Rosenbaum M. S. and Culshaw M. G. 2003. Communicating the risks arising from geohazards, *Journal of the Royal Statistical Society' Series A (Statistics in Society)*, 166, 261 -288.

Rozos D. 1989. Engineering geological conditions in Achaia province. Geomechanical characteristics of the plio-pleistocene sediments (in Greek), *PhD Thesis*, Dept. of Geology, Univ. of Patras, 453pp.

Rozos D. and Tsiambaos G. 1991. Field and laboratory engineering geological investigations and their importance for engineering purposes, *Special publications of the Geological Society of Greece*, (GSG) 2day Symposium for the 40 years of GSG, Athens, Greece.

Schon J. H. 2004. Physical Properties of Rocks': Fundamentals' and Principles of Petrophysics, Pergamon Press. Handbook of Geophysical Exploration: Seismic Exploration Series, p. 18.

Tsangaratos P., Ilia I. and Rozos D. 2011. Case Event System for landslide susceptibility analysis, *The Second World Landslide Forum Abstracts, WLF2 - 2011– 0389*, Rome, p. 10.

Tsangaratos P. 2012. Research on the engineering geological behaviour of the geological formations by the use of information systems, *PhD Thesis*, School of Mining Engineering Geology, Department of Geological Section, NTUA, Athens, pp. 363.

Tzamos A. and Sofianos A.I. 2007. A correlation of four rock mass classification systems through their fabric indices, *International Journal of Rock Mech. & Mining Sciences*, 44, 477-495.

Turner A.K., and Schuster R. L. 1996. Landslides-Investigation and mitigation: National Research Council, *Transportation Research Board Special Report*, 247, National Academy Press, Washington, D.C., 673 p.

Van Westen C.J. 2004. Geo-information tools for landslide risk assessment: an overview of recent developments, *In proceedings of the 9th International Symposium on Landslides*, London: Balkema, 36-59.

Van Westen C.J., Asch T.W.J. and Soeters R. 2006. Landslide hazard and risk zonation-why is it still so difficult?, *Bull. Eng. Geol. Env.*, vol.65, 65-184.

Van Westen C.J., Castellanos E. and Kuriakose S.L. 2008. Spatial data for landslide susceptibility, hazard, and vulnerability assessment: An overview, *Engineering Geology,* doi:10.1016/j.enggeo.2008.03.010.

Varnes D.J. and IAEG Commission on Landslides and Other Mass-Movements, 1984. Landslide Hazard Zonation: A Review of Principles and Practice, UNESCO Press, Paris.

Wood R. and Curtis A. 2004. Geological prior information and its applications to geoscientific problems, *Geological Society, London, Special Publications*, vol. 239, 1-14.

Zeleny M. 1987. Management Support Systems: Towards Integrated Knowledge Management, *Human Systems Management,* 7 (1), 59–70.

Zins C. 2007. Conceptual Approaches for Defining Data, Information, and Knowledge, *Journal of the American Society for Information Science and Technology,* 58 (4), 479–493.

Δελτίο της Ελληνικής Γεωλογικής Εταιρίας, τομ. XLVII , 2013
Πρακτικά 13ου Διεθνούς Συνεδρίου, Χανιά, Σεπτ. 2013

Bulletin of the Geological Society of Greece, vol. XLVII 2013
Proceedings of the 13th International Congress, Chania, Sept. 2013

PRODUCING LANDSLIDE SUSCEPTIBILITY MAPS BY APPLYING EXPERT KNOWLEDGE IN A GIS – BASED ENVIRONMENT

Tsangaratos P.[1] and Rozos D.[1]

[1] *National Technical University of Athens, School of Mining and Metallurgical Engineering, Department of Geological Studies, ptsag@metal.ntua.gr, rozos@metal.ntua.gr*

Abstract

In this paper two semi - quantative approaches, from the domain of Multi criteria decision analysis, such as Rock Engineering Systems (RES) and Analytic Hierarchical Process (AHP) are implemented for weighting and ranking landslide related factors in an objective manner. Through the use of GIS these approaches provide a highly accurate landslide susceptibility map. For this purpose and in order to automate the process, the Expert Knowledge for Landslide Assessment Tool (EKLATool) was developed as an extension tightly integrated in the ArcMap environment, using ArcObjects and Visual Basic script codes. The EKLATool was implemented in an area of Xanthi Prefecture, Greece, where a spatial database of landslide incidence was available.

Key words: *ArcObjects, Landslide Assessments, Multi – Criteria decision analysis, Rock Engineering Systems, Analytical Hierarchal Process.*

Περίληψη

Στην εργασία αυτή εφαρμόζονται δυο ημι – ποσοτικές προσεγγίσεις, από το πεδίο των πολυκριτηριακών μεθόδων ανάλυσης, η Rock Engineering System (RES) και η Analytic Hierarchical Process (AHP), για τον υπολογισμό και την κατάταξη των παραμέρτων που σχετίζονται με το φαινόμενο των κατολισθήσεων. Για το σκοπό αυτό και για την αυτοματοποίηση της διαδικασίας, δημιουργήθηκε ένα υπολογιστικό εργαλείο, το Expert Knowledge for Landslide Assessment Tool (EKLA-Tool) ως δυναμική επέκταση του λογισμικού πακέτου ArcMap. Για την κατασκευή του γράφτηκε σχετικός πηγαίος κώδικας με την βοήθεια της γλώσσας Visual Basic και των εργαλείων ArcObjects που βρίσκονται ενσωματωμένα στο λογισμικό Γεωγραφικών Συστημάτων Πληροφοριών, ArcMap. Η επέκταση εφαρμόστηκε στην περιοχή του νομού Ξάνθης, όπου υπήρχε διαθέσιμη σχετική χωρική βάση δεδομένων με καταγραφές κατολισθητικών φαινομένων.

Λέξεις κλειδιά: *ArcObjects, Κατολισθητική επιδεκτικότητα, Γεωγραφικά Συστήματα Πληροφοριών, Πολυκριτηριακές μέθοδοι ανάλυσης.*

1. Introduction

Natural disasters result from the interaction of physical impact and human or environmental vulnerability (Burton et al., 1993). Landslides are identified as geophysical and hydrological disasters referred to as unexpected and unpredictable movement, usually on unstable surface layers,

making them one of the most frequent natural hazards with significant consequences to human life and incalculable social - economic consequences (Schuster, 1996, Aleotti & Chodwdhury, 1999). In most cases the complexity of the causative and triggering factors, their unknown interrelationship and the lack of knowledge, makes the analyses of such phenomena a very demanding task (Gokceoglu et al., 2005). Landslide susceptibility is the likelihood of a landslide occurring in an area on the basis of local terrain conditions (Brabb, 1984). It is the degree to which a terrain can be affected by slope movements, i.e., an estimate of "where" landslides are likely to occur. As reviewed through the literature, there is no agreement on the methods for susceptibility maps production as several qualitative and quantitative methods have been proposed for landslide susceptibility evaluation. Reviews on these techniques and methodologies are given by numerous researchers (Carrara et al., 1995, Aleotti & Chodwdhury, 1999, Guzzetti et al., 1999, Dai et al., 2002, Glade et al., 2005). According to van Westen (1997), a landslide susceptibility analysis involves essentially four main phases: (a) the production of a landslide inventory map, (b) the assessment of event – controlling factors that influence the landslide manifestation, (c) the application of appropriate methods for determining the weights of each factor and (d) the compilation of the landslide susceptibility map using a GIS procedure. Landslide susceptibility and hazard assessments often use Multi criteria decision analysis (MCDA) techniques since in most cases, the types and format of data that are available are qualitative and quantitative, therefore requiring a semi - quantitative method that incorporates both types of data (Ayalew & Yamagishi, 2005). In contrast to conventional MCDA, spatial multi-criteria decision analysis requires data on both criterion values and the geographical locations of alternatives. The data are processed using GIS and MCDA techniques to obtain information for making decisions. The most common approach involves obtaining expert opinion, such as Analytical Hierarchy Process and Rock Engineering System, to assigning weights and then combining weights additively by weighted linear combination (WLC) to produce landslide susceptibility maps (Park et al., 2004, Komac, 2006). These methods have been incorporated into a variety of GIS-based decision making procedures but in only a few GIS programs (e.g. IDRISI and ILWIS) (Eastman et al. 1993, Jankowski, 1995, Lai & Hopkins, 1995, Malczewski, 1999). According to Ozturk & Batuk (2011) although ArcGIS is one of the most widespread GIS software, MCDA procedures has not been fully implemented in the standard GIS functions. The main objective of this article is to present an Expert Knowledge for Landslide Assessment Tool, developed in the ArcGIS 9.3 environment, that utilizes the above referred two semi-quantitative methods, Analytical Hierarchy Process (AHP) and Rock Engineering System (RES) for determining landslide susceptibility.

2. Materials and Methods

The most essential phase in a landslide susceptibility analysis is to establish a spatial database for landslides in a GIS environment, involving landslide inventory data and the landslide related factors. The use of GIS provides a powerful tool to model the landslide phenomena, since the collection, manipulation and analysis of the related data can be accomplished much more efficiently and cost effectively. All factors that contribute to landslide manifestation are collected and archived from a variety of qualitative or quantitative factors such as topographic characteristics (elevation, slope, aspect, curvature, relief, etc.), hydrological features (river network, hydrographic density, wetness index, etc.), geological settings (lithology, faults, tectonic features, seismicity, etc.), and environmental conditions (precipitation and temperature, land use, land cover and other anthropogenic factors). Following the construction of the GIS database, the analysis continues with the selection of the appropriate method for deriving the weight assigned to each factor. The selection of the appropriate method is based on the availability, quality of the data and desired output. The focus of our study is on MCDA techniques that are introduced for solving the problem of weighting the related landslide factors. Specifically, two semi-quantitative landslide assessment approaches, RES and AHP where applied. These techniques can be considered as an effective expert's tools for weighting and ranking the chosen parameters in an objectively optimal and simple way (Barthelos et al., 2009, Rozos et al., 2011). In the following sections (2.1, 2.2, 2.3

and 2.4) a brief description of the main tools and methods that were utilized though the developed methodology are presented.

2.1. Rock Engineering System

The Rock Engineering System (RES) has been developed in the early 90' as a semi-quantitative technique to approach increasingly complex rock engineering problems (Hudson, 1992). The implementation of RES is achieved through the use of an interaction matrix. The concept of an interaction matrix dates from the 1970s (Leopold et al., 1971) when it was used to evaluate the cause-and-effect relationship between existing (environment/natural) factors and human actions. Since then it has been modified and applied to rock stability problems (Hudson, 1992, Hudson & Harrison, 1992, Mazzoccola & Hudson, 1996), landslide susceptibility and hazard analysis (Pachauri & Pant, 1992, Golceoglu & Aksoy, 1996, Turrini & Visintainer, 1998, Donati & Turrini, 2002, Rozos et al., 2006, 2008), rock engineering (Benardos & Kaliampakos, 2004). Parameter interactions can be evaluated using a matrix display and are presented using a clockwise convention, as they might be path independent as shown in Figure 1 (Hudson, 1992). All factors that influence the studied system are arranged along the main diagonal of the interaction matrix, while the influence of each individual factor on each other corresponds to the off-diagonal values. To quantify the varying importance of the interactions, a coding method is required. Hudson (1992) proposed an expert semi-quantitative (ESQ) method shown in Figure 1.

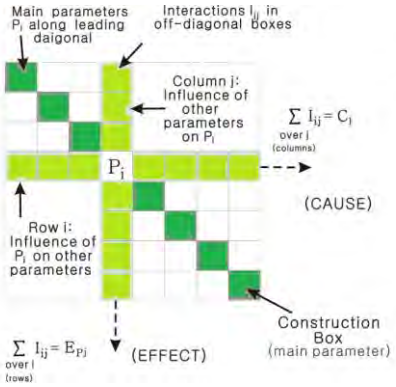

ESQ - coding of the factors interaction intensity (Hudson, 1992)

Coding	Description
0	No interaction
1	Weak interaction
2	Medium interaction
3	Strong interaction
4	Critical interaction

Figure 1 – The Interaction Matrix and the ESQ coding.

The influence of each parameter on the system (named cause, C) and the influence of the system on each parameter (named effect, E) are presented in an external row and column, respectively. The interactive intensity, which equals the addition of C and E, is transformed into a percentage format acting as weighting coefficients, which express the proportional share of each parameter (as failure causing factor) in slope failure and standardized by dividing with the maximum rating, giving the weight according to Equation 1.

Equation 1 – weighting coefficient

$$Fw_i = \frac{1}{4}\frac{(C+E)}{\sum_{i=1}^{n} C + \sum_{i=1}^{n} E}\%$$

A careful compilation of the interaction matrix optimizes the expert's judgment and eventually the resulting weighting coefficients are expressing the maximum possible objectivity, which can be revealed from a given experience.

2.2. Analytical Hierarchy Process

The AHP method is used in this study to systematically assign preferences based on Saaty's proposal (Saaty, 2000). The AHP reduces the complexity of a decision problem to a sequence of

pair-wise comparisons which are synthesized in an interaction matrix. The AHP method constructs a hierarchy of decision criteria and through the pair-wise comparison of each possible criterion pair a relative weight for each decision criterion is produced. Each comparison is a two-part question determining which criterion is more important, and how much more important, using a numerical relational scale (Table 1).

Table 1 - Scale of importance between two parameters in AHP (Saaty, 2000).

Scale	Intensity of importance	Definition
1	Equally	Two activities contribute equally to the Objective
3	Moderately	Experience and judgment slightly to moderately favour one activity over another
5	Strongly	Experience and judgment strongly or essentially favour one activity over another
7	Very strongly	An activity is strongly favoured over another and its dominance is showed in practice.
9	Extremely	The evidence of favouring one activity over another is of the highest degree possible of an affirmation.
2,4,6,8	Intermediate values	Used to represent compromises between the references in weights 1, 3, 5, 7 and 9

By applying AHP, one has the ability to evaluate pair-wise rating inconsistency. The eigenvalues enable to quantify a consistency measure which is an indicator of the inconsistencies or intransitivities in a set of pair-wise ratings. Saaty (2000) proved that for a consistent reciprocal matrix, the largest eigenvalue λ_{max} is equal to the number of comparisons n. A measure of consistency, called consistency index CI, is defined as follows (Equation 2):

Equation 2 – Consistency Index (CI)

$$CI = \frac{\lambda_{\max} - n}{n-1}$$

Saaty (2000) randomly generated reciprocal matrixes using scales 1/9, 1/8,…, 1, …, 8, 9 to evaluate a so called random consistency index RI. Saaty (1977) also introduced a consistency ratio CR, which is a comparison between the consistency index and the random consistency index. Since human judgments can violate the transitivity rule and thus cause an inconsistency, the consistency ratio (CR) is computed to check the consistency of the conducted comparisons (Equation 3).

Equation 3 – Consistency Ration (CR)

$$CR = \frac{CI}{RI}$$

If the value of the consistency ratio is smaller or equal to 10%, the inconsistency is acceptable, otherwise if the consistency ratio is greater than 10%, the subjective judgment needs to be revised (Saaty, 1977). After formatting the matrix, the numerical values must be normalized by diving each entry in a column by the sum of all the entries in that column, so that they output sums up to 1. Following normalization, the values are averaged across the rows, in order to give the relative importance weight for each parameter. Because of its simplicity and robustness in obtaining weights and integrating heterogeneous data, the AHP has been used in a wide variety of applications, including multi-attribute decision making, total quality management, suitability

analysis, resource allocation, conflict management, and design and engineering (Vargas, 1990, Jiang & Eastman, 2000, Vaidya & Kumar, 2004).

2.3. Estimating the Landslide Susceptibility Index

The next phase is to combine all the weighted factors by using the Weighted Linear Combination (WLC) method in order to produce the landslide susceptibility map. WLC is one of the best known and most commonly used MCDA methods (Malczewski, 1999, Ayalew et al., 2004). In the procedure for MCDA using WLC, it is essential the weights of the factors to have a sum of 1 and also the classes of each factor to be standardized to a common numeric range. The rating of the classes within each factor was based on the relative importance of each class obtained from field and expert knowledge according to the obvious relationship between each conditioning factor and the spatial distribution of the landslides in the research area. To standardize the classes to a uniform susceptibility rating scale, the formula of Equation 4 has been applied.

Equation 4 – standardized rank values

$$newValue = \frac{(oldValue - \min(oldValue))}{\max(oldValue) - \min(oldValue)} * [\max(newRange) - \min(new(Range)] + \min(newRange)$$

where, min (newRange) = 0.1, and max (newRange) = 1.0.

By applying the WLC method, the weight value assigned for each factor was multiplied by the standardized rank values given to the classes and numerically added according to Equation 5 in order to produce a Landslide Susceptibility Index (LS_I) map. Each pixel of the final landslide susceptibility map, obtained a value that ranged between 0.1 and 1, whereas 0.1 corresponds to the most stable conditions and 1 corresponds to the most critical value of slope instability.

Equation 5 – Landslide susceptibility index (Ls_i) for each pixel

$$LSi_{pi} = \sum_{j=1}^{n} Fw_j * c_{k\,Fj}$$

where pi the i^{th} pixel, Fw_j the weight of the j^{th} factor and cf_j the standardized ratings of class k^{th} of the j^{th} factor.

To complete the analysis, a validation procedure follows, according to which the actual location of landslides are superimposed on the landslide susceptibility map. The performance of the method is estimated by implementing the simple rule:

IF the actual location of a landslide is within the High and Very High Landslide Susceptibility Zone THEN Lp = 1 ELSE Lp = 0

The accuracy the method is calculated through Equation 6 as follows:

Equation 6 –Estimating the accuracy of the method applied

$$OverallAccuracy = \frac{\sum_{i=1}^{n} Lp_i}{n} x100\%$$

where, n is the total number of landslide events in the entire area.

2.4. The ArcGIS Environment and ArcObjects

The main core of the developed tool is the ESRI's ArcGIS software. ArcGIS, is a Geographic Information System (GIS) for working with maps and geographic data and information. It is used for creating and using maps, compiling geographic data, analyzing mapped information, sharing and discovering geographic information, using maps and geographic data and information in a

range of applications, as well as managing geographic information in a database. The system is based on a common library of shared GIS software components called ArcObjects (Burke, 2003). ArcObjects include "objects" like data frames, layers, features, tables, cartographic symbols, and the pieces that make up these "objects": points, lines, polygons, records, fields, colors, and so on. They provide a way to integrate GIS with external models and is thought as powerful tool for customizing any application that serves specific needs (Zeiler, 2001).

The Expert Knowledge for Landslide Assessment Tool (EKLATool) extension is tightly integrated in the ArcMap environment. The tool is developed as an ArcMap 9.3 extension, using ArcObjects and Visual Basic script codes. The EKLATool manipulates with raster-based data sets allowing users to input raster layers, execute multi-criteria decision analysis functions, and present the analysis outputs as a layer map in ArcMap environment. EKLATool includes five main procedures: (a) reclassify and standardize input layers, (b) choosing the appropriate multi-criteria analysis method, (c) calculate weights, (d) produce the landslide susceptibility map and (e) validation procedures.

3. Case Study

This section presents a case study to determine the landslide susceptibility using the Expert Knowledge for Landslide Assessment Tool. The study area concerns the wider area of the Perfection of Xanthi, bounded to the north by the Greek-Bulgarian borders and extended to the south up to the Neogene Thrace basin (Figure 2).

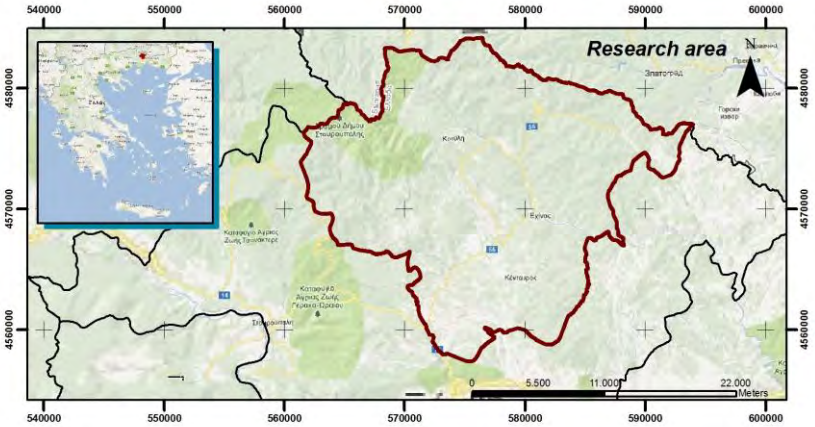

Figure 2 – Location map.

Regarding the geological structure, the study area consists of four units: (i) a marble unit (marbles and schists), (ii) a gneissic unit (magmatites, gneisses, amphibolites and ultra mafic rocks) of Palaeozoic age, (iii) a Tertiary unit (mollasic formations) and (iv) a unit from igneous rocks. The elevation values of the entire research area, varied between 30 to 1800 m approximately. From a morphological point of view, the area is characterized as mountainous and the dominant drainage pattern is dendritic.

3.1. Estimating the Landslide Susceptibility Index

First, the effective factors causing landslide instability problems were evaluated and accordingly eight evaluation factors were taken into account in this study: lithology, elevation, slope, aspect, distance to river network, distance to tectonic characteristics, distance to geological boundary, and distance to road network (Figure 3).

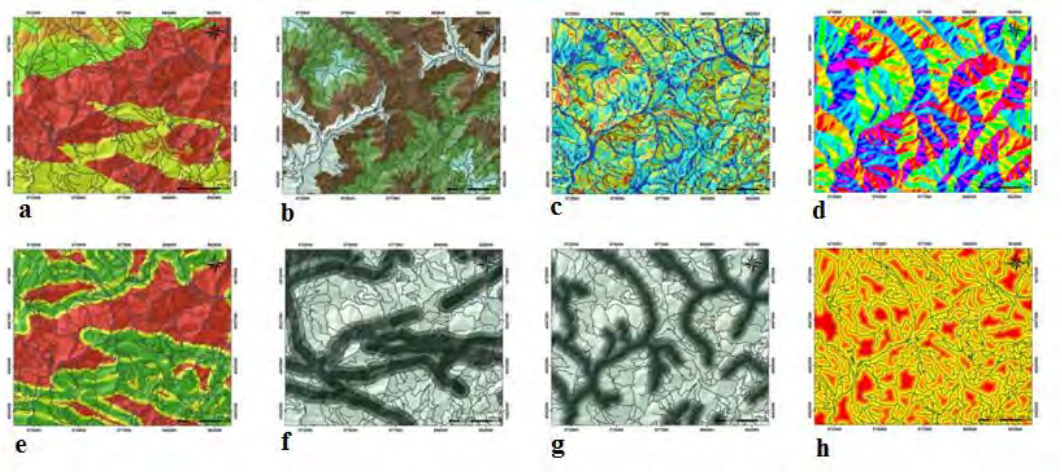

Figure 3 – The causative factors, a. lithology, b. elevation, c. slope, d. aspect, e. distance to geological boundary, f. distance to tectonic characteristics, g. distance to road network, h. distance to river network.

Since the factors greatly differ from each other, a uniform coding technique was adopted. Accordingly, each factor was classified into different categories that represent specific conditions and assigned with a value ranging from 0.1 to 1. The value 0.1 represents stable conditions, while the value 1 unstable conditions. The estimation of weights is made through the two methods RES and AHP, which combine all the relevant variables for the final calculation of landslide susceptibility with the help of the knowledge and experience of experts. Figure 4 and Figure 5 provide the weight coefficients of the eight factors used in the estimation of the landslide susceptibility by using the EKLATool for both of the methods.

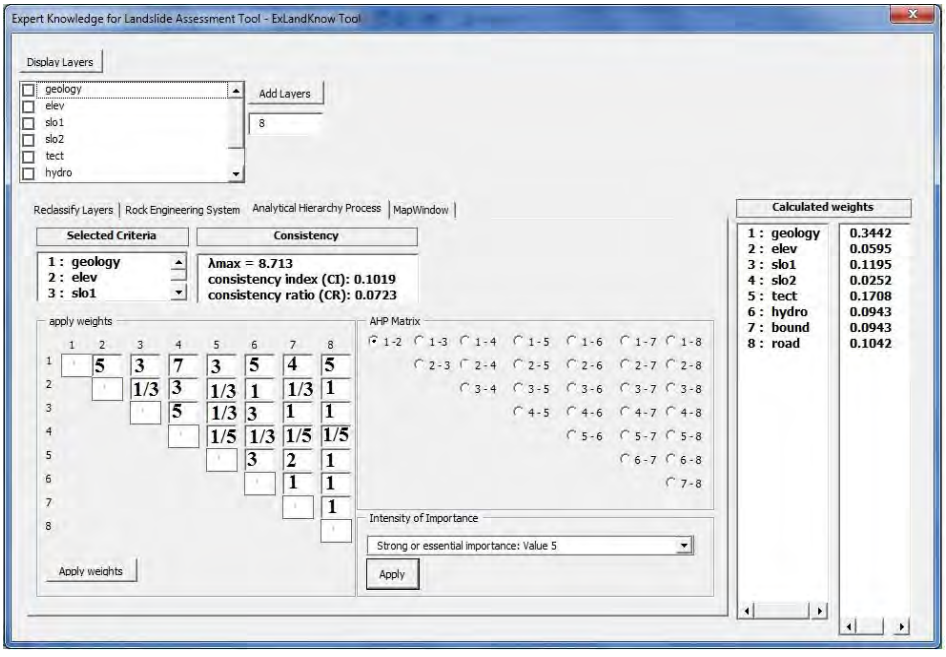

Figure 4 – The calculation of weight coefficients with the use of AHP method.

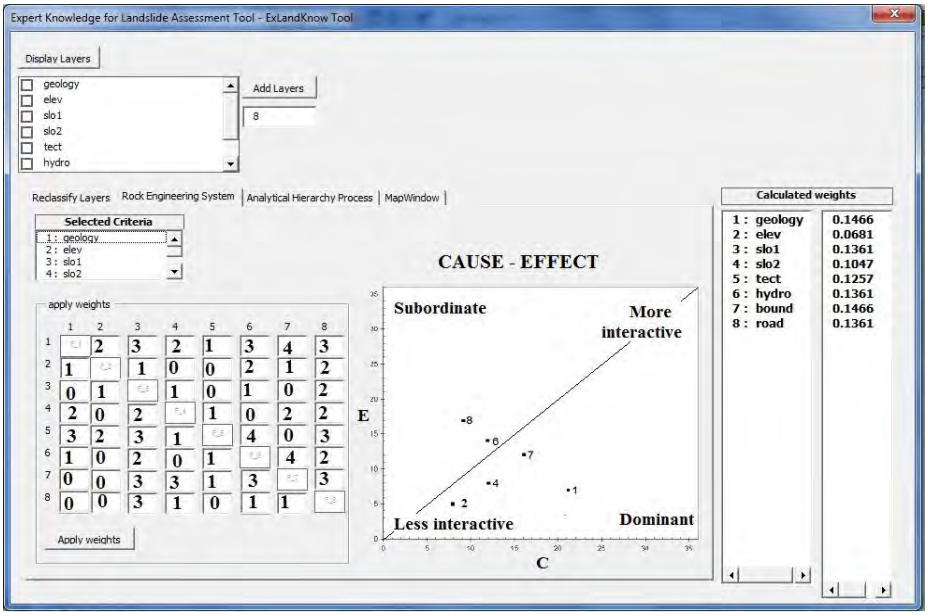

Figure 5 – The interaction matrix and the weight coefficients of RES method.

The next phase of the procedure requires the linear correlation of the weight coefficients by applying the WLC method. The result of this procedure is the compilation of the final susceptibility maps as shown in figure 6.

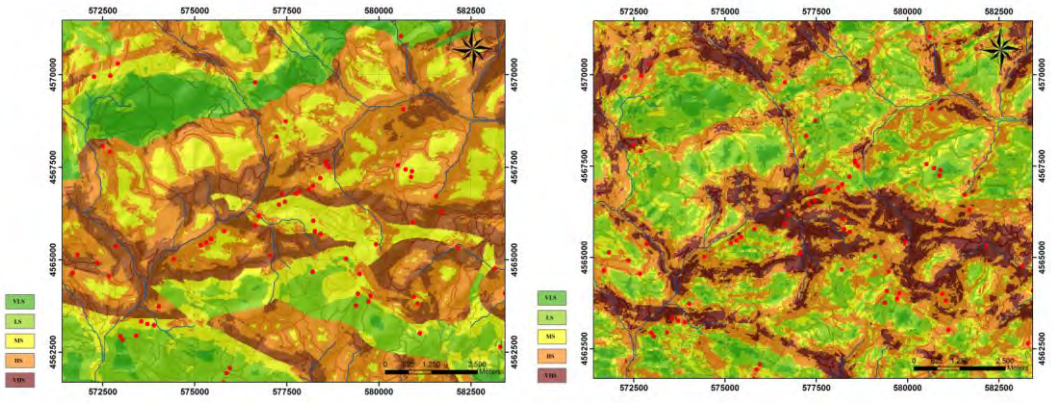

(a) **(b)**

Figure 6 – The Landslide Susceptibility Maps: (a) AHP and (b) RES method.

The final phase of the procedure requires the evaluation of the performance by applying the simple rule and afterwards calculating the accuracy of the two methods using Equation 6.

4. Results

According to the AHP method the percentage of the high and very high landslide susceptibility zone is estimated to be 22.91% and 14.34 %, while according to the RES method the percentage of the same zones is estimated to be 23.34% and 11.32% (Table 2). Table 3 shows the estimated accuracy of the two methods. RES method performs better, as it shows a higher accuracy value than AHP. From a database of 67 previously recorded landslide events the 70.15 % (47 locations)

were correctly classified, as belonging to the high and very high landslide susceptibility zone by the AHP method.

Table 2 – Landslide Susceptibility Index – RES – AHP.

Susceptibility classes RES	Surface (%)	Susceptibility classes AHP	Surface (%)
Very Low	18.97	Very Low	22.23
Low	26.50	Low	19.45
Medium	19.76	Medium	21.07
High	23.45	High	22.91
Very High	11.32	Very High	14.34

The RES method correctly classified the 79.10 % (53 locations) of the same database. The outcome of the analysis seems to confirm previous studies that compared the performance of the two methods in estimating landslide susceptibility and gave a slight advantage of the RES method against AHP method (Rozos et al., 2011).

Table 3 – Overall accuracy RES – AHP.

Method of analysis	n	$\sum_{i=1}^{n} Lp_i$	Overall accuracy (%)
AHP	67	47	70.15
RES	67	53	79.10

From the analysis performed by the RES method it is concluded that the most interactive factor is lithology and the distance from the geological boundaries (W = 0.1466), while the less interactive is the elevation factor (W = 0. 0681). Also, the lithology with the highest cause value (21) is the parameter which dominates the system and the elevation with the lowest cause value (8) is dominated by the system. From the analysis performed by the AHP method it is also concluded that lithology play the most significant role as it receives a higher weight coefficient (W=0.3442), while the less significant appears to be the aspect (W=0.0252).

5. Conclusion

The presented study focused on developing a tool that integrates Multi Criteria Decision Analysis techniques in a GIS environment for the estimation of landslide susceptibility. This approach was implemented with the usage of Visual Basic script codes in the ArcGIS environment. The tool has a range of multi-criteria evaluation capabilities including, criterion standardization, criterion weighting, decision making analysis and validation procedures. It provides access to functionality not available though the ArcMap interface, allowing the customisation of the interface for the end up users. More analytically, this study presents an application of GIS-based MCDA by applying Expert Knowledge for Landslide Assessment Tool to a real-world problem that involved determining landslide susceptibility in Xanthi Prefecture in Greece, by using two semi-quantitative methods, Analytical Hierarchy Process (AHP) and Rock Engineering System (RES). Both methods, AHP and RES, gave realistic results with an accuracy of 70.15 % and 79.10 %, respectively. The developed tool helped in managing landslide related factors in a much easier and automated manner, maximizing the functionality of GIS environment.

6. References

Aleotti P. and Chowdury R. 1999. Landslide hazard assessment: summary review and new perspectives, *Bulletin of Engineering Geology and the Environment*, 21- 44.

Ayalew L., and Yamagishi H. 2005. The application of GIS-based logistic regression for landslide susceptibility mapping in the Kakuda-Yahiko Mountains, Central Japan, *Geomorphology,* 65(1–2), 15–31.

Ayalew L., Yamagishi H. and Ugawa N. 2004. Landslide susceptibility mapping using GIS-based weighted linear combination, the case in Tsugawa area of Agano River, Niigata Prefecture, Japan, *Landslides*, 1, 73–81.

Bathrellos G.D., Kalivas P.D and Skillodimou H.D. 2009. GIS-based landslide susceptibility mapping models applied to natural and urban planning in Trikala, Central Greece, *Estudios Geológicos*, 65(1): 49–65.

Benardos A.G. and Kaliampakos D.C. 2004. A methodology for assessing geotechnical hazards for TBM tunneling - illustrated by the Athens Metro, Greece, *International Journal of Rock Mechanics and Mining Sciences*, vol. 41, no. 6, 987-999.

Brabb E.E. 1984. Innovative approaches to landslide hazard mapping. *Proceedings of IV International Symposium of Landslides*, Toronto, 1, 307-324.

Burke R. 2003. Getting to know ArcObjects: Programming ArcGIS with VBA. ESRI Press, Redlands, CA.

Burton I., Kates R.W. and White G.F. 1993. *The Environment as Hazard*, 2nd edition, Guilford Press, New York, 304 pp.

Carrara A., Cardinali M., Guzzetti F. and Reichenbach,P. 1995. GIS-based techniques for mapping landslide hazard, In A. Carrara and F. Guzzetti (eds), *Geographical Information Systems in Assessing Natural Hazards*, Kluwer Publications, Dordrecht, The Netherlands, 135–176.

Dai F.C., Lee C.F. and Ngai Y.Y. 2002. Landslide risk assessment and management: an overview, *Engineering Geology*, 64 (1), 65-87.

Donati L. and Turrini M. C. 2002. An objective method to rank the importance of the factors predisposing to landslides with the GIS methodology: application to an area of the Apennines (Valnerina; Perugia, Italy), *Engineering Geology*, 63, 277–289.

Eastman J.R., P.A.K. Kyem, and J. Toledano J. 1993. A procedure for Multi-Objective Decision Making in GIS Under Conditions of Competing Objectives, *Proceedings EGIS'93*, 438-447.

Glade T., Anderson M. and Crozier M.J. 2005. *Landslide Hazard and Risk*, John Wiley & Sons, Ltd., Chichester, England, 802pp.

Gokceoglu C. and Aksoy H. 1996. Landslide susceptibility mapping of the slopes in the residual soils of the Mengen region (Turkey) by deterministic stability analyses and image processing techniques, *Engineering Geology*, 44, 147–161,

Gokceoglu C., Sonmez H., Nefeslioglu H.A., Duman T.Y. and Can T. 2005. The 17 March 2005 Kuzulu landslide (Sivas, Turkey) and landslide-susceptibility map of its near vicinity, *Engineering Geology*, 81 (1), 65-83.

Guzzetti F., Carrara A., Cardinali M. and Reichenbach P. 1999. Landslide hazard evaluation: a review of current techniques and their application in a multi-scale study, central Italy, *Geomorphology*, 31, 181–216.

Hudson J.A. 1992. *Rock engineering systems. Theory and practice*, Ellis Horwood series in Civil Engineering, pp. 185.

Hudson J.A. and Harrison J.P. 1992. A new approach to studying complete rock engineering problems, *Quarterly Journal of Engineering Geology,* 25, 93 – 105.

Jankowski P. 1995. Integrating geographical information systems and multiple criteria decision making methods, *International Journal of Geographical Information System,* 9(3), 251-273.

Jiang H. and Eastman J.R. 2000. Application of Fuzzy Measures in Multi-Criteria Evaluation in GIS, *International Journal of Geographical Information Science*, 14, 2, 173-184.

Komac M. 2006. A landslide susceptibility model using the analytical hierarchy process method and multivariate statistics in penialpine Slovenia, *Geomorphology,* 74(1–4), 17–28.

Lai S.-K. and Hopkins L.D. 1995. Can Decision Makers Express Multi attribute Preferences Using AHP and MUT? An Experiment, *Environment and Planning B: Planning and Design*, 22 (1), 21-34.

Leopold L.B., Clarke F.E., Manshaw B.B. and Balsley J.R. 1971. A Procedure for Evaluating Environmental Impacts, U.*S. Geological Survey Circular*, No. 645, Government Printing Office, Washington, D.C.

Malczewski J. 1999. *GIS and Multicriteria Decision Analysis*, (John Wiley and Sons, New York, 1999).

Mazzoccola D.E and Hudson J.A. 1996. A comprehensive method of rock mass characterization for indicating natural slope instability, *Quartile Journal Engineering Geology*, 29, 37–56.

Ozturk D. and Batuk E. 2011. Implementation of GIS-based multicriteria decision analysis with VB in ArcGIS, *International Journal of Information Technology & Decision Making*, 10(6), 1023–1042.

Pachauri A.K. and Pant, M. 1992. Landslide hazard mapping based on geological attributes, *Engineering Geology*, 32, 81–100.

Park N.W., Chi K.H. and Kwon B.D. 2004. Application of fuzzy set theory for spatial prediction of landslide hazard, In *Proceedings of the Symposium on Geoscience and Remote Sensing*, vol. 5, 2988–2990.

Rozos D., Bathrellos G.D. and Skillodimou H.D. 2011. Comparison of the implementation of rock engineering system and analytic hierarchy process methods, upon landslide susceptibility mapping, using GIS: a case study from the Eastern Achaia County of Peloponnesus, Greece, *Environmental Earth Sciences*, 63(1), 49-63.

Rozos D., Pyrgiotis L., Skias S. and Tsagaratos P. 2008. An implementation of rock engineering system for ranking the instability potential of natural slopes in Greek territory. An application in Karditsa County, *Landslides*, 5, 261–270. doi:10.1007/s10346- 008-0117-4.

Rozos D., Tsagaratos P., Markantonis K., and Skias S. 2006. An application of rock engineering system (RES) method for ranking the instability potential of natural slopes in Achaia County, Greece, In: *Proc. of XIth international congress of the society for mathematical geology*, University of Liege, Belgium, S08-10.

Saaty T.L. 1977. A scaling method for priorities in hierarchical structures, *J Math Psychol*, 15, 234–281.

Saaty T.L. 2000. *Fundamentals of Decision Making and Priority Theory with the Analytic Hierarchy Process*, 2nd Edn., RWS Publications, Pittsburgh, USA.

Schuster R.L. 1996. Socioeconomic significance of landslides, In: A.K. Turner & R.L. Schuster (E ditors), *Landslides: Investigation and Mitigation*, National Academic Press, Washington, D C, *Special Report*, 247, pp.12-36.

Turrini M.C. and Visintainer P. 1998. Proposal of a method to define areas of landslide hazard and application to an area of the Dolomites, Italy, *Engineering Geology*, 50, 255–265.

Vaidya O.S. and Kumar S. 2004. Analytic Hierarchy Process: An overview of applications, *Europ ean Journal of Operational Research*, Vol. 169, 1, 1–29.

van Westen, C., 1997. Statistical landslide hazard analysis. ILWIS 2.1 for windows application gui de. Enshede, The Netherlands, *ITC Publication*, N. 15, 73-84.

Vargas L.G. 1990. An overview of the analytic hierarchy process and its applications. *European J ournal of Operational Research*, 48, 2−8.

Zeiler M. 2001. *Exploring ArcObjects*, ESRI, Redlands, CA. pp.578.

Δελτίο της Ελληνικής Γεωλογικής Εταιρίας, τομ. XLVII, 2013
Πρακτικά 13ου Διεθνούς Συνεδρίου, Χανιά, Σεπτ. 2013

Bulletin of the Geological Society of Greece, vol. XLVII, 2013
Proceedings of the 13th International Congress, Chania, Sept. 2013

POLLUTION ASSESSMENT OF THE DRAPETSONA-KERATSINI COASTAL SEABED

Kapsimalis V.[1], Talagani P.[2], Panagiotopoulos I.P.[1], Kaberi H.[1], Rousakis G.[1], Kanellopoulos Th.D.[1], Iliakis S.[1] and Hatzianestis I.[1]

[1] Hellenic Centre for Marine Research, Institute of Oceanography, Anavyssos, kapsim@hcmr.gr, jpanagiot@hcmr.gr, ek@hcmr.gr, rousakis@hcmr.gr, thkan@hcmr.gr, jhat@hcmr.gr

[2] National and Kapodistrian University of Athens, Faculty of Geology and Geoenvironment, Department of Hist. Geology - Paleontology, Athens, pentalag@windowslive.com

Abstract

The pollution status of the Drapetsona-Keratsini coastal environment is assessed through sedimentological and geochemical analyses of surface sediments. The results show that the sedimentary seabed consists of sandy silts and silty sands with relatively high moisture content (up to 114%) and carbonate concentration (24-86%), whilst the levels (measured in μg/g) of some harmful heavy metals, i.e., As=8-2677, Cd=0.2-15.4, Cr=82-428, Cu=18-567, Fe=5700-289,000, Hg=0.05-0.71, Mn=101-1477, Ni=25-122, Pb=18-1394, Sn=1-18, and Zn=118-4821, are particularly high. The implementation of various pollution indices, such as Geoaccumulation Index (Igeo), Potential Ecological Risk Index (RI), Pollution Load Index (PLI), Combined Contamination Index (W), and Modified Contamination Degree (mCd), together with the evaluation of biological risk using the Sediment Quality Guidelines (ERL/ERM and TEL/PEL) of NOAA indicate a very high degree of pollution with great possibility for serious and irreversible impairments for aquatic communities. The most polluted sector, probably the most heavily contaminated marine environment in Greece, is located in front of the Drapetsona rocky coast (and particularly in the Sfageion Bay), where the synergistic action of urban untreated sewage deposited in the past (before the operation of the sewage treatment plant in Psyttalia) and wastes from local industries or facilities has caused significant degradation of the marine system.

Key words: *Heavy metals, sediments, pollution indices, urban coast.*

Περίληψη

Ο βαθμός ρύπανσης του ιζηματογενούς πυθμένα στο αστικό παράκτιο περιβάλλον της Δραπετσώνας-Κερατσινίου διερευνάται μέσω ιζηματολογικής και γεωχημικής ανάλυσης. Τα αποτελέσματα δείχνουν ότι τα επιφανειακά ιζήματα αποτελούνται από αμμώδεις ιλύες και ιλυώδεις άμμους με σχετικά υψηλή περιεκτικότητα σε υγρασία (έως 114%) και ανθρακικά άλατα (24-86%), ενώ παρουσιάζουν ιδιαίτερα υψηλά επίπεδα συγκεντρώσεων (οι τιμές σε μg/g) σε κάποια επικίνδυνα μέταλλα όπως As=8-2677, Cd=0,2-15,4, Cr=82-428, Cu=18-567, Fe=570-28.900, Hg=0,05-0,71, Mn=101-1477, Ni=25-122, Pb=18-1394, Sn=1-18 και Zn=118-4821. Η εφαρμογή διαφόρων δεικτών ρύπανσης, όπως του Δείκτη Γεωσυσσώρευσης (Igeo), Δείκτη Δυνητικής Οικολογικής Επικινδυνότητας (RI), Δείκτη Ρυπαντικού Φορτίου (PLI), Συνδυασμένου

Δείκτη Ρύπανσης (W) και Τροποποιημένου Βαθμού Ρύπανσης (mCd), καθώς και η αξιολόγηση της βιολογικής επικινδυνότητας των υφιστάμενων ιζημάτων με βάση τις Κατευθυντήριες Οδηγίες Ποιότητας Ιζημάτων της NOAA (ERL/ERM και TEL/PEL) δείχνουν ένα πολύ υψηλό βαθμό ρύπανσης με μεγάλη πιθανότητα για σοβαρές και μη αναστρέψιμες βλάβες στους θαλάσσιους οργανισμούς. Η πιο ρυπασμένη περιοχή, ίσως το πιο βαριά ρυπασμένο θαλάσσιο περιβάλλον στην Ελλάδα, βρίσκεται μπροστά από τη βραχώδη ακτή της Δραπετσώνας (και ιδιαίτερα στον Όρμο των Σφαγείων), όπου η συνεργιστική δράση των αστικών ανεπεξέργαστων λυμάτων, που είχαν αποτεθεί πριν από τη λειτουργία της μονάδας επεξεργασίας λυμάτων στην Ψυττάλεια, και των αποβλήτων από τις τοπικές βιομηχανίες έχουν προκαλέσει σημαντική υποβάθμιση του θαλάσσιου περιβάλλοντος.
Λέξεις κλειδιά: *βαρέα μέταλλα, ιζήματα, δείκτες ρύπανσης, παράκτιο αστικό μέτωπο*.

1. Introduction

Heavy metal pollution of marine ecosystems is a global problem resulting from numerous human activities, such as uncontrolled disposal of urban or industrial wastes, deliberate operational discharge or accidental spills of oil from ships, mining and smelting of metalliferous ores, and draining of intensively cultivated agricultural soils. Many metals, when they exceed a certain concentration, have toxic (e.g., Cr, Ni, Pb, Cd, and As), carcinogenic (e.g., Cr (VI), Ni and Cd) and teratogenic (As and Cd) effects on the health of aquatic organisms (Forstner, 1990). Although some other metals, such as Fe, Mn, Co, Cu, and Zn, are essential micronutrients for fauna and flora, they are harmful at high concentrations (Berkowitz et al., 2008). Contaminants may eventually pass through the food chain to humans and result in a wide range of adverse effects.

Marine sediments are a major "storehouse" of heavy metals and, therefore, they are used for assessing the environmental quality of aquatic areas (Solomons and Förstner, 1984). One of the approaches to estimate the degree of pollution in coastal sediments is based on combining geochemical and statistical methods (Wu et al., 2007), which distinguish the natural from anthropogenic inputs and determine the concentration of the excess heavy metal load and the potential impact of pollutants on the marine life.

This paper aims: (1) to investigate the spatial distribution of heavy metals in the surface sediments of the coastal urban stretch in front of Drapetsona and Keratsini; (2) to define the relationship between the chemical contamination of the sediment and the toxic biological effects on aquatic organisms through widely adopted Sediment Quality Guidelines (SQGs) and quantitative pollution indices for heavy metals.

2. The Study Area

The area under investigation is the coastal region that extends from the Krakaris jetty, at the exit of the Piraeus Port, to the western part of the Keratsini Port (Figure 1). It includes the rocky coast of Drapetsona, the bays of Sfageion and Foron (or Drapetsona), the Akrokeramos Harbour, the Drapetsona quay wall, and the Keratsini Port. Until the mid-1990s, the study area was receiving untreated domestic and industrial wastes from the Attica Basin (Figure 1 shows the location of the sewage outfall). The total daily discharge of sewage was about 600,000 m^3 according to Theodorou and Perissoratis (1991). The operation of the waste treatment plant in Psyttalia has resulted in the gradual improvement of the environmental status of the Drapetsona-Keratsini coastal area and Saronikos Gulf (Krasakopoulou and Karageorgis, 2005). However, there are still many medium- to small-scale industries and facilities, such as a fertilizer plant (see FP in Figure 1), factories of plaster and cement, units of storage of petroleum and shipyards, as well as intense shipping activities (including transport of fuel, chemicals and other harmful compounds) that continue to degrade the quality of the marine environment.

Recently, Gkaragkouni (2005) studied the distribution of heavy metals and natural radionuclides in sediment cores from the Psyttaleia-Keratsini Strait identifying the pollution load of the sewage sludge deposited there before the operation of the wastewater treatment plant (WWTP) in Psytallia. In addition, Galanopoulou et al. (2005, 2009) have determined the concentrations of heavy metals and synthetic organic compounds in the surface sediments of the Keratsini Port, characterizing the sediments as highly-heavily polluted, exceeding the toxic effect range.

Figure 1 - Location map of the Drapetsona-Keratsini coastal area showing the sampling positions of: (a) the analysed sediments (1-12); and (b) the reference sediment (DSS-5).

3. Laboratory Analyses and Data Processing

During the winter of 2010 twelve sediment samples (Figure 1) were collected from the Drapetsona-Keratsini coastal area using a grab sampler. All samples were separated into the different grain-size fractions using a set of sieves for the coarser fraction (>0.063 mm) and a grain size analyser (Sedigraph 5100) for the finer fraction (<0.063 mm). The sediment texture was classified according to Folk (1974) nomenclature. Total carbon was measured by a CHN elemental analyser (EA-1108, Fisons Instruments) with the precision of the method being within 5% (Karageorgis et al., 2005), whilst the organic carbon (orgC) portion was determined following the procedure described by Verardo et al. (1990) with the detection limit of the method being 2.3 μg/g^{-} per 10 mg of dry sample. The elemental geochemistry of the bulk sediment samples (<1 mm) was determined using a Philips PW-2400 X-Ray Fluorescence (XRF) system, with the relative uncertainties of the system being within 2% for the major element concentrations (Al, Ca, Fe, K, Mg, Na, P, Si, Ti, S) and within 5% for the trace element concentrations (As, Ba, Bi, Br, Ce, Co, Cr, Cu, Hf, I, La, Mn, Mo, Nd, Ni, Pb, Rb, Sb, Sc, Sn, Sr, Th, V, Y, Zn, Zr) (Karageorgis et al., 2005). In addition, Cd concentrations were determined using the inductively coupled plasma combined with mass spectroscopy technique (ICP-MS), while Hg concentrations were estimated using cold vapor atomic absorption spectrometry.

The determination of major and minor element interrelationships and their association with grain size fractions and organic carbon content was achieved through a principal component analysis (PCA) using Varimax Rotation together with Kaiser Normalization (IBM SPSS statistics).

The assessment of the pollution status and toxicity of examined sediments was based on the following indices: (a) Geoaccumulation Index (*Igeo*) (Müller, 1969, 1981); (b) Pollution Load Index (*PLI*) (Tomlinson et al., 1980); c) Potential Ecological Risk Factor (*Eri*) and Index (*RI*) (Hakanson, 1980); (d) Modified Contamination Degree (*mCd*) (Abrahim and Parker, 2008); and (e) Combined Contamination Index (*W*) (Widianarko et al., 2000). The reference concentrations taken into account for the calculation of *RI*, *PLI*, *mCd,* and *W* were the element contents in the deepest sample (20-22 cm) of a box-core (DSS-5) recovered from the inner Saronikos Gulf at 71 m depth (Figure 1). Due to the low sedimentation rates recorded in the area (<0.6 cm 100 y^{-1}; Lykousis and Anagnostou, 1992); this sediment represents pre-industrial period and can be considered as non-contaminated. The baseline for the *Igeo* calculation was taken from the average composition of continental shale (Turekian and Wedepohl, 1961). The adverse effects of heavy metals, such as As, Cd, Cr, Cu, Hg, Ni, Pb, and Zn, on the aquatic organisms were estimated by the use of two sets of empirical Sediment Quality Guidelines (SQGs) developed by the National Oceanic and Atmospheric Administration (NOAA), i.e., the Effects Range Low (ERL) and Effects Range Median (ERM) approach (Long et al., 1995) and the Threshold Effects Level (TEL) and Probable Effects Level (PEL) approach (McDonald et al., 1996).

4. Results

4.1 Sediment Physical Characteristics

The sediments of the coastal seabed of Drapetsona-Keratsini are characterized as sandy silt (sZ) and silty sand (zS) according to Folk (1974) nomenclature. The sand, silt and clay contents (see Table 1) range from ~19-90% (average ~53%), ~10-81% (average ~46%) and 0-8% (average 1.2%), respectively. The clay fraction is almost absent from all the examined sediment samples except in KER 2 and KER 8, where its proportion is less than 10%. The highest sand contents are found within the Keratsini Port (KER 11, 89.6%) and near the Sfageion Bay (KER 2, 73%), while the highest silt contents occur within the Keratsini Port (KER 10, 80.8%) and in front of the Krakaris jetty (KER 1, 77.4%) outside the Piraeus Port. The organic carbon (orgC) content (Table 1) can not be considered as very high, since its maximum value reaches ~2.8% (KER 10), whereas

the water content (w) and wet bulk density (ρ_t) of the analysed sediments fluctuated from ~14-117% and 1442-1989 kg/m^3, respectively (Table 1).

4.2 Sediment Chemical Characteristics

A synopsis of the results of the geochemical analysis is presented in Table 1.

The spatial distribution of several chemical elements shows that their highest concentrations (in μg/g) occur mainly in two sectors: (a) in front of the Drapetsona coast (particularly nearby the Piraeus Port exit) [Fe (289,400), P (4800), Hg (0.71), La (28.5), Nd (26.3), Y (47.9), and Zr (88.3)], in the Sfageion Bay [Si (138,200), As (2677), Bi (19.1), Cd (15.4), Ce (84.2), Co (40), Cu (567), Hf (25.2), Mn (1477), Pb (1394), Sb (45) and Zn (4821)] and the Drapetsona Bay [Sn (18]; and (b) in the central part of the Keratsini Port [Al (33,500), S (10,900), Ba (247), Cr (428), Mo (6.3), Ni (122), Rb (39.6), Sc (12.5), and V (74.4)].

In contrast, minimum element contents (in μg/g) are mainly found in two sites of the Keratsini Port: (a) between the piers I and II (KER 9), where Fe=5700, K=1300, Na=430, P=200, S=700, Si=19,400, Ti=600, As=8.1, Ba=14.3, Bi=1.4, Br=26.9, Ce=18.2, Co=2.4, Cr=81.8, Cu=17.7, Hf=2.9, La=4.8, Mo=1, Nd=4.3, Pb=18.1, Rb=5.3, Sr=190, V=10.9, Y=3.2, and Zn=53.3; and (b) in the inner Keratsini (Heracleous) Port (KER 11), where Al=10,200, Cd=0.2, Hg=0.05, I=10.8, Mn=99.7, Ni=25.3, and Zr=1.1.

Finally, the spatial distribution pattern of Ca, Sr and Th shows an inverse trend, compared to that of all the other elements, with higher contents occurring in KER 11 and lower ones being in front of the Drapetsona coast (KER 1 and KER 2).

Table 1 - Physical and chemical characteristics of the surface sediments in the Drapetsona-Keratsini coastal area.

	Min	Max	Mean	StDev		Min	Max	Mean	StDev
Sand %	19.3	89.6	53.3	22.1	**Co** μg/g	2.4	40.0	10.0	10.6
Silt %	10.4	80.8	45.6	22.9	**Cr** μg/g	81.8	427.7	229.1	105.9
Clay %	0.0	8.0	1.2	2.7	**Cu** μg/g	17.7	566.7	189.5	168.6
w %	13.7	117.0	55.7	25.9	**Hf** μg/g	2.9	25.2	7.0	6.4
ρ_t kg/m^3	1442	1989	1.702	0.148	**Hg** μg/g	0.05	0.71	0.23	0.19
orgC %	0.295	2.812	1.615	0.754	**I** μg/g	10.8	72.9	38.0	17.6
$CaCO_3$ %	24.0	86.3	54.5	18.6	**La** μg/g	4.8	28.5	14.6	7.0
Al %	1.02	3.35	2.17	0.76	**Mn** μg/g	99.7	1476.8	391.1	386.4
Ca %	9.69	34.86	22.02	7.52	**Mo** μg/g	1.0	6.3	3.3	1.6
Fe %	0.57	28.94	5.43	8.20	**Nd** μg/g	4.3	26.3	12.2	5.9
K %	0.13	0.79	0.50	0.21	**Ni** μg/g	25.3	122.1	77.6	32.7
Mg %	1.22	3.78	2.00	0.73	**Pb** μg/g	18.1	1393.6	330.6	403.3
Na %	0.43	1.87	1.26	0.42	**Rb** μg/g	5.3	39.6	26.6	9.2
P %	0.02	0.48	0.13	0.15	**Sb** μg/g	4.5	45.0	22.1	17.0
S %	0.07	1.09	0.55	0.30	**Sc** μg/g	5.3	12.5	10.2	2.1
Si %	1.94	13.82	7.25	3.23	**Sn** μg/g	1.2	18.3	9.0	5.8
Ti %	0.06	0.23	0.15	0.05	**Sr** μg/g	190.0	2435.9	649.0	707.5
As μg/g	8.1	2677.4	411.3	802.6	**Th** μg/g	4.4	32.4	11.6	8.5
Ba μg/g	14.3	246.7	147.6	72.0	**V** μg/g	10.9	74.4	42.6	16.6
Bi μg/g	1.4	19.1	6.1	5.5	**Y** μg/g	3.2	47.9	17.7	12.6
Br μg/g	26.9	154.3	91.5	38.1	**Zn** μg/g	53.3	4820.9	908.2	1369.9
Cd μg/g	0.20	15.39	2.52	4.36	**Zr** μg/g	1.1	88.3	44.4	24.4
Ce μg/g	18.2	84.2	39.1	19.8					

The results from the applied statistical analysis (PCA) (Table 2) allowed us to classify the geochemical elements, grain-size fractions and organic carbon contents into four groups (components). The first group is characterized by a high positive interrelationship among Al, Ti, K, Mg, Rb, Na, V, and to a lesser extent among Ni, Si, Mo, Cr, Ba. This group clearly represents the "terrigenous aluminosilicates" component, since its principal element, i.e., aluminium, is mainly derived by terrestrial sources and it is extremely immobile in the marine environment (Bischoff et al., 1979). The second group demonstrates high positive loadings primarily for As, Bi, Zn, Cu, Pb, Y, Sb, Ce, Mn, La, Fe, Co, Hf, Cd, P, Nd, Si, Mo, S and secondarily for Ba and Hg. The strong inter-correlation among almost all the harmful heavy metals (i.e., As, Cd, Cu, Pb, Zn) implies their common origin from anthropogenic activities. The third group mainly consists of Br, Sn, I, Cr, Hg, Zr, Ni, Sc, Ba, Rb, and organic carbon, but also V, P, S, Fe are markedly loaded in this group. The third group corresponds to the "organic component" that represents the organic rich silty sediments that scavenge effectively some metals, eventually in the form of sulfides (Calvert and Pedersen, 1993). Finally, a strong correlation is evident among Ca, Sr, Th, and sand contents, which constitute the fourth group. However, this group shows an inverse geochemical behavior compared to the other defined components (i.e., "aluminosilicate", "anthropogenic" and "organic"). The fourth group represents the autochthonous biogenic fraction of the sediments, comprising shells of calcareous organisms and their fragments. Strontium often substitutes for Calcium due to their similar ionic radii (Shankar et al., 1987).

Table 2 - Principal component analysis (PCA) using Varimax Rotation (rotation converged in 7 iterations).

Element	Components				Element	Components			
	1	2	3	4		1	2	3	4
Al	.070	.190	.964	-.082	Hf	.840	.176	.225	-.274
Ca	-.881	-.392	-.173	.116	Hg	.451	.789	-.082	.097
Fe	.866	.447	.105	-.157	I	.121	.814	.210	-.023
K	.193	.288	.911	-.129	La	.870	.259	-.012	.073
Mg	.127	.120	.696	.174	Mn	.877	.171	.349	-.226
Na	.440	.335	.639	.094	Mo	.743	.197	.530	.137
P	.796	.574	.073	-.023	Nd	.788	.349	.042	.196
S	.666	.531	.248	.270	Ni	-.020	.669	.660	-.176
Si	.750	.078	.586	-.114	Pb	.913	.216	.322	.015
Ti	.275	.149	.932	-.128	Rb	.115	.619	.659	.172
As	.950	.198	.099	.032	Sb	.910	-.333	.000	-.192
Ba	.519	.635	.453	.001	Sc	.453	.650	.571	-.029
Bi	.939	.227	.161	-.016	Sn	.270	.837	.194	.241
Br	.219	.838	.294	.087	Sr	-.025	.015	.038	.945
Cd	.840	.142	.155	-.385	Th	-.392	.213	-.055	.848
Ce	.908	.218	.276	-.175	V	.391	.606	.616	.010
Co	.856	.150	.294	-.270	Y	.911	.361	.090	.089
Cr	.215	.813	.461	.005	Zn	.926	.209	.284	.008
Cu	.925	.279	.221	-.011	Zr	.480	.693	.288	-.299

5. Assessment of Heavy Metal Pollution in Sediments

5.1 Pollution Indices

The Geoaccumulation Index (*Igeo*) values of As, Cd, Pb, and Zn (Table 3) are greatly enhanced in front of the Drapetsona coast (particularly nearby the Piraeus Port exit) and in the Sfageion and Drapetsona bays, indicating strongly, strongly-to-extremely and extremely contaminated sediments, respectively. Slightly lower values are found westwards up to the Drapetsona jetty as well as in the central basin of the Keratsini Port. Therein, the *Igeo* values reveal moderate and moderate-to- strong contamination. At the other sites the *Igeo* values are low indicating an absence of pollution. The *Igeo* values of Cr, Cu and Sn (Table 4) show a similar trend to those of As, Cd, Pb, and Zn, but being quite lower. They indicate moderate or moderate-to-strong contamination for the sediments in the Drapetsona coastal area and in the central basin of the Keratsini Port, but no-to-moderate contamination for the sediments of the other sites. The *Igeo* values of Co, Hg, Mn, and Ni (Table 4) range into the classes 0 and 1, suggesting uncontaminated or uncontaminated-to-moderately contaminated sediments. Finally, the *Igeo* values of Fe are higher (2.0) nearby the Piraeus Port exit, lower (0.1-0.9) in the Sfageion and Drapetsona bays, and minimum (<0) in the rest of the study area (Table 4). This distribution pattern exhibits an increasing trend for Fe towards the Piraeus Port.

The Pollution Load Index (*PLI*) is a quick tool for determining the pollution status of sediments in different sites. The *PLI* of most of the examined sediments is extremely high indicating "progressive deterioration". Only the surface sediments located between the piers I and II of the Keratsini Port (KER 9) exhibit "baseline pollution" (Table 4).

The Potential Ecological Risk Index (*RI*) implies "severe" and "serious" risk for the majority of the sediments, except for these that occur in the inner basin of the Keratsini Port (low risk) and at the sites KER 7-KER 9, where the risk is moderate (Table 4).

Table 3 - The Geoaccumulation Index (*Igeo*) of twelve elements in the analysed sediments (KER) is presented. The *Igeo* is categorized into seven classes: 0 (values ≤0, uncontaminated), 1 (values 0-1, uncontaminated to moderately contaminated), 2 (values 1-2, moderately contaminated), 3 (values 2-3, moderately to strongly contaminated), 4 (values 3-4, strongly contaminated), 5 (values 4-5, strongly to extremely contaminated), and 6 (values >5, extremely contaminated).

ID	*Igeo* As	*Igeo* Cd	*Igeo* Co	*Igeo* Cr	*Igeo* Cu	*Igeo* Hg	*Igeo* Fe	*Igeo* Mn	*Igeo* Ni	*Igeo* Pb	*Igeo* Zn	*Igeo* Sn
1	5.1	4.6	-1.1	1.0	2.7	0.2	2.0	-1.3	-0.5	4.2	3.2	0.5
2	7.1	6.7	0.5	-0.1	3.1	-2.6	0.1	0.2	-1.1	5.5	5.1	-1.9
3	6.0	5.2	-0.5	1.3	2.3	-0.8	0.9	-0.8	-0.1	4.6	3.9	1.0
4	2.9	2.7	-2.4	0.9	1.2	-0.7	-1.3	-2.3	-0.4	2.9	1.7	0.6
5	1.2	1.5	-2.8	0.5	0.8	-0.9	-2.3	-2.7	-0.8	2.0	0.9	0.2
6	1.1	2.5	-2.4	1.3	1.3	-1.1	-1.7	-2.3	0.2	2.4	1.7	0.6
7	-0.1	1.3	-2.1	0.4	0.2	-2.2	-2.2	-2.6	-0.3	1.3	0.5	-0.6
8	-0.2	0.9	-2.2	0.5	0.2	-2.9	-2.3	-2.7	-0.1	1.1	0.3	-0.6
9	-1.3	2.0	-3.6	-0.7	-1.9	-3.1	-3.6	-3.7	-1.8	-0.7	-1.4	-2.9
10	1.0	3.1	-2.0	1.7	1.6	-1.9	-1.4	-2.1	0.3	4.0	2.3	0.9
11	-0.2	0.4	-3.6	-0.6	-0.7	-3.5	-3.5	-3.7	-2.0	0.7	-0.3	-1.6
12	0.9	2.3	-2.1	0.9	0.5	-2.7	-1.7	-2.0	0.2	2.1	0.8	-0.8

Table 4 - The Pollution Load Index (*PLI*), Potential Ecological Risk Index (*RI*), Modified Degree of Contamination (*mCd*), and Combined Contamination Index (*W*) of the analysed sediments (KER) are presented. *PLI* indicates "perfection", "baseline pollution" and "progressive deterioration", when values are 0, 1 and >1, respectively. *RI* demonstrates "low risk" (values <150), "moderate risk" (values 150-300), "severe risk" (values 300-600), and "serious risk" (values >600). *mCd* shows whether the degree of contamination is zero to very low (values 0-1.5), low (values 1.5-2), moderate (values 2-4), high (values 4-8), very high (values 8-16), extremely high (values 16-32), and ultra high (values >32). *W* classifies the sediments as unpolluted (values ≤0), slightly polluted (values 0-1), polluted (values 1-2), and heavily polluted (values >2).

ID	*PLI*	*RI*	*mCd*	*W*
1	31,519	2652	23.1	9.0
2	92,130	9157	75.8	9.9
3	58,846	3758	33.6	9.5
4	1254	792	7.3	6.2
5	147	420	3.9	4.3
6	649	607	5.8	5.6
7	39	276	2.8	3.2
8	24	219	2.5	2.8
9	1	291	1.7	0.1
10	1656	801	8.4	6.4
11	3	149	1.5	1.0
12	144	450	4.1	4.3
Mean	15,534	1631	14.2	5.2

The Modified Degree of Contamination (*mCd*) reveals low pollution for KER 9 and KER 11 (Keratsini Port), moderate pollution for KER 5, KER 7 and KER 8, high pollution for KER 4, KER 6 and KER 12, very high pollution for the central basin of the Keratsini Port; extremely high pollution for the site nearby the Piraeus Port exit, and Ultra high pollution for the Sfageion and Drapetsona bays (Table 4).

Finally, the Combined Contamination Index (*W*) suggests that the sediments in the inner basin of the Keratsini Port and in the sector between the piers I and II are slightly polluted. For the rest of the study site, the *W* index indicates heavily polluted sediments (Table 4).

5.2 Sediment Quality Guidelines

The biological impact of heavy metal concentrations on aquatic life has been assessed by comparing these concentrations to the marine ERL/ERM and TEL/PEL thresholds (Figure 2). The sedimentary seabed stretching from the Piraeus Port exit to the Aktokeramos Harbour is an area of high concern, since the enhanced contents of As, Cd, Cr, Cu, Ni, Pb, and Zn can cause irreversible adverse effects to marine organisms. To a lesser extent this may also happen in the central basin of the Keratsini Port. However, the rest of the study area does not face this threat.

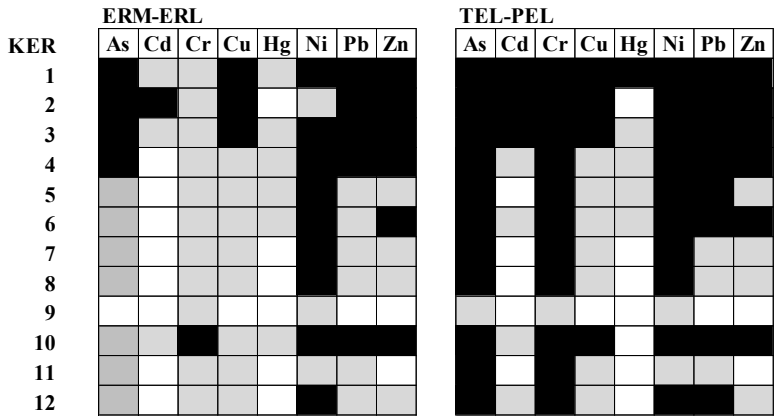

Incidence of adverse biological effects (%)

	ERM-ERL								TEL-PEL							
	As	Cd	Cr	Cu	Hg	Ni	Pb	Zn	As	Cd	Cr	Cu	Hg	Ni	Pb	Zn
	5.0	6.6	2.9	9.4	8.3	1.9	8.0	6.1	2.7	5.6	3.5	9.0	7.8	3.3	5.8	3.8
	11.1	36.6	21.1	29.1	23.5	16.7	35.8	47.0	12.9	20.1	15.4	21.9	23.6	8.4	25.8	27.2
	63.0	65.7	95.0	83.7	42.3	16.9	90.2	69.8	70.8	70.8	52.9	55.9	36.7	9.4	58.4	64.8

Figure 2 - Evaluation of aquatic life impairment due to the heavy metal load of the study area sediments using the marine ERM/ERL and TEL/PEL Guidelines.

6. Conclusions

The Drapetsona-Keratsini coastal area is a highly polluted area, since it has received for decades untreated urban sewage effluents (until the operation of the Psyttalia WWTP in 1994), industrial solid and liquid wastes and by-products of shipping activities. The distribution patterns of harmful chemical elements, organic carbon content, values of various pollution indices (*Igeo*, *PLI*, *RI*, *mCd*, and *W*) and the Sediment Quality Guidelines of NOAA show that the sector in front of the Drapetsona coast (from the Piraeus Port exit to the Drapetsona jetty), and particularly in the bays of Sfageion and Drapetsona (Foron), is extremely polluted with great possibility for the marine life to be severely and irreversibly impaired. However, the quality of the surface sediments in the adjacent Keratsini Port is relatively better, although the pollution conditions in the central basin of the port are comparable to those of the Drapetsona coast.

7. References

Abrahim G.M.S. and Parker P.J. 2008. Assessment of heavy metal enrichment factors and the degree of contamination in marine sediment from Tamaki Estuary, Auckland, New Zealand, Environmental Monitoring and Assessment, 136, 227-238.

Berkowitz B., Dror I. and Yaron B. 2008. Contaminant Geochemistry: Interactions and Transport in the Subsurface Environment, Springer-Verlag, Berlin, 412 pp.

Calvert S.E. and Pedersen T.F. 1993. Geochemistry of recent oxic and anoxic marine sediments: Implications for the geological record*, Marine Geology*, 113, 67-88.

Folk R.L. 1974. Petrology of Sedimentary Rocks, Hemphill Publications Company, Texas, 182 pp.

Forstner U. 1990. Contaminated sediments, *Lecture Notes in Earth Science*, vol. 21, Springer-Verlag, Berlin, 157 pp.

Galanopoulou S., Vgenopoulos A. and Conispoliatis N. 2005. DDTs and other chlorinated organic pesticides and polychlorinated biphenyls pollution in the surface sediments of Keratsini harbour, Saronikos gulf, Greece, *Marine Pollution Bulletin*, 50, 520-525.

Galanopoulou S., Vgenopoulos A. and Conispoliatis N. 2009.Anthropogenic Heavy Metal Pollution in the Surficial Sediments of the Keratsini Harbor, Saronikos Gulf, Greece, *Water, Air, and Soil Pollution*, 202 (1-4), 121-130.

Gkaragkouni 2005. Heavy metals and natural radionuclides in marine sediments from the Psyttalia-Keratsini strait,Saronikos Gulf, *MSc thesis*, University of Patras, 180 pp.

Hakanson L. 1980. Ecological risk index for aquatic pollution control. A sedimentological approach, *Water Research*, 14 (5), 975-1001.

Karageorgis A.P. Anagnostou C.L. and Kaberi H. 2005. Geochemistry and mineralogy of the NW Aegean Sea surface sediments: implications for river runoff and anthropogenic impact, *Applied Geochemistry*, 20, 69-88.

Krasakopoulou E. and Karageorgis A. 2005. Spatial and temporal distribution patterns of suspended particulate matter and particulate organic carbon in the Saronikos Gulf (eastern Mediterranean, Greece), *Geo-Marine Letters*, 25, 343-359.

Long E.R., MacDonald D.D., Smith S.L. and Calder F.D. 1995. Incidence of adverse biological effects within ranges of chemical concentrations in marine and estuarine sediments. *Environmental Management*, 19 (1), 81-97.

Lykousis V. and Anagnostou C. 1992. Sedimentological and paleogeographic evolution of the Saronikos Gulf in the end of Quaternary, *Bull. Geol. Soc. Greece*, 28(1), 501-510.

MacDonald D.D. Scott C.R., Calder D.F., Long R.E. and Ingersoll G.C. 1996. Development and evaluation of sediment quality guidelines for Florida coastasl waters, *Ecotoxicology*, 5, 253-278.

Müller G. 1969. Index of geoaccumulation in sediments of the Rhine River, *Journal of Geology*, 2 (3), 108-118.

Müller G. 1981. Die Schwermetallbelstung der sedimente des Neckars und seiner Nebenflusse: eine estandsaufnahme, *Chemiker Zeitung*, 105, 157-164.

Solomons W. and Forstner U. 1984. Metals in the Hydrocycle. *Springer-Verlag*, New York, 349 pp.

Theodorou A. J. and Perissoratis C. 1991. Environmental considerations for design of the Athens sea outfall, Saronikos Gulf, Greece, *Environmental Geology*, 17 (3), 233-248.

Tomlinson D.C., Wilson J.G., Harris C.R. and Jeffery D.W. 1980. Problems in the assessment of heavy metals levels in estuaries and the formation of a pollution index, *Helgol. Wiss. Meeresunters*, 33 (1-4), 566-575.

Turekian K.K. and Wedepohl K.H. 1961. Distribution of the elements in some major units of the earth's crust, *Geological Society of America* Bulletin, 72 (2), 175-192.

Verardo D.J., Froelich P.N. and McIntyre A. 1990. Determinations of organic carbon and nitrogen in marine sediments using the Carlo Erba NA-1500 Analyzer, *Deep-Sea Research*, 37, 157-165.

Widianarko B., Verweij R.A., van Gestel C.A.M. and van Straalen N.M., 2000. Spatial distribution of trace metals in sediments from urban streams of Semarang, Central Java, Indonesia, *Ecotoxicology and Environmental Safety*, 46, 95-100.

Wu Y., Hou X., Cheng X., Yao S., Xia W. and Wang S. 2007. Combining geochemical and statistical methods to distinguish anthropogenic source of metals in lacustrine sediments: a case study in Dongjiu Lake, Taihu Lake catchment, China, *Environmental Geology*, 52, 1467-1474.